

10TH INTERNATIONAL CONFERENCE
MEDSI 2018

**MECHANICAL ENGINEERING DESIGN
OF SYNCHROTRON RADIATION
EQUIPMENT AND INSTRUMENTATION**

25-29 JUNE

**CITÉ
INTERNATIONALE
UNIVERSITAIRE
PARIS**

**MEDSI focuses
on mechanical
engineering challenges
in accelerator-based
research facilities:**

- Beamline optics and end-stations
- Accelerator design, upgrades and infrastructures
- Sample environments
- High precision mechanics
- Vacuum technology
- Insertion devices

MEDSI IOC Chair: J. Kay (Diamond Light Source)
Conference Chair: K. Tavakoli (Synchrotron SOLEIL)
Scientific Committee Chairs: J-L. Giorgetta – N. Jobert (Synchrotron SOLEIL)

medsi2018@synchrotron-soleil.fr

WWW.MEDSI2018.ORG

MAISON INTERNATIONALE





Preface

The 10th Mechanical Engineering Design of Synchrotron Radiation Equipment and Instrumentation (MEDSI) conference took place from June 25th to 29th 2018 at the Cité Internationale Universitaire, Paris, France. This important biennial conference, hosted in 2018 by Synchrotron SOLEIL, gathers worldwide experts of the accelerator community and related technologies. MEDSI provides a forum for engineers from facilities around the world to meet and share their experience. The conference fulfills the need to improve information exchange on technical issues and equipment design.

The Scientific committee has reviewed all the abstracts to select the contributions and distribute them between oral and posters presentations. We invite you to see the presentations of the three Keynotes that we selected for the knowledge and background information that they give.

About 340 participants attended the conference and nearly 200 persons followed the Synchrotron Soleil lab tour. 171 abstracts (poster + talks) were submitted which finally summed up into the 128 contributions presented in these proceedings. The event program included 44 oral contributions, including 3 keynote talks, and 128 posters covering almost all engineering disciplines of particle accelerators and showing the vitality of our community. The MEDSI'18 with an unprecedented number of industrial partners (46 companies) was the most successful edition so far from this point of view.

We enjoyed a beautiful Parisian venue, including the gala dinner with a relaxing boat tour on the famous Parisian "bateaux-mouche". We hope that you have enjoyed your stay at Paris and went back to your respective labs with renewed ideas and motivations.

I will take the opportunity to deeply thank all the Local Organizing Committee for their dedication in making this event possible. Thanks to the local Scientific Committee members for such a quality selection for the oral contributions and the excellent choices for the Keynote Talks. Special thanks to the Jacow edition board for their patient work in editing this final version of the proceedings and also to the International Organizing Committee for their unconditional support.

Keihan TAVAKOLI
Synchrotron SOLEIL
MEDSI 2018 Chair



INTERNATIONAL ORGANIZING COMMITTEE

James Kay (Chair)

Diamond Light Source

Sushil Sharma

Brookhaven National Laboratory

Deming Shu

APS/Argonne National Laboratory

Yves Dabin

ESRF

June-Rong Chen

National Synchrotron Radiation Research Center
(NSRRC)

Ping He

Chinese Academy of Sciences

Robert M Duarte

Lawrence Berkeley National Laboratory

Sunao Takahashi

SPring-8/JASRI

Lin Zhang

LCLS/SLAC

Brad Mountford

Australian Synchrotron

Keihan Tavakoli

SOLEIL Synchrotron

Lixin Yin

Shanghai Synchrotron Radiation Facility

Regis T. Neuenschwander

Brazilian Synchrotron Light Laboratory

Carles Colldelram

ALBA Synchrotron

Martin Dommach

European XFEL

Gordon Barkway

Canadian Light Source

Karl Åhnberg

MAX-IV Laboratory

Ralph Döhrmann

PETRA

LOCAL ORGANIZING COMMITTEE

Keihan Tavakoli (Chair)

Filipe Alves

Jean-Michel Dubuisson

Christian Herbeaux

Stephanie Hustache

Deborah Iorio

Manuel Tilmont (JACoW editor)

LOCAL SCIENTIFIC COMMITTEE

Jean-Luc Giorgetta (Chair)

Nicolas Jobert (Chair)

Keihan TAVAKOLI

Manuel Tilmont

Contents

Preface	i
Foreword	iii
Committees	iv
Contents	v
Papers	1
TUOPMA03 – Development of the new UE38 Undulator for the Athos Beamline in SwissFEL	1
TUOPMA04 – Apple II Insertion Devices Made at MAXIV	6
TUOPMA07 – RF Fingers for the New ESRF-EBS Storage Ring	11
TUOPMA08 – Deformable RF Fingers with Axial Extension	15
TUPH01 – Installation and Alignment of SESAME Storage Ring	20
TUPH02 – Collimator for ESRF-EBS	23
TUPH03 – U15 Design and Construction Progress	26
TUPH04 – Progress on the Final Design of the APS-Upgrade Storage Ring Vacuum System	30
TUPH05 – Design of a Radiation Tolerant, Indexing Profile Monitor for the LCLS Electron Beam	33
TUPH08 – Aluminium and Bimetallic Vacuum Chambers for the New ESRF Storage Ring (EBS)	36
TUPH09 – Friction Stir Welding and Copper-Chromium Zirconium: a New Concept for the Design of Sirius' High-Power Absorbers	39
TUPH10 – Interfaces with Operational Systems APS Upgrade Project Removal and Installation	43
TUPH11 – Retractable Absorber (Mask) and White Beam Imager Diagnostic for Canted Straight Section	45
TUPH12 – Multipole Injection Kicker (MIK), a Cooperative Project SOLEIL and MAX IV	48
TUPH13 – Mechanical Design Challenges Building a Prototype 8-Pole Corrector Magnet	50
TUPH14 – Status of the Conceptual Design of ALS-U	53
TUPH15 – Friction Stir Welding Attempts for UHV Applications: Stainless Steel/Aluminum	57
TUPH16 – Hammerhead Support Design and Application at SSRF	60
TUPH17 – Design Considerations Associated with the Replacement of a Sextupole Magnet by a Short Wiggler in a Cell of the Diamond Storage Ring Lattice	63
TUPH18 – Vacuum Performance Test of CuCrZr Photon Absorbers	66
TUPH19 – A Mechanical Undulator Frame to Minimize Intrinsic Phase Errors	69
TUPH21 – Design of Vertical and Horizontal Linear Flexure Stages for Beam Size Monitor System	72
TUPH22 – Study on Cooling Technology of the Superconducting Undulator at SSRF	75
TUPH23 – Field Quality From Tolerance Analyses in Two-Half Sextupole Magnet	78
TUPH24 – Front End of Dual Imaging and Diffraction Beamline at Diamond Light Source	81
TUPH25 – Morphologies of Oxygen-Free Titanium and Palladium/Titanium Thin Films: New Non-Evaporable Getter (NEG) Coatings	84
TUPH26 – A Quasi-Periodic Elliptically Polarized Undulator at the National Synchrotron Light Source II	88
TUPH27 – Structure Design of a Multi-Wire Target	92
TUPH28 – Calculation of Orbit Distortions for the APS Upgrade Due to Girder Resonances	95
TUPH29 – Next Generation X-ray Beam Position Monitor System for the Advanced Photon Source MBA Upgrade	99
TUPH30 – ALBA Synchrotron Light Source Liquefaction Helium Plant	102
TUPH31 – Development of a Revolver Type Undulator	105
TUPH32 – Overview of Sesame Water Cooling System Design & Operation	108
TUPH33 – Vibration Measurement & Simulation of Magnet & Girder in SESAME	111
TUPH34 – The Use of AM Technologies for HV and UHV Components and Vessels	114
TUPH35 – Stainless Steel Vacuum Chambers for the EBS Storage Ring	118
TUPH36 – Metal 3D Additive Machining for in-Vacuum Beam Instrumentation	121
TUPH37 – A New Sealing Technology for High Precision Wide Open UHV Vacuum Flange and Waveguide Connections With Metal Gaskets	125
TUPH38 – Preliminary Design of the Magnets of HALS	129
TUPH39 – The Design of LCLS-II Photon Beam Containment System	133
TUPH41 – Investigation of Regulation Plan for the Vibration Utility Equipment of HEPS	136
TUPH42 – A Novel Attempt to Develop a Linear Polarization Adjustable Undulator Based on Magnetic Force Compensation Technology	140
TUPH43 – The LNLS Metrology Building - Environmental Control Results	143
WEOAMA01 – The Status of the New High-Dynamic DCM for Sirius	147

WEOAMA02 – Sample Stabilization for Tomography Experiments in Presence of Large Plant Uncertainty . . .	153
WEOAMA03 – High-Accuracy Small Roll Angle Measurement Method Based on Dual-Grating Diffraction Hetero- dyne Interferometer	163
WEOAMA04 – The Design of Exactly-Constrained X-Ray Mirror Systems for Sirius	173
WEOAMA05 – FE Model of a Nanopositioning Flexure Stage for Diagnosis of Trajectory Errors	179
WEOPMA03 – Application of Additive Manufacturing in the Development of a Sample Holder for a Fixed Target Vector Scanning Diffractometer at SwissFEL	158
WEOPMA04 – Mechanical Design of a New Precision Alignment Apparatus for Compact X-ray Compound Re- fractive Lens Manipulator	168
WEOPMA05 – Application of Industry Recognised Development Tools and Methodologies, such as Six Sigma to Facilitate the Efficient Delivery of Innovative and Robust Engineering Solutions at Synchrotron Facilities	184
WEOPMA06 – A Compact and Calibratable von Hamos X-Ray Spectrometer Based on Two Full-Cylinder HAPG Mosaic Crystals for High-Resolution XES	189
WEOPMA07 – Development of a New Sub-4k ARPES Endstation at PSI	193
WEPH01 – Evaluation of Anisotropic Simulations & Redesign of the BXDS High Energy Monochromator Bent Laue Diffraction Crystal Holders	199
WEPH02 – Thermomechanical Analysis of SESAME High-Heat-Load Front Ends Components	202
WEPH03 – Design of New Beam Instrumentation for the ISOLDE Isotope Separator at CERN	205
WEPH04 – Finite Element Analysis of a Combined White Beam Filter and Visual Screen Using CVD Diamond for the BXDS Beamline	208
WEPH06 – Upgrade of Magnetic Measurements Laboratory at ALBA Synchrotron	211
WEPH07 – Photon Beam Applied as Heat Flux on Irregular Surfaces in FEA	214
WEPH08 – Application of Remote Installation and Measurement Smart Vehicle in Accelerator	217
WEPH09 – Vibrational Stability of a Cryocooled Double Crystal Monochromator at SSRF	220
WEPH12 – Thermo-Mechanical Aspects of the MOBIPIX, a Compact X-Ray Imaging System with Embedded GPU	223
WEPH13 – Vibration Monitoring at TPS Storage Ring	227
WEPH14 – Optomechanical Optimization for a Sagittally Bent Double Crystal Monochromator, Using Finite Ele- ments and Ray Tracing	231
WEPH15 – Experimental Modal Analysis Vibration Measurement to Inform Engineering Design	235
WEPH16 – Thermal Analysis of High Heat Load Mirrors for the in-Situ Nanoprobe Beamline of the APS Upgrade	238
WEPH17 – Adjusting Mechanism of Inter-Undulator Section for PAL XFEL	241
WEPH18 – Operation Status of HLS System Installed to Measure Ground Change of Large Scientific Equipment in Real Time	245
WEPH21 – A Family of Redundant Positioning Devices for Synchrotron Applications	249
WEPH22 – Le Guide for Support: A Cookbook for Modeling of Accelerator Structures*	252
WEPH23 – FEA Simulations of the Aluminium Vacuum Chamber for LOREA Insertion Device at ALBA Synchrotron Light Source	255
WEPH24 – Design of an Integrated Crotch Absorber for ALBA Synchrotron Light Source	258
WEPH26 – High Rigidity Girder System for the Sirius Machine	261
WEPH28 – A Note of Thermal Analysis in Synchrotron Radiation Accelerator Engineering	264
WEPH29 – NSLS-II Vibration Studies to Characterize Beamline Stability	267
WEPH30 – Energy Efficient Air-Conditioning System Design	270
WEPH31 – Optimization Method Using Thermal and Mechanical Simulations for Sirius High-Stability Mirrors . .	273
WEPH32 – DESIGN OF A LAYERED HIGH PRECISION MAGNET GIRDER	277
WEPH34 – Research on Active Vibration Isolation System	280
WEPH36 – From Plate Screening to Artificial Intelligence: Innovative developments on PROXIMA 2A at Syn- chrotron SOLEIL	283
WEPH38 – Mechanical Design and Construction of the Coherent X-ray Scattering Beamline at Taiwan Photon Source	286
WEPH39 – Validation Results for Sirius APU19 Front End Prototype	290
WEPH41 – The Detector Adjustment System of Taiwan Photon Source 24A	294
THOAMA01 – Optimizing the PETRA IV Girder by Using Bio-Inspired Structures	297
THOAMA03 – Mechanical Engineering Design and Simulation for SPIRAL2 Accelerator @GANIL	302
THOAMA04 – Design and FEA of an Innovative Rotating Sic Filter for High-Energy X-Ray Beam	306
THOAMA05 – 3D Numerical Ray Tracing for the APS-Upgrade Storage Ring Vacuum System Design	312
THOAMA06 – A New X-Ray Beam for the ESRF Beamlines, Opto-Mechanical Global Survey	316

THOPMA01 – Piezo Technology in Synchrotron	321
THOPMA02 – Beamline Engineering Overview for the APS Upgrade	324
THOPMA04 – A New Procurement Strategy to Challenge the Supplier Constraints Created When Using a Fully Developed Reference Design	327
THOPMA06 – Development of Low Vibration Cooling Systems for Beamline Optics Using Heat Pipe Technology	331
THPH02 – LCLS Pulse Selector, A Multifunction Shutter for the LCLS-I 120 Hz FEL	336
THPH03 – The XBPM Project at MAX IV Frontends, Overview and First Results	340
THPH04 – Fast X-Ray Beam Intensity Stabilization for Absorption Spectroscopy and Spectromicroscopic Imaging	343
THPH05 – An Improved Polarisation Analyser for the I16 Beamline at Diamond	346
THPH06 – TMO - a New Soft X-Ray Beamline at LCLS II	349
THPH07 – Nanosurveyor 2: A Compact Instrument for Nano-Ptychography at the Advanced Light Source	352
THPH09 – Design of Indirect X-Ray Detectors for Tomography on the Anatomix Beamline	355
THPH11 – LCLS-II FEL Photon Collimators Design	358
THPH12 – Granite Benches for Sirius X-ray Optical Systems	361
THPH14 – Beam Conditioning Optics at the ALBA NCD-SWEET Beamline	365
THPH15 – A New High Precision, Fully Motorized 6-DoF Sample Stage for the ALBA PEEM Endstation	368
THPH16 – Compact Mirror Bender With Sub-Nanometer Adaptive Correction Control	371
THPH17 – NCD-SWEET Beamline Upgrade	374
THPH18 – A Multi-sample Holder for the MSPD Beamline at ALBA	377
THPH19 – Engineering Design of the XPD & PDF Beamline Sample Environment for Safe Experimental Use of Hazardous Gases	379
THPH21 – DREAM - A New Soft X-ray (Dynamic REAction Microscopy) COLTRIMS Endstation at LCLS-II	382
THPH23 – Interlock System for a Magnetic-Bearing Pulse Selector	385
THPH24 – Front End Designs for the Advanced Photon Source Multi-bend Achromats Upgrade	388
THPH26 – Mechanical Conversion of a Vertically Reflecting Artificial Channel-cut Monochromator to Horizontally Reflecting	391
THPH27 – Mechanical Design of a Compact Non-invasive Wavefront Sensor for Hard X-rays	394
THPH28 – The Development of PAL-XFEL Beamline	397
THPH31 – Design of a flexible RIXS Setup	400
THPH32 – Dual Beam Visualizer - Intensity Monitor for Lucia Beamline at SOLEIL Synchrotron	403
THPH33 – Direct LN2 Cooled Double Crystal Monochromator	406
THPH36 – Engineering Challenges for the NEH2.2 Beamline at LCLS-II	409
THPH37 – MAGSTAT V3: An In-Vacuum Variable-Gap Quadrupole with Rotary Permanent Magnets	412
THPH38 – Design & Development of an Innovative 6 Axis Sample Manipulator.	415
THPH39 – Novel Comprehensive UHV Lens Changer at the PETRA III Beamlines P22, P23 and P24	418
THPH40 – Training the Next Generation of Engineers for Photon Based Light Sources	421
THPH41 – Frontend Slits for Closely-Spaced Wiggler Beams	424
THPH43 – New Holder for Dual-Axis Cryo Soft X-Ray Tomography of Cells at the Mistral Beamline	427
FROAMA02 – A High Heat Load Double Crystal Monochromator and Its Cryo Cooling System for Heps	430
FROAMA05 – Engineering Design and Commissioning Performance of the ESM and Six Soft X-Ray Beamlines at NSLS-II	435
FROAMA07 – ESRF Double Crystal Monochromator Prototype Project	440
Appendices	445
List of Authors	445
Institutes List	453

DEVELOPMENT OF THE NEW UE38 UNDULATOR FOR THE ATHOS BEAMLINE IN SwissFEL

H. Joehri[†], M. Calvi, M. Hindermann, L. Huber, A. Keller, M. Locher, Th. Schmidt, X. Wang,
 A Zandonella, Paul Scherrer Institute, 5232 Villigen, Switzerland

Abstract

For Athos, the second beamline of SwissFEL, we profit from the experience of the U15 undulator development. The U15 undulator is in use at the Aramis-beamline in SwissFEL. But for Athos, there are new requirements, because it will be a polarized undulator with a period of 38mm. We developed a new arrangement of the drives in a X-arrangement. The magnet keepers are optimized for bigger forces also in the beam direction. A vacuum pipe with only 0.2mm of wall thickness is realized.

Currently, the undulator is in fabrication at MDC Max Daetwyler AG. All the main parts are manufactured and the assembly is close to be finished. For measurement and alignment, separate tools had to be designed.

For the vacuum pipe we have a prototype, which is close to the requirements. Some points of the fabrication process have to be optimized to realize a better straightness.

OVERVIEW

The general arrangement is an Apple II undulator, but the movements of the magnets are not in vertical direction. The opening of the gaps, is like an X (Figure 1).

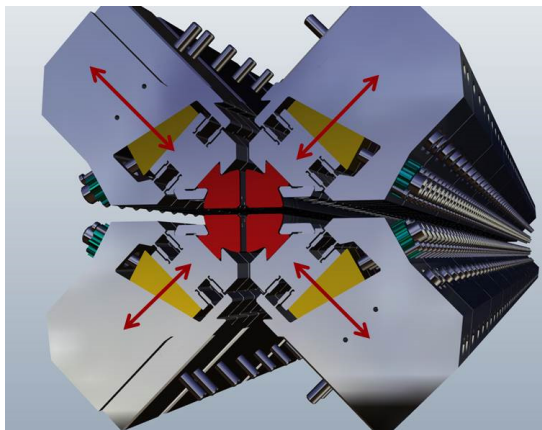


Figure 1: X – Arrangement.

Each magnet can be adjusted with a screw. The screw with two different threads moves a wedge. This wedge moves the magnet in the direction of the gap movement. This enables to use a robot system to adjust each magnet individually within a tolerance of 1.5 μm

Main Specification

Length	: 2 m
Number of periods	: 52
Length of period	: 38 mm
Gap range	: 3 – 21 mm
Shiftrange	: +/- 21 mm
Magnetic force in X	: 1.6 tons
Magnetic force in Y	: 1.6 tons
Magnetic force in Z	: 2.0 tons

See figure 2 for the definition of gap and the direction of the forces

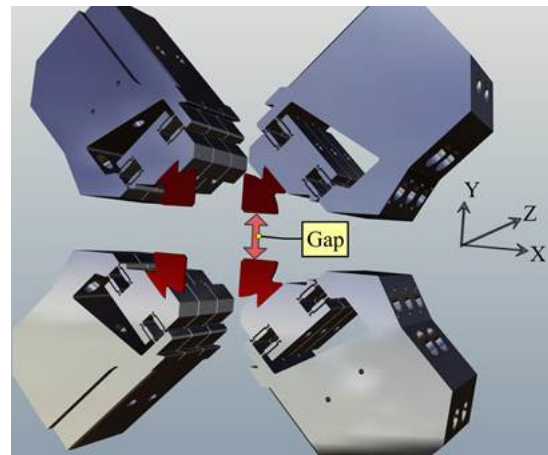


Figure 2: Definition of gap and the coordinates.

DRIVES AND ENCODERS

One goal of the development was to find an arrangement in a way, that the drives are independent of each other (see figure 3).

The gap is changed by a wedge drive. The wedge is driven by a servomotor and a spindle with a satellite roller screw. The slope of the spindle is 0.5 mm.

The shift drive is solved directly with a spindle and a servo-motor. Also here, a spindle with satellite roller screws is used. The slope is 1.0 mm.

To allow the baseplate with the keepers to move in both directions (gap and shift), a separate plate is positioned between the frame and the baseplate (violet plate in figure 3). This plate is connected to the frame with 7 linear guides to give the stiffness of the system.

All movements are controlled by linear encoders

Motors: Beckhoff AM8023-OE21

Encoders: Heidenhain LC 415-ML70

[†] haimo.joehri@psi.ch

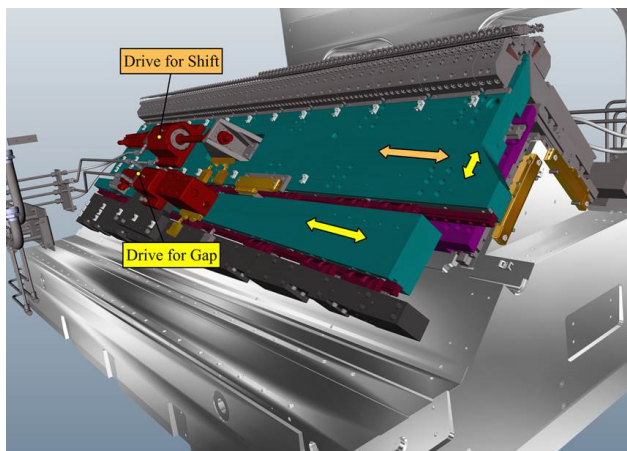


Figure 3: Drives.

FRAME

The frame has to fulfill different requirements

- Due to the big forces of the magnets, it has to be stiff.
- The production has to be cost-effective for a series of 20 units
- All parts should have the same thermal expansion, because the arrangement of the guides is very sensitive to differences in the expansion.
- For service of the components, the main parts should be accessible in case of failures

To fulfill these requirements, we chose a concept with two baseplates and two sidewalls, which gives a closed structure at the end. The two baseplates (upper and lower) are identical.

The sidewalls have openings to gain access to the drives.

We chose cast iron as material. This gives more freedom in the design than mineral cast and it can be milled. To prevent differences in thermal elongation, all parts that are shown in figure 4 are made in cast iron.

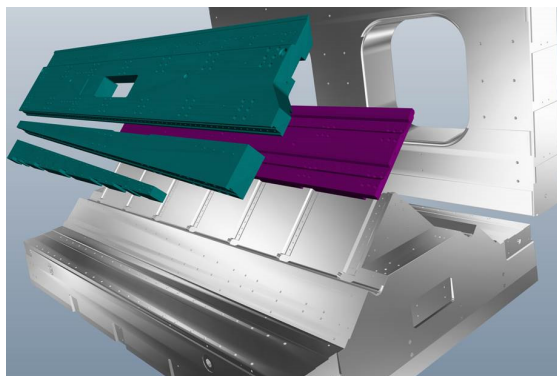


Figure 4: Parts in cast iron.

At the beginning of the design we tried tools with topological optimization. First result is shown in figure 5. As a

first impression, the result looks a bit strange. Main finding was, that in the baseplates should be a rib over each linear guide from the gap movement. So we took that principle and designed the structure in the classical way with design rules for cast iron and optimized it with normal finite element analysis.

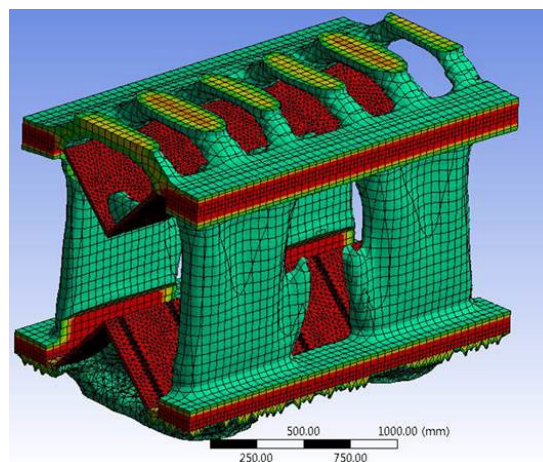


Figure 5: Result of topologic analyses.

KEEPER DESIGN

For U15 Undulator of Aramis (First beamline in Swiss-FEL), we developed a keeper, where each magnet can be adjusted by a screw [1]. This gives the possibility to use a robot screwdriver to automatize the adjustment of the magnets.

For the UE38-Undulator, we wanted to profit from that experience. Some new requirements had to be taken into account.

- Forces from the magnets in each direction
- Limited space
- Bigger range for adjustment : $\pm 0.1\text{mm}$

To fulfill these requirements, we made two general changes:

The flexible part of the keeper is pulled to the wedge by a spring.

The screw to move the wedge is designed as a differential screw. One thread has a slope of 0.907mm , the second thread has a slope of 1.0mm . This gives a small movement of the wedge of only 0.093mm by one turn of the screw. The design is shown in figure 6.

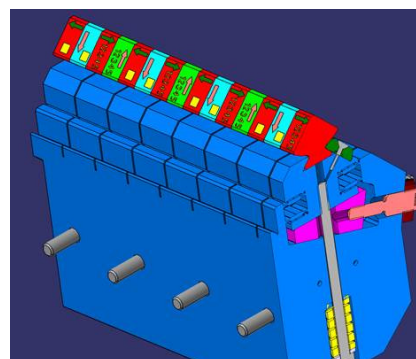


Figure 6: Keeper design.

The keeper is made of aluminium. The wedge is made of bronze with dicronite coating to minimize the friction. The differential screw is made of stainless steel with dicronite coating.

For the assembling of the wedge and the screw, it is important that wedge is in the correct position. If both treads of the screw are in mesh during the positioning, it results in differences of 1mm depending of the starting point of the thread. To solve that problem, a separate part is used to define the second thread. The assembling procedure is shown in figures 7 to 9:

In a first step, the wedge is put to the neutral position and the screw is turned in the wedge (figure 7)

Then a special nut is turned until it is in contact with the keeper (figure 8)

In the last step, the nut is fixed with two screws (figure 9).

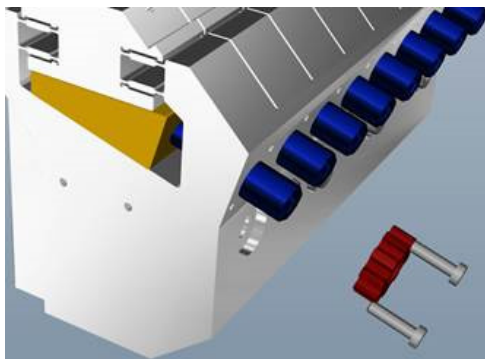


Figure 7: First step of assembling the keeper.

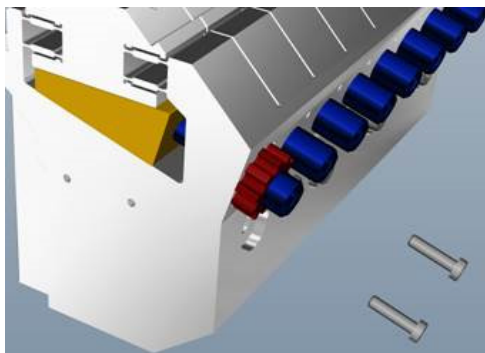


Figure 8: Second step of assembling the keeper.

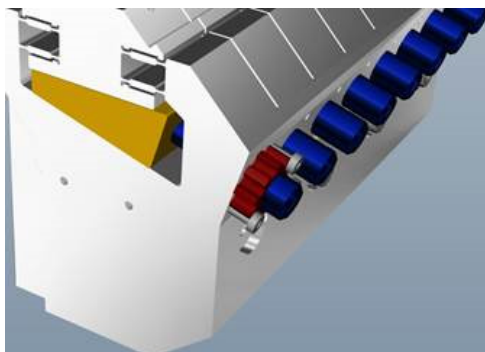


Figure 9: Third step of assembling the keeper.

The whole system has to withstand the forces of the magnets. The analysis with finite element tools showed, that the critical forces are in beam direction.

The stiffness is higher, when the magnet is adjusted to a higher position, because the flexor gives an additional pressure to wedge. Therefore it is less stiff in the lower position. The simulations showed, that the flexor should be as wear as possible and the force of the spring must be maximized.

Figure 10 shows one of the simulations

Figure 11 shows the details of the flexor

The spring has a load of 576 N. It is a spring with inner diameter of 6.3mm and an outer diameter of 12.5mm. The spring has a rectangular cross section and is mainly used in cutting tools.

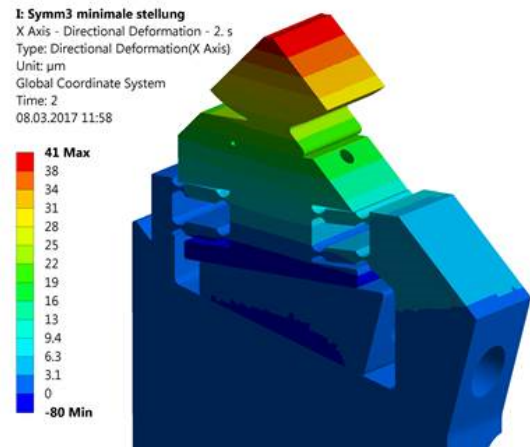


Figure 10: Simulation with force in beam direction.

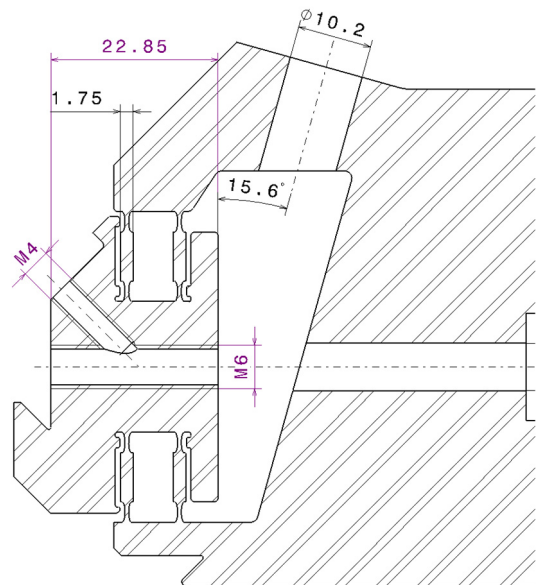


Figure 11: Detail of the flexor.

VACUUM PIPE

The space between the magnets is very limited with a diameter of only 6mm. Therefore, we developed a pipe with an inner diameter of 5mm and a wall thickness of 0.2mm. The pipe is manufactured in copper by a galvanic process. The galvanic process is done by an external company: Galvano-T in Germany.

The pipe itself with its copper support and the external support, that places the vacuum chamber in the frame, is shown in figure 12. The process of manufacturing is explained step by step in the following figures:

Figure 13: The flanges are in stainless steel together with a conical interface, that will be enwrapped by copper. The flanges are put over a silicone wire. This wire has an internal steel wire to stretch it. It is coated with silver powder to enable electrical conductivity.

Figure 14: The flanges and the wire are fixed in a frame. All parts must be covered with an electrically insulation, except the parts that will be galvanized.

Figure 15: After the galvanizing, the silicone tube can be removed by pulling it out. After that step the result is a pipe with the flanges.

Figure 16: A copper support, that is manufactured separately is connected to the pipe also with a galvanic process. For that process, the pipe and the support are fixed in a frame. Everything except the interface from the pipe to the support is electrically insulated



Figure 12: Vacuum pipe with frame.

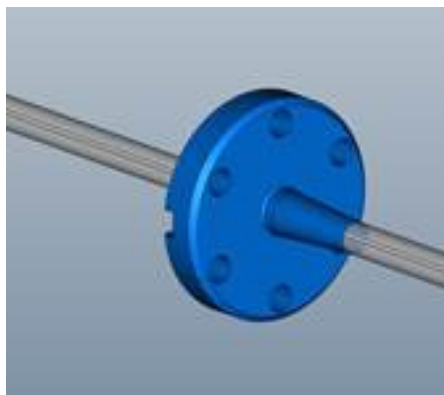


Figure 13: Flange with silicone wire.

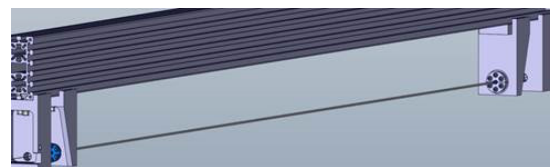


Figure 14: Stretched wire before galvanizing.



Figure 15: Pipe with flanges.



Interface of pipe and support

Figure 16: Galvanizing the support.

MEASUREMENT

For the precision of the whole system, the interface to the keepers has to be in a straight line at the correct position. During the assembling of the prototype, the upper line of the mounting plate (red chain dotted line in figure 17) is measured with gauges and lasertracker. After optimizing, we reached a straightness of 10µm



Figure 17: Measurement with laser tracker.

After optimizing the lower and upper mechanism, the frame can be completed with the sidewalls. To guarantee the position of the whole system, the system will again be optimized by lasertracker measurement. To avoid shimming with the sidewalls, the final height of the sidewalls is milled after the measurement of both mechanisms.

ACTUAL SITUATION, NEXT STEPS

In June 2018, the assembling of the frames and the mechanics are short to the final step. We expect the delivery from MDC Max Daetwyler AG in July.

The keepers for the prototype are ready (Figure 18) for assembling with the magnets.

Next step will be the final assembly, that will be done at Paul Scherrer Institut by the Insertion Device Group.



Figure 18: Keeper after assembling the wedges.

CONCLUSION

For the new Apple X Undulator (Figure 19) for Athos-Beamline at SwissFEL, we developed a new concept of frame and vacuum pipe.

For the keeper design we profit from the experience of the U15 Undulator.

At the moment, we are short to the final assembling. Whether everything works as planned will be revealed after an intensive testing with the magnets.

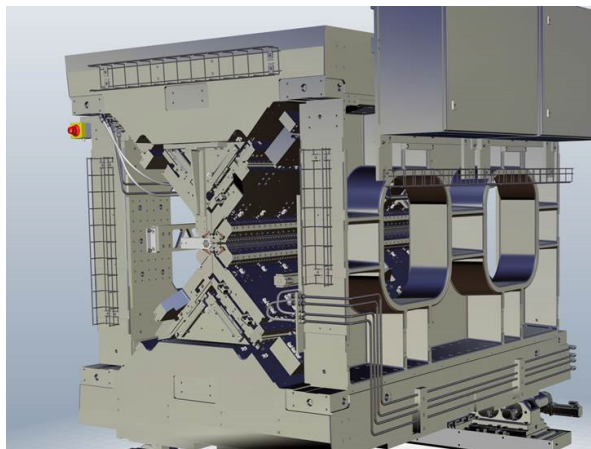


Figure 19: UE38 Undulator.

ACKNOWLEDGMENT

We want to thank the whole ID-Group, the Vacuum Group, the Engineers from the department of mechanical engineering and the external partners, especially the companies MDC Max Daetwyler AG and Galvano-T.

REFERENCES

- [1] P. Boehler *et al.*, “Experience With the Commissioning of the U15-Undulator for SwissFEL-Aramis Beamline and New Developments for the Athos Beamline”, in *Proc. 9th Edition of the Mechanical Engineering Design of Synchrotron Radiation Equipment and Instrumentation Conf. (MEDSI'16)*, Barcelona, Spain, Sep. 2016, paper WECA03, pp. 283-287, ISBN: 978-3-95450-188-5, <https://doi.org/10.18429/JACoW-MEDSI2016-WECA03>

APPLE II INSERTION DEVICES MADE AT MAX IV

A. Thiel, M. Ebbeni, H. Tarawneh, MAX IV Laboratory, Lund, Sweden

Abstract

At present five Apple II insertion devices were made and installed at MAX IV [1], three of them in the 1.5GeV-ring, and two in the 3GeV-ring. The assembly of the last one of a total number of six Apple II undulators made at MAX IV is currently going on. The undulators have period lengths of 48mm (two devices), 53mm, 58mm, 84mm and 95.2mm. The operational gap range of the 3GeV devices is between 11mm and 150mm, the range of the 1.5GeV devices is 14mm to 150mm. Structural analysis was applied to assure a minimum deflection of the main frame and the magnet array girders. The main frame is made of nodular cast iron, while the girders are made of aluminium alloy. In order to optimize the magnetic tuning the position of the magnet keepers can be adjusted by wedges. The undulators were fiducialized before the installation in the ring tunnel and were aligned in the straight section using their magnetic centre as reference. All MAX IV made undulators have three feet with vertical adjustment and separate horizontal adjusters. This paper describes the design, assembly, shimming and installation of the MAX IV Apple II devices in more detail.

OVERVIEW OF INSTALLED APPLE II

Three Apple II undulators (EPU: elliptically polarising undulator) are in place at the 1.5GeV-ring and two EPU's in the 3 GeV-ring. A sixth EPU is currently in assembly for the 3 GeV-ring. Table 1 shows the overview of the EPU's with some characteristic properties.

Table 1: Summary of Styles

	Beam-line	Period length	Inst. length	Magn. gap	K_{eff}
3 GeV	Hippie	53mm	4m	11mm	3.30
	Veritas	48mm	4m	11mm	3.30
	Softim ax	48mm	4m	11mm	3.30
	Bloch	84mm	2.6m	14mm	8.65
1.5 GeV	FinEst	95.2mm	2.6m	14mm	10.40
	MAX peem	58mm	2.6m	14mm	4.95

These six undulators were manufactured at the MAX IV magnet laboratory between 2015 and 2018. The initial design bases on an EPU designed in collaboration with Bessy (HZB) [2].

MECHANICAL DESIGN FEATURES

Undulator Cast Frame

The backbone of MAX IV EPU's is the cast iron frame made of nodular cast iron EN-GJS-400-18-RT according to DIN EN1563. The material combines high strength and

good machining properties with low deformation at present forces. The cast pattern of the frame was designed by the foundry based on the calculated magnet forces and estimated magnet array weight. Figure 1 shows the force pattern and Table 2 the allowable deformation.

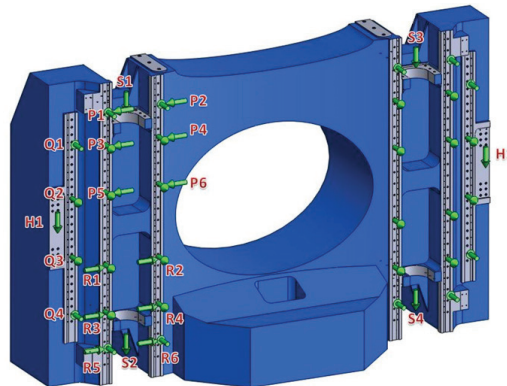


Figure 1: Force pattern on the EPU-model frame.

Table 2: Maximum Allowable Deformation

	Horizontal [mm]	Vertical [mm]
P-R		< 0.050
P1-P6 / R1-R6	< 0.015	
Q1-Q2 / Q3-Q4	< 0.010	
Q1-Q4	< 0.020	

The foundry's engineering team optimized the cast model respectively [3], also in regard of the manufacturing procedure. MAX IV used two standardized wooden cast patterns to cover the two different straight section lengths of the two storage rings. The cast frames have a weight of approximate 6.2t. Figure 2 shows the EPU53 cast frame during machining.

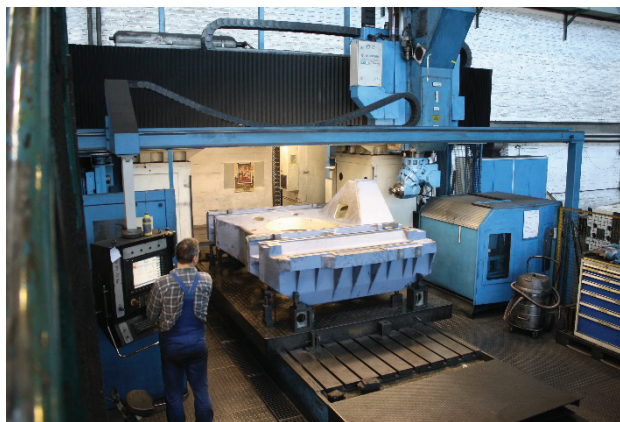


Figure 2: EPU53 cast frame during machining.

Undulator Feet Arrangement

The EPU's manufactured by MAX IV have three feet, which carry the entire weight. Three additional side adjusters take care of the horizontal alignment. The

vertical feet are standard machinery feet with precise vertical adjustment based on wedges. Bearings on the vertical feet allow the undulator to slide in the horizontal plane. This design separates the vertical and the horizontal alignments, which allows for smooth alignment in the ring tunnel saving tunnel access time. Figure 3 shows the vertical feet design.

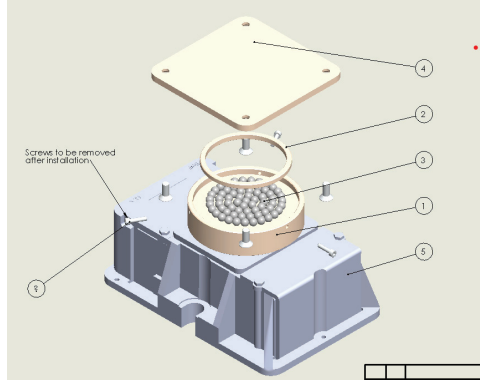


Figure 3: Feet for vertical adjustment.

A typical alignment of a MAX IV EPU takes about one hour, the most time in the ring is needed for the laser tracker to warm up (about 2...3 hours).

Magnet Keepers

Wedges realize the vertical position tuning of the MAX IV EPU magnet keepers. All magnet keepers are made of aluminium AW-6082. The wedges are made of copper alloy CW713 (2.0550). Two pins (CW614N) fix the position of each keeper on the respective subgirder. The position of the keeper on the wedge is defined by a M4 bolt, which is secured by a left hand threaded set screw, and a respective counter screw. The keeper is bolted down on the subgirder by a M8 screw. Each keeper holds a pair of magnets, horizontally and vertically magnetized. Figure 4 shows the explosion drawing of the magnet keeper assembly. Loctite 222 is used to secure all screws.

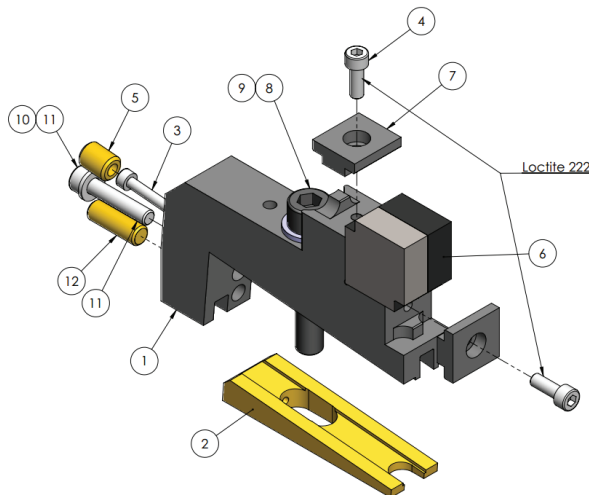


Figure 4: Dual magnet keeper of MAX IV EPU's.

The magnet keeper sees forces in all three axes and a respective torque in addition to the mounting force introduced by the screws. The individual magnet keeper of EPU95.2, the undulator with the longest period at MAX IV, sees a maximum horizontal force of 460N, a vertical force of 380N and a force of 440N in longitudinal direction at a gap of 14mm at different phase shifts. Figure 5 shows the corresponding calculated deformations in vertical direction.

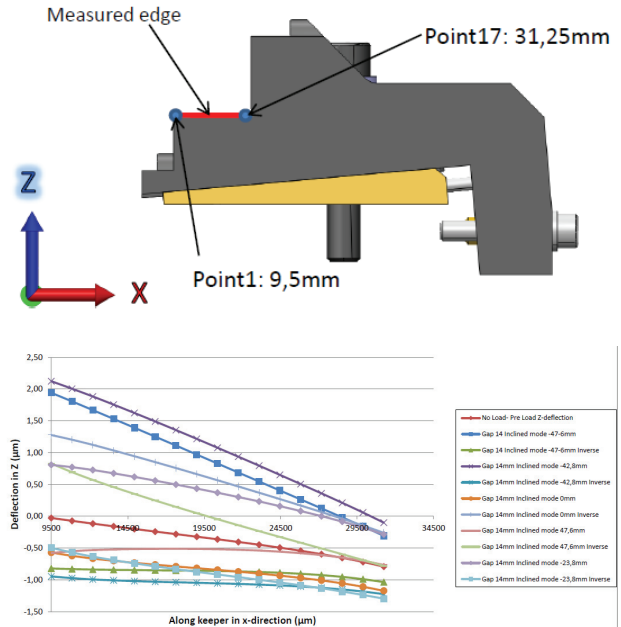


Figure 5: EPU95.2 magnet keeper vertical deflection.

According to the calculations the maximum deflection of the dual magnet keepers is below $3\mu\text{m}$ in all directions and all phases.

The assembly of the magnets on the keepers was done with the help of a mounting jig in order to have a reproducible placement of the magnets on the keepers. The jig, showed on Figure 6, can match to all magnet sizes used on MAX IV EPU's.

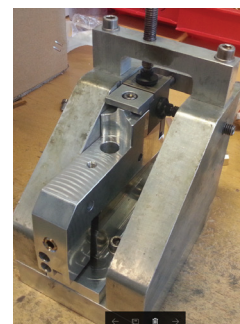


Figure 6: Magnet mounting jig.

Girders

The magnet keepers sit on four subgirders, which themselves are mounted on two main girders as shown in Figure 7.



Figure 7: Main girder assembly.

The main girders deflect by the resulting magnet forces depending on gap distance and phase shift. The main design focus was to keep the vertical deflection of the main girder below $10\mu\text{m}$ under all conditions. There is no force balancing system on MAX IV EPU's. The deflection is limited by the cross section design of the main girder ($400\text{mm} \times 400\text{mm}$). The girders are made of aluminium ACP5080. Figure 8 shows the calculated deformation in vertical direction of the main girder with subgirders in phase shift to realize inclined polarization.

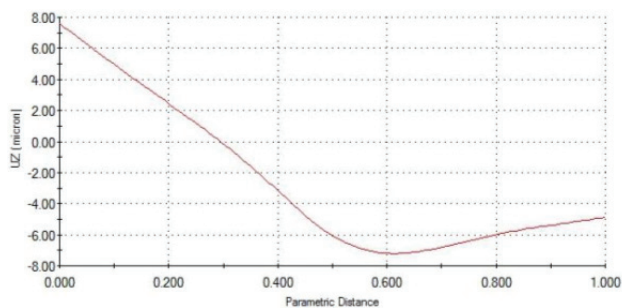


Figure 8: Vertical deflection of the main girder in inclined mode.

The maximum calculated vertical deflection due to magnetic force and weight is $7.5\mu\text{m}$.

In operation the undulator gap deflects significantly more than that. The undulator gap is not only determined by the magnet forces and weight of the girders but also by the deflection and tolerances of the entire undulator structure. Adding up the tolerance chain of the main girder assembly of a 4m-EPU gives a number of $490\mu\text{m}$. Adding the deformation induced by the magnet force the undulator gap might change by $500\mu\text{m}$ without motor motion.

TUOPMA04

Thorough mechanical design can decrease that number. Still all MAX IV EPU's operate with linear encoders measuring the gap change and motors in closed loop in order to correct for the deformation and backlash of the mechanical system.

Magnetic Tuning

After the assembly is finished, all undulators are magnetically tuned (shimmed) at the MAX IV Hall probe and wire bench [4]. The device is released for installation in the ring tunnel when,

- the residual first integral error is below 100Gcm ,
- the phase error (calculated with B2E code [5]) is below 5°
- the second integral error is below 20000Gcm^2 .
- The device is measured at different gaps and phases.

A typical shimming campaign takes about 2 weeks for a 2.6m EPU, and 4 weeks for 4m EPU. The EPU's allow for all polarizations in between horizontal and vertical polarization. Measurements show, that all these modes become good enough in magnet field quality if successfully shimmed for horizontal and vertical mode. MAX IV EPU's are therefore shimmed at horizontal and vertical polarization mode at the respective minimum undulator gap.

Figure 9 shows the initially measured orbit of EPU84 before the start of the magnetic tuning.

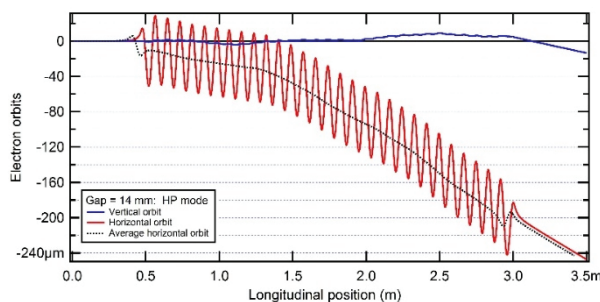


Figure 9: Measured orbit of EPU84 before shimming.

After 10 days of shimming the orbit was tuned as Figure 10 shows:

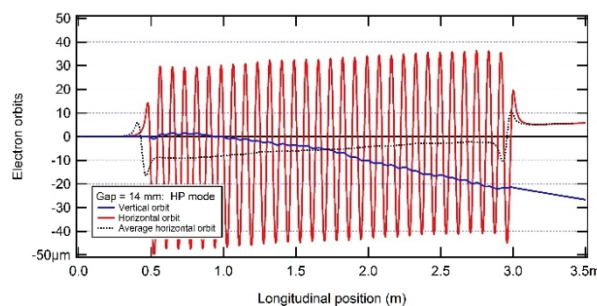


Figure 10: Measured orbit of EPU84 after 10 days shimming.

Figures 11 and 12 show the first and second integral in the horizontal plane after shimming.

Accelerators

Insertion Devices

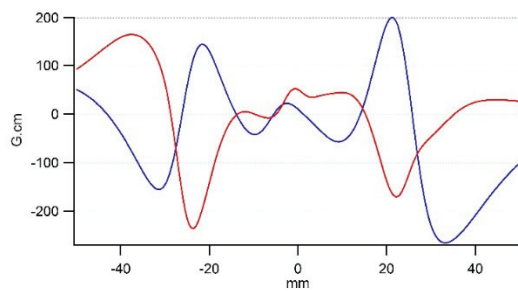


Figure 11: Measured first integral of EPU84 after shimming.

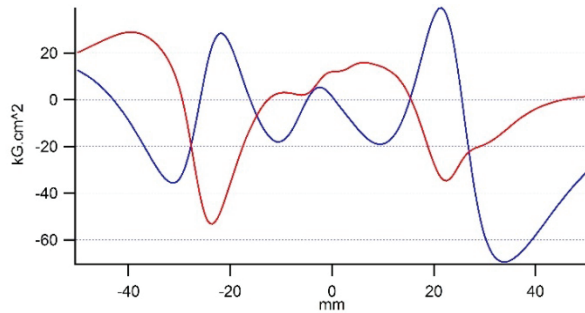


Figure 12: Measured second integral of EPU84 after shimming.

The measurements proof that the magnetic tuning with the wedge system assured the magnetic field quality, and allows for relatively quick shimming period for Apple II devices.

The measured field frequency in Figure 13 shows the achieved period length of 83.998mm of the assembled EPU84.

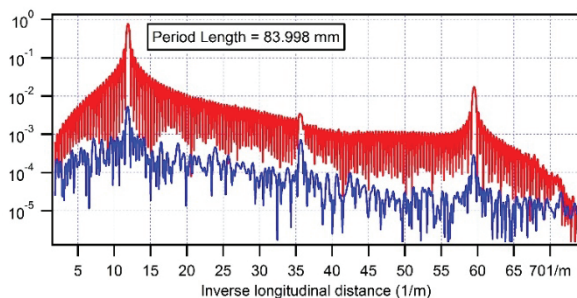


Figure 13: Measured magnet field frequency of EPU84.

Machine Protection

A possible damage of the straight vacuum chamber section is a major concern when operating Apple II devices in the storage ring. All EPU's installed at MAX IV have therefore a software limit, which prevents the user for commanding gap values outside the operation range. In addition, redundant limit and kill switches are mounted. The switches are adjusted in steps of 0.15mm below or above the operational limit and would stop the motion and activate the motor breaks. On top of this, all EPU's have a

hard stop, a chunk of metal mounted in a way that the girders could not pass. The hard stops are adjusted to 0.3mm...0.4mm below or above the respective operation limit. A high precision tilt meter (Tuff Tilt 420, high gain version) mounted on each of the girders monitors any angular change of the respective girder position. Figure 14 shows the mounted tilt meter on EPU58.



Figure 14: Mounted tilt meter.

An alarm would be triggered if the measured angle is outside the defined range. The EPU's girders are expected to operate without any taper. It turned out, that some of the tilt meters of installed EPU's triggered despite the fact they were not operated. The assumption is, that the tilt meters even measures the floor motion of the relatively fresh MAX IV concrete. That means, the tilt meter may also indicate a necessary realignment of the undulator.

CONCLUSION

Six EPU's have been built and characterized at MAX IV laboratory where of five are already installed in the two storage rings. The current design and work shop set up allows the manufacturing of Apple II undulators with magnetic and mechanical properties within specifications. All six EPU's were manufactured on time and budget.

There is still a lot of potential optimization to discover. Different magnet sorting and assembly procedures were tried. About twenty small design upgrades from the first to the last EPU already improved the mechanical behaviour and handling during assembly.

ACKNOWLEDGEMENT

Many thanks go to Morten Boettcher for his work on ID assembly and shimming, his many input on measurement systems are highly appreciated. Many thanks also to Ewcon AB who delivered all EPU machined parts in high quality.

REFERENCES

- [1] MAX IV Laboratory, <https://www.maxiv.se>
- [2] J. Bahrtdt *et al.*, “Apple Undulator for PETRA III”, in *Proc. EPAC’08*, Genoa, Italy, June 2008, paper WEPC096, pp. 2219-2221.
- [3] Heidenreich & Harbeck GmbH, Development report frame EPU84/95/58, 2015.
- [4] M. Ebbeni, A. Thiel, H. Tarawneh, “Status of Insertion Device Measurement Systems at MAX IV Laboratory”, in *Proc. IPAC’16*, Busan, Korea, May 2016, paper THPOW046, pp. 4047-4049, doi: 10.18429/JACoW-IPAC2016-THPOW046
- [5] Scientific Software B2E, <http://www.esrf.eu/Accelerators/Groups/InsertionDevices/Software/B2e>

RF FINGERS FOR THE NEW ESRF-EBS STORAGE RING

Th. Brochard[†], L. Goirand, P. Brumund, J. Pasquaud, S. White
 European Synchrotron Radiation Facility, 38043 Grenoble, France

Abstract

In the new ESRF-EBS (Extremely Brilliant Source) storage ring vacuum chambers assembly, with a reduced aperture and the new omega shape, RF fingers are a key component to ensure good vacuum conditions and reach the best possible machine performance. As a result, dedicated efforts were put into producing a more compact more robust more reliable and easier to assemble RF finger design for the new machine. The work was done in parallel on the beam coupling impedance reduction, which have a direct impact on the electron beam lifetime, and on the mechanical aspect with FEA validation and geometry optimization. Many test have been made, in a mechanical laboratory, including high resolution 3D computed tomography images in order to measure the electrical contact, and also in the existing ESRF storage ring with the electron beam, to validate the final design before launching the series production.

INTRODUCTION

In order to absorb chamber-to-chamber misalignments, thermal expansion, for instance during bake-out, bellows are used to inter-connect a large number of chambers along the ring circumference. These bellows however are seen as resonant cavities by the beam hence breaking the geometrical continuity of the beam pipe and leading to degraded vacuum and stability performance. The continuity is restored by electrically shielding the bellows from the beam using so-called RF fingers which consist of conductors matching the vacuum chamber profile and connecting the beam pipes on either side of the bellow. The RF fingers are meant to absorb mechanical movements while providing the best possible mechanical and geometrical continuity: designing such a device is therefore far from trivial since many aspects have to be carefully optimized.

The new omega-shaped chamber profile is not compatible with the present RF finger design if geometrical continuity is to be enforced. A dedicated in-house design based on new concepts and principles was therefore devised for the ESRF-EBS ring. Figure 1 shows the final design. It is the result of several iterations and optimizations of beam coupling impedance and mechanical properties.

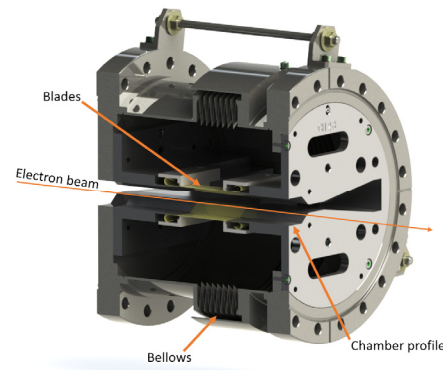


Figure 1: RF Finger placed in a bellows.

BEAM COUPLING IMPEDANCE REDUCTION

The first step was to ensure that the cavity formed by the bellow was properly shielded from the beam. This was achieved by 10 blades (5 top and 5 bottom) as seen in Fig. 2. Once the bellow is invisible to the beam, the beam coupling impedance is strictly given by geometrical discontinuities of the inner volume: in this case the steps and tapers angle at the entrance and exit of the RF fingers can be seen in Fig. 2. The step height was fixed to 0.3mm for mechanical criteria and the only parameter left for optimization was the taper angle, a good compromise was found with a reduction of the taper angle from 5° to 2° leading to a reduction of the beam coupling impedance by a factor 4. This result was found satisfactory as the resulting full contribution of the RF fingers to the total impedance of the machine became significantly smaller than the contribution of beam pipes themselves.

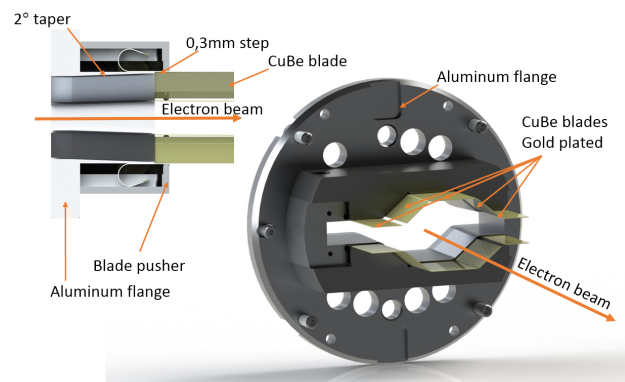


Figure 2: RF Finger cut view.

[†] brochard@esrf.fr

MECHANICAL ASPECTS, FEA VALIDATION AND GEOMETRY OPTIMIZATION

The shielding blades (the RF fingers) are made with copper-beryllium ($CuBe2$) and the flange parts with an aluminium alloy. Copper-beryllium is a high resistance, highly conductive alloy perfectly fitting for the RF finger's function whereas an aluminium alloy is easier to machine to achieve the desired complex shape of the flange part.

A profound structural mechanical finite element analysis (FEA) was performed to validate the new RF finger design as regards occurring mechanical stress and the necessary electrical contact. At the same time the FEA served to study the design optimization possibilities considering the specific component requirements. A parameter study of three key geometrical dimensions was carried out to gain knowledge about their influence on the performance and mechanical safety. One of the parameters that varied in the course of this thorough analysis was the blade thickness of the fingers.

In the structural analysis the new component concept generally showed good compliance for the defined requirements as the electric contact quality is very high. The latter mainly depends on the contact force which is comparably high for all parameter variations and of at least 1.5N per blade. As generally the image current on the surrounding walls is rather a surface current, this contact should be sufficient. In all load cases and movements the blades are in good contact at the relevant contact position.

The required flexibility can be safely guaranteed. This counts for different promising configurations of different blade thicknesses. While thinner blades tend to be more flexible, their contact force drops but the safety margin of occurring mechanical stress is higher. The usage of thinner blades that lead to a lower contact force could be a solution to reduce friction-caused wear while maintaining a very good electric contact, as the analysis showed. The safety factor of occurring mechanical stress against the elastic limit is at least 1.2 for the analysed parameter variations during a relative flange movement of 2mm between both flanges which was considered as sufficiently flexible. Small plastic deformations in the flange part turned out to be tolerable and the component's functionality can also be maintained.

The new design, patented [1], will be used on all chamber profiles, high, low and straight section profiles. Table 1 shows the mechanical performance achieved.

Table 1: RF Finger Mechanical Performances

Axial stroke	+8 / -19 mm
Radial stroke (all directions)	+/- 1 mm
Angular stroke (flange / flange)	+/- 5 degrees
Mechanical safety at 2mm flange radial movement	>1.2

RF-FINGER VALIDATION

Computed Tomography (CT) Imaging

The electrical contact validation has been made using the computed tomography imaging technique at the ESRF BM5 beam line. RF Finger images were made with filtered white beam on a dedicated tomography setup. Data acquisition was made by a PCO Edge ccd camera mounted on an X-ray optic with a 13.4 μm pixel size resolution.

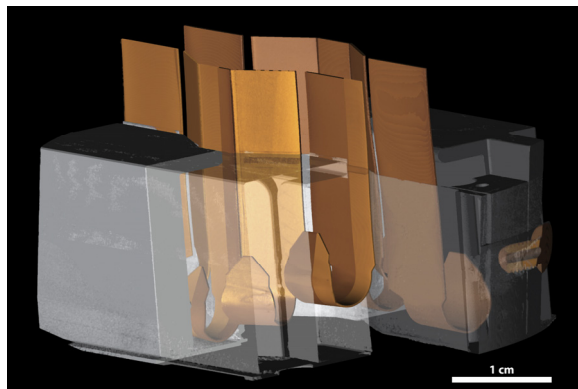


Figure 3: 3D generated volume view from CT images reconstructed.

After image reconstruction, as seen on Figure 3, it is possible to see the mechanical contact between blades and flanges at any position. The main point is the mechanical contact at the flange sleeve (Fig. 4 – Fig. 5).

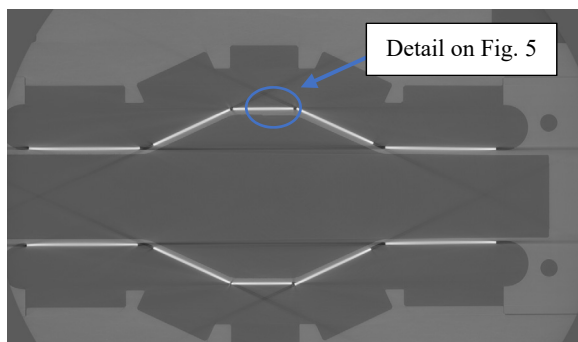


Figure 4 : 10 blades contact view on CT image.

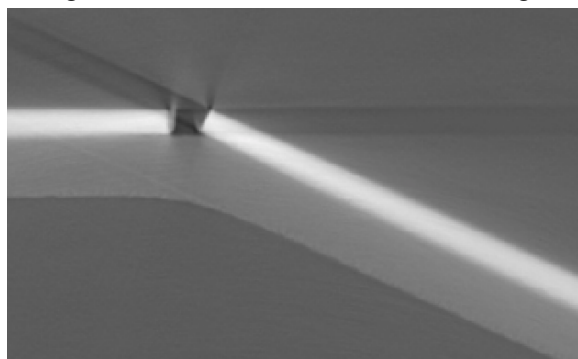


Figure 5: Detailed view of blade contact on CT image.

On Figure 6, at the 13.4 μm pixel size resolution, the mechanical contact between the blade and the flange sleeve did not shows any gap.

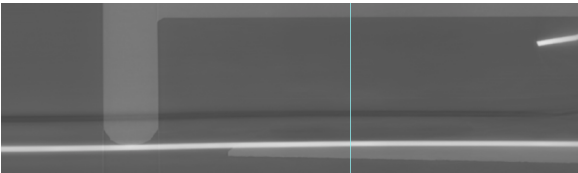


Figure 6: Longitudinal cut of upper central blade on CT image.

Synchrotron Beam Test

For RF performance validation, a test in the existing storage ring has been performed during a machine dedicated time (MDT).

Test bench description The test bench used (Fig. 7) was made with a dedicated vacuum chamber equipped on both ends with an edge welded bellows and RF-Fingers in the bellows. Thermocouples were welded on the middle of the external part of the upper and lower central blades, and connected to the data acquisition system. On the four thermocouples connected to the RF strips, only 2 were working during the test, Th3 and Th5. The central part of the chamber is mounted on a double remote controlled translation setup, one vertical (z) perpendicular to the beam and one horizontal (y) perpendicular to the beam. The x is the electron beam direction. Pressure gauges, penning type, were mounted on the upstream and downstream chambers.

The setup was placed in the European Synchrotron Radiation Facility (ESRF) storage ring, at a dedicated place.

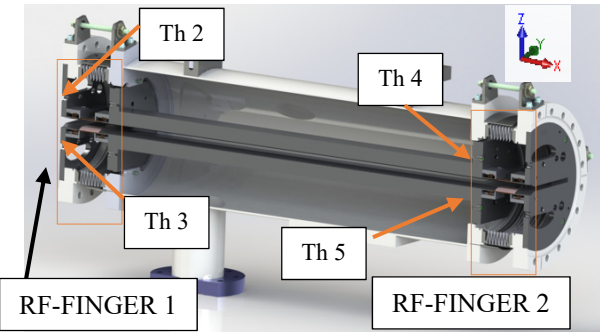


Figure 7: Cut view of the test chamber.

Test procedure The machine mode and ring current went up, step by step, in order to increase the current per bunch, as shown in Table 2. At each step, the chamber is moved by 0.1 mm from the central position to -1 mm and from the central position to +1 mm in Z. A Y translation is also performed using the same criteria but no variations, vacuum pressure and temperature, were observed during this scan.

Table 2: Machine Modes And Ring Current Used		
Machine mode	Ring current [mA]	Current / bunch [mA]
uniform	20	0
16 bunches	16	1
16 bunches	32	2
16 bunched	64	4
16 bunches	92	6
4 bunches	31	8

Test results On the plot pressure versus Z position of the vacuum chamber (Fig. 8) the correct vertical alignment correspond to the minimum pressure observed. The pressure increase on miss alignment is linked to an increase of the temperature of all the system.

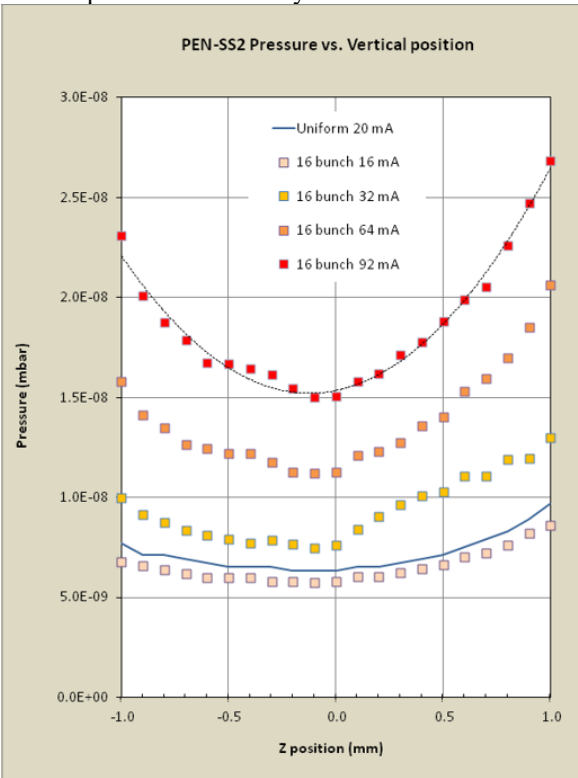


Figure 8: Pressure versus Z position.

No vacuum problem signature seen.
The temperature increase with the current per bunch in normal conditions with a maximum temperature measured at 130 °C (Fig. 9).

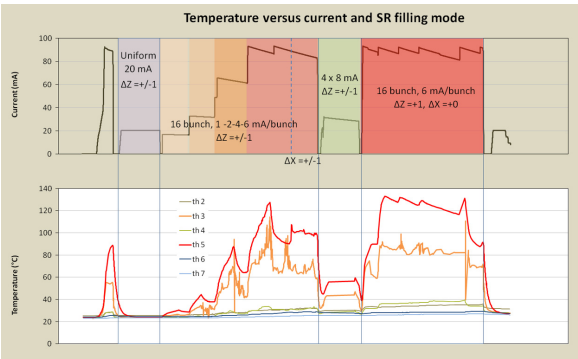


Figure 9: Temperature vs ring current and filling modes.

The temperature and pressure observed during the test are acceptable considering that the test conditions are the more demanding modes. After dismounting, we did not observe any damage or marks on the two RF-Fingers devices

CONCLUSION

The new RF Finger design is flexible and compact. It can be adapted to any chamber profile. The full assembly is light, less than 1 kg, and made with machined pieces easy to assemble. No welding or brazing are used during the manufacturing process. It is easy to mount in any position, vertically or horizontally. The axial and radial strokes are large enough to compensate any chamber-to-chamber misalignments or chamber thermal expansion during the bake out. The reduction of the beam coupling impedance is archived with a very good electrical contact. The new ESRF-EBS storage ring will be equipped with this RF Finger design on all vacuum bellows and on all vacuum chambers where a RF Finger is needed.

REFERENCE

- [1] Th. Brochard, L. Goirand, J. Pasquaud, “Dispositif de raccordement entre tronçons d'anneau de synchrotron”, B14959 EP, request number 17160419.2 -1211 / 3223591 claiming priority of patent FR 16/52454, March 22, 2016.

DEFORMABLE RF FINGERS WITH AXIAL EXTENSION

S. Sharma[†], F. DePaola, F. Lincoln, J. Tuozzolo, NSLS-II, BNL, 11973 Upton, NY, USA

Abstract

RF fingers in a bellows assembly provide electrical continuity for the image current between adjacent vacuum chambers. They are required to absorb all misalignments between the two chambers while minimizing abrupt changes in the beam aperture. In addition, during bake-outs of the chambers the fingers are required to accommodate their large thermal expansions. The latter is achieved either by having a sliding-contact finger design or a deformable finger design. In this paper we describe a version of the deformable finger design which permits large compression, significant misalignments and axial extension. A novel method of fingers' fabrication, FE analysis and test results are presented.

INTRODUCTION

Bellows assemblies are used as flexible interconnections between adjacent vacuum chambers. The flexibility of the stainless steel bellows compensates for transverse misalignments and axial gap of ~ 2 mm for the NSLS-II chambers. During bake-outs of the vacuum chambers the bellows compress by ~ 10 mm to absorb the combined thermal expansion of the chambers. RF fingers made from copper alloys are used inside the bellows to provide electrical continuity and the continuity of the beam aperture. These fingers must also compensate for the chambers' misalignment, axial gap and thermal expansion.

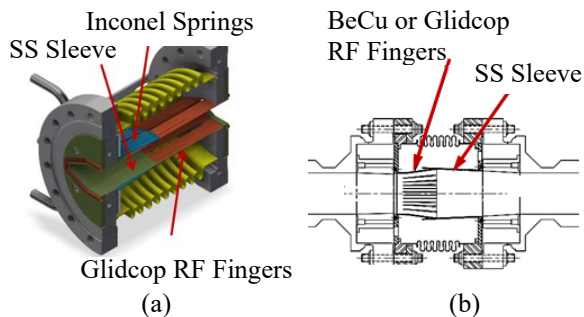


Figure 1: Conventional designs of RF fingers sliding on SS sleeve, (a) outside sliding type, (b) inside sliding type.

The conventional design of RF fingers relies on the fingers sliding on the outside surface or on the inside surface of a sleeve usually made from stainless steel. RF fingers for NSLS-II [1] and APS [2], shown in Fig. 1(a) and 1(b), are examples of the two designs. In the case of the outer-sliding RF finger design the fingers are compressed by cantilevered Inconel springs to ensure good contact pressure. A lack of good contact pressure can lead to thermal deformation and even melting of the fingers in storage rings with high beam current or high current per bunch.

[†] sharma@bnl.gov

A deformable finger design with fixed contacts has been proposed recently [3, 4] for the interconnection module of the LHC vacuum chambers. The RF fingers are pre-deformed in a corrugated shaped (Fig. 2(a)). The design is optimized to prevent buckling and over-extension. In the as-installed position, Fig. 2 (a), the fingers are compressed. During operation the fingers are almost fully extended (Fig. 2(b)) leaving some slack to compensate for axial gap.

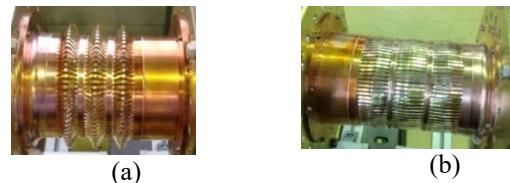


Figure 2: LHC deformable finger design, (a) as installed, (b) in operation.

In this paper we present a fixed-contact RF finger design that utilizes large nonlinear deformation including buckling to compensate for thermal expansion of the chambers. The RF fingers in this single-piece design can be offset by up to 2 mm to compensate for transverse misalignments between the vacuum chambers. They can also be extended by up to 2 mm to compensate for axial gaps. The RF fingers are designed to remain straight during operation.

PROPOSED DESIGN

Figure 3 depicts the proposed design of the RF fingers with typical overall dimensions. RF fingers are made as a single-piece spool (Fig. 3(a)) from a stock of CuCrZr or Glidcop (AL-15) alloys. These alloys are chosen in place of a more commonly used alloy, BeCu, because of their higher electrical and thermal conductivities (Table 1). Glidcop RF fingers are in use at PEP-II [5], APS and NSLS-II, and CuCrZr RF fingers have been proposed for the ITER project [6].

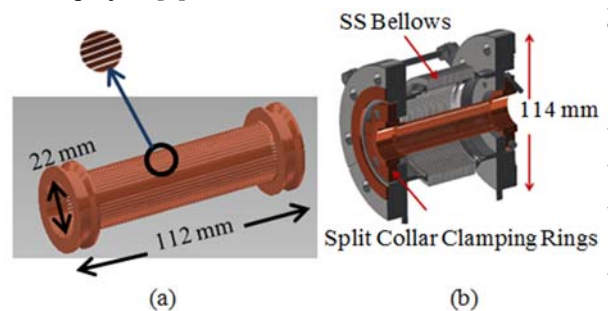


Figure 3 : Proposed RF finger design, (a) single-pièce RF finger spool, (b) assembly inside SS bellows using split collar clamping rings.

Table 1: Electrical and Thermal Conductivities

Conductivity	Glidcop (AL-15)	CuCrZr C18150	BeCu C172000
Thermal (W/m.K)	365	320	107
Electrical (%IACS)	92	76-90	22

During installation the RF fingers can be extended by up to 2 mm to compensate for axial gap. Therefore, the temper for Glidcop or CuCrZr is selected for higher elongation at fracture (preferably > 15%) instead of higher ultimate strength. The elongation at fracture can vary from 6% to 30% depending on the shapes (thin sheets to round bars) and temper [7, 8].

The RF-finger spool is integrated in the bellows assembly by split-collar clamping rings (Fig. 3(b)) which can be joined tightly for good electrical and thermal contacts. The two ends of a CuCrZr RF-finger spool can also be directly welded to stainless steel flanges using a process developed at TPS [9].

The design of the RF finger spool and its manufacturing is illustrated in Fig. 4. A hollow pipe of 112 mm length with two grooved ends is first created by machining (drilling and turning in this example). The inside bore of the pipe, ϕ 19 mm, is machined to be 3 mm smaller than the required beam aperture (ϕ 22 mm) for rigidity. The outer profile in the center is made 3.4 mm thicker than the bore providing RF fingers of 0.4 mm thickness. A wire electric-discharge machining (EDM) is used to remove the extra 3 mm thickness of the inside profile. In the same EDM setup the cutting wire is moved in and out radially by 0.4 mm beyond the inside profile, repeating it every 7.2° circumferentially. This leads to 50 fingers of approximately 1.25 mm width at the beam aperture profile. A distinct advantage of this manufacturing approach is that the RF-fingers' profile can be matched to the beam aperture profile of any geometry (e.g., elliptical) without any step discontinuity.

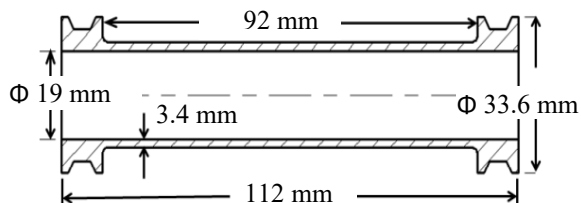


Figure 4 : RF-finger spool before wire EDM cut. EDM enlarges the inside profile by 3 mm and creates 50 fingers of 0.4 mm thickness by radial cuts at 7.2° .

During the bellows assembly process an axial compression of 10 mm is applied to the RF-finger spool. The fingers are guided to bend radially outward by a small inflatable rubber tube placed inside the bore. Residual stresses developed from this initial preset ensure that in subsequent cycles the fingers would bend outward.

FINITE ELEMENT ANALYSIS

An ANSYS finite element analysis was performed for a single flat finger of 72 mm length, 1.25 mm width and 0.4 mm thickness. As shown in Fig. 5, two stiffened ends of 10-mm length were added to represent the ends of the RF finger spool and to apply fixed and displacement boundary conditions (BCs). One of the ends was fixed in all three directions whereas displacement BC was applied to the other end to simulate transverse tolerances, axial gap and compression during bakeout. The analysis included large deformation with stress stiffening and a bilinear elastic-plastic material model with kinematic hardening. An elastic modulus of 125 GPa, yield stress of 350 MPa, Poisson's ratio of 0.3 and tangent modulus of 1,300 MPa were specified based on mechanical properties of CuCrZr at room temperature.

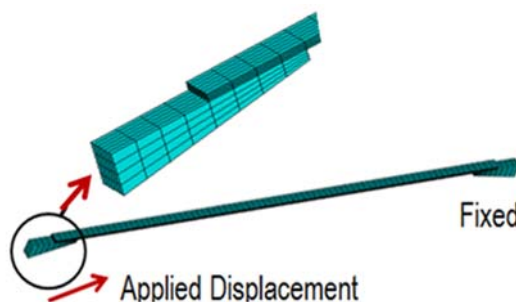


Figure 5: Finite element model of a single RF finger. Displacement BCs are applied to one end representing transverse offset (3mm), axial gap (3mm) and displacement cycles in the range +3 mm to -12 mm.

The analysis was performed for 3 compression cycles. In the first cycle a compressive displacement of 6 mm is applied to introduce preset in the fingers. In the preset cycle itself the buckling direction is imposed by an artificial pressure of 0.03 MPa during the initial 1 mm of compression. The transverse offset of 3 mm and the axial extension of 3 mm are applied after the preset cycle. The applied axial displacement is then changed from +3 mm to -12 mm in the next 2 cycle to simulate compression during bake-outs.

Figure 6 shows transverse deflection of the finger at the center (U_y) versus axial displacement (D_x). Data from an experimental test (described in the next section) for the compression part of the first compression cycle is also plotted showing a good match between the ANSYS and test results. The two curves for the compression cycles are essentially the same. The results show that U_y is several times (~ 5) larger than D_x at the beginning of compression but by the end of compression $U_y = 0.6 D_x$. A maximum U_y of 20.6 mm is obtained at full compression, $D_x = -12$ mm.

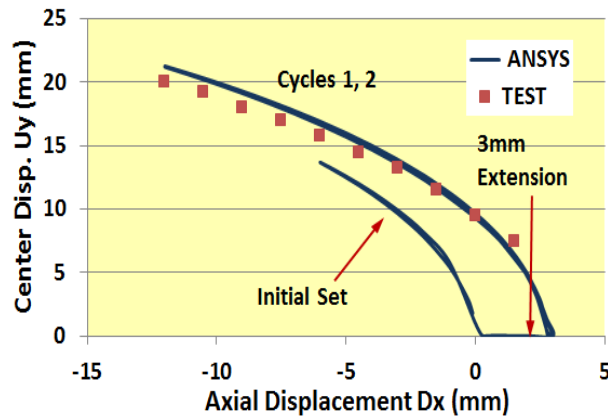


Figure 6: Transverse displacement at the center, U_y , versus applied axial displacement, D_x , for the initial preset cycle, 3 mm extension and 2 compression cycles.

Equivalent stress contours at the end of the first compression cycle are shown in Fig. 7. The equivalent stress is maximum (437 MPa) at the center and is considerable above the yield stress of 350 MPa, which is indicative of large plastic deformation.

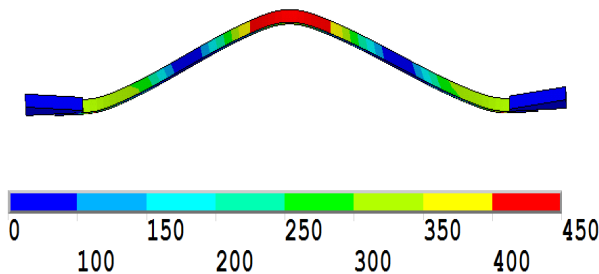


Figure 7: Equivalent stress (MPa) contours at the end of the first compression cycle.

Axial stress and strain at the center (top) are plotted in Fig. 8 starting from 3 mm extension to the end of the first compression cycle. The preset cycle and the second compression cycle are omitted for clarity. In the figure, letters A to F denote the following load excursions: A: 3 mm extension to the nominal position denoted by ●, B+C: buckling at the beginning of compression cycle, D: continued compression, E: extension and F: stress reversal in extension.

Large tensile plastic deformations occur during the 3 mm extension, A, and continued compression beyond buckling. During extension, E, there is elastic unloading followed by a large compressive plastic deformation and then by a tensile reversal which straightens the finger. Axial strain at the nominal position is ~ 4% and the strain range for the compression-extension cycle is 3.3%. In the second compression cycle (not shown) the strain range reduces to 2.69% due to mean stress-strain relaxation.

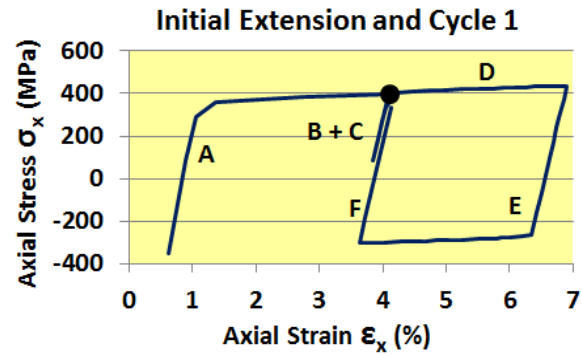


Figure 8: Axial stress versus axial strain at the center-top of the finger for 3 mm extension and the first compression-extension cycle. A: 3 mm extension, B+C: buckling at the start of compression, D: continued compression, E: extension and F: stress reversal in extension.

EXPERIMENTAL TESTS

Experimental tests were performed to determine the low-cycle fatigue life of the RF fingers. Initially the RF fingers were made in a planar geometry for ease of fabrication and testing. Subsequently the tests were repeated on RF finger spools of the geometry shown in Fig. 4.

Planer RF Fingers

The Planer RF fingers were made from 50 mm-thick plates of CuCrZr and Glidcop. Thin plates, of 106 mm x 60 mm size, were first made by wire EDM. The cross-section of the thin plates had a thickness 3 mm larger in the middle than the cross section shown in Fig. 9(a). In the second wire EDM step the extra 3 mm thickness was removed and 0.4 mm deep cuts were made for the fingers (Fig. 9(b)). The test samples of 3 fingers each (Fig. 9(c)) were then cut from the larger sample.

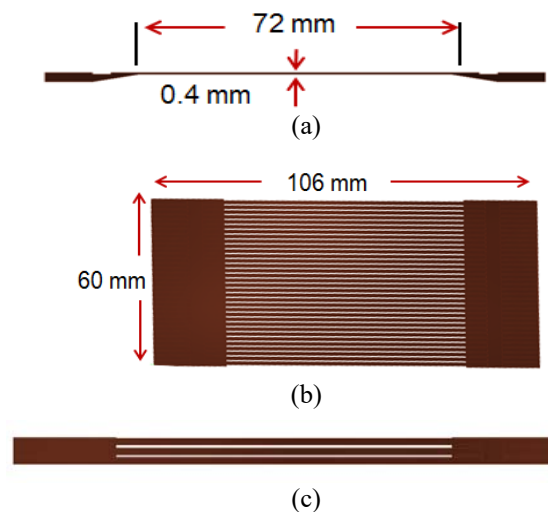


Figure 9: Wire EDM of the RF fingers, (a) cross section of the fingers, (b) fingers in the thin plate, (c) test sample of 3 fingers.

Content from this work may be used under the terms of the CC BY 3.0 licence (© 2018). Any distribution of this work must maintain attribution to the author(s), title of the work, publisher, and DOI.

The test setup for cyclic fatigue testing of the fingers is shown in Fig. 10. Clamping fixtures holding the two ends of the fingers were attached to the two jaws of a precision machine vise. One of the clamping fixtures was adjustable and provided a transvers offset of 2-3 mm. The vise was operated manually to apply compression cycles. A Starrett® dial indicator (0.025 mm resolution) was placed between the jaws to measure the applied displacement. Another dial indicator (not shown) was used for one compression cycle to measure the transverse displacement at the center of the finger.

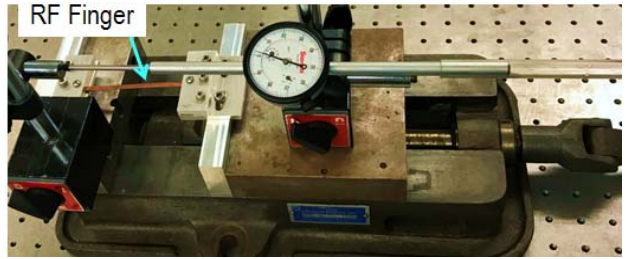


Figure 10: Test setup for cyclic fatigue testing of the RF fingers.

Four test samples, 2 of CuCrZr and 2 of Glidcop were cycled to fatigue failure. All samples had an initial preset compression cycle of 6 mm, a transverse offset of 3 mm and an axial extension of 3 mm. The first CuCrZr and Glidcop samples were guided to buckle upward by a slight application of index-finger pressure. The second CuCrZr and Glidcop samples were guided to buckle downward which is opposite to the direction preferred by the finger geometry.

Table 2 shows number of compression cycles to failure for the 4 test samples with 3 fingers each. Bending in the reverse direction reduced the cycles to failure significantly. In all cases the cycles to failure exceeded the expected number (< 30) of bake-outs of the chambers during the life time of the machine. Glidcop fingers showed a better fatigue life than the CuCrZr fingers. Subsequent tensile tests showed that elongations to failure for the CuCrZr and Glidcop fingers were 7.6% and 11.6%, respectively. A higher elongation to failure, >15%, can be specified with the selection of proper shape and temper of the copper-alloy stock.

Table 2: Compression Cycles to Fatigue Failure

Test Sample	CuCrZr		Glidcop	
	1	2	1	2
Finger 1	130	69	268	208
Finger 2	199	74	288	218
Finger 3	222	158	392	225

Deformed shapes of the fingers for different cycles were almost identical up to a few cycles (~ 10) before failure. In the last few cycles the fingers start separating with kinks appeared at the center. The fingers broke in the

middle except for a couple of cases when they broke at the ends. For the Glidcop sample 1, the normal bent shape (cycle 200) is shown in Fig. 11(a), extended shape at the second finger break (cycle 288) in Fig. 11(b), and the shape at the third finger break (392 cycles) in Fig. 11(c).

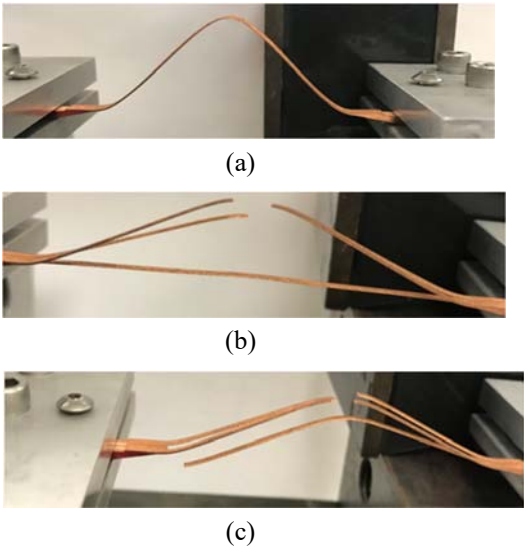


Figure 11: Deformed shapes of the fingers of Glidcop sample 1: (a) nominal bent shape after 200 cycles, (b) extended shape at the second finger break after 288 cycles, (c) shape at the third finger break after 392 cycles.

RF Finger Spools

RF finger spools were tested with the same test setup as described above but with different clamping fixtures. Three spools were tested, one made from CuCrZr and the other two made from Glidcop AL-15. The CuCrZr spool and the first Glidcop spool had 10 mm taper at the top ends of the fingers (see Fig. 12(a)) instead of a 1 mm radius (Fig. 12(b)) used for the second Glidcop spool. Eliminating the taper increased the effective length of the fingers from 72 mm to 90 mm (see Fig. 4).

The CuCrZr spool and its setup experienced two problems. A preset compression of 12 mm (compared to 6 mm for the planer fingers) was applied to ensure that higher residual stresses will result in outward bending in the subsequent compression cycles. The higher compression, however, kinked the fingers in the middle. The aluminium clamping fixtures also turned out to be weak. They distorted when a 2 mm extension was applied causing uneven extension and probably a reduction in fatigue life. Thicker steel clamping fixtures were used for the Glidcop spools and only 10 mm of preset compression was applied. For all three spools a small inflatable tube was used to control the bending direction during the preset compression cycle.

Before compression cycles a 2 mm transverse offset and a 2 mm extension was applied to the spools. Then the spools were cycled at different compression levels. The goal was not only to determine if the fingers could sur-

vive > 30 cycles at 10 mm compression, but also to see if cycles at higher compression levels were possible.

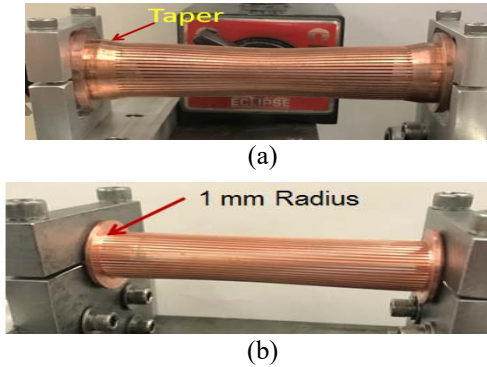


Figure 12: Test setup for the RF finger spools, (a) CuCrZr spool with aluminium clamping fixtures, (b) Glidcop spool with steel clamping fixtures.

There was no noticeable difference in the deformed shapes of the finger spools (see Fig. 13) during most of the cycles. The 10 mm tapers at the ends of the CuCrZr spool and Glidcop #1 spool appeared to keep the deformation symmetric even under the transverse offset of 2 mm. A few cycles before the break of a finger a small kink was usually formed at the failure location.

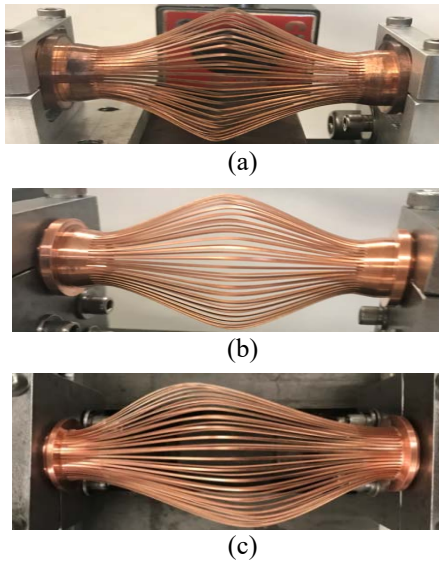


Figure 13: Deformed shapes of the finger spools during cyclic tests at 10 mm compression, (a) CuCrZr spool, (b) Glidcop spool #1, (c) Glidcop spool #2.

The results of cyclic tests are shown in Table 3. Following 30 cycles at 10 mm compression, the first break of a finger of CuCrZr spool occurred after only 8 additional cycles at 12 mm compression. The first finger of Glidcop spool # 1 (70 mm finger length) broke after 132 cycles at 10 mm compression. For Glidcop spool # 2 the first break occurred after a combined number of 137 cycles at different compression levels as follows: 50 cycles at 10 mm, 60 cycles at 12 mm and 27 cycles at 14 mm. The failure of the first finger occurred in the middle for the CuCrZr spool but at one of the ends for the Glidcop spools.

Table 3: Cyclic Tests on the RF Finger Spools – Number of Cycles at First Finger Break

CuCrZr Spool		Glidcop Spool # 1		Glidcop Spool # 2	
Compr. (mm)	Cycles	Compr. (mm)	Cycles	Compr. (mm)	Cycles
10	30	10	132	10	50
12	8			12	60
				14	27

CONCLUSION

A new design of deformable RF fingers with fixed ends and axial extension is presented together with FE analysis and test results. Beam aperture through the RF fingers is continuous without steps. The design is based on large nonlinear deformation including buckling of the RF fingers. The RF finger spool piece is made from high conductivity copper alloys such as CuCrZr and Glidcop. Fabrication of the fingers requires simple machining (drilling, turning and EDM) operations. Cyclic fatigue tests on the RF finger spools show that the typical design requirements of transverse misalignment and axial gap can be met with a good safety margin. The margin is expected to increase further with the selection of a copper-alloy stock and its temper such that the minimum elongation to failure is > 15%.

ACKNOWLEDGMENTS

The authors acknowledge the contributions of our co-workers M. Calderaro, A. DiMauro, J. Mondi, K. Wilson and the support of our Division Director, T. Shaftan.

REFERENCES

- [1] C. Hetzel *et al.*, "Design and Fabrication of NSLS-II Storage Ring Vacuum Chambers and Components", in *Proc. IPAC2012*, New Orleans, Louisiana, USA, January 2012, paper WEPPD026, p2560.
- [2] J. Jones *et al.*, "APS SR Flexible Bellows Shield Performance", in *Proc. PAC99*, New York, USA, 1999, p3095.
- [3] C. Garion, *et al.*, "Development of a New RF Finger Concept for Vacuum Beamline Interconnections", in *Proc. IPAC2012*, New Orleans, Louisiana, USA, January 2012, paper WEPPD017, p2533.
- [4] C. Garion, "Design and Tests of the Shielded Beam Screen", HL-LHC Annual Meeting, Spain (2017). <https://indico.cern.ch/event/647714/timetable/?view=standard>.
- [5] M. Nordby *et al.*, "Bellows Design for PEP-II High Energy Ring Arc Chambers", in *Proc. PAC95*, Dallas, Texas, USA, 1995, p2048.
- [6] Arxiv, <https://arxiv.org/ftp/arxiv/papers/1710/1710.03632.pdf>.
- [7] <http://conductivity-app.org/alloy-sheet/19>.
- [8] <https://www.hoganas.com/en/business-areas/glidcop/>.
- [9] C-C. Chang, "Recent Vacuum R&D in Vacuum Group of TPS" (2017), https://medsi.lbl.gov/NSLS_II_Seminar_Series_Talks-164.html

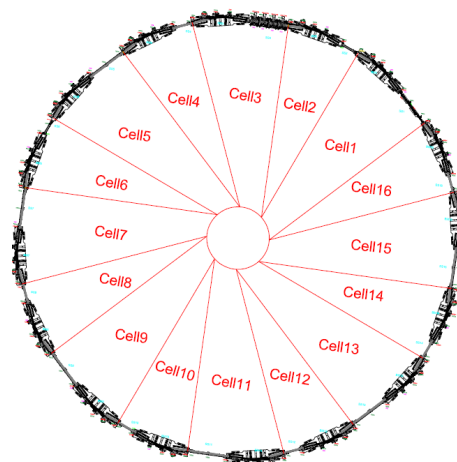
T. Abu-Hanieh, SESAME, P. O. Box 7, Allan 19252, Jordan

SESAME (Synchrotron-light for Experimental Science and Applications in the Middle East) is the first international 3rd generation synchrotron light source in the Middle East region. This paper presents the method used for installing the Storage ring girders, magnets, vacuum chambers, straight sections, and how the alignment was done. The Installation have been done in a short time with few staff. It was hard and difficult but went great.

INTRODUCTION

[illegible]

The storage ring is composed from 16 cells connected with straight sections, as shown in Fig. 3.



Girder length = 5.2m, Flatness error $< \pm 50 \mu\text{m}$, Magnet position error $< \pm 50 \mu\text{m}$. Girder-to-girder position error $< \pm 100 \mu\text{m}$, Girder deflection under load $< 50 \mu\text{m}$.

Table 1: Storage Ring Parameters

TUPH01

20

INSTALLATION STEPS

Floor Preparation

SESAME floor consists of two layers; 22 cm reinforced concrete, and 8 cm solid concrete. In order to avoid the cracks or deformation of the upper 8 cm slab, we decided to remove it, then install the baseplates of girders, and inject epoxy resin that is dedicated for such loads with good stability. Figure 5 shows the baseplates of one girder after alignment and injection of epoxy resin.



Figure 5: Girder Baseplates installed.

Girders Installation

Once the baseplates have been installed and aligned, the girder can be lowered into position. The girder then is surveyed with respect to the local network and its position adjusted as required to enable the vacuum chamber connections to be made. Figure 6 shows one girder installed and aligned on its final location.

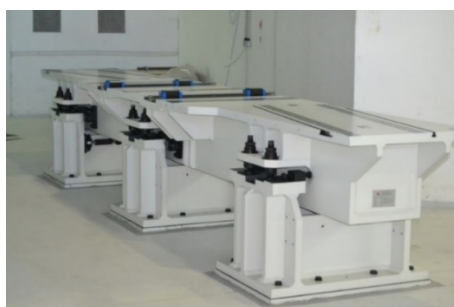


Figure 6: Girder installed on Baseplates.

For aligning the girders, the following Fig. 7 shows the adjusting mechanism.

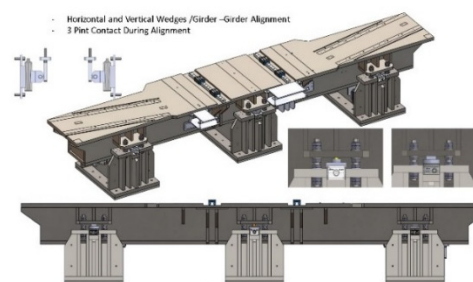


Figure 7: Girder adjusting system.

Magnets Installation

All magnets are magnetically measure, shimmed, and self-aligned on girders with pins. Only girder to girder alignment is required.

We have started by installing the dipole bending magnet, Fig. 8.



Figure 8: Dipole Bending Magnet.

Then, sextuples and quadrupoles are installed, Fig. 9.



Figure 9: Magnets installed on Girder.

Vacuum Chamber Installation

For installing the vacuum chamber, upper half of multi-poles is removed, as shown in Fig. 10.

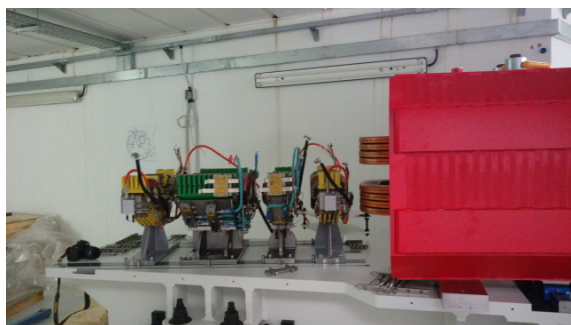


Figure 10: Multipoles upper half removed.

Then, the dipole is raised on rails and pushed back as described in Fig. 11 below.

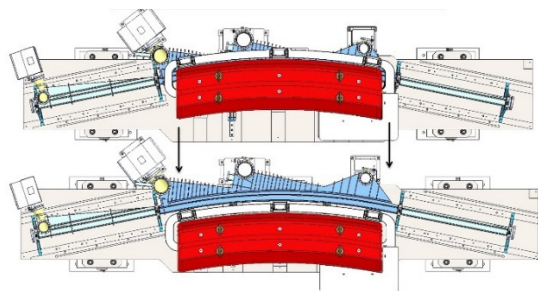


Figure 11: Pushing the dipole out.

Now, the system is ready to have the vacuum chamber, where it is installed using a skeleton with the crane as shown in Fig. 12.

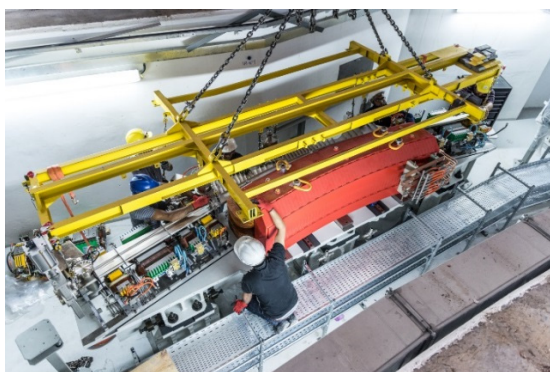


Figure 12: Installing Vacuum Chamber.

Finally, the dipole is pulled back to its location, and the upper half of multipoles is assembled again. Now, a final alignment girder to girder is done, and a survey of all magnets was succeeded. The 16 cells are ready to be connected with the straight sections. Figure 13 shows a complete aligned cell.



Figure 13: One Complete Cell.

CURRENT STATUS

Storage ring is fully installed and commissioned, Fig. 14. Two beamlines are commissioned, other beamlines are foreseen. A plan for full energy injector is under investigation.



Figure 14: Fully Installed Storage Ring.

CONCLUSION

The commissioning trials of the machine started with the conditions of good alignment. After a few days of injection trials, it was possible to circulate and accelerate the beam. The successful circulation and acceleration of beam verifies the great installation and alignment with no gross error in alignment.

SESAME is now passing from the stage of construction to the phase of exploitation. A number of technically oriented scientists and engineers participated actively in the design and construction of the facility and this provides a valuable stock of professionals when some of the Members will build their own SR facilities.

ACKNOWLEDGEMENTS

We are highly thankful to the collaboration between SESAME and CERN through CESSAMag project; which provides continuous support and coordination of design, tender, production, measurement, installation and alignment activities along during critical period.

REFERENCES

- [1] SESAME website: www.sesame.org.jo

COLLIMATOR FOR ESRF-EBS

J. Borrel*, Y. Dabin, F. Ewald, P. Van Vaerenbergh, ESRF, Grenoble, France

Abstract

The function of the Collimator is to localize the majority of the electron losses in the ESRF-EBS storage ring (SR). In addition, the Collimator of the ESRF-EBS should absorb about 1200 W of synchrotron radiation. For ESRF-EBS, the electron losses due to intra bunch scattering (Touschek scattering) will be higher than in the current ESRF SR. To limit the level of radiation outside the storage ring, and the activation level of the vacuum chambers, it is more efficient to localize the electron losses and block the radiations at one place rather than reinforce all of the SR tunnel shielding. Once the collimator is put on line with the electron beam at nominal intensity, it will no longer be possible to intervene on it (due to the activation of the materials). As a consequence, a high level of reliability is required.

The design takes into account all the diverse requirements from a safety, accelerator physics, thermal and mechanical point of view.

INTRODUCTION

The ESRF-EBS storage ring is very different with the previous one. Electron losses from intra bunch beam scattering is higher. This is the reason to introduce a Collimator to localize the majority of electron losses in two places, surrounded by a heavy concrete block.

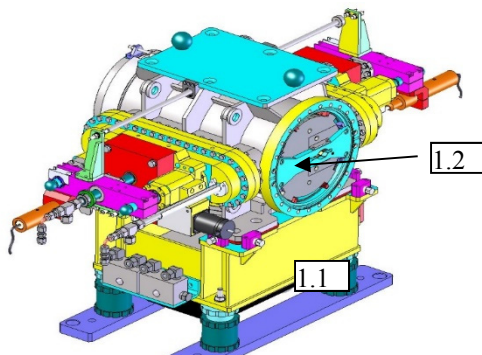


Figure 1: Collimator General assembly.

DESCRIPTION

As shown in Figures 1 to 3, the ESRF-EBS Collimator is composed of: the vacuum chamber and its support (1.1), the inner fixed shielding (1.2), fixed blades (2.1) and movable blades (2.2), its motorization (3.1) and the guiding system (3.2). In addition, concrete fixed shielding (Fig. 10) is placed around the collimator to absorb radiations outside

the collimator vacuum chamber. This paper will only describe the Collimator itself (Fig. 1). The ESRF-EBS Collimator is designed to have a 300 mm active length with a 15 mm fixed aperture in the vertical and 12 mm (+/-2 mm) adjustable aperture in the horizontal plane. The maximal horizontal opening is 32 mm.

At the entrance and at the exit of the Collimator there are "RF fingers" (Fig. 4.1). Their specific shape makes the transition between the omega internal shapes of the ESRF-EBS high profile chamber and the square shape of the Collimator inner section (Fig. 2).

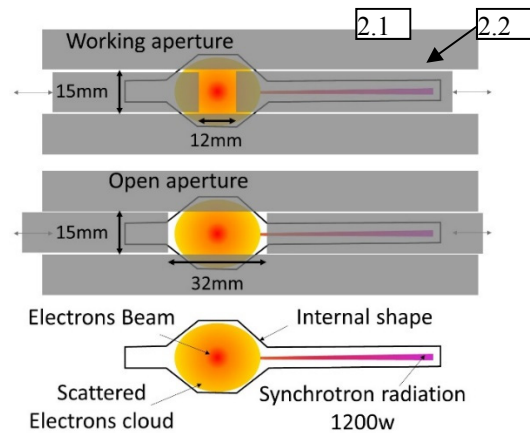


Figure 2: section of the collimator blades in two positions: the working position and fully open.

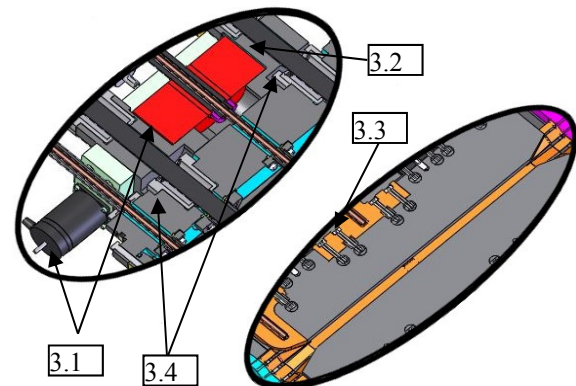


Figure 3: Details of internal view in horizontal cut.

Inside the collimator there is an absorber (Fig. 4.2) to stop the synchrotron radiation from the upstream dipoles. This absorber is made in "Glidcop Al 15©" with cooling in a concentric shape.

In order to adapt the shape of the horizontal blades as smoothly as possible, there is a 30mm taper at each end of the horizontal blades.

In addition to the blades (fixed and movable), there is a fixed shielding (Fig. 8) in the vacuum chamber to block the radiation from the scattering of the electrons absorbed by the Inermet IT180 blades.

* Email address: borrel@esrf.fr

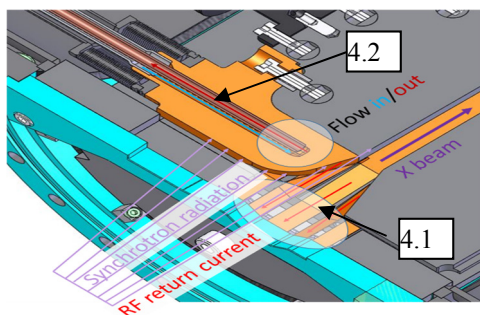


Figure 4: Detail of the entrance of the Collimator.

DESIGN

The design of the movable blade, exposed to synchrotron radiation, was critical. At the initial stage of the study, tungsten was envisaged as a material able to absorb the radiation. Nevertheless, the integration of a cooling circuit in the tungsten blade is by no means trivial and the results were not conclusive (Figs. 5 and 6). In addition, water connection was not possible. The most suitable solution was to split the function of radiation and electron absorber. The last thermal calculation shows that maximum temperature will be 186°C for Glidcop (Fig. 7) instead of 360 °C or 300 °C for Inermet.

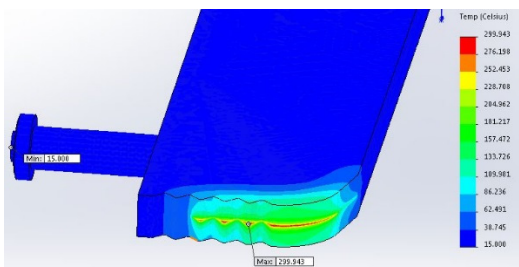


Figure 5: Example of FEA calculation W absorber.

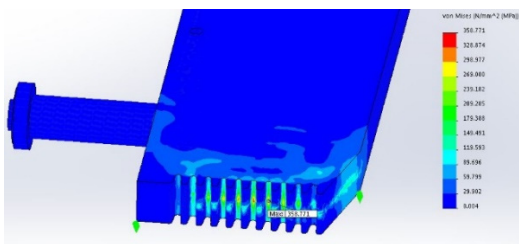


Figure 6: Example of FEA calculation W absorber.

In the final version, the temperature calculated for the surface in contact with water is still relatively high (88 °C, Fig. 7), but it is the lowest result obtained from a series of scenarios.

The final shape of the absorber is flat (Fig. 7). Initially, a shape with teeth was envisaged to enlarge the projected surface in contact with the radiation but this implied moving the cooling channel in the absorber further away from the exposed surface. An additional cooling circuit was added in the middle of the blade (Fig. 3.3) to cool the

longitudinal surface as well in order to achieve a better average temperature of blade.

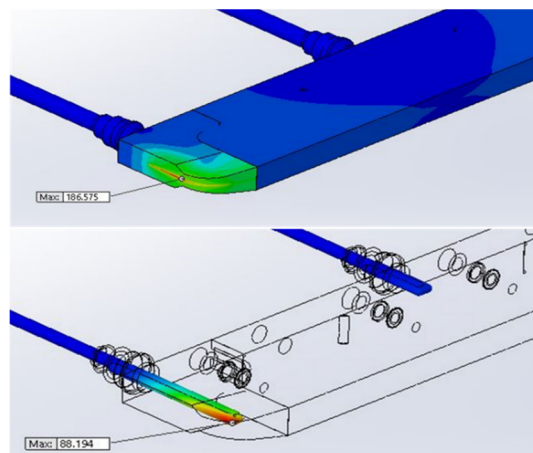


Figure 7: Final FEA calculation.

The material chosen for the collimator blades, and for the fixed shielding, is Inermet© IT180 manufactured by Plansee (Fig. 8); a solution inspired by the CERN-LHC Collimator [1]. This material has very good mechanical and thermal properties, with thermal conductivity rather close to pure tungsten (110 W/m.°C as compared to 160 W/m.°C), it is non magnetic and density is very high (18 kg/dm³- 19.3 for pure W) which has major advantages for absorbing electrons and scattering radiations from absorbed electrons. The calculation made by the ESRF Safety Engineer shows that only high energy (gamma range) radiations can pass through the collimator.

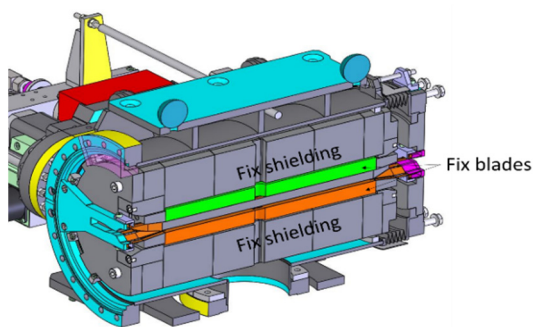


Figure 8: Vertical cut through the collimator: fixed shielding (grey) and fixed vertical blades (green, orange).

To guarantee high level movement of the adjusted blade, out-of-vacuum recirculating ball bearings guided the bars holding each blade (Fig. 3.4). The blade movement system is motorised by stepper motors and a non-reversible gear box (Fig. 3.1). Guides and motorization are fixed to the reference flange to enable consistent metrology phases to be set prior to assembly. There is also an anti-collision system to prevent contact between the two movable blades. An LVDT sensor controls the position of each blade.

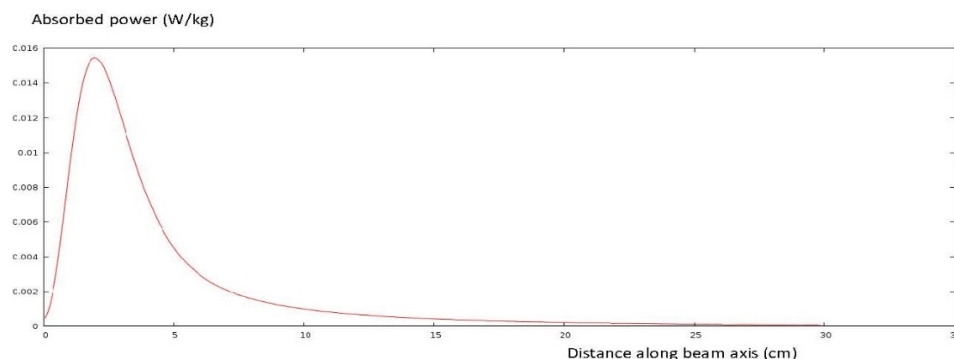


Figure 9: Absorbed dose distribution as a function of the longitudinal distance from the entrance face of the collimator.

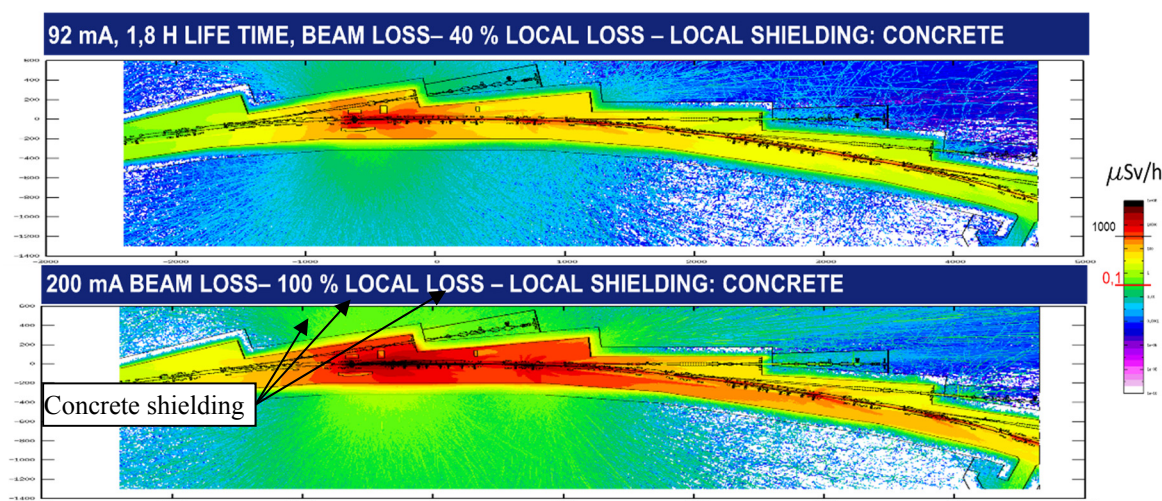


Figure 10: Radiation emission of the Collimator.

SAFETY

The Collimator is a safety apparatus designed to reduce the level of radiation outside the storage ring tunnel as much as possible. The collimator also makes perturbations on the electron beam. The Collimator inner aperture should be adjusted to perturb the electron beam as little as possible but to absorb as many scattered electrons as possible. Figure 9 shows how electrons are absorbed by 300 mm of Inermet IT180. Figure 10 shows how the radiation is absorbed in the storage ring tunnel in two cases: normal operation at 90mA and beam lost on Collimator at 200 mA. In both cases, the simulation shows that maximum radiation level is less than 0.1 mSv/h outside of the storage ring tunnel, thus respecting the safety criteria.

CONCLUSION

Two units of the Collimator will concentrate about 80% of the total electron losses of the ESRF-EBS storage ring in two dedicated and shielded areas of the storage ring. This reduces activation in the rest of the storage ring, which is obviously important from a radiation safety point of

view. But also, other storage ring equipment will benefit from this protection. The collimator is a complicated device due to the different requirements concerning the stopping of 6 GeV electrons, absorption of synchrotron radiation, reliability, and very limited available space. The ESRF design accommodates all of these requirements but will still have to prove its expected performance during the ESRF-EBS commissioning in 2020.

ACKNOWLEDGEMENTS

Special acknowledgements to the main contributors to the project: P. Berkvens, J. C. Biasci, L. Goirand, H. Pedroso-Marques, and R. Versteegen from ESRF France, C. Malosse and P. Tardieu from ASERCAO France and M. Izaguirre and P. Nogera from AVS Spain.

REFERENCES

- [1] M. Cauchi *et al.*, "Thermomechanical response of Large Hadron Collider collimators to proton and ion beam impacts", *Phys. Rev. ST Accel. Beams*, vol. 18, iss. 4, April 2015, doi:10.1103/PhysRevSTAB.18.041002.

U15 DESIGN AND CONSTRUCTION PROGRESS

F. Briquez, C. Arrachart, N. Baron, N. Béchu, P. Berteaud, F. Blache, C. Bourgoïn, M.-E. Couprie, J. Da Silva Castro, C. De Oliveira, J.-M. Dubuisson, J.-P. Duval, C. Herbeaux, F. Lepage, A. Lestrade, F. Marteau, A. Mary, F. Michel, S. Morand, M.-H. Nguyen, A. Rouquié, M. Sebdaoui, G. Sharma, K. Tavakoli, M. Tilmont, M. Valléau, M. Vandenberghe, J. Vétéran, Synchrotron SOLEIL, Gif-sur-Yvette, France.

Abstract

A 15 mm period PrFeB Cryogenic Permanent Magnet Undulator (CPMU) is under construction at SOLEIL, relying on the experience gained from the two PrFeB CPMU already installed at SOLEIL [1, 2]. The improved design includes a magnetic length of 3 m and a minimum gap of 3 mm, leading to a polyvalent device of interest for both synchrotron radiation sources and free electron lasers. A dedicated magnetic measurement bench is also under development to perform measurements at cryogenic temperature, based on the SAFALI system. The designs of both undulator and measurement bench will be explained, the construction progress will be detailed and first results will be given.

INTRODUCTION

The SOLEIL synchrotron light source has been in operation since 2006. 27 insertion devices are installed, including 4 electromagnetic undulators [3, 4], 12 APPLE-II ones [5], 8 in-vacuum ones [6], 2 wigglers [7, 8] and one EMPHU-type device [9]. Two of the in-vacuum devices are cryogenic U18 undulators and a third device of the same type was built and installed at the COXINEL experiment [10, 11], which is part of the LUNEX5 project [12]. A fourth CPMU is under construction in the frame of a collaboration agreement with the MAX-IV laboratory. This U15 undulator is called a cryo-ready one since it can be used at both cryogenic and room temperatures, thanks to the high coercivity material used for the permanent magnets. This particularity leads to a polyvalent device of interest for both synchrotron light sources and Free Electron Lasers. A view of the whole device design is shown in Figure 1.

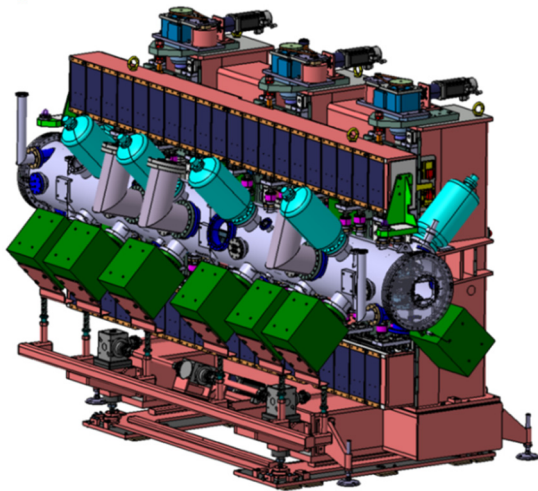


Figure 1: Design of the fully equipped U15 undulator.

MAIN PARAMETERS

The U15 design can be seen as an improvement of the SOLEIL U18 CPMU one since it is longer, has a reduced period, and can reach a smaller gap. The main parameters of both CPMU are compared in Table 1. With these characteristics, U15 has twice periods as compared to U18, leading to a higher radiated flux. By decreasing the period and increasing the peak field, one enlarges the wavelength range of the light emitted by the device.

Table 1: U15 Main Parameters Compared To U18 Ones

Parameter	U15	U18
Length (m)	3	2
Period (mm)	15	18
Min. gap (mm)	3	5.5
Max. field @77 K (T)	1.35	1.15
Nb. Periods	200	100

MAGNETIC DESIGN

The magnetic structure is a hybrid one with poles made of Vanadium Permendur and permanent magnets made of Pr₂Fe₁₄B (CR53 grade). As this material does not experiment Spin Reorientation Transition phenomenon [2], it is thus possible to cool down the magnets directly at liquid nitrogen temperature with no remanent field reduction, leading to a quite simple thermal scheme [13]. The magnetic system characteristics are given in Table 2.

Table 2: U15 Permanent Magnet Properties

Parameter	Value
Remanent field @293 K (T)	1.32
Remanent field @77 K (T)	1.55
H _{cB} @293 K (kA/m)	1016
H _{cJ} @293 K (kA/m)	1906
Pole dimensions (mm)	33x26x1
Magnet dimensions (mm)	50x30x5.5

UNDULATOR MECHANICAL DESIGN

The general design is based on the usual SOLEIL CPMU concept: the jaws are made of extruded aluminium parts which are drilled all along, enabling the liquid nitrogen to flow directly in the material and obtain an efficient magnet cooling. The main element designs are very similar between the two undulators, once taken into account the higher length of the device and the stronger magnetic force between the jaws, which is expected to reach 10 t. In order to support this strength, the carriage includes 3 motorized axes rather than 2. Moreover, the design also offers the possibility to generate a 1.5 mm taper, which can be very useful, especially for FEL operation.



Figure 2: View of the tooling used to install the girders inside the vacuum chamber.

The main difficulty of the 3 m length consists in managing the 12 mm jaw contraction at 77 K, which results in a 6 mm displacement of the extremity rod linking the in-vacuum jaw and out-vacuum carriage girder. This displacement effect on the bellow is minimized by positioning the rod always off-axis, in the range ± 3 mm according to the temperature. In addition, very tight mechanical tolerances are needed on both jaw and vacuum chamber machining operations to guarantee the correct positioning of the rods through the chamber apertures.

Another consequence of the increased force and length lies in the difficulty of every handling operation, especially the one which consists in inserting the equipped jaws inside the vacuum chamber. A dedicated tooling was constructed to operate such an operation, which needs a 8 m available length when the chamber is aligned with the jaws, as shown in Figure 2.

The holding system of the magnetic elements consists of a simple module type with one magnet inserted between two half-poles, in order to facilitate the magnetic assembly operation. The design of the holders, shown in Figure 3, was improved to minimize deformation and to make it possible to insert thermal sensors after the device assembly, without disassembling the module.

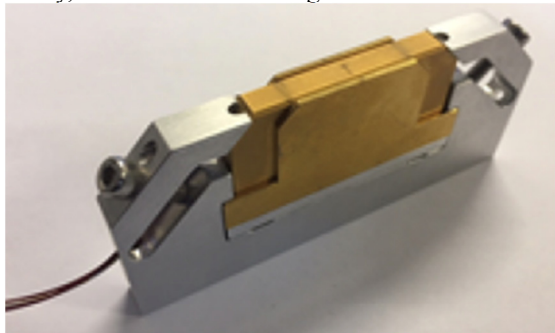


Figure 3: Photo of one module equipped with a thermal sensor.

BENCH MECHANICAL DESIGN

In order to characterize the magnetic field generated by the undulator at low temperature, a dedicated measurement bench is under construction, consisting of a Hall effect probe and a stretched wire system.

Whereas the wire system is very close to the U18 one [1], the Hall effect probe system takes advantage of our experience gained with the U18 bench, especially in the improvement of the holding structure, the guiding mechanical design and the choice of ultra-vacuum compatible elements. Figure 4 illustrates the probe guiding system improvement performed by utilizing twice rails and bearings compared to the previous design.

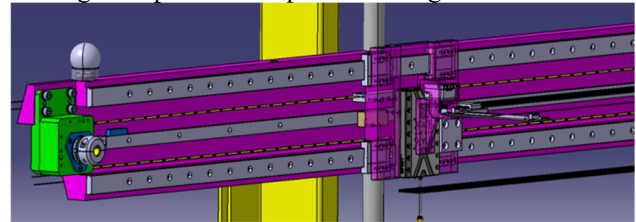


Figure 4: Design of the Hall effect probe bench: girder, sliding carriage, piezo motors and probe holder.

Moreover, it will be possible to operate measurements off-axis in order to get the contribution of each jaw on the on-axis field, and to reconstruct the longitudinal distribution of the skew quadrupole.

Because it is difficult to position precisely the probe in a 3 mm gap along 3 m, a transverse position feedback will be implemented in a comparable way as the SAFALI system [14], thanks to a laser pointing through a pinhole fixed on the probe holder, and received by a PSD placed at the other extremity of the undulator. The scheme of this system is shown in Figure 5.

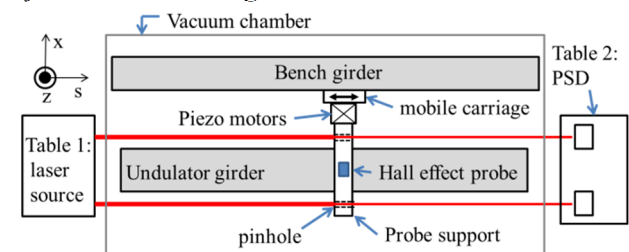


Figure 5: Scheme of the probe transverse position feedback system.

Finally the probe holder is also considerably improved: it will be made of ceramic to assure good tolerances and will operate a temperature regulation.

CONSTRUCTION PROGRESS

Difficulties were encountered to provide the vacuum chamber and the jaws, mainly explained by the increased length and the tight tolerances. All the undulator elements were constructed and most of them assembled. In order to minimize the magnet height variation along the device, every magnet and holder was mechanically measured and these elements were matched by sorting when assembling the modules. The poles were also shimmed, leading to standard deviation on module height of $19\text{ }\mu\text{m}$, as shown in Figure 6.

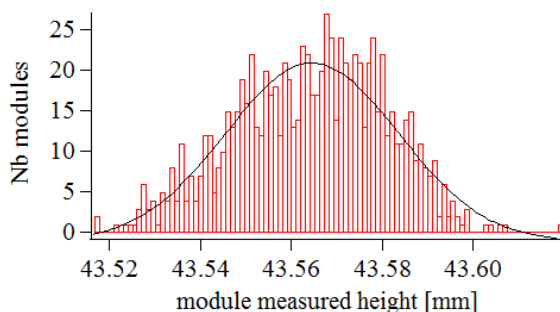


Figure 6: Height distribution of the modules.

The magnetic characterization of every module shows that there is no systematic magnetic effect on the magnets, which means no huge difficulty should be encountered during the undulator magnetic assembly.

A fake assembly of the jaws on the carriage was performed to test their positioning reproducibility, which was measured of $200\text{ }\mu\text{m}$. A photo of this positioning test is given in Figure 7.



Figure 7: Jaw assembly reproducibility test.

A fake assembly of the carriage, jaws and vacuum chamber is under progress in order to anticipate any mismatch due to wrong machining or any vacuum leakage, since it is easier to solve such a problem now, rather than when the device is magnetically assembled. Figure 8 shows a view of the fake assembly before cooling down.

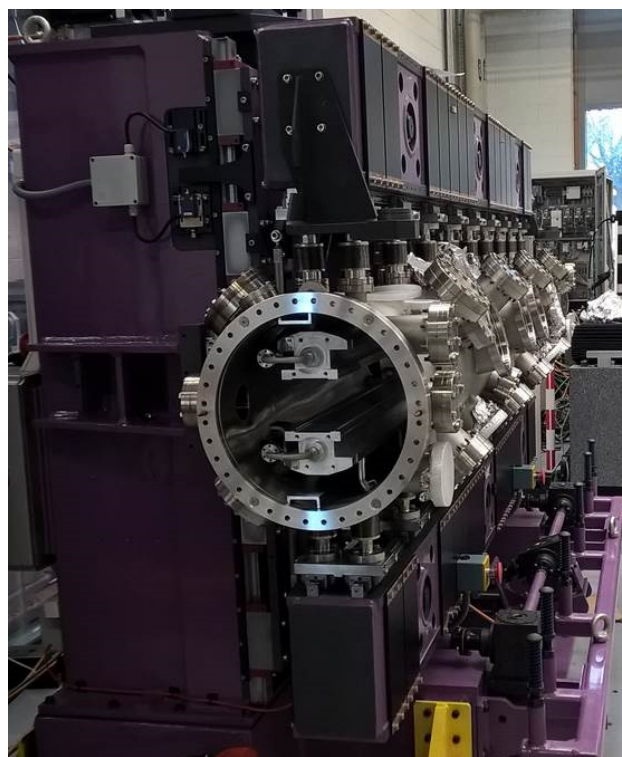


Figure 8: Undulator after fake assembly at room temperature.

Once this checking step is completed, the undulator magnetic assembly will start.

ACKNOWLEDGEMENTS

The authors would like to thank the ultra high vacuum group, mechanical workshop and alignment group people for their precious help during the different assembly tests.

U15 was developed in the frame of a collaboration agreement between SOLEIL and MAXIV laboratories.

REFERENCES

- [1] C. Benabderrahmane *et al.*, “Development and operation of a $\text{Pr}_2\text{Fe}_{14}\text{B}$ based cryogenic permanent magnet undulator for a high spatial resolution x-ray beam line”, in *Phys. Rev. Spec. Top. Accel. Beams*, vol. 20, pp. 033201, 2017.
- [2] C. Benabderrahmane *et al.*, “ $\text{Nd}_2\text{Fe}_{14}\text{B}$ and $\text{Pr}_2\text{Fe}_{14}\text{B}$ magnets characterisation and modelling for cryogenic permanent magnet undulator applications”, in *Nucl. Instr. Meth. Phys. Res. A*, vol. 669, pp. 1-6, 2012.
- [3] O. Marcouillé *et al.*, “Design, construction and magnetic measurements of the HU640 (OPHELIE2) undulator dedicated to the DESIRS VUV beamline at SOLEIL”, in *AIP Conf. Proc.*, vol. 879, pp. 311, 2007.
- [4] I. Churkin *et al.*, “Elliptical Undulator HU256 for Synchrotron Soleil: Magnetic Design, Computations and Measurements”, in *IEEE Trans. Appl. Supercond.*, vol. 16, no. 2, pp. 1852-1854, 2006.
- [5] C. Kitégi *et al.*, “Development of a short period high field APPLE-II undulator at SOLEIL”, in *Proc. 1st Int. Particle Accelerator Conf. (IPAC'10)*, Kyoto, Japan, May 2010, paper WEPD008, pp. 3099-3101.

- [6] F. Marteau *et al.*, “Development and installation of insertion devices at SOLEIL”, in *Proc. PAC’09*, Vancouver, Canada, May 2009, paper WE5RFP080, pp. 2453-2455.
- [7] O. Marcouillé *et al.*, “In vacuum permanent magnet wiggler optimized for the production of hard x rays”, in *Phys. Rev. Spec. Top. Accel. Beams*, vol. 16, pp. 050702, 2013.
- [8] O. Marcouillé *et al.*, “W164: a wiggler dedicated to the PUMA beamline and the femtoslicing project at SOLEIL”, in *Proc. IPAC 2014*, Dresden, Germany, Jun. 2014, paper WEPRO027, pp. 1998-2000.
- [9] F. Marteau *et al.*, “The 65 mm period electromagnetic/permanent magnets helical undulator at SOLEIL”, in *Proc. IPAC2011*, San Sebastián, Spain, Sept. 2011, paper THPC151, pp. 3239-3241.
- [10] T. André *et al.*, “Control of laser plasma accelerated electrons for light sources”, in *Nature Commun.*, vol. 9, 1334, 2018.
- [11] M. E. Couprie *et al.*, “An application of laser plasma acceleration: towards a free-electron laser amplification”, in *Plasma Phys. Control. Fusion*, vol. 58, pp. 034020, 2016.
- [12] M.-E. Couprie *et al.*, “The LUNEX5 project in France”, in *J. Phys.: Conf. Ser.*, vol. 425, no. 7, pp. 072001, 2013.
- [13] T. Hara *et al.*, “Cryogenic permanent magnet undulators”, in *Phys. Rev. Spec. Top. Accel. Beams*, vol. 7, no. 5, pp. 050702, 2004.
- [14] T. Tanaka *et al.*, “In situ correction of field errors induced by temperature gradient in cryogenic undulators”, in *Phys. Rev. Spec. Top. Accel. Beams*, vol. 12, pp. 120702, 2009.

PROGRESS ON THE FINAL DESIGN OF THE APS-UPGRADE STORAGE RING VACUUM SYSTEM

J. Carter, B. Billett, B. Brajuskovic, M. Lale, A. McElderry, J. Noonan, M. O'Neill, K. Wakefield, D. Walters, G. Wiemerslage, J. Zientek, Argonne National Laboratory, Lemont, IL, USA

Abstract

The final design phase is underway for the APS-Upgrade project's storage ring vacuum system. Many aspects of the design are being worked on to address challenging interfaces and to optimize vacuum system performance. Examples of recent work include updates to ray tracing and vacuum analysis, new developments in vacuum chamber and photon absorber design, and further refinement of vacuum pumping plans to achieve the best possible pressure distributions. Recent R&D work and results from a vacuum system sector mockup have also informed designs and installation plans. An overview of progress in these areas and remaining challenges is presented.

APS-U VACUUM SYSTEM REQUIREMENTS

The APS-Upgrade will retrofit the existing 1.1 km circumference APS storage ring with a new 6 GeV, 200 mA storage ring optimized for brightness above 4 keV. The scope of the APS-U storage ring vacuum system design group includes the vacuum system and component design of 40 sector arcs as shown in Figure 1 and 5x specialty 'Zone F' straight sections. The goal is to install and commission the new ring with only one year of down time for the users and to condition vacuum to 2 nTorr average pressures at 200 mA beam current by 1000 A*hrs conditioning time.

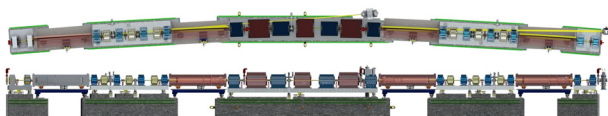


Figure 1: One 22 meter length sector of APS-U storage ring (excludes straight section).

The new storage ring design pushes magnet poles close to the electron beam and calls for narrow vacuum chambers, typically with a 22 mm inner diameter and 1 mm wall thickness. This is a substantial reduction from the previous APS design with an 84 mm wide x 42 mm tall elliptical aperture, see Figure 2 for comparison. A standard, 22 meter length arc of the vacuum system (not including straight sections) will include 27x custom vacuum chambers, 14x BPMs, 2x gate valves, 6x photon absorbers, 3x gauges, and photon extraction chambers. Of the 27x vacuum chambers, 19x will be round and NEG coated, 2x are keyhole, 2x vacuum crosses, and 4x are extruded aluminum 'L-bend' chambers. In total, 11.2 meters of the 22.1 meter length will be NEG coated.

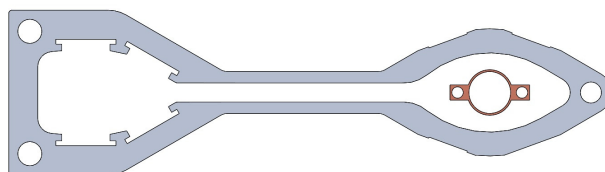


Figure 2: Cross section comparison of current APS-style vacuum chamber to new APS-U-style chamber.

INTERFACES

The APS-U vacuum systems are designed around careful interfaces with the needs of APS-U physics, magnets, and more. Vacuum components, flange seals, and absorbers must minimize impedance losses through the use of subtle transitions and reliable rf seals. The magnet's quantities, spacing, and narrow pole gaps drive thin walled vacuum chamber designs with narrow spaces to seal flanges and rout cooling water. Figure 3 demonstrates narrow installation and maintenance access between magnets to a compact BPM housing assembly. The vacuum system is also designed around numerous internal interfaces. Photon absorbers, both mounted and compact 'inline' style, are used to shadow and protect uncooled components such as BPM's, flange joints, and gate valves.



Figure 3: Narrow access between magnets to a compact BPM assembly demonstrated on a mockup.

VACUUM SYSTEM ANALYSIS

Ray tracing and vacuum analyses are performed using both 2D and 3D tools to understand and improve the limits of the vacuum system and to ensure design requirements are met. An analysis of vacuum pressures using programs like VACCALC for 2D models and MolFlow+ for 3D models helps predict the pressure profile through a hybrid pumping system. A standard arc pressure profile at 1000 A*hrs conditioning is shown in Figure 4. Pressures are typically low where distributed pumping is incorporated and

high pressure bumps are found across conductance limited, small vacuum apertures. APS-U's vacuum analysis helped inform the decision to increase the preliminary design NEG coating scope from just the FODO section to now all round vacuum chambers. This is to reduce pressures across the arcs, build margin for developing straight section vacuum designs, and speed up vacuum system conditioning.

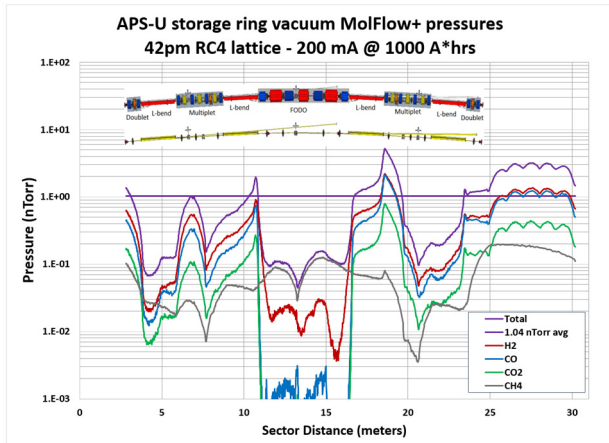


Figure 4: MolFlow+ analysis of standard arc vacuum system pressures at 200 mA, 1000 A*hrs conditioning.

Ray tracing reveals 'hot' zones in the vacuum system including the FODO section (1 kW/m) and B-Quad Doublet (700 W/m) where copper chambers are needed to absorb synchrotron loads. The B-side crotch absorber intercepts 3.4 kW, the most of six absorbers, with the A-side crotch next at 1.1 kW. Ray tracing is performed using 2D layouts and also new 3D tools which reveal missteering possibilities for conservative thermal analysis and have helped inform BPLD limits to protect narrow straight section chamber apertures.

VACUUM R&D

A major R&D activity for vacuum has been the construction of a mockup of one full standard arc of storage ring vacuum system components, see Figure 5. Manufacturing and assembly was completed in the Fall of 2017 and represent the vacuum system at the conceptual design level. Numerous tests are being informed on the mockup including pump down and NEG activation, validating vacuum gage readings to simulations, and water-flow induced vibration testing.

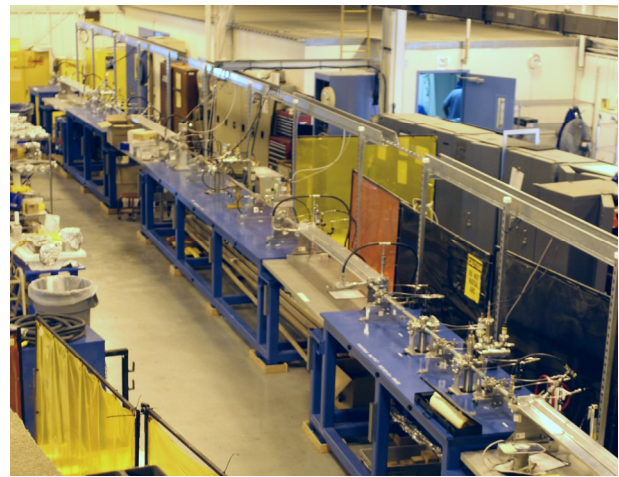


Figure 5: Full sector mockup of one standard arc of storage ring vacuum system components at conceptual design level, Fall 2017.

Water flow tests helped build confidence that turbulent flows can be used to cool irradiated vacuum chambers without transmitting significant vibrations through the bellows and onto BPMs. NEG activation tests helped build a recipe for activating NEG coated components in the presence of non-coated crosses and chambers. This also helped inform to remove 2x gate valves (of 4x total) originally designed to isolate the NEG coated FODO chambers. Remaining R&D activities include in-ring testing of new BPM button and housing designs.

FINAL DESIGN OF VACUUM COMPONENTS

APS-U's storage ring vacuum system is in its final design phase through early 2019. A standard arc's set of vacuum chambers will be manufactured from four separate common UHV materials and with respect to the total length per 22.1 m sector there will be 55% aluminium chambers (8 chambers, 12.1 m), 27% copper (7 chambers, 6.1 m), 9% Inconel (4 chambers, 2.0 m), and 9% 316 stainless steel (4 chambers + BPMs and Gate Valves, 2 m). Common chamber designs are compared in Figure 6. Aluminum chambers will include bent and extruded L-bend chambers with antechambers and also straight round tube-style chambers and integrated crosses. Copper chambers will be used when radiation loads across chamber walls are too hot for aluminum and are primarily round with some featuring slight bends. Stainless steel is used for keyhole and simple pumping crosses. Inconel will be used for tube chambers passing through 8-pole 'fast corrector' magnets where a low magnetic permeability is required.



Figure 6: Rendering of standard vacuum chamber designs (top) aluminum round chamber, (middle) aluminum vacuum cross, (bottom) copper round chamber.

Both the stability requirements for beam position monitors (BPMs) and their quantity, 14x per sector, dictate many of the challenges across the vacuum system design. APS-U BPMs must keep signal drift below 2 microns and vibrations less than 400 nm rms so a central housing with two bellows decouples the BPM button's from chamber motions. The quantity of both BPMs and magnets leads to narrow installation and maintenance access typically between 100-150 mm. The compact 74 mm length BPM design saves space on all parts of the length by using welded BPM buttons, compact bellows with +/- 5 mm travel, and Quick CF (QCF) flanges. The quantity of independent BPMs also drives the count of 44 flange joints per sector along the electron beam path.

APS-U requires that magnets should not need to be split during maintenance. This drives the decision to put rf-liners onto the removable BPM housing assembly and off of vacuum chambers whose relative simplicity should allow them to remain permanently between magnets. Figure 7 shows a cross section of the BPM assembly featuring an internal rf liner assembly which shields the bellows and includes a glidcop liner with fingers compressed by a stainless steel spring.

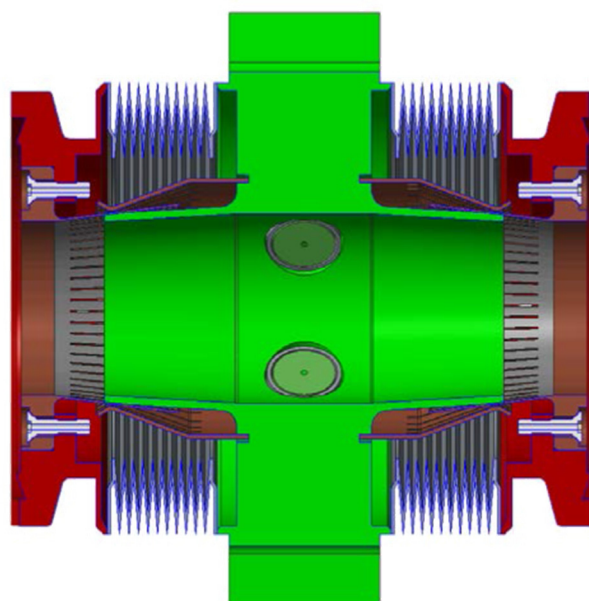


Figure 7: Cross section of compact BPM housing design with BPM buttons, GlidCop fingers, and two bellows all welded to a central stainless steel housing.

FUTURE WORK

APS-U vacuum will complete R&D by the end of 2018 and continue through final design of all vacuum components through early 2019. Some of the major design challenges ahead include two keyhole shaped BPM designs and developing and testing a robust, compact rf seal design for both round and keyhole flange joints. Manufacturing of production level components will run from 2019-2022. Pre-assembly of vacuum/magnet/support modules will happen from 2021-2022 followed by final assembly and installation in the tunnel and commissioning from 2022-2023.

ACKNOWLEDGMENT

Argonne National Laboratory's work was supported by the U.S. Department of Energy, Office of Science under contract DE-AC02-06CH11357.

DESIGN OF A RADIATION TOLERANT, INDEXING PROFILE MONITOR FOR THE LCLS ELECTRON BEAM*

A. Cedillos[†], R. Clive Field, SLAC National Accelerator Laboratory, 94025 Menlo Park, CA, USA

Abstract

The Linac Coherent Light Source (LCLS) electron beam can damage YAG:Ce scintillation screens. After one year of use, the existing profile monitor has diminished fluorescence of the screen. The decrease in performance has resulted in distorted beam images which can compromise the acquired data. Scheduling a YAG screen replacement is difficult, resulting in weeks of diminished performance. We have developed a unique profile monitor that incorporates multiple YAG screens (Ø40 mm, 50 µm thick) and methods to reduce device downtime. This device uses unique geometry to direct coherent optical transition radiation (COTR) away from the optical path, which preserves the high resolution beam image. We are presenting the operational requirements, device design and installed device operational results.

INTRODUCTION

The profile monitor upstream of the electron beam dump is used to image the beam after passing through a transverse accelerating radio frequency (RF) cavity situated 30 meters upstream [1]. The LCLS electron beam, with an intensity range of 1.5-2.0 pC per pulse at 120 Hz, damages the YAG:Ce after one month of usage. Retracting the YAG screen when not in use increases the lifespan of the screen to 10-12 months but damage still occurs. Even if damage is not visible, beam tests have shown that fluorescence in a localized area is diminished which greatly compromises the useable data from the beam image. Using a green-orange filter and a blue light, instead of the usual UV light, this damage can be seen as a dark discoloration on the YAG screen. The shape of the damage matches the beam profile which is elongated vertically due to the upstream bend magnets (Figure 1).

One solution is to replace the YAG screen after one year of usage but this is costly and inconvenient. Replacing the YAG screen requires shutting the beam off for 8 hours which is problematic. This paper describes the key components of the updated profile monitor that improve the service interval period, serviceability and operation.

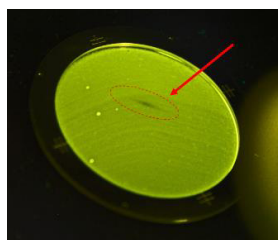


Figure 1: Photo of YAG with indicated damage.

* Work was performed in support of the U.S. DOE, Office of Science, LCLS project, under contract DE-AC02-76SF00515.

[†] cedillos@slac.stanford.edu

DESIGN REQUIREMENTS

The first requirement of the upgraded profile monitor was multiple YAG screens to increase the service interval period. The second requirement was to allow immediate operation after installation to reduce user downtime. This second requirement dictates that the new device use the proven geometry which successfully directs the OTR away from the optics path. To further decrease the potential for damage, the third requirement was that the device not fail into the beam during a power failure. The fourth requirement was to have easily removable YAG scintillators and a fifth requirement was to assess damage in situ.

Motion

Having the device near the electron beam dump prohibits the use of motors with onboard electronics or optical encoders which are susceptible to radiation. We chose a guided, double-acting pneumatic actuator because it achieves the required maximum stroke of 134.6 mm with a compact design (Figure 2). The actuator is sized to overcome the combined vacuum, spring and gravity force of 250 N while providing adjustable velocities to minimize shock to the YAG screens. Since compact pneumatic actuators don't exist with four positions, a manually adjusted hard stop is used to set the YAG screen location (Figure 2). This feature makes it quick and easy to change to the next YAG screen and simplifies the control scheme to two positions.

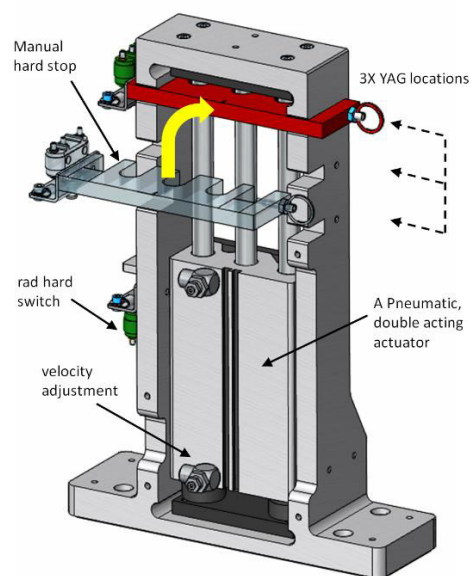


Figure 2: Actuator assembly using a 2-position pneumatic actuator to achieve 4 total positions.

The orientation of the YAG screens with respect to the beam is controlled by attaching the YAG array assembly to a fixed, UHV compatible linear guide mounted inside the chamber (Figure 3). Having the YAG array assembly on a fixed linear path reduces the repeatability and precision requirements of the actuator.

Adjusting the YAG location within the chamber is achieved by a simple coupler rod that has RH threads on one end and LH threads on the other. Rotating the coupler CW pulls the YAG array upward and rotating the coupler CCW pushes the YAG downward. Once the desired location is reached hex nuts are used to lock the coupler in place.

The first location on the YAG array assembly is a large ring to allow the beam to pass through when the device is not being used (Figure 3). Power is applied to the system to insert the YAG screen into the beam. This configuration ensures that the device fails out of the beam if power is lost.

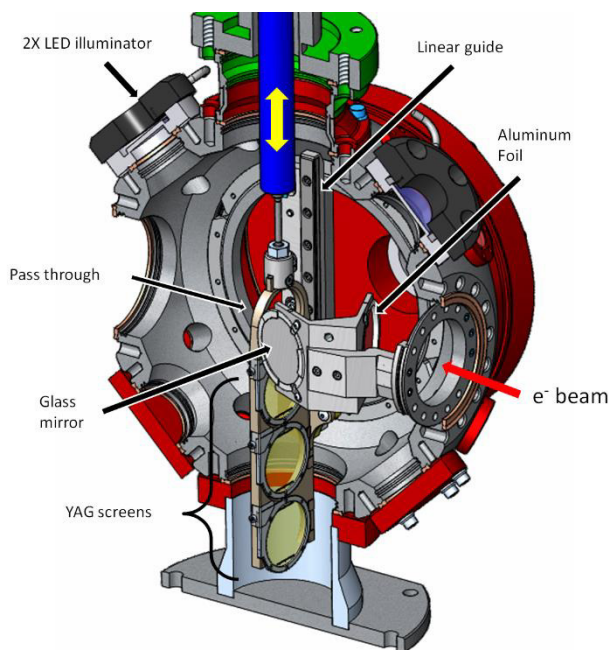


Figure 3: Isometric cross section of vacuum chamber showing internal components.

Optics

The typical configuration of a YAG screen orthogonal to the beam axis with a 45° foil (in front or behind) creates coherent optical transition radiation (COTR) that is directed into the camera [2]. This light obscures the higher resolution beam image that is created when the electron beam impinges upon the surface of the YAG screen. The optics inside the chamber was designed to address this issue by placing the YAG at 3° relative to the electron beam axis. This orientation effectively redirects the OTR away from the camera optics (Figure 4, top). To maximize the horizontal effective width and eliminate the need for a larger diameter, the foil is placed at 22.5° to the beamline

with a glass mirror added to reflect the resulting image to the camera (Figure 4, bottom). The large YAG, foil and mirror ensures that no beam reflections on the frames show up on the camera image. Furthermore, the configuration allows for easy access to the YAG screens during replacement and keeps the existing optics box location.

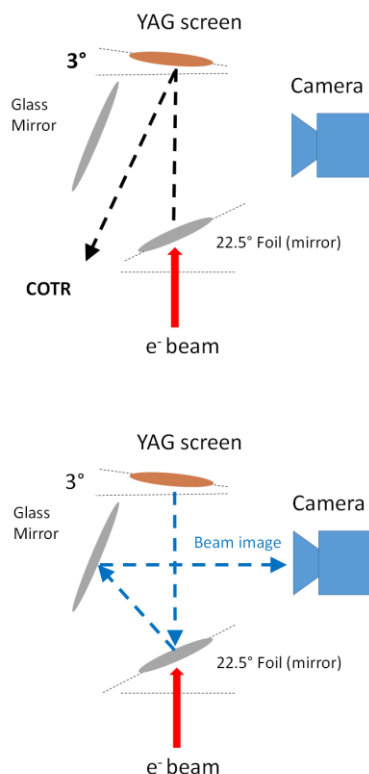


Figure 4: Orientation of YAG screen to direct COTR away from optical path to camera (top). Optical path of beam image to camera (bottom).

YAG:Ce Screen & Foil

A large YAG is required to image the transversely kicked beam and accommodate for beam jitter and slight misalignment of the beam. The large diameter allows for the addition of a chromium scale, located at the top and bottom center of the YAG screen, which is used to assist with focusing the camera on the YAG surface. This feature eliminates the need for an additional target location used only for setting the focus. With a YAG screen bonded to a keyed circular aluminum frame, the orientation of the YAG is consistent during actuation, installation and replacement. Scribe marks on the frame are used as reference markers for the camera orientation and are used to determine the initial focal distance. The YAG screen and frame cartridge design reduces the service time since they are easily inserted and removed and held in place with a screw and spring clip.

The large YAG screen is paired with a large foil (Ø42.4 mm, 1 µm thick). The prototype design had the YAG screen and foil as part of one assembly and moved as one

unit. This method was not feasible for multiple YAG screens of this size due to space constraints, and thus, the solution was to keep the foil stationary and only move the YAG screen array.

Chamber

A stock spherical square vacuum chamber was chosen for its many features. The chamber has DN160 (203mm) flange ports for easy access to the foil and YAG screen and many smaller ports for testing various illumination locations (Figure 5). The groove grabber features near the ports provide various internal mounting locations not typical of vacuum chambers. This attachment method was used to mount the linear slide and foil-mirror holder assembly. Since vertical space below the device is limited, the custom base flange was designed to provide a stable mounting location and minimize the retraction distance of the YAG array.

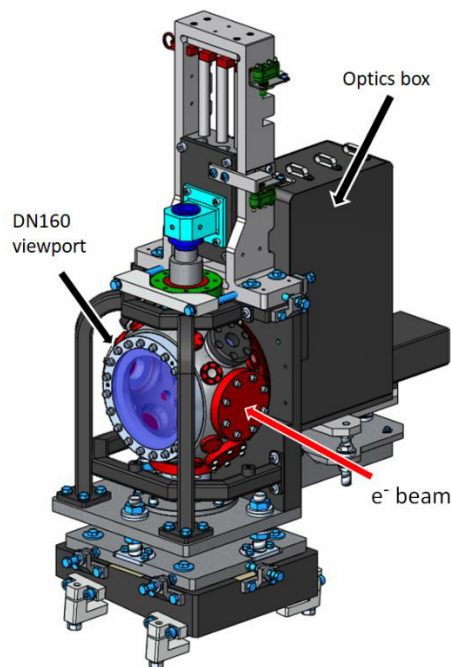


Figure 5: Model of fully assembled profile monitor.

Illumination

A dedicated light source is required to help with focusing the camera on the YAG screen surface. We chose a solution that utilizes a circular array of dimmable bright white LEDs in a compact design that mounts onto the DN40 (70 mm) CF viewport flanges. The vendor fabricated a custom version that contains bright blue LEDs which will be used for in situ inspection of the YAG screen (Figure 6, top). For in-person inspection, the YAG screen can still be viewed through the viewport when the LED illuminator is mounted to the flange.

CONCLUSION

We have designed a radiation tolerant, indexing profile monitor that has increased the service interval period from one year to three years with improved serviceability. Working with the space limitations and the existing controls system, the device was installed on the LCLS beam-line in August 2017 and is currently performing better than before. Multiple features of the previous design were improved upon from multiple YAG screens with a pneumatic actuator, ease of YAG replacement, optics to mitigate OTR light and YAG inspection methods.

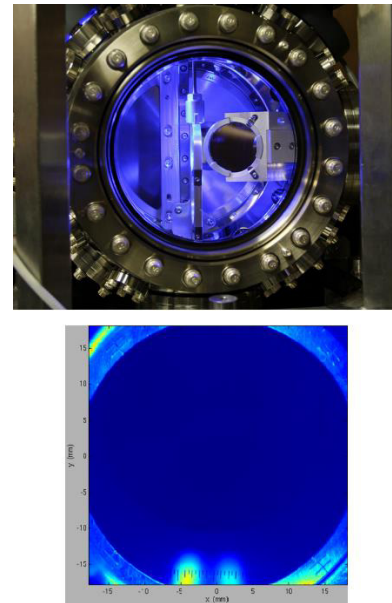


Figure 6: Photo of internal components viewed through DN160 CF viewport flange (top). Camera image of YAG screen showing scale and fiducial markings (bottom).

ACKNOWLEDGMENTS

We thank Jim Turner for initiating and supporting this project. The success of this project was the result of having a team comprised of various disciplines. Initial design work was performed by Randy Whitney and completed by Navtej Hundal. Additional design and FEA analysis was contributed by Tim Montagne. Assembly and testing was performed by Peter Noonan and Jeremy Mock respectively, and installation supervision was handled by Jeff Garcia. Additional contributors include, Jacek Krzywinski, Dehong Zhang, Georg Gassner, Aaron Monteleone, Paul Regalado, Bill Misson, Luciano Piccoli, Richard Burgess, Marco Alcazar, Craig Butler and Eli Regalado Baez.

REFERENCES

- [1] P. Krejcik *et al.*, "Commissioning the new LCLS X-band transverse deflecting cavity with femtosecond resolution" in *IBIC2013*, Oxford, UK, Sept. 2013, pp. 308-311.
- [2] H. Loos *et al.*, "Observation of coherent optical transition radiation in the LCLS linac," in *Proc. of FEL08 Conf.*, Gyeongju, Korea, Aug. 2008, pp. 485-489.

ALUMINIUM AND BIMETALLIC VACUUM CHAMBERS FOR THE NEW ESRF STORAGE RING (EBS)

F. Ciansiosi, P. Brumund, L. Goirand,
 ESRF (European Synchrotron Radiation Facility), 38000 Grenoble, France

Abstract

The ESRF is proceeding with the design and procurement of its new, low emittance EBS storage ring (Extremely Brilliant Source project). This completely new storage ring requires a new vacuum system including UHV chambers with complex shape and strict geometrical and dimensional tolerances. Due to these complexities, it was decided to build some of the chambers in an aluminium alloy machined from bulk material; the only technology permitting to respect these challenging requirements. This project now consists of 128 chambers, 2.5m long, built in alloy 2219 with custom-built Conflat flanges made by explosion bonding. The production phase is nearly finished and the chambers that have been produced fully satisfy expectations. A second generation of experimental aluminium chambers was also designed as a substitute for some of the steel chambers in an attempt to resolve part of the geometrical difficulties. These chambers are highly complex as they contain steel-aluminium junctions in the body in order to accommodate bellows and beam position monitor buttons. The delivery of the first prototype of this type of chamber is planned for June 2018.

CHOICE OF THE TECHNOLOGY

The new storage ring requires a very complex vacuum chamber system [1]. The magnets lattice and its dimensions leave very little space for the chambers, resulting in a rather complex shape. Furthermore, the beam has a very curved path, due to the presence of 4 dipole arrays (each comprising 5 permanent magnet modules with 5 different bending radii), and 3 dipole-quadrupoles. For the chambers inside the dipoles, the only technology that can be used to produce such a difficult shape is machining from bulk material. For the other chambers, it is possible to use a construction of formed and welded sheet metal.

CHOICE OF MATERIALS

The material of the chambers shall have a very low magnetic permeability, sufficient strength at bake-out temperature (150°C), to be electrically conductive and, of course,

UHV compatible (down to pressure levels of 10^{-10} mBar). The only affordable choice for the dipole chambers that are made of bulk material was an aluminium alloy, while for the other chambers the best option was stainless steel AISI316LN ESR, which is more resistant in thin sheets and easily weldable [2]. The decision to make some of the chambers from steel meant that the EBS cell could be designed in such a way that all the bellows and the BPMs could be located on the chambers. These components are very difficult to integrate in aluminium chambers (see Fig. 1). A careful analysis of the available weldable aluminium alloys for the dipole chambers revealed that the best material used at high temperatures during bake-out is the 2219T851 (ultimate tensile strength at 150C for 1000h: $\sigma_{UTS} = 220$ MPa [3]).

MECHANICAL DESIGN

Flanges

Two types of flanges were investigated, both based on the CF standard. The first is the aluminium type produced by Kurt J. Lesker. It has the advantage of being made of the same alloy as the chambers (2219 T851). However, these flanges are only compatible with pure aluminium gaskets and are sensitive to damage. The second flange type was a bimetallic flange, which is compatible with copper gaskets and is more robust, although they do present a danger of galvanic corrosion and leaks in the joint between the two materials. After a profound analysis of tender offers for the production of these flanges, the ESRF accepted the tender from CECOM, Italy, whose proposal consisted of custom-made bimetallic flanges machined from bimetallic sheets carefully controlled in order to avoid the risk of leaks due to bad bonding. CECOM assumed full responsibility for the quality of the flanges even after their installation on the chamber, thus avoiding liability issues in the event of problems between the supplier of the bimetallic material and the manufacturer of the chambers.

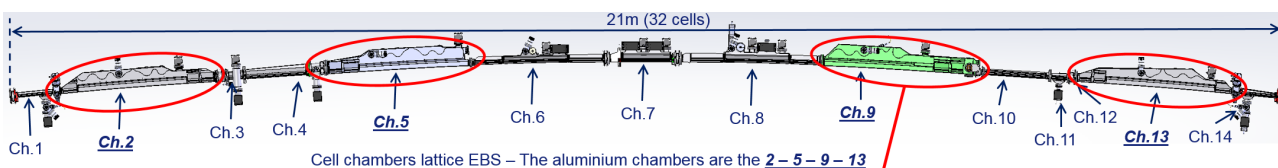


Figure 1: Vacuum chambers on one cell of EBS.

Bodies and Welding

The bodies of the chambers are machined from bulk material Al2219 T851 plates. The drawback of this material is its weldability, which is slightly lower compared to 5XXX and 6YYY alloys. To investigate this aspect a welding test campaign and a prototype chamber were commissioned to *ALCA TECHNOLOGY* (Schio, Italy) (see Fig. 2). The welding is done on the exterior, on relatively thin lips. This is sufficient as the main efforts coming from the vacuum pressure are compensated by the body surfaces in contact near the joints and in some specific areas inside the chambers (see Fig. 3). As no cleaning is possible after welding, special attention is required to keep the chambers clean during the welding process.

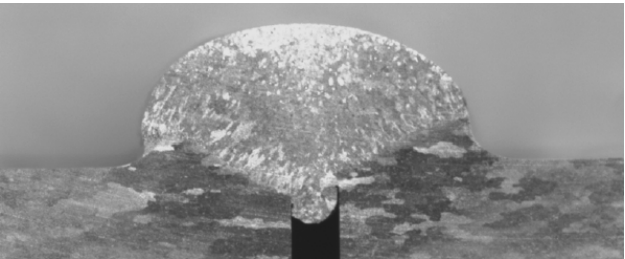


Figure 2: Welding test.

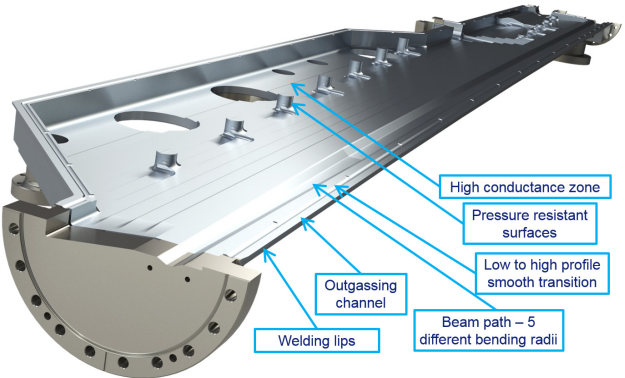


Figure 3: Bodies and welding (CH9).

Typical tolerance levels for the body are $\pm 0.05\text{mm}$, whilst critical flange orientations of the final assembly are $\pm 0.06^\circ$. Roughness levels are requested down to $Ra = 0.4$ in the beam zone.

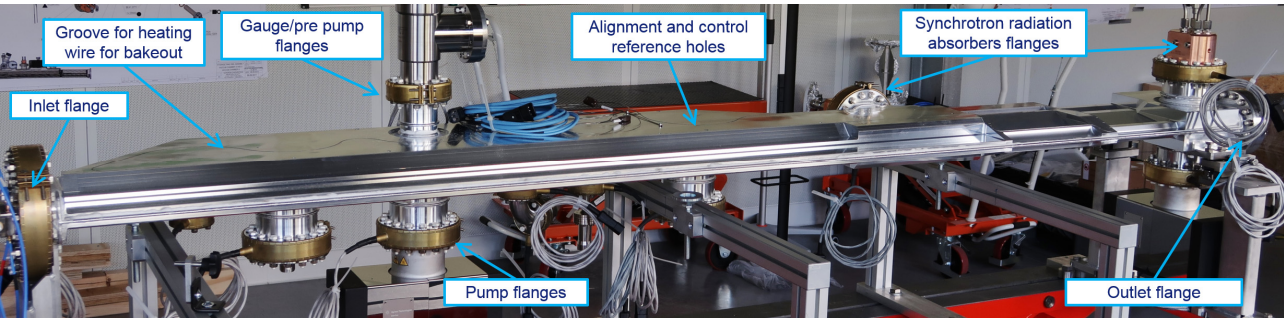


Figure 4: Series vacuum chamber (CH9) built by CECOM.

CALCULATIONS

Static

The chambers have to resist the static loads resulting from the vacuum and gravity. A FEM analysis was performed to ensure sufficient resistance of the material with respect to these loads, especially in proximity to welding and even at the bake-out temperature (150°C). The maximum stress in the material, mainly due to the vacuum pressure, is below $\sigma_{VM} = 50\text{MPa}$, so the safety coefficient is 4. This relatively high value is necessary because of the possibility of imperfections in the welding. The maximum deformation of the chamber under its own weight including equipment (pumps and other vacuum equipment) is below 0.1mm .

Thermal

The aim of the thermal calculation is to study the uniformity of the temperature field and the power needed during the bake-out. The heating is made with an electrical wire pressed into a groove in each of the two chamber halves and heating collars on the flanges. A strong thermal insulation of the chambers is impossible due to space constraints (especially in vicinity of the magnets), so even if each thermal source is closed-loop controlled with an independent thermocouple, significant temperature deviations can still occur. If the temperature is too low, the bake-out is not effective; if it is too high the chamber can be damaged. The calculations show that the maximum deviation from the target temperature $T = 150^\circ\text{C}$ is around $\Delta T = 25\text{K}$, which is acceptable (see Fig. 5).

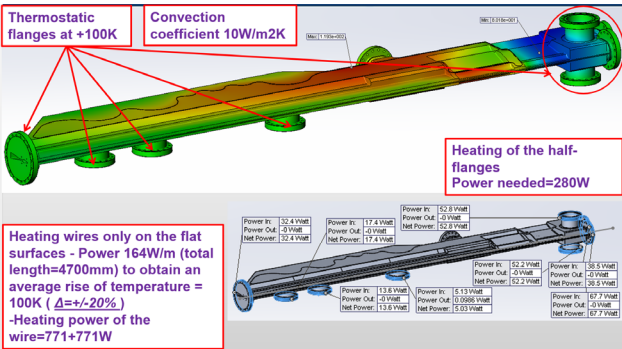


Figure 5: Thermal calculations

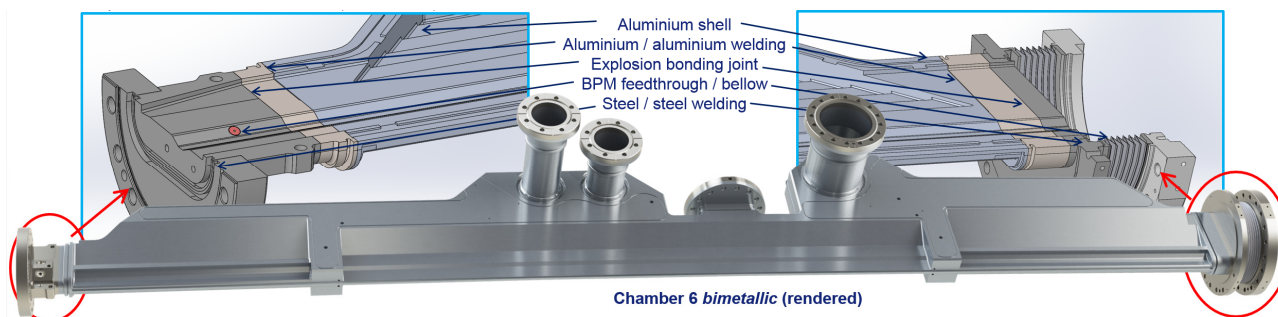


Figure 6: Vacuum chamber bimetallic (CH6).

BIMETALLIC CHAMBERS

Introduction

A new chamber series with bimetallic design was added most recently to the ESRF vacuum chambers for the EBS machine: the CH6-7-8 aluminum version. These chambers are highly complex in shape and technology as they contain both aluminum alloy and stainless-steel parts and have to guarantee very tight mechanical tolerances.

Origin of the Design Need

The chambers 6, 7 and 8 have a complex geometry, primarily due to their location within the quadrupole and dipole-quadrupole zones of the EBS cell. They contain both bellows and beam position monitor (BPM) blocks made of stainless steel as well as absorber ports. The initial design of the chambers was entirely of stainless steel due to this additional equipment installed on the chambers. The design involved welded sheet metal and plates, even though the complexity of the shape makes the dimensional and geometrical tolerances very hard to reach. Because of these technical difficulties, it was decided to create an alternative design in order to have spare chambers in case of problems.

Technical Details

The success of the aluminum chamber series CH2-5-9-13 through the collaboration with CECOM and the experience gained from this series paved the way for the design of a new generation CH6-7-8-series. This new design incorporates relevant parts in stainless steel AISI 316LN to hold the BPMs, the bellows and equipment ports. Nevertheless, a crucial difference from the initial series design is that the main section, the chamber body, is made of aluminum alloy 2219 bulk material. This alloy proved to be a very good choice regarding machinability and its welding capacity for the series CH2-5-9-13, as presented in the previous section.

The main difficulty in the new series lies in the junction between the two materials: Al2219 and AISI 316LN. Each chamber of the CH6-7-8-series contains a custom-designed bi-metallic part that serves as junction. These custom-built parts incorporate the material transition zone, the BPM blocks, as well as the corrector magnet and wiggler magnet zones. To avoid excessively high temperatures in the bi-metallic zones, sufficient material remains between the welding lips to the chamber and the bi-metallic section. The bi-metallic part is fed through the corresponding entry

and exit flanges towards a welding from the chamber outside to the flange disks to keep raw material consumption low for the bi-metallic material (see Fig. 6).

The required geometrical and dimensional tolerances for the body and the bi-metallic areas are comparable to the chamber series CH2-5-9-13 - at some points slightly lower to leave an error margin due to difficulties with the bi-metallic junctions and additional welds.

The first prototype of the new design series is expected by the end of July 2018.

CONCLUSION

The aluminium vacuum chambers designed and produced for EBS conform to the specifications and have been successfully mounted inside the magnets on the girders ready for installation in the tunnel during 2019.

The preliminary results of the bimetallic chambers are very encouraging and demonstrate that this new technology can be used to produce affordable chambers with very complex shape and tight geometrical tolerances.

REFERENCES

- [1] P. Marion, "Status of the ESRF EBS Storage Ring Engineering and Construction", presented at the 10th International conference on Mechanical Engineering Design of Synchrotron Radiation Equipment and Instrumentation (MEDSI'18), Paris, France, 25-29 June 2018, paper TUOPMA06, this conference.
- [2] P. Van Vaerenbergh, "Stainless Steel Vacuum Chambers for the EBS Storage Ring", presented at the 10th International conference on Mechanical Engineering Design of Synchrotron Radiation Equipment and Instrumentation (MEDSI'18), Paris, France, 25-29 June 2018, paper TUPH35, this conference.
- [3] J. Gilbert Kaufman, "Parametric Analyses of High-Temperature Data for Aluminum Alloys", ASM International, p. 50, doi:10.1361/paht2008p003

FRICION STIR WELDING AND COPPER-CHROMIUM ZIRCONIUM: A NEW CONCEPT FOR THE DESIGN OF SIRIUS' HIGH-POWER ABSORBERS

G.V. Claudiano†, L.M. Volpe, P.T. Fonseca, E.B. Fonseca¹, M.H.S. Silva,
Brazilian Synchrotron Light Laboratory (LNLS), Brazilian Center for Research in Energy and
Materials (CNPEM), 13083-970, Campinas, Sao Paulo, Brazil

¹ also at School of Mechanical Engineering, University of Campinas, 13083-860 Campinas, Sao
Paulo, Brazil

Abstract

Sirius, the new Brazilian fourth-generation synchrotron light source, is currently under construction. Due to the high brilliance and low emittance of its source, the photon beam on each undulator beamline can have power densities as high as 55 W/mrad². To protect the components downstream, the Front-End power absorbers need to manage this power in a limited space, but also having precision in alignment and being reliable all over their lifetime. To achieve this behaviour, the selected alloy was the copper-chromium-zirconium (CuCrZr, commercially known as C18150) because of improved thermal and mechanical properties. In order to seal the vacuum chamber (path on which the cooling water flows), friction stir welding was the selected joining method. During the welding process, the material passes through a grain refinement process which results in a high-resistance joint. The manufacturing process could also result on a reduction of costs and lead times. Finally, it will be presented the final versions of the component with its support and the characterizations done to validate the welded joint under vacuum and water pressure requirements.

INTRODUCTION

Sirius is the new 3-GeV low-emittance high-brightness fourth-generation Brazilian synchrotron light source. As a research facility, it is going to provide resources for high-level scientific studies after its beamlines are finished. Also, as can be seen by the monochromators [1] and mirrors projects [2], new concepts and technologies are already being developed.

Regarding the undulator-beamlines FE (Front-end) power absorbers (*i.e.* fixed mask, photon shutter and high-power slits), their designs were already finished, tested and validated. Those are the components which manage the high power emitted by the storage ring, protecting the components downstream by blocking portions of the white beam. On [3], it can be found specifically the function of each power absorber along with their apertures and design criteria. Their design was based on brazing of Glidcop [4] and stainless-steel parts as described on [5].

Despite of their proven utility, their manufacture chain was highly demanding in some points, such as: human sources, time and machining services (in order to refine mechanical adjustments between parts). Those facts were the main motivation for the proposal of the system optimization done in the current study. A copper-chromium-zirconium alloy (CuCrZr, commercially known as C18150) was the chosen alloy for this application because of the following reasons: it is cheaper and available on national market, its mechanical and thermal properties are alike the Glidcop [6], and it is vacuum compatible [7]. It should also be emphasized that other synchrotron facilities have already replaced Glidcop by CuCrZr alloy on their FE power absorbers [8-9].

On other hand, due to their high thermal conductivity, copper and copper alloys are difficult to weld using conventional techniques (*i.e.* techniques that involve fusion). Usually, a high heat input is necessary to melt the material and it is particularly compromising when working with precipitated-hardened alloys, such as CuCrZr [10], once strengthening nano-precipitates can be largely eliminated due to the welding thermal cycle. During welding, the previous thermal cycle usually effaces the heat treatment, and along with recrystallization, results in lower yield and ultimate strength than the aged base metal [10, 11]. Moreover, copper is susceptible to embrittlement due to oxygen dissolution into the melt pool. Furthermore, reference [12] points out that a long exposure of the CuCrZr alloy to high temperatures could cause over aging and recrystallization. Thus, it is necessary not only to limit the temperatures during manufacturing of the component, but also during its operation in the beamline. It was defined as a constraint because of a proposal to do the flange manufacturing on the CuCrZr workpiece itself as a manner to reduce the number of welding spots (a reduced material strength could cause a greater deformation on the flange's knife, leading to a vacuum leakage).

Differently from conventional processes, friction stir welding (FSW) is a solid-state joining technique capable of overcoming the problems related to welding of copper [13]. FSW consists of a rotating non-consumable tool, which is inserted in the material and translates along the weld path to create a joint. The tool generates heat from friction and deformation. Since maximum temperatures lay

† gabriel.claudiano@lnls.br

below the melting point of the alloy, solidification-related phenomena are eliminated. Besides, FSW promotes grain refinement, thus improving mechanical performance.

FSW of copper and its alloys has been reported in the literature by a number of authors, asserting its weldability. The effects of welding parameters have been studied in a wide range of rotational speeds, welding speeds, axial loads, and thicknesses for pure copper [13-17]. However, during cooling grain growth may take place depending on the parameters employed, which may cause grain coarsening and softening. Researchers demonstrated that accelerating the cooling rate could successfully result in higher hardness and better tensile properties in the stir zone (SZ) [18-19]. Another possibility is to use large axial forces and very low heat input parameters [17].

Available literature describes mostly plate butt-welding. In this work, circumferential lap-welding was performed on bulk cylinders of CuCrZr alloy covered by pure copper sleeves. The FE components were then machined from the welded parts, which already contained the cooling water circuit. Welding procedure was validated by means of microstructural characterization, hardness measurement, and leak and hydrostatic pressure tests. It is also presented the final version of the component with its support.

EXPERIMENTAL PROCEDURE

As quoted before, it is instrumental that the material preserves its mechanical resistance even when exposed to high power densities. Seeing this constraint, some common (GTAW and oxy-fuel) and unconventional techniques (FSW and sealing by mechanical clamping and deformation) were evaluated. The most promising one, given the temperature constraint and the results on the preliminary tests, was the FSW method.

Friction stir welding was performed in a dedicated TTI machine, model RM-1 at the Brazilian Nanotechnology National Laboratory (LNNano/CNPEN). FSW tools were machined in AISI H13 steel. A turn-table was used to perform circumferential welds. The welding parameters and their range of analysis were as follows: tool rotational speed (from 400 to 1500 rpm); tool travel speed (from 20 to 100 mm/min); lateral tool offset (from 1 to 3 mm); and power input (from 2.5 to 4.0 kW).

A solid machined round bar of CuCrZr alloy, with a diameter of 73 mm was covered by a pure copper sleeve with 1,6 mm in thickness (C122 alloy). It can be noticed that, at this point, the copper sleeve was already silver-welded on copper tubes (for was inlet and outlet) and on CuCrZr bushes (for attachment of temperature sensors and alignment targets). Also, there was an helicoidal water chamber machined on the CuCrZr bar (for cooling purposes). The welding process and the welded component can be seen on Figure 1.



a)



b)

Figure 1: (a) Friction Stir Welding (FSW) on the CuCrZr component. (b) FSW-welded component.

Joints subjected to conventional metallographic procedure were cut transverse to the welding direction for microscopy and microhardness testing.

The hydrostatic pressure test was conducted by connecting the component to a water pump. Firstly, all the interfaces between the water chamber (path inside the component through which the water flows) and the air were closed, except for two: one used to purge the air from the system and another one to pressure the inner side of the component. After the air was purged out, only one connection was left open. Thus, that valve was used to increase the water pressure inside the component until it reached a desirable level. By standards, the pressure needs to be at least 50% greater than the operating pressure of the component. Finally, the last connection valve was closed and then the component was maintained at constant hydrostatic pressure for at least two hours.

The leak test was included as a manner to keep track of the component tightness along its manufacture chain. The main advantage of this test is that it does not damage the component and can be easily done on single parts or welded components, being a comparison parameter of the product quality after a process. It should be noticed that it is not a substitute for the water pressure test, once a helium leakage does not suggest a water leakage (the size of the molecules is significantly different) and the hydrostatic pressure test is more aggressive (because of the higher differential pressure).

RESULTS AND DISCUSSION

Firstly, it should be considered that a metrology facility [20] has been built in order to create a controlled environment for the verification and validation of the manufactured components. The tests described on the current study were also conducted inside this building.

As for microstructure analysis the component must be destroyed, only leak and water pressure tests are done to guarantee the operational quality of a manufactured component. All the Sirius components that were already manufactured were approved for values of leak rate below $5 \cdot 10^{-10} \left[\frac{\text{mbar}}{\text{L.s}} \right]$. Hydrostatic pressure tests were conducted during, at least, 3 hours under pressures greater than 15 bar. The validated components were approved on this test also. The operational pressure of those components will be 8 bar.

It can be seen on Figure 2 an optical microscopy of the welded region. The sample was extracted of a prototype welded by FSW using the same materials and conditions. On the image is shown the copper sleeve (at the top of the figure), the external diameter of the CuCrZr part and the joint region. There is also a small gap between the parts, which is partly originated by the fine mechanical adjustment determined for the assembly and partly by the large forces involved on the welding process.

Furthermore, on Figure 3 there is a detail of the interface between the stir zone and the base material. On the stir zone, due to the magnitude of the forces and heat involved on the joint process, the grain size was significantly reduced (as intended for better mechanical properties). On other hand, on the bulk zone it is possible to distinguish the grain contours.

Figure 4 was originated by a micro-hardness analysis on the region illustrated on Figure 2. By that it is possible to notice: the different materials (a soft copper sleeve on the top and a harder CuCrZr bulk on the bottom); the hardening caused by the grain refinement on the welding zone; and the annealing caused to the soft copper on the sides of the joint region (shown as the dark-blue zone). It is also possible to conclude that the temperatures reached on the process had only local effects.

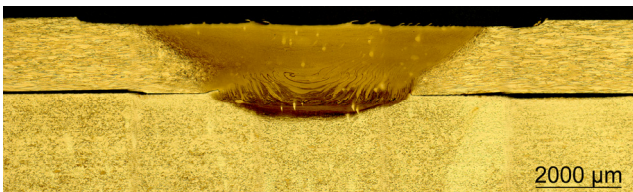


Figure 2: Cross-section image of the welded region done by optical microscopy.

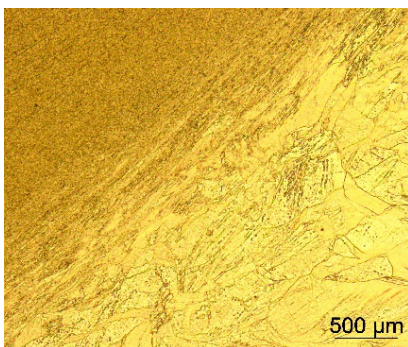


Figure 3: Microstructure of a FSW welded region.

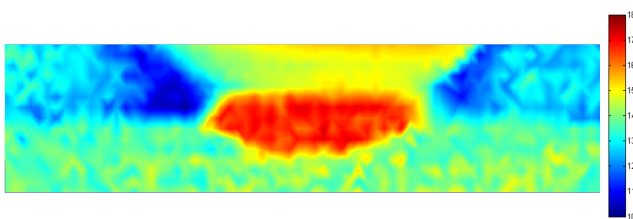


Figure 4: Microhardness analysis of a FSW welded region (in units of micro-Vickers).

Regarding the component support, as can be seen on Figure 5: one of its sides is used as a stiff reference to guarantee the alignment of the component's aperture. Pre-load and a guide pin are used to create a fixed reference for the component. On the other side it is used an elastic support, which is deformable in order to accommodate possible machining misalignments while still constraining the necessary degrees of freedom. To achieve this behaviour, a thin sheet is applied as a flexure.

Finally, on Figure 6 it is presented the final version of the welded component, including temperature sensors, support and alignment features.

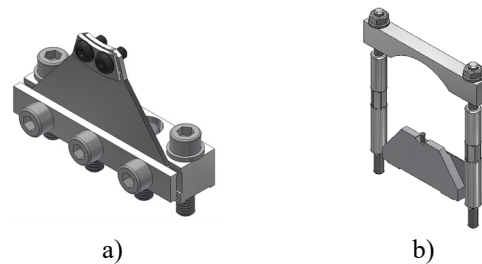


Figure 5: Front-End components support. In (a) it is represented the elastic support and in (b) the reference support.

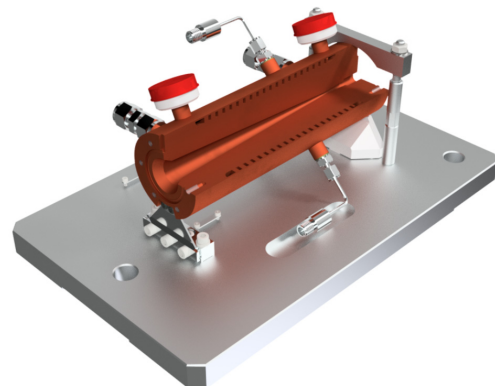


Figure 6: Final component assembly of the fixed mask for undulator-beamline Front-Ends.

NEXT STEPS

Once the integrated project, regarding the manufacture chain and the component's operational conditions, is already well developed, the next challenges are going to be related to the fiducialization and alignment in the beamline.

CONCLUSIONS

By the study conducted it is possible to observe that there are still available points of optimization in the Sirius power absorbers, but the level of quality reached for both the component and its manufacture chain is now better and more robust. The welding was already done for the first bunch of Front-End elements and the leak and hydrostatic pressure tests were conducted. They are going to be installed latter this year.

ACKNOWLEDGMENT

The authors would like to gratefully acknowledge the funding by the Brazilian Ministry of Science, Technology, Innovation and Communication and the contribution of the LNLS team. Also, a special thanks must be offered to some people who really had a noticeable role in this research. It can be named Alex Matos da Silva Costa, Victor Ferrinho Pereira and Joel Souza de Alencar.

REFERNCES

- [1] R. R. Galdes *et al.*, “The Status of the New High-Dynamic DCM for Sirius”, presented at MEDSI’18, Paris, France, June 2018, paper WEOAMA01, this conference.
- [2] R. R. Galdes *et al.*, “The Design of Exactly-Constrained X-Ray Mirror Systems for Sirius”, presented at MEDSI’18, Paris, France, June 2018, paper WEOAMA04, this conference.
- [3] L. M. Volpe *et al.*, “High Heat Load Front Ends for Sirius”, in *Proc. MEDSI’16*, Barcelona, Spain, September 2018, paper WEPE06, DOI: 10.18429/JACoW-MEDSI2016-WEPE06
- [4] Glidcop, <https://www.hoganas.com/en/business-areas/glidcop/>
- [5] G. V. Claudiano *et al.*, “Glidcop Brazing in Sirius’ High Heat Load Front-End Components”, in *Proc. MEDSI’16*, Barcelona, Spain, September 2018, paper TUPE23, DOI: 10.18429/JACoW-MEDSI2016-TUPE23
- [6] M. A. Hussain *et al.*, “Bending Magnet and 3-Pole Wiggler Frontend Design”, in *Proc. MEDSI’14*, Melbourne, Australia, October 2014, https://medsi.lbl.gov/SysIncludes/retrieve.php?url=https://medsi.lbl.gov/files/page_156/Presentations/Bending_Magnet_and_3_Pole_Wiggler_Frontend_Design_Muhamad_Aftab_Hussain.pdf
- [7] C. Shueh, C.K. Chan, C.C. Chang, and I.C. Sheng, “Investigation of Vacuum Properties of CuCrZr Alloy for High-Heat-Load Absorber”, *National Synchrotron Radiation Research Center A*, vol. 841, pp. 1-4, 2017
- [8] S. Sharma *et al.*, “A Novel Design of High Power Masks and Slits”, in *Proc. MEDSI’14*, Melbourne, Australia, October 2014, https://medsi.lbl.gov/SysIncludes/retrieve.php?url=https://medsi.lbl.gov/files/page_156/Presentations/A_Novel_Design_of_High_Power_Masks_and_Slits_Sushil_Sharma.pdf
- [9] I.C. Sheng, C.K. Chan, C.-C. Chang, C. Shueh, and L.H. Wu, “The Development of CuCrZr High Heat Load Absorber in TPS”, in *Proc. MEDSI’16*, Barcelona, Spain, September 2018, paper MOPE30, DOI: 10.18429/JACoW-MEDSI2016-MOPE30
- [10] K. Jha *et al.*, “Friction Stir Welding (FSW) of Aged CuCrZr Alloy Plates”, *Metall. Mater. Trans. A*, vol. 49, p. 223-234, 2018, doi: 10.1007/S11661-017-4413-2
- [11] R. Lai *et al.*, “Study of the Microstructure Evolution and Properties Response of a Friction-Stir-Welded Copper-Chromium-Zirconium Alloy”, *Metals*, vol. 7, no. 9, 2017, doi: 10.3390/met7090381
- [12] M. Li and S.J. Zinkle, “Physical and Mechanical Properties of Copper and Copper Alloys” In *Comprehensive Nuclear Materials*, volume 4, Amsterdam : Elsevier, 2012, pp. 667-690.
- [13] R.S. Mishra and M.W. Mahoney, *Friction Stir Welding and Processing*. ASM International, 2007.
- [14] Xie *et al.*, “Development of a fine-grained microstructure and the properties of a nugget zone in friction stir welded pure copper”, in *Scripta Materialia*, vol. 57, p. 73-76, 2007.
- [15] Y.F. Sun, and H. Fujii, “Investigation of the welding parameter dependent microstructure and mechanical properties of friction stir welded pure copper”, in *Mater. Sci. Eng. A*, vol. 527, p. 6879-6886, 2010.
- [16] J.J. Shen *et al.*, “Effect of welding speed on microstructure and mechanical properties of friction stir welded copper”, in *Mater. & Des.*, vol. 31, p. 3937-3942, 2010.
- [17] N. Xu *et al.*, “Achieving good strength-ductility synergy of friction stir welded Cu joint by using large load with extremely low welding speed and rotation rate”, in *Mater. Sci. Eng. A*, vol. 687, p. 73-81, 2017.
- [18] N. Xu *et al.*, “Modification of mechanical properties of friction stir welded Cu joint by additional liquid CO₂ cooling”, in *Mater. & Des.*, vol. 56, p. 20-25, 2014.
- [19] P. Xue *et al.*, “Microstructure and mechanical properties of friction stir processed Cu with an ideal ultrafine-grained structure”, in *Mater. Charact.*, vol. 121, p. 187-194, 2016.
- [20] H. G. P. de Oliveira, M. Bazan, C. S. N. C. Bueno, and L. Sanfelici, “The Lns Metrology Building – Environmental Control Results”, presented at MEDSI’18, Paris, France, June 2018, paper TUPH43, this conference.

INTERFACES WITH OPERATIONAL SYSTEMS APS UPGRADE REMOVAL AND INSTALLATION*

R. Connatser, Argonne National Laboratory, Argonne, IL, USA

Abstract

A critical time for the Advanced Photon Source Upgrade (APS-U) Project is the twelve month dark period in which the current accelerator, front ends, and insertion devices will be removed and the new MBA will be installed. In addition to the technical interfaces, there are a number of operational support systems and utilities that will be affected. For the dark period to be a success, all of these interfaces need to be described and their interaction with the removal and installation processes defined. This poster describes some of these systems and their interfaces.

ASSEMBLY, REMOVAL, AND INSTALLATION

The APS-U project will have an extended pre-installation phase where the 200 magnet modules will be assembled and tested prior to being placed in storage. The dark period will be kicked off with an extensive Lock Out Tag Out procedure prior to the removal of the current accelerator. The current plan calls for installation of all tray, cabling, fibers, and any other modifications to the tunnel to be complete prior to installation of the new magnet modules. Once installed, all necessary connections will be made up and testing without beam can commence.

Access Control Interlock System

The Access Control Interlock System (ACIS) of the APS consists of control systems, shutters, physical personnel gates and barriers, and associated control and sensor cabling. A block diagram is indicated in Figure 1. Entering the tunnel via various penetrations, the cabling in the tunnel runs in dedicated conduit or in shared cable trays. In order to facilitate the removal and installation work, a majority of the physical barriers and gates that are part of the ACIS will be removed at the beginning of the dark period. The sensors and interlocks that are conjoined with this equipment will need to be accounted for in that period. The current plan is that the physical barriers will be reinstalled at the same locations after the installation of the new MBA. Plates are provided for recommended software and authors are advised to use them. Please consult the individual conference help pages if questions arise.

* Work supported by Argonne National Laboratory which is a U.S. Department of Energy laboratory managed by UChicago Argonne, LLC. The Advanced Photon Source is a U.S. Department of Energy Office of Science User Facility operated for the U.S. Department of Energy Office of Science by Argonne National Laboratory under Contract No. DE-AC02-06CH11357.

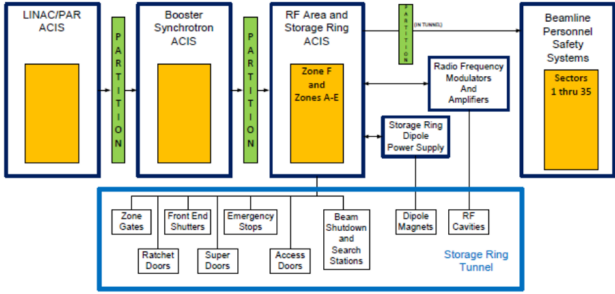


Figure 1: ACIS block diagram.

Cooling Water and Bakeout System

Cooling water for the APS storage ring is routed via two different headers and piped in parallel to the accelerator components. During the removal phase the connectors to the components will be severed after the headers are drained. The APS-U configuration has yet to be fully engineered. The current storage ring at the APS has dedicated, hot water based, bakeout systems. For the 40 storage rings sectors of the APS, there are 20 independent bakeout systems and cooling systems, located in the even sectors. The baking skid is typically located in the maintenance corridor on the inboard of the SR tunnel while the cooling skids are on the mezzanine, as shown in Figure 2. These systems are planned to be reused for the new MBA, so how they are disconnected during the removal phase, and how much work there will be during the installation to bring these systems will need to be sorted out during the removal and installation planning.

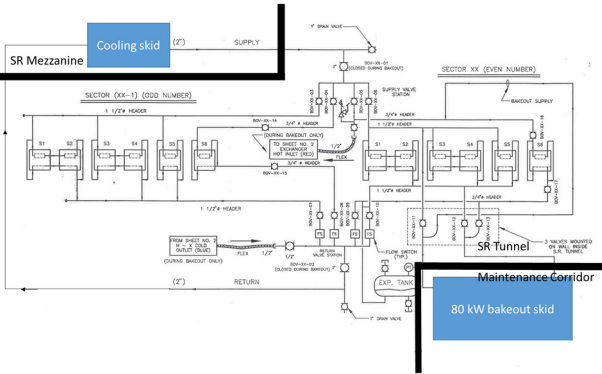


Figure 2: Water systems block diagram.

Vacuum System

The APS-U storage ring vacuum system for each sector will consist of a pair of racks with controllers located on

the mezzanine, and vacuum components in the tunnel. The vacuum components will be installed on the magnet modules during the pre-installation phase. The high voltage and control cabling will need to be pulled from the mezzanine to the tunnel during the dark year through the shielding penetrations, before being connected to the components. The current vacuum system will be completely removed, with only the racks remaining. A typical block diagram is shown in Figure 3.

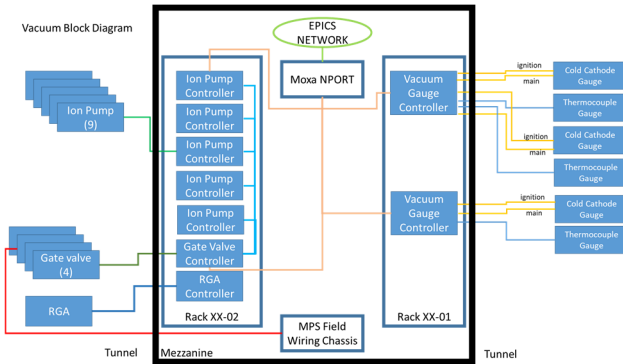


Figure 3: Vacuum system block diagram.

Beam Position Monitoring

The Beam Position Monitoring system of the APS-U will utilize new, dedicated racks mounted at the mezzanine for each of the 40 sectors. A typical block diagram of a single BPM unit is shown in Figure 4.

Matched heliax cable bundles for each of the 570 BPMs will be pulled from the mezzanine to the SR tunnel via the shielding penetrations and connected to the on module connector panel during installation. The current BPM system will be completely removed.

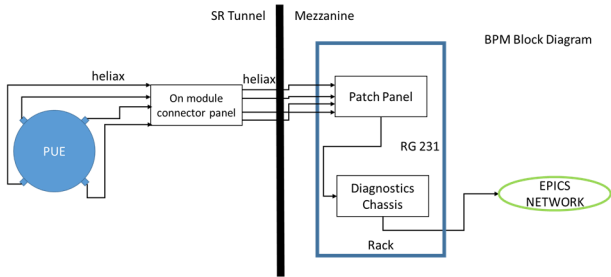


Figure 4: BPM system block diagram.

CONCLUSION

The details for all of the interfaces will be necessary to make the removal and installation of the APS-U a success. While this work has started, there is a significant amount of work remaining to be done.

ACKNOWLEDGMENTS

Assistance from Greg Markovitch, Gene Swetin, Bob Lill, and Ben Stillwell of the APS Accelerator Sciences and APS Engineering Services Divisions was much appreciated.

RETRACTABLE ABSORBER (MASK) AND WHITE BEAM IMAGER DIAGNOSTIC FOR CANTED STRAIGHT SECTION

J. Da Silva Castro, M. Labat, F. Lepage, N. Hubert, N. Jobert, A. Mary, K. Tavakoli, N. Béchu,
 C. Herbeaux, Synchrotron SOLEIL, 91190 Gif-sur-Yvette, France

Abstract

At the SOLEIL synchrotron, as in other accelerators, two canted sources can coexist on the same straight section for space and economic reasons. For its two long beamlines (ANATOMIX source upstream and NANOSCOPIUM source downstream) SOLEIL has made the choice to equip one of his long straight section with two canted insertion devices capable to operate simultaneously. That implies to take into account the degradation risk management of equipment, due to radiation. As the beam power deposition from the upstream undulator can seriously degrade the downstream one, or even other equipment. To handle these risks, Soleil first designed and installed in 2016 a retractable vertical absorber between both insertions to protect the downstream source from the upstream one. In 2017, Soleil then designed and installed a white beam imager, redundant an existing photon beam monitor (XBPM), to verify the correct positioning / alignment of equipment and beams relative to each other. For the vertical absorber as for the white beam imager SOLEIL had to meet some interesting technological and manufacturing aspects that we propose to present in a poster.

INTRODUCTION

In one of the long straight sections of SOLEIL, SDL13, two canted insertion devices have been installed for X-rays delivery to the ANATOMIX (upstream) and NANOSCOPIUM (downstream) beamlines. For the insertion devices to be operated and used simultaneously by those two independent beamlines, they were canted in the horizontal plane. But the canting angle remains small, so that the upstream ID radiation passes through the downstream ID. To prevent any damage of the downstream ID magnets from the upstream ID radiation, it was first decided to install an absorber in between the two IDs, to shadow the downstream ID magnets. But the efficiency of this mask relies on an accurate relative alignment of the upstream ID, the mask itself and the downstream ID. Those diagnostics to do the survey are mandatory. An XBPM in the beamlines front-end is in operation since 2016. But to ensure a redundancy in the measurements, it was decided in 2017 to add nearby a white imager. This paper summarizes the design of both the absorber and the white imager.

THE ABSORBER

The absorber first aim was to shadow the downstream ID magnets from the upstream ID radiation. Installed in between the two IDs, this gave a vertical aperture of 2.8 mm. Detailed studies were then carried out to define its geometry in order not to jeopardize the performance of the storage ring in terms of collective effect induced instabilities, beam losses, injection efficiency and beam time. The absorber is a piece of copper with an asymmetric 90 degree U-shape (see Figure 1). It encloses the photon beam produced upstream while the electron beam is located at -11 mm from the U-border of the absorber (see inset in Figure 1 b).

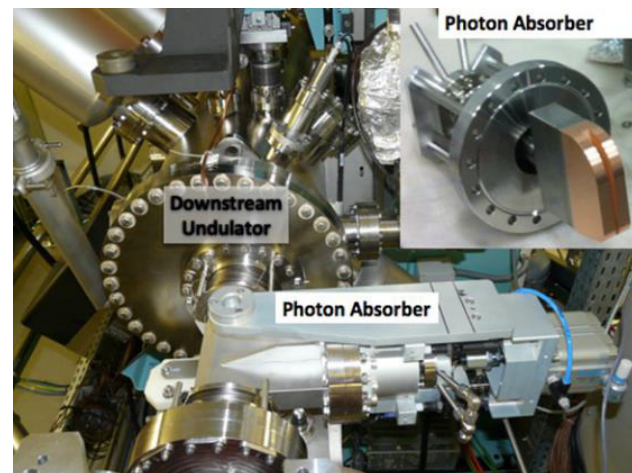
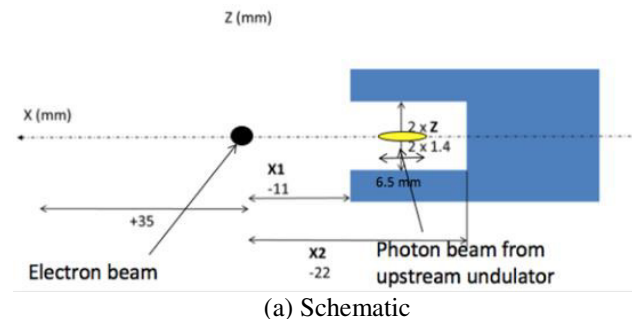


Figure 1: Schematic and pictures of the absorber.

The absorber is maintained inserted in between the IDs using a spring based system. For security reason, the stage is by default inserted. It can be retracted when needed, thanks to a remote controlled jack (see Figure 4).

THE WHITE IMAGER

The white imager first aim is to check the relative alignment of the upstream ID, the absorber and the downstream ID. Its principle is the following: a diamond disk is inserted on the upstream ID photon beam path after passing through the downstream ID. The photon beam hits diamond imperfections (Nitrogen) causing scintillation of the diamond in the visible range. This scintillating pattern is then imaged on a CCD. It is then checked on this image that the upstream radiation is correctly “clipped” by the absorber, meaning that the downstream ID magnets are protected.

The Diamond

Given the upstream ID radiation pattern dimensions together with the absorber shadow geometry in the imager plane, the diamond disk had to reach a minimum diameter of 26 mm: a clear aperture of 28 mm was chosen. To ensure sufficient light collection but also to limit the expected temperature elevation to $+40^{\circ}\text{C}$, the diamond thickness was chosen to be 0.3 mm. Because the incident power on the diamond is of the order of 10 W/mA , it can only be inserted at low ($<10\text{ mA}$) currents. To enable the water cooling of the diamond, it was brazed on a copper ring (see Figure 2). A $30\text{ }\mu\text{m}$ silver coating was deposited on the diamond surface to increase its thermal conductivity. The whole system (diamond + ring) was realized by Diamond Materials.

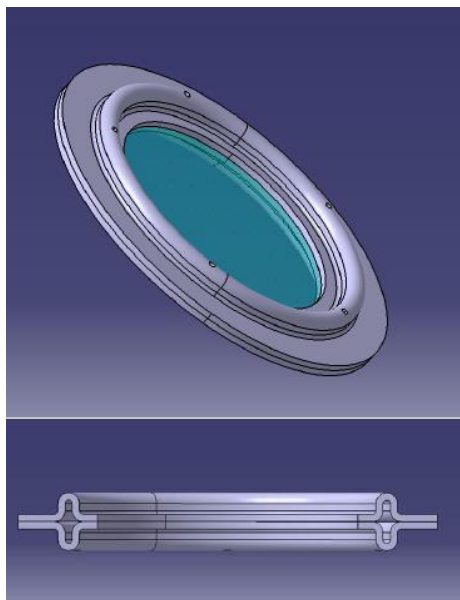


Figure 2: Schematic of the diamond disk brazed on its cooling copper ring.

The Diamond Holder and Cooling System

The diamond is mounted on a holder which ensures both the diamond supporting and cooling (see Figure 3). The diamond copper ring is held by a refined pressuring system using Belleville rings to ensure a homogeneous stress on the ring. To evacuate the heat load on the dia-

mond, water flows through the holder in and out around the copper ring with a limited speed to prevent vibrations.

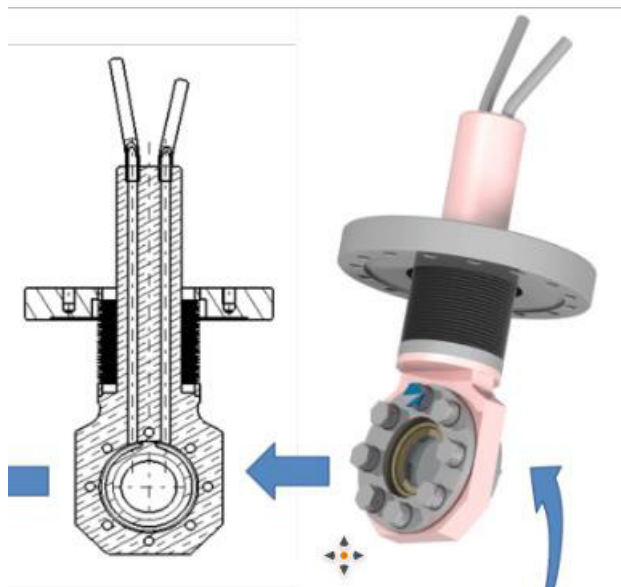


Figure 3: Diamond holder and cooling system.

The Diamond Insertion Stage

The insertion of the diamond in its holder on the photon beam path is enabled by a pneumatic jack. For machine and diamond security reasons, the diamond has to be by default extracted: this was ensured using two strong springs that have to be compressed by the jack for diamond insertion.

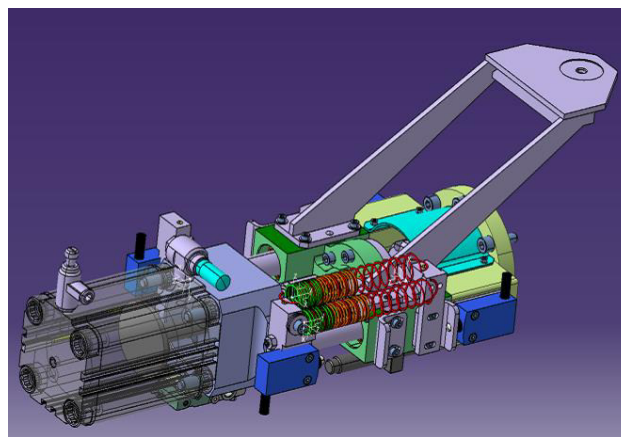


Figure 4: The diamond insertion stage.

The Imaging System

In order to image the scintillation pattern on the diamond disk, an imaging system is mounted behind an UHV window on the top of the diamond vacuum chamber (see Figure 5). This imaging system simply consists in an objective with extender and of a CMOS camera. The photon pattern is demagnified by about a factor 0.55 which allows a spatial resolution better than $10\text{ }\mu\text{m}$.

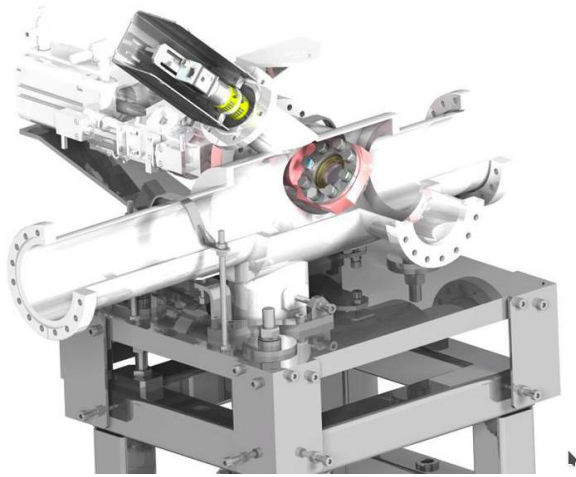


Figure 5: White imager general view.

ABSORBER AND IMAGER OPERATION

The absorber was successfully installed and commissioned in 2016. In users operation, it is systematically inserted to allow the simultaneous operation of the SDL13 beamlines. It is only extracted during specific machine studies.

The white imager was successfully installed and commissioned in 2017. It was found out that using a current of 6 mA is already sufficient in terms of photon flux to operate the diagnostics. The white imager is used after each machine shutdown and after each extraction/insertion of the absorber. It gives complementary information to the XBPM measurements and even revealed more straight forward and easy to use.

CONCLUSION

The absorber and the white imager were designed at SOLEIL to secure the operation of two canted IDs. Both rely on simple thus robust mechanical concepts which rend their commissioning easy and straight forward. They are now successfully used to operate routinely ANATOMIX and NANOSCOPIUM beamlines simultaneously.

ACKNOWLEDGEMENTS

Acknowledgements to N. Jobert and support groups of Soleil (Vacuum and Alignment).

MULTIPOLE INJECTION KICKER (MIK), A COOPERATIVE PROJECT SOLEIL AND MAX IV

J. Da Silva Castro, P. Alexandre, R. Ben El Fekih, S. Thoraud, Synchrotron SOLEIL, 91190 Gif-sur-Yvette, France

Abstract

The cooperative MIK project SOLEIL / MAX IV started in 2012 and is part of the Franco-Swedish scientific collaboration agreement, signed in 2009 and followed by framework agreements signed in 2011. The MIK is a particular electromagnet using theoretical principles of the 1950s and recently used by the new generation of synchrotrons to significantly improve the Top-Up injection of electrons into the storage rings. Indeed, this type of magnet can drastically reduce disturbances on stored beams and also offers substantial space savings. The MIK is a real opportunity for synchrotrons wishing to upgrade their facilities. One of the first MIK developed by BESSY II in 2010 gave significant results. These results motivated SOLEIL and MAX IV to develop together their own MIK. Many technical challenges have been overcome in the area of mechanical design and manufacture as well as in magnetic and high voltage design of the MIK. Currently the first series is in operation at MAX IV and displays already outstanding performances. Optimization work is in progress.

COMPLEMENTARY DESCRIPTION

Figure 1 shows the principles of the MIK. Figure 2 shows more technical details. The MIK is composed of a chamber in two part of synthetic monocrystalline Sapphire. Parts are assembled by diffusion bonding (Kyocera Japan). Chamber can also be made in alumina with two parts assembled by glass gluing or brazing depending on the subcontractor (Friatec or Coorstek). The chamber has to be machined with a very high precision to ensure a good magnet. 8 grooves positioning the 8 conductors (copper) are machined in the hundredth of a millimeter. The conductors formed and there insulating bars (alumina) are glued in the grooves, with specific tools designed and used by Soleil team. The connection between the chamber and the flanges is ensured by a brazed Sapphire/copper interface, then a brazed copper/ stainless steel interface and finally a stainless steel / flange weld.

A titanium coating of a few microns inside the sapphire vacuum chamber (made at ESRF) allows the flow of the image current without disturbing the magnetic field.

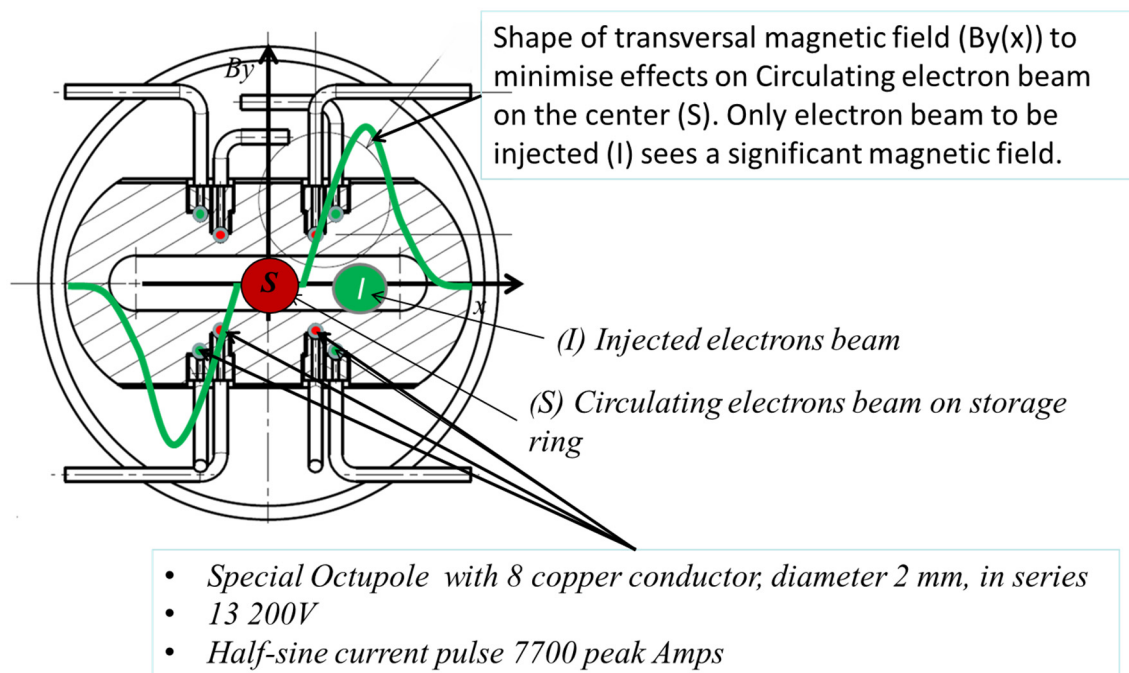


Figure 1: Cross-sectional view and principals of the MIK.

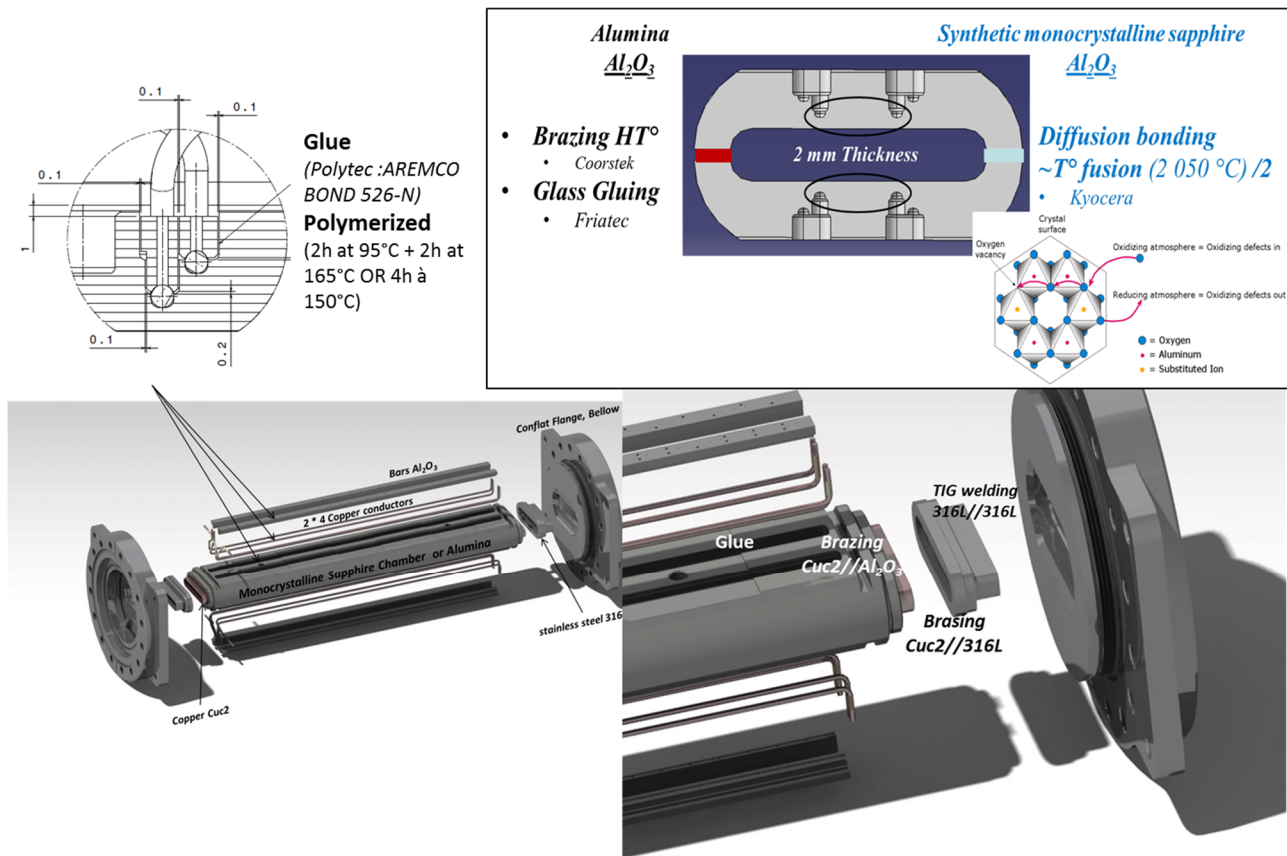


Figure 2: A few technical details.

CONCLUSION

MIK is a good example of collaborative project involving many partners. This particular electromagnet is an opportunity for the new generation of synchrotrons by reducing drastically disturbances on stored beams during top up injection, and also offers substantial space savings. Technical challenges have been overcome and a great know-how has been acquired. The first MIK displays already outstanding performances in MAX IV.

ACKNOWLEDGEMENTS

Acknowledgements to: P. Alexandre, R. Ben El Fekih, S. Thorau. from SOLEIL, Support groups from SOLEIL: Pulsed magnets, Mechanical Engineering, Vacuum, Metrology and Alignment, Electronics & Computer Control, Accelerator physics, Purchase & Juridical & Collaborations. MAX-IV team: P. Fernandes Tavares, E. Al d'Mour, J. Ahlbäck, S. Leeman, M. Johansson, L. Dallin, B. Jenssen, K. Ahnberg, M. Grabski, M. Gunnarsson, V. Hardion, J. Thanel, J. Jamroz. BESSY II (Berlin): O. Dressler, P. Kuske. LAL (Orsay): B. Leluan. ESRF (Grenoble) : M. Dubrulle and H. Marques.

A special tribute to a friend, Pierre Lebasque, project manager for the MIK at SOLEIL and Team Leader of Pulsed Magnets Group of SOLEIL for many years, who just left us and with whom I had collaborated for 15 years on different projects.

MECHANICAL DESIGN CHALLENGES BUILDING A PROTOTYPE 8-POLE CORRECTOR MAGNET

F. DePaola, R. Faussete, S. Sharma, C. Spataro
Brookhaven National Laboratory (BNL), Upton, New York, USA
A. Jain, M. Jaski, Argonne National Laboratory (ANL), Lemont, Illinois, USA

Abstract

An innovative design was developed for an 8-pole corrector magnet for the APS upgrade program. This is a combined function magnet consisting of horizontal and vertical correctors as well as a skew quadrupole. This paper describes technical challenges presented by both the magnetic design and the interface constraints for the magnet. A prototype magnet was built, and extensive testing on the magnet confirmed that all magnetic and mechanical requirements were achieved. The final design of the magnet has incorporated improvements that were identified during the manufacturing and testing of the prototype magnet.

INTRODUCTION

Multi-purpose 12-pole corrector magnets have been used in the past at several laboratories [1] but these tend to be quite large and there is not much space between the poles for mounting the coils. An 8-pole structure was developed which is more compact than a 12-pole design, yet offers a way to zero out the sextupole and decapole terms in the dipole mode and the skew octupole term in the skew quadrupole mode [2]. The magnet was designed to meet the requirements shown in Table 1.

Table 1: Design Parameters

Parameter	Value	Units
DC steering (at 6 GeV)	≥ 300	microradian
Dipole H-V field integral	≥ 0.006	T-m
Skew Quad filed integral	≥ 0.25	T
Maximum Current	15	A
Maximum required power	minimized	W
Steering at 1 kHz	$> 1\%$ or 3 microradian	
Cooling method	Air cooled	
Maximum insertion length	160	mm
Maximum insertion length with feet	90-U/S, 106-D/S	mm
Minimum Aperture	26	mm
Minimum Pole tip-to-pole tip gap	10	mm
Minimum coil-to-coil gap	16	mm
Magnet center height	279.5 ± 0.25	mm
Maximum Half-width from the vertical mid-plane	270	mm

Extensive testing was performed on the prototype 8-pole corrector magnet, photo shown in (Figure 1). This testing confirmed that the magnet is capable of providing the horizontal and vertical steering and skew quadrupole strength with good field quality and meets the specifications within the given space constraints.

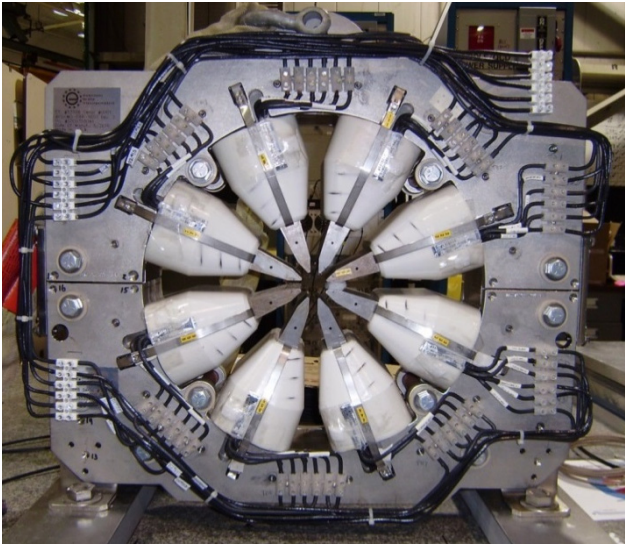


Figure 1: Prototype 8-Pole Corrector Magnet.

The magnet aperture was chosen to achieve a minimum pole-tip to pole-tip gap of 10 mm. Pole length and thickness are optimized to fit all the coils with a minimum coil-to-coil gap of 16 mm which is required at the horizontal mid-plane for the vacuum chamber extraction ports. The backleg thickness is optimized for low peak field, mechanical strength, and overall size.

COIL ASSEMBLIES

The coil pack for the 8-pole corrector magnet features three different coils on each pole, which are combined in series in a specific sequence to produce normal and skew dipole steering as well as a skew quadrupole corrector (see Figure 2).

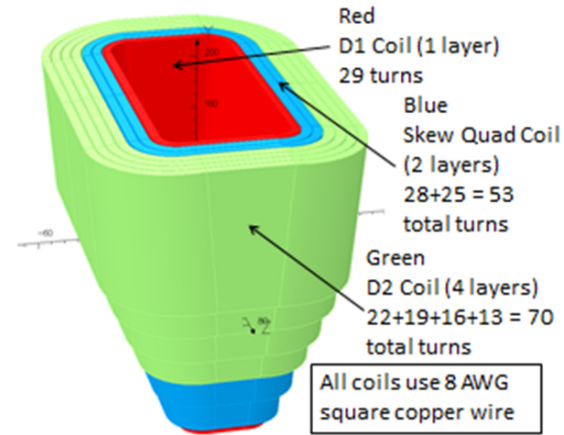


Figure 2: Coil Configuration.



Figure 3: Prototype Wound Coil.

This compact design presents demanding challenges for the coil manufacturer. Tooling similar to the tooling described in [3] is necessary to maintain the tight mechanical tolerance requirements and for producing coil assemblies with the most consistent shape and size. Building the prototype magnet verified that producing this compact coil design is possible by winding all 3 coil circuits directly on top of each other using a single winding fixture (see Figures 3 and 4).

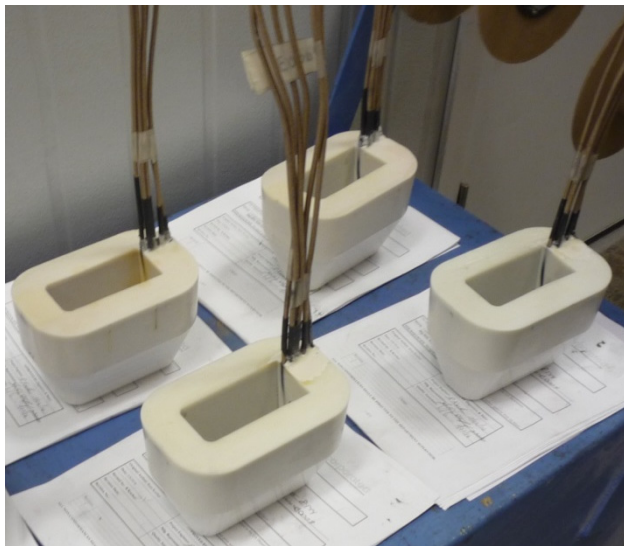


Figure 4: Prototype Potted Coil Assemblies.

Coil to coil connections between the eight coil assemblies that would typically be brazed or soldered together will instead be wired to terminal blocks. Terminal blocks are required in order to accommodate a possible future reconfiguration of the skew quadrupole circuit. The APSU accelerator physics group requested to have an option that would allow the reconfiguration of the skew quadrupole circuit into two circuits, a skew quadrupole circuit plus an octupole circuit. To accommodate this reconfiguration of the skew quadrupole circuit, the power input terminal block will have an extra pair of connections for future wiring of the octupole circuit.

POLE SEGMENTS

The 8 pole structure consists of 8 identical laminated pole segments. Each pole segment is made from 26 gauge (0.47 mm thick) M19 non-oriented steel that has a C-5 surface insulation coating on both sides. The laminations are bonded together to a length of 84.6 mm in the axial direction (see Figure 5).



Figure 5: Prototype Bonded Pole Segments.

Tooling will be required for stamping the laminations as well as stacking and bonding the pole segments. An assembly fixture will be used to precisely locate the 8 bonded pole segments that will form the magnet yoke. The assembled overall yoke cross section is 510 mm wide x 510 mm high (see Figure 6).

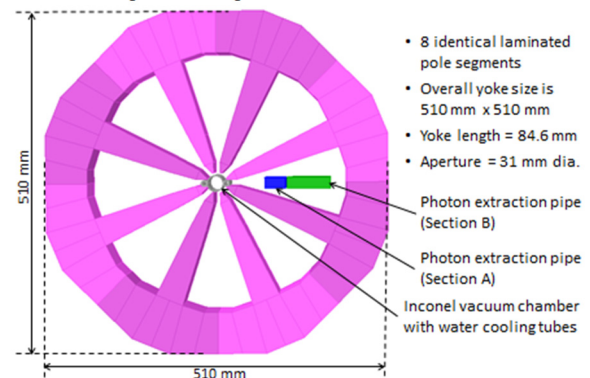


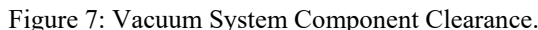
Figure 6: Magnet Yoke Cross Section.

Delamination on one of the pole tips was observed on the prototype magnet. Because there is such a small surface area at the pole tip, special attention will be required on the production magnets to ensure that there is an even distribution of pressure being applied across the entire stack of laminations during the bonding process. Each pole segment will be visually inspected for delamination after bonding, and if necessary a repair procedure will be used to apply room temperature curing epoxy to the unbonded area. In addition, a pole tip clamp has been designed that can be installed onto the magnet and used to mechanically secure the pole tips if needed.

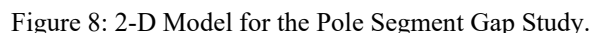
MAGNET ASSEMBLY

Requirements for the assembled magnet include being able to split the magnet at the horizontal mid-plane to allow vacuum chamber installation, also removal and

The magnet must also provide adequate clearance for the vacuum system components such as the vacuum chamber which passes through the central aperture of the magnet formed by the pole tips, and the photon extraction pipes which pass between the coils at the horizontal mid-plane of the magnet. This requires that the coils also be accurately located using an alignment fixture during assembly of the magnet (see Figure 7).



Having a tight positional tolerance for the pole tip alignment while requiring the pole segments to make contact with each other created an over constrained condition in the assembly. An Opera 2D study was undertaken to investigate this problem [4]. A 2D model with all 3 correctors powered was analysed first with no gaps between the mating surfaces of the pole segments and then finally with a 125 μm gap between each of the 8 pole segments. The gap was added between the light blue regions as shown in (Figure 8). Because the gap study showed negligible effects on both the strength and the harmonics, the 8-pole corrector can be assembled with priority given to the symmetrical positioning of the pole tips about the central axis in their ideal location. A tolerance has been added to the drawings allowing a pole-segment to pole-segment gap of no more than 100 μm .



Manufacturing and assembly tolerances were established to meet the magnet field quality requirements and to ensure adequate clearance is provided between the magnet and mating vacuum system components. Tooling will be used to ensure that a manufacturing tolerance of ± 0.05 mm is held on the component parts and fixtures will be used to align the component parts to a tolerance of ± 0.1 mm on the assembled magnet.

The prototype magnet demonstrated that the magnetic and mechanical designs are achievable. Improvements identified from manufacturing and testing the prototype magnet have been incorporated into the final design.

REFERENCES

- TUPH13
- 52

STATUS OF THE CONCEPTUAL DESIGN OF ALS-U*

C. Steier[†], A. Allézy, A. Anders, K. Baptiste, E. Buice, K. Chow, R. Duarte, G. Cutler, R. Donahue, D. Filippetto, J. Harkins, T. Hellert, M. Johnson, J.-Y. Jung, S. Leemann, D. Leitner, M. Leitner, T. Luo, H. Nishimura, T. Oliver, O. Omolayo, J. Osborn, C. Pappas, S. Persichelli, M. Placidi, G. Portmann, S. Reyes, D. Robin, F. Sannibale, S. De Santis, C. Sun, C. Swenson, M. Venturini, S. Virostek, W. Waldron, E. Wallén, LBNL, Berkeley, CA 94720, USA

Abstract

The ALS-U conceptual design promises to deliver diffraction limited performance in the soft x-ray range by lowering the horizontal emittance to about 70 pm rad resulting in two orders of brightness increase for soft x-rays compared to the current ALS. The design utilizes a nine bend achromat lattice, with reverse bending magnets and on-axis swap-out injection utilizing an accumulator ring. This paper shows some aspects of the completed conceptual design of the accelerator, as well as some results of the R&D program that has been ongoing for the last years.

INTRODUCTION

To achieve diffraction-limited performance for soft x-rays, ALS-U uses a nine bend achromat lattice with on-axis swap out injection. The improvement in coherent flux will be achieved by a big reduction of the emittance as well as smaller horizontal beta functions and insertion devices with smaller gaps (vertically and horizontally). This requires to replace the existing triple bend achromat lattice with a multi bend Achromat (MBA) lattice [1, 2]. The design produces round beams of 70 pm rad emittance, about 30 times smaller than the horizontal emittance of the existing ALS. ALS-U received approval of Mission Need (CD-0) from DOE/BES in September 2016 and the conceptual design was finished in spring 2018 and has been reviewed by a series of nine external technical reviews. Table 1 summarizes the main accelerator parameters and Figure 1 shows the nine bend achromat including the magnet supports based on plinths and rafts.

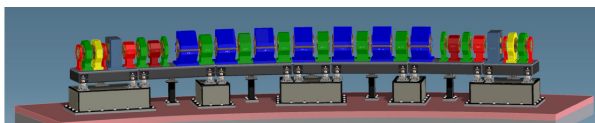


Figure 1: CAD model of ALS-U showing one of the twelve sectors of the nine bend achromat lattice as well as the support system based on plinths and rafts.

Because ALS-U is a low energy machine (with strong intrabeam scattering), it requires design solutions different from those of hard x-ray projects. Therefore an R&D program was started in early FY14 with the goal of reducing the

* This work was supported by the Director, Office of Science, Office of Basic Energy Sciences, of the U.S. Department of Energy under Contract No. DE-AC02-05CH11231.

[†] CSteier@lbl.gov

Table 1: Parameter List Comparing ALS with ALS-U

Parameter	Current ALS	ALS-U
Electron energy	1.9 GeV	2.0 GeV
Beam current	500 mA	500 mA
Hor. emittance	2000 pm rad	70 pm rad
Vert. emittance	30 pm rad	70 pm rad
rms beam size (IDs)	251 / 9 μ m	≤ 14 / ≤ 14 μ m
rms beam size (bends)	40 / 7 μ m	≤ 7 / ≤ 10 μ m
Energy spread	0.97×10^{-3}	1.04×10^{-3}
Bunch length (FWHM)	60–70 ps (harm. cavity)	120–140 ps (harm. cavity)
Circumference	196.8 m	~ 196.5 m
Bend magnets per arc	3	9

technical risks. The main areas studied were swap-out injection, harmonic cavities with large lengthening factors [3, 4], vacuum design/NEG coating, and high gradient magnets. Substantial progress has been made in all areas and an improvement in brightness by two orders of magnitude at 1 keV is achievable (see Figure 2).

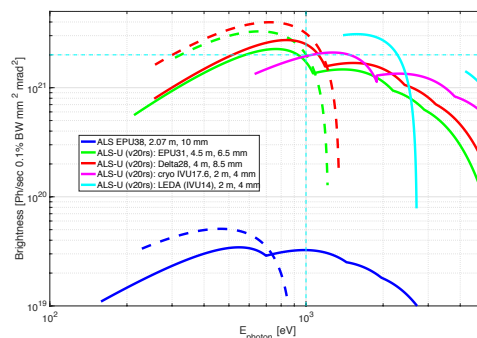


Figure 2: Soft x-ray brightness of planned new insertion devices on ALS-U compared to the existing ALS showing 2 orders of magnitude improvement at 1 keV.

LATTICE

During the conceptual design phase, a defined process was used to improve the lattice and, once a significant improvement was achieved, to update the baseline lattice, after evaluating the impact on the design of the individual technical systems. The work first focused on making the lattice more robust to errors, and to improve the lifetime. Later on, 5 T Superbends were included to maintain the ALS hard

x-ray capabilities. Finally, reverse bending magnets were included to lower the natural emittance. The resulting lattice uses 9 bending magnets, as well as 10 offset quadrupoles per arc which provide about 10% reverse bending. Six Superbend magnets with 5 T field [5] are included in three arcs to support the twelve existing hard x-ray beamline ports. Figure 3 shows the dynamic and momentum aperture as well as Touschek lifetime of about 1.5 h taking into account lattice errors and physical apertures. The adoption of frequent on-axis swap-out injection allowed to optimize the lattice for the small emittance and beta function and allows to successfully handle the short lifetime. Beam based lattice correction is essential during the commissioning period [6].

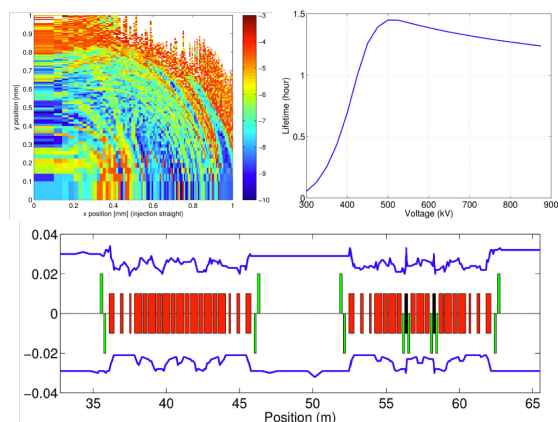


Figure 3: (Top Left) Frequency map for the 9BA lattice. (Bottom) Local momentum aperture for two periods including Superbends. (Top Right) Touschek lifetime as a function of RF voltage. All calculations include lattice errors and physical apertures.

The baseline lattice fulfills all high level project goals, including emittance, brightness, lifetime, as well as the ability to maintain the ALS hard x-ray capability. Other lattice options were studied as well, including hybrid MBAs with longitudinal gradients, different numbers of bending magnets, and an MBA design with combined longitudinal/transverse gradient magnets [7]. However, overall it was deemed that the 9BA with reverse bends and Superbends was the preferred choice.

COLLECTIVE EFFECTS

Because of the narrow vacuum chamber aperture (13 to 20 mm in the arcs; as small as 6 mm in the straights) the resistive wall impedance is a large contributor to the overall impedance. We have developed a conceptual impedance budget using numerical models for the short-range wake functions and their effects on the beam. Preliminary results show the single-bunch instability threshold with moderate chromaticity and harmonic cavities to be comfortably above the design current (see Fig. 4).

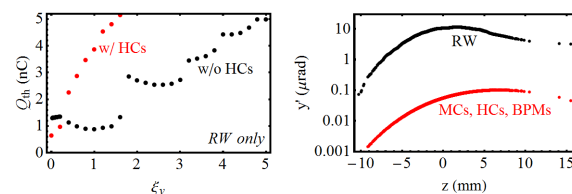


Figure 4: (Left) TMCI threshold as a function of chromaticity. (Right) Transverse wakefield kick due to resistive wall effect in small gap undulator chambers as well as selected other impedance sources.

INTRA BEAM SCATTERING

Scattering effects are stronger in low energy rings and have two consequences: they cause emittance growth (IBS) and induce particle loss. This is the main motivation for introducing harmonic cavities. Additional mitigating strategies consist of operating the machine in full-coupling mode with round beams and maximizing the occupation of the RF buckets. Thanks to these provisions, scattering effects become manageable but are still quite noticeable (see Fig. 5). The planned operating energy of ALS-U at 2.0 GeV is just above the beam energy at which the minimum emittance (including IBS) is achieved. The Touschek lifetime of the current baseline is about 1.5 h at 500 mA. The radiation damping of undulators helps to counteract some the emittance increase due to IBS. This effect of course depends on photon energy settings of each undulators [8]. A model has been developed based on historical data on the ALS and the prediction is that the emittance for ALS-U will be constant to a few percent for typical undulator operation. The average emittance with all effects included for the baseline lattice is 70 pm rad.

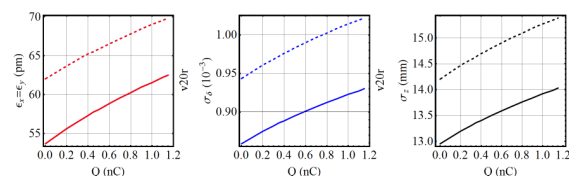


Figure 5: Emittance, energy spread and bunchlength increase due to IBS as a function of current for nominal fill pattern, round beams, harmonic cavities, both with and without the damping effect of a typical set of undulators.

MAGNETS

Strong focusing in single-function quadrupoles with gradients in excess of 100 T/m and combined-function bending magnets with gradients of about 46 T/m are required to achieve the target emittance. The latter will be realized with radially off-set geometric quadrupoles. To minimize power consumption and magnet size, we use a C-shaped design with asymmetric poles (see Fig. 6). The production of an R&D demonstration magnet with this design has

started. Further prototype magnets have been designed and production of those will start soon [9].

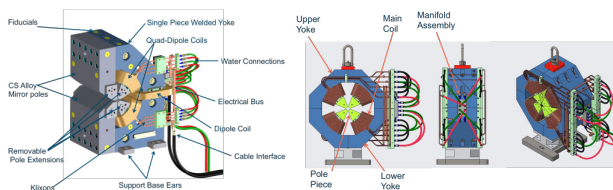


Figure 6: (Left) Design of the transverse gradient dipole which is being built as the first R&D magnet to demonstrate the critical technical features of ALS-U magnets. (Right) Design of the reverse bend quadrupole starting construction.

ACCUMULATOR AND SWAP-OUT

On axis-injection [10, 11] with bunch train swap-out and a full energy accumulator ring will be used. The accumulator will be housed in the storage ring tunnel and will act as a damping ring (see Figure 7).

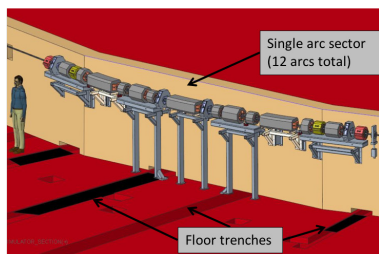


Figure 7: Mounting scheme for the accumulator on the inner shielding wall of the storage ring.

Its lattice will allow for off-axis injection from the booster and the extracted low emittance beam is injected on-axis into ALS-U. This allows ALS-U to be fully optimized for brightness. The main technical challenge of swap-out before the start of our R&D program was the fast magnets and pulsers needed for swap-out. To retire this risk, we designed, built, installed and tested a full prototype system of a small (6 mm) gap stripline kicker and an inductive voltage adder (5.5 kV) on the ALS (see Figure 8). The in-house designed inductive voltage adder has demonstrated pulses with the necessary very short rise times [12].

The stripline kicker has been installed for about one year in the ALS and has been tested in all fill patterns and operations modes. The TMCI threshold is the same as without the kicker and the heating of the kicker is manageable. Kicking the ALS beam with the stripline kicker and using turn-by-turn BPMs measurements of the pulse amplitude, duration, and shape, as well as reproducibility were carried out. The results confirm that the system fulfills the requirements.

VACUUM

The most promising technology to achieve good vacuum pressures with the small apertures necessary are Non Evaporable Getter (NEG) coated vacuum chambers. Substantial

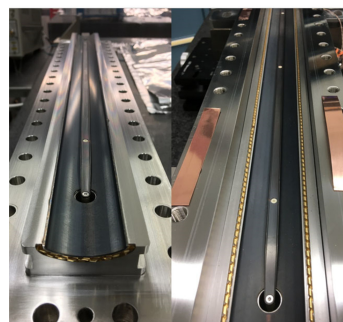


Figure 8: Top and bottom section of the stripline kicker with 6 mm full aperture, which is installed in the ALS.

progress has been made, bringing NEG coated chambers with less than 6 mm diameter within reach. The conceptual design of the ALS-U vacuum system has been completed (see Fig. 9) and pumping tests with 6 mm inner diameter copper vacuum chambers that have been NEG coated at LBNL have shown H_2 stickiness coefficients close to the best values reported for larger chambers.

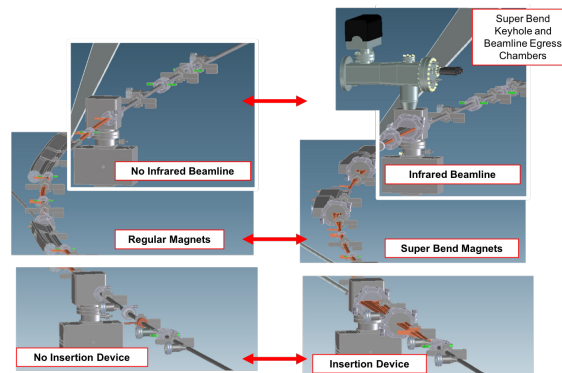


Figure 9: Conceptual layout of the arc sector vacuum chamber, photon extraction ports and absorbers.

TRANSFER LINES

An advantage of placing the accumulator in the same tunnel as the storage ring is a simplification of the layout for the transfer. Because the accumulator and storage rings have the same RF system frequency (500 MHz) there are path length constraints for two of the transfer lines. A feasible conceptual design for the three transfer lines connecting booster, accumulator and storage ring has been finished, that fulfills all physics requirements.

SUMMARY

A conceptual design of ALS-U has been completed. It uses a nine bend achromat lattice with reverse bending magnets and promises to achieve diffraction limited performance for soft x-rays up to 2 keV. In parallel, an R&D program has been successful in reducing major technical risks.

REFERENCES

- [1] H. Tarawneh *et al.*, “ALS-II, a Potential Soft X-ray, Diffraction Limited Upgrade of the Advanced Light Source”, *J. Phys.: Conf.* vol. 493, pp. 012020, 2015, doi:10.1088/1742-6596/493/1/012020
- [2] C. Sun *et al.*, “Optimization of the ALS-U Storage Ring Lattice”, in *Proc. IPAC2016*, Busan, Korea, May 2016, pp. 2959–2961, doi:10.18429/JACoW-IPAC2016-WEPOW050
- [3] S. De Santis *et al.*, “Injection/Extraction Kicker for the ALS-U Project”, in *Proc. IPAC2014*, Dresden, Germany, June 2014, pp. 1977–1979, doi:10.18429/JACoW-IPAC2014-WEPR0016
- [4] Z. Pan *et al.*, “Beam-Loading Transients and Bunch Shape in the Operation of Passive Harmonic Cavities in the ALS-U”, in *Proc. IPAC2018*, Vancouver, BC, Canada, Apr-May 2018, doi:10.18429/JACoW-IPAC2018-THPAK037
- [5] C. Swenson *et al.*, “Super Bend Magnet Design Options for the Diffraction Limited Light Source Lattices”, in *Proc. IPAC2018*, Vancouver, BC, Canada, Apr-May 2018, doi:10.18429/JACoW-IPAC2018-THPMF079
- [6] T. Hellert *et al.*, “Simulation of Trajectory Correction in Early Commissioning of the Advanced Light Source Upgrade”, in *Proc. IPAC2018*, Vancouver, BC, Canada, Apr-May 2018, doi:10.18429/JACoW-IPAC2018-THPMF078
- [7] S. Leemann *et al.*, “A Novel 7BA Lattice for a 196-m Circumference Diffraction-Limited Soft X-Ray Storage Ring”, in *Proc. IPAC2018*, Vancouver, BC, Canada, Apr-May 2018, doi:10.18429/JACoW-IPAC2018-THPMF077
- [8] F. Sannibale *et al.*, “Compensation of Insertion Device Induced Emittance Variations in Ultralow Emittance Storage Rings”, in *Proc. IPAC2018*, Vancouver, BC, Canada, Apr-May 2018, doi:10.18429/JACoW-IPAC2018-WEXGBE2
- [9] J. Jung *et al.*, “Design of Asymmetric Quadrupole Gradient Bending R&D Magnet for the Advanced Light Source Upgrade (ALS-U)”, in *Proc. IPAC2018*, Vancouver, BC, Canada, Apr-May 2018, doi:10.18429/JACoW-IPAC2018-THPAL020
- [10] C. Steier, “Possibilities for a Diffraction-Limited Upgrade of a Soft X-ray Light Source”, *Synchrotron Radiation News*, vol. 27, no. 6, pp. 18–22, 2014, doi:10.1080/08940886.2014.970934
- [11] M. Borland, “Concepts and performance for a next-generation storage ring hard x-ray source”, in *Proceedings of the SRI’09*, Melbourne, *AIP Conf Proc* vol. 1234, pp. 911-914, 2010, doi:10.1063/1.3463364
- [12] C. Steier *et al.*, “Progress of the R&D towards a diffraction limited upgrade of the Advanced Light Source”, in *Proc. IPAC2015*, Richmond, VA, USA, May 2015, doi:10.18429/JACoW-IPAC2015-TUPMA001

FRICTION STIR WELDING ATTEMPTS FOR UHV APPLICATIONS: STAINLESS STEEL/ALUMINUM

A. Ermakov[†], C. Martens, U. Naujoks, DESY, Hamburg, Germany

Abstract

At DESY in Hamburg an investigation was started to join aluminium chambers with stainless steel flanges by friction stir welding. First results will be presented. It will be shown that there is only a small effect of hardening in the contact zone at the stainless-steel side, a small amount of particles are given and the diffusion zone is about 3 microns, but with a very irregular effect on the structured junction.

Because of that, the influence of the surface and the welding parameters on the process will be investigated in the future.

OBJECTS FOR WELDING

The choice between different materials in UHV applications becomes more and more important. An investigation was started to combine aluminium chambers with standard UHV-flanges from stainless steel. Friction stir welding attempt was implied on standard UHV-flange type of NW100 (316LN) with Al insert (AN EW 6082 T6) as blind flanges for UHV usage. An industrial enterprise welded a series of flanges with different welding parameters (part of flange presented on Fig. 1). The samples #1, 2 taken from two welded flanges were investigated by means of hardness (Vickers, HV1), X-Ray fluorescence (Al is not visible due to technical limitations) and SEM/EDX element analysis measurements.

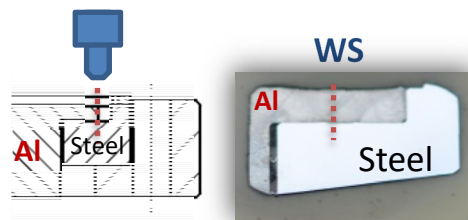


Figure 1: Part of flange with Al-insert. Position of welding seam.

HARDNESS

On Fig. 2 shown the results of hardness measurements in welding seam HAZ/TMAZ areas of sample #1. The hardness values in Aluminium part along the joint interface in WS area has in average 61.5HV1.

In both HAZ/TMAZ in measured region the Al alloy material is ca. 10% harder as in welding seam. The initial hardness of Al alloy is about 90HV so the softening of Al alloy close to welding seam area is obviously due to the temperature rise by welding. The distribution of hardness values in stainless steel shows the hardening of material in welding seam area close to joint interface. Due to relative lower thermal conductivity of stainless steel the hardness values are normalized in distance of about 1mm away to the hardness of stainless steel of ca. 160HV1. Similar variation of hardness of welding partners observed in articles [1-3]. It is reasonable to assume that hardening of material can be caused by at least 3 factors: one of them is deformation or pressure from the welding tool coming from Al side, temperature influence or the building of associated phases.

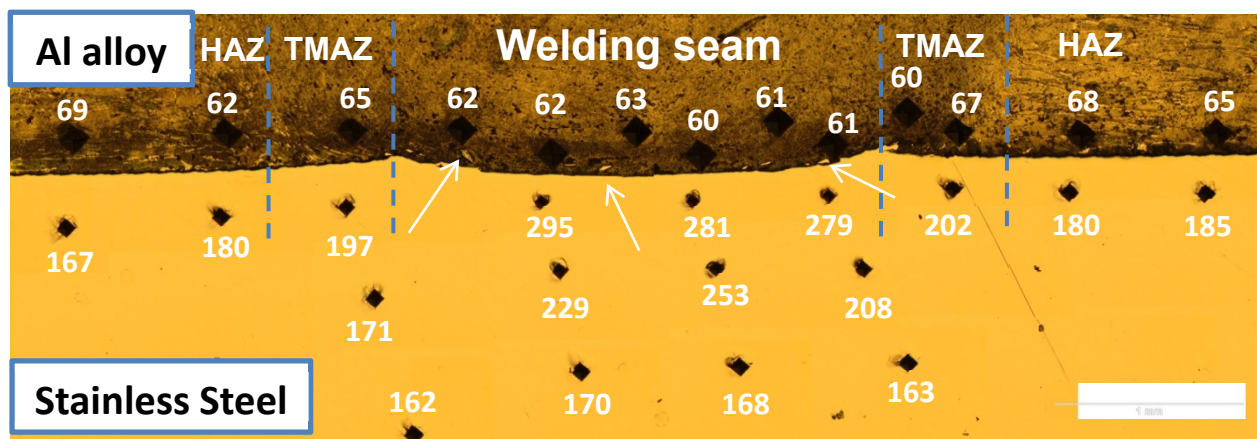


Figure 2: Distribution of HV hardness values measured along welding seam area and TMAZ/HAZ areas. Arrows show the small particles of stainless steel fraction mixed by welding with Al alloy.

[†] alexey.ermakov@desy.de

The deformation and subsequent temperature influence applied by submerging the welding tool into the depth could cause the hardening of stainless steel partner. The number of friction stir welding attempts done by different researches on similar metals confirm also the building in relative narrow welding seam band the phases like Al_5Fe_2 , $Al_{13}Fe_4$, Al_3Fe or Fe_3Al [4-8]. The detection of these phases in scope of this task is not possible due to technical limitations. The hardness measured in stainless steel part close to joint interface is ca. 285HV1. This hardness level can be attributed most likely to stainless steel surface mechanical deformation.

MICROSTRUCTURE OBSERVATION

The appearance of small particles of stainless steel fraction in narrow band in Aluminium alloy part close to joint interface is observed (some visible particles are marked with arrows on Fig. 3). These particles are visually observed and its presence confirmed by X-Ray fluorescence element analysis done in some locations of Al partner close to joint interface as well as in one location as reference in stainless steel (Fig. 3).

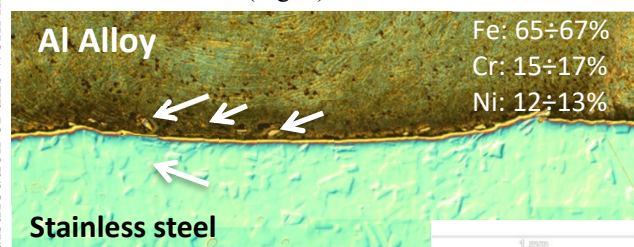


Figure 3: Elements composition measured in some locations of Al alloy and stainless steel parts (shown with arrows) of welding seam area.

The appearance of such particles is mainly associated with the mechanical deformation of the upper layer of stainless steel when the welding tool is touched. Similar structure observed also in [1, 2]. The size and distribution of those particles is evidently depends on some welding parameters such as rotation speed of welding tool and/or speed of feed.

The concentrations profiles of the main elements done by means of SEM/EDX at the welding interface between Stainless steel and Aluminium Alloy show slight mutual diffusion (See Fig. 4). These profiles show particularly the diffusion of stainless steel components Fe, Ni, Cr in deep of Al alloy part up to 2 μm , the diffusion of Al in stainless steel is ca. 1 μm . This difference in diffusions depths could be connected with local temperature, difference in diffusion coefficients of base metals and also the ratio of solubility one component in each other. The similar diffusion behaviour is also observed in [1, 7, 8].

3D MICROSCOPY

To investigate the internal structure of welding seam in details by means of 3D Microscopy the aluminium alloy and stainless steel's parts of samples #1, 2 were mechanically separated from each other.

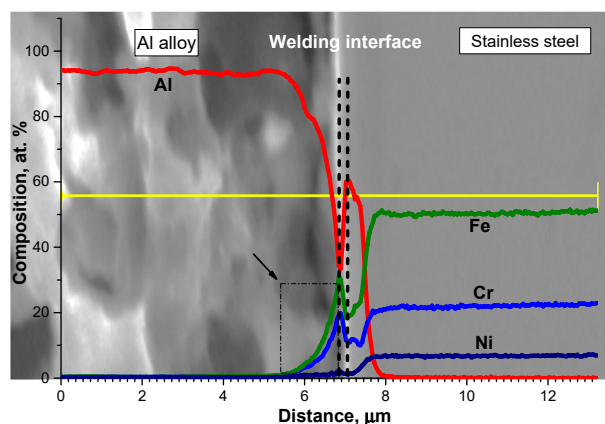


Figure 4: Concentrations profiles of Fe, Ni, Cr and Al across the EDX analysis line at the welding interface between Al alloy and stainless steel.

The circle-like structure observed in welding seam area after separation on sample #2 (Fig. 5) and stripes-like structure on sample #1 (Fig. 6) by means of 3D Microscopy.

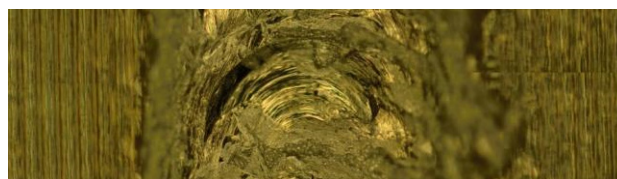


Figure 5: The microstructure of WS area of sample #2.

The circle-like structure in welding seam area of sample #2 show the traces of touching of welding tool of stainless steel partner by welding tool feeding. The welding seam area of sample #1 looks different and consists itself of two different regions: the stripe structure (circle-like structure for sample #2) (mainly in the middle of welding seam) and areas where the diffusion Al – Stainless steel can take place. The stripe structure is similar to base surface of the sample (outside of welding joint) and obviously didn't mechanically deform by welding tool. It can be assumed that the roughness of the stainless steel surface and the penetration depth of the welding tool play an important role. The mutual diffusion takes place only in edge areas and partly in the middle of welding seam area. For example the analysis of chemical composition done in the top of welding seam area (marked by orange circles, see also Fig. 6) by means of SEM/EDX confirms the diffusion of main base components in each other. Also the element analysis by X-Ray fluorescence performed on some locations inside and outside the welding seam area also confirms the diffusion: in location marked with green squares the amplitude (concentration) of base stainless steel components has maximum while in locations marked with red squares the amplitude has significantly lower magnitude (see Fig. 6).

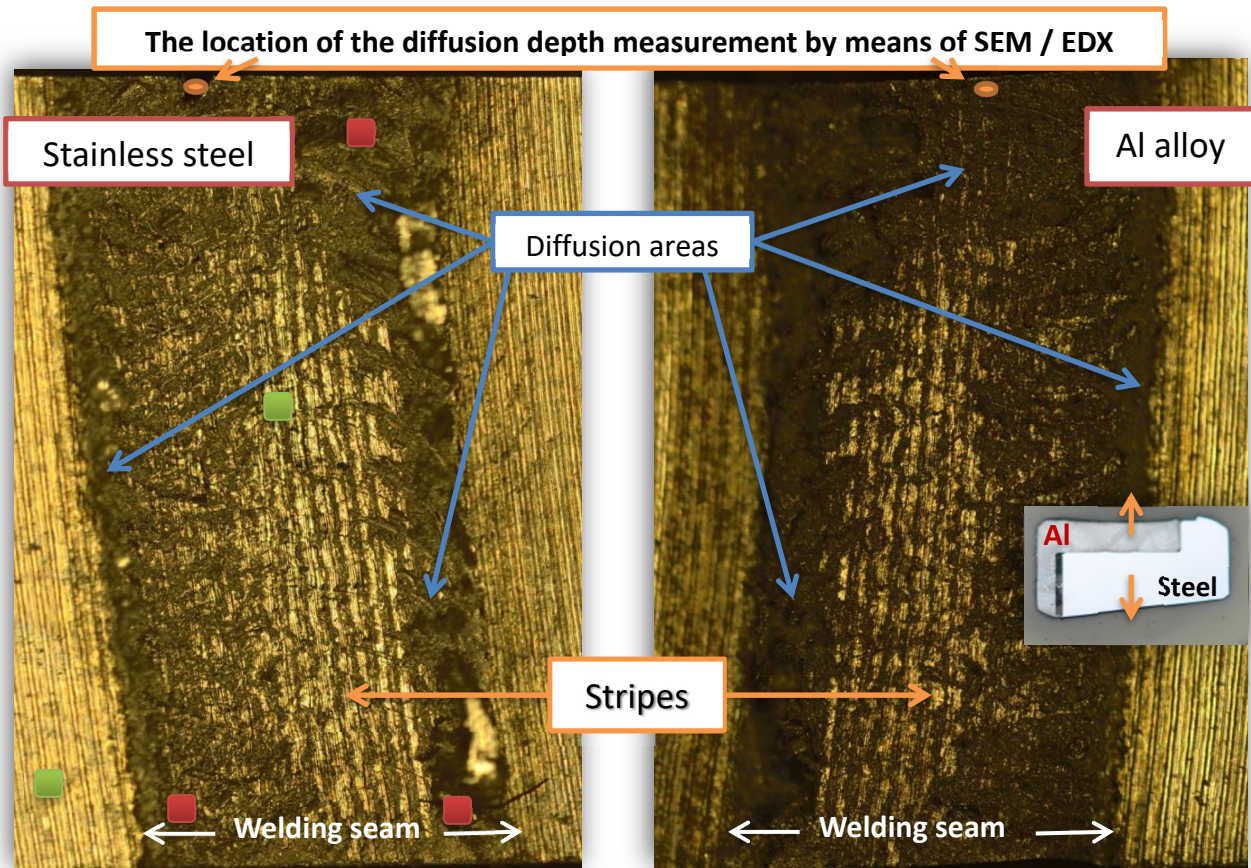


Figure 6: Mirror display of two opposite surfaces of the interface joint of sample #1. The green and red squares show the location of measurements of chemical composition.

CONCLUSION

The obtained results show the hardening of stainless steel partner and softening of Al alloy in area close to interface joint most likely due to the local temperature treatment/mechanical deformation. The welded seam has a non-homogeneous structure and mutual diffusion obviously occurs only in some regions, mainly along the edges. Obviously, the parameters of welding, the material thickness and the roughness of the surface of stainless steel are highly important.

ACKNOWLEDGEMENTS

We would like to thank Fa. Riftec GmbH (Geesthacht, Germany) for the provided samples of welded joints for investigation [9, 10].

REFERENCES

- [1] H. Uzun, C. D. Donne, A. Argagnotto, T. Ghidini, C. Gambaro, "Friction stir welding of dissimilar Al 6013-T4 to X5CrNi18-10 stainless steel", *Materials and Design*, vol. 25, issue 1, Feb. 2005, pp. 41-46.
- [2] A. Elrefaey, M. Gouda, M. Takahashi, and K. Ikeuchi, "Characterization of aluminum/steel lap joint by friction stir welding", *Journal of Materials Engineering and Performance*, vol. 14, March 2004, pp.10-17.
- [3] Z. Shen a, Y. Chen b, M. Haghshenas b, *, A.P. Gerlich, "Role of welding parameters on interfacial bonding in dissimilar steel/aluminum friction stir welds", *Engineering Science and Technology, an International Journal*, vol. 18, issue 2, June 2015, pp. 270-277.
- [4] M. Dehghani, A. Amadeh, S. A. A. Akbari Mousavi, "Investigations on the effects of friction stir welding parameters on intermetallic and defect formation in joining aluminium alloy to mild steel", *Material and Design*, vol. 49, August 2013, pp. 433-441.
- [5] K. Kimapong, T. Watanabe, "Lap Joint of A5083 Aluminum Alloy and SS400 Steel by Friction Stir Welding", *Materials Transactions*, Vol. 46, No. 4, 2005, pp. 835-841.
- [6] K. Kimapong, T. Watanabe, "Effect of Welding Process Parameters on Mechanical Property of FSW Lap Joint between Aluminum Alloy and Steel", *Materials Transactions*, Vol. 46, No. 10, 2005, pp. 2211-2217.
- [7] W.-B. Lee, M. Schmoecker, U. A. Mercardo, G. Biallas, Seung-Boo Jung, "Interfacial reaction in steel-aluminum joints made by friction stir welding", *Scripta Materialia*, vol. 55, issue 4, August 2006, pp. 355-358.
- [8] M. Mazar Atabaki, M. Nikodinovski, P. Chenier, J. Ma, M. Harooni and R. Kovacevic, "Welding of Aluminum Alloys to Steels: An Overview", *J. Manuf. Sci. Prod.*, vol.14, issue 2, July 2014, pp. 59 – 78.
- [9] EN ISO 25239-1:2012: Friction stir welding-Aluminum-Part 1: Vocabulary
- [10] Riftec GmbH, Geesthacht, Private Communications

HAMMERHEAD SUPPORT DESIGN AND APPLICATION AT SSRF*

F. Gao, R.B.Deng ,S.W.Xiang, Z.Q.Jiang, L.X.Yin
 Shanghai Institute of Applied Physics,CAS, 201204 Shanghai, China
 S.Sharma, NSLS-II, Brookhaven National Laboratory, NY, USA

Abstract

Electron beam stability is very important for Shanghai Synchrotron Radiation Facility (SSRF). One of the major players on beam stability is the vibration stability of magnet support systems. This paper describes several kinds of hammerhead magnet support prototypes with different structures, materials and ground fixation. Modal and response analyses of these prototypes are contrasted by finite-element analysis (FEA) and tests. The design can be applied to guide and improve the mechanical structures and the stability of magnet support systems at SSRF and other light source facilities.

INTRODUCTION

The Shanghai Synchrotron Radiation Facility (SSRF) is a third-generation light source, which requires high electron beam stability [1-2]. The electron beam stability is one of the most import elements that influence the properties of light sources. SSRF locates near the Huangpu River which flows to the east sea from west to east of Shanghai, which makes the soil soft. What makes things worse is the heavy traffic day and night and the nearby magnetic levitation. So the fact is that the ground vibrations at SSRF are larger than at other light sources due to altogether these factors [3].

The important demands of electron beam stability result in the high mechanical stability requirement for the light sources key parts such as quadrupole magnets. Since the mechanical support system for the magnets provides supporting, location and position adjustment, the high mechanical stability of the support is indirectly expected. The first eigenfrequency is an important index for the stability and performance of girders, based on the condition of SSRF, which motivates us to take measures to improve the stability of mechanical support system for magnets.

Marble bases produced from Shandong Province of China have been used as the main component of the support for quadruple in Shanghai Soft X-ray FEL (SXFEL) infrastructure [4]. S. Sharma proposed a girder-free support system. The system took account of several main aspects such as mechanical stability and thermal stability [5]. Based on these references, we developed several kinds of girder prototype for magnets at SSRF.

This paper describes an attempt to understand and increase the first eigenfrequency of different kinds of hammerhead support with different structures, materials and

ground fixation to improve the stability. Modal hammering experiments and the Finite-element (FE) analysis of prototypes were carried out at SSRF. The results are discussed in this paper.

STRUCTURE OF PROTOTYPES DESIGN

Figure 1 shows the mechanical structure of hammerhead support design for magnets. Figure 2 shows the size of one support. Two hammerhead supports are connected with two C-channel beams. The beams bolted to hammerhead supports are 2.9m in length and 0.4m in height, welded by steel plates. Magnets are assembled accurately on the top of supports with required good alignment techniques. Eight wheels fixed on both sides of the hammerhead supports can make the heavy support system move easier in the tunnel in the future. One prototype is about 2m long, with two quadrupoles and two sextupoles. Different materials and fixation methods between supports and floor are used for the design of prototypes.

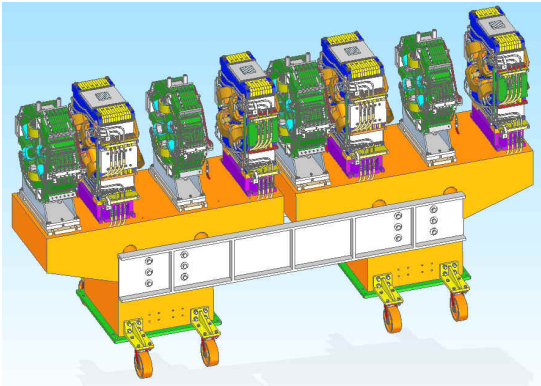


Figure 1: Structure of the hammerhead support system.

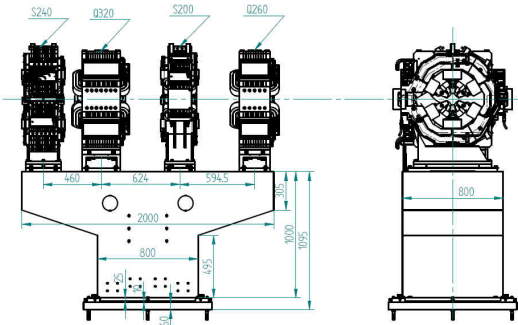


Figure 2: Size of the hammerhead support.

Design of Prototypes

Figure 3 shows the prototypes was designed to have two main parts, steel blocks instead of magnets are assembled on the top of supports, which are similar with real condition in the tunnel in the future. We proposed two types of hammerhead support.

- Prototype1 support contains two components of a marble block with a low thermal expansion coefficient and three layers of steel plates (see Fig. 4a). The bottom steel plate called grouting plate is fixed on ground with 4 tightening bolts and non-shrinkage cement having high strength. The four shims located on the four corners between grouting plate and marble fixed plate. 3 directions adjusting can be done by adjusting shims located on steel and 4 M16 jack screws.
- Prototype2 is similar to prototype1, Prototype2 support also contains two components of a steel welded box and two layers. Shims are sandwiched between the bottom of box and upper surface of grouting plate (see Fig. 4b). Compared with prototype 1, the prototype2 has no such a layer like marble fixed plate.

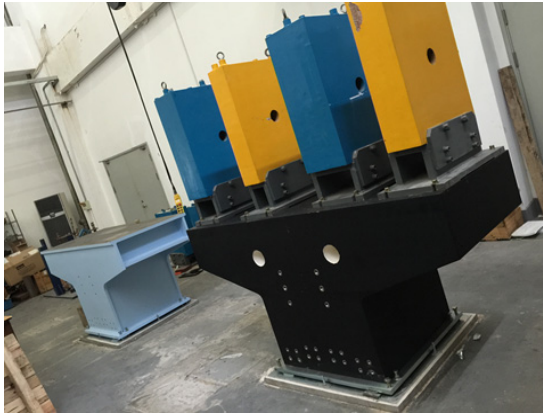


Figure 3: Hammerhead support Prototypes (Left: Steel base support; Right: Marble base support).

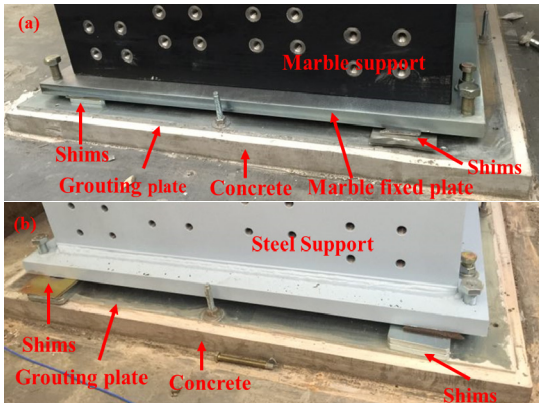


Figure 4: Fixation of Hammerhead support Prototypes on the floor (a: Marble base; b: Steel base).

FE ANALYSIS & MODAL HAMMERING MEASUREMENT OF PROTOTYPES

Table 1: First Eigenfrequency (Hz) (Transverse) of Two Prototypes

	Steel FE/Measurement	Marble FE/Measurement
With shims, and grouting plate and magnets assembled	63.5 Hz / 20.5 Hz	75.43 Hz / 18.75 Hz
Without shims and magnets	— / 56.15 Hz	— /66.25 Hz

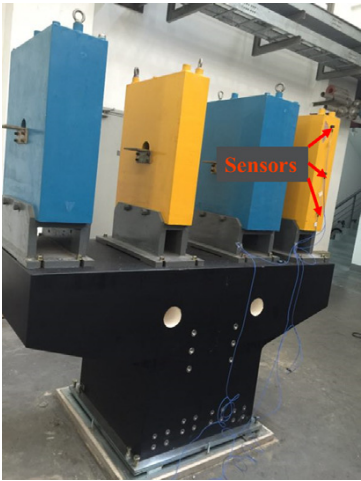


Figure 5: Modal measurement by acceleration sensors.

FE Analysis and Modal Analysis & Measurement

This section aims to investigate the dynamic performance of prototypes with different structure, materials and connections with floor and improve the mechanical design from a mechanical point of view. FE analysis (ANSYS Workbench14.0) and dynamic measurements (Device: DH5902N Data Collector system , Donghua Testing Technology. Co.,LTD and PCB333B30 Acceleration sensors) have been performed on prototypes . In the modal analysis, different connections between the bases and the floor are considered. In the modal measurement (see Fig. 5), 3 accelerometers are adhered evenly to the side of bases of two prototypes. Table 1 shows the results of FE and modal measurement. It is obvious to see the measured values are lower than FE calculations (see Fig. 6) both in marble support and steel support. This big difference can be explained by the different boundary condition in the FE modals. The results suggest that the layers between support and ground make the support system more weakness than the simulated fixed restriction in FE models.

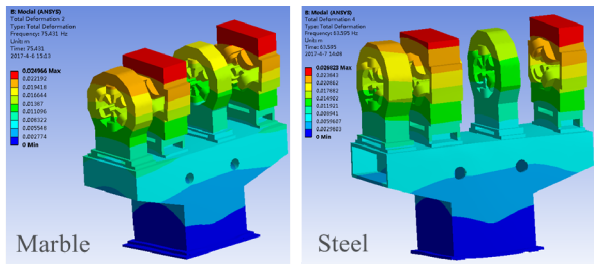


Figure 6: Hammerhead support Prototypes (1st modal in transverse -Mable: 75.35 Hz; Steel: 63.5 Hz).

Table 2: First Eigenfrequency (Hz) (Transverse) of Two Prototypes

	Steel Measurement	Marble Measurement
Full grouted without magnets	69.33Hz	48.75Hz
Full grouted with mag- nets	24.1Hz	23.2Hz

The results also suggest the first eigenfrequency of marble support is a little higher than steel support. To further understand the influence of the connection layers, the bases with magnet assembled or not were grouted directly by concrete (see Fig. 7) on the floor without any shims and grouting plates. In addition, there was still a marble fixed plate located between the marble base and the floor, because the holes on the marble fixed plate was needed for marble base installation. Then, we did the previous modal measurement again. Table 2 shows the results of the two bases. Figure 8 shows the first modal shape of two prototypes with full grouted in transverse direction. Base on the above FE and modal analysis, the full grouted connection between bases and floor is proposed to improve the first eigenfrequency of the prototypes. The first eigenfrequency of steel base is higher than that of marble base, which can be explained there was still a marble fixed plate between marble base and grouted concrete, the bolted connection makes the lower eigenfrequency.



Figure 7: Prototypes with full grouted bottom surface.

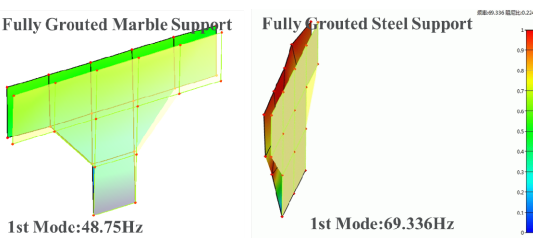


Figure 8: First modal shape of prototypes without magnet assembled.

CONCLUSION

In this paper the dynamic performance of hammerhead magnet support prototypes has been studied by FE analysis and modal measurement. Both FE calculations and modal measurement have been performed on two prototypes. The comparison of different connections between bases and floor has been also performed. Based on the result of FE analysis and modal measurement, the connection of full grouted is better than the case of bases with shims because of its higher first eigenfrequency, but the bases without shims were more difficult to installation and adjustment. In addition, the marble base of shims and magnets assembled has better performance than steel base in first eigenfrequency aspect. In FE calculations, maybe the fixed boundary applied at the bottom of bases prevents bending of plates and hides the weakness of tightening bolts. The boundary condition in the FE modals should be considered again in order to reflect the real connection between bases and floor. Further research about connection will be carried out to find a better way to design and installation of supports.

ACKNOWLEDGEMENTS

The authors would like to acknowledge financial support from The National Key Research and Development Program of China (No.2016YFA0402000) and The National Natural Science Fund (Grant No.114052550) .

REFERENCES

[1] X. Wang *et al.*, “Mechanical stability of the magnet girder assembly at the SSRF”, *J. Synchrotron Rad.*, vol.15-4, Jul. 2008, pp. 385-391, doi:10.1107/S090904950800650X.

[2] X. Wang *et al.*, “Dynamic performance of the beam position monitor support at the SSRF”, *J. Synchrotron Rad.*, vol. 16-1, Jan. 2009, pp. 1-7, doi:10.1107/S0909049508028872.

[3] L. Ouyang *et al.*, “The SSRF Ground vibration measurements and the beam COD calculations”, presented at MED-SI18, this conference, to be published.

[4] F. Gao *et al.*, “Dynamic performance of a support system for BBA components in SXFEL”, in *Proc. MEDSI 2016*, Barcelona, Spain, June 2017, paper MOPE31, DOI: 10.18429/JACoW-MEDSI2016-MOPE31.

[5] S. Sharma, “A girder-free magnet support system design”, in *Proc. MEDSI 2016*, Barcelona, Spain, June 2017, paper TUPE32, DOI:10.18429/JACoW-MEDSI2016-TUPE32

DESIGN CONSIDERATIONS ASSOCIATED WITH THE REPLACEMENT OF A SEXTUPOLE MAGNET BY A SHORT WIGGLER IN A CELL OF THE DIAMOND STORAGE RING LATTICE

N. P. Hammond, I. P. S. Martin, Diamond Light Source, Oxfordshire, UK

Abstract

All of the original straight sections in the Diamond storage ring are now occupied, and novel ways of converting bending magnet beamline locations into insertion device beamlines are being considered. Recently one cell of the 24 cells was reconfigured in to a Double-Double Bend Achromat (DDBA) to provide a new location for an Undulator and enable a formerly designated bending magnet beamline to become an Insertion Device Beamline [1]. Extending this concept for the new Dual Imaging and Diffraction (DIAD) Beamline proved to have a strong impact on lifetime and injection efficiency, so instead a proposal was made to remove a Sextupole magnet in the corresponding storage ring cell and substitute it with a short fixed gap Wiggler. The accelerator physics, mechanical and electrical design aspects associated with the change are described.

INTRODUCTION

One of the proposals emerging from the initial studies into a suitable cell configuration for an upgraded Diamond Storage Ring was a modified 4-bend achromat [1], referred to as DDBA. This had the additional benefit of providing a new achromat mid-straight for locating an Insertion Device (ID), which could replace the original bending magnet as a beamline source. Although initially developed as an upgrade for the whole storage ring it was decided to trial it in one cell to provide a new ID source for the VMX beamline. A number of factors described below prevent this solution from being deployed in a second location to provide an ID for the DIAD Beamline.

A SECOND DDBA CELL?

Although the ability of the Storage Ring to function under all operating conditions has been proved for a single DDBA cell [2], detailed studies (unpublished) have indicated that adding cells, reconfigured to a DDBA, reduces the dynamic and momentum apertures; and hence injection efficiency and lifetime to an unacceptable extent, refer to Figs. 1 and 2.

Additionally, modifying a cell to a DDBA configuration requires a complete new suit of reduced aperture magnets and vacuum vessels. Combined with re-cabling, the capital expenditure required is considerable, in the region of £2.6M excluding the cost of the new Insertion Device.

Limiting the shutdown for DDBA installation time to a maximum of eight weeks required an extensive programme of cabling up to two years in advance of the girder exchange. A set of temporary cables replicating the

existing ones was installed. The existing cell was then reconnected to the temporary cables, once this was completed the existing cables could be removed and replaced by the new DDBA cables. This way when the new girder assemblies were installed they could readily be connected to the pre-terminated cables [1]

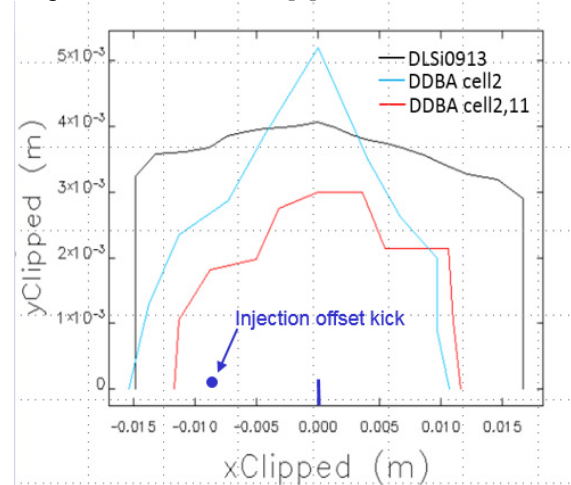


Figure 1: Reducing Dynamic Aperture for successive DDBA cell reconfigurations

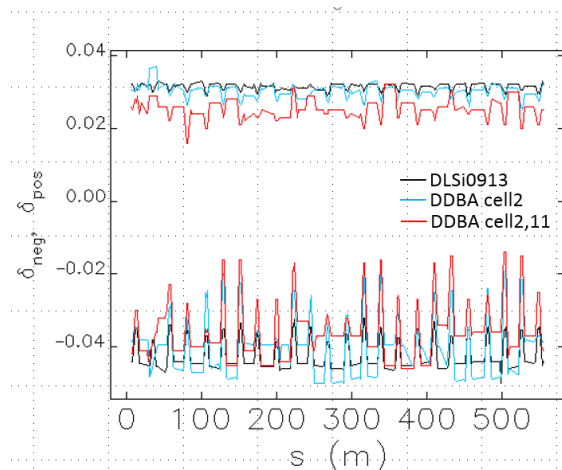


Figure 2: Reducing Momentum Aperture for successive DDBA cell reconfigurations.

The reduced machine performance combined with the associated costs of procurement, preparation, and installation have made an alternative configuration an attractive proposition.

An alternative reconfiguration was proposed whereby the first sextupole magnet upstream of the second dipole in the standard DBA configuration was replaced by a short 10 pole fixed gap Wiggler.

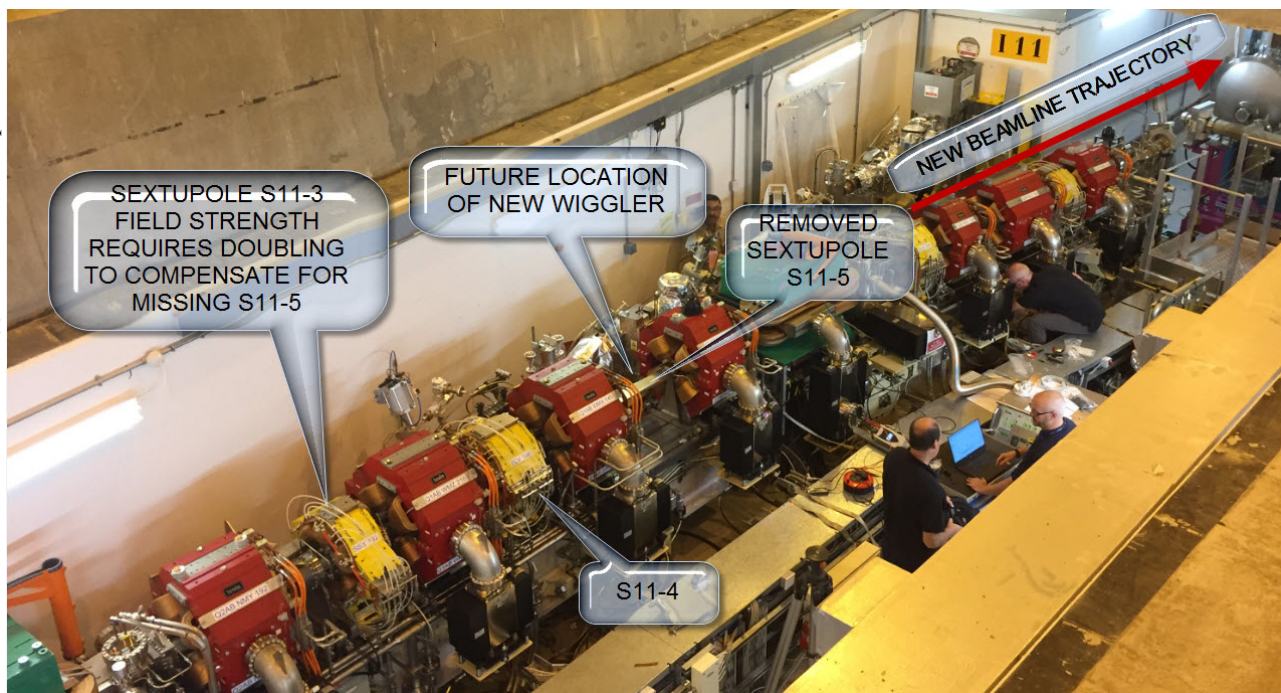


Figure 3: Illustration of newly installed storage Ring Cell for DIAD.

CELL RECONFIGURATION FOR DIAD

Overall, the inclusion of a Wiggler upstream of dipole 2 of the DBA changes the trajectory of the emitted light. Dipole Beamlines are provided with light between 5 and 25 mrad around the dipole arc (see Fig. 3). As a result, the aperture through the concrete shield wall is centred on 15mrad from the straight-ahead direction. Placing the Wiggler before the dipole fan switches trajectory back to the zero degree direction as illustrated in Fig. 4.

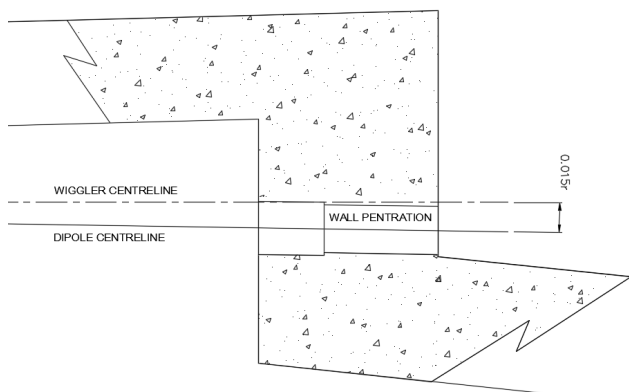


Figure 4: Differing trajectories of Wiggler and dipole light with respect to the Storage Ring wall penetration.

The difference between the new and old photon trajectory is significant and a new penetration through the concrete shield wall had to be prepared. This was achieved by core drilling an enveloping hole through the concrete and existing steel penetration liner, positioning a new liner in the void and back filling the interspace with high-density grout. The drilling process is illustrated in Fig. 5.

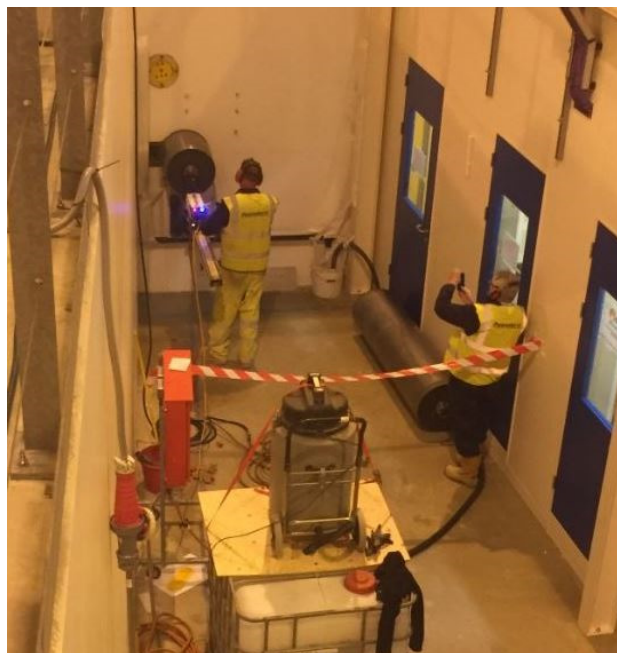


Figure 5: Core drilling for the new shield wall penetration.

The altered trajectory also meant that access to the out-board area between the new Front End and the shield wall will not be possible. Services and search routes will be redefined, as access will only be possible from the in-board side.

In addition, a number of design and component changes are required due to the altered trajectory:

1. A new shield wall penetration is required.
2. The photon absorbers in dipole 2 vessel require redesign.

3. The photon leg of the crotch vessel requires redesign to correspond to the new photon exit trajectory.
4. The yoke of the downstream quadrupole requires modification to avoid the new photon leg of the crotch vessel, see Fig. 6.
5. The inclusion of an insertion device on girder 2 with a pole tip gap of 22mm in place of a sextupole required a reduced aperture vacuum vessel (external height 21mm).

Capital expenditure for these cell modifications was in the region of £0.5M.

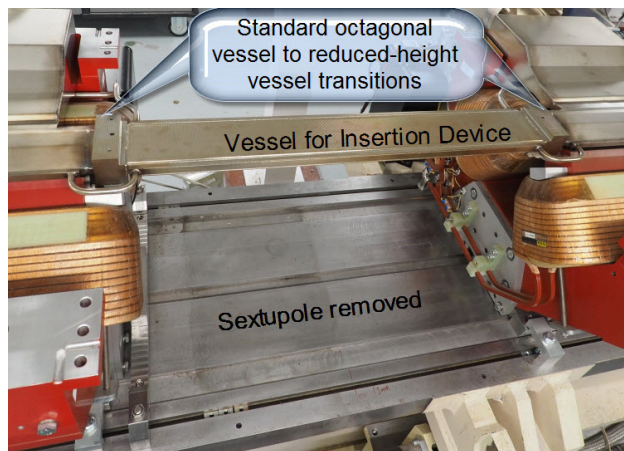


Figure 6: Vessel transition to the profile required to pass through the Wiggler (Magnet tops removed).

The girders removed from the storage ring for the DDBA installation were partially dismantled and reconfigured for DIAD. This allowed fully configured girders to be prepared in advance of the swap over during a shut-down.

The build of the 0.7 m long 10 pole Wiggler was scheduled to allow a trial fit at the girder build stage which was successful, see Fig. 7. The intention is to complete the Wiggler build after installation of the girders. To enable installation and removal of the Wiggler in situ a manually operated loading platform was designed which can span the cable tray stack adjacent to the girder in the storage ring. A short section of this apparatus is permanently fixed to the girder to enable the Wiggler to be moved horizontally when it is required to take it offline.

EFFECT ON MACHINE PERFORMANCE

At the proposal stage, a number of computer simulations and experiments were carried out to assess the impact of switching off the chromatic Sextupole magnet corresponding to the new Wiggler location (S11-5). Simply powering off this magnet was found to have an unacceptable impact on lifetime and injection efficiency. In order to recover the original performance level, the strengths of two local Sextupoles had to be adjusted (S11-3 and S11-4), combined with a small correction to the remaining sextupole families around the ring [3]. This solution required the magnet field strength of S11-3 to be doubled, which could only be achieved by replacing the existing power supply. Rebalancing of the water cooling

circuit for the sextupole magnets was also necessary to compensate for the removal of S11-5 and the increased cooling requirement of S11-3.

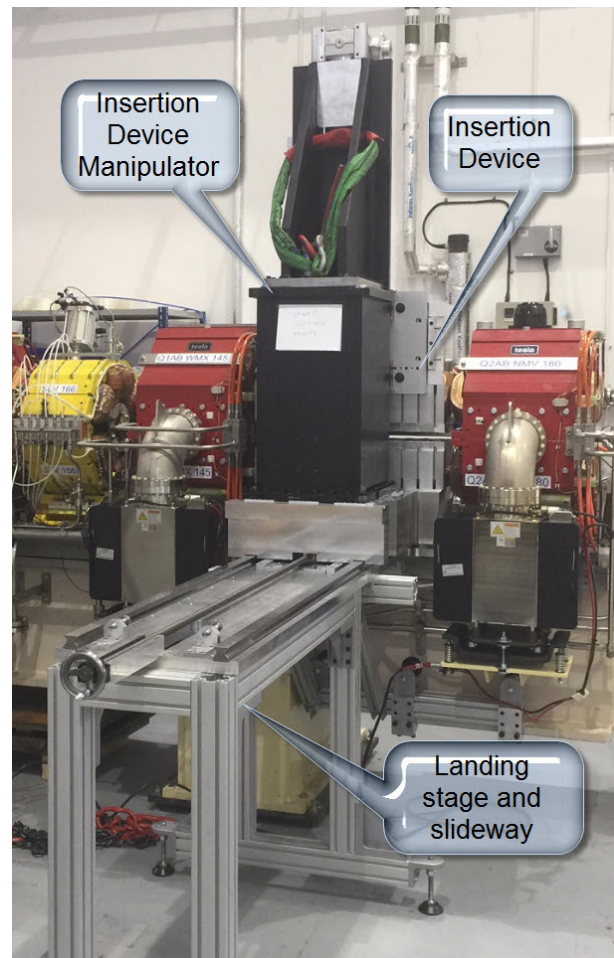


Figure 7: Trial fit of the 10 pole Wiggler in the Girder Build area.

CONCLUSION

The proposal of the inclusion of a short Wiggler as a source for the DIAD Beamline has delivered an alternative to the DDBA configuration that was trialled for the VMX Beamline with minimal impact on machine performance. The capital cost for DIAD represents a £0.5M cost saving and a one year reduction in delivery timescale when compared with DDBA.

REFERENCES

- [1] R. P. Walker *et al.*, "The Double-double Bend Achromat (DDBA) Lattice Modification for the Diamond Storage Ring", in *Proc. IPAC'14*, Dresden, Germany, pp. 34-52, doi:10.18429/JACoW-IPAC2014-MOPR0103
- [2] I. P. S. Martin and R. Bartolini, "Optimising the Diamond DDBA upgrade lattice for low alpha operation", in *Proc. IPAC'15*, pp. 525-527, 2015, doi:10.18429/JACoW-IPAC2015-MOPMA002
- [3] B. Singh *et al.*, "Studies to Install a Multipole Wiggler by Removing a Chromatic Sextupole in Diamond Storage Ring", in *Proc. IPAC'16*, Busan, Korea, May 2016, pp. 3518-3521, doi:10.18429/JACoW-IPAC2016-THPMR050

VACUUM PERFORMANCE TEST OF CuCrZr PHOTON ABSORBERS

Q. Li[†], P. He, D. Z. Guo, B. Q. Liu, Y. S. Ma, T. Z. Qi, X. J. Wang,
 Institute of High Energy Physics Chinese Academy of Sciences, Beijing, China
 P. Manini, SAES Getters S.p.A., Lainate, Italy

Abstract

To test the pumping performance of NEG coated CuCrZr absorber, we performed a comparative experiment on the two absorbers, one with NGE coating and the other one without coating. First, we run the Monte Carlo simulation by using MolFlow+ code to estimate the pressure inside test chamber at different thermal outgassing rate. And then two absorbers are mounted inside the chamber for the pressure vs. time profiles testing. The experimental set-up and pressure profiles will be presented here.

INTRODUCTION

We have developed two absorbers made of CuCrZr materials. The CuCrZr alloy is the right material for handling high heat load of synchrotron radiation. It has high yield and tensile strength, it has much lower cost than GlidCop, also it can be easily welded with stainless-steel (no brazing process) and also UHV compatibility. The two absorbers were similar in structure and the vacuum sealing flange was integrated with the absorber without any brazed or welded junctions. The 1st absorbers are similar to the ALBA absorber structure [1] and parts of the surface have NGE coating as shown in Fig. 1. The other one refers to the ESRF EBS [2] absorber structure but has no NEG coating on its surface, see Fig. 2. These two absorbers were made up by SAES RIAL and 1st one NEG coated by SAES Getters.

This experiment is to measure the pump-down curves of two absorbers and to see whether the NEG coating on the absorber has pumping effect. In the following sections, we will show the experimental set-up and present the measurement results.

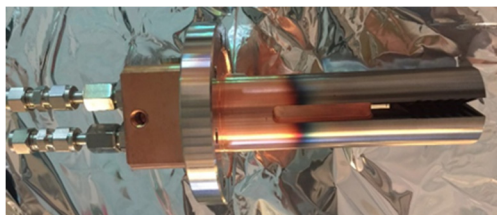


Figure 1: 1st absorber with NEG coating.



Figure 2: 2nd absorber without NEG coating.

MONTE CARLO SIMULATION

In order to choose the structure of a reasonable experimental system, we performed a simulation calculation using the Monte Carlo simulation code MolFlow+ which was developed at CERN [3].

We designed two types of experimental systems. One was to connect the vacuum chamber directly with a 150 L ion pump. The other was to add a 10mm diameter orifice conductance to the ion pump port. The simulation model is shown in Fig. 3. The simulated pressure results at different thermal outgassing rates are shown in Table 1.

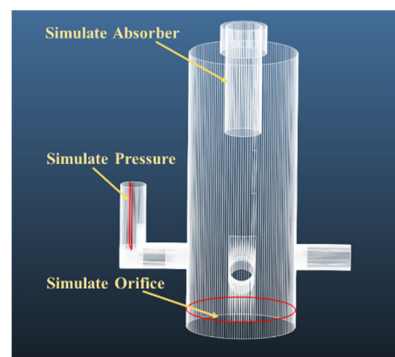


Figure 3: Simulation model.

Based on the simulation results, we set up the experimental chamber with small orifice conductance, so as to the pressure difference between the two absorbers can be more clearly displayed.

EXPERIMENTAL PROCEDURE

NEG coating can be activated after 24 hours baking at temperatures above 180°C. Before NEG coating activation, we need to bake the vacuum chamber to desorb the adhering gas on the inner surface. We developed our own activation curve with reference to the programs of SAES [4] and SOLEIL [5] and combined with the actual conditions of our baking, see Fig. 4.

Bake out operation procedure:

- Assemble the vacuum system including one of two absorbers and flanges.
- Put on the heating equipment (thermocouples and heating tapes) in three parts (absorber and vacuum chamber up and down).
- Start pump-down by primary pump and TMP.
- Switch on Helium Mass Spectrometer Leak Detector to perform leak detection.
- Keeping TMP pumping.

[†] liqi@ihep.ac.cn

Table 1: Simulation Parameters and Results

Assumed Vacuum Chamber Thermal Outgassing Rate 2E-10 mbar L/s/cm^2								
Assumed Absorber Pumping Speed on NEG Surface 0.3L/s/cm^2								
Assumed Absorber Thermal Outgassing Rate on Without NEG Surface (mbar L/s/cm^2)								
			5E-10	1E-10	5E-11	1E-11	5E-12	1E-12
Pressure (mbar)	Without Orifice	Without NEG film	1.24E-9	2.80E-10	1.62E-10	6.60E-11	5.36E-11	4.44E-11
		With NEG film	4.77E-10	1.20E-10	7.51E-11	4.16E-11	3.65E-11	3.30E-11
	With Orifice	Without NEG film	2.05E-8	4.63E-9	2.60E-9	9.68E-10	7.68E-10	6.04E-10
		With NEG film	1.45E-9	3.48E-10	2.18E-10	1.07E-10	9.46E-11	8.15E-11

- Bake-out for 24 h, heating stainless-steel vacuum chamber components up to 250°C and absorber parts to 150°C, respectively. In this way, water molecules desorbed by stainless steel under baking cannot stick to the NEG coating. In fact, heating this part to 100°C is enough, but the baking of the stainless-steel vacuum chamber passively heats the absorber part to 150°C under natural cooling conditions only. Heat up vacuum gauges and sputter-ion pump also, compatibly with their temperature limitations.
- At the end of the 24 h bake-out, start NEG activation by heating up NEG-coated parts to 230°C. Keep activating at the temperature for 24 h. When the temperature of the NEG-coated parts increases, cooling down stainless-steel vacuum chamber ones to 100°C and maintaining for about 5h.
- When the vacuum chamber temperature down to 150°C, flash the sputter-ion pumps and keep it switched on. When the vacuum chamber down to 100°C, degas the vacuum gauges and let it on to the end.
- When vacuum chamber temperature is cooled down to 100°C for 1 hour, close the valve to isolate the vacuum system and the molecular pump and start to record the pressure.
- Cool down the system to room temperature.
- Continue to record the pressure 12 to 13 hours for the pressure profiles.

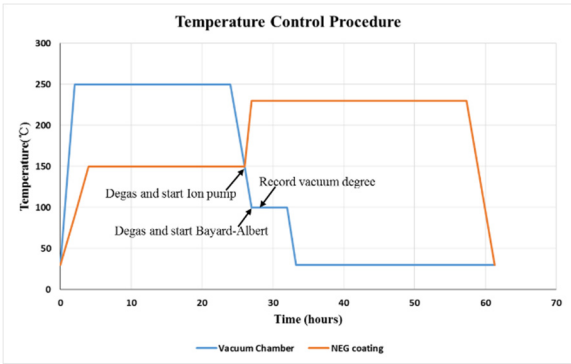


Figure 4: Temperature Control Procedure.

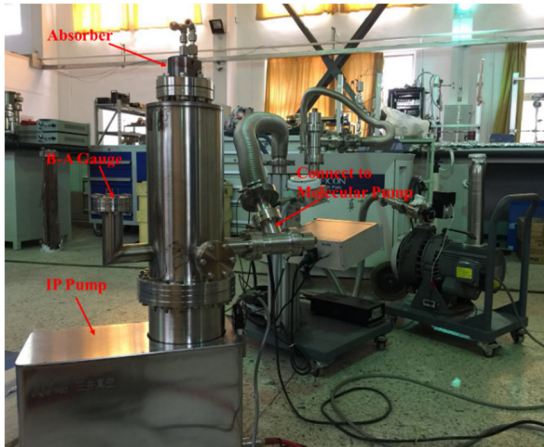


Figure 5: Experimental Set-up.

PRESSURE CURVES AND CONCLUSION

We set up a test system (Fig. 5) and conducted the experiments on two absorbers (one with NGE coating and the other one without coating). The two test conditions were kept as same as possible. Comparing the pressure vs. time curves of the two experiments, the NEG-coated absorber has a lower pressure (Fig. 6). This shows that the NEG-coated one has some pumping effect, and more coated surface area may help pumping more. Further investigation will be needed.

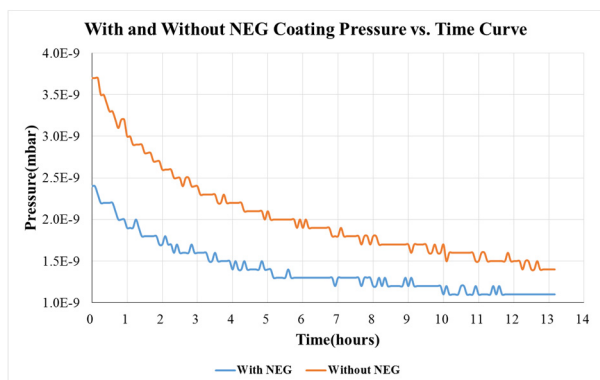


Figure 6: Pressure vs. Time Curve.

REFERENCES

- [1] M. Quispe *et al.*, "Development of the Crotch Absorbers for ALBA Storage Ring", in *Proc. MEDSI'08*, Saskatoon, Saskatchewan, Canada, June 2008, https://medsi.lbl.gov/2008_-_CLS-137.html
- [2] E. Gagliardini *et al.*, "A New Generation of X-ray Absorbers for the EBS Storage Ring", presented at the 9th Mechanical Engineering Design of Synchrotron Radiation Equipment and Instrumentation (MEDSI'16), Barcelona, Spain, September 2016, paper TUPE27, unpublished.
- [3] M. Ady and R. Kersevan, "MolFlow+ user guide", <https://molflow.web.cern.ch/content/molflow-documentation-0>
- [4] SAES Getters S.p.A., NEG coating activation procedure.
- [5] C. Herbeaux *et al.*, "NEG Coated Chambers at SOLEIL: Technological Issues and Experimental Results", in *Proc. EPAC'08*, Genoa, Italy, June 2008, paper THPP147, pp. 3696-3698.

A MECHANICAL UNDULATOR FRAME TO MINIMIZE INTRINSIC PHASE ERRORS

Jui-Che Huang[†], Chih-Sheng Yang, Ching-Kang Yang, Cheng-Hsing Chang, Ching-Shiang Hwang,
 National Synchrotron Radiation Research Center, Hsinchu, Taiwan
 H. Kitamura, RIKEN / SPring-8, 1-1-1 Kouto, Mikazuki-cho, Sayo-gun, Hyogo, Japan
 S. Mizumoto, T. Kohda, NEOMAX ENGINEERING Co., Ltd, Suita-shi, Osaka, Japan

Abstract

A PrFeB-based cryogenic permanent magnet undulator (CPMU) is under construction at the Taiwan Photon Source (TPS) to generate brilliant X-rays. When magnets are cooled to 77 K, a CPMU with a period length of 15 mm can generate an effective magnetic field of 1.32 T in a gap of 4 mm. A main feature of the TPS CPMU is its low-intrinsic-phase errors by the installation of force-compensation modules on the out-of-vacuum girders in a four-support-points configuration. Moreover, adjusting the spring settings one can obtain very low undulator phase errors. In this paper, a mechanical frame design for the TPS-CPMU with force-compensating spring modules will be discussed. Observations of deformation effects of the out-of-vacuum girders on the CPMU will be presented.

INTRODUCTION

Together with a high strength parameter, low phase errors are required characteristics an undulator to allow the generation of higher harmonics without significant degradation of SR brilliance and are therefore an important consideration to evaluate the undulator magnetic field quality. The X-ray brilliance degradation (I/I_0) due to RMS phase errors scales like $I/I_0 = \exp[-(n\sigma_{PE})^2]$ [1], where n is the undulator harmonic order and σ_{PE} the RMS phase error. The phase error derives from magnetic field errors, which can result from (1) differences of individual magnet blocks, such as remnant field and height of the magnet, (2) gap errors from manufacturing tolerances, such as the flatness of the in-vacuum girder, the length of link rods and assembly accuracy of the mechanical frame, (3) gap errors caused by mechanical deformations and (4) thermal effects in magnet arrays. During the construction of a TPS-CPMU, individual differences of magnet blocks can be greatly eliminated by magnet sorting. Gap errors from manufacturing tolerances can be corrected by adjusting gaps locally. These two error sources are of a static nature and careful corrections can be made to minimize phase errors. The gap errors caused by mechanical deformations are gap-dependent, since the magnetic forces increase exponentially with decreasing undulator gap. A counter force system, especially at small gaps, becomes necessary to retain low intrinsic RMS phase errors. Thermal effect in the magnet arrays can be corrected by temperature control systems, which however will not be discussed in this note.

MECHANICAL FRAME WITH FORCE-COMPENSATING SPRING MODULES

The magnetic force in the CU15 reaches up to 32 kN at a gap of 4 mm and 77 K, so a conventional two-support configuration is no longer rigid enough to keep the net RMS phase errors small. Yet, an optimized four-support configuration can reduce the intrinsic rms phase errors to less than 0.5 degrees [2]. Moreover, strong magnetic forces not only cause gap errors but also the deformation of the mechanical frame and heavy load to the gap drive system. Based on these considerations, the design goal of a counter force system in a four-support configuration of the mechanical frame is not only to compensate the magnetic force but also to obtain a mostly stress-free mechanical frame. Therefore, a force-compensation spring module in a compact and moment-free design is introduced and installed on four support-points of the mechanical frame (Fig. 1). The spring module is an invention of Hitachi Metals Co. Ltd. and international patents are pending. Attractive characteristics of the force-compensating spring modules are, (1) that the system is set-up in-air, so the adjustment of springs is easy, (2) machined -springs results in good reproducibility, (3) the low weight and compact design allows easy removal of the spring module during maintenance and assembly of vacuum components and (4) effective compensation of strong magnet forces without undesirable side effects. The spring module is installed between upper and lower out-of-vacuum girder and can compensate the attractive magnetic forces by repulsive spring forces. The rotational moments of the upper and the lower girders act in opposite directions as shown in Fig. 1b. The linear guides have sufficient stiffness to allow the changes of the magnetic gap while absorbing the rotational moments since, there is no mechanical connection between spring module and the pillars of the mechanical frame. The deformed spring module can keep the mechanical frame mostly stress-free with only a small deformation.

Figure 2 illustrates the deformation of the mechanical frame with and without spring modules by a finite element analysis. With the spring module, the transverse pillar tilt becomes small and the deformation of the out-of-vacuum girder due to magnetic forces can be reduced from 2.1 μm to 0.12 μm for a force of 32 kN (Fig. 3). Including the in-vacuum-girder deformation, the intrinsic phase errors are estimated to be less than 1 degrees. The spring module will deform and compensate the magnetic force, so the stress and deformation of the out-of-vacuum girders and pillars are reduced.

[†] email address : huang.juiche@nsrrc.org.tw

Content from this work may be used under the terms of the CC BY 3.0 licence (© 2018). Any distribution of this work must maintain attribution to the author(s), title of the work, publisher, and DOI.

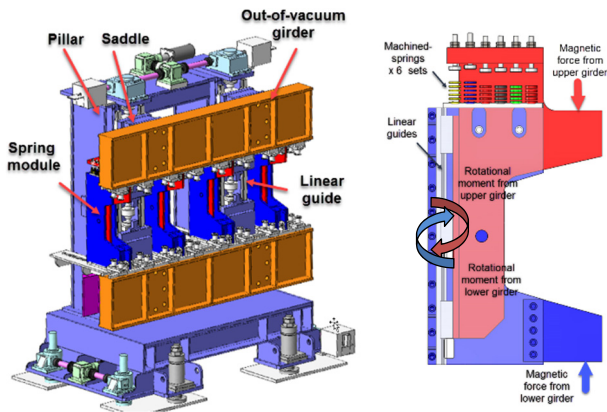


Figure 1: Force-compensating spring module on the CU15 (left) and spring module (right).

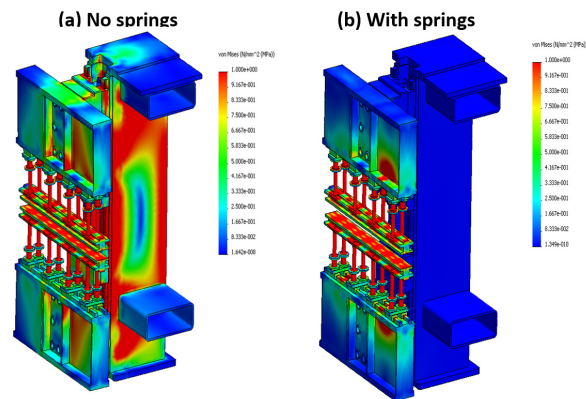


Figure 2: Stress distributions of the mechanical CU15 frame with and without spring modules under magnetic load of 32 kN.

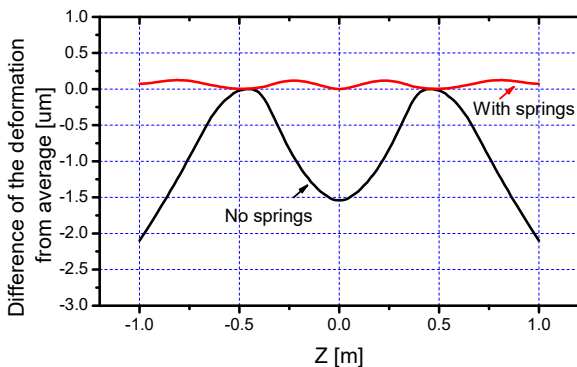


Figure 3: Finite element analysis on a deformed out-of-vacuum girder d with and without spring modules under magnetic load of 32 kN.

The spring module consists of six sets of machined-springs with various coefficients to allow a close fit to the exponential characteristics of the magnetic forces. The weakest spring start engaging at gap of 11.05 mm and then as the gap is reducing additional springs come into play. Figure 4 shows the repulsive force generated by the springs to compensate the magnetic force with exponential characteristics at CT and RT. The spring settings must be adjustable when the CPMU is cooled down and therefore easy access and tuning in air is desired.

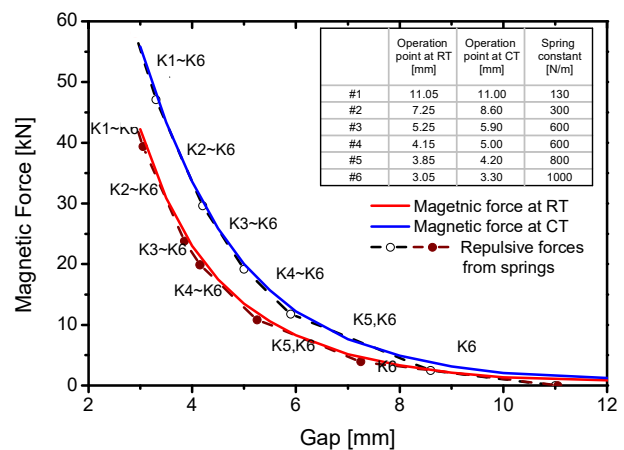


Figure 4: Dependence of magnetic (solid lines) and repulsive (dashed lines) forces on gap size at 300 K and 77 K.

DEFORMATION OF OUT-OF-VACUUM GIRDERS

The spring modules can reduce gap errors caused by the deformation of out-of-vacuum girders and to monitor the gap errors, we use 16 digital SONY magnescale gauges (DF-830SLR) with a resolution of 0.1 μm. A pair of gauges are located along the magnet arrays as shown in Fig. 5. The forces at a gap of 15 mm are negligibly small and we quantify gap errors by the difference between deformed and undeformed (gap of 15mm) structure. Figures 6 and 7 show the effect of the spring modules on gap error and transverse tilt of the out-of-vacuum girder, respectively. When there are no springs used for force compensation, the gap error is around ± 3 μm at a gap of 5 mm although this gap error and transverse tilt of out-of-vacuum girder can be reduced with the spring modules. The gap errors can further increase when the gap is less than 5 mm but can be reduced again for different spring settings. Larger gap errors were observed in contrast to simulations (Fig. 3). Since, the springs can only compensate magnetic loads, other errors, for example, coming from the drive system, may be included in the observation but not in the simulation.

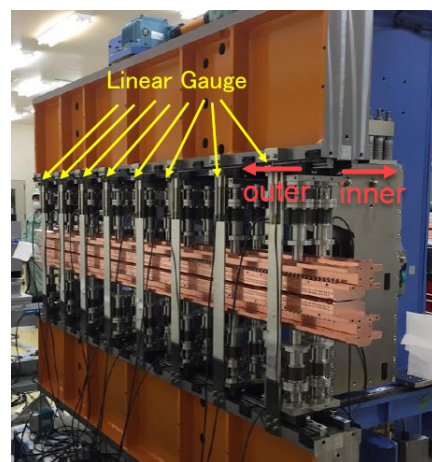


Figure 5: Gap error measurement setup on out-of-vacuum girder.

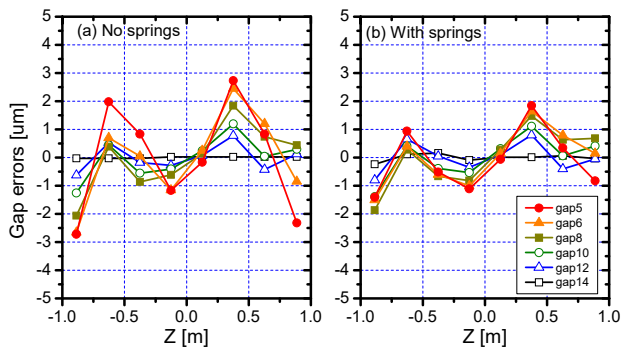


Figure 6: Effect of spring modules on gap errors for out-of-vacuum girders.

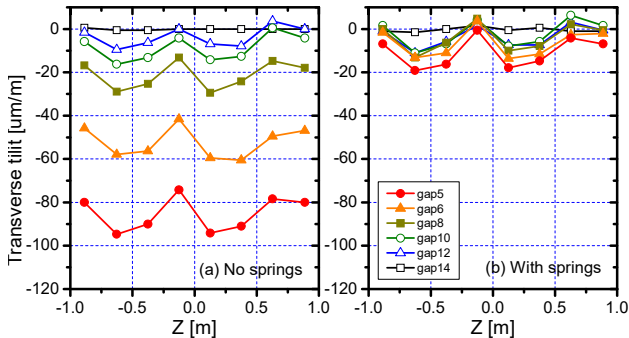


Figure 7: Effect of spring modules on the transverse tilt of out-of-vacuum girders.

GAP ERRORS CAUSED BY OPERATIONAL ERRORS

In the gap range of 15 to 25mm, where the magnetic force is negligibly small, the gap errors from magnetic loads can be ignored. Figure 8 shows observed gap errors at the inner side, near the ball screws/linear guides, and the outer side of the frame being $\pm 2 \mu\text{m}$ and $\pm 1 \mu\text{m}$, respectively. These results suggest that the errors come from the drive system, for example, from tolerances in the parallelism of the linear guide resting on the pillars. We assume such gap errors to be caused by operation and to eliminate them in the measurement, gap errors were measured for small gap changes only (1 mm step of gap closing), so that gap errors come mainly from the magnetic load. When the gap is changed from 4 to 3 mm, a gap error of $\pm 0.7 \text{ mm}$ is generated by magnetic forces of up to 20 kN (Fig. 9), which, while ignoring operational errors, can be compensated by the spring module.

The source of operational errors could come from poor parallelism of the linear guides. When the gap changes, angular errors are introduced at support positions, and as a result, the internal forces cause deformation of the out-of-vacuum girders. Figure 10 illustrates gap errors derived from such operational error. The CU15 mechanical frame has an assembly tolerance for the linear guides of around $1 \mu\text{m}$ and the deformation of the out-of-vacuum girders is around $\pm 2 \mu\text{m}$. If a gap error in the sub-micrometre-range is required, one could add a sliding mechanism to the connection between out-of-vacuum girders and support points of the frame like the mechanism used for tapered-undulators at the TPS.

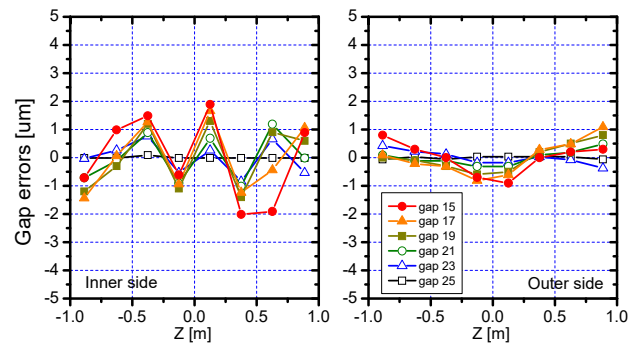


Figure 8: Gap errors of out-of-vacuum girders due to operational errors.

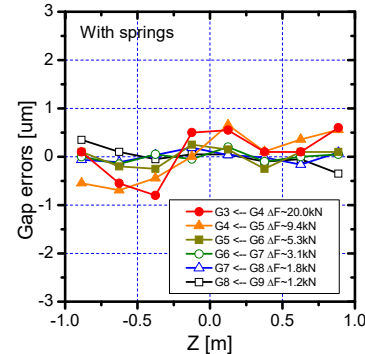


Figure 9: Gap errors of out-of-vacuum girders due to magnetic forces.

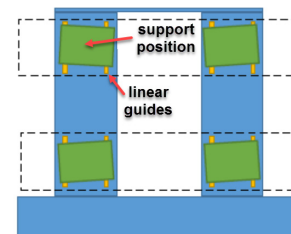


Figure 10: Sketch for the deformation of out-of-vacuum girders due to tolerances in the parallelism of the linear guides.

SUMMARY

Adoption of spring module, the gap errors are less than the TPS IVUs. A rms phase-error of 2 degree less at gap 4 mm to 10 mm can be obtained by fine adjustment of spring modules. At current design, the gap errors derived from a combined effect of operational errors and magnetic loads. A new tapered function mechanical frame with spring compensation modules will be used in the next TPS undulators to reduce the operational errors.

REFERENCES

- [1] B. Diviacco and R. Walker, "Recent advances in undulator performance optimization", *Nucl. Instr. Meth.*, vol.368-2, Jan. 1996, pp.522-532.
- [2] J. C. Huang, H. Kitamura *et al.*, "Challenges of in-vacuum and cryogenic permanent magnet undulator technologies", *Phys. Rev. ST ACCEL. Beams*, vol. 20, iss. 6, June 2017, DOI: 10.1103/PhysRevAccelBeams.20.064801

DESIGN OF VERTICAL AND HORIZONTAL LINEAR FLEXURE STAGE
 FOR BEAM SIZE MONITOR SYSTEM

W.Y. Lai, S.Y. Perng, H.S. Wang, C.J. Lin, D. G. Huang,
 H.C. Ho, K.H. Hsu, T.C. Tseng, C. K. Kuan

National Synchrotron Radiation Research Center, No 101, Hsin-Ann Road, Hsinchu 30076, Taiwan

Abstract

Taiwan photon source is a third-generation accelerator with low emittance and high brightness. The electric beam size is one of important parameters to indicate the stability and to measure the emittance and coupling of light source. The aperture size of beam slit is a crucial part to calculate the value of beam size in the X-ray pine-hole system. In order to obtain the more precise result of beam size, the flexure mechanism on beam slit is applied for the adjustment of the aperture. This paper shows that the design concept and the measurement of the beam size are obtained by the new adjustment system.

INTRODUCTION

The Taiwan Light Source (TPS) is a 3-GeV synchrotron radiation light facility. The construction started on February 2010 and after five years of construction and hardware developments, commissioning of the beam began on December 2014, and the 8 insertion devices were installed from April 2015 to now for user of beam line. Now the beam current of TPS storage ring can be up to 400mA for beam line used. TPS is a third-generation accelerator with the characters of low emittance and low coupling. Those beam parameters are routinely measured by the synchrotron radiation light produced from a dipole magnet, and the emittance can be measured indirectly by obtaining the transverse beam size. There is a dedicated beamline for photon diagnostics at the TPS storage ring utilized visible light and X-ray of the synchrotron radiation [1].

The structure of X-ray pine hole was oxidized seriously by the ozone resulted from reaction of ultraviolet in air after several years. It made the measurement of beam size to be instable and unreliable, because of that there was some fluff on the aperture of X-ray pine hole generated by the oxidation of structure. The measurement of beam size is relating to the aperture of beam slit sensitively and the energy peak of spectrum slightly [2]. Considering of that, the X-ray slit at upstream is designed to be ability of scanning for obtaining the optimum aperture at different spectrum situation.

MECHANISM DESIGN

The previous measurement of the beam size at TPS was about 63µm and 40µm in the X and Y direction respectively. The result is large than the result of calculation [3]. In order to get the more precise beam size of TPS, the existing equipment need to be upgraded. To find the best

aperture at the dedicated beam is the direction of promotion. Considering the purpose, an adjustable aperture mechanism with the ability of high resolution in a limited space was designed. The advantages of compliant structure are well known in no backlash motion and absence of lubrication and wear. Considering that the requirement of a stroke is also few and the requirement of space is limited, an adjustment system with vertical and horizontal linear flexure stage was designed at dedicated beam line as shown in Figure 1.

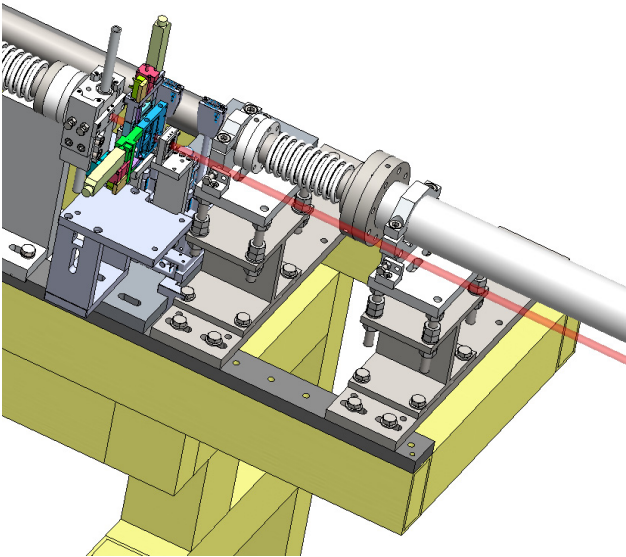


Figure 1: Layout of the adjustment system.

Introduction of Components

Figure 2 shows all the components of adjustment mechanism. The original structure of X-ray pine hole was set on commercial X, Y stages. The new adjustment system was set on the other X, Y stages. We can choose one those slitters by using those stages. Another function of stages is tuned for scanning the position of X-ray.

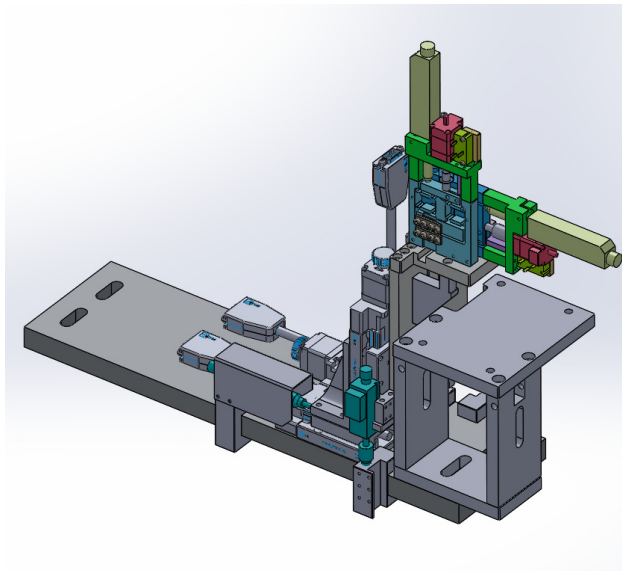


Figure 2: Components of the adjustment system.

The blue parts are the main structure of linear flexure stages in vertical and transverse direction. The flexure structure of leaf can provide a function of parallel motion. The main structure would be set on a two-axis stage. The 2-axis stage is used for searching the best position of X-ray. The black parts are the tungsten blade mounted on flexure mechanism for the function of slit. The red parts are the two-phase stepper motor for adjusting the aperture of tungsten blade. The absolute length gauges are used for the feedback of aperture as shown in olive parts, and the purple parts are potentiometers for the function of limit switch and the alternate length gauges.

Result of Simulation

The material of flexure mechanism is aluminium, and the adjustment range was design form 1 mm to 0.005 mm. When displacement is 1mm and the thickness of leaf is 0.3 mm, the maximum stress is close to the yield stress of aluminium from the result of simulation as shown in Figure 3. Base on the simulation, the thickness of the leaf is designed at 0.3 mm to get the maximum stiffness and keep the required stroke.

According to the simulation, the mechanism is needed to be exerted a 17.26 N for 1mm displacement. Considering the convenience of system integration, the two-phase step-per motors are used for the actuators of the adjustment sys-tem. According to the torque transform formula as shown in Equation 1. The symbol F, T, η , and R is the meaning of the output force, input torque, efficiency parameter and the pitch of screw respectively. We used screws with 1.25 mm pitch and take the efficiency parameter to be 0.67. The mo-tors can produce 0.02 N·m torque and generate 67 N of load force on the flexure structure by the translation of a screw. That is three times of required force, so no more decelera-tor is needed in the adjustment mechanism.

$$F = \frac{2\pi\eta T}{R} \quad (1)$$

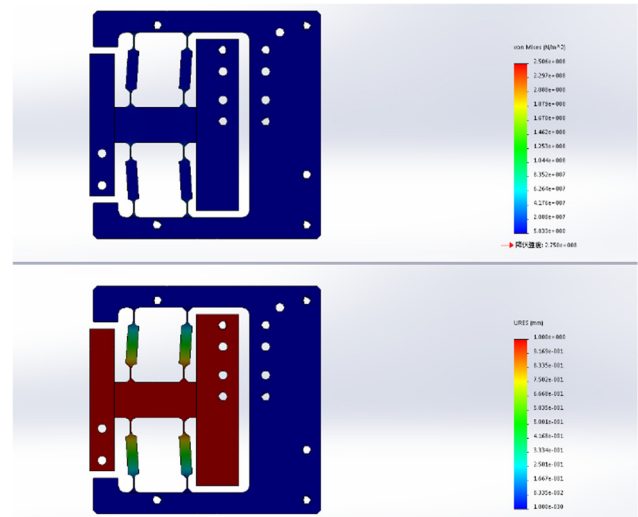


Figure 3: Simulation of a flexure mechanism.

MEASUREMENT AND RESULT

The adjustment system is used for finding the optimum aperture in the beam size monitor system. The difference in aperture can be verified by absolute length gauge. Even if the the system is power off, the actual size of aperture can be obtained by the absolute legth gauge. In order to get the size of an aperture which corresbond with the reading of absolute length gauge, the adjustment mechsanism will be assembled and measured in a laboratory. To confirm the aperture of tungsten blades, the system was measured by a microscope and compared with the absolute length gauges and potentiometers as shown in Figure 4.

The adjustment mechanism was set on the microscope, and we can confirm the parallelism between two blades by the optical observation. After the inspection, the aperture was tuned to achieve 5 μ m observed by a microscope, and the reading of length gauge and potentiometer was rec-ordered for a threshold at the same time. Afterwards, we ad-justed different aperture and compare with a microscope and a potentiometer as shown in Table 1.

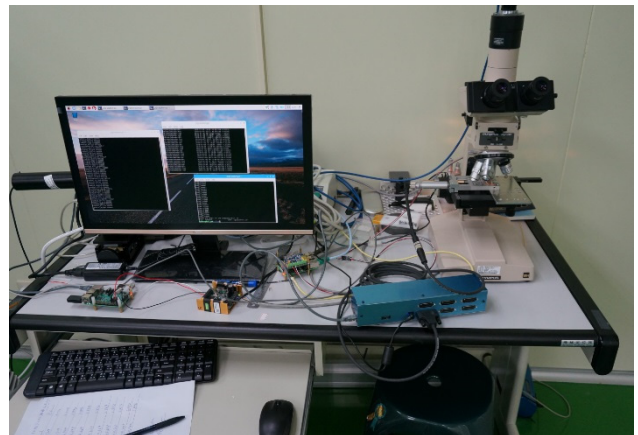


Figure 4: Measurement equipment.

Table 1: Result of Measurement

Micro-scope (μm)	Absolute length gauges (mm)	Potentiometers (mm)
100	64.826	4.040
90	64.816	4.034
80	64.806	4.026
70	64.796	4.019
60	64.786	4.012
50	64.776	4.002
40	64.766	3.995
30	64.756	3.986
20	64.746	3.977
10	64.736	3.970
5	64.731	3.967

The microscope was used to reconfirm the parallelism at the different size of aperture, and the potentiometer was to set the boundary of limit switch and the alternate length gauges by those table. After those measurements, the vertical and horizontal flexure stages are installed on commercial X, Y stages. The commercial stages are used for scanning the position of X-ray. When the Y stage moved up to the edge, the X-ray can pass without obstruction, and the original function of pine holes structure can keep being used. The absolute length gauges are covered with 2mm thickness lead as radiation protection as shown in Figure 5.

Figure 6 show the relations of gaps of blades and the beam size. The result shows the optimum aperture is about 25 μm , and the result is similar to the calculation [3]. In the original intention, the adjustment system can be suitable in different spectrum situation. However, the system is not stable in the beginning, the aperture was influenced with the change of temperature. According that, we measure the relation between temperature and the gaps of blades. We heated the mechanism and raised the temperature by 10 degrees. The aperture would increase 10 μm . According the result, cooling fans and temperature sensors were installed on the adjustable system.

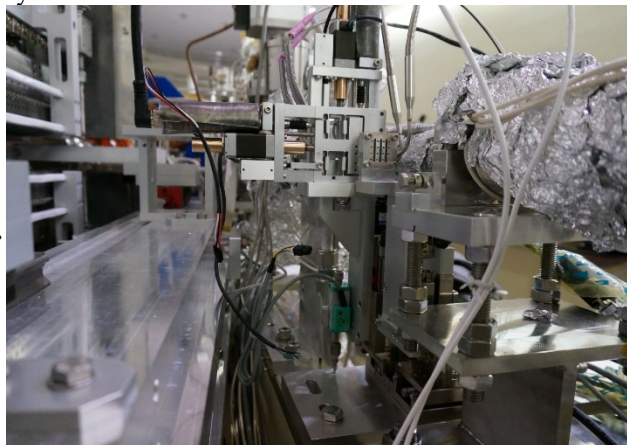


Figure 5: Adjustment system on front end.

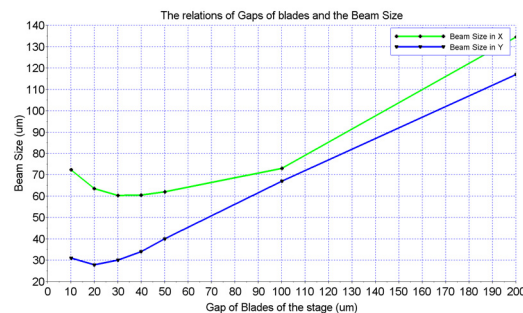


Figure 6: Graph of result.

After completing the installation of cooling fans, the amount of raising temperature decreased to 6 degree, and the temperature of system was stable within 1 degree. The measurement of beam size is stable presently and the measurement of beam size is about 56 μm and 22.5 μm in the X and Y direction respectively.

SUMMARY

The X-ray of the synchrotron radiation is used for measurement of beam size routinely. The aperture of slit is the critical parameter on this diagnostic system. The optimum aperture of slit is also related to the peak of spectrum of light source. According to that, a linear flexure stage for the adjustable aperture was designed and applied on beam size monitor system. The result shows that the optimum aperture of slit can be adjusted by this system easily and correctly. In the beginning, the measurement of beam size is not very stable. After the cooling fans being installed, the measurement of beam size is stable. The measurement of beam size is about 56 μm and 22.5 μm in the X and Y direction respectively.

REFERENCES

- [1] C. Y. Liao *et al.*, "Preliminary Beam Test of Synchrotron Radiation Monitoring System at Taiwan Photon Source", in *Proc. 6th Int. Particle Accelerator Conf. (IPAC'15)*, Richmond, Virginia, USA, May 2015, paper MOPTY074, pp. 1109-1111.
- [2] C. Thomas, G. Rehm, and I. Martin, "X-ray pinhole camera resolution and emittance measurement", *Phys. Rev. ST Accel. And Beams*, vol. 13, p. 022805, Feb. 2010.
- [3] C. K. Kuan *et al.*, "Beam Size Monitor for TPS", in *Proc. 1st Int. Beam Instrumentation Conf. (IBIC'12)*, Tsukuba, Japan, October 2012, paper MOPB88, pp. 291-293.

STUDY ON COOLING TECHNOLOGY OF THE SUPERCONDUCTING UNDULATOR AT SSRF *

Yiyong Liu[†], Li Wang, Jian Wang, Sen Sun, Shuhua Wang
 Shanghai Institute of Applied Physics, CAS, Shanghai, China

Abstract

A superconducting undulator (SCU) prototype with the period of 16 mm and the magnetic gap of 9.5 mm has been designed and fabricated at the Shanghai Synchrotron Radiation Facility (SSRF) since late 2013. A set of cooling system is designed to cool down cold masses, this paper presents the details of their design, calculation and test: 4 small cryogenic refrigerators are used as cold sources, and the superconducting coil and beam pipe are independently cooled down; The 4.2 K superconducting coil is mainly cooled by the liquid helium tube of thermal siphon loop; The 10~20 K ultra-high vacuum beam tube is cooled by Cu strips conduction. The main sources and mechanism of thermal loads for the SCU were analyzed. And experimental test of cooling technology for SCU prototype had been performed, the feasibility of cooling scheme and the rationality of the cooling structure for the SCU prototype were verified. The cryogenic test and operation of the SCU doesn't require the input of liquid helium from the outside, and is not limited by the liquid helium source. This is the characteristic of SSRF's SCU cooling technology.

INTRODUCTION

The superconducting undulator (SCU) with the advantage of producing high peak magnetic field at smaller period length can bring higher photon brilliance, as a result, technologies of SCU attract more and more attention for the synchrotron facilities in the world [1].

The Shanghai Institute of Applied Physics (SINAP) has started the research and development of SCU technology such as the winding skill of the coils since 2009. SINAP decided to develop one SCU prototype in order to study all the key technologies including coil winding, cooling technology, magnetic field measurement, cryomodule integration and alignment for the future FEL (Free Electron Laser) projects and SSRF (Shanghai Synchrotron Radiation Facility) upgrade project in China in 2013. The SCU prototype mainly consists of superconducting coil, beam chamber and cryostat. The coils include one set of main coils, two sets of end coils, their support frames and quench protection diodes. The SCU prototype is expected to be installed at the SSRF for on-line test in the winter of 2018.

The SCU superconducting coils are made from commercial copper matrix niobium titanium conductors. Both the pole and the mandrel are made of the soft iron.

* Work supported by by the Shanghai Institute of Applied Physics, Chinese Academy of Science and Shanghai Key Laboratory of Cryogenics & Superconducting RF Technology.

[†] email address : liuyiyong@sinap.ac.cn

The parameters of the SCU prototype are summarized in Table 1.

Table 1: Parameters of Superconducting Undulator Prototype

SC conductors	NbTi/Cu=0.93(+/-0.05):1
Material of pole and mandrel	Soft iron (DT4C)
Period length (mm)	16
Period number	50
Magnetic gap (mm)	9.5
Minimal beam gap (mm)	7.5
Central peak field (T)	≥ 0.67
Phase error (degree)	≤ 4
Operating current (A)	Main coil: 400A; 2 End coils: 34 A
Magnetic storage energy (kJ)	7
Coil length (mm)	800+32=832
Length of Cryostat along the beam line (m)	1.8

COOLING SCHEME

High efficient and stable cryogenic cooling system is a necessary condition to ensure the operation of the SCU. In order to realize and maintain the cryogenic environment for superconducting coils, the cooling technology needs to be studied in consideration of the complicated structure of the coil arrays, UHV beam chamber, current leads, and thermal loads and so on.

The coils length of the SCU prototype is only 0.9 m, using low temperature superconducting material NbTi / Cu wound, the running temperature margin for the coils is only about 0.8 K, the operating current of the main coils is 400 A. The magnetic clearance and beam clear area of the prototype is 9.5 mm and 7.5 mm respectively, and the thickness of beam chamber is 0.5 mm, that means 0.5 mm space between the coils and the beam chamber. Considering that the measured dynamic heat load of the SSRF beam is about 30 W, in order to avoid the direct influence of beam dynamic thermal load on the stable operation of the coils, the overall cooling scheme of the SCU is as follow:

1. Using 4 cryogenic refrigerators as cold sources, which is more easier for operation and maintenance, and the equipment cost and operating cost is lower compared with large helium refrigerator system.

2. The coils and the beam chamber are independently cooled: The two upper refrigerators cooled the coils, the two down refrigerators cooled the beam chamber. The 4.2 K superconducting coil is mainly cooled by the liquid

helium tube of thermal siphon loop, also it is zero evaporating; The 10~20 K vacuum beam chamber is cooled by Cu strips conduction.

3. Current leads and their cooling: Binary current leads made of conventional copper leads and high temperature superconducting leads (HTS) are used to reduce the heat load.

4. Cold mass cooling and liquid He accumulation: Two upper refrigerators are used not only as cold source for the normal operation of the SCU, but also cold source for helium liquefier. SCU system The cooling down procedure and normal operation do not require the input of liquid helium from the outside, only high-purity helium gas is required.

The overall cooling scheme of the SCU prototype is shown in Figure 1.

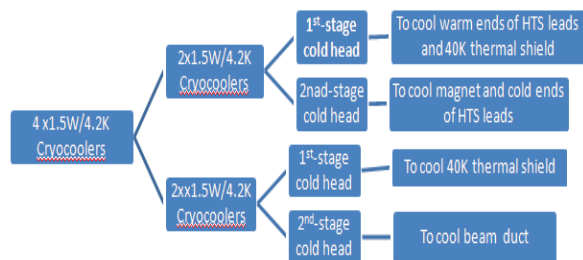


Figure 1: The overall cooling scheme of the SCU prototype.

As shown in Figure 2, the coils are cooled by the two refrigerators in the upper part of the thermostat. It is necessary to take into account the possibility to accelerate the re-cooling and cooling rate after quenching the coils. For more cooling capacity, a 30 L liquid helium tank is set to store liquid helium and provide a source of liquid helium for the thermal siphon circulation circuit.

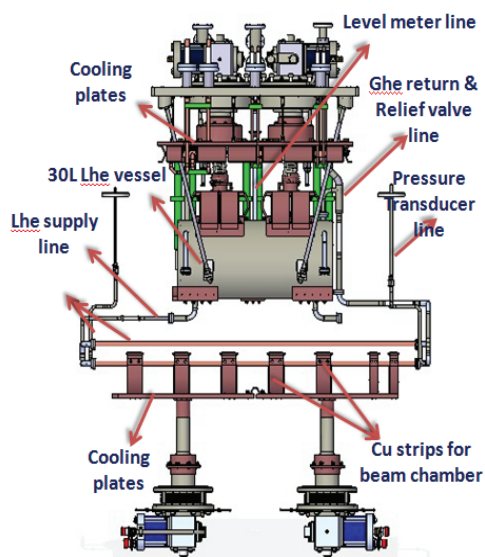


Figure 2: Cooling structures for SCU coils and beam chamber.

OPTIMIZATION OF COOLING STRUCTURES

The re-condenser is used to liquefy helium, it is directly connected to the secondary cold head and is located in the upper part of the liquid helium tank. Its structure is shown in Figure 3.

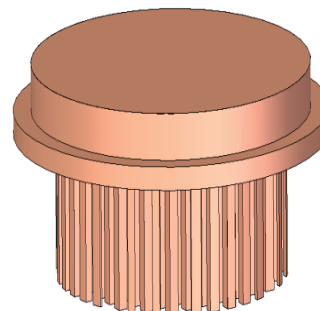


Figure 3: Re-condenser structure.

The optimal design of the re-condenser can minimize the temperature difference between the He gas and the condensing surface. According to Nusselt's pure saturated vapor laminar film condensation theory, the average temperature difference ΔT_c of the condensing surface can be obtained as [2,3]:

$$\Delta T_c = \left[\left(\frac{Q}{A} \right) \left(\frac{4\mu_l H}{\rho_l^2 g h_{fg} \lambda_l^3} \right)^{1/4} \right]^{4/3} \quad (1)$$

In equation (1), (Q/A) is the heat flux density at the condenser surface; μ_l is the dynamic viscosity of the liquid helium; H is the height of the condenser fins; ρ_l is the liquid helium density; g is the gravitational acceleration; h_{fg} is the latent heat of vaporization of liquid helium; λ_l is the thermal conductivity of liquid helium.

The results are as follows: The cross-sectional dimension of a single fin is 3 mm × 3 mm, the number of complete fins is 121, the total heat exchange area is at least 0.06 m², and the calculated heat transfer temperature difference is 0.021 K, which satisfies the design requirements. Taking into account the complexity of the actual heat transfer, the actual design, the total heat transfer area gives 2.5 times the margin, that is 0.15 m², fin length is 42 mm, round copper diameter is 100 mm, thickness is 5 mm.

The beam chamber is independently cooled by the secondary cold heads of the two refrigerators at the lower part of the thermostat. The secondary cold head is connected with the copper plate firstly, the soft copper strips is connected between the copper plate and the beam chamber. In order to ensure the temperature uniformity of the beam chamber, 7 soft copper strips are arranged along the beam direction, and are distributed on both sides of the beam chamber. According to the performance of small refrigerators, the operating temperature of the beam chamber with dynamic thermal load can be ~20 K, which is shown in Figure 4.

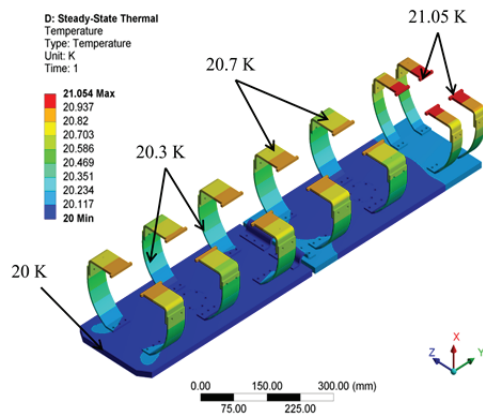


Figure 4: Temperature distribution of the beam chamber cooling structure.

EXPERIMENTAL TEST OF COOLING TECHNOLOGY

Experiments were conducted to monitor the temperature change of the cold masses to obtain the cooling down rate of each part. Figures 5 shows the cooling down curves of the secondary cold heads of the 1 and 2 coolers, the upper and lower ends of the liquid helium tanks, the HTS cold ends. In the 4 K temperature zone, about 160 kg of cold mass, from the beginning of cooling to a stable temperature, lasted about 51.5 hours, the minimum temperature of the liquid helium tank reached approximately 4.2 K, and the liquid helium pressure range in the liquid helium tank was 1~ 5 kPa.

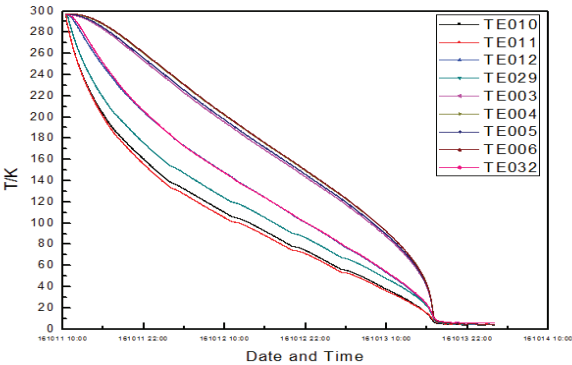


Figure 5: Cooling down curves at Liquid He temperature range of the SCU prototype.

After cooling down to 4.2 K, the cryogenic line in the cryostat was continuously filled with helium, and the liquid helium tank began to accumulate fluid. Figure 6 shows the time curve for accumulation. The whole process takes 53 hours when the L He level is up to 90% of the total volume.

The above experimental results verified: 1) The feasibility of the cooling design scheme of the SINAP SCU, that is, 4 small refrigerators used as cold sources, no need for liquid nitrogen pre-cooling or liquid helium input, only room temperature high purity helium needed to achieve cooling down cold mass and accumulating liquid helium; 2) The optimization of the cooling structure de-

sign of each cold mass successfully enables the superconducting coils to reach the operating temperature .

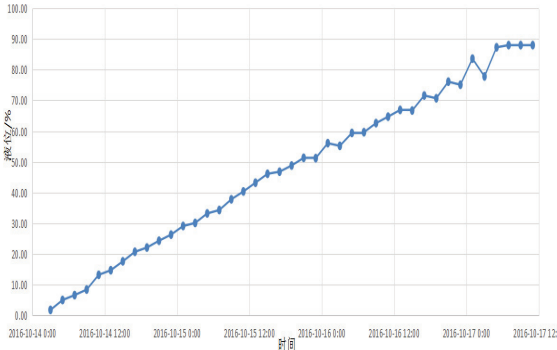


Figure 6: Liquid He accumulation curve of the SCU prototype.

ESTIMATION OF HEAT LOADS

Table 2 shows the thermal load calculation results for each temperature zone of the SCU prototype. The thermal shield is set to 40 K, the beam chamber is set to 20 K, and the superconducting coils is set to 4.2 K.

Table 2: Total Heat Loads at 4.2 K and 40 K (Unit: Watts)

Heat Source	Heat Load at 4.2 K	Heat Load at 40 K
Radiation heat	0.404	8.7
Conduction heat through pipes	0.076	3.2
Conduction heat through supports	0.025	4.1
500+100A HTS leads	0.258	64.4
Instrument wires	0.002	0.1
Total	0.765	80.5
Cooling power	3	88

As can be seen from Table 2, the current lead is the main load source in the 40-60 K temperature zone, accounting for about 80%, followed by radiation heat. The main sources of heat load in the liquid helium temperature zone are current leads and radiation heat, which account for 60% and 30%, respectively.

REFERENCES

[1] Y. Ivanyushenkov *et al.*, "A design concept for a planar Superconducting Undulator for the APS," *IEEE Trans. Appl. Supercond.*, vol. 21, no. 3, pp. 1717-1720, Jun. 2011.
[2] R. E. Barron, *Cryogenic heat transfer*, Taylor & Francis, Philadelphia, 1999, pp. 180-181.
[3] E. R. G. Eckert, "Introduction to the Transfer of Heat and Mass", McGraw-Hill, 1950, pp. 172-175 .

FIELD QUALITY FROM TOLERANCE ANALYSES IN TWO-HALF SEXTUPOLE MAGNET*

J. Liu[†], M. Jaski, A. Jain, A. Donnelly, C. Doose, R. Dejus
Argonne National Laboratory, 60439, Argonne, USA

Abstract

Sextupole magnets are used extensively in particle accelerators, synchrotrons, and storage rings. Good magnetic field quality is needed in these magnets, which requires machining the magnet parts to high precision and is the primary driver of the high fabrication costs. To minimize the fabrication costs, a magnetic field quality study from tolerance analyses was conducted. In this paper, finite element analysis (FEA) using OPERA was performed to identify key geometric factors that affect the magnetic field quality and identify the allowable range for these factors. Next, geometric and dimensional tolerance stack-up analyses are carried out using Teamcenter Variation Analysis to optimize the allocation of the geometric tolerances to parts and assemblies. Finally, the analysis results are compared to magnetic measurements of a R&D sextupole magnet.

INTRODUCTION

The Advanced Photon Source (APS) at Argonne National Laboratory (ANL) is upgrading the current double-bend achromat, 7-GeV, 3rd generation storage ring to a 6-GeV, 4th generation storage ring with a multi-bend-achromat lattice that provides dramatically enhanced hard x-ray brightness and coherent flux [1]. The new lattice has 40 sectors with 13 bending magnets per sector, including six reverse bends. Each sector includes 6 sextupoles of two different types. One has steel pole tips and produces nominal integrated sextupole field of up to 727 T/m, and the other contains vanadium permendur (VP) pole tips and produces nominal integrated sextuple field of up to 1315 T/m.

The allowable rms values for random multipole errors in units at 10 mm reference radius for the sextupoles (one unit is 0.01% of the main field component) are listed in Table 1. The requirement for magnet-to-magnet alignment within a module consisting of four quadrupoles and three sextupoles is 30 μm rms. The magnetic center of each magnet should be close to its mechanical center for ease of alignment using mechanical reference surfaces. Furthermore, the magnetic roll angle should be less than 0.4 mrad rms. These requirements place stringent demands on the magnet fabrication tolerances.

In order to achieve the required magnetic field quality and alignment accuracy at reasonable fabrication cost, magnetic and mechanical tolerance analyses are conducted to identify the key driving factors and their allowable limits, and to specify the proper mechanical tolerances for

parts and assembly to control the driving factors within allowable limits.

Table 1: Allowable rms Values for Rrandom Fractional Multipole Errors for Sextupoles at 10 mm Radius

Harmonic	Normal (unit)	Skew (unit)
Octupole	8.9	8.9
Decapole	9.1	9.1
Dodecapole	4.5	0.9
14-pole	2.6	1.8
16-pole	0.7	0.7
18-pole	0.8	0.3

MAGNETIC TOLERANCE ANALYSES

Sextupoles for APS Upgrade are made of two solid steel yoke halves (top and bottom) with removable poles tips [2]. This study was carried out on the sextupole with VP pole tips, but the results can be applied to both magnets. For a two-piece design, since it is assembled from outside yokes inward to the pole tips, all the machining errors, including size, form, orientation, and location on mating features, contribute to the variation of the final pole tip surface locations. The machining and assembly errors that will affect the magnetic field quality include: i) pole tip surface profile errors; ii) top half offset horizontally; iii) top half offset vertically; iv) top half rotated relative to the bottom half; and v) pole tips misalignment along the mounting surfaces. Opera-2D finite element analyses are carried out to study the effect of these mechanical errors on the field quality. The geometric configuration for magnetic analyses in Opera is shown in Figure 1.

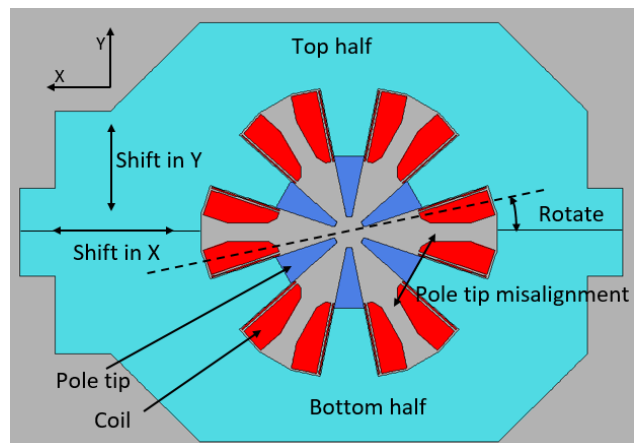


Figure 1: Configuration for magnetic analyses.

* Work supported by the U.S. Department of Energy, Office of Science, under Contract No. DE-AC02-06CH11357

[†] Email address: jliu@aps.anl.gov

In 2D magnetic analysis using Opera, each pole tip top region was discretized into 10 small segments. The segment vertex points on the tip surface were allowed to move normal to the surface within the profile tolerance's outer and inner boundary, as shown in Figure 2. In each case, random displacement values within the profile tolerance specifications were assigned to each vertex point. One hundred random cases were simulated using this method in order to find out the rms of multipole errors caused by the profile errors on pole tips surfaces.

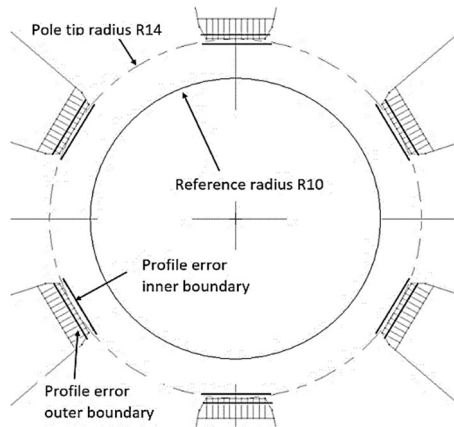


Figure 2: Sextupole pole tip configuration for profile error analyses (not to scale).

To study the effect of the top and bottom halves' shift in X direction relative to each other, the top half is deliberately shifted in the +X direction and the bottom half in the -X direction by equal amounts. Three X shift displacements, $\pm 15 \mu\text{m}$, $\pm 25 \mu\text{m}$, and $\pm 50 \mu\text{m}$ were simulated.

To study the effect of shift in Y direction, only the top half was moved by $30 \mu\text{m}$, $50 \mu\text{m}$, and $100 \mu\text{m}$ since in reality, the bottom half is normally bolted down to the girder and seldomly removed. In a similar manner, to study the effect of relative rotation, only the top half is rotated relative to a stationary bottom half about the mechanical center of the magnet. Shift in Y may be caused by small debris or dust getting stuck between the mating surfaces of the top and the bottom halves. Relative rotation of the top half is generally caused by unequal tightening torques of the clamping screws or debris on one of the two mating surfaces.

Pole tips could be misaligned and displaced along their mounting surfaces and cause pole tips asymmetry around the beam. In the study, each pole tip is assigned a random displacement within the designated range to either the right or the left along its mounting surface. Four levels of displacement ranges were studied, $\pm 25 \mu\text{m}$, $\pm 50 \mu\text{m}$, $\pm 75 \mu\text{m}$, and $\pm 100 \mu\text{m}$.

MECHANICAL TOLERANCE ANALYSES

Mechanical tolerances stack-up analyses were carried out using commercial package Teamcenter Variation Analysis. In this software, parts are virtually made with the specified dimensional and geometric tolerances on geometric features. Parts are assembled and measured virtually

in the same manner as they will be assembled and measured in the real world. The configuration for the mechanical tolerance stack-up analyses is shown on the right side of Figure 3. The distribution and the statistics of one of the measurement results is shown on the left side of Figure 3. The software then assigns errors within the specified tolerance range to parts using the Monte Carlo method. In our simulation, three machining tolerance levels, $12.5 \mu\text{m}$, $25 \mu\text{m}$ and $50 \mu\text{m}$ are assigned to parts. Five thousand cases were simulated and measured for each level.

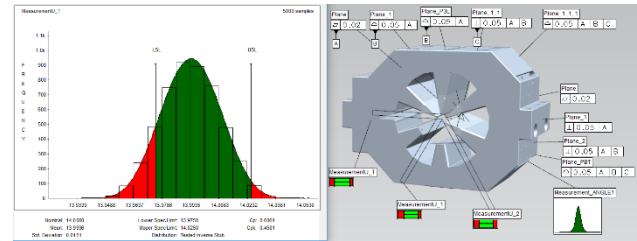


Figure 3: Configuration for mechanical tolerance stack-up analyses.

RESULTS AND DISCUSSION

The Effect of Surface Profile Error

It is found from the finite element magnetic analyses that the pole tip profile affects the rms value of all lower order random errors. The result is shown in Figure 4. In order to keep the rms random errors within specification, the profile error on pole tips must be smaller than $\pm 7 \mu\text{m}$.

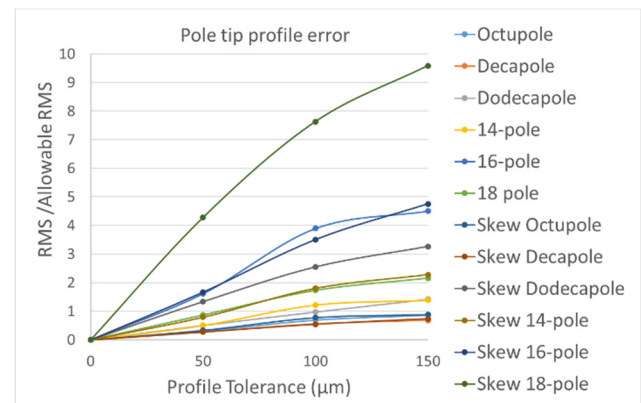


Figure 4: Effect of surface profile on the rms value of multipole errors.

From mechanical tolerance stack-up analyses, it is found that for the machining tolerance of $12.5 \mu\text{m}$, $25 \mu\text{m}$ and $50 \mu\text{m}$, the rms values of pole tip surfaces point variations is $5 \mu\text{m}$, $7.4 \mu\text{m}$ and $14 \mu\text{m}$, respectively. To keep the random errors of the magnet within spec, the machining tolerances on the pole tips need to be $25 \mu\text{m}$ or smaller. This is hard to do with conventional machining methods.

The Effect of Top and Bottom Relative Shift in X

Top and bottom relative shift in X direction affects skew sextupole, skew decapole, skew 14-pole, and skew 18-pole linearly. If the horizontal misalignment of top and bottom

halves is kept below 10 μm , the largest harmonic error (octupole and above) will be 0.5 units for the skew 18-pole term which is inside 2σ of the specified rms error.

From mechanical tolerance stack-up analyses, it is found that the offset in X direction caused by machining errors on parts has a mean of 4 μm and 2 μm , and rms of 12.5 μm and 6.4 μm , at 50 μm and 25 μm machining tolerance level, respectively. This means 25 μm machining tolerance is sufficient to keep top and bottom relative offset within spec.

The Effect of Top and Bottom Relative Shift in Y

Top half offset in Y direction affects the normal decapole, and the normal 14-pole linearly. If the vertical misalignment of top and bottom halves is kept below 30 μm , normal decapole and the normal 14-pole will be kept inside 2σ of the specified rms error.

From mechanical tolerance stack-up analyses, it is found that the offset in Y direction caused by machining errors on parts has a mean of 3 μm and 3 μm , and rms of 30 μm and 16 μm , at 50 μm and 25 μm machining tolerance level, respectively. This means 25 μm machining tolerance is sufficient. However, it is critical to keep the mating surfaces clean and follow a tightening procedure to ensure even clamping of the top half to the bottom half.

The Effect of Top and Bottom Relative Rotation

Top and bottom relative rotation mainly affects the normal octupole, normal dodecapole, and skew sextupole. If the top and bottom relative rotation is kept below 0.9 mrad, normal octupole and the normal dodecapole and magnetic roll error will be kept inside 2σ of the specified rms error.

From mechanical tolerance stack-up analyses, it is found that relative rotation caused by reasonable machining errors of parts are extremely small and is negligible. However, it is critical to keep the mating surfaces clean and follow a tightening procedure to ensure even clamping of the top half to the bottom half.

The Effect of Pole Tip Misalignment

Pole tip misalignment causes both the mean and standard deviation of random harmonics to change. Figure 5 plots the ratio of multipole error rms with regard to the allowable rms value against pole tip misalignments. From Figure 5, it can be seen that if the pole tip misalignment is kept below $\pm 10 \mu\text{m}$, the rms value for all random errors will be below 100% of the spec.

From mechanical tolerance stack-up analyses, it is found that the pole tip misalignment caused by machining and assembly errors has rms value of 25 μm and 16 μm , at 50 μm and 25 μm machining tolerance level, respectively. This means 25 μm machining tolerance is not sufficient. More stringent machining precision is required.

Based on the magnetic and mechanical tolerance analyses, it can be seen that in order to produce magnets that meet the design requirements, high machining tolerance better than 25 μm is needed, however, it is very costly to machine parts at this precision level. Moreover, all these factors will add up to affect the overall magnetic field quality and requires a machining and assembly precision level

that is not realistic. To address this issue, we have decided to use the wire EDM method for the pole tip profile at the assembled state. This way, the part level tolerances do not affect the final assembly and can be relaxed to reduce machining costs. At the same time, the pole tip surface profile, top bottom relative offset and rotation, and pole tip misalignment can all be maintained within $\pm 10 \mu\text{m}$. Although wire EDM is expensive, the overall cost using this method is lower than that using conventional machining method since it is limited to only the pole tip region.

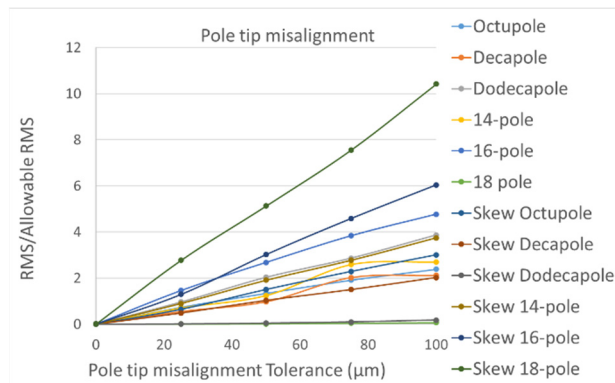


Figure 5: The effect of pole tip misalignment.

A prototype magnet with wire EDM machined VP pole tips was fabricated and measured. The measurement results of the prototype magnet matched the simulation results very well. However, we found that the hardened straight dowel pins have poor repeatability in soft magnet steels. To solve this problem, we tested taper dowel pins for yoke halves and metal filled epoxy keys for the pole tips and yokes. They can retain repeatability during reassembly within 10 μm .

CONCLUSION

Magnetic and mechanical tolerance studies were carried out for APS upgrade sextupoles. The effects of pole tip profile error, top and bottom half relative offset and rotation, and pole tip misalignment on magnet field quality in terms of random multipole errors were studied. Based on the analyses results, it is found that the conventional fabrication and assembly methods are not sufficient to achieve the tight tolerance requirements of sextupoles for APS upgrade. A new fabrication plan was developed to wire EDM the pole tips in an assembled state and to include features that ensure the repeatability of the alignment. A prototype made with this method was tested and proved satisfactory.

REFERENCES

- [1] M. Borland, V. Sajaev, Y. Sun, A. Xiao, "Hybrid Seven-Bend-Achromat Lattice for the Advanced Photon Source Upgrade", in *Proceedings of 6th Int. Particle Accelerator Conf.*, Richmond, USA, May 2015, paper TUPJE063, pp. 1776 – 1779.
- [2] M. Jaski, J. Liu, A. Jain, C. Spataro, D. Harding, V. Kashikhin, "Magnet Designs for the Multi-Bend Achromat Lattice at the Advanced Photon Source", in *Proceedings of 6th Int. Particle Accelerator Conf.*, Richmond, USA, May 2015, paper WEPTY003, pp. 3260 – 3263.

FRONT END OF DUAL IMAGING AND DIFFRACTION BEAMLINE AT DIAMOND LIGHT SOURCE

X. Liu[†], R. K. Grant, N. P. Hammond, R. K. Rawcliffe, Diamond Light Source, Oxfordshire, UK

Abstract

The Dual Imaging and Diffraction (DIAD) beamline X-ray source is a ten-pole mini wiggler. By locating the mini wiggler in place of an existing sextupole magnet, the DIAD beamline is built at a bending magnet beamline position in Diamond. To accommodate the unusual beam trajectory, a new front end was designed for the DIAD beamline. The particular designs and specifications, including an improved front end slits design, as well as the synchrotron and dipole ray tracing of the front end are presented in this paper. The development process of delivering the front end - the project challenges, approach and activities are also described along with the technical challenges.

INTRODUCTION

All of the original straight sections in the Diamond storage ring are now occupied. After an extensive study at the beginning of the DIAD beamline project, the decision was made that the DIAD beamline would be built at a bending magnet (BM) beamline position by replacing an existing sextupole magnet with a ten-pole permanent magnet wiggler [1]. DIAD X-ray beam radiates in the same direction as the first bend of the double-bend achromat. The schematics of the beam trajectory are shown in Figure 1. The field strength of the mini wiggler is 1.56T, the period length is 117mm and the total power at 500mA is 4.8kW.

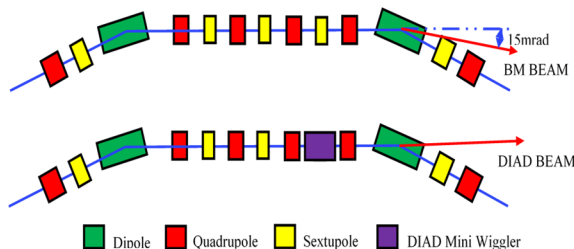


Figure 1: Top: Schematic diagram of the double-bend achromat layout. Bottom: Schematic diagram of the mini-wiggler replacing the sextupole.

This unusual beam trajectory means that the front end will be exposed to the radiation from the dipoles of the double-bend achromat. It will be necessary to shield the uncooled part of the front end from dipole radiation. Further engineering challenges include the front end having to cope with a wide wiggler beam of a fan size of 6 (horizontal) x 0.4 (vertical) mrad. The beamline also requires the front end slits to be the first optics of the beamline. It is important for the front end slits to perform according to the beamline needs.

[†]xia.liu@diamond.ac.uk

The delivery of the Front End is on the critical path of the beamline project. A new approach of “Management of the Fuzzy Front End of Innovation” [2] was tried in the concept design stage to manage the technical uncertainties effectively at the early stage of the project. We have gained more understanding of how to be more efficient in the design and development of front ends, which is an innovation process, and deliver the project successfully.

ENGINEERING SOLUTIONS

The DIAD front end design is shown in Figure 2. It consists of Zero Aperture module, 1st Aperture module, Absorber module and fast shutter, Access Pipe module, Slits module, Twin Port Shutter Module and Optics Hutch module. Radiation shielding and modules using DLS generic designs [3] are not part of the discussions in this paper. The more challenging front end ray trace and front end slits will be discussed.

Front End Ray Trace and General Layout

Ray tracing using AutoCAD was employed to study the optical path of the wiggler X ray radiation and dipole radiations and to identify aperture needs. General Layout of the front end was carried out in parallel with the ray tracing to optimise the component sizes and locations of assembly modules. The ray tracing (Figure 3) has the following findings:

- A zero module is necessary to connect the front end to the storage ring (SR) as it is almost 12 meters from the end of the SR vessel to the ratchet wall, while the standard length of an undulator front end at Diamond is around 10.4 meters.
- The crotch absorber in the SR vessel needs to be wider to provide more shielding to prevent radiation from dipole 2 shining on the uncooled zero module vessel.
- A zero aperture, in addition to the wider crotch absorber, is also needed to provide shielding to the uncooled zero module vessel. The zero aperture is also designed to replace the Beam Port Absorber fitted at the end of the SR vessel to make the easy connection of the front end to the storage ring.
- For the benefit of the project timescale and cost, a decision was made at the ray tracing stage that Absorber, Access Pipe, Twin Port Shutter and Optics Hutch module will use DLS generic designs [3]. However, the 6mrad wiggler beam size is too wide for the standard 1st Absorber. The solution was to design the 1st Aperture to trim the wiggler beam to 0.86(H) x 0.34(V) mrad so that the standard 1st Absorber can be used.

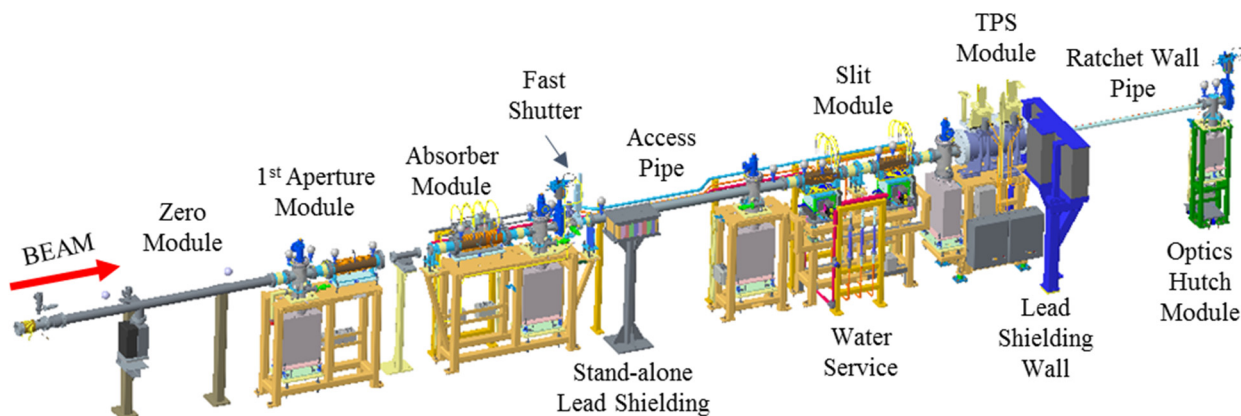


Figure 2: The DIAD Front End (Steel Wall Penetration is not shown). The fabrication design from FMB Berlin [4] is shown.

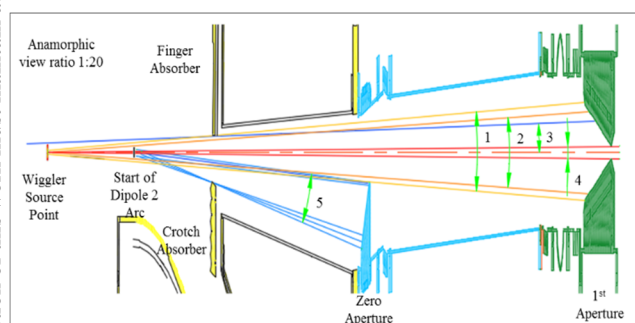


Figure 3: Plan view showing the wiggler and dipole light ray tracing. 1: wiggler fan including mis-steers; 2: 6 mrad wiggler fan nominal position; 3: 5 mrad dipole 1 fan; 4: 0.86(H) mrad wiggler light exiting the 1st aperture; 5: dipole 2 light including mis-steers.

Front End Slits – the First Optics of the Beamline

The Slits Module Assembly is shown in Figure 4. Each slit block is mounted on a motorised stage. A middle bellows assembly connects upstream and downstream slit blocks. By clamping down the central section of the middle bellows to the support frame, the bellows forces exerted on the motion stages are more balanced when the slit blocks move, and the slits can have stable motion.

The slit blocks are made from OFHC copper and are designed using DLS Finite Element Analysis criteria [5]. Four independent 3mm thick slit blades made from Tungsten are fixed to the end faces of the copper blocks forming the aperture. The distance between the pair of slit blades is 858 mm.

Slit Blade Alignments The slit blades alignment is critical for the successful operation of the slits. It is required that the upstream and downstream slit blades are parallel and orthogonal to $10\mu\text{m}$ in operation. A slits alignment protocol was defined and kinematic mounts were designed for the fine adjustment. Firstly the slit blades are aligned parallel to the travel of their own motion stages. Secondly, the upstream slit blades together with its motion

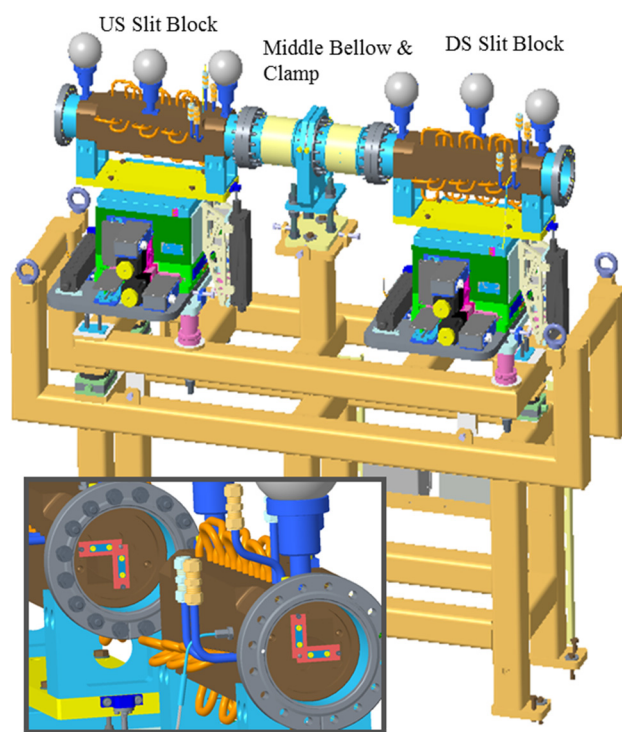


Figure 4: the DIAD front end slits. The detailed view shows the arrangement of the L shaped slit blades. The fabrication design from FMB Berlin [4] is shown here.

stages are aligned parallel to the downstream blades and its motion. It is required to take measurement records of the height between the survey monument and slit blade for the survey reference during the installation in the storage ring.

Slits Motion The motion stage is FMB Berlin YZ Stage 40/40 [4]. DLS traditionally used Renishaw incremental encoders, which demands skilled intervention when resetting is required, often with a significant delay and the risk of introducing inaccuracies. A new linear encoder that has both absolute and incremental outputs is chosen for the slits motion. The encoder is Transformation Measuring Systems (LT-100-PI) from TR Electronic [6]. Its incre-

mental outputs will be used for normal operation and connected to the Geo Brick LVTM [7] driving the slits motors. The absolute output will be connected to an EPICS IOC supervisory and will be used to update the position record while the stage is static. This allows the monitoring of the absolute position.

Machine Protection There is a need for a machine protection function to prevent slits opening too wide and allowing a damaging amount of radiation into the beamline. This is achieved by fitting Linear Variable Differential Transformers (LVDTs). LVDTs monitor the position independently of the control system and report motion stage position to a PLC that has values set to represent the limits of illumination of downstream equipment with the synchrotron light.

PROJECT CHALLENGES

The front end was identified on the critical path. Successfully delivering the DIAD front end is vital for delivering the beamline project on time. The core challenge was to quickly transform ideas, inputs and previous build experiences into the designs that meet the scientific needs. An understanding of the front end design process will help us to apply methods and tools to manage the project effectively and efficiently.

The DIAD Front End Design and Development is an Innovation Process

The beamline scientists, who are the customers of the project, envisaged to put the first pair of slits for the beamline in the front end. This idea initiated the concept of the DIAD front end. Driven by this scientific requirement and the advancement of technologies, the design and development of the DIAD front end is an innovation process.

The Fuzzy Front End of the Front End Design

In the innovation management literature, Fuzzy Front End ranges from the generation of an idea to either its approval for development or its termination. It has the highest impact on the whole project. In Fuzzy Front End, the degree of freedom in design and influence on project outcomes are high, whereas costs for changes are low [8]. With this understanding, the focus of DIAD front end design process was on managing the Fuzzy Front End phase. Figure 5 illustrates the DIAD front end design process.

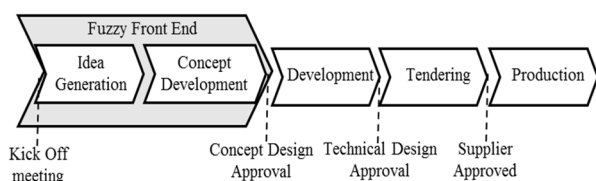


Figure 5: The DIAD front end design process.

Identifying customer needs is a key challenge in the Fuzzy Front End [2]. Focus was aimed at designing a slits module that would become a customer-specified instrument. Beamline scientists were asked about their needs of

alignment, commissioning and motion control during operation, and beamline equipment protection. Another important source of input to the concept design is the multi-functional team. The team's past experience and knowledge generate good ideas of a better building of the front end. The needs were then transformed into technical specifications and concept designs were developed. At the end of the concept phase, the DIAD front end had a fully developed General Layout. Core Technical Specifications were defined for the scientific and technical needs. The need to run a separate project for the zero module to decouple tasks was also identified. There wasn't any design change in the development stage of the design process and the project timescales were kept.

CONCLUSION

The DIAD front end design and development is an innovation process. The stage-gate approach with a focus on managing the Fuzzy Front End at initial stage of the process has proved to be successful in managing the DIAD front end project. All the project mile stones in the development stage were met. The front end will be installed in November 2018 and the slits module will be tested after the beamline commissioning in 2019.

ACKNOWLEDGEMENTS

We thank valuable inputs from DLS mechanical team members: M. Small, J. Margerum, A. Martin and B. Greening. Your feedback helps us to design better products.

REFERENCES

- [1] N. P. Hammond and I. P. S. Martin, "Design Considerations Associated with the Replacement of a Sextupole Magnet by a Short Wiggler in a Cell of the Diamond Storage Ring Lattice", presented at the 10th Int. Conf. on Mechanical Engineering Design of Synchrotron Radiation Equipment and Instrumentation (MEDSI'18), Paris, France, June 2018, paper TUPH17, this conference.
- [2] O. Gassmann and F. Schweitzer, "Managing the Unmanageable: The Fuzzy Front End of Innovation", in *Management of the Fuzzy Front End of Innovation*, O. Gassmann and F. Schweitzer, Springer International Publishing, Switzerland, 2014, pp. 3–14, doi:10.1007/978-3-319-01056-4
- [3] J. Strachan *et al.*, "Front Ends at Diamond" in *Proc. EPAC'06*, Edinburgh, Scotland, June 2006, paper THPLS06, pp. 3335–3337.
- [4] FMB Berlin, <http://www.fmb-berlin.de/en>
- [5] H. Huang *et al.*, "Elasto-Plastic Analysis of Heat Absorbers in Diamond Light Source" presented at the NWC 2013, Salzburg, Austria, June 2013, <https://www.nafems.org/events/congress/2013/presentations/pres11jun/>.
- [6] TR Electronic, <http://trelectronic.com>
- [7] DELTA TAU, <http://www.deltatau.com>
- [8] C. Herstatt, B. Verworn, "The 'Fuzzy Front End' of Innovation", in *Bringing Technology and Innovation into the Boardroom*, Palgrave Macmillan, London, 2004, pp. 347-372.

MORPHOLOGIES OF OXYGEN-FREE TITANIUM AND PALLADIUM/TITANIUM THIN FILMS: NEW NON-EVAPORABLE GETTER (NEG) COATINGS

T. Miyazawa*, SOKENDAI (The Graduate University for Advanced Studies),
 305-0801 Tsukuba, Japan

A. Hashimoto¹, M. Yamanaka, National Institute for Materials Science, 305-0047 Tsukuba, Japan

T. Kikuchi, K. Mase², KEK, 305-0801 Tsukuba, Japan

¹also at University of Tsukuba, 305-0047 Tsukuba, Japan

²also at SOKENDAI (The Graduate University for Advanced Studies), 305-0801 Tsukuba, Japan

Abstract

Non-evaporable getter (NEG) coatings are ideal for maintaining an ultrahigh vacuum (UHV) in the range 10^{-8} Pa and they are widely used for accelerators because they are oil free, magnetic-field free, vibration free, economical, space saving, and energy efficient. We recently fabricated new NEG coatings consisting of low-oxygen-content Ti or oxygen-free Pd/Ti by sublimation under a clean UHV in the range 10^{-8} to 10^{-7} Pa. Here, we report the determination of the morphologies of these films by scanning electron microscopy, transmission electron microscopy, and energy-dispersive X-ray spectroscopy. The Ti and Pd films had almost uniform thicknesses of about 1.3 μm and 50 nm, respectively, and the Pd film completely overcoated the Ti film. Both the Pd and Ti thin films were uniformly deposited in plane on the stainless steel 304L substrate and they had polycrystalline structures. The interface between the Pd and Ti thin films was not abrupt.

INTRODUCTION

A non-evaporable getter (NEG) is a material, such as Al, Ti, V, Zr, Hf, Ta, Nb, Fe, or their alloys, that can evacuate reactive residual gases after activation under a clean ultrahigh vacuum (UHV) [1–3]. The NEG coating technique involves coating the inner walls of a vacuum chamber with thin film of a NEG material [4–6] and it is widely used in accelerators for synchrotron radiation facilities, because NEG thin films suppress outgassing from substrates and pump reactive residual gases, and because they are space saving. The most popular NEG coating consists of Ti, Zr, and V, deposited by dc magnetron sputtering; this technique was developed by Benvenuti *et al.* [4,5]. The resulting TiZrV thin film can be fully activated by baking at 180 °C for 24 hours. Recently, thin films of TiZrHfV deposited by dc magnetron sputtering have been reported to be fully activated by baking at 150–160 °C for 24 hours [6].

We recently developed a new NEG coating, and named it as oxygen-free Pd/Ti coating, principally for pumping H_2 and CO [7,8]. The oxygen-free Pd/Ti coating has the following advantages: (1) it can be activated after baking

at 133 °C for 12 hours; (2) the Pd overcoat prevents oxidation of the Ti film, even after repeated venting–baking cycles; (3) the initial and running costs are low; (4) its fabrication does not require skilled technicians; (5) it can be applied to chambers having a complex structure; and (6) it can be applied to narrow tubes, where Pd and Ti filaments can be arranged.

To produce this coating, a thin film of Ti is initially deposited and subsequently overcoated with Pd under clean UHV conditions in the range 10^{-8} to 10^{-7} Pa. The activation and pumping processes for the oxygen-free Pd/Ti thin film differ from those used for conventional NEG coatings [9]. In the activation process of conventional NEG, C and O atoms chemisorbed on the NEG surface diffuse into the bulk to provide a clean and reactive surface [3]. Consequently, the activation temperature of conventional NEG films is determined mainly by the diffusion activation energies of C and O atoms. On the other hand, the oxygen-free Pd/Ti thin film is activated by the diffusion of H atoms from the Ti film through the Pd overcoating to the surface, where they desorb into the vacuum as H_2 molecules. The activation energies for surface adsorption and bulk dissolution of H are –0.53 and –0.1 eV, respectively, for Pd, and –0.92 and –0.47 eV, respectively, for Ti [10]. During this activation process, CO chemisorbed on the Pd surface is also desorbed, leaving the surface available for CO absorption [11]. Because the activation temperature of oxygen-free Pd/Ti thin film is determined by the diffusion and desorption energies of hydrogen as well by the desorption energy of CO, the activation temperature can be reduced to as low as 133 °C [7,8]. When an ionization gauge is used in a vacuum system, oxygen-free Pd/Ti is expected to pump hydrogen-containing molecules, such as H_2O or CH_4 , because electrons emitted from the gauge dissociates these molecules into H atoms and radicals such as O and C.

Here, we report the morphologies of the low-oxygen-content Ti and oxygen-free Pd/Ti thin films as determined by scanning electron microscopy (SEM), transmission electron microscopy (TEM), scanning transmission electron microscopy (STEM), and energy-dispersive X-ray spectroscopy (EDS).

*miyazate@post.kek.jp

EXPERIMENTAL METHODS

The apparatus that we used for the preparation of low-oxygen-content Ti and oxygen-free Pd/Ti samples for SEM, TEM, STEM, and EDS observations is described elsewhere [9]. The oxygen-free Pd/Ti film was deposited on a substrate of electropolished stainless steel 304L (SS304L) by the following procedure. An UHV chamber was baked for 12 hours at 150 °C, then cooled to room temperature. A Ti filament was sublimed at 50 A for 333 minutes under a pressure of 2.2×10^{-7} Pa. Next, a Pd filament was sublimed at 22 A for 111 minutes at a pressure of 1.8×10^{-8} Pa. Low-oxygen content Ti samples were similarly prepared, but without deposition of Pd. The concentration of oxygen in the Pd/Ti film and the Ti bulk was estimated to be less than 0.05% [7].

Sample observations were carried out at the National Institute of Material Science (NIMS) TEM station. SEM observations were carried out by using JSM-7000F instrument (JEOL Ltd., Tokyo) operated at an accelerating voltage of 15 kV. TEM observations were carried out by using a JEM-2100F microscope (JEOL) operated at an accelerating voltage of 200 kV.

RESULTS

Figure 1a shows an SEM image of the cross section of the low-oxygen-content Ti thin film. This had a uniform thickness and a columnar structure. Figures 1b and 1c show SEM images of the surface of the Ti thin film, which had a scale-shaped structure. The grooves observed on the Ti surface derive from those present on the SS304L substrate. X-ray photoelectron spectroscopy (XPS) has shown that the Ti surface oxidizes when it is exposed to the atmosphere [7].

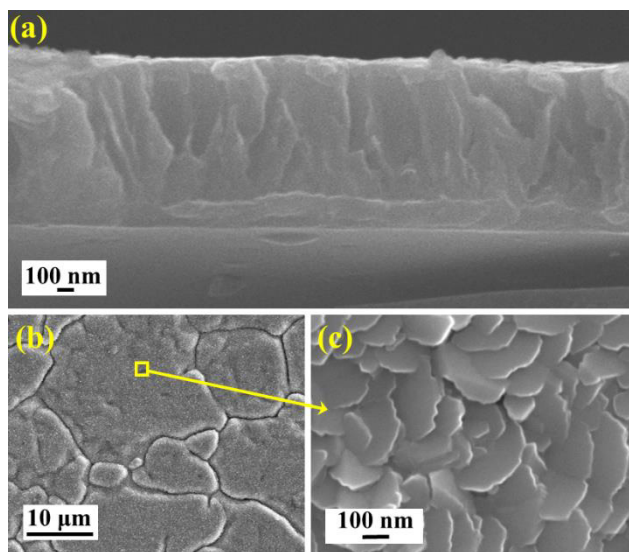


Figure 1: SEM images of (a) the cross section, (b) the surface, and (c) the enlarged surface of the low-oxygen-content Ti thin film.

Figures 2a and 2b show SEM images of the surface of the oxygen-free Pd/Ti thin film. The surface has an uneven structure with irregularities of several tens to several hundreds of nanometers, as shown in Fig. 2b. Figures 2c and 2d show the EDS elemental maps for Pd and Ti, respectively, in the same region as Fig. 2a. The fluorescence X-rays of Pd and Ti were both uniformly mapped, indicating that the Pd and Ti thin films were uniformly deposited in plane on the SS304L substrate. Because the depth resolution of EDS is approximately 1 μm, fluorescence X-rays from the Ti thin film under the Pd thin film were also detected. The SEM image of the cross section of the oxygen-free Pd/Ti film was similar to that shown in Fig. 1a [7].

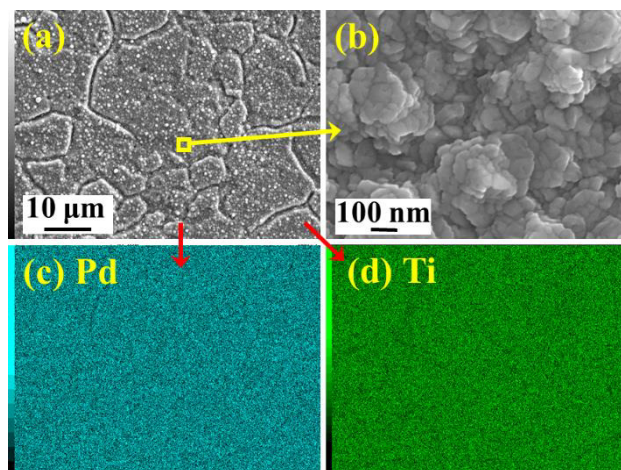


Figure 2: SEM images of (a) the surface, and (b) the enlarged surface of the oxygen-free Pd/Ti thin film. The EDS elemental maps of (c) Pd, and (d) Ti show the same region as (a).

Figures 3a and 3d show TEM bright-field images of the cross sections of the Pd and Ti thin films, respectively, whereas Figs. 3b and 3e show fast-Fourier-transform (FFT) patterns of Figs. 3a and 3d, respectively. These images indicate that the Pd and Ti thin films have polycrystalline structures. Figures 3c and 3f show TEM images of the cross sections of the interfaces between the Pd and Ti thin films, and between the Ti thin film and the SS304L substrate, respectively. The interface between the Pd and Ti thin films was not abrupt, whereas the interface between the Ti film and SS304L substrate was abrupt. At the interface, atomic layers with an atomic weight smaller than that of Ti were observed, as shown in Fig. 3f, suggesting that Cr_2O_3 segregates to the SS304L surface [12]. XPS measurements have shown that the Pd surface does not oxidize, even when it is exposed to the atmosphere [7].

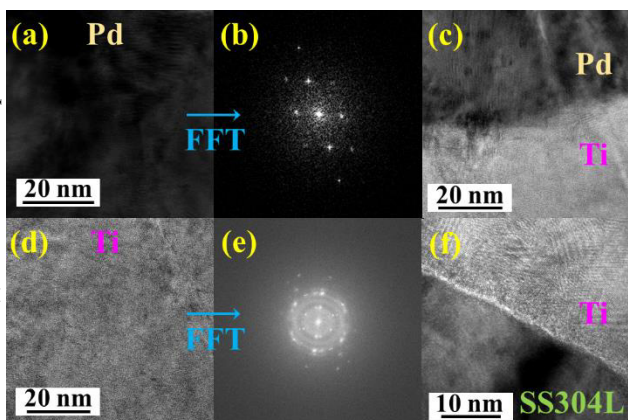


Figure 3: TEM bright-field images of cross sections of (a) Pd and (d) Ti thin films of the oxygen-free Pd/Ti thin film. Fast-Fourier-transform images of cross section of (b) the Pd and (e) Ti thin films. TEM images of cross sections of (c) the interface between the Pd and Ti thin films, and (f) the interface between the Ti thin film and SS304L substrate.

Figures 4a and 4b show STEM dark-field images of a cross section of the oxygen-free Pd/Ti thin film, prepared by focus ion milling. Figures 4c and 4d show EDS elemental maps of Pd and Ti, respectively, in the same region as Fig. 4b. These results show that the Ti and Pd films have an almost uniform thickness of approximately 1.3 μm and 50 nm, respectively, and that the Pd film completely overcoats the Ti film.

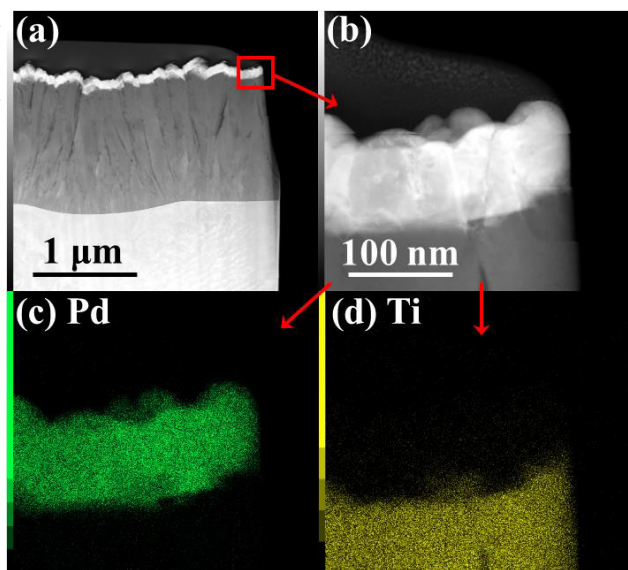


Figure 4: (a) STEM and (b) enlarged STEM dark-field images of the cross section of the oxygen-free Pd/Ti thin film. EDS images of (c) Pd and (d) Ti in the same region as (b).

Figures 5a and 5b show STEM dark-field images of cross section of the oxygen-free Pd/Ti thin film. Figures

5c, 5d, 5e, and 5f show EDS elemental maps for Ti, Fe, Cr, and Ni, respectively in the same region as Fig. 5b. At the interface between the Ti and SS304L, atomic layers with a smaller atomic weight than that of Ti were observed. The elemental map of Cr was slightly thicker than those of Fe and Ni, as shown in Figs 5d, 5e, and 5f. These results also support that Cr_2O_3 segregates on the SS304L surface [12].

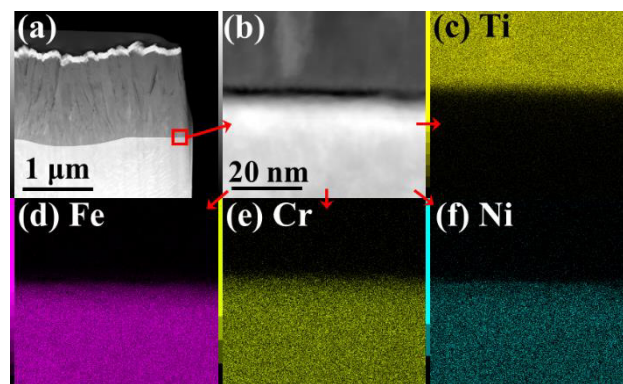


Figure 5: (a) STEM and (b) enlarged STEM dark-field images of a cross section of the oxygen-free Pd/Ti thin film. EDS images of (c) Ti, (d) Fe, (e) Cr, and (f) Ni in the same region as (b).

CONCLUSIONS

The morphologies of low-oxygen-content Ti and oxygen-free Pd/Ti films were examined by SEM, TEM, STEM, and EDS. The Ti and Pd films had almost uniform thicknesses of approximately 1.3 μm and 50 nm, respectively, and the Pd film completely overcoated the Ti film. Both the Pd and Ti thin films were uniformly deposited in plane on the SS304L substrate and had polycrystalline structures. The interface between the Pd and Ti thin films was not abrupt.

ACKNOWLEDGMENTS

The authors are grateful to Mr. A. Toyoshima (KEK), Mr. H. Tanaka (KEK), Mr. H. Nishiguchi (Baroque International Inc.), and Ms. E. Kazama (Baroque International Inc.) for their invaluable advice and support. This research was partly supported by a TIA-Kakehashi grant and by the Global Research Center for Environment and Energy based on Nanomaterials Science.

REFERENCES

- [1] LEP Vacuum Group, "LEP vacuum system: present status", *Vacuum*, Vol. 41, pp. 1882–1886, 1990, doi: 10.1016/0042-207X(90)94121-6
- [2] C. Benvenuti and P. Chiggiato, "Pumping characteristics of the St707 nonevaporable getter (Zr 70 V 24.6–Fe 5.4

- wt%)", *J. Vac. Sci. Technol., A*, Vol. 14, pp. 3278-3282, 1996, doi: 10.1116/1.580226
- [3] P. Manini, "Non evaporable getter (NEG) pumps: A route to UHV-XHV", *AIP Conf. Proc.*, Vol. 1149, pp. 1138–1142, 2009, doi: 10.1063/1.3215608
- [4] C. Benvenuti *et al.*, "Vacuum properties of TiZrV non-evaporable getter films", *Vacuum*, Vol. 60, pp. 57–65, 2001, doi: 10.1016/S0042-207X(00)00246-3
- [5] C. Benvenuti *et al.*, "Influence of the elemental composition and crystal structure on the vacuum properties of Ti–Zr–V nonevaporable getter films", *J. Vac. Sci. Technol., A*, Vol. 19, pp. 2925–2930, 2001, doi: 10.1116/1.1414122
- [6] O. B. Malyshev *et al.*, "Pumping properties of Ti–Zr–Hf–V non-evaporable getter coating", *Vacuum*, Vol. 100, pp. 26–28, 2014, doi: 10.1016/j.vacuum.2013.07.035
- [7] T. Miyazawa *et al.*, "Oxygen-free palladium/titanium coating, a novel non-evaporable getter coating with an activation temperature of 133 °C", submitted for publication.
- [8] High Energy Accelerator Research Organization, PCT patent pending, JP2017/042682.
- [9] T. Miyazawa *et al.*, "Non-evaporable getter (NEG) coating using titanium and palladium vacuum sublimation", *Vac. Surf. Sci.*, Vol. 61, pp. 227–235, 2018, doi: 10.1380/vss.61.227
- [10] M. Wilde and K. Fukutani, "Penetration mechanisms of surface-adsorbed hydrogen atoms into bulk metals: Experiment and model", *Phys. Rev. B*, Vol. 78, 115411 (10 pp.), 2008, doi: 10.1103/PhysRevB.78.115411
- [11] X. Guo and J. T. Yates Jr., "Dependence of effective desorption kinetic parameters on surface coverage and adsorption temperature: CO on Pd(111)", *J. Chem. Phys.*, Vol. 90, pp. 6761–6766, 1989, doi: 10.1063/1.456294
- [12] C. R. Cole, R. A. Outlaw, R. L. Champion, B. C. Holloway, and M. A. Kelly "Electron stimulated desorption of H₃O⁺ from 316L stainless steel", *Appl. Surf. Sci.*, Vol. 253, pp. 3789–3798, 2007, doi: 10.1016/j.apsusc.2006.07.093

A QUASI-PERIODICELLIPTICALLY POLARIZED UNDULATOR AT THE NATIONAL SYNCHROTRON LIGHT SOURCE II*

M. Musardo[†], T. Tanabe, O. Chubar, Y. Hidaka, D. Harder, J. Rank, P. Cappadoro and T. Corwin,
 Energy Sciences Directorate, Brookhaven National Laboratory, 11973 Upton, NY, USA
 C. A. Kitegi, Synchrotron SOLEIL, Saint-Aubin, France

Abstract

A 2.8 m long quasi-periodic APPLE II type undulator has been commissioned at the National Synchrotron Light Source II (NSLS-II) for the Electron Spectro-Microscopy (ESM) beamline in the framework of the NEXT (NSLS-II Experimental Tools) project [1]. It provides high brilliance photon beams in circularly and linearly polarized radiation from VUV to soft X-Rays. The mechanical structure implemented to achieve the quasi-periodicity in the magnetic field profile is described together with the optimization techniques utilized to correct the undesirable phase-dependent errors. The final magnetic results are presented as well as the spectral performance of the device. Although this EPU (Elliptically Polarizing Undulator) was procured as a turn-key device, the vendor was only responsible for the mechanical frame and the control system. Sorting and assembly of the magnet modules and the magnetic field tuning - Virtual Shimming and Magic Finger - were performed at the NSLS-II Magnetic Measurement Lab.

MAGNETIC AND MECHANICAL STRUCTURE

The magnetic structure of EPU105 is configured as four Halbach arrays in four adjacent quadrants. The support structure is equipped with four translation units for the polarization control (linear, circular, and elliptical). The period length (λ) is 105 mm and the minimum magnetic gap of the device is 16 mm. The main magnet dimensions are 34 mm (H) x 34 mm (V) x 26.25 mm (L). The remanence of the NdFeB magnets is 1.25 T. The longitudinal air-gap between the magnets is 50 μm and the gap between the magnet arrays is 1 mm. The full length of the magnetic core is 2654.25 mm, excluding girder movement and the trim magnet holders. The device has two different types of terminations, both composed of one vertically magnetized full block, two vertically magnetized half blocks and four horizontally magnetized half blocks. The end section configuration block width and the space between blocks is optimized to minimize trajectory steering and field integrals. A NEG-coated vacuum chamber with current strip corrections used for dynamic field integral correction is employed [2]. ESM EPU105 is a quasi-period undulator (QPU). The Quasi-Periodicity (Q-P) is obtained by modulating the magnetic field amplitude along the length of the device. This is achieved by vertical displacement of B-magnets (blocks magnetized longitudinally) at six specific locations. In order to reduce the magnetic field strength at

those locations the standard magnet holders were replaced with special holders that displace the magnets vertically by 13 mm with respect to the mid-plane, as shown in Fig. 1.

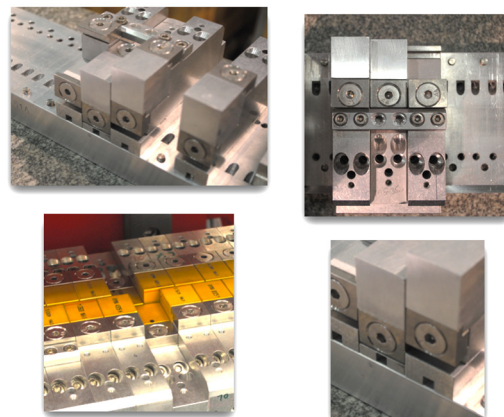


Figure 1: Magnet holders for the Q-P configuration.

During the assembly process only those magnets with longitudinal magnetization are shifted in order to minimize the deleterious effects of the Q-P adjustment on the first and second magnetic field integrals. Figure 2 shows the measured magnetic field on-axis and the 3 GeV electron trajectory in the horizontal plane at the minimum gap and phase 0.

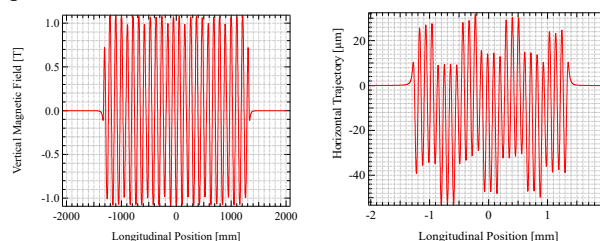


Figure 2: Measured vertical magnetic field on axis (left) and horizontal trajectory (right) in the Q-P configuration.

The quasi-periodicity in the magnetic field profile was introduced in order to modify the properties of the emitted photon beam - a reduction in intensity and shift in energy of the higher harmonics compared to the fundamental. Because of the shift in energy the higher harmonics are no longer proportional to an integer multiple of the fundamental energy, which drastically reduces the amount of unwanted higher harmonic radiation transmitted through the monochromator in the ESM beamline.

Quasi-periodic undulators were originally proposed as a method to reduce contamination from high order spectral harmonics where optical filtering is not possible or convenient [3].

* Work supported by DOE under contract DE-SC0012704

[†] musardo@bnl.gov

MAGNETIC FIELD OPTIMIZATION

The magnetic module assembly of ESM EPU105 has been carried out using a sorting scheme which progressively optimizes the magnetic field quality of the device to improve the electron trajectory straightness. After assembly, a virtual shimming process was performed to further reduce the radiation phase error and the integrated multipole variation at different phases. Fine tuning of the device using multiple trim magnets - Magic Finger (MF) - has been implemented to correct the field integral imperfections and to compensate the residual multipole effects. These optimizations were implemented using IDBuilder, a genetic algorithm-based computer code for magnetic tuning of undulators [4].

Sorting Method and Results

The sorting technique is an accurate and efficient method of field optimization. This method was first developed at ESRF [5] and then successfully used by other laboratories and industries [6]. The magnetic structure of the device is modularized. The magnets are grouped in small compensated modules. They are clamped on individual holders and arranged in modules containing either three (M3) or five (M5) magnets by means of small aluminum bars as shown in the Fig. 3.

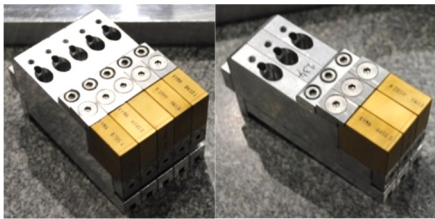


Figure 3: M5 (left) and M3 (right) modules for EPU105.

Symmetry in the design allows placement of the modules in any of the four quadrants of the EPU structure. The M5 and M3 modules form a double period that is repeated 24 times through the central region of all four magnetic arrays. These compensated modules are accurately characterized by measuring their field integral. The average of the magnetic field integral measurements of all M3 and all M5 modules are shown in Fig. 4.

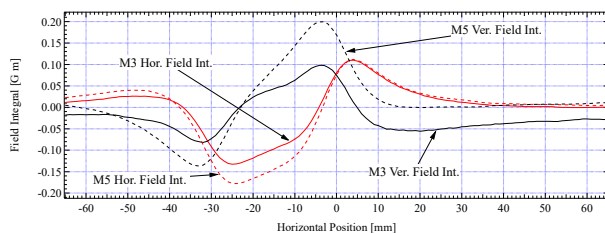


Figure 4: Horizontal (red) and vertical (black) average field integral of M3 (continuous line) and M5 (dashed line) module populations.

These measurements are used to optimize the arrangement of the modules within the undulator in order to minimize the unwanted field integrals and multipole errors, and to

ensure a straight electron beam trajectory through the device. The optimization is iterative and provides a good control of the field integral errors, reducing the post-assembly field correction effort. The assembly process consists of successive and repetitive installation of M3 and M5 magnet modules onto the mechanical frame in order to build up the 24 periods of the EPU. Because the phase dependent errors cannot be corrected by sorting, the undulator was set to zero phase mode (purely vertical field) during all of the measurements. The sorting process can be briefly summarized as follows: assembly of two period of the device, i.e. one M3 and one M5 magnet module on each array of the mechanic frame and measurement of the magnetic field integral of all assembled modules. The measured data of the current configuration and the previously measured field integrals of each module are used as inputs to IDBuilder. The software then optimizes the selection of the next two sets of M3/M5 modules to be installed. Following that process for each successive installation of two magnet modules, permits IDBuilder to minimize the first and second field integral for the fully assembled EPU. The first field integrals at a gap of 16 mm and five phases ($\pm\lambda/2$, $\pm\lambda/4$ and 0) are shown in Fig. 5. A maximum variation in phase of the horizontal field integral on-axis of about 1 G m occurs at $\pm\lambda/4$. These results demonstrate that the assembly/sorting process has been very effective: the peak to peak field integral of the fully assembled device (consisting of 48 M3 and 48 M5 magnet modules) is comparable to the field integral of the individual modules.

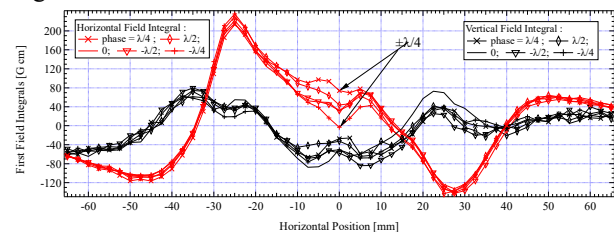


Figure 5: Horizontal (red line) and vertical (black line) field integral at minimum gap and at different phases.

In order to meet the requirements for installation in the NSLS-II storage ring a virtual shimming of the device followed by Magic Finger correction has been performed after assembly to further reduce the field integral distribution and to minimize the multipole variation in phase.

Virtual Shimming and Magic Finger Correction

Virtual Shimming is a well-established magnetic optimization technique for post-assembly tuning of an insertion device. Virtual shimming is accomplished by making small horizontal and vertical displacements of a limited number of magnets. The horizontal and vertical displacement of magnets is an efficient way to compensate the magnetic field errors of the device and thus reduce the phase error of the emitted radiation. The shimming procedure is performed based on magnetic measurement data and pre-calculated shim signatures. The shim signatures are defined as the variations of given components of the magnetic field and/or the field integral with displacements of specific

types of magnets along a given direction and at a given gap and phase. Figure 6 shows a comparison between the measured and computed vertical and horizontal field integral variation due to a horizontal displacement of 50 μm (shim thickness) of magnet #1 (A+) with the gap set at 16 mm. The magnetic interaction effects of the longitudinal shift of the magnet arrays are taken into account.

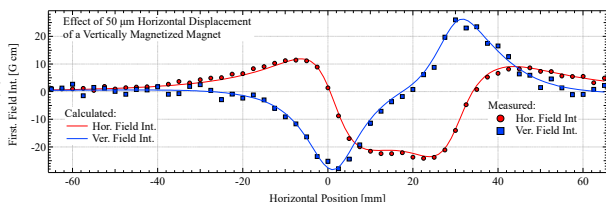


Figure 6: Shim Signatures. Predictions vs. Measurements.

Four successive iterations of virtual shimming were performed in the Q-P configuration and seven Magic Finger iterations were necessary to achieve the NSLS-II specification. MF is another corrective technique used for magnetic tuning of undulators. The MF optimization was carried out using cylindrical permanent magnets inserted into appropriate holders located at both ends of the upper and lower magnetic arrays. An optimal arrangement of these small cylindrical magnets further reduces the residual field integral and the multipole variations. After five successive MF iterations the magnetic field errors were significantly reduced. Figure 7 shows an envelope of the first and second field integral for all gaps and phases of the device.

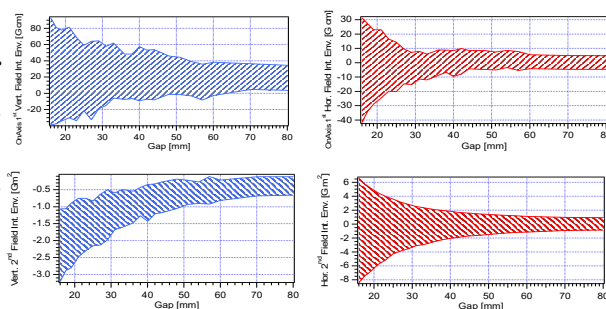


Figure 7: On-axis first (upper) and second (lower) vertical (blue) and horizontal (red) field integral variation for all gaps and phases.

The final normal and skew multipole components are shown in Fig. 8. Both field integrals and integrated quadrupoles are kept well within the tolerances over a large horizontal range. The vertical and horizontal field integral variation with respect to the phase is about ± 20 G cm over the measurement range of ± 65 mm.

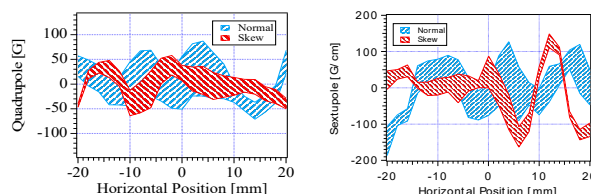


Figure 8: Envelope of the Normal (blue) and Skew (red) Quadrupole (left) and Sextupole (right) variation as function of the horizontal position for all gaps and phases.

Spectral Performance Results

The spectral flux measured at the ESM beamline reveals the quasi-periodic performance of the device [7]. The two Q-P effects, reduction in intensity and a shift in energy of the higher harmonics with respect to multiples of the fundamental (red lines), are clearly visible in the spectrum shown on Fig. 9. The spectral flux was measured with a ring current of 2 mA at a gap of 65 mm. This result is in a good agreement with the flux calculation based on the measured magnetic field as shown in Fig 10.

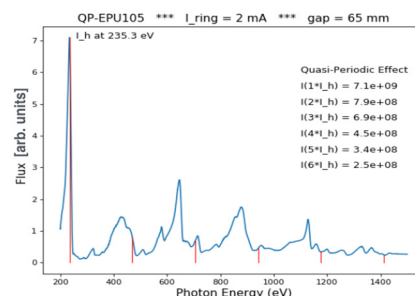


Figure 9: Spectral Flux measured at ESM beamline.

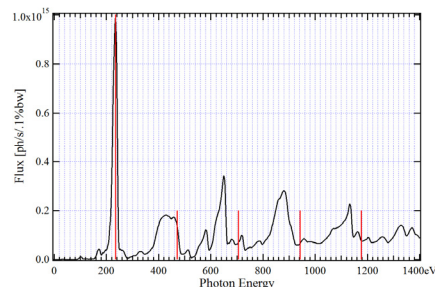


Figure 10: Spectral flux calculation based on the measured magnetic field.

CONCLUSION

Introduction of the Q-P in the device resulted in a large variation of the second field integral as a function of phase. This unwanted variation cannot be corrected using MF, but rather requires additional virtual shimming or, most efficiently, the use of external correction coils. The coils were installed and energized to quantify their correction. The maximum variation was successfully corrected by setting a current of 6.6 A.

REFERENCES

- [1] NEXT, <https://www.bnl.gov/ns1s2/project/NEXT>.
- [2] T. Tanabe *et al.*, “Latest experience on insertion devices at the National Synchrotron Light Source-II”, *Journal of the Vacuum Society of Japan*, Vol. 59, No. 8, Sep 2016, pp. 205-212.
- [3] S. Sasaki *et al.*, “Conceptual design of quasiperiodic undulator”, *Rev. Sci. Instr.*, vol.66(2), March 1995, DOI: 10.1063/1.1145768.
- [4] O. Rudenko and O. Chubar, “An evolutionary approach to shimming undulator magnets for synchrotron radiation sources”, in *Proc. PPSN IX*, Reykjavik, Iceland, Sept. 2006, pp. 362-371.
- [5] J. Chavanne *et al.*, “In-vacuum undulators at ESRF”, in *Proc. Particle Accelerator Conference*, Portland, USA, June 2003, paper TOPA013, p. 253-255, DOI: 10.1109/PAC.2003.128894.
- [6] M. Musardo *et al.*, “Magnetic characterization of an APPLE II undulator prototype for FERMI@Elettra”, in *Proc. EPAC*, June 2008, Genoa, Italy, p. 2294-2296.
- [7] E. Vescovo *et al.*, “QP-EPU105: operational experience with a quasi-periodic undulator at NSLS II”, presented at MEDSI 2018, Paris, France, June 2018, this conference.

STRUCTURE DESIGN OF A MULTI-WIRE TARGET*

Xiaojun Nie [†], Anxin Wang, Jilei Sun, Taoguang Xu, Ling Kang, Jiebing Yu, Huayan He, Jia-xin Chen, Donghui Zhu, Lei Liu, Changjun Ning, Guangyuan Wang, Yongji Yu, Junsong Zhang,
 Dongguan Branch of the Institute of High Energy Physics, Chinese Academy of Science(CAS),
 523803 Dongguan, China

Abstract

Introduce a structure design of a Multi-Wire Target. The plan of wire alignment was decided by analysis. The wire tightening device with interlaced alignment was used to solve the wire alignment in narrow space. The vacuum chamber was designed by optimization. The displacement pickup was used to make the movement control of translation stages.

INTRODUCTION

The multi-wire target is a device which is used to measure the section of beam. The measuring mental wire is bombarded by the beam and gets the low-energy electron. The low-energy can output the voltage signals. The multi-wire target can use this signal to measure the density of beam section. The mental wires are aligned according to the beam measuring requirement.

The multi-wire target has a complex structure, which includes measuring part, vacuum chamber, moving part and so on. It also demands high motion accuracy to reach high measuring accuracy. According to the running requirement of China Spallation Neutron Source, one multi-wire target (RDMWS) is demanded on the ring to dump transportation to the beam section[1-2].

WIRE ALIGNMENT PLAN

Wire alignment plan is the wire distribution pattern. Two group wires, which are vertical each other, are designed to detect two directions of beam. The horizontal and vertical directions are selected the wire directions to simplify the structure of multi-wire target. According to the beam parameter, the dimension of beam section can be reached. The dimension (1σ) of

horizontal direction is 20mm, while the dimension (1σ) of another direction is 10mm. The wire alignment plan can be concluded by the above information, which is stated as the following.

- (1) Wire direction: horizontal and vertical directions.
- (2) Wire quantity on horizontal direction: 35 wires are distributed on this direction. The distance between the wires is 7mm. The width of covered area is about 238mm. 17 wires are include in 6σ range ($\sigma_x=20\text{mm}$).
- (3) Wire quantity on vertical direction: 41 wires are distributed on this direction. The distance between the wires is 6mm. The width of the covered area is about 240mm. 10 wires are include in 6σ range ($\sigma_y=10\text{mm}$).

The wire distribution figure can be reached by the plan, which is illustrated as Figure 1.

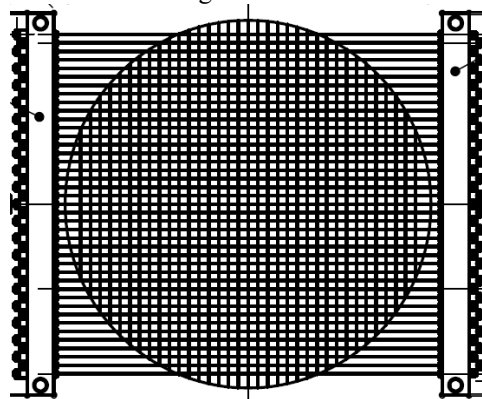


Figure 1: Wire distribution plan.

DESIGN OF WIRE TIGHTEN COMPONENT

Design Requirements

Wire tighten component is an important part for the multi-wire target, which is used to locate and fix the wires. It is important to optimize this part because of the dense distribution of wires in narrow space.

The component should fix and locate wires reliably. Any two components should avoid position interference each other. The material for this part should not be hard. Otherwise it is easy to harm the wires. Meanwhile any two wires should be insulated each other. The vacuum working condition should also be considered for design.

Structure of Wire Tighten Component

Wire tighten component is composed of wire tighten clamps, located blocks and tighten bolts. The oxygen-free copper was selected as the material of wire tighten clamp, while the ceramic was selected for the located block. Each wire is strained by the spring and fixed by bolts. The tungsten wire is used for measurement, which has good electrical conductivity and mechanical property. But the diameter of the wire is very small to ensure the measuring precision. So the stretching force of the spring should not be too high.

One group stepped holes were designed on the located block. The stepped holes can be used to locate the wire tighten clamps and install the springs. The distribution of wire tighten clamps are very dense. So they are aligned by interlaced alignment to get a gap between two clamps and avoid short circuit for the rotation of wire tighten clamp. In order to make interlaced alignment, two type clamps

[†] Email address : niexj@ihep.ac.cn

have been considered. One type clamp takes the spring, while another type does not take spring. The two type clamps were illustrated as Figure 2&3.

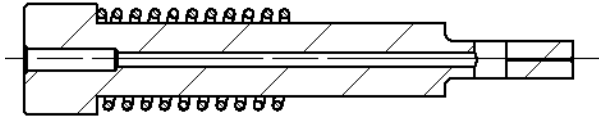


Figure 2: Clamp with spring.

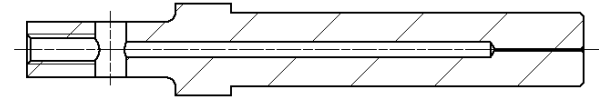


Figure 3: Clamp no spring.

The final Wire tighten component is shown as Figure 4. It is clear that the interlaced alignment of the two type clamps has made the clamps avoid each other.

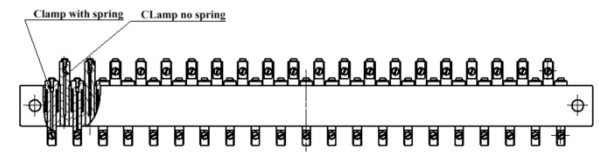


Figure 4: Final assembly of wire tighten component.

DESIGN OF VACUUM CHAMBER

Structure of the vacuum chamber

The vacuum chamber is another important part of the multi-wire target. It is used to maintain the vacuum condition and support the weight of above part of the multi-wire target. The section of vacuum chamber has many types, such as the circular section, rectangular section, irregularly shaped section and so on. The concrete section depends on the working condition.

The vacuum chamber of the multi-wire target should contain the measuring component and leave enough space for movement. The section of the vacuum chamber has been designed as rectangle for the section of the measuring component of the multi-wire target is rectangular [3].

Finite element analysis of vacuum chamber

The vacuum chamber has a big space and bears the atmospheric pressure and the weight of the above part of multi-wire target. It is important to optimize the vacuum chamber structure. Three type structures, which include the chamber without rib reinforcement, the chamber with horizontal rib reinforcement and the chamber with horizontal and vertical rib reinforcement, have been designed for optimization.

It is a valid method to make the finite element analysis for different vacuum chamber structures. Finite element method is a scientific calculation method. This method divides the whole engineering structure as many discrete element models, which are connected by nodes. The force acting on the element model is replaced by the force on

the node. In this way, the calculation can be simplified and the computational accuracy can be improved [4].

The following is the edge-restraint condition of the vacuum chamber. The bottom of the vacuum chamber will be fixed with the bracket. And the two end faces will be connected with other devices. So this two spot can be considered fully constrained. The outside of the chamber bears the atmospheric pressure. The top plate bears the weight of the above part of the multi-wire target. The material of the vacuum chamber is 316L. The characteristic parameter can be reached as Table 1 [5].

Table 1: 316L Characteristic Parameters

Tensile Strength, Yield (MPa)	Modulus of Elasticity (GPa)	Poisson ratio	Density (g/cm ³)
290	193	0.28	8

Three vacuum chamber structures were designed to compare. The first structure is the chamber without rib reinforcement (NB). The second is the chamber with horizontal rib reinforcement (HB). The third is the chamber with horizontal and vertical rib reinforcements (HV). The stress and deformation of the vacuum chambers can be reached as Figure 5 and Table 2.

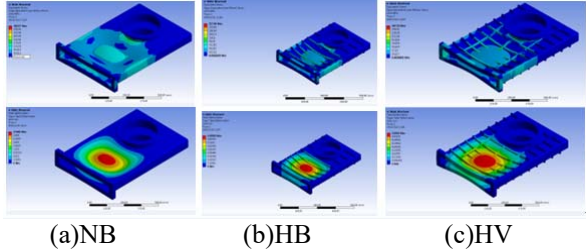


Figure 5: Distribution of stress and deformation of the vacuum chamber.

Table 2: Maximum Stress and Deformation of the Vacuum Chamber

Vacuum Chamber	Maximum Stress (MPa)	Maximum Deformation (mm)
NB	400	2.7
HB	217	0.9
HV	167	0.5

It can be concluded that the rib reinforcement can improve the stress state of the vacuum chamber significantly. The vacuum chamber with horizontal and vertical rib reinforcements (HV) has the best stress state.

DESIGN OF VACUUM CHAMBER

Movement Control by the Displacement Sensor

The measuring part of the multi-wire target is above of the beam on the free time. It just comes to the position of the beam when working. The measuring part is fixed on the slider of the translation stages. The movement of slider can take the measuring part to the working position.

It is necessary to check if the measuring part has reached the working position. The displacement sensor is used to check and control the movement.

Displacement sensor is also called as linear sensor, which can translate the movement to the electrical signal. LVDT displacement sensor can be selected as the control sensor for its simple structure, good endurance to the bad environment and high working reliability [6]. The structure of this sensor is shown as Figure 6.

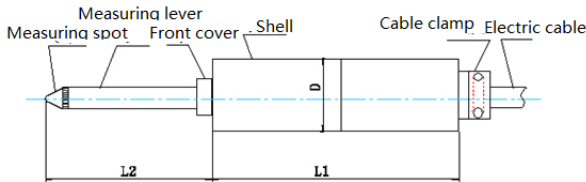


Figure 6: Structure of displacement sensor.

The output of displacement sensor is voltage signal, which is proportional to the movement of the measuring spot. The value of output voltage (V) and displacement (D) were provided by the seller, which is listed as table 3.

Table 3: The value of Displacement and Output Voltage

D/ mm	0	2	4	6	8	10
V/ mV	0	500	1000	1500	2000	2500
D/ mm	12	14	16	18	20	
V /mV	3000	3500	4000	4500	5000	

The correlation of the displacement vs the voltage is shown as Figure 7. So the voltage signal of the displacement sensor can be used to control the position of the measuring part of the multi-wire target. The deviation between the computed displace and the real displace is within 0.05mm by the spot test. It can demand the control requirement.

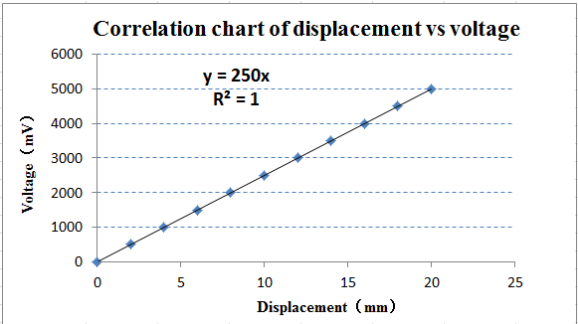


Figure 7: Correlation chart of displacement vs voltage.

Assembly of the Displacement Sensor

The displacement sensor should be located accurately and replaceable after assembly. If the displacement sensor is broken, it can be replaced by another one without adjustment. V-type block can be applied to locate the displacement sensor and realize the replacement. The located mechanism is shown as Figure 8.

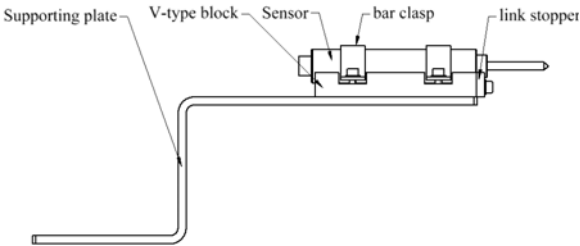


Figure 8: Located mechanism of displacement sensor.

CONCLUSIONS

Multi-wire target is an important beam testing device, which is used to check the section shape of the beam. The wire alignment plan, wire tighten component, vacuum chamber and the movement control have been discussed preliminarily in this article. It can provide some reference for the design and manufacturing of the similar devices.

ACKNOWLEDGMENTS

The authors would like to give acknowledgments to all the colleagues who have contributed to this project.

REFERENCES

- [1] Liu Bao-jie, “EPICS-Based Beam Profile Monitor System”, in *Information Security and Technology SEP.*, 2014, pp. 75-78.
- [2] YU Neng-Jie, TANG Chuan-Xiang, ZHENG Shu-Xin, *et al.*, “2-D Beam Profile Measurement Based on CT Algorithm with Rotating Multi-Wire Target”, in *Chinese Physics C*, vol. 29, No.4, Apr 2005, pp. 408-412.
- [3] DONG Hai-yi, SONG Hong, LI Qi *et al.*, “Research and development of vacuum system for China spallation neutron source”, in *Vacuum*, vol.52, no.4, Jul. 2015, pp 1-6.
- [4] Zhang Xiang-hua, Qu Hua-min, Luo Yang *et al.*, “Finite Element Analysis on Structure Design of the Antechamber of BEPC II”, in *Journal of Heilongjiang Institute of Technology*, vol.18, no.3, 2004, pp. 25-28
- [5] <http://www.matweb.com/search/DataSheet.aspx?MatGUID=1336be6d0c594b55afb5ca8bf1f3e042&ckck=1>
- [6] Liu Yan, Wang Ye, “Present Status and Trend of Technical Development of Displacement Sensor”, *Instrumentation and Measurement*, vol.32, no .6, 2013, pp. 76-80

CALCULATION OF ORBIT DISTORTIONS FOR THE APS UPGRADE DUE TO GIRDER RESONANCES*

J. Nudell[†], Z. Liu, V. Sajaev, C. Preissner, Argonne National Laboratory, Argonne, IL, USA

Abstract

Maintaining sub-micron-scale beam stability for the APS-U Multibend Achromat Lattice places strict requirements on the magnet support system. Historically, magnet vibration requirements have been based on physics simulations which make broad generalizations and assumptions regarding the magnet motion. Magnet support systems have been notoriously difficult to analyze with FEA techniques and as a consequence, these analyses have been underutilized in predicting accelerator performance. The APS has developed a procedure for accurate modeling of magnet support systems. The girder mode shapes are extracted from these analyses and exported to accelerator simulation code *elegant* to calculate the static beam amplification factor for each mode shape. These amplification factors, along with knowledge of damping coefficients and the character of the tunnel floor motion, may then be used to predict the effect of girder resonances on beam stability and validate the magnet support designs.

INTRODUCTION

Typical magnet support stability requirements for light sources are specified by physicists with a girder-to-girder motion specification and a magnet-to-magnet motion specification (for elements mounted on a common girder) as shown in Table 1 for the APS Upgrade (APS-U). As the required stability of fourth-generation light sources becomes more stringent, so too do the requirements for support systems. The goal for APS-U is to limit mechanical sources of beam motion to less than one micron in each direction, without orbit feedback.

Table 1: APS-U Vibration Tolerances [1]

Specified over 1-100 Hz	X (rms)	Y (rms)
Girder Vibration	20 nm	20 nm
Quadrupole Vibration	10 nm	10 nm

Although the tolerances in Table 1 are useful to provide engineers with simple design requirements, they are based on broad generalizations regarding the character of the magnet motion which may be inaccurate. For instance, magnet-to-magnet vibration within a girder is simulated by physicists as uncorrelated motion, when in reality, this motion is mostly correlated and due to girder deformations (which can be simulated). In addition, the specifications are based upon a particular magnet grouping arrangement, making it difficult to accurately evaluate alternate magnet grouping arrangements in terms of beam dynamics.

*Argonne National Laboratory's work was supported by the U.S. Department of Energy, Office of Science, Office of Basic Energy Sciences, under contract DE-AC02-06CH11357.

[†]jnudell@aps.anl.gov

The APS has developed a procedure for modeling of magnet support system dynamics which has proven to be accurate in predicting modal response within 10%, as shown in reference [2]. The paper below describes a procedure for utilizing these modal analyses in order to predict the effect of measured ground motion and simulated magnet support system dynamics on beam motion. The procedure has been used to evaluate a previous magnet support grouping, as described in reference [3] and the results here are used to evaluate a new magnet support grouping.

APS-U MAGNET GROUPING

The APS-U magnets will be placed on three long and two short supports (girders) per sector. Three larger supports will rest on three concrete plinths, and two smaller supports will straddle between the three plinths. The plinths are used to effectively raise the floor and reduce the height of the girders. The middle module containing focusing and defocusing quadrupoles and dipoles is called "FODO", and the side modules, which contain the quadrupole doublet, longitudinal gradient dipole, and multipoles, are called "DLM-A" and "DLM-B".

The tolerances listed in Table 1 assume a magnet grouping arrangement where all quadrupoles between dipoles are located on a common girder. This arrangement does not allow for bellows in between modules, which makes fabrication, installation, and alignment of the accelerator components infeasible given the short period of time allotted for installation. The new magnet grouping arrangement places the quadrupoles adjacent to the dipole magnets on a common support with bellows on either end, called "QMQ". Since the tolerances in Table 1 do not reflect this grouping, the strategy described in this paper is used to evaluate the magnet support design. The new and old magnet grouping arrangements are shown in Figure 1.

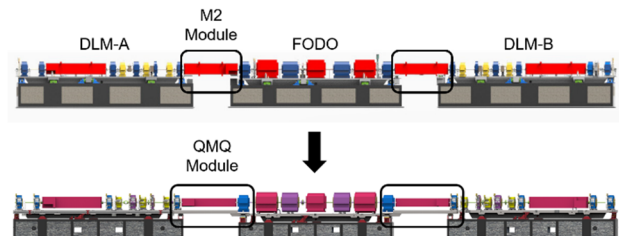


Figure 1: Previous (top) and current (bottom) APS-U magnet grouping arrangement.

GIRDER VIBRATION MODES

The girder modal analysis is performed using ANSYS Mechanical, Release 18.1 [4]. In order to accurately predict the modal response of the modules, dynamic stiffness testing is completed on the support components. Each support component is preloaded between two weights, hung from

a crane, and an experimental modal analysis is performed. Using the equations of motions for this simple dynamic system along with the experimentally determined rigid body mode values, the 6×6 diagonal stiffness matrix of the component is determined. This stiffness matrix for each support component is input into the ANSYS modal analysis along with the geometry of the magnets, girder, and plinth. During R&D, it was found that the storage ring concrete floor can be considered a rigid boundary condition. All modules in the arcsector are included in the same analysis.

The analysis is limited to modes with resonant frequencies below 100 Hz due to the rapid drop in ground vibration amplitude at higher frequencies. Figure 2 shows the mode shape and a plot of magnet displacements corresponding to one of the modes of the DLM module.

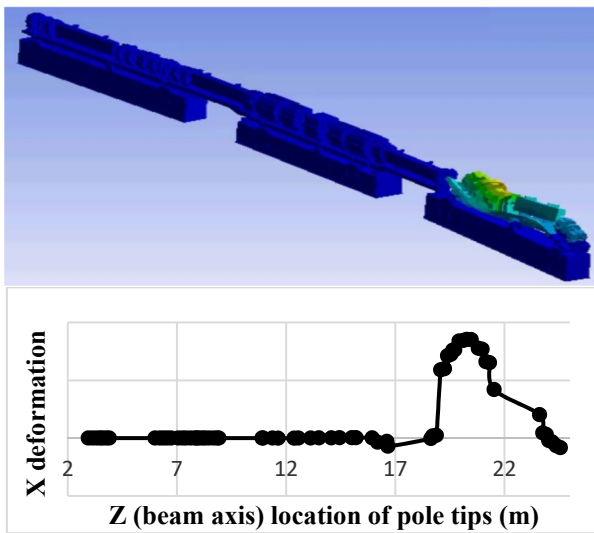


Figure 2: Mode shape illustration and plotted X-direction deformation for mode #10 – a mode which causes a relatively large orbit distortion.

LATTICE AMPLIFICATION FACTORS

Analysis shows the modes are lightly coupled and damped. This allows for the assumption that the modes can be assumed to be non-coupled, single-degree-of-freedom systems. Then, the effect of the modes on the orbit can be considered separately and then the overall effect can be obtained by adding corresponding rms amplitudes of orbit motion in quadrature. An *elegant* [5] parameter file is generated that contains the displacements and tilts of each magnet for every mode, like the one shown in Fig. 2. To generate the parameter file, the modal displacements are normalized to make the maximum of all three displacements equal to 10 μm. Then *elegant* is used to calculate the closed orbit due to magnet displacements on a single girder for each resonant mode. The ratio of the maximum orbit distortion at the ID location to the maximum magnet displacement (10 μm in our case) is the single-girder lattice amplification factor f_m for a particular mode m .

Consider the orbit motion due to a single mode in all girders. The orbit displacement at the ID locations due to a single girder displacement in a resonant mode m is

$$q = f_m u \cos(\phi_q - \pi v_q),$$

where q stands for x or y , u is the girder mode displacement amplitude and ϕ_q is the horizontal or vertical phase advance between the girder and the observation point. There is no beta function in this expression because the single-girder amplification factor f_m was calculated for orbits at ID locations only. The motion of every girder in the same mode is also independent because the coherence length of ground motion at frequencies above 30 Hz is less than 5 m [6], therefore, we can add the rms motion caused by each girder in quadrature. The total motion Q due to all N girders for one mode is:

$$Q^2 = \sum f^2 u_i^2 \cos^2(\phi_i - \pi v) = f^2 N \langle u_i^2 \cos^2(\phi_i - \pi v) \rangle \\ = f^2 N \langle u_i^2 \rangle \langle \cos^2(\phi_i - \pi v) \rangle = 0.5 f^2 N u_{rms}^2,$$

where we averaged \cos^2 to 0.5. The girder motion is driven by the ground motion, and since the ground motion spectrum is approximately the same at any location around the ring, the ground motion amplitude at some frequency is on average the same around the ring. The rms displacement of a single girder is the rms of a sine function, or $u_{rms} = 0.7 u_{max}$, where u_{max} is the ground motion amplitude at the frequency of interest. Therefore, the amplification factor of N girders vibrating at a resonance mode is:

$$F = \frac{Q}{u_{max}} = 0.7 f \sqrt{0.5 N} \approx 0.5 f \sqrt{N}.$$

To make amplification factors independent of beta function values at the ID locations, we divide the amplification factors by $\sqrt{\beta_{ID}}$.

GIRDER VIBRATION

It is assumed that the excitation for the girder vibration comes from the ground motion. The spectrum of the ground motion at APS was measured on several occasions, and the most recent measurement can be found in [6] and are used in the calculations below.

For frequencies close to widely spaced resonances, the response amplitude x can be described by the resonance curve:

$$\frac{x(\omega)}{X} = \frac{Q}{\sqrt{(\omega - \omega_0)^2 \left(\frac{2Q}{\omega_0}\right)^2 + 1}},$$

where X is the driving motion amplitude (amplitude of the ground motion), ω_0 is the resonant frequency, and Q is resonator quality factor. A value of 50 is used for the quality factor (damping ratio = .01) based on measurements of prototype girder resonances. The process of calculating the contribution of one mode is as follows. First, the driving motion PSD is multiplied by the resonance curve. Then, the resulting PSD is multiplied by the square of the corresponding mode amplification factor to get the PSD of the

Table 2: Effect on beam motion from each girder mode below 100 Hz considering ground motion, girder dynamics, and amplification factors (some rows hidden).

Mode	Freq. (Hz)	Description	Amp. Factor (X)	Amp. Factor (Y)	Beam Motion (X)	Beam Motion (Y)
1	37.3	QMQs rocking, in-phase	2.0	0.7	46	18
2	37.4	QMQs rocking, opposite phases	9.9	0.3	228	6
3	41.9	FODO rocking	15.4	0.3	180	6
4	43.6	Upstream QMQ vertical buckling	2.0	0.9	20	16
5	43.6	Downstream QMQ vertical buckling	1.2	1.0	12	16
6	47.9	FODO twisting	8.4	1.3	97	13
7	53.3	Downstream DLM twisting-buckling	12.8	6.2	144	107
8	53.5	Upstream DLM twisting-buckling	20.6	5.6	227	94
9	56.5	Upstream DLM twisting-buckling	6.7	5.1	104	98
0	57.5	Downstream DLM twisting-buckling	22.3	11.8	468	270
27	97.9	FODO wave-like distortion	0.5	20.1	2	111
Total					680	610

orbit motion caused by this mode. Finally, the orbit motion PSD is integrated between $0.5 f_0$ and $2 f_0$ to get the rms orbit motion due to this mode.

A summary table of each girder mode, amplifications factors, and resulting beam motion is shown in Table 2. This table is extremely useful to determine the relative importance of each mode in inducing beam motion. For example, mode 10 contributes significantly to the total beam motion.

The overall orbit motion due to ground vibration consists of non-resonant and resonant contributions. Non-resonant contribution can be calculated by simply multiplying the PSD of the ground motion by the girder amplification factors calculated assuming girders to be rigid bodies and considering all six girder displacements and rotations. These amplification factors were calculated similarly to what was described above for the mode amplification factors. The obtained amplification factors are 58 and 63 for the X and Y directions.

RESULTS

The total beam motion due to girder resonant modes is 680 nm and 610 nm in the horizontal and vertical directions respectively, assuming no orbit correction is applied. Including the effect of non-resonant girder motion, the total open-loop beam motion due to ground motion and girder dynamics is 0.8 microns in both the x and y directions. A PSD plot of the measured ground motion and calculated beam motion is shown in Figure 3.

Using this analysis, the effect on rms beam motion of artificially changing the resonant frequencies of all girder modes by the same value may be explored (assuming modal order is unchanged), as shown in Figure 4. This plot shows the trend with frequency shift as larger amplitude floor motion in the lower frequency band is amplified, and also as narrow-band peaks in the floor motion are amplified. In general, one can see that designing for higher girder resonant modes is preferred. Since the goal is to keep the total beam motion in each direction below 1 micron, the

current girder design is acceptable as long as modal frequencies are within roughly 5 Hz of the predicted values.

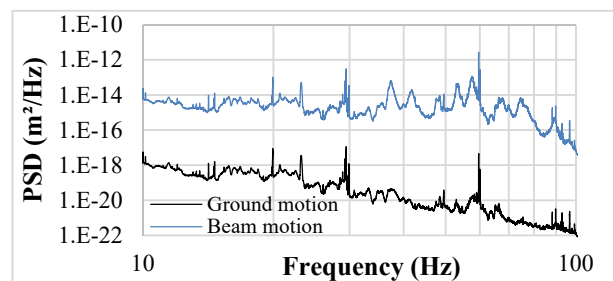


Figure 3: Measured X-direction ground motion (black) and expected X-direction beam motion (blue) including resonant and non-resonance girder vibration effects.

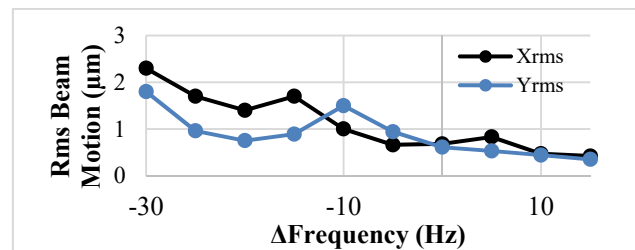


Figure 4: Rms beam motion vs. artificial frequency shift of all girder resonances.

CONCLUSION

A process has been developed which uses modal FEA data for a given magnet support design to predict the contribution of measured ground motion and girder dynamics to beam motion. The results are then used to evaluate the performance of the support system and determine a lower bound on modal frequencies, as well as provide useful information on the relative importance of higher order modes which may be used to further optimize the support system.

A new magnet support scheme is evaluated using the method presented above. The results show that the open-

loop beam motion caused by the new support scheme is 0.8 μm in the x and y directions, which is larger than for the previous support design, but acceptable.

REFERENCES

- [1] APS Upgrade Preliminary Design Report, APSU-2.01-RPT-002, 2017, <https://www.aps.anl.gov/APS-Upgrade/Documents>
- [2] C. Preissner *et al.*, “Le Guide for Support: A Cookbook for Modeling of Accelerator Structures”, presented at MEDSI 2018, Paris, France, paper WEPH22, this conference.
- [3] V. Sajaev *et al.*, “Calculation of Orbit Motions Due to Girder Resonant Vibration at the APS Upgrade”, in *Proc. IPAC’18*, Vancouver, BC, Canada, Apr.-May 2018, doi:10.18429/JACoW-IPAC2018-TUPMF011
- [4] ANSYS – Engineering simulations and 3D design software www.ansys.com, 2018.
- [5] M. Borland, Advanced Photon Source, ANL/APS LS-287, 2000.
- [6] V. Sajaev *et al.*, “Determination of the Ground Motion Orbit Amplification Factors Dependence on the Frequency for the APS Upgrade Storage Ring”, in *Proc. IPAC’18*, Vancouver, Canada, 2018, doi:10.18429/JACoW-IPAC2018-TUPMF012

NEXT GENERATION X-RAY BEAM POSITION MONITOR SYSTEM FOR THE ADVANCED PHOTON SOURCE MBA UPGRADE*

S. Oprondek[†], F. Westferro, S.H. Lee, B. Yang, Y. Jaski, J. Downey, J. Mulvey,
 and M. Ramanathan, Advanced Photon Source, Argonne National Laboratory,
 Lemont, IL 60439, USA

Abstract

The Advanced Photon Source (APS) upgrade from double-bend achromats (DBA) to multi-bend achromats (MBA) lattice has increased the need for reliable diagnostic systems. This upgrade will decrease the size of the photon beam drastically and beam current will be increased from 100 mA to 200 mA. The small beam and intense heat loads provided by the upgraded APS requires unique and innovative approaches to beam position monitoring. To meet the need for a reliable diagnostic system for the APS upgrade, the next generation X-ray Beam Position Monitoring System (XBPM) is required which includes the first XBPM (XBPM1), the Intensity Monitor (IM1) and the second XBPM (XBPM2). This paper presents progress and status of the current configuration of the XBPM system especially the development work involving the IM1 and XBPM2.

The R&D work to develop an alternative XBPM1 using the Compton scattering principle is also presented.

INTRODUCTION

Improved beam stability is critical for the Advanced Photon Source Upgrade (APS-U). The APS-U will require keeping short-term beam angle change below $0.25 \mu\text{rad}$ and long-term angle drift below $0.6 \mu\text{rad}$. In conjunction with four Radio Frequency Beam Position Monitors (RFBPM) in the accelerator ring, the front ends of the APS-U will have three diagnostic components devoted to maintaining orbit control. Beam stability will rely on two unique components that will detect X-Ray Fluorescence (XRF): the first XBPM (XBPM1) and the Intensity Monitor (IM1). The second XBPM (XBPM2) will use photoemission current to help maintain beam stability. The XBPM1 is the initial source of feedback control during user operation. The IM1 and XBPM2 are secondary devices that provide complementary data during user operation. The IM1 provides intensity measurements while a photon shutter is closed and is used to calibrate the XBPM1. The XBPM2 is not in the orbit feedback loop and is mainly used to assess feedback performance. The layout for the devices is shown in simplified form in Figure 1.

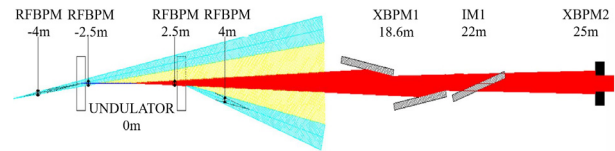


Figure 1: Layout of XBPM system.

FIRST X-RAY BEAM POSITION MONITOR (XBPM1)

The XBPM1 for the high heat load front ends (HHLFE) for the APS-U [1] uses pinhole optics and an array of silicon PIN photodiodes to monitor both vertical and horizontal displacement of the X-Ray beam as the beam is absorbed by two grazing incident insertion device (GRID) GlidCop absorbers. The XBPM1 is called the GRID-XBPM for this reason. The HHLFE is downstream of two inline undulators. The GRID absorbers are incident with the beam at 1° and will absorb 11.5 kW during normal operation. Missteering conditions require the absorbers to be able to withstand absorbing 17 kW and for this reason, GlidCop was the necessary material for this application. A cross-section of one of the GRID masks and detectors is shown in Figure 2.

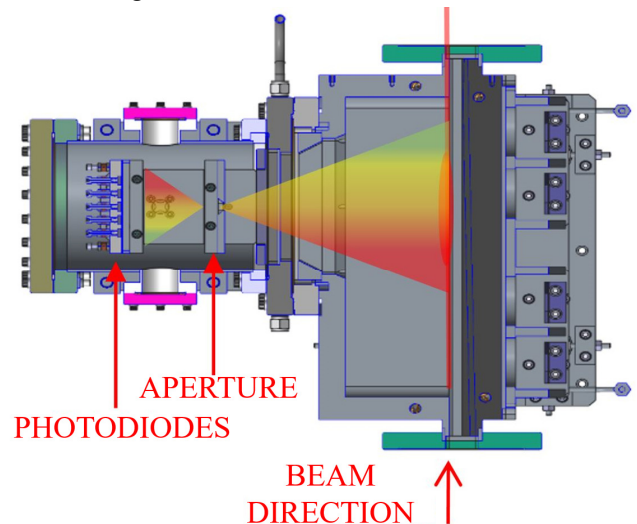


Figure 2: Cross-section of one GRID mask, with fluorescence overlay.

The unique design of the detectors is the major upgrade for this component as the GRID-XBPM style of XBPM1 has been proven effective in the current APS [2]. The detector uses an array of nine photodiodes as shown in Figure 3.

* Work supported by the U.S. Department of Energy, Office of Science, under Contract No. DE-AC02-D6CH11357

[†] soprondek@aps.anl.gov

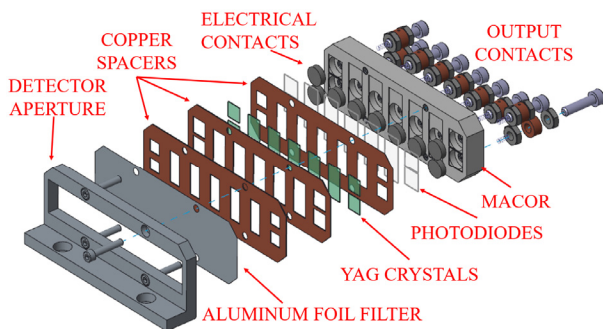


Figure 3: Detector Assembly for the GRID-XBPM.

The photodiodes are grounded to the same copper sheet to provide a basis of comparison to use for signal processing. In front of the photodiodes are Yttrium Aluminum Garnet (YAG) crystals that scintillate the XRF from the absorbers and produce visible light for the photodiodes. The photodiode lead that is not grounded is connected to an output connector, which is then connected to the feedback system.

The design of the array allows for both vertical and horizontal beam position monitoring by comparing the relative signals produced by each photodiode. Horizontal measurements are done by the middle five photodiodes and vertical measurements are done by the outer four photodiodes. As seen in Figure 2, the pinhole optics allow for upstream fluorescence on the GRID absorber to be observed by only the downstream photodiodes. By using the difference-over-sum for the signal between the upstream and downstream photodiode signal, it can be determined where on the GRID mask the beam is incident horizontally. The vertical measurement is done similarly. Figure 4 shows the layout of the photodiodes more clearly.

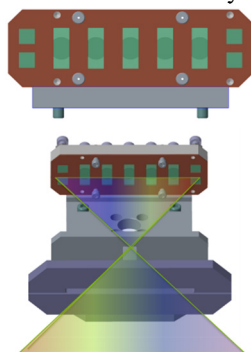


Figure 4: Front View Detector Array for the GRID-XBPM.

The GRID-XBPM will be tested in late 2018 and outlook is hopeful, as similar designs with less photodiodes have proven successful [2].

INTENSITY MONITOR (IM1)

The IM1 for the HHLFE measures XRF from a photon shutter. The full beam is absorbed by a GlidCop absorber at 1.1° when the shutter is closed. XRF reaches the upstream and downstream ends of the shutter where detectors are located. The top view of the IM1 at the beam orbit plane is shown in Figure 5.

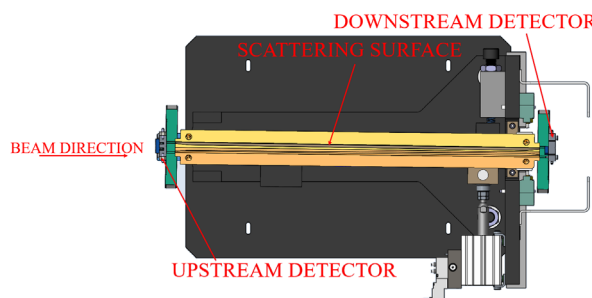


Figure 5: Cross-section of IM1 Detector System.

The detectors are single photodiodes behind aluminum filters electrically isolated from other components of the photon shutter. Detector design is shown in Figure 6.

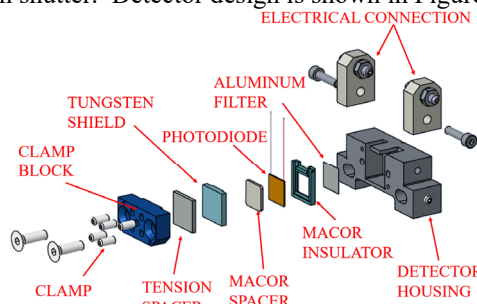


Figure 6: Detector Assembly for the IM1.

At the upstream end, a detector is placed above the nominal beam center, and at the downstream end, a detector is placed below the nominal beam center. The sum of these signals will not be dependent on the position of the undulator beam. The arrangement allows the difference-over-sum to be calculated for the two signals, which will give horizontal beam position information.

The IM1 is expected to be installed in the first upgraded front end, 28-ID, for the APS-U in late 2018. This front end will receive the current APS undulator beams but will provide test data for this type of IM1.

SECOND X-RAY BEAM POSITION MONITOR (XBPM2)

The XBPM2 design for the HHLFE is an integrated scattering mask and detector in the same unit that will ease on-site alignment. The XBPM2 uses four Invar collectors that are electrically isolated, using Macor, from the body of a GlidCop mask to determine the absolute position of the beam by collecting photoelectrons. Figure 7 shows the layout of the XBPM2.

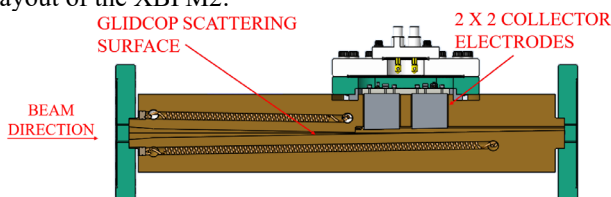


Figure 7: Cross-section of XBPM2.

Signals are expected to exceed milliamperes because of the detector's proximity to the undulator beam, as the aperture at the end of the mask is 2 mm x 2 mm. This will reduced the electronics necessary for the XBPM2 to simple

resistors and floating power supplies. Since the collectors are metal and ceramic, the XBPM2 is expected to be radiation resistant and should require little maintenance. The detector is shown in Figure 8.

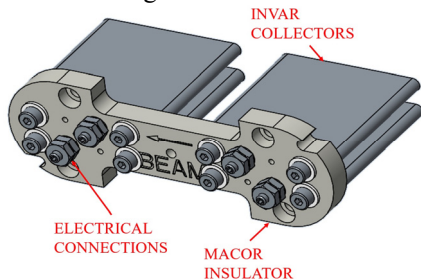


Figure 8: Photoelectron Collector for XBPM2.

The collectors are positively biased to attract photoelectrons straight away from the incident surface of the mask.

The XBPM2 is currently being tested in the APS at 27-ID with original APS undulators, and the results are very promising. High signal levels show that this design is viable.

NORMAL-INCIDENCE COMPTON SCATTERING X-RAY BEAM POSITION MONITOR (COMPTON XBPM)

An XBPM R&D project for the APS-U was a low-cost-alternative XBPM to replace the GRID-XBPM. The Normal-Incidence Compton Scattering X-Ray Beam Position Monitor (Compton XBPM) was developed and tested in mid-2017 and results are presented here.

The design includes two blades that are placed above and below the beam to absorb the halo of the beam at normal incidence. To be an effective alternative for the XBPM1, the blade material needed to be able to absorb a direct hit from the photon beam at the blade edge, absorbing half the beam in comparable conditions to the APS-U canted undulator front ends. High thermally conductive materials were chosen because of the severe condition of normal incidence. The Compton XBPM tested one chemical vapor deposition (CVD) diamond blade and one pyrolytic graphite blade as absorbers. To detect the Compton scattering from the carbon absorbers, silicon photodiode detectors and YAG scintillators were placed normal to each blade on the opposite side of the beam. A pair of photodiodes corresponded to each blade, which allowed for both horizontal and vertical beam position monitoring. A cross section is shown in Figure 9.

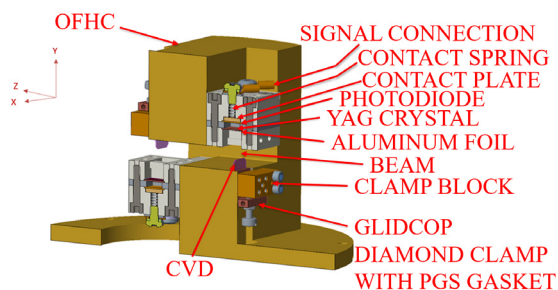


Figure 9: Cross-section of Compton XBPM.

The Compton XBPM was tested in two locations at the APS, one canted undulator beamline and one high heat load front end. The canted undulator test subjected the Compton XBPM to single undulator beam at 28 m from the source behind a beryllium window and a 3 mm x 2 mm aperture mask at 25 m. The power experienced at this location, which totaled less than 100 W was survivable for the Compton XBPM and this test gave usable results. This was a proof of concept test. For applications with relatively low power, the Compton XBPM may be a cost-effective design. During the high heat load test, which was a survivability test, dual undulators were steered directly at the blades. This test was at 20 m with no beryllium window and it simulated the power that the APS-U canted undulator front ends would produce. The test confirmed that the Compton XBPM was effective as long as the absorbers were far from the beam. When the beam was steered directly at the blades, the diamond cracked and the pyrolytic graphite sublimated. This was predicted by simulation and confirmed during the experiment. The Compton XBPM failed the survivability test.

The testing done with the Compton XBPM led to the development of the current GRID-XBPM design with undoped YAG crystals as well as determining that the Compton XBPM worked comparably to the GRID-XBPM for low power. Horizontal and vertical beam position monitoring was reliable with RMS resolution near 0.3 μm vertically. There was low bending magnet background signal-to-noise ratio of better than 30:1, which was comparable to the GRID-XBPM.

Further testing could be done to develop this technology further, but for the purposes of the APS-U, the reliable GRID-XBPM was chosen as XBPM1.

CONCLUSION

The work done to develop the XBPM system for the APS-U has built iteratively on previous designs that have been successfully used in the current APS for years. The development of array detectors will lead to interchangeable printed circuit boards instead of Macor supported designs to assist in maintenance and replacement of radiation-damaged detectors. Similar designs to what has been presented will be done for the APS-U canted undulator front ends (CUFE) and will use the technology bred from this work.

REFERENCES

- [1] Y. Jaski *et al.*, "Front Ends Design for the Advanced Photon Sources Multi-bend Achromats Upgrade," presented at the 10th Mechanical Engineering Design of Synchrotron Radiation Equipment and Instrumentation (MEDSI'18), Paris, France, June 2018, paper THPH24, this conference.
- [2] S. H. Lee, J. Mulvey, M. Ramanathan, B. X. Yang, "Design of X-Ray Beam Position Monitor for High Heat Load Front Ends of the Advanced Photon Source Upgrade" in *Proc. MEDSI'16*, Barcelona, Spain, Sept. 2016, pp. 318, doi.org/10.18429/JACoW-MEDSI2016-WEPE04

ALBA SYNCHROTRON LIGHT SOURCE LIQUEFACTION HELIUM PLANT

M.Prieto[†], Y. Nikitin[‡], C. Colldelram[§], J. Casas[#]
 ALBA Synchrotron Light Source, 08290 Cerdanyola del Vallès, Spain

Abstract

ALBA is a 3rd generation Synchrotron Light facility with: 8 operational Beam Lines (BLs), a 2nd BL of Phase II under construction and 3 first Phase III BLs in design phase. Some user experiments require Liquid Helium (LHe) as a coolant. The resulting LHe consumption at ALBA is about 650 l/week.

Thus far the vaporized helium, which results from the refrigeration of experiments and equipment, has been released into the atmosphere without being reused. Due to the increasing price of LHe, ALBA agreed with ICN2 (Catalan Institute of Nanoscience and Nanotechnology) to invest in a Liquefaction Helium Plant. Internal staff has carried out the project, installation and pressure equipment legalization of the plant, which is located in a new 80 m² construction. Under operation the plant allows recycling up to 24960 litres of LHe per year, which is an 80% of the helium consumed at ALBA, by making the gaseous helium undergo through 3 main stages: recovery, purification and liquefaction.

The plant, unique in Catalonia, will entail cost savings about 77% and will reduce vulnerability to supply disruptions. ICN2 will benefit from a part of the production due to their initial investment.

SIGNIFICANCE OF RECYCLING HELIUM

Due to the fact that helium is an inert gas and it has a really low boiling-point (-268.93 °C) [1], it is used in a wide range of applications.

Once gaseous helium is released into the atmosphere there is no economical way to recovery it, because most of it escapes into the space; leading to a very low and relatively constant atmosphere helium concentration of only 5.2 ppm [2], which is too low so as to separate it from air. By contrast, the highest helium content is in a few natural gas fields around the globe.

Owing to the balance between increasing demand and helium availability, helium is a finite non-renewable resource. Thus, gaseous helium should be recovered.

OPERATION

So as to meet ALBA's liquid helium demand, the plant subjects the vaporized helium to 3 stages: **recovery**, **purification** and **liquefaction**.

[†] mprieto@cells.es
[‡] ynikitin@cells.es
[§] ccolldelram@cells.es
[#] jcasas@cells.es

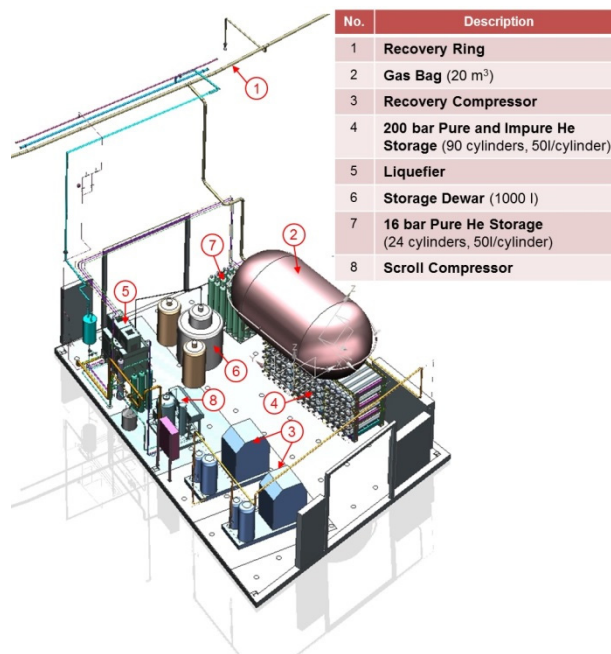


Figure 1: Liquefaction Helium Plant (LHeP) equipment identification.

Recovery

The **recuperation** initiates when the vaporized helium, which results from the thermal exchange between the liquid helium and the beamlines' components to cool, is slightly heated and inserted in the 400 m perimeter **recovery ring** that carries the gaseous impure helium to a **20 m³ gas balloon**. The helium warm-up is vital prior to being introduced into the recovery ring in order to avoid damaging the canvas, which composes the 20 m³ gas bag, because it cannot handle extreme temperatures. The helium stored in the balloon is compressed up to 200 bar by the **recovery compressor** for the purpose of saving space as well as averting the bag's collapse. The resulting 200 bar helium is stored in the **200 bar impure helium storage** (see Fig. 1 and Fig. 2).

Purification

Prior to liquefying this gas, it must be purified by the **liquefier's** internal purifier (see Fig. 2) that is capable to clean helium gas with up to 10 % air impurity. Thus, once the 200 bar storage contains a reasonable amount of impure helium, the **purification** commences starting the **liquefier** up.

The liquefier's purifier works as long as it is cooled below pre-set temperatures, which can solely be reached by circulating cold pure helium through it. The required pure helium is sucked of the **16 bar pure helium storage**,

which is at room temperature. So this reserve's content (16 bar pure helium) must be chilled before flowing through the purifier, otherwise, this pure gas would not be able to cool the purifier down. In order to decrease pure helium's temperature, the liquefier:

- can optionally use liquid nitrogen so as to speed the cooling up,
- removes heat using the main heat exchanger and,
- carries out consecutive expansions of this gas (see Fig. 2).

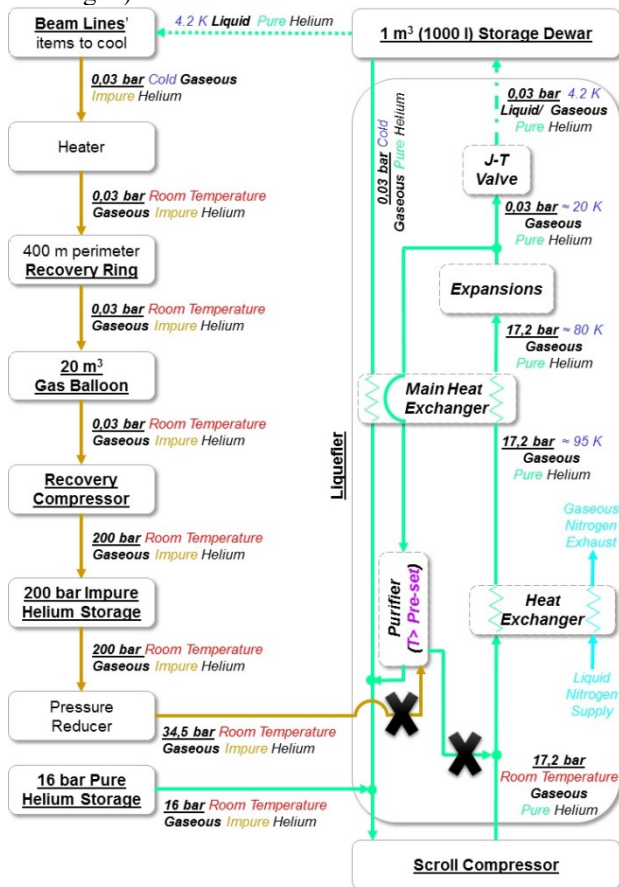


Figure 2: Plant's flow diagram when liquefier's internal purifier is not cooled below pre-set temperatures.

Therefore, before going through the successive expansions, the pure helium has to be compressed by the **scroll compressor** that delivers 17.2 bar to the liquefier where the gas is cooled (by means of the above-mentioned processes). As it is shown in Fig. 2, the resulting 17.2 bar cold pure helium stream flows through the liquefier's purifier so as to hit its pre-set temperatures. Hereafter the liquefier stops sucking the gas of the 16 bar pure helium storage and starts working with the gas of the 200 bar impure helium storage with the aim of starting the plant's final stage: the **liquefaction**.

Liquefaction

As it is shown in Fig. 3, the sucked 200 bar impure helium is led to the liquefier's internal purifier so as to remove its impurities. Then, the purified helium undergoes the different expansions that take place inside the liquefier

er and gets colder. The cold pure helium eventually is subjected to a final expansion that takes place inside in the Joule-Thomson (J-T) valve, where the gas cools below -268.93 °C, that is to say, 4.2 K. The resulting liquid/gas mixture flows through into the **1000 l storage Dewar**, but the gaseous portion comes back into the liquefier so as to be cooled and liquefied.

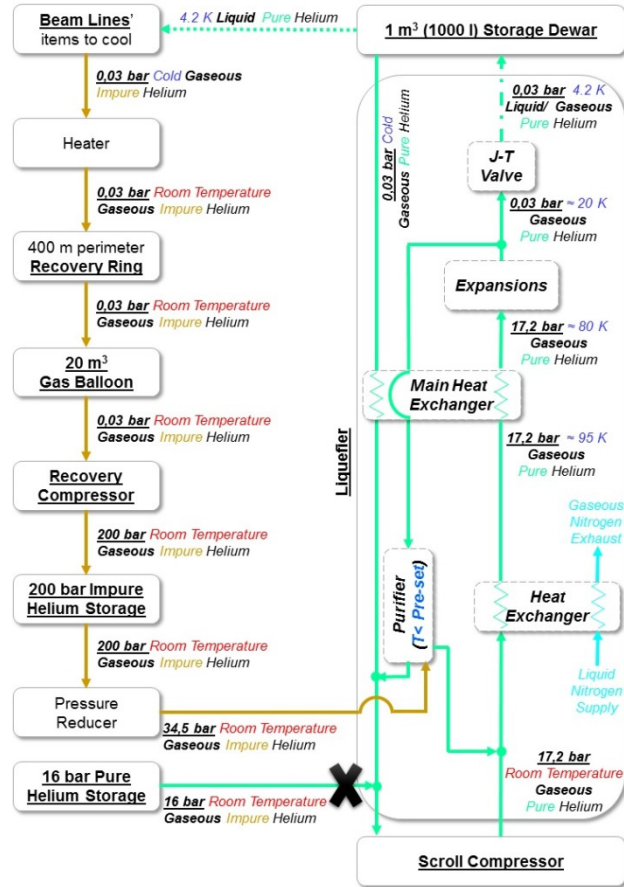


Figure 3: Plant's flow diagram when liquefier's internal purifier is cooled below pre-set temperatures.

PRODUCTION MANAGEMENT

Taking into account that the plant's liquid helium production is about 24 l/h, the strategy plan is to store the recovered gaseous helium in the 200 bar impure helium storage for two weeks. After that, 3 days will be spent to liquefy helium so as to ensure the liquid helium demand for a week.

BENEFITS

The plant allows recycling up to an 80% of the helium consumed at ALBA and implies cost savings about 77%.

Consequently, in institutions than use a significant amount of liquid helium, recovery and re-liquefaction of helium not only entail significant long-term returns but

also reduce vulnerability to supply disruptions. For instance, ALBA's Liquefaction Helium Plant can ensure from now on enough helium for 2 weeks without any new supply.

Despite the economic benefit and the fact that ALBA owns the single liquefaction helium plant in Catalonia, **ALBA will not supply liquid helium to external companies.** Nonetheless, a percentage of its production will be delivered to ICN2 as a result of their investment on the plant.

Last but not least, ICN2 also contributed money to the plant's training that has already been performed by a field service supervisor. This course entailed the installation check, commissioning and the plant's operation modes training.

ACKNOWLEDGEMENT

The author appreciates the technical advice and support as well as the superb installation task to ALBA's workshop chief, José Ferrer, and his crew. An example of their outstanding work is the 400 m perimeter ring, which has about 100 weld beads.

REFERENCES

- [1] LINDE,
http://www.lindeus.com/en/products_and_supply/helium/index.html
- [2] B.M. Oliver, J. G. Bradley, "Helium concentration in the Earth's lower atmosphere", *Geochemica et Cosmochimica Acta*, vol. 48, Sept. 1984, p. 1759-1767.

DEVELOPMENT OF A REVOLVER TYPE UNDULATOR

T. Ramm*, M. Tischler, Deutsches Elektronen-Synchrotron DESY, 22607 Hamburg, Germany

Abstract

A revolver-type undulator is developed for the SASE section of the FLASH Free-Electron Laser (FEL) at DESY. Currently, a 1.2 GeV linear accelerator injects electrons into two undulator lines to provide fully coherent VUV light to different experimental stations in two experimental halls. The more recently built FLASH2 branch consists of 12 planar undulators with a fixed magnet structure of 32 mm period length.

Within plans for refurbishment of the original FLASH1 undulator section and also to open up new operation schemes with an extended photon energy range, an undulator development was started that allows for a change of different magnet structures. Once installed, it will be possible to change the wavelength range or the FEL operation scheme within a short period of time. Magnet structures can then be switched at any time without any observable effect on the electron beam orbit or the photon beam position.

The single design steps are described in the following article: profile of requirements, choice of an applicable changing mechanism, development of a new magnet structure, the position of the bearing points, a new floor assembly and improvement of the cantilever arm.

INTRODUCTION

The motivation for the development of a magnet structure changing undulator is to open up the photon energy range for the users within a short period of time without manpower-intensive hardware exchange in the tunnel or impact on the beamline. This development is still ongoing; the paper reflects the present status of design.

PROFILE OF REQUIREMENTS

The magnet structure changing undulator should be based upon the currently installed planar insertion devices with a length of 2.5 m. Its new dimension should neither exceed the available space nor result in changing a lot of assemblies in the surroundings. Another requirement for the construction is to switch between as many as possible magnet structures automatically within a short period of time. Effects on the electron beam are undesirable. The currently installed magnet structure shall possibly be used further on and also be part of the new ones. The changing mechanism is to be mounted on the currently used base frame of the FLASH2 insertion device (ID) with all its installed components. The length of the new ID should still be 2.5 m and the whole assembly shouldn't pass the existing limits. The shutdown-time for exchanging the undulators with another magnet structure and the necessary manpower has to be minimized.

* torsten.ramm@desy.de

SELECTION OF THE CHANGING-MECHANISM

There are at least four different concepts how an exchangeable magnet structure has been realized in the past. Generally it is required to open the gap before changing the magnet arrays.

The first type has been built at DESY already in the early days of undulators and has a rotating cylinder pivot-mounted and electrically driven at the outer ends (see Fig. 1). The advantages are that you are free at the number of installed magnet structures and only restricted by their magnitude. Also, there are no disturbing influences on the magnetic field along the magnet structure. However, the cylinders, not pivot-pointed at the "Bessel-points", causing a large bending in the middle of the ID, which varies with gap and also from one to the other magnet structure [1].

The second version is similar to the first one with the difference that the pivot-points are positioned at the calculated "Bessel-points" or at the four optimum points in case of two further links. Both, upper and lower cylinder can carry three structures at maximum because the other space is preserved for bow bearings. This is the most common way of design and has been built at several labs [2, 3].

In the third solution the magnet structures are mounted side by side on an intermediate plate which can be moved transversally on a stiff magnet girder in order to change the structure. It has the advantage that a rotating mechanism with inevitable angular and phase errors can be avoided. On the other hand, the full magnetic force of all three structures is always present. In principle, the magnetic attraction of the girders can be canceled e.g. by compensation magnets beside the actual magnets which of course holds for any of the four discussed schemes. Besides, large and exact linear guides and adjustments are required [4, 5].

The fourth solution is an ID with a rotation mechanism based on multiple strap hinges which connect the movable with the fixed part of the girder. This is an innovative, compact and rigid design. Drawbacks of this concept are the limitation to only two magnet structures and in particular a complex and expensive fabrication of the strap hinge as a bearing [3].

The four alternatives have been investigated in detail and assessed under consideration of various boundary conditions with different impact, among those: an integration of possibly three magnet structures, compatibility with the existing magnet structure, keeping the 2.5 m girder length, minimization of girder bending, small overall size, reuse of the well-proven undulator frame, further use of the existing vacuum chamber, and finally costs.



Figure 1: Former DESY revolver undulator.

Finally, decision was made for a rotating cylinder with distributed support points. The changing mechanism of the new undulator is a revolver-like and loaded with up to three magnet structures per rotating cylinder (see Fig. 2). The present Flash2-structure can be integrated. The bearings of the strongback have been positioned at the optimum points. The whole length of the ID can be used for the magnet structure. Without regard to a few small changes, the current frame and power unit will also be used as is. Only a few minor changes of neighbored components will be necessary with this concept. Though, a change of the vacuum chamber and its holders is required due to the larger cross-section of the rotating structures. Also affected is the width of the ID and therefore the transport space for other assemblies behind it.

THE NEW MAGNET STRUCTURE

The development of a new magnet structure is caused by the restricted space between the different structures. The new structure has to achieve the same functions as the old structure, but in a minimized space. Positioning the magnets and adjusting the poles in height and angle must still be possible. Beneficial is a mounting of the poles and magnets from the upper side of the structure, because there is not much space for tools between them.

Finally there are three variants of new magnet structures, which must be tested under real conditions with small prototypes. The first structure is similar to the actual one, but with a transverse moving wedge instead of two counter screws for adjusting the poles. The screws for holding the magnets and poles are positioned more vertically beside the magnets and poles. The whole structure becomes smaller with another clamping mechanism on the rotating cylinder. The second structure has square magnets to find the best of four positions for a well-directed magnet field. The magnets are positioned with clamps from the top. The poles are mounted in two lateral pushers, which can be moved and adjusted with screws parallel or with a small difference (that effects the rotating of the poles). The third structure moves the poles with two independent screws equipped with an eccentric

orbiting bolt. The right position is fixed with counter nuts on the screws. The vertical moving height in this version depends on the eccentricity of the small pins and is therefore strongly limited. The vertical adjustment is not permanent in relation to the rotating angle of the screw. If the counter nut is unfastened, the force of the pole is effective and affects its position. So readjusting the poles seems to be difficult. Small tests will show, which variant is more effective to be implemented onto the revolver cylinder.

A further requirement for the new undulator is to reuse the actual Flash2 magnet structure. That means to sink this structure with an equivalent nut into the rotating cylinder. The aim is to keep the poles on the same rotating radius. It is possible, if this structure is clamped from besides or with long screws from the bottom through the rotating cylinder. A discussion point for all three structures is, whether it is still necessary to fasten the poles with counter screws or other means from the bottom side. Tests will be made to find out whether the pole position is still stable without those screws. If the result is positive the counter screws could be left out and problems with space for tools are not present anymore.

THE POSITION OF THE BEARING POINTS

The main topic for an undulator is to have a strong and homogenous magnetic field over the whole length of the structure. So the magnet girders and the supporting frame have to be built stable to provide these demands. After it came to the decision to develop a revolver undulator, first step was to find the right positions for the bearings, carrying and rotating the cylinder with the magnet structures. Finding the four bearing points only for the rotating cylinder and the magnet force was influenced by space for the rotating mechanism, the weight of the structures and of the cylinder and of the cylinder's diameter. Experience of FE-analysis has shown that it is a great difference to carry only the cylinder or to look at the whole structure. A sinusoidal form of the cylinder results in a parabolic arc, when hanging at the frame. After the four bearing points were found for a structure, mounted at the frame with minimum and constant bending, the result of the FEA-calculations shows a reduced spacing between the main side-parts of the undulator. The difference for each part was 65 mm. That is why another requirement could not be kept: the exchangeability between the actual FLASH-ID and the new Revolver-ID on the same floor assembly. As a minimum only the anchor rods could remain at their positions.

THE NEW FLOOR ASSEMBLY

Adapting the floor assembly also included rearranging the three feet of the ID. The disadvantage of the old arrangement was the danger of overturning in several stages of production. The base, resulting from those three feet, was small and sharp and needed particular care when adapting the support mechanics for other geometric requirements. The new arrangement has two feet under the rotating mechanism

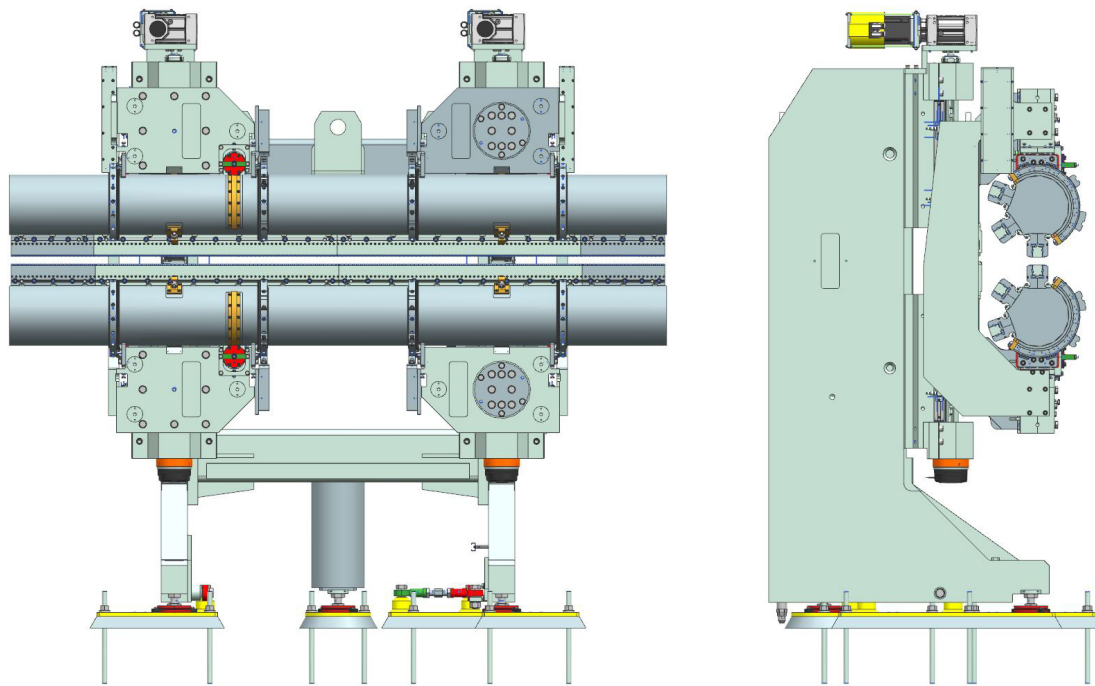


Figure 2: New DESY revolver undulator.

and the third foot on the backside of the frame. This base is much bigger than the old one and the centre of mass is secure in the near of the middle of this triangle.

THE IMPROVEMENT OF THE CANTILEVER ARM

This cantilever arm replaces the primary support plate, which carries the flat magnet girders together with the magnet structures and moved them vertically. The diameter of the rotating space for the three structures instead of the current slim outline requires a long connection to the drive train. It should be stable against bending moments and torque and lightweight. Different models came up to solve this problem: a full iron cantilever arm, a welding construction with an included thick tube (difficult to weld), another weldment with stiff plates and at least a full aluminum milled part. The final decision on this ongoing work will be made after FEA-simulations. The remaining final steps will be

- Prototyping and testing of the various magnet structures
- Construction of a hard stop for the middle structure
- Recheck the drive chain
- Recheck the whole ID-assembly with a FE-analysis to confirm the new distance of the bearing points and the minimum sinusoidal bending of the magnet girder.

REFERENCES

- [1] T. Hara, T. Tanaka, T. Seike, T. Bizen, X. Marechal, A. Nisawa, S. Fukushima, H. Yoshikawa, H. Kitamura, "Revolver undulator for BL15XU at SPring-8", *Nucl. Instr. Meth. A*, 467-468, 2001, pp. 161-164.

- [2] J. Chavanne, G. Le Bec, L. Goirand, C. Penel, F. Revol, "Up-grade of the insertion devices at the ESRF", in *Proc. IPAC2010*, Kyoto, pp. 3105-3107.
- [3] B. Stillwell, J. H. Grimmer, D. Pasholk, E. Trakhtenberg in *Proc. IPAC2012*, New Orleans, Louisiana, USA, pp. 750-752.
- [4] R. Z. Bachrach *et al.*, The SSRL insertion device beamline "Wunder", SPIE, 582:251267, 1985.
- [5] C. Baribeau, L.O. Dallin, J. Helfrich, T. Pedersen, M. Sigrist, W.A. Wurtz, "Simulated and measured magnetic performance of a double APPLE-II undulator at the Canadian Light Source", in *Proc. IPAC2016*, Busan, South Korea, pp. 4025-4027.

OVERVIEW OF SESAME WATER COOLING SYSTEM DESIGN & OPERATION*

M. Al Shehab[†], SESAME, 19252 Allan, Jordan
M. Quispe, ALBA, 08290 Barcelona, Spain

Abstract

SESAME started operation in January 2017. In order to receive heat deposited in various synchrotron devices during operation, a low-conductivity water cooling system was installed. Within this paper the design, construction and operation of the water cooling system will be discussed, Both Hydraulic and Thermal Behaviour of the system will be analysed and discussed with numerical simulation means as well as real operation pressure and temperature data for the purpose of a better understanding of the cooling system.

INTRODUCTION

SESAME cooling system basically based on two Air-cooled chillers, with a total capacity of 2314Kw. The cooling water coming from chillers feeds thermally insulated buffer tank, the buffer tank provides the cooled water to the accelerator subsystems (injector, Booster, Storage Ring & Beamlines) through two plate heat exchangers with a total capacity on 1762Kw of thermal exchange.

The air temperature inside the experimental Hall, Booster & Storage Ring tunnels are conditioned through five AHU's, two of them are used for the Experimental Hall with a total capacity of 500Kw, one for the Booster Tunnel with a capacity of 500Kw, and two for the Ring Tunnel with a total capacity of 30kw.

The general scheme of SESAME cooling system is shown in Figures 1 and 2, and the accelerator thermal loads are shown in Table 1 below. for this phase of operation at SESAME the only existing beamlines are (XAFS/XRFS) and IR Beam line including the Front ends. a future plane is foreseen to increase the cooling capacity through the installation of a third chiller of 1157kw cooling capacity and increase the Heat exchange with a third heat exchanger of 880Kw exchange capacity to cope with the future needs at SESAME which includes the Air Conditioning of the Experimental and optical Hutches as required for the current

operation the hydraulic system is working in manual mode. The group of pumps is fixed to a constant RPM, through VFD system, the users select manually the percentage of RPM that they need and do a final optimization by controlling the differential pressure sensor available between the inlet and outlet rings. This operational mode is stable if the system is a circuit closed without and modification to the local consumption. For the moment the system meets the criteria but in future operation the scenario will be different: the map of pressure and water flow velocities will be not constant for different reasons

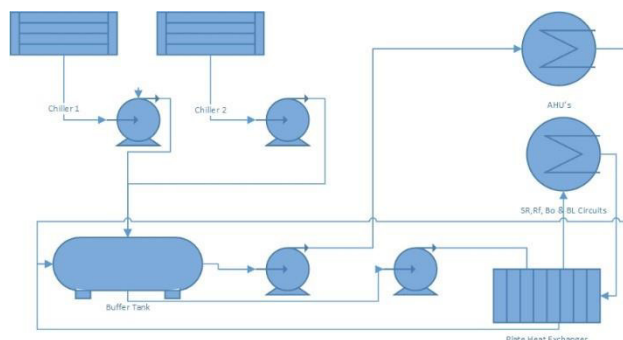


Figure 1: General scheme of the cooling system.

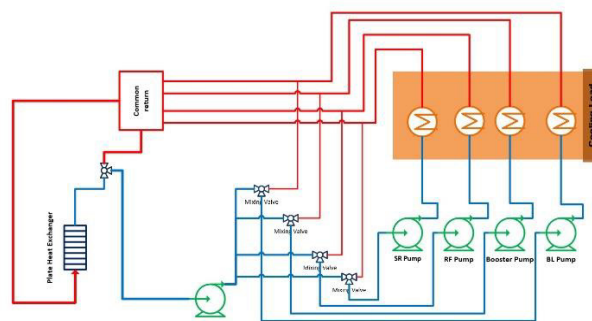


Figure 2: Scheme of the cooling circuits of the accelerator (SR, RF, Bo & BL).

SR COOLING SYSTEM

For the Storage Ring the main supply cooling pipe line Starts with DN150 Pipe size which is divided by a Tee and reduced gradually from DN100, DN80, DN65 and Ends with DN50 Pipe size, the total Flow in the SR Circuit is 24L/s with a differential pressure of 8bars. The water flow inside the ring is 180° Circulated with Zero Velocity Point at the ends (Figure 3), at each girder the flow is branched with a supply and return cross equipped with a

Table 1: Thermal Loads for Subsystems

Component	Power (Kw)
SR	774.8
RF+Dipole PS	640
Booster+Injector	70
AHU'S	600

* Work supported by IAEA & OPEN SESAME Project

[†] maher.shehab@sesame.org.jo

main ball valve. the crosses supplies the upstream & downstream Manifolds on the girders and directly supplies the dipole.

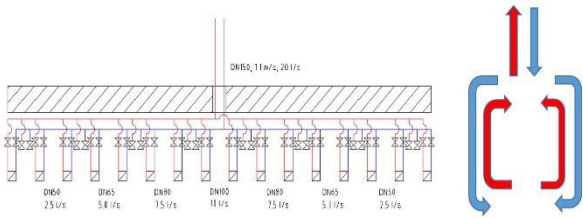


Figure 3: SR Cooling water circulation configuration.

SR Manifolds & Instrumentations

The storage ring consists of 16 girders each is equipped with two supply and two return manifolds which feeds and receive the cooling water of the short and Lunge quads, Focus and defocus sextuples as well as four crotch absorbers, three of the crouches are installed on the Arc chamber and the fourth one is on the straight section of the cell. the supply manifolds receive cooled water from the cross distributor located in the inner side of the ring. there is no pressure regulation installed on the manifolds return flow. instead a flow limiter is installed at each branch of supply manifold as shown in Table 2, this limiter restricts the flow rate to the quantity required by the multipoles and absorbers.

Table 2: Supply Manifold Flow Limiters

Flow Limiter	Q (l/min)	Location
REG-1212D	11.2	Absorber2
REG-1206D	5.3,5.6	QF&Absorber1
REG-1205D	4.6	Absorber3
REG-1203D	2.4,	SF&SD
REG-1202D	1.2	QD
REG-1201D	0.5	Absorber4

For the return manifolds flow switches are installed as means of protection to make an interlock incase the flow rate required by the magnets and absorbers get below the minimum required flow. In Table 3 the flow switches types & ranges for magnets & absorbers are shown., Figure 4. Also shows a 3D view of the Assembly.

Table 3: Return Manifold Flow Switches / Consumption

Flow Switch	Q (l/min)	Location
BVO-1235	29	Dipole
SWK2216	11.2	Abs. 2
SWK2290	5.6,4.6,5.3	Abs.1,3 & QF
SWK2240	2.4,2.4	SF&SD
SWK2218	1.2	QD
SWK2208	0.5	Abs.4

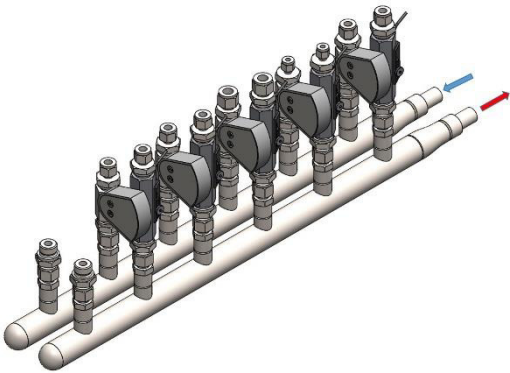


Figure 4: SR girders manifolds.

RF COOLING SYSTEM

The cooling of the RF system consists of three major cooling circuits, the first cooling circuit delivers cooled water for the cooling of the solid-state amplifiers, the second one feeds the cooling racks of the RF cavities, and the third circuit is used for the cooling of the secondary circuit of the RF cavity.

The main supply & Return line sizes are DN150, which delivers and collect cooling water through DN50 pipe size to four SS Amplifiers, four RF cooling Racks and the secondary circuit of the RF cavity as shown in Figure 5.

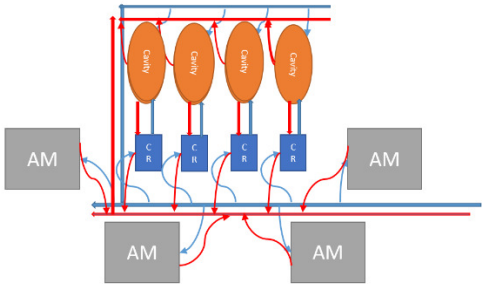


Figure 5: RF system Cooling Circuits Scheme.

The major cooling load is consumed by the Solid State amplifiers and the RF cavity cooling Racks. Table 4 contains the load distribution as well as the flow required by each component.

Table 4: Flow and Power Parameters

Component	Q (l/min)	Power (Kw)
Cavity Sec. Cir.	29.4	4
SS Amplifiers	200	90*4
Cooling Rack	75	66*4
Dipole P.S.	40	1.44

COOLING SYSTEM OPERATION

The operation of the cooling system went smoothly with a minor difficult at the early stage operation due to the Air inside the cooling system, to overcome the problem the cooling team performed a manual venting process to ensure that the remaining air inside the cooling circuits is minimum and could be handled by the automatic vents installed on the main piping as well as the distribution manifolds.

The water cooling temperature entering the four cooling circuits (SR, RF,Bo & Bl) is 24 ± 1 °C, mixing valve is used to control the temperature entering the cooling circuits , the mixing valve opening is automatically actuated based on the set temperature vale feedback . In Table 5 the operation pressure and flow values are shown.

Table 5: Pressure and Flow Operation Parameters

Cooling circuit	Q (l/s)	Pressure (Bar)
SR Circuit	24	8
RF Circuit	22	6.5
Booster Circuit	5.5	6
Beam Lines Circuit	5.5	6

Concerning the thermal regulation currently the three way valves are regulated by using a temperature sensor located at the return, after the rings. the thermal regulation is inside the acceptable levels because the amount of power to be dissipated is far from the nominal value. As the power in the system is going to increase significantly then the regulation mode will be a source of thermal instabilities.

Operational Issues

The operation of machine, SESAME encountered some problems related to the cooling system, one of the important issues we have is the frequent interlock of some sextuples flow switches, SWK (Figure 6) which consists of a small movable orifice cap equipped with a permanent magnet and restrained by a spring, the spring mass system (orifice cap and magnet) responds the flow return and interacts with a coil fixed on the body of the flows witch which sends an interlock signal to the control system based on the location of the magnet.

SESAME exploring the different possibilities for the interlock problem as well as the different possible solutions. But in general since the operation of the machine the sextuple flow interlock problem recorded for 8 times and two times for the long quads.



Figure 6: KOBOLD flow limiter.

Another issue is the difficulty to keep the minimum straight hydraulic length to get a fully developed flow entering the flow switch and leaving the flow limiter in order to get a stable and reliable reading and signal of the flow switch and a stable and fully developed flow entering the magnets and the absorbers after passing the limiter. Figure 7 below is a CFD simulation showing the minimum straight length of tube required to get a stable flow leaving the limiter which is not possible to achieve with the current configuration of connections we have.

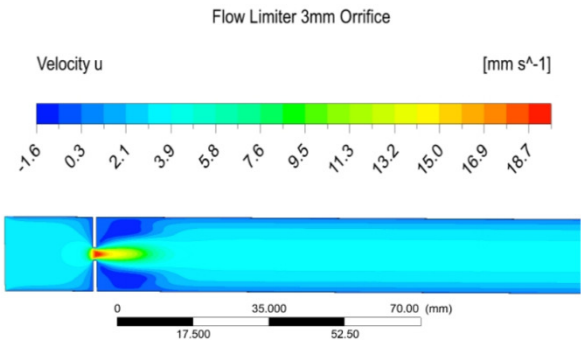


Figure 7: Flow limiter flow simulation.

CONCLUSION

For the future upgrades of the cooling system, replacement of the flexible tubes and rubber hoses for absorbers and magnets to manifolds is foreseen with a stainless steel tubes. for the hydraulic regulation an automatic control of frequency for each group of pumps. and a change of the temperature reference sensor position for the three-way valve regulation should be considered as recommended by system review report [1].

REFERENCES

- [1] Marcos Quispe, “Notes on SESAME Cooling System”, *OPEN SESAME Project Report No. 001*, 28/04/2017

VIBRATION MEASUREMENT & SIMULATION OF MAGNET & GIRDER IN SESAME*

M. Al Shehab[†], SESAME, 19252 Allan, Jordan
E. Lakovakis, L. Lancy, 1211 Geneva, Switzerland

Abstract

SESAME (Synchrotron-light for Experimental Science and Applications in the Middle East) started operation in January 2017. During the design phase several FEA studies were performed to optimize the girder and the magnet design taking into account all the constraints such as the tight spacing between magnets, the vacuum chamber installation interactions with the magnets. In this paper the experimental and Numerical modal analysis are presented as well as the result comparison between the experimental and simulation work.

INTRODUCTION

Finite Element Analysis Using ANSYS were used during the design phase in order to calculate the Eigen Frequencies and to extract the mode shapes of the Girder-Magnets Assembly [1]. After that experimental modal analysis had been conducted at CERN vibration labs. The outcome results are then used to perform Model Tuning for the Girder-Magnet assembly FEA model used in the calculations of Eigen frequency and mode shape as well as the magnets PSD response to the ground vibration.

INITIAL FEA MODEL RESULTS

Initial Modal Analysis for the girder system design before modifications during manufacturing phase was performed using ANSYS workbench15 finite element analysis software. In which over 20 modes have been extracted. the lowest natural frequency found to be 22 Hz with a longitudinal bending shape (bending the around beam axis), as shown on Table 1. The second mode Eigen frequency was 23 Hz with a longitudinal bending shape as well, the 3rd mode related to the dipole magnet with a transversal shape (rotation around beam direction) and 45.4 Hz frequency, for the 4th mode the mode take a longitudinal bending shape with an Eigen frequency of 62.8 Hz related to the long quadrupoles magnets.

Table 1: Eigen Frequencies For The Initial Design

Mode	Freq.(Hz)	Shape
1	22	Sext Longitudinal Bending
2	23	SQ Longitudinal Bending
3	45.4	Dipole Transversal Rotation
4	62.8	LQ Longitudinal Bending

* Work supported by IAEA

[†] maher.shehab@sesame.org.jo

PROTOTYPE EXPERIMENTAL MODAL ANALYSIS

In the following part of this paper the results of the experimental modal analysis performed by the Mechanical Measurement Lab of the EN -MME group at CERN to characterize the dynamical behaviour of the magnets and the girder impact of SESAME are described.

Test Setup

For measuring the dynamic response of the structure, five tri-axial accelerometers were used, two PCB Piezotronics 356A33 (sensitivity of 10 mV/g, frequency range from 2 Hz to 7 kHz and a mass of 5 grams) & two PCB Piezotronics 356B08 (sensitivity of 100 mV/g, frequency range from 0.5 Hz to 5 kHz and a mass of 50 grams. One PCB Piezotronics 356A15(sensitivity of 100 mV/g, frequency range from 2 Hz to 5 kHz and a mass of 10 grams).

In addition to the accelerometers, two impact hammers (PCB Piezotronics models 086D05 and 086D20) were used to excite the magnets and the girder respectively.

Measurement Positions

The measurement positions of the accelerometers were chosen in order to know the behaviour of the different parts of the structure. The measurements were carried out for four separate parts of the structure: the sextuple, the long and the short quadrupole and the girder as shown in Figure 1. The girder was not fixed to the floor during the measurements.

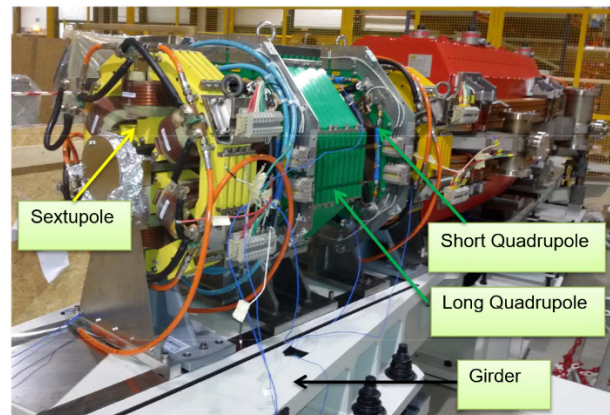


Figure1: Position of the accelerometers.

The accelerometers A1, A2, A3, A4, A5 were placed in such a way as to obtain the natural modes of the structures. Three accelerometers were glued in the front side of the Sextupole. Two in the top in antisymmetric positions A1, A2 and one the A3 to the bottom. In the back side, A4 was placed in the top and A5 in the antisymmetric position in the bottom as shown in Figure 2. Similar positions are used the configuration of the acidometers in both Long and Short Quadrupole.

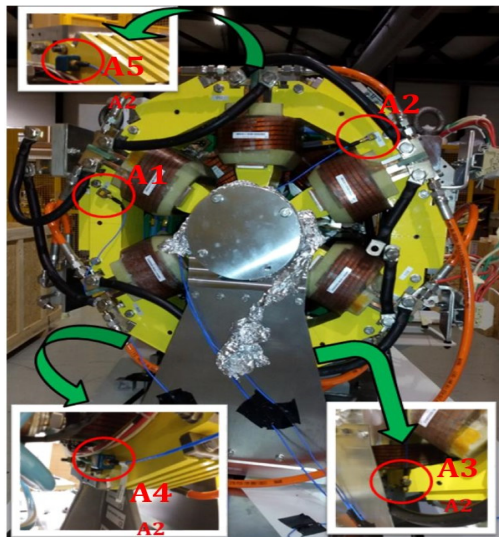


Figure 2: Positions of the accelerometers for the Sextupole.

Acquisition System

The acquisition system used was the MKII made by Müller-BBM. The MKII system is a real time spectrum analyzer and a compact data acquisition system. It contains 16 input channels with DSP (Digital Signal Processing) for each channel, with a sampling frequency rate up to 200 kHz. The dynamic resolution is 24 bits for ICP42 cards and 16 bits for ICP41 cards, and can be used in a range between 10 mV and 60 V.

The system is controlled by PAK® Software 5.6 SR4, which allows to control the hardware that measures the signal and allows different post-processing functions such as FFT (Fast Fourier Transform), PDS (Power Signal Density) and CPS (Cross Power Spectrum) to be carried out.

Post-Processing

In order to determine the mode shapes of the magnets and the girder it was necessary to create virtual structures with all points of measurement. During the post processing, each transfer function (magnitude, phase and direction) is associated with each point. The virtual geometry used for the experimental modal analysis is shown below in Figures 3 and 4.

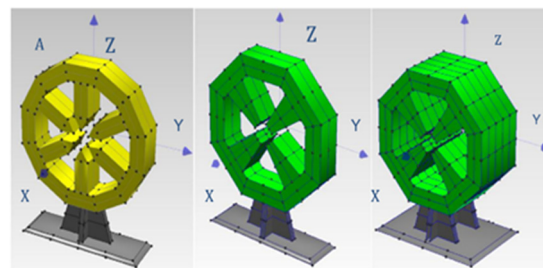


Figure 3: Simplified Model of the Multipoles.

ME'scopeVES® software V5.0 (Vibrant technology, Inc.) was used to obtain the modal parameters (modal frequencies, modal shapes) from the transfer functions obtained from PAK® Software. It allows graphical presentation of the test structure and animation of the motion.

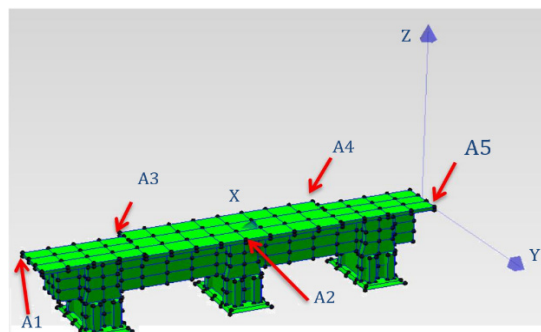


Figure 4: Simplified Model Girder.

Experimental Modal Analysis Results

After the acquisition of all transfer functions, the last step of the modal analysis is to extract the modal deformations using the FRF function obtained from the experiment. The first and most critical step of modal parameter estimation is to determine how many modes have been excited (and are therefore represented by resonance peaks) in a frequency band of a set of FRF measurements. Figure 5 shows a sample of FRF for the results of one of excitation points. The software has a choice of three different Mode Indicator functions; the Complex Mode Indicator Function was used. Table 2 presents the results.

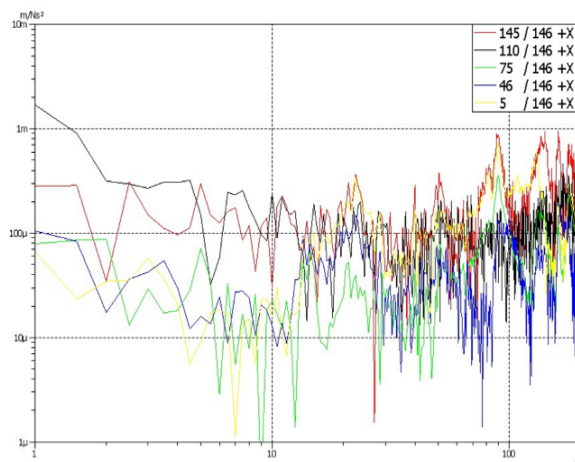


Figure 5: Sample FRF for the girder.

Table 2: Experimental Modal Analysis Results

Model	Frequency [Hz]	Damping [%]	Description
Sextuple	13.4	0.83	1 st longitudinal bending
	40.4	0.24	1 st transverse bending
	41.4	0.29	2 nd longitudinal bending
Short Quadrupole	15.4	0.87	1 st longitudinal bending
Long Quadrupole	65.9	1.05	1 st transverse bending
	86.4	1.25	2 nd longitudinal bending
	28.8	0.94	1 st longitudinal bending
	44.9	0.81	1 st transverse bending
	51.0	1.42	transverse bending
Girder (with magnets)	14.2	1.23	rigid body (low frequency)
	40.8	0.29	1 st torsional of the ends
	44.6	0.43	in-plane bending
	48.2	0.96	in-plane torsional mode

FEA MODEL TUNING

The FEA model (Figure 6) for the Modal Analysis have been tuned to using the mass and stiffness (Modules of Elasticity for the Girder and Magnets material) in order to get to an agreement with the experimental results. this step is necessary for further analysis such as PSD and to explore any modifications which may be applied to the system. The low frequency modes experimented by the sextuple and short quad magnets could be enhanced by some modifications on the magnets support and the clamping system between the magnets and the girder, the following Table 3 shows the FEA results after model tuning compared to the experimental Modal analysis results.

Table 3: FEA & Experimental Modal Analysis Results

Mode	FEA Freq. (Hz)	Experimental Freq. (Hz)	Shape
1	13.44	13.4	Sext Longitudinal Bending
2	15.92	15.4	SQ Longitudinal Bending
3	26.14	28.8	LQ Longitudinal Bending
4	62.8	42	LQ Longitudinal Bending

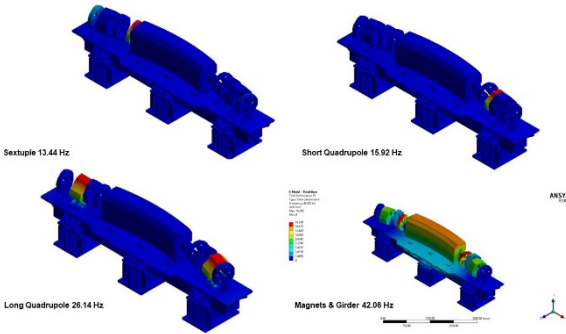


Figure 6: Girder & Magnets Assembly Mode Shapes.

CONCLUSION

The result obtained through the experimental measurements are lower than the ones obtain through FE calculations. the cause of the discrepancy is due to several reasons. one important cause is the clamping of the magnets on the girder which encountered major changes another reason the experimental modal analysis was performed without taking into account the actual fixation of the Girder-Magnets System to the Floor [2].

REFERENCES

[1] H. Ward, L. Stefa, S. Paul, “Modal analysis theory and testing”, *Beijing Institute of Technology Press*, 2001, pp. 1-70.
[2] C. Doose, S. Sharma, “Investigation of Passive Vibration Damping Methods for the Advanced Photon Source Storage Ring Girders”, in *Proc of MEDSI’02*, Chicago, USA, 2002, pp. 133-139, <https://www3.aps.anl.gov/News/Conferences/2002/meds02/papers/MED021.pdf>

THE USE OF AM TECHNOLOGIES FOR HV AND UHV COMPONENTS AND VESSELS

A. Stallwood, G. Duller, D. Butler, Diamond Light Source, Didcot, England

Abstract

AM (Additive Manufacturing) technology (3D Printing) in plastics and metals has now been in commercial use for over 30 years. However, the application of this technology in vacuum environments has been limited, due to the material porosity and additives used in the manufacturing techniques. This paper reports on the testing and use of FDM (Fused Deposition Modelling) PEEK (Polyether ether ketone) and DMLS (Direct Metal Laser Sintering) metal components inside a UHV (Ultra-High-Vacuum) environment. Specifically covering the use of DMLS to successfully produce a complex vacuum vessel operating at 10^{-6} mbar, as used on the new VMXm beamline at Diamond Light Source. Vacuum testing the vessel has demonstrated that this manufacturing technique has the potential to produce vessels that are capable of holding 10^{-10} mbar.

FDM PEEK

FDM Technology and Material Development

FDM technology has increased in popularity over the last 10 years since the launch of the RepRap self-build hobby machines in 2005. These cheap machines with open source software has allowed hobbyists and engineers to invest in the technology at home and in small offices. The boom lead to a number of competitors copying the technology and then an increased number of materials on offer. Initially limited to thermoplastics such as PLA (Polylactic acid), ABS (Acrylonitrile Butadiene Styrene) and Nylon, now materials include high percentages of fillers such as wood and metal to generate different material finishes and properties. In 2015 the German company INDMATEC [1] (now Apium) produced the first FDM PEEK material.

FDM PEEK

PEEK is a popular material to choose when looking for a vacuum compatible plastic; it has low moisture absorption, good stability and is very strong compared with other plastics. Its most useful property is the high temperatures it can withstand, thus enabling PEEK components to go through the vacuum bake out process. Having the ability to produce complex parts locally and quickly would clearly be a benefit. However, the common low cost FDM machines cannot reach the temperatures required for the production of PEEK parts. Specialised FDM machines have been produced to combat the issues with high temperature heads, heated beds and enclosed build areas.

Vacuum Testing FDM PEEK

The vacuum group at Diamond tested 19 samples supplied by Apium. The samples were specified by Apium as 100% build density and were in the form of flat tensile test samples with a surface area of 1.42 cm^2 each. Testing the samples uncleaned, as delivered direct from the supplier, the outgassing rate reached $1.33 \times 10^{-6}\text{ mbar l s}^{-1}\text{ cm}^{-2}$. Ultrasonic cleaning in IPA (Isopropyl alcohol) made the outgassing increase to $1.7 \times 10^{-6}\text{ mbar l s}^{-1}\text{ cm}^{-2}$. After baking at 150°C for 12 hours the outgassing rate improved significantly to $3.98 \times 10^{-11}\text{ mbar l s}^{-1}\text{ cm}^{-2}$ meeting our specifications for use in UHV. These results compared favourably to machined PEEK components and it is possible that they could be baked longer to improve outgassing rates.

Forming Components Using FDM PEEK

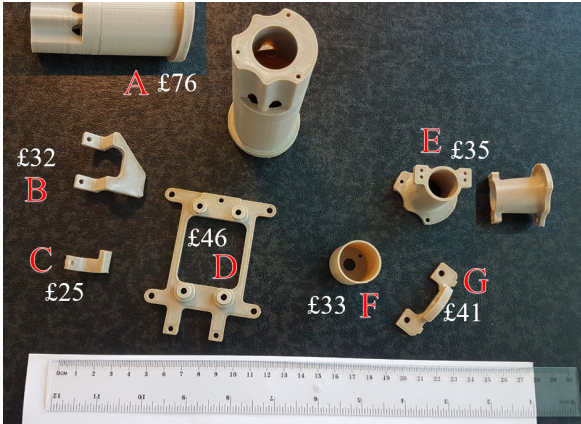


Figure 1: PEEK components produced using FDM, with costs in sterling 2017.

Seven components were ordered from Apium and a visual and dimensional inspection was carried out on five of them (A-E). The visual inspection clearly showed some build issues:

- Poor surface finish
- Unpredictable distortion
- Unpredictable component shrinkage

Detailed inspection reports were carried out on the components using a CMM. Although many feature dimensions were within tolerance, components B, C and D (Figures 1 and 2) were distorted and warped by up to 1 mm in the extremes. Component E showed no signs of warping and most dimensions within $\pm 0.1\text{ mm}$. Component A showed no signs of warping, but the internal diameter was 1 mm undersize and the outer flange diameter 0.5 mm oversize. Surface finishes also varied considerably; the base plate build surface came out polished while all other external

surfaces were rough and had cavities - adding doubt to the 100% build density.

Hole sizes under 5mm diameter tended to be produced undersize.



Figure 2: Component D, shown with base plate build surface facing upwards. Clear warping can be seen in the reflections.

Cleaning and Baking FDM PEEK

No issues were discovered through the washing and baking process.

DMLS VACUUM VESSEL

Reasons for Considering DMLS

The 2nd use of AM technologies on the VMXm beamline was the sample vessel. This vessel is complex, as many sensors and detectors converged at the sample position as well as an exit window large enough to cover a 100° inclusive diffraction cone (Figure 3).

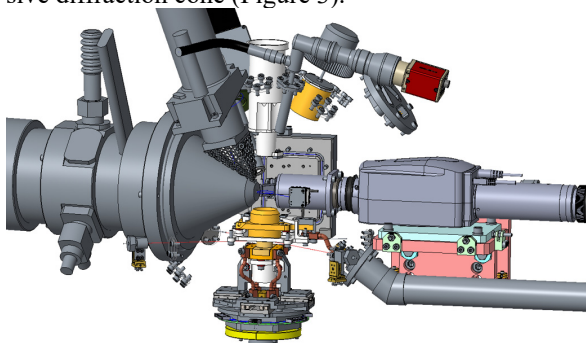


Figure 3: Equipment converging at the sample position on the VMXm beamline at Diamond Light Source.

At this time, the specification for base pressure was 10 mbar (this specification later changed to 10^{-4} mbar). DMLS suppliers were advertising 100% build densities, and existing applications already used the manufacturing process to contain fluids and gasses above 1 bar pressure differential.

A vessel design was created that could be fabricated using standard manufacturing techniques (Figure 4). This was quoted using fabrication in stainless steel and DMLS in aluminium. Note; fabrication was not available in aluminium due to welding restrictions.

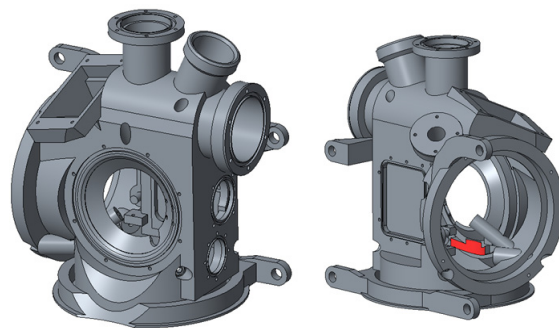


Figure 4: VMXm fabricated sample vessel design.

Finding a Supplier and Choosing the Material

Although DMLS is now an established technology there are still only a small number of suppliers and their responses varied enormously. Our chosen supplier CA Models [2] agreed to take on the work and finish the component to our specification with minimal changes, that we could implement ourselves.

The material chosen was aluminium as we only required O ring seals, the build times are quicker and the clean-up and 2nd op machining operations are easier. A stainless-steel version of this vessel would double the cost.

Price comparison showed the stainless steel fabricated vessel would be £19,750-£22,600 and the DMLS vessel in aluminium with secondary machining operations to be £12,350. The decision was made to progress with the DMLS solution.

Design Freedom

Once the decision to go ahead with AM technologies had been made, the design could now be revised to suit the manufacturing technique (Figure 5). Flowing curves and gradual changes in wall section suit this manufacturing process much better than sharp edges and ninety degree wall changes.

With this in mind, a sphere was chosen as the base shape. From this all features were either cut into, or extruded out, with generous fillet radii added at all wall intersections. The wall sections varied from 3 mm to 12 mm.

This method of manufacture also allows for undercuts and hard to access internal cavities. Whilst these features can be designed into the vessel, access for support tools needs to be considered for the removal of the support material after build.

Another advantage is that many additional features can be added to the vessel, effectively free of charge, as part complexity does not change the price. Many more brackets, view ports and other features were added in to the DMLS version compared with the original fabricated design.

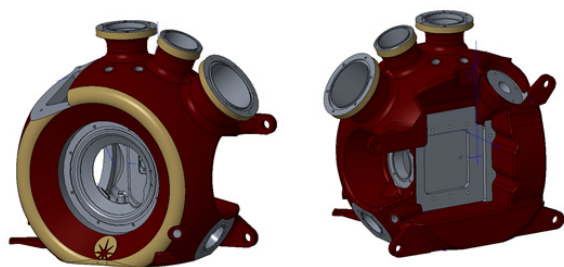


Figure 5: VMXm sample vessel designed for DMLS.

Build Errors and Issues

With a vessel of this complexity, regardless of the manufacturing method, errors are likely to occur. At the start of the project it was decided to create a prototype which could later be used as an off-line test vessel. A second vessel would then be built for use on the beamline.

An AM plastic vessel could have been produced to test for fit, but this would not have proven the technology as a vacuum vessel.

After delivery, inspection and leak testing the list of errors on the prototype vessel were as follows:

- Failed build due to power cut – *supplier remade the part free of charge*
- Thread breakthrough – *supplier locally welded*
- Some 2nd Op machining was omitted from the drawing – *Our technician carried out the machining*
- Missing O ring groove – *Vessel sealed with sealant*
- Internal clash SEM secondary detector – *Technician filed vessel*
- External clash (slits) – *Technician filed part*
- Fluorescence detector hole not machined – *Technician machined hole*
- Access to internal polishing and support removal – *Supplier observation; new vessel had re-entrant bores fabricated*
- External painting prevented bakeout – *New vessel was unpainted*

Testing and Vacuum Performance

The prototype vessel after being modified, glued and welded, achieved a vacuum pressure of 10^{-5} mbar, well exceeding the initial specification of 10 mbar and now exceeding the new specification for the vessel of 10^{-4} mbar. This vessel had only been wiped clean with alcohol as a pump and bake was not possible with the painted surfaces.

We also tested the vessel that failed during build. This had not been painted and could go through a thorough cleaning process with ionised water. The vessel was then pumped and baked and placed inside larger vessel to check outgassing rates.

Results showed no difference detected from standard aluminium with 3.9×10^{-12} mbar L s⁻¹ cm⁻².

Current Situation

The production vessel was installed onto the VMXm endstation in May 2018 ready for the first experiment (Figure 6). No issues have yet been discovered and the vacuum has reached 10^{-6} mbar comfortably.

The prototype vessel is used as an off-line testing vessel for new beamline equipment and upgrades.

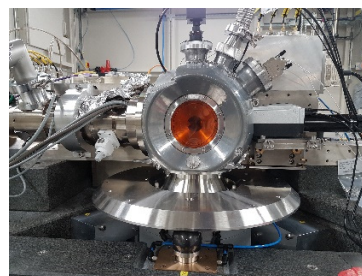


Figure 6: VMXm Sample vessel installed into end station.

Final Version Specification

- Manufactured by CA Models
- Material: Aluminium
- Mass: 4 kg
- Machine: SLM 500HL
- Build time: 60 hours
- Dimensions HWD: 262 mm x 300 mm x 200 mm
- Wall section: 3 – 12 mm
- 17x Equipment ports
- 3mm X-Ray input hole and 100° diffraction cone
- Internal and external features for mounting additional equipment
- 70 Tapped Holes
- Polished internal surfaces

CONCLUSION

AM technologies have come along way in the last 10 years, but it is not always the solution that it is cracked up to be. The FDM PEEK sounded great but in reality, the quality of the components is not up to scratch for many applications. Overall, this process is cheap and offers a quick turnaround. Components are vacuum compatible and survive the cleaning process. Complex geometries can be produced but the end results can be unpredictable.

Not yet ready to be used as a substitute to machined PEEK components but works as a quick replacement when geometry is not critical.

On the other-hand DMLS offers the ability to produce a very complex vacuum vessel in aluminium quicker and cheaper than conventional methods suitable for HV. Changing the material to stainless or coating the seal faces will allow for metal seals to be used and the vessel has the capability of being used for UHV applications 10^{-10} mbar.

REFERENCES

- [1] INDMATEC 2015, renamed to Apium Additive Technologies GmbH, Willy-Andreas-Allee 19, 76131 Karlsruhe, Germany, <https://apiumtec.com/en/home>
- [2] CA Models, AFS (Scotland) Limited, 15 Borrowmeadow Road, Springkerse Industrial Estate, Stirling FK7 7UW, <http://www.camodels.co.uk/>

STAINLESS STEEL VACUUM CHAMBERS FOR THE EBS STORAGE RING

P. Van Vaerenbergh*, J.-C. Biasci, D. Einfeld, L. Goirand,
J. Léonardon, H. P. Marques, J. Pasquaud, K. Scheidt,
ESRF, 38000 Grenoble, France

Abstract

The upgrade of the ESRF (ESRF-EBS) is a highly challenging project in many respects. One major challenge is to manufacture vacuum chambers within extremely tight tolerances. Indeed, the chamber envelope is constrained by the very limited space available between the beam stay clear and the magnets pole tips, requiring profile tolerances of just 500 μm over the full length of the chamber for a width of 55 mm. An additional challenge is guaranteeing the perpendicularity (up to 0.75 mrad) between the CF flanges and the chamber body. While a design using discrete removable absorbers was chosen, one family of chambers contains a distributed absorber required to protect the insertion devices from 600 W of upstream dipole X-rays. Two companies have been selected to produce a total of 296 stainless steel chambers. Given the unusual tolerance requirements, the manufacturers have been obliged to adapt and develop their production techniques to overcome the challenges. During manufacture, vacuum leaks were discovered on some of the BPM buttons. This paper will also present the two techniques that ESRF has developed in order to prevent the integration of potentially leaking buttons.

INTRODUCTION

After the successful delivery of the first phase of the upgrade programme in the period 2009-2015, the ESRF launched in May 2015 the ESRF – Extremely Brilliant Source (ESRF – EBS) project [1, 2]. This ambitious 150 M€ programme aimed, amongst other things, to construct and commission a brand new 844 m circumference ESRF-EBS storage ring. The goal is to increase by a factor of 100 the brilliance and coherence of the beam whilst reducing by 20 % the electrical cost of operating the storage ring.

In 2015, the Mechanical Engineering Group of ESRF initiated the design and calculations for the EBS project vacuum chambers. The design difficulties of these chambers included the narrow aperture constraint within the magnets, the density of equipment (free space between magnets within a cell is 3.4 m instead of 8 m previously), the overall ring impedance budget and synchrotron radiation handling.

* email address: vanvaer@esrf.fr

GENERAL DESIGN OF A STANDARD CELL

Besides the exception of the injection cell, all 32 cells of the storage ring share an identical vacuum chamber shape (with minor variations in the diagnostic equipment installed on some chambers that replaces the generic CH12).

The design phase led to a set of 424 vacuum chambers of which 296 were designed in 316LN stainless steel and 128 in 2219 aluminium alloy. Aluminium vacuum chambers are equipped with bimetal Conflat flanges (custom made from the chamber supplier by explosion bonding) [3]. All BPM blocks are part of the stainless-steel vacuum chambers. Some of the stainless-steel chambers can also accommodate fast correctors operating at high frequencies that cannot be installed on aluminium chambers due to the Eddy current. Figure 1 presents the general layout of a cell as well as the associated vacuum assembly.

DESIGN OF THE CHAMBERS

Space constraints and tight tolerances were the major challenges in the chamber design and production. The chambers were made as large as possible within the magnets, using anti-chambers to improve conductance and discrete absorbers to collect the synchrotron radiation. The limited available space also restricts the locations where vacuum chamber hardware such as flanges, bellows, pumps and the diagnostic equipment can be installed. Typically, the stainless-steel chambers have an “elliptical shape” with variable dimension antechambers to provide the path for X-ray extraction. The wall thickness is 1.625 mm with reinforcement at the location of the antechambers. In order to fit inside the magnets, a strict geometrical tolerance of the profile was compulsory. Figure 2 shows that for 55 mm width, and over the full length of the chamber, we have limited the shape deviation to 500 μm . Such tolerances have been verified, during the Factory Acceptance Tests, by using customised “Go-No-Go” jigs [4] and CMM (portable of fix devices).

Electron beam welding has been widely used to limit the distortion of the 316LN sheets during the welding process.

The stainless-steel chambers family has been split in two categories, the “High Profile” and the “Low Profile” (see Fig. 2 and Table 1). The vacuum chambers pass through the inside of the lattice magnets (quadrupoles, sextupoles, octupoles) with a minimum clearance smaller than 1 mm. This limited space has to accommodate the bake-out environment, the manufacture tolerances and the alignment errors (see Fig. 3).

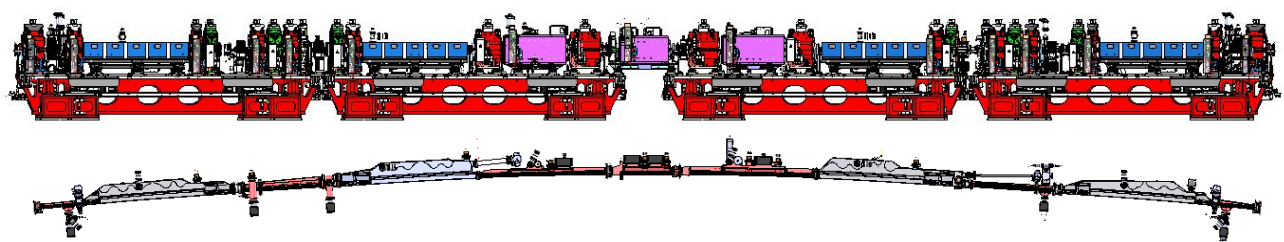


Figure 1: Front view of a cell (upper figure) and top view of the corresponding vacuum assembly (lower figure). Stainless steel chambers are highlighted in red in the lower figure.

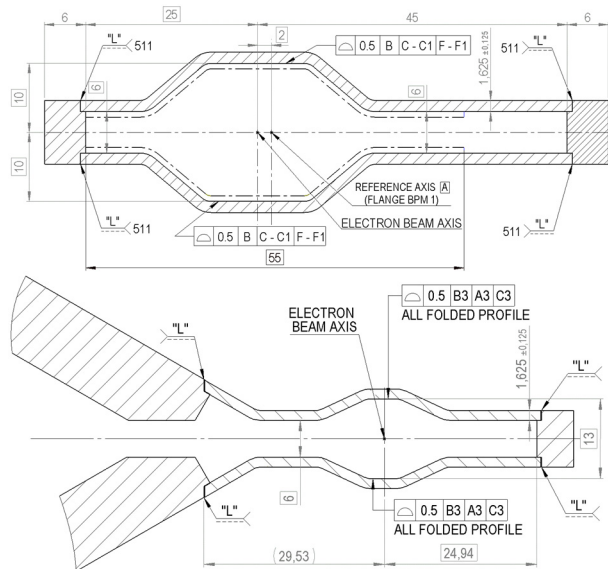


Figure 2: Side cut of a “high profile” chamber (upper figure) and of a “low profile” one (lower figure).

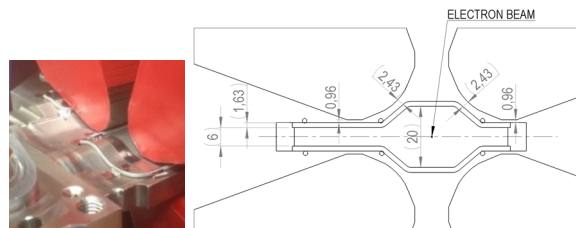


Figure 3: Picture and drawing showing the limited space available between the chamber and the pole tips. Heating wire elements are visible.

In the present design of a cell, the incorporation of the bellows has been made difficult due to lack of space. As a result, a good perpendicularity of the flanges (in the order of 0.75 mrad) was necessary to assemble the vacuum chambers and ensure their good positioning in the magnets. To do so, an extra thickness of material (typically 0.3 mm) was left on the side of the knife edge and the final machining of the fixed flange took place after its welding to the body. This ensured the best match between internal profiles of adjacent chambers (a step of just a few tenths of millimetres was allowed between two consecutive profiles). To

avoid any internal gap between two flanges, soft aluminium RF gaskets have been designed and used.

Table 1: Stainless Steel Chambers Ordered

	Qty ordered	Qty delivered on 13/06/18	Profile type	Length [mm]
CH01	33	24	High	746
CH03	33	21	High	1386
CH04	37	1	High	269
CH06	34	10	Low	2290
CH07	34	1	Low	1202
CH08	34	7	Low	2366
CH11	35	19	High	1119
CH12	23	21	High	310
CH14	33	33	High	746

Out of a total of 296 chambers, 46 % have been successfully delivered, assembled in the girders and commissioned as of 13/06/2018.

CHAMBER WITH INTEGRATED ABSORBER

All along the length of a standard cell, discrete removable absorbers have been used. On the other hand on chamber CH14, to protect the beginning of the straight section chamber, a distributed absorber has been used due to lack of space. Impinging power (600 W) originating from the upstream dipoles, is stopped by a compound strip of OFHC copper and 316LN stainless steel (obtained by explosion bonding) welded in the chamber.

The design (Fig. 4) included cooling of this strip as well as cooling of the opposite side of the chamber (in order to cope with the reflected power).

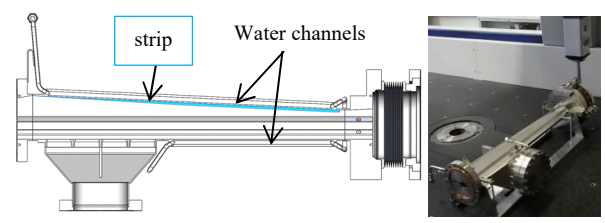


Figure 4: Cut view of the CH14 design (left) and measurement of this chamber on a CMM (right).

VACUUM CONSIDERATIONS

CH01 and CH14 are integral parts of the straight section vacuum sector. These chambers are connected to the ID chambers: in-vacuum undulators or aluminium, 8 mm internal gap, ID chambers. ID chambers are required to be coated with NEG (Non-Evaporable Getter) to achieve the necessary vacuum performance.

NEG coating was applied on CH14 to better pump photo-desorbed gases from the distributed absorber on the narrow cross section. This avoids higher pressure at the entrance of the ID chamber.

Although in terms of vacuum the storage ring could be operated with an uncoated CH01, it was decided to also coat CH01 so that the complete straight section is NEG coated (the coating is produced in-house [5]). This will maintain low pressure all along the straight section and the ID chambers will be better pumped from both extremities.

BPM BUTTONS AND ASSOCIATED DEFECTS

With the exception of CH04 and CH12, all the stainless-steel chambers have up to 8 BPM buttons each. Two analysis techniques have been used in order to detect mechanical defects within the buttons, as well as to prevent the welding of vacuum-leaking buttons to the chamber body.

A 3D X-ray tomography technique was used to identify defects within the bulk of a sample. In the present case, we have identified numerous “straw”-like defects within the 316L material (which serves as the BPM body). Some of these “straws” (see Fig 5, left picture, the black line crossing the button is the defect) have been identified as through holes and therefore lead to a vacuum leak. Their diameters are in the range of the micrometer. This problem has been solved by selecting a 316L raw material manufactured specifically according to the ESR (Electro-Slag Remelting) process.

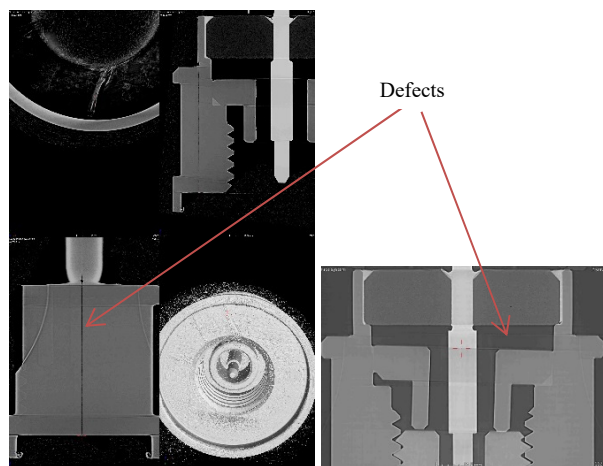


Figure 5: Tomographies of BPM buttons. Presence of a “straw”-like defect crossing the whole button (left picture) and wrong mechanical assembly (right picture). Courtesy: P. Tafforeau (BM05/ID19 – ESRF).

A second technique has been used to confirm the vacuum tightness of the buttons: a special attachment was fitted to a leak detector, the BPM button rim was put in direct contact with a customised *Viton* gasket and a cap was fitted on top (Fig. 6). By spraying helium through the cap, it was possible to identify leaks in the range of 10^{-10} mbar.l/s. [6]



Figure 6: Leak detection device for an individual BPM button.

CONCLUSION

The building of an ultra-bright synchrotron source, with performances 100 times superior to present day synchrotrons, is well underway and shall deliver its first beam to users in August 2020. The production of the associated chambers is ongoing and as of 13/06/2018, 57 girders of a total 129 have been successfully equipped with their chambers. To do so it has required the development of specific machining techniques to cope with the requirement of flange perpendicularities and other tight tolerances.

ACKNOWLEDGEMENTS

The authors would like to thank the FMB-Berlin and PINK employees for their dedication in producing the EBS stainless steel chambers with their peculiar design which embedded tight tolerances and all within a narrow schedule.

REFERENCES

- [1] EBS program, <http://www.esrf.fr/about/upgrade>
- [2] Orange book, http://www.esrf.fr/Apache_files/Upgrade/ESRF-orange-book.pdf
- [3] F. Ciansiosi *et al.*, “Aluminum and Bimetallic Vacuum Chambers for the new ESRF Storage Ring”, presented at MEDSI’18, Paris, France, June 2018, paper TUPH08, this conference.
- [4] E. Al-Dmour *et al.*, “The Status of the Vacuum Systems of the MAX IV Laboratory”, in *Proc. IPAC’13*, Shanghai, China, May 2013, paper THPF0143, pp. 3382-84.
- [5] M. Hahn *et al.*, “Non-Evaporable Getter Coatings at the European Synchrotron Radiation Facility”, *Journal of the Vacuum Society of Japan*, Vol. 53 (2010) Issue 8, pp. 493-496, <https://doi.org/10.3131/jvsj2.53.493>
- [6] F. Ewald, “BPM button leaks at ESRF-EBS”, presented at DEELS workshop, Diamond Light Source, UK, 18-19 April 2018, <https://indico.cern.ch/event/690828/contributions/2964149/>

METAL 3D ADDITIVE MACHINING FOR IN-VACUUM BEAM INSTRUMENTATION

R. Veness, W. Andreazza, D. Gudkov, A. Miarnau Marin, S. Samuelsson,
 CERN, Geneva, Switzerland

Abstract

3D additive machining by selective laser melting (SLM) has great potential for widespread use in the field of accelerator instrumentation. However, as with any new process or material, it must be adapted and qualified for use in the specific in-vacuum accelerator environment.

This paper outlines recent developments of this technology for beam instrumentation in CERN accelerators. It covers topological optimisation, design and production methods for SLM, validation and testing of samples and components to qualify the production process. It also reports on experience with operation in multiple machines.

INTRODUCTION

The CERN Beam Instrumentation Group manages more than 2000 in-vacuum instruments across the whole accelerator chain with several hundred different designs. With tens of designs in progress at any time for consolidation and new projects, there is a strong interest in taking advantage of emerging technologies and processes that offer either enhanced functionality or more cost effective production.

SLM offers both of these possibilities, allowing for the simple and rapid production of forms that are not readily machinable. In addition, it is a process that is well suited to the small series of parts generally required.

The capital cost of metal SLM equipment is falling rapidly and desktop plastic 3D printing equipment allows easy prototyping.

SLM LIMITS AND QUALIFICATION

There are a number of well-documented constraints that apply to SLM. Typical powder grain size of 30 μm limits feature sizes and wall thicknesses to a minimum of ~ 0.4 mm, as a minimum number of fused grains are required to ensure mechanical integrity. This also limits achievable surface roughness without post-machining to Ra 12.5 (ISO N10). Tolerances are limited by thermal deformations and component design, but typically are not better than 0.1 mm between two separated points. Although many geometries that are not possible using conventional machining can be produced by SLM, some forms, particularly flats parallel to the plane of product build-up are not possible. Thus an understanding of the production process is needed by the designer. A specific training course for CERN designers on 3D additive manufacture was therefore organised with a manufacturer.

Additional constraints are imposed by the application of the final component to an in-vacuum, accelerator environment. SLM uses a powder semi-product of which only a small fraction is integrated into the part. The rest is re-used

in successive cycles, sometimes up to 20 times. This recycling was considered a risk factor for introducing impurities into the powder, particularly as it is an abrasive dust manipulated by technicians with plastic gloves. Any powder sintering process such as SLM tends to produce products with some porosity and reduced mechanical strength compared with smelted materials. This could also cause problems of virtual leaks if pores are open.

In order to address these potential issues, three cuboid samples were produced using SLM with dimensions $2 \times 2 \times 1$ cm. One sample was made with new powder the second with powder after 10 re-uses and the third with powder after 18 re-uses. They were tested on a standard 'vacuum qualification' bench at CERN, measuring outgassing rate via pressure variation across a known conductance and measuring gas spectra with a Residual Gas Analyser (RGA) [1]. No difference was seen between the three samples either for outgassing or in the RGA spectrum, within the limits of the measurement (1.55×10^{-8} mbar.l.s $^{-1}$.cm $^{-2}$, limited by the background outgassing). A further test, putting all three samples together gave a value for total outgassing of 6.23×10^{-9} mbar.l.s $^{-1}$.cm $^{-2}$ H $_2$ O equivalent after 10 hours of pumping. The pump-down curve showed a 1/t slope, typical of a clean, unbaked, metallic surface. The RGA was also typical of an unbaked, metal surface with mass elements greater than 44 all 4 orders of magnitude below the 18 (H $_2$ O) peak, indicating no heavy contamination (see Figure 1).

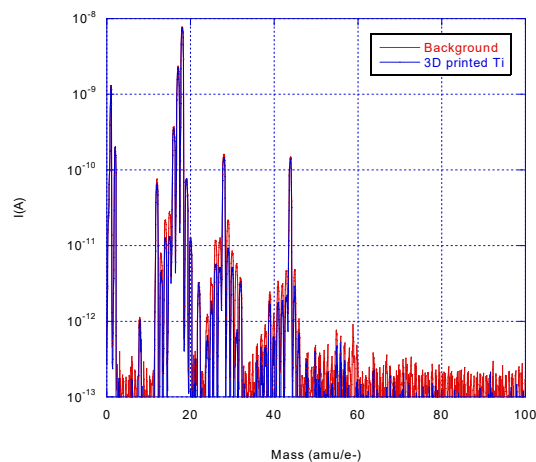


Figure 1: RGA scan of titanium blocks made by SLM from 'recycled' powder blocks.

APPLICATIONS FOR BEAM INSTRUMENTATION

Fast Beam Wire-Scanner Forks

The first application selected for this process was a ‘fork’ for fast Beam Wire-Scanners (BWS). A BWS functions by rapidly passing a thin ($\sim 30\text{ }\mu\text{m}$) carbon filament, held in place with a fork, across the beam (see Figure 2). The intensity of the secondary particle shower produced by these interactions is measured downstream of the scanner with a scintillator outside the vacuum chamber. By combining an accurate measurement of the wire position with the shower intensity, a transverse beam profile measurement is achieved. A new generation of BWS is being built at CERN for the high brightness beams foreseen following the LHC injector chain upgrade [2]. These require wires that can scan the beam at 20 ms^{-1} and a wire position measurement accurate to within $10\text{ }\mu\text{m}$, which is a factor of 50 more precise than the existing fast scanners. The scanner must accelerate the wire to its maximum speed in $\frac{1}{4}$ of a rotation, giving a peak acceleration of 15600 rad.s^{-2} . These two requirements imply an optimised fork design with a high stiffness in two planes and low inertia to minimise motor torque requirements.

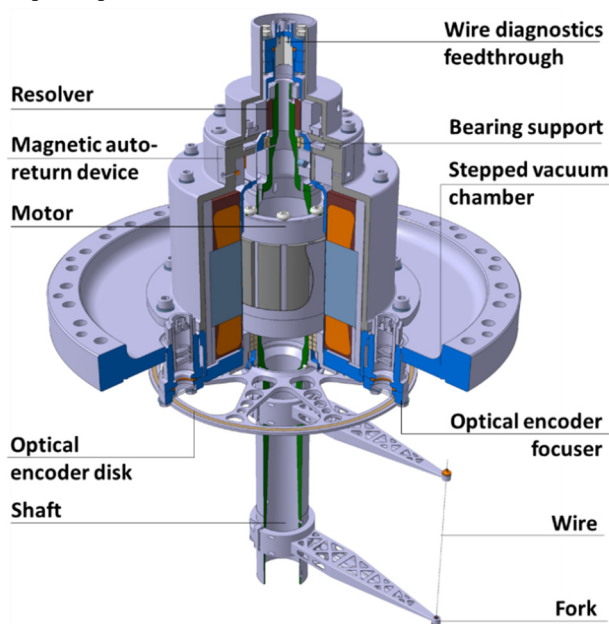


Figure 2: Part-section of the new wire scanner design showing the fork and wire.

The approach taken was first to use a topological optimisation code to generate a fork shape, iteratively removing material to converge towards an optimum for the given loads and displacement maxima (see Figure 3a) [3]. This shape was then refined into a 3D model which was further optimised based on dynamic stress analysis using the ANSYS FE code (see Figure 3b). The design was then adapted for production by SLM. The direction of ‘growth’ was defined along the long axis of the fork, and horizontal surfaces either removed or reinforced with removable tabs.

Considering the requirements for high stiffness and low inertia, the Titanium alloy Ti6Al4V was selected as the most suitable from the limited choice available (Figure 3c).



Figure 3(a-d): Design and production process for titanium wire scanner forks, showing successively: Optimisation; analysis; SLM product and finished fork.

Overall form tolerances and surface roughness from production were sufficient for the application, however, grain size limitations, thermal distortions and stress relaxation heat treatment meant that tightly-toleranced interface features needed to be post-machined (Figure 3d).

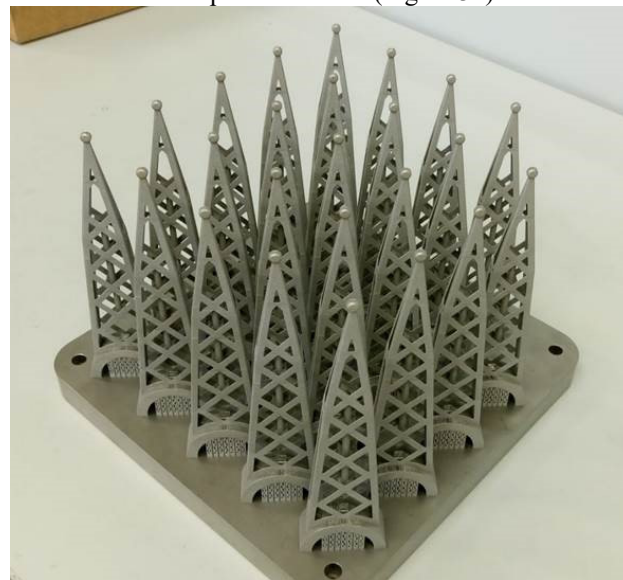


Figure 4: Series production of wire scanner forks.

Some prototypes and samples were produced for process development and test. A series of 56 forks with slightly different lengths and geometries was then produced in three batches using this process (see Figure 4). The series production was highly cost-effective, with each high-precision fork costing $\sim 35\%$ of the original, conventionally fabricated part.

Scanner Cable Chains

A major programme of instrumentation consolidation is in progress at CERN’s ISOLDE (on-line isotope mass separator) facility. This includes the re-design of several beam needle scanners which function by scanning a needle across the beam and measuring the deposition of electrical

charge from the beam on the needle. These scanners cover 350 mm horizontal apertures at speeds of up to 100 mm.s^{-1} with the signal extracted through a coaxial cable that must be properly constrained in order to avoid interfering with the beam. The redesign of these scanners is described in detail in another contribution at this conference [4], with the focus here being on the 3D additive machining used in their manufacture.

Cable-carrying chains are widely used for moving machinery. At ISOLDE, vacuum and radiation-tolerance requirements coupled with space constraints imply that off-the-shelf chains cannot be used. The solution was to design and produce a custom metallic chain.

The first step was to print several single links using thermoplastics. The links could be easily assembled together and used as a proof-of-concept. Typically, ABS or PLA are used for plastic 3D printing, the latter was used for this application. Soluble PVA supports were added to the holes. The chain links were then placed in water such that these could dissolve and the final part was ready to be tested.

In order to fully validate the design, two small chains composed of six pre-assembled links were then made in Ti6Al4V using SLM. The clearance between any two moving surfaces was $150 \mu\text{m}$, which was found to be too small for the chain links to move smoothly. Additionally, the holes on each link had slightly collapsed as the top of the hole was not supported. The chain was saw cut from the base plate rather than using wire Electrical Discharge Machining (EDM) cutting as the former option was faster. A new chain was designed to address the aforementioned issues. The clearance was increased to $200 \mu\text{m}$ and a key-hole feature was added at the top of all holes. Additionally, the length of the printed chain was increased from 6 to 32 links, to validate the full-length design. In this instance, the chain was cut from the base plate using wire EDM cutting which is more precise.

The resulting chain had a good clearance between parts and the hole geometry was accurately reproduced, however, the chain had almost no bending radius, collapsing onto itself and rendering it unusable. This was found to be caused by the change in cutting process. Saw cutting removes less material from the chain and therefore the final result does not fully represent the nominal design. This masked a fault in the original design.

Taking this into account, two new designs were made to ensure the bending radius was properly defined. One design included a feature to limit the rotation of each link to 15° as seen in Figure 5. In the second design the chain height was increased by adding material at the chain base – as it proved to be useful in the first prototype.

The final chain prototypes have a full length of approximately 280 mm and were printed as a whole assembly. The links move smoothly relative to one another and the individual link features as well as the chain bending radius are well defined.

This validated design can now be adopted for similar applications in moving instruments.

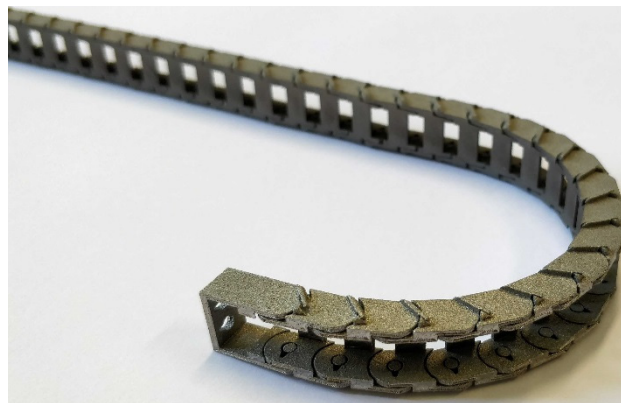


Figure 5: Titanium cable chain made by SLM.

EXPERIENCE WITH ACCELERATOR OPERATION

Wire scanner forks produced by SLM have been used in fast wire scanner prototypes installed in operating CERN accelerator rings, each scanner fitted with one fork composed of two SLM supports. The first prototype was installed in the Super Proton Synchrotron (SPS) ring in January 2015, with a second installed in the Proton Synchrotron Booster in 2016 and a third in the Proton Synchrotron (PS) in 2017. The three prototypes have slightly different fork designs to accommodate the different beam apertures in the machines. SPS and PSB installations used forks produced by an external company (3T-RPD Ltd.) with the PS and subsequent series produced in-house at CERN. A total of 6 prototype scanners were produced, with all forks passing vacuum qualification for installation without issue, irrespective of production path.

These prototype scanners have been extensively used with more than 100,000 cycles on test benches and 10,000+ cycles with beam. No issues – mechanical, vacuum or machine impedance related – have been encountered with the forks. A series of 25 scanners is now in production for installation in 2019.

ACKNOWLEDGEMENTS

The authors would like to thank the following people: Romain Gerard in the CERN/MME group for expert support in SLM production; C.Pasquino in the CERN/VSC group for performing the vacuum testing; Phil Kilburn ex-3T RPD Ltd for development of the production process.

REFERENCES

- [1] C.Pasquino, “Outgassing rate measurement before bake-out of three 3D printed Ti64 samples”, *CERN Technical Note*, <https://edms.cern.ch/document/1335390/1>.
- [2] R. Veness *et al.*, “Installation and Test of Pre-series Wire Scanners for the LHC Injector Upgrade Project at CERN”, in *Proc. 8th Int. Particle Accelerator Conf. (IPAC'17)*, Copenhagen, Denmark, May 2017, paper MOPAB121, <https://doi.org/10.18429/JACoW-IPAC2017-MOPAB121>.
- [3] S.Samuelsson. “Mechanical optimisation of a high-precision fast wire scanner at CERN”, *CERN-THESIS-2013-112*.

- [4] W.Andreazza *et al.*, “Design of new Beam Instrumentation for the ISOLDE Isotope Separator at CERN” presented at MEDSI’18, Paris, France, June 2018, paper WEPH03, this conference.

A NEW SEALING TECHNOLOGY FOR HIGH PRECISION WIDE OPEN UHV VACUUM FLANGE AND WAVEGUIDE CONNECTIONS WITH METAL GASKETS

S. Vilcins*, M. Holz, DESY, 22607 Hamburg, Germany
D. Bandke, DESY, 15738 Zeuthen, Germany

Abstract

The European-XFEL X-Ray laser facility is located in Hamburg. Since its commissioning in September 2017, this large X-ray laser opens new research opportunities for industrial users and scientists. For many beam diagnostic devices ultra-high vacuum components with high mechanical precision and additional strict requirements on particle cleanliness were produced. A vacuum chamber for the bunch compressor (BC) with a cross section of 400 mm*40.5 mm made of stainless steel blocks 1.4429 (316 LN) has been installed. These chambers have integrated flange-connections for large VATSEAL® gaskets. The tolerances for these flanges are extremely tight to ensure save vacuum tight sealing.

This contribution will report of a new technology for such large rectangular or other large flange surfaces. Furthermore this contribution will compare the present with this new technology. This new technology can be used as well for other vacuum flange metals like aluminium or titanium. Using of this technology for applications under special conditions, like particle free applications due to the non-lubricated conditions, are conceivable.

INTRODUCTION

The European X-ray Free-Electron Laser (E-XFEL) [1] is a 3.4 km long international facility, starting from DESY in Hamburg/Lurup and ending in Schenefeld (Schleswig-Holstein) in Germany. The bunch is compressed in two of three magnetic chicanes by factors of 20 and 5, respectively. Details about the chicane properties can be found in [2].

Particle accelerators like the E-XFEL are using various beam diagnostics, e.g. Beam Position Monitors (BPM) for measuring the beam orbit and diagnostics to measure longitudinal beam properties [3]. The XFEL bunch compressor (BC) incorporated three magnetic chicanes. These BC's are equipped with large vacuum chambers to ensure a beam transport with no losses under different conditions. In each of the straight sections of BC 1 and BC 2 beam diagnostic elements are located, namely an 'Energy' BPM (BPMS) and an Optical Transition Radiation (OTR) station. The vacuum chamber for these devices had to be extended to a rectangular cross section of 400 mm * 40.5 mm to fit the large vacuum beam pipe. This big cross section causes a new sealing technology of the vacuum

chambers and their flanges. The flange connections have to be leak tight up to Ultra-High-Vacuum (UHV) properties better than $1 \cdot 10^{-10}$ mbar leak rate.

GASKETS FOR NON-SYMMETRICALLY APERTURES

For wide open or non-symmetrically flange apertures flange connections with VATSEAL [4] gaskets are used, instead of normal Conflat (CF) with copper gasket rings. VATSEAL connections are made for special vacuum connections, RF structures and as well as for synchrotron beamlines. Further requirements for all-metal seal connections with VATSEAL gaskets are low permeation, low outgassing, baked-able, no hydrocarbons, low particle emission and radiation resistive. Figure 1 shows a few VATSEAL gaskets.

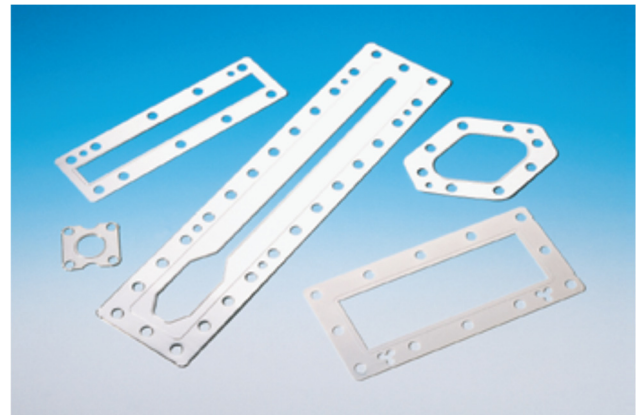


Figure 1: VATSEAL gaskets from VAT, CH [4].

A VATSEAL gasket consists of an all-metal gasket with a raised, contiguous "gasket lip" on both sides. The cross section of the raised sealing strip is highly precise and designed to follow the real vacuum outline, close to the inner diameter. Most of VATSEAL gaskets are conceptual customer design. The major factor of reliable vacuum connections is the quality and appearance of the stainless-steel flange surfaces. The applied manufacturing process after machining vacuum chambers is a handmade process step! This technology will be described in the next chapter before the new technology will be discussed.

* silke.vilcins@desy.de

® Trademark of <http://www.vatvalve.com/home>

Table 1: VATSEAL Parameters [5]

Parameter	Value
Maximum flange size	500 mm*600 mm
Distance edge to flange	1 mm
Flange material	Stainless steel
Flatness over largest length	Max. 0.2 mm
Flatness over 50 mm	Max. 0.02 mm
Surface finish	N4 (Ra=0.2 μm)
Distance between holes	Max. 50 mm
Sealing force	Min. 2000 N/cm sealing line

STATE OF THE ART

The vacuum tightness and reliability of VATSEAL connections are direct consequence to the flange design and the appearance of sealing surfaces. Therefore critical issues are surface finish, roughness and flatness of the flange sealing area.

While the former is a matter of applying correct processes during fabrication, the latter requires consideration of the forces required to adequately compress the seal. In addition, because the seal protrudes only 70 μm on either side of the gasket body, flanges with insufficient rigidity will interfere with the seal gasket or opposing flange face during tightening before sufficient sealing forces are achieved [6]. The technology parameter and boundaries are written in Table 1.

The leading fabrication process is a milling technology for pre-fabrication of rectangular or beam pipes with multi geometric cross section. The second step is leveling the surface to get a very good flatness and roughness of the surface. In this process the defined surface parameter will be prepared. Then the parts will hand over to the last step for finishing the surface in a manual made grinding step. Therefore special grinding oil, a special grinding machine and several sand papers are necessary. The surfaces will be sprinkled with this oil before the manual grinding process starts. Slowly and with the right pressure the grinding machine has to slip over the flange surface with consistent circular motions.

The risks of this manual finalizing process are pressing too strong or too soft and producing dents or rising surfaces. Furthermore oil will introduce in the sealing face, which causes that hydrocarbons will penetrate into the materials. This can be a negative impact to UHV requirements.

These conditions could produce many possibilities of higher failure rates and implicates often reworking of components. This increases the cost, time delays or sometimes defective devices. Therefore a new technology has to be formed to produce these special diagnostic BC vacuum chambers for the E-XFEL BC. This technology has to be a reliable, repeatable and well documented machining process. In close cooperation with the DESY Zeuthen

mechanical division a new sealing technology for high precision had been worked out.

OBJECTS

The 16 special vacuum chambers have been fabricated completely in DESY Zeuthen as an in-house fabrication. Each vacuum chamber with weight over 35 kg have been fabricated out of a single massive 316 LN block.

The vacuum leak requirement for the XFEL UHV system rate has to be below $1 \cdot 10^{-10}$ mbar l/s.

The geometry of these chambers had to be chosen such that they match the requirements of independency and stability; therefore this massive stainless steel (SST) block was used. Two vacuum chambers are shown in Fig. 2. The first production step was pre-milling of outer contour and wire eroding of the inner geometric, followed by heating of blocks and the second turn of milling and wire eroding. After these steps the pre-chambers were cleaned by electro polishing. Continued by final wire eroding, milling of knife edges and final outer geometric. The next chapter will describe the new technology.

NEW SEALING TECHNOLOGY

Many man-hours and efforts are necessary to build these vacuum chambers. 8 to 10 weeks of production time are necessary for one chamber; therefore the last finishing step has to be a machined technology with high repeatability.

The new technology should cover the following requirements:

- Easily repeatable, easy feasibility
- High processability and well documented
- UHV suitable and low particle emission
- No hydrocarbons
- Long-time stability and suitable for VATSEAL gaskets and wide flange apertures
- For multi-use designed and re-machinable
- And at least non-abrasive process

Starting from these requirements the project was started with a benchmark of sealing technologies. And after this benchmark a new idea arises from the mechanical technique of roller burnishing, which serves to smooth the surface as well as to increase the surface hardness for strain-hardening.

The new technology consists of a hardened metallic pin rounded, at the tip, describes a previously programmed desired path. This pin follows a defined contour with an exactly determined contact pressure and uninterrupted process speed. The pin formed a “groove” into the sealing surface. Beginning from the inside-vacuum contour, as a groove of a long-playing-record, it follows the predefined path outwards evenly. This new technique gives many positive aspects, like no use of any oil or lubrication.

Following **positive aspects** are carried out:

- Easily repeatable, well documented, high processability and easy feasibility by used well-known machining processes and CNC technology

- UHV suitable, no oil, no lubrication or other liquids
- Higher vacuum tightness due to this special (long-playing-record) rill
- Smoothing of sealing surfaces in one step, no further manufacturing steps necessary (no pre-smoothing the surfaces or getting highly flatness)
- Eliminated the manual process steps of finishing sealing surface, reducing of failure rate
- Re-machinable and non-abrasive process

Figure 2 shows the two different types of vacuum chambers at two significant process studies, pre-machining, final wire-eroding and electro polishing. On the right OTR chamber with the “sealing groove” is shown. It covers and protects the beam pipe vacuum to atmosphere. The aperture is large and therefore more screws are used to bring up the tightening forces. The sealing areas follow as close as feasible the inner vacuum structure. The radius of the groove is designed for easy production. The width of the groove is bigger than the sealing edge of gasket to have an overlap.

“Sealing-groove” with rounded edge

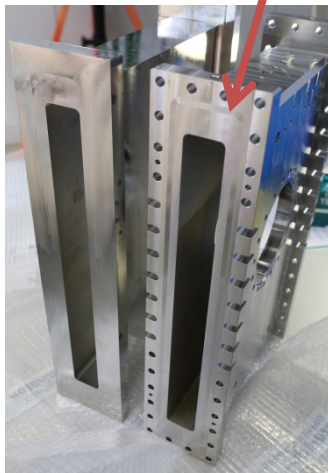


Figure 2: Left side BPMS as pre-part and on right a “ready part” of OTRS chamber with integrated “sealing groove”, see arrow. (Photo taken by D. Nölle, DESY, Hamburg).

By using this technology, it is not necessary to finish the surface. The require VATSEAL parameters for roughness and flatness, shown in Table 1 are much more relaxed. The surface has to be milled conventionally with using normal machining tools for SST materials. A roughness in the range of $R_a 0.6 \mu\text{m}$ is sufficient.



Figure 3: A macro image 10:1 of the “sealing groove”.

In Figure 3 the concentric rills are visible. The positive effect of cold-hardening and smoothing of surface are challenges of this method.

QUALITY TESTS

In a first step some test flanges with this technology were made. These flanges, see Fig. 4, were used for vacuum leakage test and first microscope inspections. Later one of the flanges was used for further quality inspections like white light interferometry (WLI), shown in Fig. 6 and micro hardness measurements, see Fig. 5. WLI is a non-contact optical method for surface height measurement on 3-D structures. Surface profiles between tens of nanometres and a few centimetres can be observed.

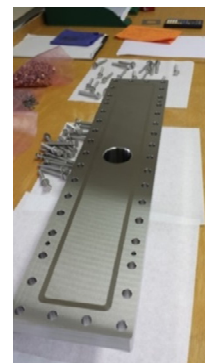


Figure 4: A special vacuum test adapter for all principle tests and for the final acceptance test like rest gas analysis and leak check.

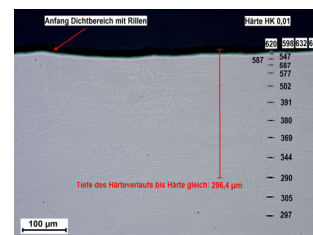


Figure 5: The micro hardness (HK 0.01) profile measurement (BAM, Berlin, Germany [7]).

In Figure 5 the deepness of the hardness profile is approximately 0.3 mm. The hardness increases from 297 HK 0.01 to 587 HK 0.01. After 30 μm the hardness dropped down a little bit. Between 30 and 100 μm the hardness dropped down 200 points. The raw material has been a value between 300 and 400 maximum.

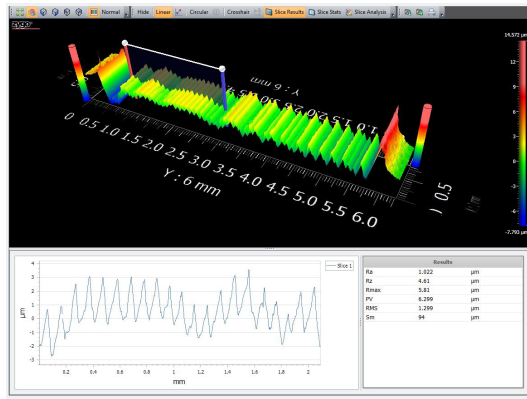


Figure 6: Special white light interferometry profile (BAM, Berlin, Germany [7]).

In Figure 6 the continuously profile roughness is shown. The width of the “sealing-groove” is between 0.5 mm up to 6.0 mm. The profile show peaks up to 3 μm and the roughness is Ra 1.022 μm.

CONCLUSION

This new technology is created and worked out for easily repeatability, high processability and easy feasibility by using well-known machining process of CNC technology. This method was tested for SST flange material. Other materials like aluminium or titanium seems to be possible, too. All flange profiles can be realise. This technique is suitable for vacuum, fluids and solid particles too. The patent for this technology is pending.

ACKNOWLEDGEMENTS

The authors thank the mechanical workshop of DESY Zeuthen for their close team work, cooperation and excellent work to produce these chambers and work out this technology.

Many thanks also to Jürgen Kruse and Dennis Renner for cleaning, testing, assembling and many good ideas to realise these massive vacuum parts with a huge number of vacuum connections.

REFERENCES

- [1] M. Altarelli *et al.*, “The European X-Ray Free-Electron Laser”, Technical Design Report, 2007, http://xfel.desy.de/technical_information/tdr/tdr
- [2] Y. Kim *et al.*, “Injector and Bunch Compressor for the European XFEL”, in *Proc. EPAC'04*, Lucerne, Switzerland, Jul. 2004, paper MOPKF018, pp. 342-344.
- [3] European XFEL, https://www.xfel.eu/facility/accelerator/index_eng.html
- [4] J. Öhri, “Valve Technology Basic Introduction“, p. 18, https://indico.cern.ch/event/565314/contributions/2285748/attachments/1467496/2275676/VAT_ValveTechnology_CAS2017.pdf
- [5] VAT, company homepage, “Flange connection components”, http://www.vatvalve.com/business/valves/catalog/H/350_1_A
- [6] B. K. Stillwell, J. D. Fuerst, J. Liu, G. J. Waldschmidt, G. Wu, “Evaluation of VATSEAL Technology to Seal Waveguide Serving High-field Superconducting RF Cavities”, in *Proc. IPAC'12*, New Orleans, LA, USA, May 2012, paper WEPPC040, pp. 2298-2299.
- [7] Bundesanstalt für Materialforschung und -prüfung, <https://www.bam.de/Navigation/EN/BAM-Services/Reviews-and-Assessments/reviews-and-assessments.html>

PRELIMINARY DESIGN OF THE MAGNETS OF HALS*

Bo Zhang[†], Zhiliang Ren, Hongliang Xu, Xiangqi Wang, Wang Yong
University of Science and Technology of China, Hefei, Anhui, China

Abstract

The Hefei Advanced Light Source (HALS) is a future soft X-ray diffraction-limited storage ring at National Synchrotron Radiation Laboratory (NSRL) of China. This project aims to improve the brilliance and coherence of the X-ray beams and to decrease the horizontal emittance. The lattice of the HALS ring relies on magnets with demanding specifications, including combined function dipole-quadrupoles (DQs) with high gradients, longitudinal gradient dipoles (DLs), high gradient quadrupoles and sextupoles. All these magnets have been designed using Radia and POSSION, as presented in this paper.

INTRODUCTION

Hefei Light Source (HLS) at National Synchrotron Radiation Laboratory is a dedicated secondary generation VUV and soft X-ray light source. The upgrade of HLS was completed in 2014 and the performance has been improved a lot. With the development of accelerator technologies and requirements from the user community, a new light source named Hefei Advanced Light Source (HALS) was brought forward about three years ago. HALS will be a soft X-ray diffraction-limited storage ring. Pre-research project of HALS was funded by Chinese Academy of Sciences and Anhui Province of China in 2017. Most key technologies, such as lattice design, vacuum, magnet, radio frequency, will be studied in the next two years.

According to the accelerator physics design, longitudinal gradient dipoles, combined dipole quadrupoles, quadrupole and sextupole magnets will be studied and prototypes of them will be constructed. Preliminary design of them will be stated in this paper.

STORAGE RING OF HALS

The lattice of the HALS has been studied using a new concept of multi-bend achromatic (MBA), locally symmetric MBA, which can promise large dynamic aperture and momentum acceptance [1,2]. Main Parameters of the HALS is shown in Table 1. It should be noted that the lattice is still evolving, and the parameters will be changed with it.

Table 1: Main Parameters of HALS

Parameter	Value	Units
Energy	2.4	GeV
Average current	300	mA
Natural emittance	18.4	pm·rad
Circumference	~680	m
Number of cells	32	-
Long straight section	5.1	m
Energy loss per turn	220	keV

MAGNETS OF HALS

In the MBA lattice of HALS, high gradient quadrupole magnets are used to compress the beam emittance, sextupole magnets are used to correct the chromaticity, longitudinal gradient dipole magnets (DLs) are used to bend the beam and weaken the negative effect of sextupole on dynamic aperture, and combined dipole-quadrupoles (DQs) are good for saving space. The magnets need to be studied are shown in Table 2.

Table 2: Magnets of HALS

	DL	DQ	Quad	Sextu
Field strength	0.2~0.5T	0.5T 25T/m	80T/m	4000T/m ²
Bore diameter		26 mm		
Reference radius		3 mm		
Homogeneity	5×10 ⁻⁴	5×10 ⁻⁴	5×10 ⁻⁴	1×10 ⁻³

All magnets except the DL should be optimized to improve the field quality. The shape optimization method developed in ESRF [3] was adopted. Pole profiles of the magnets are parameterized using Legendre polynomials. A cost function such as the sum of multipole field are reduced with Newton-Gauss iteration until the optimized profile is obtained.

Longitudinal Gradient Dipole

Permanent magnets (PM) have drawn much attention in recent years, although there exist some challenges such as the variation of remanent field with the temperature and radiation damage. The greatest advantage of PM is the almost zero operation cost. So, we design a PM based longitudinal gradient dipole, as shown in Fig. 1.

The DL magnet has seven modules. All modules have the same gap and pole shape but are filled with different amounts of permanent magnet volumes to achieve the longitudinal field gradient. The PM material used for the

* Work supported by Chinese Academy of Sciences and Anhui Province
[†] email address: zhbo@ustc.edu.cn

DL is $\text{Sm}_2\text{Co}_{17}$ due to its resistance to radiation damage and temperature stability [4]. To achieve higher temperature stability, a passive temperature compensation system based on Fe-Ni shunts [5] will be studied. Structure modification to add the field tunability will also be considered.

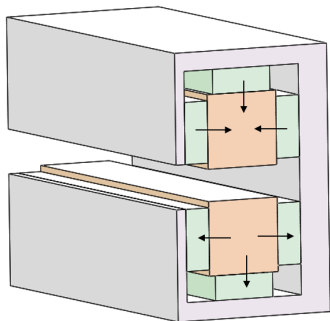


Figure 1: One module of the PM dipole.

The field along the DL and homogeneity of field integral are shown in Figs. 2 and 3 respectively. The fields of the seven modules ranges from 0.2 to 0.5 T. The error of field integral is less than 1×10^{-4} .

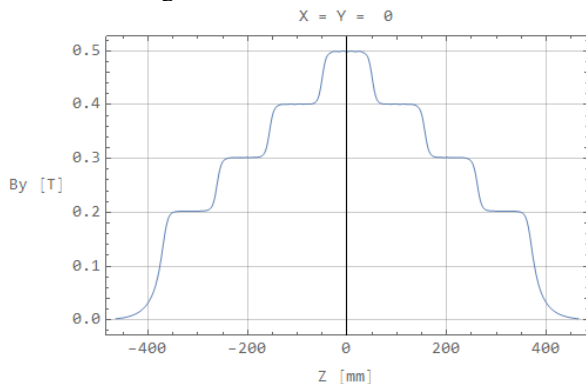


Figure 2: Field versus longitudinal position.

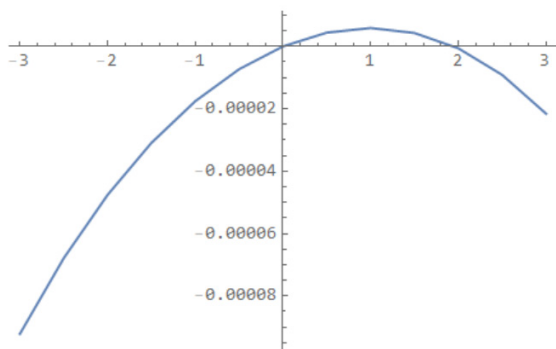


Figure 3: Homogeneity of field integral.

Combined Dipole Quadrupole

The central field of the DQ is 0.5 T, while the field gradient is 25 T/m. Because of the high field gradient, tapered dipole isn't appropriate and offset quadrupole was adopted. The offset distance is 20 mm and the beam chamber is completely located in the right side of the magnet bore, as shown in Fig. 4 (a). To maintain a gap between the pole and out wall of the beam chamber, bore diameter of the quadrupole should be more than 49 mm.

The size of the left auxiliary poles, which improve the field quality, can be reduced to decrease the construction and operation cost. Recent work showed that the auxiliary poles may be substituted by a septum plate made of soft iron. Further research on it will be performed.

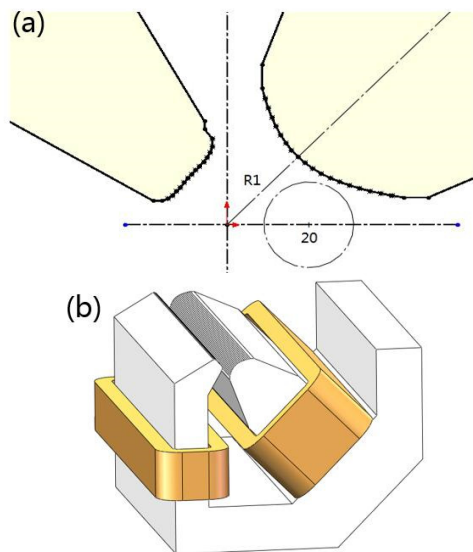


Figure 4: (a) Optimized pole profile and (b) Schematic diagram of DQ magnet.

The multipole fields of DQ within ± 3 mm are all below 5×10^{-5} , as shown in Table 3. The homogeneity of dipole and quadrupole field are shown in Figs. 5 and 6.

Table 3: Multipole Field of DQ

n	b_n/b_2	n	b_n/b_2
3	-5.35E-6	4	-4.85E-5
5	-9.54E-7	6	-1.56E-6

(By-G·x)/B0-1

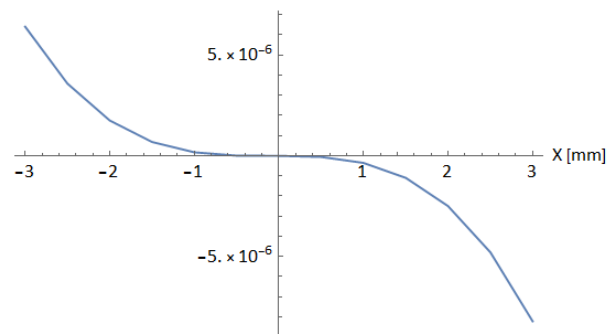


Figure 5: Homogeneity of field.

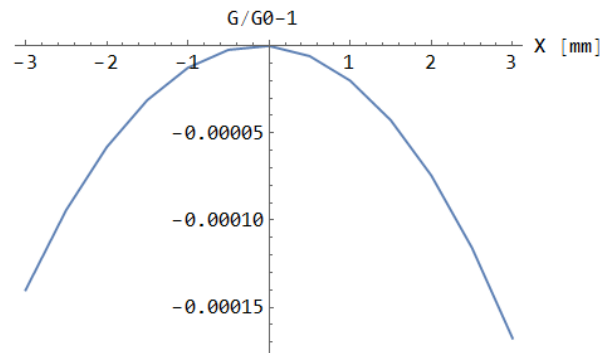


Figure 6: Homogeneity of field gradient.

Quadrupole

The initially proposed field gradient of the quadrupole was 90 T/m and recently it has been reduced to 80 T/m considering the technical risk. The optimized profile and schematic diagram of quadrupole magnet are show in Fig. 7. The gap between the adjacent poles is 11 mm, which can accommodate the beam antechamber or cooling water tube.

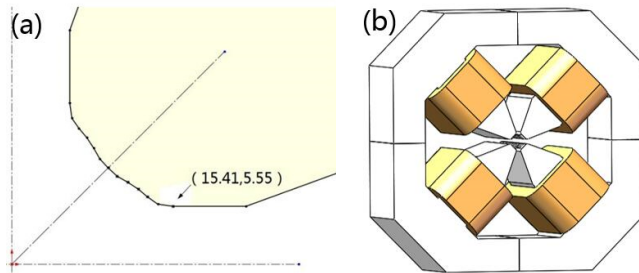


Figure 7: (a) Optimized pole profile and (b) Schematic diagram of quadrupole magnet.

The multipole fields of quadrupole within ± 3 mm are all below 5×10^{-6} , as shown in Table 4. The homogeneity of quadrupole field within ± 3 mm is better than 5×10^{-6} , as shown in Fig. 8.

Table 4: Multipole Field of Quadrupole

n	b_n/b_2	n	b_n/b_2
4	-4.84E-6	6	2.17E-6
8	7.57E-9	10	-2.56E-8

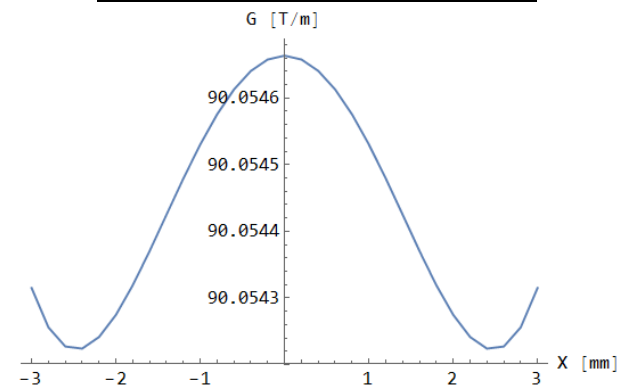


Figure 8: Homogeneity of quadrupole field.

Sextupole

The optimized profile and schematic diagram of sextupole magnet are show in Fig. 9. Because the small bore diameter, the pole width was about 6 mm and gap between adjacent poles was 7.74 mm.

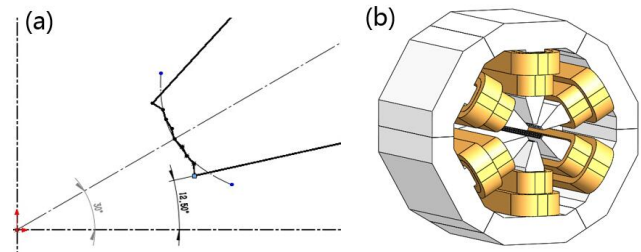


Figure 9: (a) Optimized pole profile and (b) Schematic diagram of sextupole magnet.

The multipole fields of sextupole within ± 3 mm are all below 2×10^{-7} , as shown in Table 5. The homogeneity of quadrupole field within ± 3 mm is better than 1.5×10^{-4} , as shown in Fig. 10.

Table 5: Multipole Field of Sextupole

n	b_n/b_2	n	b_n/b_2
9	-2.08E-7	15	-3.77E-9
21	3.01E-14	27	5.33E-15

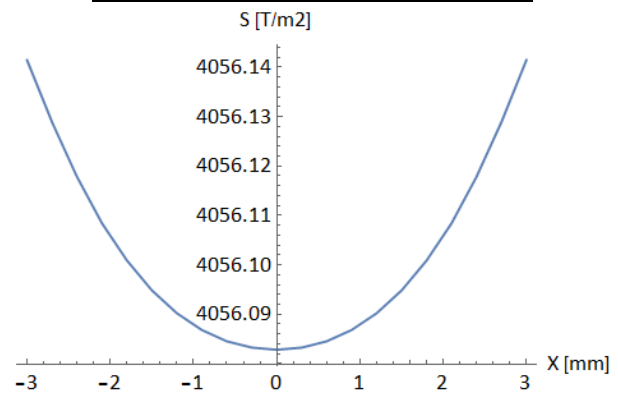


Figure 10: Homogeneity of sextupole field.

CONCLUSION

Preliminary design of the HALS magnets, including longitude gradient dipole, combined dipole quadrupole, quadrupole and sextupole have been carried out. Permanent magnet dipole was adopted because of its low operation cost. Other magnets are all traditional electromagnet and their pole profiles were optimized to obtain better field quality. More detailed research and engineering design will be performed next.

REFERENCES

- [1] Z. H. Bai, P. Yang, W. Li and L. Wang, "Design Study for the First Version of the HALS Lattice", in *Proc. IPAC'17*, Copenhagen, Denmark, May 2017, pp. 2713-2715, doi: 10.18429/JACoW-IPAC2017-WEPAB060
- [2] N. Hu, Z. H. Bai, Q. Luo, W. Li and L. Wang, "Estimates of Collective Effects in the HALS Storage Ring Having the First Version Lattice", in *Proc. IPAC'17*, Copenhagen,

Denmark, May 2017, pp. 3770-3773,
 doi: 10.18429/JACoW-IPAC2017-THPAB032

- [3] G. Le Bec, J. Chavanne and P. N'gotta, "Shape Optimization for the ESRF II Magnets," in *Proc. IPAC'14*, Dresden, Germany, June 2014, pp. 1232–1234, doi: 10.18429/JACoW-IPAC2014-TUPRO082

- [4] T. Bizen *et al.*, "Demagnetization of undulator magnets irradiated high energy electrons," *Nucl. Instr. Meth. Phys. Res. A*, vol. 467–468, Part 1, pp.185-189, 2001.

- [5] K. Bertsche, J.-F. Ostiguy, W. B. Foster, "Temperature Considerations in the Design of a Permanent Magnet Storage Ring," in *Proc. PAC'95*, Dallas, America, May 1995, paper FAP21, pp. 1381–1383.

THE DESIGN OF LCLS-II PHOTON BEAM CONTAINMENT SYSTEM

H. Wang*, Y. Feng, S. Forcat Oller, J. Krzywinski, E. Ortiz and M. Rowen
 SLAC National Accelerator Laboratory, Menlo Park, USA

Abstract

LCLS-II will produce very powerful and collimated FEL photon beams. Unlike conventional synchrotrons, the LCLS-II beam containment components withstand not only the high average beam power and/or power density, but also the instantaneous thermal shocks from the pulsed beam structure, which can potentially reach 9mJ/pulse. With a beam repetition rate up to 1MHz, regular metal based beam collimators and absorbers used in synchrotrons will no longer work, because of the likelihood of fatigue failure. And because of the poor thermal conductivity, the old LCLS B4C based absorber would need very shallow glancing angle and take valuable beamline space. Hence, a low-Z and high thermal conductivity CVD diamond based photon beam collimator and absorber systems have been developed in LCLSII. The initial damage tests using LCLS FEL beam provided positive results that graphite coated CVD diamond can endure per pulse dose level to 0.5eV/atom. For the beamline and personnel safety, in addition to the passive CVD diamond collimators and absorbers, newly developed photon diode beam mis-steer detection systems and conventional SLAC pressurized gas burn-through monitors have been also introduced in the photon beam containment system design.

INTRODUCTION

At a typical third generation synchrotron light source, the photon beam divergence can range from a few mrad for undulator beamlines and up to 10 mrad for some wiggler beamlines. The beam containment systems are designed to trim the beam divergence and define a beam size that can be accepted for experiments, as well as addressing the beam mis-steering conditions. It is not the same case for LCLS-II photon beams, which have divergence ranging from a couple of μrad to a few tens of μrad and highly coherent. The conventional scheme for containing a synchrotron photon beam won't be appropriate for the LCLS-II photon beams. On the one hand, the collimators or apertures for LCLS-II are not used to define the size of the beam, and in contrary, the photon collimators apertures try to stay clear from the beam to avoid generating noises for the experiments. On the other hand, the collimators are still needed to contain the beams in case of beam mis-steered away from its normal course, i.e. the golden trajectory. Moreover, due to the FEL beam pulses may carry tremendous power that can damage most materials by single shot ablations, and high repetition rates (up to 1MHz) may cause the fatigue failure for most of the metals even for lower beam fluences. Therefore, low atomic weight (low-Z) materials that can tolerate thermal shocks with high repetition rates may be suitable for the

construction of beam containment component. B4C is one of the low-Z materials used LCLS and other FEL facilities. However, because the LCLS-II beam can potentially have up to 880W of integrated power, good thermal conductivity becomes necessary for the application. In the meantime, large and thick chemical vapor deposition (CVD) diamond has become economically viable, hence, it has been chosen as the major heat absorption material [1].

In this article, firstly, a brief description of engineering design and analysis of the CVD diamond based beam containment components, i.e. collimators and stoppers, are presented. Secondly, in order to detect a breach caused by the FEL beam to the collimators and stoppers, diode and gas based sensing systems are also integrated with the design. And finally, the basic working principle of the photon beam containment system is briefly described.

LCLS-II BEAM PARAMETERS

Table 1 and Table 2 show the beam parameters that can produce the most thermal loads to the devices. In some extreme cases, the power load on the collimator upstream can be up to 1000 W/mm². For the soft-xray beamline, single pulse fluence (up to approx. 9mJ/pulse) may even induce damages that are not purely due to thermal effects, but directly breakdown of the bond between atoms.

GRAPHITE COATED CVD DIAMOND PHOTON ABSORBERS

To further improve the thermal shock resistance, a thin pyrolytic graphite is coated on all sides of the diamond used in collimators and stoppers. Figure 1 shows the transient behavior of a single pulse FEL beam hits the diamond absorber with 4 μm coating. One can see that the sharp instantaneous temperature rise is located in the thin graphite coating. The temperature in diamond doesn't have this sharp rise. Figure 2 shows one of the damage tests done to the graphite coated diamond by taking LCLS beam with a fluence of approx. $0.6 \pm 0.15\text{eV/atom}$. After 100,000 shots, one can visually observe the footprints of the beam, but no obvious morphological damage to the coating [2].

Figure 3 shows an absorber assembly with graphite coated CVD diamond and light-tight box installed.

A BRIEF DESCRIPTION OF LCLS-II PHOTON BEAM CONTAINMENT SYSTEM

Even equipped with graphite coated diamond absorbers, under extreme conditions, a few photon collimators upstream won't survive the extreme heat loads and ablations. As described previously, under normal operation conditions, the

* hengzi@slac.stanford.edu

Table 1: LCLS-II Soft X-ray Beam parameters at 0.1MHz, 300pC

Energy (eV)	Beam Divergence (μ rad)	Max Integrated Power (W)	Max Single Pulse Power (mJ)
250	11.8	880	8.8
750	4.6	570	5.7
1250	3.2	339	3.4

Table 2: LCLS-II hard X-ray Beam parameters at 0.3MHz, 100pC

Energy (eV)	Beam Divergence (μ rad)	Max Integrated Power (W)	Max Single Pulse Power (mJ)
1500	2.8	519	1.73
3250	2.0	185	0.62
5000	3.3	1.8	0.06

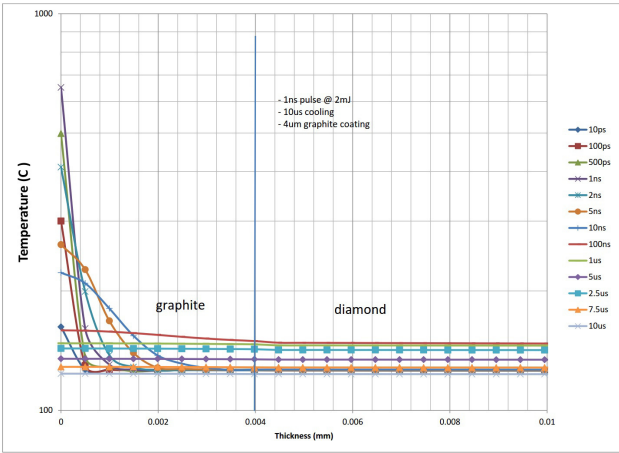


Figure 1: Instantaneous temperature rises in graphite coated diamond absorber.

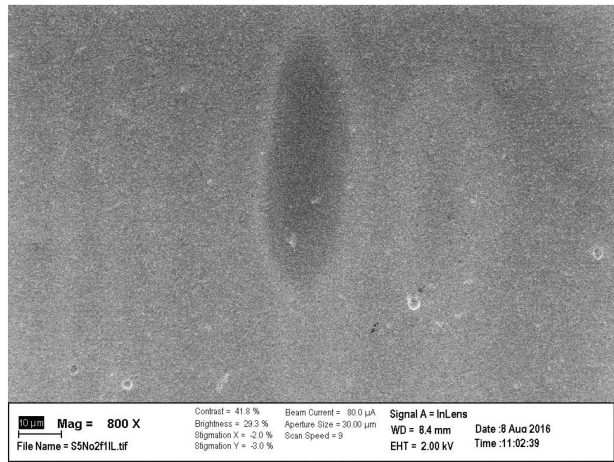


Figure 2: Damage test done to a graphite coated diamond specimen.

photon beam will stay clear from the collimators, and they will only take the beam when abnormal mis-steered conditions occur. Hence, the problem becomes how to detect the beam mis-steering conditions, and minimize duration of

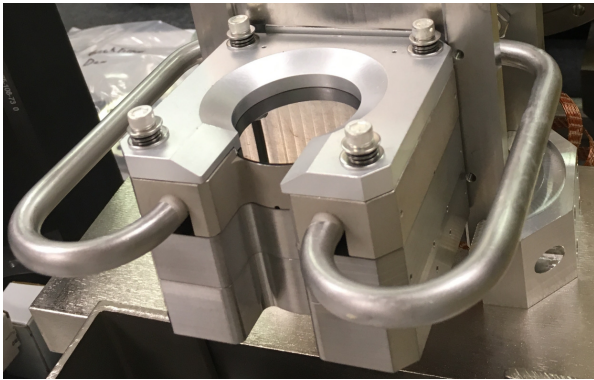


Figure 3: BCS photon absorber assembly.

the ablation time. To address this problem, a diode based sensing system is employed to provide fast feedback to shut-down the hazard as soon as it happens. To stop the beam from going downstream to the experimental stations, a redundant pair of diamond absorbers are integrated with the heavy metal for personnel safety (Figure 4). In the first absorber assembly, a fast diode based sensing system is kept in a light-tight box to detect any possible breaches of the diamond absorber. In the second absorber assembly, a gas based burn-through monitor (BTM) is sandwiched between the absorber and the heavy metal block. In case the photon beam breaks the absorbers and melt a hole on BTM chamber, the bleeding of gas will cause a pressure drop and in turn it will be trip the beam off by shutting down the RF directly.

For a safe operation of LCLS-II beamlines, especially during the commissioning phase, engineered interlock limits will be established based on modeled temperature from the optimized FEL yield and the controlled operating parameters. A temperature map from the optimized yield in photon energy is shown in Figure 5.

To stop the high harmonics and hard x-ray beams, SiC discs are also included in the absorbers. Diamond together with SiC absorbers will absorb and stop the beam up to 25keV.

Content from this work may be used under the terms of the CC BY 3.0 licence (© 2018). Any distribution of this work must maintain attribution to the author(s), title of the work, publisher, and DOI.

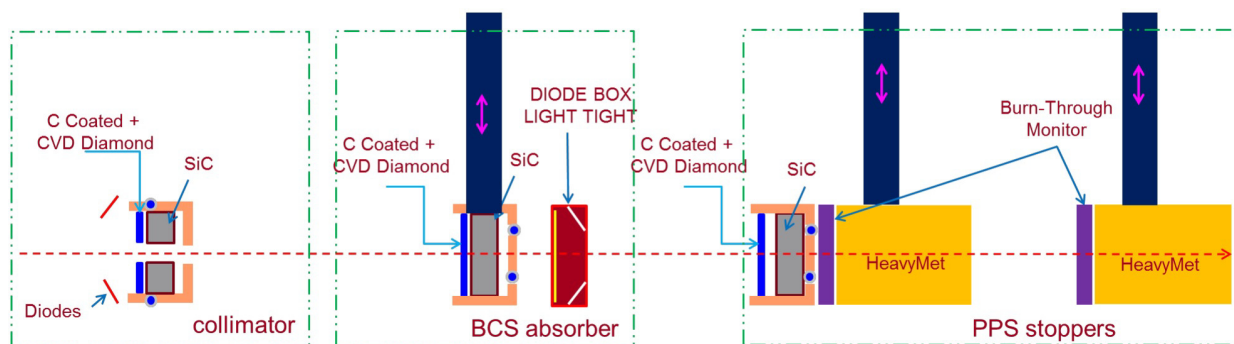


Figure 4: Schematic layout of the BCS system for Soft X-ray beamline.

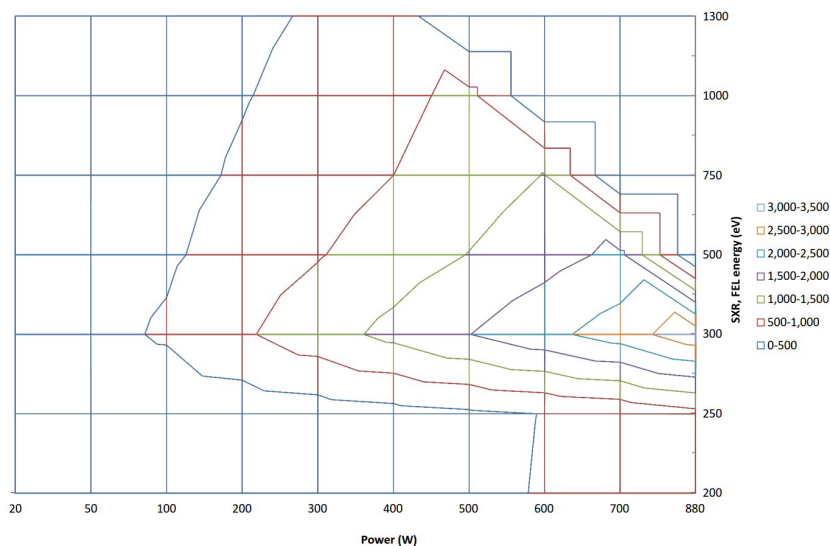


Figure 5: Temperature map on photon energy and power.

CONCLUSION

Diamond coated with graphite is a feasible solution to absorb and stop LCLS-II FEL beams, therefore, it has been used to construct the photon collimators and stoppers as major part of the beam containment system. Safe operation conditions have been estimated and mapped with input powers and photon energies.

ACKNOWLEDGEMENTS

Work supported by the U.S. Department of Energy under contract number DE-AC02-76SF00515.

REFERENCES

- [1] H. Wang, *et al.* "Thermal Studies of CVD Diamond Based FEL Photon Stoppers and Collimators", SLAC, California, USA, Rep. LCLSII-3.5-EN-0772-R1, 2017.
- [2] J. Krzywinski, *et al.* "Multi-shot Damage Study of CVD Diamond Samples Performed at 330 eV Photon Energy", SLAC, California, USA, Rep. LCLSII-3.5-EN-0779-R0, 2017.

INVESTIGATION OF REGULATION PLAN FOR THE VIBRATION UTILITY EQUIPMENT OF HEPS

Fang Yan[†], Gang Xu, Zhizhuo Wang, Daheng Ji, Yi Jiao, Chunhua Li
 Key Laboratory of Particle Acceleration Physics and Technology, Institute of High Energy
 Physics (IHEP), Chinese Academy of Sciences, Beijing, China
 Qilong Sun, Longwei Lai, Zhiqiang Jiang, Shanghai Institute of Applied Physics (SINAP),
 Shanghai, China

Abstract

For the third or fourth generation synchrotron light sources, the brilliance of the x-ray beam is 2 to 3 orders higher than other generations, and in the meanwhile the beam emittance is at least one order smaller. To ensure the stability of the beam, the vibration caused beam motion is usually controlled to be within 10% of the RMS beam size. Thus the smaller beam emittance is, more restrict of the regulation plan to the vibration sources should be. Inside of the light source site, one major vibration source is the utility equipment such as water pump, compressors and so on. There are two controlling approaches for the vibration amplitude of those sources, one is damping, and another way is decay. However reasonable specification is the key of the controlling method. This work will present the detailed establish process of the regulation plan for HEPS in China.

INTRODUCTION

Currently, the low emittance storage ring has considered being the future development direction of the photo sources. However, with the decreasing of the designed emittance of the ring, the problems caused by the ambient ground motion have been increasingly highlighted. Delicate research has to be done during the design stage for the inducing beam instabilities caused by those sources. HEPS has a very challenging beam stability requirements with the transverse beam emittance specification of 0.1 nm.rad and designed natural emittance of ~ 0.03 nm.rad while the effective vertical emittance of ~ 5 pm.rad [1-2]. To ensure the stability of the beam on the experimental station, the vibration caused beam size increment has to be controlled being smaller than 10% of the RMS beam size. Thus, according to the current designed 34 pm.rad lattice, the RMS beam position and angular motion has to be smaller than $1 \mu\text{m}$ & $0.2 \mu\text{rad}$, $0.3 \mu\text{m}$ & $0.1 \mu\text{rad}$, transverse and longitudinal respectively. [2] Special cares are mandatory in developing site vibration specifications, stable building design concepts, and passive and active ways to minimize effects on the stability of the photon beam and critical accelerator and beamline components caused by ambient ground motion sources.

To investigate the vibration influence to the beam, one has to identify the critical vibration sources, including the Egan frequencies and the amplitudes of the vibrations. There are two controlling approaches for the vibration amplitude of those ambient ground sources, one is damping,

and another way is decay. The vibration amplitude attenuate with distance as it propagates along the ground from the source to each element of the main ring with certain speed. The ambient ground motions caused by all sources transmit through the slab and girder-magnet assembling inducing orbit instability of the beam. Usually these two methods have to be combined together to realize the final specifications, and the damping level is determined, to some extent, by the decay ability of the HEPS ground. Once the critical vibration sources are identified and the decay of the vibration on HEPS ground is measured, the specification and regulation plan for the ambient ground motion of HEPS could be established.

AMBIENT GROUND MOTION SOURCES

The ambient ground motion includes ground motion of the HEPS site and other ambient motions caused by critical vibration sources around the HEPS ring including utilities (such as pump, compressor, air conditioner et. al), machine related vibrations sources (such as pulsed booster magnet, water flow et. al) and cultural noises which has day-night cycle (such as traffic and other human activities). The former one has been introduced in another paper [3], this paper will only focus on the latter one.

2 Hz Booster

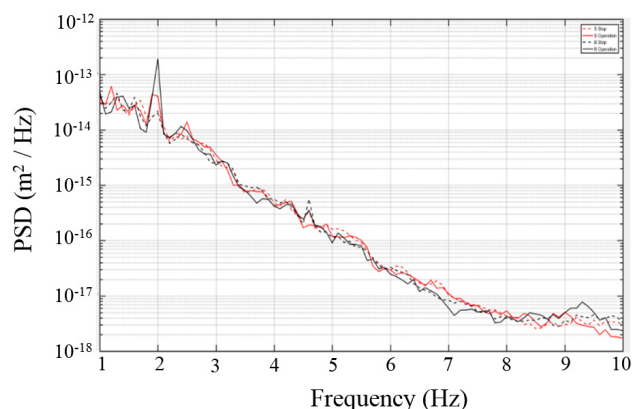


Figure 1: The black line and dash line represent PSD spectrum (in x direction) measured at booster derivation part while booster on (real line) and off operation (dash line) respectively, the red line and dash line represent PSD spectrum on main ring ground while booster on (real line) and off operation (dash line) respectively.

The HEPS booster will be operated on pulsed mode with repetition rate of 2Hz. As the AC dipole of the

[†] yanfang@ihep.ac.cn

CSNS/RCS operating at 25Hz sinusoidal alternating current caused severe vibration [4], we decided to do some measurement of the vibration caused by the 2Hz booster magnet in SSRF tunnel. We put one detector in the tunnel of SSRF booster derivation part and another one in the main ring tunnel close by the injection part (the closest position from the booster to the ring). The vibration data are collected while the booster on and off operation respectively. Comparing the data, the vibration influence (in x direction but no such influence in vertical direction) at 2Hz is clearly observed in the booster tunnel while booster magnet is on, but no such effect is observed on the main ring ground as shown in Figure 1. We learned that the booster ground is isolated from the main ring tunnel in SSRF. The same measures might need to be taken for HEPS.

Besides the influence of 2Hz booster, we also noticed from the collecting data in the main ring tunnel that the frequencies of culture noises are mainly under 15Hz, and noises with frequencies of 30 to 100Hz are mainly induced by the operated machine as shown in Figure 2.

PSD spectrum in the Storage ring tunnel before and after shut off

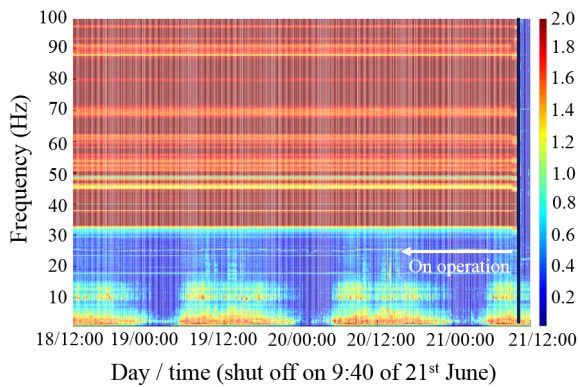


Figure 2: The comparing of vibration PSD spectrum in the SSRF main ring tunnel on & off operation.

Air Conditioner & Compressor



Figure 3: The constant temperature lab of IHEP.

A problem emerged during the alignment in the constant temperature lab (as shown in Figure 3) of IHEP as the alignment line was oscillating during the measurement. The vibration sources are investigated to get troubleshooting. The lab are equipped with air conditioner with variable frequencies of 50Hz / 45Hz / 42Hz / 40Hz / 35Hz / 30Hz. Beside the air conditioner, there are also a water pump for the magnet cooling and a compressor providing fluorine gas pressure for the alignment and magnet field measurements. We arranged a series of measurements using seismometers on the floor of the alignment lab with one equipment operating each time.

Accelerators

Storage Rings

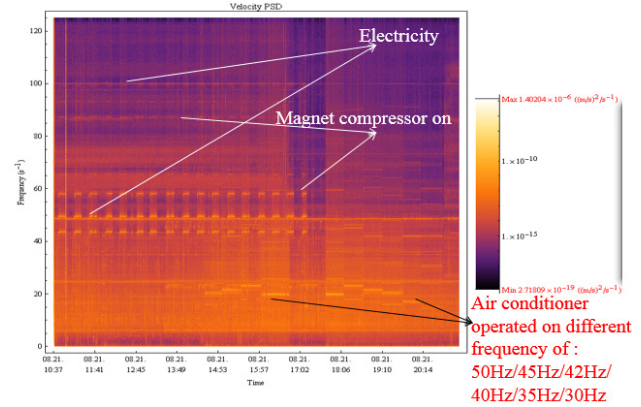


Figure 4: The vibration PSD spectrum with variable frequency air conditioner on and compressor on respectively in the constant temperature lab of IHEP.

The vibration PSD spectrum of these equipment are shown in Figure 4 illustrating the Egan frequency of each vibration source. The vibration frequency of the compressor and air conditioner operating on 35Hz / 40Hz might coincided with the Egan frequency of the alignment line leading to the resonant oscillation. The real culprit is still under investigation.

Water Pump

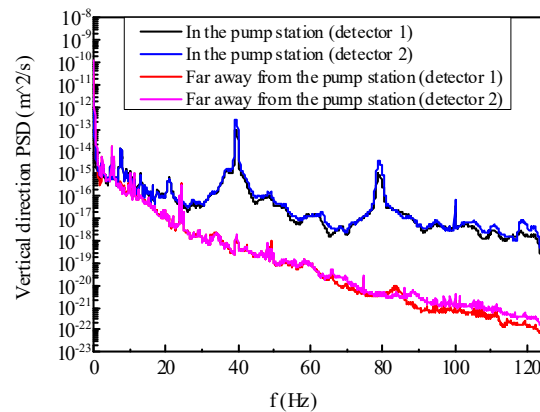


Figure 5: The comparing of vibration PSD spectrum measured in the pump station and far away from the pump station (to approximate the pump off situation).

A steam heat exchange station is planning to be built in HEPS site. The vibration influence was measured in an existing station to determine the necessary distance between the station in plan to the main ring or the at least damping level of the vibration equipment. As shown in Figure 5, the black and blue lines represent the PSD spectrum measured in the pump station by two seismometers simultaneously. The pink and orange lines represent the PSD spectrum 100 meters away from the pump station to approximate the pump off case as they are operated 24 hours a day. From the figure, we can see that the resonant frequency of around ~40Hz and ~80Hz are clearly observed and the RMS displacement is around 300nm vertically integration over frequency of 1-100Hz. According to the beam dynamics results, the allowed equipment vibration influence in the

TUPH41

137

main ring tunnel is 1nm, the damping level of the vibration pump could be determined according to the location of the station and the decay of the vibration on the HEPS ground. Besides, it is also necessary to avoid frequency overlap between machine related mechanical designs with the pump.

WAVE VELOCITY AND DECAY FACTOR



Figure 6: The seismometers used for the ground motion measurement of HEPS (left) and the measurement position on HEPS site (right).

The beam orbit vibration is closely related to the wave velocity of the vibration. And the wave velocity is different for different geology conditions. We use three CMG seismometers (as shown in Figure 6: left) equipped with GPS for the wave velocity measurement and five monitors for the decay factor measurement. The time accuracy of the seismometer with GPS is 10^{-9} s. The sampling rate could be 1000Hz, corresponding to 1000 collecting points within one second. Cooperating with CEEDI institute, we dug eleven holes to accommodate the monitors as shown in Figure 6 (right figure) and cover with plate on the top to avoid impacting of wind. The distance between the holes is 30 m. The five seismometers equipped with GPS are placed in the 2#, 3#, 4#, 6#, 8# pits. A truck loaded with ~30t construction waste were arranged to go through in the vertical direction of the measurement line. When the truck going through, the vibration caused by the truck at 1# position decay along the measurement line because of long distance.

Shifting the vibration data measured by the second detector to derive the best overlap between the first detector and the second one. The best overlap gives the smallest ratio. Take out the ratio valleys as shown in Figure 7 (above) caused by the periodically emergent vibrations because of the intrinsic resonant frequencies for truck crossing, the wave velocity could be deduced accordingly. Figure 7 (below) shows the vibration PSD spectrum of truck crossing. There is a one-to-one correspondence between the labeled resonant peaks to the valley ratios as shown in the above figure. After analyzation, the wave velocity on HEPS site is deduced to be 268m/s for the vibration vertically. The velocity is close to the shear wave velocity (193m/s) measured for HEPS ground by the initial survey group [5].

Shifting the data taken by 5 seismometers according to the wave velocity deduced above. Taking RMS displacement integration of the vibration data (when truck crossing) within 1 second over frequency of 1Hz up to 100Hz. Plot the RMS displacement detected in 5 different positions as shown in Figure 8 (the black points), the decay factor (68.6) is obtained by the fitting curve of five data points.

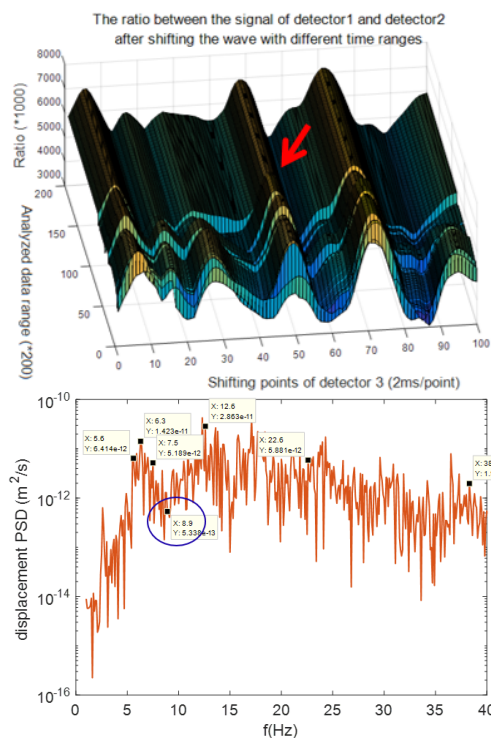


Figure 7: Vertical PSD spectrum of ground motion measured by five seismometers placed in 2#, 3#, 4#, 6#, 8# holes.

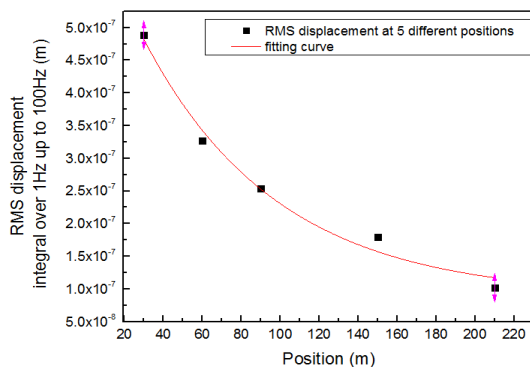


Figure 8: RMS displacement vertically at 5 measurements positions on HEPS ground when truck crossing 1# position.

CONCLUSION

To control the vibration influence of the ambient ground motion, there are two approaches. One is damping, another one is decay. Usually a practical way is combining these two measures to meet the specifications of one particular project. In this paper, the critical ambient motion measurement results have been introduced. The Egan frequencies and the amplitude of each vibration source have been obtained. The wave velocity and the decay of the vibration on the HEPS ground have been measured and analyzed. According to the beam dynamics results, the allowed equipment vibration influence in the main ring tunnel is 1nm, the damping specification of the vibration sources could be set according to the distance and the decay of the vibration on the HEPS ground.

REFERENCES

- [1] Gang Xu *et al.*, “Progress of Lattice Design and Physics Studies on the High Energy Photon Source”, presented at the 9th Int. Particle Accelerator Conf. (IPAC’18), Vancouver, Canada, Apr.-May 2018, paper TUPMF052, doi:10.18429/JACoW-IPAC2018-TUPMF052
- [2] Zhe Duan *et al.*, “Estimation of the orbit feedback performance for HEPS”, GM2017 Workshop, Beijing, Dec. 2017.
- [3] Fang Yan *et al.*, “Ambient Ground Motion Measurement and Analysis for HEPS”, presented at the 9th Int. Particle Accelerator Conf. (IPAC’18), Vancouver, Canada, Apr.-May 2018, paper MOPMF021, doi:10.18429/JACoW-IPAC2018-MOPMF021
- [4] Ren-Hong Liu *et al.*, “Study of the dynamic characteristics of the AC dipole-girder system for CSNS/RCS”, *Chinese Physics C*, Vol. 38, No. 7 (2014) 077003.
- [5] Initial survey results of the geology condition for HEPS site, Oct. 2017.

A NOVEL ATTEMPT TO DEVELOP A LINEAR POLARIZATION ADJUSTABLE UNDULATOR BASED ON MAGNETIC FORCE COMPENSATION TECHNOLOGY *

W. Zhang[†], Y. Zhu, Shanghai Institute of Applied Physics, CAS, Shanghai, China

Abstract

A linear polarization adjustable undulator is proposed in this paper. This undulator can reach 1.5T magnetic peak field with a period length 68mm and magnet length 4m. By adding two repulsive magnet arrays beside centre array the magnetic force between girders can be reduced from 70kN to near zero. Such an approach can result in a significant reduction of the undulator volume, simplification of the strong back design and fabrication. By means of rotating through the centre of undulator we can achieve magnetic field from vertical orientation to horizontal orientation. The linear polarization of radiation can be adjusted between zero and 90 degree.

INTRODUCTION

In majority of linear polarized PM undulators operating in synchrotrons and FELs, magnetic field strength is controlled by varying the gap between magnet arrays by moving arrays in vertical plane. Usually, arrays are mounted using rails on C-shape strong back. The C-shape enables lateral access to magnetic field region. Because of magnetic forces between arrays are very strong and required precision for the gap control is very high, the strong back structures must be extremely rigid. To provide such rigidity, these structures are usually built with massive and heavy components. As a result, gap varying undulators are very large, heavy and quite expensive.

There are three different method have been developed to cancel the attractive force [1-5]. One is the mechanical system composed of a number of springs having different lengths and coefficients attached to the both sides of the main magnets, which was applied to an in-vacuum wiggler developed at Synchrotron SOLEIL and SSRF for CLS. Spring-8 suggested that adding magnetic system composed of two rows of magnet array generating a repulsive force attached to the both sides of the main magnets. None of them led to a reduction in undulator dimensions or noticeable simplification of the undulator mechanical system. APS used a custom-designed conical spring system for the dynamic compensation of the undulator magnetic forces and achieved vertically polarized radiation in one 3.4-meter-long undulator prototype [6]. Such an approach resulted in a significant reduction of the undulator volume, simplification of the strong back design and fabrication but needed dozens spring tuning and calibration work.

Table 1: U68 Specifications

Periodic Length	68 mm
Length/Segment	4.0 m
Number of Periods	58
Maximum Field	1.5 T
Minimum Gap	7.2 mm
Nominal Gap	7.5 mm
Maximum Gap	80 mm
Magnet Material	NdFeB
Magnet Structure	PPM
Beam Deformation	Less than 10μm

In this paper we propose a relative compact undulator design based on Spring-8 suggestion that using repulsive magnet arrays method. Thanks to the magnetic force cancellation for all gap range 7.2-80 mm we design a very compact and thin aluminum alloy girder 80mm thickness as magnet array base beam. The deformation of the beam is just from gravity-induced deformation which is stable 5μm as the magnetic gap changes. The C-shape strong back can be simplified and the whole undulator can be weight loss less than 2t. The undulator mechanical system designed can be rotated around the centre axis. We can achieve magnetic field from vertical orientation to horizontal orientation. The linear polarization of radiation can be adjusted between zero and 90 degree.

CRITICAL DESIGN FEATURES

This U68 has 58 periods with period length 68 mm corresponds to six standard Halbach-type magnet arrays which consist of two centre magnet arrays provided the magnetic field 1.5T and four magnet arrays beside the centre arrays above and below to produce repulsive force. The specification of the undulator is list in Table 1.

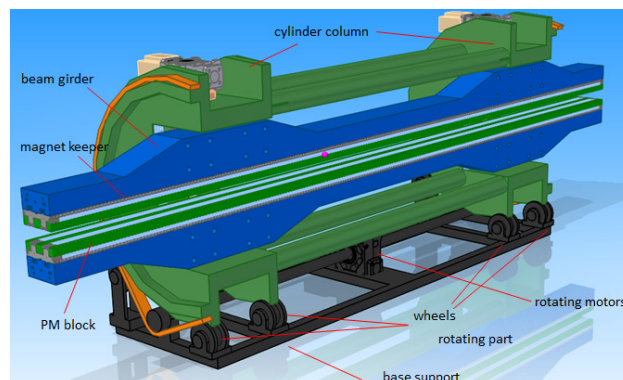


Figure 1: Overview of undulator structure: (1) –cylinder column; (2) -permanent magnet blocks soldered to aluminum keepers (3); (4) – beam girder ;(5) – base support

* Work supported by the Youth Innovation Promotion Association of CAS (Grant No: 2017305)

[†] email address : zhangwei3@sinap.ac.cn

and wheels (6); (7) –rotating parts and chain; (8) –servo motors.

The undulator frame is a welded steel structure consists of two semicircular cylinders and five joint rods. The center of two cylinders is designed to coincide with magnetic axis. Supported on one base plate though a set of wheels the undulator can be revolved on magnetic axis, shown in Figure 1.

There are two motors used for gap change. The gap should be adjusted with an accuracy of less than $2\mu\text{m}$ level. And one motor have to be used for rotating: linear polarization adjustment from horizontal to vertical.

MAGNETIC DESIGN

The magnetic fields for U68 were calculated by RADIA [7]. The usual halbach configuration is adopted. The centre blocks are chosen $45\text{mm} \times 35\text{mm}$ (width \times height) section with two side mounting cuts, see Fig. 2. The remanence of the NdFeB magnet with grade N40SH is supposed to be 1.28T. At the minimum gap 7.2mm, the effective magnetic field can reach 1.5T, see Fig. 3. The magnetic force between upper and down centre magnet arrays is about 70kN. Therefore additional repulsive force magnet arrays are designed on both sides of centre arrays. After the magnetic force compensation the magnetic force between upper and down arrays can be reduced to zero for all gaps, see Fig. 4.

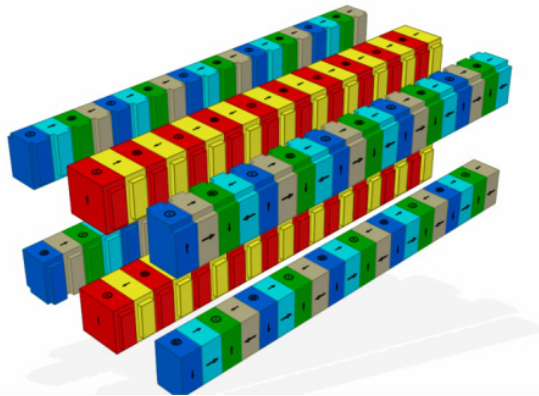


Figure 2: Layout of U68 magnet arrays model.

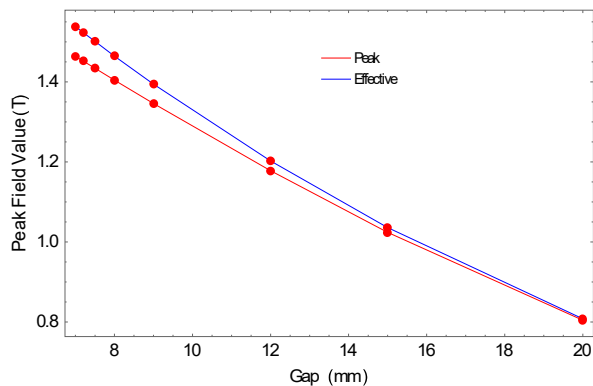


Figure 3: The effective peak field values vs gaps.

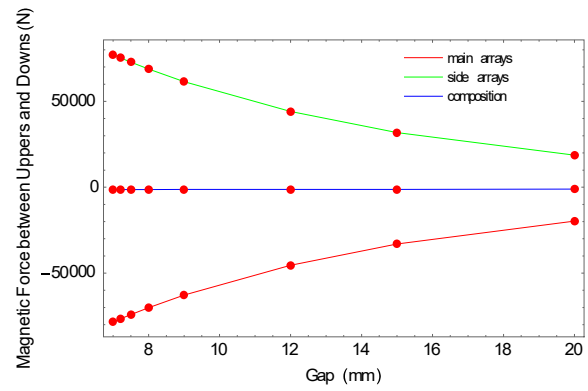


Figure 4: The magnetic force for different gaps: red represents for centre magnet arrays attractive force, green represents for repulsive force from side magnet arrays, blue line acts as composition of forces.

STRUCTURE

Figure 5 shows a closer view of magnetic structure details. Magnets are mounted to module keepers, made of aluminum alloy to match the thermal expansion characteristics of the beams. Each magnet keeper mounts three magnets together and be fixed to beams which allow for magnetic tuning by keeper height adjustment and rearrangement technique based on flipping and swapping keepers. Keepers are precisely located along the beam direction by pins to maintain precise periodic spacing.

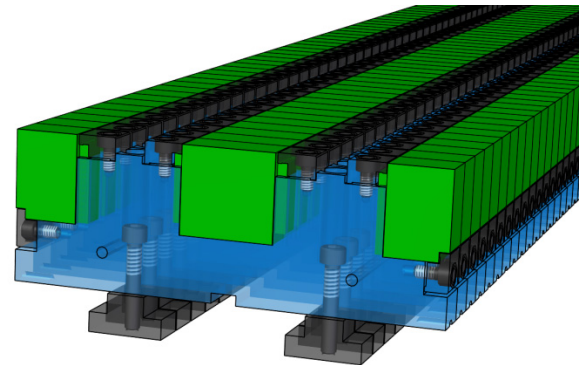


Figure 5: Magnet keeper configuration.

The magnetic attractive force between the top and bottom magnetic structures is very tiny in this undulator. In horizontal polarization mode the constant gravitational force acts gap variation in the same direction as the magnetic force for the top beam, but is opposite for the lower beam. In vertical polarization mode only the magnetic force acts gap variation. To weightless and ensure the rigidity of beams is very critical in mechanical design. Figure 6 shows the simulation results of upper and down beam in horizontal polarization mode. The maximum deformation is about $5.2\mu\text{m}$ for each beam mostly origin from beam gravity and have the same direction. The gap variation along the undulator is not to exist. And in vertical polarization mode the gap variation is inconsiderable also is shown in Fig. 7. Most of the deformation is in

Content from this work may be used under the terms of the CC BY 3.0 licence (© 2018). Any distribution of this work must maintain attribution to the author(s), title of the work, publisher, and DOI.

gravity direction perpendicular to gap direction, nearly same for two beams.

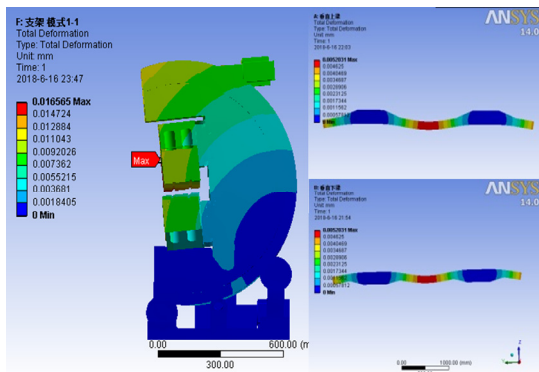


Figure 6: FEM analysis of upper beam deformation (left) and down beam deformation (right) in horizontal polarization mode.

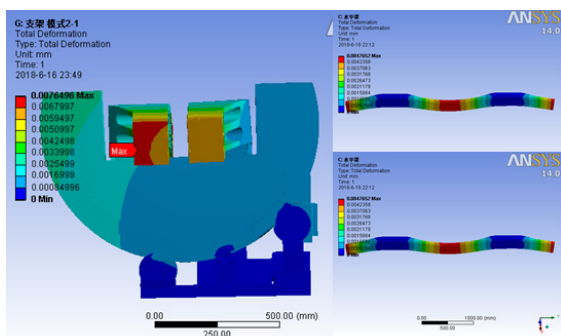


Figure 7: FEM analysis of beam deformation in vertical polarization mode: most of the deformation is in gravity direction perpendicular to gap direction, nearly same for two beams.

Table 2: U68 Beam Deformation Calculation

	Conventional		Proposed
Material	Al.	C.ST	Al
Width (mm)	150	150	150
Length (mm)	4	4	4
Height (mm)	600	400	80
Magnetic Force (kN)	70	70	0.2
Weight (kN)	10	19	1
Deformation			
Magnetic force (μm)	11	11	<1
Gravity (μm)	2	3	5
Top beam (μm)	13	14	5
Low beam (μm)	-10	-8	5
Gap Variation	22	22	5

Table 2 gives an approximate calculation with two-point support model for 4 meter undulator 70kN magnetic

force load. To satisfy the beam deformation less than $10\mu\text{m}$ level, the single beam height should more than 600mm for aluminum alloy, or 400mm for carbon steel. In the case of conventional undulator, the supporting structure is formed by strong-back made of steel base plate and two large aluminum or steel beams supporting magnet arrays. The whole structure is approximately more than 2.0 m high, 1m wide, 4.0 m long and has approximately weight of more than 8000 kg. However, in our proposed the whole structure can be much more compact: 1.0 m high, 0.6m wide and weight reduction less than 2000 kg.

CONCLUSIONS

This paper proposes the design of a linear polarization adjustable undulator based on magnetic force cancellation method. Compared to usually designs in FELs this design gives a much more reduction of beam girder height due to magnetic force load cancellation, thence we can weightless the whole mechanical structure and support to less than 25%. With a rotary mechanism design the linear polarization radiation can be adjusted that gives a great convenience for undulator design and is very attractive for facility photon users.

REFERENCES

- [1] R. Carr, "Magnetic Counterforce for Insertion Devices", *SLAC Report No. SLAC-PUB-9594*, 2002.
- [2] R. Kinjo, T. Tanaka, T. Seike, A. Kagamihata, S. Yamamoto, "Development of a magnet system to cancel the attractive force toward structural reform of undulators", in *Proc. 36th Int. Free Electron Laser Conf. (FEL'14)*, Basel, Switzerland, Aug. 2014, paper MOP023, pp. 75-79.
- [3] R. Kinjo, T. Tanaka, "Phase combination for self cancellation of magnetic force in undulators", *Phys. Rev. ST Accel. Beams*, vol. 17, 2014, 122401.
- [4] O. Marcouill , P. Brunelle, O. Chubar, M.-E. Couprie, J.-M. Filhol, C. Herbeaux, J.-L. Marlat, A. Mary, K. Tavakoli, "An in vacuum wiggler WSV50 for producing hard x rays at SOLEIL", in *Proc. 11th European Particle Accelerator Conf. (EPAC'08)*, Genoa, Italy, Jun. 2008, paper WEPC120, pp. 2288-2290.
- [5] D. Waterman, "Support structures for planar insertion devices", U.S. Patent No. 7956557, 2011.
- [6] N. Strelnikov, I. Vasserman, J. Xu, D. Jensen, O. Schmidt, E. Trakhtenberg, K. Suthar, E. R. Moog, G. Pile, E. Gluskin, "Vertically polarizing undulator with dynamic compensation of magnetic forces", *Physical Review Accelerators and Beams*, vol. 20, 2017, 010701, doi.org/10.1103/PhysRevAccelBeams.20.010701
- [7] <http://www.esrf.eu/Accelerators/Groups/InsertionDevices/Software/Radia>

THE LNLS METROLOGY BUILDING – ENVIRONMENTAL CONTROL RESULTS*

H. G. P. de Oliveira[†], M. Bazan, C. S. N. C. Bueno, L. Sanfelici, LNLS, Campinas, Brazil

Abstract

Modern synchrotron light sources require high mechanical stability throughout its facilities, frequently demanding characterization processes in the micro and nanometer scales. In this context, the Brazilian Synchrotron Light Laboratory (LNLS) built a new facility with several controlled environment rooms to minimize disturbances during optical and mechanical metrology procedures and to support advanced instrumentation development for the new Sirius' beamlines. The building design imposed very strict requirements regarding temperature, humidity and particles. This work presents the environmental control validation results and the floor vibration assessment enlightening the influence of the building machinery. Temperature variations below $\pm 0,1$ °C were successfully achieved for all rooms, relative humidity is also better than 50 ± 5 % and the floor RMS displacement did not exceed 15 nm. The building is fully operational since early 2017 and currently hosting several tests on monochromators, mirrors, front-ends and many other systems for the Sirius beamlines.

INTRODUCTION

Sirius is a 4th generation 3 GeV synchrotron light source currently under construction [1] by the Brazilian Synchrotron Light Laboratory (LNLS), designed to provide high brilliance and coherent flux based on a 5-bend achromat lattice with 0.25 nm·rad natural emittance [2,3]. The beamlines of this new generation synchrotron have started to be designed with highly demanding requirements to preserve the extraordinary properties of the source. To achieve such requirements, it is necessary to develop high-end mechanical and optical elements and instrumentation able to guarantee precision and stability during beamline operation. However, before installation of any instrumentation in the beamlines, it is necessary to validate the equipment performance, which can only be done with precision metrology. Also, to take reliable measurements, several parameters must be considered, like the uncertainties of the measurement equipment, the test setup and the environmental disturbances, which can be related to temperature stability, air convection and turbulence, air cleanness, atmospheric pressure and humidity, and vibration [4].

This paper describes the environmental control results of the new LNLS Metrology Building, whose design concepts were detailed at the 2016 MEDSI Conference [5]. Also, the performance of the inertial bases/floor on top of which the metrology laboratories were installed is presented considering the influence of the building machinery.

* Work supported by the Brazilian Ministry of Science, Technology, Innovation and Communication

[†] henrique.oliveira@lnls.br

PROJECT REQUIREMENTS

The LNLS Metrology Building was designed following a layer-based architecture, in which the outer layers have a proper environmental control that contributes for the stability of the inner ones. The goal of this architecture is to provide the laboratories (inner layers) a highly stable environment, minimizing the influence of the large thermal and humidity variations that may naturally occur outside the building [5]. The building contains three layers and each of them has one or more rooms controlled by independent air handling units (AHUs). The design requirements for each area inside the building are presented at Table 1:

Table 1: Environmental Requirements

Room	T [°C]	RH [%]	Particle
Building Shed	23±1.5	-	-
Assembly Room 1	22±1.0	50±10	-
Assembly Room 2	22±0.5	50±10	-
Mech. Metrology	22±0.1	50±5	-
Optical Metrology	22±0.1	50±5	ISO 7
Gowning Room and Buffers	22±0.1	50±5	ISO 8

ENVIRONMENTAL CONTROL RESULTS

The whole layer concept efficiency is based on stabilizing an outer layer to diminish the external thermal load on the inner layers walls. Aiming to that result, the first system tuned was the main shed, which has the more relaxed requirements and where more general and less precise tests take place. Figure 1 shows the comparison between the shed and external temperature variation, measured along a day. All the results displayed on this paper refer to the same day, 28/04/2018.

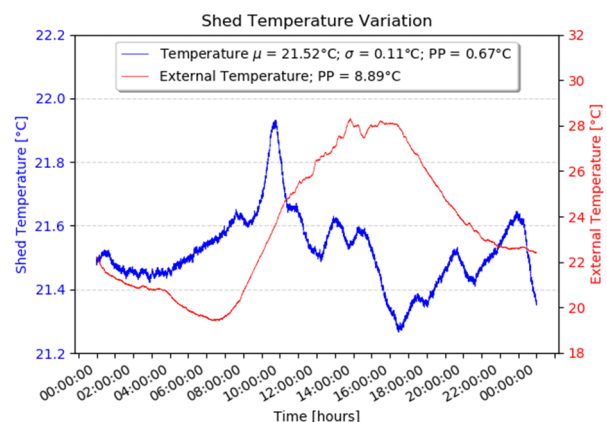


Figure 1: Temperature variation inside and outside the Metrology Building over one day.

Content from this work may be used under the terms of the CC BY 3.0 licence (© 2018). Any distribution of this work must maintain attribution to the author(s), title of the work, publisher, and DOI.

For the Sirius beamlines, mirrors and crystals are being specified with figure errors at the nanometer-level, which must be carefully verified before final installation. Such verifications are conducted at the Optical Metrology Laboratory (OML). For that, the applied instrumentation (autocollimators, interferometers) is required to work at its full performance, avoiding any external disturbances. Aiming to enable measurements at this scale, the OML had the strictest environmental project requirements, as exhibited in Table 1. Figure 2 shows the room temperature and humidity variation over one day.

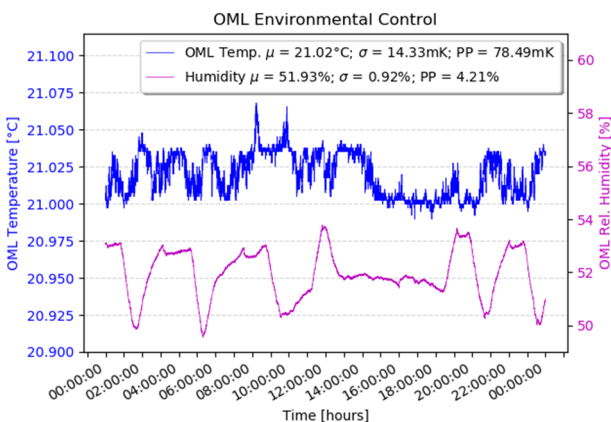


Figure 2: OML temperature and humidity variation during a day. A peak-to-peak value of 78.49mK is achieved.

Even with the OML temperature stabilized, there were some locations more influenced by the air flow fluctuations, specially near the air diffusers. One problem faced during the room commissioning was that the Long Trace Profiler (LTP) [6,7] was installed right below one of the air diffusers, consequently its capacitive sensors being affected. Aiming to circumvent that situation, an enclosure was installed around the LTP bench, providing a passive thermal insulation to the area and physically blocking the air flow. That configuration eliminated forced air flow and reduced the temperature variation on the LTP test area by a factor of 2, considering peak-to-peak (PP) values, enabling high precision optical metrology to be conducted. Figure 3 show a comparison between the temperature variation in and out the LTP enclosure.

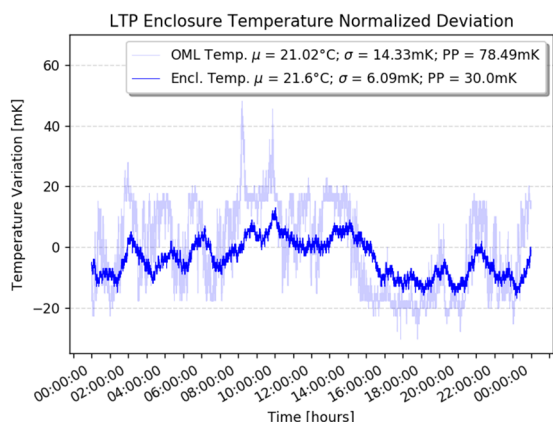


Figure 3: Normalized Temperature Variation at the OML room and inside the LTP enclosure.

Although the other rooms had more relaxed requirements, equivalent results were achieved regarding temperature and humidity control.

VIBRATION ASSESSMENT

Besides the environmental control, another aspect that could influence on the metrology results is the vibration transmission throughout the floor. Although the laboratories were built on isolated foundations, the building is near the LNLS Machine Shop and may also suffer influence from the HVAC system machinery.

About Inertial Bases/Floors

In 2013, the LNLS Mechanical Design Group conducted a study to define the Sirius tunnel floor foundation. After analyzing the soil geophysics, two special blocks prototypes were constructed based on the MAXIV and DLS designs. Several vibrational tests were carried out to characterize the blocks and, although both performed well, the MAXIV option offered slightly better results and was chosen as the base-design for the Sirius' tunnel.

To take advantage of these existing foundations, the Metrology Building was constructed around it.

Instrumentation and Methodology

In order to evaluate the influence of each HVAC component, measurements of the machines sequential starting were carried out. Six regions of the building area were analyzed, from the chillers and pumps yard to the metrology laboratories special foundations. As the observed vibration levels were small, the Wilcoxon 731A seismic accelerometer was used (1000V/g sensitivity and 0.05-450Hz frequency range). For each region, the measurement consisted in a 30 minutes acquisition at a rate of 1kHz, starting the machines one by one and giving each one sufficient time to reach permanent regime before starting the next.

Results and Conclusions

From the data collected it was inferred that the greatest contribution on the building overall vibrational level is from the HVAC system water pumps. Even though they are supported by spring-isolated inertial bases, the pumps system excited the larger frequency range as demonstrated in Figure 4. Nevertheless, the vibration levels inside the metrology rooms (special foundations) were attenuated by a factor of 3 when comparing to the shed and machine room (industrial floor). Also, the final integrated RMS displacement at the metrology rooms is at 20nm. The RMS offset data presented in Table 2 is integrated from 1 to 450Hz and the column *Cultural Noise* refer to the vibration level with the HVAC system turned off.

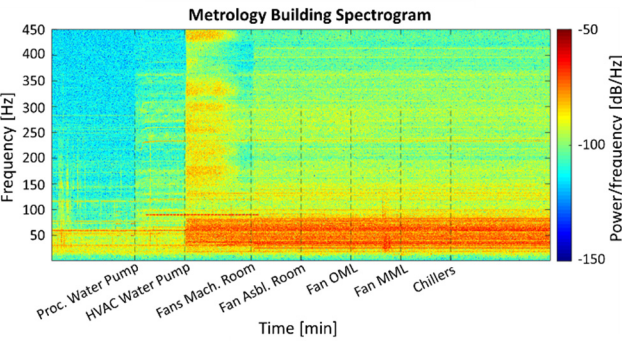


Figure 4: Frequency contribution analysis on HVAC machinery sequential start.

Table 2: Comparison Between Integrated RMS Displacement (1-450 Hz) with HVAC Machinery Turned On and Off

Room	RMS Displacement[nm]	Cultural Noise[nm]
Pump Hall	70	7
Machine Room	50.2	4.5
Building Shed	33.6	2.2
Assembly Rooms	12.7	1.25
Mech. Metrology	11.5	1.1

STATUS

Metrology Equipment

The building is now fully operational and several metrology equipment were installed since its inauguration on the beginning of 2017. The portfolio now includes big stationary equipment such as a high-end Coordinate Measuring Machine (CMM) used to gauge dimensional and geometrical features on parts and assemblies, and fiducialize beamline components; a Spindle Error Analyzer (SEA) with a granite structure and capacitive sensors to characterize rotating stages at the nanometer scale; a LTP with a full granite base and a Fizeau Interferometer to characterize the beamline optics with sub-nanometer resolution; among some other portable equipment such as autocollimators, interferometers, laser trackers and measuring arm.

Tests and Systems Examples

With the Sirius Storage Ring to be delivered until the end of 2018, the LNLS groups dedicated to beamline instrumentation are already testing the first prototypes from a whole bunch of in-house developments. The High Dynamics Double Crystal Monochromator (DCM) is already on final phase of its assembly, with a stability performance never achieved before [8]. The first mirror system prototype was designed, manufactured and tested for mechanical stability [9]. Also, some of the optics were already received and are being assembled on the system prototype to be characterized at the OML. The PIMEGA-135D real time X-ray imaging detector being developed at LNLS [10] had its most critical mechanical parts verified at the CMM. A whole front-end prototype was assembled and

commissioned inside the building [11]. In summary, the Metrology Building has become one of the main LNLS infrastructures, and it is already contributing for the development and validation of Sirius' instrumentation [12].

Upgrade to Clean Rooms

Although very stable, the building still lacks space for careful vacuum-compatible assemblies. The Assembly Room #2, where the CMM is installed and where monochromators such as the DCM are assembled, has already been upgraded to a clean room. An absolute filter was installed on its AHU and the room access was restricted to authorized staff with proper clothing.

ACKNOWLEDGEMENTS

The authors would like to thank the Biotec Company, responsible for the design and installing the HVAC system; the colleagues from ESRF, ALBA, DLS and BESSY for the fruitful discussions regarding Metrology Laboratories; and the Beamline Optics Group for improving the LTP environment.

REFERENCES

- [1] A. R. D. Rodrigues *et al.*, "SIRIUS Status Report", presented at IPAC'18, Vancouver, Canada, May 2018, paper THXGBD4, to be published.
- [2] L. Liu, F. H. de Sá, and X. R. Resende, "A New Optics for Sirius," in *Proc. IPAC'2016*, Busan, Korea, May 2016, paper THPMR013, pp. 3413–3416, DOI:10.18429/JACoW-IPAC2016-THPMR012
- [3] Wiki-Sirius, <https://wiki-sirius.lnls.br>
- [4] V. V. Yashchuk *et al.*, "Advanced environmental control as a key component in the development of ultrahigh accuracy *ex situ* metrology for x-ray optics", *Optical Engineering*, vol. 54, no. (10), p.104104, Oct. 2015.
- [5] H. G. P. de Oliveira *et al.*, "The LNLS Metrology Building", in *Proc. MEDSI'16*, Barcelona, Spain, Sep. 2016, pp. 17-19, doi.org/10.18429/JACoW-MEDSI2016-MOPE08
- [6] B. C. Meyer, M. B. Silva, "A New Optics Metrology Laboratory at CNPEM: Metrology Capabilities, Performance, and Future Plans", in *Proc. SPIE Vol. 10385*, 103850C (2017).
- [7] B. Meyer *et al.*, "Commissioning of the LNLS Long Trace Profiler (LTP VI)", presented at IWXM 2018, Hsinchu, Taiwan, June 2018.
- [8] R. Galdes *et al.*, "Offline Results of the New High-Dynamic DCM for Sirius", presented at MEDSI'18, Paris, France, June 2018, paper WEOAMA01, this conference.
- [9] R. Galdes *et al.*, "The Design of Exactly-constrained X-ray Mirror Systems for Sirius", presented at MEDSI'18, Paris, France, June 2018, paper WEOAMA04, this conference.
- [10] J. Polli *et al.*, "Medipix Detectors Developments at the Brazilian Synchrotron Light Laboratory LNLS for Sirius", presented at IFDEPS 2018, Annecy, France, March 2018.
- [11] L. M. Volpe *et al.*, "High Heat Load Front Ends for Sirius", in *Proc. MEDSI 2016*, Barcelona, Spain, Sep. 2016, paper WEPE06, pp. 324-326, doi:10.18429/JACoW-MEDSI2016-WEPE06

- [12] L. Sanfelici *et al.*, “Solutions for the SIRIUS’ Beamlines in a Nutshell”, presented at the 13th International Conference on Synchrotron Radiation Instrumentation (SRI2018), Taipei, Taiwan, June 2018, to be published.

THE STATUS OF THE NEW HIGH-DYNAMIC DCM FOR SIRIUS

R. R. Gerales^{†1}, R. M. Caliar, G. B. Z. L. Moreno, M. Saveri Silva, L. Sanfelici,
 H.C.N. Tolentino, H. Westfahl Jr., Brazilian Synchrotron Light Laboratory (LNLS),
 Brazilian Center for Research in Energy and Materials (CNPEM), Campinas, São Paulo, Brazil
 T. A. M. Ruijl, R. M. Schneider, MI Partners, Eindhoven, The Netherlands
¹also at Technische Universiteit Eindhoven, Eindhoven, The Netherlands

Abstract

The monochromator is known to be one of the most critical optical elements of a synchrotron beamline, since it directly affects the beam quality with respect to energy and position. Naturally, the new 4th generation machines, with their small emittances, start to bring higher stability performance requirements, in spite of factors as high power loads and variations, high radiation levels, ultra-high vacuum compatibility and vibration sources. In response to that, an innovative concept of a high-dynamic vertical DCM (Double Crystal Monochromator) with angular range between 3 and 60 degrees (equivalent to 2.3 to 38 keV with Si(111)) has been developed at the Brazilian Synchrotron Light Laboratory. A highly repeatable dynamic system, with servo control bandwidth of 250 Hz, has been achieved and will be installed at Sirius macromolecular crystallography beamline – MANACA – still in 2018. The complete offline results of the in-vacuum cryocooled high-dynamic DCM, showing stability between crystals around 15 nrad RMS up to 2.5 kHz, even during the Bragg angle motion for flyscans, are presented.

INTRODUCTION

The beamlines of the new generation of synchrotrons, the so-called Diffraction Limit Storage Rings (DLSR), have started to be built with ever more demanding requirements to preserve the extraordinary properties of the sources. In double-crystal monochromators (DCMs), the main performance bottleneck has been proven to be the stability of the parallelism between the two crystals, since it affects the position of the virtual source with a scaling factor given by the distance to the source, which is typically about 30 m [1]. Indeed, for sources of a few microns, this angular stability must be kept within a few nrad to keep the variation of the virtual source within about 10% of its size.

Considering the frequency range between 0 and 2.5 kHz, figures as low as 20 nrad RMS (root mean square) have been reported for horizontal DCMs [2], whereas for vertical DCMs the best performances seemed to be stuck around 50 nrad RMS [3]. Yet, it must be noticed that still today most of the available data about DCMs unfortunately cannot be directly compared to each other. This is because, although for given disturbance levels the outcome of a measurement does strongly depend on acquisition parameters like frequency and integration time, the RMS values are hardly ever displayed as a function of frequency,

but often mentioned as single numbers without further acquisition details. This means that many official numbers show averaged optimistic values, which may not be consistent with the needs and timescales of different experiments at the beamlines. Indeed, with experiments reaching the sub-millisecond range, performances in the kHz range must be proven. Moreover, it must be emphasized that even the best results rely on braked systems only, whereas about 100 nrad RMS could be expected in active control [3]. Finally, during energy flyscans, the stability levels may exceed the microradian range. Consequently, to the best of our knowledge, no vertical DCM had been close to the 10-nrad-level performance as required by DLSR beamlines.

Convinced that incremental improvements in traditional systems was insufficient to reach the new requirements, the Brazilian Synchrotron has developed over the last three years an innovative DCM, the so-called High-Dynamic DCM (HD-DCM), an active high-performance mechatronic system with a closed-loop bandwidth of 250 Hz [4]. The conceptual design, the mechatronic principles and thermal management solutions were presented in MEDSI 2016 [5–7]. More recently, the results of in-air validation of the core, together with system identification and control techniques, were presented in ICALEPCS 2017 [8,9]. In the following sections, the most recent updates, together with the offline performance of the full in-vacuum cryocooled system, are presented, showing unprecedented stability and scanning performances.

The HD-DCM is now ready to be tested online and is expected to be installed at Sirius macromolecular crystallography beamline – MANACA – in the second semester of 2018. Sirius is in an advanced construction phase, with the LINAC and the booster currently being commissioned and installed, respectively.

SYSTEM STATUS

Goniometric System

Figure 1 shows the complete system and highlights its sub-modules, including the goniometric system, the vacuum vessel and the granite bench, which were not addressed in previous publications.

As planned from the beginning, the goniometric system was realized by means of double-side bearings, to improve the load capacity and stiffness in a symmetric design. To save development time and costs, a commercial direct-drive ball-bearing rotary stage has

[†] renan.gerales@lnls.br

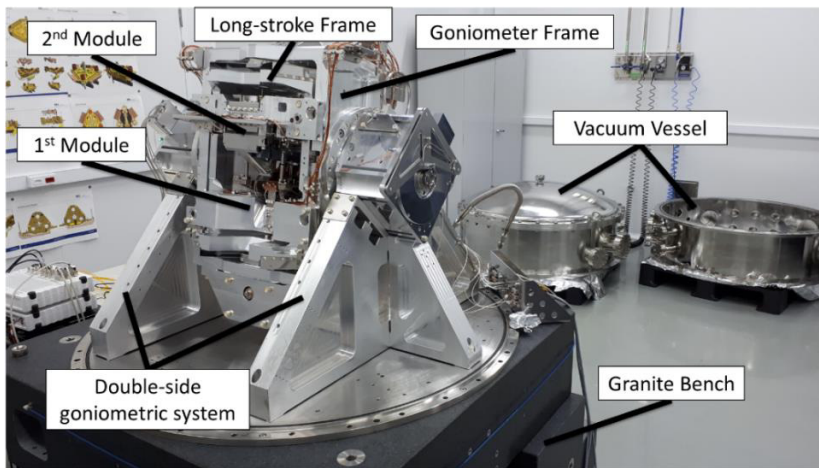


Figure 1: Overall view of the HD-DCM with its major subparts, namely: granite bench, double-side goniometric system, goniometer frame, long-stroke frame, 1st and 2nd modules, and the vacuum vessel. (For references, see [5].)

been selected, being enough to have one active stage and an equivalent passive bearing at the opposite side. The supports consist of aluminium frames, designed for maximum supporting stiffness while preventing excessive loads and deformations in the bearings, which might lead to loss of performance and premature wear. Before assembling the core, the rotary stages were mounted to the supports and aligned to each other with a laser tracker within 250 μm and 0.6 mrad. The residual misalignment is within the design budget of the elastic membranes that couple the stages to the goniometer frame.

The supports are deterministically mounted to the bottom flange of the vacuum vessel, which, in turn, is clamped to the top element of the granite bench, both from the top side in the perimeter and from below in the center. This way, the internal mechanics may greatly benefit from the stiffness of the granite bench. The vessel is completed by a bottom section, with all functional feed-throughs, a top section, with viewports and beam entrance and exit ports, and a cover. Sealing between these parts can be made either with o-rings or elastic seals. The granite bench is a topic in its own and more details are given in [10].

For the moment a closed-loop control bandwidth of 25 Hz has been used to control the Bragg angle with in-position stability of 24 nrad RMS up to 2.5 kHz. It is worth mentioning that, although this measurement is indirectly given by the encoder inside the rotary stage, not only does the core have a large moment of inertia (12 kg.m²), but also the rotor of the stages decouples from it at about 1.2 kHz, so that the real stability with respect to the bench is expected to be very close to this value. This does not take the tilting of the bench with respect to the floor into account, but this shall be evaluated by other means at the beamline.

Crystal Alignment

The Si(111) and Si(311) crystals have been designed for high eigenfrequencies and deterministic performance with respect to their metrology frames, while allowing for

cooling and beam propagation compatibilities. Both crystal sets, with their unusual triangular shapes and extended ears to increase rotational modes, have been manufactured by the team of Elina Kasman at the Advanced Photon Source (APS). Figure 2 shows the crystals during inspection in a coordinate measurement machine (CMM).

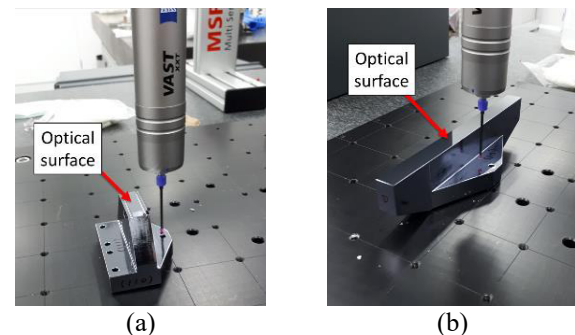


Figure 2: 1st and 2nd crystals being inspected at CMM.

Crystallographic orientation and machining tolerances are inherent limitations in the manufacturing process of crystals, such that in these crystals the angles between the diffraction planes and the bottom surface of the crystals, which make the interface with the metrology frames, reached as much as 0.17°. Therefore, as the interferometers used in the embedded metrology loop have angular operational range around $\pm 0.1^\circ$, an alignment procedure has been developed to bring the parallelism between the diffraction planes and surfaces of the mounting surfaces down to the millidegree range by means of dedicated machined shims. The procedure is based on an iterative process of measurements made in the diffractometer of the XRD2 beamline at LNL and at a CMM, as seen in Fig. 3, and fine machining of the shims. The results after two iterations are shown in Table 1, where the values were systematically reduced to at least 0.002°, which is the estimated practical repeatability limitation of the overall process. The value for the 2nd crystal of Si(111) in roll was intentionally made relatively larger to test practical aspects of the technique, but it does not affect the tuning between crystals.

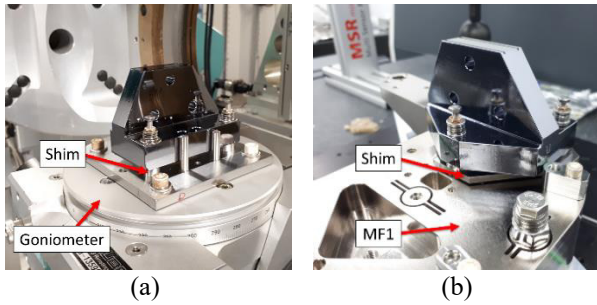


Figure 3: Parallelism correction procedure: (a) crystal on diffractometer at XRD2 beamline at LNLS; (b) crystal on metrology frame (MF1) during measurements at a CMM.

Table 1: Parallelism

	Pitch [deg]		Roll [deg]	
	before	after	before	after
1 st Si(111)	0.054	0.002	0.087	0.005
1 st Si(311)	0.173	0.003	0.043	0.002
2 nd Si(111)	0.026	0.002	0.131	0.012
2 nd Si(311)	0.015	<0.001	0.172	0.003

Manifold

The stainless-steel manifold that had been designed for reducing flow-induced vibrations in the system [11] was produced by additive manufacturing (3D-printing) by the team of Prof. Andre Jardini from the University of Campinas (UNICAMP). Next, to improve external surface roughness for vacuum purposes and refine the more precise dimensions, it went through a finishing machining step at LNLS' workshop. Finally, the full assembly, with the previously brazed tripartite copper cooling blocks and the stainless-steel tubes, was brazed by the Materials group at LNLS. Related pictures are shown in Fig. 4.

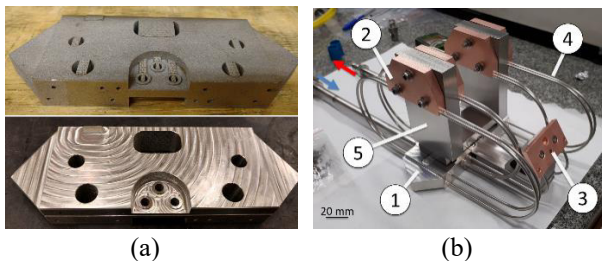


Figure 4: (a) 3D-printed manifold as sintered (top) and after finishing machining. (b) Assembly mounted to brazing tooling: manifold (1), cooling block (2) (x4), manifold extension (3), distribution tubes (4) (x18), and tooling (5).

Furthermore, to effectively compare the influence of the optimized flow distribution in the performance of the HD-DCM with that of a non-optimized design, another assembly was manufactured with a manifold produced by simple machining and welding processes. Indeed, as shown in the Results section, both have been tested in operational conditions with significant differences in the final stability levels. Figure 5 shows an isometric section view of the two manifold designs, with the optimized solution, resembling arteries, in (a), and a simple design, with abrupt flow changes in (b).

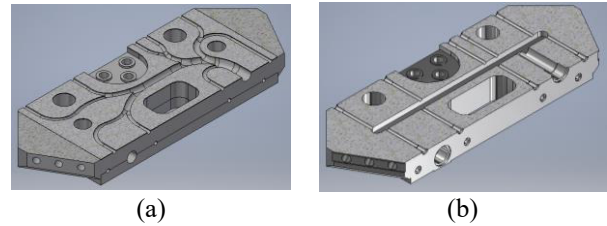


Figure 5: Isometric section view of two manifold designs: (a) optimized solution, resembling arteries; (b) simple design, with abrupt flow changes.

Thermal Management

The system includes 20 RTDs (resistance temperature detector) divided in two types, namely: PT10K, for low-temperature measurements, and PT2K, for room-temperature measurements. Some are used for monitoring purposes only, whereas the others are used in active temperature control of a few critical parts. Particularly, the Y-frame (YFM) and the short-stroke frame (SHF) are parts with direct interface with the crystal modules. So, to control heat leakage and avoid cooling of adjacent parts, they are actively temperature controlled at 24°C by local heaters in closed-loop. The temperature of the 2nd crystals are controlled at 155 K to match the lattice parameter of the 1st crystals. Finally, some heating power is put on the voice coils (VCF) to stabilize their temperature regardless the operation condition of the HD-DCM. This control is achieved by means of 16 low-power (up to 4 W) Kapton foil heaters.

Except for the actual beam power load, all the remaining thermal aspects have been evaluated offline. Table 2 compares the designed with the final temperature distribution of the parts, showing that the desired temperatures of sensitive elements have been successfully met. The main differences were found in the SHS and the VCFs, due to blackbody radiation absorption over limited thermal conductivity links.

Table 2: Comparison between Designed and Experimental Offline Temperature Distribution. (For element reference, see [5].)

Element	Designed [K]	Experimental [K]
CR1	78	78
MF1	170	180
YFM	297	297
BRC	95	102
CR2	155	155
SHS	210	250
VCF	250	267
SSF	297	297

Except for the first crystals, which reach the operational temperature in just a few minutes due to the very efficient cooling scheme, the time constants of the remaining parts are relatively large. The consequence is two-fold: on the one hand, the complete cooldown thermalization is in the order of 24 hours, which can be somewhat inconvenient; on the other hand, however, the system will probably be rather insensitive to fast power load variations, which

may not only simplify the timing requirements in the temperature control loop, but also minimize thermal-drift problems in most scanning applications. Studies for more advanced thermal control strategies, including feedforward are currently in progress.

SYSTEM PERFORMANCE

In-position Performance

As mentioned, analysing the system as a function of frequency is of fundamental importance to understanding the different effects that the mechanical instabilities may have. Therefore, the cumulative amplitude spectrum (CAS) (in [SI]), which is the square root of the cumulative power spectrum (CPS) (in [SI²]) and provides the integrated RMS value as a function of frequency, has been chosen as the standard output format for performance evaluation.

Figure 6 shows the in-position relative pitch (*ShsRx*) performance of the HD-DCM up to 2.5 kHz as measured by the embedded interferometric metrology system for different LN₂ flows, both for the 3D-printed (solid lines) and the machined (dashed lines) manifold assemblies. It is clear from the data that all experimental conditions show virtually the same error levels up to about 300 Hz, with an RMS value close to 5 nrad. This is a direct result of the efficiency of the closed-loop control of the short-stroke module, with a bandwidth of 250 Hz. Also clear is the positive impact of the optimized manifold solution, typically reducing the integrated values up to 2.5 kHz by a factor 2. Indeed, the greatest contribution for the total errors (even more clearly seen in PSD spectra) is the internal resonance at about 450 Hz, namely, the first mode between the metrology frame of the 1st crystals and the YFM, which is directly excited by the flow disturbances in the manifold. Considering the optimized manifold, RMS_{2.5kHz} values are between 12 and 25 nrad. In terms of roll (*ShsRz*) and gap (*ShsY*) stabilities, similar results are found, with typical values of 18 nrad and 1.8 nm RMS_{2.5kHz}, respectively. All measurements were made over periods of 10 s.

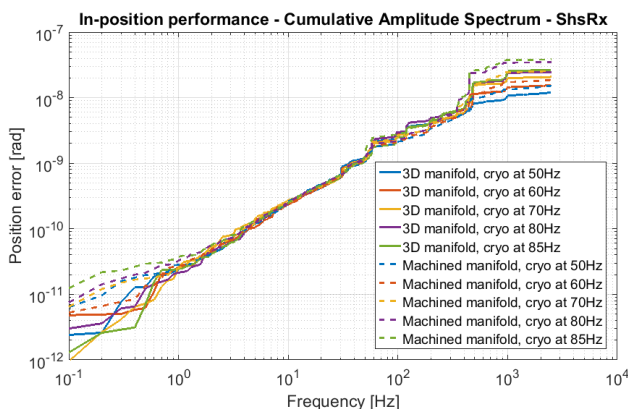


Figure 6: In-position CAS for the relative pitch between crystals (*ShsRx*), taken at different flow levels, both with the 3D-printed and the machined manifold assemblies.

The flowmeter of the cryocooler was not functioning, so, unfortunately, the only parameter available for comparisons was its pumping frequency. For reference, from preliminary measurements, 60 Hz and 85 Hz are estimated to reflect flows of 4 and 6 l/min, respectively. The actual operational flow will be determined online.

Two relevant comments need to be made regarding measurement noise levels and the indirect metrology. Evaluating the noise levels of the interferometers up to high frequencies require careful experimental investigations. Preliminary analyses suggest that in vacuum these levels would be at least below 0.5 nm, translated to and 5 nrad RMS_{2.5kHz}, which was considered good enough for the moment. Next, the interferometers do not directly see the relative position between the crystals, which can only be evaluated with enough resolution and bandwidth at the beamline. However, modal analyses realized in the 1st module suggest that the decoupling frequencies between the metrology frame and the crystals indeed exceed 1 kHz, as targeted in design. Then, the errors that are invisible to the interferometers are expected to have very small contribution.

Finally, it is worth mentioning that, the rotary stage is constantly under control, i.e. the results do not depend on additional brakes or limited operational conditions. Measurements made with brakes engaged to the rotary stage did not result in any improvement in performance.

Scanning Performances

Considering the dynamic concept of the HD-DCM, more interesting than the in-position performance is the scanning capacity of the instrument. Thanks to the two-level design, two energy scan modes are available:

Standard scanning mode In the standard mode, the Bragg angle is a setpoint to both the long-stroke and the short-stroke modules, which move together to adjust the gap while stabilizing pitch and roll. Thus, scans of any size can be made within the operational energy range. However, specially at low energies, for which large motions are required, the stability levels suffer from disturbances of the stepper-driven long-stroke actuator.

High-performance scanning mode In the alternative mode, the long-stroke is kept still while the Bragg setpoint is sent to the short-stroke only. Naturally, the scan ranges become limited to reasonable gap ranges in the short-stroke. However, particularly for energies above 8 or 10 keV, more than 1 keV scans can be performed with virtually the same stability levels of in-position performance even for scanning speeds as high as 1 keV/s.

Figure 7 shows *ShsRx* RMS_{2.5kHz} values for scans in standard and high-performance modes. As cases of interest, 1keV scans were made around different energy values for different speeds, so that every point in the graph corresponds to the CAS value at 2.5 kHz for a full scan with constant eV/s speed. In standard mode, at 20 and 30 keV the angular and gap motions are small, so that the performance is equivalent to in-position stability. As the energy

is reduced, however, the stroke and speed of the long-stroke actuator get increasingly larger, with clear disturbing effects, reaching as much as 80 nrad RMS_{2.5kHz} around 3 keV, for example. It is also worth noticing that around 3 and 5 keV the scanning speeds are limited to 30 eV/s and 100 eV/s, respectively. This is due to a practical limit of about 1 mm/s in the variation of the gap between the crystals, which is partly given by present speed limitations in the acquisition rate of the interferometers, but also by acceleration levels and heat dissipation limitations in the mechanics and actuators, respectively. Regarding the high-performance mode, 3 keV has very limited range and even 5 keV is limited to 500 eV scans. Above 10 keV, however, 1keV scans are perfectly feasible. Moreover, up to 1 keV/s all points overlap with performances around 15 to 18 nrad RMS_{2.5kHz}. Then, above 1 keV/s, high speeds and accelerations are present and the error levels increase. Nonetheless, significant improvement can be expected with feedforward control (not yet implemented).

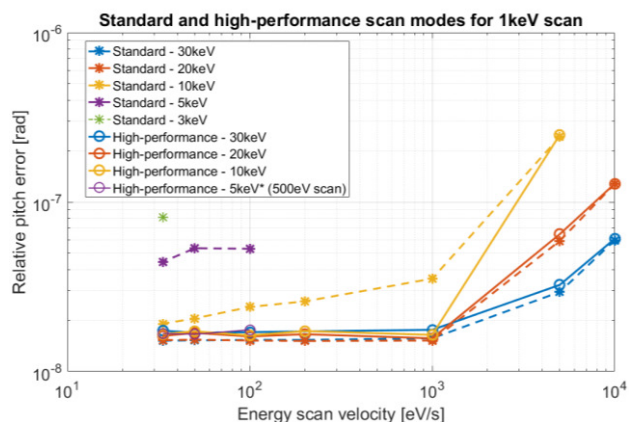


Figure 7: RMS_{2.5kHz} relative pitch between crystals (ShsRx) for standard and high-performance 1 keV scans for speeds between 30 and 10.000 eV/s.

Source Degradation Frequency Analysis

In the beginning of the project, the desired target for ShsRx was 10 nrad peak (3 σ) up to 2.5 kHz. However, this is even probably limited by the noise floor of the interferometers alone. Yet, with the present results, 3 σ 10 nrad is achieved somewhere between 100 and 200 Hz. Therefore, evaluating the effective source degradation effects as a function of frequency may be an instructive exercise. Figure 8 shows the equivalent RMS values of the maximum vertical position deviation of the virtual source and its size increase in microns for a 30-meter distance between source and monochromator as a function of the integration time for a typical stability CAS. For integration times above 100 ms all instabilities are reflected as an increase in source size. For a source of 10 μ m FWHM, the size increase is of about 2.5%, if quadratic sum is used. At the other extreme, for integration times in the order of 1 ms, most of the instabilities are reflected as position deviations of the source, with minimum effect in size increase. Again considering a source of 10 μ m FWHM, the RMS deviation is about 9.5% of the size, which is still within the initial specifications.

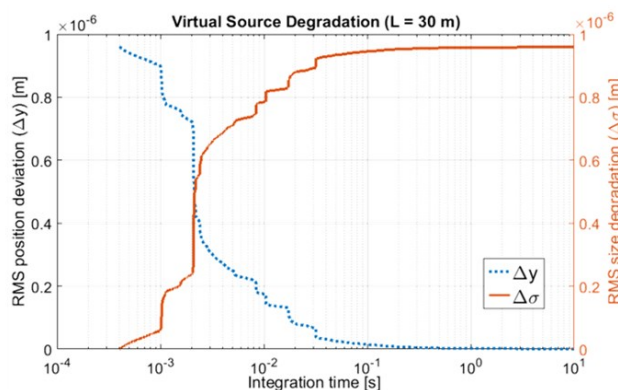


Figure 8: RMS values for virtual source vertical size degradation and maximum position deviation as a function of integration time for typical ShsRx instability levels (16 nrad RMS_{2.5kHz}) in the HD-DCM for a distance of 30 m.

CONCLUSIONS

The offline characterization of the HD-DCM proved cryogenic operation and showed performance around 15 nrad RMS_{2.5kHz} for in-position pitch stability. More remarkably, it was shown that even 1keV energy scans at up to 1 keV/s can be made with the same performance. Intrinsic limitations of an embedded metrology system, as insensitiveness to deviations associated to cosine, cyclic and Abbe errors, or thermal and wavelength instabilities, for instance, can be in principle greatly reduced via calibration, thanks to the high repeatability that is obtained by the design principles upon which the system is based. Finally, the high eigenfrequencies in the metrology loop reduces the dynamic errors in the indirect metrology to a minor contribution. In any case, the achieved results must naturally be validated under operational conditions at the beamline.

FUTURE WORK

The control platform is currently being migrated from Speedgoat's xPC to National Instruments' cRio. Moreover, in the near future, feedforward and optimized thermal control are expected to be implemented soon. The unit that is ready is expected to be installed at the MANACA beamline in the second semester of 2018 to start online commissioning. A second unit is in production and should be installed shortly after at the EMA beamline. Finally, an upgrade in the LOS actuator has been designed, with the purpose of allowing for high-performance scanning over the full energy range.

ACKNOWLEDGEMENTS

The authors would like to gratefully acknowledge the funding by the Brazilian Ministry of Science, Technology, Innovation and Communication, the contributions of the LNLS team, the MI-Partners team and those of the synchrotron community who directly or indirectly built the path to this development, and also the collaboration with Elina Kasman's team at APS.

REFERENCES

- [1] *ESRF DCM Workshop*, Grenoble, France, May 2014, unpublished.
- [2] P. Kristiansen, “Vibrational Stability of a Cryocooled Horizontal-Bounce Double Crystal Monochromator”, presented at MEDSI’16, Barcelona, Spain, Sept. 2016, paper TU-CA04, unpublished.
- [3] P. Kristiansen, J. Horbach, R. Doehrmann, J. Heuer *et al.*, “Vibration measurements of high-heat-load monochromators for DESY PETRA III extension”, *J. Synchrotron Rad.*, vol. 22, pp. 879-885, Jul. 2015.
- [4] R. R. Geraldés *et al.*, “Instrumento para movimentação de posicionamento de elementos ópticos com resolução e estabilidade mecânica nanométricas em linhas de luz”, PCT/BR2017/050262, 2017, Patent Pending.
- [5] R. R. Geraldés *et al.*, “The New High Dynamics DCM for Sirius”, in *Proc. MEDSI’16*, Barcelona, Spain, Sep. 2016, paper TUCA05, pp. 141-146, doi:10.18429/JACoW-MEDSI2016-TUCA05
- [6] R. R. Geraldés *et al.*, “Mechatronics Concepts for the New High-Dynamics DCM for Sirius”, in *Proc. MEDSI’16*, Barcelona, Spain, Sep. 2016, paper MOPE19, pp. 44-47, doi:10.18429/JACoW-MEDSI2016-MOPE19
- [7] M. Saveri Silva *et al.*, “Thermal Management and Crystal Clamping Concepts for the New High-Dynamics DCM for Sirius”, in *Proc. MEDSI’16*, Barcelona, Spain, Sep. 2016, paper TUPE15, pp. 194-197, doi:10.18429/JACoW-MEDSI2016-TUPE15
- [8] R. M. Caliri *et al.*, “System Identification and Control for the Sirius High-Dynamic DCM”, in *Proc. ICALEPCS’17*, Barcelona, Spain, Oct. 2017, paper TUSH203, pp. 997-1002, doi:10.18429/JACoW-ICALEPCS2017-TUSH203
- [9] G.B.Z.L. Moreno *et al.*, “Rapid Control Prototyping Tool for the Sirius High-Dynamic DCM”, in *Proc. ICALEPCS’17*, Barcelona, Spain, Oct. 2017, paper THPHA214, pp. 1941-1946, doi:10.18429/JACoW-ICALEPCS2017-THPHA214
- [10] R. R. Geraldés *et al.*, “Granite Benches for Sirius X-ray Optical Systems”, presented at MEDSI’18, Paris, France, June 2018, paper THPH12, this conference.
- [11] R. M. Caliri *et al.*, “Studies on Flow-Induced Vibrations for the New High-Dynamics DCM for Sirius”, in *Proc. MEDSI’16*, Barcelona, Spain, Sep. 2016, paper MOPE02, pp. 8-11, doi:10.18429/JACoW-MEDSI2016-MOPE02

SAMPLE STABILIZATION FOR TOMOGRAPHY EXPERIMENTS IN PRESENCE OF LARGE PLANT UNCERTAINTY

T. Dehaeze^{1,†}, M. Magnin-Mattenet, ESRF, Grenoble, France
 C. Collette¹, Université Libre de Bruxelles, BEAMS department, Brussels, Belgium
¹also at Precision Mechatronics Laboratory / A&M department, Liege, Belgium

Abstract

A new low emittance lattice storage ring is under construction at the ESRF. In this new instrument, an upgraded end station for ID31 beamline must allow to position the samples along complex trajectories with a nanometer precision. In order to reach these requirements, samples have to be mounted on high precision stages, combining a capability of large stroke, spin motion, and active rejection of disturbances. First, the end station will be presented with the associated requirements. However, the precision is limited by thermal expansion and various imperfections that are not actively compensated. Our approach is to add a Nano Active Stabilization System (NASS) which is composed of a 6DoF Stewart platform and a 6 DoF metrology system. A 3D model of the end station updated with experimental data is developed. As the mass of the samples may vary by up to two orders of magnitudes, robust control strategies are required to address such plant uncertainty. The proposed control strategy are presented and applied on the developed model by conducting time domain simulations of tomography experiment in presence of instrumentation noise and system uncertainty.

INTRODUCTION

Within the framework of the ESRF Phase II Upgrade Programme, a new state-of-the-art end station for the high-energy beamline ID31 is under development. Research in many scientific areas such as material and life sciences are increasingly looking for instruments with higher spatial resolution. The design of the new end station will enable many hard X-ray characterization techniques such as reflectivity, wide angle diffraction and diffraction tomography. The need of great versatility induces many constraints on the end station such as combining large stroke (≈ 10 mm), high precision (≈ 10 nm) while accepting samples with mass ranging from 1 kg to 50 kg.

Many positioning end stations have been developed with an increasing positioning precision [1–3].

However, when nanometer precision is needed, thermal expansion and vibrations are becoming the main source of positioning error that cannot be compensated by encoders used for each stage. Therefore, a direct metrology system is usually needed [2].

The aim of this study is to develop a short stroke Stewart platform that actively stabilizes the sample position and compensate for all sources of perturbations and imperfection.

This paper is organized as follows into three sections. The first section presents the ID31 positioning end station and its associated specifications. The second section is dedicated to the Nano Active Stabilization System (NASS) and the associated metrology frame. A model of the ID31 positioning station is also developed and presented. In the third section, after presenting the control strategy, simulations of tomography experiments are conducted using the developed model. These measurements are used to estimate the performance gain of using such active stabilization system.

ID31 SAMPLE-STATION

In order to position the samples along complex trajectories with a nanometer precision, a versatile positioning platform is developed. A simplified schematic representation of the system is shown Fig. 1.

Design

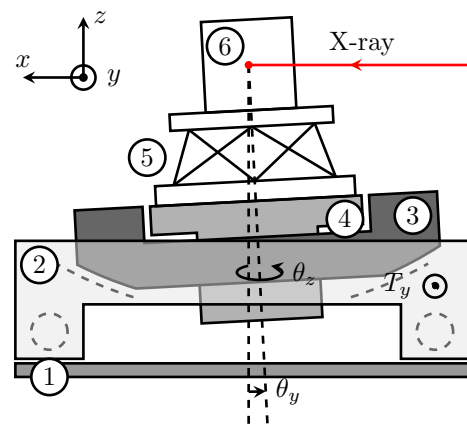


Figure 1: Schematic representation of the ID31 end station. (1) granite, (2) Translation Stage, (3) Tilt Stage, (4) Spindle, (5) Long Stroke Hexapod, (6) Sample.

This platform consists of multiple stacked stages, each of which is described below.

First, a translation stage offers a travel range of $T_y = \pm 5$ mm in the y direction which permits to scan the sample through the X-ray. A linear encoder is used to drive a brushless linear motor in a feedback loop with a Proportional-Integral-Derivative (PID) control law.

A tilt stage then rotates the sample around the y axis by $\theta_y = \pm 3^\circ$. The rotation axis is aligned with the focusing point of the X-ray in order to allow experiments such as X-ray reflectivity. The tilt stage is driven by a stepper motor and a PI position feedback using linear encoders.

[†] thomas.dehaeze@esrf.fr

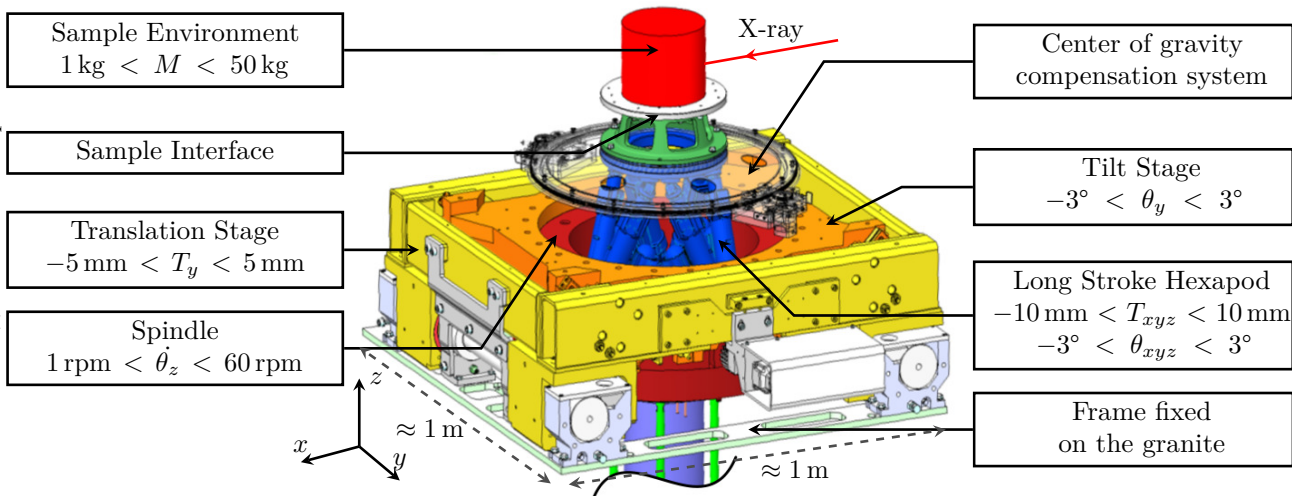


Figure 2: CAD view of the ID31 end station.

An air bearing spindle permits to rotate the sample around the vertical axis with an angular speed that varies from $\dot{\theta}_z = 1$ rpm for light samples ($M < 1$ kg) to $\dot{\theta}_z = 60$ rpm for heavy samples ($M = 50$ kg).

A long-stroke Stewart platform developed by Symetrie is placed on top of the spindle. It allows a fine positioning of the sample in all 6 degrees of freedom (DoF). Each leg of the Hexapod has an absolute linear encoder and a DC motor.

As the center of mass of the stages above the spindle is not perfectly aligned with the spindle axis, centrifugal forces generate parasitic motions. To overcome this issue, a center of gravity compensation system is used (Fig. 2). It consists of two motorized mass that can be positioned around a circular guidance in order to perfectly aligned the center of mass with the spindle rotation axis.

Finally a sample environment is positioned on top of all the stages. The sample environment permits to study samples under wide range of condition: low (1.2 K) to high (2000 K) temperatures, high magnetic field (8 T), etc.

A CAD view of the platform is shown Fig. 2. The green mechanical element shown below the sample environment is a rigid element that support the sample interface. It will later be replaced by the NASS.

Specifications

As shown in the previous section, the positioning system is composed of numerous stages in order to allow complex trajectories for various experiments.

As the precision needed on the sample position is very depending of the experiment conducted, only the most stringent requirements are summarized on Table 1. Moreover the metrology system must remain stable for 8 hours within 10 nm.

As the experiment with the most stringent requirements is the diffraction tomography, it will be used for simulations in order to test the performances of the system.

Table 1: Summary of the Most Stringent Specifications on the Motions of the ID31 End Station

	T_{xy}	T_z	θ_y	θ_z
Repeatability	20 nm	10 nm	5 μ rad	2 μ rad
MIM ¹	3 nm	3 nm	2 μ rad	0.5 μ rad

Measurements on the Existing End Station

Measurements have been conducted on each stage separately in order to characterize their positioning precision and mechanical properties.

Moreover, measurements have been done on the mounted end station (Fig. 3) to identify its mechanical behavior. These measurements will permit to tune the parameters of the developed model to better match the physical system.

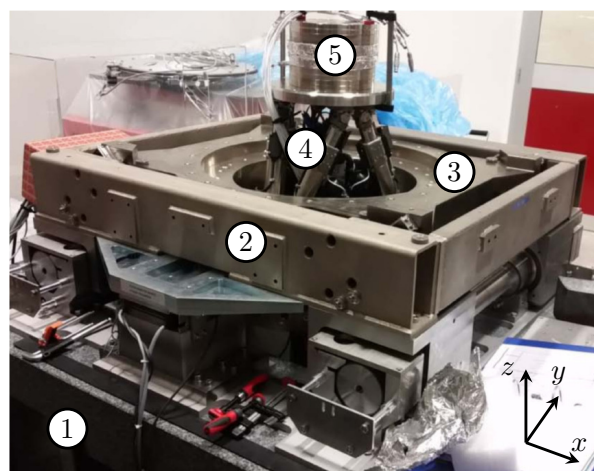


Figure 3: Picture of the ID31 end station. (1) Granite, (2) Translation stage, (3) Tilt stage, (4) Long stroke hexapod, (5) Mass representing the sample environment. The spindle is hidden by the translation and tilt stages.

¹ Minimum Incremental Motion

NANO ACTIVE STABILIZATION SYSTEM

6 DoF Metrology System

Even though the precision of each stage has shown to be excellent, thermal drifts and various parasitic motions cannot be compensated by the encoders used. Moreover, we want to control the position of the sample with respect to the X-ray that is determined by the position of the optical elements.

In order to achieve the positioning accuracy and stability requirements (shown on Table 1), a direct measurement of the relative position from the sample to the optical element is mandatory. Laser interferometry is chosen as it offers many advantages such as high resolution, high stability and large measurement range.

A 6 DoF metrology system is still under developed. Therefore, this is not developed in this paper.

6 DoF Active Stabilization Stage

In order to actively compensate the positioning error of the sample in all 6 DoF, a short stroke Stewart platform (the NASS) is added between the long stroke hexapod and the sample (Fig. 4).

A Stewart platform is a parallel robot that consists of two platforms connected by 6 active legs. Each leg has one actuator and two rotational joints [4]. The actuators can either be piezo electric stacks or voice coil linear actuators.

By inverting the dynamics of the Stewart platform, it is possible to control independently the position of the mobile platform in all 6 DoF with respect to the fixed platform [5].

These Stewart platforms have been extensively used for vibration control [6, 7] as it offers many advantages over conventional stacked stages such as high stiffness and high load over weight ratio.

Control Objective

The control objective is to stabilize the position of the sample using the NASS actuators based on the 6DoF measurements provided by the metrology system.

By this way, all the imperfections that are presently corrected (thermal drifts, guidance flexibilities, etc.) will be measured and compensated using a feedback control loop.

Figure 4 shows a simplified control architecture which will be used for the NASS. The validation and optimization of this control is done on a separate test bench.

Requirements for the NASS

The required stroke for the NASS should correspond to the maximum global positioning error of the end station without the NASS. This has been estimated to be around 10 μm in translations. This value will be confirmed as soon as full tests of the micro-station will be finalized.

Then, the minimum repeatability of the NASS is determined by the global specifications (Table 1). The requirements obtained for the NASS are shown Table 2.

Other requirements such as stiffness and dynamical properties will be determined using the model presented below.

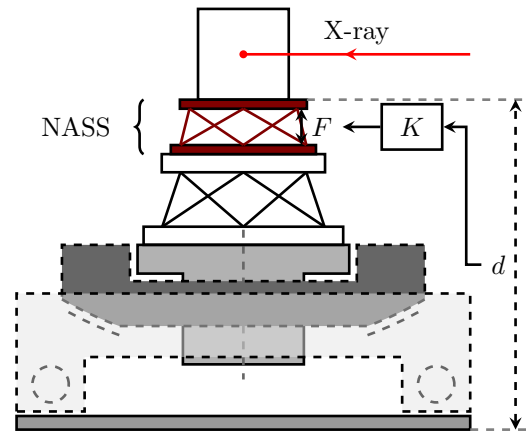


Figure 4: Schematic representation of the NASS added below the sample and the control architecture used.

Table 2: Rough Estimation of the NASS Specifications

Motion	Stroke	Repeatability
T_{xyz}	$\pm 10 \mu\text{m}$	10 nm
θ_{xyz}	$\pm 10 \mu\text{rad}$	1.7 μrad

Model Based Design

Such positioning system with multiple stages is highly coupled and presents many physical effects such as wobble that are difficult to model with a simple model based on measurements. Therefore, we have chosen to develop a 3D finite mass model. The software used is Simscape which is a toolbox for modeling multidomain physical systems within the Simulink environment.

Each stage is represented as a 3D rigid body connected with the other stages by joints. Springs and dampers are added to take into account the finite stiffness of the mechanical guidance. Actuators and sensors dynamics are also included in the model. Finally, sources of perturbation and noise such as ground motion and sensor noise are also modeled.

Thanks to the individual identification of each stage, stiffness and damping representing the flexibilities can be tuned properly.

This model has numerous utility. First, it allows to conduct simulations of experiments such as tomography. That will help us to attest the performances of the system and compare various control architecture. Second, it permits to study the effect of the sample mass on the mechanical behavior of the system and verify the robustness properties of the controlled system. Finally, this model will be of great help for designing the NASS. Indeed, many parameters have to be properly chosen such as geometric configuration, leg stiffness, actuator type and rotational joints.

In the following, the NASS is modeled as a Stewart platform with a cubic configuration, voice coil linear actuators and ideal rotational joints.

RESULTS

Plant Identification

Various transfer functions of the system can be identified using the model. The most important one for control is G which is the transfer function from a force applied by the NASS to the measurement of the sample displacement. This represent the transfer function from F to d on Fig. 4.

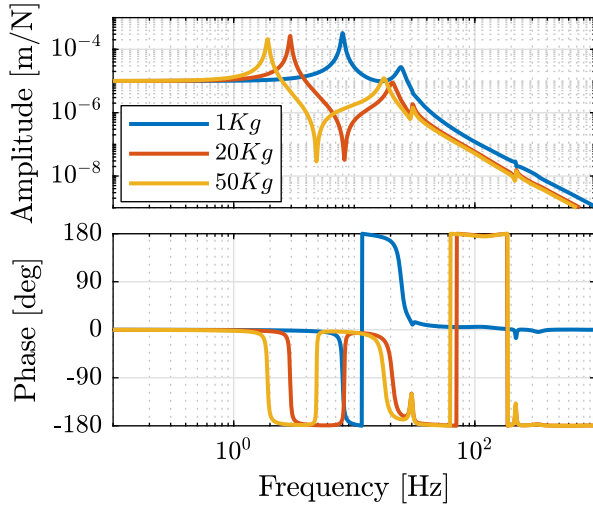


Figure 5: Transfer function from a force applied by the NASS in the x direction to the sample displacement with respect to the granite in the x direction. This is shown for 3 values of sample mass.

As the measurement and the force applied by the NASS are in 6DoF, G is a 6 by 6 transfer function. Figure 5 represents the bode diagram of the first element of G for 3 values of the sample mass. It shows that the sample mass has an important impact on the dynamic of the system and it confirms that we will have to be very cautious about the robustness of the controlled system.

Control Synthesis

In order to control such a system, we choose to start with a simple centralized feedback control as shown Fig. 6. The controller takes the signal of the metrology system in 6DoF and generates the forces applied by the NASS in 6DoF. It has therefore 6 inputs and 6 outputs and contains 36 elements. We first choose to only have diagonal elements in the controller has a decoupling compensator has been used. Tanks to that, each diagonal element can be tuned separately.

A typical loop gain obtained for the x direction is shown Fig. 7. An integral action is added at low frequency to have no static error, and a lead is added near the crossover frequency to add some phase margin. A pole is further added in high frequency to reduce the effect of noise (not shown).

Tomography Experiment

In order to test the performances obtained with the current controlled system, a simulation of a tomography experiment

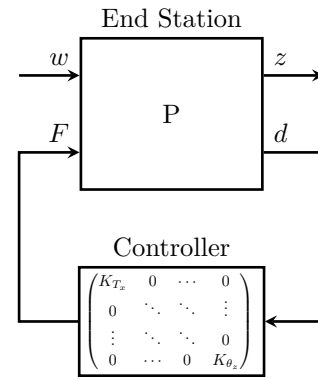


Figure 6: General control configuration applied to the end station. P represents the model developed of the end station. w represents the exogenous inputs such as ground motion and sensor noise, d the 6DoF measurement, F the 6DoF forces applied by the NASS and z the exogenous output that we want to minimize.

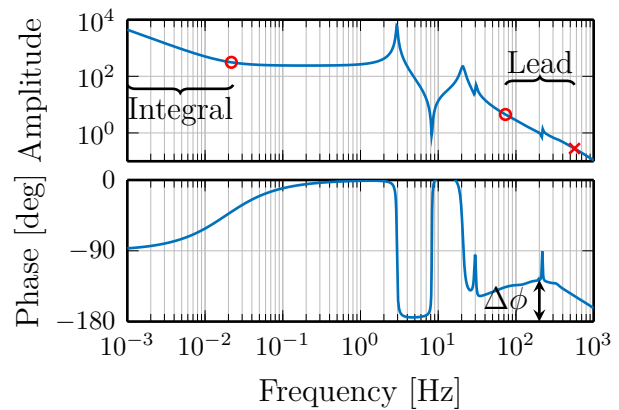


Figure 7: Bode plot of the loop gain for the control in x direction. The red circles and the red crosses represent respectively the zeros and poles of the controller. $\Delta\phi$ represents the phase margin.

is conducted. The rotation speed of the spindle is set to $\dot{\theta}_z = 30rpm$, the mass of the sample is chosen to be $M = 20$ kg, and ground motion is taken into account.

The result is shown Fig. 8. The blue and the red curves represent the $x - y$ motion of the sample for the positioning system respectively without the NASS (corresponding to the Fig. 1) and with the NASS (corresponding to the Fig. 4).

The residual motion of the sample when using the NASS is less than 50 nm in the xyz directions.

CONCLUSION

A high precision and versatile positioning platform has been presented. In order to obtain nanometer precision, a Stewart platform based stabilization system (the NASS) is proposed. A 3D finite mass model has been developed to test such stabilization system. It has been showed that even with a simple control architecture, the parasitic motions of the sample can be reduced down to 50 nm.

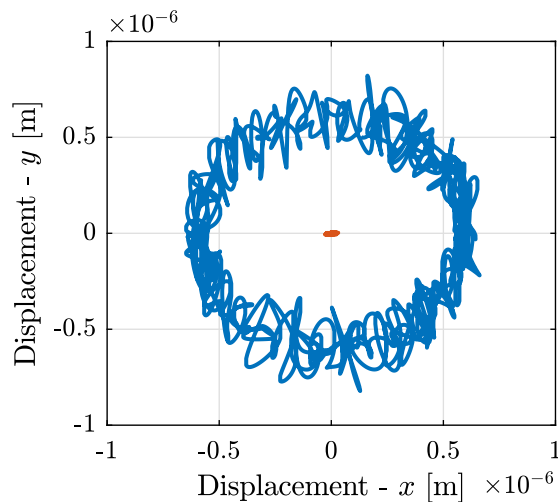


Figure 8: Positioning error of the sample in the x and y direction during the simulation of a tomography experiment. The blue curve correspond with the ID31 without the NASS and the red curve with the NASS added. The sample used has a mass $M = 20$ kg and the rotational speed is $\dot{\theta}_z = 30$ rpm.

These type of stabilization platform associated with a precise 6 DoF metrology system could be used for many other positioning systems.

To further improve the performance of the system, many control architecture could be developed such as a hybrid feedback-feedforward control or HAC-LAC feedback control. Moreover, to address the robustness issue, control techniques such as \mathcal{H}_∞ loop-shaping and μ -synthesis would be of great help.

ACKNOWLEDGMENTS

This research was made possible by a grant from the ESRF. We thank the following people for their support, without

whose help this work would never have been possible: V. Honkimaki, A. Jublan, L. Ducotte, C. Carole, M. Brendike and M. Lessourd and the whole team of the Precision Mechatronic Laboratory.

REFERENCES

- [1] Gema Martinez-Criado *et al.*, “ID16B: a hard X-ray nanoprobe beamline at the ESRF for nano-analysis”, *Journal of synchrotron radiation* 23, Jan. 2016, pp. 344–352. doi: 10.1107/S1600577515019839.
- [2] L Ducotte *et al.*, “The new ID11 nanoscope end-station - a nanotomography scanner”, presented at MEDSI’16, Barcelona, Spain, Sept. 2016, unpublished.
- [3] M Ogurreck *et al.*, “The nanotomography endstation at the PETRA III imaging beamline”, *Journal of Physics: Conference Series*, vol. 425-18, 2013, doi: 10.1088/1742-6596/425/18/182002.
- [4] J.E. McInroy, “Dynamic modeling of flexure jointed hexapods for control purposes”, in *Proc. of the 1999 IEEE International Conference On Control Applications, Kohala Coast, Hawaii, USA, 1999*, pp. 508–513. doi: 10.1109/CCA.1999.806694.
- [5] John E. McInroy and Jerry C. Hamann, “Design and control of flexure jointed hexapods”, *IEEE Transactions on Robotics and Automation*, vol. 16.4, 2000, pp. 372–381, doi: 10.1109/70.864229.
- [6] Zheng Geng and Leonard S Haynes, “Six-degree-of-freedom active vibration isolation using a stewart platform mechanism”, *Journal of Robotic Systems*, vol. 10.5, 1992, pp. 725–744, doi: 10.1109/87.273110.
- [7] A. Preumont *et al.*, “A six-axis single-stage active vibration isolator based on Stewart platform”, *Journal of Sound and Vibration*, vol. 300, 2007, doi: 10.1016/j.jsv.2006.07.050.

HIGH-ACCURACY SMALL ROLL ANGLE MEASUREMENT METHOD BASED ON DUAL-GRATING DIFFRACTION HETERODYNE INTERFEROMETER*

S. Tang^{†, 1, 2}, M. Li^{†, 1, 2}, H. Liang¹, W. Sheng^{1, 2}, J. Yang², Beijing Synchrotron Radiation Facility,
 Institute of High Energy Physics, Beijing 100049, P. R. China

¹also at Laboratory of X-ray Optics and Technology, Institute of High Energy Physics,
 Beijing, P. R. China

²also at University of Chinese Academy of Sciences, School of Physics, Beijing, P. R. China

Abstract

Small roll angle (ROLL) is a crucial parameter for the motion performances of ultra-precision guide way often applied in fine mechanics and instruments of synchrotron radiation, such as long trace profiler (LTP). However, it is difficult to be measured by conventional methods including interferometer and autocollimator owing to their low sensitivities in axial direction. There is an orthogonal dilemma between measured direction and angular displacement plane for ROLL measurement. Therefore, a novel method based on dual-grating diffraction heterodyne interferometer is presented, which uses the combining scheme of diffraction grating and heterodyne interferometer to overcome the orthogonal problem. Moreover, the design of differential structure with dual-grating and grating interferometer instead of pure interferometer is adopted to improve the practicability against the environment, e. g. air fluctuation, inconstant rotation centre. It has inherited advantages of high-resolution up to 2nrad, high sampling rate up to 50kHz, and contactless by mathematical model and analysis. So, theoretical and experimental verifications are both implemented to its validation.

INTRODUCTION

Nano-radian accuracy small roll angle (ROLL) measurement method would be very urgent for the ultra-precision optical metrology and precision instrument [1-5], especially, long trace profiler (LTP). It will be benefit the development of two-dimensional LTP used for the test of X-ray mirrors. Besides, the ROLL is also important issue in the field of the industries, such as Numerical Control (NC) machine tools, Coordinate measuring machines (CMM), advanced manufacturing technology, and precision motion engineering. No matter which field, there is indeed a common technique which is application of precision linear motion guideway pair. But, it is very difficult to achieve high-performance measurement for the ROLL, especially field testing. Because the orthogonal problem of Roll displacement plane and linear motion direction of the

guideway disables the typical methods of interferometer and autocollimator, compared with pitch or yaw measurement, as shown in Fig. 1.

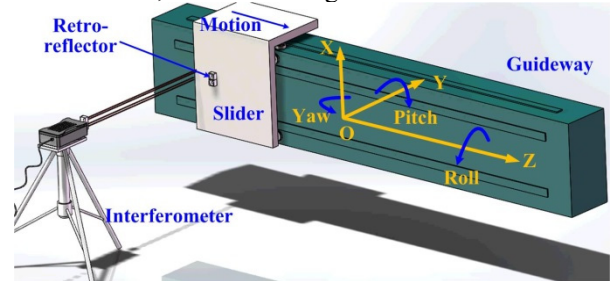


Figure 1: The diagram of angle deviations of the guideway.

So, there are exploration researches on it, such as:

- 1) Polarization detecting based on interferometry, including intensity [6, 7] and phase sensing [8-15].
- 2) Using special shape component based on interferometry, such as using wedge prism and its derivative [16, 17].
- 3) Geometrical transfer test using position sensitive detector (PSD) [18-20].
- 4) Synthetization of other optical methods [21-24], such as grating interferometer for ROLL measurement.

And there are maybe other instruments like level meter or inclinometer. They are all proved the progress in laboratory. However, there is a little far way for practical application, especially, ROLL compensation of LTP and 3-axis NC machine tools or CMM. In this paper, a synthetization dual-grating heterodyne interferometric ROLL measurement method is presented, which uses grating for overcoming the orthogonal problem and heterodyne interferometer for high-accuracy, good stability, high-sampling rate.

CONFIGURATION AND MATHEMATICAL MODELING

As show in Fig. 2, the configuration of proposal method is composed of dual-frequency laser measuring head, polarizing beam splitter (PBS), right-angle prism (RAP), dual-grating, and dual-retroreflector (using RAPs), etc.

A beam emitted by the dual-frequency laser measuring head, containing two orthogonal linear polarized compounds with a stable frequency difference of ~3 MHz, which is split into two beams (called P-beam and

* Work supported by National Natural Science Foundation of China (NSFC) (No. 61505213).

† email address: Shanzhit@gmail.com and lim@ihep.ac.cn.

S-beam) by PBS. The P-beam transmits the PBS and one of the dual-grating with diffractions. Its +1 order diffractive beam with a normal incidence is reflected by one of the dual-retroreflector, which transmits the grating and occur diffraction again. The +1 order beam of the second diffraction transmits the PBS, is lastly received by the laser head. This beam is considered as the measuring beam of heterodyne interferometer. The S-beam is reflected by the PBS and RAP, transmit the other of dual-grating with diffractions. Similarly, the +1 order diffractive beam reflected by the other of the dual-retroreflector, and return parallel to the incident beam, successively transmits this grating and rebounded by RAP and PBS to arrive at the laser head. The S-beam considered as the reference beam of heterodyne interferometer. Then, the two beams of measuring and reference have the interference which beat frequency regarded as measuring signal. It is used for getting difference by using reference beat signal offered by the laser head.

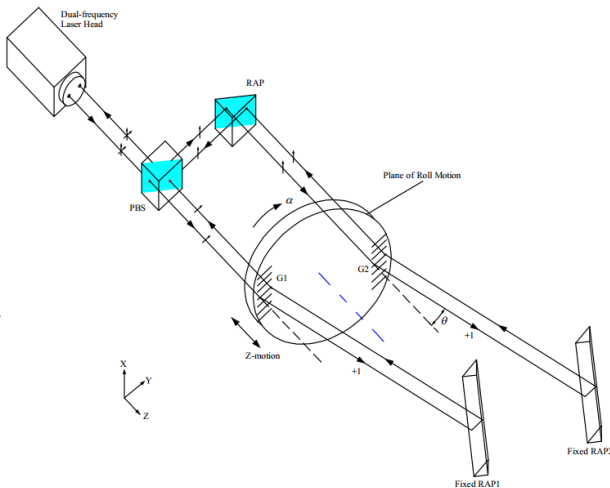


Figure 2: The principal diagram of the proposal method.

Thus, the mathematical model can be rigidly derived as follow.

For +1 order beam of the first diffraction of the measuring beam, and the grating equation is expressed as:

$$d \sin \theta = \lambda \quad (1)$$

Where, d means the grating constant or grating pitch; θ means the diffractive angle of the +1 order beam; λ means the wavelength of the laser.

Similarly, Eq. (1) is still applicable to the second diffraction of the measuring beam.

The slight arc displacement of the grating can be approximate to linear when the target has a motion with ROLL, which causes the Doppler frequency shift of the measuring beam. Due to the superimposed effect of the first and second the frequency shifts for two diffractions respectively. So, it can be expressed as:

$$\Delta f_M = \frac{2V_M}{\lambda} \cos\left(\frac{\pi}{2} - \theta\right) \quad (2)$$

Where, Δf_M means the total Doppler shift of the measuring beam; V_M means the velocity of the grating for the measuring beam.

From Eq. (1) and (2),

$$\Delta f_M = \frac{2V_M}{d} \quad (3)$$

For the reference beam, it can be similarly expressed as:

$$\Delta f_R = \frac{2V_R}{d} \quad (4)$$

Where, Δf_R means the total Doppler shift of the reference beam; V_R means the velocity of the grating for the reference beam.

From Eq. (3) and (4), the difference of the measuring and reference beams can be obtained as:

$$\Delta f = \Delta f_M - \Delta f_R = \frac{2}{d}(V_M - V_R) = \frac{2}{d}V \quad (5)$$

Where, Δf means the difference of the Doppler shifts of the two beams; V means the relative velocity of the two gratings each other.

Eq. (5) can be also written as:

$$V = \frac{d}{2} \Delta f \quad (6)$$

By time integral on the both sides of Eq. (6),

$$s = \int_0^T V \cdot dt = \frac{d}{2} \cdot \int_0^T \Delta f \cdot dt \quad (7)$$

Where, s means the relative displacement of the two gratings each other; t and T mean the time variable and particular time respectively.

Equation (7) reveals a grating interferometer for the measurement of the roll angular displacement with a natural resolution of $d/2$, which is similar to the pure optical displacement interferometer.

By the geometrical relationship, the ROLL is expressed as:

$$a = \frac{s}{L} = \frac{d}{2L} \cdot \int_0^T \Delta f \cdot dt \quad (8)$$

Where, a means the ROLL under test; L means the distance of the two gratings.

Therefore, the final measuring model is shown as Eq. (8). It inherits many advantages from the interferometer, such as high-accuracy, real-time, high sampling-rate, and so on.

THEORETICAL ANALYSIS

According to Eq. (8), there are two factors deciding the resolution of the ROLL measurement: one is the displacement measurement resolution based on the grating interferometer. The other is the distance of the two gratings, whose increase will enhance the final angle measurement resolution.

Apparently, the performance of the displacement grating interferometer is crucial for the ROLL test. We know, it is not enough for the high accuracy due to the nature resolution of $d/2$, which needs many subdivision techniques for higher resolution. Its resolution can be

up to d/λ nano-meter or better if using by the same with electronic subdivision technique of the typical Michelson interferometer with 1nm resolution. So, the ROLL measurement resolution can be expressed as,

$$a_r = \frac{s_r}{L} = \frac{d}{\lambda L} \quad (9)$$

Where, a_r and s_r mean the resolutions of the ROLL with the unit of nano-radian and displacement measurements with the unit of nano-meter respectively. And L has the unit of meter.

From the geometrics as shown in Fig. 2,

$$\sin \theta = \frac{H}{D} \quad (10)$$

Where, H means the height of the RAP1 or RAP2; D means the maximum of linear displacement of the object under test.

From Eqs (1) and (10),

$$\sin \theta = \frac{H}{D} = \frac{\lambda}{d} \quad (11)$$

By the substitution of Eq.(11) into Eq.(9),

$$a_r = \frac{d}{\lambda L} = \frac{D}{HL} \quad (12)$$

Equation (12) implies that decrease of the grating constant d is an effective approach to enhance the test resolution when the wavelength λ is known (e.g. 633 nm), accordingly, the H should be expected to be increased unlimitedly for a better resolution. But the way will be restricted by the geometric dimension of the RAP (H) due to fabricating techniques. So, the resolution a_r should be optimized by feasible choice of H and D to match a better grating constant d .

For the conditions of $\lambda = 633\text{nm}$, $L = 1000\text{mm}$, $H = 500\text{mm}$, the theoretical resolution is up to 2nrad for the range of $D = 1000\text{mm}$ if the grating constant is 1.266 μm . Admittedly, the surface error will introduced a measurement uncertainty of several nrad if the height error is several nm because of beam moving on the optical surface of the RAP. But, it can be reduced or eliminated by the mapping the error.

EXPERIMENT

As shown in Fig. 3, a based-heterodyne interferometer test setup is built for the experimental verification, which consists of laser head of 5519A (Agilent, He-Ne laser with 633nm), PBS, Mirror, Gratings with 300 lines/mm (Thorlabs), and home-built RAPs with a length of 200mm. Additionally, a tilt stage with a scale is employed to implement ROLL motion on the guideway. The indicating values of the tilt stage are regarded as nominal ROLL though its resolution is not high. Correspondingly, the values of the proposal method are test values.

Before the test, the key systematic parameter, the distance of two gratings L , was accurately given by the angle calibration, which is equal to 96.20 mm. So, the resolution of the ROLL test system can be obtained as

55 nrad (0.01 arcsec) by the substitution of the parameters of λ , d , and L into Eq. (12).

Then, the ROLL tests are implemented for feasible validation in the common experimental room. By the measurement of many nominal ROLLs with bi-direction variable, the comparison results can be achieved as shown as in Fig. 4. Whether positive stroke or negative stroke of the tilt or ROLL motion, testing and nominal values coincide each other. The standard deviation of the two values between the proposal and tilt stage is 94.96 arcsec, but the average of relative errors of each point is 0.052%, and its standard deviation is also calculated, which is 0.069%.

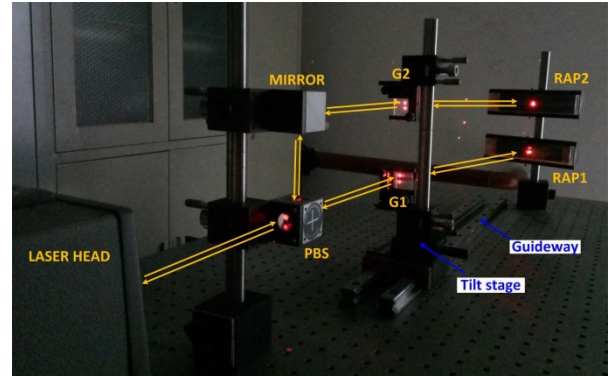


Figure 3: The prototype of the test setup based on the proposal method.

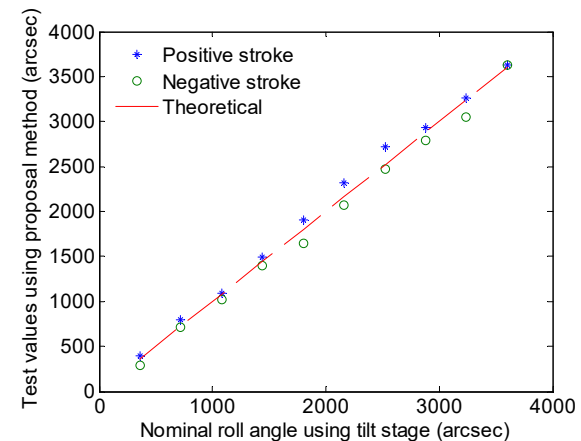


Figure 4: The results of the ROLL test.

Admittedly, the accuracy of the contrast could be much better if using a higher performance angle measurement instrument or comparator. However, it is indeed feasible for dual-grating heterodyne interferometric ROLL measurement method. Furthermore, it inherits lots of merits from pure Michelson displacement/angle interferometer, such as high-sampling rate. Figure 5 shows that the test curve of step-manual ROLLs using the proposal with simpling rate of 100Hz, which monitor the whole the motion process of the ROLL including the detailed step during the time of 500s. So, it features real-time and dynamical performance.

Actually, it is simple, in which the dual-grating just moves with the motional target under test, and other components all keep static. The procedures and configurations look like the straightness test based on the commercial laser interferometer. Therefore, it is high-accuracy, very simple and stability.

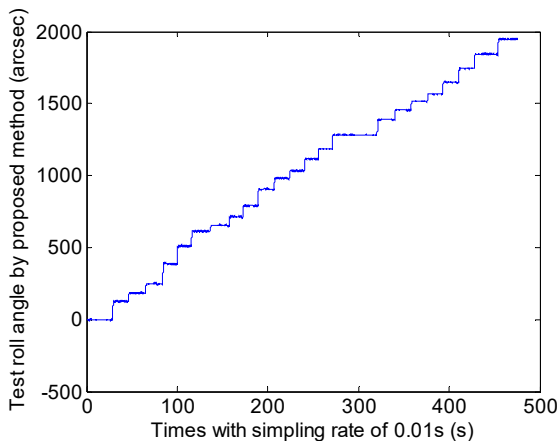


Figure 5: The test curve of step-manual ROLLs using the proposal with sampling rate of 100Hz.

CONCLUSION

A synthetization method for ROLL measurement based on dual-grating diffraction heterodyne interferometer has been presented and discussed in this paper. Both of theoretical model and experimental verification are implemented to validate the performance including high-resolution, high-sampling rate, and good operation of the proposal method. In a word, it offers a feasible and effective approach for ROLL monitoring and compensation for the R & D of advanced LTP, advanced manufacturing technology, and other relative fields.

ACKNOWLEDGEMENT

This research is supported by National Natural Science Foundation of China (NSFC) (No. 61505213).

REFERENCES

- [1] F. Siewert *et al*, “Ultra-precise characterization of LCLS hard Xray focusing mirrors by high resolution slope measuring deflectometry”, in *Opt. Express*, vol. 20, no. 4, pp. 4525-4536, 2012, doi: 10.1364/OE.20.004525.
- [2] S. Tang *et al*, “Error analysis of a plane mirror interferometer based on geometric optical paths”, in *Opt. Express*, vol. 25, no. 5, pp. 5108-5118, 2012, doi: 10.1364/OE.20.005108.
- [3] S. Tang *et al*, “Influence of tilt on collinear calibration of a laser interferometer”, in *Appl. Optics*, vol. 52, no. 4, pp. B46-B51, 2013, doi: 10.1364/AO.52.000B46.
- [4] S. Tang *et al*, “Influences of misalignments on circular path measurement based on dual-beam plane mirror interferometer”, in *Optik*, vol. 124, no. 20, pp. 4576-4580, 2013, doi: 10.1016/j.ijleo.2013.01.074.

- [5] L. Huang *et al*, “One-dimensional angular-measurement-based stitching interferometry”, in *Opt. Express*, vol. 26, no. 8, pp. 9882-9892, 2018, doi: 10.1364/OE.26.009882.
- [6] E Shi *et al*, “Theoretic study on new method for roll angle measurement of machines”, in *Proceedings of International Conference on Automation and Logistics, ICAL*, Qingdao, China: IEEE, 2008, pp. 2722-2726, doi:10.1109/ICAL.2008.4636635.
- [7] P. Zhang *et al*, “Measuring roll angle displacement based on ellipticity with high resolution and large range”, in *Opt. Laser Tech.*, vol. 65, pp. 126-130, 2015, doi: 10.1016/j.optlastec.2014.06.011
- [8] H. Jiang, C. Yin, “Sensitivity enhanced roll angle measurement”, in *Opt. Eng.*, vol. 39, no. 2, pp.516-519, 2000, doi: 10.1117/1.602390.
- [9] Z Liu *et al*, “Roll angle interferometer by means of wave plates”, in *Sensor and Actuators A*, vol. 104, pp. 127-131, 2003, doi: 10.1016/S0924-4247(03)00003-7.
- [10] C. M. Wu, Y. T. Chuang, “Roll angular displacement measurement system with microradian accuracy”, in *Sensor and Actuators A*, vol. 116, pp. 145-149, 2004, doi: 10.1016/j.sna.2004.04.005
- [11] R. C. Twu *et al*, “A single-beam probe method for roll angle measurement”, in *Proceedings of 2nd International Conference on Photonics, ICP*, Kota Kinabalu, Sabah, Malaysia: IEEE, 2011, doi: 10.1109/ICP.2011.6106881.
- [12] S. Tang *et al*, “Note: A small roll angle measurement method with enhanced resolution based on a heterodyne interferometer”, in *Rev. Sci. Instrum.*, vol. 86, no. 9, p. 096104, 2015, doi: 10.1063/1.4930241.
- [13] S.Tang *et al*, “Note: Optimal choice of the reflector by phase analysis for heterodyne interferometric roll angle measurement”, in *Rev. Sci. Instrum.*, vol. 87, no. 2, p. 026101, 2016, doi : 10.1063/1.4940985.
- [14] J. Qi *et al*, “Note: Enhancing the sensitivity of roll-angle measurement with a novel interferometric configuration based on waveplates and folding mirror”, in *Rev. Sci. Instrum.*, vol. 87, no. 3, p. 036106, 2016, doi: 10.1063/1.4943297.
- [15] J.Qi *et al*, “Resolution-enhanced heterodyne laser interferometer with differential configuration for roll angle measurement”, in *Opt. express*, vol. 26, No. 8, pp. 9634-9644, 2018, doi : 10.1364/OE.26.009634.
- [16] A. Ju, W. Hou, Y. Le, “Enhanced roll-angle measurement interferometer”, in *Opt. Eng.*, vol. 54, no. 3, p. 034101, 2015, doi: 10.1117/1.OE.54.3.034101.
- [17] T. Jin *et al*, “High resolution and stability roll angle measurement method for precision linear displacement stages”, in *Rev. Sci. Instrum.*, vol. 88, no. 2, p. 023102, 2017, doi: 10.1063/1.4974816.
- [18] Y. Zhu *et al*, “Roll angle measurement based on common path compensation principle”, *Opt. Eng.*, vol. 67, pp. 66-73, 2015, doi: 10.1016/j.optlaseng.2014.11.006.
- [19] Y. Zhai *et al*, “A high-precision roll angle measurement method”, in *Optik*, vol. 126, no. 24, pp. 4837-4840, 2015, doi: 10.1016/j.ijleo.2015.09.049.
- [20] W. Li *et al*, “Roll angle measurement with a large range based on the photoelectric autocollimator”, in *Optoelectronics Letters*, vol. 12, no. 1, pp. 0074-0076, 2016,

doi: 10.1007/s11801-016-5213-4.

- [21] S. Tang *et al*, “Measurement method for roll angular displacement with a high resolution by using diffraction gratings and a heterodyne interferometer”, in *Rev. Sci. Instrum.*, vol. 85, no. 4, p. 045110, 2014, doi: 10.1063/1.4870904.
- [22] H. L. Hsieh, S. W. Pan, “Development of a grating-based interferometer for six-degree-of-freedom displacement and angle measurements”, in *Opt. Express*, vol. 23, no. 3, pp. 2451–2465, 2015, doi: 10.1364/OE.23.002451.
- [23] X. Yu *et al*, “Moiré fringe method for roll angular displacement measurement”, in *Proc. SPIE*, Vol.9677, 2015, pp. R-1~5, doi: 10.1117/12.2199823.
- [24] Y. P. Kumaar, S. Chatterjee S. S. Negi, “Small roll angle measurement using lateral shearing cyclic path polarization interferometry”, in *Appl. Opt.*, vol. 55, No. 5, pp. 979-983, 2016, doi: 10.1364/AO.55.000979.

THE DESIGN OF EXACTLY-CONSTRAINED X-RAY MIRROR SYSTEMS FOR SIRIUS

R. R. Galdes, G.V. Claudiano, L.M. Volpe, M. S. Souza, A. Sikorski, V. Z. Ferreira, L. Sanfelici, H.C.N. Tolentino, H. Westfahl Jr., Brazilian Synchrotron Light Laboratory (LNLS), Brazilian Center for Research in Energy and Materials (CNPEM), 13083-970, Campinas, Sao Paulo, Brazil.

Abstract

The first set of Sirius beamlines is expected to start operating in early 2019. Regarding X-ray mirror systems, a single design concept has been possible thanks to the standardization of side-bounce fixed-shape mirrors. To preserve the extreme quality of both the mirror figures and the source, the main design targets were minimizing mechanical and thermal distortions in the mirrors while maximizing mechanical and thermal stabilities. A deterministic high-resolution exactly-constrained flexure-based mirror support provides pitch tuning within 100 nrad and resonances above 150 Hz, while dealing with clamping and thermal expansion effects. The adopted cooling strategy was indirect cryocooling via cryostats, drastically minimizing thermal gradients and distortions in the mirrors, decoupling vibration sources and simplifying cooling circuits. Finally, a 5-degree-of-freedom granite bench, based on high-resolution levellers and air-bearing solutions, support the vacuum chamber, on which the internal mechanics is stiffly mounted. The specifications, design and partial results are presented.

INTRODUCTION

The design of mirror systems is one of the most revisited topics in beamline designs, since ever-increasing power management and figure error requirements continuously drive either innovative or optimized concepts, particularly for cooling and figure shaping [1–6]. For many solutions, however, it is often unclear how complex mechanics and cooling schemes may limit performance either in terms of slope errors or mechanical stability.

To comply with height and slope budget errors as low as a few nanometers and tens of nanoradians, respectively, Sirius X-ray mirrors were standardized in fixed-figure configuration, thus preventing the use of benders. Next, looking forward to superior passive mechanical stability, the decision for side-bounce deflection standardization was made. These two conditions, together with generally low absorbed power levels, i.e. below 50 W, have created the opportunity for the development of an alternative standard design for mirror systems, as illustrated in Fig. 1.

From the experience gained with the High-Dynamic Double Crystal Monochromator (HD-DCM) [7], deterministic design concepts have been applied to seek simple yet accurate and highly-stable thermo-mechanical solutions. Details about the vacuum vessel, cryocooling scheme based on cryostats and cooling braids, fixation of the mirrors and internal mechanics are given in the following sections. More information about the granite bench and the

designing process for the mirrors are found in [8] and [9], respectively.

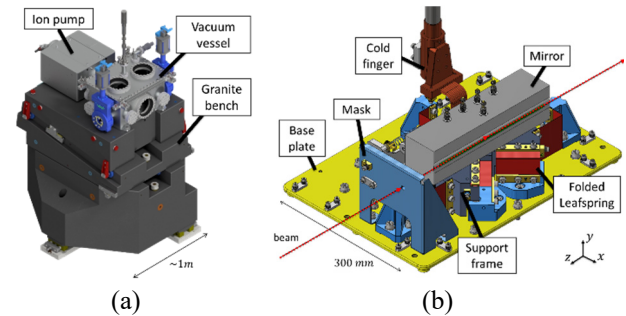


Figure 1: Example of the new standard mirror systems for Sirius X-ray beamlines. (a) Vacuum vessel on granite bench; (b) mirror mounted to fine-tuning mechanism.

CONCEPTUAL DESIGN

The concept of the mirror systems was, from the very beginning, based on a few deterministic design guidelines. From the bottom to the top, the mirrors should be built on highly stable granite benches, having only as many of degrees of freedom (DoF) as those necessary for positioning and alignment at the beamline [8]. Then, as approached in the HD-DCM, the vessel should be treated as an interface between the mirror and the bench, and by no means as a reliable and stable mounting structure in itself. Next, the mirrors should be deterministically fixed to an UHV-compatible high-resonance-frequency fine-tuning mechanism, which should be directly mounted to the vessel to benefit from the high stiffness of the bench. Finally, mechanically complex colling schemes should be avoided. Then, gathering the specifications, error budgets and alignment requirements for the mirrors of the first set of Sirius X-ray beamlines, common ground could be defined for the development of standard systems. The summarized specs are gathered in Table 1.

Table 1: X-ray Mirror Systems Summarized Specs

Description	Spec
Ry range:	> 1 mrad
Ry resolution:	< 100 nrad
Ry stability:	< 30 nrad RMS _{2.5kHz}
Resonances:	> 150 Hz
Thermo-mechanically induced slope errors:	< 50 nrad
Power load:	< 50 W
Cooling scheme:	indirect cryocooling via copper braid and cryostat

Vacuum Vessel

The vacuum vessel module is depicted in Fig. 2. The stainless-steel vessel consists of a main square-shaped box and a top flange, sealed by means of aluminium wire. In the main vessel, all the required electrical feedthroughs for the motors, encoders, temperature sensors and heaters used in the internal mechanism are available, so that the mirror can be functionally tested before the lid is put on. It also has ports for: the entrance and exit of the beam (both with gate valves); viewports, which are also used for accessibility during assembly and maintenance; the standardized 600 L ion pump; vacuum sensors; and venting valves. The top flange hosts the cryostat port and auxiliary viewports.

A few key design choices regarding the chamber were made to improve the overall mechanical stability of the assembly. Firstly, benefiting from some torsional compliance of an open box, four contact pads are machined at the outer limits of the bottom surface of the vessel to deterministically define the mounting points on the granite. Thus, fixation lever-arms and, consequently, the rotational vibration modes of the chamber can be maximized. The preload is made through four bolts in extended ears in the bottom flange. Then, to optimize the stiffness chain between the internal mechanism and the granite by preventing excessive bending of the vessel's bottom flange due to the vacuum forces (and a possible loss of contact with the granite), a central pad is also machined in the center of the bottom surface and is preloaded against the granite by means of a SMW workpiece positioning system. Finally, the suspension frequency of the ion pump is also optimized by a stiff pre-loaded connection to the granite.

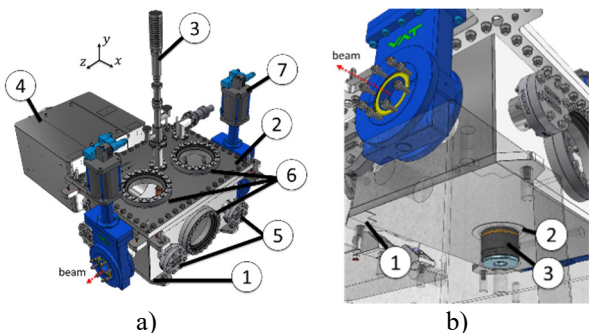


Figure 2: (a) Isometric view of vessel module: (1) main vessel, (2) top flange, (3) cryostat, (4) ion pump, (5) electrical feedthroughs, (6) viewports and (7) gate valves. (b) Isometric view through transparent granite, highlighting the outer (1) ($\times 4$) and central (2) contact pads, and the workpiece positioning system embedded in the granite (3).

These choices make in-situ baking a potential problem, due to temperature limits and thermal expansion effects between the vessel and the granite. In addition to that, designing the internal mechanism to allow for both low and high temperature ranges would offer additional limitations in terms of stresses. Finally, decoupling the vessel from the granite for baking might lead to alignment issues. All considered, in-situ baking was considered a disadvantageous option. Therefore, to complement pre-assembly baking of

the parts, a hot-nitrogen purging system is currently under development for in-situ pumping improvement.

Mirror Fixation

To achieve high-stability performances without active dynamic stabilization, two basic approaches are mitigating disturbance sources and designing for high-frequency resonances. For the mirrors: the first is obtained by decoupling the cooling source via braids; whereas the latter depends on materials and design. Practical limitations are given by the compromise between high clamping forces for high contact stiffness and the introduced stresses and deformations, which might spoil mirror figures.

For the HD-DCM, a three-point flexure-based solution for fixing the crystals with deterministic mechanical and thermal performance was implemented [10]. There, dynamic coupling above 1 kHz was achieved, while dealing with thermal expansion effects between the crystals and their supports for temperature differences as high as 100 K. Hence, a similar solution was considered for the mirrors, as shown in Fig. 3.

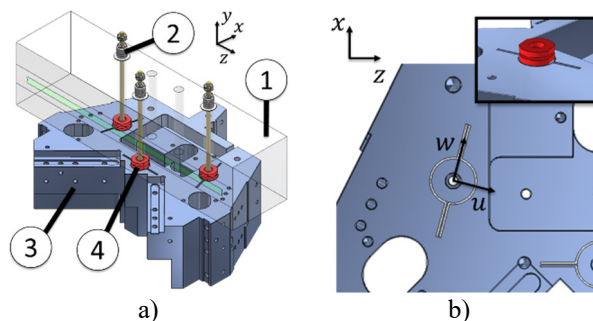


Figure 3: Mirror fixation concept with flexures and flexural hinges: a) isometric view of the assembly: (1) mirror (transparent for visualization), (2) threaded rods, (3) support frame and (4) hinges; b) top view of one of the flexures, indicating its local coordinate system (uwy), and inset with hinge.

Regarding thermal effects, the three flexures machined in a support frame create a thermal center with respect to which the optics may deterministically shrink or expand. Although this concept alone was enough for the crystals in the HD-DCM, the extreme error budget requirements of the mirrors led to the development of an additional elastic layer. Indeed, since each flexure has one weak translation (u) and one weak rotation (R_w), but high stiffness in all other directions, machining height and flatness limitations in the contact surfaces of the support and the mirror would lead to bending moments and, consequently, unacceptable deformations in the mirrors. This problem was reduced by adding flexural hinges between the mirror and the flexures, having the compliant rotation of the hinge (R_u) perpendicularly aligned to the compliant rotation of the flexure. Thus, a spherical joint is emulated in each contact region and a *quasi*-kinematic mount is achieved.

Naturally, if compared to the crystals in the HD-DCM, lower modes can be expected, due to the much larger masses of the mirrors and limitation in clamping forces. Nonetheless, modes above 200 Hz are typically feasible, provided that the fixation points in the mirror are properly

chosen. As for preload and the connection to the cooling braids, controlled nearly-constant forces can be applied via threaded rods and proper arrangements of spring-washers.

Internal Mechanics

Considering that all the necessary DoF of the mirrors should be covered by the granite bench, the internal mechanics may simply provide a few high-resolution DoF with enough range to complement that of the bench when necessary. Thus, after the development of the HD-DCM, the possibility of designing short-range mechanisms for mirrors based on folded leafsprings (FLS) was very appealing due to several reasons.

Firstly, clean, high-resolution, high-repeatability and nearly frictionless mechanisms are possible. Secondly, as FLS constrain a single DoF [11], not only is it relatively simple to add or remove DoF, but also the support frame of the mirror may be exactly-constrained, preventing bending moments and deformations from connections with other parts, which would be, otherwise, propagated to the mirror to some extent. In addition to that, a thermal center can be designed for the support, so that its working temperature may have much more design flexibility while thermal expansions are conveniently handled. In that sense, another advantage is that FLS may also work as an efficient thermal isolation layer between parts at different temperatures. Moreover, they do not present shortening effects, as many flexural options do, so that parasitic effects can be reduced.

Another key advantage in this concept is that through careful design the mechanism stiffness in different axes can be optimized so that the driving forces can be significantly reduced. This not only expands the range of actuation options, allowing for simple and cost-effective piezowalkers, for instance, to be selected, but also paves the way for dynamic mirror systems, if active mirrors are to be developed for improved stability or scanning performance. In fact, a scanning Kirkpatrick Baez (KB) system is already envisioned for Sirius CARNAUBA beamline. So, within this conception the resolution is simply defined by the actuator resolution and/or the actuation lever-arm; the range, by the driving force capacity, or ultimately by the stresses in the FLS; whereas linearity, repeatability and parasitic motion are direct outputs of the concept and its realization.

Figure 4 shows the proposed internal mechanism for the first mirror of CATERETE beamline: CAT-1-VFM. The fine pitch (R_y) DoF is implemented by means of: three vertically-oriented FLS, constraining the vertical translation T_y , and the two rotations R_x and R_z ; and two horizontally-oriented FLS, constraining the two horizontal translations T_x and T_z , and defining the rotation axis and the thermal centre of the mechanism. The actuation is made with a linear piezo-walker actuator preloaded by a spring. The selection of this low-cost actuator was driven by resolution, force, range, control options, volume, UHV compatibility and cost. Comparing piezo-walker and piezo-stack actuators, for example, the first have significant range and volume advantages, at the same time that they may also result in improved passive stability. Indeed, piezo-stacks are ac-

tive systems which may suffer from control noise and thermal drift. With a lever-arm of about 80 mm, step sizes of 100 nrad should be feasible. Moreover, the optimized FLS design allows for 3 mrad stroke with less than 5 N, leaving at least 15 N for preloading forces without exceeding the capacity of the actuator, so that good contact stiffness between the actuator tip and the support can be achieved.

For metrology and feedback, resolution in the order of 10 nrad RMS up to 2.5 kHz was desired to allow for online local in-position stability measurements. Absolute linear encoders with 1 nm resolution were selected over other non-contact probes options, such as capacitive sensors and interferometers (IFM). The reasons were: resolution and range are not conflicting factors, as they are in capacitive sensors; alignment tolerances are broader than in most IFM options; as in capacitive probes, but differently from IFM, absolute encoders save time in homing and alignment procedures; electronics are simpler and free of multiple-channel constraints; costs can be a factor 3 or 4 smaller.

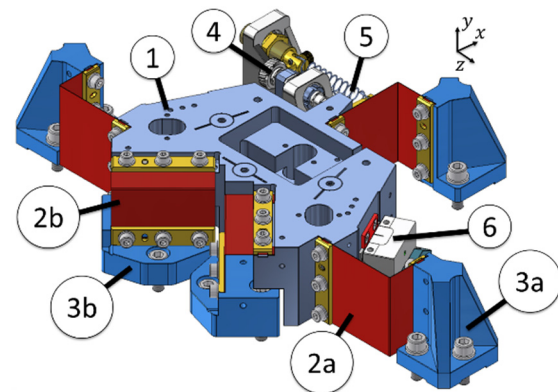


Figure 4: CAT-1-VFM mechanism isometric view: (1) support frame; (2) vertical (a) (x_3) and horizontal (b) (x_2) FLS; (3) vertical (a) (x_3) and horizontal (b) (x_2) FLS supports; (4) piezo actuator; (5) preload spring; and (6) optical encoder (x_2).

Cooling and Thermal Management

Silicon, which is the substrate material of all X-ray mirrors of the first set of Sirius beamlines, is known for remarkable thermal properties at low temperatures. Indeed, not only does the thermal expansion cross zero around 125 K, but also the thermal conductivity even exceeds that of copper for temperatures between 80 and 150 K. Thus, when compared to room-temperature operation, and particularly if the absorbed power levels and power densities are low enough, having the operational temperature of a mirror around 125 K may considerably reduce its thermal gradients (due to the high thermal conductivity) and nearly eliminate thermal bumps in the footprint (due to the very low thermal expansion). Considering the very small numbers in height and slope error budgets, this becomes an interesting option if the remaining challenges of working in cryogenic temperatures can be properly handled.

Regarding design, different alternatives can be envisioned once the heat conduction in the silicon body itself may not be the bottleneck in the heat extraction chain. For low powers, an elegant solution consists in indirectly cooling the mirror via a copper braid and a cryostat, as adopted

for handling 20 W in an artificial channel-cut monochromator at the XFEL [12]. Some key advantages of this solution over conventional water cooling schemes are: the drastic reduction in number of parts and masses around the optics; the decoupling from the cooling vibration source; and the elimination of water-vacuum interfaces or vacuum guards. Therefore, this was chosen as the standard solution for Sirius X-ray mirrors. In most cases, with power levels below 10 W, the solution is fairly straightforward. A few cases, however, do require some more work as they approach 40 or 50 W, which seems to be a practical limit due to the limited conductivity of the interfaces and the braids.

In cryogenic applications materials selection deserves special attention. When dealing with flexures linking parts with large temperature differences, two opposite choices can be considered. Either high-conductivity materials may be used to prevent excessive temperature gradients, or low-conductivity materials with small thermal expansion coefficients and high yield strengths are required, so that the large gradients may result in bearable deformations and stresses. For the support frame, aluminium was the material of choice because of: availability and costs; low density, reducing mass and inertia for improved dynamic performance of the assembly; good thermal diffusivity, allowing for faster thermal stabilization and temperature control; and small bending sensitivity, reducing bending moments and deformations. Thus, differently from the HD-DCM in which the invar flexures worked as an efficient thermal resistance, the mirror support flexures resulted in poor thermal insulation. Nonetheless, the insulation requirements between mirror and frame could be easily fulfilled by the hinges, made of Ti-6Al-4V. Moreover, considering 125 K as the target temperature of the mirrors, 283 K becomes a suitable operational temperature for the support frame, since the secant thermal expansions of aluminium and silicon match, minimizing in-plane elastic forces introduced by the deflection of the flexures.

Finally, with such large cold parts, if thermal shields were not used, blackbody radiation would generally be the major player in heat transfer to the optics, easily overcoming the beam load. Therefore, shields at about 240 K, also cooled by the cryostat via copper braids, almost completely cover the internal mechanics.

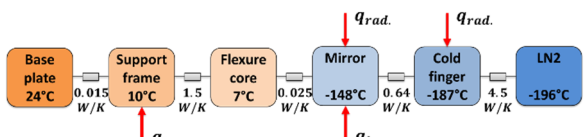


Figure 5: Simplified lumped-mass model for CAT-1-VFM, with expected temperatures and thermal conductivities.

Figure 5 and Figure 6 respectively show the simplified lumped-mass thermal model for CAT-1-VFM, with temperatures and thermal conductivities, and thermal FEA for the mirror, the hinges and the support frame in full operational conditions. It can be seen that the temperature in the body of the aluminium support frame is nearly constant and that the thermal gradient in the mirror is expected to be in the order of 0.1 K for a beam load of 9 W. In the hinge, on

the other hand, a temperature drop of 150 K is seen. Thus, once the stresses in the flexures of the support frame are negligible, in the hinges it may exceed 100 MPa.

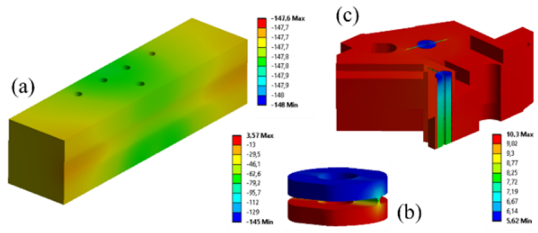


Figure 6: Thermal FEA (in °C) for the key parts in CAT-1-VFM mirror system under full operational loads (9 W beam + radiation), shown separately for readability: (a) mirror, (b) Ti-6Al-4V hinge; (c) aluminium support frame.

RESULTS

As a proof of concept, a prototype based on CAT-1-VFM mechanical system was built and characterized in air on an optical table (see Fig.7). Beginning with the results of modal analysis, Table 2 lists its first eigenmodes, showing remarkable agreement between FEA simulations and experimental data, which not only validates the concept with respect to the high-frequency targets, but also proves that the designing process has been consistent.

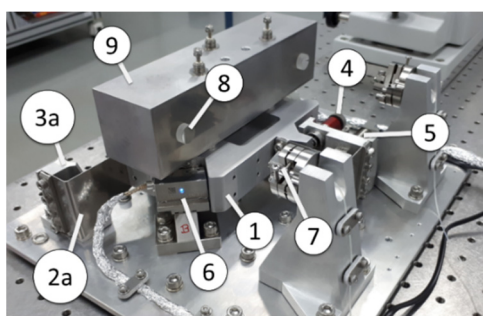


Figure 7: CAT-1-VFM prototype: (1) support frame; (2a) vertical FLS (2); (3a) vertical FLS support; (4) piezo actuator; (5) preload spring; (6) optical encoder; (7) IFM; (8) IFM target mirror; (9) dummy mirror.

Table 2: Modal Analysis for CAT-1-VFM Prototype

Mode	FEA [Hz]	Experimental [Hz]
1 (T_x)	249,7	250
2 (R_y)	312,5	313
3 (T_z)	342,4	341
4 (T_y)	408,9	403
5 (R_z)	602,5	554
6 (R_x)	614,9	851

Next, the motion performance was evaluated for resolution, range, linearity, parasitic motion errors and position stability. Figure 8 shows an open-loop resolution measurement with a 22nm-resolution actuator and the average signal of two 5nm-resolution optical encoders. With lever-arms of 0.1 and 0.08 m, respectively, it is clear that the step size is limited by the actuator and that the feedback signal has significant noise limitations. For the final systems, better resolution is expected in both actuation and metrology.

Content from this work may be used under the terms of the CC BY 3.0 licence (© 2018). Any distribution of this work must maintain attribution to the author(s), title of the work, publisher, and DOI.

Moreover, the asymmetry is step-size is a known behaviour in this type of piezo linear actuator.

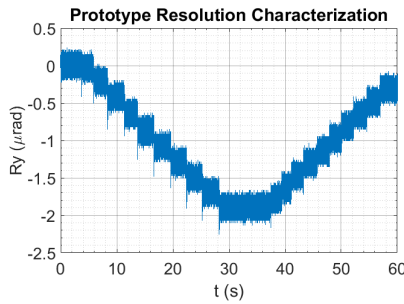


Figure 8: CAT-1-VFM prototype open-loop resolution characterization with preliminary piezo actuator and optical encoders.

With sufficient alignment tolerances in the encoders, a total range of ± 5 mrad was achieved. Then, an Elcomat 3000 autocollimator was used to measure the linearity and R_x and R_z parasitic rotations as a function of the feedback signal. Figure 9 shows that the residual errors from a linear fit (ϵ_{Ry}), as well as the parasitic rotations are below $\pm 0.1\%$ of the motion range, and mostly within ± 2 μ rad. Additionally, as the two encoders are orthogonal to each other, the parasitic translation in the x direction can be extracted from the two signals. Over the full range a symmetric parabolic runout of 2 μ m was found.

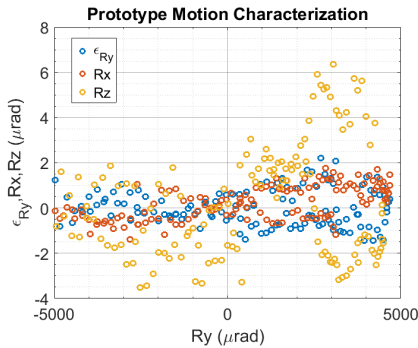


Figure 9: CAT-1-VFM prototype residual linearity errors (ϵ_{Ry}) and parasitic R_x and R_z rotations, as a function of the feedback signal.

The prototype still allowed for the evaluation of Lion Precision's C8-2.0 capacitive probes, tested in high and low-resolution modes, and SmarAct's PicoScale standard IFM as feedback sensors. Thus, all three alternatives could be compared, as summarized in Table 3. In terms of range, as expected, the encoders have a significant advantage. Regarding linearity, all sensors showed similar performance. As for stability, looking at the power spectrum density plots, all sensors seemed to be noise-limited over most of the large frequency range. In the table, the cumulative amplitude spectrum up to 2.5 kHz is given and the best results were achieved with the capacitive probe in high-resolution mode. Similar levels are expected from the 1nm-resolution encoders. Finally, the IFM was tested as an option of direct metrology (see Fig. 7), as the other sensors work over the support frame. Thanks to the high-frequency modes of the system and the limited bandwidth of the disturbance

sources, no significant differences were observed. As similar conditions are expected in real operation, having the encoders as feedback should be sufficiently reliable.

Table 3: Sensors Comparison at CAT-1-VFM Prototype

Mode	Range [mrad]	ϵ_{Ry} [μ m]	Stability (RMS)	
			Ry [nrad]	x [nm]
Encoder	± 5	< 3	55	5
Cap. (h.r.)	$\pm 0,25$	—	10	1
Cap. (l.r.)	$\pm 1,25$	< 2	50	3
IFM	$\pm 2,95$	< 1	35	3

Lastly, some results reporting problems in mirror coatings at low temperatures, especially involving multilayers, can be found [13]. Thus, to validate the use of cryogenic temperatures, the CARNAUBA beamline CAR-1-MC mirror, with Rh and Ni coating layers, has been cycled between 125 K and room temperature a few times. Transversal height measurements performed with a Fizeau DynaFiz interferometer before and after cycling are shown in Fig. 10, from where no risks or problems could be identified. Complementary measurements with results for the deformations caused by the clamping forces can be found in [8].

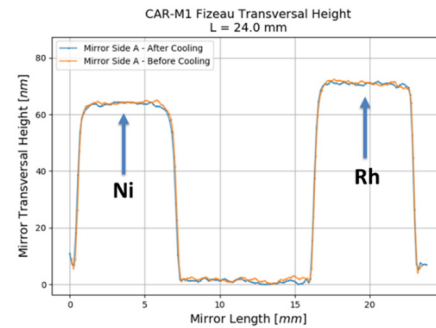


Figure 10: Transversal height measurement with Fizeau DynaFiz for CARNAUBA CAR-1-MC mirror, before and after cryocooling cycles. (Courtesy of OPT group.)

CONCLUSION

By means of deterministic design and system approach, an innovative concept for mirror systems has been developed, in which thermal, mechanical and optical challenges are simultaneously addressed. Decoupling vibrations sources via copper braids, preventing stresses by means of FLS, flexures, hinges and proper material selection, and limiting DoF and ranges of motion were some of the key aspects that resulted in this cost-effective high-performance system. Successful results in terms of eigenfrequencies and motion have been demonstrated in a functional prototype in air, while thermal and clamping performances started to be investigated in parallel. In the forthcoming months, a full set of complete mirrors systems shall be commissioned.

ACKNOWLEDGEMENTS

The authors would like to gratefully acknowledge the funding by the Brazilian Ministry of Science, Technology, Innovation and Communication and the contribution of the LNLS team.

REFERENCES

- [1] R. Baker *et al.*, “New generation mirror systems for the ESRF upgrade beamlines”, *J. Phys.: Conf. Ser.* 425 052015, 2103.
- [2] M. Mattenet *et al.*, “Optimization of X-ray mirror mounting: test bench and results”, *Proc. MEDSI 2012*, Shanghai, China, Oct. 2012.
- [3] C. Colldelram *et al.*, “The nanobender: a new X-ray mirror bender with nanometer figure correction”, in *Proc. MEDSI 2016*, Barcelona, Spain, Sep. 2016.
- [4] L. Zhang *et al.*, “LCLS-II KB mirror systems: technical challenges and solutions”, presented at MEDSI 2016, Barcelona, Spain, Sep. 2016.
- [5] L. Zhang *et al.*, “Minimization of mechanical constraint effects of Eutetic GaIn as thermal interface”, presented at MEDSI 2016, Barcelona, Spain, Sep. 2016.
- [6] T. Noll *et al.*, “The generic mirror chamber for the European XFEL”, in *Proc. MEDSI 2016*, Barcelona, Spain, Sep. 2016.
- [7] R. Gerales *et al.*, “The new high dynamics DCM for Sirius”, in *Proc. MEDSI 2016*, Barcelona, Spain, Sep. 2016.
- [8] R. Gerales *et al.*, “Granite benches for Sirius X-ray optical systems”, presented at MEDSI 2018, Paris, France, Jun. 2018, this conference.
- [9] L. Volpe *et al.*, “Optimization method using thermal and mechanical simulations for Sirius high-stability mirrors”, presented at MEDSI 2018, Paris, France, Jun. 2018, this conference.
- [10] M. Saveri Silva *et al.*, “Thermal management and crystal clamping concepts for the new high dynamics DCM for Sirius”, in *Proc. MEDSI 2016*, Barcelona, Spain, Sep. 2016.
- [11] H. Soemers, “Flexural mechanisms”, in *Principles for precision mechanisms*, Twente University, Twente, Netherlands. 2010.
- [12] X. Dong *et al.*, “Design of a Cryo-Cooled Artificial Channel-Cut Crystal Monochromator for the European XFEL”, in *Proc. SRI2015*, New York, USA, Jul. 2015.
- [13] X. Cheng, “Thermal stress issues in thin film coatings of X-ray optics under high heat load”, Université de Grenoble, Grenoble, France, 2014.

FE MODEL OF A NANOPositionING FLEXURE STAGE FOR DIAGNOSIS OF TRAJECTORY ERRORS

S. P. Kearney, D. Shu,

Advanced Photon Source, Argonne National Laboratory, Argonne, IL., USA

Abstract

The Advanced Photon Source Upgrade project includes upgrading several beamlines, which desire nanopositioning and fly-scan capabilities. A step towards achieving this is through the use of flexure stages with minimal trajectory errors. Typically, parasitic motion is on the order of micrometer-level displacements and tens of microradian-level rotations. The cause of such errors is difficult to diagnosis due to the scale and complexity of the overall mechanism. Therefore, an FE model of a flexure pivot nanopositioning stage with centimeter-level travel range [1, 2] has been developed to aid in trajectory error diagnosis. Previous work used an FE model and relative error analysis to quantify the effects of assembly error on trajectory errors [3]. Relative error analysis was used due to the difficulty in validating a complex FE model. This study develops an experimentally validated FE model of a single joint to quantify the expected error in the full FE model. The full model is then compared experimentally to the flexure stage to assess the model accuracy and diagnosis trajectory errors.

INTRODUCTION

The Advanced Photon Source Upgrade project includes upgrading several beamlines, which desire nanopositioning and fly-scan capabilities. This will require a better understanding the cause of trajectories that are typically on the order of micrometer displacements and microradian rotations [1]. We have previously developed a flexure pivot nanopositioning stage with centimeter-level travel range [1, 2] that could benefit from more focused analysis of its trajectory errors. Previously, relative error analysis was used due to the difficulty in validating a complex FE model. This study hopes to improve the quality of the FE model to be used in absolute analysis. In this paper we will present a more accurate model of the single flexure pivot that was validated through experiment, and use this more accurate model in the complete flexure stage model. The flexure stage FE model will then be compared to experimental results.

The flexure stage has four main components in its construction. A commercially available flexure pivot from C-Flex Bearing Co., Inc. and Riverhawk Co, Fig. 1, is used at each mechanical joint. These pivots are then assembled in a deformation compensated orientation four-bar mechanism, see Fig. 2. Two of these four-bar mechanisms can be joined (Fig. 3), known commonly as a double parallelogram mechanism [4], to provide rectilinear motion with the parasitic motion of the four-bar cancelled. However, there is now two degrees of freedom with the double parallelogram so we employ a 2:1 stabilizing mechanism (Fig. 4 item 2) to control the floating middle-bar, which is similar to the mechanism in [5]. A complete flexure stage, Fig. 4,

can then be assembled using these fundamental units, a vertical stage using these units can be seen in [3]. The stage in Fig. 4 will be used in this analysis.

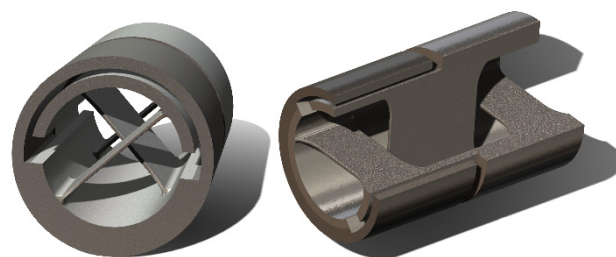


Figure 1: Flexure pivot used as a main element in the flexure stage design.



Figure 2: Four-bar deformation compensated flexure mechanism.



Figure 3: Double four-bar deformation compensated flexure mechanism.

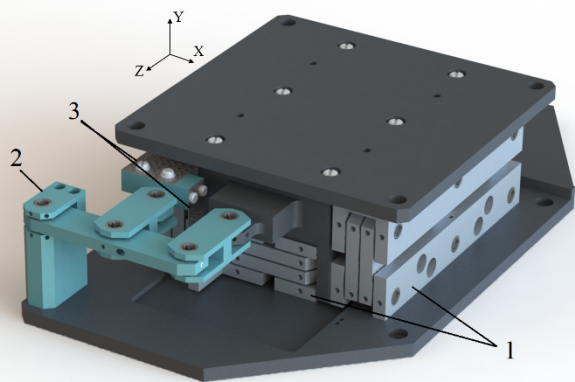


Figure 4: Complete model of flexure stage: (1) Double four-bar mechanisms (3 are actually used, the third is not visible on the opposite side), (2) 2:1 stabilizer mechanism, and (3) leaf flexure connections to the middle-bar. The co-ordinate frame used throughout this study is also shown.

VALIDATION OF FLEXURE PIVOT

Experimental Setup

For the FE model to more accurately predict trajectory errors, it must first accurately model the parasitic stiffness of a single flexure pivot. A setup to measure the parasitic stiffness can be seen in Fig. 5. A single flexure and link from the larger four-bar mechanism is used as the test bed. A load is applied at the end of the link, which causes the pivot to rotate about Z (using coordinate frame Fig. 4), a parasitic motion. The load is measured by a force gauge and the displacement by a 3-channel Attocube Systems AG laser interferometer (IDS3010). All 36 flexure pivots used in the stage assembly were measured and the results can be seen in Table 1. The COV for 36 flexure pivots was found to be 4%, which means that there is measurable variance in the stiffness of the pivots. The entire minimum to maximum range of stiffness varied by +8.5% and -9.2% from the mean, which agrees well with the manufacturer, C-Flex Bearing Co., Inc., rotational stiffness variance of $\pm 10\%$. All of this variance in flexure pivot stiffness suggests there may be more difficulty accurately modelling the complete flexure stage.

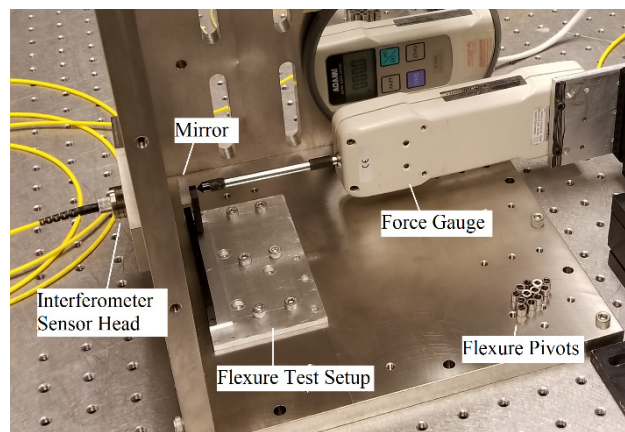


Figure 5: Experimental test setup to measure the parasitic stiffness of the flexure pivots.

FE Model Single Flexure Pivot Results

The first base FE model of the experimental setup can be seen in Fig. 6. This model was used to theoretically measure the parasitic stiffness. It can be seen that this model resembles the experiment, however this first setup, FE results row 1 in Table 1, show a 16% error. It was thought that decreasing the element size at the flexure, Fig. 7, from 0.2 mm to 0.1 mm would reduce this error, however the error was only reduced by 0.2% to 15.8%. Then the model fixture was improved to simulate the mounting screws with a no penetration but sliding and lifting virtual wall and local fixtures, Fig. 8. This also turned out to have little effect with only a 0.7% reduction in error. Finally, the bonding condition of the flexure bearing surface was redesigned to simulate the use of set screws, Fig. 9. The effect was that the error reduced to -2.4%, which is within the COV of the experimental setup. This final model was then used to find the smallest number of mesh elements and type of mesh that would keep the same accuracy. It was found that a curvature based mesh with 0.25 mm elements for the flexures, 0.65 mm elements for the simulated set screws, and that removal of the flexure side rounds was the optimal mesh, see Fig. 10.

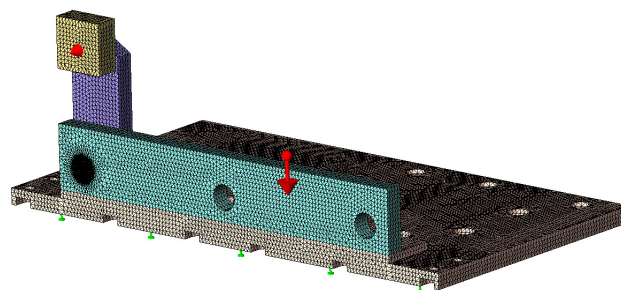


Figure 6: FE model of single flexure pivot setup. The green arrows represent fixtures, red arrow in center is the gravity force, and red arrow protruding from the mirror if the force direction and measurement point.

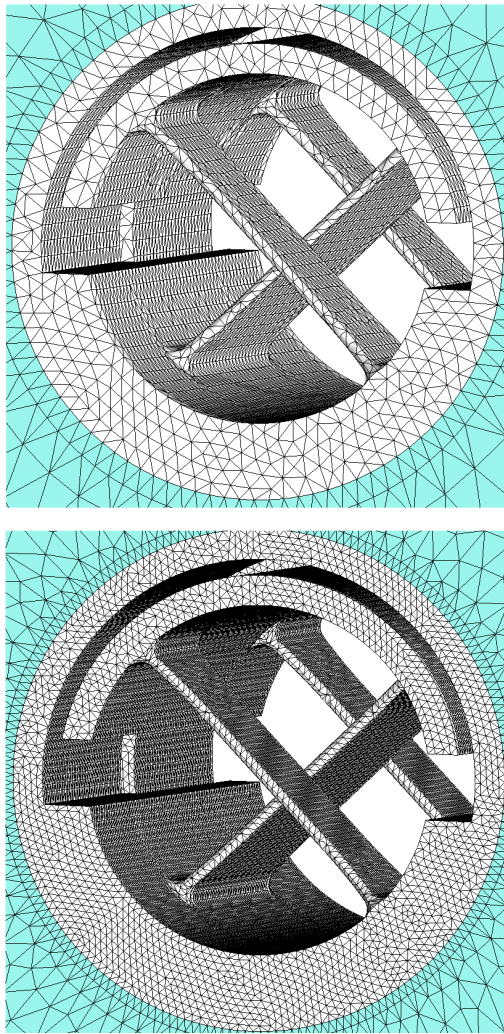


Figure 7: Varying mesh element size: top element size is 0.2 mm and bottom element size is 0.1 mm.

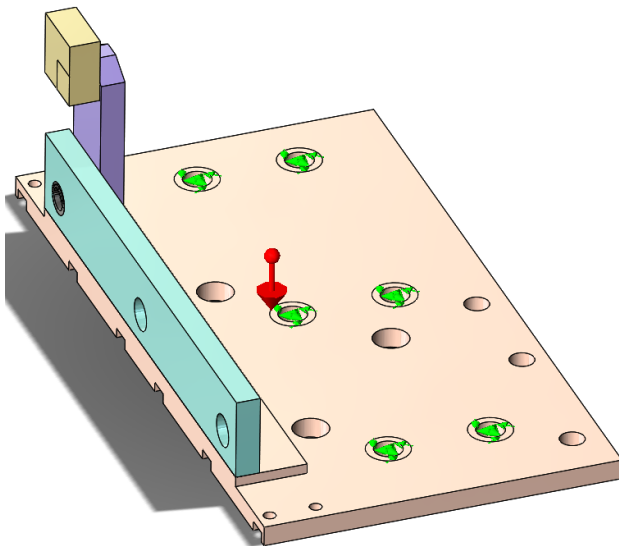


Figure 8: Base fixture now simulated by virtual wall with no penetration and simulated bolt fixtures.

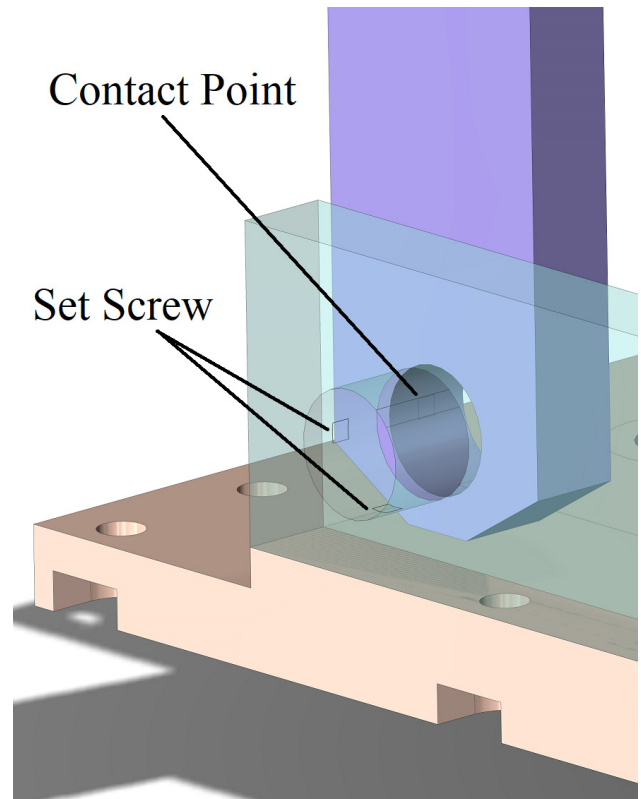


Figure 9: FE model using simulated set screw contact instead of bonded contact for the entire pivot bearing face.

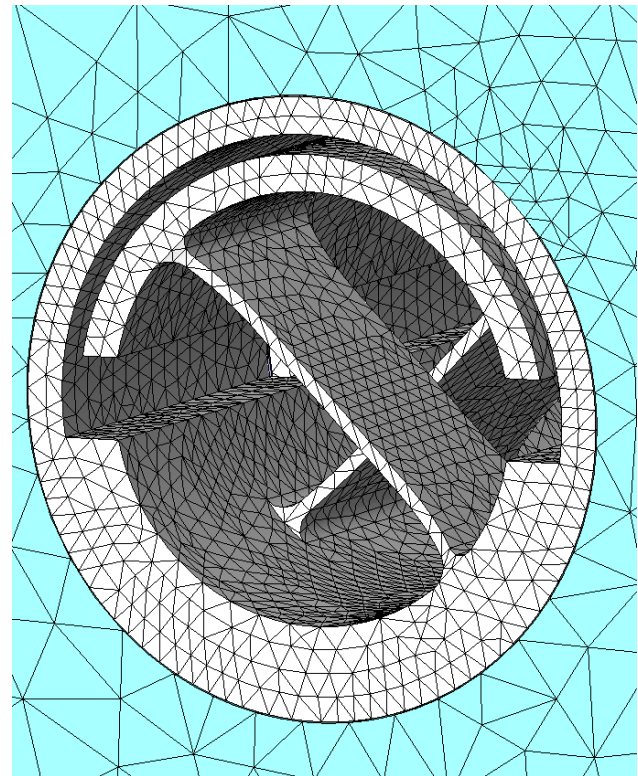


Figure 10: Optimized curvature based mesh with fillet features on the flexure sides removed. The fillets at the weld points of the flexure are retained.

Table 1: Experimental and FEA Results. K, is the parasitic stiffness of the flexure pivot, 36 pivots were measured, σ is the standard deviation, and COV is the coefficient of variation. Each row in the FEA results represents a different FE model

Experiment Results	K (N/ μ m)	σ	COV
Flexure Pivots	0.0317	0.0013	4.0 %
FEA Results	K (N/ μ m)	Error	
1. 0.2 mm Elements	0.0368	16.0 %	
2. 0.1 mm Elements	0.0367	15.8 %	
3. Base Fixture Complex Simulation	0.0365	15.3 %	
4. Set Screws Simulated	0.0309	-2.42 %	

COMPLETE FE MODEL COMPARED TO EXPERIMENT

A larger complete FE model using the refined model from the single flexure pivot experiment was then compared to experiment using the complete flexure stage. Figure 11 shows the experimental setup of the flexure stage. It was driven using a Newport Co. PZA12 piezo actuator over a range of ± 3 mm. The same interferometer was used to measure the stage displacement and pitch about the Z axis. It was clamp-mounted to an Invar frame at three points that were simulated in the FE model. The FE model can be seen in Fig. 12. The orientation of the flexure pivots was matched between the FE model and the actual stage. The entire model had approximately 4.5×10^6 elements and used the large displacement method, which applies a percent of the load in each step and updates the model deformation before moving on to the next step. Each solution point took from 30 min – 1.5 hours depending on the size of the displacement step.

A comparison of the FEA data to the measured experimental data of 3 runs can be seen in Fig. 13. Each individual run is offset from the previous due to thermal drifting variances in the mounting interface between the mirror and the moving plate of the stage. It can be seen that the FE model does not agree with the experimental results. The trend of the FEA data does go in the same direction as the experimental data, so there may be some parts of the model that are working. However, the model and experiment are so far off that there must be some major mechanical bending, assembly error, or manufacturing tolerance that is not being modelled. This is especially evident by the approximate first order linearity of the FEA data, which does not match the exponential pitch curve of the experiment.

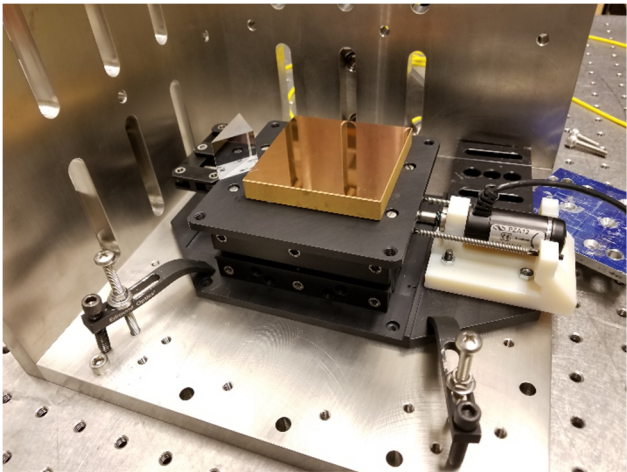


Figure 11: Experimental setup of the complete flexure stage. The mirror on the left was used to measure displacement and a flat rectangular mirror on the right to measure pitch and roll.

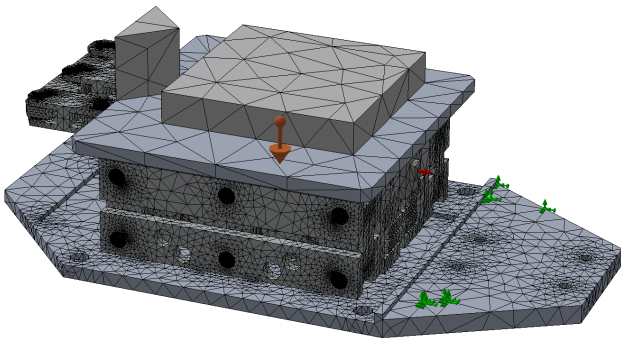


Figure 12: FE model of complete flexure stage. The orange arrow in the center is the gravity force, the red arrow an applied displacement, and the green arrows the fixed points.

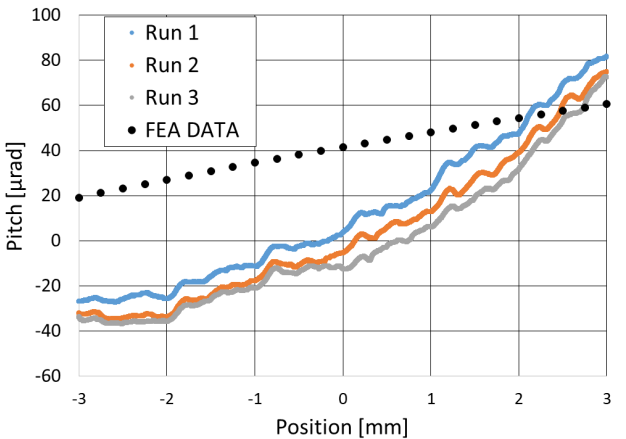


Figure 13: Pitch trajectory errors (about X) for three experimental runs in the same direction compared to the FEA results.

CONCLUSION

The parasitic stiffness of 36 flexure pivots was experimentally measured in order to validate an FE model of a single flexure pivot. The FE model of a single flexure pivot was found to be accurate to an experimentally measured flexure pivot with -2.4% error. In order to achieve this accuracy it was found that it is crucial to include an accurate simulation of the mounting method used for the flexure pivot. In addition, the entire range of flexure pivot stiffness was found to be 8.5% to -9.2% from the mean, which means that this tolerance may need to be incorporated into future FE models.

The FE model of a single flexure pivot was then used in a larger FE model of a flexure pivot stage. It was expected that with the more accurate single unit the larger FE model would predict the trajectory errors of the actual flexure pivot stage. However, it was found that this was not the case. The FE model was unable to predict the trajectory errors of the flexure stage. This result suggests that many physical features have yet to be accurately modelled in this complex FE model such that it is not yet ready for absolute prediction. Future work into this model will need to incorporate the following features:

- Geometric tolerance from manufacturing
- Set screw holding torque
- Set screw tightening order
- Assembly errors
- Flexure pivot stiffness variance
- All components interfaces (bonded vs. simulated bolt fixture)

Previous work in [3] used a large and complex FE model with relative analysis to identify design features that were sensitive to misalignment. Such relative analyses will be useful in identifying key features of the above list. By identifying which features must be modelled and which are not as sensitive we can keep the complete FE model to a practical level of complexity in regards to computing capability. A better understanding how these features affect the model as compared to the actual stage will provide more than just better FE models, but will contribute to better design insight that will aid in the design of future nanopositioning flexure stages.

ACKNOWLEDGEMENTS

Work supported by the U.S. Department of Energy, Office of Science, under Contract No. DE-AC02-06CH11357.

REFERENCES

- [1] D. Shu *et al.*, "Design and test of precision vertical and horizontal linear nanopositioning flexure stages with centimeter-level travel range for x-ray instrumentation", in *Proc. SPIE*, vol. 10371, 2017.
- [2] U.S. Patent granted No. 8,957,567, D. Shu, S. Kearney, and C. Preissner, 2015.
- [3] S. Kearney, D. Shu., "Trajectory error analysis of a flexure pivot type guide for linear nanopositioning", In *Proc. SPIE*, vol. 10371, 2017.
- [4] S. T. Smith, *Flexures: elements of elastic mechanisms*, CRC Press; 2000.
- [5] R. M. Panas, "Large displacement behavior of double parallelogram flexure mechanisms with underconstraint eliminators", in *Precision Engineering*, 46, 2016, pp. 399-408.

APPLICATION OF ADDITIVE MANUFACTURING IN THE DEVELOPMENT OF A SAMPLE HOLDER FOR A FIXED TARGET VECTOR SCANNING DIFFRACTOMETER AT SwissFEL

Xinyu Wang[†], Jan Hora, Patrick Hirschi¹, Haimo Jöhri, Claude Pradervand, Bill Pedrini,
 Paul Scherrer Institut, 5232 Villigen, Switzerland
¹also at HELVETING Engineering AG, Neuenhof, Switzerland

Abstract

Whilst the benefit of additive manufacturing (AM) in rapid prototyping becomes more and more established, the direct application to 3D printing is still demanding. Exploitation of AM opens the door for complex and optimized parts which are otherwise impossible to fabricate. Therefore, consistent efforts are currently directed to gain specific knowledge on the numerical simulation and the design process.

For a vector scanning diffractometer foreseen for fixed target protein crystallography at the Swiss X-ray free electron laser (SwissFEL) [1], we developed, manufactured and tested a 3D-printed sample holder with carbon fibre reinforced polyamide material. The diffractometer serves to collect diffraction patterns at up to 100 Hz rate on many small protein crystals ($< 5 \mu\text{m}$) by scanning the sample in the X-ray beam following the custom trajectories. The large accelerations in the motion plane transverse to the beam require the holder, which is tightly fixed on the diffractometer stages, to be particularly light and stiff.

Our work on the design and the dynamic tests for the 3D-printed holder is presented here. For sake of comparison, the numerical analysis and tests were extended on a CNC-machined aluminium holder realized to fulfil the same function.

INTRODUCTION

The collection of X-ray diffraction images with the fixed target protein crystallography instrument SwissMX [2], currently under realization at SwissFEL, relies on scanning the sample in the X-ray beam using an advanced diffractometer with translation axes in x - and y -directions (Fig. 1). In the specified error budget of $1.2 \mu\text{m}$ in total between the impact position of a femtosecond SwissFEL X-ray pulse and protein crystal position, the contribution from the deformation of sample holder is restricted to be less than 200 nm. The benchmark motion of the stages is sinusoidal with 50 Hz frequency and a maximum acceleration of 2.5 m/s^2 , corresponding to a motion amplitude of $25 \mu\text{m}$. The weight of the sample holder is crucial due to the large accelerations acting on the moving parts. The

total mass allowed by the performances of the stages must be below 100g. Given the weight of the sample unit of 30 g (including sample chip, sample pin and pin-holder magnet), the sample holder maximal weight is 70g. The natural frequencies of the sample holder have been requested to be above 400 Hz.

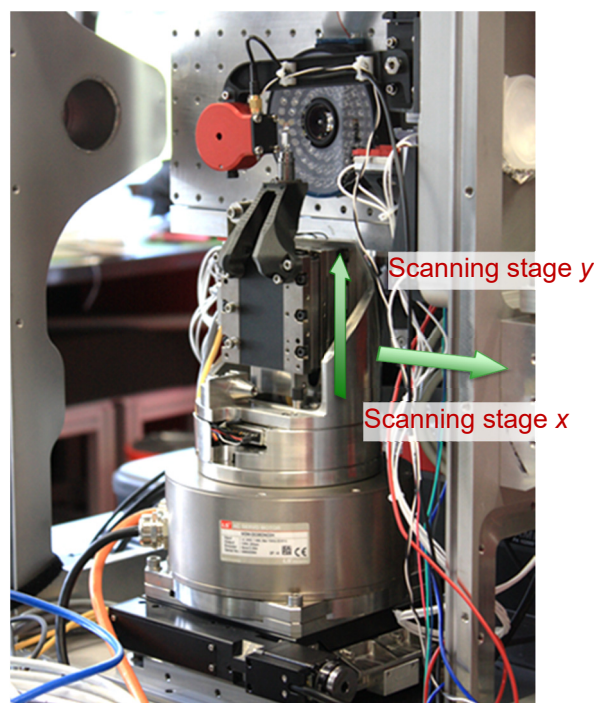


Figure 1: Sample diffractometer with sample holder and sample chip.

DESIGN OF THE SAMPLE HOLDER

To realize the sample holder, we considered both possibilities of aluminum material, i.e. by traditional CNC manufacturing, and by 3D printing with carbon fiber reinforced polyamide. In the Continuous Filament Fabrication (CFF) printing process, endless carbon fibers are printed layer by layer in predefined orientations and embedded in melted polyamide matrix material ([3]) to achieve high stiffness and low weight. The lack of material data for general 3D printing application limits the numerical predictions of the dynamical properties. In Table 1, material properties are given for uni-directional (UD) fibre orientation and for matrix material. UD composite shows the highest

[†] xinyu.wang@psi.ch

stiffness but only in the direction of the fibres and is anisotropic. The more common composites with fiber orientation in 0°/45°/90°-directions have lower stiffness, but has the advantages of being quasi isotropic and showing higher shear strength.

Table 1: Materials Properties [3]

	Alu	Carbon Pomposite UD	Micro- Carbon Reinforced Polyamide
Density [g/cm ³]	2.7	1.4	1.2
Tensile modulus [GPa]	70	54	1.4
Bending modulus [GPa]	70	51	2.9

Topology Optimisation

Since the introduction of topology optimisation (TO) theory in 1988, many algorithms have been rapidly developed [4]. With additive manufacturing, more and more complex shapes can be realized. TO is the key feature for form-finding of optimized geometry. Recently, TO has been integrated into many existing CAD and CAE environments. Thus, in addition to providing ease in the transition of results and geometries between TO and finite element (FE) analysis, the further advantage is that all features and functionalities of reliable finite element (FE) solver are made accessible to TO. The TO and FE analysis reported here has been performed with ANSYS workbench Release 19.

The design space was defined after a collision analysis in CAD (Fig. 2a). In the final design of the holder, the goal was to occupy 25% of the volume with a part of highest stiffness and highest natural frequencies. Constraints were defined at bolted connections to stage, kept fixed in the model. The pin and the sample chip were defined as a point mass located at the gravity center. The first analysis aimed to maximize the first natural frequency, which resulted in the geometry shown in Fig. 2b. Because of the motion is both in x- and y-directions, also the second mode is relevant, and therefore further optimisation was carried out to maximize both the first two natural frequencies. The new obtained geometry is illustrated in Fig. 2c. Further consideration was devoted to the static stiffness under acceleration of 2.5 m/s² in both directions. Figure 2d shows the output design with two static loads of equal weight factors. For general applications with multiple requirements, TO leads not only to sole optimum, but to many optima. Giving consideration of all requirements to possible weighting factors leads to a threshold of optimized regions, and leaves a freedom of design to engineers. The optimization results are only as good as the definition of

objectives (goals, responses) based on specification. Before a TO solution is accepted, the design has to be validated by FE analysis.

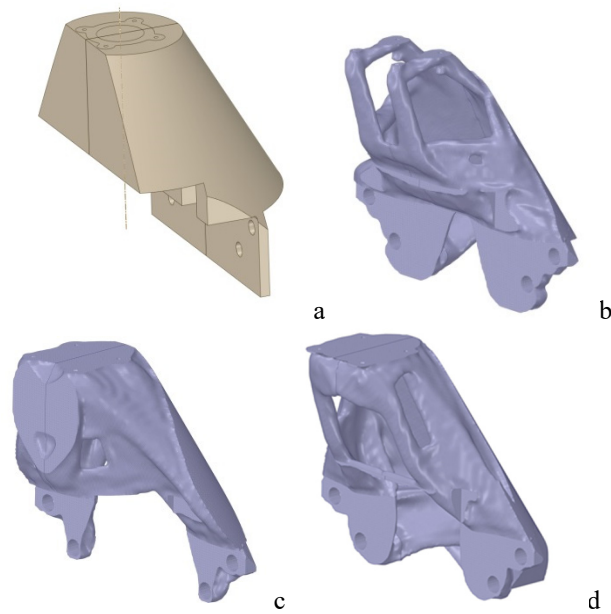


Figure 2: Design space for the stiffness optimization (a) and optimized structure (b, c, d).

Simulation to Design

The simulation employs body-fitted Cartesian all-hex meshing which is especially suitable for 3D printing simulations. Figure 3a shows the retained elements after TO of the most regular final geometry. Figure 3b shows the smoothed geometry from STL cleanup, which still requires a lot of fine tuning to make it eventually suitable for direct printing.

The final design is based on the compromise that the sample holder is both CNC manufacturable and 3D printable (Fig. 4).

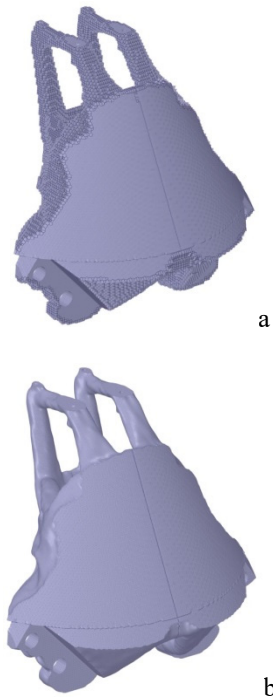


Figure 3: Retained elements (a) and smoothed geometry (b).

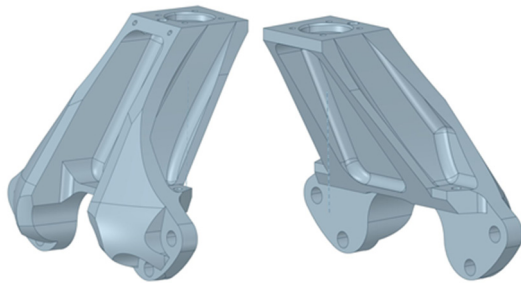


Figure 4: Final design geometry.

Design Validation

FE analysis has been performed for design validation with both aluminium and UD carbon fibre composite materials. A summary of the results for static and natural frequency analysis can be found in Table 2. The aluminium part has a weight of 64 g and is just within the specification. The carbon composite part of 33 g weight is much lighter. Figure 5 shows the deformation patterns of the aluminium part under vertical and horizontal accelerations of 2.5 m/s². Deformations for both load cases and with both materials are below 32 nm, thus well within the specified 200 nm. Figure 6 shows the shape of the first two modes: the first is a vertical bending mode, while the second is a torsional one. The first natural frequency of aluminium sample holder is 790 Hz, and of UD carbon composite is 713 Hz. With both materials, the requirement of the lowest natural frequency to be above 400 Hz is achieved. Due to the lack of material data of carbon fibres in general orientation, the calculation was performed based on stiffness of UD composite in fibre direc-

tion which is higher than that achieved in the real production. The final deformation of the 3D printed sample holder is therefore expected to be higher and the natural frequency to be lower than calculated due to material property deviations.

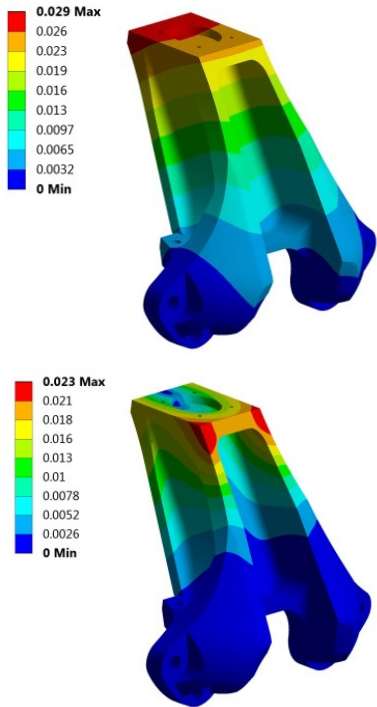


Figure 5: Deformation [μm] of the aluminium part under vertical (upper) and horizontal (lower) acceleration of 2.5 m/s².

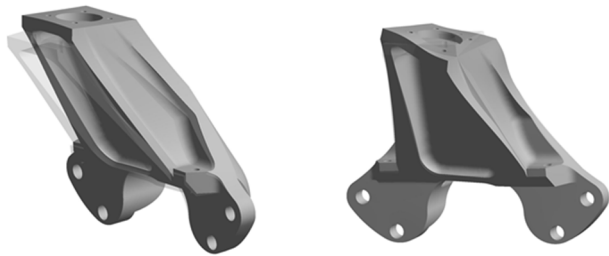


Figure 6: Mode shapes of the 1st and 2nd modes.

Table 2: Summary of FEA Results		
	Aluminium	Carbon Composite UD
Weight [g]	64	33
Deformation [nm]		
Vertical	29	32
Horizontal	23	30
Natural frequency [Hz]		
f_1	790	713
f_2	1350	1206

DYNAMIC TESTING

A modal shaker (Mini SmartShaker TMS K2007/E01) was utilized to apply the appropriate acceleration of 2.5 m/s^2 at 50 Hz for a qualification test.

The sample holder was mounted via an adaptor to the shaker. For the vertical excitation, two tri-axial accelerometers (PCB 356B18) were used: one was placed on the adaptor and the other on the sample holder (Fig. 7). The accelerometer with the joining plate had a weight of 30 g, corresponding to the total mass of pin-holding magnet and pin. The input acceleration is recorded by the accelerometer on the adaptor, and the output acceleration is measured by the accelerometer on the sample holder. For the transversal motion, the adaptor was rotated to the vertical direction (Fig. 8). Two 3D printed sample holder parts were tested simultaneously to prevent the out-of-axis motion due to eccentric mass centre. The input signal to the sample holders was recorded by an impedance sensor PCB 288D01 on the top of adaptor.

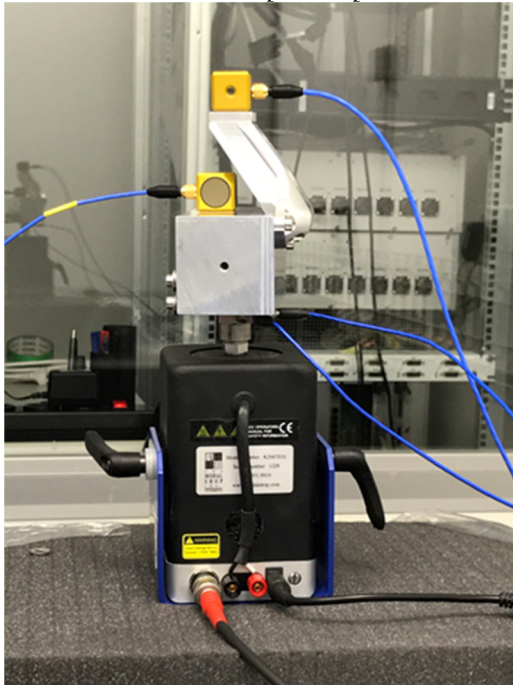


Figure 7: Vertical dynamical test setup with aluminium sample holder.

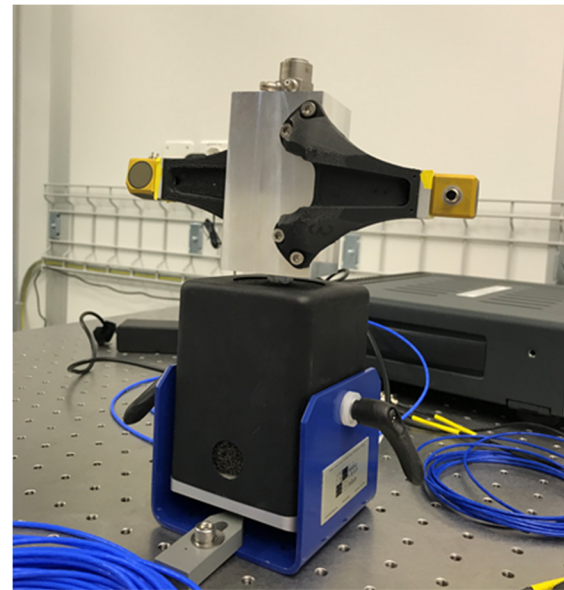


Figure 8: Transversal dynamic test setup with two composite sample holders.

The response of the following four sample holders under forced harmonic vibration was investigated:

- M1: 3D printed micro-fiber reinforced polyamide
- M2: 3D printed carbon fiber composite with quasi-isotropic orientation, printed from the curved back side
- M3: 3D printed carbon fiber composite with quasi-isotropic orientation, printed from the flat front side
- M4: Aluminum

The shaker was set to a harmonic motion at 50 Hz with a maximum acceleration up to 3.3 m/s^2 . The phase shift of the output and input was calculated from cross spectrum functions. Figure 9 depicts a 3D color map of the phase as a function of time on the vertical axis and frequency on the horizontal axis, with phase value encoded in the color corresponding to the scale on the left of the picture. As the forced vibration excitation is at 50 Hz, the phase shift is correlated at this frequency. Beyond the excitation frequency, the phase information has no physical meaning, and therefore no correlation can be found.

Content from this work may be used under the terms of the CC BY 3.0 licence (© 2018). Any distribution of this work must maintain attribution to the author(s), title of the work, publisher, and DOI.

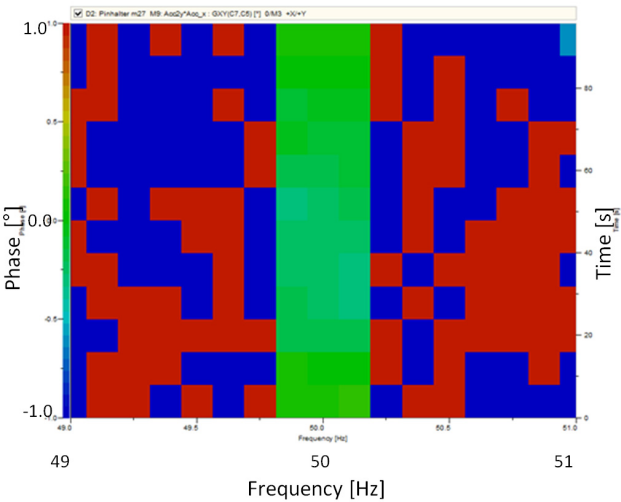


Figure 9: Color map of phase shift from 49 to 51 Hz.

Table 3: Summary of Measurement Results

	Aluminium M1	Composite M2/M3
Weight [g]	63	40
Vertical excitation		
Phase [°]	0.16	0.36
Pos. Error [nm]	70	157
Transversal excitation		
Phase [°]	-	0.31
Pos. Error [nm]		135

The phase shifts tested at various amplitudes with accelerations up to 3.3 m/s^2 are scaled linearly to the acceleration of 2.5 m/s^2 . The main measurement error is the off-axis motions resulting from the tilting of the shaker output mounting, which is restricted to be below 10% of the axial motion amplitude. With the sample stage the tilting motion can be eliminated, and the measurement with the shaker corresponds to a worst case behaviour of the sample holder. A summary of the measured phase shifts is given in Table 3.

The aluminium sample holder has the lowest phase shift of about 0.16° . The two composite parts printed from different sides and therefore with different support structures behave similarly, with phase shift around 0.36° . The maximum position error related to 0.36° phase shift at $25 \mu\text{m}$ amplitude is estimated to be

$$25 \mu\text{m} \cdot \sin(0.36^\circ) = 0.157 \mu\text{m}.$$

The error is therefore within the 200 nm specification. For the aluminium holder, the position error estimate (0.16° phase shift giving 70 nm) is even lower, but the part is 50% heavier. The micro-fibre reinforced polyamide part has a phase shift of more than a factor of four larger, resulting in a position error of 600 nm which is too high for practical use.

CONCLUSION

Topology optimisation plays a key feature in advanced manufacturing. Its application is not only beneficial to 3D printing but also to traditional CNC manufacturing.

In the case of the sample holder considered here, the design resulted from the compromise of both CNC machinable and 3D printable. Holders made with aluminium and endless carbon fibre reinforced composites turned out to qualify for the foreseen application. Micro-fibre reinforced polyamide was too soft, with the holder exhibiting a phase shift four times larger than the part with endless carbon fibre. The aluminium part was the stiffest but 50% heavier. The 3D printed composite part was chosen as the preferred option for the fixed target protein crystallography diffractometer in the SwissMX instrument.

The lack of general material properties of carbon fibre composites material limits the numerical prediction possibilities of the mechanical behaviour of the parts. Further knowledge on material properties, influence of printing process still need to be gained.

ACKNOWLEDGEMENTS

We want to thank Peter Hottinger for the support in mechanical testing.

REFERENCES

[1] Christopher J. Milne *et al.*: “SwissFEL: The Swiss X-ray Free Electron Laser”, *Appl. Phys. Lett.*, vol. 7, 720 (2017)
[2] SwissMX (former ESB-MX) concept design report, available at <https://www.psi.ch/swissfel/swissfel>
[3] MarkForged, Inc. & Mark3D GmbH: “Fertigung neu definiert”, 04 2018.
[4] Ole Sigmund and Kurt Maute, “Topology optimization approaches, a comparative review”, *Structural and Multidisciplinary Optimization*, 48:1031–1055, DOI 10.1007/s00158-013-0978-6

MECHANICAL DESIGN OF A NEW PRECISION ALIGNMENT APPARATUS FOR COMPACT X-RAY COMPOUND REFRACTIVE LENS MANIPULATOR*

D. Shu[†], Z. Islam, J. Anton¹, S. Kearney, X. Shi, W. Grizolli, P. Kenesei, S. Shastri, L. Assoufid
 Advanced Photon Source, Argonne National Laboratory, Argonne, IL, USA
¹University of Illinois at Chicago, Chicago, IL, USA

Abstract

A prototype of compact x-ray compound refractive lens (CRL) manipulator system has been developed at the Argonne National Laboratory for dark-field imaging of multi-scale structures. This novel full-field imaging modality uses Bragg peaks to reconstruct 3D distribution of mesoscopic and microscopic structures that govern the behavior of functional materials, in particular, thermodynamic phase transitions in magnetic systems. At the heart of this microscopy technique is a CRL-based x-ray objective lens with an easily adjustable focal length to isolate any region of interest, typically in the energy range of 5-100 keV or higher, with high precision positional and angular reproducibility. Since the x-ray CRL manipulator system for this technique will be implemented on a high-resolution diffractometer detector arm that rotates during diffraction studies, compactness and system stability, along with the ability to change focal length ("zooming"), became key design requirements for this new CRL manipulator system. The mechanical designs of the compact x-ray CRL manipulator system, as well as finite element analysis for its precision alignment apparatus are described in this paper.

INTRODUCTION

The macroscopic properties of functional materials (including most technologically relevant properties) are controlled by microscopic and nano-scale features and processes. It is important to deepen our understanding of couplings between such multi-scale structural features (e.g. as twin boundaries, grain orientations, lattice distortions, or magneto-striction) and average materials properties (thermodynamic, magneto-caloric, pinning, transport, critical current, etc.) as well as order parameters. Furthermore, the nature of hysteretic magnetic and/or structural transitions and related phenomena (e.g. memory effects, domain network, fluctuations, and relaxation) tuned in by magnetic fields at cryogenic temperature is of great interest. So, there is a growing need, especially in the wake of near diffraction-limited sources being on the horizon, to develop imaging techniques ideally suited for problems alluded to above and to complement well-known resonant and non-resonant diffraction methods.

While there is a plethora of x-ray microscopy techniques that are poised to provide high-resolution real-space images of inhomogeneous materials at multiple length scales and their evolution through phase transitions, dark-field x-ray microscopy (DFXM) stands out as a fast imaging method [1-6]. This full-field imaging modality uses Bragg peaks to reconstruct 3D distribution of mesoscopic and microscopic structures in materials. A Bragg peak is excited and its intensity distribution is recorded using an area detector. However, the diffracted beam is passed through an x-ray objective lens to magnify and project onto a scintillator before detection with a high-resolution CCD camera. The key is to collect diffraction data of a particular Bragg peak as the sample is rotated around the momentum transfer, with a high precision, over a range of full 360°.

A CRL-based x-ray objective lens [7-9] with an easily adjustable focal length to isolate any region of interest is a central piece of this microscopy technique. For such application CRL-based x-ray objective lens operating over a wide energy range (e.g. 5-100 keV, or even higher), with high precision positional and angular reproducibility, need to be implemented on a high-resolution diffractometer detector arm that rotates during diffraction studies. As such, compactness and system stability, along with the ability to change focal length, became key design requirements for this new CRL manipulator system.

In this paper, we present a proof-of-principle prototype design for the compact x-ray CRL manipulator along with its preliminary x-ray test results first, followed by the designs of the manipulators for 16-mm- and 32-mm-long CRL stacks, and conclude with the design options of the CRL manipulators integration.

PROOF-OF-PRINCIPLE PROTOTYPE

The novelty of the new mechanical design is the compactness and positioning stability as well as repeatability of its unique flexural lens holder alignment structure. It is using commercial high precision V-rail for linear roller bearing [10] as a reference base.

Figure 1 shows a 3D-model of the prototype for demonstrating proof-of-principle of operation. As shown in Fig. 1, the prototype CRL manipulator includes a base subassembly with stage support and a base V-rail, a lens holder V-rail with lens holder frame subassembly, a commercial miniature piezo-driven linear stage (SmarAct™ 1720s) [11], and a multi-dimensional flexural link subassembly. As shown in Fig. 2, a group of eight CRL is confined by a thin metal lens confiner, which is mounted on the bottom of the lens holder frame. A short linear bearing V-rail is

* Work supported by the U.S. Department of Energy, Office of Science, under Contract No. DE-AC02-06CH11357.

[†] shu@aps.anl.gov

mounted in the lens holder frame as the top half of the lens alignment structure. At the linear stages lower limit position, the flexural link subassembly, as shown in Fig. 3, provides multi-dimensional flexibility to ensure the CRL group to be fully aligned between the lens holder V-rail and the base V-rail.

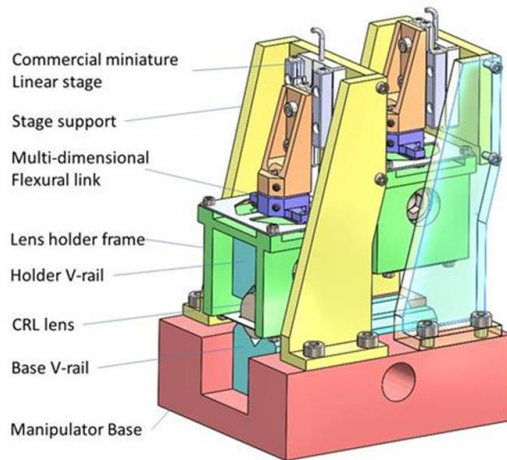


Figure 1: A 3-D model of the proof-of-principle prototype design for the compact x-ray CRL manipulator.

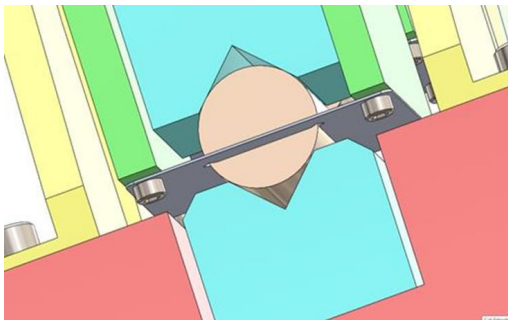


Figure 2: A 3-D model of the eight CRL confined by a thin metal lens confiner, which is mounted on the bottom of the lens holder frame.

X-RAY TEST FOR THE PROOF-OF-PRINCIPLE PROTOTYPE

A proof-of-principle prototype for the compact x-ray CRL manipulator was manufactured with 3D-printing technique as shown in Fig. 4. It is designed to hold a group of eight 2-D parabolic beryllium CRL lenses with 50 micron radius of curvature from RXOPTICSTM. The 2D-lenses have a circular frame with a diameter of 12 mm and a thickness of 2 mm for each lens. The x-ray test was performed at the APS 1-BM beamline using an 8 keV beam. The measured focal size of the lens stack is $4.1 \times 1.7 \mu\text{m}^2$ FWHM at 589 mm downstream of the lens stack as shown in Figs. 5 and 6. The total transmission of the stack is 36% within the $390 \times 390 \mu\text{m}^2$ aperture, which gives a gain of ~ 8000 .

The repeatability of the prototype manipulator was tested by moving the lens stack up and down. No measurable difference was observed. A second stack of 8 lenses was tested as well with a similar measured focal size. It indicates a good quality consistency of these lenses.

Core technology developments

New Technologies

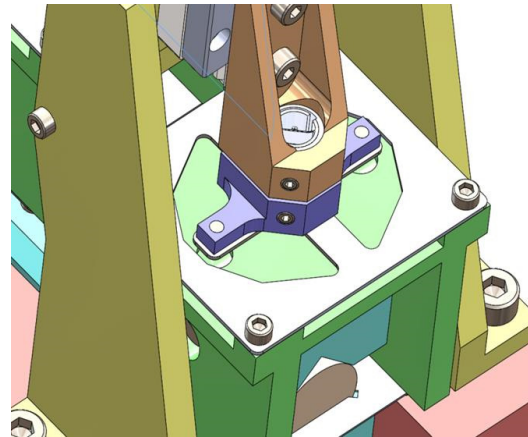


Figure 3: A 3-D model of the multi-dimensional flexural link subassembly which links the lens holder frame with the carriage of the miniature piezo-driven linear stage.

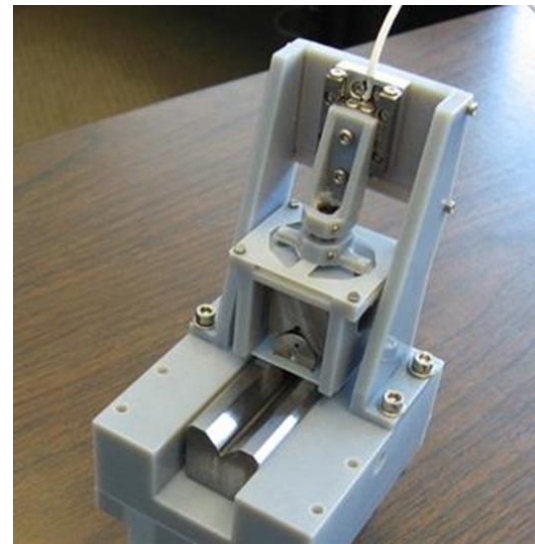


Figure 4: Photograph of the proof-of-principle prototype for the compact x-ray CRL manipulator manufactured with 3D-printing technique and modified commercial THK™ linear bearing V-rail.

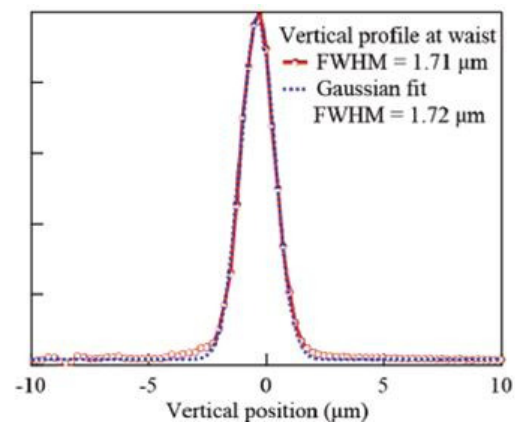


Figure 5: The measured vertical focal size of the lens stack is $1.7 \mu\text{m}$ FWHM at 8 keV.

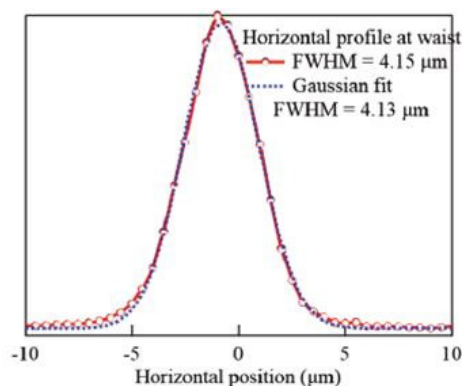


Figure 6: The measured horizontal focal size of the lens stack is 4.1 μm FWHM at 8 keV.

DESIGN OF THE COMPACT MANIPULATOR FOR 16-MM CRL LENS STACK

Based on the experiences gained from the proof-of-principle prototype, a compact manipulator APS Y9-5101 for 16-mm CRL lens stack was designed using commercial miniature piezo-driven linear stage, such as SmarAct™ 1720s, as a lens manipulating driver. As shown in Fig. 7, a group of four Y9-5101 CRL manipulators are mounted on a pair of linear guiding rails and linked together as a unit to be driven by a manual or motorized linear motion driver for focal length adjustment. Since the manipulator precision alignment structure is based on the commercial high precision V-rail, a regular linear guiding system can be used for the focal length adjustment. Figure 8 shows two options of the linear guiding system for focal length adjustment.

To accommodate to the operation conditions on a diffractometer detector arm that may rotate in horizontal as well as vertical planes during diffraction studies, a micro-bearing has been added on the stage support structure as shown in Fig. 9 to confine the vertical tilting range of the flexural link subassembly. Figure 10 shows a 3D FEA model for the flexural link subassembly of the Y9-5101 CRL manipulator. The results showed that the maximum Von-Mises stresses on the 250 micron thick flexural link with various operation conditions are well below the material yield stress for 17-7-PH stainless steel.

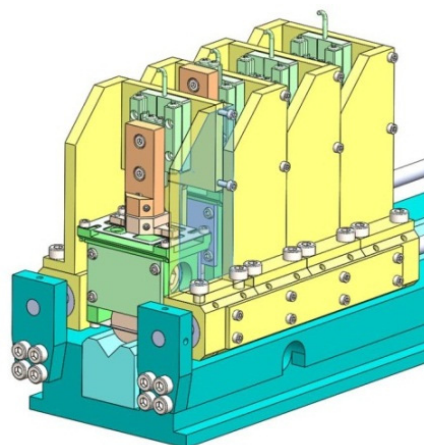


Figure 7: A 3-D model of a group of four Y9-5101 CRL manipulators mounted on a pair of linear guiding rails and linked together as a unit.

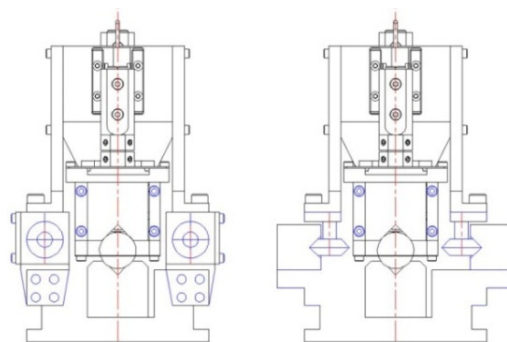


Figure 8: Schematic diagrams for the two options of the CRL manipulators linear guiding system for focal length adjustment. Left: using Thomson™ ball Bushing™ system [12]. Right: using THK™ V-rails and rolling wheels.

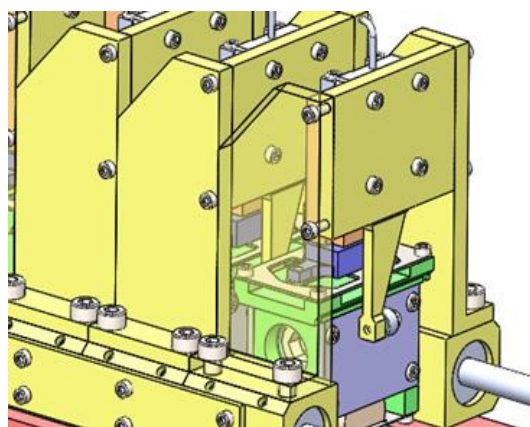


Figure 9: A 3-D model of the APS Y9-5101 compact manipulator with micro-bearing added on the stage support structure to confine the vertical tilting range of the flexural link subassembly.

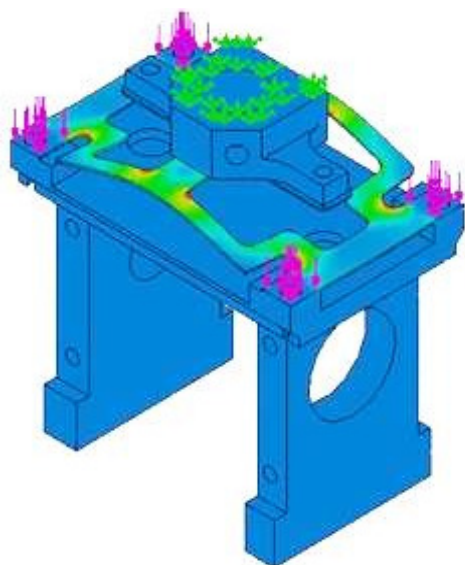


Figure 10: A 3-D FEA model for the flexural link subassembly of the Y9-5101 CRL manipulator.

DESIGN OF THE COMPACT MANIPULATOR FOR 32-MM CRL LENS STACK

To manipulate CRL lens stack with longer total length, a compact manipulator APS Y9-5102 for 32-mm CRL lens stack was designed using commercial piezo-driven linear actuator, such as Picomotor™ 8353 [13], as a lens manipulating driver with maximum axial driving force of 13 N. Figure 11 shows a 3D model of the Y9-5102 compact manipulator for 32-mm CRL lens stack.

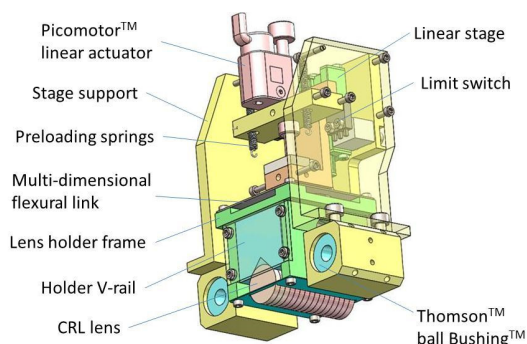


Figure 11: A 3-D model of the Y9-5102 compact manipulator for 32-mm CRL lens stack.

SUMMARY

The mechanical designs of a new precision alignment apparatus for compact x-ray CRL manipulator system are presented in this paper. This CRL manipulator system is specially designed for dark-field imaging of multi-scale structures at the APS. Comparing with existing CRL manipulator designs [14, 15], it is compact, and suitable to be implemented on a high-resolution diffractometer detector arm that rotates during diffraction studies with limited load capacity. A prototype for proof-of-principle has been built and tested at the APS with promising results.

Meanwhile, the compact modular designed CRL manipulators are compatible with high-vacuum (HV) or ultra-high-vacuum (UHV) operation conditions. The manipulators integration flexibility provides wide range of applications for synchrotron radiation instrumentation. Figure 12 shows a 3D model of a combination of four Y9-5101 and one Y9-5102 manipulators for a total of 48 CRL to be mounted on a Thomson™ rail system with 140-mm travel range for focal length adjustment on a high-resolution diffractometer detector arm for dark-field imaging application. Figure 13 shows a schematic diagram for a combination of four Y9-5101 and nine Y9-5102 manipulators for a total of 159 CRL with an overall manipulators dimension of 468-mm. The 1+2+4+8+16x9 CRL lenses arrangement provides the flexibility to select any number between 0 – 159 for the numbers of CRLs to be aligned into the x-ray beam.

ACKNOWLEDGMENT

The authors would like to acknowledge Patricia Fernandez and Dean Haeffner for their management support. Work supported by the U.S. Department of Energy, Office of Science, under Contract No. DE-AC02-06CH11357.

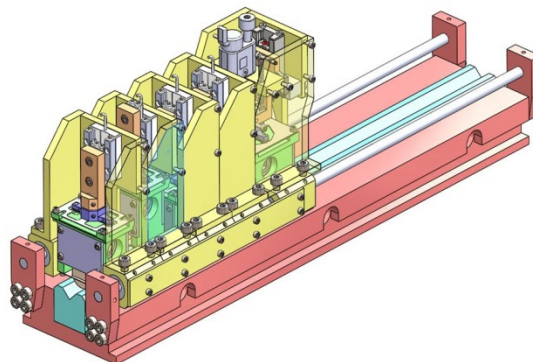


Figure 12: A 3-D model of a combination of four Y9-5101 and one Y9-5102 manipulators for a total of 48 CRL to be mounted on a Thomson™ rail system with 140-mm travel range for focal length adjustment. The motorized linear actuator for focal length adjustment is not shown in the figure.

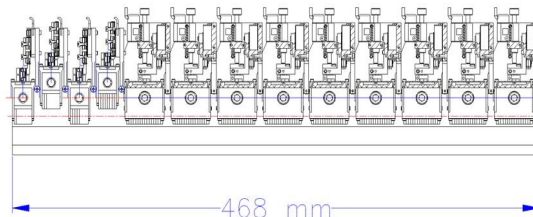


Figure 13: A schematic diagram for a combination of four Y9-5101 and nine Y9-5102 manipulators for a total of 159 CRL with an overall manipulators dimension of 468-mm.

REFERENCES

- [1] H. Simons, A. King, W. Ludwig, C. Detlefs, W. Pantleon, S. Schmidt, F. Stöhr, I. Snigireva, A. Snigirev, and H. F. Poulsen, “Dark-field X-ray microscopy for multiscale structural characterization,” *Nat. Comm.*, 6, Jan. 2015, paper 6098, DOI: 10.1038/ncomms7098.
- [2] H. Simons, A. C. Jakobsen, S. R. Ahl, C. Detlefs, H.F. Poulsen, “Multiscale 3D characterization with dark-field x-ray microscopy,” *MRS Bulletin*, 41, June 2016, pp. 454-459, DOI: 10.1557/mrs.2016.114.
- [3] J. Hilhorst, F. Marschall, T. N. Tran Thi, A. Last, and T. U. Schüll, “Full-field X-ray diffraction microscopy using polymeric compound refractive lenses”, *J. Appl. Cryst.*, 47, 2014, pp. 1882-1888, DOI: 10.1107/S1600576714021256.
- [4] W. Ludwig, P. Cloetens, J. Härtwig, J. Baruchel, B. Hamelin, and P. Bastie, “Three-dimensional imaging of crystal defects by ‘topo-tomography’”, *J. Appl. Cryst.*, 34, Oct. 2001, pp. 602-607, DOI: 10.1107/S002188980101086X.
- [5] F. Marschall, A. Last, M. Simon, M. Kluge, V. Nazmov, H. Vogt, M. Ogurreck, I. Greving, and J. Mohr, “X-ray full field microscopy at 30 keV”, *J. Phys. Conf. Ser.*, April 2014, DOI: 10.1088/1742-6596/499/1/012007.
- [6] S. R. Ahl, H. Simons, A. C. Jakobsen, Y. B. Zhang, F. Stöhr, D. Juul Jensen, and H. F. Poulsen, “Dark field X-ray microscopy for studies of recrystallization”, *IOP Conf. Ser.: Mat. Sci. Eng.*, vol. 89-1, 2015, DOI: 10.1088/1757-899X/89/1/012016.
- [7] A. Snigirev, V. Kohn, I. Snigireva, B. Lengeler, “A compound refractive lens for focusing high-energy X-rays”, *Nature*, vol. 384, iss. 6604, Nov. 1996, pp. 49-51, DOI: 10.1038/384049a0.
- [8] B. Lengeler, C. Schroer, J. Tummler, B. Benner, M. Richwin, A. Snigirev, I. Snigireva, M. Drakopoulos, “Imaging by parabolic refractive lenses in the hard X-ray range”, *J. Synchrotron Rad.*, vol. 6, 1999, pp. 1153-1167, DOI: 10.1107/S0909049599009747.
- [9] RXOPTICS, <http://www.rxoptics.de/intro.html>.
- [10] THK, <http://www.thk.com>.
- [11] SmarAct, <http://www.smaract.com>.
- [12] Thomsonlinear, <https://www.thomsonlinear.com>.
- [13] Newport, <https://www.newport.com>.
- [14] G. M. A. Duller, D. R. Hall, and A. Stallwood, “F-Switch: Novel 'Random Access' Manipulator for Large Numbers of Compound Refractive Lenses”, in *Proc. MEDSI'16*, Barcelona, Spain, Sep. 2016, paper WEPE22, pp. 345-347, DOI: 10.18429/JACoW-MEDSI2016-WEPE22.
- [15] JJ X-ray, <https://jjxray.dk>.

APPLICATION OF INDUSTRY RECOGNISED DEVELOPMENT TOOLS AND METHODOLOGIES, SUCH AS SIX SIGMA TO FACILITATE THE EFFICIENT DELIVERY OF INNOVATIVE AND ROBUST ENGINEERING SOLUTIONS AT SYNCHROTRON FACILITIES

S.A.Macdonell†, Diamond Light Source, OX11 0DE Didcot, UK

Abstract

Synchrotron facilities play a key part in the delivery of world leading science to facilitate research and development across multiple fields. The enabling technology designed by engineers at these facilities is crucial to their success.

The highly academic nature of Synchrotron facilities does not always lead to working in the same way as a commercial engineering company. However, are the engineering requirements at Synchrotrons different to commercial companies? Exploring the parallels between research and commercial companies, can we show that the tools and methodologies employed could benefit engineering development at Synchrotrons?

This paper provides a theoretical discussion on the commonality between engineering developments at Synchrotron facilities compared to commercial companies. How methodologies such as Design for Six Sigma and in particular tools such as stakeholder analysis, functional tree analysis, FMEA and DoE could be utilised in the design process at Synchrotrons. It also seeks to demonstrate how implementation could aid the development of innovative, robust and efficient design of engineering solutions to meet the ever-increasing demands of our facilities.

INTRODUCTION

Diamond Light Source [1], as other Synchrotron facilities around the globe, generates brilliant beams of light from infrared to X-rays, used for academic and industrial research. This research can be at the cutting edge of scientific discovery and therefore requires innovative enabling technology, engineered to meet unique requirements. Diamond Light Source like other facilities is a ‘not for profit’ organisation that is primarily government funded.

Commercial companies, on the other hand must develop innovative products that meet the needs of particular markets. Markets and the opportunity they present are constantly changing and companies must adapt and develop new innovative products and technology to meet these ever-changing needs. Commercial companies operate to make a profit that can fund business growth and the development of next generation products.

Synchrotron facilities and commercial companies oper-

ate and are funded differently, but at the heart of both of these organisations is a need to develop new and innovative solutions to meet unique engineering requirements. The ability to deliver to these unique engineering requirements determines the success of the organisation whether it be a Synchrotron facility or a commercial company.

Many commercial companies utilise Six Sigma approaches within their organisations. The many success stories of Six Sigma implementation include organisations such as [2] GE, Motorola, Honeywell, Bombardier, 3M Ford and Toshiba. Today, many large commercial organisations have implemented Six Sigma and are reporting large profits.

However, implementation of Six Sigma is not common at Synchrotron facilities. Given the funded research nature of these types of organisation, and headlines of profit associated with Six Sigma it is perhaps possible to understand why. Six Sigma also holds a statistical association that implies it is only useful for organisations creating products for mass production. This does not necessarily match with the single unique engineering developments carried out at Synchrotrons.

However, when we explore the Six Sigma methodology further and how and why it is used. We can see that the use of Six Sigma within an organisation can provide systematic approaches to process improvement, problem solving of existing designs and improve quality in new design

Since Synchrotron facilities utilise processes, can have a requirement to solve problems and do require high levels of quality in the design of their systems it is hard to believe that the Six Sigma approach or at least parts of it would not be beneficial. In fact, if we were to deploy some of the tools embedded in the Six Sigma approach at Synchrotrons could we save time in development, could we improve the performance and ultimately increase our ability to deliver world leading scientific research?

At Diamond Light Source Ltd, we have started to investigate the Six Sigma methodology and how we might apply this to the benefit of our organisation.

ENGINEERING DEVELOPMENTS AT SYNCHROTRON FACILITIES VERSUS COMMERCIAL COMPANIES

If we strip away the input and output factors of any engineering organisation, we see that there is a core process

† sarah.macdonell@diamond.ac.uk

of converting requirements into solutions. This common ground at the heart of an organisation, be it a Synchrotron facility or a commercial company, demonstrates that however the organisation is funded or whatever its final output is, there are some aspects of these organisations that must be similar.

At a Synchrotron facility, the requirement to do some engineering development may originate from a scientific need to allow specific research to be undertaken. In a commercial company, the requirement may originate from the feedback of customers within its operating markets. Ultimately, irrespective of the origin or detail we have identified a 'need' to do some engineering development.

At a Synchrotron facility, there may be a requirement to satisfy this need in order that research can be completed and published first. In a commercial company, there may be a requirement to satisfy this need in order to hit a market window and release a product ahead of its competitors. Both of these scenarios demonstrate a requirement for needs to be satisfied within certain timescales to ensure success. Although at a Synchrotron, the timescales aspect may not be as critical due to the many unknowns associated with carrying out scientific research, delays to enabling the research to take place could mean another scientist somewhere round the world could undertake this first.

From identifying a requirement or need, we need to translate these into a specification detailing what it is we actually need to engineer. Requirements and specifications are fundamental to ensuring an agreed understanding of the criteria an engineering solution needs to meet in order to be successful. Failure to do this means that project scope may creep, designs may not be fit for purpose, the project may overspend and there may be substantial delays in the time taken for the development. For either type of organisation, this can have detrimental consequences. Therefore, delivery on time, to specification and in budget is critical to both.

As engineers, we all want to ensure whatever solutions we deliver, perform at the correct level. Requirements and specifications become critical in ensuring we define what the correct level of performance is; in fact, they allow us to define what success looks like.

The actual requirements and specifications at Synchrotrons and commercial companies may be very different in terms of content or priority; however, they still define the criteria against which the development activity will progress.

The phases that engineers may go through in development of solutions can include; concept generation and selection, detail design, prototyping, manufacture and assembly, testing and verification. All of these steps ensure we develop solutions that meets the criteria specified in our requirements and specification documents. In other words how we deliver a solution of the correct quality to meet the required performance standards.

These phases may look very different depending on the type of organisation. For example, at a Synchrotron where we are generally designing and building a one-off solu-

tion, any prototype hardware may in fact be the hardware used. Testing and verification may happen on this during installation and commissioning phases. In commercial companies where they intend to sell quantities of a product, they often manufacture several sets of prototype hardware. Each set of prototype hardware tests different aspects in terms of performance and the processes involved in mass production, particularly repeatability and reproducibility.

At a commercial company, issues with quality, cost or timescales could lead to a product that does not meet the needs of the market, higher operating costs, reduced profit and missed market windows. Ultimately, the company may lose customers and market share, severely affecting their bottom line.

For a Synchrotron issues with quality, cost or timescales could lead to solutions that are unable to facilitate some or all of the science they were required for, missed opportunities to deliver ground breaking science and delays in availability of resources to do other developments. Ultimately, this could mean cancelling users, a reduction in publications and possible loss of future funding.

Acknowledging that there are differences between these types of organisation we have also shown that the aspects of cost, time and quality apply to both. Therefore, it seems that it should be possible to use the Six Sigma approach or at least some of the tools encompassed in this approach to ensure that we are meeting the quality, cost and timescale requirements at a Synchrotron facility.

SIX SIGMA OVERVIEW AND USEFUL TOOLS

Overview

Six Sigma [2] has been around in its current form since the late 70s when Motorola developed the approach and documented savings of over \$16 billion [2]. Six Sigma has a foundation in statistics and the idea that the nearest specification limit is six standard deviations from the mean, then as the variation in a process increases the mean, the result will move further away from the midpoint of the specification limits. Consequently, fewer standard deviations will fit between the mean and the specification limit.

This statistical approach is also why it can put off organisations such as Synchrotron facilities as we may only have a data set of one.

However, when we look further into Six Sigma there are two fundamental methodologies associated with Six Sigma, DMAIC and DFSS.

DMAIC [3-5] is the most commonly used methodology and is mostly concerned with existing processes or hardware that are wasting resources. DMAIC stands for Define, Measure, Analyse, Improve and Control. In essence, define the requirements or project goals, measure current performance, determine root cause, implement corrective actions to eliminate the root cause issue and implement controls to ensure continued good performance.

DFSS [3, 4] on the other hand stands for Design for Six Sigma and is concerned with the design of a new product for Six Sigma quality. Unlike DMAIC, there are several different ways to approach Design for Six Sigma. The approach implemented at a company will depend on the type of business. Therefore, we can consider Design for Six Sigma more of an approach than a defined methodology.

As an Engineer, you can approach Six Sigma in the same way as your toolbox. Your toolbox can hold multiple tools, you do not always need to use every tool in the box for every job that you do but you do need to use your tools in the right order. Using the right tool, at the right time allows you to complete work efficiently and successfully.

Selecting and applying appropriate tools from within the Six Sigma framework and applying to development activities at Synchrotron facilities should offer improvements to the quality and efficiency of delivery.

Stakeholder Identification

When it comes to defining, the requirements for a new development at a Synchrotron facility there are many stakeholders and these can be both internal and external. Stakeholders are those people who will benefit from the project, people impacted by the project, people who will have an interest in the project and those who may have a concern regarding the project. These may be our users, members of peer review panels, senior management, engineers, scientists, specialist groups, suppliers or even partners at other Synchrotrons. Brainstorming whom the project will touch and identifying interfaces where exchanges of information or materials may occur will support developing a list of stakeholders for a project.

An Elliot Kemp Matrix [4-6] can be utilised to clarify who our stakeholders are in terms of their power and influence and their interest or concern in the project. Figure 1 shows how the Elliot Kemp matrix is constructed, with quadrants representing the different types of stakeholder. Those in quadrant 1 are key players, ready and willing to participate in the project. Quadrant 2 represents those stakeholders that would be willing to participate if they could but lack required knowledge or power. Quadrant 3 have an ability to influence the project but do not want to engage. Finally, quadrant 4 are those with no influence and minimal interest in the project.

The success or failure of a project can hinge around engaging with the right people at the right time throughout the project lifecycle. Particularly, when we consider the specialist nature of Synchrotron facilities. We are endeavouring to do things that have potentially never been done before and in order to succeed we need to engage with and have people engage in supporting us. Understanding, of who these people are and how we need to involve them can only benefit us. How often have you done months of work to find there is a problem with your solution due to something you were not aware of, perhaps there was a

stakeholder missing from initial project discussions that could have made you aware earlier?

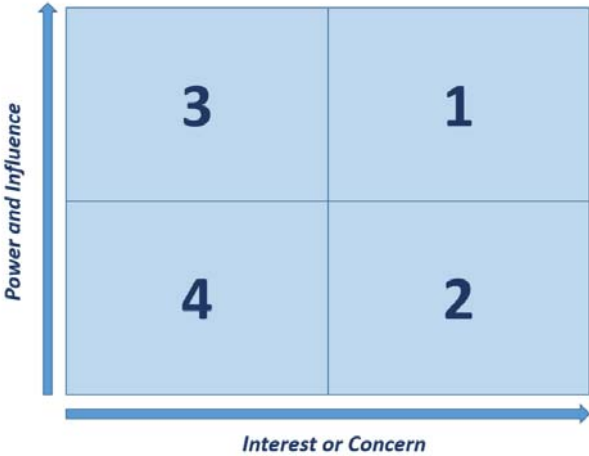


Figure 1: Elliot Kemp Matrix.

Engaging at the right level with stakeholders throughout a project can ensure that requirements, specification, design solutions and decisions are effective, preventing the need for rework because of missing information or knowledge. This can be of particular importance at a Synchrotron where there are a plethora of specialist groups with specialist knowledge.

Functions Identification

Describing the hardware we want to design by its functions, can prevent constraining elements becoming fixed in the design [4, 5]. The concept of functionality means we describe something in terms of what it does rather than what it is. Describing a design in terms of its functions and not its solutions enables us to determine design criteria, which helps us, develop the requirements specification and ultimately encourage innovation.

We could view this, as a method to get inside the head of the scientist and facilitate understanding as to what it is they want.

To do this we describe functions using two words, a verb and a noun. The noun in this case must not be part of the hardware. So for example, in designing a beamline we might say it needs to illuminate a sample, we might say it needs to generate light or provide energy; we might talk about aligning sample or presenting sample. Ultimately, we want to describe all the functions required to achieve the end goal of the scientist, starting with the top-level function or 'Task' function.

Figure 2 is an example of how from the task function we can define a functional structure or functional tree for the system we are designing. The task function sits at the top of the tree. From this starting point, you develop the next level of functions by asking 'How' we can achieve the task function. This cascades downwards until we reach the lowest level of functions. The overall size of the structure will depend on the complexity of the system.

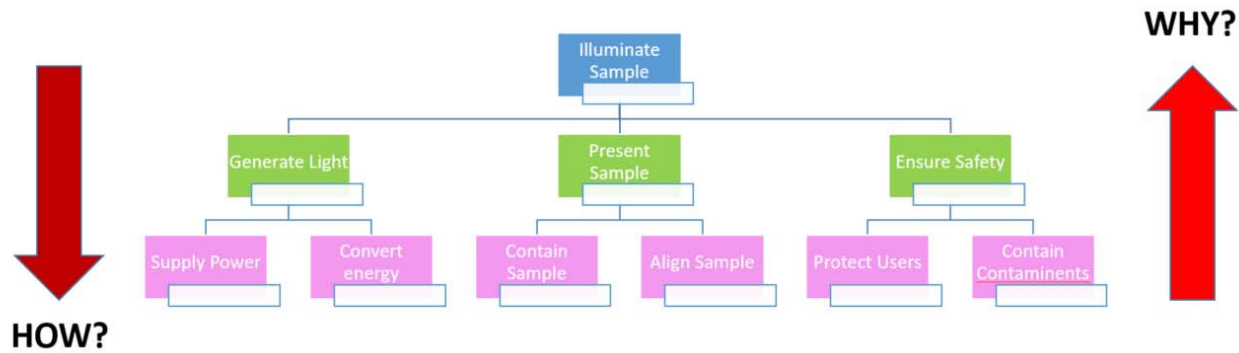


Figure 2: Example Functional Tree.

Progressing down the functional tree shows how to achieve the function above, progressing up the tree shows why we need the function. I.e. we need to ‘Protect Users;’ Why? To ‘Ensure Safety.’

Once a functional tree is established, it can help guide the development, aiding prioritisation of functions delivery and more importantly defining specifications. For example, we want to align a sample. What accuracy or resolution is required?

Use of functional trees to aid in requirements capture is being trialled at Diamond Light Source and whilst we are refining the process to suit us, this technique is proving successful and we are looking to use this more in the future.

FMEA

Finding design problems late in the development process can cause substantial disruption to a project. Particularly, in Synchrotrons where some work may need to be done in ‘shutdown’ periods. This provides a small window of opportunity for work to be completed and everything needs to be ready on time and without faults.

Risk analysis offers us the opportunity to proactively identify errors and take action in time to avoid them. FMEA [4-6] or Failure Mode and Effect Analysis is an industry standard method of carrying out risk analysis. It presents a systematic approach to establishing failure modes, effects and potential causes. FMEA is a continual process throughout the development cycle. A Systems FMEA completed following specification agreement but before design, allows us to mitigate issues ahead of creating and selecting design solutions.

A Design FMEA allows us to assess risk of failure with respect to the design solution and occurs after a concept solution is proposed and prior to detail design. This allows us to mitigate risk of failure due to the design throughout the detail design phase and supports assessment of the final design solution prior to manufacture.

A Process FMEA allows us to review things that may go wrong in the manufacturing, assembly, installation or commissioning processes. This should occur following design completion and ahead of the next development, manufacturing and testing phases.

The functional tree created previously allows identification of failure modes by analysing the functions we require. Each failure mode assessed allows us to look at the causes of failure and score them with respect to the severity of failure, the likelihood of occurrence and ability to detect the failure; creating a risk priority number.

Benefits to this method include:

- Early identification of potential problems throughout the lifecycle
- Increased quality and likelihood of being right first time
- Ability to stay on budget
- More efficient delivery, increased likelihood of being on time
- More emphasis on lessons learned and understanding of what has or has not been done before
- Prioritisation of key potential issues early

At Synchrotron facilities where budget is limited, we only want to do something once. There are particular constraints surrounding how and when installation can occur. It is critically important that we mitigate risks and deliver a working system when required. FMEA, particularly the systems level and design level FMEAs could ensure improved quality and improved efficiency in the delivery of working design solutions for our facilities.

DoE

Design of Experiments [4-6] or DoE is a controlled way of exploring the effects of different factors on system performance. In effect, the process allows us to consider different input variables and in so doing, optimise a design or system. For example, we might have a cooling system. Inputs to the system’s performance may be the material, cooling fluid, length of cooling channel and flow rates. DoE allows us to understand how these factors and their interactions affect overall system performance and subsequently optimise the design of our system for desired performance. For example, we may want to keep our component below a certain temperature. As such, we may wish to determine the optimum length of cooling channel and flow rate to achieve this. Using DoE, we would systematically plan an experiment that would vary

these two inputs and measure the results. We can then analyse these results to see which has the biggest effect and how the interaction between these two inputs effects the performance. Ultimately, allowing us to make a decision on the optimum length and flow rate.

At a Synchrotron, the performance of our systems is vital to enable our scientific experiments to continue successfully. If our systems do not perform as expected then the consequence could be that we are unable to carry out these experiments and there could be significant delays and cost associated with rectifying these issues.

DoE is relevant within both the development and operational cycles of a system. For an operational system, it could aid in understanding problem performance; for a development system, it can proactively be used to optimise performance. Whilst this is experimental testing, it does not necessarily mean that this must be tested with physical hardware, under some circumstances and with the correct setup, simulated experiments could also be used, particularly to optimise designs.

Selection and Prioritisation

Engineering development entails making many decisions and many of these decisions relate directly to how well the solution will meet the performance criteria. This can be a difficult process particularly for larger projects with many stakeholders. However, there are a couple of simple techniques that support the decision making process.

The first of which is called ‘paired comparison [6].’ This is a simple technique, ideal for use in establishing priorities, particularly of design criteria. For example, if we have criteria A, B, C, D, and E. We can compare pairs of criteria in turn and total the winning occurrences of each criteria, i.e. we can compare criteria A and B, A and C, A and D, A and E; asking which is more important.

Table 1: Paired Comparison Matrix

	A	B	C	D	E
A		A	A	A	A
B			B	D	E
C				D	E
D					D
Σ	4	1	0	3	2

Table 1 shows the results of the comparison of each pair of criteria in red. We can then count the number of winning occurrences for each criteria. The criteria with the highest number of occurrences indicates the most important criteria, in this case A with four occurrences. C has zero occurrences and therefore is the least important. This does not mean C is not important but that we prioritise decisions towards meeting criteria A, with D being the next important, followed by E and then B.

In order to select the most appropriate design solutions a commonly used technique is a Criteria Matrix [6]. This technique allows us to score design solutions against weighted criteria. The development team score each possible solution out of 10 against the design criteria, this is

multiplied by a weighting for the design criteria itself and the total weighted score for each solution summed. Highest overall score indicates the solution that best meets the design criteria.

Table 2: Example of a Criteria Matrix

Design Criteria	Weight	Design 1		Design 2	
		Score	Wtd. Score	Score	Wtd. Score
A	10	1	10	5	50
B	4	10	40	10	40
C	2	5	10	7	14
D	8	7	56	3	24
E	6	8	48	1	6
Total			164		134

Table 2 shows an example of how a criteria matrix works. In this example, the weighted scores for the criteria were determined by giving each criteria a score out of 10 based on the priorities agreed using the paired comparison.

These two simple methods for prioritising and selecting solutions are easy to use and provide a quantifiable process for decision-making.

CONCLUSION

Whilst there are many differences between Synchrotron facilities and commercial companies, at the core, both must meet quality, time and cost targets.

Six Sigma whilst in its full statistical sense may not seem applicable at Synchrotron facilities we do look for continual quality improvement of our design solutions and the improved efficiency of our delivery processes. With the size and specialist nature of our organisations the tools contained within the Six Sigma approach are of definite benefit.

Whilst only a small number of tools have been reviewed and trialled at Diamond Light Source Ltd, we will be continuing to investigate the application of Six Sigma methodologies further.

REFERENCES

- [1] Diamond Light Source, <http://www.diamond.ac.uk/industry/Synchrotron-Oxford/What-is-a-Synchrotron.html>
- [2] T. T. Burton and J. L. Sams, in *Six Sigma for Small and Mid-Sized Organizations*, Boca Raton, Florida, USA : J Ross Publishing, 2005.
- [3] iSixSigma, <https://www.isixsigma.com/new-to-six-sigma/design-for-six-sigma-dfss/design-six-sigma-dfss-versus-dmaic/>
- [4] Smallpeice Enterprises Ltd., *Lean Sigma Black Belt*. Malvern Instruments Ltd. Training Manual, 2013.
- [5] Smallpeice Enterprise Ltd., *Lean Sigma Manufacturing Green Belt*. Malvern Instruments Ltd. Training Manual, 2011
- [6] Smallpeice Enterprises Ltd., *Lean Sigma Toolkit*, 2011

A COMPACT AND CALIBRATABLE VON HAMOS X-RAY SPECTROMETER BASED ON TWO FULL-CYLINDER HAPG MOSAIC CRYSTALS FOR HIGH-RESOLUTION XES

I. Holfelder[†], R. Fliegau, Y. Kayser, M. Müller, M. Wansleben, J. Weser, B. Beckhoff,
 Physikalisch-Technische Bundesanstalt, 10587 Berlin, Germany

Abstract

In high-resolution X-ray emission spectroscopy (XES) crystal-based wavelength-dispersive spectrometers (WDS) are being applied for the characterization of the electronic structure of matter in various research fields like geosciences, chemistry or material sciences. Thereby, the von Hamos geometry provides high detection efficiency of spectrometers due to sagittal focusing using cylindrically bent crystals. To maximize the detection efficiency, a full-cylinder optic can be applied [1].

Based on this idea, a novel calibratable von Hamos X-ray spectrometer based on up to two full-cylinder optics was developed at the PTB. To realize the full-cylinder geometry, Highly Annealed Pyrolytic Graphite (HAPG) [2] was used. Besides its good bending properties, this mosaic crystal shows highly integrated reflectivity while offering low mosaicity, ensuring high resolving power [3]. The spectrometer enables chemical speciation of elements in an energy range from 2.4 keV up to 18 keV. The design and commissioning of the spectrometer will be presented. The spectrometer combines high efficiency with high spectral resolution (ten times better than in commercial WDS systems) in a compact arrangement also suitable for laboratory arrangements.

INTRODUCTION

Constant development of novel micro- and nano-materials in the industry is a huge challenge for metrology. As the research and development cycles are sometimes less than four months, reliable correlations of material functionalities and properties are called for while only few or no reference materials available. Therefore, reliable analytical methods for characterization of new material systems are needed that are not dependent on reference materials. An appropriate method is the reference-free X-ray spectrometry, which is based on the so-called fundamental parameter approach [4, 5, 6, 7, 8]. This method requires calculable synchrotron radiation and radiometrically calibratable instrumentation. In this work we present a novel compact wavelength-dispersive spectrometer that can be calibrated to ensure reference-free X-ray emission spectroscopy (XES). Due to its compactness and its high efficiency, it can be used in different experiments and at different beamlines. A laboratory X-ray source can be used as an excitation source as well.

[†] ina.holfelder@ptb.de

VON HAMOS SPECTROMETER

To ensure high efficiency, the von Hamos geometry was used. In the von Hamos geometry, the radiation source – which, in the case of the XES experiment, is the fluorescence radiation from the sample – and a CCD camera are placed along the cylinder axis of a sagittally bent crystal, see Figure 1. While the original design was based on a cylindrically bent crystal covering only a segment of a ring, the use of full-cylindrical optics allows maximizing the solid angle of detection [9, 10].

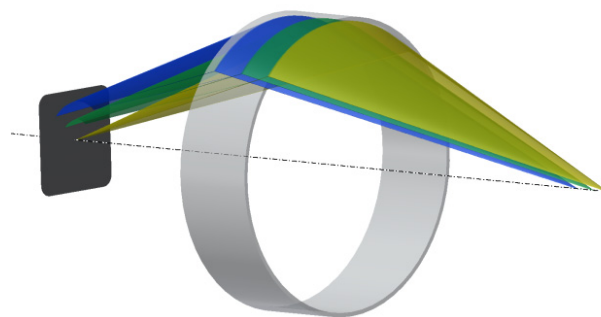


Figure 1: Von Hamos geometry.

To realize full-cylinder geometry, Highly Annealed Pyrolytic Graphite (HAPG) is especially suitable for this purpose, as it can be bent up to a 50 mm radius without any structural impact on the resolution. In the spectrometer presented here, 40 μm thick HAPG layers on cylindrical glass ceramic (Zerodur®) substrates were used. The HAPG is a mosaic crystal that consists of 50 μm to 80 μm mosaic blocks, which again consists of several approximately 1 μm sized crystallites that are tilted against each other [11]. Its mosaic structure leads to the highest integrated reflectivity of all known crystals, as all crystallites that are lying on the Rowland circle and fulfil the Bragg equation contribute to the crystal reflectivity. Simultaneously, HAPG has an especially small mosaic spread, the angle distribution function of the crystallites, and high resolving power.

For an additional increase of the resolving power, two HAPG optics are used in the beam path. An increase of the resolving power of around 40 % is expected [12]. This double reflection concept also increases the discrimination capability and improves the tailing of the spectral peaks.

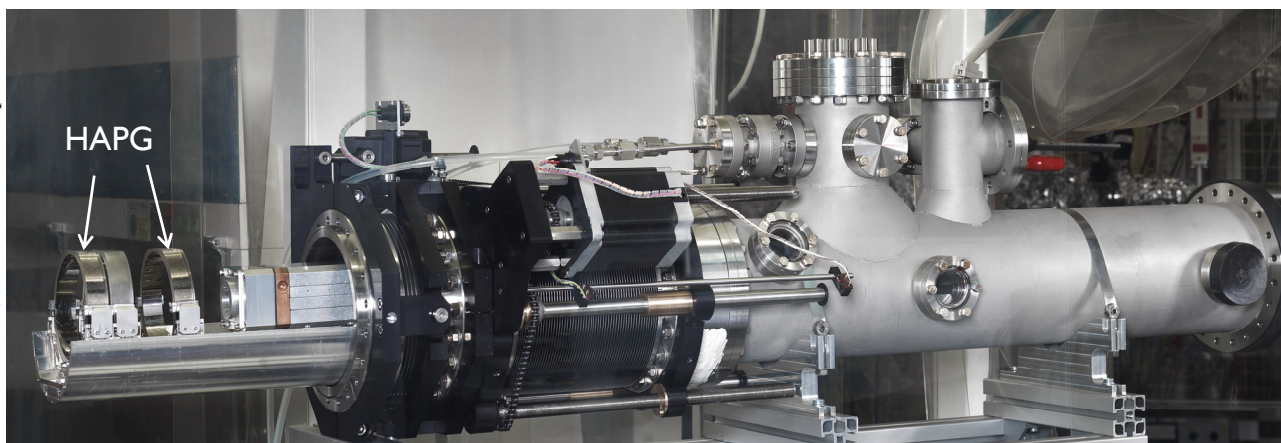


Figure 2: Picture of the presented X-ray von Hamos spectrometer.

Using the double Bragg reflection concept lowers the efficiency of the spectrometer compared to using one Bragg reflection.

In Figure 2 the spectrometer is shown. The whole front part goes into an experimental chamber. The flange inner diameter is 150 mm. The main components are three cylindrical optics and a CCD camera. The first and the third optics are HAPG optics. The second optic will be an optic based on a perfect crystal in the future. To prevent the icing of the CCD chip of the camera, an ultra-high vacuum (UHV) environment is necessary. The CCD camera is a water-cooled Princeton Instruments camera with 2048 x 2048 pixels. The pixel size is 13.5 μm . Furthermore, there is a port aligner, a linear feedthrough, and the ultra-high vacuum chamber.

THE 17-AXIS MANIPULATOR

As only a small assembly space was available to move and to adjust the 100 mm inner diameter optics in a 150 mm inner-diameter tubular chamber, piezo manipulators were used.

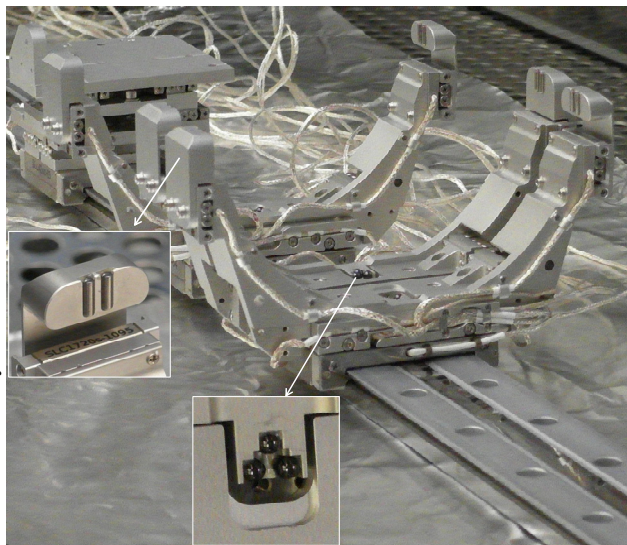


Figure 3: 17-axis manipulator from SmarAct GmbH.

As a result of a joint development of the PTB and SmarAct GmbH, a 17-axis manipulator was manufactured, which allows for the alignment of each optic and the CCD camera. The 17-axis manipulator is shown in Figure 3.

Each component can be moved by one slide, which can be used independently from one another. To ensure high reproducibility, all components were guided on one common linear slide. For each optic, two translator axes in x and y directions are included in addition to the feed motion. The rotation around the vertical axis of the optic is realized by two linear motors that are positioned on the optic sides and move against each other. Therefore, both sides of the optic as well as the bottom of the optic are equipped with a ball joint, see Figure 4.



Figure 4: HAPG optics with three ball joints.

On the manipulator, the optics holders are also equipped with ball or roll joints. At the bottom of the holder, three ceramic balls are included, Figure 3 zoomed view below, in which the below ball joint of the optics is positioned. To ensure a rotation around the horizontal symmetry axis of the optic perpendicular to the feed direction, both linear alignment-axes are moving parallel to the feed direction and in the same direction. Simultaneously the optic is tilted around the below ball joint. Thereby the horizontal

cylinder axis is shifted downwards in the direction of the tilt. The principle is shown in Figure 5. To perform a rotation of the optic around the horizontal axis in an angle α , both linear motors, labeled with number 1 in Figure 5 left, have to move about d_x which is calculated by the distance from the rotation point of the optic to the rotation point of the ball joint (=55 mm) of the optic multiplied with the sine of α . This movement has to be offset with the linear axis number 3 in the opposite direction about d_x . To compensate the vertical position change, motor number 3 has to be moved about d_y . D_y is calculated by d_x multiplied with the tangent of half α . This vertical movement is possible due to the lateral slide of the optic ball joints along the roll joints of the manipulator, see Figure 3 zoomed view left.

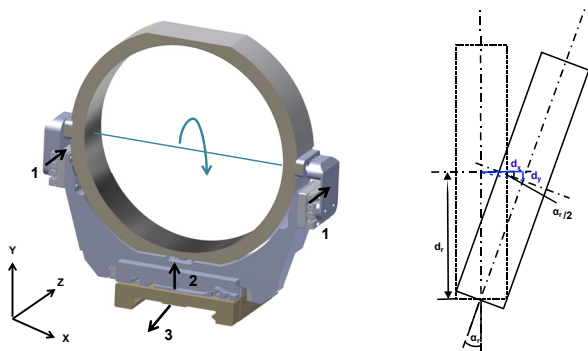


Figure 5: Principle of the rotation around the horizontal axis (perpendicular to the feed direction) using four linear motors.

This translation of the linear movement into polar coordinates enables the integration of two translational as well as two rotatory axes in limited space.

THE ENERGY CHAIN

To ensure the water supply for the Peltier element of the CCD camera a considerable challenge was to ensure a guidance of the hoses over a large travel range of around one meter. Also, the guide of the energy cable for the piezo manipulators was necessary. Because of the limited available space in the chamber it was not possible to use a conventional energy chain here, which is usually made of separate chain links. Furthermore, it has been shown that during the movement of the chain, the chain links tilt abruptly when they are bent, so that can have an impact on the CCD camera position and thereby on your spectral image [13].

Therefore, a new concept was realized for the hose as well as for the electrical cables. This concept is based on a steel strapping made of stainless spring steel, which is bent like a tape measure and has a shape of a gutter with a radius r . For the guidance of the water hoses the gutter is bent to a radius R , so that the gutter inner radius r is placed outside, see Figure 6. Thereby both radii are the same $R=r$. The bending of the steel strapping leads to tensions in the material so that the steel strapping can hold the weight of the water hoses and is stiff to act as a guide at the same time.

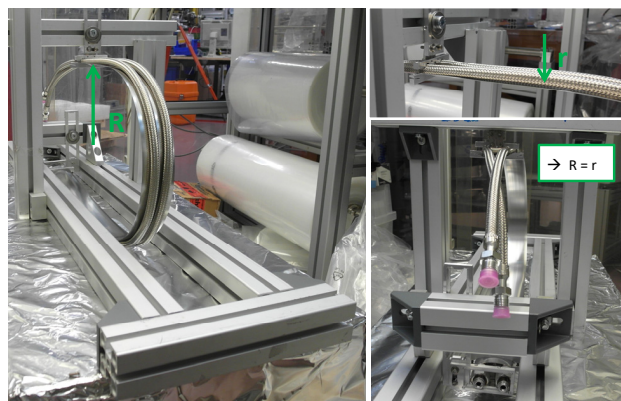


Figure 6: Guiding concept using gutter-type steel strapping.

To ensure that the electrical cable will stay in the guide they were fixed with a copper wire, Figure 7.

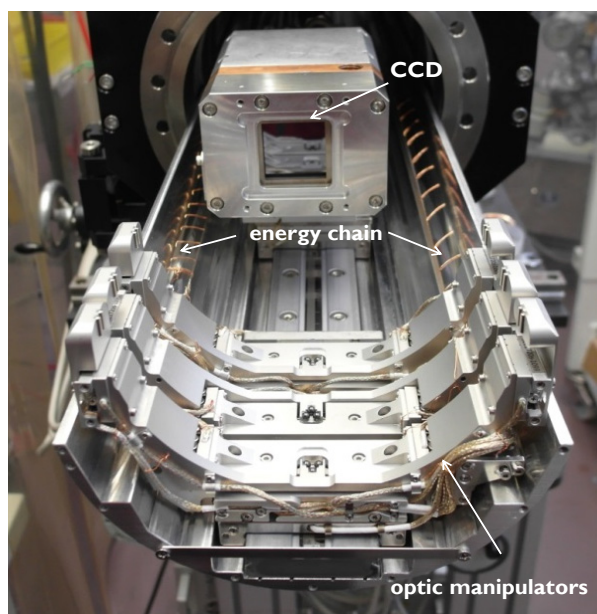


Figure 7: Energy chain for the electric cable of the optic manipulators.

With the here presented guide concept it is possible to carry and guide cables and hoses over a long travel range. At the same time this concept provides an ultra-high vacuum solution.

CONCLUSION

In this paper a novel calibratable wavelength-dispersive spectrometer was presented. The focus of the development was the compactness of the spectrometer as well as the stiffness of the mechanical system. Due to application of small sized piezo motors and a water hose guide concept two 100 mm inner diameter optics could be integrated in a 150 mm inner diameter tubular UHV chamber. Despite of the compact design a large solid angle was realized due to the full-cylinder optic. The condition for spectrometer calibration were fulfilled from the mechani-

cal side in respect to the relevant parameters such as detector response function and detection efficiency. On account of the spectrometers compactness, its high efficiency and its high spectral resolving power ($E/\Delta E = 2800$ for titanium $K\beta_{1,3}$) a transfer to a commercial laboratory tool is quite possible. It can be expected that such high-resolution X-ray spectrometers will be applied in different research fields, for ex-situ, in-situ and operando experiments for different material systems.

REFERENCES

- [1] L. Anklamm *et al.*, "A novel von Hamos spectrometer for efficient X-ray emission spectroscopy in the laboratory", *Rev. of Sci. Instr.*, vol. 85, May 2014, pp. 053110-1 - 053110-5.
- [2] H. Legall *et al.*, "A New Generation of X-Ray Optics Based on Pyrolytic Graphite", in *Proc. FEL'06*, BESSY, Berlin, Germany, Aug.-Sep. 2006, paper FRAAU04, pp. 798 – 801.
- [3] M. Gerlach *et al.*, "Characterization of HAPG mosaic crystals using synchrotron radiation", *J. Appl. Cryst.*, vol. 48, Oct. 2015, pp. 1381-1390.
- [4] A. Delabie *et al.*, "Reaction mechanisms for atomic layer deposition of aluminum oxide on semiconductor substrates", *J. Vac. Sci. Technol.*, vol. A 30, 01A12, Jan. 2012.
- [5] P. Hönicke *et al.*, "Characterization of ultra-shallow aluminum implants in silicon by grazing incidence and grazing emission X-ray fluorescence spectroscopy", *J. Anal. At. Spectrom.*, vol.27, May 2012, pp. 1432-1438.
- [6] B. Pollakowski *et al.*, "Speciation of deeply buried TiOx nanolayers with grazing-incidence x-ray fluorescence combined with a near-edge x-ray absorption fine-structure investigation", *Phys. Rev. B*, vol. 77, 235408, June 2008.
- [7] C. Streeck *et al.*, "Elemental depth profiling of Cu(In,Ga)Se2 thin films by reference-free grazing incidence X-ray fluorescence analysis", *Nucl. Instr. And Meth. B*, vol. 268, Feb. 2010, pp. 277-281.
- [8] R. Unterumsberger *et al.*, "Complementary Characterization of Buried Nanolayers by Quantitative X-ray Fluorescence Spectrometry under Conventional and Grazing Incidence Conditions", *Anal. Chem.*, vol. 83, Oct. 2011, pp. 8623-8628.
- [9] L. v. Hamos, "Röntgenspektroskopie und Abbildung mittels gekrümmter Kristallreflektoren", *Die Naturwissenschaften*, vol. 20, Sept. 1932, pp. 705-706.
- [10] L. Anklamm, "Ein hocheffizientes Von-Hamos-Spektrometer für Röntgenemissionsspektroskopie im Labor", Ph.D. thesis, Technische Universität Berlin, Berlin, Germany, 2014, <http://dx.doi.org/10.14279/depositonce-4184>
- [11] M. Gerlach *et al.*, "Röntgenoptiken aus „Highly Oriented Pyrolytic Graphite (HOPG)“, PTB, Berlin, Germany, Oct. 2012.
- [12] D. Hohlwein *et al.*, "A Graphite Double-Crystal Monochromator for X-ray Synchrotron Radiation", *J. Appl. Cryst.*, vol. 21, Dec. 1988, pp. 911 - 915.
- [13] H. J. Baecker *et al.*, "In-Vakuum Kabelschlepp", 2016, unpublished.

DEVELOPMENT OF A NEW SUB-4K ARPES ENDSTATION AT PSI

D. Trutmann*, S. Maag, L. Nue, A. Pfister, A. Schwarb, K. Zehnder, S. Hasanaj, M. Shi, N. C. Plumb
 Paul Scherrer Institut (PSI), 5232 Villigen PSI, Switzerland

Abstract

In spring 2016 a project was started to renew the high-resolution ARPES endstation of the Surface/Interface Spectroscopy (SIS) beamline at PSI. The focus lay on achieving sample temperatures below 4 K while maintaining 6 degrees of freedom.

This made it necessary to redesign all thermally active parts, such as the connection to the cryostat, the flexible braid that enables the tilt and azimuthal movement, the sample clamping as well as the thermal isolators that hold the clamping device in place. A newly introduced shield in the main analyser chamber, cooled by separate cryopumps, is used to remove nearly all radiation heat load.

A major milestone has recently been taken, by running cryogenic tests on a test stand. The simplified setup reached sample temperatures of 3.35 K. The temperature loss from the cryostat to the sample was as low as 0.6 K. Encouraged by these results, it is believed that the final endstation will be able to reach temperatures even below 3 K. With the new cryo concept, the thermal performance seems to be mainly limited by the radiative heat load emitted by the analyser lens.

The new endstation is planned to be in operation by spring 2019.

INTRODUCTION

Angle-resolved photoemission spectroscopy (ARPES) is a powerful technique to directly measure the electronic band structure and interactions in solids [1] that is widely employed at many synchrotrons. ARPES is primarily used to study materials at the cutting edge of condensed matter physics and solid state engineering. Practitioners in the field are generally interested in experimental systems that can reach ever-lower energy and temperature scales, as these provide access to many interesting, unstudied science cases and ideal conditions obtaining sharp spectra and discerning fine features.

Of course, the pursuit of lower temperature and better resolution always involves design tradeoffs. While the record lowest temperature for ARPES at a synchrotron currently is below 1 K using a He-3 cryostat [2], this level of performance is possible only by drastically reducing access to the sample in order to reduce the radiation load, which in turn introduces practical issues for sample handling, manipulation, alignment and data acquisition.

Considering the state-of-the-art in VUV beamlines – and, more importantly, the performance guarantees of commercially available ARPES analyzers – an optimistic estimate of the foreseeable best-case resolution at SIS beamline is

about $\Delta E = 1$ meV. Equivalent thermal broadening occurs around $T \approx \Delta E / (4k_B) = 3$ K. Below roughly this point, we expect drastically diminishing scientific returns on any hard-fought improvements in the temperature. In light of the above, we have therefore conceived of the SIS upgrade as a new standard in high-throughput *workhorse* systems for ARPES at synchrotrons, with the goal of sub-4 K temperature performance and an optimistic design target of 2 K to 3 K.

GENERAL OVERVIEW

The current endstation offers a six degrees of freedom (DOF) mechanical system, with no coupling between any DOF and only a negligible thermal drift along on the azimuthal axis and no drift along all other DOF. It further offers an open environment such that sample manipulation and alignment is easy. Overall, these features gives it a very competitive all-around performance among ARPES manipulators. Apart from maintaining the above features, the new endstation, figure 1 and 2, should improve or introduce new features, such as:

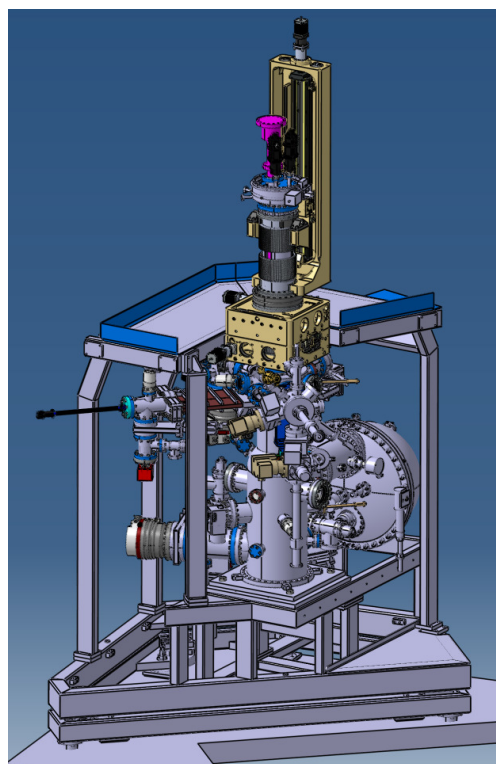


Figure 1: The current state of the new endstation.

- improved sample temperature from currently reachable 14 K (measured on the sample plate holder) to <4 K (measured on the sample plate itself)

* daniel.trutmann@psi.ch

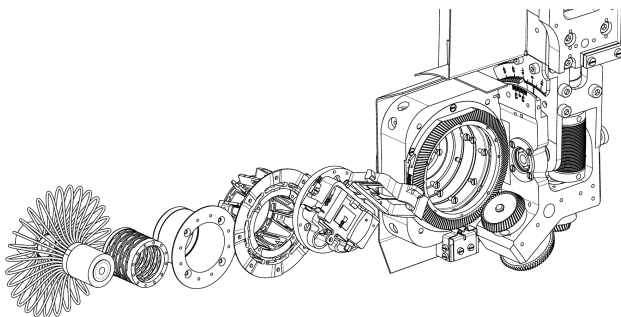


Figure 2: Disassembled manipulator head with (left to right) braid, isolator 1, shield, isolator 2, sample plate holder with shield, head support structure with tilt and azimuthal DOF.

- improved analyser resolution to <1.6 meV and adds a *deflection* scanning mode, which may be especially helpful for small samples
- improved vacuum to below 10^{-11} mbar
- switch from custom sample plates to Omicron-compatible sample plates
- introduce a way to recover sample pieces that fell down in the preparation chamber (PC)

CRYOGENIC DEVELOPMENT

The cryogenic conductors, isolators and their interfaces are designed with great care to avoid any unwanted temperature drop. Overall, every cryogenic part has the potential for causing a critical temperature loss such that the design target can be missed. The whole cooling chain, starting from the liquid helium inside the cryostat all the way to the sample plate itself was optimised for optimal heat transfer. Figure 3 gives a topological overview.

Thermal radiation onto the sample is mainly blocked through the AC-cryoshield, the analyser *nose cone* and the sample holder shield. Other *onboard* shields, directly mounted onto the cryostat, removes thermal radiation from the manipulator support structure. Among all warm parts, only the analyser lens has a direct line-of-sight with the sample. The heat load on the sample due to radiation is estimated to be approximately 5 mW.¹ Conductive heat load onto the sample plate holder, through *Isolator 1* (figure 3), is estimated to be below 1 mW. This is supported by Finite Element Analysis (FEA)^{2,3} and conducted tests on a modified test setup.

Braid

The braid must be flexible enough to do the relative motion of the tilt and azimuth DOF, but at the same time, it must have a large enough crosssection to reduce the temperature loss between both ends. Several trials, that mainly

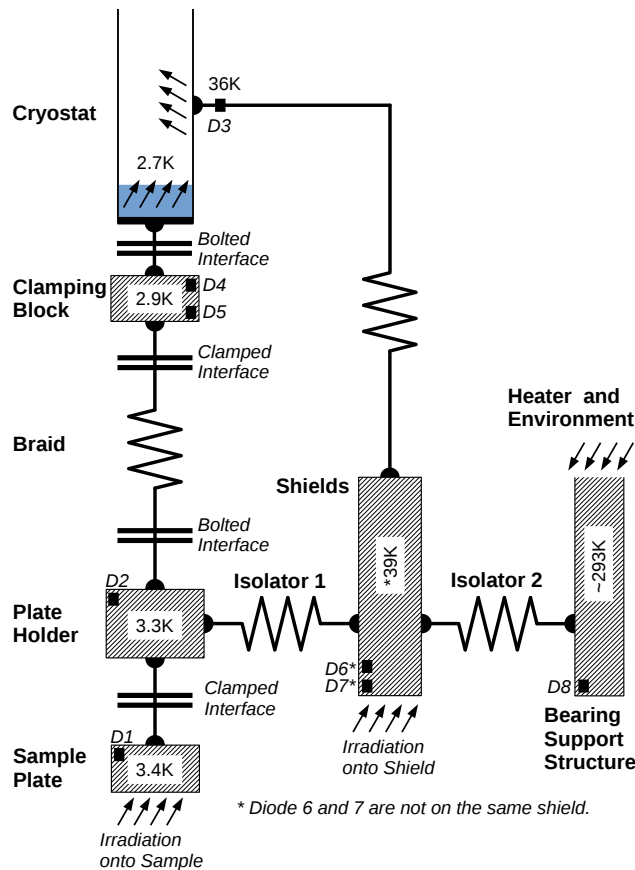


Figure 3: Simplified topological cryo-layout.

differ in the way how the strain-ends are clamped, have been developed and manufactured. In one of the first designs, shown in figure 4a, the braids were compressed by applying a radial force. Cut-ups showed that the contact between the wires and the deformed jacket is poor, figure 4b and 4c. Overall the result was not satisfactory, as an unacceptable large temperature loss across the braid was expected.

As a consequence, a new design was developed that pressed the wires between an outer and an inner cone in order to optimise the resulting contacts. Furthermore, the ends were welded using electron beam welding and later vacuum-annealed, see figure 5c. Deformation from pressing made it necessary to machine the braid ends. Cutups showed indeed that the connection between the single wires and the end-piece is very good, figure 5a and 5b. It can however not be determined what contributed more to the good conductivity that has later been observed in the tests, the pressing or the welding.

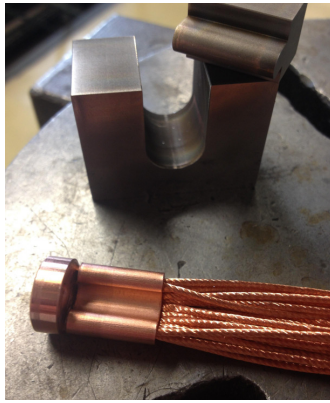
Plate Holder

Thermal contact conductance is the ability to transport heat from one body across a contact interface to another body. It depends on the force [3] with which both bodies are pressed together, but somewhat counter-intuitively, not on the area and hence not on the pressure (force per area). The temperature gradient across an interface exists, because sur-

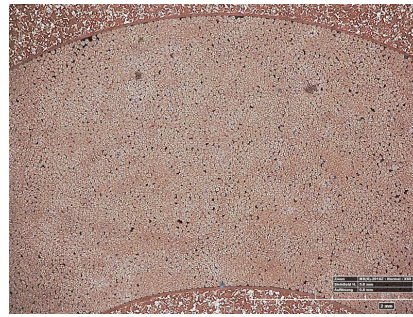
¹ Based on the exposed sample plate ($D = 10$ mm) and lens ($D = 30$ mm), located in 34 mm distance.

² Thermal conductivity for copper (OFE): [5] and [6]

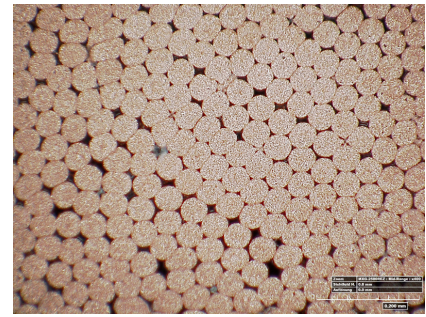
³ Thermal conductivity for Vespel SP1: [5] and [7]



(a) Photo of the pressed braid-end and the pressing tool

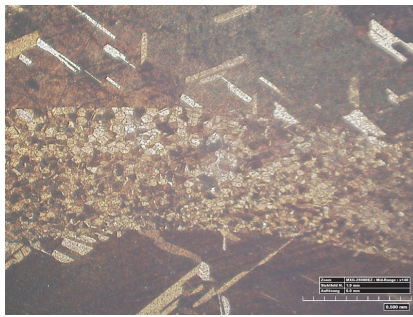


(b) Picture of a cut-up, showing the middle of the croissant-shaped cross section. Towards the very left and right end of the cut, the number of gaps increases severely.



(c) Magnified view of a central area, in the middle of the cross section. This situation is about average for such locations. The single wires have a diameter of 0.05 mm.

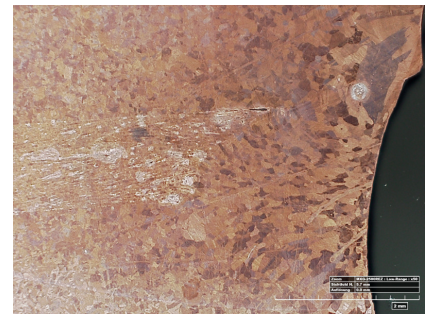
Figure 4: Early braid design.



(a) The lower part shows the inner cone, the upper part the outer counterpart. In between are the wires, which run perpendicular to the paper.



(b) Detail of the single wires, which have been deformed to hexagons. The single wires have a diameter of 0.05 mm.



(c) Axial cross section along the single braids. The braids comes from the left and enters the welding seam on the right.

Figure 5: Iterated braid design.

faces are not perfectly flat but instead have a hilly topology. Therefore, two surfaces that are in contact touch each other only on a small number of places. As the pressing force increases, small deformations occur and causes the number of contact spots and their sizes to increase, followed by an improved thermal contact conductance [4]. The thermal contact conductance is material, temperature and surface-quality specific.

Using experimental data presented in [3], it was possible to derive a *force-to-temperature-drop* diagram, such that the expected loss across the *sample plate – holder* interface could be estimated. The resulting graph, figure 6, is however not universally applicable since it is constructed for this specific use. As a consequence, it became clear that the sample plate holder must be able to clamp a sample plate with kN's of clamping force.

Several designs have been considered, such as a design based on flat springs and a design using a *car jack*-like flexure. The first was dismissed due to the limited force delivered (twice 350 N to 550 N, cause a temperature drop of 0.7 K to 1 K), while the second was rejected due to the very small travelling distance of the *jack* when the angles

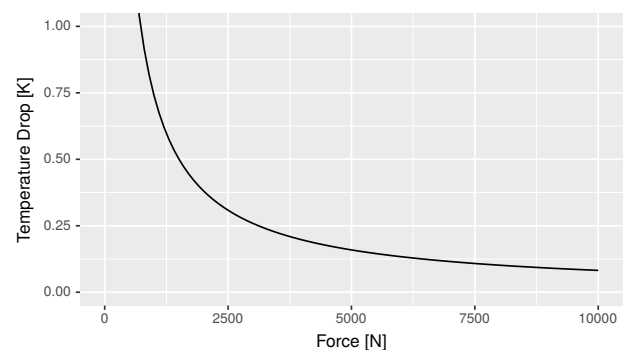


Figure 6: Force dependent temperature drop estimated for the sample plate – holder interface.

of were set appropriately such that the force was sufficiently high.

It became clear that none of these mechanisms would suffice. Instead a design using a worm-gear, a fine pitch thread and a wedge/ram pair was pursued, figure 7. While the torque of the wobblestick used to operate the holder is limited to 0.4 Nm, it is possible to see the holder (elastic)

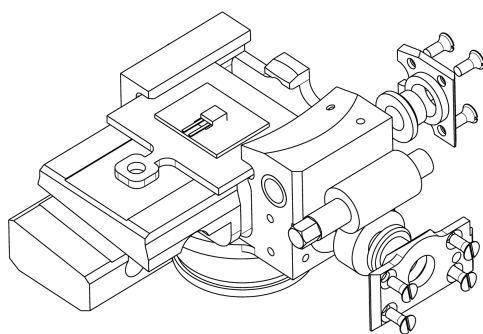


Figure 7: Final design of the sample plate holder.

deform with a torque even below 0.1 Nm. Based on this input torque (0.1 Nm), gear ratio and pitch as well as appropriate efficiencies for each mechanism, an estimated clamping force of 3.7 kN results, leading to a temperature drop of only 0.2 K.

Isolators

Experience from previous endstation upgrades and FEA investigations have shown, that better thermal decoupling is required. As the current endstation already uses an isolator that is on the edge of what manufacturing capabilities allows, an topological change was focused.

The new layout utilises two separate isolators, made of Vespel SP1, that are connected to the radiation shield in between, such that the temperature gradient across the rigid insulation assembly is in favour of the lowest temperature level. Furthermore, the thermal contraction of both isolators compensate each other, such that the overall thermal drift is expected to improve even further.

AC-Radiation Shield

The radiation heat load is essentially a function of the solid angle of the sample that is exposed to room temperature parts. The most significant portion of this load can be removed by a statically mounted shield inside of the AC chamber. While the manipulator support structure is shielded with on-board shields, cooled by the cryostat exhaust gas, the AC shield is cooled by a secondary cooling system also mounted onto the AC chamber. This allows to carry much of the shielding duty over from the cryostat to the secondary system. Meanwhile, this permanent radiation shielding in the AC chamber carries the side benefit of acting as a cryopump, thus enabling ARPES to be performed in an exceptionally clean environment.

The shield is composed of two main parts – an upper bell-shaped part that allows a good view onto the sample and manipulator through holes and cutouts and a second, bucket-like part that can be moved up such that it closes all unnecessary openings, see figure 8. The lifting is done by a vertical threaded shaft, driven by a wormgear that is coupled to a motor located outside of the AC.

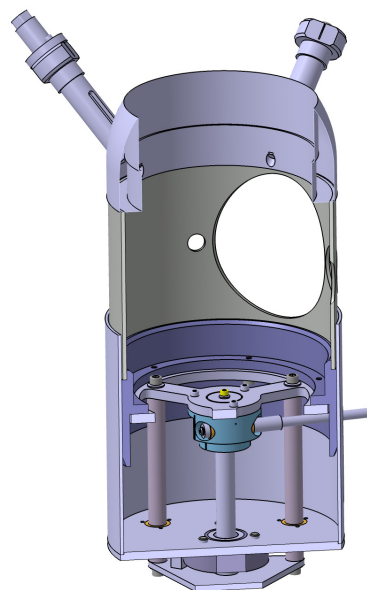


Figure 8: Stationary shield within the AC chamber.

CRYOTEST SETUP

To test the performance of the cryogenic parts, a test setup was build. It was mounted onto a CF150 flange, through which the cryostat reached down, parallel to a (room temperature) support bar. Figure 9 shows the lower parts of the setup in detail, without the outer shielding.

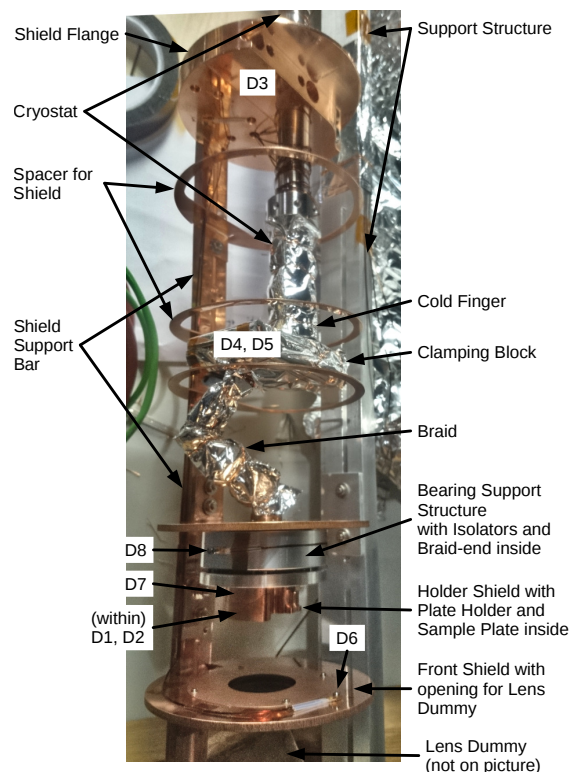


Figure 9: Test setup without the shield-wrapping. The lower part of the cryostat, the clamping block and the braid are wrapped in super insulating foil.

Support Bar

The support bar holds room temperature parts in place. It is equipped with a heater to counter the thermal radiation deficit caused by the cryogenic parts right next to it. At its lower end, a bent aluminium sheet mimed the analyser lens. The surface of the lens dummy was treated with rough grinding paper to ensure a rough and oxidised surface, such that the emissivity was sufficiently high. If further tests will be performed, it will be good to anodise this part, in order to better mimic the emissivity of the instrument. It is the main source of radiation into the cryogenic system.

A couple of centimetres above the lens dummy, the warm support bar connects to the *bearing dummy*. This part is a replacement for two ball bearings required for the azimuthal rotation. On its inner diameter, it holds the second isolator and thus the cryogenic assembly in place.

Shield

Approximately 250 mm above the cold finger a larger copper disk clamps onto the cryostat tube, *shield flange* in figure 9. On its outer diameter, a copper bar attaches and reaches down, parallel to the cryostat and the support bar. It supplies the intermediate temperature level to all shields. Approximately in the middle, a disk attaches that holds a cryoshield in place and supplies it with the shield temperature. At the lower end of the bar, another disk attaches with a hole in it, through which the lens dummy emits thermal radiation onto the sample. The complete assembly is wrapped within a thin copper sheet to protect it from the irradiation of the environment.

Cryogenic Chain

In comparison to the actual endstation, the cryogenic test setup only differs in how the braid is clamped onto the cryostat and the location of some shields. Overall the setup is the same and should perform as such. To be able to measure the temperature of the sample plate, without exposing the diode itself to the incoming irradiation, a specially designed, non-standard plate has been manufactured. While the plate has the overall shape of an Omicron plate, it has an additional extension to clamp a silicon diode on it, hidden from the incoming thermal radiation from the lens dummy.

MEASUREMENTS

Tests performed with this setup showed that the thermal design is sound. Figure 10 shows the development of the temperatures throughout the test, while the lowest stable operation point is also shown in figure 3. The diode within the cryostat was not recorded but used to adjust the helium flow. The helium consumption is within the same range as with the current endstation. During warmup, diode 1 (sample plate) seems to have made thermal contact with a shield.

ACKNOWLEDGEMENTS

A special thanks goes to the workshop crew for their quality work and flexibility.

This work is supported by the *Swiss National Science Foundation* project number 206021_164016.

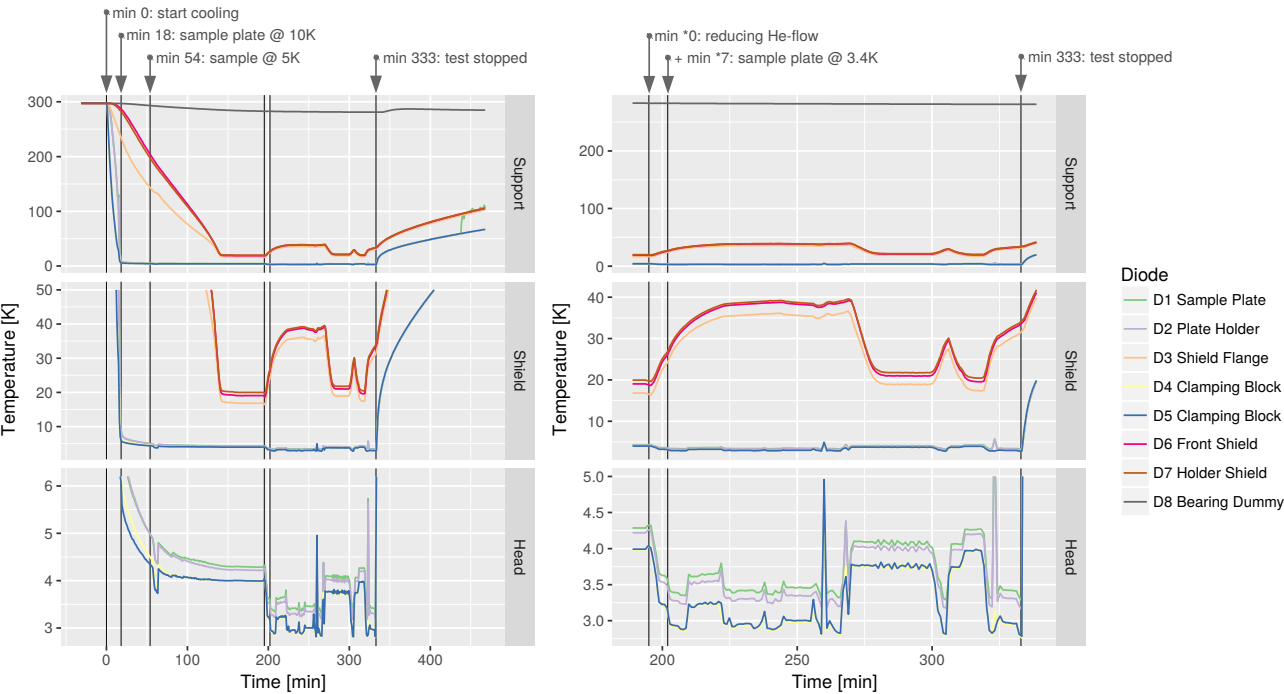


Figure 10: Temperature measurements of the test run.

REFERENCES

- [1] A. Damascelli, "Probing the Electronic Structure of Complex Systems by ARPES", *Physica Scripta*, vol. 2004, no. T109, 2004, p. 61.
- [2] S. Borisenko, "'One Cubed' ARPES User Facility at BESSY II", *Synchrotron Radiation News*, vol. 25, no. 5, 2012, pp. 6-11.
- [3] L. J. Salerno, and P. Kittel, "Thermal Contact Conductance" *NASA Technical Memorandum*, vol. 110429, 1997.
- [4] M. G. Cooper, and B. B. Mikic, "Thermal Contact Conductance" *Int. J. Heat Mass Transfer*, vol. 12, 1968, pp.279-300.
- [5] F. Pobell, *Matter and methods at low temperatures*. Berlin: Springer, 2007.
- [6] A. L. Woodcraft, "Recommended values for the thermal conductivity of aluminium of different purities in the cryogenic to room temperature range, and comparison with copper", *Cryogenics*, vol. 45, no. 9, 2005, pp. 626-635.
- [7] A. L. Woodcraft, and A. Gray, "A low temperature thermal conductivity database" in *Proc. AIP conference proceedings*, vol. 1185, no. 1, 2009, pp. 681-684.

EVALUATION OF ANISOTROPIC SIMULATIONS & REDESIGN OF THE BXDS HIGH ENERGY MONOCHROMATOR BENT LAUE DIFFRACTION CRYSTAL HOLDERS

M. J. P. Adam*, N. Appathurai†, Canadian Light Source Inc., S7N 2V3 Saskatoon, Canada

Abstract

The Brockhouse X-ray Diffraction and Scattering Sector (BXDS) High-Energy (HE) beamline includes a bent Laue diffraction monochromator. The BXDS HE monochromator achieves energy ranges of 35keV to 90 keV through the bent Laue diffraction of two silicon crystal wafers. Each wafer (460 μm & 1000 μm thick) is bent to achieve specific Sagittal Radius (R_s); subsequent anticlastic Meridional Radius (R_m) results from the anisotropic nature of silicon, creating the desired x-ray focusing parameters. During the initial conditioning of the BXDS HE monochromator spurious diffraction patterns were observed indicating that the crystal holder and crystal integrity failed. Alternative holder designs were evaluated using Finite Element Analysis (FEA; ANSYS) simulations to ensure that appropriate R_s and R_m values were achieved, verification of the crystal holder R_s was completed using contact 3D measurement (FaroArm/Leica T-Probe), and the crystal surface was assessed using 3D optical profiling (Zygo). A superior holder was chosen based on the results, and replaced. The performance of the BXDS HE monochromator has been characterized, indicating the new holder design has achieved x-ray focusing parameters.

INTRODUCTION

Each Si wafer is bent against a precisely machined cryogenically cooled block to achieve specific R_s ; a subsequent anticlastic R_m results from the anisotropic nature of Si creating the desired X-ray focusing parameters [1–3]. The theoretical design values for the BXDS HE mono bending radius are found in Table 1), and describe values required for desired focus [1], Si (111) reflection for 35keV, Si (422) & Si (533) reflections for 60-90keV.

Table 1: Theoretical Radius of Curvature

Energy (Si thickness)	R_s [m]	R_m [m]
35keV (460 μm)	0.37	-28.0
60-90keV (1000 μm)	0.72	-37.0

BACKGROUND

The original BXDS HE crystal holder system was composed of two precisely machined blocks (specifically R_s , with dimensions from Table 1).

During the initial conditioning of the BXDS HE mono spurious beam shapes were observed from both crystals. The patterns indicated that the crystal holder and crystal integrity had failed. The fluorescing patterns were observed during the initial low flux beam conditioning, suggesting that the crystal fracture resulted during cryogenic cool-down of the stage prior to x-ray attenuation.

The crystal assemblies were removed from the HE mono and inspected. Fractures for both wafers were observed (see Fig. 1), as well the crystal wafer had bonded to the indium foil, suggesting that the wafer was over constrained when assembled.

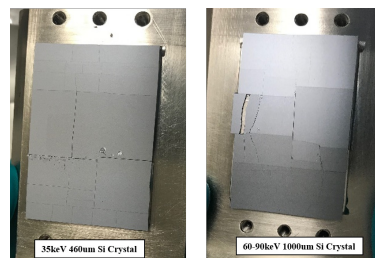


Figure 1: The fractured crystals after being removed. The silicon wafers fractured along the lattice planes (vertically & horizontally). The fractures per area were highest around the locations where the crystals were pressed against the indium foil and the cooling block.

The originally implemented design over-constrained the crystal, resulting in fractures and unusable beam (i.e. unfocused). Therefore, an evaluation of the crystal holders was required.

Objectives

1. Review the current holder design.
2. Confirm the radius induced when clamped against the cooling block & the effect of different clamps on the anticlastic radius.
3. Determine the expected performance (focusing, flux, etc.)

ANISOTROPIC SIMULATION

Initially a review of the original crystal holder was simulated using finite element methods (ANSYS 18.0) and evaluated to determine the resulting R_s & R_m . All simulations used anisotropic material properties for Si (111), and applied non-linear large deformation theory [4–7].

The original mask simulation results demonstrated an immediate issue; the R_m could not be achieved with the

* madison.adam@lightsource.ca

† narayana.appathurai@lightsource.ca

current style of clamping due to being over constrained by the mask clamped along the entire crystal surface. It was clear that the revised clamping system would require minimal contact.

Three variants of clamped holder styles were developed and evaluated (see Fig. 2). Each design emulated the best practice Laue benders [1, 3]. The variation in clamp designs were intended to maintain the appropriate holding force, bending the crystal wafer against the cooled block to allow the beamline focusing performance (R_s), and to allow the crystal to achieve the anticlastic bend (R_m).

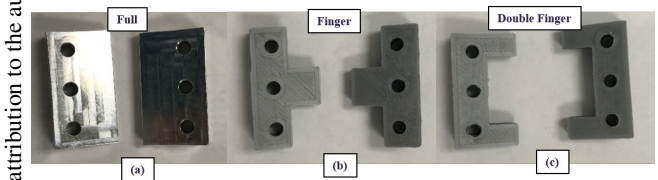


Figure 2: Three clamping styles that were evaluated for use within the BXDS HE mono. (a) the Full clamp applies a line contact to the crystal surface (AL6061), (b) the Finger clamp applies a small line contact force to the center of the crystal (rapid-prototype), (c) the Double Finger clamp applies two small line contact forces to the outer edges of the crystal (rapid-prototype).

The radius of curvature was calculated (ANSYS 18.0) to find deformation maps for each of the directions of interest (R_s & R_m). Data from the deformation paths (see Fig. 3) along each direction were fitted using Least Squared Method to a circle [8]. The results for each clamping style are summarized in Table 2. The Double Finger clamp was found to produce the best simulated curvatures that closely matched theory. Verification with the Zygo Nexview surface profiler indicated otherwise.

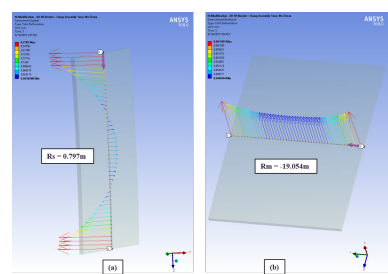


Figure 3: Total deformation results for the Full clamping style of the 1000 μm crystal. (a) the Sagittal path (b) the Meridional path.

VERIFICATION OF CLAMPING METHOD

Two test holders were machined (35keV & 60-90keV stages) so that measurements on the Zygo Nexview profiler could be completed on the crystal surfaces, and so that measurements could be made for various pretension forces for clamping. The crystals were clamped in place using the three clamping styles (Full, Finger, Double Finger), and

Table 2: Three Clamps Simulation Results for 1000 μm Si Crystal

Clamp Style	R_s [m]	R_m [m]
Full	0.797	-19.054
Finger	0.771	-13.296
Double Finger	0.754	-48.458

then measured (Table 3) on the Zygo profiler for R_s & R_m , repeated tests were conducted to assess the variability of tightening.

Table 3: Zygo Nexview Profiler Measurements Results for Si Crystals (460 μm top & 1000 μm bottom)

Clamp Style	R_s [m] ($\pm\text{SD}$)	R_m [m] ($\pm\text{SD}$)
Full	0.414 (0.121)	-22.066 (9.196)
Finger	0.375 (0.003)	+28.174 (7.719) ¹
Double Finger	0.367 (0.003)	-10.128 (0.859)
Full	0.688 (0.003)	-32.951 (8.459)
Finger	0.694 (0.001)	-64.289 (14.268)
Double Finger	0.699 (0.003)	-23.609 (3.512)

A further analysis of the 1000 μm Si crystal profile at three locations (see Fig. 4) along sagittal curvature plane illustrates the subtle parabolic curvature results.

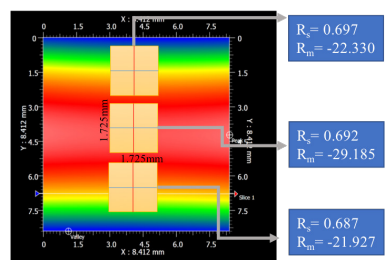


Figure 4: Evaluation of three locations of the Full clamp style using the 1000 μm Si crystal.

The parabolic curvature using the Full clamp was found from both the ANSYS Simulations and the Zygo Profiler. This observation is an unfortunate result likely from the static clamping method. Fortunately, the desired curvature areas was found to exceed the incident beam size creating the desired focusing of the full beam.

REDESIGN IMPLEMENTED

Once evaluation was complete, the Full clamp resulted in the most promising R_s & R_m for both of the 1000 μm & 460 μm Si crystals. The Full clamp was installed on the crystal holders, three Belleville washers were stacked in a parallel configuration for each screw (see Fig. 5), silver paint (Conductive Silver Paint, SPI 05001-AB) was used

¹ Interestingly, the Finger clamp for 460 μm Si resulted in a +ve R_m

as interstitial material between the Si Crystal and copper holder.

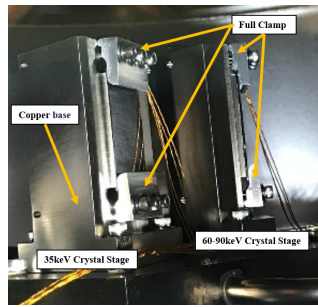


Figure 5: Currently operating within the BXDS HE Mono.

CURRENT PERFORMANCE

The performance of the BXDS HE monochromator has been characterized (see Fig. 6), indicating the new holder design has achieved x-ray focusing parameters that currently approximate the theoretical requirements, but most importantly have produced good initial diffraction from samples.

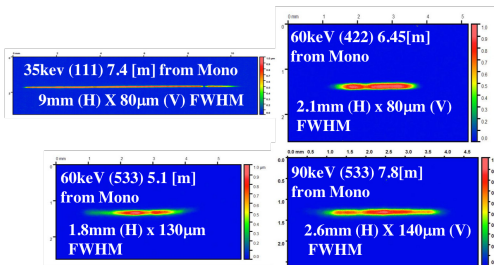


Figure 6: Beam profiles measured with current Full clamp.

The current flux measurements (Table 4) produced from the BXDS HE Mono (In Vacuum Wiggler limited to 8.4 mm gap.

Table 4: Flux Performance for BXDS HE Mono Crystals

Energy	Ion Chamber Flux [ph/s]	% of theory
35keV (460 µm)	1.34×10^{13}	22.27
60keV (1000 µm)	2.08×10^{12}	61.07
90keV (1000 µm)	8.1×10^9	4.5

CONCLUSION

With the initial unusable performance from the BXDS HE mono, an evaluation of the crystal holder was required. By removing the over constrained original mask, the Full clamp allowed the crystal to naturally bend achieving acceptable R_s & R_m .

The study conducted of the BXDS HE mono crystal holder demonstrates a simple method of reproducing Laue bent

diffraction using two clamps that hold the Si crystal over a precisely machined radius. The design changes have resulted in good X-ray focusing and have demonstrated good diffraction results.

FUTURE WORK

Thermal equilibrium analysis for crystal performance under high heat loads would greatly benefit the understanding of how each crystal behaves. The thermal analysis would consider the attenuated heat, evaluate effective differences/optimization of cooling applied to various clamping methods.

Ultimately, a dynamic bender would be ideal to achieve closer theoretical focusing values, allowing for immediate optimization of the crystal focus. A comparison between a dynamic system and the static system proposed in this work, would be useful to future designers.

ACKNOWLEDGEMENTS

Thank you to Brian Yates, David Muir, John Campbell, and David Smith. Thank you to the BXDS Technical Group.

REFERENCES

- [1] A. Gomez *et al.*, "The high-energy x-ray diffraction and scattering beamline at the Canadian Light Source", *Review of Scientific Instrumentation*, vol. 89(6), Jun. 2018, doi:10.1063/1.5017613.
- [2] K. Wyatt *et al.*, "Cryogenically cooled monochromators for the brockhouse wiggler beamlines", in *Proc. Xth Synchrotron Radiation Instrumentation Conf. (SRI 2018)*, Taipei, Taiwan, poster PD2-14, Jun. 2018.
- [3] X. Shi *et al.*, "Surface curvatures and diffraction profiles of sagittally bent laue crystals", *Applied Crystallography*, vol. 44, 2011, pp. 665-671, doi:10.1107/S0021889811018711t.
- [4] M. Krisch *et al.*, "Study of dynamically bent crystals for xray focusing optics", *Nuclear Instruments and Methods in Physics Research*, vol. 305(1), July 1991, pp. 208-213, doi:10.1016/0168-9002(91)90536-Y.
- [5] M. Hopcroft *et al.*, "What is the young's modulus of silicon?", *Journal of Microelectromechanical Systems*, vol. 19(2), Apr. 2010, pp. 229-238, doi:10.1109/JMEMS.2009.2039697.
- [6] L. Zhang *et al.*, "Anisotropic elasticity of silicon and its application to the modelling of x-ray optics", *Journal of Synchrotron Radiation*, vol. 21(3), Apr. 2014, pp. 507-517, doi:10.1107/S1600577514004962.
- [7] A. Masolin *et al.*, "Thermo-mechanical and fracture properties in single crystal silicon", *Journal of Materials Science*, vol. 48(3), Feb. 2013, p. 979-988, doi: 10.1007/s10853-012-6713-7.
- [8] D. Umbach and K. Jones, "A Few methods for fitting circles to data", *IEEE Transactions on Instrumentation and Measurement*, vol. 52(6), Nov. 2003, pp. 1881-1885, doi:10.1109/TIM.2003.820472.

THERMOMECHANICAL ANALYSIS OF SESAME HIGH-HEAT-LOAD FRONT ENDS COMPONENTS

M. AL-Najdawi[†], SESAME, 19252 Allan, Jordan

Abstract

New front-end beamline components at SESAME are designed to handle the high heat load produced by the insertion devices. A mini gap wiggler will be installed for the Material Science Beamline and the front end will receive 5.0 kW of total power and 7.79 kW/mrad² of peak power density. The power produced by the insertion device was simulated using SynRad+[1], a software using Monte Carlo simulation to simulate the synchrotron radiation from either an insertion device or any magnet source. The surface power density distribution generated by this software can be mapped directly to an FEA software to conduct a coupled thermo-mechanical analyses. The design, modelling, power source simulation and FEA analysis of the fixed mask, shutter and filter for the material science Beamline front end will be presented in this paper.

INTRODUCTION

SESAME is a third generation light source located in Allan Jordan operating with a 2.5 GeV electron beam and a design current of 400 mA. A mini gap wiggler as a source for the material science beamline will be installed and can deliver a power of over 5.0 kW with a peak power density of 7.79 kW/mrad² at 12 mm magnetic gap. The design of the fixed mask, shutter and filter had been done to handle the high heat load generated from the wiggler source, the upstream and downstream dipole magnets, to protect the first optical components in the beamline.

POWER CALCULATION

Mini-Gap Wiggler Parameters

The mini-gap wiggler will be installed in one of the storage ring long straight sections and the gap will be adjusted to 12 mm, the wiggler parameters shown in table 1 and power distribution in Figure 1.

Table 1: Mini-gap Wiggler Parameters

Overall length	2 m
Minimum magnetic gap	8 mm
Period length	60.5 mm
Number of poles (Np)	63
Maximum field (B _{max})	1.84 T
Effective field (B _{eff})	1.63 T
Deviation parameter (K)	8.6
Critical energy (E _c)	7.0 keV

[†] mohammad.najdawi@sesame.org.jo

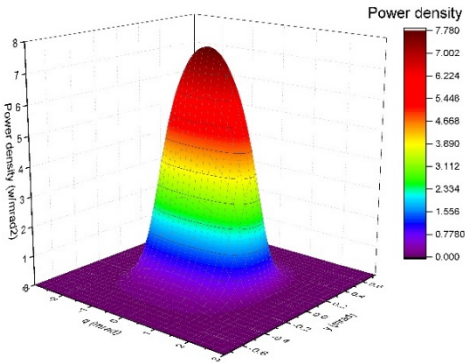


Figure 1: Power distribution of the mini gap wiggler at 12 mm gap.

Power Calculation

The power calculations had been done using SynRad+, a software using Monte Carlo simulation to simulate the synchrotron radiation from either an insertion device or any magnet source. The surface power density distribution generated by this software can be mapped directly to an FEA software to conduct a coupled thermo-mechanical analyses. The benefit from using this type of simulation is to take the whole length of the insertion device as a distribution of source points, which give us more accurate results than the traditional way of assuming one source point. Also, in this type of simulations, we can introduce the effect of the heat load produced by the upstream and downstream dipole magnets as shown Figure 2.

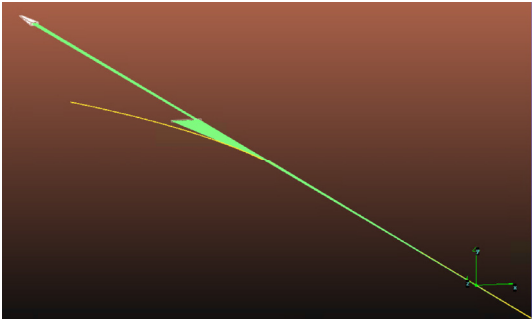


Figure 2: SynRad simulation for the wiggler source with upstream and downstream dipole magnets.

In order to have more accurate results, the tapered shape of the fixed mask had been introduced in the simulation and the power distribution has been calculated at each taper face. An example of the SynRad output is given in Figure 3 which shows the power distribution at the fixed mask from the wiggler and dipole magnet source.

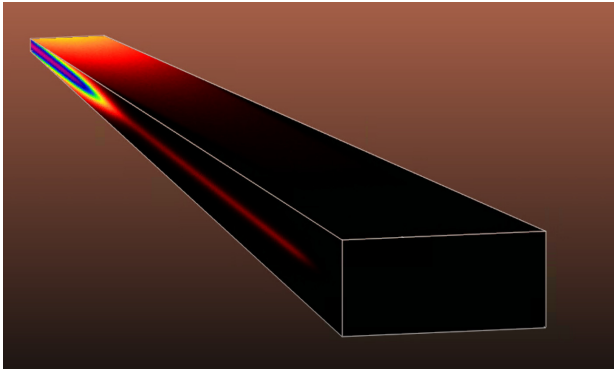


Figure 3: Power distribution at fixed mask, it shows the power distribution delivered from the wiggler and dipole magnet sources.

THERMAL ANALYSIS

Failure Criteria

Failure criteria of the fixed mask and photon shutter are used as [2]:

- The maximum stress in copper thermal absorber should be smaller than twice the ultimate tensile strength of the copper $\sigma_{VM}^{max} < 850 \text{ MPa}$ for Glidcop.
- The maximum temperature on the Glidcop body temperature should be less than 300°C .
- The maximum temperature on the water cooling channel walls should be less than water boiling temperature at channel pressure.

Fixed Mask

Fixed mask is the first high heat load components in front end to shape the beam coming from the mini gap wiggler. The fixed mask will be manufactured from a Glidcop® A115 block with a rectangular tapered tunnel fabricated using wire EDM technology to allow the beam to pass through. The tapered angle equal to 1.5° and had been defined in a way to allow the fixed mask to absorb half the total power delivered from wiggler, upstream and downstream dipole. There will be four grooved channels next to each surface defining the aperture to cool the fixed mask. Figure 4 shows the design of the fixed mask.

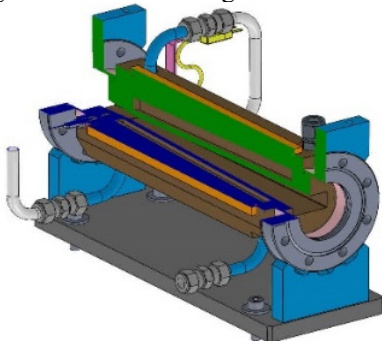


Figure 4: Fixed mask design sectional view.

The fixed mask will absorb a total power of 2.6 kW, the maximum temperature on the shutter body will reach 69°C as shown in Figure 5, thermal stress peaks to 183 MPa corresponding to an equivalent total strain of 0.14%.

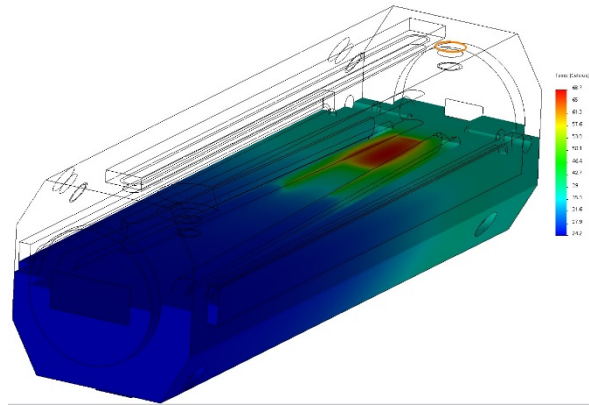


Figure 5: Fixed mask maximum temperature distribution.

Photon Shutter

The photon shutter designed in a way to protect the beamline downstream components from the synchrotron radiation either when the beamline is not in operation, in emergency case or when the beamline in service. The absorber design based on ESRF design [3] and consists of two brazed Glidcop® A115 blocks. There are two positions for the shutter: the first one, when the front end is open, allows the synchrotron radiation defined by the fixed mask to pass, the second one with the shutter closed will force the side water cooled tapered to absorb all the synchrotron radiation at incidence angle of 3° . Figure 6 shows the design of the photon shutter.

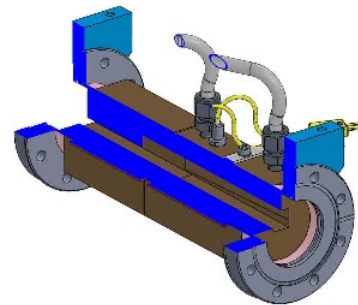


Figure 6: Photon shutter sectional view.

The shutter will absorb a 2.4 kW, the maximum temperature on the shutter body reaches 84°C as shown in Figure 7, the thermal stress peaks to 137 MPa corresponding to an equivalent total strain of 0.105%.

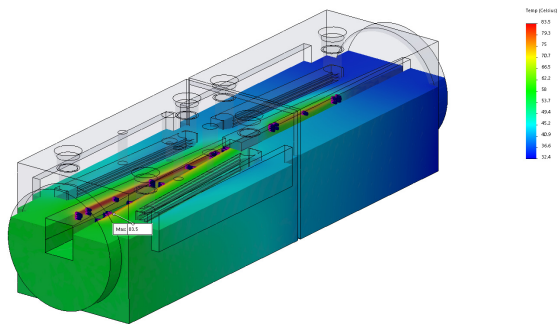


Figure 7: Shutter maximum temperature distribution.

Rotating Filter

The rotating filter is based on the SLS design [4] and is shown in Figure 8. The idea of the filter is to remove the soft X-rays and reduce the power which will be delivered to the first mirror. The rotating filter is a commercially available cylindrical crucible made from the glassy-carbon material Sigradur G [5], material properties listed in table 2. The filter is rotated using a drive shaft equipped with two bearings with silicon nitride ceramic balls [6].

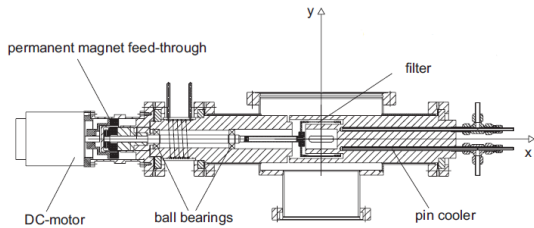


Figure 8: sectional view of rotating filter.

The drive motor is mounted outside the vacuum, and the torque is transmitted to the drive shaft via a permanent-magnet feed-through.

Table 2: Material Properties of Sigradur G

T (°C)	20	1000	2000
ρ (g/cm ³)		1.42	
K (W/m/°C)	6.3	11	12
α (°C ⁻¹)	3×10^{-6}	4×10^{-6}	5×10^{-6}
C_p (J/g/°C)	0.5	1.9	2.1
ϵ		0.3	
E (N/mm ²)		3.5×10^4	
S_f (N/mm ²)	260	>260	>260

The cooling of the carbon filter is achieved by radiation to affixed black-oxidized copper jacket (emissivity of 0.6) which is cooled via four 8 mm blind holes with inserted tubes for incoming and outgoing water. The filter thickness is 2 mm and the total power absorbed is equal to 1.6 kW, the maximum temperature of the carbon filter equal to 1240 °C and the copper jacket 94 °C as shown in Figure 9.

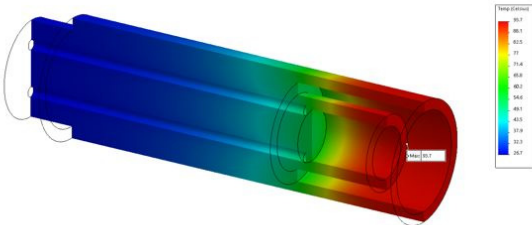
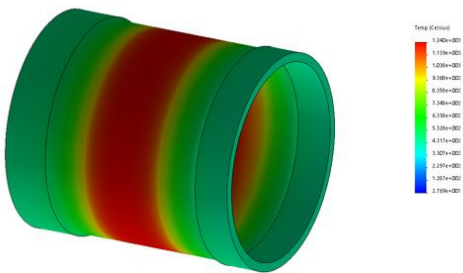


Figure 9: Filter cup and fixed jacket maximum temperature of 1240 °C and 94 °C respectively.

CONCLUSION

The design of the fixed mask and photon shutter has been done in order to handle the high heat power delivered from the mini gap wiggler. Glidcop material will be used for the body with side water cooling grooved channels. The power simulations have been done using SynRad and the results directly mapped to the FEA code which give us a very accurate results. The front end filter will be made of Sigradur G and will be cooled via radiation to a copper cooled mask.

The simulations show that the front ends components will be safe to be used for the mini gape wiggler source.

REFERENCES

- [1] R. Kersevan, "SYNRAD, a Monte Carlo synchrotron radiation ray-tracing program", in *Proceedings of the 1993 Particle Accelerator Conference*, vol.5, pp. 3848-3850.
- [2] L. Zhang *et al.*, "ESRF Thermal Absorber: Temperature, Stress and Material Criteria", in *Proc. MEDSI 2002*, APS, Chicago, 2002, p. 377-389.
- [3] J.C. Biasci *et al.*, "Design and performance of ESRF high-power undulator front-end components", in *J. Synchrotron Rad.* 9, 2002, p. 44-46.
- [4] G. Heidenreich, B.D. Patterson, "A rotating filter for the wiggler beamline at the Swiss Light Source", in *Nuclear Instruments and Methods in Physics Research A*, 577(3), pp 751-755, July 2007, DOI: 10.1016/j.nima.2007.04.136.
- [5] HTW Hochttemperatur-Werkstoffe GmbH, D-86672 Thierhaupten, Germany, <http://www.htw-germany.com>
- [6] W. Kaika, GMN Paul Müller Industrie GmbH, D-90411 Nürnberg, Germany, <http://www.gmn.de>

DESIGN OF NEW BEAM INSTRUMENTATION FOR THE ISOLDE ISOTOPE SEPARATOR AT CERN

W. Andreazza, M. Duraffourg, G. J. Focker, A. Miarnau Marin, D. Smakulska, J. Tassan-Viol, R. Veness, CERN, Geneva, Switzerland

Abstract

The ISOLDE radioactive ion beam separator facility at CERN produces beams of short-lived isotopes for experiments in physics, material and medical science. New requirements for more precise measurement of profile, position and intensity has pushed the CERN beam instrumentation group to start the study of a new generation of ISOLDE beam instrumentation dedicated to the specific needs of this facility.

This paper will describe the design and the development of a number of new ISOLDE instruments with the aim of achieving better performance, increased reliability and to facilitate maintenance in a radioactive environment.

It will explain how modern technologies such as magnetically coupled linear actuators and 3D additive machining have been used to make a modern, precise and reliable beam instrumentation design.

INTRODUCTION

The on-line isotope mass separator ISOLDE [1] is a facility dedicated to the production of a large variety of radioactive ion beams for a wide range of experiments in the fields of nuclear and atomic physics, solid-state physics, materials science and life sciences. The facility takes beam from the Proton-Synchrotron Booster (PSB) at CERN, the European Organization for Nuclear Research.

At ISOLDE, radioactive beams are produced in two fixed target areas, known as front-ends, and subsequently delivered to their respective isotope separators: the General Purpose Separator (GPS) and the High Resolution Separator (HRS). The GPS line has one mass separator magnet and the HRS line has two magnets. The extracted mass-separated beams are then delivered to different experimental lines.

BEAM DIAGNOSTIC REQUIREMENTS

Beam diagnostics in ISOLDE is comprised of wire Secondary Emission Monitor (SEM) grids, wire or needle scanners and Faraday cups in order to measure the properties of the beam during set-up and operation of the front-end and separators.

The SEM grids and scanners can be used to take beam profile measurements by moving them into the beam path. The charge depletion measured in the wires is proportional to the local beam density and thus allows for the reconstruction of the beam profile as a function of wire position. Faraday cups are used to take measurements of the beam intensity, however, in this paper the focus will be placed on SEM grids and needle scanners.

EXISTING SITUATION AND REASONS FOR CHANGE

The existing beam instrumentation was designed and built in the early 90's. The success of the ISOLDE facility, including a recent upgrade has meant that these instruments are operating far past their initial expected lifetime. Despite a surprising longevity, they are now showing their limits in terms of performance and reliability. New requirements for more precise measurement, more stringent vacuum acceptance constraints and a CERN-wide policy to reduce maintenance requirements in radioactive environments according to modern "As Low As Reasonably Achievable" (ALARA) guidelines has led to a project for the design, development and construction of a new generation of ISOLDE instrumentation.

USE OF NOVEL TECHNOLOGIES

The mechanisms that move a grid, wire or Faraday cup into the beam path do so using pneumatic actuators, lead-screws or pulleys. The current scanners use a system of in-vacuum motors and pulleys, which in turn rely on in-vacuum electronics and numerous small parts. These require frequent and costly maintenance in a hazardous area where there is a risk of radioactive contamination. Similarly, the combined scanner and Faraday cup instruments, which were recently redesigned, used pneumatic actuators coupled with edge welded bellows. Edge welded bellows allow a long movement for their nominal length, but are limited in fatigue life to some 10,000 cycles, are difficult to clean for ultra-high vacuum environments and are fragile, with the associated risk of leaks.

Magnetically coupled push-pull linear actuators (MPPL) were identified as a solution as they avoid these limitations. The MPPL is driven by a stepper motor and ball screw with a rated linear speed of 100 mm/s and a nominal linear resolution of 25 μm per half step of the stepper motor. The ball screw is connected to a thimble containing SmCo_5 magnets and running over a tube that creates the vacuum-air interface. The thimble is magnetically coupled to an in-vacuum shaft supported on a nose bearing. The MPPL is installed onto the instrument using a ConFlat® flange.

Existing MPPLs did not fully complying with CERN's requirements. A development was therefore made with a supplier to introduce some key modifications. Opto-couplers, which may fail under stray magnetic fields and radiation, have been replaced by micromechanical switches, and an over-travel hard stop has been incorporated to avoid damaging the push-pull. Finally, due to the rapid degradation of PTFE in a radioactive environment, the PTFE and

bronze matrix bushing has been replaced by a PEEK bushing. This should have no impact on the lifetime and is approved for use in accelerator vacuum.

The cantilevered load applied will be 0.18 Nm with the maximum that can be applied to the MPPL being 0.5 Nm. The maximum deflection at the end of the shaft has been calculated to be 0.134 mm.

In addition to the MPPL development, several parts were designed and manufactured by Selective Laser Melting (SLM), including a metallic cable-carrying chain that was printed fully assembled. These parts were designed iteratively and optimized for additive manufacturing as outlined in another paper at this conference [2].

SCANNERS

The current scanners use a system of motors and pulleys to actuate metallic needles, which measure the current of the beam as a function of position, thus allowing for the reconstruction of the beam profile. The scanners were designed more than 20 years ago for a few thousand scans (see Fig. 1). As aforementioned, the instruments contain numerous small parts as well as in-vacuum electronics and resins, requiring frequent and complex maintenance.



Figure 1: Existing ISOLDE beam needle scanner.

The purpose of the consolidation project is to redesign three horizontal needle scanners with the aim of simplifying the mechanisms in use, improving the reliability and minimising the required maintenance. The needles should maintain their exiting coverage of the aperture and the instrument footprint should be minimised.

One scanner is situated on top of the GPS switchyard and the other two are installed on the HRS line. The three scanners have different specifications in order to meet the requirements at each location.

The GPS scanner has two needles which, when fully retracted (Fig. 2), are at opposite ends of the instrument, centred about the vacuum chamber. The reason for this is two-fold: firstly, the total distance to be covered is larger than the maximum stroke of a single MPPL. Secondly, having two needles which overlap over a common area offers some redundancy in case of failure of one of the two needles. Each needle (Fig. 3) has a stroke of 250 mm, 70 mm more per needle than in the current instrument. With respect to the current instrument, the total coverage has been increased from 300 to 350 mm and the overlap has been increased from 60 to 150 mm. The two needles move along parallel planes 2 mm apart from each other.

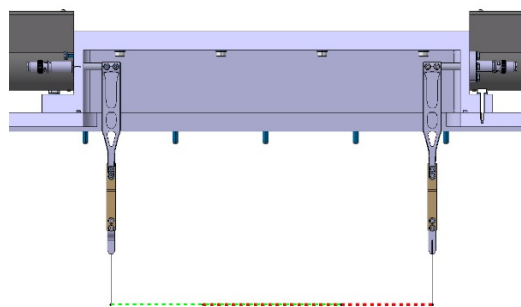


Figure 2: Section view of the scanner with both needles fully retracted.

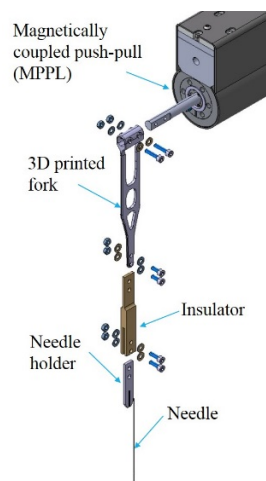


Figure 3: Push-pull to needle assembly.

Two HRS scanners have been redesigned. The first one will be installed before the separator magnets with an overall aperture to cover of 95 mm. The proposed instrument is shown in Fig. 4. The second scanner will be installed after the separator magnets, requiring a larger aperture of at least 180 mm, and having two needles for redundancy purposes. The instrument is shown in Fig. 5. Currently the needles run along parallel planes 10 mm apart from each other. For the new design, the needles have been brought closer together, running 2 mm apart from each other. This allows for the beam to be measured at almost the same transverse location regardless of the needle that is used.

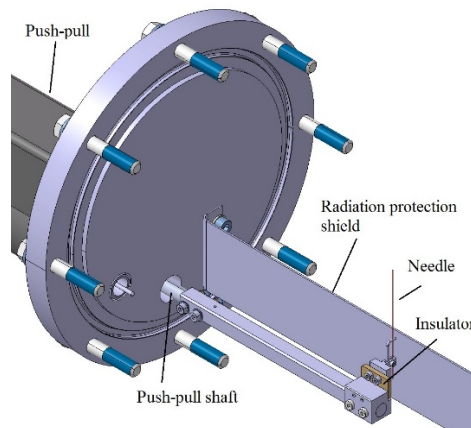


Figure 4: Cropped view of the single-needle HRS scanner.

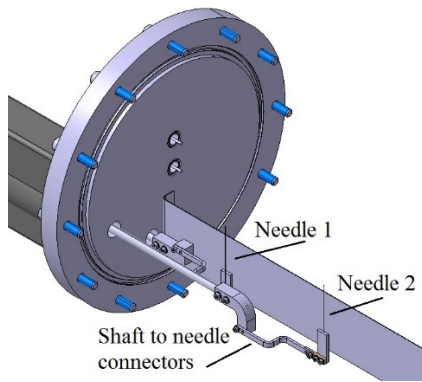


Figure 5: Double-needle HRS scanner with one needle fully retracted and one in the centre.

The motors as well as the electronics and resin currently used for the in-vacuum pre-amplifier will be removed and replaced by a new amplifier, located outside vacuum but having the same interface as the existing one. This in turn will also lead to an improved vacuum quality.

There are several advantages in undertaking this redesign. By using fewer parts and completely removing the need for bellows this system will offer much greater reliability than the pulley system, thus in turn reducing the maintenance required. When maintenance does have to be carried out, such interventions will be easier and therefore quicker, reducing the exposure of personnel to radiation and the risk of contamination. Furthermore, because of the removal of the pre-amplifier and the use of the MPPL actuators, the vacuum level will be improved. All of these changes and improvements will maintain the full functionality of the device and in some cases make the instrument even more versatile.

SEM GRID

The ISOLDE front-end areas are amongst the most radioactive areas at CERN and the existing SEM grid was rendered inoperable due to this radiation environment a few years ago. Considering this, the materials for the redesign have been limited to metal, glass, ceramic and Kapton®, a polyimide foil. The grid is made of two plates of ceramic Al_2O_3 , installed one on the top of another with Macor® ceramic spacers. Wires are placed horizontally on the first plate and vertically on the second. This allows the beam density profiles in two directions to be read simultaneously. Each ceramic plate has 31 Tungsten wires installed at 2.5 mm intervals symmetrically about the beam centre. The wires are soldered to the copper circuits printed on the ceramic plates and connected with flexible circuits (FLEX, see Fig. 6 and Fig. 7) to the D-Sub connector. FLEX is composed of two layers of polyimide foil with electro-deposited copper circuits between them. Formerly composed of 62 independent wires with a considerable risk of errors in the connections the new FLEX cable will improve the wiring phase and the outgassing rate. This significantly simplifies the assembly of the instruments. The D-Sub connectors are welded to a specially designed body, which acts

as an interface between the vacuum inside the beamline and ambient atmosphere outside.

The SEM Grid can be mechanically moved in and out of the beam. This movement is achieved through a pneumatic actuator, specially designed to be free of rubber seals. Instead, a very precise machined piston without seals is used.



Figure 6: ISOLDE SEM grid FLEX cable.

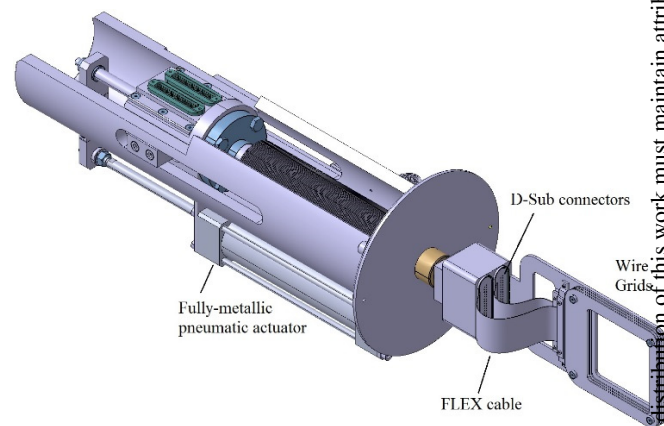


Figure 7: ISOLDE SEM grid.

CONCLUSIONS

Three new types of ISOLDE scanner and one ISOLDE SEM grid have been designed with a view to significantly increasing the reliability and maintainability of these devices.

A series of tests performed with the first prototype of the SEM grid have given good results and production of all instruments is now underway. The new design will allow for easier and faster assembly and maintenance with a significant reduction in the time spent in a hazardous area.

The installation is planned for the next ISOLDE long shutdown scheduled from January 2019 to July 2020.

REFERENCES

- [1] R. Catherall *et al*, "The ISOLDE Facility", in *J. Phys. G*, vol. 44, 094002, sept. 2017.
- [2] R. Veness *et al*. "Metal 3D Additive Machining for In-Vacuum Beam Instrumentation", presented at MEDSI 2018, Paris, France, paper TUPH36, unpublished.

FINITE ELEMENT ANALYSIS OF A COMBINED WHITE BEAM FILTER AND VISUAL SCREEN USING CVD DIAMOND FOR THE BXDS BEAMLINE

D. M. Smith*, M. J. P. Adam†, A. Janis, G. Barkway
 Canadian Light Source Inc., Saskatoon, Canada

Abstract

A white beam filter and visual screen are required for the undulator beamline at the Brockhouse X-Ray Diffraction and Scattering Sector (BXDS). Reusing a water-cooled copper paddle with a 0.1 mm thick chemical vapor deposition (CVD) diamond foil, a combined filter and screen design is presented. The Canadian Light Source (CLS) previously experienced failure of CVD diamond filters when exposed to high flux density white beam. Finite element analysis (FEA) was performed to determine if the CVD diamond would fracture under the BXDS undulator heat load. Conservative failure criteria are selected for CVD diamond based on available literature for the following failure mechanisms: high temperature, thermal fatigue, and temperature induced stress. Four designs are analyzed using FEA models simulating effects of clamping pressure and heat load on the CVD diamond. The simulations are verified by optimizing the model mesh, comparing results against hand calculations, and comparing theoretical absorbed heat load to simulated values. Details of the simulation method are reviewed and results for the different designs evaluated. Suggestions for future testing of CVD diamond in a synchrotron setting will be discussed.

INTRODUCTION

The BXDS undulator beamline at the CLS requires a white beam photon filter to reduce the heat load on downstream monochromators, and a visual screen for commissioning of the beamline. Originally planned as separate components, it was decided that a combined white beam photon filter and visual screen (PFIL/VSC) using a 0.1 mm thick CVD diamond filter could fulfill the functionality of both. A new FEA was initiated to accurately simulate the reaction of CVD diamond to a heat load and clamping forces. The purpose of this work was to apply an analysis based design process enabling good conceptualization of the design parameters for the PFIL/VSC.

FEA Objectives

1. Determine the Steady-State Thermal condition for the BXDS PFIL/VSC subjected to worst case heat loads,
2. Determine the Static Structural condition for the BXDS PFIL/VSC subjected to worst case heat loads, and
3. Determine a suitable design for BXDS PFIL/VSC.

* david.smith@lightsources.ca

† madison.adam@lightsources.ca

BACKGROUND

The primary purpose of the FEA was to determine if the PFIL/VSC could function under the undulator heat load using a recycled, water-cooled base, or whether a more robust cooling system would be required. The beam size 37.2 m from the center of the BXDS straight (the location of PFIL/VSC) is 13.0 mm (H) by 4.58 mm (V). The maximum power load and power density on the filter are 368.9 W and 6.42 W/mm² respectively when the storage ring current is 500 mA and the undulator gap is set to its minimum at 5.2 mm as shown in Fig. 1. The CLS typically operates at 220 mA, but designs require consideration for 500 and 250 mA too. For 250 and 220 mA, the absorbed power load will be 184.6 W and 163.8 W respectively.

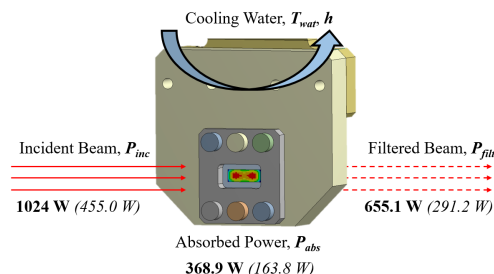


Figure 1: The undulator beam if filtered by the CVD diamond. The absorbed heat is removed while the filtered power continues downstream. Values in bold are for 500 mA and italicized values are for 220 mA.

Failure Criteria & Safety Factors

Conservative safety factors (SF) were favored from literature review when there was little experimental data available. Three failure methods are considered: high temperature, thermal fatigue, and stress.

Failure Due to High Temperature CVD diamond undergoes graphitization at high temperatures and optical degradation occurs at temperatures of 1300 °C in vacuum [1]. A SF of 1.5 allows for a maximum temperature of 866 °C on the CVD diamond foil.

Fracture Due to Thermal Cycling (Fatigue) of CVD Diamond Researchers have found that slow crack propagation, the main failure method in thermal fatigue, is not a concern with CVD diamond [2]. Therefore, fatigue effects will be considered negligible.

Fracture Due To Stress In The CVD Diamond CVD diamond is a brittle material, so Modified Mohr theory must be used to predict failure. The FEA must consider principal stresses over equivalent Von Mises stress [3]. Researchers found the average fracture stress for a 0.340 mm CVD diamond foil could be as low as 450 MPa [4]. Using 450 MPa as the fracture stress and a SF of 2, the maximum principal stress allowable in the CVD diamond is 225 MPa. If the maximum principal stress is greater than zero and greater than the minimum principal stress, Eq. (1) can be used to determine the stress SF (fracture stress has been substituted for tensile strength).

$$n = \frac{S_f}{\sigma_{max}} \quad (1)$$

FEA METHODOLOGY

The analysis of the PFIL/VSC requires an absorbed heat flux mesh, a convection boundary condition, and thermal contact conductance (TCC) values. Absorbed heat flux files were created from SPECTRA 10.1 [5]. The convection boundary condition is applied to the model along the inner diameter of the cooling lines. Convection coefficient values ranged between 10 500 W/(m² K) and 11 000 W/(m² K) for the designs depending on the cooling line inner diameter. TCC describes the capacity to conduct heat between two surfaces in contact. In-Ga eutectic is the interstitial material between the oxygen-free high conductivity (OFHC) Cu and CVD diamond. The OFHC Cu is Ni coated where it contacts eutectic to reduce corrosion. The following TCC values were used in the analysis:

- OFHC Cu/OFHC Cu = 45 000 W/(m² K) [6]
- OFHC Cu/Ni/In-Ga/Diamond = 230 000 W/(m² K) [7]

Assumptions

The following assumptions were made to simplify the analysis:

- All materials are linear, elastic, isotropic, and homogeneous,
- Contributions from bend magnets and the BXDS wiggler are negligible,
- Vibration induced by cooling lines is negligible,
- Convection coefficient and temperature of water is constant,
- Fatigue effects on the CVD diamond are negligible,
- Fracture strength is lower than ultimate tensile strength of CVD diamond, and
- All frictional contacts are assumed to have a value of $\mu = 0.2$ [8].

Model Setup

Simplified models of the PFIL/VSC were created using Inventor 2016 for import into ANSYS 18.1 [9] for four designs shown in Fig. 2. Frictional contacts were used between CVD diamond and OFHC Cu, and between stainless steel fasteners when contacting OFHC Cu. Bolt pretension forces simulated the clamping force on the diamond. Pretension was applied in step one, and the heat load in step two.

Simulation

FEA Methods

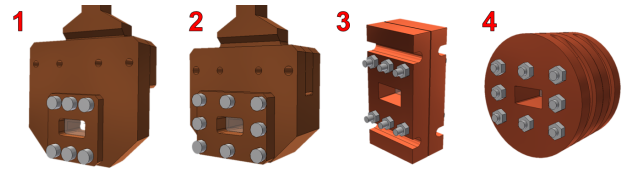


Figure 2: Four different designs for the PFIL/VSC that were assessed. Designs 1 and 2 utilized a recycled paddle from Brookhaven National Laboratory. Designs 3 (by Johnson Ultravac) and 4 were based off of filter designs used elsewhere at the CLS.

Model Verification

To ensure accuracy, the model mesh was optimized (see Fig. 3) to reduce thermal and structural error, and to reduce error in the import of the heat file. A square mesh of 0.5 mm sized elements was used on the CVD diamond foil. With this mesh, the error in the convection boundary condition was less than 1.2%. The adaptive size function with a medium relevance center was used to build the remaining mesh as it had low error and reasonable computing time. Computed clamping pressure on the diamond was within 4.1% of hand calculations.

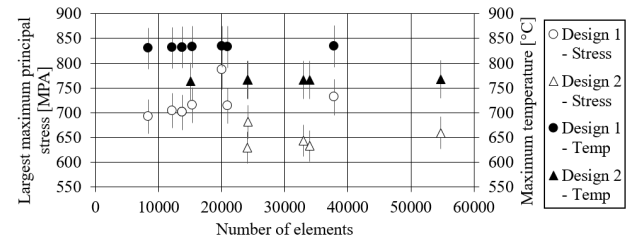


Figure 3: Maximum temperature and largest max principal stress on the CVD diamond versus number of elements. Error bars represent range of 5% above and below the calculated value.

RESULTS & DISCUSSION

Analysis was done for each design at a ring current of 500 mA. The results are shown in Table 1.

Table 1: Results for 500 mA (acceptable SF are bold)

Design	Max. Foil Temp. (SF) [°C]	Max. vM Stress [MPa]	Max. P. Stress (SF) [MPa]
1	881.2 (1.4)	1264	831.0 (0.5)
2	765.8 (1.6)	1144	681.4 (0.6)
3	492.2 (2.6)	656.8	418.2 (1.0)
4	482.6 (2.6)	670.7	343.5 (1.3)

None of the proposed designs met the 500 mA requirements. A more robust cooling system would be required to cool the diamond. Experimental data on the mechanical and thermal failure of a 0.1 mm CVD diamond filter could change the fracture stress value and reveal these designs are

viable. Designs 1 & 2 were evaluated for ring currents of 220 and 250 mA and the results are shown in Table 2.

Table 2: Results for 220 mA & 250 mA

Design (Ring Curr. [mA])	Max. Foil Temp. (SF) [°C]	Max. vM Stress [MPa]	Max. P Stress (SF) [MPa]
1 (250)	294.8 (4.4)	269.2	194.7 (2.3)
1 (220)	254.3 (5.1)	210.5	158.1 (2.8)
2 (250)	280.5 (4.6)	240.4	188.5 (2.4)
2 (220)	242.3 (5.3)	186.1	151.9 (2.9)

Either design 1 or 2 would perform well under either storage ring current. Design 1 was chosen as it required less machining time. Belleville washers were added to maintain a constant pressure on the diamond. A resistance temperature detector was added to compare temperature of the PFIL/VSC in operation to the FEA.

Model sensitivity was evaluated by altering different parameters of the designs to see which had the greatest effect in lowering the stress and temperature of the CVD diamond. The following parameters were optimized: clamping area, beam profile clearance, cooling line inner diameter, foil shape, and proximity to cooling lines. Of those tested, reducing the clearance around the beam profile had the greatest effect on reducing CVD diamond stress and temperature.

Bolt pretension was also tested to determine clamping pressure's effects on the diamond. Using a lighter clamping force lead to smaller maximum principal stress values as shown in Fig. 4. The relationship between TCC and the maximum temperature of the foil was found and is shown in Fig. 5.

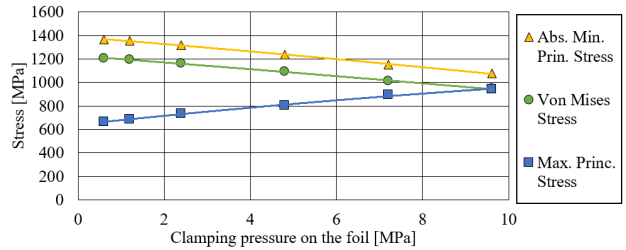


Figure 4: Stress versus clamping pressure on the CVD Diamond for 500 mA. Von Mises stress would erroneously predict a lower SF. The maximum principal stress is lower for lighter clamping pressures. Absolute values for minimum principal stress are graphed.

CONCLUSION

Reasonable results were found for brittle failure of CVD diamond using evaluation of principal stresses (Brittle Theory), allowing a design to be chosen. Sensitivity tests within FEA demonstrated design optimization changes that have the greatest positive effect on design criterion. Through evaluation of the bolt pretension, it was found that increasing clamping pressure on the CVD diamond increases the

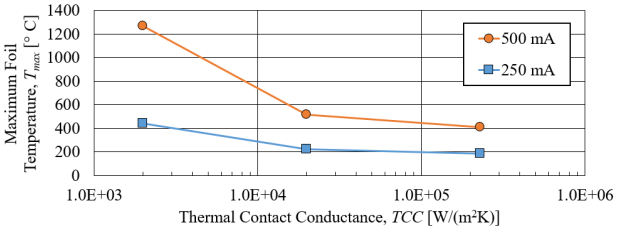


Figure 5: Maximum CVD diamond temperature versus TCC between the diamond and copper surfaces for 500 mA & 250 mA. If a TCC value is not specified in ANSYS, the program will use a large, unrealistic value. TCC should be based on experimental data.

chance of failure, therefore a balance between clamping pressure and TCC must be found.

To further improve this analysis, simulating anisotropic properties of CVD diamond would provide more accurate results. Thermal fatigue was considered negligible, but future work would benefit from empirical testing of thermal fatigue of CVD diamond under similar conditions.

ACKNOWLEDGEMENTS

Special *Thank You* to the CLS Engineering group and participants of the design review.

REFERENCES

[1] A. V. Khomich, V. G. Ralchenko, A. V. Vlasov, R. A. Khmel-nitskiy, I. I. Vlasov, and V. I Konov, "Effect of high temper-ature annealing on optical and thermal properties of CVD diamond", *Diam. Relat. Mater.*, vol. 10, pp. 546-551, 2001. doi:10.1016/S0925-9635(00)00517-3

[2] A. R. Davies, J. E. Field, K. Takahashi, and K. Hada, "Ten-sile and fatigue strength of free-standing CVD diamond", *Diam. Relat. Mater.*, vol. 14, pp. 6-10, 2005. doi:10.1016/j.diamond.2004.06.015

[3] R. G. Budynas and J. K. Nisbett, *Shigley's Mechanical En-gineering Design*. New York, NY: McGraw-Hill Education, 2015.

[4] C. S. Pickles, "The fracture stress of chemical vapour deposited diamond", *Diam. Relat. Mater.*, vol. 11, pp. 1913-1922, 2002. doi:10.1016/S0925-9635(02)00197-8

[5] SPECTRA (version 10.0.7 64bit), <http://radiant.harima.riken.go.jp/spectra/>.

[6] A. Tariq and M. Asif, "Experimental investigation of thermal contact conductance for nominally flat metallic contact", *Heat Mass Transfer.*, vol. 52, pp. 291-307, 2016. doi:10.1007/s00231-015-1551-1

[7] L. Assoufid and A. M. Khounsary, "Contact heat conductance at a diamond-OFHC copper interface with GaIn eutectic as a heat transfer medium", *Rev. Sci. Instrum.*, vol. 67, no. 9, pp. 3354, 1996. doi:10.1063/1.1147400

[8] Applied Diamond, Inc., <http://usapplieddiamond.com/wp-content/uploads/2016/02/chart3.pdf>.

[9] ANSYS Mechanical, Release 18.1, <https://www.ansys.com>.

Content from this work may be used under the terms of the CC BY 3.0 licence (© 2018). Any distribution of this work must maintain attribution to the author(s), title of the work, publisher, and DOI.

UPGRADE OF MAGNETIC MEASUREMENTS LABORATORY AT ALBA SYNCHROTRON

J. Campmany[†], J. Marcos, V. Massana, L. Ribó, F. Becheri, R.A. Petrocelli
ALBA-CELLS, 08290 Barcelona, Catalonia, Spain.

Abstract

Along 2017 and 2018, a complete upgrade of hardware and software at ALBA magnetic measurements lab has been done. Regarding hardware, a relevant innovation has been the replacement of DC motors by step motors in new Hall probe, flipping and rotating coil benches. Up to now, these kind of continuous measurements usually were done with DC motors because steppers were considered unable to fulfil the required movement smoothness. However, recent innovations in drives made feasible its use. In our case, we tested the performance of upgraded benches and they reach the same accuracy than the former DC versions. In all upgraded systems, we used the ALBA standard IcePAP motor driver [1], taking advantage of firmware upgrades, including the possibility of triggering data acquisition by signals generated from different axes selectable via software. Regarding software, control systems have been unified to Tango package.

HALL PROBE BENCH

The Hall probe bench at ALBA, used to map the magnetic field over 3D regions, was originally built in 1997 by Ramem Company as shown in Fig. 1. It was fully characterized when it was initially commissioned [2], and over the years the system had undergone several hardware and software upgrades in order to improve its performance. In particular, in 2005-2006 the control system was completely revised in order to migrate it from EPICS to TANGO and to implement the on-the-fly measurement mode, which allows acquiring data while the system is moving [3].

However, one of the critical hardware components, the motion driving system, a Delta Tau VME PMAC, had never been replaced and by the end of 2016 it has become obsolete. Therefore it was decided to replace it by a state-of-the-art motion controller providing equivalent or even better capabilities. The selected system was a Delta Tau Power Brick AC unit, which integrates a Power PMAC controller. In parallel, it was also decided to develop a new version of the control system, having it up-to-date with ALBA standards, in order to take profit of the tools that have been developed last years. The objective has been to control ID laboratory benches with the same architecture and code versions used in the controls of both Beamlines and Accelerator at ALBA.

The hardware replacement took place in Oct-Dec of 2016. Afterwards, between Dec 2016 and Feb 2017 the

hardware was tuned and adjusted. Finally, in the period Feb-Apr 2017 the new control system was successfully commissioned and debugged. Its performance is the same as the old one.



Figure 1: Old Hall probe bench based in DC motors upgraded in 2016.

In parallel, we have built a new Hall probe bench entirely based on step motors and with a control system similar to the upgraded old bench. The new bench, presented and characterized as published elsewhere [4] can be seen in Fig. 2. Software and hardware improvements are sketched in Fig. 3.



Figure 2: New Hall probe bench based in step motors.

Hardware	Old system	Upgraded system	New system
Motion controller	VME PMAC	Power PMAC	ICEPAP
Motor	DC motors	DC motors	Step motors
Hall probe current source	Agilent E3631A	Lake Shore 121	Agilent E3631A
Software			
OS	Suse9	Debian8	Debian8
Control System	Tango5	Tango8	Tango8
Hardware controllers	Tango-ds compiled in C++	New Tango-ds, mostly in Python	New Tango-ds, mostly in Python
Experiment control		Sardana SEP6	Sardana SEP6
GUI	Java with Jdraw synoptics	Taurus 3.7.0 based on QT	Taurus 3.7.0 based on QT

Figure 3: Hardware and Software upgrades of the Hall probe benches at ALBA.

[†] campmany@cells.es

According to tests published elsewhere [5], the system repeatability when measuring small-gradient magnetic fields is $\sim 10 \mu\text{T}$. In the case of measuring small period oscillating fields as those typical of in-vacuum undulators, the repeatability worsens by up to $\sim 60 \mu\text{T}$. Also, using the usual procedure of identifying poles as those points where $\partial B_y / \partial z = 0$, the rms error of the pole positions is of the order of $1 \mu\text{m}$, and the rms error of the associated peak field strength is $40 \mu\text{T}$. Thus, it is worth noting that the rms optical phase error calculated from the measured field is reproducible within 0.01° .

This performance is even slightly better than that of the upgraded old bench moved with DC motors. As a summary, in Table 1 we compare the accuracies reached with the old Hall probe bench operated with DC motors with the accuracies reached with the new system.

Table 1: Hall Probe Benches. DC Versus Step Motors

	Old bench DC motors	New bench Step motors
Error homogeneous field	$\pm 10 \mu\text{T}$	$\pm 10 \mu\text{T}$
Variable field error	$\pm 60 \mu\text{T}$	$\pm 60 \mu\text{T}$
Position error	$\pm 30 \mu\text{m}$	$\pm 20 \mu\text{m}$
Position repeatability	$\pm 1 \mu\text{m}$	$\pm 1 \mu\text{m}$
Phase error accuracy	$\pm 0.02^\circ$	$\pm 0.01^\circ$
Measurement velocity	15 mm/s	13 mm/s

FLIPPING COIL BENCH

The flipping coil bench at ALBA, designed to determine low-value field integrals from small gap devices, was purchased as a turn-key system from ESRF on 2006. The system made use of linear and rotating stages based on DC motors, controlled by a 6-axis Newport MM4006 motion controller. The control system consisted of macros running on Igor Pro software.

The copper multiturn-wire coil is arranged along the z-axis (longitudinal) and stretched between both stages (only the slave stage can be manually moved), and connected to a Digital Voltmeter (DVM). The x- and y-stages are used to position the coil for measurement and to scan the variation of field integrals. The rotational r-stage is used to rotate the coil around the z-axis and to determine the local value of the field integral. The system is shown in Fig. 4. In our case, the coil has the following dimensions: 4.1 m long, 4 mm width (nominal value) and has 15 turns. Repeatability errors have been studied and the reproducibility of first field integral measurements is $< 10^{-5} \text{ T}\cdot\text{m}$ [6].

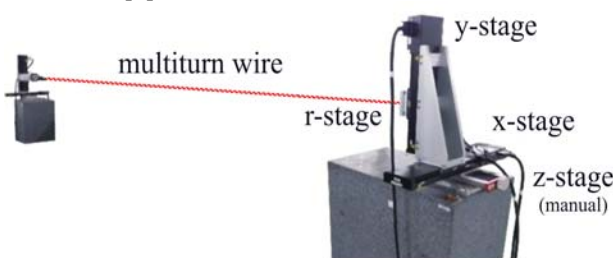


Figure 4: Flipping coil system at CELLS, with two motion stages on granite blocks.

In 2016 the motion controller unit broke down, and given that the system was not commercially available anymore and that no technical support existed, it was neither possible to replace nor to repair it. Therefore it was decided to replace the motion controller by the standard solution used at ALBA, an IcePAP unit. However, current version of IcePAP firmware only implements stepper motor control. As a consequence, it was necessary to send the linear/rotating stages to the manufacturer (Newport) in order to have their DC motors replaced by stepper ones.

The hardware refurbishment was complemented with the development of a new control system based on Tango conforming ALBA standards, as sketched in Fig. 5.

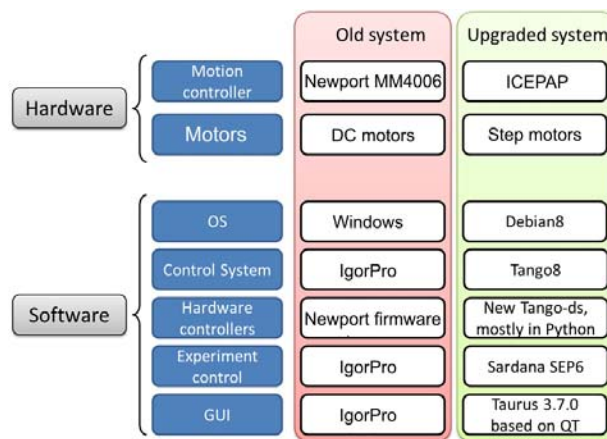


Figure 5: Hardware and Software upgrades of the Flipping Coil bench at ALBA.

This new control system, in addition to allowing for an easier maintenance, will make it possible to combine in a straight forward way the operation of the Hall probe and the flipping coil benches, which is a particularly convenient feature in the case of measuring Insertion Devices.

The hardware upgrade was carried out on Feb-Apr of 2017; the system was reassembled on May 2017 and the control system was developed and commissioned on Jun-Jul 2017. The new system displays a performance similar to the original one, with a *rms* repeatability of field integrals of $10^{-6} \text{ T}\cdot\text{m}$. Results are summarized in Table 2.

Table 2: Repeatability of Flipping Coil Bench

	DC motors	Step motors
Background	$1 \cdot 10^{-6} \text{ T}\cdot\text{m}$	$1 \cdot 10^{-6} \text{ T}\cdot\text{m}$
With field (relative)	$7 \cdot 10^{-3} \text{ T}\cdot\text{m}$	$1 \cdot 10^{-3} \text{ T}\cdot\text{m}$

ROTATING COIL BENCH

The rotating coil bench at ALBA, used to determine the integrated field harmonics of accelerator magnets with lengths up to 0.5m, is a second-hand system purchased from CERN on 2008. It is shown in Fig. 6. The system rotation is driven by a DC motor controlled by a Maxon PCU2000 unit. The coil signal is acquired by means of VME integrators based on voltage-to-frequency

converters developed at CERN, and the control system is based on LabVIEW running on a Sun Ultra workstation.

The repeatability of such a system in the determination of the main harmonic is better than $1 \cdot 10^{-4}$, and the repeatability in the determination of the normalized high order harmonics up to the 15th is of the order of $1 \cdot 10^{-5}$ [7].



Figure 6: Old rotating coil bench.

System hardware and software were obsolete and difficult to maintain. Therefore, a major upgrade of the system was mandatory. It included the substitution of the DC motor by a stepper one and the corresponding IcePAP controller; the replacement of the VME integrators by a state-of-the-art system (either a Keithley or a Keysight nanovoltmeter); and a new control system based on Tango. Also the software was upgraded with the same architecture used in other benches, as sketched in Fig. 7.

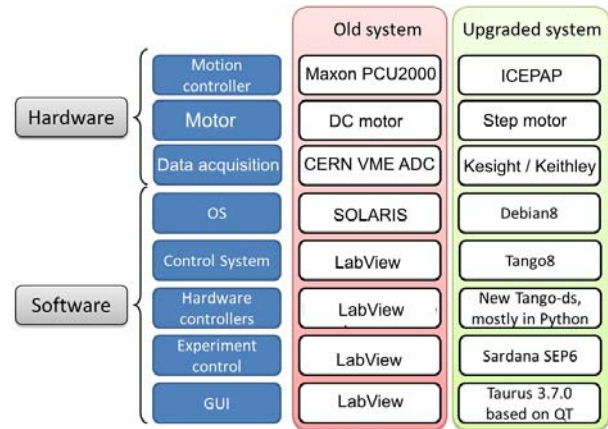


Figure 7: Hardware and Software upgrades of the Rotating Coil bench at ALBA.

In order to test the performance of the new hardware and software we have set up a mock-up integrating the three main devices of a rotating coil: the motor (step motor), the encoder and the coil. For simplicity, the coil is fixed, and the rotary part in the setup is the magnet used as a test. The prototype can be seen in Fig. 8.

Repeatability for the main harmonic is the same than for the old system, as shown in table 3. Further tests will be done to check the repeatability for high harmonics.

Table 3: Repeatability of Rotating Coil Bench

	DC motors	Step motors
Main harmonic	10^{-4}	10^{-4}

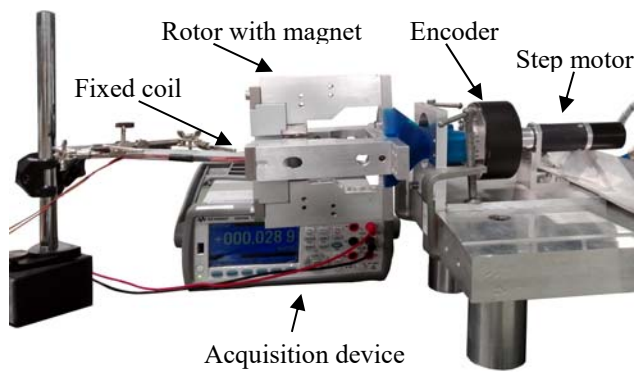


Figure 8: Mock-up of the rotating coil bench used to test the performance of new hardware setup.

CONCLUSIONS

The tests confirm that the step motors are suitable to make magnetic measurement benches requiring continuous movements at constant velocities.

We have successfully upgraded our measurement benches by new devices equipped with step motors without any loss of repeatability. This has allowed the standardization within ALBA of both the hardware (motor models, motor controller) and software (Debian 8, TANGO and SARDANA packages), simplifying accordingly the maintenance and the replacement of parts.

REFERENCES

- [1] N. Janvier, J. M. Clement, and P. Fajardo "ICEPAP: an advanced motor controller for scientific applications in large user facilities", in *Proc. of ICALEPCS2013*, San Francisco, CA, USA Oct. 2013, p. 766.
- [2] D. Beltran, J. Bordas, J. Campmany, A. Molins, J. Perlas, M. Traveria, "An instrument for precision magnetic measurements of large magnetic structures", *Nucl. Instr. and Methods A*, 4Feb. 2001, pp 285-294. DOI: 10.1016/S0168-9002(00)01008-1.
- [3] J. Marcos, V. Massana, L. García and J. Campmany, "Latest developments at the ALBA magnetic measurements laboratory", *Meas. Sci. Technol.*, vol. 29-2, Jan 2018. DOI: 10.1088/1361-6501/aa8ba2.
- [4] J. Campmany, F. Becheri, C. Colldelram, J. Marcos, V. Massana and L. Ribó "A new bench concept for measuring magnetic fields of big closed structures" in *Proc. IPAC 2015*, Richmond, USA, May 2015, paper TUPJE036 pp. 1690–1692.
- [5] J. Campmany, L. Ribó, C. Colldelram, F. Becheri, J. Marcos, and V. Massana "A new bench concept for measuring magnetic fields of big closed structures", *Physics Procedia*, Volume 75 (2015) 1222–1229. DOI: 10.1016/j.phpro.2015.12.124.
- [6] J. Marcos, "Characterization of the flipping coil bench at the ID laboratory at CELLS", Internal ALBA report AADSR-ID-AN-0194.
- [7] J. Campmany et al., "Status of magnetic measurements at ALBA", in *Proc. International Magnetic Measurements Workshop, IMM18*, Brookhaven, New York, USA, June 2013, https://indico.bnl.gov/event/609/contributions/15426/attachments/13732/16805/Day1_07_Campmany.pdf.

PHOTON BEAM APPLIED AS HEAT FLUX ON IRREGULAR SURFACES IN FEA*

D. Capatina†, Advanced Photon Source, Argonne National Laboratory, Lemont, USA

Abstract

The light source front ends and beamlines contain several devices designed to limit the size of, or completely stop, the photon beam. Most of these devices are meant to protect personnel and/or equipment, thus their failure would have serious implications for the facility operation. The photon beam carries extremely high energy, thus the system will experience very large thermal loads. Accurate temperature and stress distribution of these components, based on well-reasoned assumptions, is needed to accurately review the performance of these devices during the design process. Applying non-uniform heat flux as a thermal load in simulation presents a challenge. This work describes the steps of the thermomechanical numerical simulation for a typical component at the Advanced Photon Source (APS), subject to photon beam interception. The numerical algorithm used to apply the non-uniform heat flux distribution on an irregular type of surface is presented in detail. The algorithm was developed using the commercial Finite Element Analysis (FEA) software ANSYS Workbench of ANSYS, Inc.

PROBLEM FORMULATION

A photon mask (here after mask) is a front end or beam-line component meant to limit the size of the photon beam presented to the downstream components. During normal operation the photon beam passes through the mask aperture. By several reasons the beam could be missteered from its normal trajectory, causing the beam to partially or fully strike the mask [1]. Accurate thermal simulation of this mask is needed to review the performance of this device under the worst case load and beam missteering scenarios.

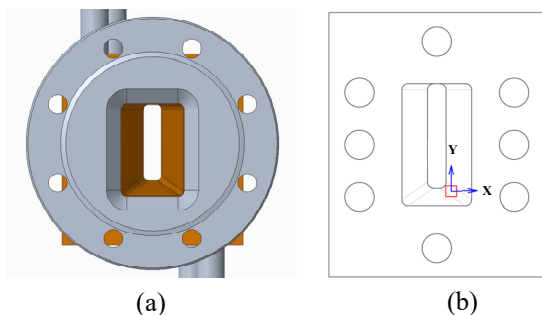


Figure 1: (a) CAD model of the mask assembly, front view; (b) CAD drawing of the mask model used in the analysis, front view, showing the beam footprint.

* Work at the Advanced Photon Source is supported by the U. S. Department of Energy, Office of Science, Office of Basic Energy Sciences, under Contract No. DE-AC02-06CH11357.

† capatina@anl.gov

A typical mask design is the boxed-cone and the aperture of such component is shown in Fig. 1a. One of the most critical scenarios is when the beam strikes the corner of the taper. The beam footprint for this case is shown in Fig. 1b.

The power density distribution corresponding to the normal beam incidence assuming a 4th order Gaussian equation was calculated using SRUFF [2]. Equation (1), generated for a particular loading scenario for demonstration purposes, was used in ANSYS to apply the heat flux thermal load:

$$q = \exp(a+bx^2+cy^2+dx^4+fy^4+gx^2y^2) \quad (1)$$

where $a=4.3828$, $b=-0.037375$, $c=-0.20196$, $d=-0.0023109$, $f=0.0045228$ and $g=-0.020031$.

Equation (1) represents the coordinate-dependent power density, q , along the beam axis, z . The power absorbed by the mask surface and thus to be applied in ANSYS is the component of the q vector perpendicular to the surface, q_n . The heat flux vector decomposition is illustrated in Fig. 2.

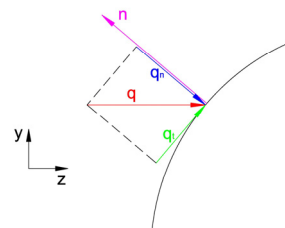


Figure 2: Heat flux vector decomposition.

Unlike the sides of the mask taper, which have a constant normal vector, on the corner surface the normal vector varies at each point of the surface. ANSYS does not have a build-in command to apply a coordinate dependent heat flux vector. The solution of this challenge is developing a code to provide the surface heat flux at each node of the element where the heat load is applied.

NORMAL VECTORS COMPUTATION

After meshing, ANSYS Workbench allows the user to obtain information about the mesh such as: element number and its nodes numbers, and coordinates with respect to the specified coordinate system [3]. In this case the coordinate system is user defined and its origin is situated in the middle of the beam footprint with respect to the x and y coordinates. Knowing the coordinates of two points one can compute a vector connecting the two points. In the same way, having the coordinates of three nodes of a surface element, one can compute two vectors which have a common point, each vector having the tail at the common

point and the head at the adjacent point. By definition the vector product of two adjacent vectors is a vector which is perpendicular to the surface defined by the initial two vectors and having the tail on the common point. The new vector divided by its length gives us the normal vector to the surface in that particular point. Based on this theory, the normal vector at each node of the beam footprint is computed [4]. In order to loop through all the elements, we need to know how many elements there are in the selection. The following command is issued in order to obtain the number of elements:

$$*get,ne,elem,0,count \quad (2)$$

Parameter ne is the user defined parameter name which stores the number of elements.

If we set the element number, e, to equal zero, the following command allows the user to get the next higher element number above e.

$$*get,e,elem,e,nxth \quad (3)$$

The routine then loops through all the elements of the selection to compute the heat flux at each node.

The core of the routine starts with obtaining the node numbers and the x, y, z coordinates of each node of the element as shown by the commands (4) through (7). There are eight nodes per element for the chosen SURF152 elements, which are quadratic elements with middle side nodes, as shown in Fig. 3.

$$*get,n1,elem,e,node,1 \quad (4)$$

$$*get,n1x,node,n1,loc,x \quad (5)$$

$$*get,n1y,node,n1,loc,y \quad (6)$$

$$*get,n1z,node,n1,loc,z \quad (7)$$

In the above commands, n1 is the node number of the first node of the element number e and n1x is the x coordinate of the node number n1, etc. After obtaining all the 8 times 3 coordinates for the first element, one can compute the normal vectors, make the projections and calculate the heat load at each node.

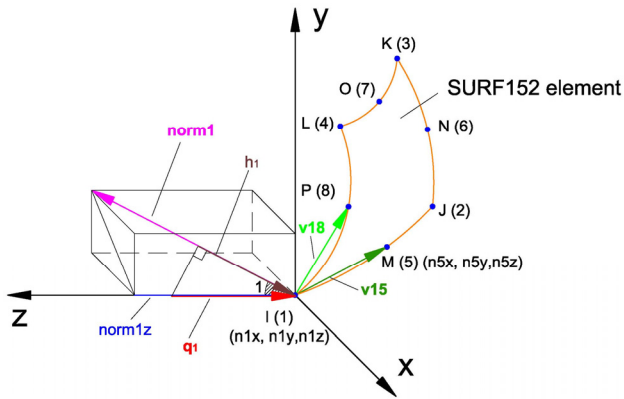


Figure 3: Normal vector at node 1 of a surface element.

The first normal vector to be computed, norm1, see Fig. 3, has the tail on node 1 and it is perpendicular on v15 and v18. The vectors v15 and v18 are connecting node 1

with its adjacent nodes: 5 and 8, respectively. Vectors v15 and v18 have v15x, v15y, v15z, and v18x, v18y, v18z as coordinates, respectively. The coordinates are computed as follows:

$$v15x=n5x-n1x \quad (8)$$

$$v15y=n5y-n1y \quad (9)$$

$$v15z=n5z-n1z \quad (10)$$

$$v18x=n8x-n1x \quad (11)$$

$$v18y=n8y-n1y \quad (12)$$

$$v18z=n8z-n1z \quad (13)$$

The vector product definition is used to find the normal vector coordinates norm1 (norm1x, norm1y, norm1z):

$$v15 \times v18 = \text{norm1} \quad (14)$$

In matrix notation this becomes:

$$\begin{bmatrix} e_1 & e_2 & e_3 \\ v15x & v15y & v15z \\ v18x & v18y & v18z \end{bmatrix} = \begin{bmatrix} \text{norm1x} \\ \text{norm1y} \\ \text{norm1z} \end{bmatrix} \quad (15)$$

where e1, e2 and e3 are the unit normal vectors of the coordinate system with the origin at node 1. Therefore, the normal vector, norm1, coordinates are:

$$\text{norm1x} = (v15y * v18z) - (v18y * v15z) \quad (16)$$

$$\text{norm1y} = (v18x * v15z) - (v15x * v18z) \quad (17)$$

$$\text{norm1z} = (v15x * v18y) - (v18x * v15y) \quad (18)$$

The modulus of the normal vector, norm1, is:

$$\text{mod_norm1} = \sqrt{\text{norm1x}^2 + \text{norm1y}^2 + \text{norm1z}^2} \quad (19)$$

The cosine of the angle between the normal vector, norm1, and the z direction can be now computed. This angle is called angle 1, as it refers to the normal vector at node number 1:

$$\cos 1 = \frac{|\text{norm1z}|}{\text{mod_norm1}} \quad (20)$$

The heat load as provided by SRUFF at node 1, q_{n1} , is obtained by substituting x with n1x and y with n1y in equation (1). Finally, the length of the normal component of the heat flux, q_{n1} , at node 1, $h1$, is obtained by multiplying q_{n1} by $\cos 1$.

Following the same procedure, the other normal components at the nodes 2 through 8, hi , can be computed. Having all the hi values for the element e allows issuing the load command:

$$\text{sfe},e,1,hflux,,h1,h2,h3,h4,h5,h6,h7,h8 \quad (21)$$

This way each node of the selection is loaded with the appropriate heat flux value.

METHOD FOR ANSYS WORKBENCH

With appropriate pre-processing, the numerical algorithm described above can be used in ANSYS Workbench as a command snippet to apply the heat flux load.

Pre-processing

The above algorithm is written for quadratic elements and therefore the hex dominant method for meshing has to be used. To be able to capture the heat load accurately it is essential to fine mesh the surfaces of interest.

The user has to define a coordinate system, as shown in Fig. 4, with the origin in the middle of the beam footprint and assign a number, 12 for instance, as the APDL name.

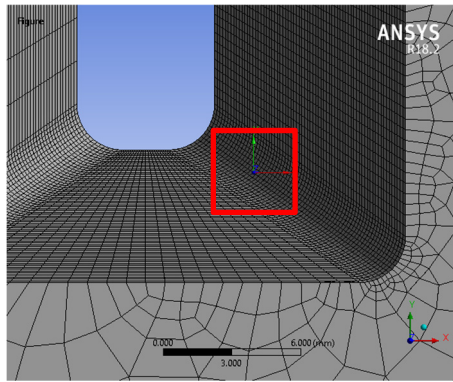


Figure 4: The mesh of the taper corner.

The surfaces of interest, in this case the corner and the adjacent sides, are selected and saved in a "Named selection" called "E_Surf". By right-clicking on the named selection just created and choosing "Create Nodal Named Selection", the user creates a collection of nodes called "E_Surf_Nodes".

In this step, the user also assigns the material, the heat transfer coefficient and the bulk temperature.

Command Snippet

The first step is to set the coordinate system to 12, then add SURF152 surface elements to the thermal analysis and enable heat flux input. Next, a subset of nodes corresponding to the beam size at the component or slightly larger is selected. The surface effect elements, SURF152, are created using ESURF and then selected as follows:

```
CSYS,12 (22)
*GET,ID_MAX_TYPE,ETYP,0,NUM,MAX (23)
ET,ID_MAX_TYPE+1,152 (24)
KEYOPT,ID_MAX_TYPE+1,8,1 (25)
TYPE,ID_MAX_TYPE+1 (26)
CMSEL,S,E_Surf_Nodes (27)
NSSEL,R,LOC,X,-1.43,1.43 (28)
NSSEL,R,LOC,Y,-1.45,1.45 (29)
ESURF (30)
ESEL,S,TYPE,,ID_MAX_TYPE+1 (31)
```

Then the number of selected elements, ne, are obtained using equation (2), the element number, e, is set to zero and

the coefficients a through g are defined. The core of the algorithm, consisting of a do – enddo loop through all of the selection elements, starts with equation (32). Following are equations (3) through (13) and (16) through (21), for the nodes 1 through 8. Equation (33) closes the loop.

```
*do,i,1,ne (32)
```

```
*enddo (33)
```

Solution

The temperature distribution within the mask body is obtained by running the solution. The temperature plot for the example chosen here is shown in Fig. 5.

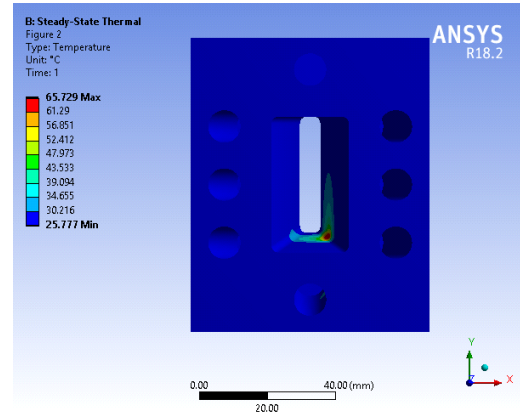


Figure 5: Temperature distribution.

CONCLUSION

The purpose of this work was to calculate the temperature distribution on a mask component subject to x-ray beam interception by means of using the commercial FEA software ANSYS Workbench of ANSYS, Inc. The analysis technique was described in detail. A sophisticated command snippet was developed. This allows applying the heat flux load generated by the x-ray beam on any surface type of a body. The technique described in this work is applicable to any component subject to x-ray beam interception. The prediction of the temperature distributions is very accurate; therefore, it is a reliable tool for the component validation procedure.

REFERENCES

- [1] Y. Jaski *et al.*, "Thermomechanical analysis of high-heat-load components for the canted-undulator front end," in *Proc. MEDSI2002*, Argonne, IL, USA, Sep. 2002, pp. 390-397.
- [2] M. Meron, "SRUFF: A Comprehensive Package for Synchrotron Radiation Spectral and Optics Calculations," unpublished.
- [3] ANSYS Inc., "Introduction to ANSYS 9.0 – Part 1: training manual", unpublished.
- [4] D. Capatina, "A computational and experimental investigation of the heat flux applied by a photon beam," M.S. thesis, Materials and Aerospace Engineering, Illinois Institute of Technology, Chicago, USA, 2008.

APPLICATION OF REMOTE INSTALLATION AND MEASUREMENT SMART VEHICLE IN ACCELERATOR*

J. X. Chen^{†1}, L. Kang¹, G. Y. Wang¹, J. S. Zhang¹, J. B. Yu¹, X. J. Nie¹, H. Y. He¹

A. X. Wang¹, C. J. Ning¹, Y. J. Yu¹, L. Liu¹, D. H. Zhu¹

Institute of High Energy Physics, Chinese Academy of Sciences, 100049 Beijing, China

¹ also at Dongguan Neutron Science Center, 523808 Dongguan, China

Abstract

The installation, alignment measurement and vibration monitoring of the accelerator equipment are cumbersome. In order to reduce the work intensity and exposure time of personnel, this paper has developed a smart vehicle that can automatically walk and automatically adjust the horizontal in the accelerator or beam line area. The smart vehicle can move forwards, sideways, oblique lines, rotations and combinations, and can automatically adjust the level according to different terrains. The auto-levelling accuracy is better than 0.001 degrees. By installing vibration measuring equipment or collimating equipment on the vehicle platform, vibration testing and collimation measurement of the equipment in the accelerator or beam-line device can be performed.

INTRODUCTION

The remote measurement smart vehicle (Figure 1) is mainly composed of a body, McNamee wheels movement module, a lifting module, a parallel six-degree-of-freedom platform [1, 2], an electrical module and a control panel. The main body of the vehicle is constructed of high-strength hard aluminium alloy and aluminium profiles. The car is equipped with four sets of McNamee wheels motion platform, which can realize forward, horizontal, oblique, and rotation and combination sports. Lifting module maximum load is greater than 2000N, can achieve 0-500mm range of lifting movement. The six-degree-of-freedom platform mainly realizes the self-levelling and angle adjustment functions required for the vibration measuring equipment and the alignment equipment. Two 24V power interfaces are reserved for the walking platform to provide power to other on-board devices.

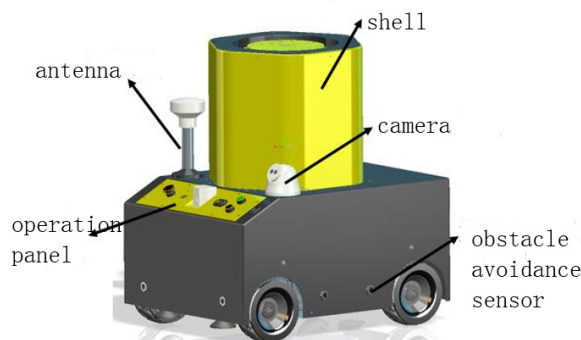


Figure 1: Structure of the smart vehicle.

*Work supported by National Nature Science Foundation of China (11375217)

[†] email address: chenjx@ihep.ac.cn

SMART VEHICLE PERFORMANCE TEST

Smart vehicle walking tests mainly include automatic walking and manual walking. The vehicle and the upper computer control system communicate data through the wireless network. The automatic walking mainly realizes the straight running, left-turning, right-turning and stopping of the smart vehicle through the two-dimensional code identification and positioning technology. The vehicle walking movement information is recorded on each two-dimensional code. The smart vehicle scans the two-dimensional code to obtain the movement. The scanning range is $\varnothing 200\text{mm}$. Before detecting the action information of the next two-dimensional code, the smart vehicle will continue to maintain the previous command. Manual walking indicates the forward and backward rotation of the smart vehicle through the control button. The infrared obstacle avoidance sensor and image acquisition system are arranged around the whole vehicle, and the environment in front of the vehicle can be obtained in the upper computer. Figure 2 shows the smart vehicle measuring in a simulated accelerator tunnel. Figure 3 shows a two-dimensional code tracking test of the smart vehicle.

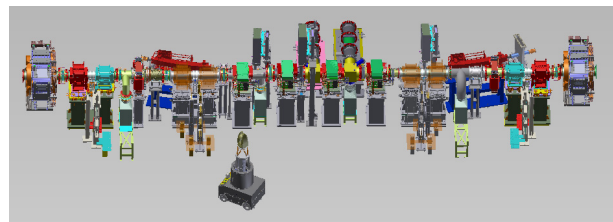


Figure 2: The smart vehicle measuring in a simulation accelerator tunnel.

SMART VEHICLE AUTO-LEVELLING TEST

When the vehicle is in place, in order to meet the level requirement of the alignment device, the level of the moving platform at the top of the smart vehicle needs to be adjusted [3]. According to the level requirement of the alignment measurement, the level of the platform needs to be better than 0.001° . After measurement, the three directions of the XYZ range of rotary angle travel are $\pm 10^\circ$ and the travel range is $\pm 29\text{mm}$. Figure 4 shows the position error curve of open-loop control of the horizontal adjustment mechanism of the smart vehicle. The open-loop position error is within 1mm. Figure 5 shows the attitude error curve of the open-loop control mechanism of the

horizontal adjustment mechanism of the smart vehicle. The accuracy is within 0.04° . After closed-loop control, the positioning accuracy of the horizontal adjustment mechanism of the carriage is shown in Table 1, and the horizontal angle accuracy is better than 0.00086° .



Figure 3: The two-dimensional code tracking test.

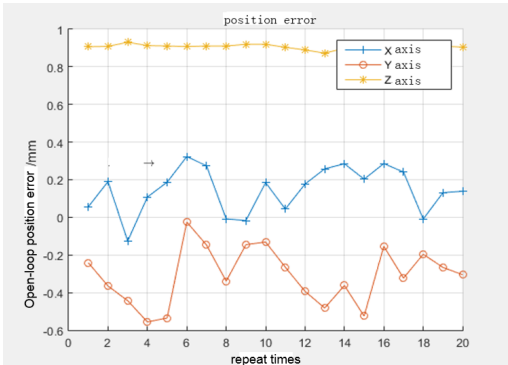


Figure 4: The open-loop position error curve.

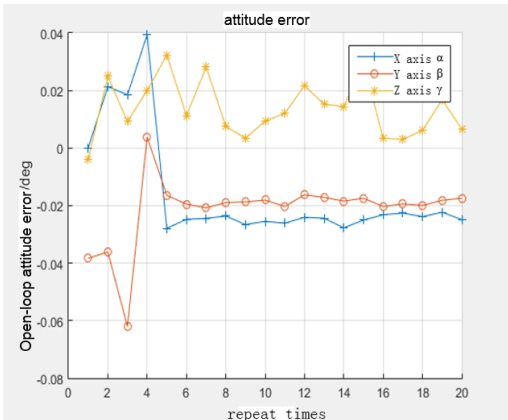


Figure 5: The open-loop attitude error curve.

Table 1: Closed-Loop Accuracy of the Horizontal

Axis	X	Y	Z	α	β	γ
Close-loop accuracy	0.004 mm	0.005 mm	0.001 mm	0.00025 deg	0.00043 deg	0.00086 deg

VIBRATION MONITORING TEST

The vehicle is equipped with a vibration monitoring system to detect the vibration of the equipment. As shown in Figure 6, the vibration monitoring system can be fixed on the smart vehicle, and the height of the vibration system can be changed by a lifting mechanism. By adjusting the attitude of the parallel 6-DOF platform, a swing of ± 10 degrees can be achieved, thereby increasing the testing range. At the front of the vehicle, there is a video monitor. Through the video monitor, the position of the vibration monitoring lens can be clearly seen. The smart vehicle simulates a vibration test in the laboratory. During the test, in order to obtain a better imaging effect, the smart vehicle needs a higher positioning accuracy or a more convenient adjustment operation. After testing, within the range of ± 200 mm of the fixed position, multiple sets of different vibration data were tested. The results show that the camera can obtain better imaging results and measure the vibration data. Figure 7 shows the target images captured by the vibration monitoring system. Figure 8 shows the data collected by the vibration monitoring system.

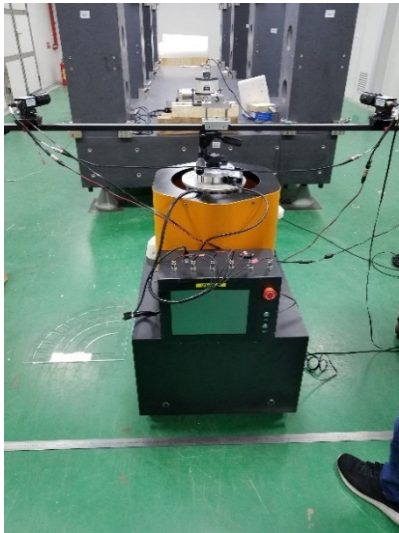


Figure 6: Vibration monitoring equipment test on the smart vehicle.

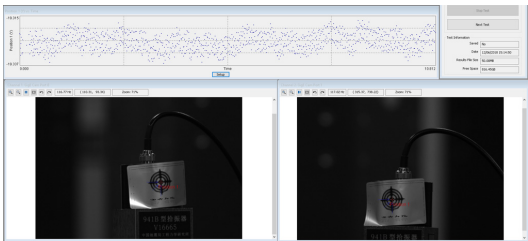


Figure 7: Vibration monitoring acquisition images.

PHOTOGRAPHIC ALIGNMENT MEASUREMENT

When the smart vehicle is equipped with an alignment device, the alignment of the device can be measured. Figure 9 shows an alignment measurement test by the

smart vehicle equipped with an alignment device at the target station of the Chinese Spallation Neutron Source. The vehicle can also be equipped with a radiation dose detection device to monitor the radiation dose in the tunnel or carry a robot to perform specific operations.

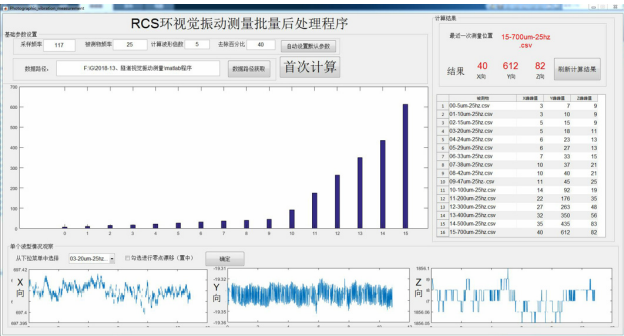


Figure 8: Vibration monitoring acquisition data.

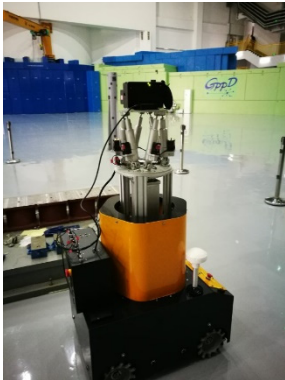


Figure 9: Photographic alignment measurement test.

CONCLUSION

The remote installation and measurement smart vehicle can carry various test devices to complete various test work in the accelerator, which can effectively reduce the labour time and labour intensity of the operator, and at the same time reduce the radiation time for the operator, and can be promoted in various accelerator devices.

REFERENCES

[1] Guo-Qing Sun, Guan-Bin Gao, “Kinematic modelling and validation of a 6-DOF industrial robot”, in *Proceedings of 2015 5th International Conference on Computer Sciences and Automation Engineering (ICCSAE 2015)* doi:10.2991/iccsae-15.2016.42

[2] TAN Shuang ,WANG Xiaoyong, LIN Zhe, YAN Nanxing, “Sensitivity Analysis of Position and Pose Adjustment of 6DOF Parallel Mechanism”, in *Spacecraft Recovery & Remote Sensing*, 2015, Vol.36, pp.78-85. doi: 10.3969/j.issn.1009-8518.2015.03.011

[3] ZHU Cheng-wei, WANG Liang, CHEN Jian-wei, ZHANG Rong-xing, “Study of Automatic Levelling System Based on 4-SPS(PS) Parallel Mechanism”, in *Chinese Hydraulics & Pneumatics*, 2016, Issue 6, pp.102-108. doi: 10.11832/j.issn.1000-4858.2016.06.021

VIBRATIONAL STABILITY OF A CRYOCOOLED DOUBLE CRYSTAL MONOCHROMATOR AT SSRF *

Y. Fan^{†,1,2}, F. Tao^{1,2}, Z. Li¹, H. Qin¹, W. Zhu¹

¹Shanghai Institute of Applied Physics, Shanghai 201800, P. R. China

²University of Chinese Academy of Sciences, Beijing 100049, P. R. China

Abstract

There is an increasingly critical demand on the angular stability of double crystal monochromator (DCM). This work focuses on a method to measure angular vibration directly at the DCM crystals using a dual-frequency interferometer. This method was applied to the off-line test of a newly developed cryocooled DCM at Shanghai Synchrotron Radiation Facility (SSRF), which can obtain a resolution of 8 nrad. The DCM was then tested on the X-ray Test Line. Both off-line and on-line results were referenced for DCM structure optimizations. In this paper, the DCM angular stability measuring method is presented, and detailed information of the results are shown.

INTRODUCTION

In the Phase-II beamline project of Shanghai Synchrotron Radiation Facility (SSRF), a fast x-ray imaging beamline will be constructed. To ensure the imaging quality, the beam stability is supposed to achieve 0.25 μrad/10min, thus the influence on the spatial resolution can be controlled within 1 μm. A cryocooled double crystal monochromator (DCM) has been designed and manufactured for this new beamline, which is under optimization at present. Main specifications of DCM stability are shown in Table 1 [1]. To achieve this target, a series of tests has been carried out on DCM stability, so as to provide references on the structure optimization.

Table 1: Angular Stability Specifications of DCM

Imaging Mode	Spatial Resolution (μm/pixel)	Angular Stability (μrad)
Monochromatic	1	≤0.25/10min
/White beam	2	≤0.5/10min
	5	≤1.5/10min

EXPERIMENTAL DESIGN

Principle and Instrument

To obtain the frequency information of DCM vibration, an Agilent[®] 10719A differential interferometer was applied to angular measurement. As the interferometer is mounted with quarter-wave plates inside, direct measurement of a mirror or a polished crystal surface is available. Figure 1 shows the schematic of the interferometer [2,3].

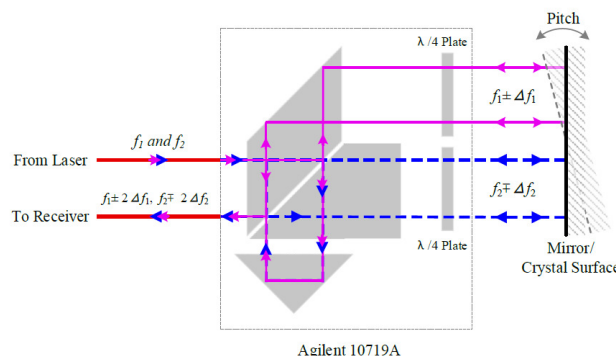


Figure 1: Schematic of 10719A.

According to Doppler effect, the angle can be worked out as:

$$\tan \theta = \frac{\lambda}{4D} \int_0^t \Delta f dt = \frac{N\lambda}{4D} \quad (1)$$

With an upgrade of the monitor board from E1735A to N1230A, the resolution of this measuring system can be increased from 50 nrad to 8 nrad [3,4]. The upgrade is now in progress.

Methodology and Experimental Setup

With a mirror located by the outlet flange, angular vibration of double-crystal could be measured directly, as shown in Figure 2. This method can also be applied to the vacuum condition. All the off-line tests were carried out in Lab 1042 at SSRF, shown as Figure3, where the floor is only 0.12m thick with no pile underground [5]. The sampling rate was set to be 500 Hz to obtain the frequency information within 200Hz. As the experimental environment was not satisfactory, more attention was paid on the frequency information.

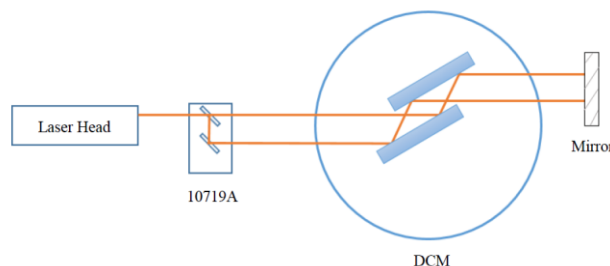


Figure 2: Direct measurement of double-crystal stability.

* Work supported by National Natural Science Foundation of China (Grant No. Y615171061)

† fanyichen@sinap.ac.cn

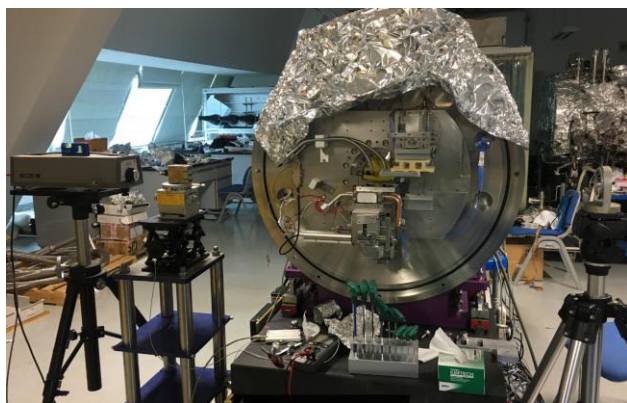


Figure 3: Off-line test of DCM angular stability.

RESULTS AND DISCUSSION

Off-line Test

To get rid of the influence of the measuring system itself, direct reflective signal from the mirror without passing through crystals was also acquired, working as the background information. The FFT results of both tests can be seen from Figure 4 and Figure 5.

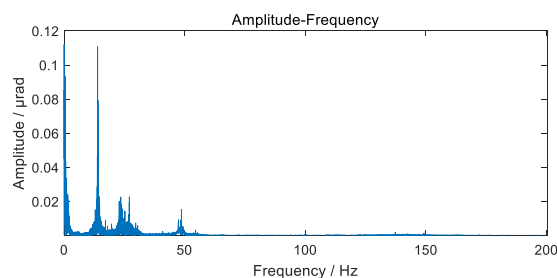


Figure 4: FFT of direct reflective signal.

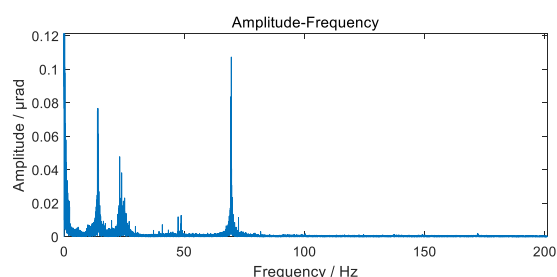


Figure 5: FFT of double-crystal pitch angle vibration.

RMS value of DCM vibration was about 200nrad. In consideration of the simplified facilities as well as the noisy experimental environment, more attention was paid on the frequency information rather than the amplitude. Comparing the two figures above, there is an apparent peak around 70Hz, which is believed to be the signal of double-crystal system. As laser has passed through the crystals back and forth, the actual amplitude should be half as shown. The off-line measurement could successfully obtain the frequency information of double-crystal vibration, which provided a useful reference on the structure optimization.

On-line Test

On-line tests of the DCM were carried out on the X-ray Test Beamline (09B) at SSRF. Altogether 3978 spots were acquired, with each image exposing for 1ms. Frequency analysis was done by picking up several line profiles and studying the rule of time-intensity, shown in Figure 6. FFT of the time domain data has been calculated and is shown in Figure 7. The main frequency distribution of vibration sources was around 30Hz, 40Hz, 50Hz, and 65Hz. Comparing Figure 7 with Figure 5, we can see both results of off-line and on-line test matched well, the calculated frequency responses are similar.

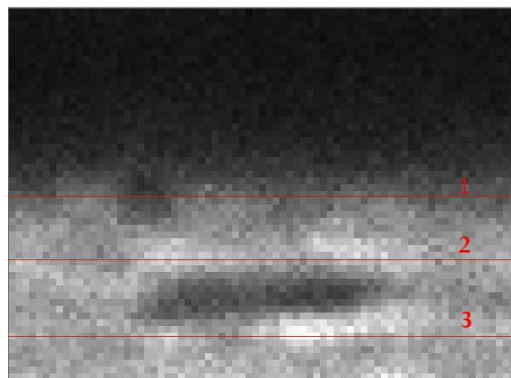


Figure 6: Picking up line profiles from spot.

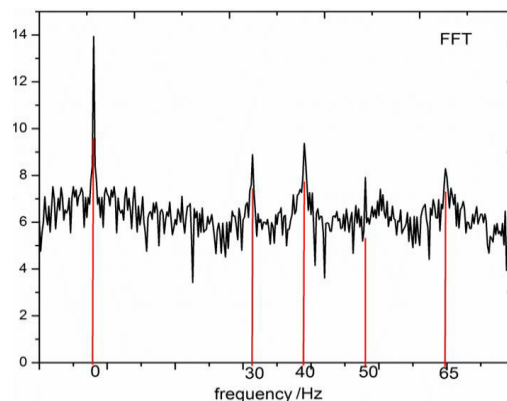


Figure 7: FFT analysis of spot vibration.

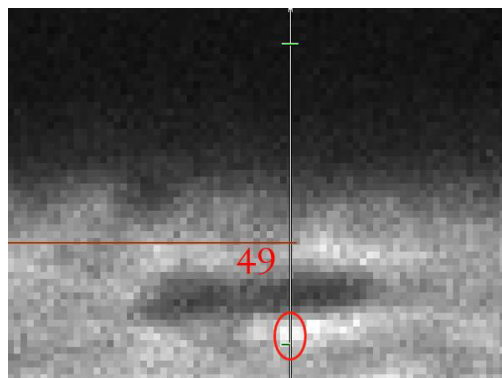


Figure 8: Picking up specific point from spot.

By picking up some specific points and observing their location change, shown in Figure 8, the amplitude analysis was done. To acquire more detailed data of the amplitude,

subpixel digital image processing was applied. Through an interpolation of 1:0.05:2, the peak-to-valley amplitude was worked out to be about $8\mu\text{m}$, shown in Figure 9. The DCM structure still needs optimization to improve the angular stability.

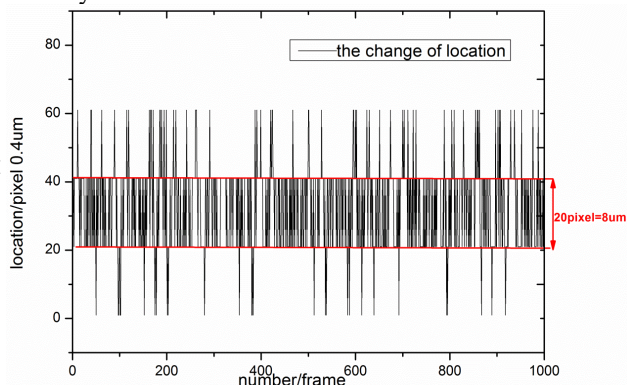


Figure 9: Amplitude analysis of spot vibration.

CONCLUSION

This paper represents a method to measure angular vibration directly at the DCM crystals using a dual-frequency interferometer, which can realize a resolution of 8 nrad. This method has been applied to the off-line test of a newly developed cryocooled DCM at SSRF, the results of which has been discussed. On-line test results have also been shown, and comparison between both measurements has been made. The DCM is currently under optimization to realize better angular stability, the tests can provide effective reference on the structure optimization.

ACKNOWLEDGEMENTS

The authors would like to acknowledge the financial support from National Natural Science Foundation of China (Grant No. Y615171061).

REFERENCES

- [1] SSRF Phase-II Beamline Project Preliminary Design Report, Shanghai, 2017.
- [2] P. Kristiansen *et al.* "Vibration measurements of high-heat-load monochromators for DESY PETRA III extension.", *Journal of Synchrotron Radiation*, volume 22, 2015, pp. 879-885.
- [3] *Agilent Laser Optics-User's Manual, Volume II*, Agilent Technologies, USA, Jul. 2017, pp.509-529.
- [4] X. Qi, L. Teng, and H. Yu, "Real-time compensation of Abbe error in measuring lead screw accuracy by dual-frequency laser interferometer", *Chinese Optics*, vol. 3, no. 3, 2010, pp. 279-284.
- [5] R. Deng, F. Gao, and L. Yin, "Ground vibration monitoring for SXFEL construction at SSRF", in *9th Edition of the Mechanical Engineering Design of Synchrotron Radiation Equipment and Instrumentation Conf. (MEDSI'16)*, Barcelona, Spain, Sept. 2016, paper TUPE36, pp. 242-245.

THERMO-MECHANICAL ASPECTS OF THE MOBIPIX, A COMPACT X-RAY IMAGING SYSTEM WITH EMBEDDED GPU*

A. Gilmour A Jr.[†], W.R. Araujo, J.M. Polli,
Brazilian Synchrotron Light Source (LNLS), Campinas, Brazil

Abstract

In the light of the high brilliance fourth generation synchrotron light sources, real-time imaging techniques became possible, boosting the demand for fast and reliable detectors. Mobipix project is a compact X-ray imaging camera designed for Sirius [1], based on Medipix3RX** [2,3]. The control and acquisition system uses System-On-a-Chip technology with embedded Graphics Processing Units (GPUs) where data processing algorithms will run in real time. The Mobipix X-ray detector is designed to perform as a video camera, enabling X-ray imaging experiments and beam diagnose, at thousands of frames per second (FPS), without external computers.

This paper presents the development of the Mobipix detector mechanics. The authors describe the path taken to design the structural aspects, ensuring robustness and versatility in the device installation to the beamlines, and the thermal aspects, regarding forced air cooling, high heat density, and small volume through which the flow will occur. The latter aspects were developed by exploiting Computational Fluid Dynamics (CFD) modelling.

The Mobipix has 28 x 28 mm² active area, composed by 260k pixels of 55 x 55 μm², and is planned to achieve continuous readout up to 2000 FPS.

INTRODUCTION

The Mobipix electronic design is composed of three boards, the upper board is the carrier board, responsible for housing a Nvidia Jetson TX-1 [4] and providing external connections. The lower board contains the analogical and digital electronics for Mobipix control and readout, being nominated Mobipix board. The board housing four Medipix3RX sensors is attached to the Mobipix board by a perpendicular connection, and is called the Medipix board. Figure 1, illustrates the three boards and their assembly disposition.

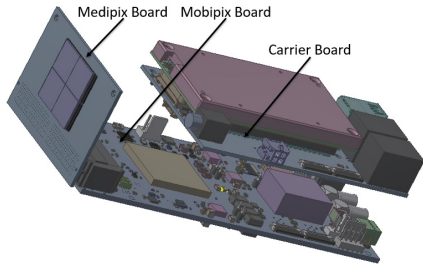


Figure 1: The three electronic boards that compose Mobipix, assembled.

* Work supported by Brazilian Ministry of Science, Technology, Innovations and Communications.

**LNLS is a member of CERN Medipix3 Collaboration.

[†] allan.gilmour@lnls.br

Simulation

Thermal

Objectives

This work aimed at keeping the volume of the device as small as possible, while ensuring that the temperature of each component is kept within its given limits. There are two different kinds of semiconductor sensors intended to be coupled to Mobipix, one made of silicon (Si) and another made of cadmium telluride (CdTe). The thermal project must attend both possibilities.

Figure 2 and Figure 3 demonstrate the position of the main heat generating components, while Figure 4 lists their description and worst-case scenario heat dissipation, according to their datasheets [2-13].

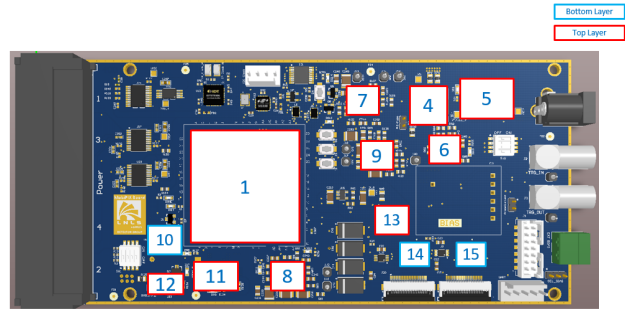


Figure 2: Heat generating components in Mobipix board.

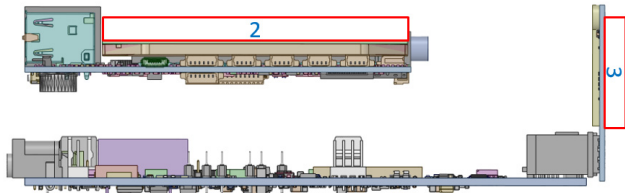


Figure 3: Heat generating components in the other two boards.

Component (ID no.)	Power [W]	P. Density [W/m ³]	Allowed T [°C]
FPGA Kintex-7 Xilinx (1)	4	1.32E+06	80
Jetson TX-1 (2)	15	4.27E+05	80
Sensor Medipix-3RX (3)	6	6.56E+06	60
LTC4358 Protection Diode (4)	1	1.83E+07	80
BNX025H01B Source Filter (5)	1	2.65E+06	80
LTM4622 Tension Adjuster (6)	1.8	1.90E+07	120
LTM4622 Tension Adjuster (7)	0.9	9.52E+06	120
LTM4622 Tension Adjuster (8)	1.2	1.27E+07	120
LTM4622 Tension Adjuster (9)	1.5	1.59E+07	120
ADP1740ACPZ-1.5 Tension Adjuster (10)	0.2	1.48E+07	80
LT3071 Tension Adjuster (11)	0.82	5.69E+07	80
ADP1740ACPZ-2.5 Tension Adjuster (12)	0.16	1.19E+07	80
LT3080 Tension Adjuster (13)	1.1	1.43E+08	125
MC20902 MIPI Protocol Driver (14)	0.5	1.36E+07	80
MC20902 MIPI Protocol Driver (15)	0.5	1.36E+07	80

Figure 4: Heat Generation, Heat Density and Maximum Allowed Temperature for Each Component.

Content from this work may be used under the terms of the CC BY 3.0 licence (© 2018). Any distribution of this work must maintain attribution to the author(s), title of the work, publisher, and DOI.

Inner Assembly

As one of the main objectives is the achievement of a portable size, it was decided that the chassis, upon which the boards will be assembled, will also act as a heat spreader, dissipating the power generated by the electronics.

The sensor heat exchanger is a copper piece fitted through two holes in the backside of the Medipix board, touching the ASICs as a cold finger. On its backside, the airflow removes the heat, through fins.

Figure 5 presents the intended interior assembly, in which the sensor heat exchanger is displaced to allow the visualization of the fitting.

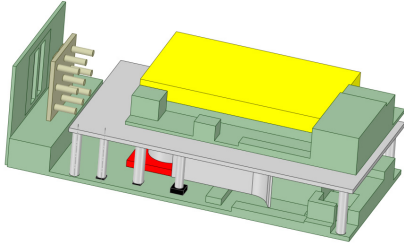


Figure 5: Projected interior assembly, with the heat exchangers.

As the front face is reserved for the sensor, and the back panel will be populated with connectors, both these sides cannot house cooler fans, and the boards arrangement, one above the other, also makes it ineffective to use the upper and bottom faces as primary dissipation sides.

The superior limit of velocity commonly adopted for air cooling of electronic components is 3 m/s. Higher values will generate interference (noise) and vibration. The convective coefficient in this case is approximately 15 W/m²K [14].

METHODOLOGY

The software Space Claim Design Modeler was utilized to prepare the model for simulation and make adjustments, and the software Ansys Fluent was used to perform the Computational Fluid Dynamics simulations.

Series of simulations were performed to determine the number of cooler fans needed, their dimensions and their locations, as well as the chassis height. Then, another series of simulations were performed to define the position, shape and size of the heat exchanger touching pads. Lastly, new series of simulations were performed to test possible enhancements, such as application and dimensioning of guiding vanes and fins, and the use of alternative materials to benefit the heat exchange with each component.

The streamlines and vectors obtained through CFD were used to understand the flow inside the system. This helped to identify zones of recirculation, stagnation and interference. With this data, it was possible to move and take advantage of the mentioned zones to reach more efficient results. The shapes of the chassis-heat spreader and the sensor heat spreader were entirely based on this analysis.

RESULTS

The simulations determined the cooler fans position presented in Figure 6, with optimal results occurring when they faced each another, and that two 50x50x12 mm coolers, blowing 13 cubic feet per minute (CFM) each, at ambient temperature 24±0.1°C, would suffice for the system cooling, with expected temperatures presented in Table 1, for both kinds of sensors, silicon and cadmium telluride.

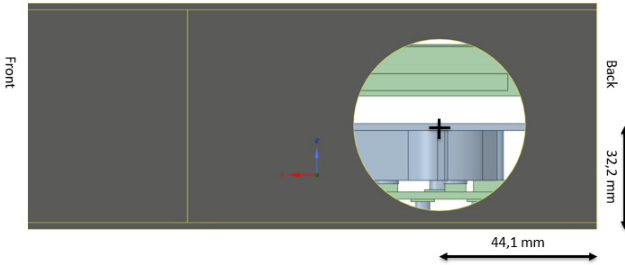


Figure 6: Positions of inlets that generated better results.

Table 1: Expected Temperatures for 13 CFM (3 m/s)		
Component	Temperature [°C]	
1	33.9	
2	59.5	
3	55.3(Si)/56.6(CdTe)	
4	58.6	
5	51.7	
6	66.4	
7	54.6	
8	68.3	
9	60.5	
10	44.9	
11	48.3	
12	35.2	
13	84.7	
14	57.5	
15	60.6	

It can be noted that every component is well within their temperature limits, except for the sensor. Future works may include improvements to the sensor heat exchanger, which would allow the same results or better with slower inlet speeds.

Different materials such as copper alloys were also tested for the composition of the main chassis-heat spreader, however, the difference in the components temperature (in average, 0.5°C) did not justify the increase in weight (approximately three times heavier) and manufacture difficulty. Also, it was observed that the convection with the exterior walls represents a negligible effect on the inside temperatures. Nonetheless, this heat exchange was kept in the simulations.

As can be observed in Figure 7, the temperature at the larger components, such as Jetson and FPGA was well below the rest of the components in the system, due to the larger area presented to the flow. With this information it is possible to avoid the use of extra fins.

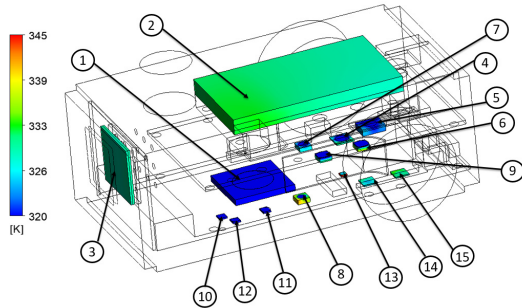


Figure 7: Heat Distribution Comparison inside the system.

Figure 8 and Figure 9 present the air flow inside the device. The cylindrical cold fingers of the chassis-heat spreader were positioned in a way that preserves the main air path toward the next components, using the recirculation to direct the flow towards other components, increasing the heat exchange efficiency.

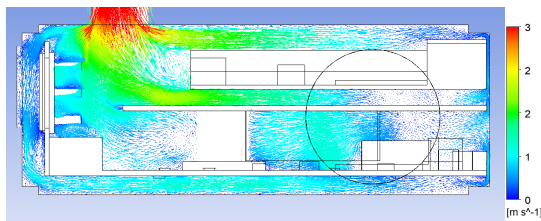


Figure 8: Velocity Vectors in the Longitudinal Plane.

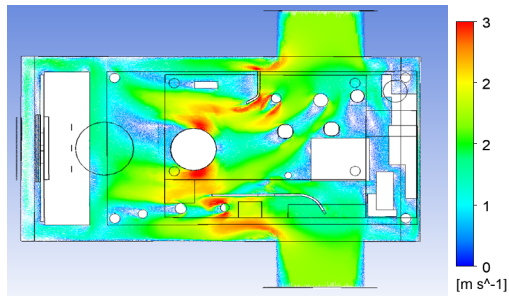


Figure 9: Velocity Vectors in the Transversal Plane.

Inside the system, as depicted in the same Figure 8 and Figure 9, the observed velocity of the stream is above the limit of 3 m/s. However, as observed in Figure 10, the velocity next to the board and components is below the limit.

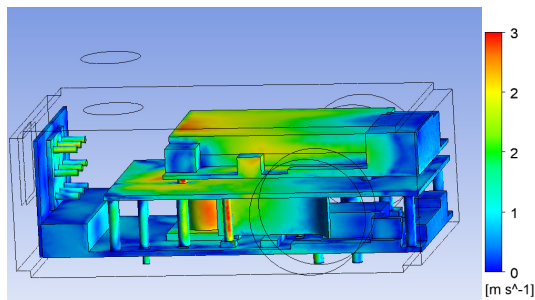


Figure 10: Velocity next to the components.

CONCLUSION

The results obtained in the simulation were satisfactory and, thus, a first prototype was built and awaits the electronic boards assembly for tests and model validation. Meanwhile, a second version of sensor heat exchanger is under development.

The external structure that allows an easy assembly and robust fixture to the beamline, preventing the obstruction of the air vents was also developed, and a preview image is presented in Figure 11.

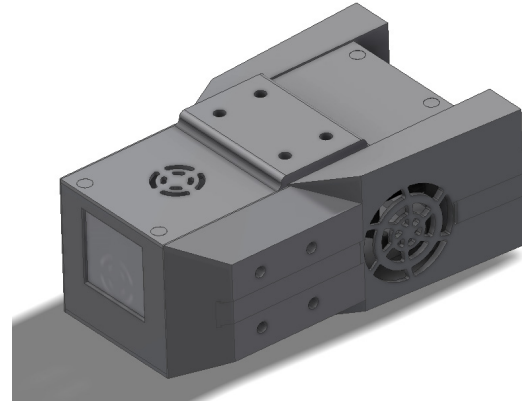


Figure 11 : Mobipix Structure.

ACKNOWLEDGEMENTS

The authors would like to thank all the colleagues that helped with the acquisition of data and experience in the developing of synchrotron devices and also those who helped revising this paper and the poster. Also thanks for the good moments and friendship.

Special thanks to Luciano Camacho, Débora Magalhães, Marcos Errada, Marlon Saveri, Alexis Sikorski and Francisco Figueiredo.

REFERENCES

- [1] L. Liu, *et al.*, "The Sirius project.", in *J. Synchrotron Radiation*, vol. 21, no.5, pp. 904–11, 2014.
- [2] R. Ballabriga, *et al.*, "The Medipix3RX: a high resolution, zero dead-time pixel detector readout chip allowing spectroscopic imaging", *Journal of Instrumentation*, vol. 8, 2013, doi:10.1088/1748-0221/8/02/C02016
- [3] CERN Medipix3 Collaboration, <https://medipix.web.cern.ch/collaboration/medipix3-collaboration>
- [4] Nvidia, "Jetson-TX1 Thermal Design Guide", <http://developer.nvidia.com>
- [5] Xilinx, "Power Estimator FPGA-7 Series", <http://www.xilinx.com>
- [6] Analog Devices, "LTC4358 Protection Diode Datasheet", <http://www.analog.com>
- [7] Murata, "BNX025H01B Source Filter Datasheet", <http://www.murata.com>
- [8] Analog Devices, "LTM4622 Tension Adjuster Datasheet", <http://www.analog.com>
- [9] Analog Devices, "ADP1740ACPZ-1.5 Tension Adjuster Datasheet", <http://www.analog.com>
- [10] Analog Devices, "LT3071 Tension Adjuster Datasheet", <http://www.analog.com>
- [11] Analog Devices, "ADP1740ACPZ-2.5 Tension Adjuster Datasheet", <http://www.analog.com>

- [12] Analog Devices, “LT3080 Tension Adjuster Datasheet”,
<http://www.analog.com>
- [13] Meticom, “MC20902 MIPI Protocol Driver Datasheet”,
<http://www.meticom.com>

- [14] J. Parry, R. Bornoff, B. Blackmore, “Move your Thermal
Strategy for Air-Cooled Electronics up in the Design Flow”,
Electronic Design, vol. 57, no. 14, p. 39, Jul. 2009.

VIBRATION MONITORING AT TPS STORAGE RING*

K. -H. Hsu [†], H.-S. Wang, W. -Y. Lai, C.-K.Kuan, National Synchrotron Radiation Research Center, Hsinchu 30076, Taiwan

Abstract

In order to locate irregular vibrations caused by the installation of new equipment or malfunctioning of the machine, a vibration monitoring system was developed for the storage ring. Totally, 72 accelerometers and 10 velocity sensors were used to detect girder and ground vibrations, respectively. Continuous long-time observation results will be presented.

INTRODUCTION

For the low-emittance, high-brightness and high-stability Taiwan Photon Source (TPS), vibration issues have been studied. Before the TPS was constructed, D.J. Wang had recorded ground vibrations in 2006 at different locations across the NSRRC [1]. These measurements show that transverse vibrations were sometimes large than vertical vibrations for displacements at frequencies above 1.12 Hz but were almost the same above 3.5 Hz. However, we assume, that after more than ten years the situation is different now with significantly different environment. In recent years, the addition of vibration sources like the utility system, may have changed the vibration characteristic for the TPS. Since the utility equipment such as pumps, cooling water systems and air handling units (AHU) need to operate continuously over years, higher vibrations may get introduced when one component fails. In order to locate irregular additional vibrations caused by the installation of new equipment or the malfunction of the machine at the earliest time, we developed a vibration monitoring system to monitor the vibration status comprehensively and continuously.

Long-term girder and ground vibrations of the TPS storage ring were performed with the vibration monitoring system and we present in this paper observations of the vibration levels at various locations and variation of those vibrations with respect to day and night, work day and holiday.

EQUIPMENT AND METHODOLOGY

The TPS storage ring has a circumference of 518.4m composed of 24 Double-Bend Achromat lattice cells. Each TPS SR cell is composed of three magnet girders and the layout of 24 cells (R01~R24) of the TPS SR is shown in Fig.1. Accelerometers (PCB 393B31) were mounted on the first girder (G1) of each cell sensitive in three directions X, Y and Z, where X, Y and Z are the horizontal, vertical and longitudinal coordinates as shown in Fig.2. Tri-axial velocity sensors (Walesch MST-1031) were installed on the ground between G1 and G2 of each cell. However, there are only 10 velocity sensors installed

in R01, R03, R05, R07, R09, R11, R13, R15, R17, and R21 due to the limited availability of equipment. Totally, 72 accelerometers and 10 velocity sensors were used to measure the vibration of girders and ground of the TPS storage ring, respectively. The sensors installed evenly in 24 cells of the TPS storage ring are connected to the corresponding DAQ devices (NI PXI-4496) which are installed in a PXI chassis in 24 control and instrument areas (CIA) on the second floor.

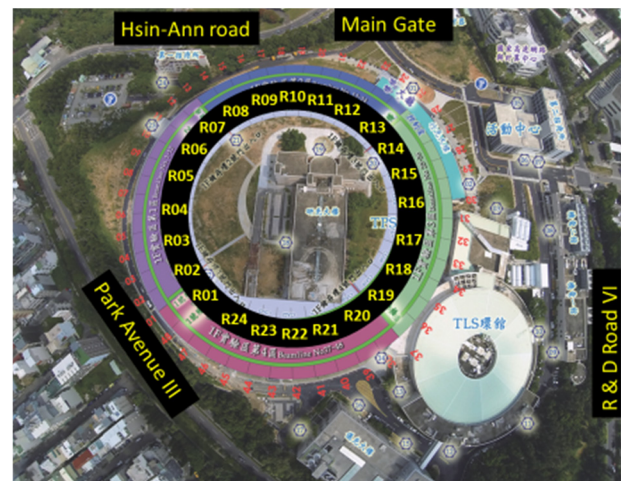


Figure 1: Layout of the 24 cells TPS storage ring on the NSRRC campus.

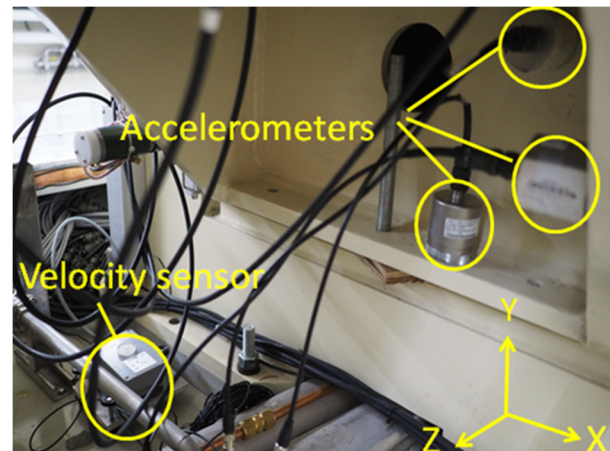


Figure 2: Vibration sensors are installed on the ground and girder of each TPS SR cell.

The Vibration signals were recorded, processed and analysed by a LabVIEW program with a sampling rate of 256Hz. We took 2048 data points for an FFT analysis to get the power spectrum density (PSD) [2]. The acceleration PSD and velocity PSD measured by accelerometers and velocity sensors are converted into displacement PSD by integration [3].

* Work supported by National Synchrotron Radiation Research Center

[†] khhsu@nsrrc.org.tw

Content from this work may be used under the terms of the CC BY 3.0 licence (© 2018). Any distribution of this work must maintain attribution to the author(s), title of the work, publisher, and DOI.

In this article, we calculate the root-mean-square (rms) displacement from the PSD from 1 Hz to 100 Hz and from 4 Hz to 100 Hz [4]. To determine the storage ring cell in which the abnormal high vibration occurs, the displacement values of 24 cells in X, Y, Z are plotted in a bar chart [5] where a very high displacement is coloured as a red bar as shown in Fig.3.

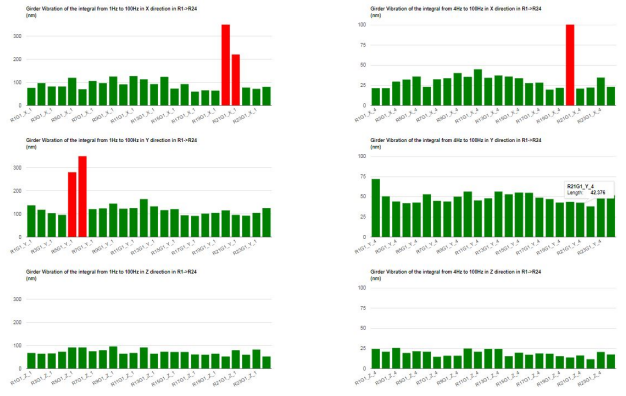


Figure 3: Integrated girders displacement of 24 cells in X, Y and Z.

For long-term observations, the historical integrated ground and girder displacement values [6] are shown in Fig.4. However, vibration spectra were not recorded due to limited hard disk space. The configuration of the vibration monitoring system is shown in Fig.5.

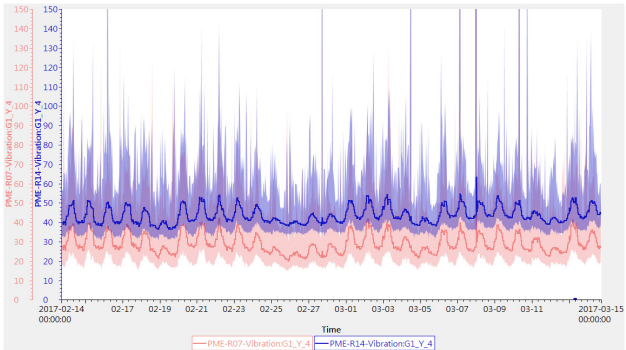


Figure 4: Monthly vertical displacement data (4-100Hz) of the girder in R07 and R14 in the CSS browser.

For further statistical analysis, we downloaded one month of the integrated displacement values from the CSS database collected during February 14th to March 14th, 2017. In order to compare the vibration levels between day and night, we separate a day into daytime and nighttime. Daytime is defined from 8:00 A.M. to 5:00 P.M. Nighttime is defined from 0:00 A.M. to 8:00 A.M. and from 5:00 P.M. to 0:00 A.M. The data were classified and the statistics were obtained with the Scilab program. Differences between vibration displacements and their mean value being more than 140 nm for frequencies above one Hz and being more than 35 nm above four Hz were filtered out, thus eliminating extreme values which may influence the mean value.

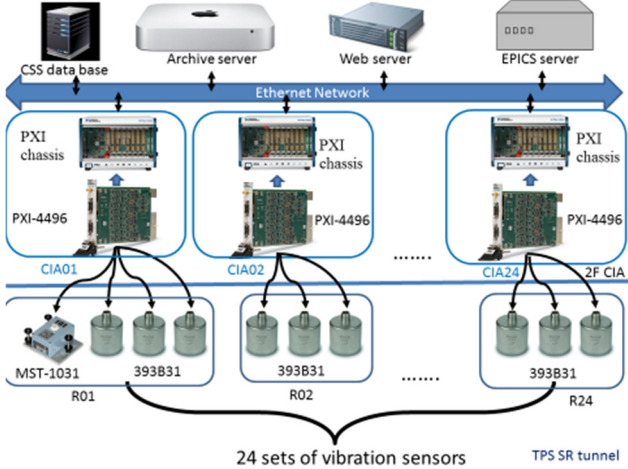


Figure 5: Configuration of the vibration monitoring system.

MEASUREMENT RESULTS

Vibration at Different Location of TPS SR

The integrated displacement observed at different locations of the TPS SR was individually averaged from February 14th to March 14th and the averaged values are plotted as a line chart as shown in Fig.6. We can find all the vertical vibrations measured at R05~R13 were higher than 130 nm above one Hz during daytime. By inference, the locations from R05 to R13 with higher vibrations were near the heavy traffic Hsin-Ann road during rush hours. The vertical vibrations of R14 were higher than 40 nm above four Hz during daytime. One of the sources we speculate is related to the nearby AHU, and the related research is still in progress.

Vibration with Respect to Time

For legibility, the individual vibrations measured for the ground and girders at R01~R24 are averaged to be one data in one direction. The daily integrated RMS displacement of that with respect to day and night in X, Y and Z directions are plotted from February 14th to March 14th in Fig. 7. In addition, the holidays are coloured red; the work days are coloured blue; the make-up workday (February 18th) is coloured green.

As a further simplification, the average monthly integrated displacement of ground and girder in the X, Y, and Z directions during day and night are shown in Table 1 and Table 2.

The measurement results are summarized as following:

- The girder vibrations are a little higher than that of the ground in all directions and the amplification is about 1.01~1.17.
- The vibration of both ground and girders in the vertical direction is much higher than that in the horizontal and longitudinal direction; the vibration in the horizontal direction is a little higher than that in the longitudinal direction.

- The mean value of vibration during daytime is 7~14 nm higher than that at nighttime above one Hz and 1~5 nm higher than that during nighttime above four Hz.
- The mean value of vertical vibrations measured during a work day was about 40 nm during daytime. On the other hand, the mean value measured on a holiday was about 30 nm during daytime.

Table 1: Average Monthly Displacement of TPS SR (1-100 Hz)

Ground	X	Y	Z
Day	92.8	114.1	92.8
Night	83.9	100.5	85.1
Girder	X	Y	Z
Day	106.9	125.5	104.1
Night	98.5	113.0	96.6

(unit: nm)

Table 2: Average Monthly Displacement of TPS SR (4-100 Hz)

Ground	X	Y	Z
Day	20.2	36.2	16.8
Night	17.3	31.8	15.1
Girder	X	Y	Z
Day	22.9	37.3	17.2
Night	20.1	33.3	15.2

(unit: nm)

CURRENT STATUS

The vibration monitoring system of TPS storage ring was developed. Moreover, the long-time continuously and overall measurement results were presented. Although the system was not in service due to the incompatibility of the PXI vibration module in Linux OS, the historical measured data of this system will also be useful references.

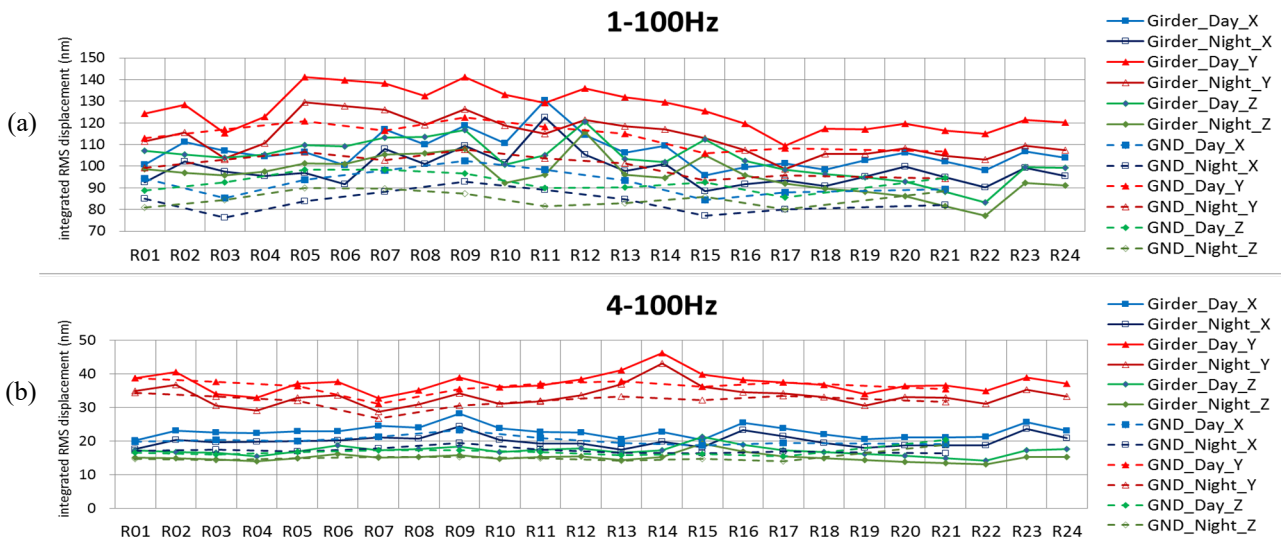


Figure 6: Integrated displacement of ground and girder in TPS SR R01~R24 in X, Y, Z (a) 1-100 Hz. (b) 4-100 Hz.

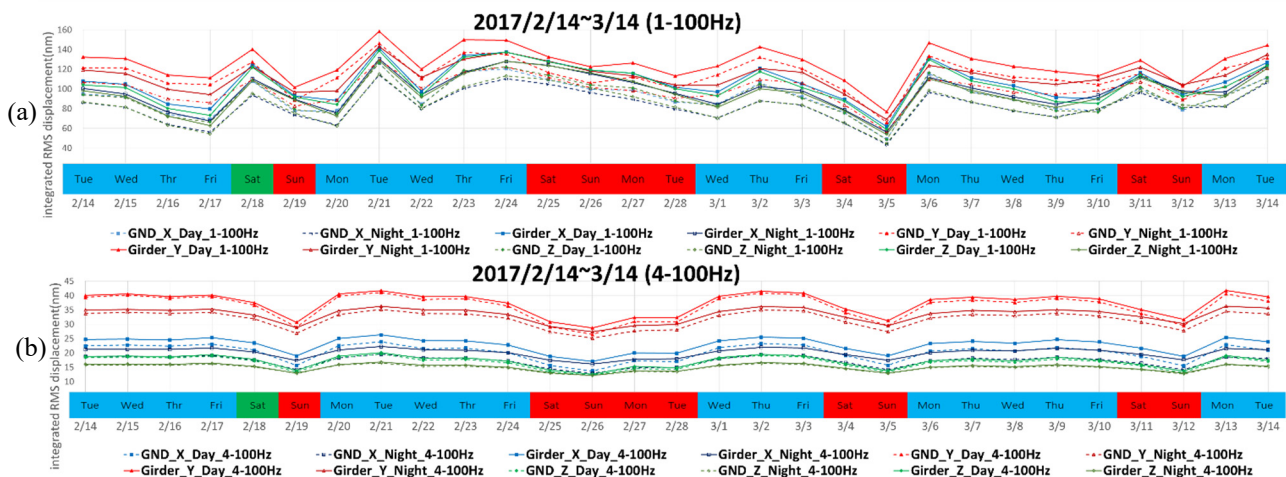


Figure 7: Averaged daily integrated displacement of TPS SR ground and girder from 2/14~3/14 (a) 1-100 Hz, (b) 4-100 Hz.

REFERENCES

- [1] D. -J. Wang, Jeremy Wang, J.-P. Wang, J.-R. Chen and H. - P. Chang, "Ground vibration measurement at NSRRC site", in *Proc. EPAC'06*, Edinburgh, Scotland, July 2006, pp. 3454-3456
- [2] NI LabVIEW 2017 Help,
http://zone.ni.com/reference/en-XX/help/371361P-01/lvwave/fft_power_spec_psd/
- [3] Tom Irvine, "Integration of a Power Spectral Density Function",
http://www.vibrationdata.com/Course_Units/UNIT15.pdf
- [4] W. Bialowons, R. Amirikas, A. Bertolini and D. Kruecker, "Measurement of Ground Motion in Various Sites", in *Proc. EPAC'06*, Edinburgh, Scotland, July 2006, pp. 691-693
- [5] H. -S. Wang *et al*, "Design and Implementation of the six-channel embedded system for reading touch sensors", presented at SRI'18, Taipei, Taiwan, June 2018, paper PA6-03, submitted for publication
- [6] Y. -S. Cheng *et al*, "Implementation of the EPICS Data Archive System for the TPS Project", in *Proc. IPAC'13*, Shanghai, China, May 2013, pp. 3255-3257

OPTOMECHANICAL OPTIMIZATION FOR A SAGITALLY BENT DOUBLE CRYSTAL MONOCHROMATOR, USING FINITE ELEMENTS AND RAY TRACING

N.Jobert[†], T. Moreno, M.Ribbens, E.Fonda, Synchrotron SOLEIL, Gif Sur Yvette, FRANCE

Abstract

Designing a second crystal for a sagittally bent Double Crystal Monochromator (DCM) requires dealing with a number of conflicting requirements. Especially when working with high-energy photons, the angular aperture (Darwin width) becomes very narrow (below 10 μ rad for Si) while simultaneously the bending radius is decreasing (down to 1.2 m for typical beamline dimensions at 40 keV). In this situation, the cross-talk between tangential and sagittal curvature becomes a key parameter, and two strategies are generally used to overcome the issue: either using a flat crystal with a specific length/width ratio, or usage of a rib-stiffened crystal. In the frame of the upgrade of the SAMBA beamline DCM, both solutions have been explored, using a suite of scripts connecting a general purpose FEM code (ANSYS) and a ray-tracing code (SpotX). This has allowed a systematic evaluation of a wide number of configurations, giving insight in the interaction between geometric parameters, and ultimately resulting in a significant increase in the photon throughput at 30 keV without comprising neither spectral resolution nor spot size at sample location.

INTRODUCTION

During the upgrade of the SAMBA (Spectroscopy Applied to Material Based Absorption) beamline DCM, the second crystal needed to be replaced, along with its bending mechanics. Two improvements were requested by the beamline scientist. Firstly, it was desired to extend the 2nd crystal usable length so that the corresponding (longitudinal) translation stage could be removed, thus improving mechanical stability. Secondly, the photon throughput at high energies had to be as high as possible (preferably no less than 50% at 30 keV).

OBJECTIVES

The beamline layout is provided in Fig. 1. Combining the Bragg law for first order diffraction (eq. 1) and the equation for sagittal focusing (eq.2), the linear relationship between sagittal curvature and energy is derived (eq. 3).

$$2d \sin(\theta_{\text{Bragg}}) = \lambda \quad (\text{eq. 1})$$

$$\frac{1}{p} + \frac{1}{q} = \frac{2 \sin(\theta)}{\rho} \quad (\text{eq.2})$$

$$\rho E = cte = \left(\frac{hc}{d} \frac{pq}{p+q} \right) \quad (\text{eq.3})$$

Where, d is the spacing between crystal planes, λ is the wavelength, h is Planck constant, c is the light celerity, p and q are the object and image distances, ρ is the sagittal bending radius, E is the photons working energy.

A Si(220) monocrystal is used, so that the Bragg Angle and the curvature in the 5-40 keV energy range are as follows (Fig. 2):

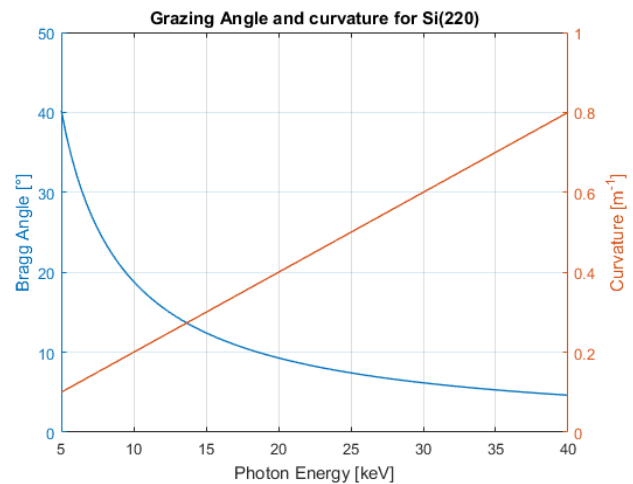


Figure 2: Bragg Angle and curvature.

In order to lose a minimal amount of photons, the parallelism between the first and the second crystals must remain well below the Darwin width of the crystal, which becomes increasingly small at high energies :

- @20keV: 9.3 μ rad
- @30keV: 6.2 μ rad
- @40keV: 4.6 μ rad

Since the footprint has a length of about 10 to 20 mm, meeting the slope error criterion makes it necessary to have longitudinal bending radius larger than 1000 m. Compared to the sagittal curvature (slightly above 1 m), this in turn requires achieving a decoupling ratio of 1000 and above. The anticlastic effect must therefore be drastically minimized.

[†]nicolas.jobert@synchrotron-soleil.fr

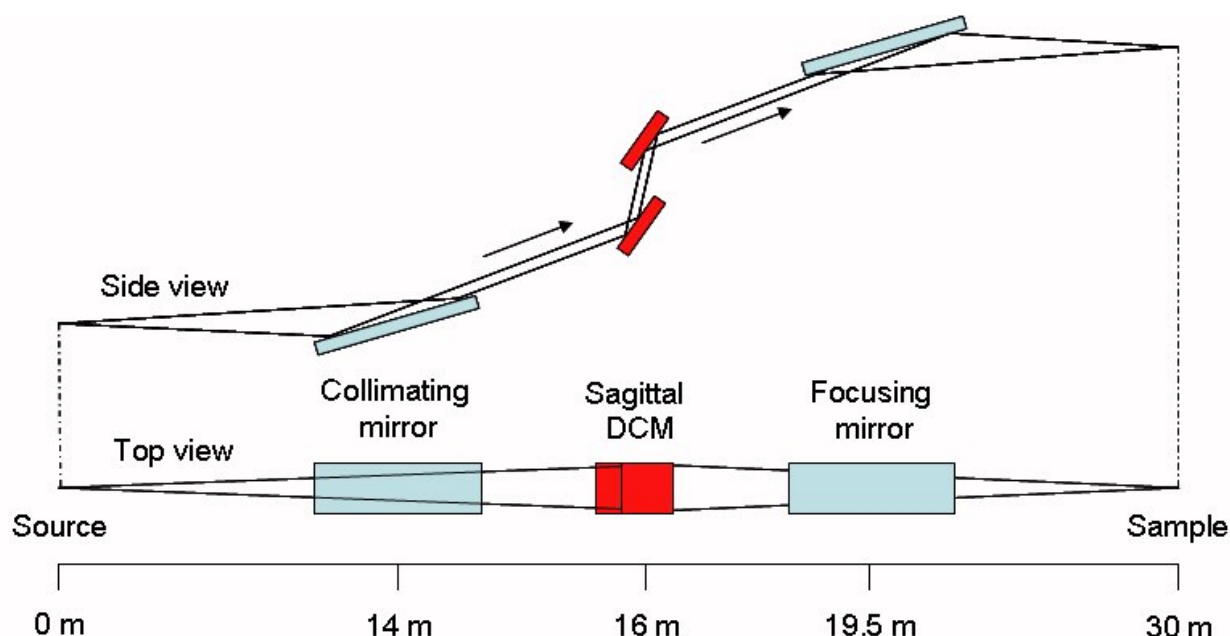


Figure 1: SAMBA Beamline Layout (simplified).

METHODS AND RESULTS

In order to achieve such a decoupling, we rely on two well known methods. The first is the introduction of ribs in order to increase the crystal longitudinal bending stiffness, while keeping the transverse bending stiffness unmodified [1]. The second is the usage of a flat crystal with a specific length to width ratio [2].

Because of the relatively large design space, a numerical Design Of Experiment (DOE) approach has been used, the 4 parameters being the crystal width and length and ribs spacing and height. For each parameter, 3 values have been used (low, base, high), resulting in a 3^4 DOE. Moreover, the results needed to be obtained for various photon energies and beam position along the crystal length, hence a systematic and efficient approach was required.

Mechanical Generation and Analysis

ANSYS Parametric Design Language (APDL) scripts have been written to generate, solve, and post process the results for each design, at 3 working energies (5, 20 and 30 keV).

The bender mechanism is supposed to be free of parasitics, perfectly stiff, and the connection effective on both sides of the jaws. Bender mechanism (virtual) rotation axes are placed so as to avoid overstressing the mirror.

All models use brick elements with mid side nodes, hence the shape functions are parabolic. In order to capture the local bending radius variation due to the presence of the ribs, two elements through thickness have been employed (Fig. 3 and Fig. 4). Analysis are conducted using linear material model and isotropic properties (Poisson ratio $\nu=0.27$).

Each model is labelled using a 4 digits code:

- digit1: width (1,2,3=30,40,50 mm)
- digit2: length (1,2,3=90,100,110 mm)
- digit3: rib height (0=flat, 1,2,3=5,7,9 mm)
- digit4: thickness (1,2,3=0.5, 0.7, 0.9 mm)

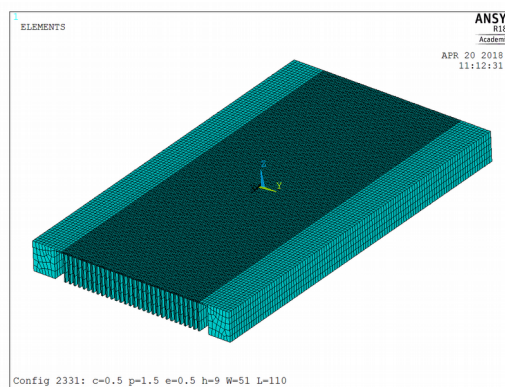


Figure 3: Ribbed design FEM.

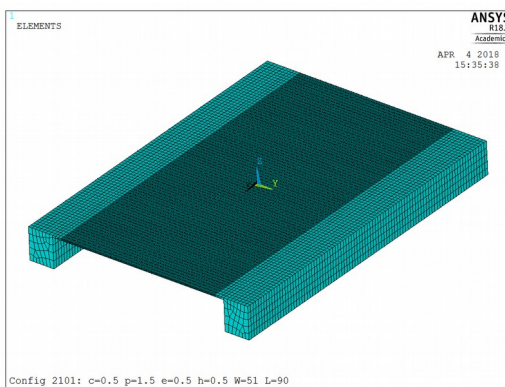


Figure 4: Flat design FEM.

Optical Surface Defect Assessment

Deformed shapes are read into Matlab, then the best fit cylinder is obtained and subtracted, giving the geometric defect. Then, for each working energy and each working position the following quantities are determined:

- Ratio of the footprint for which longitudinal slope is within Darwin Width
- RMS deviation of the sagittal bending radius.

Then the two best configurations (in terms of photon throughput) are selected (Fig. 5)

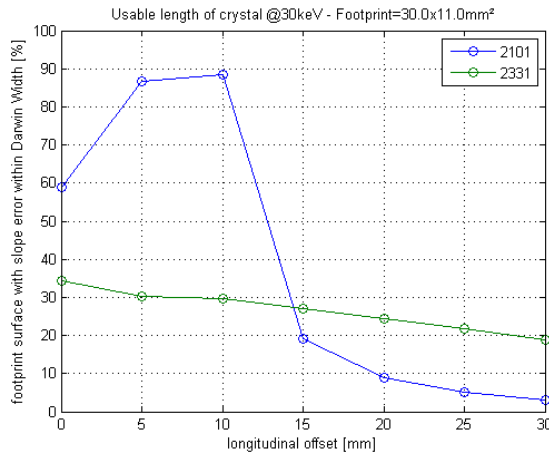


Figure 5: Photon throughput at various distances from the crystal centerline.

It clearly appears from the estimation of the slopes that the ribbed design has a nearly homogeneous anticlastic bending ratio along the length (of about 500 m, see Fig. 6), while the flat design has a saddle point near the centre (Fig. 7).

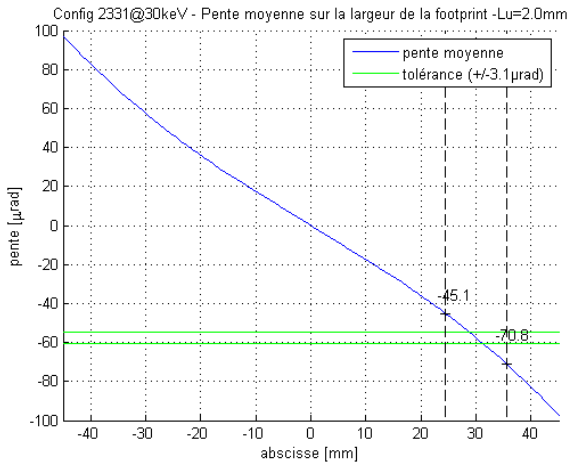


Figure 6: Longitudinal slope error for the ribbed design.

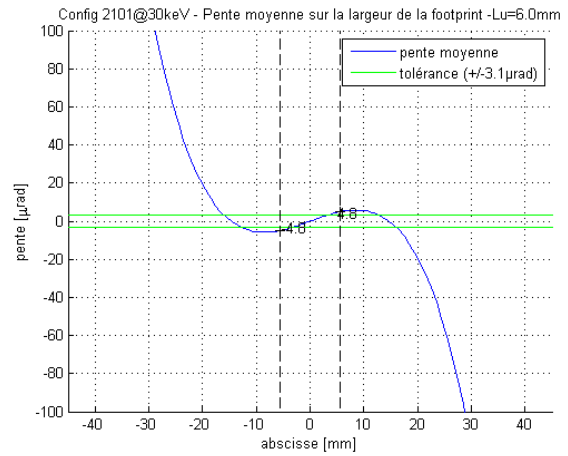


Figure 7: Longitudinal slope error for the flat design.

It must be acknowledged that those conclusions, based on purely geometric quantities, are only approximations since two effects are missing. Firstly, the anticlastic effect will not only reduce the photon throughput, it will also induce a vertical defocusing effect. Secondly, the defocusing effect of the local variation of sagittal bending radius cannot be readily estimated using such a simple indicator as the RMS bending radius (about 3% for the ribbed design, and virtually negligible for the flat design). Also, the effect of the source vertical divergence is not accounted for, and it is likely that the apparent increase in photon throughput will be somehow reduced by this effect. Therefore, to reach a consolidated conclusion, one needs to use a dedicated optical tool for X-rays.

Validation using Ray Tracing Calculations

A complete optical model of the beamline is built using the SpotX software [3]. The analysis includes the source (Bending Magnet), a Be filter, vertical collimating and focusing mirrors, along with their optical properties. Then the analysis is executed based on ray tracing algorithm and a Monte Carlo method.

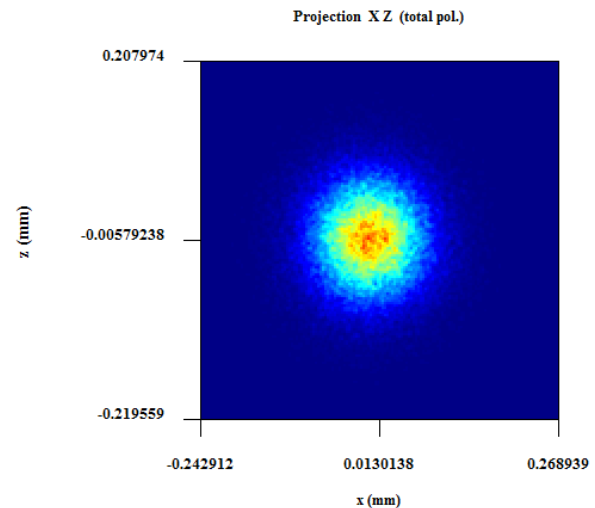


Figure 8: Projection of photon flux @30keV.

Content from this work may be used under the terms of the CC BY 3.0 licence (© 2018). Any distribution of this work must maintain attribution to the author(s), title of the work, publisher, and DOI.

At first, no geometric defect on the 2nd crystal is accounted for, this configuration serves as a reference. Then, the optical defect for the two most promising configurations are included, and the analysis is repeated. Case “Opt1” corresponds with the optimal configuration using ribs, while case “Opt2” corresponds with a flat design. The raw data consists of a 2D map of photon flux obtained at the sample location which is shown in Fig. 8. Beam horizontal and vertical profiles are provided in Fig. 9 and Fig. 10.

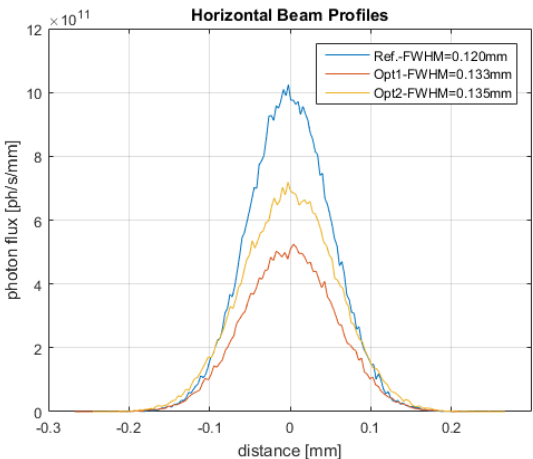


Figure 9: Horizontal Beam Profiles.

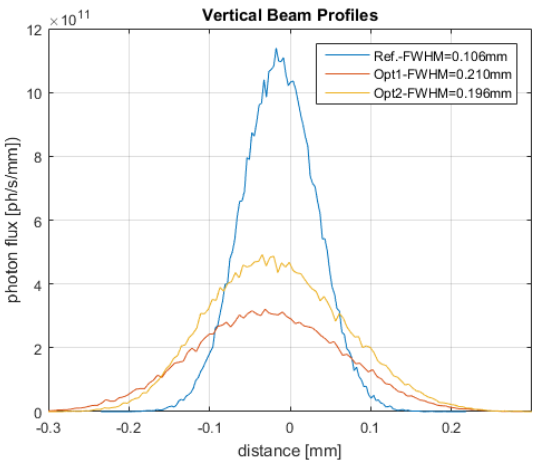


Figure 10: Vertical Beam Profiles.

For each case, one estimates the footprint dimensions (Full Width at Half Maximum), the energy resolution, and the total photon flux. Results are compiled in Table 1.

Both optimal designs are compliant with the initial request, but the Option 2 (flat design) reach 80% of photon throughput, to be compared with 60% for the ribbed design (Option1). In both cases, horizontal focusing and energy are almost not affected, while the vertical focusing is clearly degraded.

Table 1: Optical Figures of Merit

Case	FWHM (H/V) (μm)		FWHM (eV)	Flux (10^{10}ph/s)
Ref.	120	105	2.55	12.8
Opt1	138	206	2.62	7.2
Opt2	129	219	2.79	10.1
Target	<150	<300	<3.0	>6.4

CONCLUSIONS AND OUTLOOK

Using a DOE approach, it was shown that a substantial increase in photon throughput was possible, by minor modifications of the crystal geometric features:

- The ribbed design provides nearly homogeneous flatness along the length, while the flat design is only usable when the beam centre is located less than 10mm away from mirror axis
- When beam footprint is longitudinally centred on the crystal, flat design is significantly superior. This comes at the price of needing a dedicated translation
- For the ribbed design, aberrations due to the local variation of the bending radius (“microlenses” effect) were found to be insignificant at the focus position

Two major simplifications have been made. Firstly, FE analyses have been executed neglecting geometric non linearities, which is acceptable because of the bending radius being larger than the crystal width ($R/W > 30$ @30keV). However, because of the high accuracy typically required for optical calculations, taking into account those second order effect might be required, especially since high fidelity is required at those higher energies. Secondly, monocrystal anisotropic behaviour has been discarded, which could slightly modify the results [4].

Finally, the performance of the crystal will somehow be degraded due to the defects induced by the gluing process and the bender geometric imperfections and parasitics. Thermal/mechanical/optical simulations will be employed to estimate their severity and make corrections as required.

REFERENCES

- [1] C. J. Sparks, G.E. Ice, J. Wong and B.W. Batterman, “Sagittal focusing of synchrotron x-radiation with curved crystals”, in *Nucl. Instrum. Methods*, 1982, **194** 73,
- [2] Mikhail Antimonov, Ali Khounsary “On the influence of monochromator thermal deformations on X-ray focusing”, in *J. Phys. Conf. Ser.*, 2014, **493** 012003
- [3] T. Moreno, & M. Idir, “SPOTX a ray tracing software for X-ray optics”, in *J. Phys.*, 2001, IV Fr. **11**, 527–531.
- [4] L. Zhang, “Anisotropic elasticity of silicon and its application to the modelling of X-ray optics”, in *J. Synchrotron Radiation* 2014 May 1; 21(Pt 3): 507–517.

EXPERIMENTAL MODAL ANALYSIS VIBRATION MEASUREMENT TO INFORM ENGINEERING DESIGN

J. H. Kelly, The Diamond Light Source Ltd, Harwell, UK

Abstract

Experimental Modal Analysis was performed on an existing 5 degree of freedom mirror system on beamline I08 at the Diamond Light Source, by impacting the structure and measuring the response at locations of interest. Commercial software was used to generate the frequency response functions and mode shape animations. This experimental information was used to inform and optimise a design iteration for a new mirror system. The new mechanism was designed, installed and tested on the J08 branch line at The Diamond Light Source to validate the expected improvements in stability, stiffness and resonant frequency. The mirror system fundamental resonant frequency was significantly increased from 20 Hz to 49 Hz.

INTRODUCTION

Experimental Modal Analysis is a technique which allows a mechanical system's vibration mode shapes to be identified, quantified and visualised. This information can then be used to inform future design & operation. It is commonly used for everything from aircraft to tennis rackets. Modal Analysis was used at the Advanced Photon Source during the development of new magnet support structures for example [1]. There are numerous commercial systems based upon different data capture methods from large scanning laser Doppler vibrometry systems [2] to single accelerometer techniques [3].

5 Degree of Freedom Mirror System

The I08 X-ray Microscopy beamline at the Diamond Light Source uses 3 mirror systems with identical supports. The new J08 branchline project required a new mirror system. Rather than order an identical copy of an existing mirror system, the opportunity for a design iteration was taken. The original systems which were procured from Instrument Design Technology Ltd.TM (IDT), have been in service since 2013. They have operated without fault and exhibit excellent thermal stability. The design uses an orthogonal system of slides, rails and vertical jacks to provide the 5 degrees of freedom (DOF). The mirror system moving platform is mounted without over constraint. A spherical bearing forms the "cone", a single free rail & spherical bearing forms the "vee" and 2 crossed free rails & a spherical bearing forms the "flat". A horizontally deflecting mechanical mirror bender is mounted within the vessel with a fine pitch piezo mechanism incorporated into the support. The vessel is pumped by a relatively small 200 l/s ion pump, mounted in top of the system, as there was no space underneath.

An image of the system under test is given in Figure 1. Up-stream of the mirror is a diagnostic vessel and down-stream is the radiation shutter.

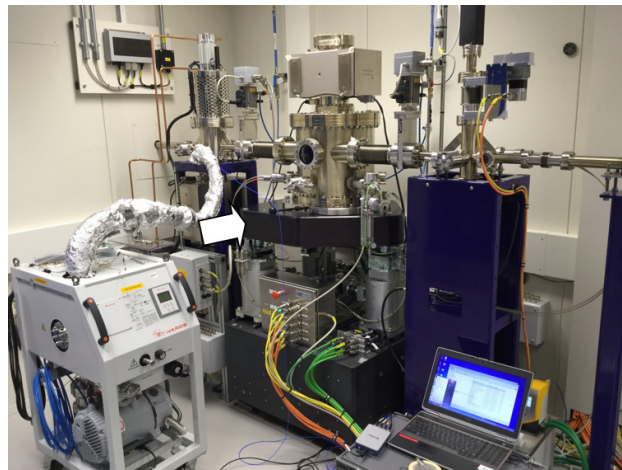


Figure 1: Mirror System I08-M4 at the Diamond Light Source. Impact location indicated by arrow.

Data Capture & Processing

The data presented within this paper was taken using a single triaxial accelerometer (PCBTM LW214478), an impact hammer (Bruel & KjaerTM 8206), a 4 channel signal amplifier (National Instruments Ltd.TM cDAQ-9171) and software from M+P International Ltd.TM (Analyzer 5.1.0 software [3]).

The method chosen for this study was to manually impact the system at the same point and move the triaxial accelerometer around. The impact location was chosen to drive the resonant mode shapes most likely to cause X-ray beam motion. The direction and location are indicated in the image above (Figure 1). This force vector drives both horizontal and rotation modes of the horizontally deflecting optic. A coarse 3D model of the mirror system was created with node locations either corresponding to physical data capture locations or simply following data capture locations. For example, the granite block was modelled with 4 data points on the top surface close to the corners with an extra 4 virtual slave points to form the bottom surface. A total of 26 data points (5 impact average per point) were measured to give a clear picture of how the mirror system base, jacks, moving platform, vacuum vessel ports, ion pump and neighbouring vessel ports move. The software processes the accelerometer data using the time, amplitude and phase information from the calibrated impact hammer to create frequency response functions (FRF) & mode shapes. The modal analysis 3D model is shown below (Figure 2). Multiple data points were taken on the

jacks & slides to enable the clear observation of the motion contribution of each rail & slide.

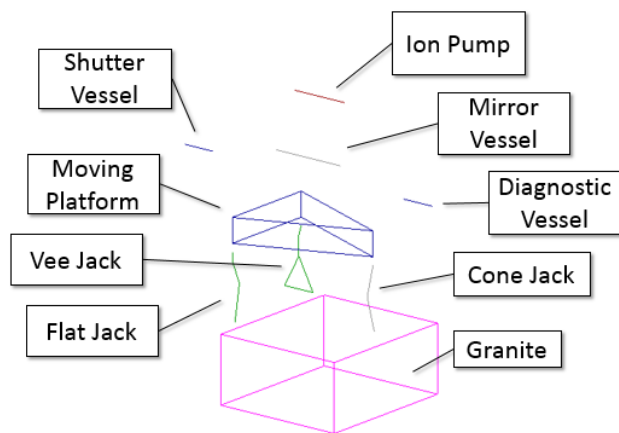


Figure 2: Modal Analysis Model of the mirror system within the M+P software.

I08-M4 MODAL ANALYSIS RESULTS

The software plots the frequency response functions (FRF) of the requested locations and gives a mode shape animation for the selected frequency. The FRF is a graph of measured acceleration per unit impact force vs. frequency. The I08-M4 system FRF for the impact location is given as the blue trace in Figure 3.

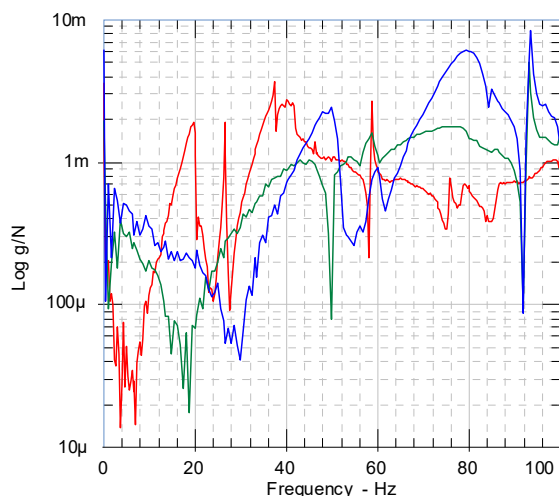


Figure 3: Impact Test Comparison of X Direction FRF: Red I08-M4, Green J08-M2 Clamps Off, Blue J08-M2 Clamps On.

It is very interesting to note that the physical acceleration of the system varies by more than an order of magnitude for the same peak force. Only the frequency is different.

The mirror system fundamental vibration mode was a translation of moving platform, normal to the optic at 19.7 Hz. Only a modal analysis will show you that the peak in the FRF is a translation rather than a rotation. An image of the mode shape is given below in Figure 4. There are a number of points to note about this image. The granite and neighbouring vessels are stationary at this frequency. The “cone” and “vee” jacks are pivoting at their base around

the preloaded ballscrew slides; whereas the “flat” jack is translating on its free slide. The mirror system vacuum vessel ports are translating less than the moving platform i.e. being restrained by the bellows. The ion pump is rocking with a larger amplitude than the moving platform due to the addition of the rotation component around the jack bases.

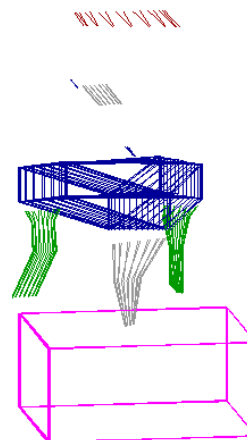


Figure 4: Fundamental Vibration Mode Shape at 19.7 Hz, looking down-stream.

A large table of system resonant characteristics was created using this quality data. The frequencies ranged from the shutter resonance at 14.4 Hz up to the granite block resonance at 111.3 Hz. It is perhaps surprising that even on the nanometre level, the preloaded rails are rolling i.e. the vibration force is greater than the friction.

A second example mode shape is given below (Figure 5) to show the effect of the ion pump resonances on the mirror stability. At 58.75 Hz the ion pump resonated with minimal damping dragging the moving platform with it.

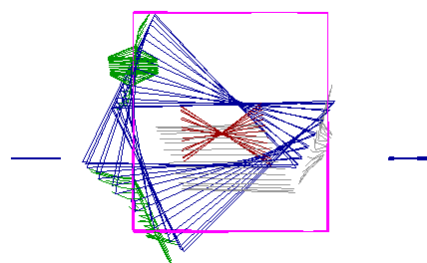


Figure 5: I08-M4 Ion Pump Resonant Mode at 58.75 Hz, plan view.

Modal Analysis Design Conclusions

The author created a list of design suggestions based upon the experimental modal analysis data. IDT used this to perform a low risk design iteration, building on the existing good performance.

1. Move the ion pump to the diagnostic assembly to reduce the moving mass & remove a resonator
2. Integrate pneumatic slide locks to fix the kinematic system during data capture
3. Redesign the system to use rails with a higher moment stiffness to increase rocking resonance frequencies

4. Reduce the mass of the motion platform
5. Recess the spherical bearings into the moving platform to reduce leg length
6. Reduce the jack travel & hence length to optimise for this application
7. Mount the granite firmly to the concrete floor

J08-M2 MIRROR SYSTEM

The new improved system was delivered by IDT and installed at the Diamond Light Source on the J08 branch line. An image of the system is given below in Figure 6.



Figure 6: J08-M2 Mirror System from Instrument Design Technology Ltd.

J08-M2 Mirror System Vibration Tests

The FRF of the new system was measured in the same way as for the original system. The data is presented in the same plot for direct comparison in Figure 3. The original fundamental of 19.7 Hz compared well with systems from other commercial suppliers. The new system resonant frequency has been pushed up to 45 Hz without clamps and 50 Hz with clamps engaged. This is particularly impressive as the resonant frequency is proportional to the square root of the stiffness [4]. The system moving mass was reduced by a factor of 0.6 and the stiffness was increased by a factor of 3 (Assuming a simple spring mass system). It is also clear from the FRF that the width of the fundamental and hence damping is significantly increased. The damping must be caused by the increased rolling element preload and contact areas. The high resonant frequency enables the support to accurately track the synchrotron floor motion and the high damping minimises the amplitude at resonance.

The new and the old systems are only mounted 2 m apart which allows a direct comparison of background stability. The system position has been calculated by a double integration of the accelerometer data. As may be seen from Figure 7 the old system position oscillated with an

amplitude of ~ 100 nm whereas the new system stability is at the background vibration level of ~ 20 nm (Measured using PCBTM 393B31). Both traces nicely illustrate how the largest amplitude motion of the floor is at the lowest frequency with the beamline optics moving together.

The slide clamps clearly stiffen the system and reduce the damping at resonance under a FRF impact measurement. However, in practice the background stability data shows little difference.

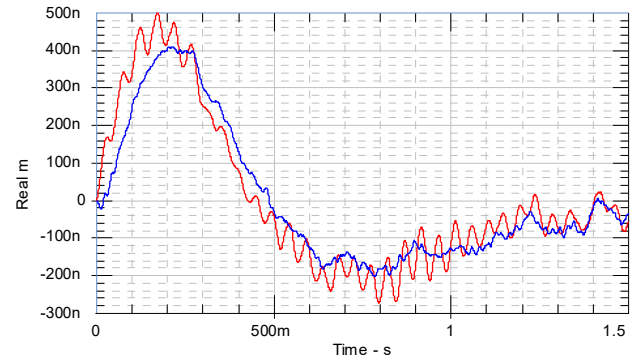


Figure 7: Comparison of Mirror System stability: Red = I08-M4, Blue = J08-M2.

CONCLUSION

An ultra-stable mirror system has been engineered, installed and tested using the experimental modal analysis technique to inform the design evolution of an existing system. The fundamental vibration mode of the system is ~ 45 Hz with the clamps off and ~ 50 Hz with the clamps on. The J08 system will form a stable focus for the J08 endstation.

REFERENCES

- [1] C. Preissner, H. Cease, J. Collins, B. N. Jensen, Z. Liu, and J. Nudell, "Nostradamus and the Synchrotron Engineer: Key Aspects of Predicting Accelerator Structural Response", in *Proceedings of the 9th Edition of the Mechanical Engineering Design of Synchrotron Radiation Equipment and Instrumentation Conf. (MEDSI2016)*, Barcelona, Spain, 2016, paper WEBA01, pp. 272-276, DOI: 10.18429/JACoW-MEDSI2016-WEBA01
- [2] M+P Intl., <https://www.polytec.com/uk/vibrometry/>
- [3] M+P Intl., <https://www.mpihome.com/en/>
- [4] R. M. Schmidt, G. Schitter, J. V. Eijk, "Dynamics of motion systems", in *The Design of High Performance Mechatronics*, Ed. Delft, Netherlands: Delft University Press, 2011, pp. 102-106.

THERMAL ANALYSIS OF HIGH HEAT LOAD MIRRORS FOR THE IN-SITU NANOPROBE BEAMLINE OF THE APS UPGRADE*

J. Knopp[†], X. Shi, Argonne National Laboratory, 60439 Lemont, IL United States
 J. Maser, R. Reininger, M. V. Fisher, Argonne National Laboratory, 60439 Lemont, IL United States

Abstract

The Advanced Photon Source (APS) is currently in the process of upgrading to a multi-bend achromat (MBA) storage ring, which will increase brightness and coherent flux by several orders of magnitude. The planned In-Situ Nanoprobe (ISN) beamline, one of the feature beamlines of the APS Upgrade (APS-U) project, is a 220 m long beamline that aims to focus the x-ray beam to a spot size of 20 nm or below by focusing with a KB pair. A double-mirror system, consisting of a high heat load mirror and a pink beam mirror, is designed to provide high harmonic rejection, reduce the power transmitted to the monochromator, and focus the beam along the vertical direction to a beam-defining aperture (BDA). One of the key issues is to manage the high power and power density absorbed by these mirrors. To attain the best focus at the BDA, the pink beam mirror needs to be mechanically bent to correct for thermal deformations on both mirrors. In this paper we report on the thermal responses of the mirror system to different undulator tunings and cooling schemes as calculated with Finite Element Analysis (FEA) and optical ray tracing.

INTRODUCTION

The ISN beamline will allow high-resolution imaging, spectroscopy, and tomography of energy materials and energy devices, as well as of other complex, hierarchical systems under in-situ and operando conditions. A flat high heat load mirror, M1, is located at 28 m from the source. A bendable pink beam mirror, M2, located 29 m from the source is used to focus the x-rays in the vertical direction from the source to the BDA, which is located at 26 m downstream of M2 (see Fig. 1). Both mirrors deflect the beam by 5 mrad (2.5 mrad grazing angle) in the vertical direction. Ray tracings show a focus at the position of the BDA without visible coma as expected from the near 1:1 focusing.

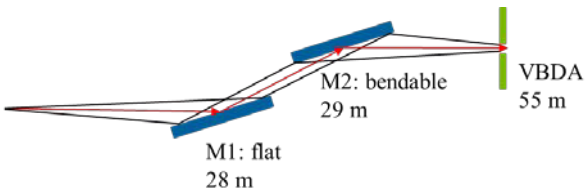


Figure 1: Schematic of the M1 and M2 mirrors of the ISN beamline focusing to the BDA.

* Work supported by the U.S. Department of Energy, Office of Science, Basic Energy Sciences, under contract #DE-AC02-06CH11357.
[†] jknopp@aps.anl.gov

M1, which is a flat mirror and deflects the white undulator beam is placed as close to the source as possible, to allow a secondary focus as far upstream as feasible, without reducing the size of the secondary source below the original source size.

To determine the effect of the heat load induced deformations on the spot size at the BDA location, the absorbed power by the mirrors was calculated using SRCalc [1] followed by several FEA calculations. The deformed output of the FEA was subsequently used in the ray tracings with and without the bending required to correct for the thermal deformation of the system.

THERMAL ANALYSIS

The insertion device designed for the ISN beamline has a 25 mm period and is 4.6 m long. Calculations were performed when the insertion device was tuned to emit photon energies between 5 keV to 12 keV at 1000 eV increments. The power absorbed by each of the mirrors was calculated assuming 200 mA stored in the 6 GeV storage ring. The power densities were imported into ANSYS and applied as a heat flux on the surface of the mirrors. The absorbed power density on the M1 mirror when the undulator is tuned to emit 5 keV is shown in Fig. 2. As seen in the figure, the absorbed power density does not vary significantly in the illuminated area. This is also the case for all energies investigated.

ANSYS Workbench version 18.2 was used in the steady state thermal analysis of the M1 and M2 mirrors. Both M1 and M2 mirrors are 400 mm long, 50 mm wide, and 50 mm thick.

Simple Side Cooling

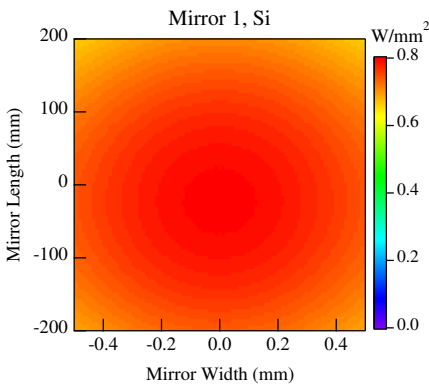


Figure 2: Absorbed power profile on M1 at 5 keV.

For this analysis we assume side cooling spanning the entire length and height of the mirror. The OHFC copper cooling blocks on both sides of the mirror are 12.7 mm in width with 9.5 mm diameter cooling channels. The cooling channel centers are 12.25 mm from the top of the block. The film coefficient between the water and the cooling channels was calculated to be $5000 \text{ W}/(\text{m}^2 \cdot \text{K})$. A schematic representation of the mirror and the cooling blocks is shown in Fig. 3.

Thermal contact resistance across the copper-silicon interface with an Indium Foil layer between them is approximately $8000 \text{ W}/(\text{m}^2 \cdot \text{K})$ [2]. The temperature distribution

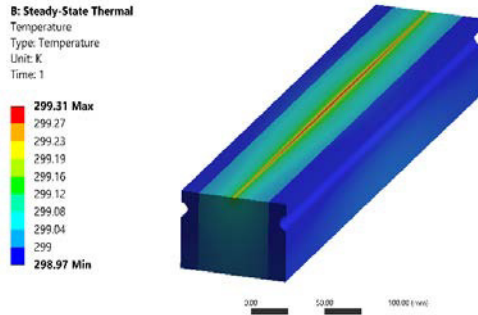


Figure 3: ANSYS model and temperature of M1 Mirror at 5 keV.

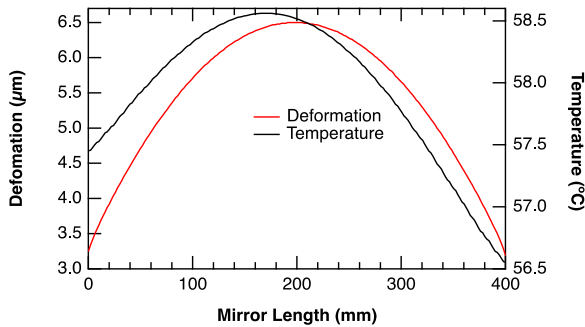


Figure 4: Temperature and deformation of M1 at 5 keV along the central line.

obtained from the FEA when the first mirror is exposed to the power emitted by the insertion device tuned to 5 keV is shown in Fig. 3. The narrow stripe along the mirror center corresponds to the area illuminated by the x-ray beam. The temperature along the mirror length at its center and the deformation normal to the optical surface are shown in Fig. 4.

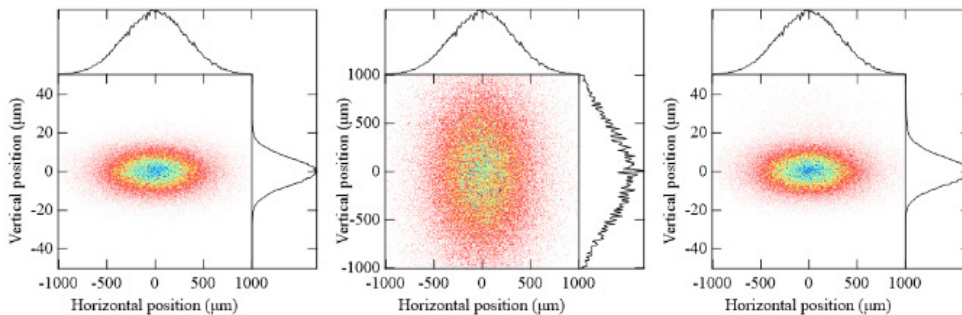


Figure 5: Ray tracing results. Beam profile at the BDA position (left) with ideal mirror surfaces, (middle) with thermal deformation from FEA calculations without M2 bending correction, and (right) with M2 bending correction.

A smaller, but similar deformation is also seen on M2. The derivative of the convex shape on both mirrors is almost linear indicating a nearly constant radius of curvature in each mirror.

The ray tracings at the position of the BDA with the ideal mirror surfaces (left panel) and those obtained from the FEA calculations (middle panel) are compared in Fig. 5. As seen in the figure, the absorbed power on the mirrors increase the vertical FWHM from $16.5 \mu\text{m}$ to more than 1 mm due to the defocus. These results allow one to calculate the radius of curvature necessary to correct for the defocus. The right panel in Fig. 5 shows ray tracings at the position of the BDA obtained by bending the M2 mirror to a cylinder with a 4.38 km radius. With the correction the vertical FWHM is nearly the same as the ideal case. Table 1 summarizes the results for four of the eight energies studied. The table lists the power absorbed by each of the mirrors, the vertical spot sizes for the ideal, the uncorrected and the corrected cases that were studied. Finally, the table shows the required radius of curvature at M2 to achieve the corrected case, which provides an almost perfect focus at the BDA.

Table 1: Summary of Results for Selected Energies

Photon Energy (keV)	5	7	9	12
Power absorbed by M1 (W)	429	260	130	20.3
Power absorbed by M2 (W)	10.6	9.06	6.23	5.79
Focal Size at BDA (μm), FWHM Theoretical	16.6	14.4	13.0	11.6
Focal Size at BDA (μm), FWHM Uncorrected	1129	589	257	47
Focal Size at BDA (μm), FWHM Corrected	16.8	14.2	13.0	11.6
Corrected M2 Radius (km)	4.38	5.72	7.51	10.1

Some experiments at the ISN beamline will require scanning photon energy. Therefore, we performed an analysis to determine the change in focal spot size at the BDA using a fixed radius of curvature. The ray tracings were performed with the radius of M2 being 4.38 km , which is optimized for 5 keV. When tuning the undulator energy from 5 keV to 5.1 keV, the beam size obtained at the BDA increased from the “ideal” $16.8 \mu\text{m}$ to $21 \mu\text{m}$. This means the

flux at the sample will vary due to lower transmission through the BDA.

Notch Design

It has been shown that the mirror deformation can be reduced by an order of magnitude by adding a notch to the mirror side and only applying cooling above the notch. By placing the notch approximately 1/3 of the way down from the optical surface, the notch dimensions can then be optimized to reduce the deformation for certain energies [3, 4].

The notch dimensions on M1 were optimized for the power absorbed at 5 keV. The temperature profile of the M1 mirror with the optimized notch are shown in Fig. 6.

Figure 7 compares the vertical deformation obtained with the simple side cooling to the optimized notch. As seen on the figure the deformation is indeed reduced by more than an order of magnitude and produced a near flat shape especially in the central portion of the mirror (slope error within the central 300 mm is 0.14 μ rad). The small increase in focal spot size could greatly reduce the amount of bending needed by the M2 mirror.

For comparison with previous energy scan results, powers at 5 keV and 5.1 keV energies were applied to this design, and then compared with the energy scan for the regular no notch design. The M2 radius was held constant at 4.38 km as before. The notched design showed a change in focal size from 17.2 μ m to 17.0 μ m going from 5.0 keV to 5.1 keV respectively. This is a significant reduction in change of focal spot size. In addition, the focal position change relative to the BDA decreased from -1.7 m to 0.1 m going from the normal side cooled design to the notch design respectively.

Internally Cooled

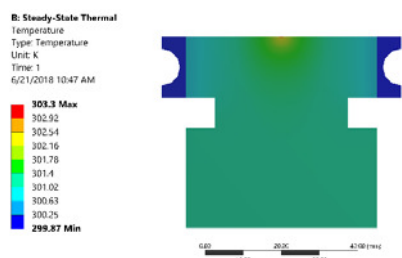


Figure 6: Temperature profile of M1 for the notch design at 5 keV.

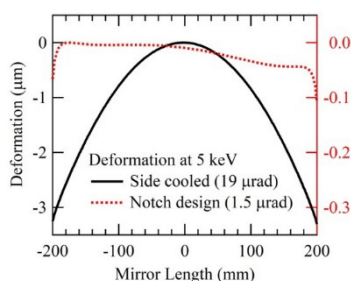


Figure 7: Thermal deformation of M1 comparison of side cooled and notch design at 5 keV.

Internally cooled mirrors have been studied previously in hopes of finding a signification reduction in thermal distortions on high heat load optics [5]. Such mirrors have also been considered as an option for the M1 and M2 mirrors of the ISN beamline. The results of the internal cooling studies show an order of magnitude less thermal deformation than a normal side cooled mirror, but not enough to completely remove the thermal bump without further correction. The surface deformation is more complicated due to the cooling channel design and coolant pressure, thus a simple bending correction may not be adequate. Since the accurate modeling of internally cooled mirrors is difficult, further studies are still needed.

CONCLUSIONS

The combined FEA and ray tracings show that the mirror system composed of a flat mirror and a bendable mirror that are side cooled will practically maintain the vertical spot size at the aperture. Scanning undulator energy without actively bending the M2 mirror will increase the spot size at the BDA when the insertion device changes power. Preliminary results show promise for the notch design in greatly reducing the beam spot size due to thermal deformation. Furthermore, the design allows scanning with a fixed radius of curvature without a significant increase in spot size. For the APS upgrade project, we are actively looking into different cooling schemes, coolants and designs.

REFERENCES

- [1] R. Reininger, private software, unpublished, June 2018.
- [2] A. Khounsary, D. Chojnowski, L. Assoufid, and W. Worek, "Thermal contact resistance across a copper-silicon interface," in *Proc. Optical Science, Engineering and Instrumentation (SPIE '97)*, San Diego, CA, United States, December 1997, doi: 10.1117/12.294497
- [3] L. Zhang *et al.*, "Thermal distortion minimization by geometry optimization for water-cooled white beam mirror or multilayer optics", in *11th International Conference on Synchrotron Radiation Instrumentation (SRI 2012)*, Lyon, France, July 2012, doi:10.1088/1742-6596/425/5/052029
- [4] A. Khounsary, "Thermal Management of Next-Generation Contact-Cooled Synchrotron X-Ray Mirrors," *SPIE annual meeting*.
- [5] A. Khounsary, "Design, fabrication, and evaluation of an internally cooled silicon carbide mirror," *American Institute of Physics*, doi:10.1103/PhysRevLett.114.050511

ADJUSTING MECHANISM OF INTER-UNDULATOR SECTION FOR PAL-XFEL

H.G. Lee, B.G. Oh, S.B. Lee, Y.G. Jung, H.S. Suh, S.H. Jeong, D.E. Kim, K.H. Park, J.H. Han, H.S. Kang, H.S. Lee, Pohang Accelerator Laboratory, Pohang, Korea

Abstract

Pohang Accelerator Laboratory (PAL) has developed a SASE X-ray Free Electron Laser based on 10 GeV linear accelerator. The inter-Undulator (IU) support section was developed to be used in the intersections of the Undulator Systems. The IU supports consist of phase shifter, quadrupole magnet with mover, beam loss monitor, cavity BPM with mover, two corrector magnets and vacuum components. The adjusting mechanism of IU Support has manual alignment system to be easily adjusting the component. The mover of quadrupole magnet and cavity BPM with submicron repeatability has auto-adjusting systems with stepping motor. The mover main specifications include compact dimensions and a ± 1.5 mm stroke in the vertical and horizontal direction. Linear motion guide based on 5-phase stepping motors have been chosen. This paper describes the design of the stages used for precise movement and results of mechanical measurements including reproducibility will be reported.

INTRODUCTION

PAL-XFEL has been providing X-rays in ranges of 0.1 to 0.6 nm for hard X-ray line and 3.0 nm to 1.0 nm for soft X-ray line by using the self-amplified spontaneous emission (SASE) Schematic [1]. For undulator system, there are 20 undulators for hard X-ray line and 7 planar undulators with additional two EPU's (Elliptically Polarized Undulator) are expected for soft X-ray line. To generate X-ray FEL radiation, the PAL-XFEL undulator section requires high resolution beam position monitoring systems with $<1 \mu\text{m}$ resolution for single bunch. It will be used in the intersections of the Undulator Systems to achieve high resolution requirement.

The inter-undulator sections, shown in Figure 1, consist of phase shifter, quadrupole magnet with mover, beam loss monitor, two corrector magnets, cavity BPM with mover and vacuum components. The quadrupole mover developed based on the EU-XFEL concept with some modifications [2]. It includes submicron repeatability for quadrupole magnet and a ± 1.5 mm stroke in the vertical and horizontal direction. Compact linear actuators based on 5-phase stepping motors have been chosen. Vertical actuator works in a wedge configuration to take mechanical advantage. A closed-loop control system has been developed to achieve this repeatability. For the feedback, one LVDT sensor for each axis was used.

Mechanical switches are used to limit movement. In addition, hard-stops are included for emergency.

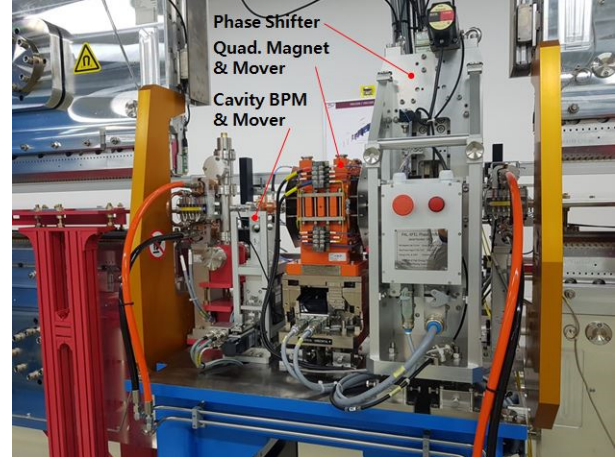


Figure 1: Lay-out of inter-undulator section.

OVERVIEW OF CAVITY BPM MOVER

The cavity BPM(C-BPM) system has installed in between each undulator with other diagnostics tools. The cavity BPM Mover had been fabricated, tested and installed for the PAL XFEL [3]. The main specifications include submicron repeatability for a 10 kg cavity BPM with support within compact dimensions and a ± 1.5 mm stroke in the vertical and horizontal direction. Linear motion guide based on 5-phase stepping motors have been chosen. For the measurement of the position, one digital probe sensor for each axis was used. Mechanical switches are used to limit movement. In addition, hard-stoppers are included for emergency.

Table 1: Main Specification for C-BPM Movers

	Value	Details
Dimensions	332x140x255.5 mm ³	Long, wide, high
Axes	2(H & V)	± 1.5 mm stroke
Load	10 kg	
Repeatability	$< 3 \mu\text{m}$	
Control Device	Digital probe closed-loop	EPICS
Ranges	± 1.5 mm Limit Switch	± 1.6 Hard Stopper
Driving System	5 Phase Stepping Motor	With brakes
Measure System	Digital Probe (DP/5/S)	$< 0.15 \mu\text{m}$
Limit Sensor	D4E-1C20N	

The main specifications for these movers are included in Table 1. The movers are composed of each stepping motor for horizontal and vertical, digital probe, limit switch and harder stopper. Figure 2 shows the 3D view of cavity BPM system. A robust and compact mover is required according to specifications therefore concept

design includes some important features. The drive mechanism adopts a 5-phase stepping motor with ball screw for Oriental Motor's. The motor achieves high positioning accuracy in a space-saving design. The compact and lightweight body houses the rotating components as well as the linear motion mechanism of the stepping motor. The load position can be held with electromagnetic brake when the power is cut off. Since the work will not fall in case of power failure or disconnection, it can safely use equipment in which the work moves vertically. Linear motion (LM) guides and high-precision motors have been selected for both axes. LM guide in each row of balls is placed at a contact angle of 45° so that the rated loads applied to the LM block are uniform in the four directions (radial, reverse radial and lateral directions). Two digital probes are used to measure at horizontal and vertical direction movement.

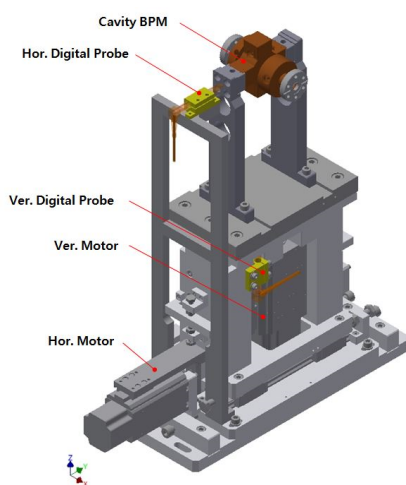


Figure 2: 3D view of cavity BPM Mover.

REPEATABILITY OF C-BPM MOVER

The repeatability is the most important specification of the movers, as submicron level must be reached. The testing set up is displayed at Figure 3. The cavity BPM mover is measured at both axes with external reference gauges. The positioning to a certain LVDT position reaches always exactly the same actual position from external references in a perfect repeatable system. The sets of measured movements are 0.2 mm steps along the vertical axis and the horizontal axis for the whole movement range. Results for direct movements from a given position have been found to have very high repeatability.

Design has showed also a high ability to keep position under certain possible conditions. Under such conditions, Repeatability is below ± 1 micron at every set of movements for both axes. Figure 4 shows the repeatability of the number 3 cavity BPM mover. Upper graph is the measuring data for horizontal movement and lower is the vertical movement. The maximum deviation is $\pm 0.3 \mu\text{m}$ for horizontal movement and the vertical movement is $\pm 0.6 \mu\text{m}$.

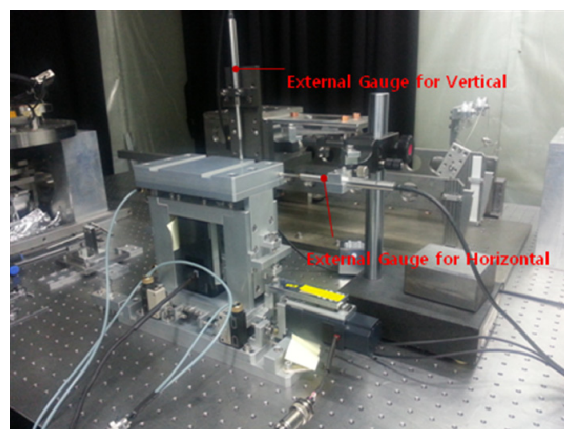


Figure 3: Test set-up for repeatability of cavity BPM Mover.

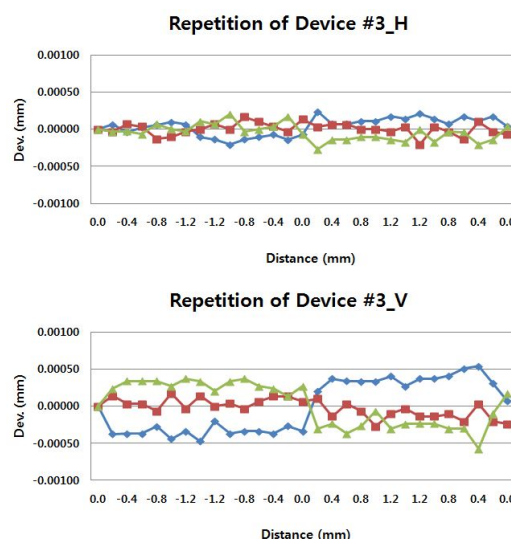


Figure 4: Repetition of cavity BPM Mover. Maximum deviation is $\pm 0.3 \mu\text{m}$ of horizontal and $\pm 0.6 \mu\text{m}$ of vertical measurement for number 3 Mover.

OVERVIEW OF QUAD MOVER

Quad mover has developed to be used for the Hard X-ray and Soft X-ray undulator line. On the basis design of EU-XFEL quad mover, we implemented some modification, fabricated and tested. The modification parts are the position of horizontal and vertical LVDT. It was located outside of the moving mechanism and sensors are touched directly the moving parts. The main specifications, shown in Table 2, include submicron repeatability for a 70 kg quadrupole magnet within compact dimensions and a ± 1.5 mm stroke in the vertical and horizontal direction. Compact linear actuators based on 5-phase stepping motors have been chosen. Vertical actuator works in a wedge configuration to take mechanical advantage. A closed-loop control system has been developed to achieve this repeatability. For the feedback, one LVDT sensor for each axis was used. Mechanical switches are used to limit movement. In

addition, hard-stops are included for emergency. Figure 5 shows the front and rear view of quad mover.

Table 2: Main Specification for Quad Movers

	Value	Details
Dimensions	360x220x175 mm ³	Long, wide, high
Axes	2(H & V)	±1.5 mm stroke
Load	70 kg	
Repeatability	< 1 µm	
Control Device	LVDT closed-loop	EPICS
Ranges	±1.5 mm Limit Switch	±1.6 Hard Stopper
Driving System	5 Phase Stepping Motor	With brakes
Measure System	LVDT (SM222.4.1.S)	SCHREIBER
Limit Sensor	PN41	SAIA-Burgess

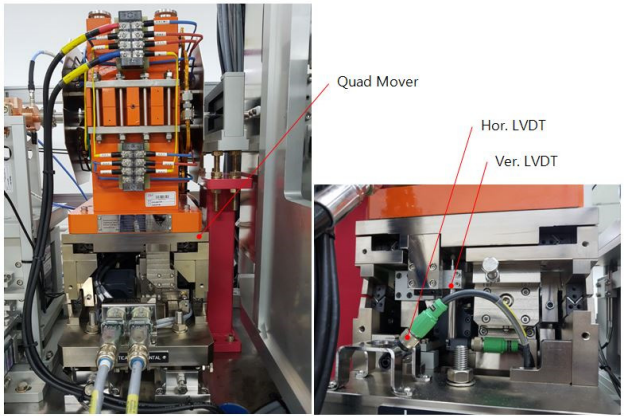


Figure 5: Front and rear view of quad mover. Left is front view and right is rear view. LVDT is attached out-side of moving parts.

A robust and compact mover was required, therefore concept design include the following important features.

High-precision linear motion guide had been selected for both axes X and Y. The wedge design has a slope so the force needed to lift the load is lower than the direct weight of the load. At the same time, diagonal movement instead of a vertical one results in a finer resolution for vertical axis. The measuring position of LVDT is very important because of backlashes. So, measuring point of LVDT is attached directly moving parts for vertical and horizontal. A closed-loop control system is implemented in order to achieve submicron repeatability. Two LVDTs are placed outside the mover to get a continuous measurement of each axis absolute position. Each LVDT has been arranged to measure just one axis at a constant contact point, which means that the LVDT and the measurement surface have no relative movement apart of the measured in-axis separation. Limit switches were added at the ends of movement of both axes to ensure that even under a failure of the LVDT sensors the mover will be reach a safe stop position. Moreover, mechanical stoppers have been implemented to exclude any possibility of over-travelling.

REPEATABILITY OF QUAD MOVER

The repeatability is the most important specification of the quad movers, as submicron level must be reached. It was measured at both axes with external reference gauges. The positioning to a certain LVDT position reaches always exactly the same actual position from external references in a perfect repeatable system. The sets of measured movements are 0.2 mm steps along the vertical axis and the horizontal axis for the whole movement range. We have to measure 5 times at both axes. Results for direct movements from a given position have been found to have very high repeatability. Under such conditions, repeatability is below ± 1 micron at every set of movements for both axes. Figure 6 shows the repeatability of the number 14 Quad Mover. Upper graph is the measuring data for horizontal movement and lower is the vertical movement. The maximum deviation is ± 0.8 µm for horizontal movement and the vertical movement is ± 0.6 µm.

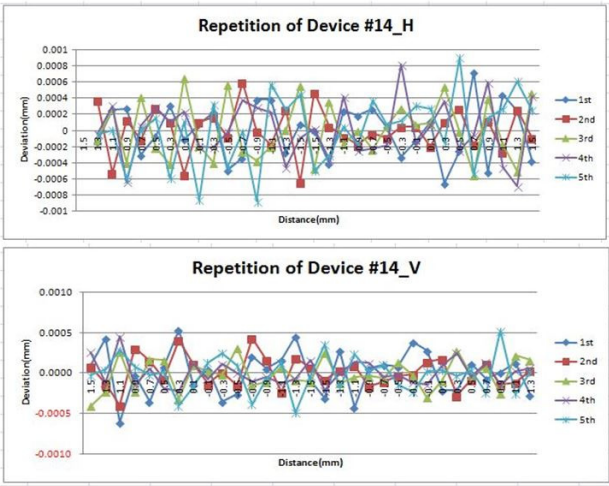


Figure 6: Repetition of Quad Mover. Maximum deviation is ± 0.8 µm of horizontal measurement and vertical is ± 0.6 µm for number 14 Mover.

SUMMARY

In this report, the status of the moving mechanism for the PAL-XFEL Inter-Undulator section is briefly described. It was supplied and installed to Hard X-ray and Soft X-ray Undulator hall. The C-BPM mover was installed 49 units and the quad mover was installed 30 units. The C-BPM Mover and the Quad Mover was supplied and tested from domestic company.

REFERENCE

[1] I.S. Ko, J.-H. Han, "Current status of PAL-XFEL project", in *Proceedings of 27th Linear Accelerator Conference*, Geneva, Switzerland, August 31-September 5, 2014, paper MOIOB04, pp. 26-30.

- [2] J. Munilla *et al*, “Design, Manufacturing and Tests of Closed-Loop Quadrupole Mover Prototypes for European XFEL”, in *Proceedings of 2nd International Particle Accelerator Conference*, San Sebastian, Spain, Sept. 2011, paper MOP0026, pp. 535-538.
- [3] H.G. Lee *et al*, “Technical Overview of Cavity BPM Mover for PAL XFEL”, in *Proceedings of 7th International Particle Accelerator Conference*, Busan, Korea, May 2016, paper TUPMB013, pp. 1136-1138.

OPERATION STATUS OF HLS SYSTEM INSTALLED TO MEASURE GROUND CHANGE OF LARGE SCIENTIFIC EQUIPMENT IN REAL TIME*

Hyojin Choi[†], Seung Nam Kim, Seung Hwan Kim, Sangbong Lee, Hong-Gi Lee, Jang Hui Han
 and Heung-Sik Kang,
 Department of Accelerator, PAL-XFEL, Pohang, Korea

Abstract

Several parts that comprise the large scientific equipment should be installed and operated at precise three-dimensional location coordinates X, Y, and Z through survey and alignment to ensure their optimal performance. As time goes by, however, the ground goes through uplift and subsidence, which consequently changes the coordinates of installed components and leads to alignment errors ΔX , ΔY , and ΔZ . As a result, the system parameters change, and the performance of the large scientific equipment deteriorates accordingly. Measuring the change in locations of systems comprising the large scientific equipment in real-time would make it possible to predict alignment errors, locate any region with greater changes, realign components in the region fast, and shorten the time of survey and realignment. For this purpose, a WPS's (wire position sensor) are installed in undulator section and a HLS's (hydrostatic leveling sensor) are installed in PAL-XFEL building. This paper is designed to introduce performance enhancements to reduce observed phenomena and measurement errors in the HLS system operation process.

INTRODUCTION

All components of PAL-XFEL were completely installed in December 2015, and Hard X-ray 0.1nm lasing achieved through its beam commissioning test and machine study on March 16, 2017. The beam line users are use the hard X-ray since March 22, 2017 [1, 2].

The HLS and WPS system has been installed since September 2016 to measure and record changes of the building floor and devices in real-time [3, 4].

HISTORY OF HLS USED ON THE ACCELERATOR

HLS was developed by the Alignment and Geodesy group at the European Synchrotron Radiation Facility (ESRF) for long term monitoring and control of rapid realignment of the storage ring machine at 1990. The concept of the non-contact capacitive sensor developed at the ESRF has been considerably improved upon by the company FOGALE-Nanotech. Various types of HLS Sensors, including Capacitive and Ultrasonic, are developed and used in recent. European Council for Nuclear Research (CERN) announced the results of the comprehensive testing of HLS and WPS in many forms [5].

*Work supported by Ministry of the Science, ICT and Future Planning
[†]choihyo@postech.ac.kr

SELF-CALIBRATION FUNCTION

Deutsches Elektronen Synchrotron (DESY) conducted In-situ experiments to develop the Ultrasound sensor for HLS in 2001 and the basic design concept of Ultrasound sensor for HLS was built based on the result of the experiments [6]. The structure of Ultrasonic pulse hydrostatic level sensor developed by Budker Institute of Nuclear Physics (BINP) in Russia is described in Fig. 1. The sound reflector made of invar metal that has a low thermal deformation acts as an absolute ruler at an interval of 7.5mm and self-calibrates the differences of water density due to the changes in temperature (sound speed) and electrical properties of the transducer. The composition and operating principle of ULS Electronics developed by BINP and its results of field tests are described in more detail in related papers [7, 8].

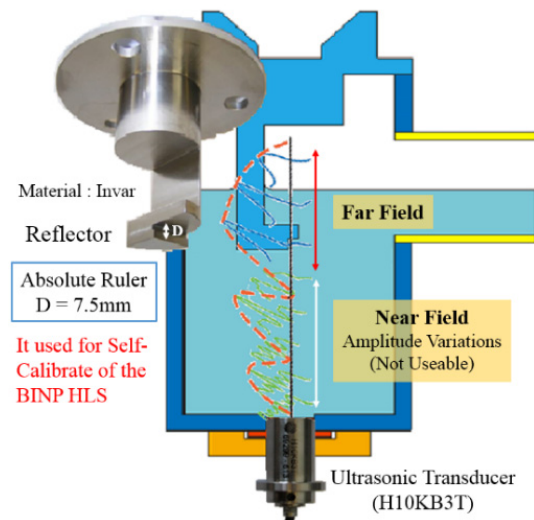


Figure 1: The HLS measurement concept using an Ultrasonic transducer and self-calibration.

INSTALLATION OF HLS AND WATERPIPE

Although it is best to survey the changing progress conditions of the building floor with a view to installing the HLS system, it is desirable to install it low and in close contact to the floor. However, since the concrete anchor, height controlling equipment, etc. is reflected in the support design, the HLS support of the Undulator section was designed to be 15cm in height and the waterpipe support to be 25cm in height. In order for the waterpipe to pass

through the walls of the building in accordance with the radiation safety regulations, the process of radiation shield with a lead block must be carried out after bending the pipe. To do so, ten 90° elbow pipes were used. Waterpipes of all sections apart from sections close to the building walls were installed in a straight line (see Fig. 2).

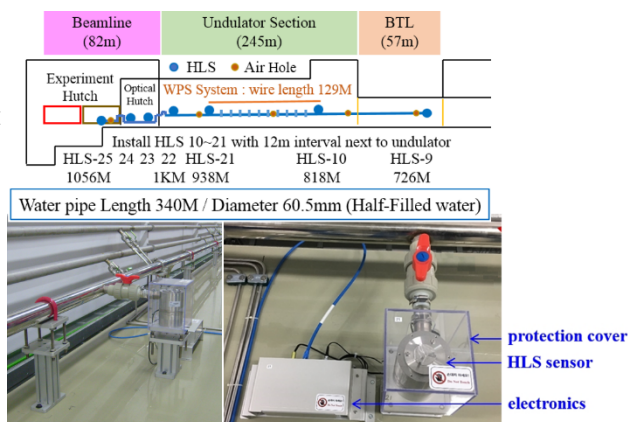


Figure 2: HLS and waterpipe of the Undulator section.

In the case of the linear accelerator (LINAC) section, with regard to maintenance work of the waveguide and the cable installed across from the accelerator tube girder, a person must pass through under the girder. This is the reason for why the waterpipe is installed beside the accelerator tube girder. The pipes in the Bunch Compressor (BC) area that moves from side to side due to the actuator had to be installed on the surface of the wall and the pipes installed in area where the Screen Monitor as well as the Beam Collimator had to be installed beside the equipment. As a result, eighteen 90° elbow pipes, twelve 45° elbow pipes and fifty-six 25° elbow pipes were used (see Fig. 3). When elbow pipes are used, the flow of the water slows down.

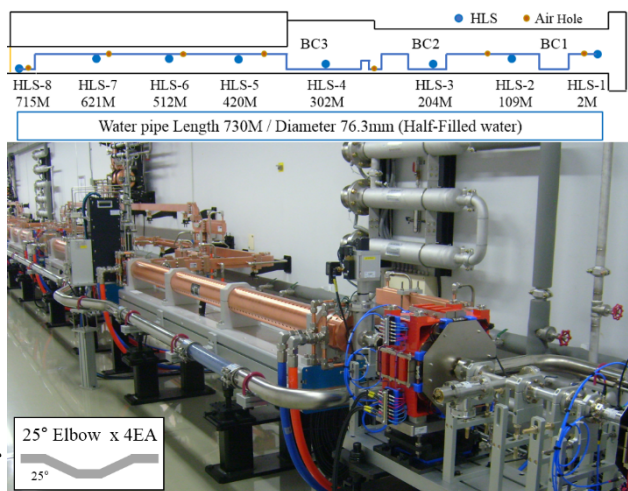


Figure 3: 25° and 90° elbow pipe of the LINAC section.

IMPROVEMENT OF PROBLEM THAT AROSE AFTER INSTALLING THE HLS SYSTEM

Utilizing the Half-Filled method to improve the water flow within the waterpipe, the height of the pipe must be installed in a uniform manner so that the water can flow in a stable and smooth fashion.

Observation of Atmospheric Pressure

Ever since the beginning of data acquisition in September 2016, after having completed the installation of the HLS system, the measurement values of HLS-1 could not be understood. We searched through many literatures and reference materials because we had to know what the measurements meant in order to find the cause of the problem and to solve it. In the process of reviewing the Meteorological Administration data of January 2017, we were able to confirm that the atmospheric pressure changes and the HLS-1 measurements coincided (see Fig. 4).

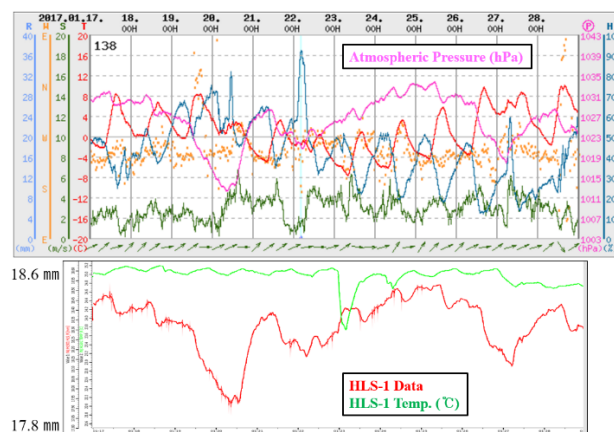


Figure 4: Reference materials of the Meteorological Administration about atmospheric pressure (above), HLS-1 data (below).

The reason why the atmospheric pressure changes were clearly observed in HLS-1 was thought to be the same as the principle of measuring the pressure of Torricelli, which we learned about during physics class in middle school. Therefore, we measured the height of the pipes around HLS-1 and were able to confirm that the pipes installed on the surface of the BC1 wall were 3~4cm and the pipes installed on the surface of wall BC2 and BC3 were installed 1~2cm lower. This was a situation that was identical to the Manometer, which measures the atmospheric pressure changes (see Fig. 5).

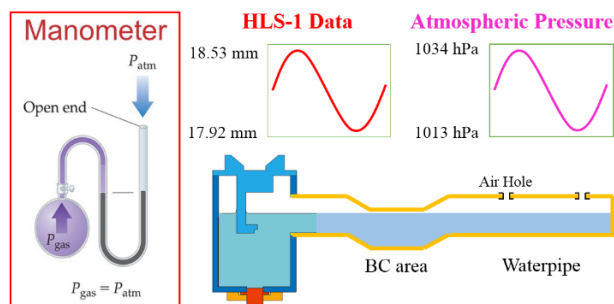


Figure 5: Manometer for measuring atmospheric pressure.

Since the support installed on the surface of the wall was not designed to control the height of the pipes, new support was designed (see Fig. 6). After the pipes near the BC were rearranged at a constant height, the phenomenon of atmospheric pressure being measured in HLS-1 disappeared.

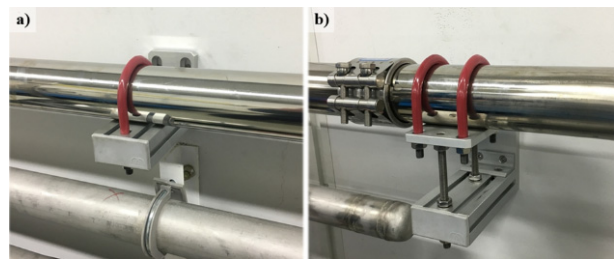


Figure 6: Surface of the BC wall (a) Preexisting support (b) Height controlling support.

Tidal-force and Air Hole

The water within the pipe is affected by the tidal-force and changes in height twice a day (see Fig. 7). In order to measure the changes of the building floor in real-time, the water within the pipe has to flow quickly and maintain balance in accordance with the influence of the tidal-force. As the water flows only by the force of the gravity, if there is a pressure difference within the pipe or if the air flow is abnormal, the flow rate of the water slows or stops. Air holes in intervals of 100 meters were installed in order to remove pressure difference within the pipe and to improve the air flow. As a result, the water flow was improved as shown in Table 1, and the time required for maintaining the balance of water was shortened.

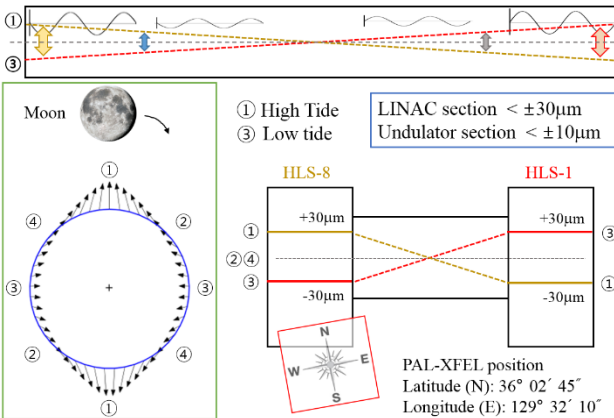


Figure 7: Change in the height of water due to tidal-force.

Table 1: Time Required to Attain Equilibrium of Water After Adding Air Holes

Section	Before adding	After adding
LINAC	14 hours (air hole 2ea)	4 hours (air hole 7ea)
Undulator	2.5 hours (air hole 2ea)	1.5 hours (air hole 4ea)

A simple way of checking the measured conditions of the HLS and the installed conditions of the waterpipe is to inject or drain water to determine the measurement range of HLS ($17.5\pm 2.5\text{mm}$). The water flow rate within the pipe can be confirmed through the balanced run-time of water while injecting or draining water and see whether the pipes have been installed at a constant height up to the measurement range of HLS (see Fig. 8).

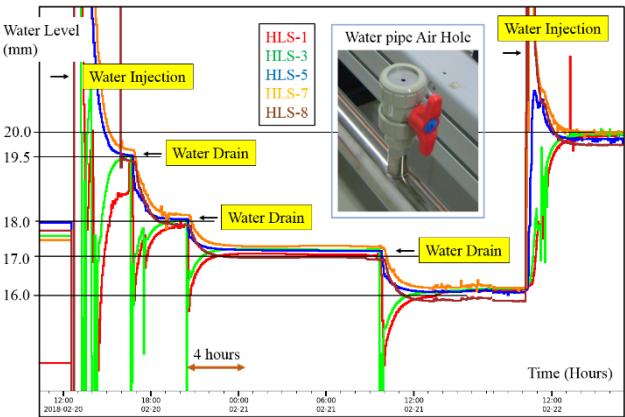


Figure 8: Confirmation of waterpipe installation condition.

The time required for the water to maintain balance within the waterpipe is determined by the length (L) and diameter (\varnothing) of the pipe. The pipe diameter was calculated so that the pipe could be installed in a straight line and so that the time required to balance the water would take about an hour [9]. However, if a lot of elbow pipes are used in the process of installing the pipes, the water flow slows down as like Table 1.

Vibration

Vibration was observed in the measurement of HLS, which was installed in the LINAC section (see Fig. 9). As a result of using the vibration sensor, it was confirmed that the 449nm vibration of the LINAC tunnel floor was amplified in HLS support and vibrated at $2.11\mu\text{m}$ in HLS (see Fig. 10). If the vibration is severe, the water within HLS sloshes. It seems that the vibration problem will be solved if the vibration-proof support is designed.

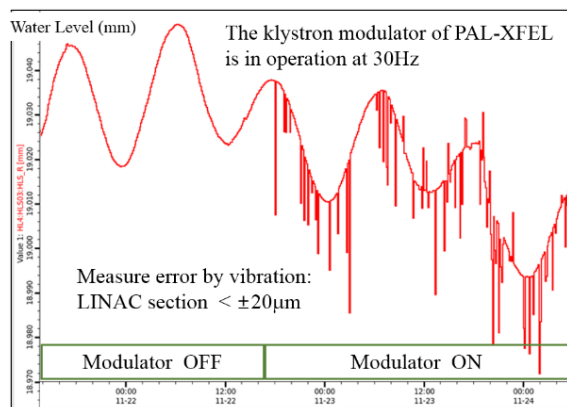
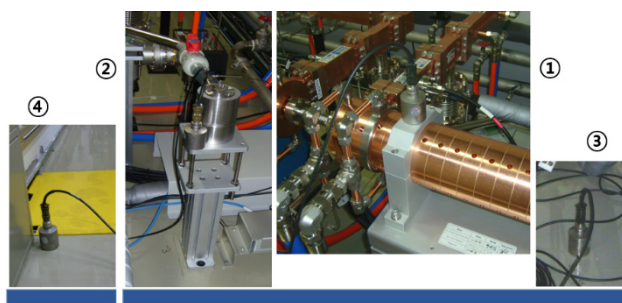


Figure 9: HLS measurement error due to vibration.



Vibration Sensor Position	Modulator OFF		Modulator ON	
	RMS	PkPk	RMS	PkPk
① Accelerator Support	96.6 nm	273 nm	134 nm	380 nm
② HLS Support	39.5 nm	112 nm	746 nm	2.11 µm
③ LINAC Tunnel Floor	60.1 nm	170 nm	159 nm	449 nm
④ Modulator Gallery Floor	25.2 nm	71.4 nm	41.3 nm	117 nm

Figure 10: Vibration measurement within the LINAC section.

SUMMARY

In order to efficiently realign the large scientific equipment, a survey system that can observe and record the

changing progress of the building floor in real-time is needed. PAL-XFEL uses a 1km-long waterpipe as well as 24 HLS to survey the changing progress of the building floor in real-time. In the event of heavy rain, earthquakes, etc. the PAL-XFEL continues to maintain its performance by rapidly realigning components by detecting areas with severe floor changes through the HLS system.

REFERENCES

- [1] I. S. Ko *et al.*, “Construction and Commissioning of PAL-XFEL Facility”, *Applied Science*, 7(5), p. 479, 2017, doi:10.3390/app7050479
- [2] H.-S. Kang *et al.*, “Hard X-ray free-electron laser with femtosecond-scale timing jitter”, *Nature Photonics*, vol. 11, p. 708, 2017, doi:10.1038/s41566-017-0029-8
- [3] H. J. Choi *et al.*, “Wire position system to consistently measure and record the location change of girders following ground changes”, *Journal of Physics: Conf. Series*, 874, 2017, 012088, doi:10.1088/1742-6596/874/1/012088
- [4] H. Choi *et al.*, “HLS System to Measure the Location Changes in Real Time of PAL-XFEL Devices”, presented at IPAC’18, Vancouver, Canada, Apr.-May 2018, paper WEPAL070, to be published.
- [5] A. Herty *et al.*, “Intercomparison Tests with HLS and WPS”, in *Proc. of IWAA 2010*, DESY, Hamburg, Germany, 2010.
- [6] M. Schlösser *et al.*, “High Precision Survey and Alignment of Large Linear Colliders – Vertical Alignment”, in *Proc. of IWAA 2002*, SPring-8, Japan, pp. 343-355, 2002.
- [7] A. G. Chuprya *et al.*, “The Ultrasonic Level Sensors for Precise Alignment of Particle Accelerators and Storage Rings”, in *Proc. of IWAA 2006*, SLAC, California, USA, Sept. 2006.
- [8] A. G. Chuprya *et al.*, “BINP Capacitive and Ultrasonic Hydrostatic Level Sensors”, in *Proc. of IWAA 2008*, KEK, Tsukuba, Japan, Feb. 2008.
- [9] C. Zhang *et al.*, “Primary Hydrokinetics Study and Experiment on the Hydrostatic Leveling System”, in *Proc. of IWAA 2002*, SPring-8, Japan, Nov. 2002.

A FAMILY OF REDUNDANT POSITIONING DEVICES FOR SYNCHROTRON APPLICATIONS

G. Olea[†], N. Huber, HUBER Diffraction GmbH & Co.KG, Rimsting, Germany

Abstract

A new family of reconfigurable devices able to work in synchrotron applications, especially in diffractometer's environments has been developed. It can provide six (6) or less than six (<6) degrees of freedom (dof) motion capabilities ($F \leq 6$) being able to pose a heavy load sample (instruments) with high precision towards an X-ray incoming beam. Based on the Parallel Kinematics (PK) Quatropod concept with redundant actuation ($R_d=2$), it was built around the fully ($F=6$ dof) basic topology 6-4(213) where 2- actuated and 1, 3- passive joints, respectively. By altering the passive joints dof, structures with less than six dof ($F < 6$) can be obtained, e.g. 5-4(213₂)/ $F=5$, 4-4(213₁)/ $F=4$, 3-4(213₀)/ $F=3$ (3₂ and 3₁ and 3₀ stand for 3dof joint with constrained/less dof – $f=2, 1$ or 0/blocked). For a perfect symmetric arrangement and using only P, and S (P-prismatic, S-spherical) joints several useful positioning mechanisms are presented. And, in the design phase, 2dof linear actuators (2P), e.g. XY stages have been proved to be a successful choice, too.

INTRODUCTION

Today, the synchrotron light has been proved to be one of the most active tools to investigate the internal structure of materials. By using the actual and/or further advanced facilities and techniques, the mysteries of our ancient and future world are waiting to be deciphered.

The X-ray Diffraction (Df) is a well-established research technique for material characterisation. In its basic and/or modern forms [1] it is actually the largest investigative technique. Previously applied exclusively for crystal-line materials, nowadays it extended to virtually any materials scattering X-rays. An appreciable number of research results have been obtained in the recent years.

The “workhorses” here have been the Diffractometers (Dm) machines. Built in standard or customized types for various specific applications they are manufactured by several companies (HUBER, NEWPORT, KOHZU, etc). Very often, the requirements are coming to use them for samples working in special environmental conditions (vacuum, cryo, magnetic) fields. These instruments could be sophisticated, large in size and heavy. In addition, they must be manipulated (together with the sample) with high precision, e.g. [2]. However, the existent working space inside of the Dm machines is relative small (constrains are coming from the beam line available room space / hutches, also). In order to comply with this restricted space (especially, height), the sample positioning systems designers must accommodate. Till now, in their concepts, they adopted a serial/stacked solution. (X, Y and/or Z motion xes have been materialized through single axis translation

and/or rotational positioning units called the stages). Subsequently, a sample (and, instrument) is posed in space in the desired position, but with relative low precision (accumulation of errors). The stages are commercially available in a large variety of standard typo-dimensions and can move a heavy load in all (6) or less than six (<6) degrees of freedom (dof). However, in the case of more than 3 dof, the available Dm working space in height sometimes is not enough for stacking all the axes, especially, when rotations around the Centre of Rotation (CoR) point are required. The CoR distance is predetermined (fixed).

Precision Hexapods based on Parallel Kinematic Mechanisms (PKM [3]) are gradually replacing them. They are precise and versatile, able to perform six (6) dof by freely choosing the CoR (variable distances), e.g. PI/Micos, SYMETRIE, NEWPORT, AEROTECH. However, they came with limitations regarding the available portfolio (standard typo-dimensions). The manipulated load & overall size (especially, the height) cannot fulfil always the specific requirements; they are too week or too big. They are not perfectly adapted to Dm environment [4]. Moreover, when less than 6 (dof <6) are necessary, another solutions must be considered.

In order to fulfil all these inconvenient, a new family of positioning devices is proposed. Based on the redundant and reconfigurable principles, at least one of the members could fulfil the above expectations. The main topological, kinematical and conceptual design features for the whole family and in particular for the members will be presented below.

RD-PPTD

HUBER Diffraction & Positioning company has been for a long time a promoter of synchrotron instrumentation pushing the limit of X-ray investigations [5].

A research project (2011) aiming to develop new positioning devices for synchrotron applications based on PKM has finally resulted into the development of a new family of Parallel Positioning Devices (P-PD) based on QUADROPOD (QP) [6] ‘species’.

By using only fundamental joints ($f=1,2,3$, f -joint dof), and in the same configuration on each level from the total of three ($j=I,II,III$) – costs saving and by choosing 2 dof actuation—compact joints, the findings resulted in three (sub) families of topological options. Each actuated level has eight dof capabilities (F_j) $_a=8$, $j=I, \dots, III$ where F_j – level dof (a -actuated) being from kinematics pov redundant one. One from the above QP6_2A (2A–2 dof actuation) (sub) families exhibits useful characteristics for positioning. The 2dof actuation subfamily having all the actuators on the base(Ia) has the advantages of low dynamical effects of motion comparing with another ones - (IIa) and (IIIa), respectively. The 6-4(2)13 (6-dof, 4-chains) representative

[†] go@xhuber.com

structure is providing 6dof motion and could have the actuation any single units, e.g. planar (2P), spherical (2R), roto-translation (RL) motors. This redundant positioning topology ($Rd=2$) is owing an increased natural static stability ($Ss=4$), and is perfect adapted to the common shape (quadrilateral) of a working table. Moreover, by the adequate modification—alteration and/or elimination of the dof of the passive joints – (1) and (3), e.g. 1_0 ; 3_2 , 3_1 , 3_0 (2-two dof, 1-one dof 0-nul dof/blocked), the resulted structures are performing less than six (6) dof positioning tasks with the same actuation setup [7].

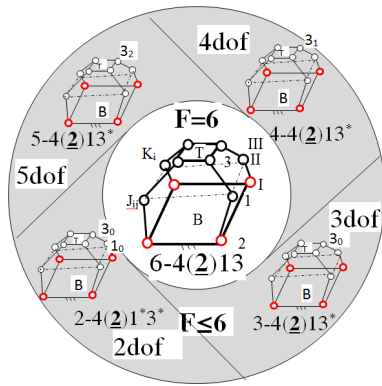


Figure 1: Rd-PPTD (QP_2A) family.

This has several advantages regarding the costs and flexibility of positioning (manufacturing, handling, etc) specific for the large scale facilities, as synchrotrons are. All the members of this family performing: a) six ($F=6$) and b) less than six ($F \leq 6$) dof, are shown in Fig. 1.

By using in each of the Kinematic chain (K_i , $i=1, \dots, 4$) only simple P–prismatic/linear (well-established technology) and upper level S– spherical (IPP, DDP simplified) joints, a new parallel mechanism (sub)family is obtained.

The 6-4(2P)PS architecture shown in Fig. 2 with the pyramidal shape is using planar units for the actuation (2P) and inclined $P\alpha$ (α - angle) passive joints. By adequate modifying the P and S joints, the resulted mechanisms become able to perform less than six (6) dof positioning motions. The members are shown in Fig. 2.

By performing a suitable choice of the elements in the design process for both, the actuation (2P) & passive joints (P, S), the improved results can be expected from the precision, stability and load manipulation point of view. Specifically, an increased precision is expected as a result of the averaging/minimizing the manufacturing & assembly errors effect (over-constrained mechanism). In addition, the total shape, e.g. height could be reduced. A direct drive (DD) planar motor (PI) for actuation (2P) and the wedges (W) principles for passive (P) joints could be among the options. By the coordinate motion of each of the pairs from the four Kinematic chains (K_i), the structure can deliver in a compact way - all translational and rotational (3T&3R) dof, respectively.

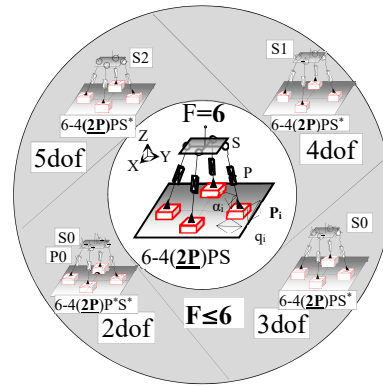


Figure 2: Rd-PPTD (QP_2P) family.

The resulted members, being able to perform either, full (6dof) and less than six (<6dof) motions of positioning with a suitable design of the components (W, S).

An overview of the whole family with these specific features is included in Table 1.

Table 1: Rd-PPTD Configurations

Rd-PPTD	F=6	F≤6
T	(2)13	(2)1*3*
M	(2P)PS	(2P)P*S*
D	(PI)WS	(PI)W*S*

* modified or missed

A short description of the design concept for the entire family and the particularities for each of the members is presented below.

RD-PPTD (6DOF)

Figure 3 shows the design concept for Rd-PPTD in the case of 6-4(2P)PS mechanism. This modular architecture stands as a base for the development of other members of the family.

Between a base (B) and table (T) four Positioning modules (Pm) are arranged around the centre of the base, each of them consisting from a well-defined combination of active(A-Actuation) and/or passive (E-Elevation, G-Guiding) positioning units (Pu). It is able to deliver 6dof (3T3R) motion of positioning in space. Active (Ac) Pu can be chosen as any compact translational XY stages with high accuracy (and, stiffness) based on DD, or electro-mechanical (e.g. motor-ball screw) principle [8].

The first passive Pu - Elevation (EI) can be built as a pair of wedges (W1/W2) materializing a precise, compact and stiff up / down motion. A compact ball & socket design based on sliding principle fit for the passive Guiding (G) unit. Generally, it consists from a vertical pillar with a high precision ball (B) at one end and two adjustable houses (H=2). Through the combined (XYZ) motion of all (or, some) Pm (Pm_i , Pm_{i+2} , $i=1,2$) precision and stiff: a) translations - X,Y,Z and/or b) rotations - Rx, Ry or Rz can be obtained. The resulted working space is rectangular (prism)

and inside of it, a Cartesian (cubic) one can be easily found as a solution for free of singularities motion.

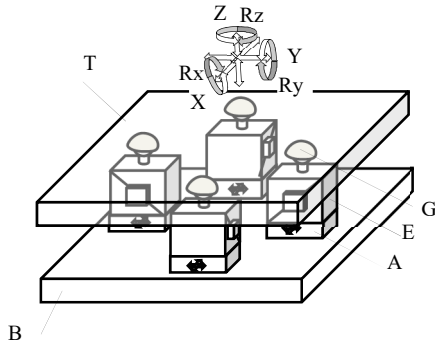


Figure 3: Rd-PPTD (F=6) design.

RD-PPTD (<6DOF)

Figure 4 shows the design concepts for Rd-PPTD with less dof (F=5, 4, 3, 2). They are derived from previously one, with full dof 6-4(2P)PS mechanism by adequate modifications of E(levation) and S(pherical) parts.

5dof Rd-PPTD device is obtained by a simply modifying the upper level joints (S), Fig.4a. In this case, the joints must perform 2dof, only. Specifically, the new joint (S2) should be able to permit only the rotations – Rx and Ry, around X and Y axis, respectively. With other words, the remaining dof – the rotation around Z axis (Rz=0) should be somehow (mechanically) blocked. A ball shaft (pins) must be able to perform combined motions along of two orthogonally channels. The final design solution depends of the specificity of joint type, e.g. sliding, rolling, etc. (Note: The redundancy is changed, Rd=3).

4dof Rd-PPTD device is obtained by adequately modifying the upper level joints (S) to perform 1dof, only. Specifically, S1 joints should be able to permit only the rotations around Z axis (Rz) by blocking the remaining dof – the rotations around X and Y axis (Rx=Ry=0). As in Fig. 4b is represented, a (modified) ball-shaft must be able to rotate inside of a precision hole manufactured in the upper house, only. Effective design solutions must adapt to the type of joints. (Note: The grade of redundancy is four, Rd=4).

3dof Rd-PPTD (Fig. 4c) is obtained by fully modifying the upper level joints (S). In this case, they must not perform any rotation (Rx=Ry=Rz=0). S0 parts, ball-shaft and house(s) must be somehow fixed against each other, e.g. screws, etc. (Note: The grade of redundancy is five / Rd=5. The device can also work with four (4) actuators, only(Rd=1). And, G positioning unit can be missed [9].)

2 dof RD-TPD, Fig. 4d is obtained from the basic RD-PPTD Pu, by using the elevations (E) and spherical (S) joints with null dof. With other words, E0 and S0 must be blocked during the mechanism motion in each of the four Pm. (Note: Rd=6, but the device is working with four (4) actuators (Rd=2); E and G units both can be missing).

An overview of the above design features for whole family is given in Table 2. (Note: Each Positioning module (Pm) is resulting from a pre-established combination of Positioning units (Pu) involving a basic set of S joints).

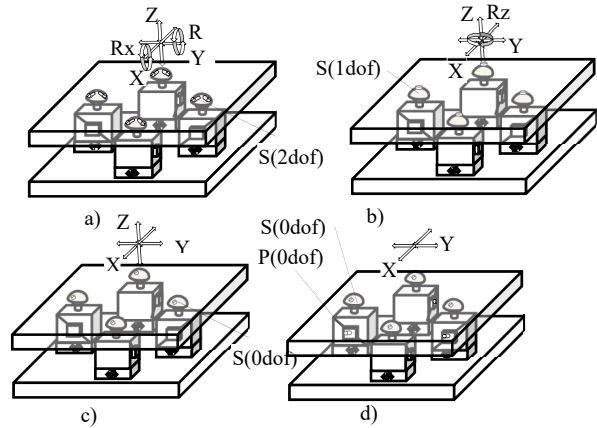


Figure 4: Rd-PPTD (F<6) design.

Table 2: Rd-PPTD Design

Pm	F=6	F=5	F=4	F=3	F=2
A			(X/Y)		
E		W1/W2			W0
G	S	S2	S1	S0	S0

0 – fixed/motionless

CONCLUSION

A new family of redundant parallel positioning table devices (Rd-PPTD) able to work in a synchrotron environment has been presented. Built on the direct requirements of the diffractometers' use, its powerful members exhibit the necessary features to qualifying it for heavy load and high precision positioning. By using the (re)configurability principle, it offers an alternative solution for fast and cost-effective positioning in synchrotrons' workshops, delivering flexibility, saving costs and time. It stands also as a first step and example towards the parallel reconfigurable positioning concept.

REFERENCES

- [1] E.J. Mittemeijer and U. Welzel, *Modern Diffraction Methods*, J.Wiley & Sons, 2012.
- [2] C. Nicklin, *et al.*, "Diamond beamline I07", in *J. Sync. Rad.*, 23, 2016, pp.1-9.
- [3] JP. Merlet, *Parallel Robots*, 2nd ed., Springer, 2006.
- [4] G. Olea *et al.* "Precision Hexapod", in *Proc.10th Int. Conf. & Exh.(EUSPEN)*, May 2010, pp.379-383.
- [5] HUBER GmbH, <http://www.xhuber.com>, 2018
- [6] G. Olea, "Redundant Parallel Positioning Table Device", patented at EPO, EP 3077162B1, 2018.
- [7] G. Olea, "Redundant Parallel Positioning Table Device", D 202014 011 139 U1, *DPMA*, 2018.
- [8] G. Olea, N. Huber, "OCTOGLIDE - Table Positioning Device for Diffraction Applications", in *Proc MEDSI'16*, Barcelona, Spain, Sep. 2016, pp. 38-40.
- [9] G. Olea, "Redundant Parallel Positioning Table Device with linear DoF", in *Proc. of Euspen2017*, pp.85-86.

LE GUIDE FOR SUPPORT: A COOKBOOK FOR MODELING OF ACCELERATOR STRUCTURES*

Curt Preissner[†], Jeremy Nudell, Zunping Liu, Scott Izzo,
 Advanced Photon Source, Argonne National Laboratory, Argonne, IL, 60439, USA

Abstract

The Advanced Photon Source-Upgrade (APS-U) project has stringent specifications and a 12 month installation schedule. Some form of these constraints appear to be common at all multi-bend achromat upgrade projects. At the APS-U, no full tests will be made of the final accelerator support design. The evaluation of the final design against the specifications will be based primarily on computer simulations using virtual inputs.

Ensuring that the final designs meet specifications solely based on simulations is much like cooking a complex, multicourse meal without a trial run. Producing a successful meal on the first try requires a prior understanding of the ingredients, techniques, and interactions between the constituents. A good cookbook can be essential in providing this understanding. Likewise, producing an accelerator support final design that meets the requirements requires a prior understanding of the materials, components, techniques, and interactions between them. This poster describes a cookbook-style approach that any design team can use to confidently predict important characteristics such as natural frequency and ambient vibration response with an error of around 10%.

MOTIVATION

Many third-generation synchrotrons are on a path to a high-brightness, multi-bend achromat (MBA) upgrade [1-3]. In addition to the orders-of-magnitude increase in brightness, these MBA upgrades are unusual in that they involve shutting down very productive machines for a period, removing and replacing the storage ring components, commissioning, and making them again available to the users in the shortest time possible. There is precedent for this in the United States with the SPEAR 3 upgrade project [4]. However, the aggressive project schedules of these MBA upgrades impose additional engineering constraints on the magnet support systems, beyond those driven by physics requirements or those found in greenfield synchrotron projects.

From the beginning of the design process the APS-U supports team assumed there would be a large reliance on computer simulation of magnet support mechanical behavior. Table 1 shows the stringent APS-U mechanical motion tolerances. In addition to these mechanical tolerances, there are space constraints dictated by installation, utilities, and front requirements. The short installation time requires magnets be grouped into larger structures and installed fully aligned and assembled, reducing in-tunnel assembly

* Argonne National Laboratory's work was supported by the U.S. Department of Energy, Office of Science, Office of Basic Energy Sciences, under contract DE-AC02-06CH11357.

[†]preissner@anl.gov

time. These constraints all have to be met within the project schedule.

Table 1: APS-U Vibration Tolerances

Specified over 1-100 Hz	X (rms)	Y (rms)
Girder Vibration	20 nm	20 nm
Quadrupole Vibration	10 nm	10 nm

The APS-U magnet support design has evolved in parallel with the magnet, vacuum system, and revised physics requirements, moving beyond that described previously [5, 6]. The only full-scale magnet support prototype has a structure quite different than the final design.

Evaluating the final APS-U magnet support design against Table 1, from ref. [1], using only a numerical model, is challenging. Finite element (FE) model and vibration modelling is convenient due to the ease of incorporating CAD data. However, it is common for synchrotron engineers to expect FE results to be unrealistic [7], to tune a FE model *a posteriori* [8], or to use the FE model to confirm the behaviour of one particular design [9]. The APS-U supports team wanted a model and a process by which the final design could be checked against requirements, the effect of design trade-offs could be evaluated, and that could be used to accurately predict beam motions [10].

RECIPE

Ingredients

The APS-U magnet support systems consist of the following components, listed in order from the floor to the magnets: 1) a thin epoxy grout line, 2) a steel-reinforced concrete 'plinth', 3) a set of support and alignment mechanisms, 4) a cast iron 'girder', and 5) individual magnets. Measurements of the APS have shown the floor can be considered to be rigid. The most basic ingredients in any mechanical dynamic model are geometry, mass, stiffness, and damping. To obtain the final result, one more ingredient is necessary, the facility vibration. In this section we explain how these ingredients can be mixed to capture the behaviour of accelerator magnet support systems, using the APS-U magnet support system as an example.

The appropriate mixing of the ingredients for each component is key to producing an accurate FE model. For the epoxy grout, plinth, and girder, CAD geometry, combined with the material property data are sufficient to accurately capture the component behaviour. The epoxy manufacturer supplies modulus data. For the steel and concrete plinth, the steel reinforcing geometry is captured in the CAD model and can be used with common steel material properties, while the concrete vendor supplied modulus data on the proprietary concrete mix. Likewise for the girder, the

CAD data accurately define the geometry and the foundry supplied the cast iron material properties. The APS-U magnets are fixed to the girder and can be well-represented with simplified CAD data that capture the mass and inertia properties.

In contrast, the support and alignment mechanisms behaviour *are not* accurately captured using CAD data and available material properties. The use of CAD geometry and material properties are the root source of the unreliability of the FE modal analyses such as those of references [7] and [8]. Regardless of the support and alignment mechanism type, threaded rods, wedge jacks, cam movers, etc., these components exhibit nonlinear stiffness and damping with respect to load. This is due to all of the interfaces within these components (threads, sliding surfaces, Hertzian contacts, spherical bearings, etc.). When relatively lightly loaded, these interfaces are fairly compliant. In addition, the slope of the stiffness vs. load curve can be steep at light loads. This means small changes in load can greatly influence behaviour. The use of CAD geometry vastly over predicts the component stiffness, and without a *posteriori* model tuning results in over predicting modal response and under predicting vibration response. Typically manufacturers do not or cannot supply the necessary component data.

The best way to capture the support and alignment component behaviour is to replace the geometric representation with a discrete stiffnesses in the FE model. The alignment component masses can be neglected if sufficiently small (m is generally $\ll 10\%$ of total system mass), or easily represented with discrete masses. Simple vibration measurements [11] can then be used to determine the load-dependent, linearized, diagonal stiffness coefficient matrix for a support component (three translational and three torsional stiffnesses).

The final ingredient to predict the overall system vibration response is the facility vibration. This is one area where upgrading an existing facility has an advantage over a greenfield site. As an existing facility, the APS has been stable and the vibration characteristics can and have been well characterized. The storage ring floor motions have been measured at various locations in three directions.

Measures

Like baking French pastry, an accurate mechanical model is highly dependent both the form (CAD vs. discrete) and amount (geometry derived vs. measured stiffness and damping) of the ingredients. Experimental modal analysis (EMA) measurements were made of the FODO plinth and girder prototypes to confirm the assumption that geometry and material properties were sufficient to predict their behavior. Whereas measurements were made of the alignment components to generate the necessary linearized stiffness coefficients.

A full (measured FRFs, curve fitting (natural frequency and damping), modal visualization) free boundary condition (BC) EMA was conducted on the plinth and girder. Figure 1 shows the girder casting rigged for an EMA. Tri-axial, roving accelerometers were used to measure the impact frequency response functions (FRFs) at 28 points,

enough to properly resolve the first 6 modes. The slings provided a very soft support, approximating free BCs.

The match between the FE and EMA modal results are a metric of dynamic model performance. A FE modal model that matches the EMA well will yield accurate random vibration results when combined with measured damping values. The model will also provide accurate static and thermal deflection results. The first five modes of the plinth and six modes of the girder matched to an average of 1.98% and 5.40% respectively. Table 2 shows the first three modes for the girder.



Figure 1: The FODO prototype girder casting at the manufacturer, rigged for a free BC EMA.

Table 2: Girder Modal Results, Average Difference 1.99%

Mode	EMA (Hz)	FEA (Hz)	% Diff.
1	106	104	1.89
2	157	154	1.91
3	232	227	2.16

Linearized stiffness coefficients were determined for a variety of wedge jack adjusters, spherical bearings, and the metal-polymer bearings used in both the vertical and in-plane adjustment stacks. Dynamic testing proved to be more reliable, flexible, and provided more information (diagonal stiffness matrix) than static stiffness measurements used in [9].

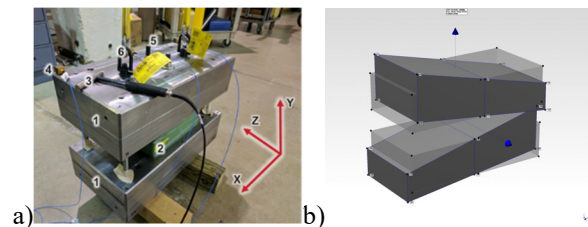


Figure 2: Stiffness test rig shown in a). The components are: 1) masses, 2) wedge jack, 3) impact hammer, 4) accelerometers, 5) threaded rods, and 6) slings. In b) The mode involving rotation about the Z axis is shown.

The component is clamped between the two rigid (in frequency range of interest) masses shown in Figure 2 and a free BC modal analysis is done at many load. A load cell measures the applied force. For each load, three translational and three rotational stiffness are determined. The assembly is symmetric and has six uncoupled modes, relating

to each of the translational and torsional stiffnesses. Modal analysis software is used to curve fit the data for each load, determining natural frequencies and damping. Modes shapes are also visualized. Stiffnesses are initially estimated at the highest applied load using a single-degree-of-freedom model. The results are refined with a FE model of the test rig. The stiffness at the lower load levels can then be determined simply by scaling the high-load stiffnesses by the square of the ratio of natural frequencies. In this manner a table of stiffnesses is determined for each component. Figure 3 shows one set of stiffness vs. load curves.

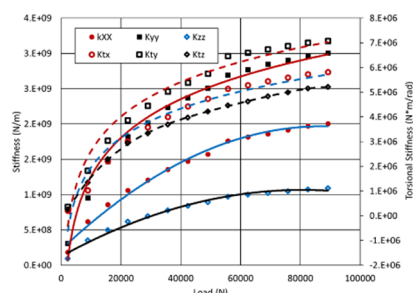


Figure 3: Airloc 1212-KSKCV translational (K_{xx} , K_{yy} , K_{zz}) and torsional (K_{tx} , K_{ty} , K_{tz}) stiffnesses.

RESULTS

The first analysis of the complete model was a modal analysis both to verify the modelling process and to estimate the first natural frequency, and provide a set of mode shapes for random vibration analysis. The first three modes matched well, with an average error of 7.3%. This is with only *a priori* knowledge. Figure 4 shows the first mode comparison.

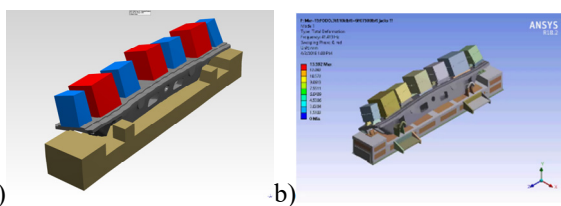


Figure 4: Grouted FODO prototype, first mode shape comparison, a) is EMA at 41 Hz, while b) is FE modal analysis at 42 Hz (2.4% difference).

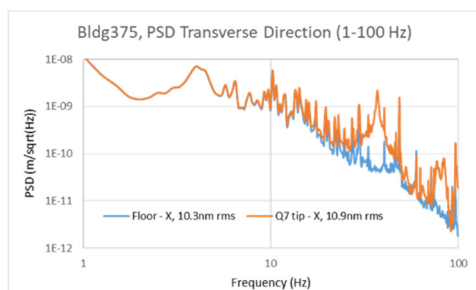


Figure 5: Predicted FODO magnet pole tip response using random vibration analysis. Blue is floor (input) while orange is magnet (response).

The modal model can then be used in a random vibration analysis to estimate magnet pole tip motion, as in Figure 5. Work is ongoing to measure and compare the experimental

response. Work is also ongoing to perform a transient dynamic analysis, from which support transfer functions and magnet-to-magnet phase relations can be estimated.

CONCLUSIONS

This paper describes a process by which accelerator magnet support structures can be accurately modelled using only data from material properties, CAD geometry, and sub-component dynamic stiffness tests. The expected error is less than 10%. The accuracy of this method allows for using only FE model results to evaluate the APS-U supports final design against requirements both dynamically and statically. It also allows for a novel approach to estimating mechanical motion-related orbit distortions [10]. The approach is also readily applied to beamline instrumentation as well.

REFERENCES

- [1] "APS Upgrade Project Preliminary Design Review Report", Argonne National Laboratory APSU-2.01-RPT-002, 2017, Available: <https://www.aps.anl.gov/APS-Upgrade/Documents>
- [2] R. Dimper *et al.*, "ESRF Upgrade Programme Phase II (2015-2022) Technical Design Study", The European Synchrotron 2015, Available: http://www.esrf.eu/Apache_files/Upgrade/ESRF-orange-book.pdf
- [3] H. Tanaka *et al.*, "SPRING-8 upgrade project", in *7th International Particle Accelerator Conference, IPAC 2016, May 8, 2016 - May 13, 2016*, Busan, Korea, 2016, pp. 2867-2870.
- [4] R. Hettel *et al.*, "SPEAR 3 upgrade project: The final year", in *PAC 2003 - Proceedings of the 2003 Particle Accelerator Conference, May 12, 2003 - May 16, 2003*, Portland, OR, United States, pp. 235-237.
- [5] J. Collins *et al.*, "Preliminary Design of the Magnet Support and Alignment Systems for the APS-U Storage Ring", in *9th Edition of the Mechanical Engineering Design of Synchrotron Radiation Equipment and Instrumentation Conf. (MEDSI'16)*, Barcelona, Spain, 2016, pp. 87-89.
- [6] J. Nudell *et al.*, "Preliminary Design and Analysis of the FODO Module Support System for the APS-U Storage Ring," in *Proc. MEDSI'16*, Barcelona, Spain, 2016, pp. 83-85.
- [7] H. Wang *et al.*, "Overall Design of Magnet Girder System for Heps-Tf " in *Proc. IPAC'16*, Busan, Korea, 2016, pp. 2382-2385.
- [8] V. Ravindranath *et al.*, "Vibration Stability Of NSLS II Girder-Magnets Assembly", in *Proc. MEDSI 2008*, Canadian Light Source, 2008, https://medsi.lbl.gov/SysIncludes/retrieve.php?url=https://medsi.lbl.gov/files/page_137/Presentations_Papers/Engineering_For_Low_Emittance/Vibrations_Stability_of_NSLS_II_Girder-Magnet_Assembly_-_V._Ravindranath_-_PPT.pdf
- [9] F. Ciani *et al.*, "The Girders System for the New ESRF Storage Ring", in *Proc. MEDSI'16*, Barcelona, Spain, 2017, paper: TUCA06, pp. 147-151.
- [10] J. Nudell *et al.*, "Calculation of Orbit Distortions for the APS Upgrade Due to Girder Resonances", Presented at MEDSI'18, Paris, France, June 2018, paper TUPH28, this conference.
- [11] T. J. Royston, I. Basdogan, "Vibration transmission through self-aligning (spherical) rolling element bearings: Theory and experiment," *Journal of Sound and Vibration*, vol. 215, no. 5, pp. 997-1014, 1998.

FEA SIMULATIONS OF THE ALUMINIUM VACUUM CHAMBER FOR LOREA INSERTION DEVICE AT ALBA SYNCHROTRON LIGHT SOURCE

M. Quispe[†], A. Gevorgyan, ALBA – CELLS Synchrotron, 08290 Cerdanyola del Vallès, Spain

Abstract

For LOREA, the new beamline at ALBA, the Insertion Device Apple-II helical out-vacuum undulator requires the installation of a suitable narrow – gap aluminium chamber.

The chamber design is based on the standard ALBA aluminium chamber which has an internal elliptical cross section, where NEG coating is deposited and bending magnet (BM) radiation from the upstream dipole is dissipated on the chamber walls. For the standard chamber the upstream distributed absorber cannot protect the entire chamber from direct BM radiation because there is a limitation for its design: the beam impedance of the machine.

Based on new studies of collective effects it has been concluded that it's possible to implement modifications on the upstream distributed absorber and protect the chamber from lateral collision of BM radiation keeping the beam impedance of the machine inside of a safe range. In spite of that still there is a contribution of the tails of BM radiation.

In this paper we describe the behavior of the new aluminium vacuum chamber for different thermal load conditions using water and air for refrigeration. Also we present the design of the modified OFHC upstream distributed absorber.

BACKGROUND

The Insertion Device (ID) for LOREA, the new beam line at ALBA for Low-Energy Ultra-High-Resolution Angular Photoemission for Complex Materials, will operate with a suitable chamber, a narrow-gap, NEG-coated, extruded-aluminium vacuum chamber.

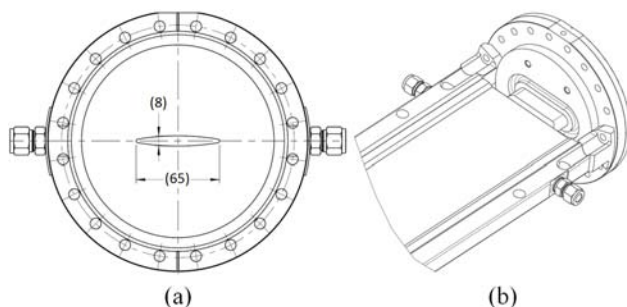


Figure 1: The ALBA narrow-gap, NEG-coated, extruded-aluminium vacuum chamber. (a) Internal elliptical cross section of 65 mm by 8 mm. (b) Detail of the end chamber joined to the flange.

The design model of this chamber is based on the standard aluminium vacuum chambers installed at ALBA. It has an internal elliptical cross section of 65 mm by 8 mm, where NEG coating is deposited (See Fig. 1).

Synchrotron radiation from the upstream dipole is dissipated on the chamber, thus two water cooling channels with 7 mm diameter each is used for cooling. The material used for the manufacturing is aluminium 6061 T6. At each end of the chamber, the aluminium extrusion is welded to an explosion-bonded bimetallic (stainless-steel/aluminium) flange to enable to make a joint to the flange (Spigot flange). The inlet and outlet flanges are bimetal made of AISI 316LN and aluminium 6061 T6. Flanges are CF type, fixed with a DN160 size.

In order to integrate the chamber into the straight section two vacuum components must be implemented: the OFHC upstream distributed absorber and the downstream tapered chamber connected to the current bellows (See Fig. 2).

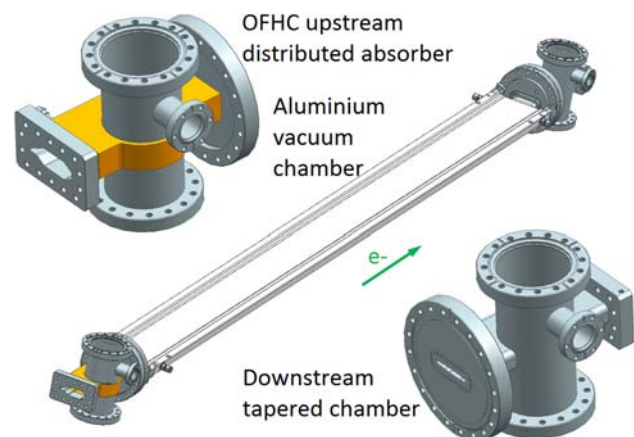


Figure 2: ALBA 3D model of the aluminium vacuum chamber, the OFHC upstream distributed absorber and the downstream tapered chamber.

For the current aluminium vacuum chambers at ALBA the BM radiation hits the wall laterally because the chamber is only partially protected by the upstream distributed absorber. This unwanted configuration is due to a geometrical restriction imposed for the design of the absorber: in order to keep the beam impedance of the machine inside of a safe range a minimum distance between the sharp end of the absorber and the electron beam trajectory must be fixed to 28.5 mm.

For LOREA, new studies of collective effect confirm the possibility to reduce the minimum distance from the sharp end of the absorber to the electron beam trajectory. Then it will be possible to avoid a lateral collision of BM radiation.

[†] mquispe@cells.es

For this new condition, still there is a contribution of the tails of the radiation on the upper and lower walls of the chamber. This radiation can be significant because of the very narrow gap of the chamber.

In this paper we present the thermal behavior of the LOREA aluminium vacuum chamber for different conditions: radiation heating the lateral, upper and lower walls, including misalignment effects, and using water and air cooling as thermal solutions. And finally details of the new OFHC upstream distributed absorber are included.

ALUMINIUM VACUUM CHAMBER

Lateral Collision

This case corresponds to the standard aluminium vacuum chamber at ALBA. The BM radiation hits the wall laterally. Because of this a maximum power and peak power density calculated are 250 W and 0.17 W/mm², respectively. These thermal variables have been obtained according with the design parameters defined in Table 1.

For the water cooling 23 °C is fixed as inlet temperature and the average velocity in the tubes (7 mm internal diameter) is kept in 2.2 m/s. For these conditions the calculated convective heat transfer coefficient is 10300 W/m²K.

Table 1: Main parameters for ALBA Storage Ring

Parameter	Magnitude
Beam energy, E	3 GeV
Design current, I	400 mA
Dipole magnetic field, B	1.42 T

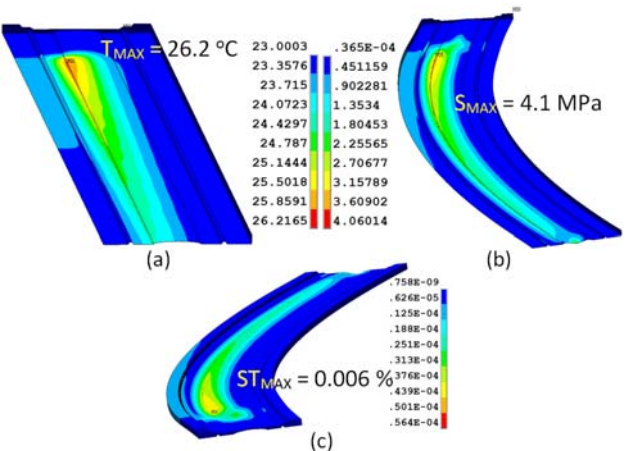


Figure 3: FEA results for the aluminium vacuum chamber for lateral collision of BM radiation. (a) Temperature map, (b) Stress map, and (c) Strain map.

FEA has been performed to estimate the maximum stress, strain and temperature on the chamber, in order to estimate the cycles that the chamber can withstand before failure. The results of this analysis are: the maximum stress is 4.1 MPa, the maximum strain is 0.006% and the maximum temperature is 26.2 °C; the results are within

the design criteria of the vacuum aluminium components [1]. Figure 3 shows the FEA results for the chamber.

Collision on the Upper and Lower Walls

The thermal conditions because of the tails of BM radiation are calculated by using the Monte Carlo software SynRad+ [2]. For the thermal characterization the design parameters in Table 1 have been applied. With the aim to guarantee an asymptotic behaviour of the SynRad+ model, the beam trajectory on the dipole chamber has been discretized with steps of 0.01 cm and surfaces of 0.0004 cm² has been defined for the discretization of the walls of the chamber. In order to be conservative the effects of the reflections have been omitted for this study.

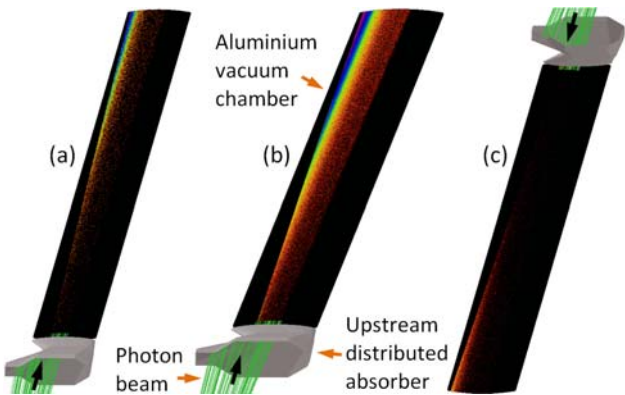


Figure 4: Footprint of the tails of BM radiation on the upper and lower walls of the aluminium vacuum chamber. (a) Nominal trajectory of the beam, (b) Radiation on the upper wall under vertical misalignment effect, and (c) Radiation on the lower wall under vertical misalignment effect.

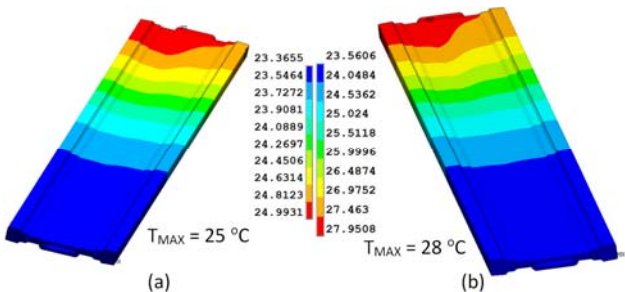


Figure 5: Thermal results for the aluminium vacuum chamber. The BM radiation is deposited on the upper and lower walls. (a) Temperature map for nominal trajectory of the beam. (b) Temperature map for trajectory of the beam under vertical misalignment effect.

The thermal behaviour for nominal trajectory and vertical misalignment of the beam has been studied. For nominal condition a maximum power and power density distribution are 2.34 W and 0.0006 W/mm², defined for each surface (the upper and lower walls). For the worst condition, the misalignment case, a vertical deviation of the beam of +1 mm has been imposed as a conservative criteria, then for the upper wall the thermal variables are 4.74 W and 0.0031 W/mm² while for the lower wall the parameters 1.6 W and 0.00019 W/mm² are calculated (See

Fig. 4). For both cases air natural convection is applied as fluid boundary condition. The convective heat transfer coefficient is calculated for quiet air: $3 \text{ W/m}^2\text{K}$ at 23°C .

Figure 5 shows the thermal results. The maximum temperatures of 25 and 28°C are obtained for nominal and with misalignment effects, respectively. These thermal results are similar to the case for lateral collision. The studies of thermal stress and strain have been omitted considering that these cases are a better situation with respect to the results obtained for the case with lateral collision.

UPSTREAM DISTRIBUTED ABSORBER

Boundary Conditions

The OFHC upstream distributed absorber is subject to BM radiation coming from the upstream dipole. Based on the parameters of Table 1 the power deposited on the absorber is estimated using the SynRad+ computer code (See Fig. 6). The total power calculated is 596 W and the peak power density is 7.3 W/mm^2 . The non-reflection condition has been established as conservative criteria for the surfaces. In order to guarantee an asymptotic behavior size elements of 0.0001 cm^2 are used for the discretization of the surfaces.

The absorber is cooled by water at 23°C inlet temperature. The velocity in the cooling channels is kept in 3 m/s and the calculated convective heat transfer coefficient is $13888 \text{ W/m}^2\text{K}$.

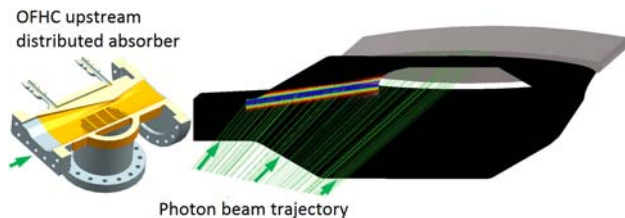


Figure 6: Representation of the surface power density distribution using the SynRad+ computer code.

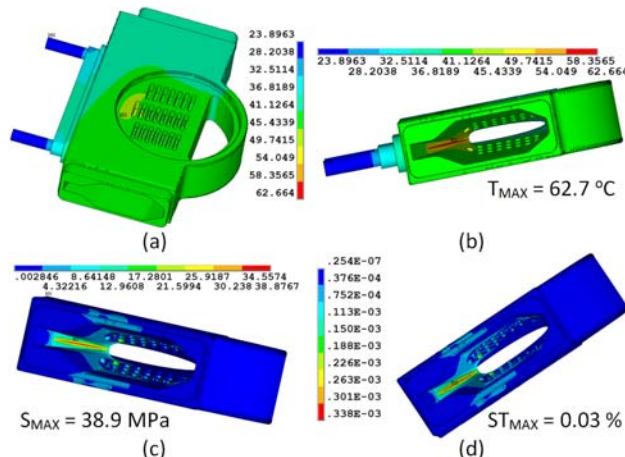


Figure 7: FEA results of the OFHC upstream distributed absorber: (a) and (b) Temperature map, (c) Stress map, and (d) Strain map.

Results

The temperature, stress and strain distribution have been calculated based on linear elastic analysis. The thermal mechanical simulations show good results, the new absorber is in a safe range according to the design criteria [3]. The maximum temperature, stress and strain are 62.7°C , 38.9 MPa and 0.03% , respectively (See Fig. 7).

CONCLUSIONS

The narrow-gap, NEG-coated, extruded-aluminium vacuum chamber at LOREA has been simulated under different BM thermal load conditions.

When the BM radiation hits the lateral wall of the chamber, water cooling is needed to dissipate the power; this is the current scenario for the aluminium vacuum chambers installed at ALBA.

When the BM radiation hits only the upper and lower walls of the chamber, that is the power load is because of the tails of the Gaussian profile of the BM radiation, the power can be dissipated only by air natural convection; this is a particular situation for LOREA because the conventional OFHC upstream distributed absorber has been modified to protect the aluminium vacuum chamber completely from any lateral BM photon collision. The absorber has been modified following the new geometrical constraints defined in a new study of collective effects made at ALBA, which confirm the possibility to reduce the distance between the end sharp of the absorber and the electron beam trajectory, keeping the beam impedance of the machine inside of a safe range.

As is well-know, because of corrosion problems the water cooling circuit for aluminium components must be separated from the water cooling circuit for cooper components. Then the dissipation of the heat on the chamber by air free convection avoids the implementation of a particular cooling circuit for the aluminium chamber.

The simulation of the new OFHC upstream distributed absorber has been made and the thermal structural results obtained are inside of the design criteria.

REFERENCES

- [1] A. Brammer *et al.*, "Strain-Controlled Low-Cycle Fatigue Properties of Extruded 6061-T6 Aluminum Alloy", *Journal of Materials Engineering and Performance*, vol. 22, issue 5, 2013, pp. 1348-1350.
- [2] SynRad+, <https://molflow.web.cern.ch>.
- [3] E. Al-Dmour *et al.*, "The conceptual design and thermal analysis of ALBA crotch absorbers", in *Proc. PAC07*, Albuquerque, NM, USA, July 2007, paper MOPAN065, pp. 299-301, DOI: 10.1109/PAC.2007.4440191.

DESIGN OF AN INTEGRATED CROTCH ABSORBER FOR ALBA SYNCHROTRON LIGHT SOURCE

M. Quispe[†], J. Campmany, A. Gevorgyan, J. Marcos
 ALBA – CELLS Synchrotron, 08920 Cerdanyola del Vallès, Spain

Abstract

This paper presents the design of an Integrated Crotch Absorber for the new beamline LOREA (Low-Energy Ultra-High-Resolution Angular Photoemission for Complex Materials at ALBA). The LOREA Insertion Device (ID) consists of an Apple II undulator with a period of 125 mm.

For the current ALBA dipole chamber the ID vertical polarized light hits the upper and lower walls because of the very narrow vertical aperture between the cooling channels. To solve this problem some modifications must be implemented both in the dipole chamber and in the crotch absorber located inside of the dipole.

The new crotch absorber, named Integrated Crotch Absorber, must absorb a significant part of the ID vertical polarized light in order to avoid radiation impinging at the post dipole chamber.

The geometry of the Integrated Crotch Absorber is a combination of the conventional crotch and the distributed absorber done at PSI for ANKA. The design has been optimized taking into account the standard thermo-mechanical design criteria as well as the reflective effects of the ID radiation from the opening towards the walls of the dipole chamber.

INTRODUCTION

The ALBA synchrotron light source is currently installing the new beamline LOREA, for Low-Energy Ultra-High-Resolution Angular Photoemission for Complex Materials. It will operate in the range of 10 – 1500 eV and will use polarized light. To produce the light an Insertion Device Apple II undulator with a period of 125 mm has been chosen. The device can operate as an undulator at low energies and as a wiggler at high energies, reaching a wide energy range.

For the vertical polarization mode, the photon beam emitted by the ID at low photon energies has a large aperture angle of ± 2.2 mrad, which is the worst case. Because of the very narrow vertical aperture between the cooling channels of the conventional ALBA dipole chamber, the ID vertical polarized light hits the chamber. To solve this problem two main modifications have to be introduced:

- Modification of the dipole chamber. The longitudinal cooling channels have to be removed to increase the vertical aperture.
- Modification of the Glidcop Crotch Absorber. Part of the ID radiation must be absorbed by the opening of the new crotch absorber in order to protect the post dipole chamber from any collision.

This paper is dedicated to the design of a new Glidcop Crotch Absorber. For ALBA this new absorber is non-conventional because the device must face the Bending Magnet (BM) and ID radiation at the same time. We name this new absorber as Integrated Crotch Absorber because its geometry is a combination of the conventional crotch absorber and the distributed absorber made at PSI for ANKA [1].

Design aspects of the geometry, the effects of the ID beam reflection from the absorber to the walls of the vacuum chamber and FEA simulations of the Integrated Crotch Absorber are included in this paper.

BASIC DESIGN

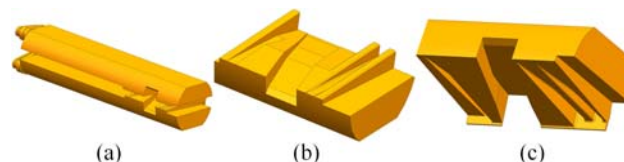


Figure 1: (a) Assembly of the Integrated Crotch Absorber, (b) The lower jaw and (c) The upper jaw.

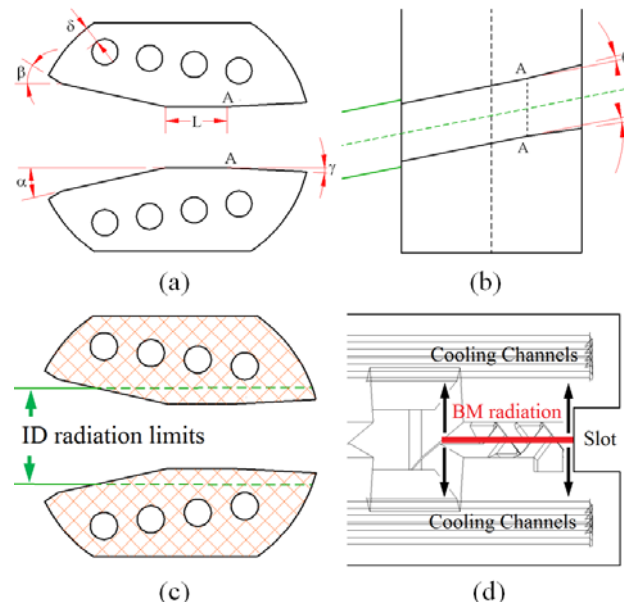


Figure 2: (a) Cross section view in the middle of the opening, (b) Details of the opening from the top view, (c) Details of the beam limits with respect to the cooling channels and (d) Position of the cooling channels with respect to the BM radiation on the teeth.

[†] mquispe@cells.es

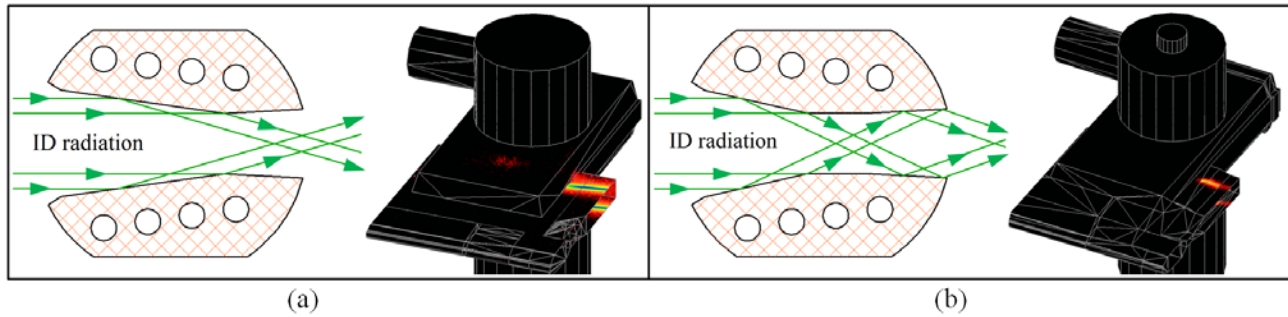


Figure 3: Collision and reflection of the ID radiation vertical mode in a cross section view of the opening. (a) The radiation hits the absorber and is reflected directly to the walls of the dipole vacuum chamber. (b) After the collision on the absorber the reflected ID radiation hits the internal walls of the Integrated Crotch Absorber.

Figure 1 shows the updated version of the Integrated Crotch Absorber presented in a previous work [2]. It consists of two jaws. A special opening has been designed in order to absorb the ID radiation in vertical mode. At the end of the absorber a slot also has been included as part of the thermal mechanical optimization.

The geometrical model is based on the following design criteria as is showed on Fig. 2:

- The inclination of the surface where the ID radiation is deposited, defined by the angle α (Fig. 2a), has been chosen under the following conditions: (i) get the lower power density distribution and (ii) capture the ID radiation reflected inside of the same absorber.
- At the entrance of the opening an additional safe angle is included, the angle β (Fig. 2a), with the aim to avoid any perpendicular collision of the beam on the absorber in case of beam misalignments.
- A horizontal surface has been included in the half-way of the opening, defined by the length L (Fig. 2a), in order to capture the reflection of the radiation inside of the absorber.
- With the aim to guarantee that all the ID radiation is always deposited below of the cooling channels, the angles θ and γ have been included in this design. In this way the end point for the first collision of the radiation will be always the point “A” (Fig. 2a and 2b).
- A minimal thickness of $\delta = 5$ mm has been defined in between the water cooling channels and the vacuum zone (Fig. 2a).
- In order to avoid any possibility of corrosion induced by radiation, the position of the cooling channels are separated from the fan of the ID radiation (Fig. 2c).
- At the end of the absorber a slot has been included. In this way the region with BM radiation is always below of the position of the cooling channels (Fig. 2d).

Photon Reflection as Design Parameter

The effect of the reflection of the ID radiation from the opening of the absorber to the dipole vacuum chamber has been investigated. This analysis has been done by using the Monte Carlo software SynRad+ [3].

The radiation of the Apple II undulator has been approximated as a Wiggler by applying the function \sin/\cos

for the magnetic field with the appropriated parameters in order to approximate the Gaussian profile of the ID radiation.

Figure 3 shows two types of reflections as a function of the internal geometry of the opening. For the first case, Fig. 3a, after the collision the photons are reflected directly to the wall of the chamber as is showed in the illuminated part. It is calculated a maximum power of 3.4 W and a peak of power density of 7 W/cm². In the second case, Fig. 3b, the previous geometry has been optimized and now the reflection after the collision hits directly the same opening of the absorber and the following reflections hit the walls of the dipole chamber. For this new case the maximum power and peak power density has been reduced to 0.6 W and 0.8 W/cm².

Figure 4 shows the SynRad+ simulations made for the Integrated Crotch Absorber based on the geometry of Fig. 3 (b). The green lines represent the photon beam coming from the ID and BM sources. The SynRad+ model allows to see the effect of the internal reflection on the opening of the absorber (Fig. 4 a).

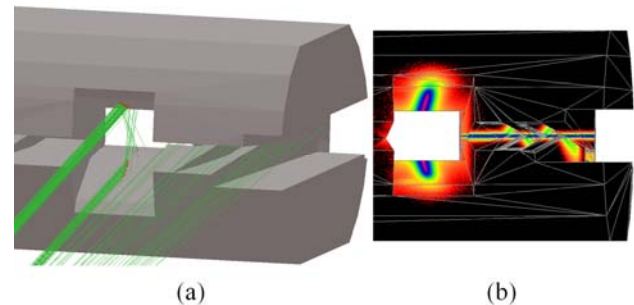


Figure 4: Absorber simulated by using SynRad+. (a) Details of the photon beam trajectory. (b) The footprint of the ID and BM radiation.

SIMULATIONS

Boundary Conditions

The main parameters which characterize the LOREA ID (vertical mode) and BM power on the absorber are shown in Tables 1 and 2.

For the ID power deposition the vertical misalignments, angular (± 0.11 mrad) and displacement (± 0.16 mm), have been imposed. For these conditions the ID power on

Content from this work may be used under the terms of the CC BY 3.0 licence (© 2018). Any distribution of this work must maintain attribution to the author(s), title of the work, publisher, and DOI.

the upper and lower jaws are 610.7 and 296.2 W, respectively, and the ID peak power density is 19.8 W/mm².

The total power (ID and BM) on the upper jaw is 2729 W and the maximum power density is because of BM radiation: 43 W/mm².

The crotch absorber is cooled by water at 23 °C inlet temperature. The velocity in the cooling channels is kept at 3 m/s and the calculated convective heat transfer coefficient is 15000 W/m²K.

For all the FEA studies only the upper jaw is simulated. This jaw is subjected to the maximum power load conditions, in comparison with the lower jaw.

The material for the absorber is Glidcop Al-15.

Table 1: Main parameters of Insertion Device for LOREA (vertical mode). The emitted power and power density are computed for an electron beam current of 400 mA.

Parameter	Magnitude
Maximum magnetic field	1.06 T
K	12.37
Power density	5.6 kW/mrad ²
Total power	5.5 kW

Table 2: Main parameters for ALBA Storage Ring

Parameter	Magnitude
Beam energy, E	3 GeV
Design current, I	400 mA
Dipole magnetic field, B	1.42 T

Results

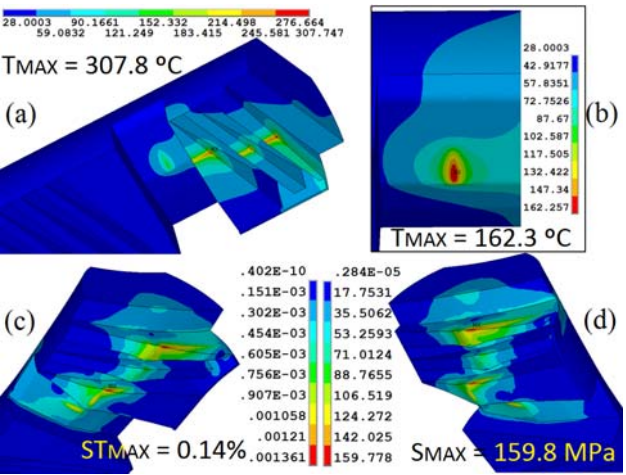


Figure 5: FEA results for the Glidcop Al-15 Integrated Crotch Absorber in the dipole chamber: (a) Temperature map, (b) Local detail of the temperature distribution at the ID power deposition, (c) Strain map, and (d) Stress map.

The temperature, stress and strain distribution have been calculated based on linear elastic analysis. The thermal mechanical simulations show good results, the new absorber is in a safe range according to the design

criteria [4]. The maximum temperature, stress and strain are 307.8 °C, 159.8 MPa and 0.14%, respectively (Fig. 5). The maximum temperature because of the ID radiation equals 162.3 °C, at the upper wall of the opening.

Figure 6 shows the Integrated Crotch Absorber for ALBA manufactured by CINEL company [5] according with the ALBA specifications.

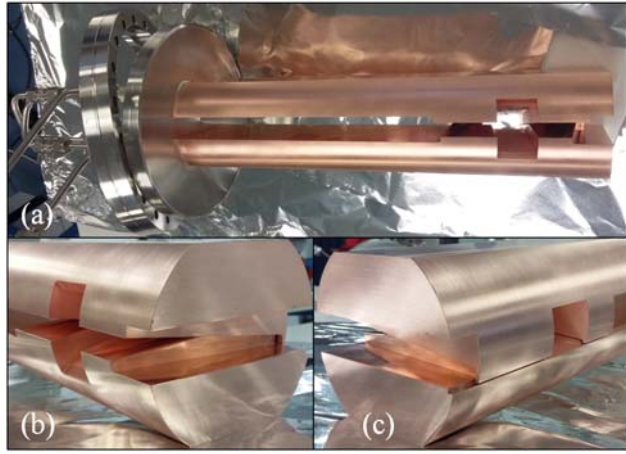


Figure 6: Integrated Crotch Absorber for LOREA. (a) The complete absorber. (b) Opening inlet reference. (c) Opening back reference.

CONCLUSIONS

Details of a non-conventional absorber at ALBA are presented. This new Glidcop Al-15 absorber is named Integrated Crotch Absorber because we combine two types of geometries: the conventional crotch absorber and the distributed type. Its optimization is based on geometrical aspects in order to have an optimal thermal mechanical behavior and also with the aim to capture the ID radiation reflected inside of the same absorber. The final design meets the thermal mechanical design criteria for the absorbers and reduces the effects of the ID photon reflection on the dipole vacuum chamber.

REFERENCES

- [1] S. Hermle *et al.*, “Layout of the absorbers for the synchrotron light source ANKA”, in *Proc. PAC99*, vol. 2, New York City, New York, USA, March-April 1999, pp.1360-1362.
- [2] M. Quispe *et al.*, “Study, Design and Optimization Analysis of the ALBA LOREA Dipole Vacuum Chamber and Crotch Absorbers Based on Finite Element Analysis”, in *Proc. MED-SI2016*, Barcelona, Spain, Sep. 2016, paper TUPE14, pp. 191–103, DOI: 10.18429/JACoW-MEDSI2016-TUPE14
- [3] SynRad, <https://molflow.web.cern.ch>.
- [4] E. Al-Dmour *et al.*, “The conceptual design and thermal analysis of ALBA crotch absorbers”, in *Proc. PAC07*, Albuquerque, NM, USA, June 2007, paper MOPAN065, pp. 299–301, DOI: 10.1109/PAC.2007.4440191.
- [5] CINEL, <https://www.cinel.com>.

HIGH RIGIDITY GIRDER SYSTEM FOR THE SIRIUS MACHINE

M. C. Rocha[†], A. L. Mesa, A. R. D. Rodrigues, F. Rodrigues, P. P. S. Freitas, R. T. Neuenschwander,
 R. J. Leão, T. Jasso, Brazilian Synchrotron Light Laboratory, Campinas, Brazil

Abstract

Sirius is a 4th generation synchrotron light source under construction in Brazil, with a bare emittance of 250 picometer rad, scheduled to have the first beam late this year. One of the most important aspects for this ultra-low emittance machine is the stability of the components, especially the magnets. This paper describes the main characteristics of the girder system, including the concrete pedestal, the levelling units, the girder itself, the clamping mechanism for the magnets and the measurements procedures. Each detail was considered in the design phase and the result is a high rigidity setup with a first horizontal mode close to 170 Hz.

INTRODUCTION

The Brazilian Synchrotron Light Laboratory – LNLS is currently installing the components of the new Brazilian light source (Sirius). This new machine will be a state-of-the-art synchrotron light source [1-2] with low emittance and capacity for 39 beamlines. First users are expected to 2019. For its proper operation, there are high demands in terms of stability of the storage ring components, especially the magnets. Their maximum vibration should not exceed 6 nm according to the specifications [3]. This tolerance implies that the whole building structure and the supports for the magnets should be designed accordingly.

When it comes to the decision as to where to install the storage ring magnets, the choice is usually to fix them on the slab, using intermediate support components such as bases, pedestals and girders. In most particle accelerators the solution is to fix concrete bases or metallic pedestals on the floor, followed by metallic girders that hold assemblies of magnets. Few studies propose girder-free magnet supports, notably [4].

To align the position of the components, levelling and positioning devices are used in-between pedestals and girders and in-between girders and magnets. For the Sirius supports, the concept of using metallic girders and concrete pedestals fixed to the slab is maintained. The main efforts were put into the design and manufacturing of the girders, although many innovations were applied to the concrete pedestals, the design of the levelling units and the fixation of the magnets on the girders. For the girder design, we built up on several girder designs, such as the Petra III [5], and optimized it in terms of rigidity.

One of the key issues for the Sirius building is its vibration characteristics, especially the special slab of the accelerators. Although this design and the civil construction details are of fundamental importance, a discussion about this is not within the scope of this paper. The intent of this work is to describe the main innovations and results related to

the high rigidity girder system for Sirius, including design, manufacturing and tests.

SYSTEM DESIGN, MANUFACTURING AND TESTS

To maintain the displacement of the magnets within 6 nm, the vibrations coming from the ground must be attenuated. To achieve this, the vibration spectrum from the environment should not match the natural frequencies of the supporting structure. The goal is, therefore, design the supporting structure to maximize the natural frequency of its first modes of vibration. Also, the structure should provide a significative damping for the environmental vibrations. In terms of geometry of the girders, we performed a Topology Optimization starting from preliminary boundary conditions based mainly on dimensional constraints. Figure 1 shows the result of this study and the resulting geometry based on the study.

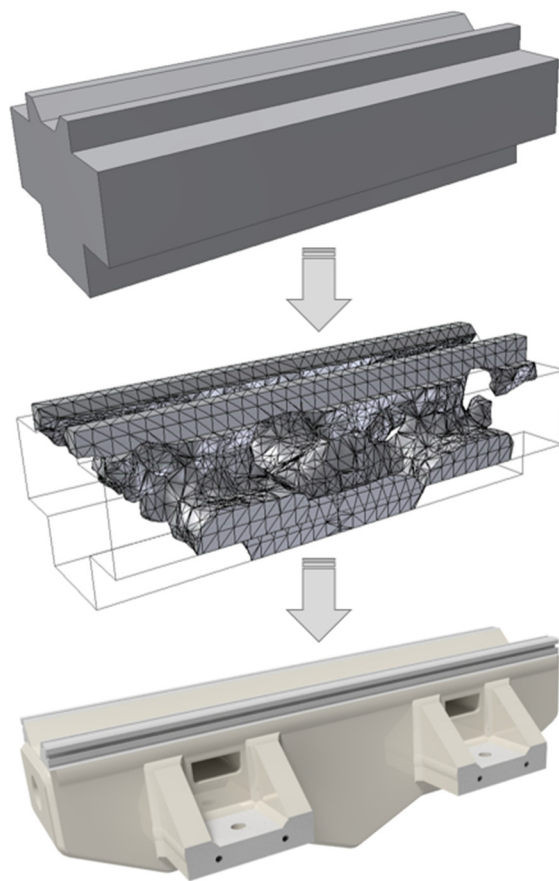


Figure 1: From the Topology Optimization to the final CAD model.

Finite Element Analyses – FEA shows that this “dolphin-shaped” design is indeed optimized in terms of vibration

[†] milton.rocha@lnls.br

modes. In terms of material, two prototypes were tested. Experimental modal analysis was performed to compare a casting iron girder (ASTM A159 G1800H) versus a welded steel girder (ASTM A36). The measurements have shown that, besides the higher natural frequencies, the damping of the welded version was relatively better (see Table 1).

Table 1: Comparison Between Two Versions of Girders

Girder Version	Natural frequency [Hz]		Damping ratio [%]			
			Excitation (1 μm)		Excitation (100 nm)	
	1 st mode	2 nd mode	1 st mode	2 nd mode	1 st mode	2 nd mode
Cast Iron	286.9	573.3	0.16	0.14	0.20	0.14
A36 Steel	511.8	826.1	0.19	0.09	0.26	0.13

The concrete base was obtained by using state-of-the-art in concrete technology and differentiated techniques and tools. The process required a technological development including new manufacturing process, dimensional controls and results to reach the production of precast concrete. The initial requirements demanded by the Sirius project involved the development of an Ultra High Performance Concrete (UHPC) that must achieve a tangent elasticity modulus of 60 GPa and compressive strength above 100 MPa. The parts should be produced with a minimum dimensional precision of 2 mm in all verified dimensions, including flatness, parallelism and perpendicularity between the plan faces. The need for this unusual dimensional check in the current precast factories and processes required the use of technology and measurement equipment of use in the automotive and aeronautical industry – laser tracker.

The development of the concrete counted on techniques of packaging, use of several aggregates and modern chemical additives of concrete. The strength of the concrete was verified through compression test and its modulus of elasticity through a pulsed ultrasonic test. The forms, executed exclusively for the project, underwent dimensional validation in their execution, assembly and during the production process of the bases.

The resulting concrete achieved compressive strengths above 120 MPa and tangent elasticity modulus above 57 GPa. Several fixation methods were tested for the concrete bases on the special slab. The chosen solution is to grout the base to the floor using a high strength bi-component Epoxy resin. For levelling the girders, special levelling wedges were developed. Each device should have a maximum deformation of 0.016 mm when a 50 kN load is applied. This parameter was demonstrated experimentally for the prototypes and a 100 % inspection process was conducted for all 1000 units produced. Approximately 60 % of the levelling units had a maximum deformation below

0.010 mm for the applied load. Tests indicated that commercial units presented a three times larger deformation under the same load.

To increased stiffness, the magnets will be screwed directly on top of girders, using transversal and longitudinal adjustment devices only. This tolerance-based approach for assembly and alignment guarantees a better result in terms of vibration, both because the weak links represented by levelling devices below the magnets are absent and because this design allows the centre of mass from the assembly to be lowered. This compromise between stability and alignment issues demands high-quality magnets and girders in terms of geometrical and dimensional tolerances. Vibration measurements for a complete prototype setup show an actual result of 168 Hz for the first horizontal mode and 270 Hz for the first vertical mode (refer to Figure 2).

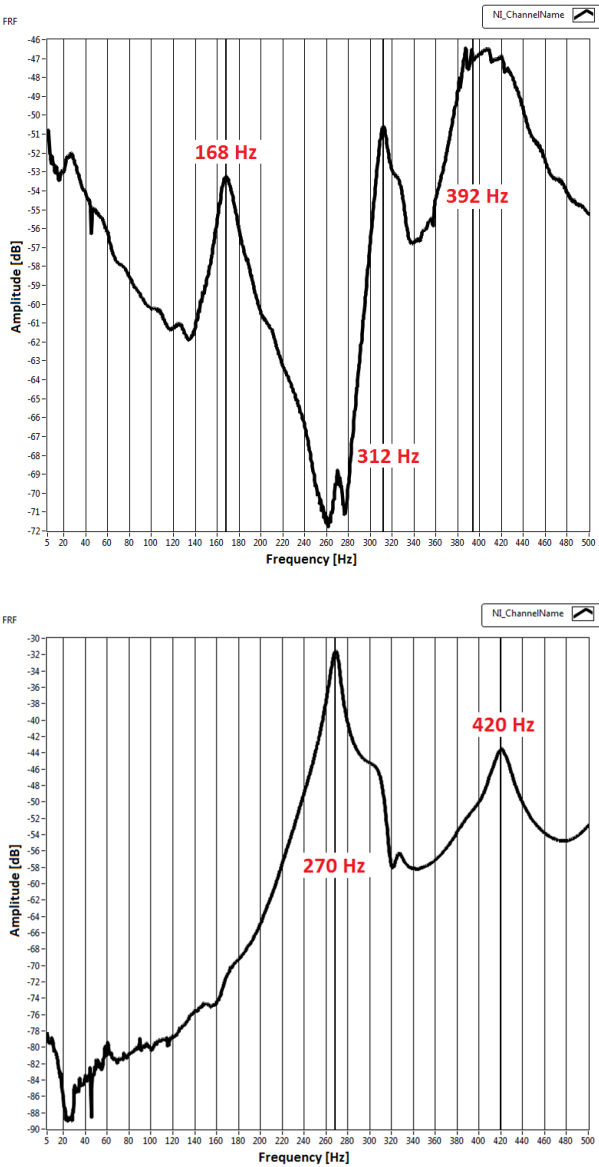


Figure 2: Experimental modal analysis of the complete assembly, results for the horizontal modes (top) and vertical modes (bottom).

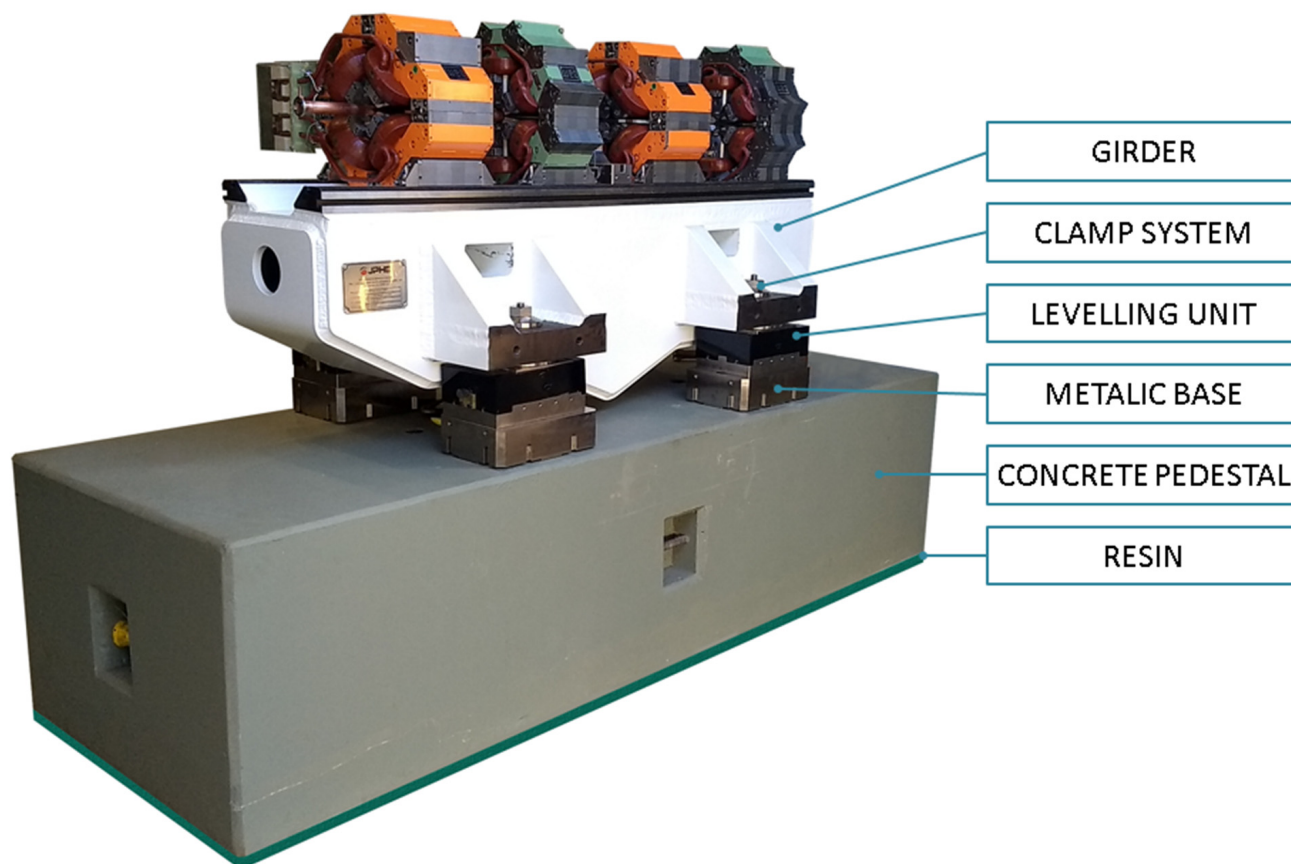


Figure 3: A complete assembly of the Sirius high rigidity girder system.

DISCUSSION AND CONCLUSIONS

The adopted vibration control is passive, that is, there is no active attenuation such as the use of piezo actuators studied for the TPS light source [6].

The so-called Sirius high rigidity girder system achieved natural frequencies outside the common and measured spectrum of vibration of the surrounding environment. The system has the potential to allow for a very stable electron beam, contributing to the success of the Sirius light source. The complete mechanical system can be seen in Figure 3.

We conclude that the Sirius magnets supporting system achieved the stiffness required for the good operation of the new light source, from the point-of-view of vibration stability. Moreover, the girder system presents natural frequencies results that stand-out from the current state-of-the-art. Reported girder systems resonances do not surpass the 120 Hz limit, including modern machines [5; 7]. This comparison is still valid if it is normalized for girder mass. The Sirius design utilizes smaller and lighter girders and magnets. This design decision contributes for the high natural frequencies, and represents another improvement in terms of design.

ACKNOWLEDGMENTS

The authors acknowledge the help from the Sirius suppliers Leonardi, Toyo Matic, JPHE and WEG. The support from the several LNLS groups involved with this project is also very much appreciated.

REFERENCES

- [1] Lin Liu, Natalia Milas, Afonso H. C. Mukai, Ximenes R. Resende, and Fernando H. de Sá, "The Sirius Project", in *J. Synchrotron Rad.*, vol. 21, 2014, pp. 904–911.
- [2] R.T. Neuenschwander, L. Liu, S.R. Marques, A.R.D. Rodrigues, and R.M. Seraphim, "Engineering challenges of future light sources", in *Proc. 6th International Particle Accelerator Conference (IPAC'15)*, Richmond, Virginia, United States, May 2015, paper TUXC2.
- [3] LNLS, https://wiki-sirius.lnls.br/mediawiki/index.php/Machine:Storage_Ring
- [4] S. Sharma, "A girder-free magnet support system design", in *Proc. of MEDSI*, Barcelona, Spain, 2016, paper TUPE32.
- [5] M. Schlösser, "The PETRA III Girder-Concept", in *Proc. of the 9th International Workshop on Accelerator Alignment (IWAA)*, Menlo Park, California, United States, September 2006.
- [6] T.C. Tseng *et al.*, "Preliminary active vibration elimination study of the TPS girder system", in *Proc. of MEDSI16*, Barcelona, Spain, 2016, paper MOPE11.
- [7] W. Haijing *et al.*, "Overall design of magnet girder system for heps-1f", in *Proc. of IPAC16*, Busan, Korea, 2016, paper WEPMR047.

A NOTE OF THERMAL ANALYSIS IN SYNCHROTRON RADIATION ACCELERATOR ENGINEERING

I. C. Sheng[†], National Synchrotron Radiation Research Center (NSRRC),
 3007 Hsinchu, Taiwan, R.O. C.

Abstract

Thermal and thermomechanical analysis is one of the key process while designing accelerator components that may subject to synchrotron radiation heating. Even some closed-form solutions are available, and yet as to complex geometry numerical analysis such as finite element method (FEM) is commonly used to obtain the result. However due to its complexity of density distribution of the heat load, implementing such boundary conditions in the finite element method (FEM) model is relatively tedious.

In this report we provide a simplified, practical and more conservative method to apply heat load both for bending magnet and insertion device. In addition, a general purpose synchrotron radiation heating numerical modelling is also introduced, and a simple FEM model with EPU power heat load is also compared

INTRODUCTIONS

As to synchrotron accelerator radiation heat load issue, typically when it comes to analysing the designs of crotch absorber, fixed masks, photon stoppers..., etc., one finds that bending magnet (BM) and insertion device (ID) are two major heat sources. The synchrotron radiation (SR) is primary in Gaussian distribution in 1D or 2D. Unless one can compile embedded programming in the FEM tool (such as ANSYS), manually applying such non-constant power density on the nodes in the FEM model is a tedious work. On the other hand, the total heat flux input may be underestimated due to human error.

Due to high speed computer capability nowadays, we find that FEM modelling for this type of analysis, during material assignment element meshing as well as solving process are fairly straightforward. Instead, applying synchrotron radiation heat load distribution is the most time-consuming task among the entire modelling process. To speed up this process, we introduce two methodologies, a simplified and a realistic model for the analysis.

SYNCHROTRON RADIATION DISTRIBUTIONS

Bending Magnet

The power distribution function for the bending magnet can be found in [1]:

$$q \left[\frac{Kw}{mrad^2} \right] = 5.425E[GeV]B[T]I[MA]f(\gamma\varphi) = q_o f(\gamma\varphi) \quad (1)$$

Where

$$f(\gamma\varphi) = \frac{1}{(1+\gamma^2\varphi^2)^{5/2}} \left(1 + \frac{5}{7} \frac{\gamma^2\varphi^2}{(1+\gamma^2\varphi^2)} \right) \quad (2)$$

is the shape function of bending magnet, $\gamma = 1957E$ is relativistic energy and φ is the vertical opening angle. Kim [2] suggested that the shape function in equation (2) can be approximated as Gaussian distribution as follows:

$$f(\gamma\varphi) = \exp \left(-\frac{\varphi^2}{2(\sigma_o/\gamma)^2} \right) \quad (3)$$

Where σ_o is the standard deviation and is found to be

$$\sigma_o = \frac{32}{21\sqrt{2\pi}} \approx 0.608 \quad (4)$$

To simplify the FEM modelling, we can approximate the above shape function to be a Heaviside step function

$$q(\varphi) = q_o \left(H\left(\varphi - \frac{\sigma_c}{\gamma}\right) - H\left(\varphi + \frac{\sigma_c}{\gamma}\right) \right)$$

As suggested in [3], the equilibrium beam half beam size σ_c is given as

$$\sigma_c = 0.608\sqrt{\frac{\pi}{2}} \approx 0.762 \quad (5)$$

This assumption is valid because in general, the bending magnet beam size along vertical direction (Gaussian profile) is much smaller than that of the designed body itself. The benefit of utilizing this simplified power distribution are the following:

- Step function distribution gives more concentrated power distribution, which leads to more conservative thermal result.
- Easy to apply power to the FEM model. Only few nodes have to be meshed on the heating surface. This dramatically reduce the modelling time.

Insertion Device

As was given by [4], power density of elliptical polarized undulator is

$$q[w/mrad^2] = 0.0844E^4[GeV]I[A] \frac{L[m]}{\lambda_o^2[m]} \times f(k_x, k_y, \theta_x, \theta_y) \quad (6)$$

Where $f(k_x, k_y, \theta_x, \theta_y)$ is the shape function defined as

[†] email address shengic@nsrrc.org.tw

$$f(k_x, k_y, \theta_x, \theta_y) = \int_{-\pi}^{\pi} \left[\frac{(k_x^2 \cos^2 \alpha + k_y^2 \sin^2 \alpha)}{(1 + (k_y \sin \alpha - \gamma \theta_x)^2 + (k_x \cos \alpha - \gamma \theta_y)^2)^3} - \frac{[(k_y^2 - k_x^2) \sin 2\alpha - 2k_y \gamma \theta_x \cos \alpha + 2k_x \gamma \theta_y \sin \alpha]^2}{(1 + (k_y \sin \alpha - \gamma \theta_x)^2 + (k_x \cos \alpha - \gamma \theta_y)^2)^5} \right] d\alpha \quad (7)$$

As you can see, the generalized power distribution for ID is quite complicated to implement into FEM as boundary conditions. Even Sheng [5] has proved that it is not only possible to approximate above shape function into Gaussian type explicit function, but also a constant peak power distribution ones. The Gaussian type shape function $f(k_x, k_y, \theta_x, \theta_y)$ in (7) is found to be

$$\exp \left(\frac{k_x^2 k_y^2}{k_x^2 \cos^2 \theta + k_y^2 \sin^2 \theta} - \frac{1}{(2\beta - \beta^2)^2} \left(\sqrt{\frac{\theta_x^2}{\left(\frac{k_y}{\gamma}\right)^2} + \frac{\theta_y^2}{\left(\frac{k_x}{\gamma}\right)^2} - 1} \right)^2 \right) \quad (8)$$

Where θ is the polar angle in $\theta_x - \theta_y$ plane. The constant power distribution is in an elliptical donut shape $\frac{2\sigma_c}{\gamma}$.

with rim width γ . Note that its area is given as [5]

$$Area = \pi \left(\left(\frac{k_y}{\gamma} + \frac{\sigma_c}{\gamma} \right) \left(\frac{k_x}{\gamma} + \frac{\sigma_c}{\gamma} \right) - \left(\frac{k_y}{\gamma} - \frac{\sigma_c}{\gamma} \right) \left(\frac{k_x}{\gamma} - \frac{\sigma_c}{\gamma} \right) \right) = \frac{2\pi(k_x + k_y)\sigma_c}{\gamma^2} \quad (9)$$

And the effective half beam width σ_c is found to be

$$\sigma_c \approx 0.762 \frac{(\beta^2 + 1)}{(\beta + 1)}, \quad \beta = \begin{cases} \frac{k_x}{k_y} & \text{when } k_y > k_x \\ \frac{k_y}{k_x} & \text{when } k_x > k_y \end{cases} \quad (10)$$

It is interesting to note that for linear undulator ($k_y = 0$) or helical undulator ($k_x = k_y$), σ_c will be exactly equal to that for bending magnet in (8).

An analytical comparison between Gaussian type power distribution and step function power distribution has been studied in [3].

IMPLEMENTATION OF ACTUAL SR POWER DISTRIBUTION IN FEM

We take Solidworks® and ANSYS® as example, since these two CAD and FEM tools are the most well-known software packages available. Solidworks is used as solid modelling tool to construct geometry and mesh, whereas ANSYS is for the FEM analysis.

In Solidworks, after solid model is built and meshed, we apply dummy heat load on the heating surface element where SR power strikes. Then the meshed model is exported as an ANSYS input file.

By default, the exported ANSYS thermal model file using SOLID87 3-D 10-Node Tetrahedral Thermal Solid element [6], there are specific surface nodes and heating surface number. With these geometry information, one can come up with an intermediate process (a script or a computer program) to read the geometry file (nodal coordinate, nodal number, element number, boundary conditions...,

etc.) exported from Solidworks, the incident angle θ_{inc} is calculated for each surface load element by applying inner product SR source unit vector and unit normal vector \vec{n} of the heating surface.

To determine the corresponding θ_x and θ_y of an arbitrary centroid coordinate of the triangular surface element (x, y, z) (determined by averaging out three vertex coordinates of the heating surface element), we simplify the geometry by, for instance, if the source coordinate of SR source is at $(x_o, 0, z_o)$ and it strikes at corresponding surface coordinate $(0, 0, 0)$, then

$$\begin{cases} \theta_x \approx \left(\frac{(y - y_o) \sqrt{x_o^2 + z_o^2}}{(x - x_o)x_o + (z - z_o)z_o} \right) \\ \theta_y \approx \left(\frac{-x_o z + x z_o}{(x - x_o)x_o + (z - z_o)z_o} \right) \end{cases} \quad (11)$$

And the power density applied on that heating surface will be

$$q[w/l^2] = \frac{0.0844 E^4 [GeV] I [A] L [m]}{l^2 10^{-6} \lambda_o^2 [m]} \sin(\theta_{inc}) \times f(k_x, k_y, \theta_x, \theta_y) \quad (12)$$

where l is the distance from source to the central coordinate of the heating surface (x, y, z) . Figure 1 illustrates the geometrical relationship.

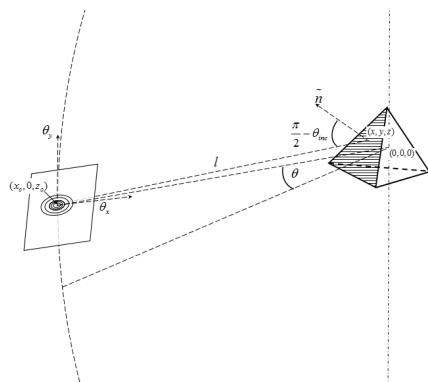


Figure 1: Illustration of one finite element heating surface element vs. heat source.

CASE STUDY

A typical EPU power thermal simulation is carried out and compared with step function type and Gaussian power distribution. As shown in Table 1.

Table 1: Simulation Parameters for EPU

Name	Sym-bol	Value
Beam energy	E	3[GeV]
Beam current	I	500[mA]
Distance from source	D	10m
Period	λ_o	4.8[cm]
Number of period	N	67
Horizontal deflection parameter	k_x	2
Vertical deflection parameter	k_y	4
Inclined angle	θ	8°

A simple FEM model is used as a comparison case, the model is a 160[mm]×25[mm] copper block with 5[mm] water channel on the other side. The heating surface is flat and has 8° inclined w.r.t. the ID source. For step function power density, as shown in Figure 2. The maximum temperature rise is found to be 252 °C

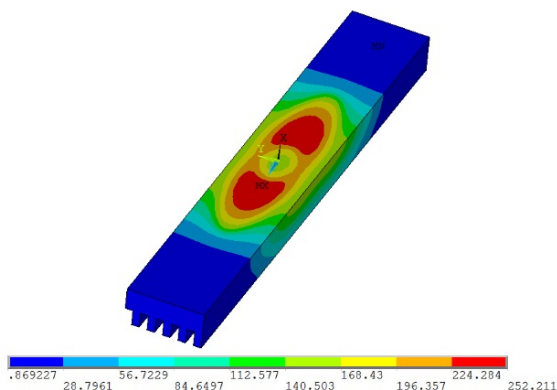


Figure 2: Temperature rise of the model with step function power distribution.

with the same model, as is shown in Figure 3, real power distribution using (12) is implemented. The maximum temperature rise is 212 °C. These two maximum temperature results agree with our predictions that the temperature heated by step function power distribution in general is higher than that of Gaussian type.

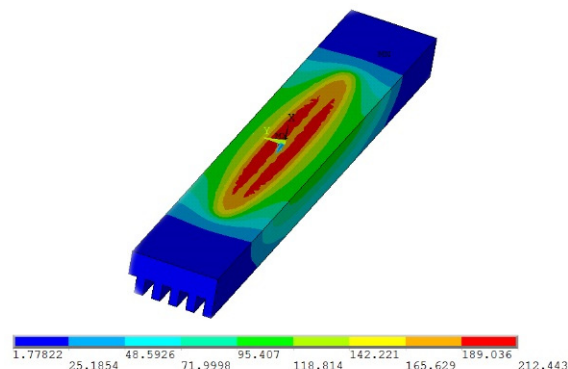


Figure 3: Temperature rise of the model with real EPU Gaussian power distribution.

DISCUSSION AND CONCLUSION

A simplified step function power heating is developed both for bending magnet and insertion device. Simplified power distribution is much more efficient to implement for FEM analysis, and yet it provides more conservative temperature result.

REFERENCES

- [1] J. D. Jackson, "Classical Electrodynamics," 2nd Edition, John Wiley & Sons, New York, 1975.
- [2] S. Kim, "Distribution of Synchrotron Radiation from a Bending Magnet", Argonne National Laboratory, Chicago, November 1988.
- [3] A. Sheng, "Note on Some Thermal Analytical Solutions in Accelerator Engineering," in *Proc. PAC'09*, Vancouver, Canada, May 2009, paper TU6RFP060, pp. 1687-1689.
- [4] R. P. Walker, "Insertion devices: undulators and wigglers", CAS - CERN Accelerator School: Synchrotron Radiation and Free Electron Lasers, Grenoble, France, 22 - 27 Apr. 1996, pp.129-190, (CERN-1998-004), doi:10.5170/CERN-1998-004.129
- [5] I. C. Sheng and C. K. Kuan, "Power Density Distribution and Associated Thermal Analysis of an Elliptical Polarizing Undulator," *Nuclear Instruments and Methods in Physics Research Section A Accelerators Spectrometers Detectors and Associated Equipment*, April 2011.
- [6] R. M. Pidaparti, *Engineering Finite Element Analysis*, Morgan & Claypool Publishers, 2017.

NSLS-II SITE VIBRATION STUDIES TO CHARACTERIZE BEAMLINE STABILITY

C. Spataro, F. Lincoln, S. Sharma, Brookhaven National Laboratory, Upton, NY, USA

Abstract

High performance goals of NSLS-II require stringent mechanical stability of its instruments such as BPMs, slits, mirrors, monochromators, and detectors. Mechanical stability of these components can be compromised by site-wide as well as local vibration sources (pumps, compressors, etc.). Several vibration studies have been performed at NSLS-II at the request of beamline users. This paper presents the results of these studies highlighting sources of vibration and mitigation strategies.

INTRODUCTION

Modern light sources, such as the NSLS-II at Brookhaven National Laboratory are designed to generate an electron beam with very low emittance and small beam size which requires a high degree of mechanical stability of the girder assembly and a low ground vibration level. The ground motion below 4 Hz is assumed to be correlated over the length of the storage ring cell (25m), and motion above 50 Hz is expected to be negligible.

MOTIVATION FOR MEASUREMENTS

Be it long (DC) or short term (AC), stability directly affects the operation and performance of NSLS-II. The beamlines also require precision mechanical and optical stability in order to meet their specifications and performance goals. At the request of the beamline users, a number of vibration studies were carried out to determine the sources of vibration instabilities that were affecting their operations.

SOURCES OF INSTABILITIES

Vibration sources can be broken down into four categories: natural, cultural, electrical and mechanical. Examples of natural sources are lunar tides, solar tides, earthquakes, wind, barometric pressure, and seasonal changes.

Heavy truck and traffic on the local expressway contribute greatly to the cultural instabilities. Mechanical vibration sources include AC handlers, water flow, liquid helium induced vibrations, and vacuum pumps. Electrical sources include power supply ripple as well as 60 Hz noise from power supplies, etc.

FLOOR MOTION OVER TIME

In October of 2012 vibration data was taken on the NSLS-II floor 2-ID SIX beamline every thirty minutes over a number of days. Measurements of the ground motion in the NSLS-II ring were made on a grouted floor plate as well as on a girder flange in cell 7 inside the tunnel. The results of the integrated displacement vs time from 2-100 Hz can be seen in Figure 1 below.

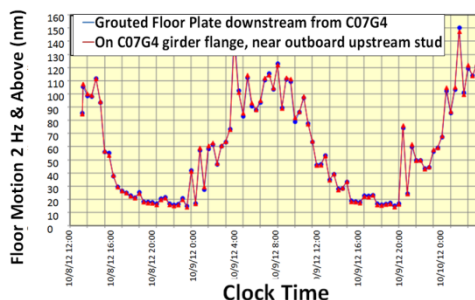


Figure 1: Vertical RMS Displacement vs Time.

The integrated displacement is periodic over a twenty-four hour period. The maximum day-time amplitude was about five times that of the night time amplitude. This was quite a surprise. The day time vertical RMS displacement from 2-100 Hz were upwards of 120 nm at mid-day while the night amplitudes dropped to 15-20 nm. Vibration measurements were taken over the next few months and were found to be very repeatable, though the weekend displacements measurements were slightly lower than the weekday and were also repeatable. The periodic nature of the vibration levels suggested the nearby Long Island Expressway which was later confirmed with measurements as the source of the vibrations.

11-BM VIBRATION MEASUREMENTS

Vibration studies have been performed over the last several years at bequest of the beamline users. The 11-BM (Bending Magnet beamline) was seeing a 200 μ m fluctuation in beam position at a rate of 1 Hz during operations. Below is Figure 2 that shows the layout of the beamline consisting of a number of optical benches, a sample chamber, two crys-tals and a single monochromator.

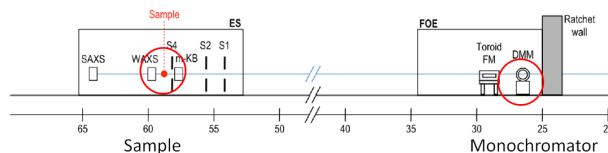
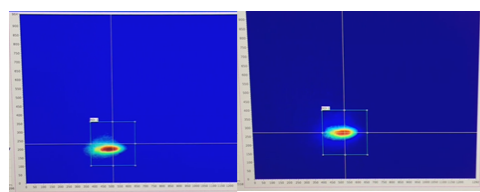


Figure 2: 11-BM layout

Vibration measurements on the floor as well as along the entire beamline on the granite tables at beam height did not find the source of the 1 Hz signal. After a thorough inspection of the beamline, it was found that the spring-loaded screws for the kinematic mount for the 1st crystal were loose. [1] Tightening of these screws resulted in the dampening of the vertical motion as shown in Figure 3.



Before
 After
 (Photos taken from video - courtesy of Masafumi Fukuto)

Figure 3: 200 μm position error and result of tightening spring-loaded screws.

2-ID SIX BEAMLINE

Prior to installation of the beamline, the SIX (Soft Inelastic X-ray Scattering) group requested a continuous study of the vertical signatures of the future detector and sample locations for a period of two weeks. Seismometers were placed 14 M apart and vibration data was taken over the two week period. Below is a graph of the displacement vs Time of the sample and detector locations. The periodic nature of the vibrations from the nearby LIE can be seen as well as a few large spikes due to the freight train activity in the early morning hours.

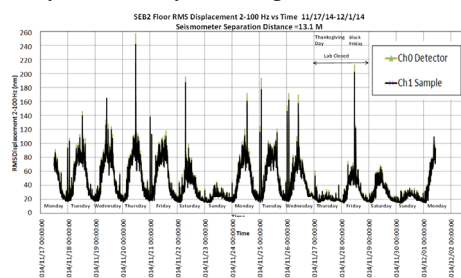


Figure 4: Vertical Displacement vs Time.

The vertical displacement varied from 15 to 100 nm (not counting vibration spikes) (Figure 4). The tight (400 nm) vertical stability tolerance across the 2.5 M vertical motion range to track energy led to a complete re-design of the experiment. (Figure 5).

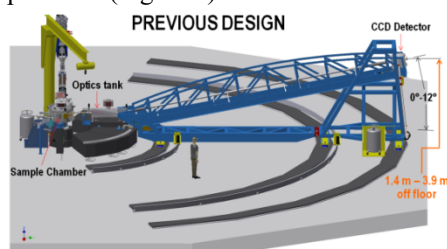
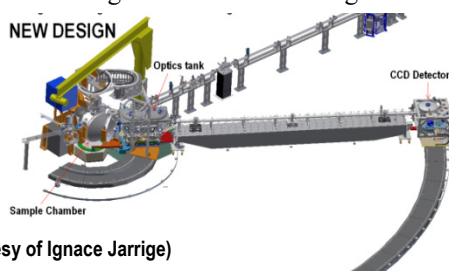


Figure 5: Previous Design.



Courtesy of Ignace Jarrige)

Figure 6: Re-design.

In this new design (Figure 6), a vertically reflecting mirror was added in the spectrometer optics tank to produce a constant output at all energies with the new detector height being only 1 M off the floor. [2]

3-ID HXN BEAMLINE

A vibration study was carried out in the satellite building that houses the HXN 3-ID beamline. The HXN Satellite Building (Figure 7) is a state of the art building designed to meet stringent technical requirements for vibration isolation and temperature stability, which are critical to operating the Hard X-ray Nanoprobe Beamline. [3]



Figure 7: HXN Satellite building.

To that end, the hutch was built with a 1 M thick concrete floor as opposed to the 27" floor of the storage ring and the 15" thick experimental floor. To characterize the hutch and experimental floors, a series of correlation measurements were made as well as a vibration study over a number of days. Correlation measurements were made by measuring the vibration levels with two seismometers side by side, then increasing the distance between them after each measurement. These were done up to 11 M separation.

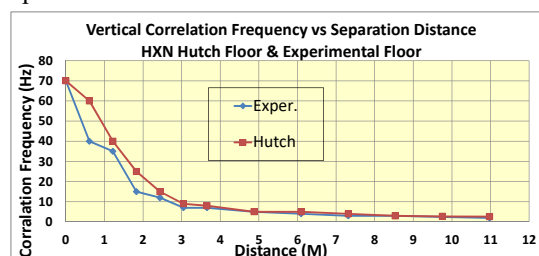


Figure 8: Correlation frequency vs separation distance.

The correlation study (see Fig. 8) shows that for short distances – up to 4.8 M, vertical correlation is slightly better on the hutch floor than the experimental floor. From 4.8 M to 11 M, the frequencies at which the correlation remains ‘good’ ($> 90\%$), are about the same. The ratio of the relative displacement/absolute displacement vs separation distance (Figure 9) shows a better relative displacement for the hutch floor up to 8.53 M due to the flatter response of the hutch floor above the correlation frequency. At 11 M, the responses of the floors are about the same (figure 10).

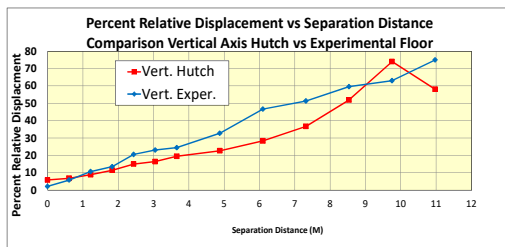


Figure 9: Ratio Rel./Abs. vertical displacement vs separation distance.

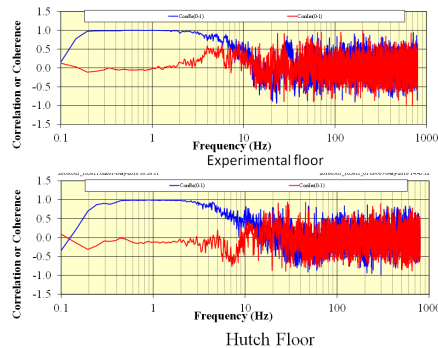


Figure 10: Vertical Correlation at a 8.53 M separation.

The horizontal correlation study shows that for all separation distances, the horizontal correlation is slightly better on the hutch floor than the experimental floor. (Figure 11).

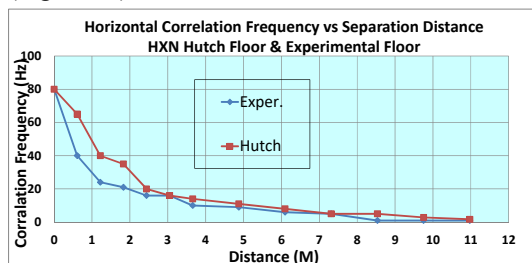


Figure 11: Correlation frequency vs separation distance

Looking at the relative displacement ratio (Figure 12), the hutch floor is better at the longer distances. At a distance of 8.53M, (Figure 13), the correlation for the hutch floor is still good at 5 Hz while that of the experimental floor falls below 1 Hz which is the lower bandwidth of the seismometer.

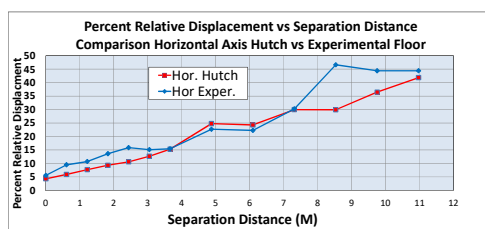


Figure 12: Ratio Relative/Absolute horizontal displacement vs separation distance.

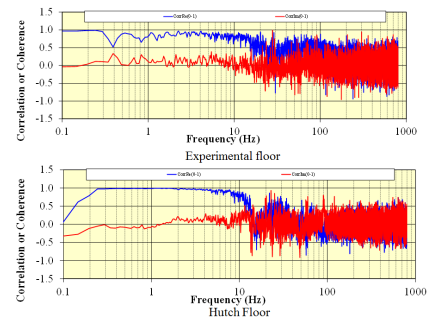


Figure 13: Horizontal correlation at 8.53 M separation.

The absolute RMS displacement maximums are slightly better on the hutch floor than the experimental floor , 55 vs 80 nm horizontally and 70 vs 90 vertically. See figures 14 & 15 below. The experimental floor minimums are slightly different for horizontal and vertical but for the hutch floor they are about the same.

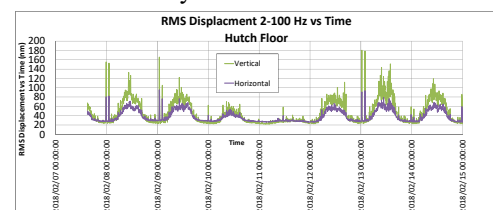


Figure 14: Hutch Floor Displacement vs Time.

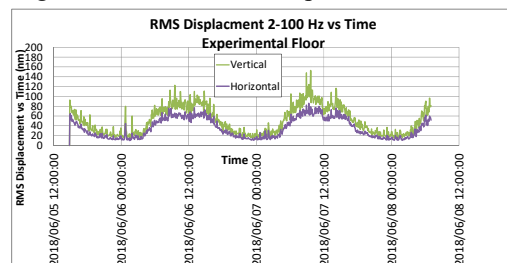


Figure 15: Experimental floor displacement vs time.

SUMMARY

Vibration studies have been used successfully to investigate the various sources of instabilities in the operation of the NSLS-II beamlines and to find the cause of these instabilities. In the one case, the vibration study led to a re-design of the experiment prior to installation, thereby saving both time and money in a costly redesign after the fact. The comparison of the experimental floor and the thickened HXN floor show that the absolute displacements are slightly less for the HXN floor. Measurements show that the vertical response of the floors are about the same while HXN floor shows a much better horizontal response at longer distances than the experimental floor.

REFERENCES

- [1] Private communication with M. Fukumo
- [2] Private communication with I. Jarrige
- [3] Preliminary Design Report for Hard X-Ray Nanoprobe (HXN) Beamline, LT-C-XFD-HXN-PDR-001, June 2011.

ENERGY EFFICIENT AIR-CONDITIONING SYSTEM DESIGN

Z. D. Tsai[†], W. S. Chan, C. S. Chen, C. Y. Liu, Y. C. Chung and Y. Y. Cheng, National Synchrotron Radiation Research Center, 30076 Hsinchu, Taiwan

Abstract

At the Taiwan Light Source (TLS) and Taiwan Photon Source (TPS), several studies related to energy savings in air-conditioning systems are underway, where heat recovery has been considered for laboratory applications. The performance of a run-around coil has demonstrated that heat recovery plays an important role in energy conservation. Based on this design of an air handling unit (AHU), we enhance this model by combining it with enthalpy control for seasonal changes. Here, we construct a new AHU to verify the practical impact of energy usage. The improvements show that both mechanisms can be achieved simultaneously.

INTRODUCTION

In general, thermal waste can be treated by circulating deionized water (DIW) and by air conditioning (AC). The main cooling water system at the TPS includes the cooling tower, chilled water, hot water, de-ionized water and heating, ventilation and air-conditioning (HVAC) systems. The air-handling units (AHU) located at the inner and outer rings provide very stable cooling air for the storage-ring tunnel, CIA, experimental hall and Linac area. The amount of HVAC systems must be well optimized so that the accelerator would be the least subject to thermal waste [1]. Besides the requirement to be stable, the utility system is designed carefully with a good satisfactory energy-efficiency ratio (EER) and coefficient of performance (COP). In general, a HVAC system always consumes energy for processes like dehumidification and reheating to maintain a constant temperature and humidity.

Since the utility system is essentially an energy wasting system, a preliminary study for energy efficiency in the HVAC system with heat moving and moisture recovery systems has been started by reviewing the designs in more detail [2]. Here, we address mainly specific designs with three flow piping schemes to verify energy efficiency. In addition, the HVAC system also should be equipped with enthalpy controls to deal with the return and fresh air damper. The control philosophy should have the goal to decrease usage of chilled water in the cooling coils.

ENERGY EFFICIENT AIR-CONDITIONING SYSTEM STRUCTURE

The main components of an AHU include dampers, supply fans, filters, humidifiers, dehumidifiers, heating and cooling coils, ducts and various sensors. We add a pre-cooling coil before the cooling coil, pre-heating coil before the heating coil and the corresponding flow piping.

The proposed AHU with extra two coils integrate into three modes, including a traditional mode, a cascade mode and a run-around mode to determine the performance among different flow methods.

The traditional mode as illustrated in Fig. 1a includes only cooling and heating coils, which serve as the basis of power usage. To maintain a suitable room humidity, the supply air temperature is controlled in a cooling coil to 12 °C, which is the dew-point temperature. To reach a final precise temperature control, the air temperature supplied by a heating coil must be maintained to a constant value of 22±0.05 °C.

Based on the traditional mode, pre-cooling and pre-heating coils are inserted and the water piping of the first three coils is also re-arranged to form a cascade mode as shown in Fig. 1b. The cascade mode has four coils including pre-cooling, cooling, pre-heating and heating coils. In principle, the larger the amount of heat transferred from the pre-cooling to the pre-heating coils by the circulating water, the greater is the required surface area of the coils and the larger is the required circulating water volume.

The run-around mode uses the same coils as the cascade mode with a circulating pump added as shown in Fig. 1c. The heat withdrawn from the warm air along the way to the pre-cooling coils is transferred by the circulating water to the pre-heating coils. The pre-heating coils then return the sensible heat to the cold air leaving the cooling coils and any heat added to the flowing air by the pre-heating coils is then exactly equal to the heat removed by the pre-cooling coils. The required refrigerating capacity thus decreases in the run-around cycle to reheat the cold air supply. In this arrangement, the required heating capacity is reduced as well.

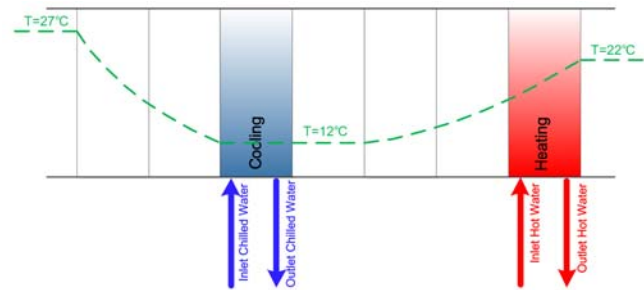


Figure 1a: Scheme of an AHU system operated in the traditional mode.

[†] zdtsai@nsrrc.org.tw

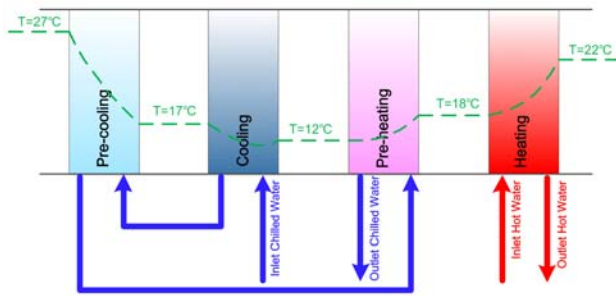


Figure 1b: Scheme of an AHU system operated in the cascade mode.

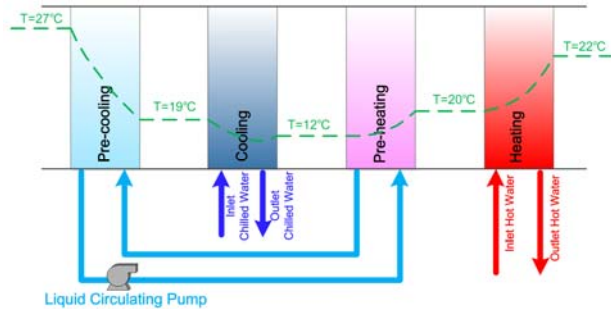


Figure 1c: Scheme of an AHU system operated in the run-around mode.

PERFORMANCE COMPARISON OF RUN-AROUND HEAT AND MOISTURE RECOVERY SYSTEMS

In traditional mode, the return air at 27 °C flows through the cooling coils and will be well controlled at the dew point of 12 °C. Thereafter, the cold air flows through the heating coils and is also well controlled to 22 ± 0.05 °C. According to this mode, the cooling and heating will operate at full or 100% power usage as shown in Fig. 2a.

In the cascade mode, inserting extra pre-cooling and pre-heating coils form a cascade of coils. The pre-cooling coils absorbs heat from the return air and the absorbed thermal energy is transferred to the pre-heating coils, where the cold supply air is heated. This design requires only 68% of cooling load and 44% heating load as shown in Fig. 2b. The chilled water flow is determined by the cooling coils, according to the dew point, which affects the amount of heat recovery related to the pre-heating coils. This uncontrollable heat source can lead to an overheated air supply, especially in summer.

Therefore, we insert a circulation pump to isolate the heat recovery, cooling and heating mechanisms. The pre-cooling and pre-heating coils having independent run-around water piping reduce cooling energy because of the lower air temperature entering the cooling coil. Water is circulated continuously through two coils. This system reduces the need for a dehumidifying and reheating source and thereby decrease system operating costs. As shown in Fig. 2c, this design involves a cooling load of only 71% and a 25% heating load.

The actual power usage as described in Table 1 is similar between cascade mode and run-around mode. However, the run-around mode includes more tuning mechanisms to adapt seasonal changes. The water circulating pump with an inverter can distribute thermal energy among four coils to achieve energy savings. The inverter can be tuned to an optimal working point of 18 Hz instead of 60 Hz as shown in Fig. 3.

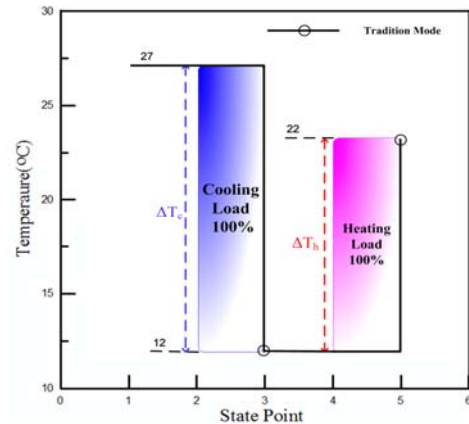


Figure 2a: Traditional mode power usage of an AHU system.

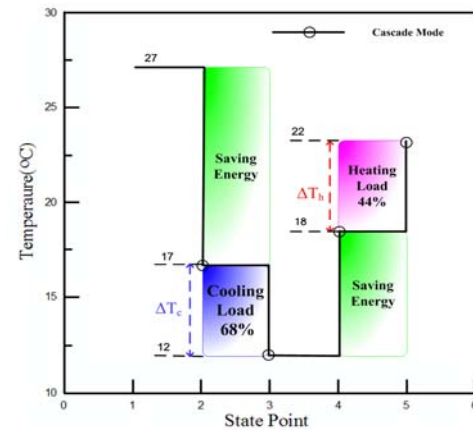


Figure 2b: Cascade mode power usage of an AHU system.

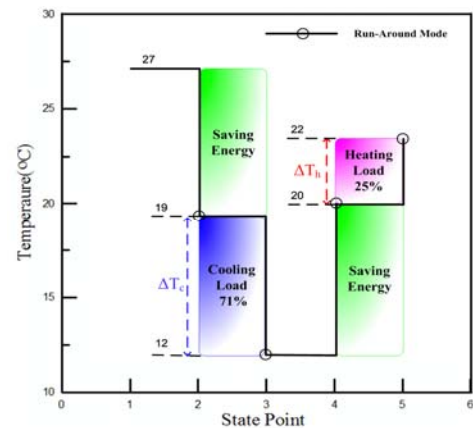


Figure 2c: Run-around mode power usage of an AHU system.

Table 1: The Comparison of Power Usage Among the Three Modes

	Traditional Mode	Cascade Mode	Run-around Mode
Chilled Water	98.6 kW	66.9 kW	70.4 kW
Hot Water	28.2 kW	12.3 kW	7.1 kW
Pump	0 kW	0 kW	1.4 kW
Power Usage	126.8 kW	79.2 kW	78.9 kW
Power Usage	100%	62%	62%

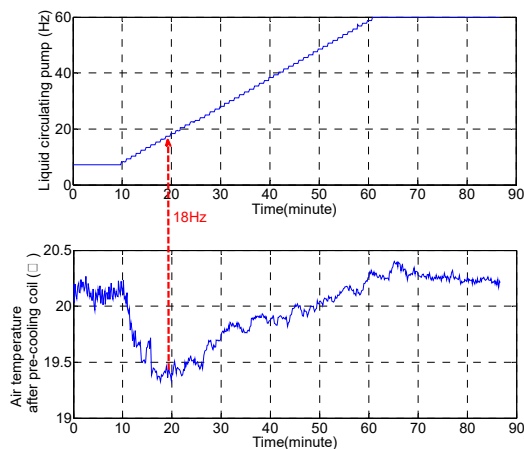


Figure 3: Temperature difference along with pump tuning with an inverter.

ENTHALPY CONTROL FOR SEASONAL CHANGES

We use enthalpy control for seasonal changes. In general, the air damper of an AHU can be controlled with a 10% opening to introduce fresh air. When the fresh air temperature is lower than the return air temperature, we open the damper more to save energy. According to the psychrometric chart, as shown in Fig. 4, the damper opening, can be controlled more efficiently based on enthalpy than temperature. Operating in zone A (Fig. 4) at a lower dry temperature and higher humidity leads to a higher load for dehumidification, while operating in zone C at a lower dry temperature and humidity can decrease the required cooling capacity. Therefore, we regulate the damper open settings for the fresh and return air by a new control logic to optimize energy efficiency and control stability.

Figure 5 shows that the enthalpy can be controlled to around 36.7 kJ/kg by adjusting the damper when the fresh air enthalpy is lower than the return air enthalpy as shown in Zone A of Fig. 5. If the mixing air enthalpy is higher than the setpoint, the damper will be fully opened as shown in Zone B of Fig. 5. Once the fresh air enthalpy is higher than the return air enthalpy, the damper will be

kept at a constant 10% opening to maintain supply air quality as shown in Zone C of Fig. 5. Therefore, the cooling capacity can be evaluated by mixing air enthalpy to obtain the lowest energy usage.

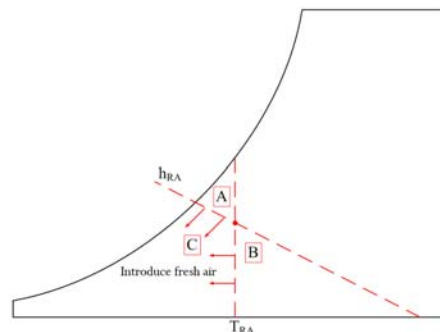


Figure 4: Difference of damper control between enthalpy and temperature on Psychrometric chart.

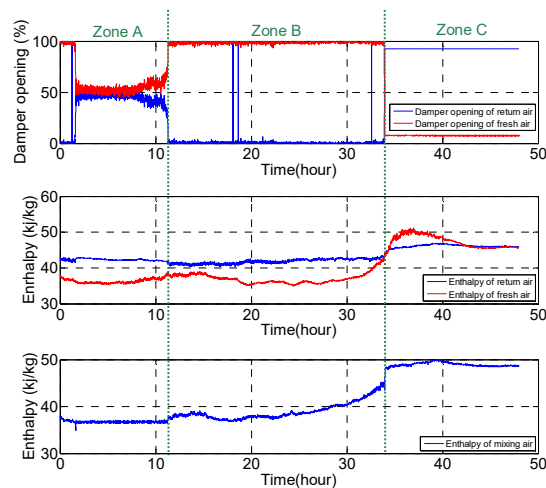


Figure 5: Enthalpy control of the damper opening.

CONCLUSION

This paper presents some heat recovery models and enthalpy controls to determine the practical influences of power usage. The efforts are devoted to developing a set of AHUs with high temperature stability and efficient energy usage at the same time. These upgrade schemes will be implemented at the Taiwan Photon Source in the future.

ACKNOWLEDGEMENT

We thank our colleagues in the utility group of the TLS and TPS for assistance.

REFERENCES

- [1] J.C. Chang *et al.*, "Operation Of Both Utility Systems Of TPS And TLS at NSRRC", in *Proc. IPAC'15*, Richmond, VA, USA, May 2015, pp. 3176-3178.
- [2] Z.D. Tsai *et al.*, "The Strategy between High Precision Temperature Control and Energy Saving for Air-Conditioning System", in *Proc. IPAC'12*, New Orleans, Louisiana, USA, May 2012, pp. 2603-2605.

OPTIMIZATION METHOD USING THERMAL AND MECHANICAL SIMULATIONS FOR SIRIUS HIGH-STABILITY MIRRORS*

L. M. Volpe[†], G. V. Claudiano, R. R. Geraldese, S. A. L. Luiz, A. C. Pinto,
Brazilian Synchrotron Light Laboratory (LNLS), Brazilian Center for Research in Energy and
Materials (CNPEM), 13083-970, Campinas, Sao Paulo, Brazil

Abstract

The mirrors for Sirius, the new 4th-generation synchrotron at the Brazilian Synchrotron Light Laboratory (LNLS), have strict requirements regarding thermo-mechanical stability and deformations, with figure height and slope errors limited to a few nanometers and tens of nanoradians, respectively. Therefore, fixed-shape mirrors have been defined with horizontally-reflecting orientation (except for vertically-reflecting mirrors of KB systems), whereas their cooling schemes (namely, air, water or liquid nitrogen cooling) depend on the particular power load. A thermal and mechanical optimization method was developed to guide the design of mirrors through the evaluation of deformations caused by power load, cooling, gravity, tightening of the fastening screws, manufacturing errors and modal analyses. Up to now, this method was already used to define the mirrors of Sirius' beamlines, which include plane, cylindrical, elliptical and ellipsoidal mirrors, as well as KB systems for microprobe and nanoprobes stations. Two examples are presented to illustrate the method.

INTRODUCTION

Mirrors are critical components to ensure a good beam quality on beamlines. With the emergence of 4th-generation synchrotron accelerators, in which it is desired to have the photon beam size near the diffraction limit and a higher coherence, the deformation and stability specifications for the mirror's design have become extremely tight.

To reach these specifications, a new fixation system was developed based on deterministic models. Thermal and mechanical simulations using finite element analysis (FEA) were done to determine the shape of the mirror, minimizing the expected deformation in its operating condition. The simulations were performed using Ansys Workbench [1].

Firstly, the works related to the design of mirrors and deterministic models are presented. In the following sections are shown the optimization methodology used to define the mirror shape, the results obtained and the conclusions.

RELATED WORKS

During the last decades several solutions of water cooling of mirrors were presented and optimized, and with the requirements increasingly tight, these solutions became more complex, requiring methods of correction of the mirror shape, for example using heaters or actuators [2-3].

Cryogenic cooling solutions can also be applied to mirrors, but are often avoided due to cost, even if better results can be obtained than water cooling. This type of cooling is widely used in monochromator crystals due to the good thermal properties of the silicon at temperatures close to 125 K, such as a coefficient of thermal expansion close to zero and high thermal conductivity [4-8].

In order to achieve movement accuracy and stiffness never seen before in double-crystal monochromators (DCM), the Sirius High Dynamic DCM utilized deterministic concepts in its design [9]. A deterministic design is made in order to obtain a system that is highly repetitive, where cause and effect relationships are well known and controlled and random behaviors are negligible [10]. Only using such techniques it is possible to achieve the necessary requirements without divergences between the design and the final product, as it was done in the present study.

CONCEPTUAL DESIGN

Since Sirius' mirrors absorb powers of at most 50W, a simple cryogenic cooling solution using cryostats and copper braids can be used, benefiting from the good properties of silicon in relation to deformation and decoupling the vibrations from the cryostat to the mirror. Thus, a new fixture concept was developed for Sirius' mirrors based on the deterministic concepts used in HD-DCM: the optical element is fixed in an exactly-constrained flexure-based support with threaded rods that passes through holes in the substrate, which achieves high stability (eigenfrequencies above 150 Hz) and still accommodates thermal deformations resultant from system cooling. More details of the conceptual design of the Sirius mirrors mechanics can be seen in [11].

MIRROR DESIGN METHOD

In order to define the shape of the mirror, a method was developed to evaluate and optimize the deformation caused by several different effects, so that each effect can be evaluated individually and the mirror design can be optimized iteratively considering each effect at a time in a way that when all effects are added, the specifications are met. The main specifications required for the development of the project are: optical area size, mirror orientation, absorbed power and maximum permissible deformation for thermal and mechanical deformations. To illustrate the method two examples of Sirius' mirrors are presented, CAT-1-HFM from the Cateretê beamline and CAR-5-KB-VFM from the Carnúba beamline. The specifications for these mirrors are shown in Table 1.

* Work supported by Brazil's Ministry of Science, Technology, Innovation and Communication (MCTIC)

[†] lucas.volpe@lnls.br

Table 1: Specifications (Mirror 1: CAT-1-VFM, Mirror 2: CAR-5-KB-VFM)

Parameter	Mirror 1	Mirror 2
Orientation	Side	Up
Figure	Cylindrical	Elliptical
Length [mm]	200	210
Power [W]	6	0
Power Area [mm]	180x0.55	200x0.55
Peak-to-Valley Error [nm]	4	1
Height Error RMS [nm]	1.3	0.5
Slope Error RMS [nrad]	110	20

Using the size of the optical area, the reflection orientation and taking into account the limitations of the production process, it's possible to define the size of the substrate and the method of fixation. An important point is that the mass and inertia should be minimized and the center of gravity kept low for greater stability. Basically, two mirror shapes have been defined according to the orientation of the optical surface. For side-bounce mirrors, a rectangular shape with the fixation preload applied on the upper surface was chosen. For the other ones, lateral flaps were added for fixation to avoid direct deformations on the polished face of the mirror and to increase the assembly lever arms length, improving the stability. The final design of the mirrors are shown in Fig. 1.

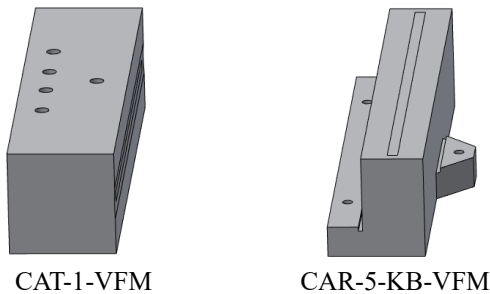


Figure 1: Example mirrors design.

The first analysis to be made is due to the gravity and tightness of the bolts. Firstly, the deformation due to gravity in the production process is evaluated by simulating the supported mirror in the same way as the optical surface is measured during the polishing process. Then the mirror is simulated on a generic support with the flexures and hinges, considering all clamping forces and the gravity. The deformation obtained in the gravity analysis is then subtracted from the deformation of the mirror fixed in the support, obtaining the deformation curve actually expected in the mirror mounted in its base. It is from this last curve that one must optimize the position of the fixation holes, the shape of the mirror and, if necessary, the support position of the mirror during the measurement in the polishing process. This procedure is done in all simulations that consider the effects of gravity and tightening forces.

In general, the mirror is supported at its Bessel points during the polishing process. It results in a very small deformation due to gravity in the optical face in mirrors with

horizontal reflection, but in a significant one in cases of vertical reflection. Therefore, it is needed to change the mirror support position during the polishing to a position closer to where the mirror will be fixed in its support. It is done in order to reduce the impacts of the gravity on the total deformation that the mirror will have under work conditions. The already optimized results are presented in Fig. 2.

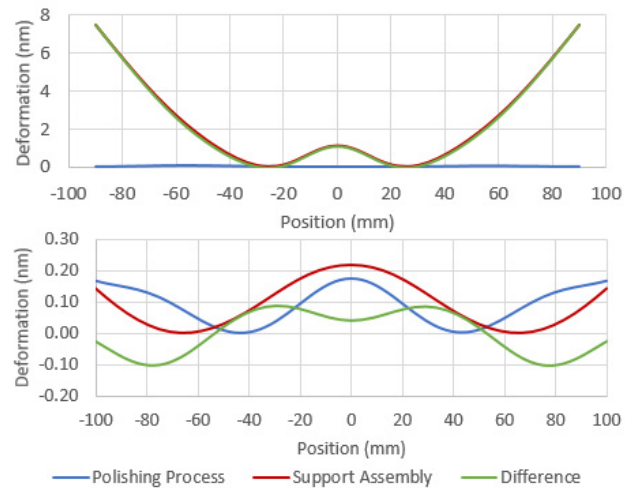


Figure 2: Polishing process, assembly and resulted deformations. CAT-1-VFM (top), CAR-5-KB-VFM (down).

A modal analysis is also performed iteratively with the previous simulation to verify if the stability conditions were reached. As an eigenfrequency above 150 Hz is desired for the a ssembled mirror mechanism, it has been established that the first frequency should be above 300 Hz for the case of the mirror mounted only on a dummy flexured-base.

Another important point to check is the deformation due to the mechanical manufacturing tolerances. Gaps between the mirror and the support due to the flatness of the parts will also result in deformations in the mirror when it is mounted. It is expected to obtain gaps of at most 1 μ m using shimming techniques in the hinge spacers between the support and the mirror. To verify the maximum deformation expected, two cases are simulated, one on which the gap is applied in the central spacer and another on which the gap is applied in one of the lateral spacers. To perform this type of simulation, the type of contact used is rough, with Lagrange Normal formulation and interface treatment adjust to touch. The results for the examples are shown in Fig. 3.

The next effect to be evaluated is the deformation relative to the temperature difference between the assembly and the work condition of the mirror, also considering the power absorbed. The temperature of the clean room for assembly is 22°C. Then, the simulation is performed for cooling the mirror to 125 K and the aluminum support to

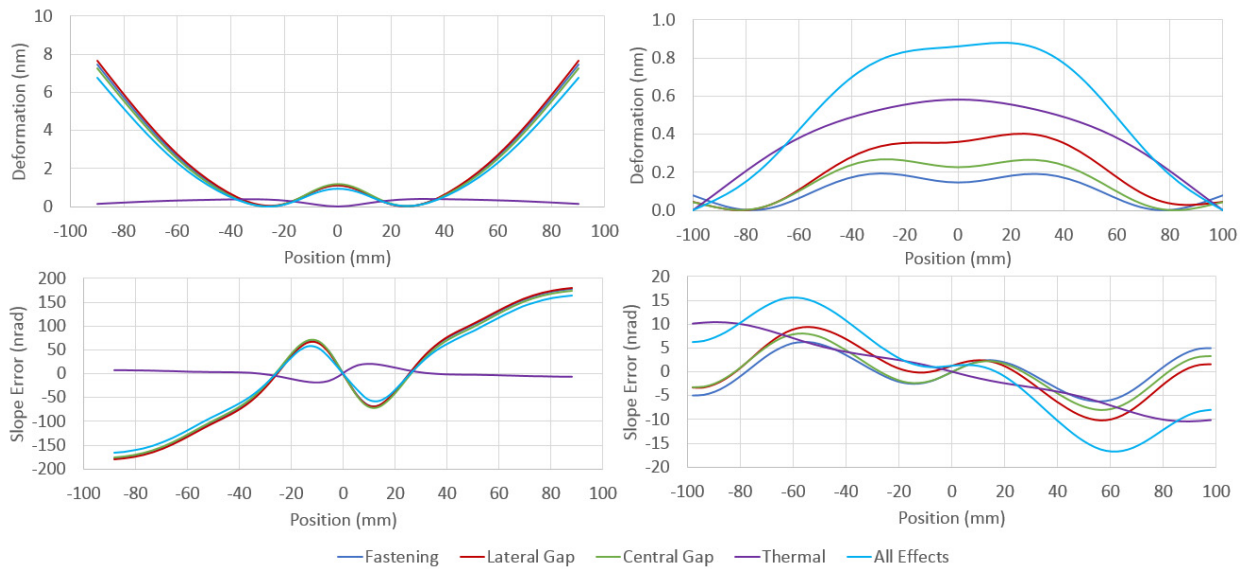


Figure 3: Deformation and slope error curves for each simulation. CAT-1-VFM (left), CAR-5-KB-VFM (right).

10.7°C in the case of cryogenic mirrors and to 24°C for mirrors without cooling (which is the temperature inside of the optical hutches). The temperature difference between the mirror and the support for the first case are chosen in a way that both components have the same thermal deformation. This simulation must be performed with the mirror mounted on the flexured-support but without considering the tightening forces, to evaluate only the thermal condition. The results for the examples are shown in Fig. 3.

A final simulation is performed to evaluate the deformation considering all the effects, analyzing the maximum deformation expected in the mirror in operating conditions. With the deformation within the specification, an optical simulation considering this deformation should be done by the Optics group to confirm that the beam profile is within the specifications for the beamline.

RESULTS

All deformation curves for the examples are shown in Fig. 3. The results optical simulation are presented in Fig. 4, demonstrating a small variation in the beam size. The final results and its criteria are shown in Table 2. It is noticed that the requirements have been met in all cases.

Table 2: Results (Mir. 1: CAT-1-VFM, Mir. 2: CAR-5-KB-VFM, criteria in parenthesis)

Requirement	Mir. 1	Mir. 2
Peak-to-Valley Error [nm]	6.8 (< 10)	0.88 (< 1.0)
Height Error RMS [nm]	2.0 (< 2.5)	0.31 (< 0.5)
Slope Error RMS [nrad]	101 (< 110)	10.4 (< 20)
1 st Eigenfrequency [Hz]	571 (> 300)	969 (> 300)

To validate the deformation simulations due to the tightening force, a measurement was made on the CAR-1-MC mirror using the Fizeau Zygo Dynafiz for the mirror only supported on the base with the clamping force. The measured and expected results are presented in Fig. 5, demonstrating an agreement between the simulation and the

Simulation

FEA Methods

low-frequency deformation of the mirror (high-frequency is due to measurement noise). Subsequently, another deformation measurement will be performed with the mirror cooled. The same agreement of results are expected.

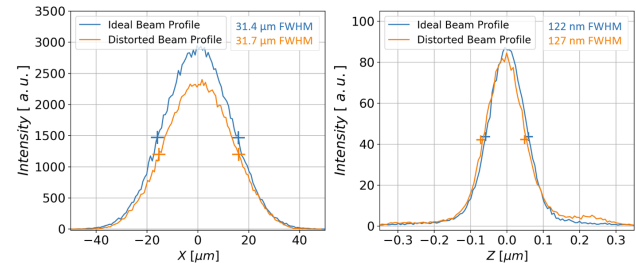


Figure 4: Beam profile from optical simulation. CAT-1-VFM (left), CAR-5-KB-VFM (right).

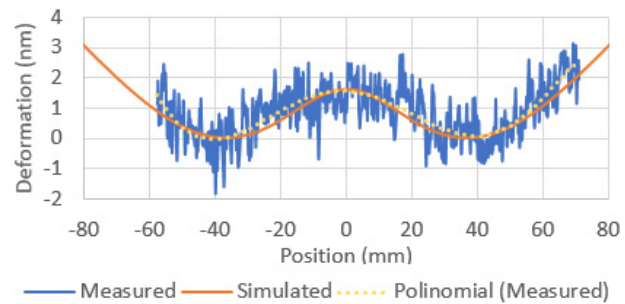


Figure 5: Measured and simulated deformation.

CONCLUSION

An optimization method through thermal and mechanical simulations was developed to define the design of the mirrors that will be used in Sirius. Through this method it was possible to reach the specified deformation levels, reaching in some cases slope error levels below 10 nrad RMS. As the mirror design and its support were made based on deterministic concepts, the results obtained in the simulations are expected to be close to the reality.

WEPH31

275

ACKNOWLEDGEMENTS

The authors would like to gratefully acknowledge the contribution of Murilo Bazan da Silva, Lucas Sanfelici, Harry Westfahl Jr., H  lio C. N. Tolentino, Bernd C. Meyer and all other members of the LNLS team that was involved with this work.

REFERENCES

- [1] ANSYS  Academic Research Mechanical, Release 19.1.
- [2] L. Zhang *et al.*, "Optimizing X-ray mirror thermal performance using matched profile cooling", in *Journal of synchrotron radiation*, vol. 22, n. 5, pp. 1170-1181, 2015.
- [3] J. Nicolas *et al.*, "Focusing and defocusing using mechanically corrected mirrors at the MX beamline at Alba", in *Journal of Physics: Conference Series*, vol. 425, n. 5, p. 052016, 2013.
- [4] G. Marot *et al.*, "Cryogenic cooling of monochromators", in *Review of scientific instruments*, vol. 63, n. 1, pp. 477-480, 1992.
- [5] W. K. Lee *et al.*, "High heat load monochromator development at the Advanced Photon Source", in *Optical Engineering*, vol. 34, n. 2, pp. 418-426, 1995.
- [6] D. H. Bilderback *et al.*, "The historical development of cryogenically cooled monochromators for third-generation synchrotron radiation sources", in *Journal of synchrotron radiation*, vol. 7, n. 2, pp. 53-60, 2000.
- [7] L. Zhang *et al.*, "Thermal deformation of cryogenically cooled silicon crystals under intense X-ray beams: measurement and finite-element predictions of the surface shape", in *Journal of synchrotron radiation*, vol. 20, n. 4, pp. 567-580, 2013.
- [8] M. Saveri Silva *et al.*, "Thermal Management and Crystal Clamping Concepts for the New High-Dynamics DCM for Sirius", in *Proc. MEDSI'16*, Barcelona, Spain, Sep. 2016, paper TUPE15, pp. 194-197.
- [9] R. R. Gerald  s *et al.*, "The new high dynamics DCM for Sirius", in *Proc. MEDSI'16*, Barcelona, Spain, Sep. 2016, paper TUCA05, pp. 141-146.
- [10] J. B. Bryan. "The deterministic approach in metrology and manufacturing", in *Proceedings of the 1993 International Forum on Dimensional Tolerancing and Metrology*, Dearborn, MI, USA, Jun. 1993, pp. 85-96.
- [11] R. R. Gerald  s *et al.*, "The design of exactly-constrained X-ray mirror systems for Sirius", presented at MEDSI'18, Paris, France, Jun. 2018, paper WEOAMA04, this conference.

DESIGN OF A LAYERED HIGH PRECISION MAGNET GIRDER

Wang Guang Yuan, Zhang Junsong, Kang Ling, Yu Jiebin, Chen Jiaxin
 Dongguan Branch of the Institute of High Energy Physics, Chinese Academy of Science (CAS),
 523803 Dongguan, China

Abstract

In order to adjust the collimation of the light source magnet, a layered magnet girder is developed, which can adjust the six degrees of freedom accurately and reduce the mutual influence of the adjustment process between the various layers of the girder. The precision of the collimation is up to 5 microns.

INTRODUCTION

The HEPS is a high energy synchrotron source with the electronic energy of 5GeV and the emittance of 0.5nmrad in 13th Five-Year Plan. The synchrotron radiation source consists of two types of accelerators, the intensifier and the storage ring [1]. The synchrotron radiation source consists of two types of accelerators, the booster and the storage ring. The main equipment of the accelerator is all kinds of magnets (including: dipole magnet, quadrupole magnet, sextupole magnet, correction magnet). The magnet girder is a device used to support, adjust and locate the magnet. Its adjusting precision directly affects the collimating accuracy of the magnet [2]. This electric magnet girder is applied to support and position precision adjustment of the dipole magnet in the booster.

THE STRUCTURE OF GIRDER

In order to save the manpower and adjusting time of the magnet collimation adjustment, the girder adopts all electric control, which can realize three directions movement of X, Y, Z direction and Rotational motion around the axis of X, Y and Z. The girder realizes the precise collimation of magnets in a small area, and the adjustment range of the horizontal X, Y and Z directions is + 15mm. The structure of the electric adjusting girder is shown in Figure 1 below.

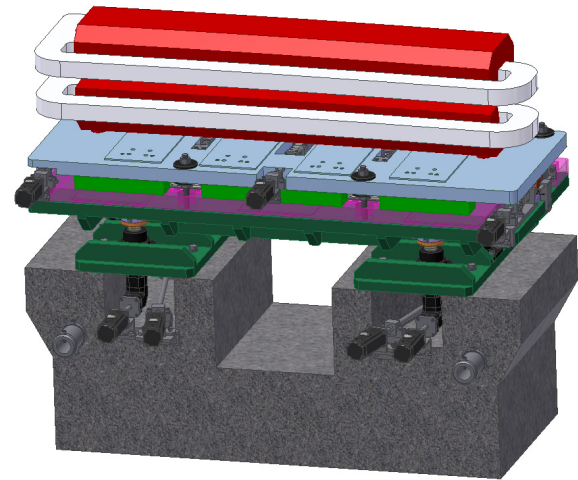


Figure 1: The structure of magnet girder.

The structure of the magnet girder is divided into two parts, namely the horizontal adjustment mechanism (shown in Figure 2) and the height adjustment mechanism (as shown in Figure 3). The horizontal adjustment assembly adopts a layering adjustment mode, and each layer realizes one direction adjustment independently. Height adjustment assembly realizes elevation adjustment by 4 adjusting mechanisms.

After the magnet collimating adjustment is completed, the girder is fixed by the height locking mechanism and the horizontal locking mechanism. The base of the magnet girder is made of marble, providing high stability support. The hoisting rod is used for lifting the whole magnet girder.

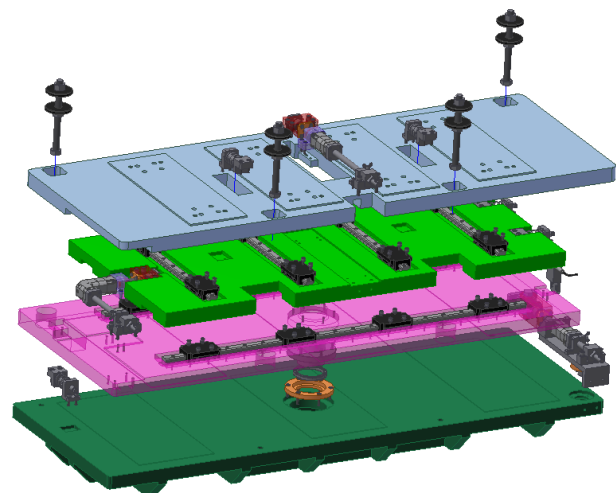


Figure 2: The horizontal adjusting mechanism.

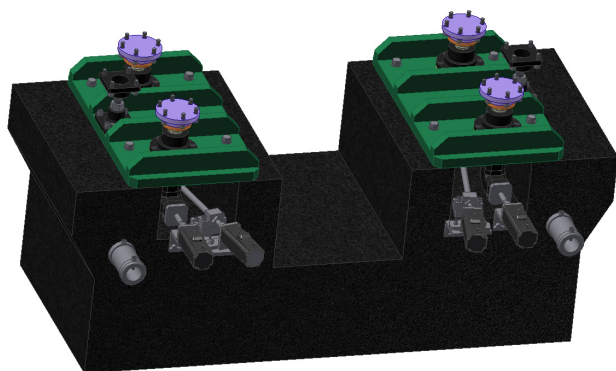


Figure 3: The height adjustment mechanism.

STRUCTURE OF THE HORIZONTAL ADJUSTING MECHANISM

The structure of the horizontal adjusting mechanism is shown in Figure 4 and Figure 5 below, which is divided into horizontal transverse moving plate, horizontal longitudinal moving plate, rotary adjusting plate and lifting plate. Each plate is regulated by an independent mechanism. A spring pre-tightening device is installed on each plate, and the pre tightening force is applied to the adjusting mechanism to reduce the screw thread clearance of the adjusting screw.

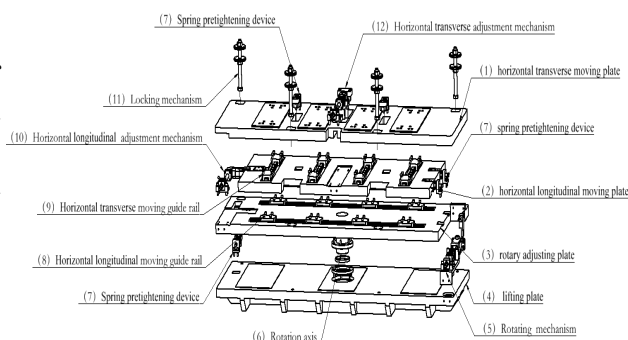


Figure 4: The structure of the horizontal adjusting mechanism.

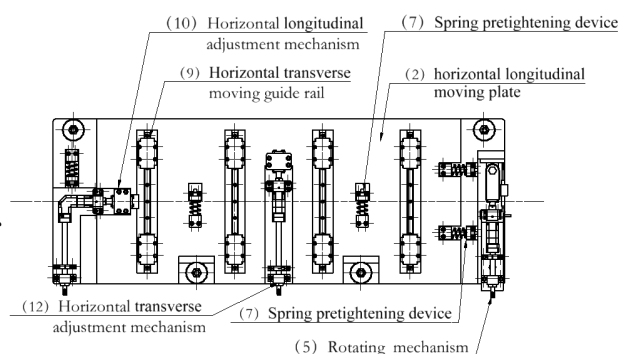


Figure 5: Second layer view of the horizontal adjusting mechanism.

THE STRUCTURAL OF HORIZONTAL ADJUSTMENT MECHANISM

Each adjustment organization takes the same structural form, shown in Figure 6. The reducer and the trapezoidal screw are connected by coupling. The adjusting nut is installed on the moving plate after being installed on the connecting seat. The push and pull of each laminate is realized by trapezoidal screw. In order to facilitate the operation and maintenance of the motor, all motors are connected with the reducer by the extending shaft. All 7 motors are elicited to the operator side. The pre tightening spring device is connected with the upper and lower plate respectively, as shown in Figure 7. Pre tightening force is applied to reduce the internal clearance of the adjusting mechanism.

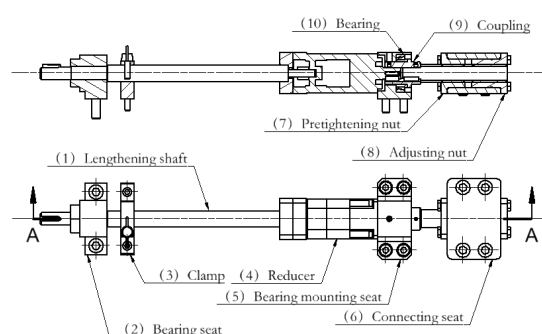


Figure 6: The structural of horizontal adjustment mechanism.

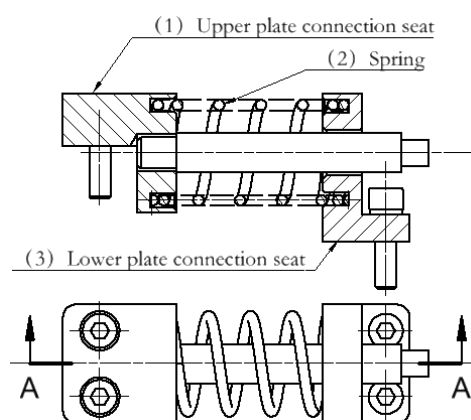


Figure 7: The structure of spring pre-tightening device.

THE STRUCTURAL OF VERTICAL ADJUSTMENT MECHANISM

The vertical adjustment mechanism connects the vertical plate and the marble base to realize the different position state of the vertical plate welding plate. Four height adjustment mechanism lift together to realize the lifting of the whole girder; Two adjusting mechanism in the same side is marked as one group. The two group of mechanism adjusted in reverse direction to realize the

rotary motion of the girder. The structure of the vertical adjustment mechanism was shown in Figure 8. The ball connection structure enables the height adjustment mechanism to have a certain rotation angle. During the adjustment process, the motor rotates the adjusting nut. Because of the positioning key, the screw rod does not rotate, and only rises and goes up and down. Thus the purpose of vertical direction lifting is achieved.

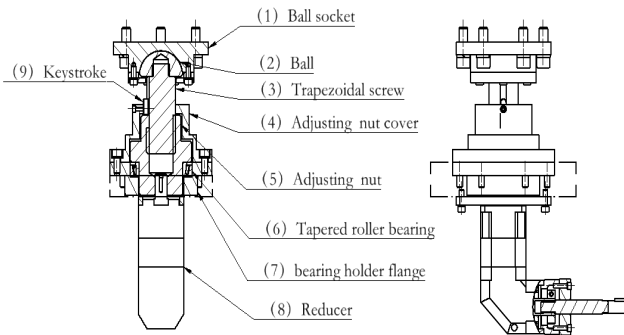


Figure 8: The structural form of vertical adjustment mechanism.

PRECISION FEEDBACK

The clearance of the adjusting mechanism will affect the adjusting accuracy of the girder. Therefore, the displacement sensor, shown in Figure 9, was installed to compensate for the movement amount, so as to ensure the adjustment accuracy of the $5\mu\text{m}$.

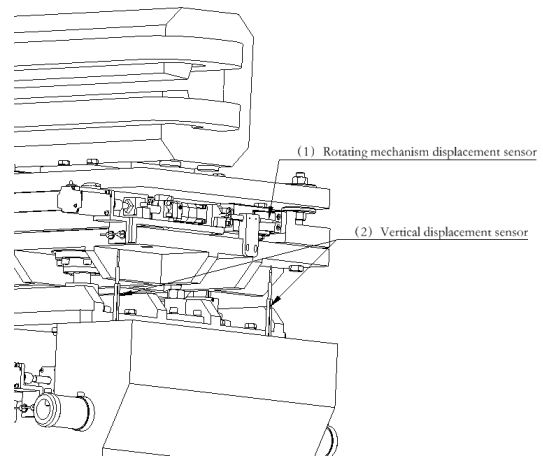


Figure 9: The displacement sensor of the each adjustment mechanism.

CONCLUSION

Layered high precision magnet girder provides a high-precision alignment scheme for the magnet. Its highest accuracy is $5\mu\text{m}$, providing stable and high precision support for the magnet of the light source.

REFERENCES

- [1]HEPS, <http://heps.ihep.ac.cn/>
- [2]R. Liu, J. Zhang, H. Qu, L. Kang, M. Wang, G. Wang, H. Wang, "Vibration research of the AC dipole-girder system for CSNS/RCS", in *Chinese Physics C*, no.6, pp. 97-102, 2014.

RESEARCH ON ACTIVE VIBRATION ISOLATION SYSTEM*

J. B. Yu^{1†}, L. Kang¹, G. Y. Wang¹, J. X. Chen¹, J. S. Zhang¹, A. X. Wang¹,
 X. J. Nie¹, H. Y. He¹, D. H. Zhu¹, C. J. Ning¹, Y. J. Yu¹, L. Liu¹

Institute of High Energy Physics, Chinese Academy of Sciences, Beijing, China

¹also at Dongguan Neutron Science Center, Dongguan, China

Abstract

Based on the increase of accuracy requirements coming from increasing instrument precision, advanced isolation components are required, and active vibration control method is proposed. This paper mainly shows the experimental system, and some work has been done at present. Now that we are still at the beginning research of active vibration isolation, we hope it will be steadily used in the support systems of some precision equipment and instruments.

INTRODUCTION

Micro-vibration study is one of the important research project in synchrotron light sources, the girder system with passive vibration isolation and damping technology which are effective for beam stability has been widely researched in different institutes, active vibration isolation system, for some uncontrollable factors exist in the control system and actors, its application in synchrotron light source has been constrained. While for the increase of accuracy requirements coming from increasing instrument precision, alone use of passive vibration can't satisfy the requirements, active vibration will play an important role in high precision instruments [1]. This paper firstly shows active vibration isolation research in accelerator, and then the experimental system and some work we have been done at present will be introduced.

The active vibration isolation system in accelerator is mainly used in the future compact linear collider (CLIC) [2], two nanometre size particle beams are accelerated and steered into collision to create high energy collisions between electrons and positrons, to achieve the expected performance, the beams need to be vertically stabilized at the nanometre scale, many institutes have done much preliminary development, early in 1996, Christoph had researched the active stabilization of mechanical quadrupole vibrations with one piezo actuator used in one support system [3]. J. Frisch et al had constructed a prototype system by using of active vibration damping to control magnet motion [4]. C. Collette et al researched on the nano-motion control system for heavy quadrupoles by using two actuators in one support [5, 6]. R. Le Breton et al. had researched on the nanometre scale active ground motion isolator with four actuators in one support [1]. All these research experiments show that active vibration isolation can play a positive role on nanometre scale. Now that we are still at the beginning research of active vibration isolation, we hope it will be

steadily used in the support system of some precision equipment and instruments.

ACTIVE VIBRATION ISOLATION SYSTEM

A two stage support system which include passive stage and active stage is shown in Figure 1, the passive stage is composed of springs and damping, while the active stage is made up of springs and actuators. High stiffness springs, which result in high normal mode frequencies, provide relatively low amplitude motion and good stability in the absence of feedback, while low stiffness springs allow large amplitude low frequency motions, but attenuate high frequencies. This paper mainly research on the active stage.

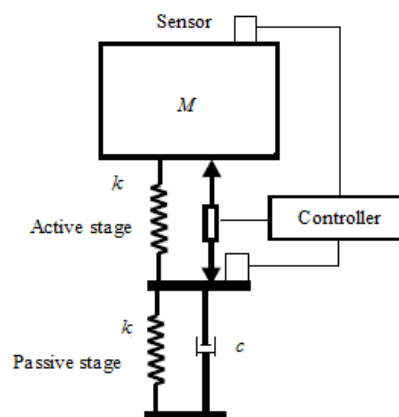


Figure 1: Single d.o.f support system.

To reduce expenditure, the active stage with three springs and one actuator is designed as shown in Figure 2. Different actuator technologies can be used for active isolation system, base on the advantages of high resolutions, wide bandwidths and strong forces, piezoelectric actuator is chosen in this stage. The load on the stage is about 100kg, and it's expected to be effective with the frequencies in the range 1-20 Hz.

*Work supported by National Nature Science Foundation of China (11375217)

† email address: yujb@ihep.ac.cn

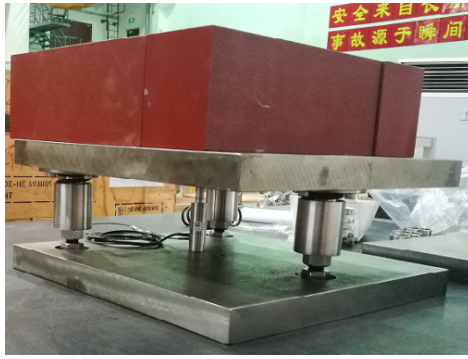


Figure 2: The structure of active stage.

As shown in Figure 3, the active isolation system consists of an actuator, an actuator power amplifier, two types of sensors measuring displacement and acceleration, two instrumentation amplifiers and a hardware for rapid control prototyping.

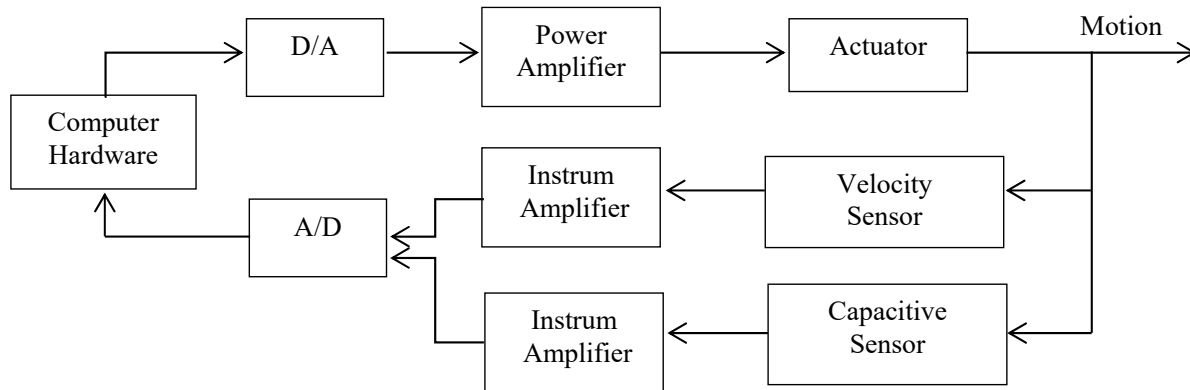


Figure 3: Control system of the active isolation system.

P-845preload stack piezoelectric actuator from PI is chosen as the actuator in the active stage, a preload ensures that the actuator will not be damaged when the driven close to the frequencies of the structure.

Because it is impossible to obtain the absolute displacement of the ground due to lack of fixed reference, the ground motion can be measured by only acceleration or velocity sensors. The sensor 941B which at different tap position can measure velocity or acceleration is chosen

to obtain the velocity of the stage. The sensor with a sensitivity of $0.3V \cdot s^2/m$ offers a suitable bandwidth for this application ($0.25 \sim 80$ Hz).

Capacitive sensor PI D-E20 is chosen to observe the elongation of the actuator, although the sensor can't give direct information about the stage motion, it's used to get the electromechanical model of the structure.

Open loop performance platform is established as shown in Figure 4, it consists of a signal generator, a power amplifier, D/A, A/D, a capacitive sensor, an instrumentation amplifier, an actuator and an actuator controller. The multimeter DMM7510 is also used to measure the precision of the piezoelectric actuator and the capacitive sensor, due to the controller is not the original controller to the actuator and error exists between them, the precision is measured within 5 nm.

Open loop response of the actuator at different frequencies with 0.1 Hz, 0.5 Hz, 1 Hz have been tested, Figure 5



Figure 4: Open loop performance platform.

shows the response at 1 Hz, in which the first curve is the signal from the signal generator, the second curve is the signal from the actuator controller, and the third curve is the signal from the capacitive sensor, these curves indicate that the actuator and the capacitive sensor have nice response to the input signal at a single low frequency.

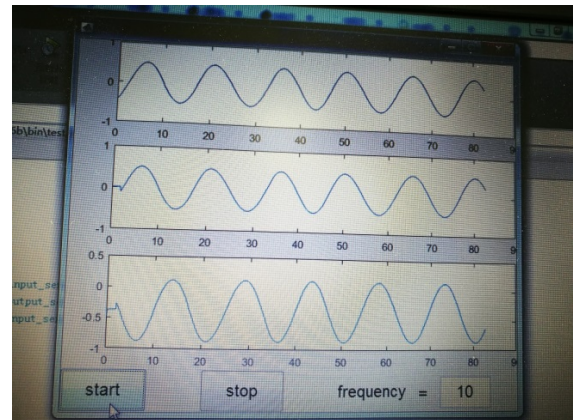


Figure 5: Open loop response at 1 Hz.

The response with the frequencies of 0.5 Hz and 1 Hz coupling has been tested, and the result is shown in Figure 6. The response with the frequencies of 0.5 Hz, 1 Hz

and also with random signal coupling has also been tested, and the result is similar to Figure 6, which is considered to be suitable.

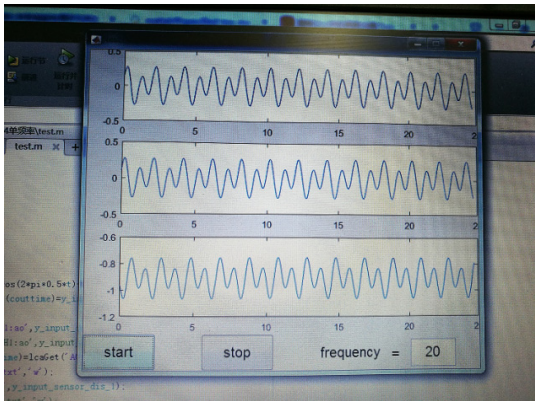


Figure 6: Open loop response with 0.5 Hz and 1 Hz coupling.

CONCLUSION

For active isolation can be widely used in different fields, like interferometers, microscopes, high precision manufacturing and so on, now we are still at the beginning research of active vibration isolation, there are much work such as closed loop response, two or three actuators work together and so on need to be done.

REFERENCES

[1] R. L. Breton, G. Deleglise, J. Allibe, *et al.* “Nanometer scale active ground motion isolator”, *Sensors and Actuators A*, vol. 204, p. 97-106, 2013.

[2] G. Riddone, D. Schulte, H. Mainaud-Durand, *et al.*, “Technical specification for the CLIC two-beam module”, in *Proc. EPAC’08*, Genoa, Italy, June 2008, pp.607-609.

[3] C. Montag. “Active stabilization of mechanical quadrupole vibrations for linear colliders”, *Nuclear Instruments and Methods in Physics Research A*, vol. 378, pp. 369-375,1996.

[4] J. Frisch, L. Hendrickson, T. Himel, *et al.*, “Active vibration suppression R&D for the NLC”, in *Proc. ICALEPCS’01*, California, USA, November 2001, p. 263-265.

[5] C. Collette, K. Artoos, A. Kuzmin, *et al.*, “Active quadrupole stabilization for future linear particle colliders”, *Nuclear Instruments and Methods in Physics Research A*, vol. 621, pp. 71-78, 2010.

[6] C. Collette, S. Janssens, K. Artoos, *et al.*, “Nano-motion control of heavy quadrupoles for future particles colliders: An experimental validation”, *Nuclear Instruments and Methods in Physics Research A*, vol. 643, pp. 95-101, 2011.

FROM PLATE SCREENING TO ARTIFICIAL INTELLIGENCE: INNOVATIVE DEVELOPMENTS ON PROXIMA 2A AT SYNCHROTRON SOLEIL

Damien Jeangerard¹, Martin Savko¹, Lidia Ciccone¹, Kewin Desjardins¹,
Antoine Le Jollec¹, Ahmed Haouz², William Shepard^{1†}

¹ Synchrotron SOLEIL, L'Orme des Merisiers, Saint Aubin BP 48, 91192 Gif-sur-Yvette, France

² Pasteur Institute, 209-211 rue de Vaugirard, 75015 Paris, France

Abstract

PROXIMA 2A is a high performance 3rd generation synchrotron beamline dedicated to X-ray micro-crystallography on biological macromolecules. Since opening in March 2013, the experimental station has hosted a large number of users who have collected vast amounts of X-ray diffraction images from thousands of crystals. In order to streamline the throughput, enhance performance and add functionality, a number of developments have been launched on PROXIMA 2A. These cover all aspects of the beamline, from the practical to the visionary: such as the design, fabrication and implementation of a dedicated high-precision motorized stage to screen crystallization plates for *in situ* X-ray data collections, and the employment of artificial intelligence and computer vision technologies for the detection of samples under liquid nitrogen. Other notable beamline projects include the addition of a vertical translation table for the EIGER X 9M detector to permit the acquisition of ultra-high (0.6 Å) resolution X-ray data, the incorporation of a miniaturized Yttrium Aluminium Garnet (YAG) coupled photodiode within a beamstop and the determination of the sphere of confusion (SOC) of a recently added kappa arm to the goniometer.

INTRODUCTION

Modern macromolecular crystallography (MX) beamlines at synchrotron radiation centres have become highly automated systems that permit the high-throughput screening and X-ray data collection of a large number of protein crystals from academic and industrial users. However, as MX experiments have become increasingly sophisticated, there is a desire and need to record more information during the experiment (e.g. variations of the incident flux, sample shape, positions collected, X-ray dose, etc.). One of the direct consequences of maintaining higher throughput is that more complex situations need to be handled automatically without any human intervention. Given that every piece of instrumentation has its own technical limitations, there is a ceiling to the throughput efficiency obtainable. Similarly, every automated procedure is designed for a specific set of tasks, which tends to constrict the overall functionality of the experimental station. As such the automation of experiments sets its own boundaries in quality assurance, efficiency and functionality, and the mission of assuring reliability and

broadening the frontiers is a continual process. Here we present some of the on-going projects on the PROXIMA 2A beamline at Synchrotron SOLEIL that improve upon the current automation available, extend the capabilities of the beamline, and add new functionalities for the user community.

RESULTS

In Situ Crystallisation Plate Screener

Crystals of biological macromolecules (proteins, DNA, RNA, and their complexes) are typically grown in 96-well SBS format crystallisation plates via sitting-drop vapour diffusion experiments. When crystals appear in a drop (few 100 nL), they are physically very fragile, sensitive to changes in humidity and temperature, and consequently difficult to harvest. Furthermore, as such crystals contain 30-80% water, flash freezing them in liquid nitrogen can destroy their crystal quality. Although collecting X-ray diffraction data from crystals in crystallisation plates has been reported previously from other beamlines [1-4], the micro-focussed X-rays on PROXIMA 2A with a beam cross-section of 5 µm full width half maximum (FWHM) necessitates a high mechanical resolution over the entire dimensions of a crystallisation plate (128 mm × 86 mm). Unfortunately, such a resolution can not be delivered by the robotic arm of the sample changer system (SOC ≈ 50 µm), and the travel range of our version of the Micro-diffractometer (MD2, Arinax, France) is too small to cover an entire crystallisation plate. Thus, we have launched a project to custom design and build a crystallisation plate screener that is suitable for a micro-focussed X-ray beam and tailored to the environment of PROXIMA 2A.

The crystallisation plate screener (Figure 1) is composed of five motorised translation tables: Three heavy duty, long range, high-resolution (100 nm) stages (Axmo Precision, France) to move the plate horizontally (Tx), vertically (Tz) and along the X-ray beam path (Ts), which also brings the drop into the focal plane of the coaxial microscope of the MD2. Two other stages (SmarAct, Germany) will align the crystallisation drop to the centre of the air-bearing ω rotation axis, which will ensure a limited movement in angular range (±45°). The supporting frame can hold SBS format crystallisation plates. A graphical user interface, written in Python Qt4, permits the user to move to any given crystallisation well and control the various data collection parameters (zone to

† email address: william.shepard@synchrotron-soleil.fr

screen, exposure time, detector frame rate, etc.). The images are automatically processed using the DIALS spot finder routine (dials.diamond.ac.uk), which searches for X-ray diffraction spots in the collected images. The number of diffraction spots per position is then rendered as a heat map.

At the moment the plate screener collects X-ray diffraction images as stills, but in the near future we envisage adding an ω rotation axis and incorporating other functionalities.

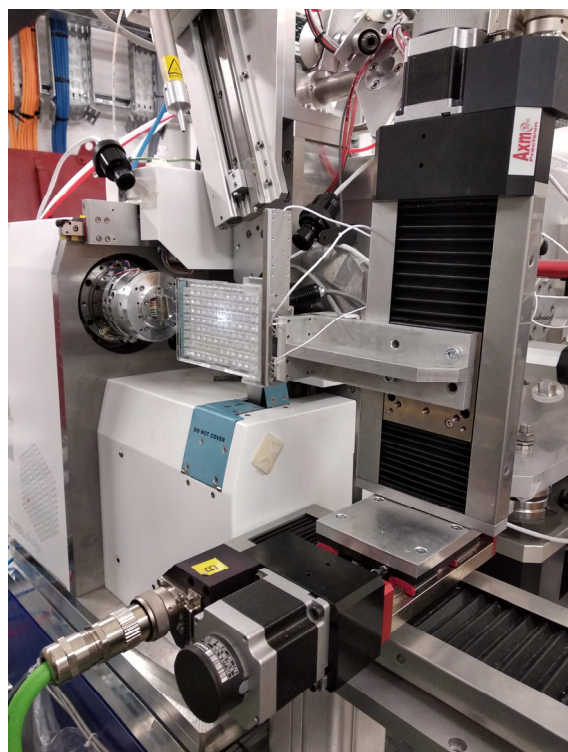


Figure 1: Photo of the Plate screener on PROXIMA 2A.

Fibre Optic Coupled YAG Beamstop

In order to record the actual flux at the sample during the experiment, we are developing a miniaturised beam monitoring system mounted inside a small beamstop of the experimental set up. For micro-crystallography experiments, it is preferable to reduce any background scatter by placing the beamstop as close as possible behind the sample. However, for MX data collections, the lowest resolution shells (>50 Å) are important in the calculation of the electron density maps. On PROXIMA 2A, the nominal beamstop is only 300 μm in height and placed 10 mm behind the sample. Making an incident beam monitor of these dimensions is a real challenge. Nevertheless, we have developed a prototype, which is a YAG crystal coupled to an optical fibre that transmits the signal to a photodiode. The prototype shows a linear response with respect to the incident flux, but it is sensitive to any movements of the crystal, which became unglued during the exposure to the intense X-rays.

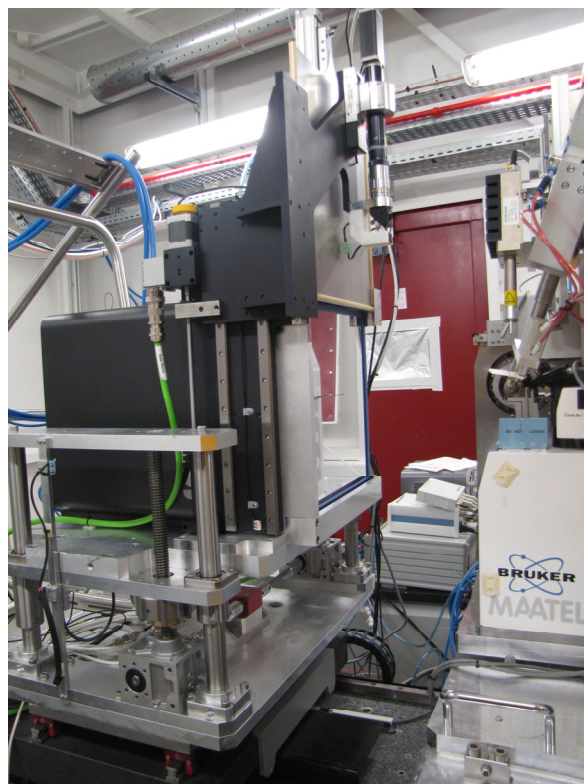


Figure 2: Photo of the vertical translation table for the EIGER X 9M on PROXIMA 2A.

EIGER X 9M Translation Table

With ever increasing frequency, many PROXIMA 2A users grow crystals that diffract to sub-atomic resolution, but until recently the experimental set up could not bring the EIGER X 9M detector close enough to permit the complete data collection to resolutions beyond 1.1\AA resolution at the nominal energy of 12.65 keV. By elevating the detector by as much as 120 mm and raising the X-ray energy to 18 keV, the PROXIMA 2A set up can readily collect complete X-ray diffraction data to 0.6\AA resolution.

The vertical translation stage of the EIGER X 9M detector is comprised of four stiff columns, which guide the lifting of a 25mm thick base plate. A single motor coupled to a transmission (Phytron, Germany) drives the two lead screws. The two struts connecting the guide columns reinforce the rigidity of the ensemble (see Figure 2). X-ray powder diffraction images of LaB_6 confirm that diffraction rings are observable beyond 0.6\AA resolution.

Determining the SOC With a Mini-Kappa

In order to provide extra functionality for the users, especially those who wish to perform sulphur SAD experiments, the PROXIMA 2A beamline recently acquired a motorised mini-kappa arm (MK3, Arinax, France) for the MD2. However, this motorised arm does not convert the system into a proper κ goniometer as the sample needs re-centring for different κ , ϕ and ω angles. Furthermore, the weight of the MK3 affects the SOC of the ω air-bearing spindle of the MD2. Thus, we are currently investigating methods to automatically characterise the shifts in the

position using a ball bearing, a thin fibre or a point, in order to create a geometric displacement map. The site acceptance tests using a point and optical microscope of the MD2 confirmed that the SOC (peak-valley) of the ω -axis degrades slightly of the extra weight of the mini-kappa arm from 2.4 μm at $\kappa = 0^\circ$ to 4.8 μm at $\kappa = 130^\circ$. However our initial attempts to reproduce these measurements with an interferometer and ball bearing yielded much higher SOC values (8.8 μm horizontally and 9.0 μm vertically at $\kappa = 0^\circ$), and the measurements were very sensitive to and depended upon the mechanical set up. Consequently, we are continuing our pursuit of more reliable methods of determining the SOC for the definition of a displacement map for the MK3 & MD2.

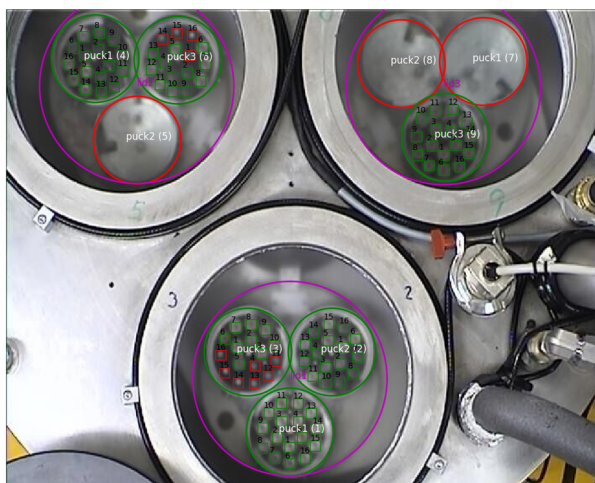


Figure 3: Result of sample detection from an overhead image of samples stored in the Dewar under liquid nitrogen (LN2): Purple circles: identified lids, red circles: missing pucks, green circles: present pucks, red squares: missing pins, green squares: present pins.

Computer Vision Detection of Samples in LN2

The automated sample-transfer system installed on PROXIMA 2A stores up to 148 samples under a layer of liquid nitrogen (LN2). A limitation of the system is its inability to detect the presence of individual samples. This sometimes leads to confusion on the part of the user and leads to unnecessary interruptions in the smooth operation of the beamline. To address this problem, we have developed a system to determine the exact content of the Dewar by the analysis of optical images acquired by a camera positioned above the storage Dewar.

Given an image of the storage Dewar (Figure 3), we determine the locations of present and missing samples. We considered the problem as that of defining segments of the image corresponding to missing and present samples and solved it as a supervised classification machine-learning task. Using human designated positive and negative examples (the training data set contained $\sim 10,000$ examples for each class), we trained a linear classifier to decide whether a particular image patch is likely to correspond to a present or missing sample. Using the results from the classification step, we could then make use of

the known geometry of the Dewar to determine the coordinates and indices of all missing and present samples. An image pre-processing and sliding window search were done using scikit-image library; feature computation, classification and clustering using scikit-learn library.

The system is robust with respect to small differences in intensity of lighting across the image, differences in pin types and the solution is also robust with respect to small changes in camera position and scale of the input image.

CONCLUSIONS

The various advances in instrumentation and methodology will render the automation of MX beamlines more robust while also offering increased functionality. *In situ* plate screening will become necessary for the crystalline systems that are particularly fragile and do not resist the cryo-cooling step, such as crystals of membrane proteins, although plate screening can also be useful to verify the diffraction limit of crystals prior to any handling. Extension of the crystallographic resolution limit to 0.6Å and implementation of an easy to use κ goniometry are obvious advantages to the MX users' arsenal. Similarly, knowledge of the incident flux will not only help monitor the stability of the X-rays on the sample, which is important for micro-crystal and anomalous scattering experiments, but it will also allow users to calculate the X-ray dose and avoid unnecessary radiation damage. Finally, the application of artificial intelligence and computer vision technologies will enable the automatic handling of more complex situations and extend the boundaries of automation on the beamline.

ACKNOWLEDGEMENTS

The authors wish to thank the various support groups at Synchrotron SOLEIL, especially Alain Lestrade, Jean-Michel Dubuisson and Bertrand Pillaud.

REFERENCES

- [1] L. Jacquamet, J. Ohana, J. Joly, F. Borel, M. Pirocchi, P. Charrault, A. Bertoni, P. Israel-Gouy, P. Carpentier, F. Kozielski, D. Blot, and J. L. Ferrer, "Automated analysis of vapor diffusion crystallization drops with an X-ray beam," *Structure*, vol. 12, no. 7, pp. 1219–1225, 2004.
- [2] A. Le Maire, M. Gelin, S. Pochet, F. Hoh, M. Pirocchi, J. F. Guichou, J. L. Ferrer, and G. Labesse, "In-plate protein crystallization, in situ ligand soaking and X-ray diffraction," *Acta Cryst. D*, vol. 67, no. 9, pp. 747–755, 2011.
- [3] N. Watanabe, H. Murai, and I. Tanaka, "Semi-automatic protein crystallization system that allows in situ observation of X-ray diffraction from crystals in the drop," *Acta Cryst. D*, vol. 58, no. 10 II, pp. 1527–1530, 2002.
- [4] J. H. Kelly, "Engineering Challenges of the VMXi Beamline," in *Proc. MEDSI'16*, Barcelona, Spain, pp. 304–308, 2016. doi:10.18429/JACoW-MEDSI2016-WECA07

MECHANICAL DESIGN AND CONSTRUCTION OF THE COHERENT X-RAY SCATTERING BEAMLINE AT TAIWAN PHOTON SOURCE

H. Y. Yan[†], C. H. Chang, C. C. Chiu, C. Y. Chang, L. Lee, L. J. Huang, C. Y. Chen, J. M. Lin,
 D. G. Liu, S. H. Chang, and Y. S. Huang,

National Synchrotron Radiation Research Center, 30076 Hsinchu, Taiwan

Abstract

The Coherent X-ray Scattering (CXS) beamline at Taiwan Photon Source has been completely constructed in the end of 2015 and opened for users in the next half year of 2016 successfully. Two In-vacuum Undulators (IU22) with lengths of 3 m and 2 m were used as the Insertion Device (ID) to provide intense synchrotron radiation for the CXS beamline. To achieve the coherent performance, the components setup in the beamline needs to be considered and designed carefully. As no white-beam diamond window was installed in the upstream beamline for the maintenance of coherent beam, a differential pumping mechanism was evaluated to prevent the worse vacuum condition influencing the front end and the storage ring. A single-crystal diamond filter was also adopted to maintain the coherence of x-ray. The protection of bremsstrahlung radiation for this beamline was designed specifically based on the optical layout. This paper will introduce the detailed mechanical design and current status for the CXS beamline.

INTRODUCTION

The Coherent X-ray Scattering (CXS) beamline, which is mainly dedicated to the experimental techniques of the Small-angle X-ray Scattering (SAXS), X-ray Photon Correlation Spectroscopy (XPCS), Coherent Diffraction Imaging (CDI), and so on with its highly coherent beam, is one of the phase-I beamlines at Taiwan Photon Source (TPS). The CXS beamline has been completely constructed and opened for users in 2016. The focused size of $10 \times 10 \mu\text{m}^2$

at sample with operating energy ranging from 5.6 to 20 keV was also accomplished. The preliminary mechanical design of the CXS beam was reported in [1]. Based on the following suggestion for optimization, the detailed design of the beamline was upgraded. This paper introduces the updated and optimized parts in the following sections, such as the radiation shields, optics, vacuum condition, and thermal analysis. The current status of the CXS endstation is also briefly described.

COMPONENTS SETUP

The latest layout of the CXS beamline and endstation is shown in Figure 1. The components setup in the beamline is mainly divided into several functional parts: The optics, radiation shields, vacuum condition, definition of beam size, monitor of beam position and size, and filter. The similar components for definition of beam size and monitor of beam position and size were introduced in [1-3]. In this section, we focus on the description for optics, radiation shields, and vacuum condition.

Optics

A liquid nitrogen-cooled Double Crystal Monochromator (DCM) manufactured by Kohzu Precision with two sets of crystals, which are Si (111) and Ge (111), was adopted for its mature technique in any sort of hard x-ray beamlines and located at 30.5 m. The crystals can be switched with a wide lateral translation. After reflected by the first and second crystals, the beam path offsets upward by 25 mm.

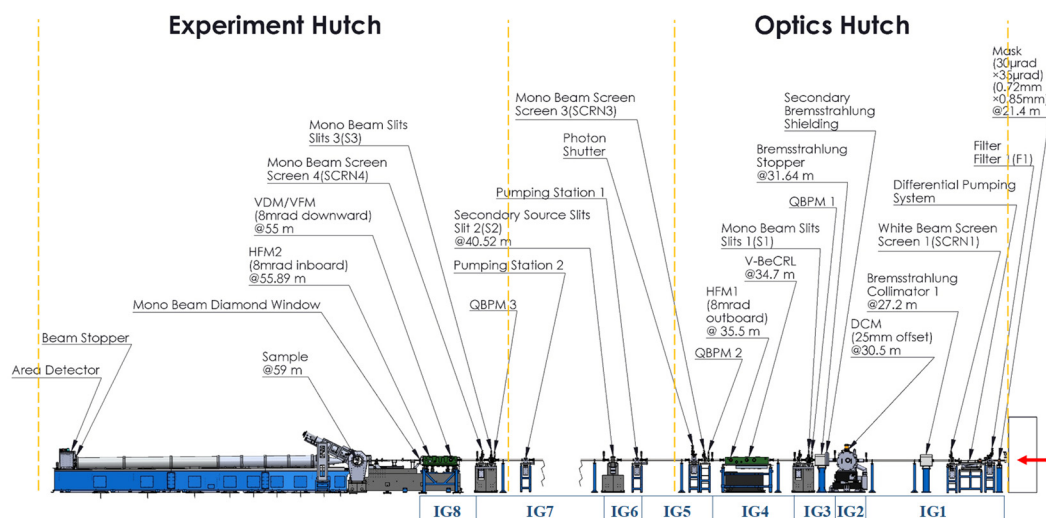


Figure 1: The layout of the CXS beamline and endstation.

[†] yan.hy@nsrrc.org.tw

gular aperture of 4 mm x 6 mm was used to isolate the vacuum incompatibility and also able to maintain the coherent beam.

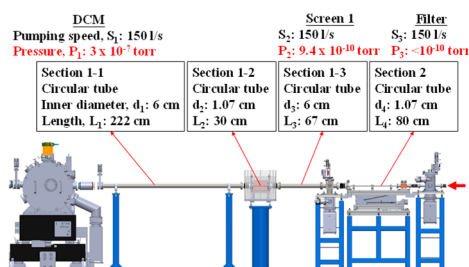


Figure 4: The evaluation of differential pumping between the filter and DCM.

THERMAL ANALYSIS

Thermal analyses were evaluated by the finite element method to verify the performance of white-beam components in the beamline. The maximum calculated power after the slits in front end with a $24 \times 29 \mu\text{rad}^2$ aperture is 84 W. The mask is the first white-beam component in the beamline for the prevention of beam missteering and designed with a $30 \times 35 \mu\text{rad}^2$ aperture. The thermal analysis is based on the assumption that energy is absorbed by the mask entirely. The single-crystal diamond filter with a thickness of 200 μm and a round aperture of 6 mm is the second white-beam component and used to absorb unnecessary energy. The diamond foil was brazed in a holder, and then the holder was assembled with the copper cooling bar. The calculated absorbed power is 27 W when the beam transmits through the center of the diamond foil. Thermal analysis is unnecessary for the liquid nitrogen-cooled DCM thanks to its wide application and experience on this level of power density. The result of thermal simulation shown in Figure 5 presents the design of these white-beam components are applicable.

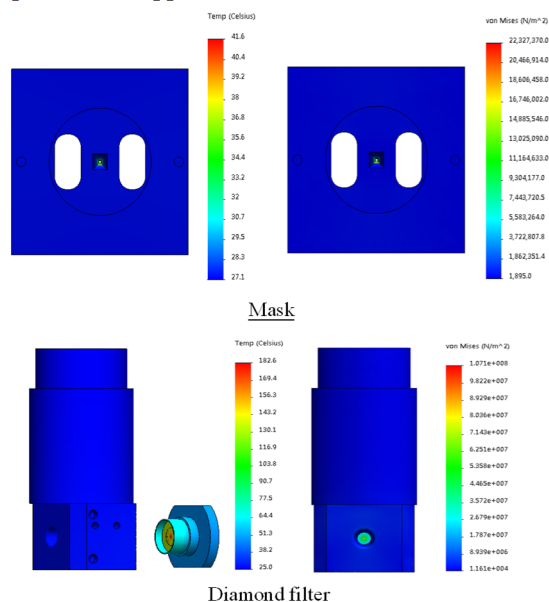


Figure 5: The result of thermal simulation representing the temperature and thermal stress for the mask and diamond filter.

BRIEF DESCRIPTION OF THE CXS END-STATION

The CXS endstation begins from the mono-beam single-crystal diamond window in the downstream beamline and consists of the slits 1, slits 2, attenuator, measurement unit of beam intensity, fast piezo shutter, sample, 12 m-long pipe section, beam stopper, area detector and its motor-actuated platform respectively. The sample position is adjusted by a 3-axis stage for its horizontal and vertical directions. The 12 m-long pipe section for the experiments of small angle can reset the distance between sample and area detector from 2 m to 12 m semi-automatically. The goniometer system for the experiments of wide angle was installed nearby the sample and capable of tilting up to 35 and 45 degrees from the horizontal when the in-vacuum area detector was at a distance of 2 m and below 1.75 m away from the sample respectively. The tests of vacuum and movement for the goniometer system was also verified. The layout and on-site view of the CXS endstation is shown in Figure 6.

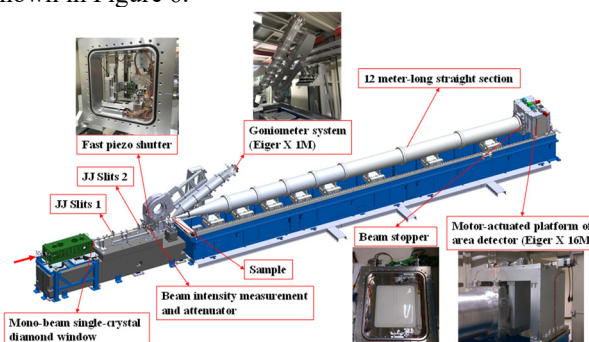


Figure 6: The layout and on-site view of the CXS endstation.

CONCLUSION

The CXS beamline at TPS has been completely constructed and opened for users, and the performance has been also achieved basically. The radiation shields and vacuum condition performed expectedly as well as the differential pumping design. The white-beam components were evaluated by thermal analysis in advance and also verified on-site. The status of the CXS endstation is briefly presented, and some functional expansion is ongoing for more experimental opportunity in the future.

REFERENCES

- [1] H. Y. Yan *et al.*, "Stable mechanical design of coherent X-ray scattering beamline at Taiwan Photon Source", in Proc. MEDSI 2014, Melbourne, Australia, Oct. 2014, https://medsi.lbl.gov/files/page_156/Posters/Stable_Mechanical_Design_of_Coherent_X-Ray_Scattering_Beamline_at_Taiwan_Photon_Source_Hong-Yi_Yan.pdf.
- [2] H. Y. Yan *et al.*, "Mechanical design of secondary source slits for hard X-ray beamlines at Taiwan Photon Source", in Proc. MEDSI 2016, Barcelona, Spain, September 2016, paper MOPE05, pp. 11-16.

- [3] M. H. Lee *et al.*, “Developing white beam components of TPS beamline 24A”, in *Proc. MEDSI 2016*, Barcelona, Spain, 11-16, September, 2016, paper TUPE12, pp. 183-186.
- [4] C. K. Kuan *et al.*, “General Design of ID Front Ends in the TPS”, in *Proc. IPAC 2017*, Copenhagen, Denmark, May 2017, paper THPVA068, pp. 14-19.

VALIDATION RESULTS FOR SIRIUS APU19 FRONT END PROTOTYPE *

H. G. P. de Oliveira†, L. C. Arruda, C. S. N. C. Bueno, H. F. Canova, P. T. Fonseca, G. Rodrigues, L. Sanfelici, L. M. Volpe, LNLS, Campinas, Brazil

Abstract

A Front End (FE) prototype for a 19-mm period length Adjustable Phase Undulator (APU19) beamline of the new Brazilian 4th-generation synchrotron, Sirius, was assembled in the LNLS metrology building in January 2017 to validate main design concepts. Regarding stability, flow-induced vibration (FIV) investigations were carried out on the water-cooled components, and modal analyses were made on the X-Ray Beam Position Monitor (XBPM) support. As for the vacuum system, final pressure levels were investigated and a vacuum breach was intentionally provoked to verify the performance of the equipment protection system (EPS). In addition, cycling tests of the Photon and Gamma shutters were conducted to verify the FE reliability. Moreover, the three-layer protection system, developed to limit the maximum aperture for the high-power slits, was functionally evaluated. Finally, the results were used to improve the FE to its final design. This paper describes the tests setups and results obtained during the validations.

INTRODUCTION

The Front-End comprehends the group of components connecting the storage ring (SR) to the beamline. They are responsible for defining the final aperture, absorbing exceeding beam power and providing radiation protection, storage ring vacuum protection and photon-beam diagnostics [1]. Figure 1 shows an overview of the FE design, highlighting its main components position. An APU19 front-end was first prototyped to validate its mechanical design concepts.

RESULTS AND DISCUSSIONS

Flow-Induced Vibrations

The FE components must handle a high-power load from the APU19 white beam, therefore they must be water-cooled. The total error budget allowed for each component is 1% of the beam size (which is ~30 mm for the APU19

FE). This analysis aimed to quantify the vibration contribution of the cooling system.

A 3D accelerometer from Kistler (8726A) was used to measure the vibration level in each component with and without a water flow of 3 m/s. With the data, it was possible to investigate the RMS displacement on the beam transversal plane. The results for each component are compiled in Table 1.

Table 1: RMS Displacement of the Front-End Components

Component	Flow on [nm]		Flow off [nm]		Variation (%)	
	X	Y	X	Y	X	Y
Mask	22	48	20	40	10	20
Photon	607	44	80	23	658	91
Slit 1	203	28	53	19	283	47
Slit 2	173	31	54	23	220	35
XBPM	15	52	15	36	0	30

The large influence of the cooling system on the Photon Shutter can be justified by the fact that its driving mechanism doesn't have a high stiffness in the X direction. As the water inlet is in the same direction, the disturbances are intensified. Even so, all the contributions are below 1% of the beam size.

XBPM Support Modal Analysis

The XBPM is the most sensitive component in the FE, demanding very strict stability requirements for it to be reliable [2]. It is mounted on the top of a granite block, which is designed for higher stiffness, aiming at the first eigenfrequency value above 100 Hz when tightened to the ground. A modal analysis of the XBPM support was conducted to verify its performance and compare the results with the Finite Element Analysis (FEA) simulation previously carried out using Ansys Workbench [3]. Simulations were firstly done considering the support as a free-body and then as rigidly attached to the ground (grouted).

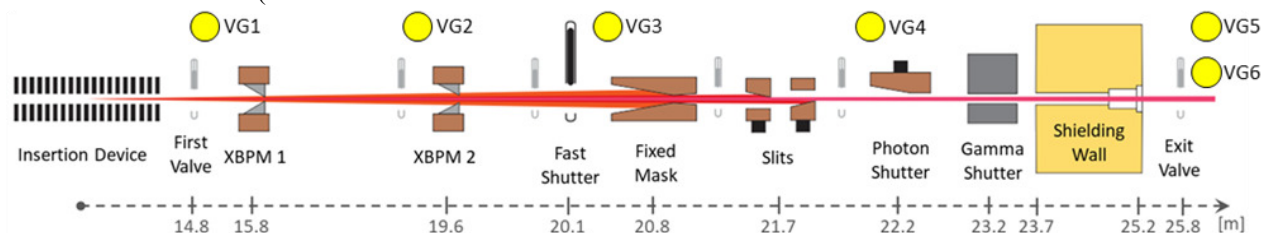


Figure 1: APU19 Front End general layout with each component's distance from the undulator. The vacuum gauges (VG) used to monitor the pressure level along the FE are represented by yellow circles. VG5 and VG6 are used in redundancy for the Fast Shutter (FS) actuation in case of an air inrush at the beamline.

* Work supported by the Brazilian Ministry of Science, Technology, Innovation and Communication

† henrique.oliveira@lnls.br

The first investigation made was a free-body analysis, aiming to evaluate the support internal vibration modes. The granite block was suspended by springs, decoupling the system around 1 Hz. Based on the simulation, some points of interest were mapped for the accelerometer positioning (Kistler 8786A5). For each point, the block was excited using an impact hammer instrumented with a force sensor (PCB Piezotronics 086C02). The results presented a good correlation with the simulation, with a maximum divergence of 1.2% on the eigenfrequency values.

The second investigation aimed to evaluate the performance of the support when tightened to the ground. The same measurement instrumentation was used, varying the interface between the granite block and the Metrology Building floor: tightened directly to the floor (no interface); or using metal shimmings (copper and aluminum) to improve the contact stiffness.

Table 2 shows the obtained results for the three first eigenfrequencies. The cooper-shimming interface presented slightly better results, but the performance is still below expected. A limitation was attributed to the stiffness of the Metrology Building floor. Further studies on this hypothesis are being carried out. However, a higher stiffness is expected for the Sirius especial foundation, and, for now, it was defined that the XBPM support for the six first beamlines will be grouted to the floor.

Table 2: Modal Analysis Results for XBPM Support

Mode	Simulation	Ground	Aluminum	Cooper
1°	230 Hz	38 Hz	48 Hz	50 Hz
2°	230 Hz	39 Hz	49 Hz	72 Hz
3°	640 Hz	326 Hz	335 Hz	353 Hz

Vacuum Breach / EPS Validation

To investigate if the FE would effectively protect the SR in case of an air inrush at the beamline, a vacuum accident was provoked downstream the FE prototype. This study was carried out to validate three design aspects of the FE: the low conductance due to the reduced straight section diameter on the vacuum pipes; the pinhole effect due to the components small apertures; and the air velocity in case of an inrush accident.

The FE vacuum pipes were initially designed with a diameter of 63 mm, but since the photon-beam size generated by an APU19 undulator is about 31 mm x 16 mm, the vacuum pipe diameter as reduced to 38.8 mm, diminishing almost 40% of its size (and thus the overall conductance). This reduction should delay a shockwave impact in a few milliseconds.

The components small apertures, e.g. the gamma shutter (ϕ 10 mm), the slits (9 x 9 mm²), and the fixed mask (ϕ 3.1 mm), also contribute for the FE protection effectiveness, through a "pinhole effect", which physically holds back an air shockwave (SW).

This experiment aimed to evaluate SW velocity achieved by considering different accident conditions. Similar studies were also conducted in other facilities to correlate the SW velocity to the leakage hole and pipe diameter [4, 5].

The test setup was prepared by adding a low-pressure chamber (LPC) with an ion pump and a vacuum gage (VG) in the FE upstream, which simulates the SR vacuum level (10^{-11} mbar). At the FE downstream, a 790 mm section of vacuum pipe and a small chamber were installed, with a pressure differential of eight orders of magnitude related to the atmosphere. This chamber includes the two redundant sensors for the FS activation and a window. To simulate the inrush accident, the window was broken by an instrumented impact hammer, and its signal was used to verify the exact moment of the breach. The acquisition system was an NI CRIO 9039, which acquired data of all the FE VGs at a rate of 90 kHz.

To determine the worst possible condition for the accident (largest aperture at window rupture with maximum SW velocity), the experiment was repeated four times, varying the window material: CuAg foils (100 μ m and 50 μ m) and Kapton foils (50 μ m and 25 μ m). Afterwards, it was repeated two more times considering the worst condition.

Figure 2 shows the obtained wave front average velocity through the FE. It varied from 121 m/s to 687 m/s on the breach moment depending on the window material: the thinnest Kapton foil presented the largest rupture aperture, thus the greatest initial velocity.

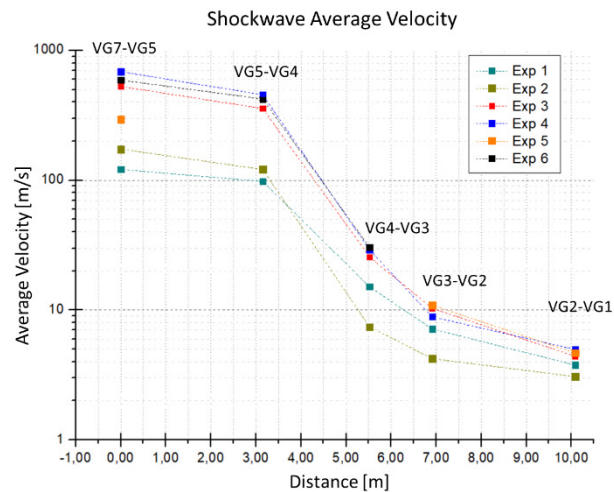


Figure 2: Average SW velocity in each FE section, calculated considering the instant on which the VG detected a pressure increase and the distance between two adjacent VGs.

Figure 2 also illustrates the "pinhole effect", verified by the great decrease on the SW velocity along the FE path, especially at the fixed mask region, which contributed for a reduction of 64% of its average values.

Figure 3 exhibits the time interval that the SW spent to reach each of the VGs. The red dashed line represents the FS closure time provided by its manufacturer (16 ms). As illustrated in the FE layout (Figure 1), the FS is located near the VG3, approximately 5.6 m from the inrush region. Considering the worst case, the SW reached VG3 in 61 ms, resulting in a safety margin of 3.8 compared to 16 ms from the FS closing time.

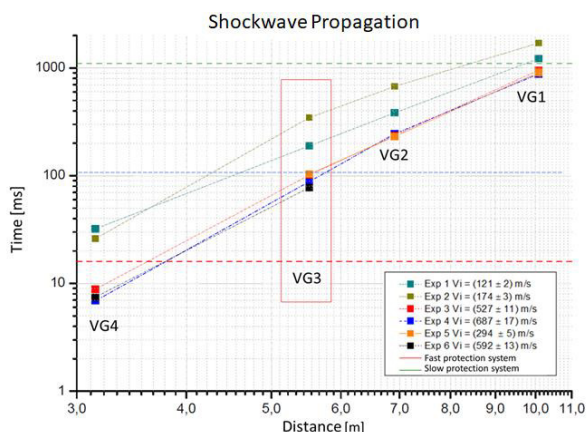


Figure 3: Comparison of the time interval for closing the fast shutter (16 ms - red dashed line) with the time that the SW reaches VG4 to VG1, and the reference time value for gate valve closure (1 s - green dashed line).

The final pressure data obtained with the EPS system online is shown in Figure 4. It demonstrates that, even with a pressure increase at the FE, the EPS system reacts to the event quick enough to preserve the vacuum level at 10^{-5} mbar in the FS region. The gauges upstream (VG2 and VG1) were not affected and the subtle pressure increase registered by PS0 (representing the SR) is due to the gate valve closure, recovering its initial state after 1.5 seconds.

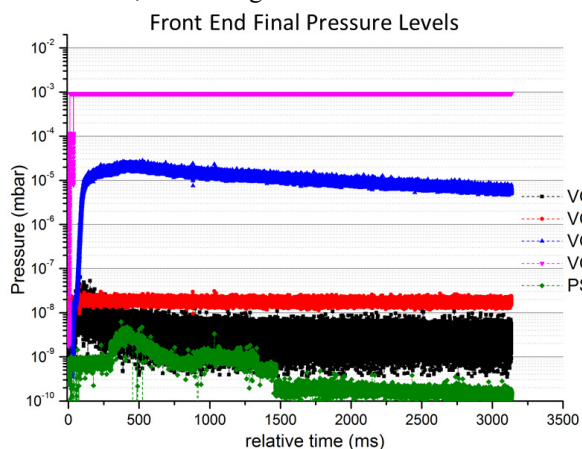


Figure 4: Pressure level after the inrush event. The FS blocked the SW and preserved the vacuum level upstream.

Cycling Stress

To verify the FE reliability, the system was submitted to a stress test, consisting of full cycles with the Gamma and Photon Shutters. During the cycling period (10 days), the components and limit switches fastening screws torque were verified daily, and the pressure level was monitored along the FE path. The system was not disturbed even after 10,000 cycles and the screws torque didn't show variations. By these results, the shutters systems were approved.

Slits Limit Switch System

The High-Power Slits motion system is based on Huber translation stages with micrometric accuracy. Even so, a three layers protection system was developed to ensure that

the slits would never move beyond its maximum permissible aperture, avoiding damages to the beamline optics. The system is based on software control, limit switches (LS) and a Hard Stop. The use of inductive LS was proposed due to its low hysteresis and good repeatability. The DW-AV-601-M4-276 sensor by Contrinex was chosen. It was embedded in a housing, which is also used as the hard stop. Figure 5 shows the developed housing and LS system assembly.

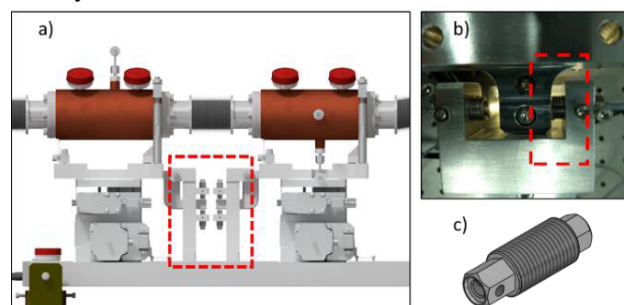


Figure 5: a) design for the LS system with 4 sensors per slit (2 vertical and 2 horizontal); b) LS system assembled for validation test; c) sensor housing.

To verify the sensor performance, a repeatability test was carried out. It consisted on evaluating the sensor activation position during several cycles, according to the Huber stage encoder reading. Each cycle consisted of: leaning the housing against the surface under test; moving this surface 50 μm on the opposite direction; mounting the sensor in the housing and pushing it to the surface until it activates; and finally, programming the stage to move away from the sensor and travel back to it until it activates and interrupts the motion. The encoder reading is then recorded. This routine was repeated 1200 times for each direction and the results are shown in Figure 6.

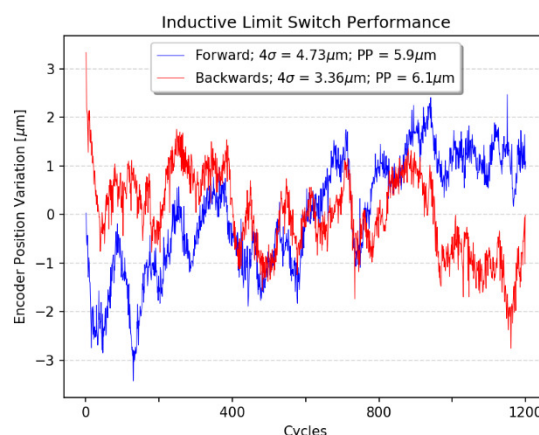


Figure 6: Inductive sensor performance on horizontal direction during 1200 cycles. The Y-axis is the deviation from the mean of the encoder reading when the sensor is activated.

With the proposed inductive LS, the system achieved a unidirectional repeatability of $4.73\mu\text{m}$ and a peak-to-peak value of $6.10\mu\text{m}$.

CONCLUSIONS

The FE prototype has fulfilled its purpose to validate the main aspects adopted on its design. It also elucidated minor details to be improved, such as the Photon Shutter mechanism stiffness, alignment mechanism, size of girders fastening holes, electronics panel positioning and bake-out tapes requirements. Based on the results, an improved design was proposed, manufactured and the first three FEs are currently on installation phase at Sirius.

ACKNOWLEDGMENTS

The authors would like to gratefully acknowledge the funding by the Brazilian Ministry of Science, Technology, Innovation and Communication and the contribution of the LNLS team involved in the FE prototype characterization.

REFERENCES

- [1] L. M. Volpe *et al.*, “High Heat Load Front Ends for Sirius”, in *Proc. MEDSI 2016*, Barcelona, Spain, Sep. 2016, paper WEPE06, pp. 324-326, doi:10.18429/JACoW-MEDSI2016-WEPE06
- [2] N. Hubert, S. Marques *et al.*, “Design of a New Blade Type X-BPM”, in *Proc. IBIC 2014*, Monterey, USA, Sep. 2014, paper WEPD22.
- [3] ANSYS® Academic Research Mechanical, Release 19.1.
- [4] G. Vandoni, M. Ady, M.A. Hermann, R. Kersevan, and D.T. Ziemianski, “Leak Propagation Dynamics for the HIE-ISOLDE Superconducting Linac”, in *Proc. 5th Int. Particle Accelerator Conf. (IPAC'14)*, Dresden, Germany, June 2014, pp. 2351-2353, doi:10.18429/JACoW-IPAC2014-WEPME039
- [5] S. Takahashi, *et al.*, “Prediction of vacuum deterioration caused by vacuum accident in the beamline”, *Vacuum.*, vol. 155, p. 325-335, Jun. 2018, doi:10.1016/j.vacuum.2018.06.029

THE DETECTOR ADJUSTMENT SYSTEM OF TAIWAN PHOTON SOURCE 24A

B. Y. Chen[†], G. C. Yin, M. Y. Hsu, X. Y. Li, D. J. Wang, L. J. Lai
 National Synchrotron Radiation Research Center, 300 Hsinchu, Taiwan

Abstract

The soft X-ray tomography endstation of TPS has the ability to provide 3D biological cell images by fluorescence structured-illumination microscopy (SIM) and soft x-ray tomography (SXT). The electron energy is design to be in the range of 200 eV to 3 keV. The detector system equipped with an Andor® iKon-L Series imaging CCD, X-Z-roll-pitch adjustment stage, and long stroke bellows system. The detector system can adjust the CCD about 10 mm in both X and Z direction, and +5 degree of roll. Moreover, the long stroke bellows system gives the CCD an extra degree of freedom in the Y direction and its range is up to 2500 mm. That can locate the CCD close to the sample to get a larger field of view, and far from the sample to get higher image resolution. In this study, the design and commission status of the detector system is studied and the mechanical structures are also presented.

INTRODUCTIONS

The soft X-ray tomography endstation (TPS 24A) is one of the phase II beamlines of Taiwan Photon Source. The main function of this endstation is aimed for the transmission full-field imaging of biological samples, such as thick cells or tissues. Most of the bio-cell or tissues are composed of carbon, oxygen, and nitrogen, etc. That gives a good chance to adopt the water window, which is between the K edge of carbon (284 eV) and oxygen (543 eV), to get the high contrast between biological sample and water. Moreover, the image contrast can be further improved when the x-ray energy decrease to the range of 2000 ~ 3000 eV for phase contrast soft X-ray tomography [1-3].

BEAMLINE LAYOUT

The beamline layout of TPS 24A is shown in Fig. 1. The X-ray comes out from bending source and focused by the horizontal focused mirror (HFM) and vertical focused mirror (VFM). The x-ray is further pass through the plane grating mirror (PGM) and vertical refocusing mirror (VRFM). Finally, the x-ray is focused by the capillary condenser (CC) and shine on the biological sample. The fluorescence structured-illumination microscopy (SIM) is used to get the 3D biological cell images. Besides, the image can be projected by zone plate (ZP) and collected by the detector system, which is performed by Andor® iKon-L Series imaging CCD. The distance between detector system and the sample can be changed in a large range of 1390 mm to 3910 mm.

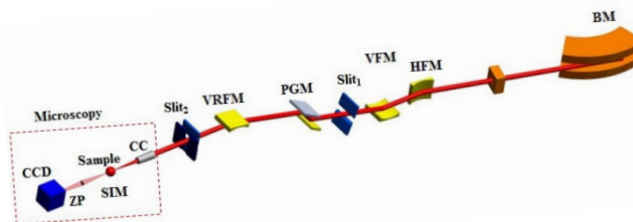


Figure 1: Beamline layout of TPS 24A.

DETECTOR SYSTEM

The image of soft X-ray beamline is collected by the detector system, which is at the very end of this endstation. The detector system has three major parts, which includes (1) foundation, (2) long linear guide way, and (3) adjustment part. The detail design concept and components are described in this section.

Design Target

The phase contrast or absorption contrast signal comes from the sample, which is shining by the soft X-ray, will be collected by structured-illumination microscopy and Andor® iKon-L Series imaging CCD. The design target of the detector system is shown in the following: (1) system stability: The pixel size of Andor iKon-L series imaging CCD is $13.5 \mu\text{m} \times 13.5 \mu\text{m}$, thus, the vibration of the detector system shall be less than $2.7 \mu\text{m}$ (20% of pixel size). (2) the position of detector: According to the optical design, the distance between detector and sample for different X-ray energy and magnification are in the range of 1390 mm to 3910 mm. (3) adjustment part: The resolution and travel range of the adjustment system is $1 \mu\text{m}$ and 10 mm, respectively. This alignment part is necessary for adjusting the position of the detector with x-ray.

Foundation of Detector System

The allowable peak to peak vibration level is $2.7 \mu\text{m}$, this value is quite larger than the ground vibration, which is around 130 nm. But the foundation of the detector system still needs to design carefully, because the system has many degree of freedoms for adjustment. Therefore, stable and strong base is required.

Consider of the structure and thermal stability, the granite bases were adopted to form the reliable foundation of whole system. Each granite was placed on a 20 mm thick stainless steel, which is well aligned by laser tracker. The accuracy of vertical and horizontal position of both the stainless steel plate and granite is about several micro-meters. The foundation of detector system is shown in Fig. 2.

[†] chen.by@nsrrc.org.tw



Figure 2: Foundation of detector system.

Long Linear Guide Way of Detector System

The long travel range of detector system is realized by a long linear guide way system. The long linear guide way system is based on thick optical table, which dimension is 3600 mm x 1000 mm x 400 mm (L x W x T). This optical table is support with six Hi-wedge® supports, each support can adjust the height level in the range of ± 6 mm. That support also provides the optical table a rotational range about 3 mrad. The long linear guide way of detector system is shown in Fig. 3.

The long bellows with 2500 mm stroke was connected in front of the detector, this bellows will be pumped down to the pressure lower than 10^{-4} torr to avoid the absorption of signal. The bellows is divided into two parts, one is used to axial compression and elongation in the range of 2500 mm, and the other is for the lateral movement in the range of ± 10 mm. The first part of the bellows is supported by seven pairs of frame, which is based on individual sliding block. The second part of the bellows is linked with the adjustment part. The THK® GSR-25T long linear guide way was adopted to transfer the bellows and the adjustment part. The rack teeth were made on the side of the linear guide, thus the alignment of the linear guide way and the teeth for the actuator gear is not necessary.

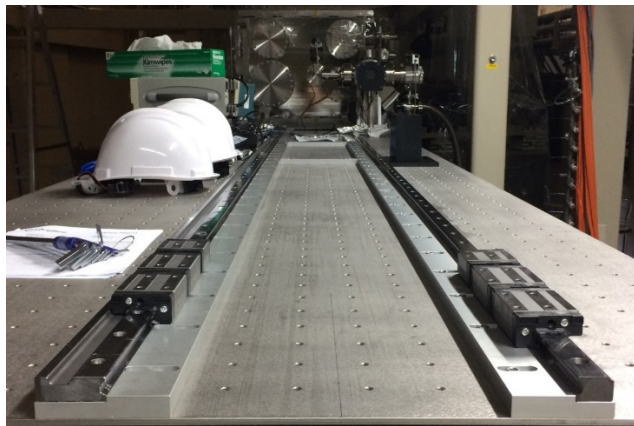


Figure 3: Long linear guide way of detector system.

Adjustment Part of Detector System

The main portion of the adjustment part is shown in Fig. 4. The heavy-duty Oriental motor® 5-phase motor combine with THK® GP6-25A pinion gear provide large push and pull force to the adjustment stage. The maximum pull and push force requirement of the system can be evaluated from the deformation of the bellows, the spring constant of bellows, cross-section of bellows, air pressure acting on the bellows, and the safety factor. Then the force shall be considered with the maximum torque and diameter of the pinion gear. The location of the adjustment stage in the Y direction is measured by Renishaw® optical encoder with the resolution better than $1 \mu\text{m}$.

The second part of the bellows is used to cover the lateral movement of the detector during adjustment only, and no axial deformation is allowable. Therefore, this portion of bellows is located on the front of the adjustable stage, and fixed with the L-shaped frame.

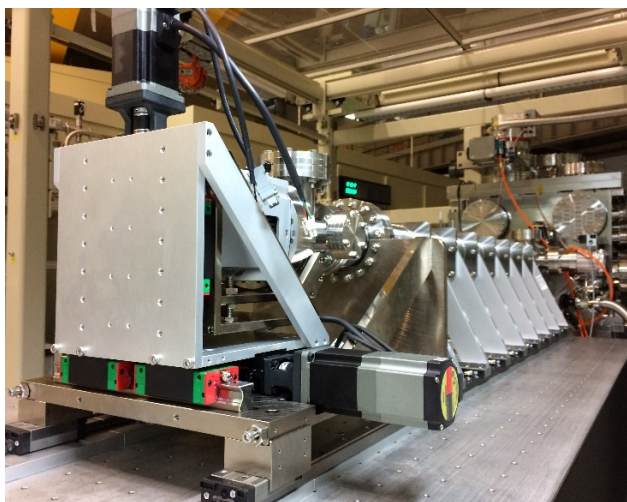


Figure 4: Adjustment part of detector system.

Two NSK® monocarriers combined with HIWIN® linear guide way and Oriental motor® are used to align the detector in the X and Z direction. The exact movement in these two directions is defined by the encoder, which is embedded in the 5-phase stepping motor. The total travel ranges in these two directions are both ± 10 mm.

In order to further align the oriental degree of freedoms, roll and pitch, there are four M10 screws, located on the bottom of the detector support plane, can manually adjust the detector during the pre-alignment process in the range of ± 5 degrees and ± 3 degrees for roll and pitch, respectively.

There is another six-way-crosses in front of the detector, which is used to mount the liquid nitrogen cryogenic pump and vacuum gauge, therefore the vacuum pressure at the end of the system can be monitored and maintained at the level of 10^{-4} torr.

Connection with Main Chamber

The connection portion between the detector system and the main chamber is an individual six-way crosses, which is fixed on the stainless steel support. The support can be adjusted ± 5 mm in the x direction, moreover the upper part of the support can tune the horizontal level of the crosses, as shown in Fig. 5.

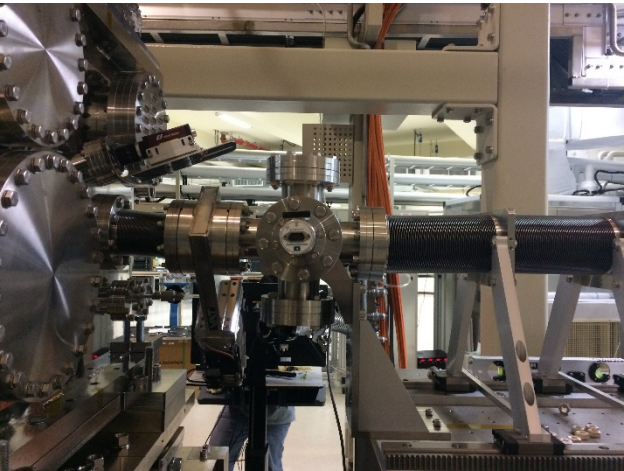


Figure 5: Six-way crosses for the connection portion.

CONCLUSION

The detector system of TPS 24A equipped with an imaging CCD, X-Z-roll-pitch adjustment stage, and long stroke bellows system was design and installed. The detector system can adjust the CCD about 10 mm in both X and Z direction, ± 5 degree of roll, and ± 3 degree of pitch. Moreover, the long stroke bellows system gives the CCD an extra degree of freedom in Y direction and its range is up to 2500 mm. That can locate the CCD close to the sample to get larger field of view, and far from the sample to get higher image resolution. This system started commission in the early of 2018, and got the first image in April, 2018.

REFERENCES

[1] L. J. Lai *et al.*, “Development of a Correlation of Soft X-Ray Tomography with Fluorescence Microscopy at Taiwan Photon Source”, in *Proc. 8th Int. X-ray Microscopy Conf. (XRM’18)*, Canada, 2018, 105403.

[2] C. A. Larabell, and K. A Nugent, “Imaging cellular architecture with X-rays”, *Current Opinion in Structural Biology*, Vol. 20, pp. 623-631, 2010.

[3] Y. J. Su, et al., “Design of the soft x-ray tomography beamline at Taiwan photon source”, *AIP Conference Proceedings*, 1741, 030046, 2016, doi: 10.1063/1.4952869

OPTIMIZING THE PETRA IV GIRDER BY USING BIO-INSPIRED STRUCTURES

S. Andresen¹, Alfred-Wegener-Institut Helmholtz-Zentrum für Polar- und Meeresforschung,
 Bremerhaven, Germany

¹also at Deutsches Elektronen Synchrotron, Hamburg, Germany

Abstract

The PETRA IV project at DESY (Deutsches Elektronen Synchrotron) aims at building a unique synchrotron light source to provide beams of hard X-rays with unprecedented coherence properties that can be focused to dimensions in the nanometer-regime.

An optimization of the girder structure is necessary to reduce the impact of ambient vibrations on the particle beam. For this purpose, several numerical approaches have been made to simultaneously reach natural frequencies above 50 Hz, a high stiffness and a low mass.

In order to define an optimal girder support, a parametric study was conducted varying both the number and location of support points. Based on the resulting arrangement of support points, topology optimizations were performed to achieve a high stiffness and a high first natural frequency. The following transformation of the results into parametric constructions allowed further parametric studies to find optimal geometry parameters leading to the aimed girder properties. In addition to that, bio-inspired structures based on marine organisms were applied to the girder which likewise resulted in improved girder properties.

INTRODUCTION

DESY (Deutsches Elektronen Synchrotron) plans to convert the PETRA III (Positron-Elektron-Tandem-Ring-Anlage) storage ring into an ultralow emittance synchrotron radiation source, able to provide beams of hard X-rays with very high coherence properties that can be focused to dimensions in the nanometer-regime and allows the analysis of physical, chemical and biological interactions which occur inside materials between atoms.

In order to receive such highly energetic and low emittance synchrotron radiation, it is fundamental to minimize the impact of ambient vibration on the girders which carry the magnets guiding the particles. An optimization of the girder design is therefore crucial to avoid resonance and

minimize vibration amplitudes.

To achieve the best results, several approaches were followed in a systematic development of new girder designs.

As the definition of boundary conditions has a strong impact on the vibration characteristics and the stiffness, a support study was conducted which varied both the number and location of support points in order to find the optimal support point number and locations. Based on the resulting arrangement of support points, topology optimizations were performed to achieve a high stiffness in combination with a high first natural frequency. The goal of a topology optimization is to find the optimal design of a structure within a specified design space [1]. The applied loads and support conditions, the volume of the structure to be designed and potentially additional design restrictions are known, whereas the size, shape and connectivity of the structure are unknown. The subsequent transformation of the topology optimization result in parametric constructions allowed further parametric studies to determine optimal geometry parameters leading to the aimed girder properties. Furthermore, structures inspired by marine organisms were applied to the girder which also resulted into improved girder properties.

The objective of the conducted studies was to develop girder designs with natural frequencies higher than 52 Hz, a maximal deflection lower than 0.5 mm and a girder mass of maximal 2500 kg.

SUPPORT STUDY

Methods

An actual PETRA III girder assembly provided the basis for the study and led to the model layout shown in Fig. 1. The girder was abstracted as a hollow cuboid and meshed with shell elements with an averaged edge size of 0.08 m. The material was characterized by a Young's modulus of $2.1 \times 10^{11} \text{ N m}^{-2}$, a density of 7830 kg m^{-3} and a Poisson's ratio of 0.3. The defined shell thickness of

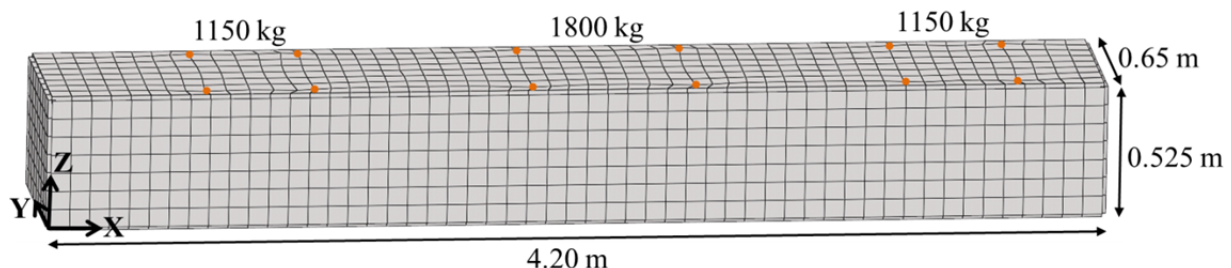


Figure 1: Model assembly considered for the support study. The orange dots show the defined point masses representing the three heavy magnets. The shell thickness of the elements is displayed.

0.03 m led to a girder mass of 2479 kg. Three heavy magnets were considered each as point masses apportioned among four points.

Table 1 summarizes the analyzed support point configurations. Regarding the study steps 1 and 2, three and four support points, respectively, were defined at the Bessel points of the girder and thus at the lower girder surface. This support point configuration has been considered in previous studies [2]. As to the study steps 3, 4 and 5, the support points were located at the upper girder edges at the specified coordinates. Parameter studies were performed varying the support point locations in the defined range with a step size of 0.1 m. At the specified support points, all translations and rotations were zero.

After the model assembly using the software Rhinoceros, Plug-In Grasshopper, the solver OptiStruct (Altair)

was considered to receive the first natural frequency of the conducted modal analysis.

For each study step, the support point locations leading to the highest first natural frequency were recorded. In addition to that, the girder pedestals were included to estimate their impact on the natural frequency (Fig. 2). Here, an optimal wall thickness of the pedestals in order to reach a high stiffness was considered.

Results

Figure 3 shows the first natural frequency depending on the support point configuration and the neglect and consideration of the pedestals. Defining the support points at the Bessel points of the lower girder surface led to low first natural frequencies of less than 15 Hz. The first mode shape showed tilts around the support points with highest

Table 1: Configurations of the support study. Depending on the five study steps, the support point (SP) positions were defined and changed along the X axis of the girder.

Study step	SP	SP position	SP start coordinates	SP displacement along X axis Range	Step size	Number of combinations
1	SP 1	Lower girder surface	(0.94; 0.325; 0.0)	-	-	1
	SP 2	Lower girder surface	(0.94; 0.325; 0.0)	-	-	
	SP 3	Lower girder surface	(3.26; 0.43; 0.0)	-	-	
2	SP 1	Lower girder surface	(0.94; 0.22; 0.0)	-	-	1
	SP 2	Lower girder surface	(0.94; 0.43; 0.0)	-	-	
	SP 3	Lower girder surface	(3.26; 0.22; 0.0)	-	-	
	SP 4	Lower girder surface	(3.26; 0.43; 0.0)	-	-	
3	SP 1	Upper girder edge	(0.94; 0.0; 0.525)	-0.9 - 0.9	0.1	6859
	SP 2	Upper girder edge	(2.1; 0.65; 0.525)	-0.9 - 0.9	0.1	
	SP 3	Upper girder edge	(3.26; 0.0; 0.525)	-0.9 - 0.9	0.1	
4	SP 1	Upper girder edge	(0.94; 0.0; 0.525)	-0.9 - 0.9	0.1	361
	SP 2	Upper girder edge	(0.94; 0.65; 0.525)	-0.9 - 0.9	0.1	
	SP 3	Upper girder edge	(3.26; 0.0; 0.525)	-0.9 - 0.9	0.1	
	SP 4	Upper girder edge	(3.26; 0.65; 0.525)	-0.9 - 0.9	0.1	
5	SP 1	Upper girder edge	(0.94; 0.0; 0.525)	-0.9 - 0.5	0.1	2475
	SP 2	Upper girder edge	(0.94; 0.65; 0.525)	-0.9 - 0.5	0.1	
	SP 3	Upper girder edge	(2.1; 0.0; 0.525)	-0.5 - 0.5	0.1	
	SP 4	Upper girder edge	(2.1; 0.65; 0.525)	-0.5 - 0.5	0.1	
	SP 5	Upper girder edge	(3.26; 0.0; 0.525)	-0.5 - 0.9	0.1	
	SP 6	Upper girder edge	(3.26; 0.65; 0.525)	-0.5 - 0.9	0.1	

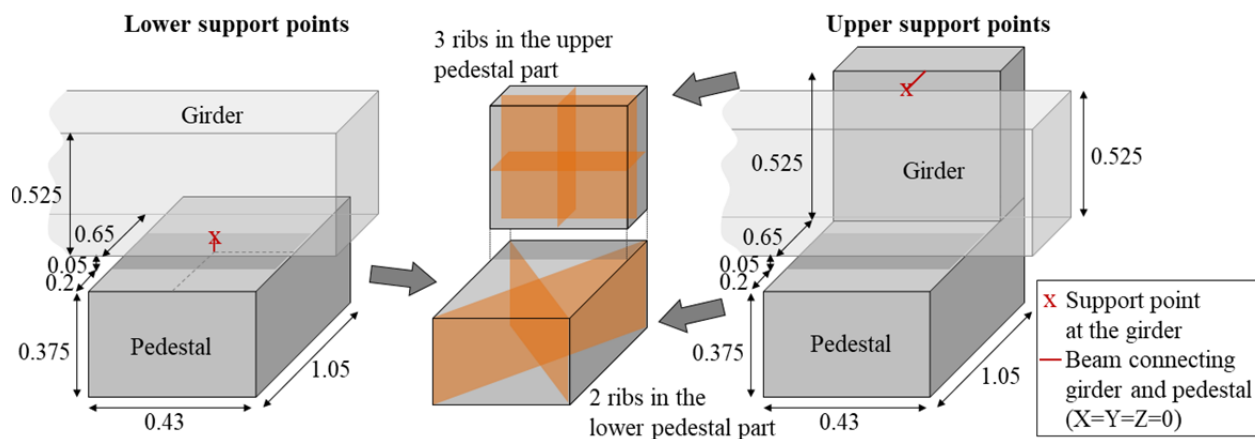


Figure 2: Design of the pedestals. In case of the lower support points, just the lower pedestal part with two ribs was considered, whereas the upper pedestal part with three inner ribs was additionally included for the upper support points.

amplitudes at the locations of the magnets.

Locating the support points at the upper girder edges led to a first mode shape of bending in the Y-Z-plane overlaid with a torsion mode. Here, the highest amplitudes appeared at the lower girder surface far away from the magnets. The first natural frequency increased with the number of support points (Table 2). Considering the pedestals strongly decreases the first natural frequency.

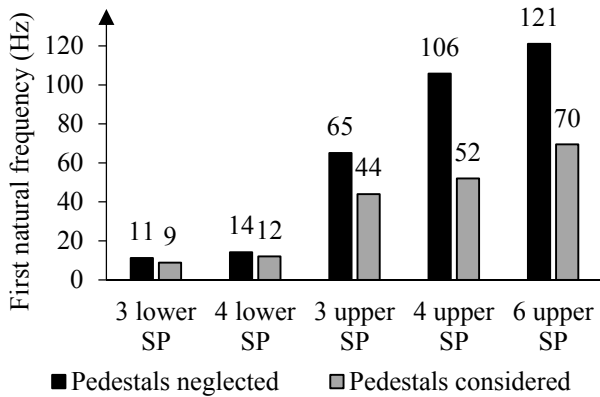


Figure 3: First natural frequency depending on the support point configuration and the neglect and consideration of the pedestals. The frequency is located on top of each bar.

Table 2: Best support point (SP) locations leading to the highest first natural frequency for the three study steps of SP at the upper girder edges.

Study step	SP	Best SP location
3	SP 1	(0.44; 0.0; 0.525)
	SP 2	(3.0; 0.65; 0.525)
	SP 3	(4.16; 0.0; 0.525)
4	SP 1	(0.24; 0.0; 0.525)
	SP 2	(0.24; 0.65; 0.525)
	SP 3	(3.56; 0.0; 0.525)
	SP 4	(3.56; 0.65; 0.525)
5	SP 1	(0.04; 0.0; 0.525)
	SP 2	(0.04; 0.65; 0.525)
	SP 3	(2.0; 0.0; 0.525)
	SP 4	(2.0; 0.65; 0.525)
	SP 5	(3.76; 0.0; 0.525)
	SP 6	(3.76; 0.65; 0.525)

Discussion

Analogous to the result of a conducted support study [3], an increasing number of support points leads to a higher first natural frequency. Moreover, locating the support points close to the magnets has also a positive influence on the vibration characteristics as already mentioned [4].

Considering the pedestals leads to a strong decrease in the first natural frequency. In order to assure a first natural frequency of more than 52 Hz, six support points at the locations listed in Table 2 should be defined. This support configuration was considered in the following studies.

Simulation

Structural Statics And Dynamics

TOPOLOGY OPTIMIZATION

Methods

The volume shown in Fig. 1 was specified as design space where elements can be removed during the optimization. Besides this, elements around the support points and point masses were manually selected as non-design space. The girder pedestals were neglected. Previous studies have demonstrated that no material in the girder middle is needed to reach a high first natural frequency. Therefore, 30% in the middle of the design space was manually removed to support the generation of clear load paths.

The best support point configuration of six support points gotten from the support study was considered. The material properties were analogous to the support study, while the mesh was made out of solid elements with an average size of 1 cm. A final volume fraction of 0.1 and a first natural frequency of more than 100 Hz were defined as constraints. For this, a modal load case with the point loads shown in Fig 1 was specified considering the first ten natural frequencies. For the second linear static load case, the magnets were abstracted as point loads resulting from the product of the magnet mass and the gravity factor. The topology optimization was conducted using HyperWorks (Altair) and the solver OptiStruct.

With the help of the smoothing function OSSMOOTH and minor manual changes, the resulting structure was 3D meshed. A modal analysis and a linear static analysis were conducted to examine the natural frequencies and the maximal deflection under the load of the three magnets.

Subsequently, curves were derived from the resulting structure and projected onto the outer girder walls using Rhinoceros and the Plug-In Grasshopper as well as algorithms developed in my research section at the Alfred-Wegener-Institut. A shell thickness optimization was conducted to determine the optimal thickness for each rib formed by the curves to meet the requirements stated initially.

Results

The topology optimization result is shown in Fig 4a. A high virtual element density represents the importance of an element to reach the desired properties. The reanalysis of the resulting structure of 863 kg led to a maximal deflection of 0.03 mm. The first natural frequency is 91 Hz and the connected mode shape showed a local vibration of the lower right bars while the structure close to the magnets revealed low amplitude (Fig. 4b). The shell thickness optimization of the ribs derived from the topology optimization resulted into a variety of structures with properties shown in Fig. 5a. A girder structure with a first natural frequency of 130 Hz, a mass of 1920 kg and a maximal deflection of 0.01 mm is shown in Fig. 5b.

Discussion

The topology optimization led to a very light structure showing a high first natural frequency and low maximal deflection. Girder structures with even higher natural

Content from this work may be used under the terms of the CC BY 3.0 licence (© 2018). Any distribution of this work must maintain attribution to the author(s), title of the work, publisher, and DOI.

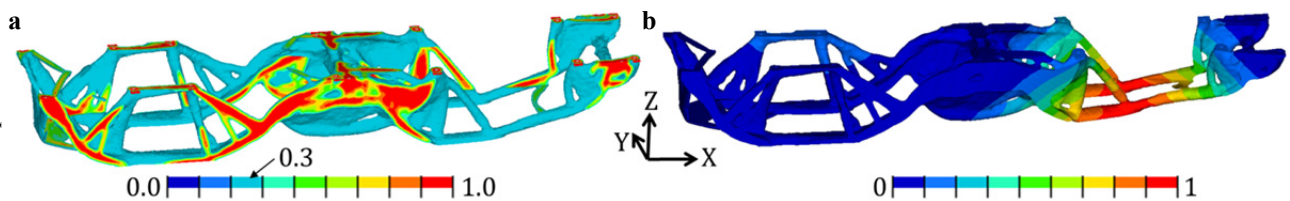


Figure 4: (a) Result of the topology optimization. The coloured scale represents the virtual element density. All elements with a density of at least 0.3 are shown. (b) First mode shape ($f = 91$ Hz) of the resulting structure of the topology optimization. The coloured scale represents the normalized vibration amplitude.

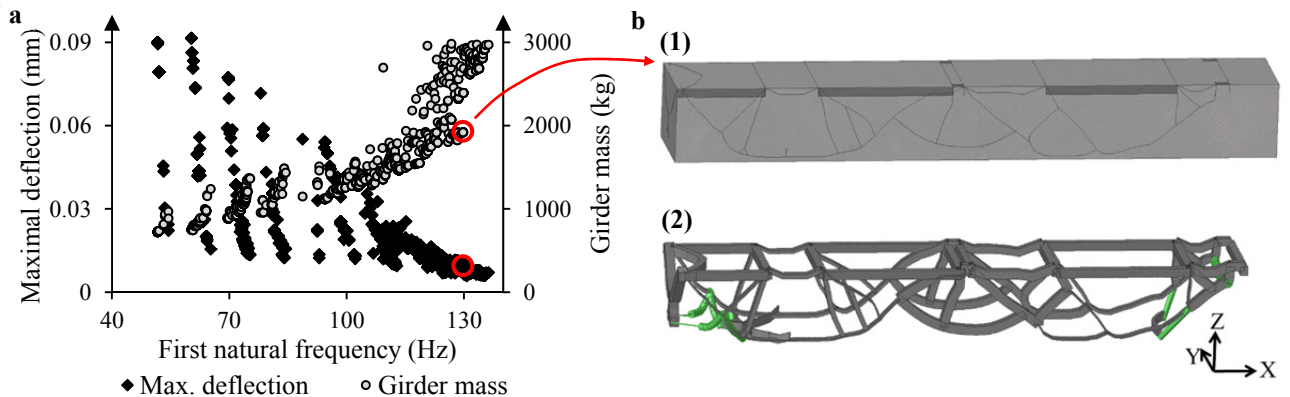


Figure 5: (a) First natural frequency, maximal deflection and girder mass of different girder structures derived from the topology optimization. The girder with the red encircled properties is shown in (b1) entirely and in (b2) with hidden outer walls to visualize the inner ribs and beams derived from the topology optimization (*bright grey*: outer surfaces of the girder, *dark grey*: ribs, *green*: beams).

frequencies can be obtained by integrating ribs and beams derived from the topology optimization results into the girder. As the girder pedestals have been neglected so far, it still has to be demonstrated that including the pedestals, the first natural frequency will remain above 52 Hz.

BIONIC STRUCTURES

Methods

Design space, boundary conditions and material properties were specified analogous to the layout of the topology optimization. Thus, the location of the support points and the point masses representing the magnets were fixed, while the girder pedestals were neglected.

The designed lattice structure was based on a point distribution inside the design space. Using the fixed magnet and support points as attractors, the point distribution density was changed locally around the attractors. The lattice was built by connecting each point with a certain number of neighboring points leading to a lattice structure which can be often observed in nature.

In order to reach a high first natural frequency, the outer walls of the design space were also considered. A parameter study was conducted generating 300 structures based on randomly defined parameter values in between the specified definition range of each parameter shown in Table 3. For each structure, a modal analysis and a linear static analysis were conducted.

Table 3: Parameters and their definition range for the lattice structure based on connection of neighboring points and attractors (Attr.).

Parameters		Range
Point distribution:	Attr. value (m):	0.10 - 0.70
	Attr. radius (m):	0.05 - 0.40
	Attr. decay factor (m):	1.10 - 2.50
	Global value (m):	0.20 - 0.70
Neighbors:	Number of neighbors:	5 - 25
Outer surfaces:	Shell thickness (m):	0.01 - 0.05
Lattice cross section:	Outer diameter (m):	0.01 - 0.06
	Wall thickness (m):	0.003 - 0.03

During the evaluation of the results, structures having a mass of more than 2500 kg and showing a maximal deflection of more than 0.5 mm were neglected. From the remaining structures, the one having the highest first natural frequency was rated as the best lattice structure. Afterwards, the pedestals were considered analogous to the support study to estimate their influence on the natural frequency and the stiffness.

Results

The inverse values of the maximal deflections (stiffness) and the girder masses were tending to increase with the squared first natural frequency similar to a simple mass oscillator (Fig. 6). However, for a specific stiffness value, structures with different first natural frequencies

were generated, whereby the girder masses remained within permitted values.

Figure 7 shows the best structure considering the pedestals, whose parameter values are summarized in Table 4. The total girder mass was 2489 kg and the maximal deflection 0.02 mm. The first mode shape at a frequency of 70 Hz showed a rotation in the Y-Z-plane with the highest amplitude at the lower girder surface far away from the magnets.

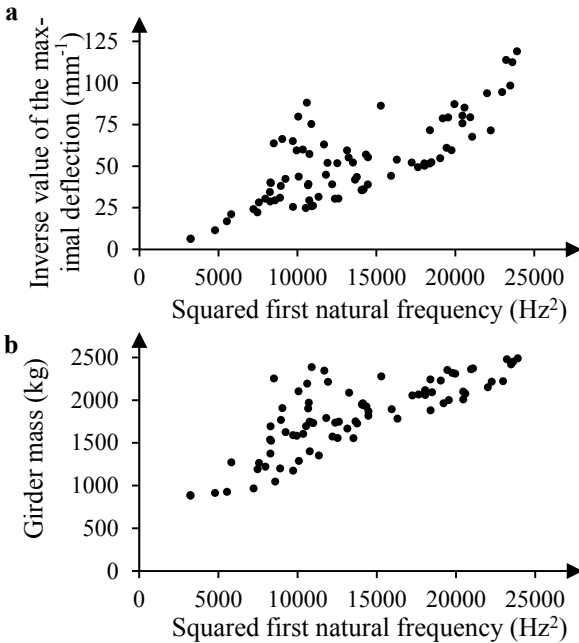


Figure 6: Inverse of the maximal deflection (stiffness) (a) and girder mass (b) depending on the squared first natural frequency for different lattice girder structure.

Discussion

Using bionic lattice structures in combination with an optimal support point configuration leads to girder assemblies with natural frequencies well above 70 Hz. Moreover, the parametric construction of the lattice structure allows the shift of natural frequencies by leaving the stiffness and mass constant or the other way around. However, production restrictions have not been included yet.

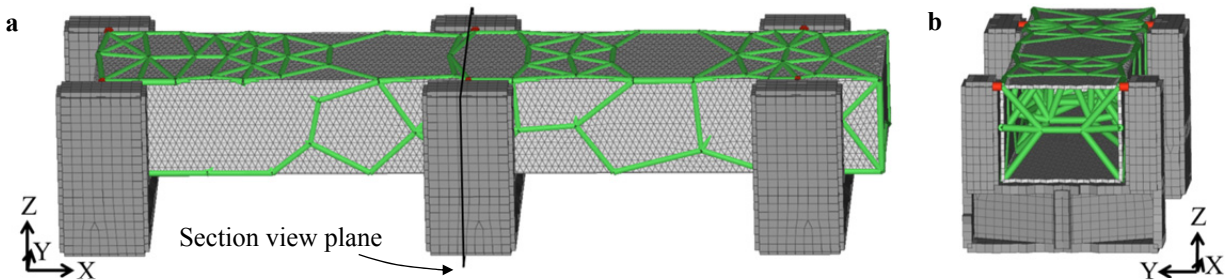


Figure 7: Best bio-inspired lattice girder structure based on connection of neighboring points. (b) shows the section view marked in (a). The shell thickness and beam cross section of the elements are displayed (green: lattice, bright grey: outer surfaces of the girder, dark grey: pedestals, red: beams connecting girder and pedestals).

Table 4: Parameters and their specified values for the best lattice structure based on connection of neighboring points and attractors (Attr.).

Parameters		Value
Point distribution:	Attr. value (m):	0.27
	Attr. radius (m):	0.17
	Attr. decay factor (m):	2.47
	Global value (m):	0.41
Neighbors:	Number of neighbors:	6
Outer surfaces:	Shell thickness (m):	0.02
Lattice cross section:	Outer diameter (m):	0.04
	Wall thickness (m):	0.014

CONCLUSION

The study shows the high potential of structural optimization for passive vibration control. A variation of the girder structure allows a natural frequency shift keeping the stiffness and the mass constant.

Innovative, bio-inspired girder structures were generated with improved properties regarding stiffness, natural frequencies and lightweight design.

ACKNOWLEDGMENTS

I would like to thank my colleagues from Alfred-Wegener-Institut for providing the algorithms to generate the bionic lattice structures and my colleagues from DESY for the collaboration and the frequent comments on my work.

REFERENCES

- [1] M. P. Bendsøe and O. Sigmund, “*Topology Optimization, Theory, Methods and Applications*”, 2nd Edition, Springer-Verlag Berlin Heidelberg, Germany, 2004.
- [2] S. Andresen “Untersuchung von Eigenschwingung und Leichtbaupotenzial unterschiedlicher Gitterstrukturen am Beispiel von Magnetuntergestellen von Teilchenbeschleunigern”, presented at NAFEMS DACH, Bamberg, Germany, May 2018, unpublished.
- [3] X. Wang, Z. Yan, H. Du and L. Yin, “Investigation of mechanical stability for SSRF girder”, in *Proc. MEDSI’04*, 2004, Grenoble, France.
- [4] D. Mangra, S. Sharma and C. Doose, “Performance of the vibration damping pads in the APS storage ring”, in *Proc. MEDSI’00*, 2000, Wurenlingen/Villigen, Switzerland.

MECHANICAL ENGINEERING DESIGN AND SIMULATION FOR SPIRAL2 ACCELERATOR @GANIL

C. Barthe-Dejean, F. Lutton, M. Michel, P. Gangnant, C. Michel, P. Lecomte, F. Daudin, C. Stodel,
R. Revenko, J.L. Vignet, M. Di Giacomo, JF. Leyge, E. Petit, SPIRAL2-GANIL, Caen, France
M. Walter, CC-IN2P3, Lyon, France.

Abstract

The SPIRAL2 project at GANIL is based on a superconducting ion Continuous Wave LINAC with two associated experimental areas named S3 (Super Separator Spectrometer) and NFS (Neutron For Science). This paper reports the main contributions of Mechanical Design Group at GANIL to the project. Mechanical engineers have been highly involved since 2005 from the pre-design of the accelerator and its development until present to finalize the installation. During the development phase, design and numerical simulation were used throughout the complete process: from the ion sources, to the LINAC accelerator, then through beam transport lines to experimental halls equipped with detectors. The entire installation (process, buildings and systems) is integrated in 3D CAD models. The paper focuses on three equipments designed in collaboration with electronics engineers and physicists: the Rebuncher in the Mean Energy Beam Transport line (MEBT); the Instrumentation of Secondary Emission Monitors (SEM profilers), and the Target Station in S3. SPIRAL2 also has to meet safety requirements, such as seismic hazard, therefore the dynamic simulations performed to demonstrate the mechanical strength in case of earthquake will also be detailed.

INTRODUCTION

The SPIRAL2 radioactive ion beam facility was launched in July 2005, with the participation of French laboratories (CEA, CNRS) and international partners. SPIRAL2 complex is built in two phases: a first one including the accelerator, the Neutron-based research area (NFS) and the Super Separator Spectrometer (S3); and a second one including the low energy RIB experimental hall called DESIR. The SPIRAL2 LINAC takes into account a wide variety of beams detailed in Table 1 to fulfill the physics requests.

Table 1: Beam Specifications [1]

Particles	H+	D+	ions	option
Q/A	1	1/2	1/3	1/6
Max I (mA)	5	5	1	1
Max energy (MeV/A)	33	20	15	8.5
Max beam power (kW)	165	200	45	51

The SPIRAL2 first phase facility is now built; the accelerator installation and connecting tasks are achieved, and the beam commissioning has started with encouraging and promising results. The goal is now to send the first beam for physical experiment in NFS in 2019.

MECHANICAL CAD INTEGRATION

One of the main task of the Mechanical Design Group was to integrate the CAD Models (CATIAv5 files) from the different laboratories participating to the project (Fig.1 and Fig.2). It was decided to use a common PLM (Product Life cycle Management) software: SMARTEAM. This PLM solution allows complex collaborative design development at large scale (Fig.3). The software license, the installation and the training for all the users in different laboratories were organized jointly by GANIL Mechanical Design Group and IN2P3-CNRS Data Center.

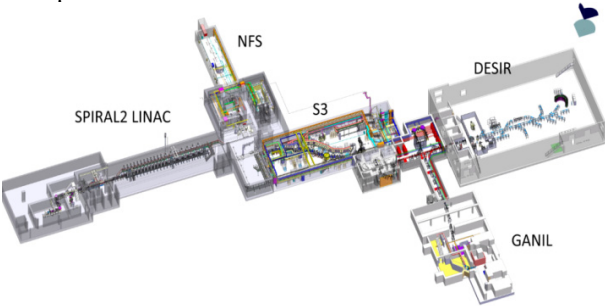


Figure 1: SPIRAL2 CAD complete assembly model.

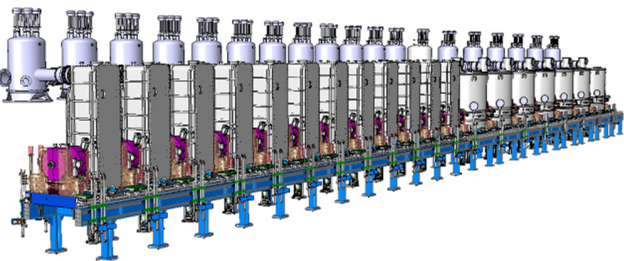


Figure 2: LINAC with its Cryomodules type A and B.

The complete SPIRAL2 CATIA v5 CAD file is 11 Gigabytes. It was assembled by GANIL designers, and is the most important CAD assembly of IN2P3 database. The CAD model of S3 experimental hall itself contains 2700 different sub-models.

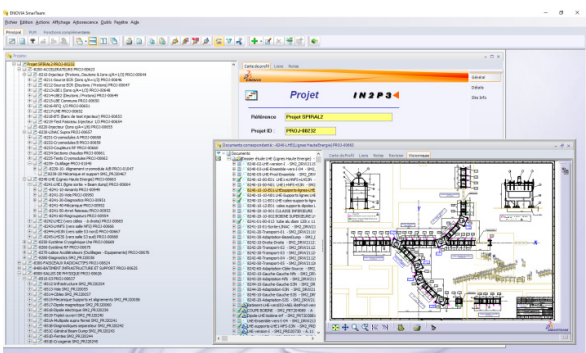


Figure 3: SPIRAL2 Project in Smarteam Data Base.

MEBT REBUNCHER

The Spiral 2 accelerator uses radio-frequency three-gap cavities to prepare high intensity beams before LINAC acceleration. Its function is to ensure and maintain the beam’s longitudinal dimension. Those cavities work at 88 MHz [2] The rebunchers are located in the Mean Energy Beam Transport line. They are made of a copper plated stainless steel vacuum chamber and solid copper parts. The central section is machined from a solid block for more accuracy. The chamber, stems, beam ports and trimmers are water cooled. The stems are cooled by a continuous layer of water flowing inside the tube (Fig. 4).

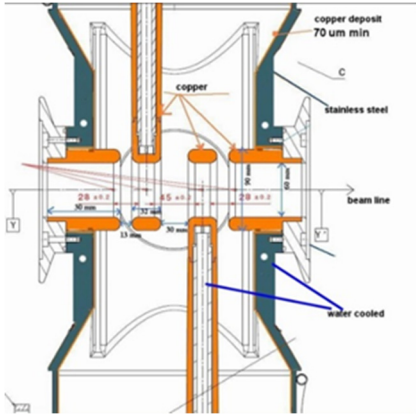


Figure 4 : Rebuncher section [3].

The several heat-transfert simulations (Fig. 5) have allowed to optimize the cooling system in order to ensure a maximum $\Delta T= 50\text{ }^{\circ}\text{C}$ between all parts [4] : an essential parameter to grants proper functioning of the cavity (the temperature distribution has to be as uniform as possible). A motorized and a manual trimmer panel are added to adjust the distance between the panels and the stem to compensate thermal expansion.

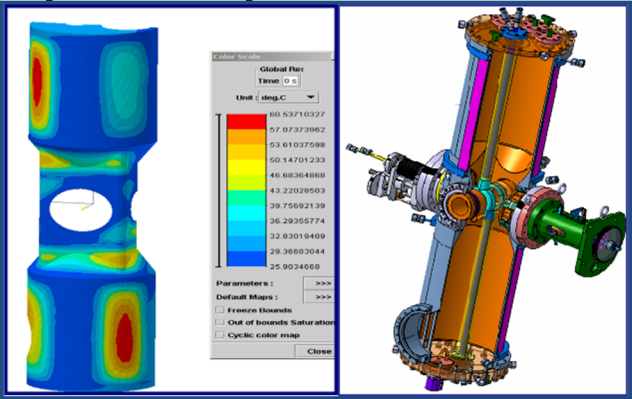


Figure 5: Rebuncher CAD and thermal simulation [4].

S3 TARGET STATION

The design of the stable target station was fully developed by GANIL Mechanical Design Group. The aim is to obtain a stable behaviour of the targets under high primary beams intensities (up to 350 MeV at 10 μA) [5,6]. In order to withstand this high beam intensity, the 18 solid targets are placed on 6 different sectors which are mounted on a large

wheel rotating at high speed (Fig. 6). One of the example of target studied is Uranium on Carbon and Titanium backings [6]. The total thickness is less than 5 μm . The station is designed for several type of targets materials which range from Carbon to Uranium.

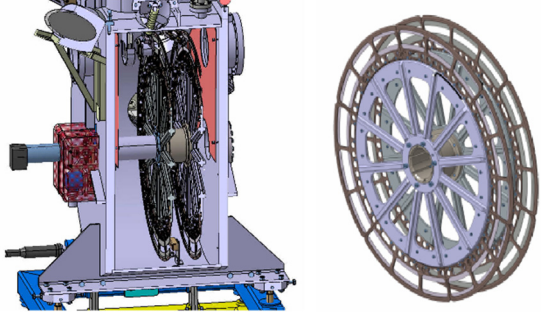


Figure 6: S3 Vacuum chamber assembly with wheel [7].

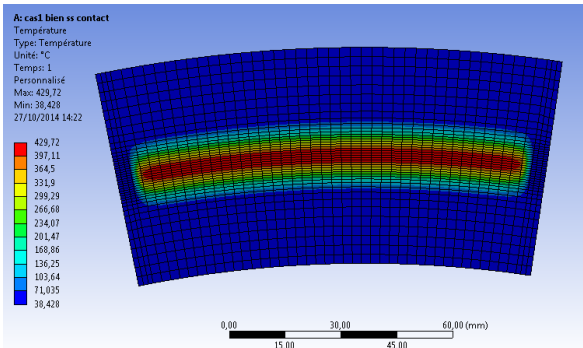


Figure 7: Carbon-Uranium Target thermal simulation [7].

The maximum rotational speed is 3000 rpm (50 Hz) [5,6]. The wheel is made of aluminium to optimize the weight and the shaft is in stainless steel. The shaft is driven by a motor located outside the vacuum chamber: the feedthrough air/vacuum is Ferro-fluidic seal technology based on magnetics sealing for high speed, and specifically designed by the supplier. Dynamic simulations and rotational tests have been realized to determine Eigen frequencies of the system and dynamic behaviour. Different thermo-mechanical simulations have been conducted (Fig. 7) to finally lead to current design with a maximum predicted temperature of 400 $^{\circ}\text{C}$ stabilized after 40 rotations (Fig. 8) [7].

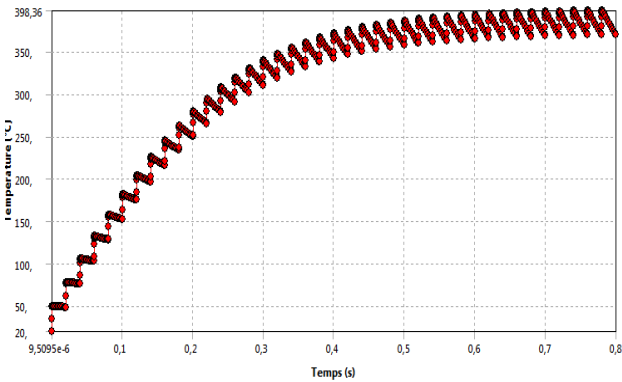


Figure 8: Temperature in the target @3000rpm [7].

SEM PROFILER

The function of the profiler is to characterize the beam position and profile. The profiler is made of tungsten wire Ø20 to Ø150 µm in two orthogonal planes. The beam is passing through the wires and extracts electrons which create an electrical current in the same ratio as the energy transferred to the wire [8]. This type of profiler is used 250 times in all SPIRAL2 beam transport lines (Fig. 9). The actuator has also been developed at GANIL and is used to translate the profiler INSIDE and OUTSIDE the beam with a stroke of 120 mm. The GANIL actuator is now used widely for different accelerators.

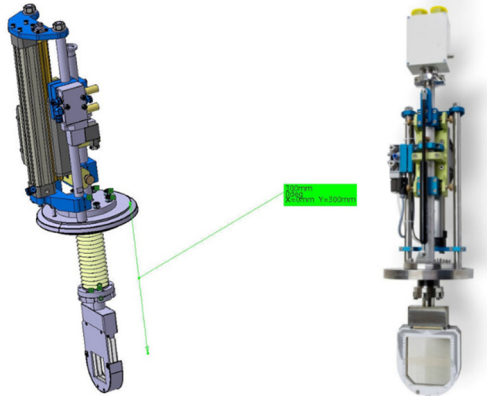


Figure 9 : EMS Profiler.

SEISMIC CALCULATIONS

Safety requirement as specified by A.S.N. (French Nuclear Authority) in terms of seismic hazard have been reinforced. The SPIRAL2 new building is used as containment barrier for radiation protection. In case of earthquake, some equipment has to be designed to ensure that it will not be projected and affect the building. For this reason, all the supporting frame, mechanical support and its anchorage to ground have been calculated to withstand dynamic load corresponding to earthquake S.M.S (Maximum Security Seism). Civil engineering have provided seismic spectral load (Fig. 10) in each building bloc [9]. The simulations have been performed for more than thirty equipments for which weight exceeds 500 kg (example Fig. 11).

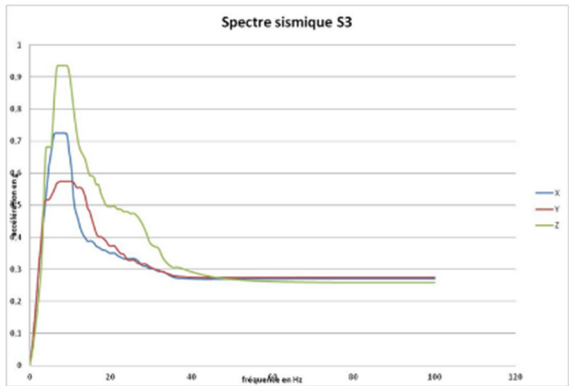


Figure 10: Spectral load for seismic simulation in S3 [9].

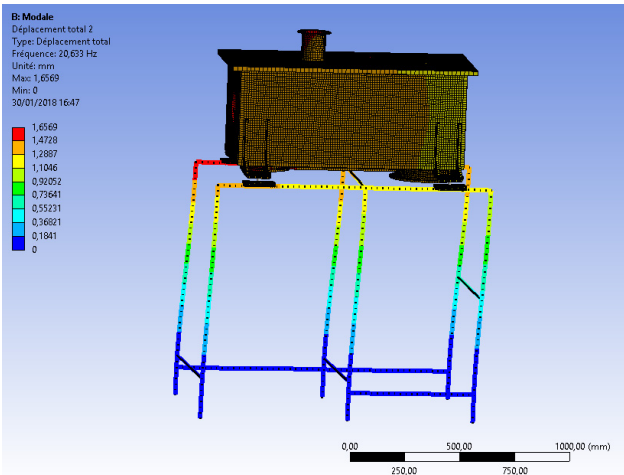


Figure 11: Modal analysis for Detection chamber [10].

The Results are post-treated in terms of Von Misès Stresses (Fig. 12) for all mechanical parts. Each fastener, anchorage and weld is calculated and analysed separately to prove it can meet the Eurocode 3 mechanical design criteria.

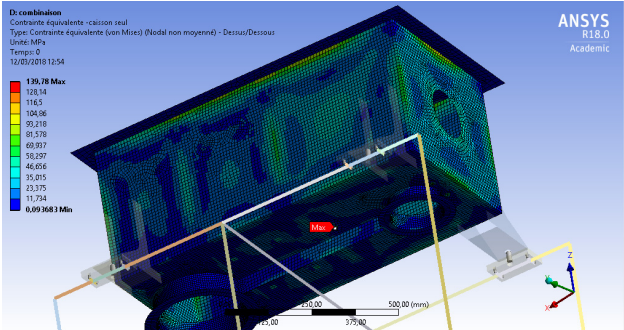


Figure 12: Detection Chamber Von Mises Stresses [10].

A specific computer program based on existing analytical method has been developed on our Finite Element software ANSYS in order to calculate the welds. For one standard mechanical equipment, the different calculation steps necessary to justify the integrity in case of earthquake last 2 months full-time for an engineer of the group.

CONCLUSION

An international project of a magnitude such as SPIRAL2 has led the designers and engineers to adopt new methods of design and simulation, and has required significant development and upgrading of skills in the mechanical design group in various technical domains including CAD large assembly, heat transfer and dynamic simulation.

ACKNOWLEDGMENT

I would like to thank E. Petit, M. Di Giacomo, F. Lutton, P. Gangnant, M. Michel, C. Michel and P. Lecomte, C. Stodel, R. Revenko (SPIRAL2-GANIL) and M. Walter (CC IN2P3) for their help to collect information presented in this document.

REFERENCES

- [1] E. Petit, "Status Report on the SPIRAL2 Facility at GANIL", *Proc. of North American Particle Accelerator Conference (NAPAC'16)*, Chicago, USA, October 9-14, 2016, paper TUA11002.
- [2] M. Di Giacomo "Design Of The MEBT Rebuncher RS for the SPIRAL2 Driver", *Proc. of LINAC 08*, Victoria, BC, Canada, 2008, paper THP047.
- [3] JF Leyge, « Présentation MEBT Rebuncher Test and Results », *GANIL*, 23 janv. 2012.
- [4] , M. Michel, F. Pellemoine, JF. Leyge, « Etude Mécanique des regroupeurs de la ligne LME », *STP00027A*, 2008.
- [5] C. Stodel, F. Pellemoine, R. Hue, F. Lutton, C. Marry «Targets for S3 at SPIRAL2» *Nuclear Instruments and Methods in Physics Research A*, 2010, vol. 613, pp. 480-485.
- [6] Ch. Stodel, J. - F. Libin, C. Marry, F. Lutton, M.- G. Saint-Laurent, B. Bastin, J. Piot, E. Clement, S. Le Moal, V. Morel, P. Gangnant, M. Authier, F. Pellemoine, « High Intensity Targets Stations for S3 », *Journal of Radioanalytical and Nuclear Chemistry*, 2015, Volume 305, Issue 3 pp 761-767 .
- [7] M. Michel, F. Lutton, C. Barthe-Dejean, «Tenue thermique cibles stables S3», *S3-NT-8514-I035728V2.0*, 2014.
- [8] J-L. Vignet, A. Delannoy, E. Guérout, P. Gangant, J.C. Foy, S. Cuzon, C. Houarner, M. Blaizot, "The Beam Profile Monitors for SPIRAL 2", in *Proceedings of DIPAC09*, Basel, Switzerland, 2009, paper TUPB07.
- [9] « Hypothèses et Méthodologie de Calcul Génie Civil pour SPIRAL2 », *Ref PH1-IES-021-NDC-03540-C*.
- [10] C. Barthe-Dejean, F. Lutton, "Calculs de Tenue sismique du Caisson de la Cellule Gazeuse REGLIS", *S3_NT_851E_AT-271894*.

DESIGN AND FEA OF AN INNOVATIVE ROTATING SiC FILTER FOR HIGH-ENERGY X-RAY BEAM

W. Tizzano*, T. Connolley, S. Davies, M. Drakopoulos, G. E. Howell
Diamond Light Source, OX11 0DE Didcot, United Kingdom

Abstract

I12 Joint Engineering, Environmental, and Processing (JEEP) is a high-energy imaging, diffraction and scattering beamline at Diamond. Its source is a superconducting wiggler with a power of approximately 9 kW at 500 mA after the fixed front-end aperture; two permanent filters aim at reducing the power in photons below the operating range of the beamline of 50-150 keV, which accounts for about two-thirds of the total [1]. This paper focuses on the design and simulation process of the secondary permanent filter, a 4 mm thick SiC disk. The first version of the filter was vulnerable to cracking due to thermally induced stress, so a new filter based on an innovative concept was proposed: a water-cooled shaft rotates, via a ceramic interface, the SiC disk; the disk operates up to 900 °C, and a copper absorber surrounding the filter dissipates the heat through radiation. We utilised analysis data following failure of an initial prototype to successfully model the heat flow using FEA. This model informed different iterations of the re-design of the assembly, addressing the issues identified. The operational temperature of the final product matches within a few degrees Celsius the one predicted by the simulation.

INTRODUCTION

I12 is a high-energy imaging, diffraction and scattering beamline located on a straight section of Diamond storage ring. Its source is a 4.2 T superconducting wiggler, and the beamline operates at 50–150 keV, providing a hard X-ray beam capable of penetrating large dense samples, for

* walter.tizzano@diamond.ac.uk

example engineering parts and assemblies (e.g., superalloy turbine blades [2], or steel and Al alloy internal combustion engines [3]). Table 1 summarizes the key parameters of the beamline and Fig. 1 shows its layout.

Table 1: I12 Key Parameters [4]

Source	Super-conducting wiggler, 4.2 T, 48 mm periodicity, 22 full field periods
Beam acceptance	1 mrad×0.3 mrad
Beam modes	White beam or monochromatic beam
Monochromator	Si (111) cryo-cooled double crystal bent Laue
Energy range	50–150 keV

The techniques available to I12 users include, among the others: static and time-resolved radiography and tomography, energy-dispersive diffraction, monochromatic and white-beam two-dimensional diffraction/scattering, and high energy Small-Angle X-ray Scattering (SAXS) [1].

The beamline has two in-line experimental hutches (EH), one inside Diamond Experimental Hall 51.7 m from the source (EH1), and the other in an external building 94.5 m from the source (EH2). EH1 allows experiments involving small and medium-sized samples and sample environments, whereas EH2 offers space for large or complex experiments [5].

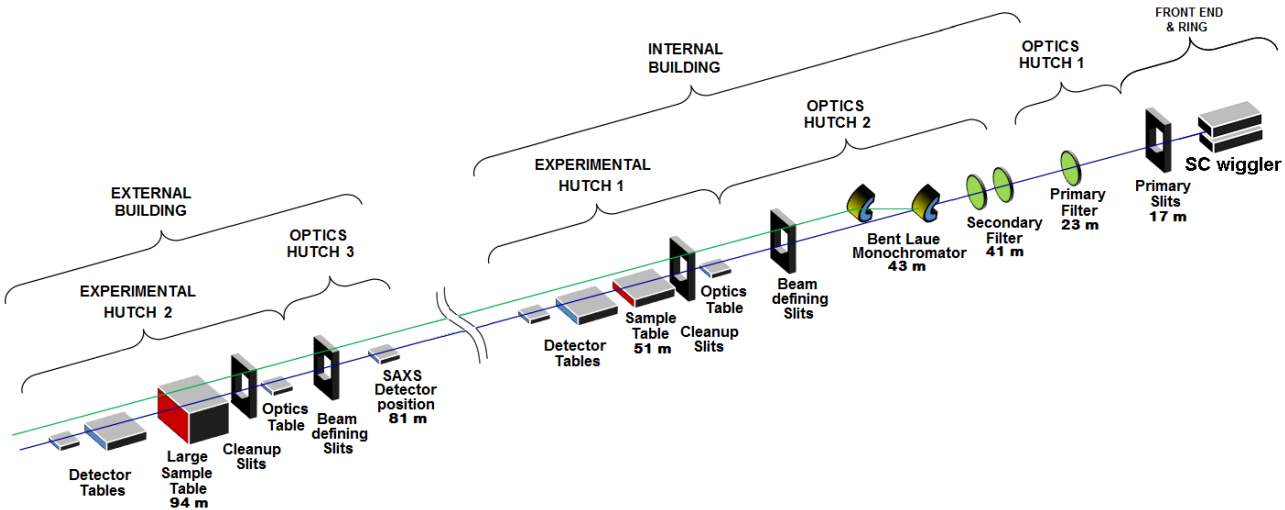


Figure 1: Schematic optical and functional layout of the I12 JEEP beamline [4].

HEAT LOAD MANAGEMENT

Diamond Light Light Source Storage Ring currently operates at 300 mA [6], with design intent up to 500 mA [7]. With this current, the total power emitted by the wiggler would be 56 kW, and the maximum power entering the beam line through the fixed front-end aperture would be 9 kW [1].

About two-thirds of this power is due to photons below the operating range of the beamline of 50-150 keV, and for this reason two permanent filters are installed upstream of the Laue monochromator (see Fig. 1). The primary filter is a series of two water-cooled Chemical Vapour Deposited (CVD) diamond disks, that reduce the total power to 6.2 kW. This paper will focus mainly on the secondary filter, that aims at reducing the power from 6.2 kW to 2.6 kW. Figure 2 shows the flux at 500 mA, and the effect of the aforementioned filters and of attenuators of different thickness.

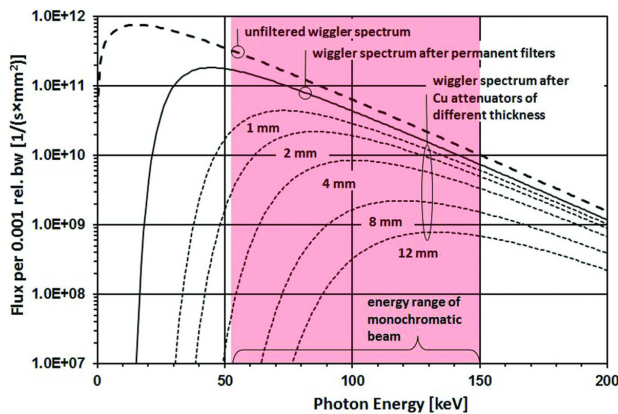


Figure 2: Photon flux at 500 mA calculated with XOP [8], in the full 1 mrad x 0.3 mrad fan accepted by the beamline at 50 m from the source. The effect of filters and attenuation is shown [1].

Static Secondary Filter

The beamline was initially commissioned with a static secondary filter, consisting in a 4 mm thick SiC disk, diffusion bonded to a water cooled Cu carrier via a Mo interface (see Fig. 3).

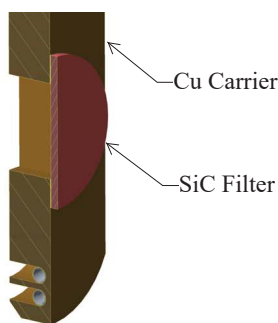


Figure 3: Static filter.

A combination of thermally-induced stress and residual stress from the diffusion bonding [1] proved to be too challenging for the filter. Following failure on first aperture of maximum beam load at 300 mA, it was necessary to replace

it with a completely different design, that would not have diffusion bonding and that would be less vulnerable to thermal stresses.

Rotating Secondary Filter

A new assembly filter, shown in Fig. 4, was designed. In this design, the SiC disk rotates at 60 RPM, in this way the thermal load is distributed on a larger area, reducing the power density the filter material is subjected to. Two Cu water-cooled absorbers collect the heat radiated by the filter; the rotating shaft (that is also water-cooled) dissipates the remaining thermal power, transmitted conductively through a series of Machinable Glass Ceramic (MACOR®) and titanium alloy parts.

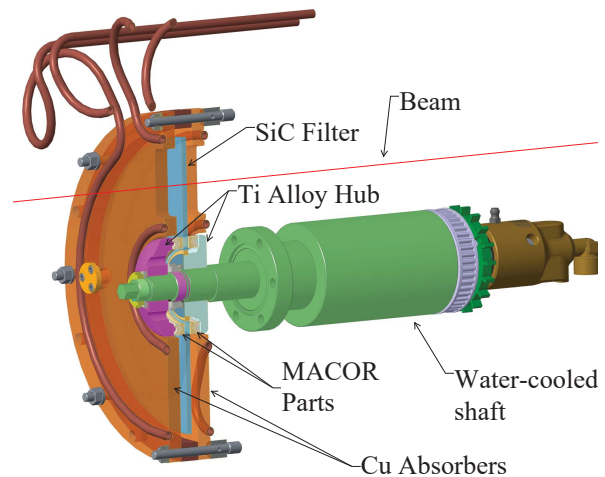


Figure 4: First prototype of the rotating filter.

A thermal finite element simulation was performed, and it showed that no part was subjected to excessive temperatures or stresses, so a first prototype was made and tested; however, the temperatures measured were higher than the ones predicted, and the ceramic parts exhibited some cracking. Further analysis was required.

FAILURE ANALYSIS

The fact that the temperature was higher than predicted suggests that the system exhibited more internal thermal resistance than the one assumed in the simulation, as the boundary conditions are known with a good degree of precision. In particular, the boundary conditions for this system are represented by the external thermal load, accurately calculated by XOP, and the convective water cooling, whose characteristic parameter h was estimated analytically with well-established formulas¹. As for the internal thermal resistance, it can be represented with the electrical circuit analogy², as shown in Fig. 5.

T_d represents the maximum SiC Disk temperature, T_w the cooling water temperature, R_{cond} is a resistance equivalent

¹ The equation for convection is $\dot{Q} = hA\Delta T$, where \dot{Q} is the thermal power, h is the convective heat transfer coefficient, A is the heat transfer area and ΔT is the temperature difference between the bulk fluid and the

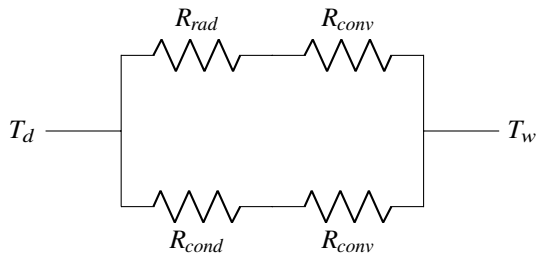


Figure 5: Circuit analogy.

to the parallel of two series of conductive resistances the heat must go through to reach the water cooled shaft, R_{conv} models the convection heat transfer, and R_{rad} is a resistance that takes into account the effect of radiation, governed (for grey bodies³) by this law:

$$\dot{Q} = \frac{\sigma(T_d^4 - T_a^4)}{\frac{1 - \epsilon_d}{A_d \epsilon_d} + \frac{1}{A_d F_{d \rightarrow a}} + \frac{1 - \epsilon_a}{A_a \epsilon_a}}, \quad (1)$$

where d and a are respectively the SiC disk and absorber surfaces interested to the radiation phenomenon, T is their temperature, ϵ their emissivity, A their area, and $F_{d \rightarrow a}$ the view factor from the disk to the absorber.

The fact that T_d from the simulation was significantly lower than the one measured during the test, suggests that either R_{rad} or R_{cond} was higher than the one in the simulation. R_{rad} was estimated with a sufficient degree of precision⁴, so by exclusion it could be assumed that the most significant source of error was likely to be R_{cond} .

As mentioned above, R_{cond} is in fact equivalent to a parallel of two series of resistances. These resistances depend on the conductivity of the materials, their geometry and the interface between them. The materials used are well known, and their conductivity can easily be found on reputable material databases, like MatWeb [11], and the geometry error is negligible, as it depends only on small manufacturing tolerances and some small approximations due to the mesh. This means that the error was probably due mostly by how the interface between the parts was modeled.

At the interface between two parts in contact along a thermal conductance path, there is a temperature drop due to the Thermal Contact Resistance (TCR). This depends on several factors, like the contact pressure between the two parts, the materials, the surface roughness etc. Figure 6

shows how the TCR changes with contact pressure for some common interstitial materials. By default, ANSYS assigns to this variable a very small value⁵, that can be considered like a 'perfect' contact, which is one where there is practically no temperature drop.

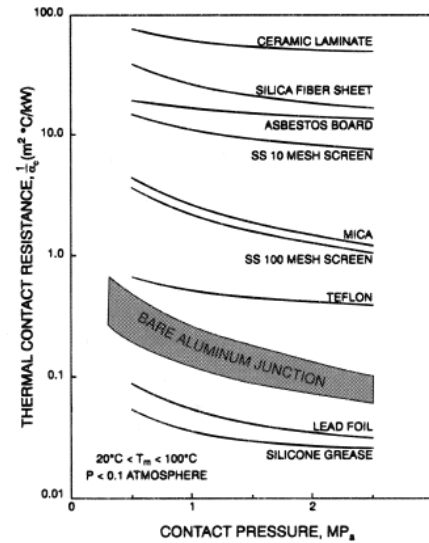


Figure 6: Contact resistance for selected interstitial materials for thermal enhancement or thermal isolation [12].

Even if tables and graphs are available in the literature (e.g., [14]), it is not easy to identify the value of the TCR for all the interfaces in the assembly, because some of the variables it depends on are not known. An alternative approach is to isolate the interface effects from the conductance through the single parts and add a resistor in our electrical model, as shown in Fig. 7. Such a resistor is variable, and by changing its value we change the calculated T_d , if all the other variables are unchanged.

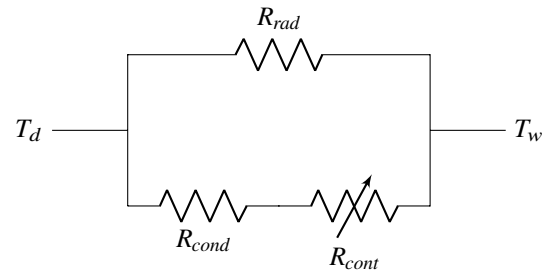


Figure 7: Circuit analogy that takes into account the TCR (R_{conv} omitted for clarity).

By varying R_{cont} until T_d matched the one measured during the test, we could identify a value of this parameter that takes into account the collective effect of all the contact interfaces in the model. In this way we could estimate how much

surface. For forced convection, the parameter h can be estimated with empirical formulas available in the literature [9].

² Ohm's law ($V_2 - V_1$) = RI can be used in thermal circuits as $(T_2 - T_1) = R\dot{Q}$, where T_1 and T_2 are the temperatures of two points of the system, R is the thermal resistance between them, and \dot{Q} is the thermal power transferred from one point to the other.

³ An approximation according which ϵ is frequency independent.

⁴ It depends on the geometry of the parts and the emissivity ϵ of the materials interested to the radiative heat exchange. For the copper absorbers, a conservative value of $7 \cdot 10^{-2}$ [10] was used, whereas the SiC disk's emissivity was measured using the cold immersion method by a Land M1 thermometer having a spectral response of $1.6 \mu\text{m}$. The measured value was 0.66 ± 0.2 at 700°C and did not vary significantly with temperature.

⁵ $TCC = K_{xx} 10^3 / ASM_{diag}$, where TCC is the thermal contact conductance, the reciprocal of TCR , K_{xx} is the largest material conductivity defined in the model, and ASM_{diag} is the geometry bounding box diagonal [13].

heat is transferred by radiation and how much by conduction. In electrical terms, estimate the relative contribution of the two branches of our circuit.

The prototype was tested with a heat load of 389 W, and a model that uses the default value for the TCR predicted a T_d of $\approx 590^\circ\text{C}$ (see Fig. 8a), which means that almost 60% of the thermal power would be dissipated conductively (the lower branch of Fig. 7). The temperature measured in the test was however significantly higher ($\approx 780^\circ\text{C}$, see Fig. 8b), and the R_{cont} that makes the calculated FEA equal to this value is $5\text{ m}^2\text{C/kW}$. Taking into account the TCR , according to the simulation, only 11% of the power is transferred conductively, which explains the higher temperature reached by the disk⁶.

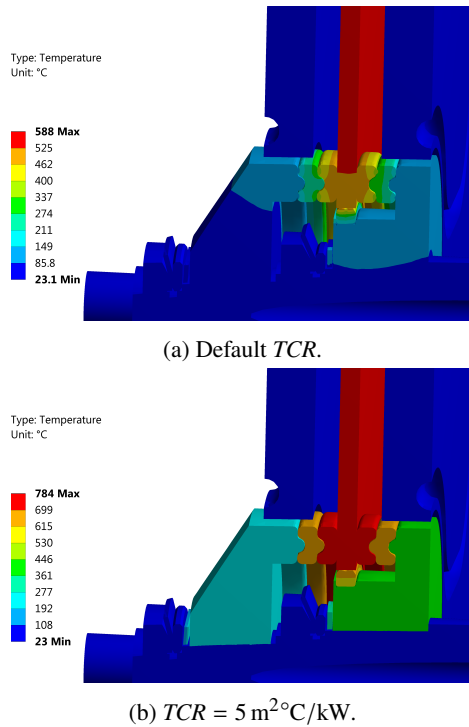


Figure 8: Simulations on the prototype with default (8a) and custom (8b) values for the TCR .

The thermal contact resistance calculated above is relatively high, but realistic, for ceramic parts. It is unacceptably high for metal parts, unless the contact pressure is extremely poor. This suggests that the interface between the Ti alloy hubs and the steel shaft did not transfer sufficient heat because there was not enough contact pressure between these components. One way to improve this is to use the Axiomatic Design principles.

Axiomatic Design

Axiomatic Design is a powerful design methodology that divides the Design World into four domains, and

⁶ The total heat load staying the same, all the heat that is not transferred by conduction must be radiated by the disk to the Cu absorbers; hence, if more heat is transferred in this way, the temperature of the disk must be higher, in accordance to Eq. (1).

models the relationships between them with matrices. The four domains are the Customer domain, the Functional domain, the Physical domain, and the Process domain. To each of these a characteristic vector is assigned ($\{CA_s\}, \{FR_s\}, \{DP_s\}, \{PV_s\}$). The method takes its name from the fact that it is based on two axioms⁷ [15]:

1. the Independence Axiom;
2. the Information Axiom.

The Independence Axiom says that the Functional Requirements should be independent. This means that if we express the relationship between Functional Requirements $\{FR_s\}$ and the Design Parameters $\{DP_s\}$ as $\{FR_s\} = [A]\{DP_s\}$, the matrix $[A]$ should be diagonal. If the design matrix $[A]$ is not diagonal, the $\{FR_s\}$ are coupled, and optimising a Design Parameter to achieve a Functional Requirement might affect other Functional Requirements too, making the optimisation harder, sometimes impossible and the design less robust⁸.

The Information Axiom says that the information content of the design should be minimised⁹.

If we consider the subassembly that includes the water-cooled shaft and the titanium alloy hubs, we have two Functional Requirements:

- $\{FR_1\}$ - can assemble;
- $\{FR_2\}$ - transfers heat.

We have however only a single Design Parameter, the difference between the hub internal diameter D_h and the shaft external diameter d_s that we can call x . We can represent this in matrix form as follows:

$$\begin{Bmatrix} FR_1 \\ FR_2 \end{Bmatrix} = \begin{bmatrix} a_{1,1} & 0 \\ a_{2,1} & 0 \end{bmatrix} \begin{Bmatrix} x \end{Bmatrix} \quad (2)$$

The matrix $[A]$ is not diagonal, hence the design is not uncoupled¹⁰; x affects both $\{FR_1\}$ and $\{FR_2\}$, but its optimal value is different for the two Functional Requirements: to make assembly easier, we want a low contact pressure, but to transfer heat we need a high contact pressure. There is a contradiction¹¹.

One way to resolve this contradiction is to follow the first axiom, and modify our system so that the matrix $[A]$ is diagonal and our system is hence uncoupled.

⁷ Self-evident statements that cannot be derived from other principles.
⁸ There is also a third possibility: the matrix $[A]$ can be triangular. In this case, the system is decoupled, which is a non-ideal scenario but still preferable to a coupled system.
⁹ The *information content* I is defined as $I = \log_2 1/P$, and it represents the probability of satisfying a given functional requirement [15].
¹⁰ All systems with more $\{FR_s\}$ than $\{DP_s\}$ are coupled.
¹¹ Also, x is temperature dependent: the greater the ΔT between hubs and shaft, the greater the TCR become, which leads to even higher ΔT . This causes a runaway phenomenon where temperature spirals out of control.

FINAL DESIGN

The analysis of the failed prototype informed the final design, that addressed the weaknesses we identified, and that were described in the previous sections. In particular, changes were made to improve the heat transfer between the hubs and the shaft without compromising the ease of assembly, and to maximise the heat dissipated through radiation.

Redesigned Hubs

A feature was added to the hubs, consisting in some wedges that allow the tightening of the hub around the shaft after it has been slid into position, as shown in Fig. 9.

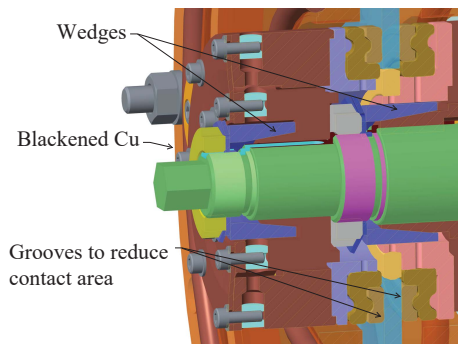


Figure 9: Final Design.

This allows for both easy installation and high contact pressure during operation. In axiomatic design terms, the new feature gives us another design parameter that we can call y , hence the system now looks like this:

$$\begin{Bmatrix} FR_1 \\ FR_2 \end{Bmatrix} = \begin{bmatrix} a_{1,1} & 0 \\ 0 & a_{2,2} \end{bmatrix} \begin{Bmatrix} x \\ y \end{Bmatrix} \quad (3)$$

In the redesigned assembly x has a different meaning, and it represents the clearance of the wedges before they are compressed. y is the clamping force and depends on the wedge geometry (height, angle etc.)¹². The matrix $[A]$ is now diagonal, and the system uncoupled¹³.

Maximising Radiation

If a 389 W heat load radiation heat transfer dominated (only 11% was transferred conductively), this would be even more true with higher heat loads (the heat transferred by radiation grows with the fourth power of temperature (Eq. (1)), the one transferred by conduction only grows linearly with the temperature¹⁴). For this reason, we decided to increase the radiation heat transfer by improving the emissivity ϵ of the copper absorbers. This could be achieved by blackening

¹² Similarly to x in the first prototype, also y varies with ΔT . However, in this case, the clamping force grows with ΔT ; consequently the TCR becomes smaller, which leads to a stable thermal equilibrium.

¹³ By design there is clearance between the uncompressed wedges and the shaft. If we had interference, the term $A_{2,1}$ would be different from 0, and our system would be decoupled.

¹⁴ $\dot{Q} = U\Delta T$, where U is the conductance.

them¹⁵. Also, we wanted to increase the conductive resistance of the chain of components supporting the disk, so that less heat would be transferred along that path. We achieved this by considerably reducing the contact surface between the ceramic parts and the disk (by adding some grooves on the ceramic, in the positions indicated in Fig. 9).

FEA

The redesigned assembly was simulated, using the thermal contact resistance value estimated with the prototype¹⁶. With a calculated thermal load of 3.6 kW at 500 mA, the predicted disk temperature is $\approx 880^\circ\text{C}$ (see Fig. 10). Diamond is currently operating at 350 mA, so the maximum condition cannot be validated with a physical measurement.

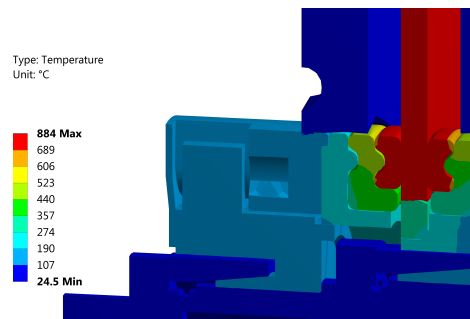


Figure 10: Thermal FEA on the final design, with the maximum 500 mA current in the storage ring.

For this reason, we simulated the assembly with other heat loads, and compared the results with the values measured in the operational assembly. The simulation is able to predict reliably and conservatively the temperatures: the error is less than 10%, and the simulated value is always larger than the measured one, confirming that the assumptions made were conservative. Also, the heat is now dissipated almost exclusively by the absorbers, as only $\approx 1\%$ goes to the water-cooled shaft¹⁷.

CONCLUSION

The redesigned rotating SiC filter has been installed in August 2016, and it has been used from September 2016 onward, with the fixed filter still in place downstream. The rotating filter has been operating since then without showing any problem. For this reason, in December 2017 the fixed filter has been removed, and we have been using just the rotating one since January 2018. We can conclude that the final design, informed by the thermal FEA described in the sections above, is robust and effective.

REFERENCES

[1] M. Drakopoulos *et al.*, "I12: the Joint Engineering, Environment and Processing (JEEP) beamline at Diamond Light

¹⁵ By heating the copper in air, the surface is covered by CuO (cupric oxide), a black solid compound with high ϵ , stable at room temperature.

¹⁶ The geometry was modified to improve that value, so using it is a conservative assumption.

¹⁷ For medium-high heatloads. For low heat-loads this value is higher.

- Source”, in *Journal of Synchrotron Radiation* (2015), vol. 22, pp. 828–838, doi:10.1107/S1600577515003513
- [2] N. Baimpas, M. Xie, C. Reinhard, and A. Korsunsky, “The application of geometry corrections for Diffraction Strain Tomography (DST) analysis of a Ni-base superalloy blade”, in *Powder Diffraction*, Sep. 2013, vol. 28, pp. S436–S447, doi:10.1017/S0885715613000857
- [3] N. Baimpas *et al.*, “A feasibility study of dynamic stress analysis inside a running internal combustion engine using synchrotron X-ray beams”, in *Journal of Synchrotron Radiation* (2013), vol. 20, pp. 316–323, doi:10.1107/S0909049513000885
- [4] Diamond Light Source, I12 Beamline Characteristics <http://www.diamond.ac.uk/Beamlines/Engineering-and-Environment/I12/Beamline-Characteristics.html>
- [5] Diamond Light Source, Introduction to I12 – JEEP <http://www.diamond.ac.uk/Beamlines/Engineering-and-Environment/I12.html>
- [6] Diamond Light Source, Storage Ring Status <http://www.diamond.ac.uk/default/MachineStatus.html>
- [7] C. Christou *et al.*, “Implications of Increased Beam Current for the Diamond Storage Ring Rf System”, presented at the 16th International Conference on RF Superconductivity, SRF 2013.
- [8] M. Sanchez del Rio and R. J. Dejus, “Status of XOP: an x-ray optics software toolkit”, in *Proc. SPIE 5536, Advances in Computational Methods for X-Ray and Neutron Optics*, vol. 5536, 21 October 2004, doi:10.1117/12.560903
- [9] W. M. Kays, *Convective Heat and Mass Transfer*, McGraw-Hill Education; 4th edition (May 1, 2004).
- [10] Mikron, Table of Emissivity of Various Surfaces http://www-eng.lbl.gov/~dw/projects/DW4229_LHC_detector_analysis/calculations/emissivity2.pdf
- [11] MatWeb <http://www.matweb.com>
- [12] L. K. Fletcher, “Review of Thermal Control Materials for Metallic Junctions”, in *Journal of Spacecraft and Rockets*, vol. 9, n. 12 (1972), pp. 849–850, doi:10.2514/3.61809
- [13] *Thermal Analysis*, ANSYS, in ANSYS Training Manual.
- [14] L. J. Salerno and P. Kittel, “Thermal Contact Conductance”, in *NASA Technical Memorandum 110429*.
- [15] N. P. Suh, “Axiomatic Design: Advances and Applications”, *New York: Oxford University Press*, 2001. ISBN: 0195134664.

3D NUMERICAL RAY TRACING FOR THE APS-UPGRADE STORAGE RING VACUUM SYSTEM DESIGN

J. Carter, Argonne National Laboratory, Lemont, IL, USA

Abstract

The APS-Upgrade project will build a diffraction limited storage ring requiring a vacuum system design with small aperture vacuum chambers passing through narrow magnet poles. The small apertures dictate that the walls of the vacuum chambers act as distributed photon absorbers. The vacuum chambers must be designed robustly so a thorough understanding of the synchrotron ray tracing with beam missteering is required.

A MatLab program has been developed to investigate 3D ray tracing with beam missteering. The program discretizes local phase spaces of deviation possibilities along the beam path in both the horizontal and vertical planes of motion and then projects rays within a 3D model of the vacuum system. The 3D model contains elements in sequence along the beam path which represent both chamber segments and photon absorbers. Ray strikes are evaluated for multiple worst-case criteria such as local power intensity or strike offset from cooling channels. The worst case results are plotted and used as boundary conditions for vacuum chamber thermal/structural analyses. The results have also helped inform decisions about practical beam position limits.

RAY TRACING FOR THE APS-U STORAGE RING VACUUM SYSTEM

The APS-Upgrade will retrofit the existing 40 sectors, 1.1 km circumference APS storage ring with a new 6 GeV, 200 mA storage ring optimized for brightness above 4 keV. The new storage ring vacuum system will feature 22 mm inner diameter vacuum chambers to fit between narrow magnet apertures, see Figure 1. Each sector will have 5x copper photon absorbers to both funnel extracted photons towards the front ends and to shadow downstream components. Each sector will also have 14x independently mounted beam position monitor (BPM) assemblies. The BPMs are not water cooled and have sensitive features including RF liners and BPM buttons and each will need shadowing by compact inline absorbers built into the immediate upstream chambers.

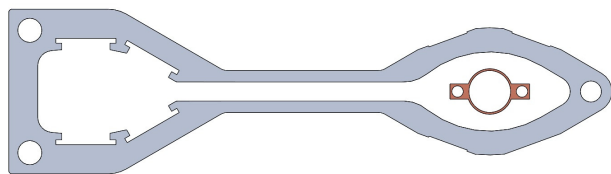


Figure 1: Cross section comparison of current APS-style vacuum chamber to new APS-U-style chamber.

In total the vacuum system will have 20x water-cooled vacuum components which will intercept synchrotron radiation either by design with a photon absorbing edge or along the chamber length as consequence of the small apertures. Figure 2 shows a cross section of three APS-U vacuum components in sequence. Here a slight taper on a vacuum chamber shadows a downstream flange joint of a compact copper inline absorber. The absorber then shadows the length of a BPM assembly past its downstream flange joint. The current APS has 6x total photon absorbing components compared to APS-U's 20x and this fits into a trend among diffraction limited light source vacuum systems with increasingly more compact vacuum chamber requirements. This increase in complexity leads to a need for more careful ray tracing constructions and calculations and considerations beyond the limits of conventional top view 2D ray traces.

A new MatLab program has been developed to investigate 3D ray tracing possibilities with missteering. Beam missteering possibilities and limits vary along the length of the lattice function and the ray tracing consequences differs from component to component in a complex system. Numerical methods are a more efficient approach to exploring missteering rather than individual CAD constructions. The new MatLab program calculates the local extents of missteering by discretizing local phase space ellipses and then projects the large quantity of rays downstream towards a model of vacuum elements. The quantity of ray strikes can be summarized to ensure the protection of sensitive components and to analyze worst case ray tracing outcomes unique to each vacuum component.

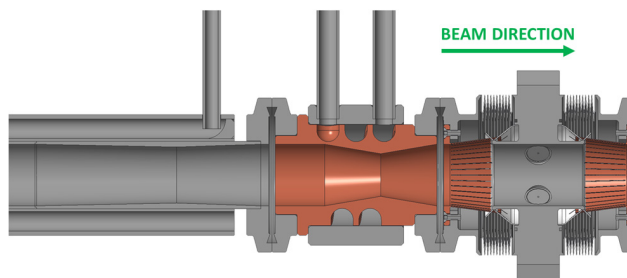


Figure 2: Top view cross section comparison of current APS-style vacuum chamber to new APS-U-style chamber.

SUMMARY OF APS-U'S 2D RAY TRACE

Building and analysing a conventional 2D ray trace remains critical as it sets the baseline for heat load distributions and shadowing of critical components. APS-U's storage ring ray trace is summarized in the table in Figure 3. APS-U's magnet lattice generates 14.3 kW per sector at 200 mA beam current. This excludes narrowly funnelled

radiation produced in the straight sections that the storage ring vacuum system will not intercept. Only 10% of the bending magnet radiation is passed to the beamlines and the rest is intercepted by vacuum components. For the photon absorbers, the 'b-side' crotch absorber takes the most bending magnet radiation at 3.4 kW and the A-side crotch absorber takes 1 kW. For the vacuum chambers, 5.3 kW (or ~1 kW/m) is intercepted along the FODO section's copper vacuum chamber walls. 600 W (or ~700 W/m) are intercepted in the B-Quad Doublet. Lighter loads (~100 W/m) are intercepted along small aperture aluminium vacuum chambers in the Multiplets.

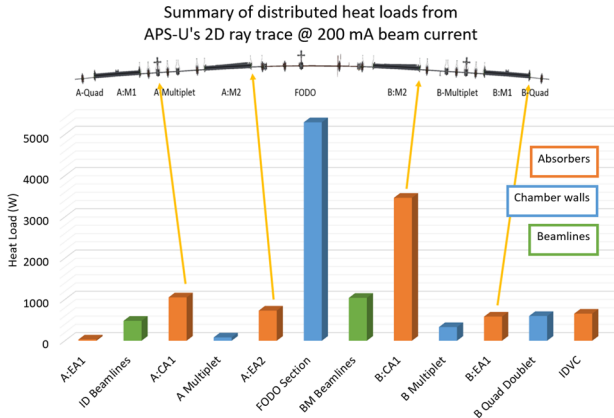


Figure 3: Summary of APS-U storage ring vacuum system 2D ray trace.

BEAM MISSTEERING LIMITS

Off-orbit ray tracing possibilities can be calculated from local phase space ellipses in both the horizontal (x,x') and vertical (y,y') phase spaces. The local ellipses are calculated for either phase space based on the Courant-Snyder parameters using equations (1) and (2) where A_x is calculated based on the half size of the limiting aperture in the storage ring and the beta function value at the limiting aperture's location. Figure 4 shows a schematic of a phase space ellipse and a corresponding mesh of ray deviation possibilities.

$$x' = -2\alpha x \pm \frac{\sqrt{(2\alpha x)^2 - 4\beta(\gamma x^2 - A_x)}}{2\beta} \quad (1)$$

$$A_x = \frac{a^2}{\beta_u} \quad (2)$$

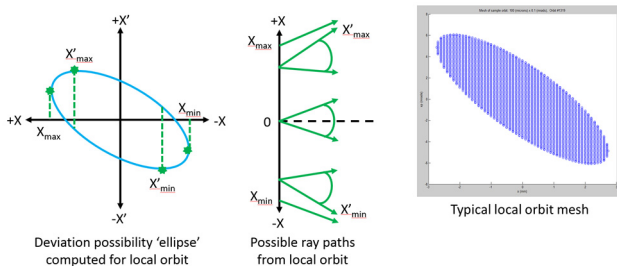


Figure 4: Local orbit ellipse concept and ray possibilities when meshed (top) and diagram of basic ray tracing schematic (bottom).

Simulation

Thermal

The MatLab program discretizes the local phase space ellipses and uses each point to deviate the positional and angular path of rays from a given base point along the arcing beam path. The extents of the ellipses in both X and Y and thus deviation possibilities at any point along the arcing beam paths are determined using lattice functions provided by APS-U physics. The deviated ray is then projected out until it strikes a geometric element in a model of the vacuum system. Finally strike parameters of interest such as power intensity are calculated using equations (3) and (4).

$$P_a \left(\frac{W}{mm^2} \right) = 5.42 * E_e^4 (GeV) * I(A) * \frac{B(T)}{L^2} * \sin(\theta_{ray}) \quad (3)$$

$$P_l \left(\frac{W}{m} \right) = 4.22 * E_e^3 (GeV) * I(A) * \frac{B(T)}{L} * \sin(\theta_{ray}) \quad (4)$$

ALGORITHM FOR 3D NUMERICAL RAY TRACING

The summary of the algorithm for the new 3D numerical ray tracing is as follows:

1. Build vacuum system geometry based on sequentially ordered geometry elements along the beam path. Figure 5 shows an example diagram of sequential geometric elements and the current types of elements allowed in the program.
2. Generate rays projected from finely spaced points where synchrotron radiation is generated along the arcing beam path
3. Determine where rays strike by checking if the intersection between a ray and a geometric element falls within the upstream and downstream extents of the element, see Figure 6.
4. Calculate data of interest from the strike including total power (W) deposited, power intensity (W/mm and W/mm²), location of strike, etc.
5. Use logic to find the 'worst case' ray to strike any given element out of a large quantity of possible strikes.

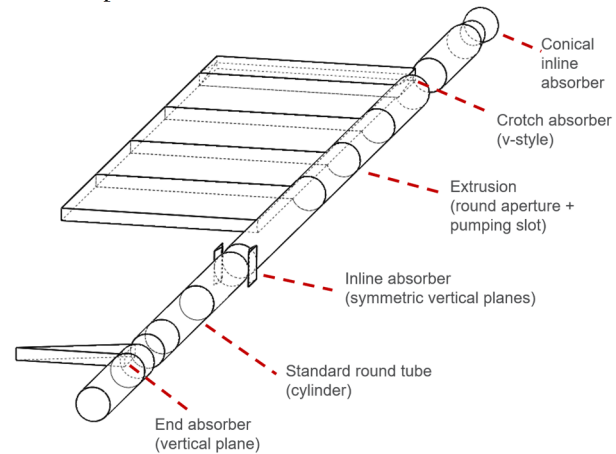


Figure 5: Diagram of a sequence of geometric elements and the element types currently available in the program.

THOAMA05

313

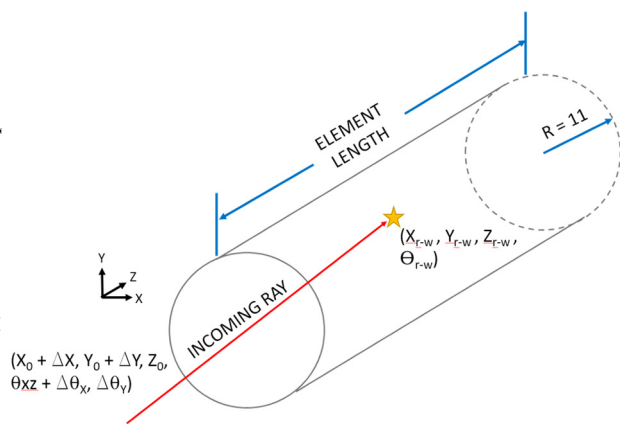


Figure 6: Diagram of a ray striking a geometric element.

The program imports lattice parameters across a typical sector. The format and types of lattice parameters were developed with input from APS-U physics and the program has now been used to quickly analyze multiple changes and iterations to APS-U's magnet lattice.

Geometry is built into the program as a sequence of geometric elements and typically requires the element's length, central global coordinates, and details of the cross section specific to each element. The input parameters are flexible and can be used to study design scenarios.

Results are provided in a large array with details of the worst ray strikes found on each geometric element. Examples of the ray strike details include ray origination and strike location, length travelled and angle of strike, and power intensity. Criteria for 'worst cases' are defined by logic with examples being 'highest power intensity' or 'furthest vertical offset from a cooling channel along the central plane'. The data is most easily viewed and manipulated in a spreadsheet program like MS Excel.

3D RAY TRACING RESULTS

The first benchmark of the program is to run it with no missteering and confirm that the results match both equivalent 2D CAD layout and 3D models in CERN's SynRad ray tracing program (part of the MolFlow+ Monte-Carlo Simulator package) [1]. Figure 7 shows a post process of numerous generated rays by the program within a top level cross section of the 3D geometry. The results are colored closely to those viewed in SynRad as a means of confirming that the calculations yield a highly similar result in 3D.

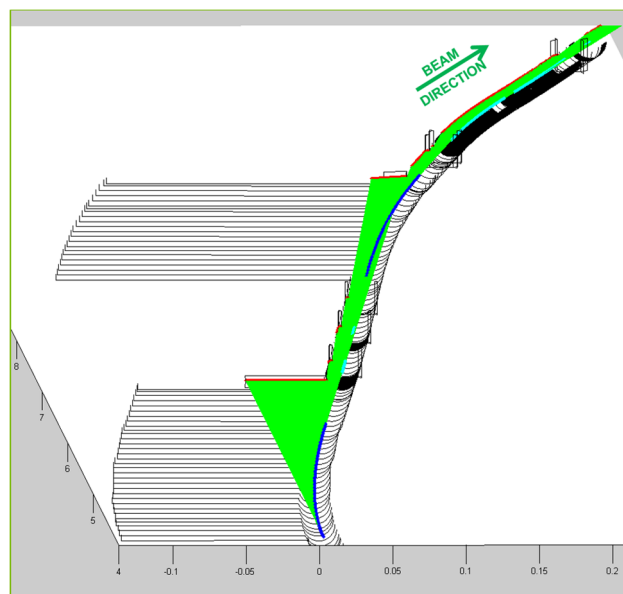


Figure 7: Angled view of an APS-U ray trace of the A-side of the vacuum system with no missteering from the new 3D numerical ray tracing program.

For APS-U the results of both individual rays and sweeping fans of rays have been found to match near equivalently between both 2D CAD and SynRad with differences usually being attributable to challenges in making equivalent geometric models between the three separate methods. Individual rays reconstructed in 2D CAD have been seen to travel the same distance and strike geometry at the same angle of incidence.

Beam missteering can be introduced following the confirmation of the 'ideal' ray trace. A user will enter a value for either a limiting aperture or a beam position limit detection system limit (BPLD limit) to determine the extents of missteering. Then discretization parameters for the local ellipses are chosen where finer rays will lead to more rays being tested during a run of the program. Figure 8 demonstrates the generation of both a single missteered ray and all of the rays generated from a discretized local x-plane ellipse.

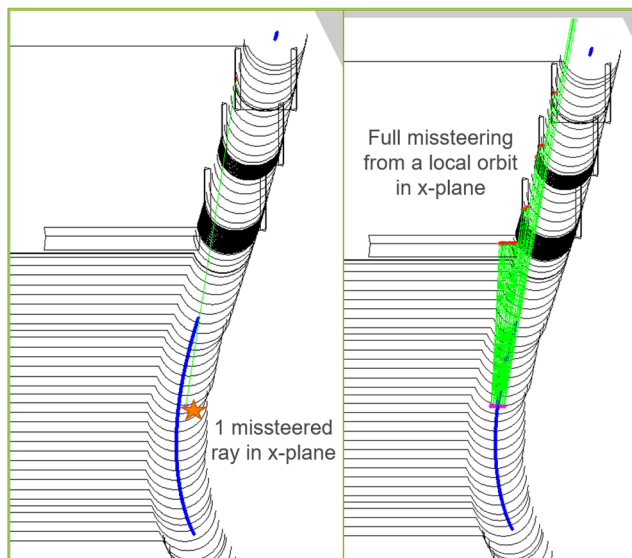


Figure 8: Comparison of one missteered ray (left) vs. all of the rays generated from a single local phase space ellipse in the X-plane (right).

When results such as linear power density and peak power density are compared across the length of the vacuum system, the set of ideally steered rays is always a lower bound to the set of ‘worst case’ rays as shown in Figure 9. Linear power is plotted across the sector and compared for both ‘ideal’ ray tracing and ray tracing with beam missteering confined by a BPLD limit. Local spikes in the results are due to tapered absorbers in the model. The figure shows a zoom in to the FODO section where copper vacuum chambers will receive high loads > 1 kW/m along their round bodies. The difference between a missteering result and a ideal steering result increases as the BPLD limit increases to an upper limit when the BPLD limit is equivalent to the limiting aperture.

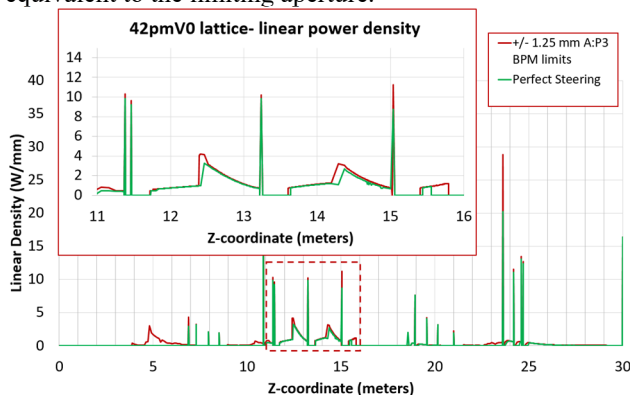


Figure 9: Comparison of linear power across a full sector for ideal steering vs missteering with BPLD limits with zoom in to the FODO section.

The results from the program can then be incorporated into a thermal/structural finite element analyses for vacuum chambers and absorbers. Figure 10 shows a typical ANSYS analysis for an APS-U vacuum chamber where a fine heat load across the water-cooled chamber is concentrated on a compact inline absorber face.

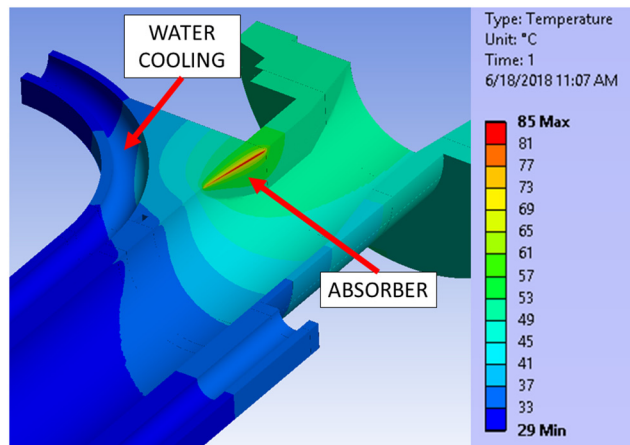


Figure 10: Typical ANSYS temperature result at downstream end of a water cooled vacuum chamber with narrow ray tracing heat load applied to an inline absorber.

Scenario studies were used to inform the BPLD limit for APS-U’s storage ring. The vacuum system will include a number of extruded chambers with uncooled narrow pumping slots designed between small magnet gaps. Rays travelling with a vertical positional or angular offset may be found to strike the chamber if not carefully confined. Recent work found ± 1 mm BPLD limits should be sufficient to protect 3.5 mm tall pumping slots spanning > 5 meter lengths in the straight sections from being struck by missteered rays.

CONCLUSIONS AND FUTURE WORK

The new 3D ray tracing program helps more efficiently explore the wide range of beam missteering consequences within a complex vacuum system. The program has been used to help ensure robust equipment protection and thermal/structural design for APS-U’s storage ring vacuum system design. The program imports familiar lattice parameters and has now been used to analyze multiple iterations to the APS-Upgrade’s magnet lattice. The program is also built on flexible geometric parameters which can be toggled to explore design scenarios.

The current program is primarily suited for calculations of vacuum components along the beam path. Future work should develop the program to explore missteering consequences down photon extraction lines towards front ends and beam lines. Geometric modelling can also be improved with the inclusion of more elements or more ideally finding a way to import external 3D CAD geometry.

ACKNOWLEDGMENT

Argonne National Laboratory’s work was supported by the U.S. Department of Energy, Office of Science under contract DE-AC02-06CH11357.

REFERENCES

- [1] R. Kersevan and M. Ady, "MolFlow+ - A Monte-Carlo Simulator Package developed at CERN," CERN VSC Group, 2015. [Online]. Available: <http://test-molflow.web.cern.ch/>.

A NEW X-RAY BEAM FOR THE ESRF BEAMLINES, OPTO-MECHANICAL GLOBAL SURVEY

Y. Dabin, R. Barrett, S. Jarjays, M. Sanchez del Rio,
 European Synchrotron Radiation Facility, 38043 Grenoble Cedex 9, France

Abstract

With the new Extremely Brilliant Source (EBS), ESRF beamlines (BL) will have to adapt their optical configurations to use the new beams optimally. Preparing the photon beam for an experiment by a BL implies successive interactions between the different components that produce, transport and manipulate this beam. A cascade of topics and cross-linked processes optimize the photon beam parameters. The scientific application defines the baseline parameters such photon energy, beam sizes and flux. These will in turn define the most appropriate source characteristics, for which an optical scheme must be developed and implemented to tailor the X-ray beam properties to the experimental requirements. In this phase simulation software tools such as OASYS, are employed for optics and source calculations and ANSYS and COMSOL for FEA thermo-elastic analyses. Finally, the implementation phase interconnects the string of technical components, involving the whole spectrum of engineering issues. This paper deals with this cascade of tasks and describes the sequence of parameters and calculations flow required to exploit an X-ray light source.

INTRODUCTION

The EBS (Extremely Brilliant Source) [1] project is based upon a reduction of the horizontal emittance of the ESRF electron storage ring. Table 1 gives details on changes in major parameters.

The new EBS straight sections are reduced in length, leading to a need to adapt the existing collection of undulator carriages. Beamlines using canted undulators reset their source point and their location.

Table 1: Emittance and Straight Section Main Parameters for the Current ESRF and New EBS Storage Rings

Configuration	Current SR	EBS
Hor_Emittance (pm)	4000	147
Ver_Emittance (pm)	4	4
Straight section (m)	6 and 7	5.5
Bending magnet source	Dipole from DBA lattice	Small Insertion device

At the same time, new undulators require specific strategies for their gaps and periods. Recent cryogenic, in-vacuum undulators with 22, 18 and now 14mm periods, 6mm (and 5mm) gap increase peak flux and energy tunability. The recent topping-up hybrid mode (7/8+1) produces a reduced vertical size of the X-ray beam as seen at some BL, modifying as a consequence the optics illumination. Thus,

monitoring on-live the X-ray beam characteristics is a “daily issue” and an important topic. Scientists at the BL must react to any changes, in collaboration with the other engineering specialists like storage-ring, optics, mech. Eng. FEA. Since recent years, optics simulation tools are implemented in user-friendly software environment to make the chain of design and optimizing beamlines faster and easier. An example of such effort is OASYS suite [2].

FROM THE PRESENT STORAGE RING TO THE NEW EBS SOURCE

The photon beam is produced by an electron beam stored in a magnetic lattice. The fundamental properties of this X-ray beam are first determined by the electron ring. The ESRF electron storage ring, implemented in 1990, is based on a double-bend-achromat (DBA) lattice. It consists of al-ternating low- and high-beta straight sections for installing insertion devices, offering respectively an electron source of small size and large divergence, or large size and small divergence, in the horizontal plane Fig. 1 shows schemati-cally the horizontal emittance characteristics of this alter-nating

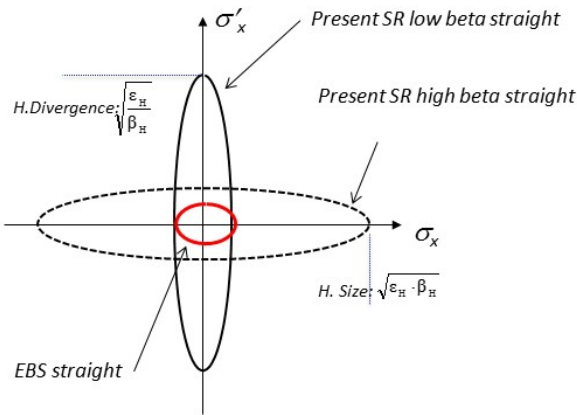


Figure 1: Schematic representation of the electron phase space in the horizontal plane comparing the case of present storage ring and the new EBS lattice. Originally the low beta was aimed at hosting wigglers, while the high beta hosted undulators. The emittance reduction factor of EBS is 1/30 as compared to the older facility.

The choice of a lattice configuration with high and low beta sections was driven at the time by the difficulties in building high performance undulators, as compared to less demanding wiggler technologies giving a broad energy spectrum without the need to tune the magnetic gap. With time and experience, undulator performance has improved

to a degree that very few ESRF beamlines still use wigglers. Device periods have had a tendency to reduce with beamlines using 42 mm period arrays moving to periods as low as 14 mm and a progressive reduction of magnetic gaps from 15 to 6 and soon 5 mm, through the use of in-vacuum undulators operating at room- or cryogenic-temperatures [1].

THE EBS-READINESS REVIEW PLAN FOR ESRF BEAMLINES

One of the strategic issues for the ESRF to secure BL optics, stands in assessing the power issues of the new beam on the existing beamlines, what we call the “EBS- readiness review” plan. This is being implemented at pre-sent, after ranking BLs according to their capability to op-erate with the new source with at least equivalent perfor-mance as with the original ESRF source, then according to the necessary degree of intervention to achieve optimum performance with the EBS. The first ones to be considered are the existing “low beta beamlines” those where the beam power is dispersed thanks to a large divergence, thus pro-ducing a lower power density on the optical elements. With EBS, these beamlines will see a smaller beam, with a new power density increased by a factor of two to five [3].

There are two parallel considerations to implement such an undulator at the beamline:

From the science applications view point, the key energies must be accessible with relevant flux. The photon energy, or the photon wavelength depends on the deflection parameter K [4], which can be approximated on axis by:

$$\lambda_{ph} = \frac{\lambda_u}{2 \cdot \gamma^2} \left(1 + \frac{K^2}{2} \right)$$

with λ_{ph} the resonance photon wavelength, λ_u the undulator period and γ = electron energy/ $m_e c^2$ (m_e = electron mass, c = velocity of light)

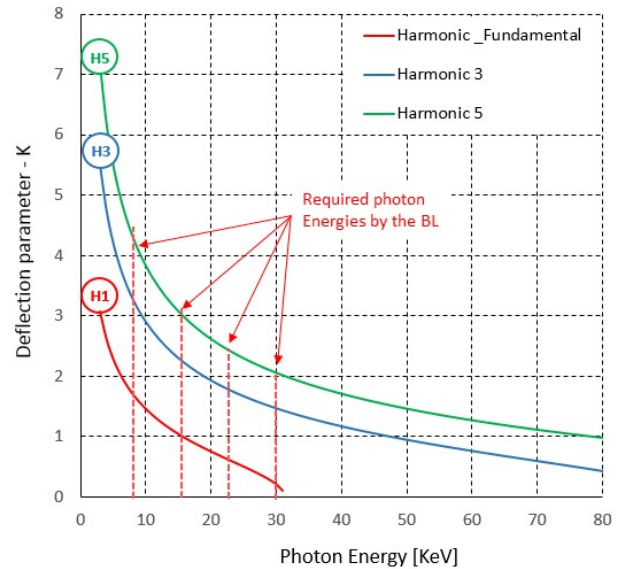
A dialog is developed between beamline scientists, insertion device, and advanced analysis calculation groups to define the possible undulator choices, this ends-up with a compromise between gap and period giving the required K value. The ID design makes use of the proportionality of K with the magnetic field at the axis \tilde{B} :

$$K = \frac{\lambda_u \cdot e \cdot \tilde{B}}{2 \cdot \pi \cdot m_e \cdot c}$$

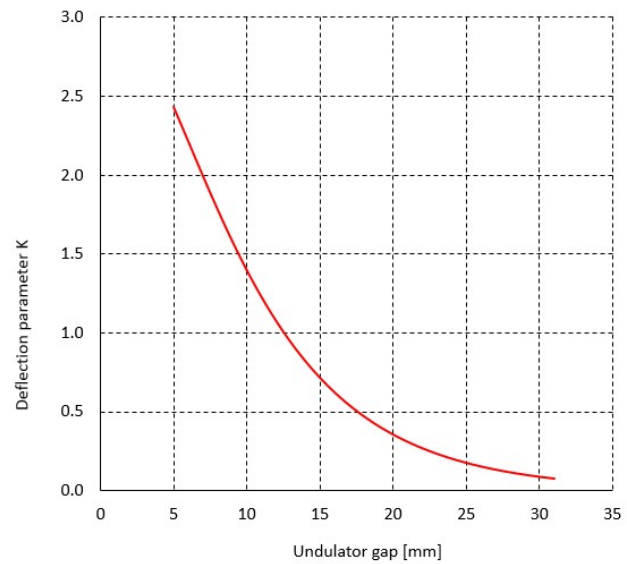
In turn, the magnetic field depends on the gap [5]:

$$\tilde{B} = \frac{1}{\cosh(\pi \cdot \frac{g}{\lambda_u})}$$

where g (und. gap) must also fit with the vacuum wall, respecting a given radio-frequency minimum distance with e⁻ beam. For the EBS, $g_{min} \geq 6$ or 5mm (likely after EBS commissioning). Figure 2 represents how gap considerations can meet with the energy choice for the scientific applications with the technical constrains. This also applies to higher spectrum harmonics, like H3, H5. In fact, from the magnetic field optimization, the ratio g/λ_u is a suitable figure of merit to optimize.



(a)



(b)

Figure 2: The K value is defined through two main processes, from science (a) where the energy targets are initially defined, and from the insertion device engineering (b), where the undulator gap provides a K value. Dotted lines in (a) represent the different energies choice from experiments. Figure 2b shows how the undulator (cryo permanent magnet with a period of 22mm) can meet the K value, enabling the BL to perform scientific research.

SEARCH FOR EXPLOITING WITH EBS HIGHER DEGREE OF COHERENCE

The lower EBS beam size (reduced by a factor of 10) increases the coherent fraction of the X-ray beam. This property is of major importance for optimizing experimental methods based on interference and diffraction of wavefronts. Experimental techniques such as phase contrast imaging, coherent diffraction imaging (CDI), holog-

raphy, ptychography and X-ray photon correlation spectroscopy (XPCS) all exploit this characteristic. The transverse coherence length gives an estimation of the length of the illuminated area across which the beam can be considered coherent, thus allowing coherence experiments. It is proportional to the wavelength λ_{ph} and beamline length L_{BL} and inversely proportional to the photon source size s [6]:

$$L_{coh} = \frac{\lambda_{ph} \cdot L_{BL}}{2 \cdot s}$$

Thus, with ESRF long beamlines and using optics that adequately preserve the wavefront quality, high coherence beamlines are available, even above 30 keV. The EBS BM18 imaging project as well as several other ESRF beamlines are specifically designed to exploit the improved coherence properties of the new source.

As an example of beam aspect, in relation with mechanical engineering, the following inquiry, qualifies the deformation works performed in the frame of the ESRF-Compound refractive lens development, a DCT (differential contrast tomography) of a single Al lens is illustrated in Fig. 3. It reveals a structure made by grains of increasing grain size, suggesting a dynamic recrystallization, due to excessive punching velocity thus inducing an adiabatic thermal process.

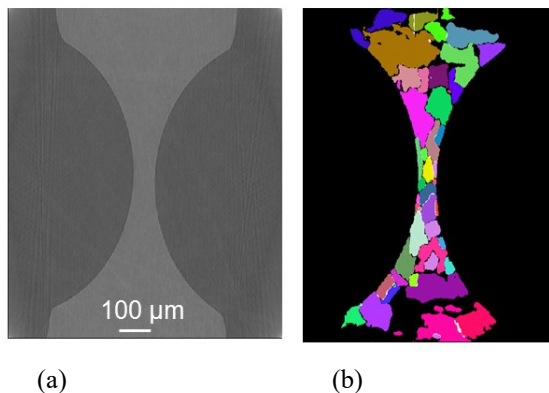


Figure 3: a) A classical transmission radiography of a single lens. b) A differential contrast tomography. The refractive lens is produced by cold-punching. Grain sizes are revealed. The quick deformation produced a high temperature rise of the material and then a dynamic recrystallization- Courtesy W. Ludwig-ESRF-ID11.

OASYS : A BEAMLINE OPTICS SIMULATION TOOL

The OASYS package [2] is an open source suite of different software tools, connected together by means of a workflow-based graphical environment implemented using Orange [7]. This package is an open source project for

synchrotron virtual experiments and data visualization, developed in an academic environment. OASYS includes modules for X-ray tracing, synchrotron wave optics (SRW), toolboxes (XOPPY), partial coherence (COMSYL), etc...

This tool, enables quick and easy analysis, from individual optical elements to a full beamline simulation. Figure 4 shows a typical workflow representing the simulation of a complete beamline.

Within the scope of the EBS-readiness project, we are particularly concerned with the beam power handling of the beamlines. A cascade of calculations is implemented for each case, where we can calculate the flux, and its related power spread and spectrum, and the way it is transmitted. The spectrum limitation by means of attenuation or critical angle reflection mirrors is simulated in the existing configuration. Thermo-mechanical analyses are then applied, in these two cases, which are aimed at determining stresses for attenuators, and deformations for mirrors. OASYS is also aimed at computing the full beamline performance, including most of beam distortions due to optical imperfection. Mirror figure errors can be provided by a specific historical measurement database, including a large collection of achieved reflecting surfaces (specific wigglets). In the same way, a database of thermal slope errors surfaces provided by FEA tools should be included soon, in order to add-up all of major effects. At present this link is operated manually.

PROCESS OF X-RAY BEAMLINE DESIGN

For the EBS source there are several scenarios for the beamline design but all involve close interaction between the ESRF engineering groups and the BL scientists. New 'EBS beamlines' are generally designed from scratch. In contrast, for existing beamlines, the design process may be limited to a check that the existing instrumentation can perform to a level which is at least equivalent to that achieved with the existing source or may include re-design/refurbishment of critical components which allow the beamline to reap the benefits, either partially or fully, of the new source parameters. One of the primary choices is the selection of the source. This is determined principally by the energies in which the experiments are planned in accordance with the scientific case of the beamline. Parameters such as energy tunability and polarization control may also influence this choice as well as the radiated power. At the ESRF the choice of source parameters is conducted in consultation with the Magnets and Insertion Device Group. Tools integrated into OASYS greatly facilitate the simulation of spectral brilliance, emitted power etc.

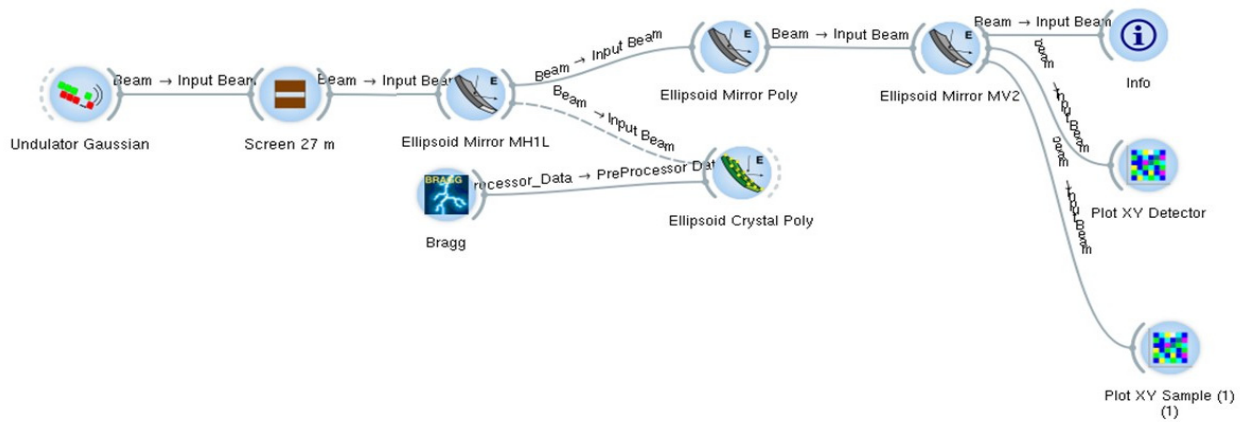


Figure 4: OASYS display window, enables to compute a full beamline string of components. Here the ID24 spectroscopy sample is illustrated. This model represents part of a beamline scheme, enabling a complete simulation of the arrangement.

The power transmitted to the critical beamline components is controlled by tuning of the primary slit opening; these are adapted to the emission angle of the central cone of the required undulator peak, in order to keep maximize the useful photon flux illuminating the sensitive optical components without subjecting them to unnecessary absorbed power.

There are several ways of dealing with the transmitted power. Amongst the most common are:

- Cut the low energy part of the spectrum by means of attenuators.
- Cut the high energy part of the spectrum with mirrors, operated in total reflection.

For the engineering design of these two cases, the material stresses, and deformations resulting from the absorbed power are simulated. Figure 5 gives an example of spectral filtering using mirror optics. The strategy commonly used at the ESRF is to reduce the thermally induced deformation of the optical surface, using a optimized notch profile of the silicon substrate [8,9,10]. The criteria in that case is defined such that thermal deformations should be negligible relative to the intrinsic polishing quality of the native optical surface. Since the two effects are essentially uncorrelated the overall slope error, ϵ_{rms} of the thermally deformed optic can be estimated by:

$$\epsilon_{rms} = \sqrt{\epsilon_{rms\ slope-error}^2 + \epsilon_{rms\ thermal_slope}^2}$$

REVIEWING QUICKLY OPTICAL CASES

Experience tells us that beam is not fixed forever. Random events come, and disturb the beamline operation.

First, the optical quality of the optics can be processed with OASYS, using specific formatted files from the optical metrology lab.

Second, thermally deformed surfaces can be provided by FEA tools, to OASYS using Matlab scripts.

The results are more complete real case optical propagation, better predicting practical sample illumination. We

are at present implementing a roadmap aimed at completing OASYS with specific modules, as shortly described in Fig. 6.

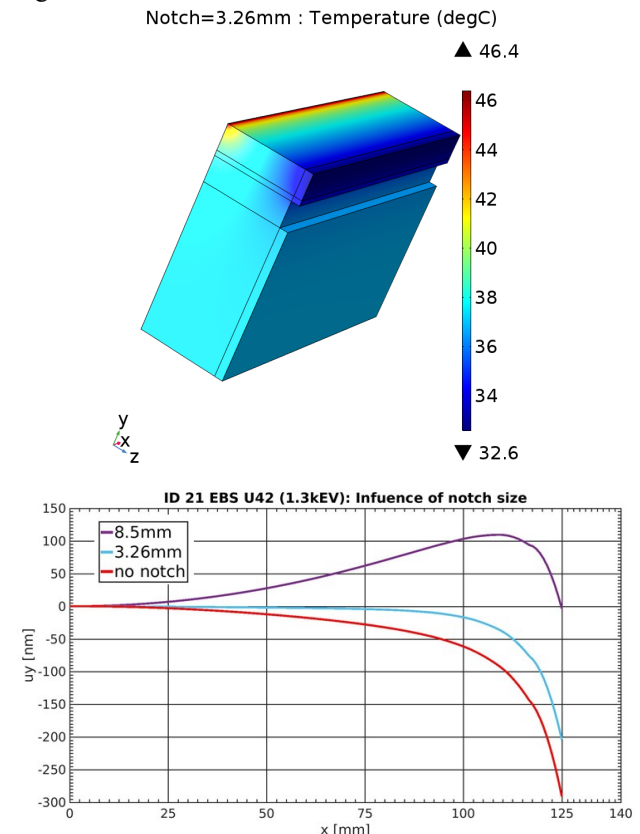


Figure 5: A 'smart' profiled mirror, consisting in making longitudinal grooves each side on the substrate, with optimised depth, in order to minimize deformation of the reflecting surface upon power absorption. The horizontal axis represents half length of the mirror, the vertical axis being the thermal slope (in nano-rad).

The thermal slope is restricted to $\epsilon_{Thermal_slope} \leq 200nrd$ although it produces smooth image density gradient.

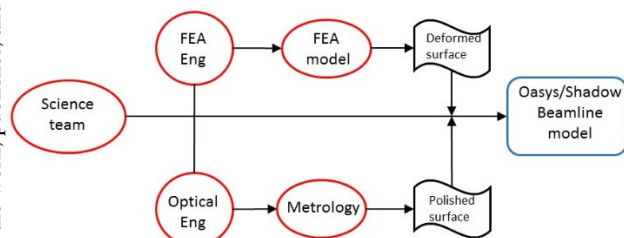


Figure 6: The science team proceeds to a beamline model with OASYS. This model can consider an ideal case. With FEA Eng, and Optics Eng, real/simulated surfaces can be implemented, involving surface distortions in the transmitted beam. This process corresponds to a specific module of OASYS, including a COMSOL application builder, operated by scientists.

CONCLUSION

The ESRF instrument division the ISDD (Instrument Support and Development Division) is committed in an optics calculation roadmap leading to better integrate the chain of actors, from scientists, to engineers, involving metrology lab phase. The OASYS suite, created 4 years ago, is also itself within a roadmap. It requires more software support, in order to resolve the various interactions with user's platforms. This should be triggered soon. For the ESRF beamlines, a review priority is set, and a relative long calculation chain is starting, including the recent new phase II beamlines, described in Technical Design Reports.

ACKNOWLEDGEMENTS

We acknowledge all of the beamline scientists who have helped in developing these approaches, in particular, S. Pascarelli, O. Mathon, R. Tucoulou, M. Wulff, M. di Michel, P. Tafforeau, W. Ludwig, as well as J. Chavanne and staff of the mechanical engineering group.

REFERENCES

- [1] EBS Upgrade Programme Phase II, Technical Design Study, ESRF Orange book, 2014.
- [2] L. Rebuffi, M. Sanchez del Rio, "OASYS (OrAnge SYNchrotron Suite) : an open-source graphical environment for x-ray virtual experiments", in *Proc. SPIE*, vol. 10388, paper 103880S, 2017, doi: 10.1117/12.2274263.
- [3] J. Susini *et al.*, "New Challenges in beamline instrumentation for the ESRF Upgrade Programme Phase II" *J. Synchrotron Rad.*, vol. 21, pp. 986-995.
- [4] A. Hofmann, *The Physics of Synchrotron Radiation.*, Cambridge University Press, 2004, Cambridge, MA, USA.
- [5] K. Wille, *Synchrotron Radiation-Lecture notes*, JUAS 24, 2005.
- [6] E. Hecht, *Optics*, 4th Ed, 2002, Addison Wesley, Boston, MA, USA.
- [7] Orange. <https://github.com/biolab/orange3> University of Ljubljana, Faculty of Informatics.
- [8] A. Kounsary, "Thermal management of next generation contact cooled synchrotron X-ray mirrors", in *Proc. SPIE*, Vol. 3773, 1999, doi: 10.1117/12.370114
- [9] L. Zhang, "Smart shape mirror for ESRF. ID21 case", internal report ESRF/ISDD, 2014.
- [10] S. Jarjays, "ID21 heat-load project", internal report, ESRF/ISDD, 2017.

PIEZO TECHNOLOGY IN SYNCHROTRON

Boris Laluc, Aurélien Riquer, Thomas Maillard
 CEDRAT TECHNOLOGIES, 38 000 Grenoble, France

Abstract

Synchrotrons need robust products. That's why the association of piezo actuator technology and CEDRAT TECHNOLOGIES (CTEC) know-how has been successful for synchrotron mechanisms projects. The technological brick is the "Amplified Piezo Actuator" (APA®) tested and widely used in space applications, it is often implemented in CTEC piezo mechanisms and provides a high level of robustness. Modifying the layout and the number of APA® allows several needs to be addressed within beamlines. Three applications developed in collaboration with the EMBL, PAL and SOLEIL will be presented in this paper. The first application consists of cutting a beam with a piezo shutter. The maximum beam diameter is 3 mm. The second mechanism allows the energy of a beam to be modified by using a series of piezo actuated filters. And the last mechanism aims at modifying the beam section shape with an active piezo micro-slits mechanism.

PIEZO TECHNOLOGY AND SYNCHROTRONS

Synchrotrons need reliable products because most of the time the actuators are working in vacuum environments and it is very time consuming and expensive to break the vacuum for a maintenance operation. That's why the association of the piezo technology and the CEDRAT TECHNOLOGIES (CTEC) know-how has been successful for synchrotron mechanisms projects around the world for over 15 years.

LINEAR ACTUATOR APA

The Amplified Piezo Actuator APA® [1] was developed, tested and approved for space applications and then industrialised to be used in other markets, for example instrumentation. Thus, the APA® can withstand more than 10^{10} cycles. The actuator is composed of a piezo ceramic which generates a translation motion. The piezo ceramic has only a 0.1 % active deformation: to get a 0.5 mm displacement motion the piezo ceramic size should be 0.5 m. That's why the APA uses a shell around the piezo-ceramic to amplify the movement and increase this deformation. As an example the APA600M with 0.55 mm stroke is only 15 mm-height. The active deformation ratio is then 3.7%. The full stroke of the APA® is achieved with a 170 V range (-20 to +150 V).

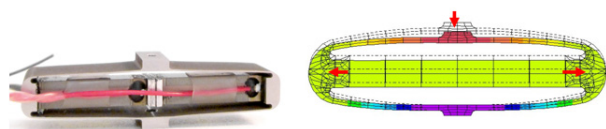


Figure 1: APA600M Actuator & Shell displacement.

In Figure 1 the dotted lines represent the actuator at rest thus not powered. When a positive voltage is applied the ceramic expands outwards and the shell moves downwards.

The robustness of the APA® is present in all CTEC mechatronics products and especially for synchrotron beamlines: the fast shutter, the fast beam attenuation actuator and the active micro-slits products.

FAST PIEZO SHUTTER (FPS)

For this mechanism 2 APA® face each other on a rigid frame, see Fig. 2. At rest the optical head cuts the beam and when a voltage is applied, the two APA200M retract and the shutter opens. The opening between the 2 APA is around 0.4 mm, giving a security factor, this shutter is designed for a beam diameter up to 0.3 mm.

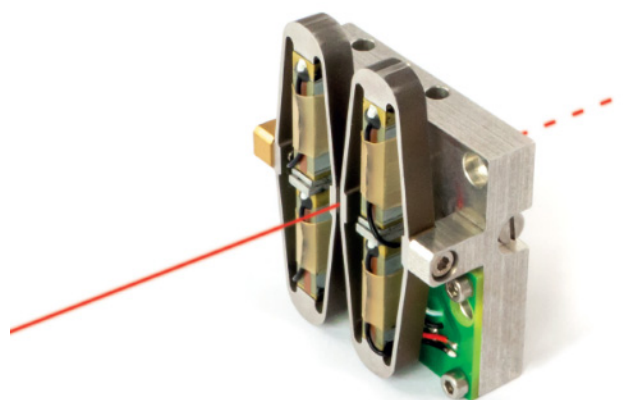


Figure 2: FPS200M.

These shutters are used to expose the sample behind it during a defined and controllable time. Aperture or closure time is directly linked to the resonance frequency of the actuator and so its stiffness. The APA200M has a mechanical resonance frequency of 900 Hz in blocked-free mode that is to say a period of 1.1 ms. The driver is optimised with a pre-shaped signal to minimise the excitation at this frequency. The mechanical ringing of the slits is reduced, even with a fast aperture and closing time of 2 ms. The APA200M actuator used in the FPS200M is a good compromise between stiffness required for fast response time, and aperture size. Other shutters FPS400M and FPS900M allow respectively a beam diameter of 0.7 and 1.1 mm with the same mechanical design but with larger strokes actuators.

If more stroke is needed, the FAPS400M (Fig. 3) developed for PAL uses a lever arm to amplify the APA movement. In this case the beam diameter could be up to 3 mm with a translation of each APA400M of 410 μ m.

Even if the lever impacts on the stiffness of the mechanism the response time remains fast, with a closing time of 8 ms.

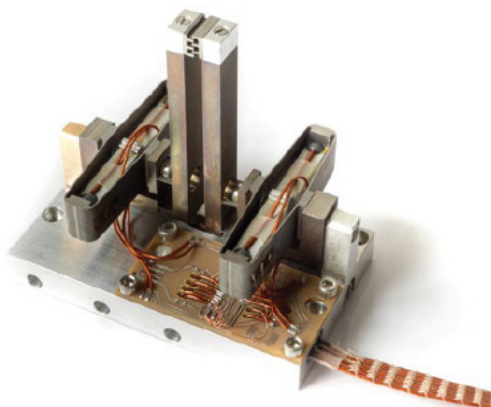


Figure 3: FAPS400M.

The FPS and FAPS piezo shutters family have a low jitter ($<100 \mu\text{s}$) thanks to a low self-heating compared to magnetics solutions.

FAST BEAM ATTENUATION ACTUATOR

When a motion greater than 1 or 2 mm is required, the APA can be integrated into a second level amplification mechanism.

For example, an APA fitted with a lever arm has been designed for the Fast Beam Attenuation project (Fig. 4) led by SOLEIL. The energy of the electron beam is controlled by putting more or less filters into the beam trajectory. It is useful to avoid detector damage and saturation. Thus the tip of each arm is moving 3 mm and a filter is mounted to it. To modify the beam attenuation, SOLEIL decides to play with 6 filters in a row.

This mechanism is installed in the SixS beamline at SOLEIL.

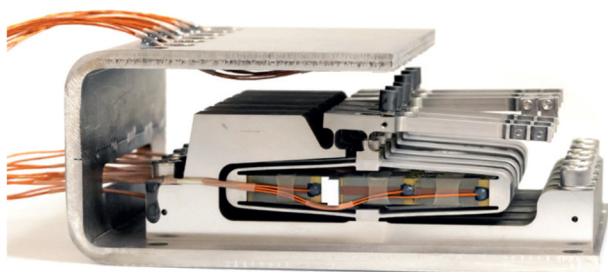


Figure 4: Fast Beam Attenuation Actuator.

The pivot links for the lever arm are done by bending and removed all mechanical friction disadvantages. Neither maintenance nor lubrication are required and the solution is cost effective.

The source of the movement is done by a piezo ceramic with a $40 \mu\text{m}$ stroke. A shell amplifies the movement to get $650 \mu\text{m}$ stroke, this actuator is the APA600MML. Then a lever arm amplifies again the translation to 3 mm (see Fig. 5, the blue area shows a 3 mm displacement). These two amplification stages leads to an 80 times amplification.

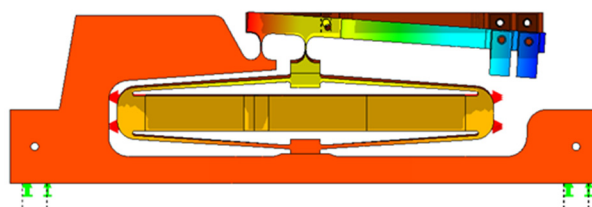


Figure 5: Displacement simulations.

The switch for each filter is achieved in 10ms that is to say a period of 100 Hz. To avoid filters ringing, the resonant frequency of the system must be twice higher than the movement period. That is why the mechanism has been designed and optimized to get a mechanical resonant frequency around 200 Hz.

Additional proprietary sensors are embedded to valid the status of the row (open or closed).

ACTIVE PIEZO MICRO-SLITS MECHANISM

Another actuator layout that has been designed with SOLEIL is to put a piezo actuator fitted with 4 lever arms to modify as required the shape of the synchrotron beam. Thanks to this mechanism the beam becomes a well-defined rectangle section and the section is adjustable in height and width. This mechanism is used in the SWING beamline at SOLEIL (Fig. 6).

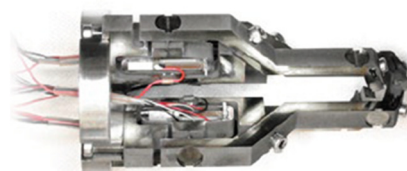


Figure 6: Active Piezo Micro-slits.

In this case, the source of the movement is done by a piezo ceramic with a $40 \mu\text{m}$ stroke. A shell amplifies the movement to get $66 \mu\text{m}$ stroke, this actuator is the APA50XS.

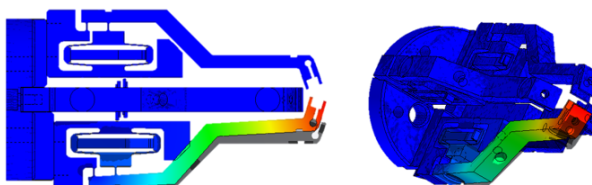


Figure 7: Displacement simulations.

Thanks to a lever arm again the stroke is increased up to $670 \mu\text{m}$ with a $-20/+150 \text{ V}$ supply (see Fig. 7, the red area shows a $400 \mu\text{m}$ displacement). These two amplification stages lead to an 18 times amplification.

The length and the height of the rectangular section can be adjusted up to $670 \mu\text{m}$.

The thermal stability was a very important criteria for SOLEIL ($\pm 0.5 \mu\text{m}$ for a 0.5°C variation). Thanks to CTEC space heritage in mechanical designs and Strain

Gauge (SG) use [2, 3], the specification has been reached. A closed loop is required because of the accuracy. Indeed, the closed loop option removes the hysteresis phenomena inherent from the piezoelectric ceramics (Fig. 8).

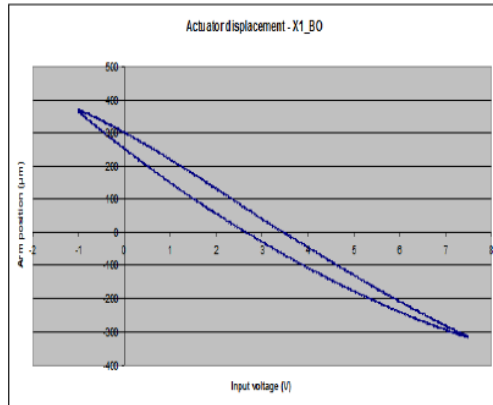


Figure 8: Mechanism displacement in open loop.

A linearization (with a 2nd order polynomial function) and calibration of the SG sensor has been done (Fig. 9).

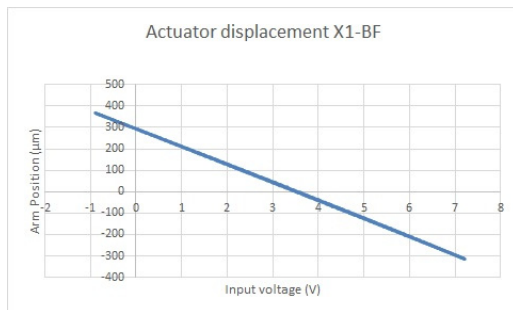


Figure 9: Mechanism displacement in closed loop.

A comparison between a laser interferometer measurement (yellow curve) and the position given by the SG (red curve) has been done (Fig. 10) in closed loop.

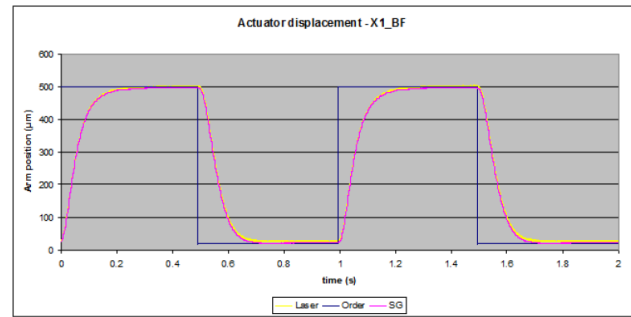


Figure 10: SG versus Laser Interferometer.

The results show that the maximal error between these two measurements is 0.4 %. SG sensors are a good solution in term of space (because they are stuck directly on the piezo stack) and accuracy to improve the performances of the mechanism.

ACKNOWLEDGMENT

The authors would like to thanks the following organizations for the fruitful collaboration in the development of the presented mechanisms:

- SOLEIL Saint-Aubin, France
- EMBL Grenoble (ESRF), France
- PAL, Pohang, Korea

REFERENCES

- [1] F.Claeyssen, R. Le Letty, F. Barillot, O. Sosnicki, "Amplified Piezoelectric Actuators: Static & Dynamic Applications", in *Proc of ECAPD 8 Conf*, Metz, Sept 2006, *Ferroelectrics*, Ed Taylor & Francis Group, LCC, Vol. 351, 2007, pp 3–14
- [2] Strain gages sensors for high stability piezo actuators, http://www.cedrat-technologies.com/fileamin/user_upload/CTEC/Publications/Publications/2015/Strain_gages_sensors_for_high_stability_piezo_actuators.pdf
- [3] T. Porchez, F. Barillot, C. Belly, CEDRAT TECHNOLOGIES, "Nanometric Linear Piezo-Actuator with integrated Strain Gages for high stability positioning", Conference Actuator 2016, Ed Messe-Bremen – Proceedings N° P8 / P489

BEAMLINE ENGINEERING OVERVIEW FOR THE APS UPGRADE*

O. Schmidt, E. Benda, D. Capatina, T. Clute, J. Collins, M. Erdmann, T. Graber, D. Haeffner, Y. Jaski, J. Knopp, G. Navrotsky, R. Winarski, Argonne National Laboratory, 60439 Lemont, IL, USA

Abstract

The Advanced Photon Source (APS) is currently in the process of upgrading to a 4th generation high-energy light source. A new multi-bend achromat storage ring will provide increased brightness and an orders-of-magnitude improvement in coherent flux over the current facility. To take advantage of these new capabilities, we will be building nine new feature beamlines and implementing numerous additional beamline enhancements, all while ensuring the compatibility of existing programs. Clear challenges exist in advancing state-of-the-art optics and developing nano-resolution instrumentation. We also need to recognize and address project scheduling, labor resources, existing infrastructure, bending magnet parameters, and possible modifications to radiation shielding in order to achieve project success.

APS-U Overview

The APS-Upgrade (APS-U) will transform the APS into a next-generation synchrotron light source, exceeding the performance of today's storage ring by up to three orders of magnitude in brightness and coherent flux.¹

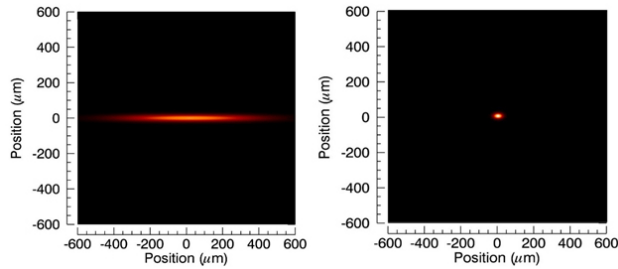


Figure 1: APS electron beam before and after upgrade.

The new storage ring will also produce a much smaller, more coherent beam (Fig 1). Currently we are in the planning and design phase of the project with the main installation planned for 2023 with one year of scheduled dark time.

Feature Beamlines

To take full advantage of the higher brightness and higher energy of the new storage ring, nine “feature” beamlines have been chosen to showcase these capabilities and provide world class scientific programs. Preliminary designs for each beamline have been completed along with detailed cost estimates and project schedules. Table 1

shows the list of feature beamlines that will be either brand new or greatly modified.

Table 1: Summary of APS-U Feature Beamlines

Sector	Name	Title
4-ID	POLAR	Polarization modulation spectroscopy
8-ID	XPCS	X-ray Photon Correlation Spectroscopy Beamline
9-ID	CSSI	Coherent Surface Scattering Imaging
19-ID	ISN	In Situ Nanoprobe
20-ID	HEXM	High-Energy X-ray Microscope
25-ID	ASL	Advanced Spectroscopy & LERIX
28-ID	CHEX	Coherent High-Energy X-ray Sector for In Situ Science
33-ID	Ptycho	Ptychography/Spectromicroscopy
34-ID	3DMN/ ATOMIC	3D Micro & Nano Diffraction/ High-Resolution Atomic Imaging

Beamline Enhancements

In addition to the nine feature beamlines, another seventeen beamlines will see major enhancements to their optics and end station instrumentation to greatly enrich the capabilities of their current programs. Proposals for beamline enhancements were submitted in February of 2017. Beamlines were chosen based on scientific impact, degree of benefit to the general user program, and alignment with upgraded APS capabilities and APS strategic plans (high energy, coherence, etc.) Enhancements include new and upgraded mirrors, monochromators, and refractive lenses, along with station modifications and end station instrumentation and detectors. These smaller beamline enhancements essentially provide value and many can be completed before the main shutdown to free up resources during the main installation period.

Long Beamlines

In order to achieve extremely small focal sizes and make the best use of the improved beam coherence, two “long” beamlines will be developed which will extend beyond the current APS building footprint. The In Situ Nanoprobe (ISN), and High Energy X-ray Microscope (HEXM) beam-

* Work supported by the U.S. Department of Energy, Office of Science, Basic Energy Sciences, under contract #DE-AC02-06CH11357.

lines, at sectors 19 and 20-ID, will extend 220 and 180 meters respectively. With both beamlines being adjacent to each other, the end stations will be in relative close proximity to one another which will allow them to share the same out-building and enable the building to be as small as possible. Final preliminary designs for this new building are complete and we are conducting studies to maximize stability and reduce vibration. The longer of the two beamlines will employ a 101 mm diameter, 146 meter long shielded transport pipe. Vacuum conductance calculations for this section have been done assuming 3×10^{-10} mbar*L/s/cm² outgassing rate (conservative for stainless steel), and we've determined that four 200 L/s pumps equally spaced along this span, with a 100 L/s pump at each end will be sufficient even if two of the pumps fail. These results were compared to calculations for the LCLS-XTOD Tunnel Vacuum System with similar results.

IDEA Beamline

Currently the APS Upgrade (APS-U) does not have a suitable testing location for X-ray optics and components (there is one station located on a bending magnet beamline at Sector 1 (1-BM-B) that is used for optics testing, but it does not provide the necessary flux to simulate the planned brightness of the APS-U source). The Instrumentation Development, Evaluation, & Analysis (IDEA) Beamline is currently being built at 28-ID which is one of the last two remaining empty sectors at the APS. Eventually becoming the CHEX beamline after the upgrade, this sector will in the meantime be used to test new undulator designs (SCUs, Revolvers, etc.), evaluate monochromator and mirror stability (thermal, vibrational, positional), including Kirkpatrick-Baez (KB) mirror systems, zone plates, compound refractive lenses (CRLs), and to verify thermal performance of photon masks. Additionally, new detector designs can be developed with vendors over a period of time prior to the completion of the APS upgrade, tested, and performance verified with pre-purchase units. In order to save money and design time, much of the beamline will be built using existing shutters and various other components that we have on hand. The contract for the shielded enclosures for 28-ID was awarded to Enterprise Caratelli and construction will begin in October of 2018. Beamline commissioning should be completed in spring of 2019.

Beamline Design Process

Initial preliminary layouts for the feature beamlines were created working with the beamline scientists based on their optical requirements, existing infrastructure constraints, and radiation safety parameters. Two-dimensional beamline ray trace diagrams were generated to determine the safety envelope, shielding positions, and ultimate component specifications for photon delivery components; i.e. photon absorbers & shutters, Bremsstrahlung collimators, general support structures, and vacuum equipment. Once all of these parameters are known, components will be designed using PTC/Creo 3D CAD software. The APS has a large library of standard time-tested designs which will be leveraged for the upgrade project.

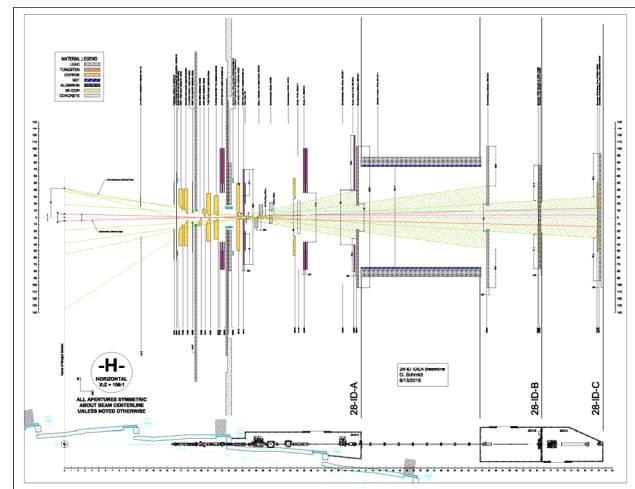


Figure 2: Example raytracing diagram.

Working groups have been established to address Nano positioning, vibrational stability, and high heat-load optics performance. Some of the more complex beamline instrumentation may be designed in-house, however it will be more efficient to specify and purchase most of our optical components from outside vendors. A few of these items have already been purchased as part of an early procurement plan to allow for testing and evaluation at various beamlines including IDEA.

Project Management

From our preliminary beamline layouts, as well as leveraging subject matter experts, we've developed a detailed list of components, hardware, and infrastructure requirements. Using recent purchase requisitions and vendor quotes, we've systematically compiled a very good basis of estimate (BOE) for overall beamline costs. Labor estimates for all resource allocations are based on previous experience and recent beamline upgrades and improvements. The work breakdown structure (WBS) for each beamline consists of Overall Design, Photon Delivery Integration & Assembly, Installation, Optical Components, Non-Optical Components, Diagnostics, Supports, Shielded Transports, Vacuum Systems, Detectors, and End Station Instrumentation, Shielded Enclosures, Mechanical Utilities, Electrical Utilities, Safety Interlocks, Beamline Controls, and Network Infrastructure. All of this information has been loaded into Primavera version 6 project management software (P6), and detailed schedules have been worked out. This is a powerful tool which will allow us to track schedule and cost variances over the life of the project.

Challenges

The new APSU storage ring will establish new source parameters that define our synchrotron and bremsstrahlung radiation safety envelopes. Since these changes will affect all ID and BM beamlines, all existing ray tracing (Fig. 2) diagrams will need to be redrawn and approved by the Radiation Safety Committee. We have achieved a great deal in standardizing our ray tracing techniques over the years and have recently developed a new template that will make

the process much more efficient. Work is presently underway to bring all of the beamlines up to the current standard, which will make this task much more manageable in the end.

ID beamlines will remain in the same locations with respect to beamline source, however the new storage ring parameters will require the re-alignment of all bending magnet beamlines. The current estimate is a lateral translation of 36mm inboard with a possible rotation of up to 0.75 mrad may be necessary.

The reuse of existing components and infrastructure will be key to lowering the cost and meeting the overall schedule. Identifying components, ensuring that they still have a usable service life, and then tracking and refurbishing them during the main installation period will take significant effort.

Conclusion

The Advanced Photon Source (Fig. 3), at Argonne National Laboratory, is a high energy synchrotron light source in operation since 1995. The upgrade of this facility to a 4th generation light source will ensure many more years of world class science and innovation.

References

[1] M. Borland *et al.*, “The Upgrade Of The Advanced Photon Source,” in *Proc. 9th International Particle Accelerator Conf. (IPAC2018)*, Vancouver, BC, Canada April-May 2018, paper THXGBD1.



Figure 3: Bird’s eye view of the Advanced Photon Source, Argonne National Laboratory.

A NEW PROCUREMENT STRATEGY TO CHALLENGE THE SUPPLIER CONSTRAINTS CREATED WHEN USING A FULLY DEVELOPED REFERENCE DESIGN

George Howell[†], Nick Baker[‡], Steve Davies[¶], Andrew Walters^β, Mirian Garcia-Fernandez^γ,
 Houcheng Huang^δ, Stewart Scott^ε, Kejin Zhou^{α1},
 Diamond Light Source Ltd, OX11 0DE Oxford, United Kingdom

Abstract

A common procurement strategy is to produce a fully optimised reference design that makes assumptions about the manufacturing process and supplier capability. This approach can restrict the opportunities for some companies to include their own specialist manufacturing capability to provide a more effective and cost efficient solution. A new approach is suggested following the recent experience at Diamond Light Source. The manufacture of high stiffness welded fabrications up to 13 m in length for the I21 RIXS² [1] Spectrometer is used as an example. The I21 RIXS Spectrometer design was optimised for stiffness and control of vibration. The use of Finite Element Analysis³ enabled different design options and compromises to be explored utilising the supplier's capabilities. The final design was tested during manufacture to verify the FEA model. With the I21 RIXS Spectrometer commissioned the data collected shows the final stability performance of the system including detector stability over full experiment durations has met the scientific goals of the design.

REFERENCE DESIGN DEVELOPMENT

The RIXS Beamline at Diamond followed the normal development process with Concept and Technical Design Review phases of Science Case and Technical Feasibility sign off. The beamline optical layout is typical for a soft X-ray beamline having a PGM⁴ and Exit Slits with focusing optics either side. However to achieve the necessary photon throughput, energy resolution and stability enhancements have been necessary.

Construction of I21 RIXS Beamline at Diamond was a complex programme of Beamline, Spectrometer, External Building and Sample Vessel projects. The Spectrometer is a 16 m long assembly that supports a detector and optics. The complete assembly is able to rotate on a vertical axis

150 degrees around the sample vessel with the sample at the centre. The optics are a series of cylindrical gratings to focus scattered X-rays from the sample on the detector with energy distributed vertically. The gratings have 4 motions and in addition the whole assembly can travel 1.5 m in beam direction. The detector is able to rotate to align with the focus of the vertical energy distribution of the X-rays by moving radially and vertically.

Project Phases

The Spectrometer project had several stages starting with a concept stage that concluded with a review by the Technical Working Group, Science Director and Head of Engineering. The first phase of work on the Spectrometer involved developing concepts for the key aspects of the design. During this phase visits were carried out to the Address Beamline at the Swiss Light Source [2] and ID32 at the ESRF [3] to discuss the approach used for similar beamlines.

At this stage, the design intention followed recognised best practice to minimise risk through the utilisation of standard parts, using developed technology and where possible solutions previously used at Diamond. With this low risk strategy in place the design of individual assemblies could then be developed including the Spectrometer Frame.

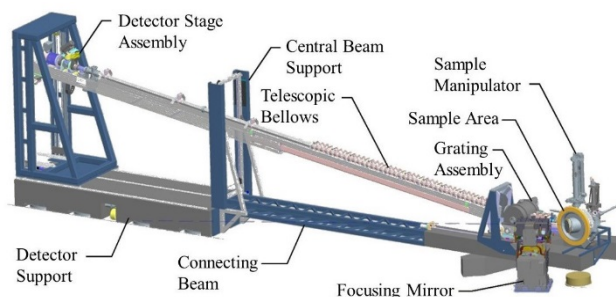


Figure 1: Concept Report Design January 2014.

In the design shown in Fig. 1 the Vertical Frame Assembly supporting the Detector Stage Assembly is able to move in the radial direction to control sample to detector distance. The range of this motion was extended in the final design to move detector from 10.3 m to 15.5 m. The completed Vertical Frame Assembly is able to move the detector 1.4 m vertically with a minimum height of 900 mm above the sample. At the concept stage it was expected the detector would need to be the same height as the sample for alignment. This requirement was later

[†] george.howell@diamond.ac.uk

^α kejin.zhou@diamond.ac.uk

^β andrew.walters@diamond.ac.uk

^γ mirian.garcia-fernandez@diamond.ac.uk

^δ houcheng.huang@diamond.ac.uk

^ε stewart.scott@diamond.ac.uk

[‡] nick.baker@diamond.ac.uk

¹ Principle Beamline Scientist for I21

² Resonant Inelastic X-Ray Scattering

³ Finite Element Analysis (FEA) or Finite Element Method

⁴ Plane Grating Monochromator

removed allowing more space for stiffening members once the optical alignment process had been defined.

Tender Stage

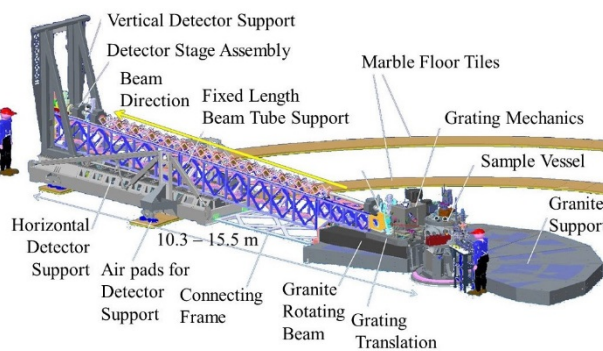


Figure 2: Tender Reference Design April 2016.

Several changes were made as the design developed for the Tender Reference Design Fig. 2. Air Pads were chosen for the Horizontal Detector Support. The telescopic bellows support was rejected in favour of a 13 m fixed length support enabling the central beam support to be removed. The rails supporting the Detector Stage Assembly could also be used to support the bellows capable of extending 7 m to link the Grating Mechanics Vessel to the Detector Stage Assembly. The chosen structure for the fixed length bellows support was a welded lattice based on a Bailey bridge [4]. The lattice design of diamonds between vertical members was found to have a significantly higher stiffness to mass ratio than a design with crossed members between verticals. In the Spectrometer application, this gives better vibration performance and reduced deflection for the same load.

Deflection of the lattice varies with radial movement of the Vertical Frame Assembly. This deflection creates a variable energy offset seen at the detector. Energy is measured by the detector through spatial separation in the vertical plane. Vibration limits the energy resolution achievable through vertical motion of the detector. Both of these effects are detrimental to the quality of data collected.

The Horizontal Detector Support material was selected as steel in preference to granite to facilitate the use of Air Pads in the support as the mass of the assembly was radically reduced. To increase the stiffness of the steel structure, towers and rigid stays were added. The overall length was increased to accommodate changes in the performance of X-Ray optics that may be available for future upgrades.

Tender Stage FEA

At this stage of the detailed design; deflection of the horizontal frame and specifically the variation of this deflection was minimised. The maximum deflection case shown in Fig. 3 is with the load from the Vertical Frame Assembly midway between supports. The maximum deflection modelled is 0.25 mm. The aim for the variation

in deflection between different load cases was ± 0.1 mm with ± 0.14 mm being achieved. This models the parasitic change in vertical position of the detector for different sample to detector distances. Modal analysis was also carried out to quantify the stiffening effect of improvements. The result Fig. 3 at tender was a first mode of vibration of 18 Hz.

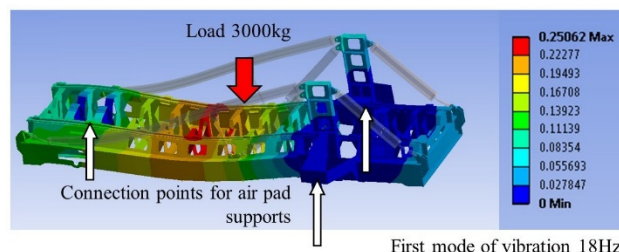


Figure 3: Horizontal detector welded frame deformation at tender stage.

PROCUREMENT

Our first challenge came right at the end of the tendering process. One of the regular suppliers to Diamond who had been contacted in the concept phase to give budget advice informed us that they would not be tendering. This was due to the scope of work being substantially outside their normal range. We had to decide whether it would be better to accept the outcome of the tender process or restart our specification and accept the delays that would follow. Since our project timescale was already under pressure we chose to accept the tender process outcome.

The second challenge was presented by the company OCSAM s.r.l.⁵ who were successful in the tender process. We agreed a rapid progression to a kick off meeting at the OCSAM manufacturing plant. The main outcome of the discussion was that they liked our project but not our reference design. In the company's opinion it was not optimised, they also advised it would be possible to offer a much better solution in a reduced delivery time. We took the opportunity, and although under time pressure, we decided to revise the design. Using the potential time saved from manufacture it was possible to investigate the performance benefits of optimising the design for the OCSAM capabilities. These capabilities included custom beam manufacture, folding steel plate (6 mm thick and 13 m in length) and machining assemblies in sections up to 18 m in length. This was far in excess of what we had expected to be easily accessible in our budget and time scale when developing our reference design.

Our initial concept based on the low risk and standard part approach had led to a design based on standard section beams for the main strength of the assembly. OCSAM suggested a custom beam based on a plate with 'C' section folded around it. This 'D' shaped profile was able to fill all the vertical space available offering signifi-

⁵ OCSAM s.r.l. Via della Tomba Antica 1-2, 33030 Basaldella di Campoformido (UD) Italy
<http://www.ocsam80.it/>

cantly improved stiffness with the increased moment of inertia from the equation (1).

$$I = \frac{b \cdot d^3}{12} \quad (1)[5]$$

Other changes included the width of frame, optimised at a wider span and removing the towers and stays without reducing the performance of the structure.

The Vertical and Fixed Length Beam Tube Support welded assemblies could then be focused on. The limitation was not the section of material or machine tool capacity, but the decision to avoid the need for an escort across Europe. This also reduced the cost of shipping the frame parts from Italy to the UK.

Achieving the Optimal Solution

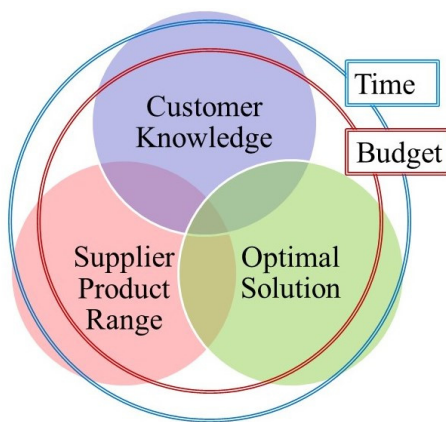


Figure 4: Venn diagram showing influences that need to converge to achieve the required outcome.

Figure 4 shows graphically how the Optimal Solution can be positioned against the Customer Knowledge and Supplier Product Range. Equally the supplier product range could be their capability or potential and Optimal Solution could also be defined as ideal specification. Also shown in Fig. 4 are the budget and time aspects, these factors provide overall constraining limitations. Recognising and responding to knowledge baseline effects is a key factor in achieving the desired outcome.

It has become clear that the convergence of Customer Knowledge and Supplier Product Range had not come together with the Optimal Solution at the Tender Stage of the Spectrometer Frame Project. The knowledge of Supplier Product Range was wrong for both companies discussed and the Optimal Solution achievable was limited by the reference design. It cannot be realistic to hope for an open ended budget to resolve these type of problems yet challenging budget contingency may be valid for projects at the fringes of customer knowledge.

Design consultancy would be a recognised route for projects where further knowledge of the optimal solution is required. The cost of doing this would need to be reflected in the overall project cost as well as potentially higher manufacturing cost of the solution. Taking a prag-

matic view in a budget conscious environment leads to the option of investing time in developing customer knowledge. This is where time spent understanding technology and supplier capability at the outset of a project are the route to eliminating higher cost routes to achieving optimal design solutions. In short a more informed Engineer or Designer will have a greater opportunity to achieve the most optimum solution. The benefits from the investment in time and Engineering knowledge are returned through achieving higher quality solutions first time and also getting closer to the optimal goals of the project, whether they are low cost, efficiency, science output or data quality.

Analysis of Final Design

Finite Element Analysis (FEA) enabled the exploration of different design options and compromises. This resulted in a new optimised design based on the design parameters OCSAM had made available. The final design included changes targeting specific load cases where the position of the vertical frame caused the most deflection. Figure 5 shows a deflection of 0.16 mm for the optimised frame FEA. The variation in deflection between different load cases was improved to ± 0.06 mm. Modal analysis showed stiffness had been significantly improved with a first mode of vibration of 36 Hz.

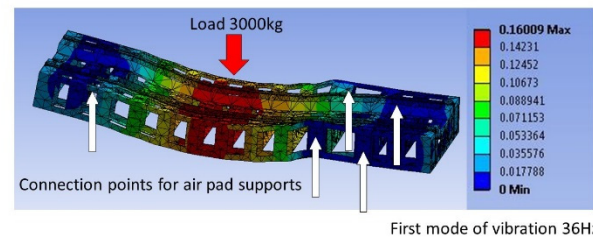


Figure 5: Horizontal detector welded frame design at FDR stage.

Changes to the vertical frame included significant additions to give lateral stiffness. The aperture for the lattice to pass through is a major weakness of the structure and stiffening this was the last priority. Following the optimisation, it was possible to hold a Final Design Review and allow manufacture to start.

MANUFACTURE AND TESTING

Manufacture included load tests designed to verify the FEA model. Simple load cases were modelled that could be easily set up by OCSAM with the frames after welding. These tests were able to verify the frames achieved the predicted stiffness. The horizontal frame performed extremely close to the model with 0.36 mm and 0.39 mm vertical deformation. The FEA prediction was 0.358 mm for both sides. The fixed length bellows support and vertical frame did not follow the prediction as closely with deflections 23-33 μ m greater than predicted. This was a significant proportion of the predicted deformation. These errors are not enough to create significant stresses and the

frames were accepted. The comparable difference in reliability of FEA prediction may be due to differences in the use of welded joints to create strength. The horizontal frame is essentially two beams with stiffening sections between them, the other assemblies are welded lattice structures. This area would require further investigation and modelling to understand the differences from the FEA model.

Stability

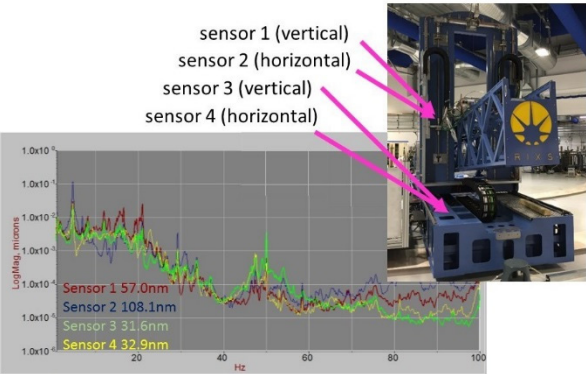


Figure 6: Spectrometer vibration measurement.

Stability measurements of the Spectrometer Frame show very good stability with a summary of results shown in Fig. 6. Vibration measurements of the frame show an RMS⁶ vibration amplitude of 108nm, which is in the lateral direction. Vertical vibration, which has a more direct relation to the quality of data collected by the beamline, is 57 nm.

CONCLUSIONS

When specifying equipment and writing tenders it is necessary to draw out the suppliers knowledge to show where the equipment would fit in their circle of capability.

The risks of a reference design are to overlook the need to write specifications in a way that allows a supplier to give their best solution to meet the functional requirements of the equipment.

There is a need to recognise and be aware of the limitations of our design baseline. These limitations taken through a specification and tender process are able to influence the level of design optimisation possible.

The challenge for future projects is to apply a strategy that identifies limitations in our knowledge and enable the procurement process to meet our functional requirements within the overriding project limitations of time and budget.

Using a budget contingency allows a broad range of procurement solutions to be considered. The most appropriate solution can then be chosen to achieve the project functional specification more efficiently. Through the development of our engineering knowledge base, especially knowledge related to supplier expertise and capability it becomes possible to provide better Customer Knowledge to a project.

The best method for achieving a delivery closer to the optimal solution is for a new strategy to facilitate convergence of Customer Knowledge and Supplier Product Range. The proposed method for this is through the development and exchange of engineering knowledge to give the largest convergence of Customer Knowledge and Supplier Product Range with the Optimal Solution for a given project.

For the I21 RIXS Beamline at Diamond the Spectrometer project has been able to make the most of a second chance. Working with OCSAM provided an opportunity to learn as well as time for development of the design to take place. This lead to improvements in structural strength and vibration performance that have a direct impact on the quality of results the beamline is able to deliver.

REFERENCES

- [1] L. J. P. Ament, M. van Veenendaal, T. P. Devereaux, J. P. Hill, J. van den Brink, “Resonant inelastic x-ray scattering studies of elementary excitations”, in *Rev. Mod. Phys.*, vol. 83, pp. 567-569, Published 24, June 2011, doi:<https://doi.org/10.1103/RevModPhys.83.705>
- [2] V. N. Strocov *et al.*, “High-resolution soft X-ray beamline ADDRESS at the Swiss Light Source for resonant inelastic X-ray scattering and angle-resolved photoelectron spectroscopies”, in *J. Synchrotron Rad.*, vol. 17, pp. 631–643, doi:10.1107/S0909049510019862
- [3] ESRF ID32 RIXS N. Brooks, F. Yakhou, F. Cianciosi and L. Eybert, <http://www.esrf.eu/home/UsersAndScience/Experiments/EMD/ID32/RIXS.html>
- [4] Think Defence, <https://www.thinkdefence.co.uk/2012/01/uk-military-bridging-equipment-the-bailey-bridge/>
- [5] W. C. Young, R. G. Budynas, “Properties of Plane Area”, in *Roark's Formulas for Stress and Strain - 7th Edition: International Edition*, McGraw-Hill, 2002, p802.

⁶ Root Mean Square

DEVELOPMENT OF LOW VIBRATION COOLING SYSTEMS FOR BEAM-LINE OPTICS USING HEAT PIPE TECHNOLOGY

J.R. Nasiatka*, S.S. Soezeri, O. Omolayo, H. A. Padmore, Advanced Light Source, Lawrence Berkeley National Lab, 94720 Berkeley, CA, USA

Abstract

Cooling of in-vacuum beamline components has always been problematic. Water cooling lines can transfer vibrations to critical components, and often require complex air guarding systems to ensure that the vacuum envelope is not breached in the event of a leak. These constraints increase design complexity, limit options, and provide challenges for assembly and maintenance.

Commercial heat pipes are inexpensive and readily available. Custom assemblies can be fabricated into vacuum flanges and may use non-water-based cooling mediums if required. A mockup of an optical assembly has been used to explore vibration reduction and cooling capacity. Other example beamline components such as a heat generating electromagnetic shutter, demonstrate the cooling capability of these heat pipes.

INTRODUCTION

A heat pipe [1] [2] is a device with a very high thermal conductivity that can transport large thermal loads. It is a passive, 2-phase device that comprises a sealed tube at sub-atmospheric pressure that contains a wicking medium and a working fluid. (Figure 1) At the hot end the working fluid absorbs energy and evaporates. It then migrates to the cold end where the thermal energy is released and the fluid condenses. The wicking material draws the condensed liquid back to the hot end. With proper design, the device can generally operate in any orientation, but if vertical with the hot end elevated, then gravity will help with the wicking.

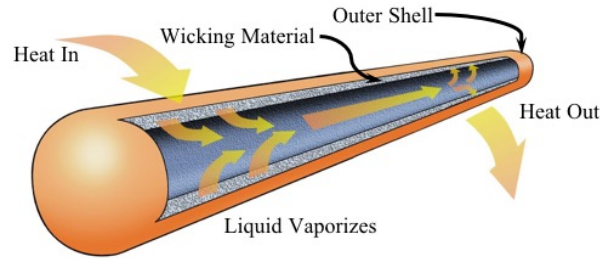


Figure 1: Heat Pipe Operation.

Table 1 lists thermal conductivities of various metals used in vacuum systems and the conductivity of a typical heat pipe. Heat pipes have an extremely high effective thermal conductivity compared to a solid metal conductor of the same size/shape $\sim 10-100$. Internal design, orientation and working temperatures as well as heat loads need

to be considered for proper selection. [3] [4] Operation ranges can be anywhere from cryogenic to over 1500°C , and determine both the working fluid and outer shell. For $0-100^{\circ}\text{C}$ operations water with a Copper shell is the most common and was used for these tests. Ethanol, methanol, and acetone can also be used. For use in UHV environments, sealing methods and materials are a factor. [5] This paper examines the suitability of heat pipes for cooling in-vacuum components on beamlines and endstations.

Table 1: Thermal Conductivities of Materials

Material	Conductivity (W/m \cdot K)
Heat Pipe	10,000 +
OFHC Copper	390
6061 Aluminum	167
304 Stainless Steel	16.2

VACUUM COMPATABILITY

Standard Commercial Off The Shelf (COTS) heat pipes are typically fused and sealed by friction welding at the filled end. This end seal is the main potential point of failure that could result in leaking the working fluid into the vacuum. To determine vacuum suitability, two commercial heat pipes were ultra-high vacuum (UHV) cleaned and placed in a testing chamber that was then baked at 180°C for 2 days. Before and after bake residual gas analysis (RGA) scans were performed and after removal they were tested by placing them in a cup of hot water where they performed as expected.

Another heat pipe was cut in two and brazed onto a standard 2.75" Conflat flange so that the sealed ends of the pipe would be exposed to vacuum. (Figure 2) This was then UHV cleaned and mounted in a testing chamber equipped with an RGA. The assembly was exposed to repeated 180°C bake cycles of 24 hours with RGA scans performed after each cycle.

* JRNasiatka@lbl.gov

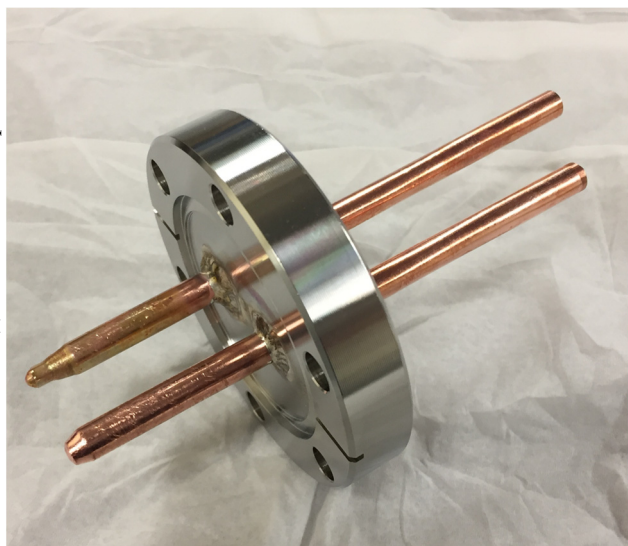


Figure 2: Heat Pipe Vacuum Test Assembly.

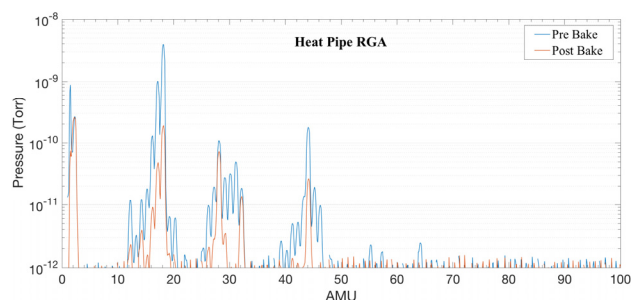


Figure 3: Heat Pipe RGA Scan.

The assembly was monitored for 5 bake cycles and no signs of leaking or contamination were found as indicated by a clean UHV RGA scan (Figure 3). It was then left on the testing chamber during testing of other UHV components for approximately another 15 cycles over 2 months. No signs of leaking were found which implies that for this heat pipe at least, the friction vacuum seal of the heat pipe is adequate for normal UHV practices.

THERMAL TESTING

In these tests, a 457mm long, 6.35mm dia. heat pipe was fabricated into a 2.75" Conflat flange (Figure 4). The in-vacuum end was coupled to an Aluminum block to represent a generic optic, and an Aluminum cold plate connected to a chiller was attached to the air end of the heat pipe. Indium foil was used to ensure good thermal contact. A 20W Kapton foil heater was placed on one face of the Aluminum block to represent X-Rays impacting the face.

For testing, the system was mounted in a vacuum chamber (Figure 5) and pumped to high vacuum ($\sim 10^{-6}$ Torr) to remove any convection effects. The chiller was set to 18°C and power was applied to the heater to output 20 W. After reaching thermal equilibrium, temperatures on the optic face, and both ends of the heat pipe were recorded and

compared to thermal finite element analysis (FEA) that was conducted based on the manufacturers specifications for the operating conditions. Figure 6 shows the thermocouple locations about the heated Aluminum block. Figure 7 shows the FEA of the system in thermal equilibrium. Table 2 shows the FEA and measured temperatures.

The FEA agrees reasonably well with the measurements – the heater block temperatures are within 5°C and the heat pipe within 2°C. Refining the thermal contact at the joints for the FEA would be needed for closer agreement.

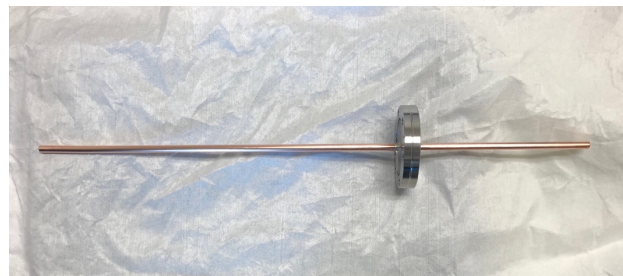


Figure 4: Custom Heat Pipe in CFF Flange.

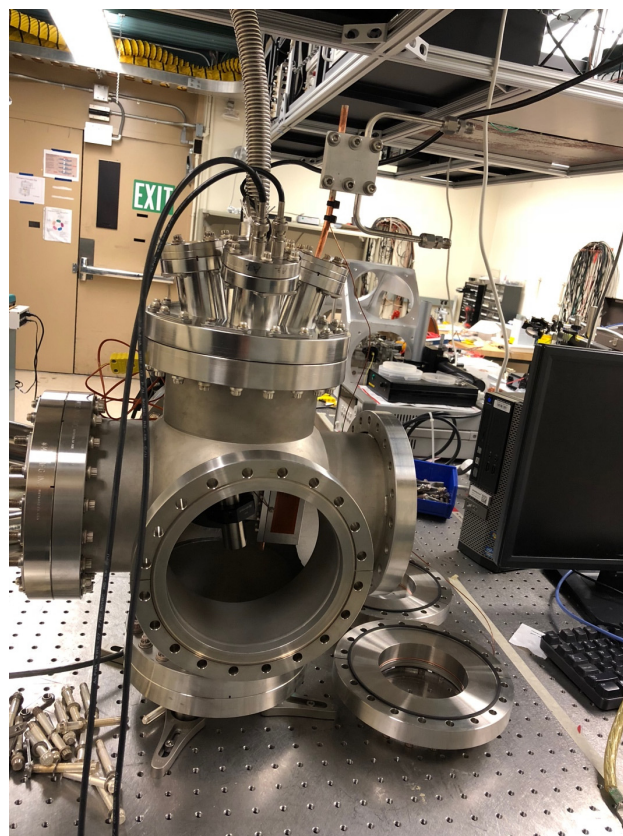


Figure 5: Test Chamber Assembly.

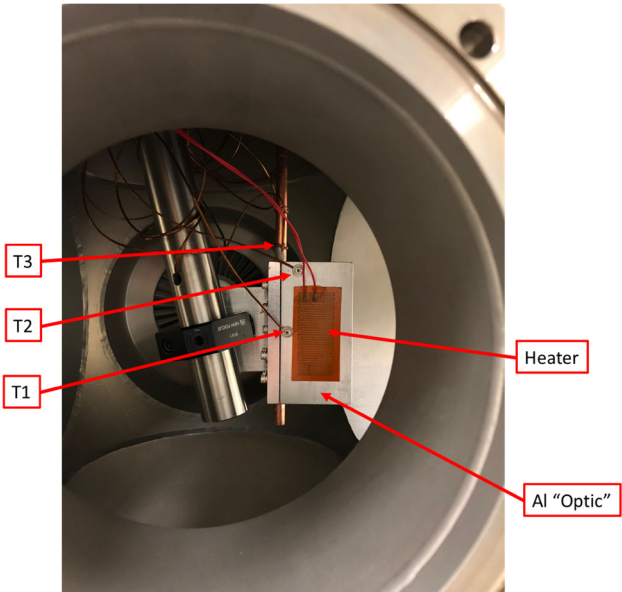


Figure 6: Al heater block and in-vacuum thermocouples.

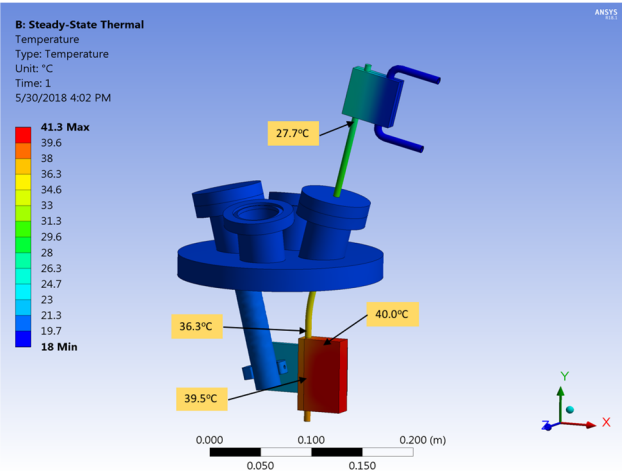


Figure 7: Thermal FEA.

Table 2: FEA Comparison to Measured Values in Figure 6 and Figure 7

Temperature	FEA	Measured
T1 – Al Block	39.5 °C	45.6° C
T2 – Al Block	40.0 °C	44.7° C
T3 – HP Base	36.3 °C	37.1° C
T4 – HP Top	27.7 °C	25.8° C

VIBRATION MEASUREMENTS

Accelerometers were mounted on the Aluminum heater block (Figure 8) and vibration measurements were taken with for various combinations of cooling water on, off and for the water cooling section directly coupled to the Aluminum heated block.

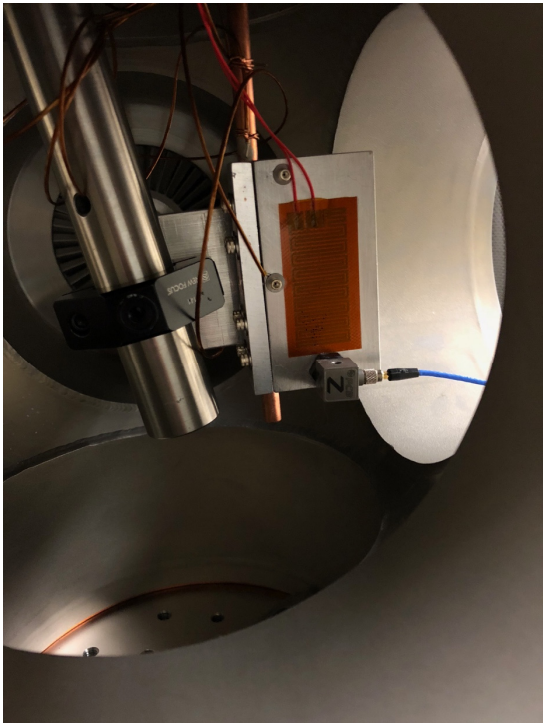


Figure 8: Test Assembly with Accelerometer.

Figure 9 shows the Power Spectrum Distribution (PSD) in the X, Y, and Z axis on the cooling block with the heat pipe attached and the cooling water on/off. The plots indicate slightly increased vibrations with the water flow on.

Figure 10 compares the PSD between the cooling block and the heater block, i.e. between the two ends of the heat pipe with cooling water on. The cooled end is fairly unconstrained and vibrations from the cooling water are greatly amplified at this end, but do not translate through to the hot end. This indicates good vibrational decoupling between the two.

Figure 11 compares the PSD of the Aluminum heater block with both the heat pipe installed and with the water directly coupled to the heater block. In both cases the cooling water on. This also indicates good vibrational decoupling from using the heat pipe, and reduced water-induced vibration by up to 10x over certain frequency ranges.

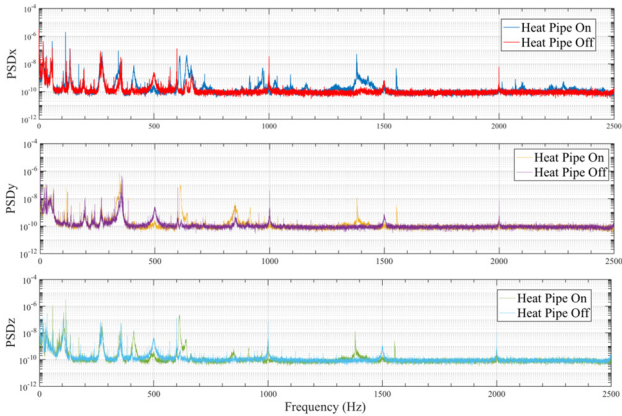


Figure 9: PSD with Heat Pipe Flow On/Off.

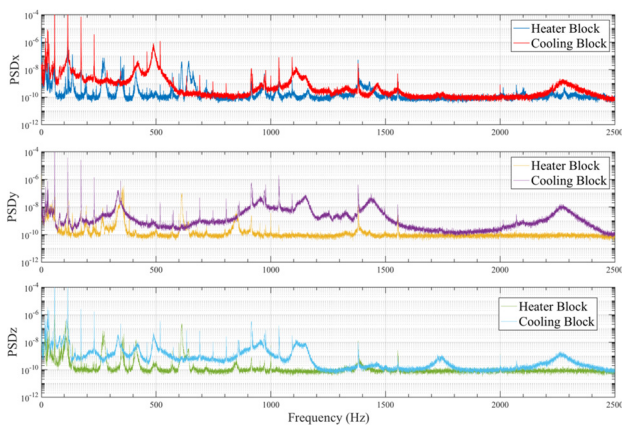


Figure 10: PSD for Hot and Cold Blocks with Flow On.

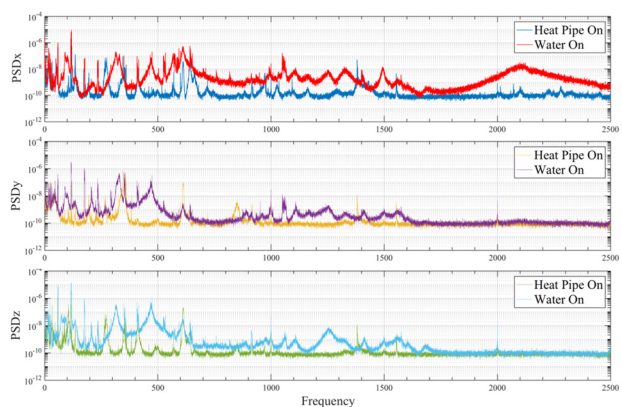


Figure 11: Vibrations - Heat Pipe vs. Direct Coupling with Flow On.

BEAMLINE APPLICATIONS

ALS Beamline 5.3.1 is a tender x-ray development beamline that uses an electromagnetically actuated laser shutter that has been modified for use in vacuum to act as a fast (<10 ms) shutter on the endstation. This modified design has been used in several other endstations at the ALS, and typically requires active water cooling of the mounting base to remove excess heat generated by the electromagnet. For this system, a COTS heat pipe was coupled to the magnet assembly to transport the waste heat to the side wall of the Aluminum vacuum chamber for thermal dissipation and subsequent air convection cooling.

Figure 12 shows the shutter assembly before installation, and Figure 13 shows the system installed in the vacuum vessel. The system has been shown to effectively cool the shutter assembly, with the contact area on the chamber wall being slightly warm to the touch. Exposure to vacuum and x-rays have not affected the heat pipe.

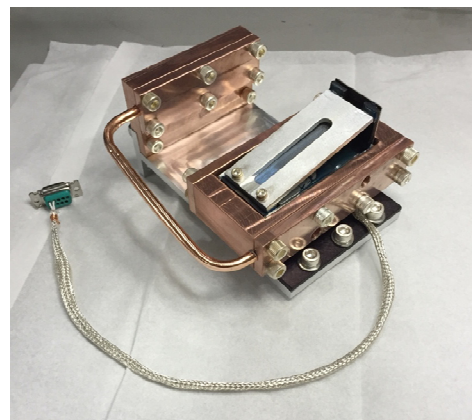


Figure 12: Shutter Assembly showing bent heat pipe conducting heat from shutter electromagnet to wall clamp support.

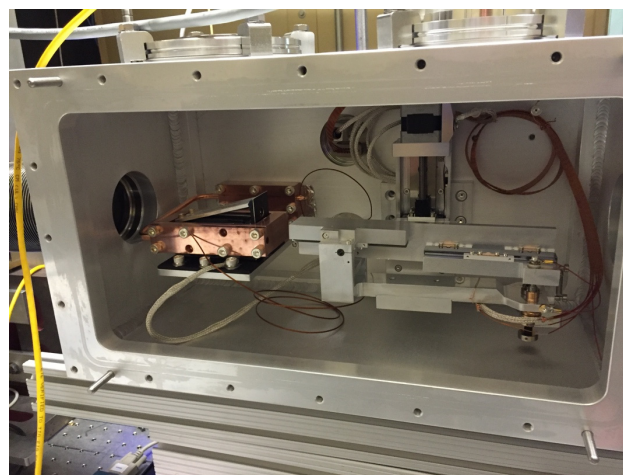


Figure 13: Chamber assembly showing shutter assembly (left of centre) clamped to the vacuum vessel.

CONCLUSION

Heat pipes, both custom and COTS can effectively be used to cool beamline components with minimal risk to UHV environments, and exposure to both vacuum and x-rays do not have deleterious effects on the system. They can also assist in reducing vibrations and offer simplified designs and reduced maintenance.

ACKNOWLEDGEMENTS

This research used resources of the Advanced Light Source, which is a DOE Office of Science User Facility under contract no DE-AC02-05CH11231.

REFERENCES

- [1] P. D. Dunn and D. Reay, *Heat Pipes*, Pergamon, Ed. Oxford, UK, 1993.
- [2] M. Kutz, *Mechanical Engineers Handbook*, Wiley and Sons, New York, USA, 2015.
- [3] C. K. Loh, E. Harris and D. J. Chou, "Comparative Study of Heat Pipes Performances in Different Orientations", in *Proc. Semiconductor Thermal Measurement and Management IEEE Twenty First Annual IEEE Symposium*, San Jose, CA, USA, April 2005, DOI: 10.1109/STHERM.2005.141278.
- [4] Advanced Thermal Solutions, "How Wicks and Orientation Affect Heat Pipe Performance," *QPedia*, Aug. 2009, http://www.qats.com/cms/wp-content/uploads/2015/03/Qpedia_Aug09_How_wicks_and_orientation_affect_a_heat_pipes_performance.pdf.
- [5] Y. Li and L. Xianghong, "US Particle Accelerator School-Vacuum Science and Technology for Accelerator Vacuum Systems", <http://uspas.fnal.gov/index.shtml>.

Content from this work may be used under the terms of the CC BY 3.0 licence (© 2018). Any distribution of this work must maintain attribution to the author(s), title of the work, publisher, and DOI.

LCLS PULSE SELECTOR, A MULTIFUNCTION SHUTTER FOR THE LCLS-I 120 Hz FEL

R. R. Armenta[†], E. Paiser

Linac Coherent Light Source, SLAC National Accelerator Laboratory, Menlo Park, USA

Abstract

The Linac Coherent Light Source (LCLS) Pulse Selector was designed to pick specific pulses and reduce the repetition rate of the 120Hz LCLS pulse train in support of widely diverse, user defined experiments. It utilizes two rotating parallel plates to alternately transmit and block pulses in a single sweeping motion. A conventional stepper motor connected to the plates provides the rotation. The key to the system is its sophisticated timing scheme. Each sweep of the shutter is synchronized (with a precise delay) with the event codes normally generated with each pulse for data acquisition use. This shutter system has the capability of reducing the repetition rate of the LCLS x-ray to any frequency less than or equal to 60Hz in order to select a single pulse of LCLS x-ray beam at 120Hz. Since its installation, the pulse selector has been used in numerous experiments with great success providing independent pulse selection to individual beamlines at the same time.

INTRODUCTION

The Pulse Selector was commissioned to provide the hard x-ray beamlines (XPP, XCS, CXI, MEC, and later, MFX) with the ability to control pulse delivery without having to change accelerator machine modes/parameters. The key requirements were that (in addition to being able to fully attenuate the beam) the selector had to provide three main functions:

1. Provide single pulse selection (Mode 1)
2. Allow for multiple (n) sequential pulse selection (Mode 2)
3. Reduce the repetition rate of the 120Hz LCLS beam to up to 30Hz (Mode 3)

Initially the concept was to create a device similar in design to chopper/picker systems integrated at other synchrotron and FEL facilities e.g. the systems described by Kudr et al. [1] and Cammarata et al. [2]. These systems typically have a rotating disk or other shape with multiple apertures.

Material Considerations*

The pulse selector is required to block a certain number of x-ray pulses, i.e. attenuate the beam by more than about 20 orders of magnitude in the LCLS hard x-ray energy range (4-25 keV). While the required attenuation can be easily reached with small material thicknesses of high Z

element containing materials, the short attenuation length in this material leads to the absorption of energy in a very small volume. Depending on the dose (energy per atom) the absorbed energy can be sufficient to melt and thereby damage the material. Melting doses for different elements are listed in the following Table.

Table 1: Melting Doses for Individual Elements

Element	Melting Dose / (eV / atom)
Al	0.186
W	1.2376
Si3N4	0.187
Co	0.554

The maximum FEL pulse energy to reach the damage dose depends on the beam size. From all hard x-ray hutches the beam size is smallest at XPP (500 um) and therefore the fluence is highest there.

The maximum pulse energy to reach the melting dose for W and Co, the main components in the stopper material selected for this application (WC/Co), is shown in Fig. 1 for the full energy range.

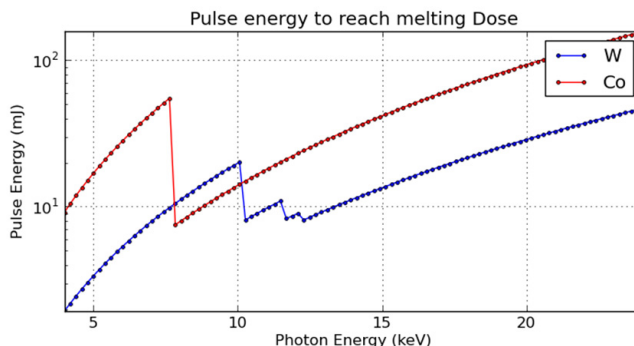


Figure 1: Pulse Energy to Reach Melting Dose.

Within the energy range of the first LCLS harmonic (4-10keV) damage might be reached. To prevent this, it was determined that coating with a lower Z material (Aluminum) would help for the following reasons: The x-ray pulse energy is reduced by attenuation in the coating material, and the material prevents melted material from leaving the x-ray exposed region. Coating of the stopper material with a metal would have been most preferable as it is mechanically very stable. However, when evaluating

[†] Contact: rebecca@slac.stanford.edu

* Material investigations performed by Henrik Lemke, LCLS staff scientist (2012)

the required thickness of the aluminium layer it was determined that 0.1mm was needed to increase the attenuation in the lower energy ranges (below 6 keV – where the material is most prone to beam damage).

DESIGN

Taking into consideration the requirement to layer the high Z tungsten carbide shutter material with at least 0.1mm of Aluminum, and the fact that 0.1mm is beyond the limitations of most conventional coating processes, it was determined that a separate layer of aluminum foil or sheet 0.02in thick (shown in Fig. 2) would be used in the assembly. This layering requirement limited the options for complex geometries such as disks with multiple channels or holes. As such, a simple parallel blade geometry was adopted. This geometry creates a single channel for the beam to pass through when aligned with the beam.



Figure 2: Parallel Layered Blades.

When clocked at a slight angle the blades block passage of the beam and when aligned with the beam allows it to pass through as shown in Fig. 3. With this simple mechanical concept methods to produce all three modes of operation were conceived.

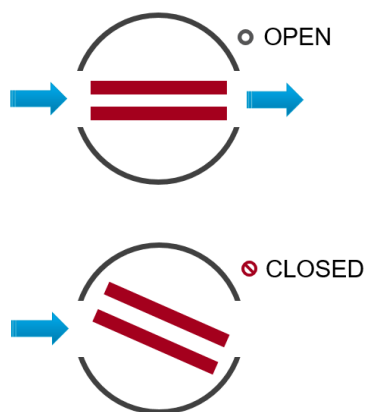


Figure 3: Opened and closed states of channel.

With only 8.3ms between pulses on the 120Hz LCLS beam the speed of the system opening and closing becomes an issue. Time taken for communication to the motor as

well as the time taken for blades to move into position easily add up to around 8-11ms. For the single pulse (Mode 1) and pulse rate reduction modes (Mode 3), in particular, the timing must be extremely efficient. To save time on each cycle in these modes the pulse selector sweeps through three states (closed-open-closed) in a single motion (and single command to motor). The timing of each sweep in alternate directions is synchronized and triggered by a simple pulse (the beamlines use the “Event Receiver” (EVR) to generate it). This concept is illustrated in Fig. 4.

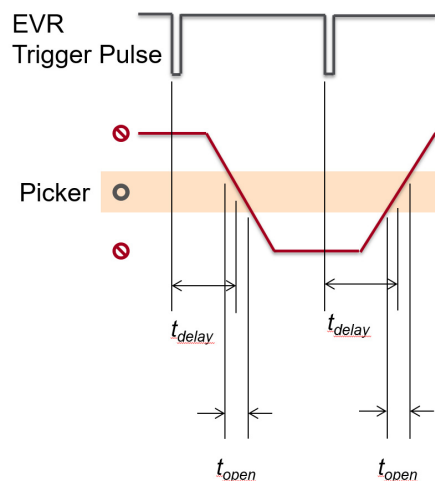


Figure 4: Open/Close cycle during a pulse rate reduction sequence (each swipe triggered by EVR Pulse).

Significant testing was performed in the lab (with offline pulses) during the conceptual design phase of the project in order to optimize the speed and tune the timing of the system. Variables such as sweep angle, motor speed/acceleration (and other parameters), gap length between blades, length of blades, trigger delay, and others were tuned to produce a robustly functioning shutter system before integration into the final mechanical system.

Mechanical

The Pulse Selector device is installed on each of the hard x-ray beamlines and shares a chamber with the hard x-ray attenuator assembly. The interface on this chamber for this device is a single 6.0 inch conflate flange. Each of the hard x-ray beamlines operate nominally at 10⁻⁷ scale vacuum in the areas in which these devices are installed.

Rotary Vacuum Feedthrough The rotation feedthrough chosen for this application is a ferrofluidic seal, so chosen because of its ability to transmit high speed rotation at this vacuum level (much testing was performed in the lab on this device pre-final design as well, testing off-gassing rates at speed as well as temperature effects on off-gassing). Although some hydrocarbons are released during continuous rotation of the seal, the levels do not exceed what can be tolerated in the zones in which these

devices are installed (for example there are no precision optics nearby). In order to position the rotational bearings within the ferrofluidic seal as close to the blades as possible the seal is mounted in a re-entrant (inverted) bellows flange. This flange can be precisely positioned by an X/Y stage which the external device structure is mounted. The structure also provides support for the stepper motor and related components.

Stepper Motor The driving motor chosen for this system is an IMS Smart Motor [3], which is a stepper motor with integrated driver and controller. These are commonly used along the beamline at LCLS and have existing accommodations in the controls system infrastructure. But most importantly the on-board controller with this particular motor system has the built-in ability to accept fast trigger pulses, which was exactly what we needed to synchronize the shutter to the FEL pulses. To operate at the speeds necessary for this application the motor needs to be powered with a 60V power supply. After several hours of continuous operation, the motor has a tendency to get quite hot. A fan is necessary to keep it within safe operating temperature.

Blade Assembly The parallel blade assembly is mechanically fastened together onto a hub and secured to the ferrofluidic feed-through shaft of the vacuum side of the re-entrant flange. To remain secure during cyclical/high vibration operation conditions, the assembly utilizes deformable locknuts and spring pins to ensure a secure connection.

Other Features The system includes a high resolution optical rotary en-coder with reference mark used for motor positioning and homing. This is mounted on the air side of the rotary feed-through assembly. High precision limit/position switches enable precise positioning of the X/Y stages used for blade alignment. These features can be seen in Fig. 5.

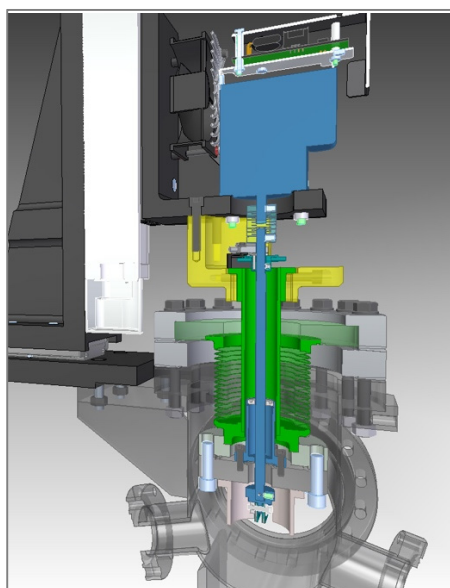


Figure 5: Cross section of Pulse Selector Device.

Controls

Using the IMS smart motors was deemed the simplest way to control the motor during design conception, but one of the big challenges during commissioning was to produce a very efficient program that, when integrated within the LCLS beamline framework, could read the EVR trigger and move the motor fast enough to accomplish single pulse selection and 30Hz (or higher) pulse rate reduction (the most difficult cases). During commissioning, the code developed during testing was refined and optimized for fast control with reduced overhead processing times. User interfaces and commands were developed for control of this device through the beamline control system.

The main beamline framework at LCLS is EPICS. Control of the Pulse Selector system is made by channel access (CA) process variables (PVs) via a Python command line (like SPEC) or through a Graphical User Interface (GUI). A dedicated GUI (referred to as EDM at LCLS) was developed for this device to select the mode of operation and to set specific motor parameters for the desired mode (if settings other than the default are desired). Alignment in X and Y directions and homing operations can also be performed from this interface.

The Pulse Selector IOC (input output control) program (EPICS software running on a generic server/computer) is used to communicate with the motor electronics sending the parameters necessary to set the mode of operation (single pulse, multiple sequential pulses, or pulse rate reduction) by serial line through a terminal server. The main program with different modes of operation is uploaded to the motor controller firmware and stored in their non-volatile memory by the IOC program only once. This allows for efficient execution of a program when the motor receives triggers.

The Pulse Selector timing configuration is done through the Event Sequencer. The Event Sequencer is a kind of command sequencer of operations that the scientists program prior to acquiring data. The output signal (Trigger) is issued after the selected timing events arrive in the EVR (Event Receiver) electronic board according to a particular set of events pre-programmed in the sequencer. A schematic for this process is shown in Fig. 6.

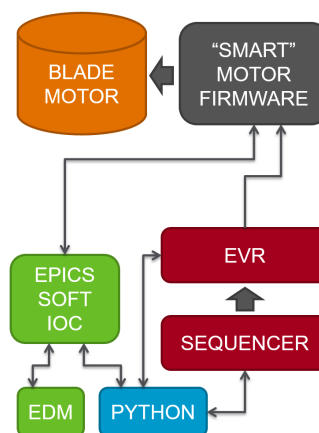


Figure 6: Motor Control System Schematic.

RESULTS

The Pulse Selector was installed and commissioned in 2013 in four hard x-ray beamlines at LCLS (XPP, XCS, CXI (two are installed at CXI), MEC) and has been running consistently ever since, with minimal required maintenance. In 2015 another unit was installed in the new hard x-ray endstation, MFX. The layout of the LCLS endstations (instruments) are shown in Fig. 7.

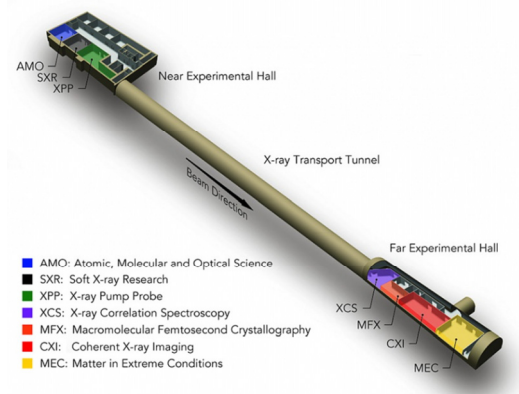


Figure 7: LCLS Instrument Map.

The Pulse Selector is typically used when running detectors that operate with readout rates lower than 120Hz as well as for alignment and detector tuning. For most beamlines this means 10-30% of the time. For MEC, an endstation that mainly runs single shot experiments, the Pulse Selector is used 100% of the time. For single shot experiment like MEC, i.e. one shot every few minutes, or low rate experiment at 10Hz, 30Hz, it allows the accelerator to run at its maximum rate (120Hz) where feedback and diagnostics are optimized to provide best stability. Additionally, the Pulse Selector is an essential element in the multiplexing scenario, when two (or three) hutches are using the same beam, where it allows experiments to control the pulse rate delivered independently of each other.

CONCLUSION

The mechanics of the Pulse Selector system are simple and robust and are designed to specifically withstand the LCLS FEL beam. The motion and timing concepts were prototyped and perfected in the lab before being integrated into final mechanical form. During the commissioning period the system software was refined and tuned, providing reliable and efficient control. The system has been in operation for five years and has become an indispensable component of LCLS standard beamline instrumentation.

ACKNOWLEDGMENTS

We are grateful for our colleagues at SLAC National Accelerator Laboratory who contributed to this project's success: M. Campell, J. Delor - Mechanical Engineering concepts and testing; J. Ludvik, K. Gumerlock - Controls integration; H. Lemke, A. Robert - Scientific guidance and support.

REFERENCES

- [1] T. Kudo *et al.*, "Vacuum-compatible Pulse Selector for Free-Electron Laser", *Review of Scientific Instruments*, 80, 093301 (2009).
- [2] M. Cammarata *et al.*, "Chopper System for Time Resolved Experiments with Synchrotron Radiation", *Review of Scientific Instruments*, 80, 015101 (2009).
- [3] Schneider Electric MDrive Motors, <https://motion.schneider-electric.com/all-products/mdrive-intelligent-motors/mdrive-plus-products/>

THE XBPM PROJECT AT MAX IV FRONTENDS, OVERVIEW AND FIRST RESULTS

A. Bartalesi[†], MAX IV Laboratory, Lund, Sweden

Abstract

All the frontends installed on the 3GeV storage ring at MAX IV are equipped with two X-Ray Beam Position Monitors. Having recently finished the installation of the acquisition system, it was possible to record and analyse data. This presentation describes the setup and shows the first results.

INTRODUCTION

Since the writing of the technical specifications for the MAX IV frontends [1], it was foreseen to include X-ray Beam Position Monitors in the design. Being the first real diagnostic tool for the photon beam, and being upstream of all the beamline optics, these devices are capable to decouple beam instabilities and fluctuations originated in the storage ring from the ones originated the beamlines. This makes them an important device when trying to pinpoint the source of a specific disturb. Additionally, they can be used to cross check the readouts of the ring BPMs, and possibly be included in closed loop orbit correction as feedback. Finally, being sensitive to energy and flux, and being the closest diagnostic tool to the synchrotron sources, they are interesting as a verification of the insertion device output.

WORKING PRINCIPLE

The XBPM working principle is based on the photoelectric effect: the emission of electrons from a material when light shine on it. Each XBPM is equipped with 4 tungsten blade that are placed in the outer region of the white beam, usually spaced in a way to have symmetries along X and Y in the beam cross section, as shown in Figure 1.

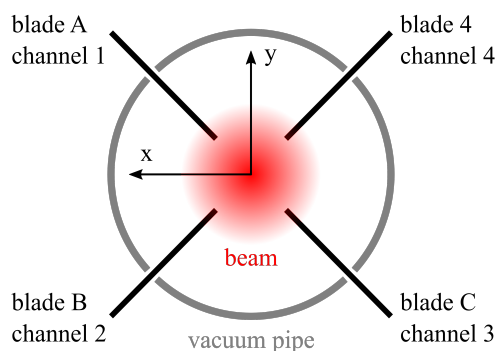


Figure 1: XBPM schematics.

These blades are then electrically connected to an elec-

trometer, so that when photons hit the blades and electrons are emitted, the electric current flowing out of the blades can be precisely measured. Knowing the photon cross-section of interaction of Tungsten, the energy and flux of the white beam and all the involved geometries, it is possible to calculate the theoretical current flowing out of each blade. But most importantly, if the symmetry is not broken anywhere else, imbalances between different blade currents are a direct sign of a difference between positions of white beam center and XBPM center.

This particular characteristic of being sensitive to *relative* signal differences makes these devices quite robust against other sources of error or uncertainties. For this reason, the XBPM are mounted on top of movable stages, and can be moved until the imbalances between different blade signals are zeroed. This placement is then fixed and maintained for long periods, so that short and long term beam movements can be both quantified.

Finally, there is one important complication: since the blades are usually close to each other, the electrons emitted from one blade can end up in another blade, and therefore alter the measurement. This is usually referred to as cross talk, but this issue can be avoided completely by applying a negative bias voltage to the blade themselves. The resulting electric field will then prevent emitted electrons from ending up in neighbouring blades, and each blade will show a reading that is closed to the theoretical one. Some XBPM designs take one step further in this direction and include an additional positive electrode in proximity of the blades, that distorts the electric field even more favourably.

Electric Measurement

The addition of a negative high voltage bias makes electric measurements slightly more complicated. Considering that we are interested in having really high accuracy, since we are interested in a differential measurement between similar blades, and also considering the small absolute value of the currents involved, it is important that all the current produced at a blade is transported to a high accuracy electrometer. The presence of the high voltage bias, however, can lead to very small, but problematic current leakages through the cable insulation. To avoid this problem, triaxial cables are adopted: they consist in a core at the bias voltage carrying the current from blade to electrometer, a first coaxial "shielding" named guard, that carries no signal but is elevated to bias voltage, and a third, proper shielding connected to ground. In this way, having the voltage difference between signal and guard equal to zero, we can guarantee no current leakages through the cable insulation. There will be leakages from guard to shield, but that has no effect on the measurement.

[†] antonio.bartalesi@maxiv.lu.se

THE ELECTROMETER

To measure the current of each blade, we adopted the high voltage EM# electrometer, fruit of a collaboration between ALBA synchrotron and MAX IV [2]. This device is fully capable of the resolution necessary for the XBPM electric measurements, it has four channel and the possibility to add a bias voltage, and finally, its acquisition frequency can go as high as 3.2 kHz. These units come with an ethernet connection and host a webserver with basic functionalities that help make the setup and first measurements extremely quick. A picture of the device is shown in Fig. 2, while Fig. 3 shows the web interface, with the four channel readings in different colors.



Figure 2: the EM# electrometer.

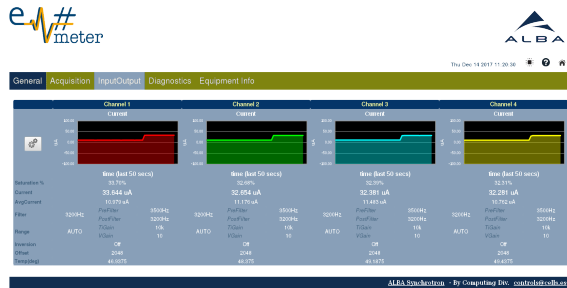


Figure 3: EM# electrometer web interface.

DATA HANDLING

The XBPMs acquisition can output the current reading of each blade with a rate of up to 3.2kHz. But more interesting than the raw data, are four derived quantities: X position, Y position, Q factor, and the sum S . Naming A , B , C , D the current readouts of the respective blades according to Fig. 1; these quantities are defined as follows:

$$S = A + B + C + D$$

$$X = \frac{A + B - C - D}{S}$$

$$Y = \frac{A - B - C + D}{S}$$

$$Q = \frac{A - B + C - D}{S}$$

The quantities X and Y represents movement of the electric signals center, Q is an indication of either a physical tilt, dipole light presence or other asymmetries, and S is mostly related to flux, and therefore stored current and insertion device gap. Two calibration coefficients K_x , K_y are then required to convert X and Y into physical displacements in μm .

Archiving Strategy

The four values X , Y , Q and S are the ones to be stored, and in particular we are planning to use the newly coming MAX IV FA archive, based on the Diamond light source FA archive [3]; to store a rolling buffer of approximately two weeks of high frequency data.

A slower, periodical beam position archiving will take the data from the fast archive, apply the calibration coefficient, and store the beam position permanently.

Finally, at regular intervals, a Fast Fourier Transformation will generate a snapshot of the beam position in the frequency domain, and these snapshots will also be stored permanently.

This will allow us to have, at the same time, extremely detailed data to investigate exceptional events, and also long term storage to observe slow phenomena, all without consuming unreasonable amounts of storage space.

THE MAX IV SETUP

As mentioned above, we will have two XBPMs per frontend on all the 3GeV ring beamlines. Having currently eight frontends installed, we are operating sixteen EM# electrometers. Due to the use of short triaxial cables, we installed the electrometers in the storage ring tunnel, with a 50 mm thick lead shielding. At the present time, we received all electrometers and all cables, we installed some of them with a temporary set up, and we have plans to finish the permanent installation during the forthcoming MAX IV summer shutdown 2018.

RESULTS

We currently have most of the XBPM functionalities on three beamlines: NanoMAX, BioMAX and HIPPIE. The control group installed the first tango devices for the electrometers in BioMAX and we were able to perform XBPM scans in this beamline: the motors controlling the X , Y stages of the XBPMs are moved, and the four signals are recorded together with the axis position. The very first plot obtained with this technique on BioMAX beamline, XBPM 01, is shown in Figure 4.

This scan allowed us to extract the calibration coefficients K_x and K_y , which for these devices are in the order of 1mm for K_x and 0.5 mm for K_y (ring current 200 mA, insertion device gap 5mm). This first difference tell us that the device is about twice as sensitive in the X direction with respect to Y , and this can be traced back to the white beam cross section.

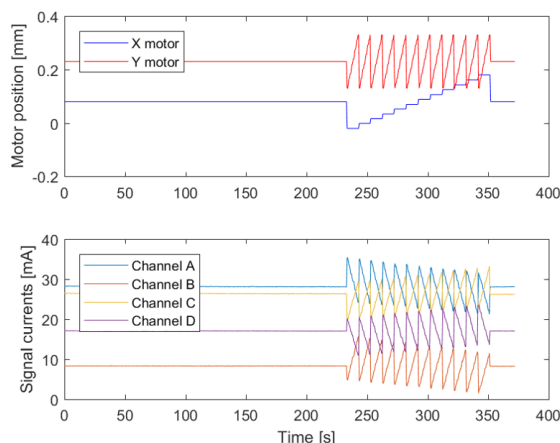


Figure 4: First scan of XBPM 01 at BioMAX.

These coefficients can then be used to plot maps of the XBPM estimated X and Y beam center with respect to real movement of the device itself.

These plots, represented in Figs. 5 and 6, show that the X and Y sensitivity of the device are fairly decoupled, while it is possible that the device itself is mounted with a very small angular error.

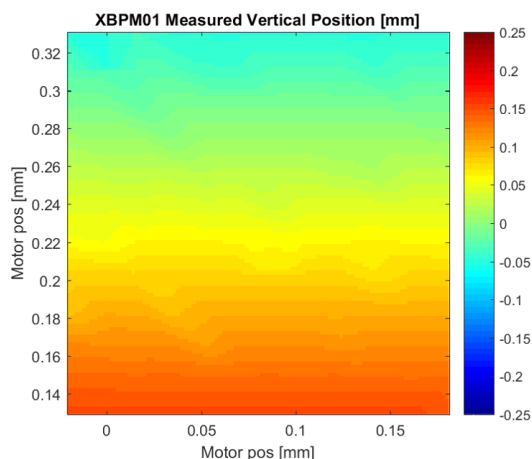


Figure 5: X readout of the calibrated XBPM 1.

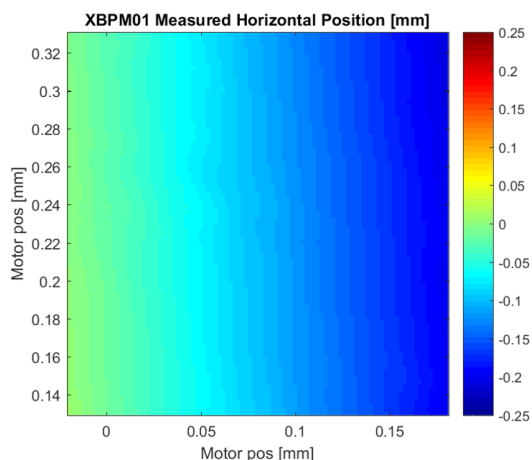


Figure 6: Y readout of the calibrated XBPM 1.

CONCLUSIONS

The XBPM project at MAX IV is starting to deliver results, as an important diagnostic tool that is showing new, unprecedented information about the 3 GeV storage ring, its alignment, its stability and its insertion devices. With the final installation planned to happen in summer 2018, we are now looking forward for a fully functioning set of XBPMs in late 2018 operations.

ACKNOWLEDGEMENTS

A great number of people have been involved in the XBPM project at MAX IV. Most notably, Dr. Krempaski Juraj from PSI, who is in charge of these devices at the SLS and has a deep knowledge of all the aspects of the design, operation and maintenance of XBPMs. Chris Bloomer from Diamond light source was also very generous in sharing his vast expertise on these, and other kinds of XBPMs. And Dr. Michael Böge from PSI contributed with his expertise on feedback system, having implemented the XBPM in the SLS slow orbit feedback himself. Precious help, interest and assistance also came from the beamline staff at MAX IV, the machine and operators group, and of course the controls and software groups both at MAX IV and ALBA. Without all these contributions, this project could never have been successful.

REFERENCES

- [1] S. Forcat, "MAX IV Front ends call for tender – Appendix B: Front end Functional Description", unpublished.
- [2] J. Avila-Abellan *et al.*, "Em# electrometer comes to light", in *Proc. ICALEPCS'17*, Barcelona, Spain, 2017, doi:10.18429/JACoW-ICALEPCS2017-TUAPL04
- [3] M. G. Abbott, G. Rehm, and I. S. Uzun, "A new fast data logger and viewer at diamond: the FA archiver", in *Proc. ICALEPCS'11*, Grenoble, France, 2011, pp. 1244, paper THCHMUST03.

FAST X-RAY BEAM INTENSITY STABILIZATION FOR ABSORPTION SPECTROSCOPY AND SPECTROMICROSCOPIC IMAGING

M. Birri[†], V. A. Samson, D. F. Sanchez, B. Meyer, D. Grolimund[‡]
 Paul Scherrer Institut, 5232 Villigen PSI, Switzerland
 M. Willmann, DECTRIS Ltd, Baden, Switzerland

Abstract

We have designed and implemented a hardware component called “Wedges” with a closed-loop feedback system to achieve a constant incident X-ray flux I_0 at the sample during spectroscopic measurement at the microXAS undulator beamline at the Swiss Light Source. Compared to existing approaches, the new system has several advantages, in particular when used in combination with mini-gap, in-vacuum insertion devices or microfocusing optics. The attenuation strength required to maintain constant I_0 flux can be adjusted in a fast, steady manner by simple linear translations of two wedge-shaped attenuators.

INTRODUCTION

The characteristics of synchrotron sources and beam-line optics commonly result in systematic and random variations of the delivered photon flux. In X-ray absorption based measurements, for example, monochromator glitches [1] or the energy dependent gap size of small gap in-vacuum undulators [2] are intrinsic sources for changes in the I_0 flux. The measured signal intensity, I , has to be normalized by taking the ratio with I_0 to compensate for such variations in I_0 . However, especially in the case of non-linear responses between the I_0 and I detectors, such normalization can introduce artifacts or signal distortions. Many types of x-ray experiments would benefit from a constant I_0 flux over the entire experimental parameter space.

Monochromator Stabilization (MOSTAB) is the current solution for most synchrotron beamlines with double crystal monochromators (DCM) to have a constant I_0 from the monochromator output [3, 4]. The MOSTAB approach is acting on the relative alignment of the two monochromator crystals (‘dynamic detuning’) in order to stabilize beam intensity (or to maintain beam position).

Obviously, any change in angular alignment of the monochromator crystals will not only result changes in the transmitted photon flux, but also induce deviations in the beam trajectory and photon energy distribution.

BEAMLINE LAYOUT

The beamline layout and relevant components are shown in Figure 1. A minigap in-vacuum undulator (U19) serves as radiation source providing high brightness X-rays in the energy range from 4 to 23 keV. The photon flux delivered at 12 keV is $> 10^{12}$ photons/sec, while the optical scheme employed used ensure an energy resolution of $\Delta E/E < 10^{-4}$. The optical layout of the beamline is composed of several pairs of slits, a bendable toroidal, horizontally deflecting mirror and a DC monochromator (Figure 1). The toroidal mirror unit serves three main purposes: (i) to collimate the beam in the vertical dimension, (ii) to allow for dynamic demagnification in horizontal dimension, and to act as a low-pass filter with an energy cut-off of ~ 23 keV given by the Rh coating. The horizontal focusing corresponds to the first part of a two-step focusing strategy that offers two main advantages: a secondary source with flexible size adjustment by precision slits (the capability of dynamical focusing and the possibility of optimizing the overall acceptance of the subsequent microfocusing optical system. The fixed-exit double-crystal monochromator is equipped with three different pairs of crystals: Si(111), Si(311) for higher energy resolution and Ge(111) for higher flux throughput. The first crystal is for energy selection while the fixed-exit is controlled by a piezo device acting the second crystal.

In the experimental hutch, the micro-probe set-up is installed on a stable optical table. Achromatic focusing in the entire energy range of 4-23 keV is done with an elliptical shape mirror pair in the Kirkpatrick-Baez (KB) geometry (or KB mirrors) producing a beam of about 1.0

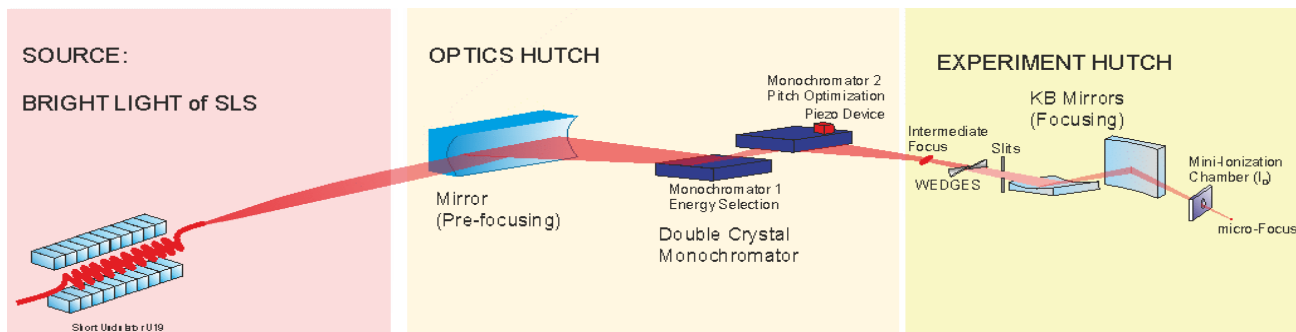


Figure 1: MicroXAS Beamline Layout.

[†] mario.birri@psi.ch

[‡] daniel.grolimund@psi.ch

(H) x 1.0 (V) μm^2 spot size on the sample (monochromatic beam). The wedges are housed inside a vacuum box with the multi-layer mirrors of the beamline (used for pump-probe experiments) and positioned about 2.5 meters away from the KB mirror box. Scattering from the wedges are limited by slits in front of the KB mirror box. Incident X-ray flux of the microfocus beam from the KB box is counted by a mini-ionization chamber (S-2274B with $5 \times 10 \text{ mm}^2$ opening produced by OHYO KOKEN KOGYO Co., Ltd) before the beam hits the sample. Different detectors are present for fluorescence, diffraction and transmission measurements.

WEDGE DYNAMIC ATTENATORS – SYSTEM DESCRIPTION

Concept

Two wedge-shaped absorbers produce a spatially uniform attenuation preserving the beam shape without changing the beam trajectory. The attenuation length can be modified by changing the relative overlap of the two wedges (transversal alignment of the wedges with respect to the beam direction) as shown in Figure 2. The wedges are mounted on linear positioners. The direction of motion and the velocity of the wedge actuators are simply linked to the deviation from the I_0 set point by an ultrafast closed-loop algorithm.

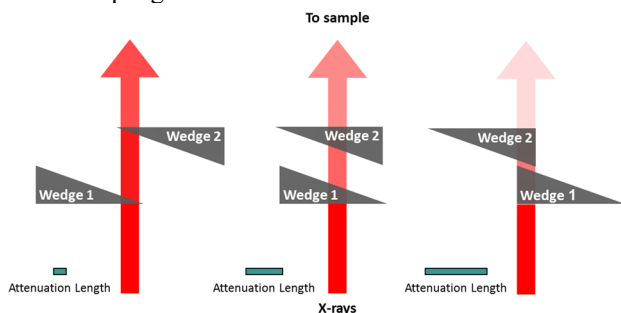


Figure 2: Attenuation length at different wedge positions.

Mechanical Part

The two wedges were made from boron carbide (B_4C) ceramic with 4mm thickness (purchased from Goodfellow). Due to the hardness of the B_4C material, it had to be diamond-grinded into the wedge shape (Stecher Ceramics GmbH).

The motion system is mainly a combination of a powerful in-vacuum linear ironless motor from Aerotech (constant force of 18.3 N) and a compact linear rail from Schneeberger AG. On the surface of the rail an optical 100 μm pitch linear scale is engraved. The rail is equipped with low vibration carriages including a sin-cos encoder reading head. These components are mounted on an aluminium support (Figure 3).

Feedback Loop

Incident X-ray flux is counted by the mini-ionization chamber before the sample position. A FEMTO© current amplifier converts the current from the ion chamber into a

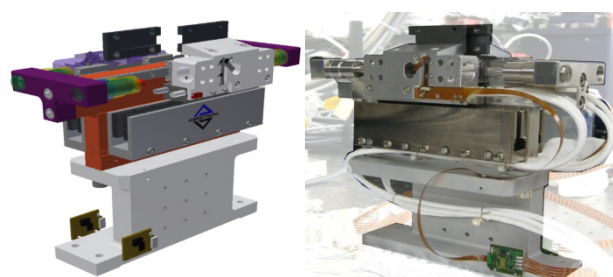


Figure 3: Design and photo of the system.

voltage between 0 to 10 VDC. The feedback loop basically takes this voltage signal “current value” coming from the amplifier (I_0). The “set value” is produced by an analog output of the control system. With the “current value” and “set value” the Aerotech controller calculates an ultrafast hardware based position profiling and generates the modulated current for the motor. This ultrafast closed loop implementation is called “autofocus” and corresponds to a standard implementation of this controller.

DYNAMICS AND PERFORMANCE

The moving mass of the axis is around 50 g. With a continuous force of 18.3 N it is theoretical possible (in open loop) to accelerate the wedge up to 366 m/s^2 . With a travel range of 50 mm a max speed of $\sim 4.2 \text{ m/s}$ is feasible for a full range step within a time of 20 ms. The response time of the system was tested using the output of the I_0 chamber as the current value and the value of the analog output from control system as the set value at $\sim 7.2 \text{ keV}$. By changing the set point it is possible to measure the response behaviour of the current value and the whole closed loop system. The data are acquired directly on the Aerotech Controller with a sample rate of 2 kHz which gives a time resolution of 0.5 ms. Figure 4 shows the step response time of a 20% drop. It shows that the current value reaches an error bandwidth of $\pm 1\%$ of the set point within $\sim 40 \text{ ms}$ (Figure 4) and for a drop of 80% $\sim 60 \text{ ms}$ (Figure 5).

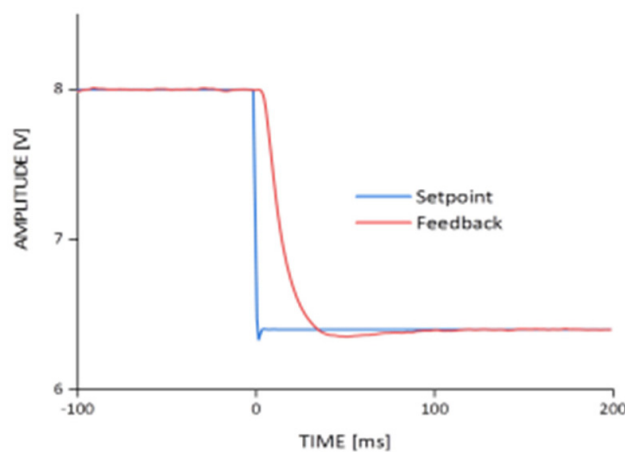


Figure 4: Step Response Time of a 20 % drop.

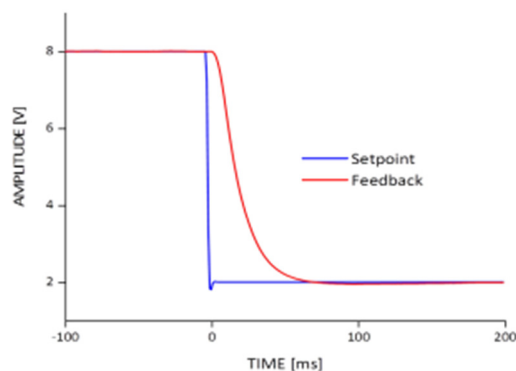


Figure 5: Step Response Time of a 80% drop.

IO MEASUREMENT AT DIFFERENT SETPOINTS

During an energy scan the wedge can remove different artifact like glitches and non-linearities. Figure 6 shows the I_0 measurement without and with the wedge operated at different set point voltages. Energy range was at ~ 17.33 keV with a prominent glitch.

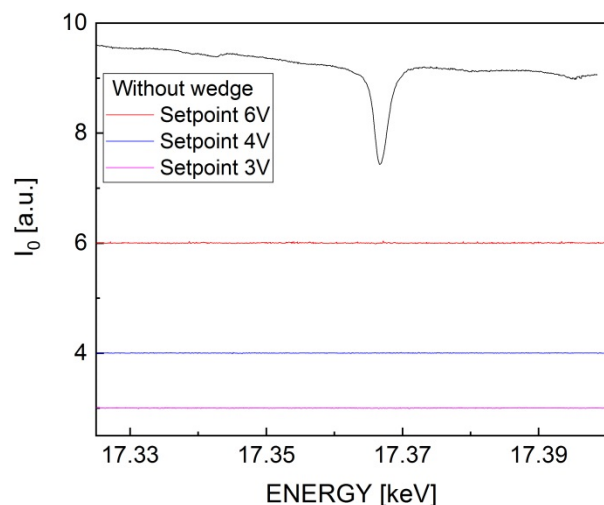


Figure 6: I_0 during Energy @ different set points.

BEAM POSITION & SIZE

By using this system it is important to realize that the beam size and position is not changed by the wedge. Based on knife-edge scans with a nano test pattern the position deviation at different attenuation factors turns out to be < 40 nm from the average beam center position. The beam size during the scans is changing by < 100 nm. Both numbers are within the typical measured errors. In contrast to the MOSTAB system, we can conclude that the wedge system does not affect beam size nor beam position.

CONCLUSION

We have designed and implemented a hardware component called “WEDGE” with a closed-loop feedback system to achieve a constant incident X-ray flux I_0 at the sample during spectroscopic measurement at the microXAS undulator beamline at the Swiss Light Source. Compared to existing approaches, the new system has several advantages, most pronounced when used in combination with mini-gap, in-vacuum insertion devices or microfocusing optics. The attenuation strength required to maintain constant I_0 flux can be adjusted in a fast, steady manner by simple linear translations of two wedge-shaped attenuators.

REFERENCES

- [1] F. Bridges, “A simple feedback system to keep the flux from an X-ray double monochromator constant”, *Nucl. Instr. and Meth. in Physics Research A*, vol. 257, 1987, pp. 447-450. doi:10.1016/0168-9002(87)90772-8
- [2] H. Kitamura, “Recent trends of insertion-device technology for X-ray sources”, *J. Synchrotron Rad.*, vol.7, 2000, part 3, pp. 121-130. doi:10.1107/S0909049500002983
- [3] A. Krolzig, G. Materlik, M. Swars, and J. Zegenhagen, “A feedback control system for synchrotron radiation double crystal instruments”, *Nucl. Instr. and Meth.*, vol. 219, issue 2, 1984, p.430-434. doi:10.1016/0167-5087(84)90355-7
- [4] https://bib-pubdb1.desy.de/record/94619/files/mostab_usermeeting2012.pdf

AN IMPROVED POLARISATION ANALYSER FOR THE I16 BEAMLINE AT DIAMOND

M. Burt, S. P. Collins, S. Green, I. Horswell, J. Li, G. Nisbet, R. Pocock, J. Spiers, K. Wilkinson
 Diamond Light Source Ltd., Harwell Science and Innovation Campus, OX11 0DE, UK

Abstract

The project to upgrade the I16 polarisation analyser was necessary to increase its functionality and to introduce a more robust and reliable construction. The requirement that the device was to be mounted on the arm of a diffractometer meant the construction needed to be as lightweight and as compact as possible. This provided opportunities to explore new collaborative ways of working with both in-house and external suppliers.

The paper describes the approach taken to develop lightweight aluminium vacuum chambers using a company specialising in additive layer manufacturing techniques. In addition, the design of lightweight and compact slit assemblies are detailed; these were developed in collaboration with a supplier of driven linear stages.

The paper also describes the process of using additive layer manufacturing to model prototypes to optimise the design of cable management systems where previously basing the design on 3d CAD models had proved unsatisfactory.

Another novel requirement for this device is having an x-ray detector mounted on a rotation axis in vacuum. The results of working with the in-house detector group to develop a design to allow this to be realised with all the necessary thermal and electrical connections, are outlined.

POLARIZATION ANALYSER

Overview

The I16 beamline at Diamond is dedicated to the study of advanced materials using X-ray diffraction; part of this process is to use a device that can analyse magnetic scattering from samples. Magnetic scattering is different to, and weaker than, normal scattering and analysis of the polarisation of this scattering can be used to gain insights into the magnetic properties of materials. This information allows details of the three-dimensional magnetic structure of the sample material to be determined.

The device in question, known as a polarisation analyser (PA), allows a crystal/detector assembly to be rotated about the axis of the x-ray beam direction in a similar way to a polaroid polarizer being rotated in visible light. In addition, utilizing a high quality crystal with the analyser can give higher resolution diffraction that allows structures to be studied on length scales that range from the atomic to 10^{-3} m.

The design of the PA essentially comprises an assembly of vacuum chambers, sets of slits to remove unwanted scattering, and various detectors which are arranged to rotate about different axes. Data collected from the detec-

tors as they are moved and rotated allow information on the polarisation of the scattering to be built up.

The project to upgrade the design of the existing polarisation analyser was an opportunity to increase its functionality and to introduce a more robust construction.

The analyser itself is mounted on the arm of a diffractometer so it was important that the construction was made to be lightweight (see Fig. 1). A lightweight construction would avoid the need for additional counterweights on the diffractometer which would reduce its performance.

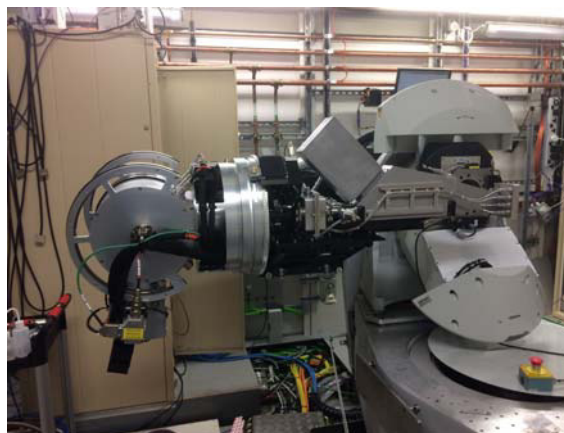


Figure 1: View of polarisation analyser mounted on diffractometer arm.

Lightweight Vacuum Vessels

A significant proportion of the structure of the PA comprises vacuum chambers. Conventionally these vessels had been constructed as two separate parts, a vessel body with a lid. In order to make an effective seal both parts have to be thick enough to accommodate an O-ring seal and also to be stiff enough to compress the seal. In addition, to compress the seal a large number of nuts and bolts are required, all of which add weight.

It was decided that by using additive layer manufacturing these vessels could be made as one piece. This would remove the need for flanges and the nuts and bolts; also the wall thickness of the vessels could be reduced to the minimum required to provide an air-tight and rigid shell.

Working in collaboration with a specialist additive layer manufacturing company: 3d-Alchemy [1], who advised on materials and minimum thicknesses to prevent porosity, the chambers were manufactured and the relevant sealing surfaces were machined to complete the finished chambers (see Fig. 2).

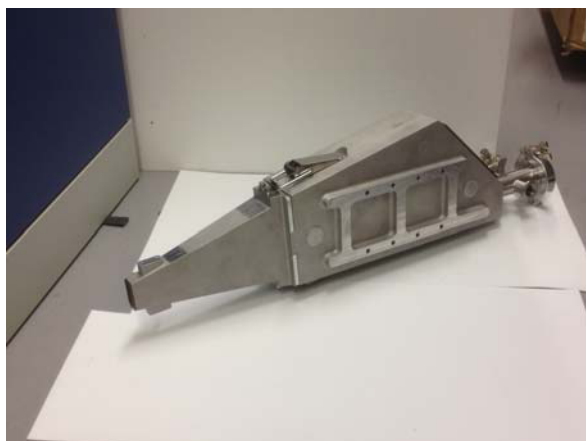


Figure 2: Two of the vacuum chambers produced by additive layer manufacture of aluminium alloy. Chambers shown are approximately 600mm long by 200mm high.

Slit Assemblies

The requirement for weight reduction extended to the slit assemblies of which there are two sets: one in air and one in vacuum. In order to keep the assemblies simple and lightweight and to minimise the complexity of installation and commissioning, a collaboration was entered into with the supplier of suitable piezo-actuated linear stages: SmarAct GmbH [2].

DLS established the design of the assemblies and free issued the main components to SmarAct who assembled the linear stages to the bases and then were able to supply the slits sub-assemblies completely wired and tested. The only additional task was to add the tungsten blades.

The in-vacuum slits are in the form of two sub-assemblies each comprising a pair of slits mounted in a casing wired to connectors. The casings are then bolted together with one orientated at 90 degrees relative to the other to form horizontal and vertical slits.

The in-air slits comprised an assembly where all four actuators with their respective blades are mounted on a single plate and wired to their respective electrical connectors, which are also contained on the same sub-assembly.

In this way for both slits assemblies, a compact and lightweight design could be realised, which could be easily incorporated into the bigger assembly (see Fig. 3).



Figure 3: An example of a compact in-air slits assembly designed in collaboration with SmarAct GmbH. Stages shown have ranges of 12mm and 20mm with sub-micron resolution.

Cable Management

The mechanism of cable management was an important consideration in the design of the analyser because the detectors are rotated about an axis that is itself mounted on a second rotary axis arranged perpendicular to the first. The wiring and detector cooling lines have to accommodate the rotations in order that they can operate over the lifetime of the analyser without the cables or hoses being subject to excessive strain or abrasion that could result in damage.

Formerly, cable management has been treated as a secondary element in the design of systems however, because of the complex combination of motions on the analyser, a different approach was needed. Previously cable management mechanisms had been designed by looking at the three-dimensional model and predicting the behaviour of cables as the various axes are operated. This has proved to be unsatisfactory in the past as making predictions about the behaviour of cables of different stiffnesses in different orientations has proved very difficult.

Access to in-house additive layer manufacturing technology means that proposed designs could be produced quickly in plastic material. The design could then be assessed using suitable lengths of the actual cables that would be used on the final design. Once a design had proved to perform satisfactorily in a full-scale prototype version then this design was carried forward to be incorporated in the final design (see Fig. 4).



Figure 4: Image showing a prototype of the cable management mechanism produced to evaluate its effectiveness.

In-vacuum Detector

An important feature of the upgraded analyser was the facility of having an in-vacuum detector, which could also be rotated about an axis within the main vacuum chamber. The detector was adapted from a Medipix [3] Merlin detector. The Medipix detectors are produced by an international consortium of which Diamond is a member.

The requirement of putting the detector into vacuum meant all the necessary wiring to the detector had to pass through the vacuum boundary and also the detector had to be thermally managed which necessitated a thermal connection passing through the vacuum boundary. The thermal connections were designed to remove a heat load of approximately 5W and limit the temperature of the detector to below 40°C. Both the electrical and thermal connections had to accommodate the rotary motion that was required of the detector.

The electrical connections were produced in collaboration with the detector group and consisted of two custom-made ribbon connectors made of DuPont AP8535R, a polyimide material. The ribbon connectors each needed to carry 78 tracks, be flexible enough to accommodate the rotational motion of the detector and be suitable to operate in a vacuum environment. One end of each connector attached to the detector and the other was potted into the feedthrough that made a vacuum tight seal with the main vacuum chamber.

The thermal management was necessary as in operation the detector generates heat which in a vacuum environment has to be removed by conduction. The method of conduction needs to accommodate the rotary motion of the detector. To achieve this the detector board with its heatsink is mounted on a copper bracket which is attached by flexible copper braids to a pillar that is situated at the centre of rotation.

The central pillar was also produced using additive layer manufacturing as it could then be manufactured as one piece incorporating the cooling channels without the need for forming joints suitable for vacuum. Again working in collaboration with 3d-Alchemy a suitable material was

chosen, this was a copper alloy which had the necessary thermal properties and, with a minimal thickness, was free from porosity.

The rotary motion of the detector is achieved by a worm and wheel mechanism, which with preloading will minimise backlash (see Fig. 5).

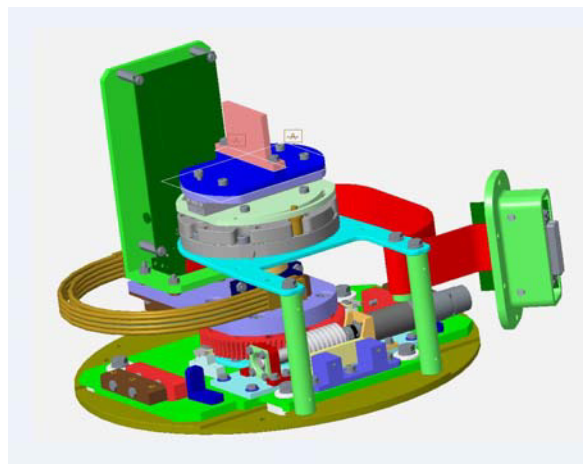


Figure 5: CAD model of the mechanism located inside the main vacuum chamber showing the detector mounted on its rotary stage with thermal and electrical connections. The face of the detector is approximately at a 100mm radius from its axis of rotation.

CONCLUSION

It is necessary to continually upgrade beamline facilities to keep them at the forefront of scientific research. In the case of the I16 beamline at Diamond, there was the requirement to improve the polarisation analyser. This provided an opportunity to work collaboratively with suppliers in ways to effectively use more advanced techniques to achieve lightweight and compact sub-assemblies.

Currently, the upgraded analyser has been installed, commissioned and is operational on the beamline. Further upgrades are planned to be carried out to improve its performance.

REFERENCES

- [1] 3d-Alchemy, <https://www.3d-alchemy.co.uk>
- [2] SmarAct GmbH, <http://www.smaract.com>
- [3] Medipix, <https://medipix.web.cern.ch>

TMO - A NEW SOFT X-RAY BEAMLINE AT LCLS II*

J.C. Castagna[†], M. Holmes, J. James, P. Walter, T. Osipov, L Amores

LCLS, SLAC National Accelerator Laboratory, Menlo Park, CA, United States

Abstract

LCLS is building 4 new soft X-ray beamlines with the LCLS-II upgrade. The TMO (Time resolved Molecular Optical science) beamline aka NEH 1.1 will support many experimental techniques not currently available at LCLS. The beamline hinges around 2 main end stations, LAMP a multi configurable end station and DREAM, dedicated to COLTRIM type of experimentation. Both the existing LAMP as well as the newly built DREAM end-station will be configured to take full advantage of both the high per pulse energy from the copper accelerator (120 Hz) as well as high average intensity and high repetition rate (up to 100 kHz) from the superconducting accelerator. Each end station will have its own focusing optic systems (KB Mirrors) which can focus the beam down to 300 nm, and have laser pump probe experiments capability. Very demanding requirements for IR and X-ray overlap as well as beam stability, make the TMO beamline a major engineering challenge. The main components of the beamline (KB optics, DREAM end stations and diagnostics components) are built on granite stands. The building structure is being reviewed for thermal stability. First light on TMO is expected in February 2020.

SCIENCE DRIVERS

TMO stands for Time resolved Molecular Optical science instrument

LCLS-II will be a transformative tool for energy science, qualitatively changing the way that X-ray imaging, scattering and spectroscopy can be used to study how natural and artificial systems function. It will enable new ways to capture rare chemical events, characterize fluctuating heterogeneous complexes, and reveal quantum phenomena in matter, using nonlinear, multidimensional and coherent X-ray techniques that are possible only with X-ray lasers. This facility will operate in a soft X-ray range (250 eV to 1.5 keV), and will use seeding technologies to provide fully coherent X-rays in a uniformly spaced series of pulses with programmable repetition rate and rapidly tuneable photon energies.

NEH beamline 1.1 aka TMO will support many experimental techniques not currently available at LCLS. High operational efficiency will be achieved through utilization of 2 fixed endstations. Stable beam trajectories will be provided through streamlined X-ray alignment to the fixed interaction points. Delivering the beam to only a few fixed locations will optimize optical laser experiments and setups.

END STATIONS

The beamline hinges around 2 main end stations; LAMP a multi configurable end station and DREAM, dedicated to COLTRIM type experimentation.

Both the existing LAMP as well as the newly built DREAM end-station will be configured to take full advantage of both the high per pulse energy from the copper accelerator (120 Hz) as well as high average intensity and high repetition rate (up to 100 kHz) from the superconducting accelerator.

The new DREAM endstation will house a well-defined geometry and COLTRIMS type spectrometer as a standard configuration to accommodate extreme vacuum, sub-micron focus spot size, and target purity requirements dictated by the pump-probe class of coincidence experiments, while accumulating data on the event-by-event basis at the rep rates in excess of 100 kHz fully utilizing the LCLS-II capabilities. Photon fluency in DREAM will reach over 1021 photons/cm² with superconducting Linac X-rays, while with copper accelerator it will be over 1022 photons/cm² at 120 Hz.

The LAMP endstation will be part of the Next generation Atomic, Molecular, and Accelerator Science and Technology Experiments (NAMASTE) and it will be optimized for performing high energy, high resolution, time, but also angular-resolved photoelectron spectroscopic measurements. NAMASTE will accept highly standardized modular endstations.

Pump-probe timing resolution of X-ray with optical laser pulses goal is sub 10 fs for both end-stations. Optical laser peak field power density will be over 1015 W/cm² (of 800 nm) on target.

FOCUSING OPTICS

Each endstation will have its own focusing optic systems (KB Mirrors). The focus size in LAMP will be around 5µ and down to 300 nm in the DREAM end station. Both end station will have laser pump probe experiments capability. The KB mirrors will be used in “series”. The focal point of the first set of mirrors for the LAMP end station being used as the source point for the second set of KB mirrors for the DREAM endstation. Only the first set of KB mirrors will be bendable to adjust focus in either endstation.

* Work supported by the United States Department of Energy

[†]castagna@slac.stanford.edu

BEAMS STABILITY AND OVERLAP

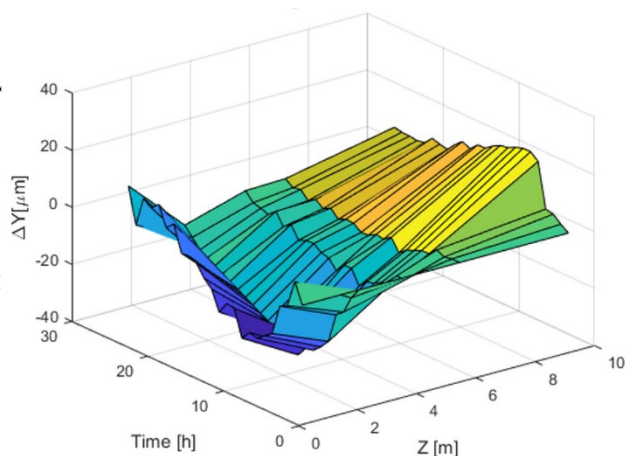


Figure 1: Floor motion measurements.

Very demanding requirements for IR laser and X-ray overlap as well as beam stability, make the TMO beamline a major engineering challenge. In the DREAM endstation we will need to overlap a 300nm X-ray focus to a 5μ IR laser focus. For this reason all the main components of the beamline (KB optics, end stations and diagnostics components) are built on common granite stands.

The thermal stability of the building itself has a direct impact on beam stability. External shifts of temperature have directly been measured as floor deviation in the sub-basement of the building where the beamline is installed. Variations of up to 30μ have been measured on the floor flatness and horizontality. In order to meet our very demanding requirements the part of the building that is directly exposed to climate and solar radiation is being thermally insulated to reduce thermal expansion of the walls.

Figure 1 shows the motion measurements of the hutch floor as a function of day time over a typical 24h period.

VACUUM REQUIREMENTS

The large range of vacuum pressure used in the 2 main end stations requires sophisticated pumping options and numerous differential pumping systems between the essential elements of the beam-line. The LAMP endstation will work at levels of up to 10⁻⁵ torr, while the DREAM endstation will continuously work in the low 10⁻¹¹ torr range as shown in Figure 2 vacuum profile.

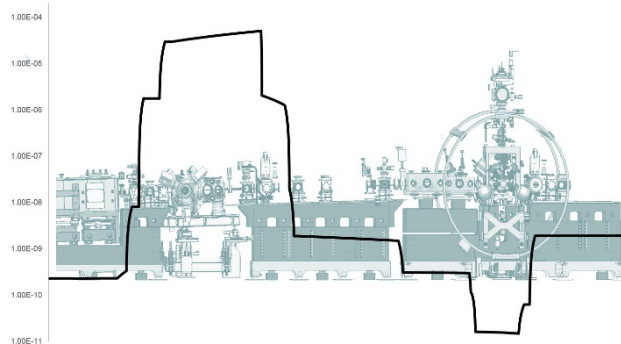


Figure 2: TMO Vacuum profile.

BEAM DIAGNOSTICS DEVICES

A whole battery of diagnostics are installed along the X-ray beam line. These include the following:

- Profile monitors to look at beam profile and position.
- Fluorescence intensity monitors. These will look at the pulse by pulse intensity of the beam by looking at the fluorescence induced by the x-ray beam on the surface of the KB mirrors.
- Wavefront sensors. Each endstation focus spot will be analysed and controlled for quality (astigmatism) and size of the focus. Focus quality and size will very much be driven by the bending and position of the optics.
- Arrival time monitors. These will monitor the synchronization of the IR pumping laser to the X-ray beam to sub 10 fs level.

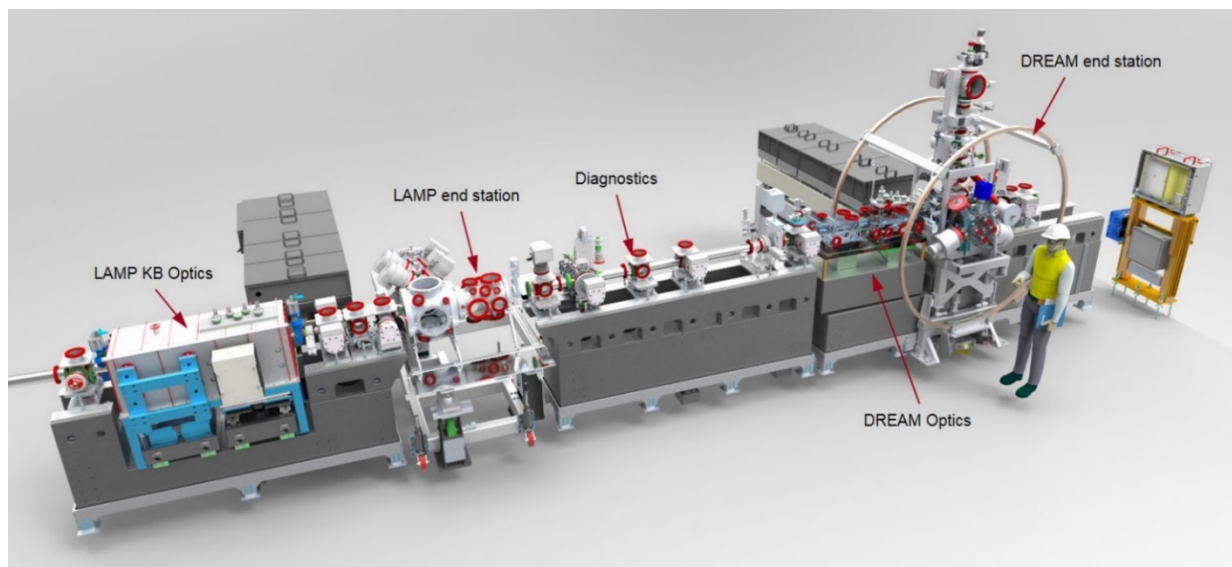


Figure 3: The TMO Beamline in its preliminary design phase.

BEAM CONTAINMENT

A number of components along the beamline provide for beam containment requirements.

These include the following:

- Solid and gas beam attenuators
- Collimators
- Slits systems
- Beam stoppers
- Safety beam dump for personnel protection

CONCLUSION

The TMO beamline is in its preliminary design phase (see Figure 3) and following a very bold schedule. The high average intensity and high repetition rate capability will open the door to new type of experiments not possible to today. It will be the first beamline of the LCLS II project to take beam. First light is expected in February 2020.

ACKNOWLEDGMENTS

Lin Zhang, Georg Gassner, Daniele Cocco, LCLS, SLAC National Accelerator Laboratory.

NANOSURVEYOR 2: A COMPACT INSTRUMENT FOR NANO-PTYCHOGRAPHY AT THE ADVANCED LIGHT SOURCE

R.S. Celestre, K.Nowrouzi ¹, H.A. Padmore, D.A. Shapiro, Advanced Light Source, Lawrence Berkeley National Laboratory, 94720, Berkeley, CA, USA
¹also at University of California, 94720,Berkeley, CA, USA

Abstract

The Advanced Light Source has developed a compact tomographic microscope based on soft x-ray ptychography for the study of meso and nanoscale materials [1,2]. The microscope utilizes the sample manipulator mechanism from a commercial TEM coupled with laser interferometric feedback for zone plate positioning and a fast frame rate charge-coupled device detector for soft x-ray diffraction measurements. The microscope has achieved scan rates of greater than 50 Hz, including motor move, data readout and x-ray exposure, with a positioning accuracy of better than 2 nm RMS and has achieved spatial resolution of better than 5 nm. The instrument enables the use of commercially available sample holders compatible with FEI transmission electron microscopes. This allows in-situ measurement of samples using both soft x-rays and electrons.

This instrument is a refinement of a currently commissioned instrument called The Nanosurveyor, which has demonstrated resolution of better than 20nm in both two and three dimensions using 750 eV x-rays. [3] The instrument has been installed on the new Coherent Scattering and Microscopy beamline at the Advanced Light Source and is in the final stages of commissioning. It will enable spectromicroscopy and tomography of materials with wavelength limited spatial resolution.

INTRODUCTION

X-ray ptychography holds the promise of overcoming the resolution, depth of field and efficiency limitations of imaging with conventional x-ray optics [1,2]. It instead relies upon phase retrieval from coherent diffraction data which can be measured to very high numerical aperture with high efficiency. The use of soft x-rays for microscopy, though limiting sample thickness to a few microns, provides very high contrast and exquisite sensitivity to electronic and magnetic states of matter. This, coupled with the high coherent flux available in the soft x-ray range at modern synchrotron sources allows for high spatial resolution with very short exposure times. The ability to image materials with near wavelength limited spatial resolution and functional systems with high time and chemical resolution has previously been demonstrated [2,3]. As x-ray source brightness increases, there is an ever increasing demand for high performance imaging systems. We present the operational instrument of an

ultra-stable, high speed scanning x-ray microscope which is fully compatible with many electron microscopy sample holders. The microscope, called Nanosurveyor 2 (Fig. 1), enables wavelength limited x-ray microscopy and facilitate correlative imaging using x-rays and electrons.

MECHANICAL AND OPTICAL DESIGN

The nanosurveyor 2 instrument is derived from the sample area hardware of an FEI CM200 series TEM. We have modified the octagon sample area hardware to create a larger vacuum chamber incorporating both upstream and downstream sections in order to house the required beam conditioning hardware and the LBNL designed fast CCD [4]. This approach was taken in order to leverage the existing design of the TEM for high stability, which also utilizes air-side motor hardware for thermal stability, and to provide for ease of measurement of samples going between EM and XRM instruments. The sample is held and positioned by a standard FEI Compustage sample manipulator that has been upgraded to higher resolution optical encoders. Most functionality present in a standard TEM installation remains in our implementation of the system. This allows users to mount samples in commercially available sample holders designed for tomography, cryo-tomography and those holders specially designed for *in-situ* experiments.

The basic configuration of the system is similar to other scanning zone plate systems in use at the ALS in that the focusing optic is mounted into a high stiffness scanning piezo flexure stage with X and Y axes (orthogonal to the x-ray beam direction) [5]. The interferometer's fiber-optics heads are mounted to the fixed assembly which supports the sample goniometer such that mechanical path lengths to the sample are minimized. These interferometer beams are returned by a polished and gold coated surface on the zone plate mounting assembly in order to track position of the zone plate in XY while scanning. A compact, three axis order sorting aperture assembly is mounted within the frame of the piezo scanner in order to facilitate tracking of the focused x-ray beam with the order sorting aperture (OSA). The OSA assembly scans with the focusing optic. This enables us to utilize the entire 100 μm range of our XY scanning system rather than being limited to a fraction of the OSA diameter (typically 50 μm).

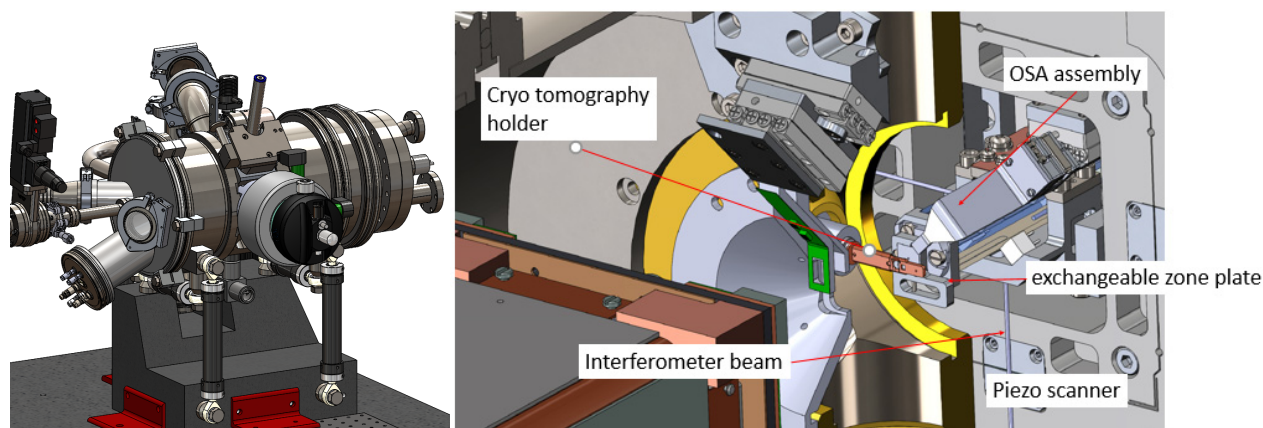


Figure 1: CAD models of the Nanosurveyor 2 instrument showing Gatan cryo tomography sample holder and internal zone plate optic scanning hardware with reference to TEM sample holder.

The focusing optic travels along the beam axis on a novel stage that integrates the motion stage with the interferometric mirror surfaces and the mounting system for the zone plate optic. This system is mounted within the open frame of the XY piezo scanner. The design of this linear travel stage is centered around an octagonal piece of sapphire that has been polished and had designated reflecting surfaces coated for use as mirrors for the interferometric tracking system. Other faces act as the bearing surfaces for stick/slip piezo actuators that provide the motive force to translate the optical elements along the beam path. This assembly is both lightweight and very stiff, leading to a high resonant frequency in the scanning system. The design specification for the system was to allow for positioning the beam on the sample at a rate matching the maximum frame rate of the fast CCD.

VIBRATION AND THERMAL STABILITY

Vibration control and stability of the entire endstation assembly is critical to reaching the ultimate planned system resolution of 1nm. To this end, the exit slit assembly is incorporated into the structure of the endstation support in order to remove effects of experimental hall floor motion. The slit assembly is installed on a cantilever section of tubular steel that is mounted to the endstation support structure (Fig. 2). Both the endstation and exit slit frames are filled with epoxy concrete (Zanite) for vibration damping and increased thermal stability. The cantilever was designed to maximize horizontal stability of the exit slits with respect to the focusing optics in the endstations. The two endstations that comprise the COSMIC Imaging station are mounted on a single 1500kg casting of Zanite. This casting is isolated from the support frame by an array of engineered viscoelastic urethane polymer isolation pads (Sorbothane) which provide passive vibration isolation. This has resulted in motion transmissibility of 19 Hz in the vertical (Y) and 5 Hz in the lateral directions (X,Z) (Fig. 3). Damping of motion is aided by the center of gravity of the experimental system being located 50 mm below the top surface of the Zanite filled steel assembly.

The endstation assembly is contained within an acoustically dampening enclosure which is thermally stabilized. The temperature of the enclosure is maintained by a recirculating, closed-loop HVAC system which has been demonstrated to maintain temperature within 0.1 degrees Centigrade over long periods of time (Fig. 4).

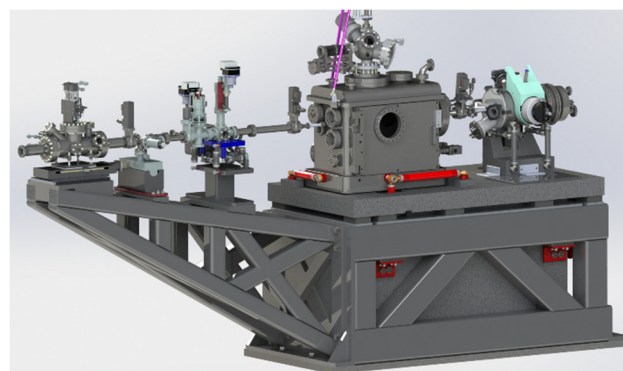


Figure 2 : COSMIC Imaging endstation with Nanosurveyor 1 and 2 instruments mounted in-line.

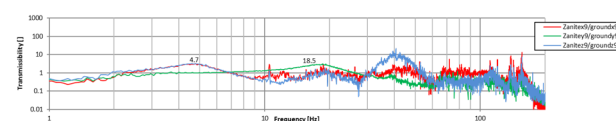


Figure 3: Vibrometer measurements showing the spectra of isolation in X,Y,Z between the experimental floor and the top of the passively isolated instrument structure.

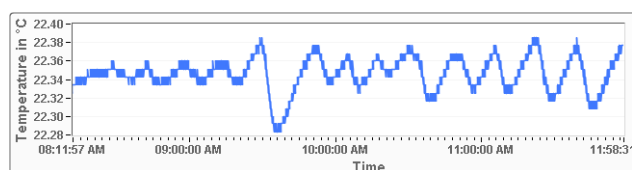


Figure 4: Plot showing typical stability of temperature in the environmental enclosure over a period of 4 hours.

COMMISSIONING RESULTS

First ptychography results from Nanosurveyor 2 at the COSMIC beamline during commissioning. The sample, provided by a Beam Technologies, is a WSi₂/Si multilayer, with fundamental linewidth of 2.8nm (all other lines are integer multiples), and thickness of 100nm. Data was collected at beam energy of 1000eV using a 45nm zone plate supplied by the Center for X-Ray Optics (CXRO).

The zone plate was scanned with a step size of 30nm and the sample was exposed for 20msec at each point. The CCD was placed further downstream than the standard operating position to increase dynamic range for commissioning, thus decreasing the Numerical Aperture and limiting the resolution to 10nm (Fig. 5).

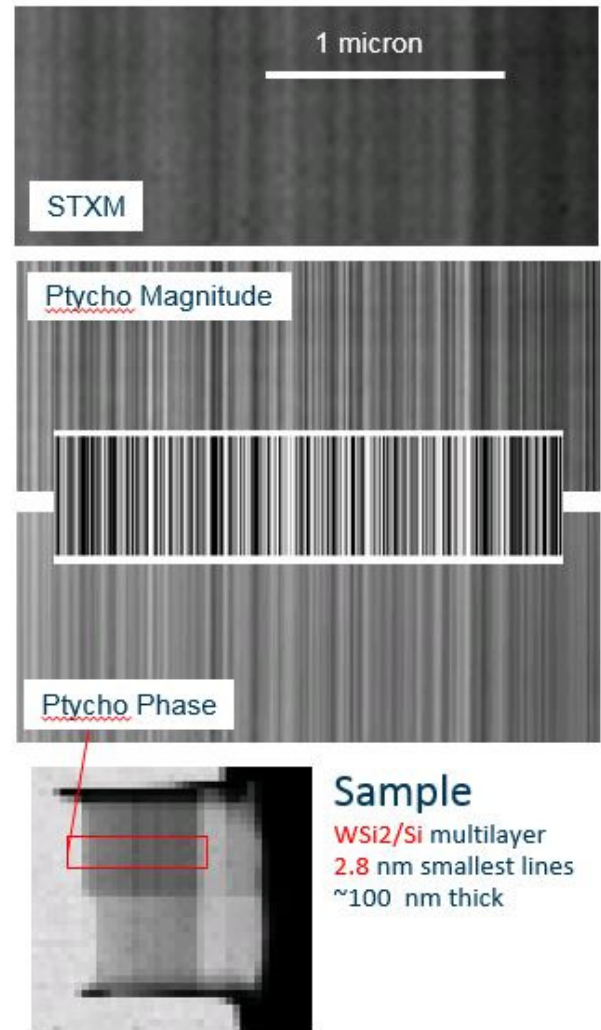


Figure 5: First ptychography results from COSMIC Imaging endstation at Advanced Light Source.

CONCLUSION

We present the design and preliminary performance results of a new compact scanning transmission x-ray microscope dedicated to ptychographic imaging at the ALS. The microscope is based upon the sample goniometer and transfer system of a commercial TEM which has been customized to also house a high performance zone plate scanning mechanism. This mechanism can perform point to point scans at well over 100 Hz which is fast enough to keep pace with the short exposure times possible at new high brightness beamlines and the short readout time of a custom fast frame rate CCD. We have also demonstrated that the stability of the instrument is suitable to reach the microscope design goal of soft x-ray wavelength limited imaging.

ACKNOWLEDGMENTS

The Advanced Light Source is supported by the Director, Office of Science, Office of Basic Energy Sciences, of the U.S. Department of Energy under Contract No. DE-AC02-05CH11231.

REFERENCES

- [1] P. Thibault, M. Dierolf, A. Menzel, O. Bunk, C. David, F. Pfeiffer, “High-Resolution Scanning X-ray Diffraction Microscopy”, in *Science*, 321, 2008, pp 379–382
- [2] D. A. Shapiro, Y. S. Yu, T. Tyliczszak, J. Cabana, R. Celestre, W. Chao, K. Kaznatcheev, A. L. D. Kilcoyne, F. Maia, S. Marchesini, Y. S. Meng, T. Warwick, L. L. Yang, H. A. Padmore, “Chemical composition mapping with nanometre resolution by soft X-ray microscopy”, in *Nature Photonics* 8, 2014, pp 765–769, ISSN 1749-4885, <http://www.nature.com/nphoton/journal/v8/n10/full/nphoton.2014.207.html>
- [3] P. Denes, D. Doering, H. A. Padmore, J. P. Walder, J. Wezeorick, “A fast, direct x-ray detection charge-coupled device”, in *Review of Scientific Instruments* 80, 083302, 2009, pp 1089-7623, ISSN 0034-6748 <http://scitation.aip.org/content/aip/journal/rsi/80/8/10.1063/1.3187222>
- [4] A. L. D. Kilcoyne, T. Tyliczszak, W. F. Steele, S. Fakra, P. Hitchcock, K. Franck, E. Anderson, B. Harteneck, E. G. Rightor, G. E. Mitchell, A. P. Hitchcock, L. Yang, T. Warwick, H. Ade, “Interferometer-controlled scanning transmission X-ray microscopes at the Advanced Light Source”, in *Journal of Synchrotron Radiation* 10, 2003, 125–136, <http://dx.doi.org/10.1107/S0909049502017739>
- [5] J. Lim, Y. Li, D. H. Alsem, H. So, S. C. Lee, P. Bai, D. A. Cogswell, X. Liu, N. Jin, Ys. Yu, N. J. Salmon, D. A. Shapiro, M. Z. Bazant, T. Tyliczszak, W. C. Chueh, “Origin and hysteresis of lithium compositional spatiodynamics within battery primary particles”, in *Science* 353, 2004, pp 566–571, <http://science.sciencemag.org/content/353/629/566>

DESIGN OF INDIRECT X-RAY DETECTORS FOR TOMOGRAPHY ON THE ANATOMIX BEAMLINE

K. Desjardins[†], M. Scheel, J.-L. Giorgetta, T. Weitkamp, C. Meneglier and A. Carcy,
 Synchrotron SOLEIL, L'Orme des Merisiers, 91192 Gif-sur-Yvette, France

Abstract

ANATOMIX is a new beamline for full-field tomography techniques at the French synchrotron SOLEIL. It will operate at photon energies from 5 to 30 keV and feature several operation modes via versatile optics configurations, including direct propagation of the polychromatic (“white”) undulator beam to the experiment position. Two different experimental methods will be used: parallel-beam X-ray shadowgraphy, for spatial resolution down to the sub-micron range, and full-field transmission X-ray microscopy down to a spatial resolution of less than 100 nm. To cover the large panel of experimental possibilities, four dedicated indirect X-ray detectors have been designed. For pixels in the sub-micron size range, a micro-tomography revolver camera for versatility, a high-efficiency camera for flux-limited experiments, and a high-resolution camera for the largest optical magnifications will be available. For experiments with a large X-ray beam and pixel sizes from several microns upward, a “large-field” camera completes the set.

INTRODUCTION

Indirect X-ray image detection is the standard concept used today for full-field tomography techniques on hard X-ray synchrotron beamlines. Detectors based on this principle have been commonly used for 20 years [1,2]; they can be in-house developments [3-4] or commercially supplied (for example from Optique Perter, Lentilly, France or Hamamatsu Photonics, Hamamatsu, Japan). They convert the X-ray image to visible light with a scintillator screen and project the visible-light image on the sensor of a digital camera using visible-light lenses.

To match the large variety of needs of the new tomography beamline ANATOMIX [5] at the French synchrotron SOLEIL, the Detector Group, the Mechanical Engineering Group and beamline team have designed four models of indirect detectors. The “Revolver X-Ray Camera”, a versatile assembly composed of a revolving cylinder with four microscope objectives, the “High-Resolution X-ray Camera” equipped with a very high resolution microscope objective, the “High-Efficiency X-ray Camera” for applications limited by X-ray flux and the “Large-Field X-Ray Camera” for fields of view of several centimeters width. Each of these models accepts different digital cameras and, with the exception of the “high-resolution” model, all are compatible with the intense white X-ray beam. In this article, we report on the different designs with the detailed components and expected performance of each solution.

[†] kewin.desjar@synchrotron-soleil.fr

INDIRECT X-RAY CAMERAS

Common Specifications

All X-ray detectors have been made to be easily customizable. The camera, objective, scintillator or mirror can be simply disassembled and changed.

The four X-ray detectors can accept different models of commercially-available digital cameras which can be plugged through a standard support (Fig. 1). Three different camera models are currently used at the beamline to cover the range of parameter space required by the user community.

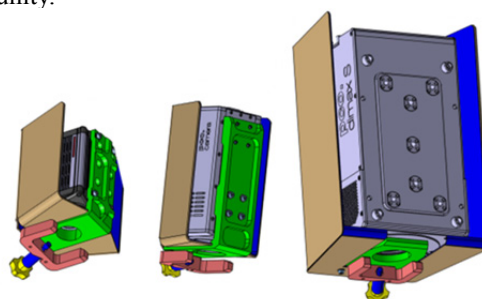


Figure 1: Standard camera support for ANATOMIX X-ray detectors. Left to the right: ORCA Flash4, PCO4000 and DIMAX HS4.

Firstly, the ORCA Flash 4 (Hamamatsu Photonics, Hamamatsu, Japan), with a scientific CMOS sensor array of 2048×2048 pixels of relatively small size of (6.5 μm) is a polyvalent camera with low readout noise (1 e⁻ rms) and high frame rate of 100 Hz. Secondly, the DIMAX HS4 (PCO AG, Kelheim, Germany), a high-speed CMOS camera with 2 kHz frame rate, 2048×2048 pixels (11 μm pixel size), especially used with the high X-ray beam flux to perform very quick tomography. Finally, the PCO 4000 based on a large CCD sensor (4008×2672 pixels of 9 μm size, sensor area 36×24 mm²) with a low dark noise < 0.05 e⁻/s. The camera bracket support is installed on a motorized rotation stage to align the pixel matrix with the tomography rotation axis (Fig. 2b).

The detectors (excepting the “high-resolution” model) have been also made to accept a polychromatic X-ray beam, so as to prevent radiation damage in lenses or electronics; all models have an L-shaped optical path, with the camera placed vertically, away from the X-ray beam path. A mirror between the scintillator screen and the objective redirects the visible light path toward the sensor (example in Fig. 2d for the revolver camera). The objectives are protected by millimeter-thick lead-glass windows which absorb the X-ray scattering from the air and mirror while remaining totally transparent to the visible.

Furthermore, a large lead frame around the objective and the camera has been added. Finally, the scintillator screen can be flushed with an inert gas to prevent degradation, especially with the white X-ray beam (Figs. 2e & 4).

The scintillator screen material is chosen as a function of the X-ray photon energy and the flux. The single-crystal scintillator materials used include YAG:Ce or LuAG:Ce supplied by Crytur (Turnov, Czech Republic) or LSO:Tb supplied by the ESRF (Grenoble, France) [6]. The scintillator thickness is optimized so as not to affect the effective spatial resolution [7].

The “Revolver X-Ray Camera”

The ANATOMIX “Revolver X-Ray camera” (Fig. 2a) is a modular indirect detector for microtomography at sub-micrometer pixel size. Its scintillator can be adapted to the experiment needs; typically, it is a thin freestanding YAG:Ce or LuAG:Ce crystal down to 20 μm thickness. The orientation of the scintillator support is adjustable in the two tilt axes (Fig. 2e). Four microscope objectives are mounted vertically into a motorized cylinder that allows easy selection and change of objective (and, thus, magnification) (Fig. 2c). The objective is focused to the scintillator screen through a mirror by a fine motorized translation. The objectives used in the revolver model are infinity-corrected with a working distance down to 20 mm. Especially, the Mitutoyo (Kawasaki, Japan) objectives as the M PLAN APO with a magnification of 2 \times to 10 \times and the super long working distance M PLAN APO SL 20 \times coupled with a tube lens $\times 1$ can be installed. Between the microscope objective and the tube lens, a filter can be added to select the scintillation wavelength range used via a fine bandpass. Three different filters are mounted in a manually-rotated cylinder.

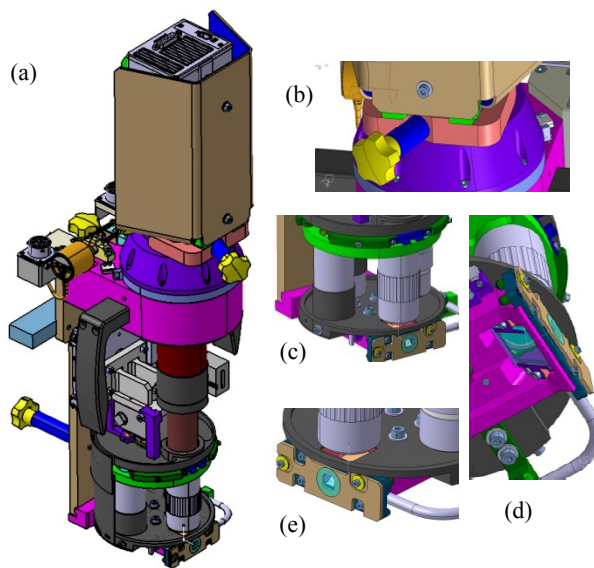


Figure 2: Revolver X-Ray Camera. (a) Complete system coupled to the PCO 4000. (b) Camera rotation stage. (c) Cylinder with four objectives mounted. (d) Support of 45° glassy carbon mirror. (e) Scintillator support, inert gas entrance tube and lead glass emplacement.

Then, the revolver X-ray camera is a relatively compact system with a large modular configuration possible.

Coupled with the ORCA Flash 4, effective image pixel sizes can be realized in a range between 3.25 and 0.325 μm , with an effective resolution of 1 μm (value for the MTF at 10 % with Mitutoyo $\times 10$ with NA 0.28 and a scintillator thickness of 20 μm).

The “High-Resolution X-Ray Camera”

The ANATOMIX “High-Resolution X-Ray Camera” (Fig. 3a) gives access to very high-resolution objectives, that means with a very high Numerical Aperture, but with a very short working distance. The optical design is similar to that of the Revolver X-Ray Camera but the mirror is placed between the tube lens and the camera. This means that the objective lens is in the beam propagation axis and the working distance is not limited by the mechanic. Objectives compatible with this model are the 20 \times , 50 \times or 100 \times and also the high-resolution objectives such as HR 5 \times , HR 10 \times or HR 50 \times from Mitutoyo. The design is made to be very rigid with optimized alignment of the different planes (sensor, objective and scintillator). Coupled with the ORCA Flash 4 CMOS camera and a very thin scintillator layer (<1 μm) on a substrate, the spatial resolution expected with this design should attain values smaller than 1 μm .

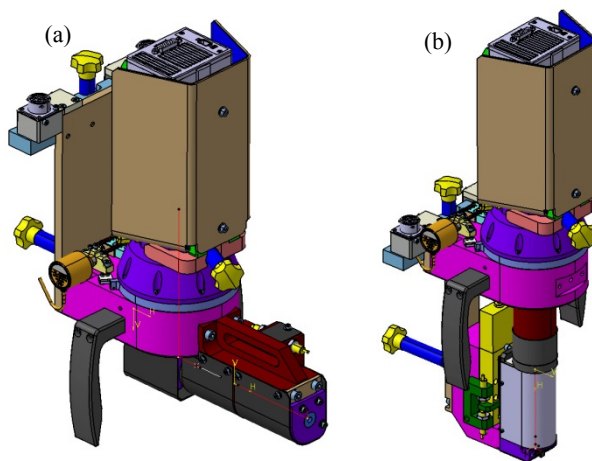


Figure 3: (a) High-Resolution and (b) High-Efficiency X-Ray Camera, both shown with the ORCA Flash 4.

The first test result (Fig. 4) using a 20 \times objective, at 10 keV photon energy, shows a resolution of 0.5 μm on a test chart (model XRESO-100 from NTT-AT, Kawasaki, Japan).

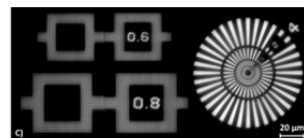


Figure 4: Radiograph of an X-ray test chart (NTT XRESO-100) with the High-Resolution X-ray Camera.

The “High-Efficiency X-Ray Camera”

The ANATOMIX “High-Efficiency X-Ray Camera” (Fig. 3b) bears features of both the revolver and the “high-resolution” designs. It differs from the revolver model by a smaller and lighter design but keeping the protections against X-ray scatter radiation. Only one microscope objective can be mounted but the minimum working distance is shorter to accept objectives with very high numerical aperture, such as the Mitutoyo HR10 \times .

This detector is optimized to collect a maximum of visible light from the scintillator and is primarily aimed at application in low-flux experiments, such as full-field transmission X-ray microscopy. A small mirror is placed between the scintillator and the objective, and the scintillator support is positioned very close to the mirror without any position adjustment. Coupled with the ORCA Flash 4 camera, the resolution is limited but allows a two times higher sensitivity than with the classical 10 \times objective.

The “Large-Field X-Ray Camera”

The ANATOMIX “Large-Field X-Ray Camera” (Fig. 5) completes this panoply of indirect X-ray detectors with a design aimed at imaging a large field of view. The optical design is based on a tandem of photographic objectives with high aperture and very low distortion (Hasselblad, Gothenburg, Sweden). The design delivers an efficient detector for magnifications down to 0.48 \times . Coupled with the PCO 4000 camera, the field of view is 74 mm (H) \times 51 mm (V). On the beamline, the field of view is actually limited by the X-ray beam size (57 mm \times 18 mm, H \times V).

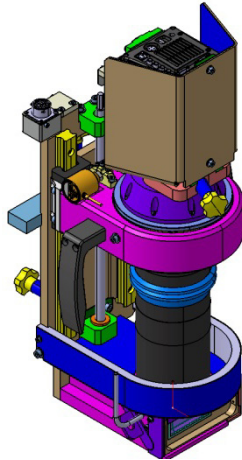


Figure 5: Large-Field X-Ray Camera (shown with Hamamatsu ORCA Flash 4 camera).

CONCLUSION

Four dedicated indirect X-ray detectors have been designed for new tomography beamline ANATOMIX at SOLEIL. A summary of the specifications and elements is given in ANNEX A, Table 1. These detectors match the wide variety of scientific requirements on the beamline; they remain totally upgradable for new generations of cameras, scintillators or lenses. The first specimen of the High-Resolution model is currently under commissioning.

ACKNOWLEDGEMENTS

The construction of ANATOMIX is largely funded by the French National Research Agency (ANR) through the EQUIPEX investment program, project NanoimagesX, grant no. ANR-11-EQPX-0031.

REFERENCES

[1] T. Weitkamp, C. Raven, and A. Snigirev, “Imaging and microtomography facility at the ESRF beamline ID 22”, in *Proc. SPIE*, vol. 3772, pp. 311–317, 1999.

[2] E. Boulard *et al.*, “High-speed tomography under extreme conditions at the PSICHE beamline of the SOLEIL Synchrotron”, *Journal Synchrotron Rad.*, vol. 25, pp. 818–825, 2018.

[3] T. Martin and A. Koch, “Recent developments in X-ray imaging with micrometer spatial resolution”, *Journal Synchrotron Rad.*, vol. 13, pp. 180–194, 2006.

[4] K. Desjardins *et al.*, “MTF, NPS and DQE characterization of an in-house developed X-ray imaging detector for synchrotron based micro-tomography”, *JINST*, vol. 9, C06001, 2014.

[5] T. Weitkamp *et al.*, “The tomography beamline ANATOMIX at Synchrotron SOLEIL”, *Journal of Physics: Conf. Series*, 849, 012037, 2017.

[6] T. Martin *et al.*, “LSO-based single crystal film scintillator for synchrotron-based hard X-ray micro-imaging”, *IEEE Trans. Nuclear Science*, vol. 56, pp. 1412–1418, 2009.

[7] A. Koch *et al.*, “X-ray imaging with submicrometer resolution employing transparent luminescent screens”, *J. Opt. Soc. of America A*, vol. 15, pp. 1940–1951, 1998.

ANNEX A

Table 1: Main Specifications of the ANATOMIX Indirect X-ray Detectors

X-ray camera	Large Field	Revolver	HR	HE
X-ray beam type	10 keV – 30 keV Pink or monochromatic beam			
Objectives	≥ 60 mm	≥ 20 mm	≥ 1 mm	≥ 15 mm
WD (mm)				
NA	0.1 to 0.22	0.05 to 0.28	0.42 to 0.75	0.42
Mag.	0.48 \times to 3.5 \times	2 \times to 20 \times	2 \times to 100 \times	10 \times to 50 \times
Expected resolution	10 μ m	1 μ m	< 1 μ m	1 μ m
Scintillator material	LuAG:Ce, YAG:Ce, LSO:Tb, ...			
Scinti. thickness	1000 μ m down to 60 μ m	250 μ m down to 20 μ m	Down to few μ m on substrate	20 μ m
Camera	Hamamatsu ORCA Flash 4 v2, PCO 4000, PCO DI-MAX HS4 and other camera with T-mount.			
Other specs	Camera motorized orientation Fine focus motorized adjustment Lead glass & lead shielding Inert gas input			

LCLS-II FEL PHOTON COLLIMATORS DESIGN*

S. Forcat Oller[†], H. Wang, E. Ortiz, Y. Feng, J. Krzywiński, M. Rowen
SLAC National Accelerator Laboratory, Menlo Park, CA 94025, USA

Abstract

The unique capabilities of LCLS, the world's first hard X-ray FEL, have had significant impact on advancing our understanding across a broad range of science. LCLS-II, a major upgrade of LCLS, is being developed as a high-repetition rate X-ray laser with two simultaneously operating FELs. It features a 4 GeV continuous wave superconducting Linac capable of producing ultrafast X-ray laser pulses at a repetition rate up to 1 MHz and energy range from 0.25 to 5 keV. The LCLS-II upgrade is an enormous engineering challenge not only on the accelerator side but also for safety, machine protection devices and diagnostic units. A major part of the beam containment is covered by the FEL beam collimators. The current photon collimator design is no longer suitable for the high power densities of the upcoming LCLS-II beam. A complete new design has been conceived to satisfy this new constraints. Moreover, a special FEL miss-steering detection system based on a photo diodes array has been designed as an integral part of the photon collimator as additional safety feature. This paper describes the new LCLS-II FEL Collimators, their mechanical design and encountered challenges.

INTRODUCTION

Due to the possibility of having a X-ray FEL beam stray from its nominal path and strike surfaces of beam-line components no able to handle the FEL power, the installation of collimators along the Front End layout is required to stop this mis-steered photon beam and also to only let pass the beam size defined by their aperture to the downstream components. The collimators are equipped with a fault detection mechanism that consists of four photo diodes that shall detect the beam scattering from miss-steered beam and inform the Machine Protection System (MPS) which will take actions such as deviating or even tripping off the beam if required.

LCLS-II BEAM PARAMETERS

The LCLS-II SXR beamline will be driven by the new superconducting radio-frequency Linac (SCRF) while the HXR beamline can be driven either by the SCRF Linac or by the normal copper radio-frequency Linac (CuRF).

The much higher average power possible with the SCRF Linac compared with the current LCLS FEL beam presents new challenges to the thermal management of the beam optics, diagnostics, slits and absorbers (see Table 1 and table 2).

[†] sforcat@slac.stanford.edu

*Work supported by the U.S. Department of Energy under contract number DE-AC02-76SF00515

Table 1: LCLS-II Soft X-ray Beam Parameters at 0.1 MHz, 300 Pc

Energy [eV]	Beam divergence [μrad]	Max integrated power [W]	Max single pulse fluence [mJ]
250	11.8	880	8.8
750	4.6	570	5.7
1250	3.2	339	3.4

Table 2: LCLS-II Hard X-Ray Beam Parameters at 0.3 MHz, 100 Pc

Energy [eV]	Beam divergence [μrad]	Max integrated power [W]	Max single pulse fluence [mJ]
1500	2.8	519	1.73
3250	2.0	185	0.62
5000	3.3	1.8	0.06

MECHANICAL DESIGN

Collimators in the Layout

A total of ten collimators are considered in the baseline for LCLS-II, five will be installed on the SXR line and five on the HXR. The Table 3 and Table 4 show the different aperture sizes and location of each collimator along the x-ray transport system. Aperture size was determined by beam stay clear and ray trace.

Table 3: HXR Collimators Location and Apertures Sizes (1.5 keV for the SC Linac and 1.5 keV for Cu Linac)

Coll. ID	Location [#] [m]	Beam size Ø [mm] SC/Cu	Beam Stay Clear Ø [mm] SC/Cu	Coll. aperture Ø [mm]
PC1H	84.2	2.92/2.44	7.69/6.73	8
PC2H	93.2	3.09/2.59	8.12/7.12	2.5
PC3H	100.9	3.24/2.72	8.49/7.46	2.5
PC4H	104.6	3.31/2.79	8.67/7.62	2.5
PC5H	98.2	3.19/2.68	8.37/7.34	2.5

[#]Location from the end of the undulator.

Table 4: SXR Collimators Location and Aperture Sizes (0.4 keV SC Linac)

Coll. ID	Location* [m]	Beam size Ø [mm] SC/Cu	Beam Stay Clear Ø [mm] SC/Cu	Coll. aperture Ø [mm]
PC1S	41.1	4.41	10.24	12
PC2S	75.6	6.32	14.41	16
PC3S	94.3	7.36	16.67	12
PC4S	97.3	7.53	17.04	12
PC5S	100.4	7.70	17.40	12

*Location from the end of the undulator.

Vacuum Chamber and Cooling System

The collimators design consists of a vacuum pipe with two fixed DN100 flanges. See Figure 1. Inside the vacuum chamber there are three main assemblies:

- A photo diodes array with their internal cabling going to a feedthrough.
- A stack of a 750 μm thick and 55 mm \varnothing CVD Diamond, 10 mm thick SiC and 10 mm Tungsten.
- A “keep-alive” system with two 660 nm pulsed visible emitters or LEDs with their internal cabling going to a second feedthrough.

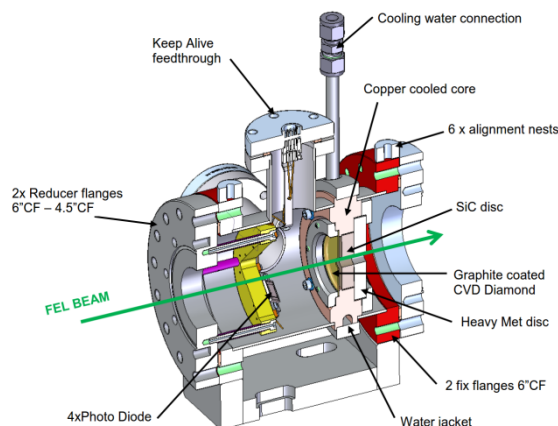


Figure 1: Photon collimator assembly section view.

A central oxygen-free (OFHC) copper core brazed to the stainless-steel chamber works as a holder for the stack-up of materials and provides cooling for the CVD Diamond through a stainless steel water jacket. Two pipes connect the device to the main water cooling system through Swagelok fittings.

The whole collimator assembly sits on top of an adjustment stage with spherical washers and pushers for alignment of the component.

Diode Array and “Keep-Alive”

In the event that the photon beam mis-steers it will hit the front surface of the diamond creating x-ray scattering which will be detected by four AXUV100Al photo diodes with a 150 nm aluminium filter on the front surface. There is sufficient visible spectrum transmission through the Al filter layer for the “keep-alive” system to confirm the diodes are working. See below Figure 2.

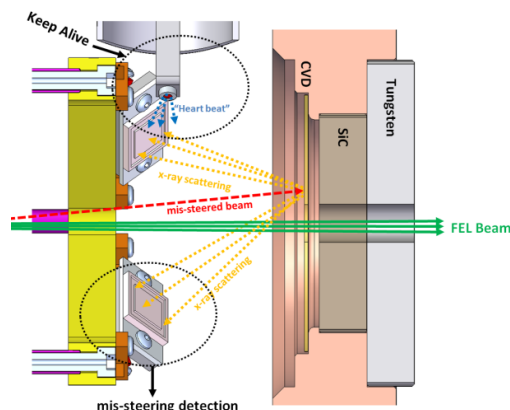


Figure 2: Section of the collimator showing half of the diodes array and keep-alive system.

The fault detection mechanism, works together with a keep-alive system that ensures the health of the photo diodes verifying their health periodically.

CVD Diamond and Graphite Coating

Due to the high power density (W/cm^2) and extremely high peak fluence (J/cm^2 per pulse) a material with high thermal conductivity and low Z number as the CVD diamond was the most suitable. [1]

To mitigate the damage of the diamond near carbon edge photon energies ($\sim 283 \text{ eV}$) and deal with the instantaneous heating of the pulsed FEL beam, a pyrolytic graphite coating of 3 μm has been applied with chemical vapor deposition. The coating absorbs the intensive pulsed beam while the diamond underneath only deals with the average power with its temperature remaining almost constant, see Figure 3.

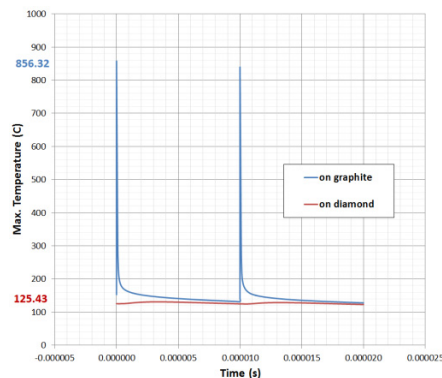


Figure 3: At 2 mJ/pulse, with energy of 290 eV for 1 ns heating and 10 μ s cooling, attenuation of the graphite coating from each pulse while the diamond material remains at near constant temperature 2 mJ/pulse at 290 eV for 1 nsec heating and 10 μ s cooling).

The diamond disc is fixed to the copper body with an aluminum clamp and using Belleville washers to control the pressure applied. As thermal interface between the diamond and the copper heat sink an indium 100 μ m thick gasket has been chosen.

THERMAL STUDIES

Analyses have been performed of the collimator installed in the SXR beamline at 40 m downstream of the last undulator (see Table 5). Simulations have been done with the beam hitting the edge of the aperture as is where we observed the highest temperature and stress. [2]

Table 5: Cases of Study, Most Upstream Collimators for SXR and HXR Beamlines

Parameters	PC1S SXR Collimator	PC1H HXR Collimator
Distance to End of Undulator [m]	41.1	101.5
Photon Energy [eV]	750	1500
Divergence [μ rad]	4.8	2.8
Beam size [rms, mm]	0.3	0.38
Incident Power [W]	400	519
Surface peak power density [W/mm ²]	712	558

Other studies with higher power and carbon edge energies showed that the diamond may not be safe once the input power exceeds 550W (see Table 6).

Table 6: Combined Temperature Steady State and Instantaneous for PC1S Collimator, SXR Beamline

Energy / Power	340 W	550 W	880 W
250 eV	422 °C	810 °C	1761 °C
290 eV	1479 °C	2386 °C	4123 °C
750 eV	993 °C	1999 °C	>4500 °C

Stress analyses were done and for boundary conditions, the peak tensile stress observed is of 57 MPa, which is less than the allowable tensile stress of 500 MPa, and the peak compression stress is of 665 MPa, which is also below the 1900 MPa of allowable compressive stress.

Looking at the results of temperature and stress, a “bootstrap strategy” will be applied. The beam power will be gradually increased while the diamond will be monitored in order to define new safe operation conditions.

MANUFACTURE AND INSTALLATION

Ten photon collimators are currently being assembled at SLAC. The chambers were received in April. In the next weeks the diodes and keep-alive systems will be assembled and tested. See Figure 4 where the chambers are shown.



Figure 4: Photon collimator chambers received.

The installation on their support stands inside the LCLS tunnel will be during the long shutdown (starting on December 2018 until December 2019) with the rest of Front End components.

CONCLUSION

A whole new LCLS-II photon collimator design has been fabricated and this incorporates a new fault detection system with a keep-alive that ensures and certifies the health of the photo diodes.

A diamond with graphite coating is appropriate to absorb the FEL photon beam and this solution has been applied in the rest of photon stoppers and apertures for the new LCLS-II.

A bootstrap strategy will be needed during commissioning in order to identify safe operation conditions for the collimators and the diamond inside them.

REFERENCES

- [1] J.Krzywiński, “Multi-shot Damage Study of CVD Diamond Samples performed at 330 eV Photon Energy”, *LCLSII-3.5-EN-0779-R0*, 2017.
- [2] H.Wang, “Thermal Studies of CVD Diamond based FEL Photon Stoppers and Collimators”, *LCLSII-3.5-EN-0772-R1*, 2017.

GRANITE BENCHES FOR SIRIUS X-RAY OPTICAL SYSTEMS

R. R. Galdes, A. Sikorski, C.S.N.C. Bueno, M. Saveri Silva, G.V. Claudiano, V.Z. Ferreira, M.S. Souza, Brazilian Synchrotron Light Laboratory (LNLS), Brazilian Center for Research in Energy and Materials (CNPEM), 13083-970, Campinas, São Paulo, Brazil

Abstract

The first set of Sirius beamlines is expected to start operating in early 2019 and over the last few years many optical systems for the X-ray beamlines have been developed in-house at the Brazilian Synchrotron Light Laboratory (LNLS). Starting with the High-Dynamic Double Crystal Monochromator (HD-DCM), passing by the Double Channel-Cut Monochromator (4CM) and continuing with new standard mirror systems, a series of granite benches, based on high-resolution levellers, and a combination of embedded and commercial air-bearings, has been designed for high mechanical and thermal stability. Specifications, designs, and partial results are presented, showing the progressive increase in complexity according to a deterministic design approach.

INTRODUCTION

Sirius, the new Brazilian synchrotron light source, is currently under construction. As a fourth-generation machine, the synchrotron beam will have extraordinary properties in terms of size, divergence and flux. Consequently, the beamline optical elements, such as monochromators and mirror systems, must have corresponding performances to allow for proper energy selection and control of position and size of the beam at the sample, which begins with robust and stable mechanical supports (see Fig. 1).

Following several successful beamline instrumentation examples [1, 2], granite was chosen as the base material for the new generation of mechanical benches, due its good elastic modulus over density ratio associated to a very low coefficient of thermal expansion, since this combination results simultaneously in good thermal and mechanical performances. Moreover, to improve the stability and reduce the complexity of the assemblies of the optical elements, it was made the choice of allowing only the essential degrees of freedom (DoF) in vacuum, whereas all other DoF needed for positioning and alignment should be provided by the benches [3, 4]. In the following sections, the practical implementation of these guidelines and partial results of the benches of the High-Dynamic Double Crystal Monochromator (HD-DCM), Double Channel-Cut Monochromator (4CM) and mirror systems are presented.

CONCEPTUAL DESIGN

Since positioning the optical elements along the beam axis (z) does not usually have strict specifications, the granite benches have been designed to allow for positioning and alignment in the remaining 5 DoF, namely: translations, in the horizontal and vertical axes, T_x and T_y , respectively; and the associated rotations, R_x , R_y and R_z .

With some effort, all the most demanding specifications of different optical elements could be meet in a standard conceptual design. At the bottom level, wedge-levellers developed for Sirius girders [5] allow for T_{y1} , R_x and R_z , for basic short-range height positioning and levelling. Next, functional air-bearing arrangements allow for the additional DoF by positioning different granite blocks with respect to each other. In the monochromators, T_x and R_y are implemented to overcome initial assembly and alignment limitations, and to allow for either the exchange between crystal sets (HD-DCM) or for pink beam operation (4CM). As for the mirrors, with side-bounce deflection, in addition to these two DoF, a large-range T_{y2} has been introduced to allow for the selection of stripes with different coating materials.

The choice of functional air-bearings was driven by the intention of maximizing the overall mechanical and thermal stability, and effectively optimizing the stiffness of the bench as a whole. Indeed, with this solution, it is even possible to combine different DoF over a single interface, which allows for designing the minimum number of granite parts and direct interfaces. As the air-bearings are used only during alignment, once the air is off the bench should behave nearly as an extension from the floor up to the optical elements. With conventional guiding elements, there would be more elements in the stiffness chain and particularly a significant number of interfaces, which are prone to performance limitations. Finally, combining embedded

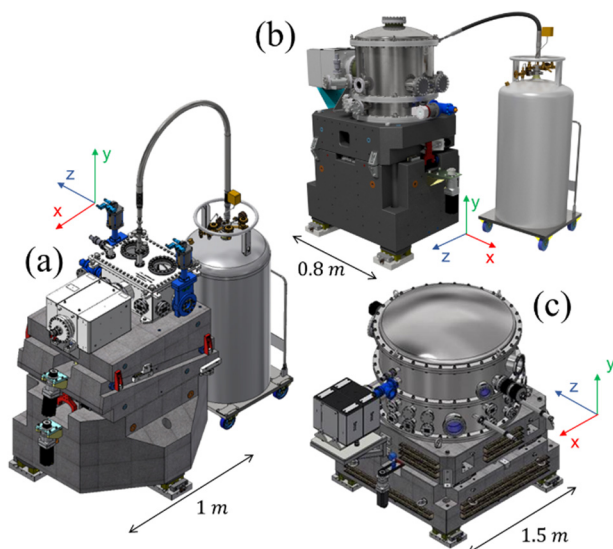


Figure 1: Optical systems mounted on granite benches: (a) mirror; (b) double channel-cut monochromator (4CM); and (c) High-Dynamic Double Crystal Monochromator (HD-DCM) (Beam direction: $+z$. Vertical up: $+y$).

and commercial air-bearing solutions gives significant design flexibility. The first are used for lifting, so that without air there can be direct contact between the granite parts. Moreover, high determinism, particularly in terms of stiffness and stability, is obtained by building the air-bearings in specific machined areas of the granite blocks, defining contact pads with optimized geometry. In the pads, textbook grooves are added to improve the pressure distribution profile, allowing for lower operational pressure levels. As for the commercial air-bearings, they are used as guiding elements, running on internal or external tracks also directly machined in the blocks. Since each element constrains a single DoF, they can be suitably arranged to provide high-quality guiding without over-constraining limitations. Indeed, this was a key characteristic in the implementation of more than one DoF over one interface.

Figure 2 shows the granite bench for the mirror systems, with the 3 granite parts and 4 interface levels. The 1st level is between the levellers and the floor, the 2nd, between the bottom granite and levellers, the 3rd and 4th, between the granite parts. In the 3rd level T_x and R_y are implemented together, whereas the combined translations of the 3rd and 4th levels provide T_y in a wedge-type solution, similar to that adopted in the APS Velociprobe [2]. Comparing the two wedge solutions, here the wedge angle was increased from 7.5° to 8.5° to reduce strokes, while keeping self-locking with a safety factor of 2.8, and a vertical guide was not compatible with the design of only 3 granite parts for all the DoF.

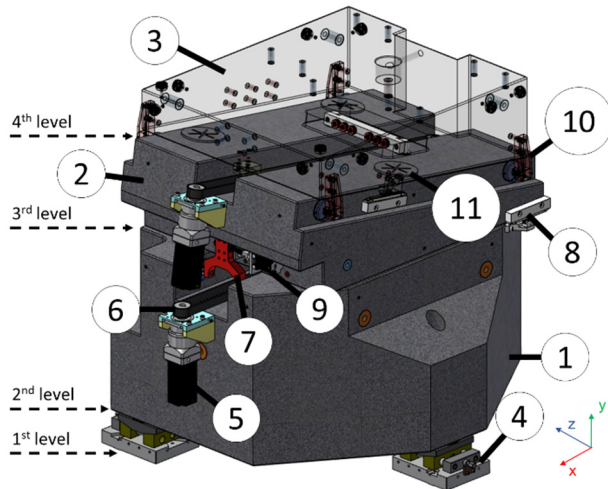


Figure 2: Three-part granite bench for the mirrors systems: (1) bottom granite; (2) middle granite; (3) top granite (transparent for visibility); (4) wedge-leveller; (5) stepper motor for T_x ; (6) timing belt for T_x ; (7) commercial air-bearing guiding for T_x ; (8) optical encoder; (9) power screw mechanism for R_y ; (10) commercial air-bearing for wedge; and (11) machined air-bearing pad.

All mechanisms are driven by stepper motors, which are connected either to power screws, for the levellers and the R_y solution, or to timing belts, for the translations between granites. The latter option also prevents over-constraining issues, not only allowing for the integration of T_x and R_y

in a single level in the first place, but also relaxing eventual alignment problems that might occur between power screws and the air-bearing guides. For feedback and metrology, all five DoF plus the additional T_y are covered by: three length gauges installed between the bottom granite and the floor; and three Renishaw REVOLUTE absolute encoders with $0.5 \mu\text{m}$ resolution, which are particularly useful to comply with the R_y DoF for having large yaw misalignments tolerances.

RESULTS AND DISCUSSION

The granite bench of HD-DCM was assembled and functionally validated in the second semester of 2017, building up confidence in the proposed approach and unlocking the design of the benches for other optical components. Next in line were the 4CM and the mirrors, with progressive complexity levels. The components for the mirror benches are still in manufacturing phase, but most of the parts of 4CM bench have already been delivered, which allowed for a new round of experimental analyses for motion and dynamic performances. Figure 3 shows this assembly at the hall of the metrology building at LNLS:

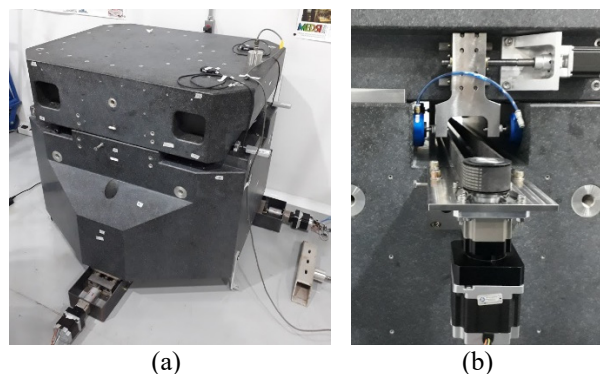


Figure 3: (a) 4CM granite bench assembled at the hall of the metrology building of LNLS; (b) Detail of T_x and R_y stepper-driven actuation mechanisms with the timing belt and power screw, guided by the commercial air pad.

Dynamic Analysis

The most stringent mechanical RMS stability specifications in the optical systems are in the order of $1 \mu\text{m}$ for translations and 50 nrad for rotations. Extracting meaningful absolute stability data of systems out of their final destinations and operational conditions, however, can be fairly difficult, because a significant part of it is a response to cultural noise. Nevertheless, to get some reference numbers, a few measurements for the integrated RMS values between 1 and 450 Hz were recently made using Wilcoxon 731A accelerometers. As a result, numbers below 40 nm and 30 nrad for the HD-DCM on a special floor of the metrology building were achieved, whereas up to 200 nm and 100 nrad were found for the 4CM in the common floor of the hall, close to the HVAC system. Sirius experimental floor is built for exceptional performance, so that, even with its cultural noise, the specs are expected to be met.

Moreover, regarding the conceptual design choices, investigations of modal analyses bring important information. In that sense a toolbox developed in Matlab to build 3D mode shapes from experimental data has proven to be extremely useful. Figure 4 shows de frequency response functions (FRF) built with signals of a Kistler 8726A accelerometer and a PCB Electronics hammer for about 25 points of interest over the complete structure. It can be seen that below 40 Hz the coherence is very level low, so that no meaningful information can be extracted. To improve the signal quality in this frequency range, measurements with a shaker are most likely needed and may actually provide relevant transmissibility information. Indeed, up to this frequency the bench and the floor are coupled, so that it is difficult to achieve good signal to noise ratio. Then, at about 45 Hz, matching very well with expected values from simulations, the first rigid body modes (R_x and R_z) appear for the whole structure and the signals generally improve. Adding a preload of 20 kN per leveller, which is equivalent to increase the preload given by weight alone by a factor 3, only caused a shift of about 4 Hz in frequency, suggesting that the stiffness link between the bench and the floor is close a practical limit within the present concept. Indeed, since the stiffness of the floor itself may be a limitation, having peaks at relatively low frequencies becomes an inevitable drawback of using such heavy granite benches. Although larger floor stiffness can be expected in Sirius experimental floor, it is arguable how much improvement can be obtained frequency-wise. Nonetheless, if needed, passive damping solutions may be introduced to keep displacements down to the nm level. Yet, knowing that the 120 and 175 Hz peaks are also related to rigid body modes, it can be seen that the first modes between granites occur above 450 Hz, which validates the design choices with the intention of creating nearly monolithic structures.

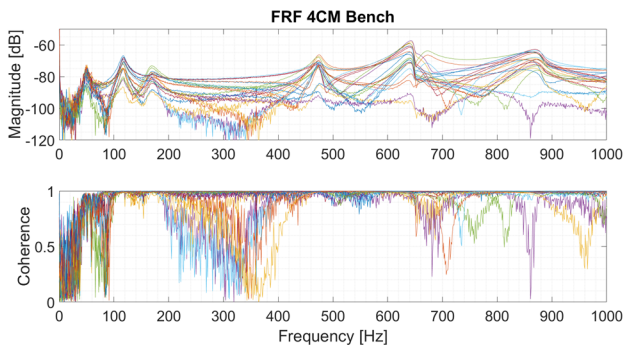


Figure 4: Frequency response function used for experimental modal analyses in the granite bench of the 4CM.

Motion Analyses

Based on the alignment and performance requirements of all the optical systems currently under design or manufacture, a set of standard specifications was defined for the benches, including: accuracy, range, resolution, repeatability, and stability. For the optical elements, accuracy is essentially defined by proper alignment with respect to the beam, so that it can be encompassed by sufficient range and

resolution. In terms of range, there were practical limitations because of design choices, but not risks. Resolution, on the other hand, tends to be dominated by friction, requiring more careful investigation. If metrology is present, in simple systems the repeatability also becomes a function of resolution, provided that the target position may be achieved within a reasonable number of iterations.

Table 1 summarizes the motion specs and the results for the DoF available in the 4CM bench. Since not all electronic parts were yet available, the motion characterization was carried with Heidenhain's MT25 length gauges, with accuracy below of $0.5 \mu m$. It can be seen that the only item that fell out of specs was the translation T_x , which was off by a factor 10. This is related to the compliance of the timing belt and to the creation and removal of the air film. This result must be rechecked with realistic preload, as expected at the beamlines due to bellows and vacuum forces. Else, the driving reasons of this spec may be reviewed or reconsidered. Yet, the tight resolutions of $1 \mu rad$ in the levellers, which were of concern, could be successfully met, even with extra preload.

Table 1: Summarized Specifications for Mirrors and Monochromators Granite Benches and Results for the 4CM

Axis	Range [mm/mrad]		Resolution [$\mu m/\mu rad$]	
	Spec	Exp.	Spec	Exp.
T_x^*	–	± 9	0.5	5.3
Ty_1	± 2.3	± 2.3	1	0.5
Ty_2^{**}	± 10	–	1	–
R_x	± 3.5	± 5	1	0.8
R_y	± 10	± 11.5	1	1
R_z	± 3.5	± 5	1	1

* Range very much dependent on the system.

** For mirror systems only.

CONCLUSION

Deterministic design concepts have been applied in the development of high-stability granite benches for Sirius X-ray optical elements. Experimental analyses of a monochromator bench proved that the innovative functional air-bearing solutions allowed for the realization of robust structures, with internal eigenfrequencies above 450 Hz, yet providing fine motion resolution which approach the sub-micrometer and sub-microradian ranges. The evaluation of the mirror benches and further investigations about stability levels, transmissibility and damping are expected in the near future.

ACKNOWLEDGEMENTS

The authors would like to gratefully acknowledge the funding by the Brazilian Ministry of Science, Technology, Innovation and Communication and the contribution of the LNLS team.

REFERENCES

- [1] R. Baker *et al.* “New generation mirror systems for the ESRF upgrade beamlines”, *J. Phys.: Conf. Ser.* 425 052015, 2103.
- [2] C. Preissner *et al.*, “Earth, wind and fire: the new fast scanning Velociprobe”, in *Proc. MEDSI 2016*, Barcelona, Spain, Sep. 2016, paper TUAA02.
- [3] R. Galdes *et al.*, “The design of Exactly-constrained X-ray mirror Systems for Sirius”, presented at MEDSI 2018, Paris France, Jun. 2018, this conference, paper WEOAMA04.
- [4] R. Galdes *et al.*, “The status of the new High-Dynamic DCM for Sirius”, presented at MEDSI 2018, Paris, France, Jun. 2018, this conference, WEOAMA01.
- [5] F. Rodrigues *et al.*, “High rigidity girder systems for the Sirius machine”, presented at MEDSI 2018, Paris, France, Jun. 2018, this conference, paper WEPH26.

BEAM CONDITIONING OPTICS AT THE ALBA NCD-SWEET BEAMLINE

N. Gonzalez, J. B. González, C. Colldelram, M. Llonch, J. Ladrera, A. Fontserè, G. Jover-Manas,
 J. C. Martínez, C. Kamma-Lorger, I. Sics, S. Ferrer and M. Malfois
 ALBA Synchrotron Light Source, Cerdanyola del Valles, Spain

Abstract

The SAXS/WAXS Experimental End Station beamline (NCD-SWEET) at ALBA Synchrotron has undergone a major upgrade in the optics and the end station to perform state-of-the-art SAXS/WAXS experiments.

In order to reduce X-ray parasitic scattering with air and maximize the photon flux at the sample, an optimized beam conditioning optics has been designed and built in the end station, integrating previously used and new components in vacuum.

The beam conditioning optics includes a fast shutter, a set of commercial guard slits and a diagnostic unit comprising three filters and a four-quadrant transmissive photodiode. In addition, a set of refractive beryllium lenses allows micro focusing of the beam. The lens system can be removed from the beam path remotely. Finally, an on axis sample viewing system, with a novel design based on an in-vacuum camera mirror and a mica window minimizes the beam path in air up to the sample.

To facilitate the alignment of the elements with respect to the beam, all the subsystems are supported by a high-stability granite table with 4 degrees of freedom and sub-micron resolution.

INTRODUCTION

As part of the upgrade project of the the Non-Crystal-line Diffraction beamline (NCD-SWEET) at ALBA, the end station has undergone a full re-design of the mechanical elements in addition to the installation of new equipment with the result of a new beamline configuration [1].

In order to improve the service to users and provide an improved basic configuration to perform transmission experiments, an enhanced beam conditioning optics system comprising new elements such as, a diagnostic unit and a set of micro focusing lenses, has been designed and built (Figure 1). Additionally, the vacuum section has been extended up to the sample and all the components have been located over an in-house developed 4-DOF granite table.

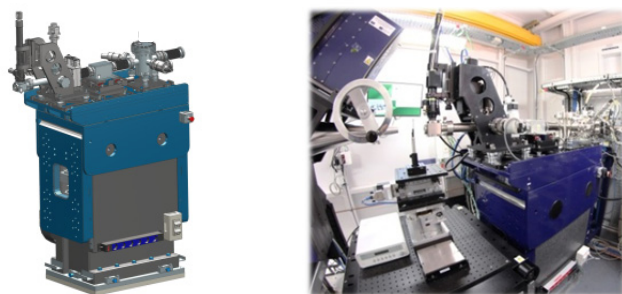


Figure 1: General overview of the Beam Conditioning Optics.

SYSTEM REQUIREMENTS

The main objective of the beam conditioning optics (BCO) upgrade was to maximize the beam transmissivity up to the sample, thus, all the elements, including the fast shutter and the on-axis sample viewing system (in air in the previous setup), were placed in vacuum. Besides, in order to have a diagnostic of the beam intensity just before the sample a new diagnostic unit compounded of a transmissive photodiode and 3 filters had to be installed. Additionally, a set of compound lenses were integrated. These lenses can be remotely inserted into the beam path in order to micro focus the beam.

So as to ease the alignment of the beam conditioning elements with respect to the beam for different optical configurations and energy ranges while ensuring the system stability, all the components had to be located over a high stability 4-DOF table.

The movement requirements of the support table are listed in Table 1.

Table 1: Motion Requirements of the BCO Support Table

	Range	Resolution
Vertical	15mm	2 μ m
Transversal	± 5 mm	2 μ m
Pitch	$\pm 0.5^\circ$ (± 8.5 mrad)	$\pm 0.001^\circ$ (17.4 μ rad)
Yaw	$\pm 0.5^\circ$ (± 8.5 mrad)	$\pm 0.001^\circ$ (17.4 μ rad)

DESIGN DESCRIPTION

The beam conditioning optics system consists of a granite based table with 4 motorized degrees of freedom that allows the alignment of the elements with respect to the beam while ensuring the stability of the components. All the beam conditioning elements, namely, the fast shutter, the compound refractive lenses, the slits, the diagnostic unit and the sample viewing camera mirror are placed inside UHV vessels located over the table. The elements have external fiducial interfaces and individual alignment stages, with edge welded bellows in between, so that all the apertures could be pre aligned during the installation. Besides, the beryllium lenses system is located over two motorized stages that permit the in-out motion and the longitudinal positioning along the beam path for the focal position adjustment. This motion, together with the vertical movement of the on axis camera that permits the focusing adjustment, gives high versatility for using sample holders of distinct sizes.

Microfocusing Lenses

A set of 35 beryllium compound refractive lenses permit micro focusing the beam at 664mm from their centre. The lenses are positioned within a vacuum chamber lo-

cated over an in-house designed two linear motions motorized stage of sub-micron resolution (Figure2). The transversal motion allows the positioning or removal of the lenses in the beam path and the longitudinal motion permits to adjust the focal point for diverse sample environments. Going from standard configuration to micro-focused beam (or the other way around) is fast and only takes 10s.

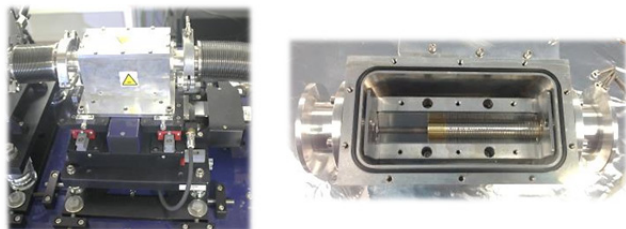


Figure 2: Images of the micro focusing lenses unit.

Diagnostic Unit

The system consists of a motorized horizontal linear motion with 4 discreet positions for different filters: none, Cobalt, Copper and Zink, and an independent vertical linear motion for a photodiode, located just upstream the filters (Figure 3). The transmissive photodiode is a $5 \times 5 \text{ mm}^2$ area and $10 \mu\text{m}$ thickness Si diode, developed in collaboration between ALBA, ESRF and IMB-CNM-CSIC [2]. It enables having a diagnostic of the beam intensity and vertical position just before the sample. The diode has been calibrated and provides absolute flux. The three filters are used together with the data collected at the diode for energy calibration.

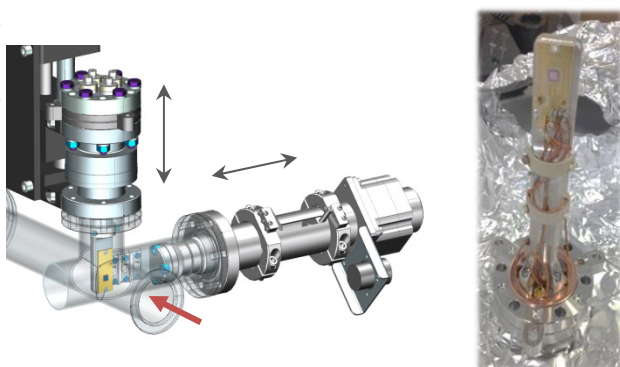


Figure 3: Pictures of the diagnostic unit.

On Axis Sample Viewing System

The on-axis viewing system is based on a novel design consisting of an in-vacuum mirror and an imaging system (commercial Navitar lens with a CCD camera) located in air. The mirror, located at 45° , is made in-house from a hard disc platter with an $\varnothing 1 \text{ mm}$ central hole for the beam. It is separated from air by a $50 \mu\text{m}$ mica window at the sample side and by a fused silica viewport and an in-house developed and patented double O-ring sealing [3] on the side of the camera lenses (Figure 4).

Besides, the camera is equipped with a vertical motion system to adjust the focal plane at sample position. The lens can be easily re-configured in order to focus at larger

distances, although at the expense of magnification, thus providing an enhanced versatility in regard to the different sample holder sizes/types.

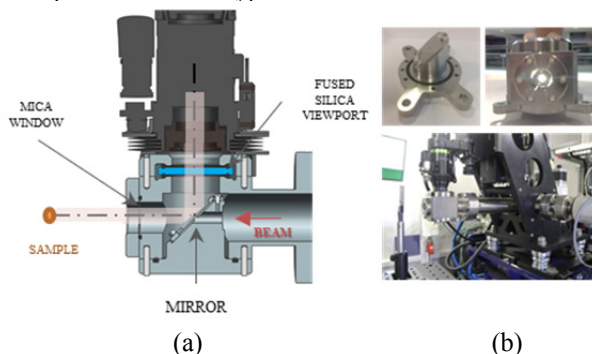


Figure 4: Sample viewing system scheme (a) and mirror, mirror support and mirror chamber (b).

Support Table

The support table is based on the in-house developed “skin concept” design which provides high stability and excellent resolution performances [4]. The motion stages are mounted as close as possible to the fixed block of natural granite, minimizing the mass lever arms and thus optimizing the stability.

Vertical movement is performed by a simultaneous displacement of the front and back rigid plates, which are connected on the top by a horizontal plate. The pitch motion is achieved by a differential movement of these two plates, which are flexure grooved (Figure 5).

Transversal movement is carried out by a linear guided stage, actuated by motors and precision ball screws on both sides. The yaw, guided by circular guides, is performed when actuating the upstream motor alone. The rotational movement on the motion system of the yaw is relieved by a flexure link.

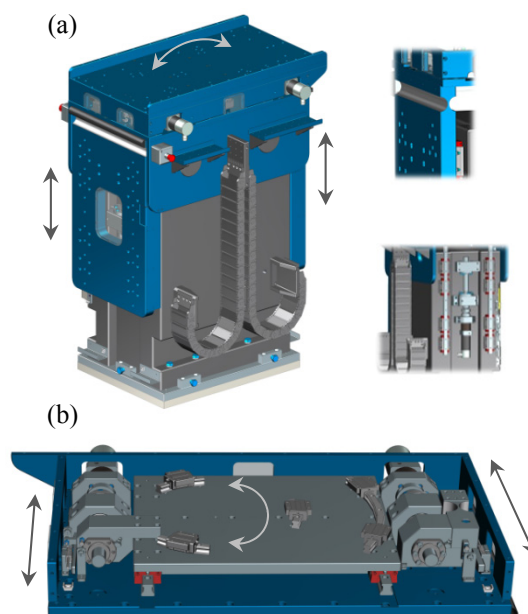


Figure 5: Vertical and pitch motions (a) and transversal and yaw motions (b).

FINITE ELEMENTS ANALYSIS

In order to study the behaviour of the whole system, both structural and modal finite elements analyses were performed in Ansys.

Structural Analysis

The maximum deformation and stresses of the BCO were 94 μ m and 20MPa respectively, well beyond the maximum admissible values in order to assure the correct performance of the system. Besides, the maximum stresses on the flexures for the pitch and yaw rotations were calculated, obtaining a maximum stress value of 340MPa, which is 1/3 below the yield stress of the high elastic limit steel used.

Modal Behaviour

A frequency analysis was also performed in Ansys to evaluate the stability of the overall system. The first 4 modes of vibration are shown in Figure 6.

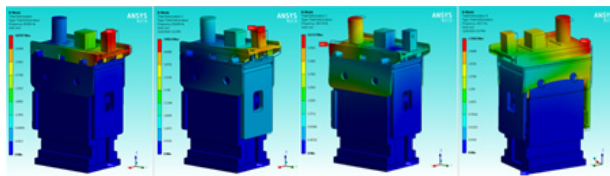


Figure 6: First four eigenmodes of the BCO; 58Hz, 84Hz, 100Hz and 103Hz respectively.

PERFORMANCE & RESULTS

Metrology Results

Metrology tests were performed using a Renishaw ML10 Interferometer in order to evaluate the performance of the different motions of the BCO support table. The results of resolution and repeatability measurements are shown at Table 2.

Table 2: BCO Support Table Metrology Results

	Stroke	Resolution	Repeatability
Vertical	90 mm	0,125 μ m	2,016 μ m
Transverse	\pm 20 mm	0,313 μ m	0,598 μ m
Pitch	\pm 9,2 mrad	0,125 μ rad	0,702 μ rad
Yaw	\pm 14,6 mrad	0,313 μ rad	1,259 μ rad

In addition, vibration tests were executed measuring the amplitudes when exciting the system with a hammer at different locations. The results quite well match with the FEA simulation results.

Table 3: Vibration Tests Results

Location	Frequencies (Hz)
Upstream	84, 92
Downstream	84, 92
Inboard	54, 65, 84, 92, 113
Outboard	56, 84
Top	53, 65, 84, 92

On Axis Viewing System

An extensive commissioning on the on axis viewing system was performed in order to evaluate the image

quality provided by the in vacuum camera mirror with the mica window sealing. Several pictures of distinct zooms are shown in the Figure 7. The field of view (FOV) at maximum zoom (Magnification) of M=5.66X is 0.85x0.64mm (H x V).

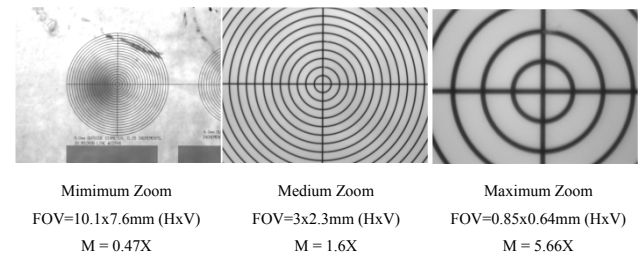


Figure 7: Test images for a 5mm diameter reticule with 0.25mm diameter increments and 0.02mm line width.

CONCLUSIONS

In summary, the overall design of the beam conditioning elements at the recently upgraded NCD-SWEET beamline has been presented, including the detailed description and results of the support table that validate the enhanced performance and stability of the system.

The beam conditioning optics assembly was installed during the summer shutdown of 2017 and it is currently used by the users. Further commissioning for optimization will be performed during this year.

ACKNOWLEDGEMENTS

The authors acknowledge Liudmila Nikitina, David Calderón, Lluís Ginés, Artur Gevorgyan, Jose Ferrer, Karim Maimouni, Jordi Navarro, Oscar Borrego, Pablo Pedreira, Bern Saló, Jorge Villanueva and Francesc Farré for their help in the design and construction of the beam conditioning optics.

REFERENCES

- [1] J. B. González *et al.*, “NCD-SWEET Beamline Upgrade”, presented at MEDSI’18, Paris, France, June 2018, paper THPH17, this conference.
- [2] J. M. Rafi *et al.*, “10 μ m-thick four-quadrant transmissive silicon photodiodes for beam position monitor application: electrical characterization and gamma irradiation effects”, presented at the 18th International Workshop on Radiation Imaging Detectors, Barcelona, Spain, July 2016, *JINST*, vol. 12, Jan. 2017, doi:10.1088/17480221/12/01/C01004
- [3] L. Roso, J. Hernandez, A. Crisol, C. Colldelram, L. Nikitina, “Ventanilla con vidrio intercambiable para cámaras de presión”, Spanish Patent and Trademark Office No. U201431357, Oct. 17, 2014.
- [4] C. Colldelram, C. Ruget and L. Nikitina, “ALBA XALOC Beamline diffractometer table skin concept”, in *Proc. MEDSI’10*, Oxford, UK, July 2010, https://doi.org/10.1017/S2044820110000754

A NEW HIGH PRECISION, FULLY MOTORIZED 6-DoF SAMPLE STAGE FOR THE ALBA PEEM ENDSTATION

N. González†, L. Aballe, A. Carballado, C. Colldelram and M. Foerster
 ALBA Synchrotron Light Source, Cerdanyola del Vallès, Spain

Abstract

A new 6-DoF sample manipulator has been designed for the ALBA Synchrotron PhotoEmission Electron Microscopy (PEEM) experimental station, based on a commercial Elmitec LEEM 3.

The new design includes full motorization of all 6 axes with position feedback, no backlash, and maximized stability, crucial to achieve the best spatial resolution of down to 8 nm (in so-called LEEM mode).

The in-plane longitudinal and transversal motions with sub-micron resolution are based on high precision linear guides, while the pitch and roll stages (sample tilt), guided by angular guides, are actuated by a double-flexure system, which enhances the overall rigidity of the system. The vertical stage is composed by a high rigidity recirculating roller screw and cross roller guides. Finally, 360° yaw rotation is supplied by a differentially pumped commercial rotary stage. On top of the stage, the sample support is mounted on a customized DN63CF flange.

This support keeps the original functionalities of the sample manipulator and holders, with 6 independent electrical contacts, and the possibility to heat the sample up to 2000 K and cool it to 100 K with an improved liquid nitrogen cooling system.

INTRODUCTION

The purpose of the project is to upgrade the PEEM endstation functionality by offering full automatization of the sample motions. In the present form, the vertical motion and the crucial sample tilt (which through non-geometrical effects is coupled with the measurement position (horizontal stage)) are still operated manually, preventing full remote control and programming of sequences.

Additionally the new design offers opportunities to improve repeatability of those motions already motorized, the easy integration into the control system through ICEpap motor controls and the improvement of the cooling stage efficiency which has deteriorated in the original design. Improvement of the sample stability, which is straight related with the microscope resolution, is also sought.

TECHNICAL SPECIFICATIONS

The main objective of the new design of the sample manipulator is to motorize the 6 degrees of freedom that allow the alignment of the sample with respect to the

microscope (main) objective lens (field of view). The motions must guarantee the correct positioning of the sample and repeatability while most of all ensuring stability, which directly influences the microscope resolution. Besides, a longer vertical movement is required in order to move the sample holder to the transfer position.

In addition, the existing liquid nitrogen cooling system has to be improved in order to obtain 100K at the sample.

The stage must be placed over the analyser chamber at the PEEM experimental station (Figure 1) so the overall system must be as compact as possible to reduce the mass over the chamber, maximize stability and leave free space for the surrounding instrumentation.

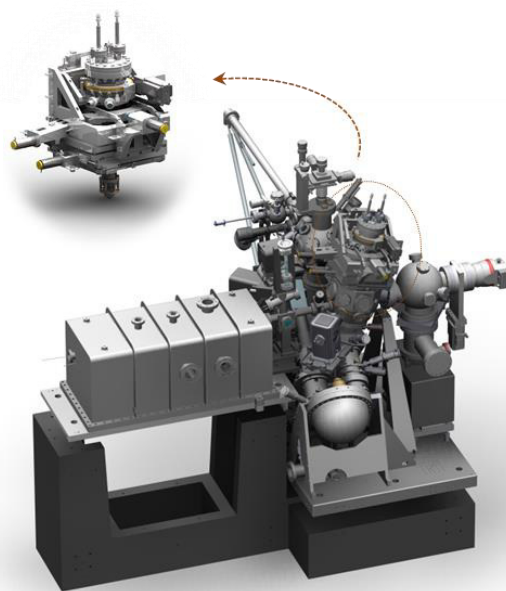


Figure 1: General view of the sample stage location at the PEEM End Station.

Moreover, the new sample stage must comply with the following specifications:

- To be UHV compatible and bakeable.
- To be compatible with the standard Elmitec sample holders.
- To keep 6 independent electrical contacts at High Voltage (20kV)
- Possibility to heat the sample up to 2000K.
- Possibility to cool the sample down to 100K.

† ngonzalez@cells.es

SYSTEM DESCRIPTION

Motion Stages

The presented solution consists of a horizontal stage in which the longitudinal and transversal linear movements are performed by high precision ball screws and cross roller linear guides.

Relative to the latter, a double angle goniometer mechanism enables the pitch and roll rotations. The linear motion on the ball screws is transmitted to the square frames guided by angular guides, which have the center of rotation at the intersection between the theoretical X ray beam and the objective axis. The small rotation between the ball screw nut and the angular motion is relieved by a double-flexure that enhances the stability of the system.

On top of the goniometer, the vertical stage is compounded by a high rigidity recirculating roller screw and cross roller guides. Finally, yaw rotation is provided by a commercial differentially pumped rotary stage.

All the movements (Figure 2) are actuated by low-backlash stepper motors and include encoder feedback. An edge welded bellow mounted on the manipulator base allows transmitting the movements in air to the sample support in UHV.

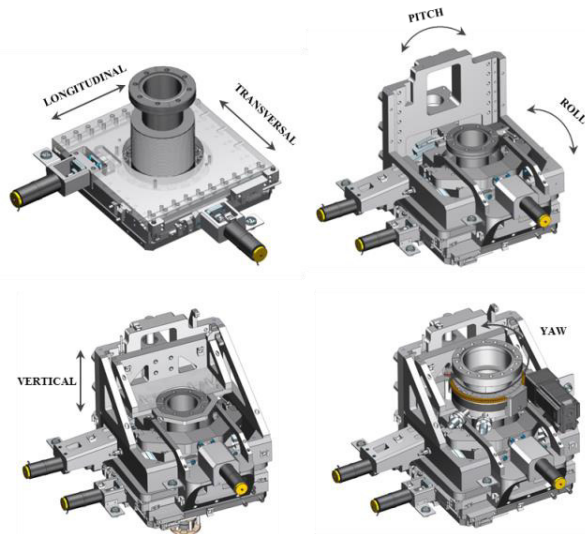


Figure 2: Pictures of the different stages that provide six degrees of freedom.

Sample Environment

The sample support (Figure 3) consists of a customized CF63 flange mounted on top of the rotary stage with a support tube in UHV that carries the sample holder interfaces at the tip in. The flange includes two CF25 flanges for the liquid nitrogen supply connections and the electrical connections at the tube end.

The sample tip, which has not been modified with respect to the existing design from Elmitec, includes 6 electrical contacts and it is connected to the support tube by means of a ceramic brazing that acts as electrical insulator. Besides, the sample holder interface is supported by 6 sapphire rods that also act as electrically

insulating thermal conductors in order to cool the sample holder support from the liquid nitrogen circuit.

The manipulator tip can be easily extracted for maintenance purposes without disassembling the manipulator mechanics.

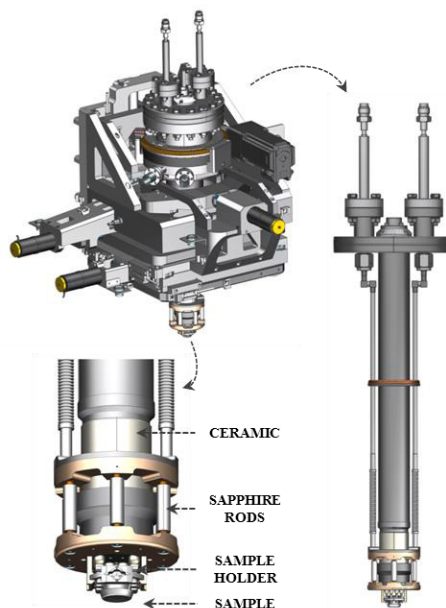


Figure 3: Pictures of the sample support.

Cooling Circuit

The cooling circuit has been upgraded so that the cooling pipes do not have any relative movements that could deteriorate the thermal conductivity up to the sample support. The tubes are connected to vacuum insulated VCR connections and they are linked to a liquid nitrogen reservoir that cools down the sample support by means of turbulence suppressive low-vibration hoses that absorb the thermal deformations of the tubes and reduce the vibrations caused by the liquid flow (Figure 4).

The use of feedthroughs designated for cryogenics should improve the long term reliability of this UHV seal, which has the risk of becoming leaky with time in the original design.

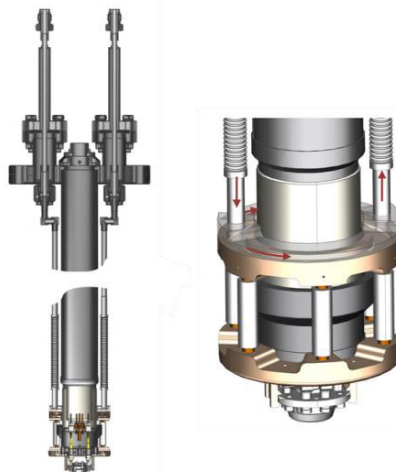


Figure 4: Liquid nitrogen cooling circuit.

SIMULATIONS

Static Behaviour

Different calculations by means of FEA have been done in order to achieve the standards of safety and technical specifications. Boundary conditions of gravity and vacuum forces were considered. The resulting displacement on the sample position (Figure 5) and maximum stress under static behaviour were 0.14 mm and 35 MPa respectively.

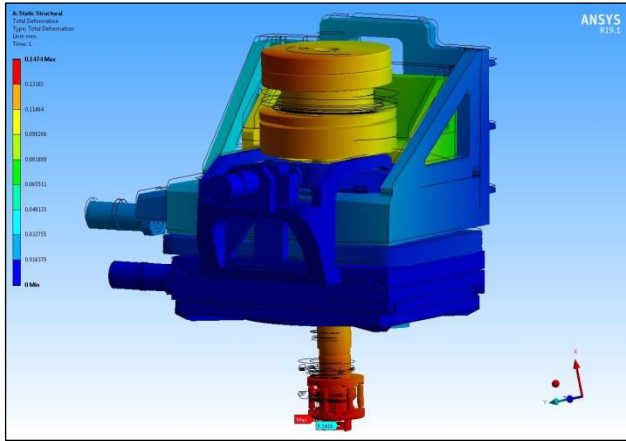


Figure 5: Displacement under static behaviour.

Regarding the stress on the flexures when pitch and roll are actuated, the resulting values were 830 MPa and 826 MPa respectively (Figure 6). Due to the critical stress that appeared on the flexure line, a high performance Cr-Mo-V steel alloy has been selected, which provides a yield strength of 1800 MPa.

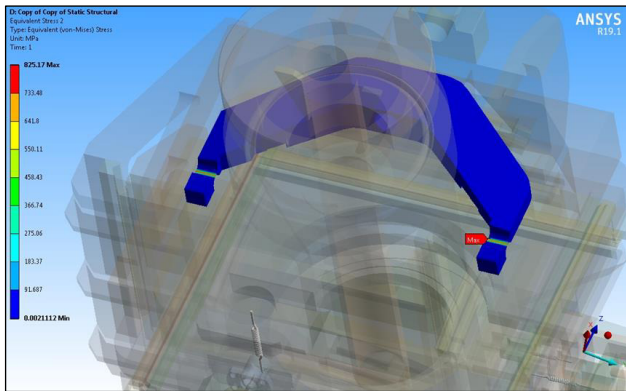


Figure 6: Stress on Roll Flexure.

Modal Analysis

Several FEA calculations studying the free vibration behaviour were done. Figure 7 shows the sample manipulator first and second resonance mode (RM). The resulting values were for 1st RM of 64.8 Hz and 2nd RM of 67.4 Hz. All values are shown in Table 1, corresponding to pitch and roll rotations on the sample respectively.

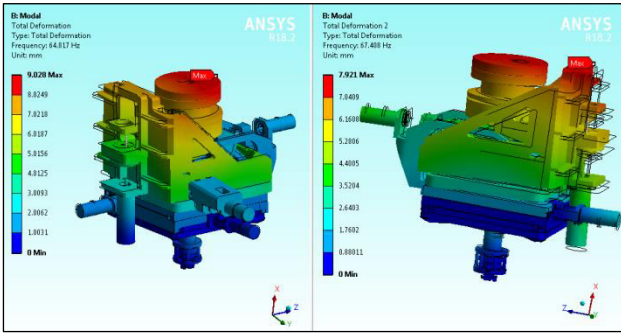


Figure 7: 1st and 2nd RM results.

Table 1: Sample Manipulator Resonance Modes

Mode	Frequency [Hz]
1	64.8
2	67.4
3	108.3
4	111.0
5	127.0
6	129.9

CONCLUSIONS

In conclusion, the development of this project has result in a compact and fully motorized 6-DoF sample manipulator. Keeping the UHV compatibility on the sample environment, enhanced functions have been integrated like the new cooling system and high precision and repeatable movements.

Even though the sample manipulator performance has been not tested yet, it is expected to obtain a maximized stability on the system, crucial to achieve the best spatial resolution on the PEEM station.

The accomplished requirements are shown at Table 2.

Table 2: Manipulator Motions Compliance Table

		Required	Accomplished
X and Y	Range	± 5 mm	± 5 mm
	Resolution	0.5 µm	0.2 µm
Vertical	Range	43.75 mm	57 mm
	Resolution	0.1 µm	0.035 µm
Roll and Pitch	Range	±2°	±2°
	Resolution	0.35 mrad	0.001 mrad
Yaw	Range	360°	360°
	Resolution	0.02°	<0.01°

The design, which is currently under production, will be tested and installed during the end of year 2018.

ACKNOWLEDGEMENTS

The authors wish to acknowledge all the ALBA staff involved in the design of the high precision sample stage, in particular, Marta Llonch, Jon Ladrera, Liudmila Nikitina, Gabriel Peña, Abel Fontseré, Fulvio Becheri, Josep Nicolás and Jordi Prat.

COMPACT MIRROR BENDER WITH SUB-NANOMETER ADAPTIVE CORRECTION CONTROL

N. González[†], J. González, C. Colldelram, J. Juanhuix, C. Ruget and J. Nicolas
 ALBA Synchrotron Light Source, 08290 Cerdanyola del Vallès, Barcelona, Catalonia, Spain

Abstract

We present a compact mirror bender with dynamic surface correction. The system is the evolution of an in-house development and will be the default focusing system for the new ALBA beamlines. The bender is now more compact and can introduce stronger curvatures, as required for microfocus applications. It allows for in-situ correction of the mirror surface, with resolution and stability below one nanometer. The bender can compensate parasitic deformations caused by thermal bumps, changes of focus, or stresses appeared during installation or bakeout.

INTRODUCTION

Surface quality of optical elements is essential to reach the performance of X-ray beamlines in 3rd and 4th generation synchrotron light sources and free electron lasers [1]. Mirror figure errors are usually the limit for the smallest achievable spot on sample and for the resolution of soft x-ray monochromators. In addition, they also limit the homogeneity of defocused beams [2,3]. In the last years, deterministic surface figuring techniques have been developed [4, 5], and sub-nanometer figure errors can be achieved by some mirror polishers [6]. On the other hand, beamline operation often requires certain adaptability: being able to change the focus position, tune the spot size, or compensate thermal bumps. This pushes for the development of active optics systems for x-ray mirrors, keeping the accuracy within the nanometer.

Existing active X-ray optical systems control the topography of the mirror surface by introducing deterministic deformation of its substrate. There are several systems that, to do this with sufficient resolution, use piezo-electric actuators [7-10]. Alternatively, the system we propose controls the deformation by applying point forces distributed along the substrate using spring-based mechanical correctors [11,12]. In order to achieve the required range, resolution, and stability of the applied force, we use a combination of springs and magnets as the elements generating the force.

Results obtained with a prototype demonstrate that the required mechanical performance is achieved, and is stable within several days.

SYSTEM DESCRIPTION

The mirror bender system we propose consists of three main parts: the frame that supports the bending actuators and the correctors, the bender actuators, that support and bend the mirror by applying forces at the ends of the mirror substrate, and the correctors, that apply smaller forces at

discrete points along the mirror (see Fig. 1). The whole system is ultra-high-vacuum (UHV) compatible.

The main frame consists of two thick plates that offer a stiff reference for the supports and for the correctors. The plates have multiple slots to allow placing the correctors at any position along the mirror substrate. The two bending actuators are located at the ends of the frame. They support the mirror and provide the bending forces. These actuators are designed to be compact in the direction of the beam, so the complete system is just 20 mm longer than the mirror substrate, and most of the length of the substrate is also clear to install correctors, or cooling pads. The bending actuators include the supports of the mirror, as well as the contacts that apply the bending force on the mirror. All these elements have rolled articulations to minimize parasitic forces that could be applied to the mirror substrate. In particular, all contact points between the bender and the mirror are free to pitch and roll, except one of the supports of the mirror, which is fixed in roll. This fixes the orientation of the mirror but avoids introducing any parasitic twist. Also, all contact surfaces are cylindrical, in order to have a reproducible contact point on the mirror, with acceptable contact stress.

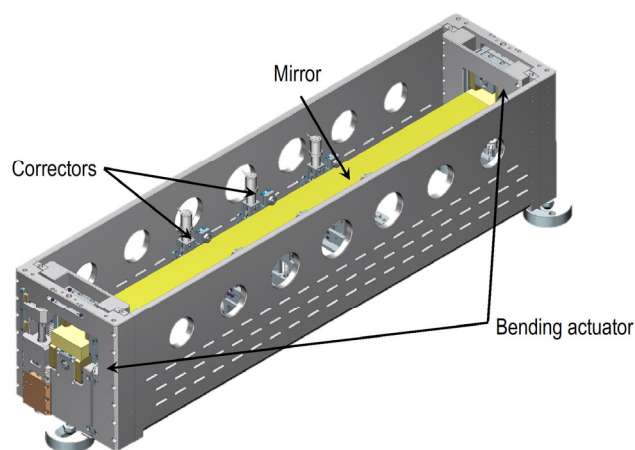


Figure 1. Illustration of the bender prototype, indicating the positions of the bending actuators and of the point correctors.

The bending force applied to each end of the mirror substrate is generated by compressing two helical springs which are connected on one end to a linear stage driven by a stepper motor, and to the mirror on the other end. In addition, the link between the spring and the mirror includes a load cell that provides feedback of the force applied to the mirror. The load cell is placed between braided cables, that compensate any misalignment that could introduce errors on the measurement of force. The load cell resolution is 0.01 N, which corresponds to a 0.5% error in a 100 km

[†]ngonzalez@cells.es

radius mirror. The resolution of the actuator is actually 0.00055 N per motor step. On the other hand, the maximum force the bender actuators can apply is 1000 N, enough to bend a mirror to a radius in the order of few hundred meters.

The correctors are mechanical modules that can be attached to the frame of the bender, underneath the mirror substrate, and that apply a force normal to the mirror surface. The force is generated by stretching a long spring and is transmitted to the mirror by a lever that can pull or push the mirror, depending on the configuration of the spring. The link between the lever and the mirror is also articulated to minimize any parasitic force, and all articulations are rolled to minimize friction. The width of the corrector is minimized to 22 mm, to allow allocating many correctors. The stretching of the spring is controlled by a simple linear motion system, motorized by a stepper motor.

The force applied by each corrector is stabilized against mechanical drifts of the mirror or support, by a pair of magnets installed at one end of the lever arm. The total force applied to the mirror is the sum of the forces exerted by the spring and by the magnets. However, while the spring force increases with the elongation, the magnetic force decreases with the gap (see Fig. 2). So, mechanical drifts of the mirror with respect to the corrector, which alter equally the elongation of the mirror and the gap between magnets, provoke force drifts of opposite sign on the spring and magnets. The gap between the magnets can be adjusted to match the stiffness of the spring at the nominal position of the mirror, so that the force drifts of the spring are exactly compensated by those of the magnets. Once the magnets are adjusted, the force applied to the mirror can be tuned by adjusting the elongation of the spring, using the corresponding stepper motor. This provides stability of the mirror correction against drifts occurred during installation, transport or during operation.

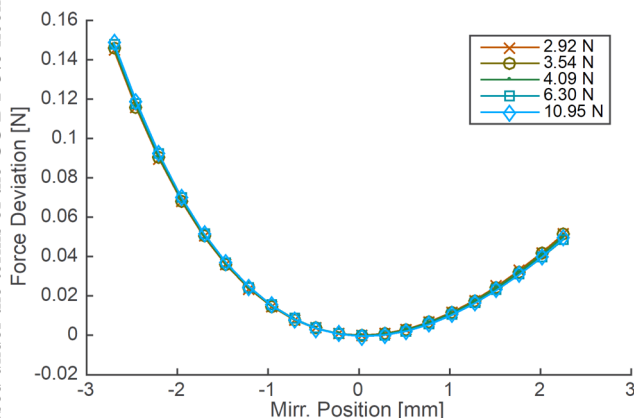


Figure 2. Deviation of the corrector force as a function of the position of the application point, measured for 5 different values of the nominal force.

The force stabilization solution has been tested in a laboratory prototype. In this case, the force applied by the corrector is measured by a load cell, with a resolution of 0.001 N. The position of the application point is scanned

using a motorized linear stage. The load cell is placed between the linear stage and the mirror contact of the corrector, which is the force application point. In order to test the stability of the point where the system is stable, the same experiment is repeated for different elongations of the spring, which are adjusted using the stepper motor of the corrector.

The corresponding results are given in Fig. 2. There, the deviation from the nominal force is represented as a function of the position of the application point. One can see that the force deviation presents a minimum at the mirror nominal position, and that in a range of 2 mm around it, the total drift of the force stays below 0.02 N. Note also that the position of such minimum does not depend on the nominal force. This means that once the magnet gap is optimized, the nominal force can be tuned by changing the elongation of the spring, while preserving the position where the stability is optimal.

The mechanical performance of the correctors has been characterized in a test bench that measures the force applied by the corrector. In particular, the resolution of the actuator has been proved to be better than 0.001 N, as shown in Fig. 3.

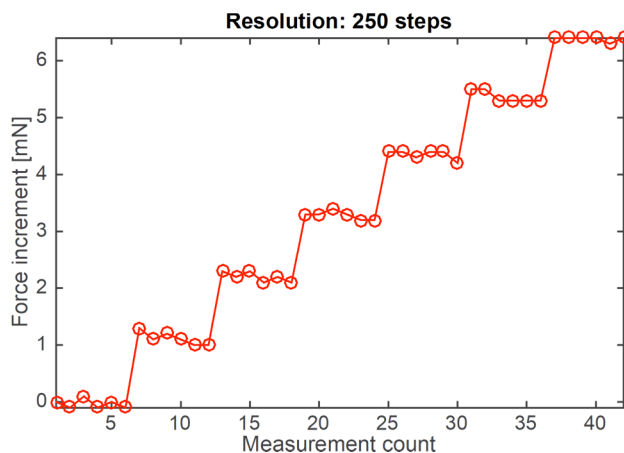


Figure 3. Resolution test results of the corrector.

CORRECTION RESULTS

The correction principle has been demonstrated in a prototype of the system. A mirror with a figure error of 23 nm rms (root mean square), equivalent to a slope error of 0.87 μ rad rms, has been corrected to 0.86 nm rms (0.115 μ rad rms) (see Fig. 4). Only four actuators at optimal longitudinal positions have been required for this case. The correction is based on the surface height profile as measured by the ALBA-NOM. The difference between the reached figure and the target figure (blue line) is 0.08 nm rms.

We have also verified that the correction is preserved when the radius of curvature of the mirror is changed. Fig. 5 shows measurements of the residual height profile for three different radii of curvature of the mirror. The total variation of the radius is 35%. One can see that the three

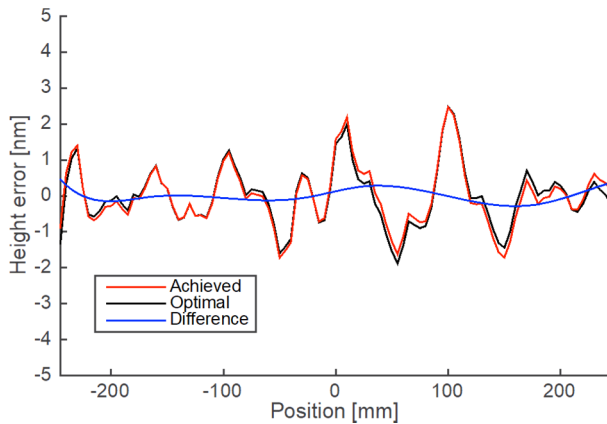


Figure 4. Mirror figure correction. The red line shows the achieved correction. The black line corresponds to the best possible figure according to the deformation model. The blue line corresponds to the difference among the two. The shadowed regions around the blue and red line indicate the repeatability of the measurement.

measurements overlap each other within the nanometer. The different measurements were taken in a lapse of 5 days, which indicates that the correction is also stable in that period of time.

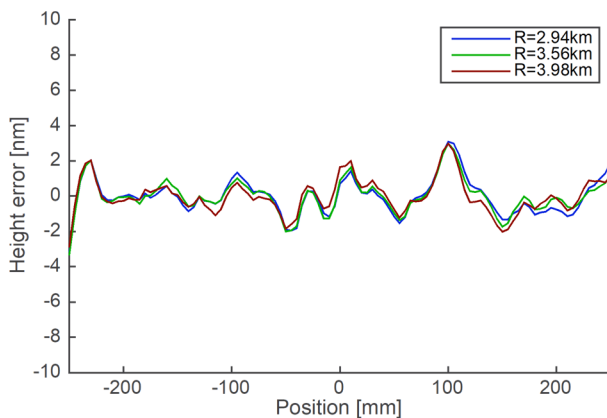


Figure 5. Residual height profile for three different radii of curvature. Corresponding to a difference of 35%.

CONCLUSION

We present a mechanical mirror bender capable of correcting the figure errors below 1 nm rms. The system is fully UHV compatible, and special care has been taken on minimizing the dimensions of the system.

The mirror bender provides bending actuators with force feedback, capable of bending the mirror to the required elliptical figure. In addition to the main bending actuators, the system has additional figure correctors that introduce local deformation of the mirror substrate. The system has been designed to provide high stability of the obtained figure by stabilizing the forces applied on the mirror in front of possible dimensional drifts of the mechanics.

A prototype has been optimized to surface error of 0.86 nm rms, starting from a moderate quality mirror

blank. The residual figure error corresponds to high spatial frequencies. The agreement between the achieved results and the theoretical optimal profile agree within 0.08 nm rms. And the correction is shown to be stable in front of changes of curvature as well as in time.

ACKNOWLEDGEMENTS

This work is partially funded by MINECO under contract FIS2015-66328-C3-2-R and by ERDF funds.

REFERENCES

- [1] D. Cocco, "Recent Developments in UV Optics for Ultra-Short, Ultra-Intense Coherent Light Source," *Photonics*, vol. 2, Jan. 2015, pp. 40-49.
- [2] J. Nicolas and G. García, "Modulation of intensity in defocused beams," in *Proc. SPIE 8848, Sept. 2013*, pp. 884810, doi:10.1117/12.2024528
- [3] J. P. Sutter, S. G. Alcock, F. Rust, H. Wang, and K. Sawhney, "Structure in defocused beams of X-ray mirrors: causes and possible solutions," in *Proc. SPIE 9208*, pp. 92080G, Sept. 2014, doi:10.1117/12.2061941
- [4] M. Weiser, "Ion beam figuring for lithography optics," *Nucl. Instrum. Methods Phys. Res. B*, vol. 267, iss. 8-9, May 2009, pp. 1390-1393, doi:10.1016/j.nimb.2009.01.051
- [5] J. Susini, D. Laberge, and L. Zhang, "Compact active/adaptive x-ray mirror: Bimorph piezoelectric flexible mirror," *Rev. Sci. Instrum.* vol. 66, iss. 2, pp. 2229-2231 (1995), doi:10.1063/1.1145715
- [6] K. Yamauchi, H. Mimura, K. Inagaki, and Y. Mori, "Figuring with subnanometer-level accuracy by numerically controlled elastic emission machining," *Rev. Sci. Instrum.*, vol. 73, iss. 11, 2002, pp. 4028-4033, doi:10.1063/1.1510573
- [7] R. Signorato, O. Hignette, and J. Goulon, "Multi-segmented piezoelectric mirrors as active/adaptive optics components," *J. Synchrotron Rad.*, vol. 5, issue 3, pp. 797-800, (1998), doi:10.1107/S0909049597012843
- [8] R. Signorato and T. Ishikawa, "R&D on third generation multi-segmented piezoelectric bimorph mirror substrates at Spring-8," *Nucl. Instrum. Methods Phys. Res. A*, vol. 467-468, part 1, 2001, pp. 271-274, doi:10.1016/S0168-9002(01)00297-2
- [9] C. Svetina, D. Cocco, A. Di Cicco, C. Fava, S. Gerusina, R. Gobessi, *et al.*, "An active optics system for EUV/soft x-ray beam shaping," *Proc. SPIE*, vol. 8503, 2012, pp. 850302, doi: 10.1117/12.929701
- [10] L. A. Poyneer, T. Pardini, T. McCarville, D. Palmer, and A. Brooks, "Control of a 45-cm long x-ray deformable mirror with either external or internal metrology," *Proc. SPIE* vol. 9208, 2014, pp. 92080F, DOI: 10.1117/12.2062072
- [11] M. Idir, P. Mercère, M. H. Modi, G. Dovillaire, X. Leveq, S. Bucourt, L. Escolano, and P. Sauvageot, "X-ray active mirror coupled with a Hartmann wavefront sensor," *Nucl. Instrum. Methods Phys. Res. A*, vol. 616 (2-3), 2010, doi:10.1016/j.nima.2009.10.168
- [12] J. Nicolas, C. Ruget, J. Juanhuix, J. Benach, and S. Ferrer, "Focusing and defocusing using mechanically corrected mirrors at the MX beamline at Alba," *J. Phys.: Conf. Ser.* vol. 425, part 5, 2013, 052016, doi: 10.1088/1742-6596/425/5/052016

NCD-SWEET BEAMLINE UPGRADE

J.B. González*, N. González, C. Colldelram, L. Ribó, A. Fontserè, G. Jover -Manas, J. Villanueva, M. Llonch, G. Peña, A. Gevorgyan, Y. Nikitin, J.C. Martínez, C. Kamma-Lorger, E. Solano, I. Sics, S. Ferrer, M. Malfois
 ALBA Synchrotron Light Source, Cerdanyola del Valles, Spain

Abstract

The SAXS/WAXS Experimental End sTation (NCD-SWEET) at ALBA Synchrotron has undergone major improvements in three main areas, beam performance, SAXS detector data quality and beamline operability, in order to perform state-of-the-art SAXS/WAXS experiments. A new channel-cut monochromator system has improved the beam quality and stability, with current vibration amplitudes under 1% of the beam size. Two sets of refractive beryllium lenses have been installed for focussing the beam. One of the sets allows to microfocus the beam size. Besides this, the former SAXS CCD detector has been replaced by a single-photon counting pixel detector, a Piltatus3 S 1M. In the end station, a full re-design of the mechanical elements with sub-micron resolution movements together with the installation of new equipment has been completed, resulting in an improved beamline configuration, and a faster and safer rearrangement of the flight tube length. New upgraded configuration also allows for GISAXS experiments. Finally, other auxiliary improvements have been done in areas like radiation protection, air conditioning, health and safety, cable management, electronics and control.

INTRODUCTION

The NCD-SWEET beamline is dedicated to Small Angle X-ray Scattering (SAXS) and Wide Angle X-ray Scattering (WAXS) experiments at ALBA Synchrotron. SAXS experiments provide structural and dynamics information from coherently scattering entities within sample at a longer length-scale (up to several hundreds of nm). E.g. large molecular assemblies, fibres or higher order structures of proteins and polymers can be explored by this technique. WAXS technique explores structure at shorter length scales on the order of Angstroms. In addition, one of the objectives of the upgrade of beamline was to make it suitable for Grazing-Incidence Small-Angle Scattering (GISAXS) experiments which are being implemented at present.

The End Station of the beamline includes the last downstream section of beam conditioning optics, a sample environment, two detectors (SAXS and WAXS) and a flight tube on rails that permits changing the camera length and minimizing the air gap between the samples and the SAXS detector (Fig. 1).

Following some years of operations of NCD beamline, Scientific Advisory Committee suggested to perform an

upgrade of the beamline in order to improve its performance. After review process by a panel of experts as well as internal discussions, a major project was developed in order to achieve the state-of-the-art for SAXS/WAXS experiments at the beamline. Present paper discusses this multidisciplinary project including all of the changes made and features added to the beamline.



Figure 1: NCD-SWEET End Station.

BEAM PERFORMANCE

In the past, NCD beamline experienced poor beam stability due to undesired vibration in the double crystal monochromator system. In order to resolve this stability issue, the former double crystal monochromator (DCM) system has been replaced with a new channel-cut system while keeping the vacuum vessel, Bragg angle goniometer and other interfaces (Fig. 2). As a result, stability has improved substantially with current vibration amplitudes under 1% of the beam size instead of 39% before the change.



Figure 2: Channel-cut monochromator system.

In addition, two sets of refractive beryllium lenses have been installed for focussing the x-ray beam. One set is located in the Optics Hutch section of the layout while the second in the End Station of the beamline. The latter enables achieving microfocus beam size at the sample position (although with the associated loss in the flux). Addition of these beryllium lenses allows for switching between the existing toroidal-collimating mirror optics

* jgonzalez@cells.es

and refractive lens optics. Consequently, the most suitable focussing configuration can be chosen depending on user.

SAXS DETECTOR DATA QUALITY

The former SAXS detector ADSC Q210R suffered a total malfunction in 2015 and was replaced with an aging ADSC Q310r kindly provided by ESRF. As a part of the upgrade project, this last detector was replaced with a new single-photon counting pixel detector Piltatus3 S 1M. This new detector has considerably improved the operation reliability of the beamline and data quality.

A new positioning table (Fig. 3) was designed and built for housing the SAXS detector, in replacement of the previously used support. This positioning table, enabling vertical, lateral and pitch movements, is based on the in-house developed “skin” concept design which provides high stability and excellent resolution performances [1]. Table consists of a sturdy granite block, two movable lateral plates driven by ball screws with linear guides actuated by stepper motors. Both lateral plates are linked together by a top plate articulated by flexure hinges, providing vertical and pitch motions. Another motion system with similar mechanics is added on top of the previously described one, providing lateral movement. Granite block functions as a stable and stiff reference for the rest of the mechanics. Ball screws have low axial clearance in order to assure good repeatability while linear guides are slightly preloaded for stiffness purposes. Metrology tests of the table movements showed sub-micron resolution and notable repeatability values (see Table 1). Finite element analysis (FEA) was performed in order to study the structural and vibration behaviour of the system (Table 2).



Figure 3: SAXS detector and flight tube in the End Station.

The SAXS detector table is able to accommodate up to two detectors for any x-ray detector currently available on the market by only changing the interface between the table and the detector.

In addition, the original WAXS detector support has been totally redesigned. The newly designed system permits ninety degrees of roll movement and includes insertion movement to adjust the detector position with respect to the sample. The active imaging area of the detector is tilted a 30 degrees fixed angle with respect to the vertical plane of the sample.

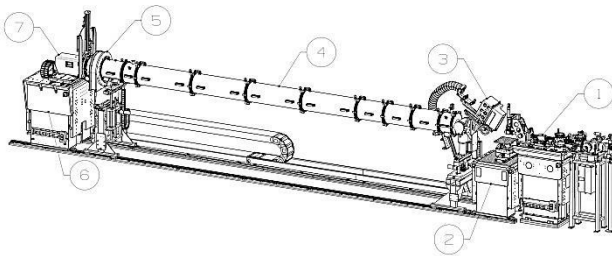


Figure 4: End Station parts breakdown. (1) BCO, (2) sample table, (3) WAXS detector, (4) flight tube, (5) beamstops, (6) SAXS detector table, (7) SAXS detector.

BEAMLINE OPERABILITY

Apart from the changes and modifications in the individual elements of the layout within the End Station (Fig. 4), the one significant is the change of SAXS *modus operandi*. Originally, SAXS detector was at fixed position while sample environment (and WAXS setup) was translated along the x-ray beam for different flight tube lengths. After years of operations it was concluded that this mode of operations is detrimental to the performance of the beamline by complicating the switching between different configurations of the SAXS experiments and reducing versatility of the beamline. New *modus operandi* involves translation of the SAXS detector assembly for different flight tube configurations, while sample environment platform is mostly stationary.

Table 1: Table Metrology Results

SAXS Detector Table			
	Range	Resolution	Repeatability
Vertical	300 mm	0.313 μm	5.934 μm
Lateral	515.5 mm	0.781 μm	0.859 μm
Pitch	± 7 mrad	0.78 μrad	-
BCO			
	Range	Resolution	Repeatability
Vertical	90 mm	0.125 μm	2.016 μm
Lateral	40 mm	0.313 μm	0.598 μm
Pitch	± 9.2 mrad	0.125 μrad	0.702 μrad
Yaw	± 14.6 mrad	0.313 μrad	1.259 μrad
Sample Table			
	Range	Resolution	Repeatability
Vertical	200 mm	0.195 μm	1.225 μm
Pitch	± 87 mrad	0.27 μrad	2.063 μrad

When the End Station is considered (Fig. 1), support structures of the main element have been replaced by new designs. A new beam conditioning optics (BCO) table [2] and new sample table have been built and metrology tested (Table 1). The sample table permits vertical, and pitch movements, and the table consists of a granite block, two lateral plates driven by ball screws with linear guides actuated by stepper motors. Both lateral plates are linked together by a top plate articulated by tapered roller bearings. The BCO assembly includes a fast shutter, a set

of commercial guard slits, a diagnostic unit comprising three filters and a four-quadrant transmissive photodiode and finally a set of refractive beryllium lenses for micro focussing of the beam.

A set of commercial translation stages have been integrated on the top of the sample table for precise positioning of elements (Fig. 5). These stages permit vertical, lateral, pitch and yaw fine adjustments. Two motorized beamstops have been installed downstream in the flight tube. The first one is a tungsten cylinder block with a photodiode incorporated inside [3] provided with X-Y positioning motion, while the second is a tungsten rod with lateral motorization. All of these improvements, apart from enhancing the original SAXS-WAXS capability, make the End Station suitable for GISAXS experiments.

An originally installed vacuum delay line system has been removed from the optical layout in the End Station, increasing the maximum length of the flight tube. The new configuration of the End Station with a stationary sample and a moving SAXS detector, along with other safety and usability enhancements has reduced the time required to change the flight tube length by 18h. Additionally, a new safety shutter has been installed in the downstream kapton window assembly of the flight tube.

Table 2: FEA Results

	Max. Stress	Max. Deformation	1 st Mode of vibration
SAXS Table	10 MPa	100 µm	28.9 Hz
BCO Table	20 MPa	45 µm	59 Hz
Sample Table	17.5 MPa	78 µm	45.7 Hz

AUXILIARY PROJECTS

The fulfilment of all the requirements of the main project has required large developments in other important areas of the beamline. The switch to a channel-cut monochromator system has compelled an update of some radiation protection shielding elements and required installation of a new bremsstrahlung radiation stop.

Besides, the cryocooler for the liquid nitrogen cooling of the monochromator, originally positioned inside the Optics Hutch, has been moved outside of the hutch with a new chicane for cryogenic hoses. This solution has improved safety by dropping the nitrogen concentration and decreasing vibration sources inside the Optics Hutch.

New air conditioning equipment has been installed in the roof of the Experimental Hutch with an air sock distribution system in order to control the uniformity of temperature inside the hutch.

General work on the cable management and electronics has been performed with all new equipment, including a main cable chain in the End Station in order to relieve cables during camera length changes. And finally, the integration of all of the new equipment has involved gen-

eral changes in the control system of the beamline, especially in the equipment protection system.

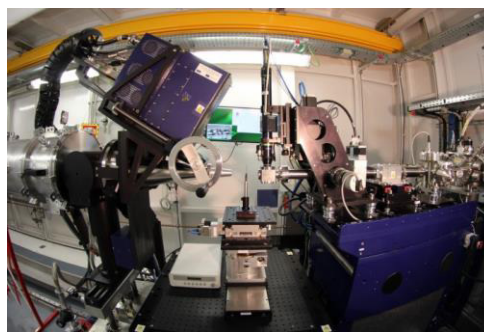


Figure 5: Sample environment in the End Station.

CONCLUSIONS

In summary, the NCD-SWEET beamline has undergone major improvements in beam performance, SAXS detector data quality and beamline operability, as well as developments in other auxiliary areas. All the described works, carried out during implementation of the project, enable beamline to perform state-of-the-art SAXS/WAXS experiments and implement GISAXS technique.

ACKNOWLEDGEMENT

The authors wish to acknowledge all those most involved in the design, construction and testing: NCD-SWEET Beamline Staff, Francesc Farré; Technical Office, Llibert Ribó and Alejandro Crisol; Mechanical Workshop, José Ferrer, Jordi Navarro, Karim Maimouni, Raúl Lorenzo, Manuel Murcia and Oscar Borrego; Electronics Section, Alberto Ruz, Bern Saló, Bernat Molas, Cristian Pérez, Joan Pagès, Jose Avila, Sergio Astorga, Xavier Serra, Óscar Matilla, Antonio Camps, Manel Baena, Domingo Alloza and Roberto Petrocelli; Control Systems, Alberto Rubio; Engineering Alignment Group, Jon Ladrera; Vacuum Group, Raquel Monge, David Calderón, and Lluís Ginés; Infrastructure Section, Jordi Iglesias and Pablo Jiménez; Optics, Development & Innovation Section, Pablo Pedreira and Josep Nicolàs; Health and Safety Group, María José García, Arnaud Devienne, Jose Aguil-lar and Carme Mármol.

REFERENCES

- [1] C. Colldelram, C. Ruget and L. Nikitina, "ALBA XALOC beamline diffractometer table skin concept", in *Proc MEDSI'10*, Oxfordshire, UK, July 2010, Vol 1, paper e44, doi:10.1017/S2044820110000754
- [2] N. González *et al.*, "Beam Conditioning Optics at the ALBA NCD-SWEET Beamline", presented at MEDSI'18, Paris, France, June 2018, paper THPH14, this conference.
- [3] J. González *et al.*, "Two-rotation Mechanism for an in Vacuum Beamstop", in *Proc MEDSI'16*, Barcelona, Spain, Sep. 2016, pp. 378-380, doi:10.18429/JACoW-MEDSI2016- WEPE40

A MULTI-SAMPLE HOLDER FOR THE MSPD BEAMLINE AT ALBA

J.B. González*, F. Farré, X. Serra, D. Roldán, P. Pedreira, F. Fauth,
 ALBA Synchrotron Light Source, Cerdanyola del Valles, Spain

Abstract

At the high resolution powder diffraction end station of the Materials Science and Powder Diffraction (MSPD) beamline at ALBA Synchrotron, several samples are measured on a daily basis. Thus, an automatic sample exchanger is a great asset to the beamline, permitting a more efficient use of beam time. Even if a robot arm is the more suitable option for a sample exchanger device, in terms of cost, compactness and versatility MSPD needs another approach. ALBA engineering division has developed a multi-sample holder that allows the loading of up to eight samples and exchanging between them with a resolution of less than a micron. This new design consists of a customized and motorized linear stage that has been designed to fit into the present three-circles diffractometer, on top of the positioning stages, avoiding any possible collision with the Eulerian cradle. In addition, this new holder permits the use of different types of samples like capillaries in fast spinners, coin cell batteries and electrochemical cells. Finally, the system is compatible with the usual sample conditioning equipment on the end station such as the hot blower, cryostream, beamstop, chiller, etc.

DESIGN

The multi-sample holder consists of a customized and motorized linear stage (Fig. 1). The mechanism involves a ball screw and linear guides together actuated by a stepper motor. The ball screw presents low axial clearance (less than 5 μm) in order to assure good repeatability and the linear guides are slightly preloaded for stiffness purpose.

Due to space restriction on top of the positioning stages of the present three-circles diffractometer, the multi-sample holder has been designed to be as narrow as possible (up to 31.5 mm) in order to not shadow the Mythen and Multicrystal Analyser detectors (Fig. 2). Also the system has been designed to avoid any possible collision with the Eulerian cradle.

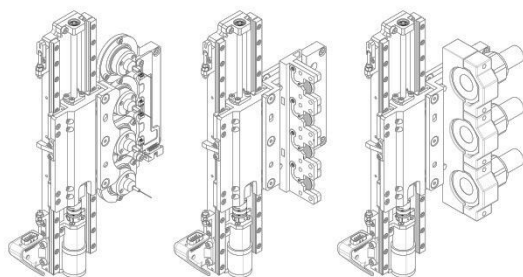


Figure 1: Multi sample holder in three configurations.

The multi sample holder permits the use of different types of samples like capillaries in fast spinners, coin cell

batteries and electrochemical cells. For this purpose, a common interface is used for all sample holders, consisting of a plate with positioning pins and fixed by screws. This common interface will be compatible with all future sample developments in the beamline.

Finally, the complete system is suitable for sample conditioning equipment use on the end station such as the hot blower, cryostream, beamstop, chiller, etc. during normal operation.

TECHNICAL SPECIFICATIONS

The multi sample holder complies with the following specifications:

- Linear resolution of 0.3 μm .
- Repeatability of 0.75 μm .
- Range of 166mm (± 83 mm).
- Compact and integrated in the Eulerian cradle.
- Compatible with sample conditioning equipment.
- It provides 4 positions for coin cell batteries.
- It provides 3 positions for electrochemical cells.
- It provides 4 positions for fast spinners in its current design or 8 in a new configuration in development.

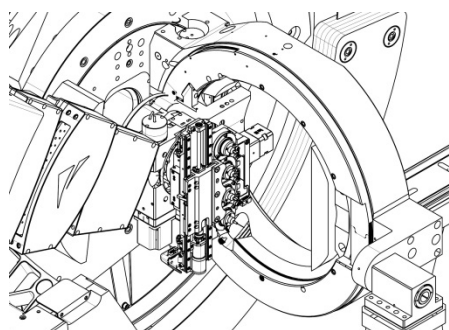


Figure 2: Multi sample holder on Eulerian cradle.

METROLOGY RESULTS

Metrology tests have been performed using a Renishaw ML10 Interferometer in order to evaluate the resolution, repeatability and other characteristics of the motion of the multi-sample holder in open loop.

Table 1: Metrology Results

Explored Range	0.156 m
Avg. resolution	0.1562 $\mu\text{m}/\text{hs}$
Backlash/Hysteresis	2.32 μm
Repeatability	0.75 μm
Linearity	4.39 μm
Sampling noise	18 nm

* jgonzalez@cells.es

The position error versus the motor position has been measured (Fig. 3), obtaining results in average resolution, hysteresis, repeatability and linearity (Table 1). Additionally, resolution tests in dynamic mode have been performed to test the mechanical response of the system to the minimum achievable step size.

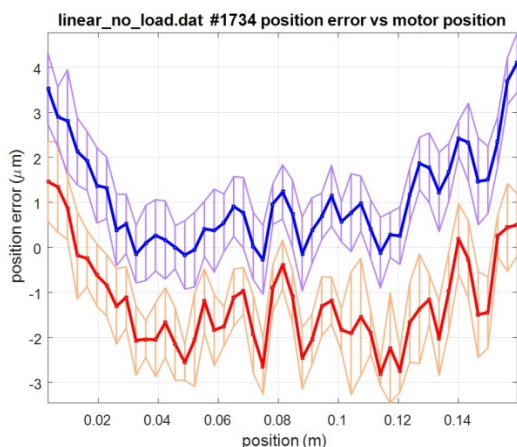


Figure 3: Position error vs motor position.

CONCLUSION

In conclusion, ALBA engineering division has developed the design of a multi-sample holder based in a linear stage mechanism that allows the loading of up to eight samples and exchanging between them with a resolution of less a micron, integrated in the high resolution powder diffraction end station.

This solution permits faster operation of the end station and a more efficient use of beam time in the MSPD beam-line.

ACKNOWLEDGEMENT

The authors wish to acknowledge all those most involved in the design, construction and test: Mechanical Engineers, Llibert Ribó and Edmundo Fraga; Mechanical Workshop, Jordi Navarro and José Ferrer; Electronics Section, Sergio Astorga; Optics, Development & Innovation Section, P. de la Rubia and Josep Nicolàs.

ENGINEERING DESIGN OF THE PDF & XPD BEAMLINE SAMPLE ENVIRONMENT FOR SAFE EXPERIMENTAL USE OF HAZARDOUS GASES

Edwin Haas, A. M. Milinda Abeykoon, PhD, Scott Buda, Eric Dooryhee, PhD, Sanjit Ghose, PhD,
 Christopher Stelmach, John Trunk, National Synchrotron Light Source II, Brookhaven National
 Laboratory, Upton, New York, 11973 U.S.A.

Abstract

The Pair Distribution Function (PDF) and X-ray Powder Diffraction (XPD) beamlines located at the 28-ID at Brookhaven National Laboratory's (BNL) National Synchrotron Light Source II (NSLS-II) require a means for safely supplying, containing, and exhausting hazardous gases to and from experimental samples. The PDF/XPD sample environment includes a sample holder, internal beam stop, sample chamber, and stages that provide eight degrees of freedom. A specially-designed window is also included for maximum X-ray transmission at minimum cost. Sensors, flow metering devices, and circuitry are included to provide proper purging, control hazardous and dilution gas flows, and integrate the safeguards needed for safe operation.

INTRODUCTION

The PDF and XPD beamlines collect X-ray pair distribution function and diffraction data from samples using high energy (i.e. > 25 keV) X-rays. A specially-designed Gas Handling System (GHS, see Acknowledgments) supplies a variety of hazardous and non-hazardous gases to an outlet port for in-situ and in-operando studies of chemical reactions. A specially-designed sample environment is needed to contain and supply gases to experimental samples, position samples quickly, accurately, and remotely, collect scattered X-rays over a wide-angle without distortion, dilute hazardous gases after flowing through the samples, and then safely exhaust the gas mixtures. Excluding inert and non-reactive gases, the GHS supplies hydrogen, methane, ethylene, oxygen, carbon monoxide, NO_x, SO_x, and CH₃S_x (e.g. methyl mercaptan and methional) gases and mixtures.

SAMPLE ENVIRONMENT DESIGN

The sample environment includes: a sample chamber, a sample holder and sample, an internal beam stop, and stages to remotely position the sample, sample chamber, and beam stop. The samples are contained in capillary tubes and retained by miniature collets in a holder designed to allow gases to pass through the samples. The sample chamber is vented externally and inert gas dilutes hazardous gases after flowing past each sample. Seals and materials are compatible with the gases used, and the sample chamber has windows to cost-effectively allow entrance of a .5 mm x .5 mm X-ray photon beam and undistorted exit of scattered X-rays over a wide ($\pm 30^\circ$)

angle from the sample center. Lastly, the sample environment requires similar protections and safety provisions as the GHS. Two cameras, a goniometer, and X, Y, and Z stages are used to align the capillary tubes. Once aligned, electrical power is disconnected for safe operation when using flammable gases. The sample chamber is large enough to contain a goniometer and an internal beam stop (to prevent X-ray scatter from the downstream window) yet small enough for $\pm 30^\circ$ unobscured collection of scattered X-rays. An image of the sample environment is shown in Figure 1.

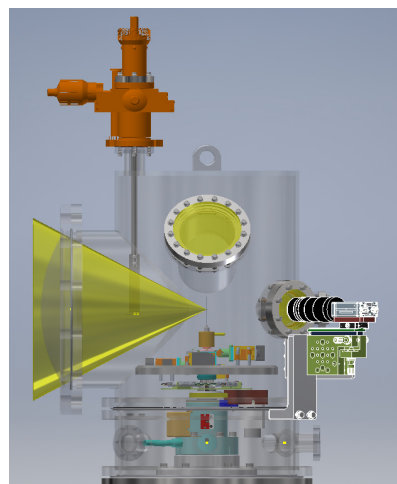


Figure 1: Sample environment with transparent sample chamber and $\pm 30^\circ$ scattered X-ray exit cone.

The X-ray sample chamber is composed of two sections, the upper section has an upstream Be window for monochromatic photon beam input, a large port downstream to collect scattered X-ray data, an internal beam stop (with remote X and Y stages), two camera ports, and a view port. It connects to a lower spool section which contains the feedthroughs for gas inputs, exhaust, sensors, electrical power, and controls. The upper section can be removed quickly for non-hazardous gas experimental use.

To meet BNL safety requirements, the sample chamber materials must be compatible with all gases used and the chamber must withstand 1 atmosphere external pressure (and internal vacuum for leak-check verification) with a safety factor of 3.0 on yield stress. The chamber wall thicknesses were determined by iterative finite element analysis (FEA) modeling using standard material stock sizes. Since all gases used are compatible with stainless steel, 304/304L stainless steel

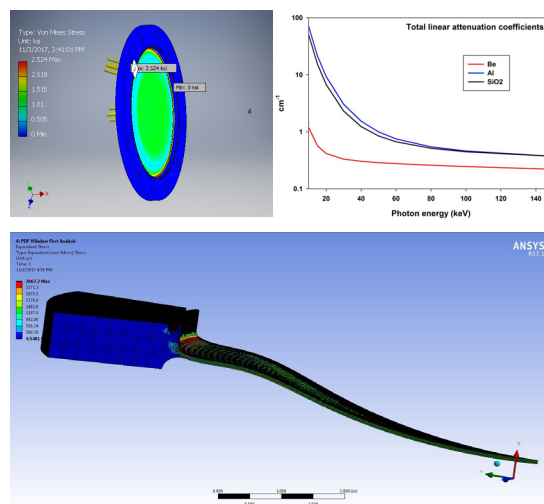
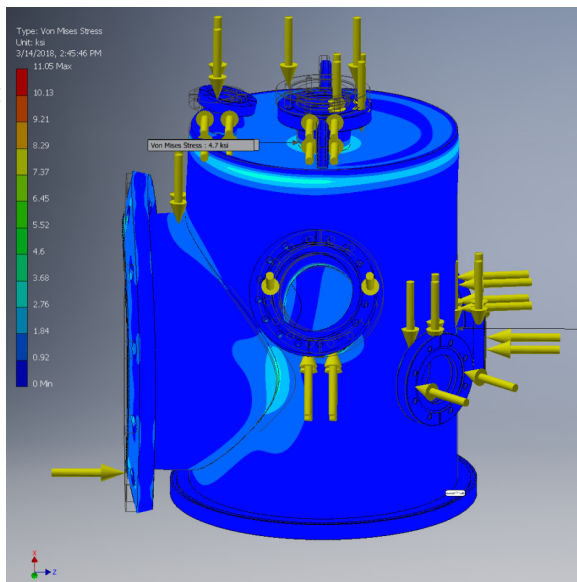


Table 1: Flammable and Explosive Gas Dilutions

Gas	LFL/LEL (% volume of air)	Gas Flow (SCFM inert, ml/min Haz)
Hydrogen (H ₂)	4 / 18.3	0.042 @ 50 ml/min
Methane (CH ₄)	5 / -	0.034 @ 50 ml/min
Ethylene (C ₂ H ₄)	2.7 / -	10 @ 50 ml/min
Methional (CH ₃ SCH)	3.9 / -	10 @ 3.6 ml/min

Table 2: Toxic Gas Dilutions

Gas	REL EL (PPM)	TLV (PPM)	LC ₅₀ /100 (PPM)	Gas Flow (SCFM inert, ml/min Haz)
Carbon Monoxide (CO)	35 \ 50	25 TWA	37.6	10 @ 7 ml/min
Nitric Oxide (NO)	25 \ 25	25 TWA	1.15	10 @ 0.3 ml/min
Nitrogen Dioxide (NO ₂)	1 \ 5	0.2 TWA	1.15	10 @ 0.06 ml/min
Sulfur Dioxide (SO ₂)	2 \ 5	.25 STEL	25.2	10 @ 0.07 ml/min
Ethylene (C ₂ H ₄)	200 \ Not Found	200 TWA	Not Found	10 @ 57 ml/min
Methional (CH ₃ SCH)	Not found	Not found	12.67	10 @ 3.6 ml/min
Methyl Mercaptan (CH ₃ SH)	0.5 / 10	0.5	13.5	10 @ 0.14 ml/min

Two gases (ethylene and methional) used are both toxic and flammable and are therefore listed in both tables. The PDF and XPD beamlines will use boil-off gaseous nitrogen (GN₂) from the NSLS-II utility system. The NSLS-II GN₂ system should provide adequate flow for nearly continuous 10 SCFM flow without the need to change compressed gas cylinders. During experimental operations, minimal down-time is desirable for recurring tasks such as sample change, and experiment set-up; the sample environment therefore uses quick-change fittings and other methods to allow rapid experimental set ups. Additionally, the use of engineering controls (sensor and circuitry) are included to prevent accidental hazardous gas release into occupied spaces.

CONCLUSIONS

The capability to safely use a variety of hazardous gases is needed for in-situ and in-operando X-ray diffraction studies. The chamber and system described herein safely contains hazardous gases while reacting with materials being studied, dilutes the hazardous gases to safe breathing levels, and then exhausts the effluent safely. A hazard analysis was conducted with mitigations for each hazard. Engineering and chemical compatibility studies were also undertaken for each component, gas, and material to assure all requirements were met. The exhaust flow needs for each branch were considered and ducts were all sized for ample flow.

ACKNOWLEDGEMENTS

Several BNL staff members provided review, direction, and guidance. BNL's Safety and Health Services personnel (Michael Gaffney, Mario Cubillo, and Joseph Terranova) provided ongoing review and guidance, as did the NSLS-II Environmental, Safety and Health staff (Lori Stiegler, and Robert Lee).

The sample environment requires two additional systems for safe operation, an external exhaust system and a fire protection system. Thanks go to BNL's Fire Protection Engineer Michael Kretschmann for design oversight of the fire protection system and to Modernization Plant Office engineer Sriya Adhya for the local connections. Also thanks go to Al Boerner and BNL Electricians for wiring and Chris Stebbins for task coordination.

The GHS referenced herein was designed, built, and installed by Applied Energy Systems (AES) company of Malvern, Pennsylvania, USA with some support and guidance from Mark Winter of Abbie Gregg Incorporated in Tempe, Arizona, USA. Thanks go to AES President Steven Buerkel and Project Manager Robert Holloway who may acknowledge and thank the numerous AES personnel individually. Without the GHS, hazardous gases could not be provided safely.

Lastly, thanks go to Kristen Rubino for the assistance in putting this paper together.

DREAM - A NEW SOFT X-RAY (DYNAMIC REACTION MICROSCOPY) COLTRIMS ENDSTATION AT LCLS-II*

M. Holmes[†], L. Amores, J. C. Castagna, J. James, T. Osipov, P. Walter
 LCLS, SLAC National Accelerator Laboratory, Menlo Park, CA, United States

Abstract

SLAC National Accelerator Laboratory is building new soft X-ray beamlines to take advantage of the LCLS-II upgrade to 1 MHz. One of the new beamlines is called TMO (Time resolved Molecular Optical science) also known as NEH 1.1. It will be a soft X-ray beamline featuring a sub-micron X-ray focus at its second, most downstream interaction region where the DREAM (Dynamic REAction Microscopy) COLTRIMS (COLd Target Recoil Ion Momentum Spectroscopy) endstation will be situated.

DREAM will feature; large magnetic coils to provide a strong uniform magnetic field through the spectrometer, rigid in-vacuum laser in- & out-coupling optics decoupled from the chamber support stand for pump-probe experiments, a multi-stage differentially pumped gas jet with catcher, insertable diagnostics, a long-distance microscope, scatter slits, a steerable gas jet, jet slits, and an adjustable stand to bias the spectrometer off-center from the interaction region.

In order to achieve a spot overlap spec of 0.5 μm ; the KB mirrors, laser optics, & beam position diagnostics all sit on a common granite support structure to minimize mechanical vibrations and thermal drifts. An in-vacuum UHV hexapod will be utilized for fine positioning of the laser in-coupling optic.

BACKGROUND

For the new DREAM endstation at SLAC National Accelerator Laboratory, the required X-ray spot size is 0.3 μm , and the required pump laser spot size is 5 μm . They need to be overlapped with incredibly tight precision to achieve spatial overlap of the pump laser with respect to the X-ray laser with sub-micron repeatability. In addition to this challenging requirement the DREAM endstation needs to achieve an outstanding UHV (Ultra High Vacuum) base pressure of $3\text{e-}11$ Torr. It also needs to have a multi-stage differentially pumped gas jet for delivering the sample and a Helmholtz coil pair for generating a magnetic field around its COLTRIMS spectrometer at the center of the chamber. Figure 1 shows the complete model of the DREAM endstation and labels its major components.

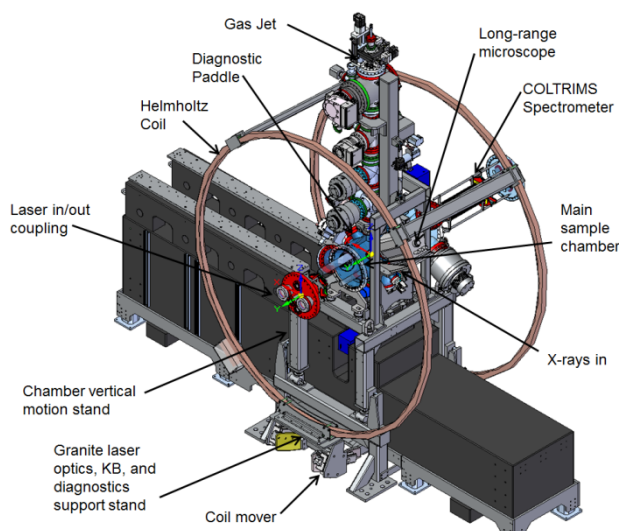


Figure 1: The DREAM endstation in its preliminary design phase. The major components of the endstation are listed.

HELMHOLTZ COILS

A pair of high-power Helmholtz coils is used for providing a linear magnetic field of up to 30 Gauss through the central ion/electron spectrometer. The coils will each be built by winding 16 turns of hollow rectangular copper tubing around a fixture, and curing a high-temperature fiberglass/epoxy mixture. At a diameter of approximately 2.2 meters, the total cross sectional amperage needed for each main coil ring is about 3800 amps; therefore each section of coil tubing will have 1/16th of the total; about 240 amps. The expected voltage required to drive both coils in series is 16 volts DC, resulting in a total power requirement of 3.7 kW. The Helmholtz coils will be water-cooled to keep them safe to touch while additionally not contributing unwanted thermal currents to the surrounding air near the endstation.

In order to correct the magnetic field vector of the earth, the coils have two motorized angular degrees of freedom to correct both roll and yaw of the coils. This will ensure the resultant magnetic field vector from the combination of earth's magnetic field and the coil's magnetic field is running axially horizontal along the center of the main chamber perpendicular to the two detectors in the spectrometer.

* Work supported by the United States Department of Energy

[†] holmes@slac.stanford.edu

SUPPORT STANDS

There are a total of three unique and separate support structures on this endstation. First, the large granite base is meant to support all the critical elements on a common module; the KB mirrors, the DREAM laser in-coupling and out-coupling optics, the DREAM diagnostics paddle for tuning spot overlap, and the downstream X-ray beam diagnostics. The laser optics in the center of the granite at the DREAM endstation are then decoupled by bellows, allowing the chamber to vibrate independently of the rigid pump laser optics.

The second support structure supports the weight of the main chamber, spectrometer, gas jet, and gas jet catcher system. This stand has 6-degrees of freedom of mechanical adjustability with one motorized degree of freedom in the vertical direction to move the main chamber and spectrometer vertically below the X-ray beam axis by up to 20 mm to accommodate the space needed for gas ions to make a 90-degree turn into the spectrometer detectors at either end of the main chamber. This stand will be constructed primarily of non-magnetic stainless steel to minimize any distortion to the magnetic field lines from the Helmholtz coil pair.

The 3rd stand is for holding and moving the Helmholtz coils, and is a separate stand that is packaged tightly below the granite stand and main chamber support stand. While located relatively far away from the main chamber, it too will be constructed primarily of non-magnetic stainless steel to minimize field distortions of the coils. Using large bearings, it will support the coils and move them by up to ± 3 degrees in both roll and yaw with respect to the X-ray beam axis.

BEAM OVERLAP

Perhaps the most demanding requirement of this endstation is the goal to have an overlap of the X-ray spot and pump laser spot to within 0.5 μm . Once this requirement became solidified, a few metrology studies of the building that the endstation will occupy were performed to get a better understanding of the floor that DREAM will be bolted to. To summarize our findings, we discovered that the floor itself can move roughly between 20-40 μm daily depending on the outside temperature and sun exposure, which is way beyond the required beam overlap specification of 0.5 μm . If the beamline were constructed with a single set of KB mirrors focusing to this endstation, the floor motion error would be de-magnified, but in the case of this beamline, there are two sets in series. With simulations we found that the spot overlap error (x-ray spot to laser spot distance) would roughly correspond around a 1:1 ratio with the floor motion amplitude, which was very undesirable. Through experience gained at our other lightsource, the SSRL (Stanford Synchrotron Radiation Lightsource) we learned that insulating the concrete buildings can have a large reduction on solar-induced daily floor deflection amplitudes by over 10X at SSRL, and simulations showed up to a 40X reduction for the NEH (Near Experimental Hall,) therefore in order for the

DREAM endstation to work properly with minimal spot drift, the NEH housing the DREAM endstation will have exterior siding and insulation installed prior to first light in this endstation.

In order to find beam overlap, a 3-step alignment process is envisioned. First, the diagnostics paddle with YAG screens will be inserted into the center of DREAM. A long-range microscope with a resolution of 2.2 μm will view the two spots and work out a delta X (horizontal error) and delta Y (vertical error.) The in-vacuum hexapod will then steer the OAP (off-axis parabola) to overlap the pump spot to the x-ray spot to within a few μm . In step two, the insertable diagnostics paddle will scan two knife edges vertically and horizontally to map out the two spot positions in an effort to further refine the pump laser focus position. In step three, the paddle is retracted, a pre-calibrated sample gas is turned on into the main chamber, and the spectrometer is used to look for maximum overlap as the pump laser spot is carefully rastered in a small (few μm x few μm) space to achieve sub-micron spot overlap by using the OAP on an in-vacuum hexapod. At LCLS-II, it is a goal to automate these steps to facilitate faster beam overlap. Figure 2 shows the interaction region of the DREAM endstation, while Fig. 3 shows a cross-section view of the interaction region.

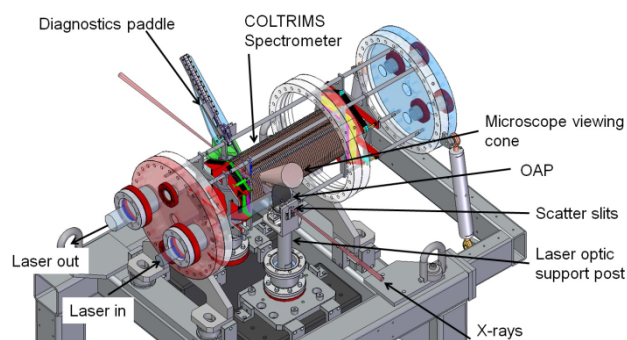


Figure 2: The DREAM interaction region noting positions of spectrometer, microscope view, diagnostics paddle, x-ray path, laser path, and optics support post with integrated scatter slits.

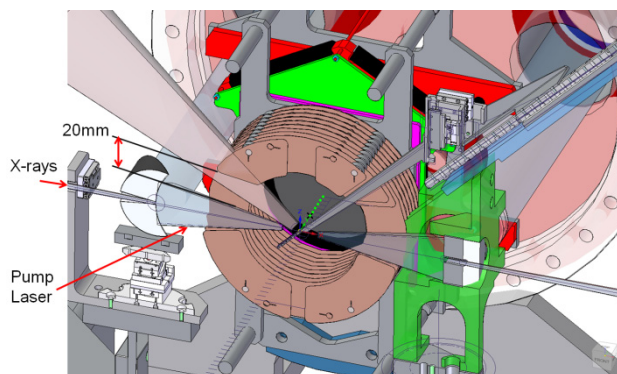


Figure 3: Cross section view at the center of the DREAM instrument. Note that the clearance cuts in the spectrometer voltage plates allow for 20 mm of vertical movement of the main chamber while the laser in-coupling and out-

coupling optics and support posts stay rigidly coupled to the stationary granite stand below the main chamber. The Insertable paddle is shown coming in from the upper-right of the image and the microscope viewing cone through the spectrometer is shown in the upper-left of the image.

VACUUM

The DREAM endstation has a physics requirement for the vacuum pressure in the experimental chamber to be $3\text{e-}11$ Torr or better. If the pressure is higher, there is a chance that the background noise in the spectrometer will be so high that no meaningful signals are visible in the noise. This is challenging for a static chamber, but even more challenging for an endstation featuring a gas jet sample where the gas jet chamber operates up to $1\text{e-}3$ Torr. In order to reach the main chamber pressure goal, a 4-stage differentially-pumped skimmed gas jet, and a 2-stage differentially-pump catcher will be built. Figure 4 shows a cross-section of the gas jet assembly.

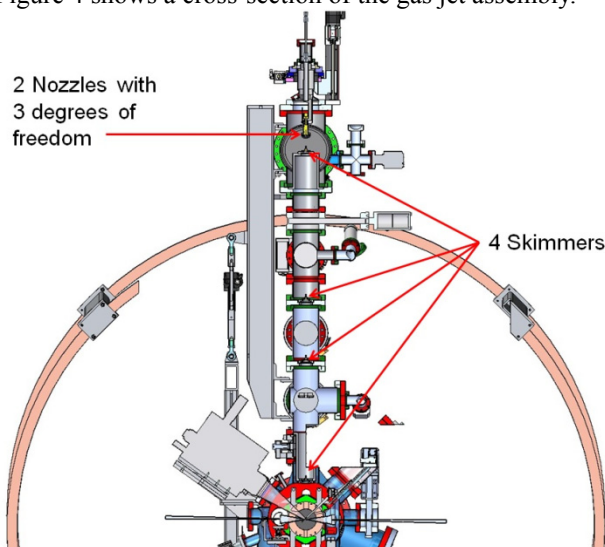


Figure 4: Cross section view of the multi-stage skimmed gas jet assembly.

The resulting gas load into the chamber from both the jet and the catcher should end up being less than a tenth of the total gas load of the main chamber, therefore by using a highly pumped gas jet and catcher, the dominant gas load in the main experimental chamber becomes the outgassing loads. We will extensively treat surfaces by electro-polishing, firing, baking, etc. to drive out as much hydrogen, water and impurities from the SST bulk material as possible. A final long-duration low-temperature bake-out is envisioned for when the entire system is assembled. The main chamber will have a combination of getter pumps and turbo pumps to optimize pumping of outgassed materials and jet gasses with an estimated total nominal pumping speed of 9,000 liters/second. Figure 5 shows the expected pressure profile across all chambers of the DREAM endstation.

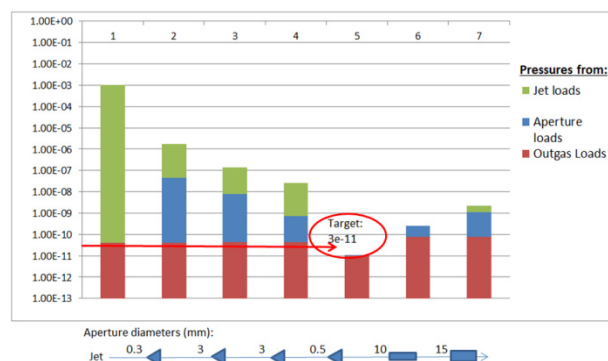


Figure 5: Calculated pressure profile in DREAM starting from the gas jet chamber on the left through 4 skimmers to the catcher chambers on the right. Starting with a pressure of $1\text{e-}3$ Torr in the gas jet chamber, the main chamber at bar graph position 5 should still be able to reach a base pressure of $3\text{e-}11$ Torr, but will be highly dependent on the outgassing rate of parts in the main chamber.

CONCLUSION

The DREAM endstation has numerous technical challenges: tight beam overlap requirements, extremely low UHV vacuum pressure in the main chamber with a gas jet providing the gas sample, very tight space constraints for packaging a large number of features (in-vacuum optics, insertable diagnostics paddle, scatter slits, a 2-axis Helmholtz coils, steerable gas jet assembly, large COLTRIMS spectrometer) but the design seems well on its way to achieving the ambitious set of requirements laid out for this instrument. First light in DREAM is expected near the end of 2020, but will be dependent on SLAC project priorities and resources.

INTERLOCK SYSTEM FOR A MAGNETIC-BEARING PULSE SELECTOR

H. Ishii, J. Adachi, H. Tanaka, T. Kosuge,
 High Energy Accelerator Research Organization, Tsukuba, Ibaraki, Japan

Abstract

A new pulse selector with a magnetic bearing has been developed for a hybrid operation mode which has been introduced in the Photon Factory (PF) 2.5 GeV ring of the High Energy Accelerator Research Organization. The pulse selector is used to permit only the passage of an X-ray pulse that comes from the single-bunch part of the hybrid filling pattern. It is mainly comprised of a slit dish-shaped disk fixed at a rotation axis and a motor system synchronized with the radio-frequency signal of the ring. We have adopted a commercially available motor system with a very low jitter of the rotation, which was developed not for a heavy load. The slit disk is so heavy that a rapid deceleration of the rotation can cause a large current to flow back to the motor driver. To avoid the current flow-back problem in the pulse selector system, we have implemented a software interlock and have developed a prototype of a programmable logic controller-based interlock system. The operation of the interlocks in five possible situations has been checked.

INTRODUCTION

A hybrid operation mode has been introduced in the Photon Factory (PF) 2.5 GeV ring of the High Energy Accelerator Research Organization (KEK) [1]. A pulse selector, a type of optical chopper, is used to permit only the passage of an X-ray pulse that comes from the single-bunch part of the hybrid filling pattern. We have developed a new pulse selector which comprises of a magnetic bearing, a dish-shaped and many-slit disk fixed at the rotation axis, a phase-locked-loop (PLL)-controlled motor system, and other parts. The speed and phase of the rotating disk are controlled by transistor-transistor logic (TTL) signals obtained by dividing the radio-frequency (RF) signal of the PF 2.5 GeV ring. A commercially available motor system has been adopted for a sufficiently low jitter of the rotation. The slit disk for the new pulse selector was so heavier than the previous disks in our previous pulse selectors with an air bearing that a rapid deceleration of the rotation can cause a large current to flow back to the motor driver, causing it to fail. An interlock to avoid the current flow-back problem in the pulse selector system is required. We have implemented a software interlock and have developed a prototype of a programmable logic controller (PLC)-based interlock system.

INTERLOCK SYSTEM FOR MAGNETIC-BEARING PULSE SELECTOR

The magnetic-bearing pulse selector system consists of an amplifier module, trigger and clock delay module, pulse-selector controller, magnetic-bearing controller, pulse-selector main body, and interlock system (Fig. 1).

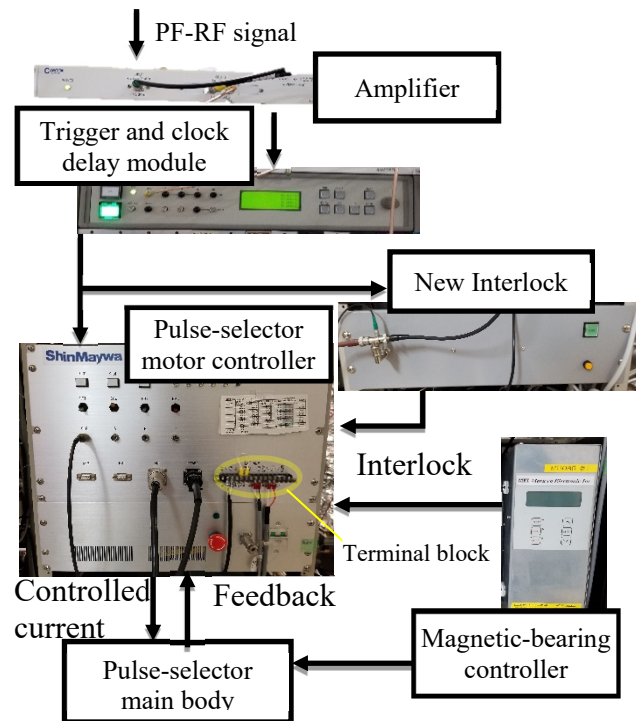


Figure 1: Pulse-selector control system.

The RF signal for the PF 2.5 GeV ring is amplified by the amplifier module and input into the counter circuit. The trigger and clock delay module divides the amplified RF signal into TTL-pulse sequences with a frequency-dividing rate. The TTL-pulse sequence is sent both to the new interlock system and to the pulse-selector motor controller. The pulse-selector motor controller drives the motor of the pulse selector with monitoring encoder. The new interlock system responds according to the TTL-signal frequency to protect the pulse-selector motor controller from the ill effects of the current flow-back.

The pulse-selector motor controller has an emergency button and a terminal block for the external input to protect the equipment. The terminal block is connected to the following three types of interlock.

- Power-off detection
- Detection of magnetic-bearing controller errors
- Newly developed PLC-based interlock system

The slit disk part of the pulse selector is floated by the magnetic bearing and the controller is connected to an uninterruptible power supply (UPS). If a power stoppage to the UPS input is detected, the drive signal of the pulse selector will be cut immediately. The magnetic-bearing controller is connected to the terminal block to signal an error to the motor controller.

Content from this work may be used under the terms of the CC BY 3.0 licence (© 2018). Any distribution of this work must maintain attribution to the author(s), title of the work, publisher, and DOI.

The newly developed PLC-based interlock system is also connected to the terminal block. The trigger and clock delay module is controlled through the simple transmission and retrieval system (STARS) [2,3], which is used as a beamline control system at the KEK-PF. We also developed a software-interlock system with STARS to protect the system from any errors.

A simplified schematic of the pulse selector is shown in Fig. 2. The dish shape, in which the pulse selector revolves, is controlled by the pulse-selector motor controller. The control method is the PLL.

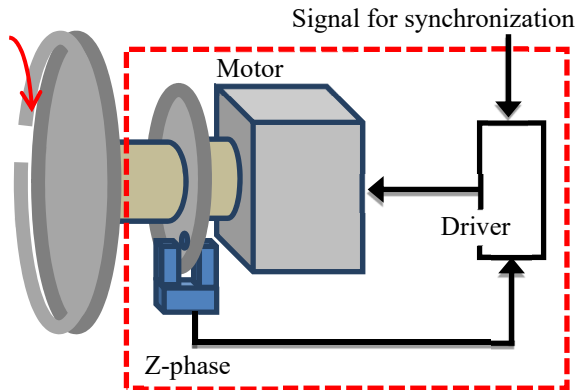


Figure 2: Pulse selector.

Software interlock

The maker of the trigger and clock delay module, Candox Systems Inc., provides a graphical user interface (GUI) to control the module, originally through the Ethernet. The GUI can communicate with the module directly; however, we decided to place STARS between the GUI and the module to log the communications. We also developed a software interlock for this system using STARS (Fig. 3).

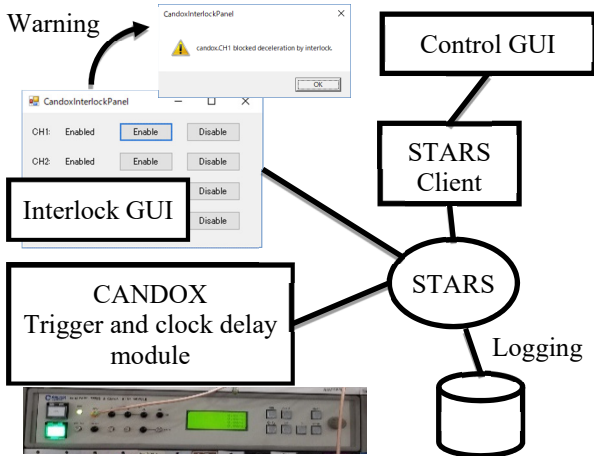


Figure 3: Software interlock system.

When users wish to change the setting of the frequency dividing rate, they must request permission from the interlock GUI. The software interlock system reduces operational errors.

PLC-Based Interlock

The function that detects the frequency deceleration of the TTL signal is implemented in the new PLC-based interlock system. The interlock monitors the frequency of the TTL signal. If it detects a deceleration, the motor-drive signal of the pulse-selector controller is cut. The requirements of the monitoring TTL signal are shown in Table 1.

Table 1: Requirements of the Counter Module

Condition	Value
Sampling interval	10 ms
Input signal type	TTL (3.3 V)
Maximum input frequency	10 kHz

A sufficient sampling-time window is required for monitoring the TTL-signal frequency; however, an overlong time window causes a delay in protecting the pulse-selector controller. We chose 10 ms for the sampling-time window.

The RF signal of PF 2.5 GeV ring (500.1 MHz) is divided by the trigger and clock module, and the module outputs a signal around 10 kHz (maximum). A maximum frequency input of 10 kHz is required for the counter module.

PLC and Hardware

We decided to use a PLC made by OMRON, used widely at the KEK-PF beamline. The PLC-based interlock system consists of the CPU module (CJ2M-CPU13), power module (CJ2M-PA202), DC24V power module for the output (S8VS-06024), counter module (CJ1W-CT021), power relay (MY-4N), a push button, and a lamp (Fig. 4).

The control program was written with Cx-programmer, provided by OMRON for PLC programming. The CPU module stores the count data for the interlock logic program, the configurations, etc. The counter module has frequency inputs and digital inputs and outputs. The power supply module (CJ2M-PA202) supplies DC 24 V to the PLC module and the S8VS-06024 power module supplies DC 24 V to the power relay.



Figure 4: PLC.

Interlock Logic

Figure 5 shows the flowchart of the interlock logic. When the input RF signal frequency is lower than the minimum value (F_{\min}), the interlock system inhibits the motor-drive signal. The minimum input frequency is always renewed. Pushing the reset button resets the interlock system and inputs the minimum frequency. If the RF signal frequency is zero, the interlock cannot be reset.

In the calculation, the input frequency value (f) is copied to the data memory area of the PLC and compared with the minimum frequency value (F_{\min}).

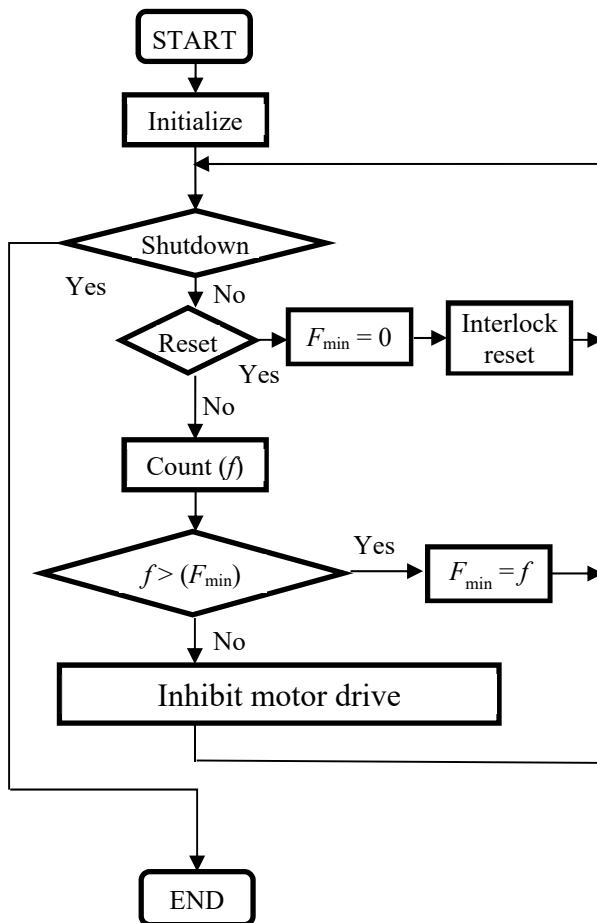


Figure 5: Flowchart of prototype interlock system.

DEVELOPMENT TESTING OF PROTOTYPE INTERLOCK

The prototype of the PLC-based interlock system was implemented and tested with the magnetic-bearing pulse selector (Fig. 6).

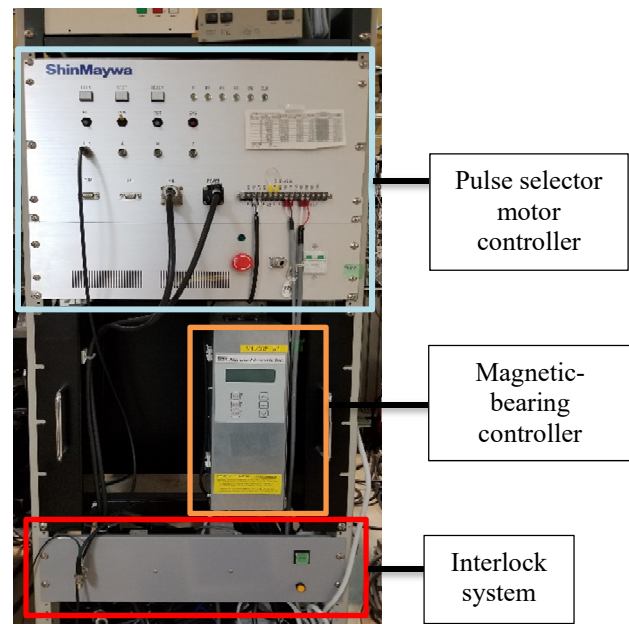


Figure 6: Interlock system and controllers.

The results of the prototype interlock test were as follows:

- When the TTL input-signal frequency rose or was fixed, the motor-drive signal stayed on.
- The motor drive was cut off when the TTL signal frequency fell below the setting value.
- The reset button of the interlock system was disabled without the TTL signal.
- The indicator lamp worked properly in both states (inhibited or enabled) of the interlock system.
- When the TTL input frequency was not zero, the reset button of the interlock system was enabled.

CONCLUSION

We developed a prototype of an interlock system to protect the pulse-selector controller from the current flow-back that occurred during the pulse selector's practical use. Input setting mistakes were reduced by the interlock GUI. The motor-drive signal was turned off immediately by the PLC-based interlock system when the TTL-signal frequency decreased. We verified that these interlock systems worked satisfactorily.

The development of a STARS interface for the PLC-based interlock system has been planned, and sufficient functions, e.g., logging, will be implemented.

REFERENCES

- [1] R. Takai *et al.*, "Test of Hybrid Fill Mode at The Photon Factory Storage Ring", in *Proc. IPAC'10*, Kyoto, Japan, May 2010, paper WEPEA035.
- [2] T. Kosuge and Y. Nagatani, "STARS: Current Development Status", in *Proc. PCaPAC2014*, Karlsruhe, Germany, Oct. 2014, paper WPO019.
- [3] STARS, <http://stars.kek.jp>

FRONT END DESIGNS FOR THE ADVANCED PHOTON SOURCE MULTI-BEND ACHROMATS UPGRADE *

Y. Jaski†, F. Westferro, S. Oprondek, S. Lee, B. Yang, M. Abliz, J. Downey, J. Mulvey
and M. Ramanathan, Argonne National Laboratory, Lemont, IL 60439, U.S.A

Abstract

The Advanced Photon Source (APS) upgrade from double-bend achromats (DBA) to multi-bend achromats (MBA) lattice is underway. This upgrade will change the storage ring energy from 7 GeV to 6 GeV and beam current from 100 mA to 200 mA. All front ends must be upgraded to fulfil the following requirements: 1) Include a clearing magnet in all front ends to deflect and dump any electrons in case the electrons escape from the storage ring during swap-out injection with the safety shutters open, 2) Incorporate the next generation x-ray beam position monitors (XBPMs) into the front ends to meet the new stringent beam stability requirements, 3) For insertion device (ID) front ends, handle the high heat load from two undulators in either inline or canted configuration. The upgraded APS ID front ends will only have two types: High Heat Load Front End (HHLFE) for single beam and Canted Undulator Front End (CUFE) for canted beams. This paper presents the final design of the HHLFE and preliminary design of the CUFE.

OVERVIEW OF APS FRONT ENDS

APS has a total of 35 sectors that can extract user beams. Currently there are 33 existing ID front ends (FE) and two vacant ID ports. The APS upgrade (APSU) will build out all 35 ID front ends with either a HHLFE for inline undulators or a CUFE for canted undulators. Out of the 33 existing ID front ends, 21 of them were built in the 1990s and are not capable of handling the heat load of the APSU ID sources and must be replaced with new FEs. The remaining 12 front ends that were built in the 2000s are capable to handle the heat load but must be retrofitted to have the next generation XBPMs and the clearing magnets. The APS existing ID front ends and their heat load limit is shown in Table 1.

Type of FEs	FEv1.2	FEv1.5	CUFE	HHLFE
P _{total} (watts)	6.9	8.9	10×2	21
P _{peak} (w/mrad ²)	198	245	281	590
Existing Qty.	17	4	7	5

HIGH HEAT LOAD FRONT END

The original HHLFE was designed in 2003 [1]. The original design was focused on the design of high heat load components. All photon masks and photon shutters were designed to handle the heat load limit of 21 kW total power and 590 kW/mrad² peak power density, equivalent of two inline 3.3-cm-period undulators at 10.5 mm gap at 180 mA. This heat load limit was sufficient for the APSU and was adopted as the design requirement for the APSU front ends. The first major redesign of the HHLFE was in 2012 to incorporate the next generation XBPMs into the front end [2]. Since then many improvements have been made to the front end. This paper presents the new HHLFE for APSU MBA to include a clearing magnet in the front end and refine the design of the XBPMs to reduce cost and ease alignment, and introduce a new design of exit mask and XBPM2 combined unit. The layout of the new HHLFE is shown in Fig. 1. The aperture of key components are shown in Table 2. The design will be initially installed in the vacant port of 28-ID for the current storage ring to test out the new designs of the XBPM system.

Table 2: HHLFE Aperture Table for APSU MBA

Components	Aperture H×V (mm)
Pre-Mask	36×26
FM1	38×26 (inlet)/ 20×16 (outlet)
FM2	24×20 (inlet)/ 9×12 (outlet)
Clearing Magnet	13×20 (optical minimum) 18 (magnet gap)×65 (stay clear)
Lead Collimator	19.5×19.5 (optical) 26×26 (shielding)
GRID-XBPM	15.3×50 (inlet)/ 1.6×50 (outlet)
FM3	16×47.8 (inlet)/ 3.6×6 (outlet)
Photon Shutter	10×47.8 (inlet)/ 5×47.8 (outlet)
Safety Shutter	72×20 (optical) 72×20 (shielding)
Wall Collimator	27×17 (optical) 37×26 (shielding)
Exit Mask	10×38 (inlet)/ 2×2 (outlet)
Exit Collimator	5×5 (optical) 5×5 (shielding)

* Work supported by the U.S. Department of Energy, Office of Science, under Contract No. DE-AC02-06CH11357
† email address jaskiy@aps.anl.gov

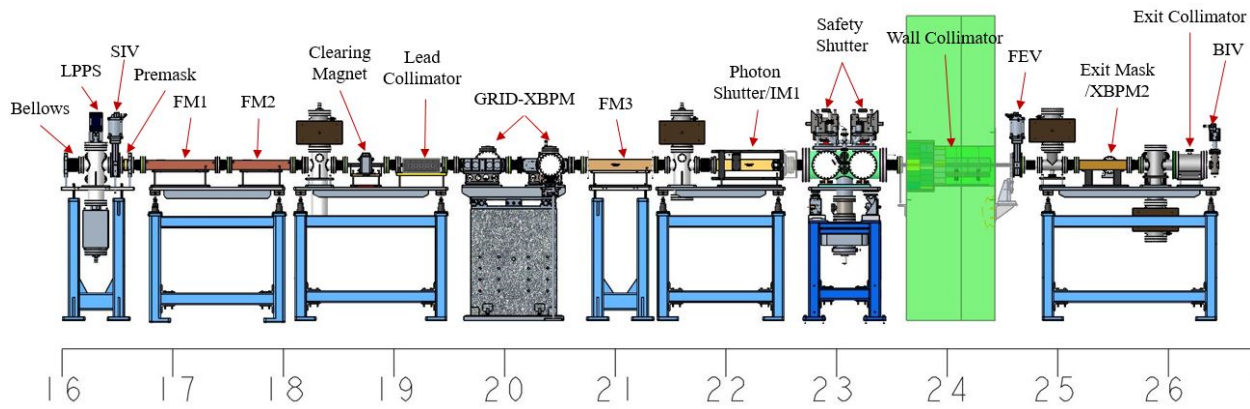


Figure 1: Layout of the HHLFE for APS MBA upgrade.

HHLFE Description

The front end starts with a bellows to be connected to the storage ring photon extraction tube, followed by a Low Power Photon Shutter (LPPS), a Storage Ring Isolation Valve (SIV), and a Premask. This table will be installed along with the storage ring vacuum system. This table is the same for HHLFE and CUFE except the aperture of the premask. The SIV provides the vacuum interface between the storage ring and the front end. As long as the LPPS and SIV is closed, the storage ring can operate without the rest of the front end being installed.

For the photon components, the first fixed mask (FM1) and second fixed mask (FM2) together provide the required aperture for the GRID-XBPM and protect the clearing magnet and lead collimator aperture from synchrotron beam. The FM1 and FM2 are box-cone design confining beam both horizontally and vertically. FM1 and FM2 are made from solid GlidCop bar. The third fixed mask (FM3) protects all components downstream of it. The FM3 is made from brazing two OFHC based halves. Each half has a GlidCop beam striking plate explosion bonded to the OFHC base material. The exit mask is a new design. It combines the exit mask and XBPM2 function into one unit. The beam intercepted by the inboard surface is detected by the detectors mounted to the outboard flange. The exit mask is made by brazing two halves of GlidCop bars. All three styles of masks are shown in Fig. 2.

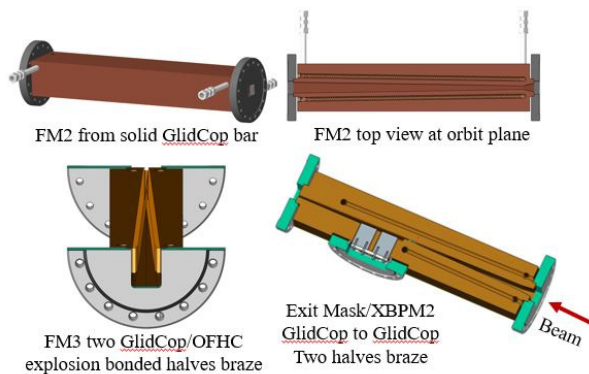


Figure 2: Three styles of masks in HHLFE.

The clearing magnet is a new component. It is a passively safe device to dump the electron beam in case the electron beam enter the front end due to the storage ring magnet steering errors. Due to HHLFE has small horizontal apertures, the clearing magnets has 18 mm horizontal magnetic gap to deflect the beam vertically towards the floor. The required deflection angle is calculated to be 6.52 mrad [3]. The magnet design and analysis has been completed and the preliminary mechanical model is shown in Fig. 3. The radiation caused by dumping the electron beam in the front end is still under evaluation.

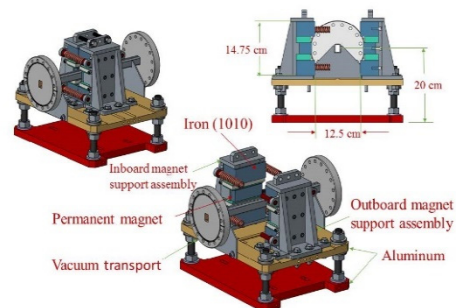


Figure 3: Preliminary mechanical model of the clearing magnet for HHLFE.

The next generation XBPMs consists of three components: 1) GRID-XBPM which is in the storage ring feed-back system, 2) Intensity Monitor 1 (IM1) which is an alignment tool for GRID-XBPM, 3) XBPM2 which is not in the storage ring feed-back system and functions as an independent check to ensure that the beam is centered at the exit mask aperture. Since the original design of GRID-XBPM, many improvement has been made to its support and the motion structures, and the detector system to reduce the cost, and increase the signal to noise ratio. For the IM1, the new design is to mount the detectors directly onto the photon shutter's upstream and downstream flanges. These detectors measure the copper fluorescence generated by the photo shutter at it closed position to aid the alignment of the GRID-XBPM. The new XBPM2 integrated the exit mask and the detectors into the same unit. [4]

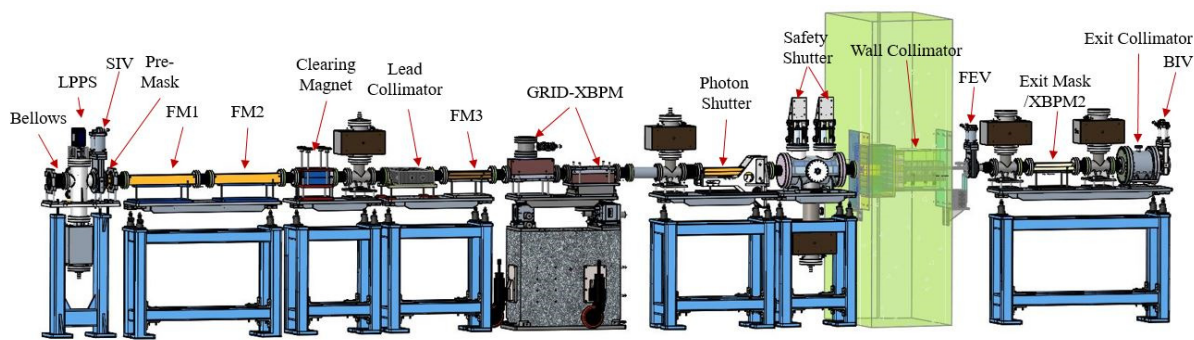


Figure 4: Layout of the CUFE for APS MBA upgrade.

CANTED UNDULATOR FRONT END

CUFE is designed for two canted beams with 1.0 mrad canting angle. Currently there are 7 CUFEs in the existing storage ring. The high heat load components in the existing CUFEs are designed to handle the heat load limit of 20 kW total power which is 10 kW per beam and 281 kW/mrad² peak power density, equivalent to two 2.07-m-long 3.3-cm-period undulators at 10.5 mm gap at 200 mA. [5] This heat load limit is sufficient for the APSU and is used as the design requirement for the APSU. The layout of the CUFE is shown in Fig. 4 and the aperture table is shown in Table 3. The layout is similar to that of the HHLFE. The first table is identical to that of the HHLFE except the aperture of the premask. The FM1 and FM2 are existing designs to protect clearing magnet and lead collimator. Due to CUFE has large horizontal aperture to pass the two canted beams, the clearing magnet must use vertical magnetic gap to deflect beam horizontally. The principle for the GRID-XBPM in CUFE is the same as that in HHLFE. It is rotated 90°. CUFE GRID-XBPM has inclined scattering surface intercepting beam vertically with detectors mounted on the top and bottom respectively. To prevent the cross talks of the two beams, a divider must be installed in the center of the

GRID-XBPM. To protect the divider from synchrotron beam strike, a splitter mask of FM3 is introduced to ensure that the beam passing through the FM3 has proper horizontal separation and will not strike the divider in the GRID-XBPM. The photon shutter and safety shutter are existing designs. A new exit mask is needed to function as XBPM2. A new exit collimator design uses in-vacuum tungsten.

CONCLUSION AND DISCUSSIONS

HHLFE final design was completed for all components except the clearing magnets. All high heat load components are made out of GlidCop or GlidCop to OFHC copper explosion bond material. All three styles of masks were successfully fabricated by three vendors. The exit mask/XBPM2 combination unit was already installed in 27-ID in May 2018 shut down and are producing good data. A complete front end without clearing magnet will be installed in 28-ID in September 2018 shutdown. For CUFE, preliminary design is completed. Currently in detail design of the XBPMs. For all front ends, The Bremsstrahlung radiation caused by electron beam dumped by clearing magnet into the front end need to be evaluated by radiation physicist as soon as possible to ensure that this radiation is within the allowed limit.

Table 3: CUFE Aperture Table for APSU MBA

Components	Aperture H×V (mm)
Pre-Mask	62×26
FM1	64×26 (inlet)/ 40×14 (outlet)
FM2	46×17 (inlet)/ 26×5 (outlet)
Clearing Magnet	32×9 (optical minimum) 40 (clear)×16 (v. magnet gap)
Lead Collimator	40×16 (optical) 46×22 (shielding)
Splitter mask FM3	50×10 (inlet)/ dual 10×4 (outlet)
GRID-XBPM	50×10 (inlet)/ 50×1 (outlet)
Photon Shutter (PS)	50×10 (inlet)/ 50×5 (outlet)
Safety Shutter (SS)	50×16 (optical) 50×16 (shielding)
Wall Collimator	47.6×16.8 (optical) 56×26 (shielding)
Exit Mask (EM)	50×9 (inlet)/ dual 2×2 (outlet)
Exit Collimator	7×6 (optical) 7×6 (shielding)

REFERENCES

- [1] Y. Jaski, "New Front-End Design for Multiple In-line Undulators at the Advanced Photon Source," *AIP Conf. Proc.* 705, pp. 356-359, 2004; doi: 10.1063/1.1757807
- [2] Y. Jaski *et al.*, "New Front Ends with the Next-Generation XBPMs for the Advanced Photon Source Upgrade," in *Proc. MEDSI 2012*, Shanghai, China, Oct. 2012, URL: <https://pdfs.semanticscholar.org/presentation/5a2f/184b17805b9b85d17bd7ae7c15fc3a2389ef.pdf>
- [3] M. Abliz *et al.*, "Clearing Magnet Design for APS-U," in *Proc. NAPAC2016*, Chicago, IL USA. Oct. 2016, paper THPOA62
- [4] S. Oprondek *et al.*, "Next Generation X-ray Beam Position Monitor System for the Advance Photon Source MBA Upgrade," presented at MEDSI 2018, Paris, France, June 2018, paper TUPH29, this conference.
- [5] Y. Jaski *et al.*, "Thermomechanical Analysis of High-Heat-Load Components for the Canted-Undulator Front End," in *Proc. MEDSI 2002*, Argonne, IL, USA, pp. 390-397, 2002

MECHANICAL CONVERSION OF A VERTICALLY REFLECTING ARTIFICIAL CHANNEL-CUT MONOCHROMATOR TO HORIZONTALLY REFLECTING*

S. P. Kearney[†], E. Dufresne, S. Narayanan, A. Sandy, D. Shu, Advanced Photon Source, Argonne National Laboratory, Argonne IL. 60439, U.S.A.

Abstract

The mechanical conversion of a high-resolution artificial channel-cut monochromator (ACCM) from a vertically reflecting orientation to a horizontally reflecting orientation is presented. The ACCM was originally commissioned for the 8-ID-I beamline at the Advanced Photon Source (APS), Argonne National Laboratory [1, 2]. The ACCM was intentionally designed at commission to have the potential to be reoriented to the horizontal direction. After nearly a decade of operation in the vertical orientation the ACCM was rotated to the horizontal orientation. The details of the design which allowed this conversion and the preparation steps needed to assure the continued performance of the ACCM will be discussed.

INTRODUCTION

An ultra-high-vacuum double crystal monochromator (DCM) was previously designed for the 8-ID-I beamline at the Advanced Photon Source [1]. The DCM was designed to meet the same stability performance as a single channel-cut crystal using an overconstrained weak-link mechanism for positioning alignment of the second crystal [3]. In addition, features were incorporated into the design for the potential conversion of the vertically reflecting geometry to horizontally reflecting. This paper will discuss the mechanical conversion of the DCM from vertical to horizontal reflecting geometry and the optical results.

MECHANICAL CONVERSION

The original vertical orientation can be seen in Fig. 1(a-b). For the conversion to work the entire vacuum tank was designed so that when rotated 90° about the x-ray beam path (Fig. 1(a)) the crystal assembly would be at the same height. The support frame was designed with this in mind, which can be seen in Fig. 1(b), and the table was also designed with a hole through the top plate for clearance of the main Bragg rotation stage flange. Rotation of the DCM was done in the end station with little modification and the final horizontal orientation can be seen in Fig. 1(c). Internal components were kept in place during the rotation and only the x-ray vacuum lines, cooling lines, and electrical components were detached. Modifications included new supports for the ion pumps shown in Fig. 1(c), and two internal support straps, Fig. 2, for the water cooling lines. The straps were installed to reduce the strain on the connection points due to gravity. All crystal mounts, stages, and supports needed no modification for the new orientation.

* Work supported by the U.S Department of Energy, Office of Science, under Contract No. DEAC02-06CH11357.

[†]skearney@aps.anl.gov

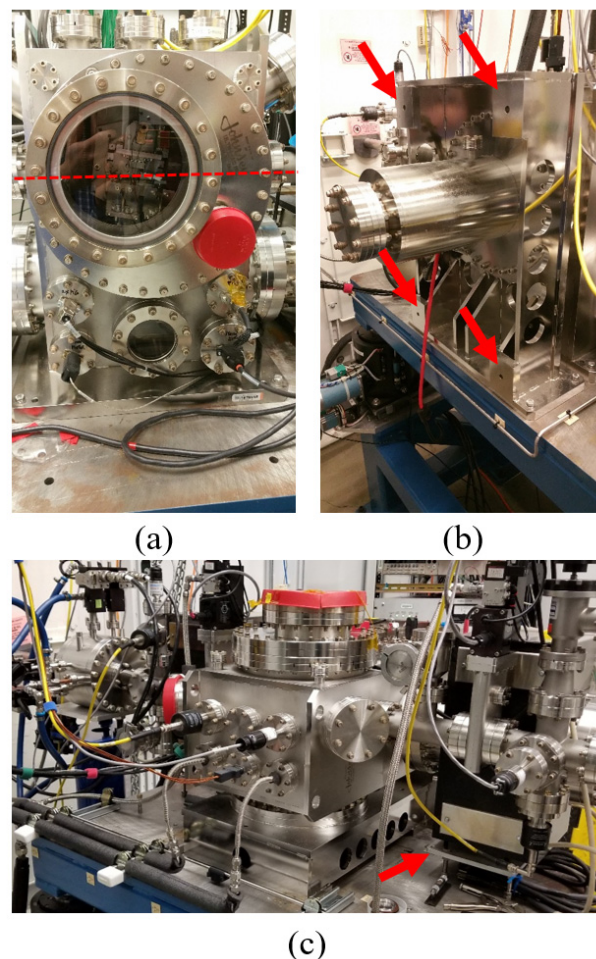


Figure 1: (a) Front view of DCM in vertical orientation with a dashed line representing x-ray path. (b) Back view of DCM showing new mounting surfaces (red arrows) for horizontal orientation. (c) Isometric view of DCM in the new horizontal orientation with red arrows showing new ion pump supports.

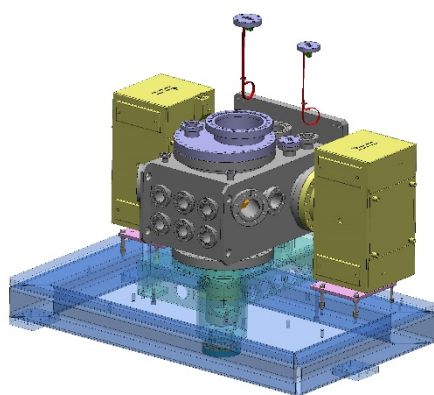


Figure 2: Model of the DCM in horizontal orientation showing the support straps for the cooling lines mounted to the back of vacuum flanges.

OPTICAL CONVERSION OF DCM

The electron beam source size (σ) in the current third generation storage rings is highly asymmetric with a vertical source size of $\sim 10 \mu\text{m}$ and the horizontal source size being higher by more than an order of magnitude. As a result, the transverse coherence lengths at a longitudinal distance R from the source and for a wavelength λ is defined as, $\lambda R/\sigma$. At the X-ray Photon Correlation Spectroscopy (XPCS) beamline 8-ID-I at the APS, the vertical and the horizontal transverse coherence lengths are $\sim 150 \mu\text{m}$ and $7 \mu\text{m}$ respectively at a distance of 65 m from the source where the monochromator is located. For coherent scattering experiments, it is imperative to utilize the entire transverse coherence area of the beam. Additionally, for XPCS experiments, there is another level of signal to noise optimization [4] that is involved which requires the angular speckle size (diffraction limited scattering from the sample) to match the solid angle subtended by the pixel. For the state-of-the-art pixel array detectors (PADs), the pixel size is typically in the range of 50-75 μm . In order to fulfill this condition, the beam size at the sample should be in the order of 1-10 μm for a sample to detector distance at 8-ID-I of 4 m.

It is well known that the thermal load of a polychromatic synchrotron x-ray beam incident on the first crystal of a double crystal monochromator induces significant thermal bumps leading to distortion of the crystal surface. This distortion results in a broadening of the rocking curve leading to a loss in the reflectivity. Additionally, this also causes significant wave front distortion which negatively impacts the functioning of downstream optical components such as focusing optics.

Previously, a detailed thermal analysis of this monochromator was carried out to understand the effect of the thermal bump [5] on the focal length of the downstream focusing optics based on a Beryllium Compound Refractive Lens (CRL). Thermal analysis verified the experimental observations that the thermally deformed first crystal acts as a lens creating a virtual source that is much closer to the crystal (ca. 1.5 m) than the real source (ca. 65 m) thereby increasing the focal distance of the CRL assembly

by as much as 100% from the theoretical 2 m to an experimentally observed ca. 4.5 m.

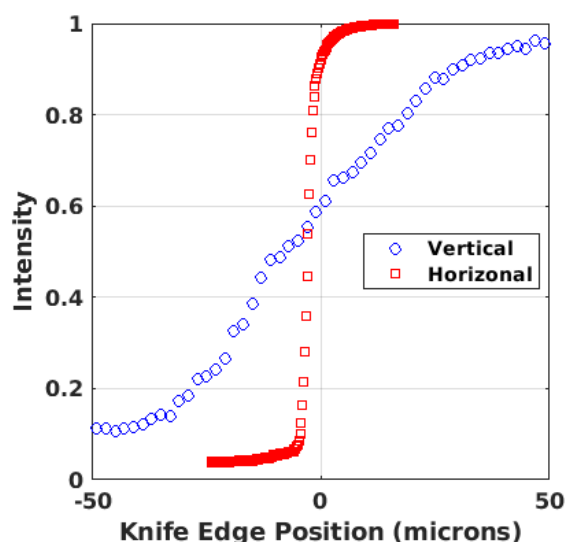


Figure 3: Knife edge scan of the vertically focused beam with the monochromator in the vertical versus the horizontal diffraction geometry.

While it is possible to mitigate the thermally induced distortions by cryogenic cooling for a Silicon monochromator to a regime of zero thermal expansion, the same is non-trivial for Germanium as the zero thermal expansion occurs at ca. 50 K. Since such a mitigation was beyond the scope of the beamline in its current state, we embarked on flipping the orientation of the monochromator to be horizontally diffracting from the original vertical scattering geometry. The monochromator was originally designed by taking this option into consideration [1].

This also aligns well with the fact that the transverse coherence length of the x-ray beam in the horizontal direction is far more forgiving than in the vertical which allows us to mitigate the thermally induced distortions without going to the extreme of cryogenic cooling. The effect of the flipping of the monochromator on the focusing is shown below. Figure 3 shows the knife edge scan through the focused x-ray beam under both orientations of the monochromator. Figure 4 shows the derivative of the knife edge scans yielding the focal spot sizes. The horizontal orientation yields a focal length and a focal spot size that matches the theoretically estimated values based on ray tracing. Figure 5 shows the knife edge scan and its derivative in the case of the horizontal orientation of the monochromator.

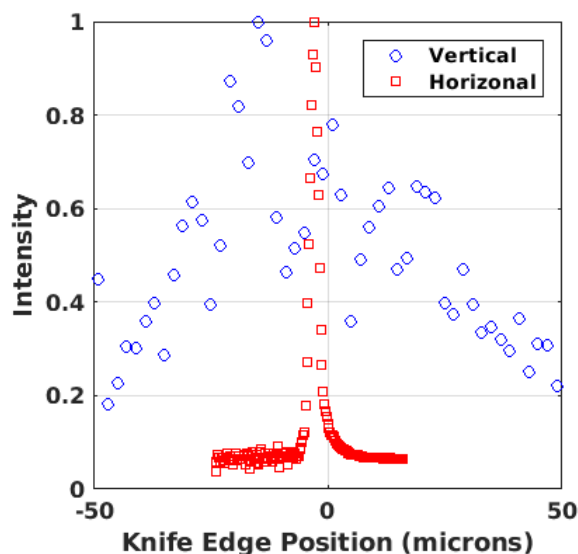


Figure 4. Derivative of the knife edge scan of the vertically focused beam with the monochromator in the vertical versus the horizontal diffraction geometry.

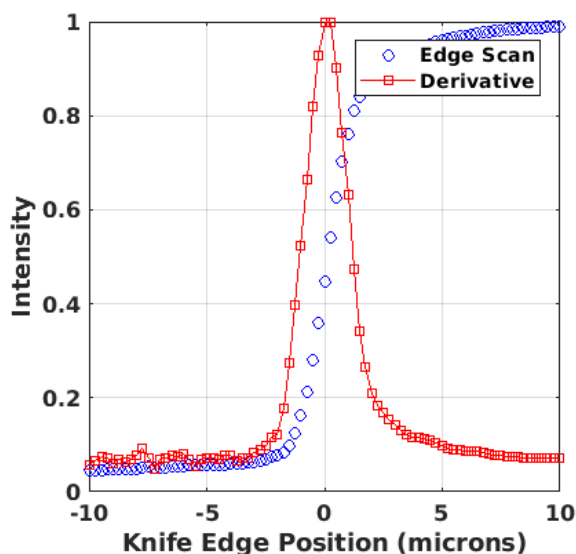


Figure 5: Knife edge scan along with the derivative showing the theoretical focus size of the vertically focused beam with the monochromator in the horizontal diffraction geometry.

CONCLUSION

Previously, a high stability DCM was designed to operate in both vertical and horizontal reflection geometry. It was originally installed at the 8-ID-I beamline at the APS in the vertical orientation. A thermal analysis of the DCM found that a thermal bump was having negative effects on the downstream optical components. Instead of using cryogenic cooling to create a non-zero thermal expansion it was decided to flip the DCM to a horizontally reflecting geometry, which would take advantage of the more forgiving transverse coherence length of the x-ray beam in the horizontal direction.

Changing the orientation of the DCM was successfully completed. Mechanically, only slight modifications were required, which included internal support straps for cooling lines and new ion pump supports. Optically, the horizontal orientation was found to improve the focus. The focal length and focal spot size matched theoretical ray tracing values.

REFERENCES

- [1] Narayanan S., Sandy D., Shu D., Sprung M., Preissner C., Sullivan J., "Design and performance of an ultra-high-vacuum-compatible artificial channel-cut monochromator", in *J. Synchrotron Radiation* 15, 2008, pp. 12–18.
- [2] *U.S. Patent granted No. 6,607,840*, D. Shu, T. S. Toellner, and E. E. Alp, 2003.
- [3] Shu D., Narayanan S., Sandy A., Sprung M., Preissner C., Sullivan J., "Precision mechanical design of a UHV-compatible artificial-channel-cut x-ray monochromator", in *Proc. SPIE*, Vol. 6665, 66650O-1, 2007, doi: 10.1117/12.733101.
- [4] Falus P., Lurio L., Mochrie S., "Optimizing the signal-to-noise ratio for X-ray photon correlation spectroscopy", in *Journal of Synchrotron Radiation* 13, 2006, pp. 253–259.
- [5] Antimonov M. A., Khounsary A. M., Sandy A. R., Narayanan S., Navrotsky G., "On the influence of monochromator thermal deformations on X-ray focusing", in *Nuclear Instruments & Methods in Physics Research Section A*, 820(C), 2006, pp. 164–171.

MECHANICAL DESIGN OF A COMPACT NON-INVASIVE WAVEFRONT SENSOR FOR HARD X-RAYS

S. P. Kearney[†], L. Assoufid, W. Grizolli, T. Kolodziej, K. Lang, A. Macrander, Y. Shvyd'ko, X. Shi, D. Shu, and M. Wojcik,

Advanced Photon Source, Argonne National Laboratory, Argonne, IL 60439, U.S.A.

Abstract

This work describes mechanical design of a prototype compact wavefront sensor for in situ measurement and monitoring of beam wavefront of hard x-ray beamlines. The system is based on a single-shot grating interferometer [1, 2] and a thin diamond single-crystal beam splitter. The beam splitter is designed to be inserted in the incident beam and oriented to diffract a fraction of the incident beam bandwidth into the interferometer, for wavefront measurement and reconstruction. The concept is intended to study the feasibility of a non-invasive wavefront sensor for real time wavefront monitoring and diagnostics, with possible application in adaptive mirrors for wavefront preservation and control [1, 3]. The design focus was on compactness to enable easy portability and implementation in a beamline.

Z8-83 OVERALL DESIGN

The wavefront sensor, see Fig. 1 and 2, was designed for in situ measurement and monitoring of beam wavefront of hard x-ray beamlines. It works by placing a single-crystal beam splitter into the incident x-ray beam and then using the grating interferometer to measure the diffracted wavefront in a non-invasive manner. The design is based on the designs in [1, 2] with the focus being compactness so that it could be easily implemented in any beamline. The entire assembly is only 26 kg (Table 1), which can be easily lifted by two people without lifting equipment. A total of 9 controlled stages were used in its various sub-assemblies and the camera and grating assemblies were designed to be manually positioned along the rotation arm. The support structure is modular such that the legs can be removed completely or replaced with longer legs all while maintaining alignment of the crystal rotation axis and main diffraction axis.



Figure 1: Fully assembled wavefront sensor.

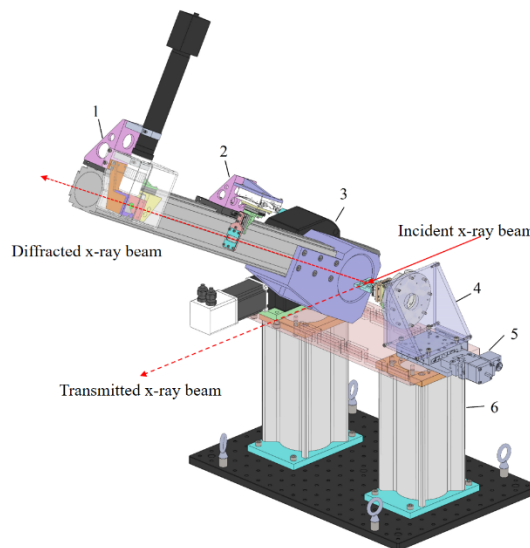


Figure 2: Complete assembly of Z8-83 wavefront sensor: (1) camera assembly, (2) grating assembly, (3) rotation arm, (4) crystal assembly, (5) Kohzu Precision Co. linear stage, and (6) modular support table.

Z8-830200 Crystal Assembly

The crystal assembly holds the single-crystal beam splitter, see Fig. 3. A SmarAct SR-7021 rotation stage is used to rotate the crystal to diffract a fraction of the incident beam, all other stages are used for fine positioning alignment of the crystal. The crystal holder is designed with a U-shaped cut-out to let the incident beam pass through non-invasively.

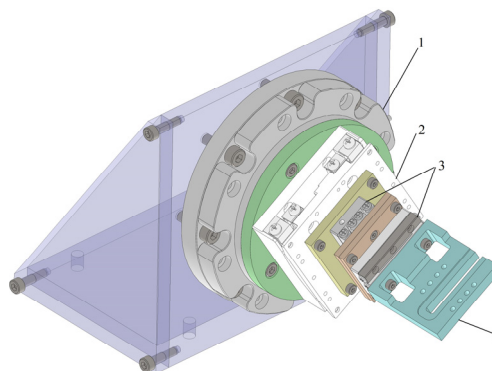


Figure 3: Z8-830200 crystal assembly: (1) SmarAct GmbH SR-7021 rotation stage, (2) SmarAct GmbH SGO-60.5 tilt stage, (3) SmarAct GmbH SLC-1730 linear stage, and (4) crystal holder.

[†]skearney@aps.anl.gov

Z8-830300 Grating Assembly

The grating assembly can be seen in Fig. 4. It is placed between the crystal and the camera assembly. The grating holder is made as narrow as possible so that it can get as close as possible to the crystal.

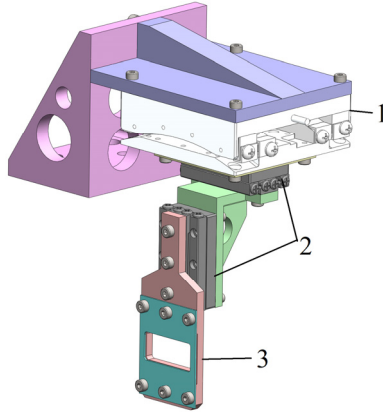


Figure 4: Z8-830300 grating assembly: (1) SmarAct GmbH SGO-60.5 tilt stage, (2) SmarAct GmbH SLC-1730 linear stage, and (3) grating holder.

Table 1: Specifications of Z8-83 Wavefront Sensor and the Commercial Stages Used in its Design

Specification	Value
Z8-83 Wavefront Sensor	
Volume (L x W x H) mm ³	(884x502x393)
Mass	25.9 kg
Controlled Degrees of Freedom	9
SmarAct GmbH SLC-1730 Linear Stage	
Smallest/Largest Step Size	1 nm/1.5 μ m
Range	± 10.5 mm
Mass	20 g
SmarAct GmbH SGO-60.5 Goniometer	
Smallest/Largest Step Size	0.7/7 μ rad
Range	$\pm 5^\circ$
Mass	140 g
SmarAct GmbH SR-7021 Rotation Stage	
Smallest/Largest Step Size	3.5/35 μ rad
Range	∞°
Mass	400 g
Kohzu Precision Co. XA07A-R201 Linear Stage	
Resolution Full/Half Step	1/0.5 μ m
Range	± 10.0 mm
Mass	600 g
Aerotech® Inc. AGR50 Rotation Stage	
Resolution	58 μ rad
Range	∞°
Mass	2.5 kg

Z8-830400 Camera Assembly

The camera assembly, Fig. 5, supports the camera (GS3-U3-120S6M-C, FLIR Integrated Imaging Solutions Inc.), 45° reflecting mirror (#45-595, Edmund Optics Inc.), 10X Mitutoyo objective lens with a 33.5 mm working distance (#46-144, Edmund Optics Inc.), and the scintillator. All of these components are enclosed by an opaque 3D printed plastic cover. The scintillator holder can be adjusted in the along the x-ray beam direction using an SLC-1730 piezo stage and the entire scintillator holder can be removed without disassembling any other components allowing for quick changes in scintillator types. The scintillator is clamped using a 3D printed ring, which is then held in place by a metal retaining ring.

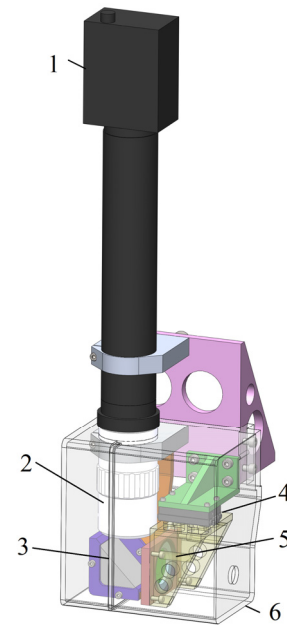


Figure 5: Z8-830400 camera assembly: (1) FLIR Integrated Imaging Solutions Inc. GS3-U3-120S6M-C camera, (2) Mitutoyo Co. 10X objective lens, (3) Edmund Optics Inc. #45-595 45° reflecting mirror, (4) SmarAct GmbH SLC-1730 linear stage, (5) scintillator holder, and (6) opaque cover.

ROTATION ARM DESIGN

The pitch arm assembly, Fig. 6, is mounted to a rotation stage (AGR50, Aerotech Inc.) for pitch rotation with 180° rotation range and 58 μ rad resolution. Both the camera and grating assemblies are mounted to dovetail carriages (XT95P11/M, Thorlabs Inc.), which can be manually adjusted over a range of 438 mm on the rotation arm. A counterweight support extends through the aperture of the rotation stage to increase the structural rigidity of the pitch arm. The rigidity is increased due to the sliding fit contact between the counterweight support and the rotation stage aperture hole. In addition, this geometry allows for complete

180° free rotation of the counterweight. Two counterweight position are required to utilize the entire working length of the arm and can be seen in Fig. 6.

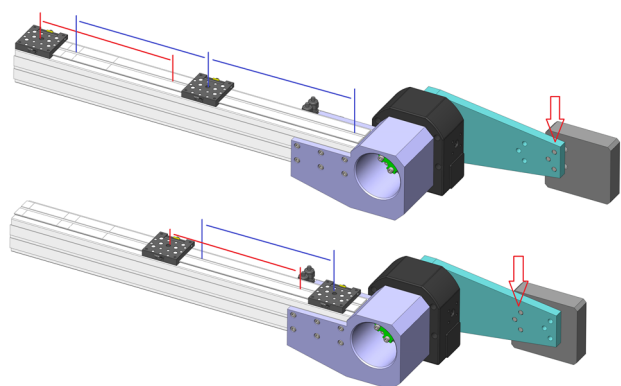


Figure 6: Balance configurations of Z8-830100 rotation arm with the potential positions of the camera assembly (red lines) and grating assembly (blue lines): (top) furthest extent configuration and (bottom) closest configuration.

FEA of Rotation Arm

There were concerns about the stability of such a long arm with the potential of a concentration of mass at the end. A design goal of >100 Hz for the first mode shape with the grating and camera assemblies at the extreme end of the arm was set. The grating and camera assemblies are represented by the points in the model and were modelled as extended inertia points to reduce model complexity.

In Fig. 7 it can be seen that the design goal was not achieved; this was due to weight constraints on the rotation stage. In Fig. 7 the first 3 mode shapes can be seen. The first mode of 50 Hz is much lower than the design goal, but looking at the mode shape it can be seen that the majority of the motion was in the counterweight and likewise with the second mode. It is the third mode that was found to influence the main arm the most and was at 94 Hz putting the design reasonably close to the design goal.

ACKNOWLEDGEMENTS

Work supported by the U.S. Department of Energy, Office of Science, under Contract No. DE-AC02-06CH11357.

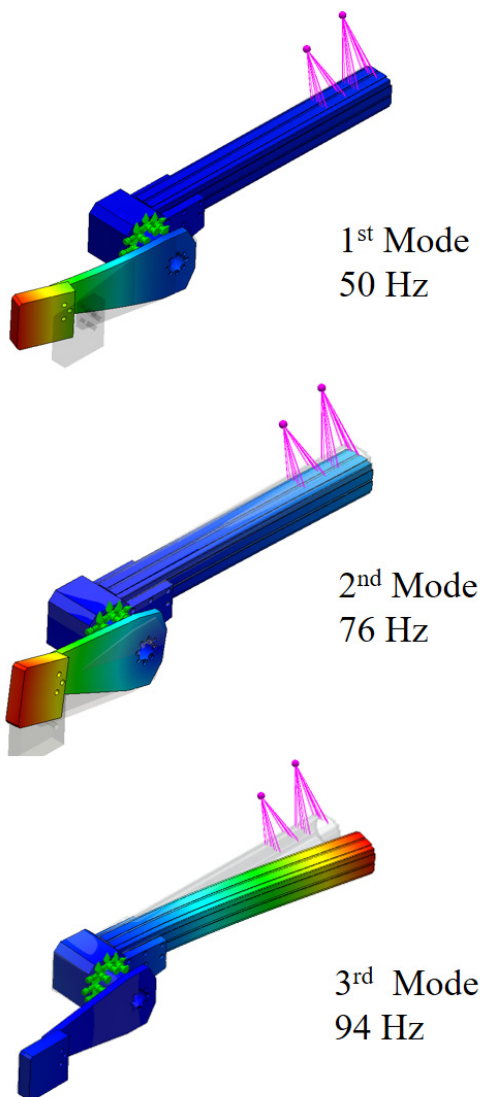


Figure 7: First 3 mode shapes of the rotation arm assembly.

REFERENCES

- [1] L. Assoufid *et al.*, “Development and implementation of a portable grating interferometer system as a standard tool for testing optics at the advanced photon source beamline 1-BM”, *Rev. Sci. Instrum.*, 87(5), 052004, 2016.
- [2] W. Grizolli, X. Shi, T. Kolodziej, Y. Shvyd’ko, L. Assoufid, “Single-grating Talbot imaging for wavefront sensing and x-ray metrology”, in *SPIE Proc.*, 1038502, 2017.
- [3] S. Marathe, X. Shi, A. M. Khounsary, M. J. Wojcik, N. G. Kujala, A. T. Macrander, and L. Assoufid, “Development of single grating x-ray Talbot interferometer as a feedback loop sensor element of an adaptive x-ray mirror system”, *Adaptive X-Ray Optics III*, in *SPIE Proc.*, 92080D, 2014.

THE DEVELOPMENT OF PAL-XFEL BEAMLINE

Seonghan Kim*, Seungnam Kim, Myeongjin Kim, Seonmin Hwang, Hyojung Hyun,
 Intae Eom, Kisoo Park, Jaehyun Park, Jaeku Park, Kyungsook Kim, Sangsoo Kim,
 Sunam Kim, Chaesun Lee, Seungyu Nah,
 Pohang Accelerator Laboratory, POSTECH, Pohang, Gyeongbuk 37673, Republic of Korea

Abstract

Pohang Accelerator Laboratory X-ray Free Electron Laser (PAL-XFEL) is a research facility, which is designed to generate extremely intense (assuming 1×10^{12} photon/pulse at 12.4 keV) and ultra-short (10-200 femtosecond) pulsed X-rays. Now two beamlines were constructed, the one is hard X-ray and the other is soft X-ray. Each beamline is consisted of UH (Undulator hall), OH (Optical hall), and EH (Experimental hall). We have two hutches, XSS (X-ray Scattering Spectroscopy) and NCI (Nano-crystallography and Coherence Imaging) in hard X-ray beamline. They are connected each other, and sharing main optics (Mirrors and DCM, etc). PAL-XFEL is a very precise facility and has very large heat power, so mechanical analysis is required. Now vacuum components of beamline are installed and completed performance test. In here, beamlines of the PAL-XFEL is introduced in briefly, and two components, GMD (Gas Monitor Detector) and MICOSS (multifarious injection chamber for molecular structure study), are also reported.

INTRODUCTION

PAL-XFEL (Pohang Accelerator Laboratory X-ray Free Electron Laser) project, which provides 10 times the brightness of the beam than the third generation and a very short pulse of <100 fs, started construction in 2011. The installation of all machines and devices was completed at the end of 2015 and the commissioning was proceeded in 2016. The XFEL (X-ray Free Electron Laser) has been officially provided to users from 2017. Figure 1 shows the PAL-XFEL installed near the PLS-II (Pohang Light Source II).



Figure 1: Scene of PAL-XFEL and PLS-II.

The PAL-XFEL features as the world's most notable source of radiation in recent years are using higher electron energy and a longer undulator than PLS-II to produce much shorter and stronger light. The average brightness is about 100 times and the maximum brightness is more than 100 million times stronger, and the pulse length is shorter than 1/100, which makes it suitable for dynamic phenomenon research. PAL-XFEL beamline is divided into UH (Undulator hall), OH (Optical hall) and EH (Experimental hall). There are three experimental area at EH, which are XSS (X-ray Scattering Spectroscopy), NCI (Nano-crystallography and Coherence Imaging), and SSS (Soft X-ray Scattering and Spectroscopy).

Beamline [1,2]

Figure 2 shows the layouts of the hard X-ray and soft X-ray beamlines. The performance of various optical devices which are consisted of beamline were verified during the commissioning. In the PAL-XFEL beamline, the role of the diagnostic device is very important and needs to be developed separately. Therefore, various diagnostic devices were developed. GMD (Gas Monitor Detector) that one of the diagnostic device has been developed with a lot of verification test and modification and installed at the beamline. In experimental area, NCI beamline's SFX (Serial Femtosecond Crystallography) experiment uses micro focused X-ray pulse and needs to provide efficient operational performance. Thus, the MICOSS (the multifarious injection chamber for molecular structure study) is developed. By using this system, clear diffraction patterns can be obtained for lysozyme microcrystal experiment.

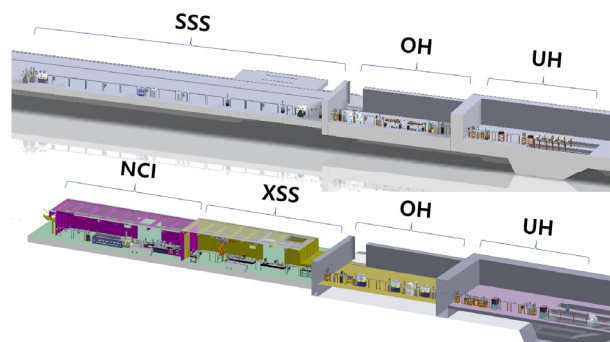


Figure 2: The layouts of hard x-ray beamline (bottom) and soft x-ray beamline (top).

*kimsh80@postech.ac.kr

Gas Monitor Detector (GMD) [1,2]

GMD can measure the intensity of X-ray beam by using photoionization of Xenon gas. A gas-based transmissive measurement such as GMD has some advantages:

- On-line intensity monitoring of each pulse is possible
- The wavefront of the coherent beam is preserved
- The gas target does not degrade with time
- The gas detector is not easily saturated by the peak power of the highly intense and strongly XFEL

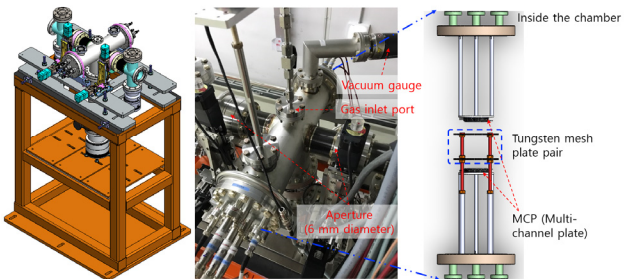


Figure 3: GMD installed at UH and schematic drawing.

The GMD of PAL-XFEL is installed at the downstream of the solid attenuator in the UH and uses xenon gas with $< \text{low} \times 10^{-5}$ torr. Figure 3 shows the schematic drawing and installed GMD at UH. Xenon gas can be controlled by motorized leak valve as shown in Fig. 4. Since the gas is used, it is necessary to maintain a vacuum without any influence on the beam. Accordingly, the chamber is further provided with a vacuum maintained by differential pumping at both ends of the detector. UH area is important area for beam transporting. Vacuum test has been performed many times to get the stable result. Table 1 shows differential pumping test result. The vacuum level was kept stable when leak valve was changed.

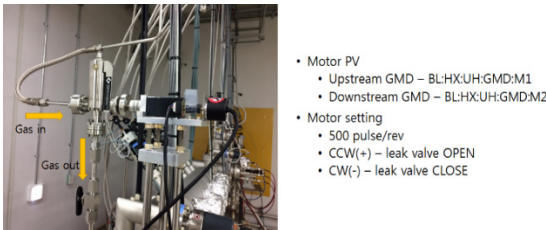


Figure 4: Motorized leak valve of GMD.

Table 1: Differential Pumping Test Result

Motor	Upstream GMD		Downstream GMD		Safety shutter	
	FRG (GMD cell)	Solid attenuator	FRG (GMD cell)	IG #5	IG #6	
-1500	8.06×10^{-7}	3.85×10^{-8}	1.70×10^{-7}	2.1×10^{-8}	3.5×10^{-9}	
-1200	8.05×10^{-7}	3.83×10^{-8}	1.73×10^{-7}	2.1×10^{-8}	3.6×10^{-9}	
-1000	8.05×10^{-7}	3.84×10^{-8}	1.86×10^{-7}	2.1×10^{-8}	3.6×10^{-9}	
-750	8.04×10^{-7}	3.93×10^{-8}	3.01×10^{-7}	2.4×10^{-8}	3.9×10^{-9}	
-500	8.03×10^{-7}	4.42×10^{-8}	9.82×10^{-7}	3.7×10^{-8}	5.6×10^{-9}	
-250	8.03×10^{-7}	1.11×10^{-8}	9.88×10^{-6}	2.0×10^{-7}	2.7×10^{-8}	
0	8.08×10^{-7}	5.68×10^{-8}	4.08×10^{-5}	1.2×10^{-6}	9.7×10^{-8}	

GMD's aperture size is 6 mm in diameter, and it caused to block or interfere the XFEL. Therefore, it should be tested about the vibration sensitivity. Figure 5 shows the characteristics of vibration displacement at the four measurement points. The results at each measuring position are summarized in Table 2. All of them are in nm range, so it proved that the aperture of the GMD did not affect to the XFEL.

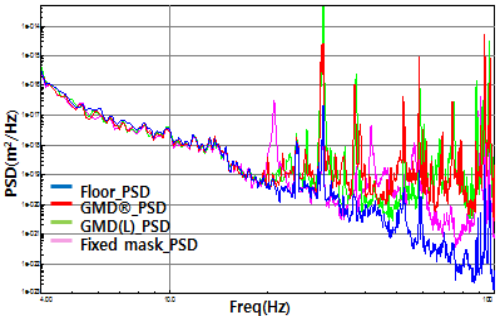


Figure 5: The characteristics of vibration displacement around GMD.

Table 2: The RMS and Peak to Peak Values at Four Measurement Points

	RMS	Pk-Pk
1-Floor	12.7 nm	36 nm
2-GMD(Right)	55.8 nm	159 nm
3-GMD(Light)	105 nm	296 nm
4-Fixed mask	129 nm	36.5 nm

Multifarious Injection Chamber for Molecular Structure Study System (MICOSS) [3]

The MICOSS has been developed for SFX experiments and installed at NCI beamline. It is composed of several instruments such as a dedicated sample chamber, sample injectors, sample environment diagnostic system, and detector stage for convenient distance manipulation.

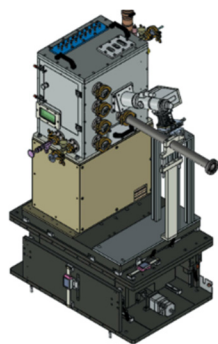


Figure 6: Schematic drawing of MICOSS and position manipulation stage.

Figure 6 and figure 7 show the design including stage system and manufactured chamber, respectively.

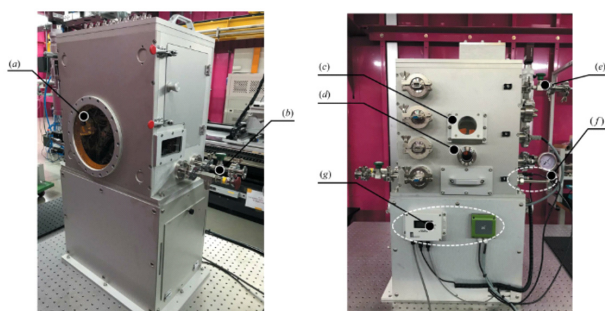


Figure 7: Manufactured MICOSS: (a) window for passing diffraction signal to detector, (b) pumping port, (c) view port for microscope, (d) XFEL pulse input port, (e) helium gas input port, (f), (g) Sensors & signal.

Sample Injector Sample injectors do main function for SFX experiment, and they are developed into two types, multi injector type and LCP (Liquid Cubic Phase) injector type as shown in Fig. 8.

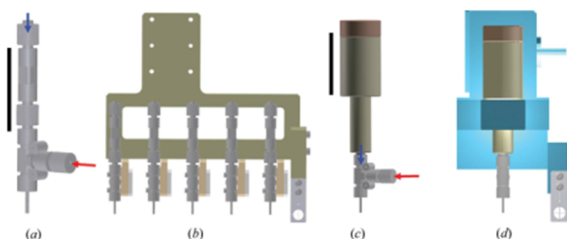


Figure 8: Two sample injector types: (a), (b) Multi-injector nozzle; (c), (d) LCP injector nozzle.

Chamber A helium-gas filled sample chamber provides relatively a low signal to noise. Basically, motorized stage of the MICOSS has 3 directions, X, Y and Z. It designed for easy access to exchange sample and sample injectors. The MICOSS also has motorized Photodiode (PD) and cross wire for sample positioning. Oxygen & humidity sensor can monitor the inner status of the chamber. Figure 9 shows the inner design of the chamber.

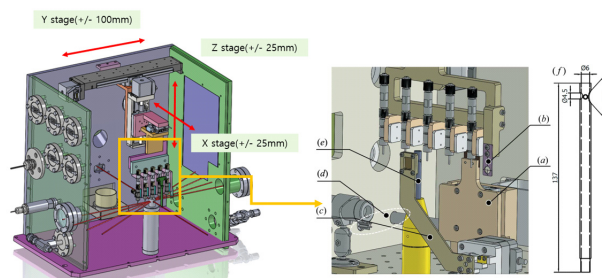


Figure 9: Sample injector: (a) pinhole position, (b) cross wire holder, (c) PD manipulator, (d) oxygen & humidity sensors (e), (f) sample catcher.

CONCLUSION

The construction of PAL-XFEL beamline has been completed, and the performance verification and the commissioning of several experiments are successfully done. The PAL-XFEL is operating for scientific experiments. During the construction and commissioning, key devices are developed, and the performance is verified. In the future, components of the beamlines will be upgraded for better scientific results.

ACKNOWLEDGEMENTS

The authors would like to thank beamline support team for helpful discussions and gratefully acknowledge.

REFERENCES

- [1] SeungNam Kim, Yeongduk, Yoon, Myeongjin Kim, Bongsoo Kim, "A study of vacuum pump at PAL-XFEL beamline", PAL-INT/ME-2013-002, 2013.
- [2] Seonghan Kim, Myeongjin Kim, Chaesun Lee, Seonmin Hwang, Jiwha Kim, Hocheol Shin, SeungNam Kim, "The installation report of hard & soft X-ray beamline at PAL-XFEL", PAL-INT/TS-2016-004, 2016.
- [3] Jaehyun Park, Seonghan Kim, Sangsoo Kim, Ki Hyun Nam, "Multifarious injection chamber for molecular structure study (MICOSS) system: development and application for serial femtosecond crystallography at Pohang Accelerator Laboratory X-ray Free-Electron Laser", *Journal of Synchrotron Radiation*, vol. 25-2, March 2018, DOI: 10.1107/S160057751800022X.

DESIGN OF A FLEXIBLE RIXS SETUP

D. Meissner*, S. Adler, M. Beye, A. Bühner, H. Krüger,
 R. Platzter, T. Reuss, M. Röhling, E.-O. Saemann, E. Saithong
 Deutsches Elektronen-Synchrotron DESY, 22607 Hamburg, Germany

Abstract

We present a new mechanical design for a RIXS experiment setup consisting of a sample environment vacuum chamber and corresponding spectrometer. It allows variable beam incidence angles to the sample as well as observation angles of the spectrometer.

The dispersive element of the spectrometer can be aligned in five DOF by motors inside the UHV chamber. The alignment of the CCD detector can be adjusted independently in the lateral and longitudinal position as well as incidence angle. In combination with a tiltable detector chamber this design allows for multiple observation methods, not limited to variable energies but also for use of different optics or direct observations of the sample.

REQUIREMENTS AND EXPERIMENT SETUP

Requirements for the setup are according to Fig. 1, as well as Table 1. In Addition the entire spectrometer Setup must rotate around the Sample Chamber.

The setup need not support changing the entire scattering angle field without breaking vacuum. Rather a cost effective yet easy to use and quickly changeable support structure has to be chosen.

The design of the sample chamber is fixed from the beginning of the design phase which also restricts placement of mechanics and supporting infrastructure.

To observe RIXS photons at the energy spectrum from 50 eV to 650 eV the positions of grid and detector have to be changed. The optical parameters are optimized to space constraints (available area at end station as well as placement of objects and assembly space required) and imaging qualities on the detector.

In addition to the ranges of movement of grid and detector according to Fig. 1 and Table 1 the setup can move the detector to any position in the rectangle defined by the two extreme points. Also horizontal view from sample to detector is possible.

SAMPLE ENVIRONMENT AND SUPPORT STRUCTURE

Figure 2 shows an overview of the experiment. The sample is located in a vertical, cylindrical vacuum chamber and is inserted from the top. Figure 3 shows the sample holder mechanism. The top flange of the chamber is a rotating feedthrough which supports the sample holder and addi-

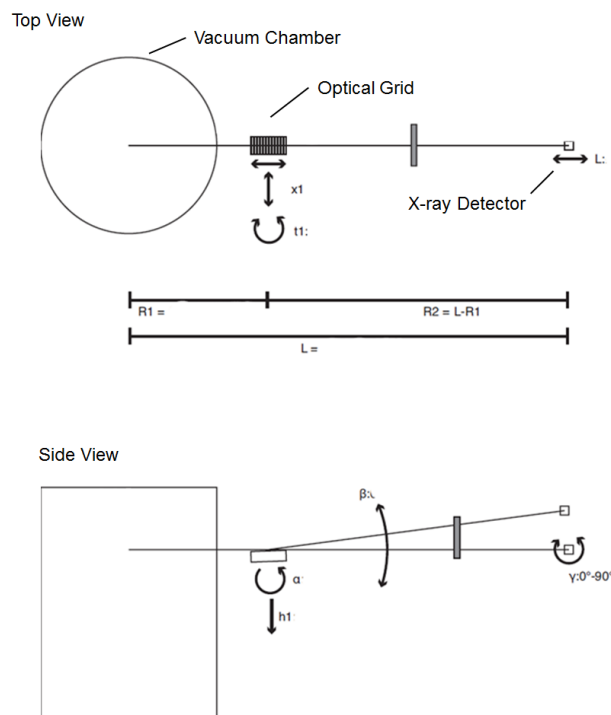


Figure 1: Position and movement parameters for optical elements.

Table 1: Correlation of RIXS Photon Energy and Positions of Optical Elements (Refer to Figs. 2 and 5)

Energy eV	R_1 mm	L mm	α deg	β deg	γ deg
50	300	1347	87,9	75,8	53,5
200	364	1240	87,9	82,7	23,1
400	399	1183	87,9	84,6	17,4
650	422	1146	87,9	85,6	13,9

tional infrastructure. The sample can be cooled to 25K or heated to about 350K.

To vary the angles between beam incidence on the sample and observation angle of the spectrometer a cost-effective solution was chosen. The beamline is connected to the chamber by a motor driven bellow system (see Fig. 4) that can vary incidence angles of $\pm 15^\circ$. For larger changes of incidence angle however the vacuum connection has to be broken and the bellow system has to be attached to another flange. By using all ports on the sample chamber any scattering angle can be reached.

The chamber is mounted on a support structure that can be adjusted to multiple beam heights above the floor and has

* daniel.meissner@desy.de

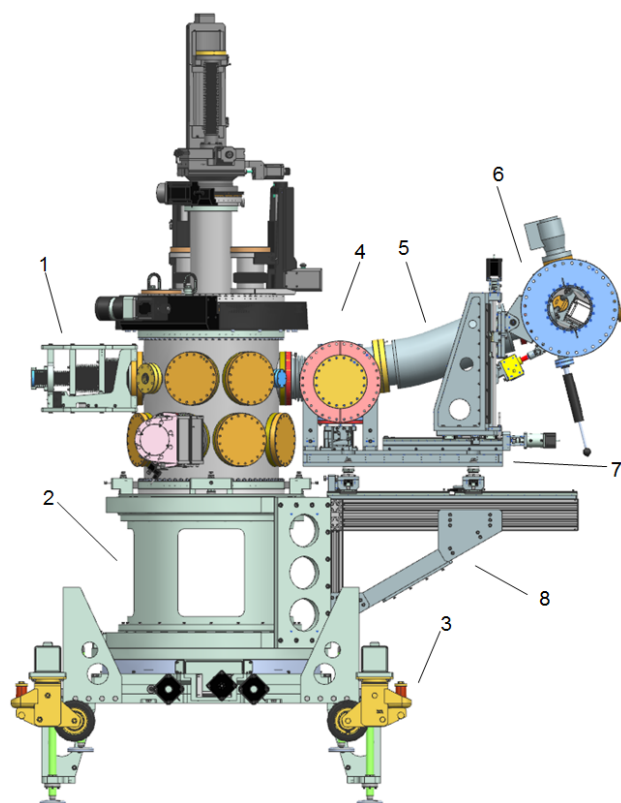


Figure 2: Overview of the experiment. Motor driven bellow system (1), support structure (2), gear system (3), grid chamber (4), DN150 bellow (5), detector chamber (6), spectrometer alignment table (7), rotating spectrometer support structure (8).

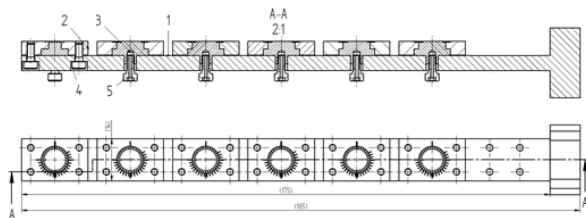


Figure 3: 6 way sample holder and adjustment system.

foldable wheels for easy transport of the entire setup. The lower alignment system of the setup has motor driven x- and y-stages as well as a rotational stage about the z axis for fine tuning of the position. Figure 5 shows an overview of the support structure.

To allow for variable observation angles with the spectrometer the support structure features a DN500 diameter rotational bearing that connects the spectrometer support to the chamber support. This rotational support can be locked in positions perfectly aligned with the flanges of the chamber.

SPECTROMETER DESIGN

The vacuum layout of the spectrometer consists of a grid chamber (DN250) that is connected to the sample chamber,

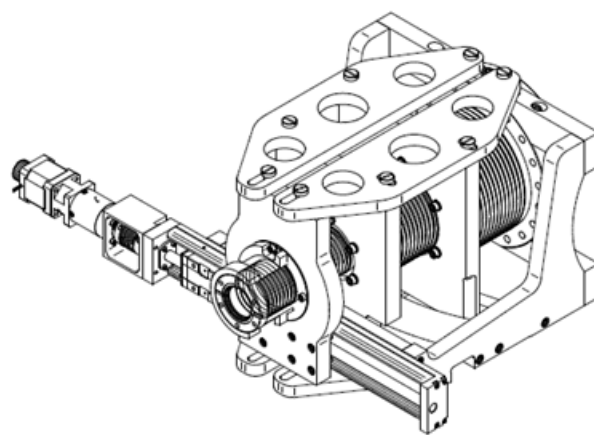


Figure 4: Motor driven bellow system to connect the beam-line to the sample chamber.

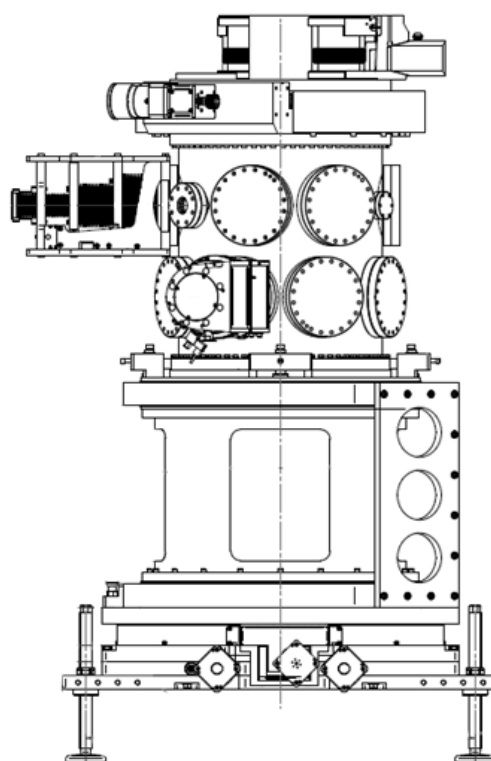


Figure 5: Support structure of the sample chamber.

and a detector chamber (DN300) connected to the grid chamber via a DN150 edge welded bellow. The grid chamber is fixed on a alignment table that sits on top of the rotating spectrometer support structure. It is used to perfectly align the spectrometer inlet flange with one of the sample chamber flanges. In addition it allows the spectrometer to be moved away from and clear the sample chamber during rotation to another sample chamber flange.

The detector chamber is supported in a three axis motor driven frame which sits on top of the alignment table. This frame can move the chamber in the x and z direction and

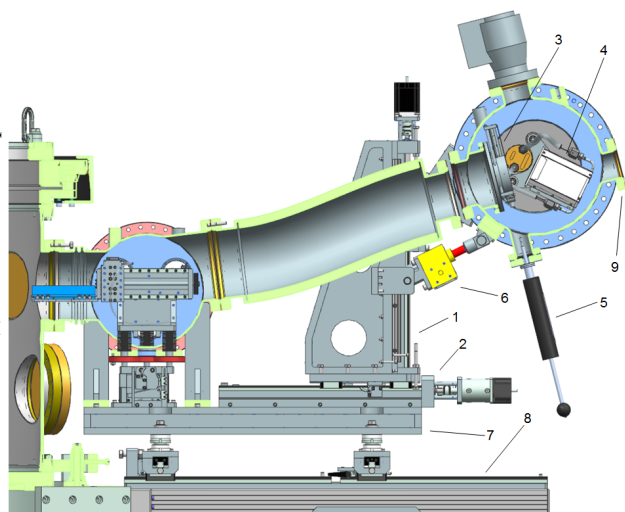


Figure 6: Cross-section view of the Spectrometer.

also tilt the chamber so that its inlet flange always points in the direction of the sample.

Figure 6 shows a cross-section overview of the spectrometer with the following positions: 1: Detector chamber z lift support and actuator, stepper motor with trapezoidal threaded shaft, two parallel linear guides; 2: Detector chamber x actuator and support, actuator same as for z lift; 3: Filter/Shutter Unit; 4: Detector, mounted on rotating feedthrough on the backside flange of detector chamber, electrical and cooling feedthrough; 5: manual linear feedthrough to operate Filter/Shutter unit Pos. 3; 6: Detector chamber tilt actuator. Allows to optimize the inlet aperture to be optimized and also to provide direct view to sample through flange Pos. 9; 7: Spectrometer support structure. Adjusts detector chamber to sample chamber and slides back on rails of rotating support Pos. 8 when changing flanges; 8: Rotating support structure. Fixed on sample chamber support structure, rotates 360°; 9: Observation port with DN63 window flange.

The internals of the grid chamber are shown in Fig. 7 with the following positions: 1: Grid holder, easily changeable; 2:

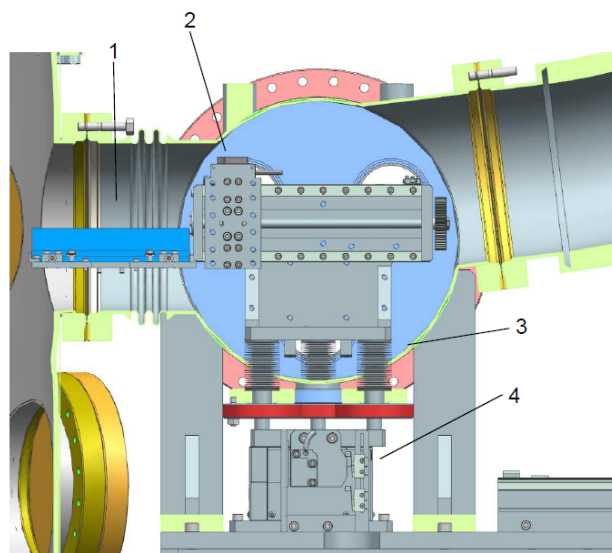


Figure 7: Cross section detail view of the grid chamber.

Grid stage x axis (see Table 1, parameter R_1); 3: Grid z axis feedthrough, 4: Grid z axis actuator, lower the grid to allow direct incidence from sample to detector. The positioning unit that supports the grid from the x axis stage is not shown due to a pending patent application at the time of paper submission.

CONCLUSION AND OUTLOOK

Design, manufacturing and assembly of this first stage is complete and the first measurements are ongoing. Even with not all motorized axes yet available the alignment and handling of the setup is very easy. Also the alignment, handling and stability of the dispersive element and the detector is well within the specified parameters for precision.

The design of the positioning unit for the dispersive element is currently patent pending.

A planned upgrade of the setup will rotate the spectrometer by 90° so that the detector moves in the horizontal plane.

DUAL BEAM VISUALIZER - INTENSITY MONITOR FOR LUCIA BEAMLINE AT SOLEIL SYNCHROTRON

C. Menneglier[†], V. Pinty, D. Vantelon, D. Roy and K. Desjardins,
 Synchrotron SOLEIL, L'Orme des Merisiers, Saint-Aubin, 91190 Gif-sur-Yvette, France

Abstract

LUCIA is a micro-focused beamline dedicated to X-ray fluorescence and X-ray absorption spectroscopy at SOLEIL Synchrotron. With its recent optical upgrade and photons flux increase, the three pink-beam diagnostics of the beamline have been upgraded to sustain a beam flux reaching 10^{13} ph/s and a power deposition of 20 W/mm^2 . This paper presents the thermomechanical study and the realization of new diagnostic detector adapted to the current constraints of use, making possible to both visualize the shape of the pink beam and to measure its intensity simultaneously in the same compact device. The X-ray beam is visualized by a piece of Al_2O_3 - Cr ceramic, soldered to a copper heat sink, whose fluorescence image detected in visible light with a suitable camera and optical system. The measurement of the photonic intensity is made by a polarized CVD diamond used as a photosensitive element, the current reading is made by a suitable low noise current to voltage amplifier. The design of this dual beam visualizer and intensity monitor, made by the SOLEIL Detector group with thermomechanical studies done by the Mechanical Design Office, will be presented in details in this paper. In-lab measurements will be also presented.

INTRODUCTION

The LUCIA beamline [1] is dedicated to micro-X-ray Absorption Spectroscopy (μXAS) and micro-X-ray Fluorescence (μXRF) experiments in "tender" X rays range of energy 0.6 - 8 keV. The range of energy offered by LUCIA allows μXAS experiments at the K-edge of the elements from sodium (Na) to iron (Fe) and L-edges of nickel (Ni) to gadolinium (Gd) and to the M-edges of rare earths and actinides. It makes it possible to apply these two non-destructive techniques to the measurement of heterogeneous samples, to make elementary maps at the photon spot scale ($2 \mu\text{m} \times 2 \mu\text{m}$), and to describe the local environment around these elements. In order to adjust the beam on the focusing and low-pass mirror, and on the monochromator, the beamline has several imagers and intensity monitor in pink beam. The monochromatic beam is finally sent on a sample placed on an x-z translation stage. (Fig. 1).

Typical imagers consist of a YAG scintillator screen placed perpendicular to the beam and a visible light camera

oriented at 45° to the screen. The intensity monitors consist of AXUV100 diode in the direct beam. Both are motorized for insertion/extraction.

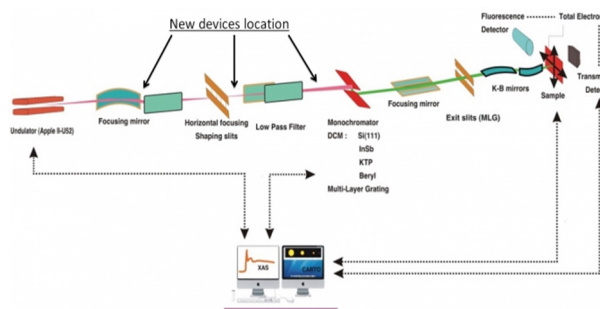


Figure 1: General layout of the Lucia Beamline.

TECHNICAL ISSUES

As a result of an upgrade of the first focusing mirror of the beamline, and a gradual increase in the intensity of the SOLEIL electron beam, the diagnostic elements of the line have undergone constraints exceeding their initial design limit. Degradations and alterations of their performance have appeared over time.

In addition, the orientation of the camera with respect to the scintillator screen requires closing the diaphragm of the camera to increase the depth of field. A long exposure time is necessary to compensate for the loss of light. This prevents detection of beam movement and creates latency during direct visualization of the beam for adjustment of optical alignments. This device had to overcome these limitations.

TECHNICAL SPECIFICATION

The new diagnostic devices must meet several functional needs:

- Image and monitor the X-ray beam;
- Totally extractable;
- Compatible with the pink beam properties;
- A incident power density of 20 W/mm^2 ;
- A maximum beam size of $300 \mu\text{m} (\text{H}) \times 1.2 \text{ mm} (\text{V})$.

The new diagnostics must also take into account technical constraints specific to the beamline:

- The imager and the intensity monitor must be designed on a single package (compact design), but will not be used simultaneously;
- They must be compatible with a level of 10^{-8} mbar vacuum;

[†] claud.menneglier@synchrotron-soleil.fr

- The scintillator screen and the camera optics will have to be perpendicular to ensure completeness of the beam in the same focal plane.

MECHANICAL DESIGN

Soft X-Ray Pink Beam Imager

Due to radiation hardness, thermal constraints and beamline energy, a Al_2O_3 ceramic scintillator has been chosen for X-rays conversion to visible light ($\sim 650 \text{ nm}$). This ceramic of 1 mm thick (AF995R Durox from Solcera, Moissy-Cramayel, France) is brazed directly on the copper finger to ensure holding and effective cooling (Fig. 2). This scintillator plate is placed at 45° from the X-ray beam axis. A camera and its objective, located in air, record the scintillator visible image through a classical optical viewport. (Fig. 3).

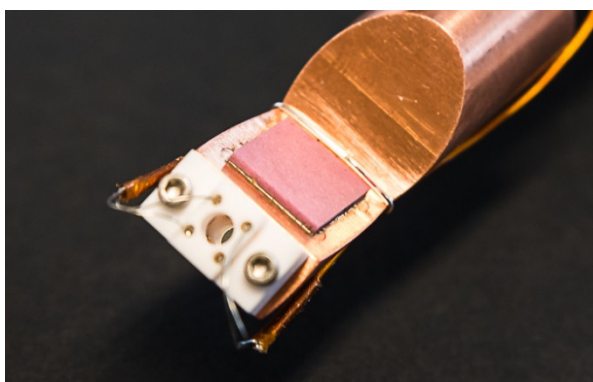


Figure 2: Brazed ceramic on copper finger.

In order to collect a maximum of light and to produce image with a good resolution, a lens with a large optic aperture is necessary. The ceramic scintillator screen is placed perpendicular to the optical axis. This allows us to use an objective with a larger resolution than the previous imager. An Edmund MMS R4 optics with an Obj-11 lens were chosen. The camera and its optics are located on the air side, and record the scintillator image through an optical quality viewport.

Camera is a *SOLEIL standard* Basler camera. Model acA1300-60gm with 1296×966 pixel resolution and with $3.75 \times 3.75 \mu\text{m}^2$ pixel size. These setup properties are given in table 1.

Table 1: Final Camera System Characteristics

Working distance	141 mm
Field of view	$6.7 \times 5.0 \text{ mm}$
Magnification	1.1
Image pixel size	$4.8 \mu\text{m}$
Resolution	36.0 lp/mm

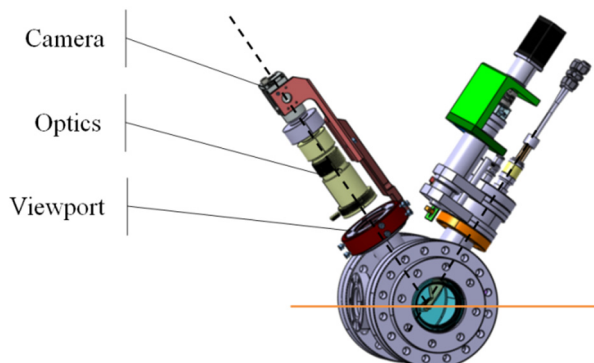


Figure 3: Camera and optics (modelized).

Soft X-Ray Pink Beam Monitor

As for the scintillator, the intensity monitor has to face with radiation hardness, thermal constraints and beamline energies. To record the X-ray beam intensity a high-purity single-crystal chemical-vapor-deposition (sc-CVD) diamond (from Element 6, Berkshire, UK) with a $50 \mu\text{m}$ thickness and a 200 nm Al deposit has been used as solid “ionization chamber” detector (Fig. 4).

Synchrotron beam tests have shown that for a wide range of photon energies from 0.2 up to 25 keV , the diode-like responsivity of diamond sensors is predictable, and efficient to provide absolute power measurements for sources of known energy bandwidth [2-3].

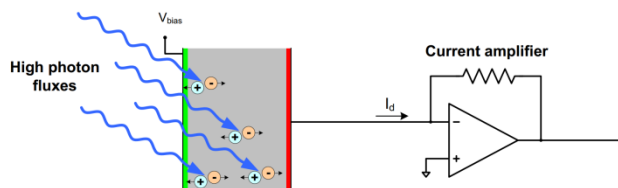


Figure 4: Photon conversion & readout principle.

The sc-CVD Diamond is glued to the same copper holder than the ceramic. It is positioned by centering pins and held in position by four Feinmetall pins made of gold-plated beryllium copper (HV compliant). These pins ensure contact with the Al electrode and allow the collection of charges created by the interaction of X-ray photons with diamond (Figs. 2 & 5). Four wires connect these pins to a UHV-BNC feedthrough where a low noise current to voltage amplifier located in air (FEMTO DDPCA300 low-current amplifier) allows recording the X-ray photocurrent generated.

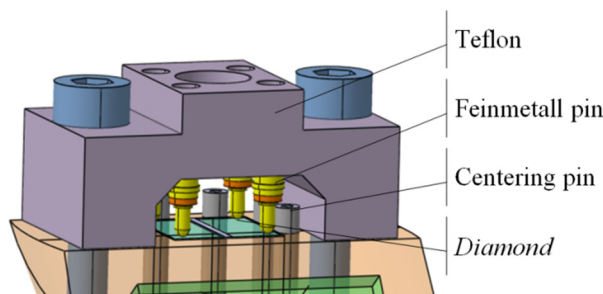


Figure 5: Diamond with holding system.

Manipulator and Motorization

The manipulator allows insertion and extraction of the ceramic screen and diamond in the beam, on a single axis. It is a commercial part (ref ZLMT25) of Vacgen (St-Leonard-on-Sea, UK). Because of air/vacuum pressure difference, it requires a 1.2 N.m momentum for extraction.

It is motorized by a *SOLEIL compliant* stepper motor and a moto-reductor.

THERMAL STUDIES

A thermal study has determined the most efficient cooling system between air or water. It deals only with the diamond, as it is the most critical element in the system, because of its distance from the cold point of the copper rod, and its lower thermomechanical resistance. The study was based on a system modeled under ANSYS. The maximum power of the beam absorbed by the diamond (30 W) on a spot size of $300\text{ }\mu\text{m} \times 1.2\text{ mm}$ (H \times V) has been use for the simulation. The results with air cooling show a hot spot at a maximum temperature of 255°C as illustrated on Figure 6 (a). On the contrary, water cooling limits the hot spot to 66°C (see Figure 6 (b)).

As the maximum admissible temperature on sc-CVD is 100°C , water cooling is the only exploitable option.

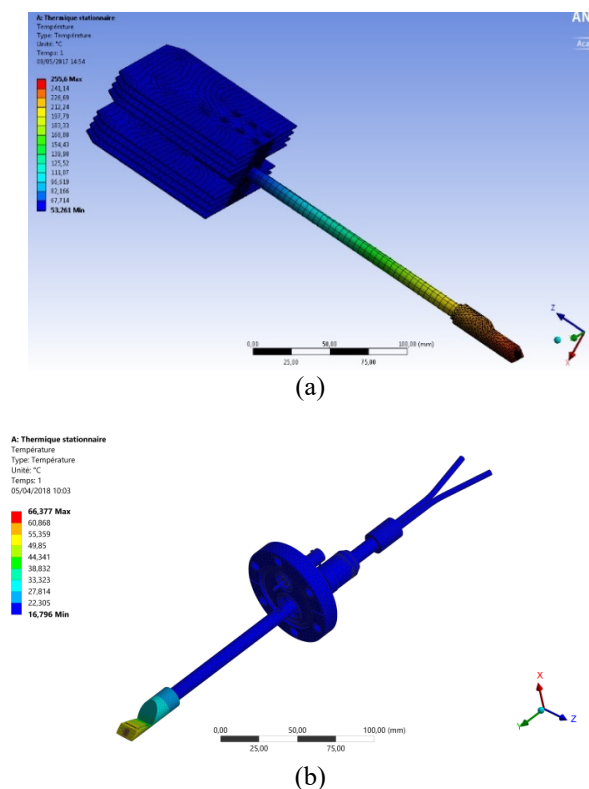


Figure 6: Thermal simulation of cooling with air (a) and water cooling (b).

INSTALLATION ON BEAMLINE

The installation of three complete dual beam visualizer-intensity monitors was made with success in June 2018 on the beamline. First images were recorded by the camera to adjust the closing of the beamline front-end diaphragm as shown of Figure 7. Other tests are on-going.

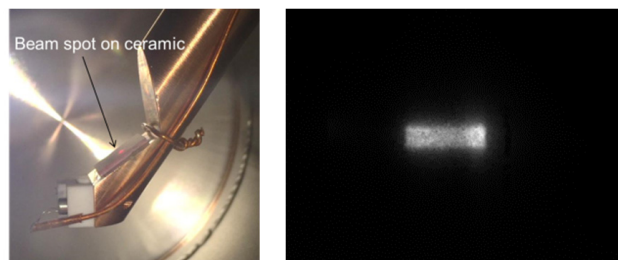


Figure 7: First beam image of LUCIA beam $653\text{ }\mu\text{m}$ (H) \times $206\text{ }\mu\text{m}$ (V) obtain with the new imager placed just before the monochromator.

CONCLUSION

A new concept of dual system (beam visualizer + intensity monitor) has been designed, realized and installed with success on the LUCIA beamline at SOLEIL synchrotron in June 2018. First tests of the new devices are very promising.

Nevertheless, some adjustment of the mechanics remains to be done as well as a characterization of the diamonds for the measurement of intensity.

This concept can be reused for now on other beamlines and especially for SOLEIL upgrade.

REFERENCES

- [1] Vantelon D. *et al*, "The LUCIA beamline at SOLEIL", *Journal of Synchrotron Radiation*, Vol 23, part 2, Mar. 2016, pp. 635-640, DOI: 10.1107/S1600577516000746.
- [2] J. W. Keister *et al*, "Diamond X-ray photodiode for white and monochromatic SR beams", *Nucl Instrum Methods Phys Res A*, vol. 649-1, Sep. 2011, pp. 91-93, DOI:10.1016/j.nima.2010.11.135.
- [3] Desjardins K. *et al*, "Ultra-thin optical grade scCVD diamond as X-ray beam position monitor" in *Journal of Synchrotron Radiation*, vol. 21-6, Oct. 2014, pp1217-1223, DOI: 10.1107/S1600577514016191.

DIRECT LN2 COOLED DOUBLE CRYSTAL MONOCHROMATOR

Tetsuro Mochizuki[†], Kazuteru Akiyama, Katsumi Endo, Hirotsugu Hara, Takumi Ohsawa,
 Junki Sonoyama, Tetsuya Tachibana, Hisataka Takenaga, Koji Tsubota,
 TOYAMA Co. Ltd., Kanazawa, Japan
 Klaus Attenkofer, Eli Stavitski, BNL, Upton, Long Island, New York, USA

Abstract

A liquid-nitrogen-cooled (LN) X-ray double crystal monochromator has been designed and built for the high power load damping wiggler beamline of the NSLS2. It was designed as the direct LN first crystal to dissipate the max heat load of 2 kW and the second is in-direct-braid LN. It is designed to operate for beam energy 5 to 36 keV with fixed exit beam mode, and for QEXAFS compatible with channel cut mode. It is designed to rotate the Bragg axis with using AC servo motor and achieve up to 10 Hz scan.

INTRODUCTION

Directly fin-cooling cryogenic crystal is designed and built for the first crystal of NSLS-II ISS beam line monochromator. The ISS damping wiggler source incident power to the first crystal is total power of 2 kW and its power density of 7 W/mm².

Directly water cooled silicon crystal was designed and built for use in high power synchrotron radiation beam-lines. The fin-cooling crystal used at KEK-PF BL16 multi pole wiggler source beamline showed its cooling effectiveness at the total incident power up to 1.6 kW and power density up to 0.7 W/mm² [1]. The total heat load is comparable to the incident power of ISS monochromator but the power density is one tenth.

Another crystal cooling method of direct LN2 cooling was designed and used for cooling the high heat load and high power density source at AR-NE3 in-vacuum undulator beamline [2, 3]. The maximum heat load is 800 W and the power density is 4.2 W/mm². The crystal is cooled by LN2 pool boiling. The power density is comparable to that of the ISS crystal but the total power is about half.

Cryogenic internal cooling and side cooling crystals were tested at NSLS on beam lines X25 and X17[4]. The tests are carried out for power density: 150 W/mm², total power: 75 W and power density: 0.5 W/mm², total power: 100 W. The power density is very high but the total power is small.

As cryogenic silicon crystal is adequate thermo-mechanical property for cooling the high power density radiation source and directly fin-cooling crystal can handle the high heat load, a new direct fin-cooling cryogenic silicon crystal was designed and fabricated for the ISS monochromator first crystal. The design of this crystal depends on critically on a number of mechanical dimensions. One is the Si thickness between the diffracting surface and the top of the LN2

channel. As this thickness is reduced, but the temperature and the heat flux on the LN2 channel are increased. If the temperature of the channel exceeds the starting point of nucleate boiling, LN2 boiling begins on the cooling channel surface. When the heat flux go through the critical heat flux, the heat transfer is suddenly decreased, and part of the channel surface is insulated with a vapour film and then the cooling of the crystal fails.

The individual widths of the cooling channels and Si fins, and the geometry of the crescent inserts influence the effectiveness and uniformity of the cooling, and should be matched to the parameters of the cooling system.

The Si top thickness, the channel widths, the geometry of inserts, the over-all Si thickness and the coolant flow rate were optimized by the simulation with using FEA analysis.

DESIGN OF SI CRYSTAL

The Si (111) first crystal is a cylindrical shape and has a disc shape thick flange in the middle of it with which it is mounted to a manifold and seals the vacuum. The cooling semi-circular channels are cut into the backside through which LN2 is circulated. The size of the crystal is 62.5 mm in height, 77 mm in top surface diameter, 125 mm in flange diameter.

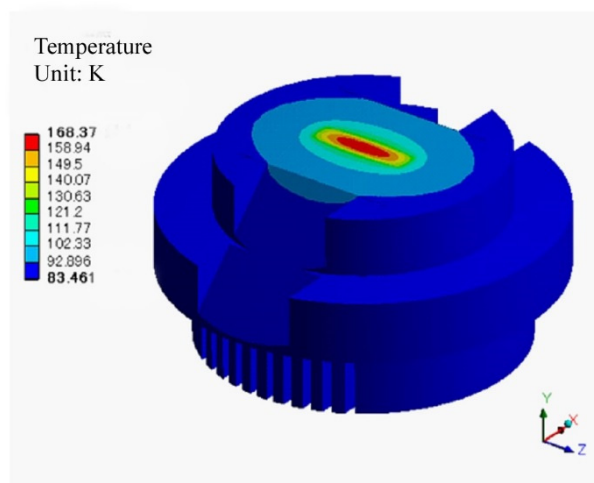


Figure 1: Temperature profile of the first crystal. Total heat load=2 kW; power density=7 W/mm²; foot print=33.6 mm x8.51 mm (H x V); T-LN2=80 K; h=0.0103 W/mm²K. This calculation model is for the thermal design phase.

[†] mochizuki@toyama-jp.com

Thermo-mechanical analyses were carried out by using FEA software ANSYS and the results are shown in Fig. 1 and Fig. 2.

The heat load on diffraction surface is 2 kW and the heat flux is 7 W/mm². The LN2 flow rate is 0.52 l/min for each channel and its temperature is 80 K. Figure 1 shows the temperature profile of the crystal, the maximum temperature is 168.4 K at the diffraction surface and the minimum is 83.5 K. Figure 2 shows the temperature profile at top of cooling channels and the maximum is 97 K. The calculated maximum heat flux of cooling channel is 0.18 W/mm² which is much smaller than the critical flux of 1.4 W/mm² estimated by using the CHF correlation [5, 6].

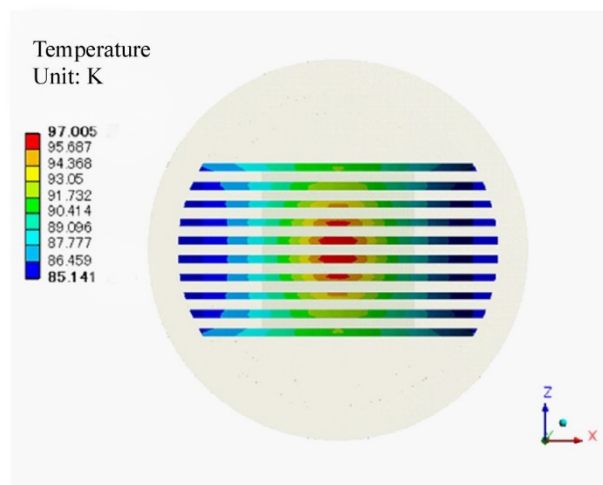


Figure 2: Temperature profile of the top of channel. The maximum heat flux of the channel is 0.18 W/mm².

Thermal deformation profile perpendicular to the crystal surface is shown in Fig. 3. Figure 4 shows the thermal slope error of the crystal is much smaller than the angular width of the reflectivity curve (Darwin width).

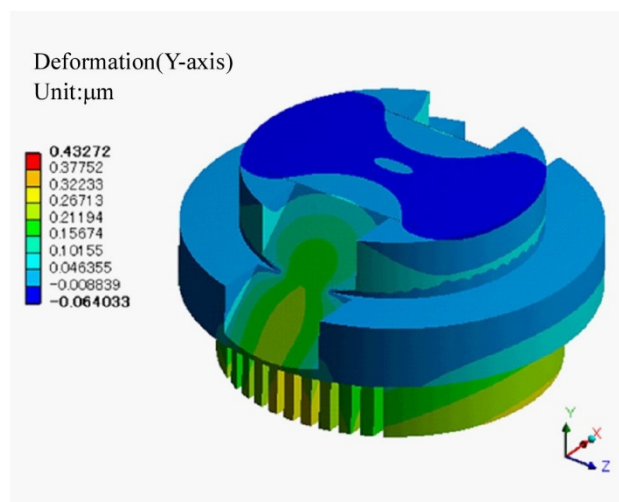


Figure 3: Deformation profile in perpendicular to the diffraction surface. Reference temperature for the calculation of thermal deformation=83.5 K. LN2 pressure=0.5 MPa absolute.

The appropriate size and shape of DCM first crystal and the shape of its cooling channel were evaluated by FEA analysis of various crystal designs.

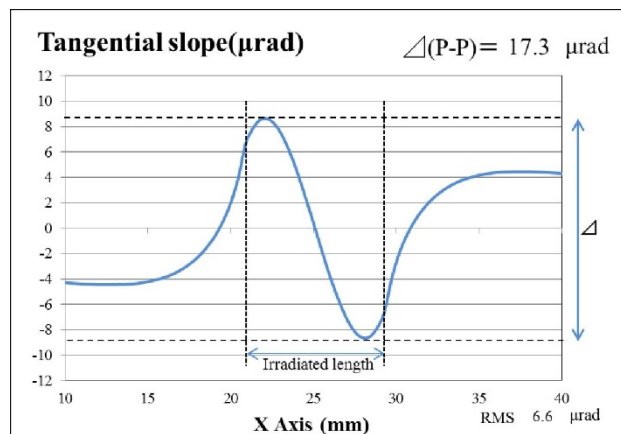


Figure 4: Tangential slope error of Si first crystal.

The final crystal shape is slightly different from the FEA model. From the reviewing the range of Bragg angle to be used, the notches in the upstream and downstream portions of the diffraction surface were unnecessary and it was enough to chamfer the peripheral portion. The final first crystal shape is shown in Fig. 5 and Fig. 6.

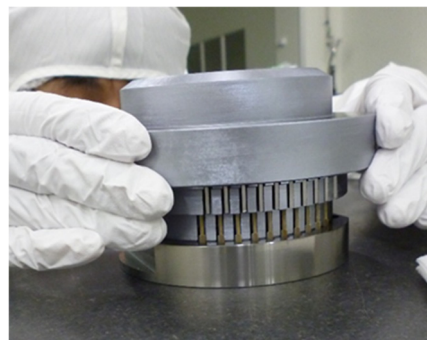


Figure 5: Si first crystal and crescent inserts assembly.

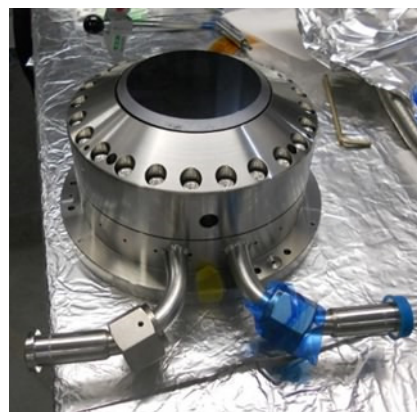


Figure 6: Si first crystal mounted to the manifold.

Figure 5 shows the engagement check of Si first crystal and the crescent inserts assembly. Figure 6 shows the assembled crystal mounted to the manifold. The vacuum seal between the crystal and the manifold is kept with using Indium wire.

SUMMARY

A directly LN2 cooled crystal for double crystal monochromator has been designed and built for the damping wiggler source ISS beamline of NLSL-II. It is in successfully operation.

The full heat load condition is 2 kW of total power and 7 W/mm² of the power density. The maximum heat flux on LN2 cooling channel is 0.18 W/mm² which is 13 % of critical heat flux at full heat load condition.

This crystal is installed in the ISS DCM and the scan mode was tested up to 10 Hz.

REFERENCES

- [1] T. Oversluisen, T. Matsushita, T. Ishikawa, P. M. Stefan, S. Sharma, A. Mikuni, "Performance of a directly water-cooled silicon crystal for use in high-power synchrotron radiation applications", *Rev. Sci. Instrum.* 60, July 1989, pp. 1493-1500.
- [2] S. Yamamoto, T. Shioya, M. Hara, H. Kitamura, X.W. Zhang, T. Mochizuki, H. Sugiyama, M. Ando, "Construction of an in-vacuum type undulator for production of undulator x rays in the 5-25 keV region", *Rev. Sci. Instrum.* 63, 1992, pp. 400-403.
- [3] T. Mochizuki, X. W. Zhang, H. Sugiyama, J. Zhao, M. Ando, "Cooling of silicon crystal monochromator for the undulator x rays at beamline NE3", *Rev. Sci. Instrum.* 66, February 1995, pp. 2167-2170.
- [4] G. Marot, M. Rossat, A. Freund, S. Joksche, H. Kawata, L. Zhang, E. Ziegler, L. Berman, D. Chapman, J.B. Hastings, M. Larocci, "Cryogenic cooling of monochromators", *Rev. Sci. Instrum.* 63, 1992, pp. 477-480.
- [5] W.R. Gambill, "Generalized Prediction of Burnout Heat Flux for Flowing, Subcooled, Wetting Liquids", *Chem. Engr. Progr. Sympos. Series* 59, 1963 pp. 71-87.
- [6] W.R. Gambill, T. Mochizuki, Advanced Neutron Source Design: "Burnout Heat Flux Correlation Development", in *Proceeding ANS/ENS* 1988.

ENGINEERING CHALLENGES FOR THE NEH2.2 BEAMLINE AT LCLS-II*

F. O'Dowd[†], D. Cocco, J. Defever, S. Guillet, C. Hardin, D. Morton, M. Owens, T. Osier, D. Rich,
 L. Zhang, G. Dakovski, SLAC National Laboratory, Menlo Park, USA

Abstract

SLAC National Accelerator Laboratory is developing LCLS-II, a superconducting linear accelerator based free electron laser capable of repetition rates up to 1MHz. The NEH2.2 Instrument at LCLS-II will use this combination of exceptionally high flux of monochromatic photons to achieve multidimensional and coherent X-ray experimental techniques that are possible only with X-ray lasers. The challenges, which emanate from delivering the beam from the sub-basement level to the basement of the Near Experimental Hall (NEH) along with the stringent requirements for providing a stable beam at the interaction points, necessitate unique engineering solutions.

With this paper we present the conceptual design for the NEH2.2 Instrument along with an overview of the R&D program required to validate design performance. Furthermore, it will show the design of the proposed Liquid Jet Endstation (LJE) and Resonant Inelastic X-Ray Scattering Endstation (RIXS) that will be installed on the beamline. After introducing the context and the layout of the beamline, this paper will focus on the main technical challenges and present the mechanical design solutions adopted for beam delivery and other strategic components.

INTRODUCTION

The LCLSII is a nextgeneration facility based on advanced superconducting accelerator technology (continuouswave RF) and tunable magnetic undulators. The Xray FreeElectron Laser (FEL) is being designed to deliver photons between 200eV and 5keV with an unprecedented flux, approximately 10^{18} ph/s ($0.1\text{mJ/pulse} = 10^{12}\text{ph/pulse}$), at repetition rates as high as 1MHz using a superconducting RF linac (SCRF) while still providing pulses at short wavelengths and high Xray pulse energy over the photon range of 1 to 25keV using the existing copper RF (CuRF) LCLS linac at 120Hz.

The unique LCLS-II capability opens the possibility to follow chemical dynamics with time resolved x-ray absorption and emission spectroscopy as well as time resolved inelastic X-ray scattering. LCLS-II will enable the full implementation of time-resolved resonant X-ray Raman spectroscopy (resonant inelastic X-ray Raman scattering, RIXS). RIXS uniquely provides information on both occupied and unoccupied valence states probed from core levels to achieve chemical specificity.

NEH2.2 BEAMLINE

The NEH2.2 beamline fulfils the need for high throughput spectroscopic and resonant scattering applications with

the high repetition rate LCLS-II beam (see key requirements in Table 1). It will take advantage of the unprecedentedly high flux of narrow-band, nearly transform-limited femtosecond soft X-ray pulses to open new scientific opportunities for spectroscopic studies of elementary excitations. The major components include a beamline monochromator, bendable re-focusing optics, pump laser integration and two endstations: Resonant Inelastic X-ray Scattering (RIXS) Endstation and Liquid Jet Endstation (LJE).

Table 1: Key Requirements

Parameter	Range	Comment
Photon Energy	250-1600eV	Reject 3 rd harmonic at O
Beamline Transmission	20%	Zero Order
Bandwidth Control	>50,000; 5-10,000	High resolution RIXS
Spot Size	2-1,000 μm	Adjustable

X-ray Optical Layout

The layout of the beamline stretches from the Front End Enclosure (FEE) into the Near Experimental Hall (NEH) and ultimately to the upper level, as shown in Figure 1. The beam will be deflected vertically by the soft X-ray monochromator (through a combination of mirrors and a grating) and will rise at an angle of $\sim 7^\circ$. A horizontally deflecting flat mirror directs the beam south by $\sim 3^\circ$ towards NEH 2.2, while the straight-through beam continues to NEH 2.1. The beamline exits the FEE high on the east wall and enters Hutch 1 (AMO), where the exit slit is mounted. The beam continues in Hutch 1, penetrates the ceiling and continues to the basement level of the NEH. The beam is then deflected back down by a combination of a flat and vertically re-focusing mirror, so it is again horizontal, and enters the RIXS Sample Chamber, Figure 2.

The beamline monochromator is projected to house four gratings ruled at different groove densities. Three of them are used to provide very high spectral resolution. The fourth one has a low groove density (50l/mm) and will provide transform limited beam with resolution between 5 and 10,000. The footprint of the beam on the grating is controlled using the elliptical bendable mirror upstream of the monochromator. For the very high resolution option, approximately 10^{15} ph/s, in first diffraction order, at resolving power (RP) up to 50,000 will be made available at the sample location in high repetition rate mode.

* fodowd@slac.stanford.edu

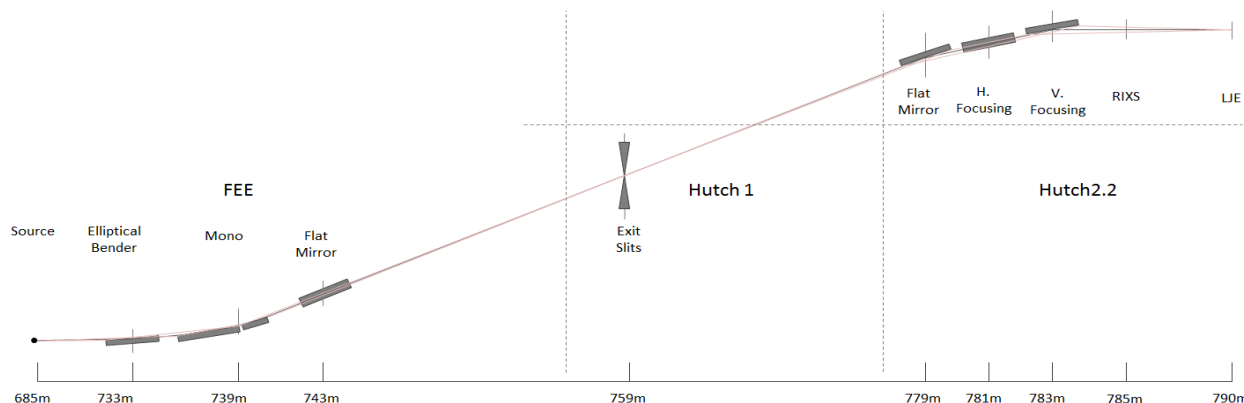


Figure 1: NEH2.2 Beamline Layout.

Liquid Jet Endstation

LJE is comprised of a sample chamber, designed with emphasis on soft X-ray spectroscopy experiments on liquid samples, and two X-ray emission spectrometers, the Varied Line Spacing (VLS) portable spectrometer and the Transition Edge Sensor (TES) spectrometer. The VLS is a grating-based spectrometer which disperses the beam and the spectrum is recorded by a 2D position-sensitive detector. Here resolving power $>2,000$ can be achieved. Alternatively the TES spectrometer allows for higher count rate at resolving power of $\sim 1,000$.

For typical liquid-based experiments, samples in solution are introduced via a jet, mounted on a manipulator. Adequate pumping must be provided to ensure no beamline contamination and proper detector operation. Key requirements for this endstation include ensuring spatial and temporal overlap of x-ray, pump laser and sample jet; sample positioning and stability; sample delivery and extraction and data acquisition rates.

RIXS Endstation

The RIXS spectrometer at LCLS-II will have a target resolving power (RP) of 50,000 and a combined (beamline + spectrometer) RP of better than 30,000 at 1keV. A unique aspect of the RIXS instrument enabled by LCLS-II is the capability of performing time-resolved measurements with high energy resolution (e.g., 100fs correspond to 18meV at the Fourier-transform limit) to study the dynamics of these collective excitations and photo-induced non-equilibrium states. Upon photo-excitation, one can readily probe the temporal evolution of elementary excitations.

For typical RIXS experiments, solid samples are mounted on in-vacuum diffractometer and cooled to low (down to few K) temperatures. The soft x-ray fluorescence is spectrally dispersed by a diffraction grating and the spectrum is recorded by a 2D position-sensitive detector. In order to accurately map out the momentum transfer-dependent excitations, the spectrometer (grating and detector) needs to rotate over a large angular range (40° - 150°).

The spectrometer consists of a combination of horizontally collimating mirror and vertically displacing set of gratings, together with a multilayer polarization analyzer

and 2D detector. The positioning of the detector in the focal plane along with its stability and that of the gratings are key parameters in delivering performance. Sources of vibration in and around the RIXS endstation need to be minimized so as not to adversely affect measurements.

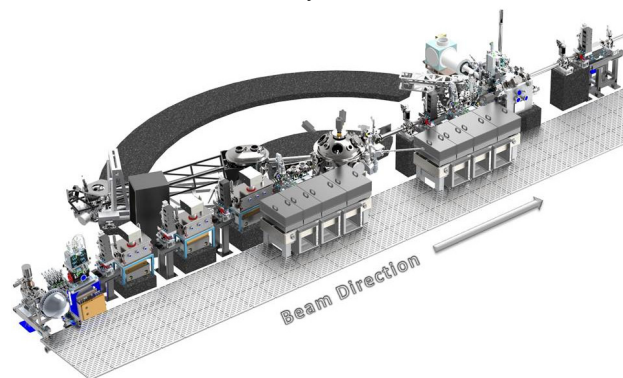


Figure 2: NEH2.2 Endstations.

CHALLENGES

The NEH consists of three floors: a ground floor, basement and sub-basement levels. The basement floor on which the NEH2.2 instrument will be installed is 36" thick reinforced concrete, which then reduces to 18" on the North end of the hutch and extends to the walkway beyond. Delivering stable beam, in both position and energy, while also maintaining overlap with the optical laser and sample delivery system provides significant challenges for the design of this instrument. This section will present some of the main challenges and proposed design solutions.

Building Structure

The layout of the optical system is a multifactorial optimization to meet scientific requirements through trade-offs between technical, resource and space constraints. Delivering beam from the FEE to an upper level of the NEH is not without significant challenges and risk. Foremost among those is maintaining the required spectral resolution. A concept solution is currently being developed which will use a photoemission spectrometer for diagnostic purposes. In this design, the exit slit will be used as a pick-off to send an offset beam to this diagnostic, allowing a non-destructive feedback on energy resolution, Figure 3.

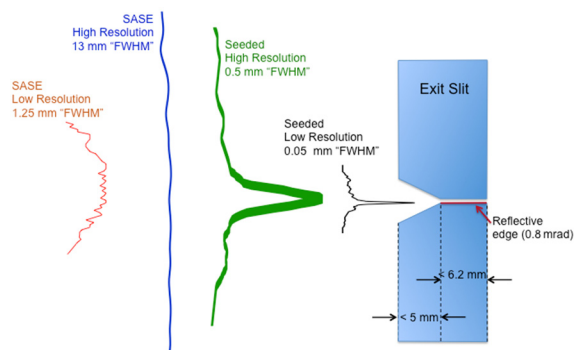


Figure 3: Relative dimension of the dispersed beam at the exit slit location.

Stability

The South and East sides of the building are fully underground, while the North and West are exposed to the elements. The induced heating by solar radiation on the building has led to noticeable bowing of the basement and sub-basement floors over a diurnal cycle. Thermal measurements of the NEH building show large variations in temperature over this cycle, which is manifested in relative variation in floor-to-ceiling heights and across individual slabs. Figure 4 shows hydrostatic levelling system (HLS) measurements on the floor of the NEH2.2 hutch.

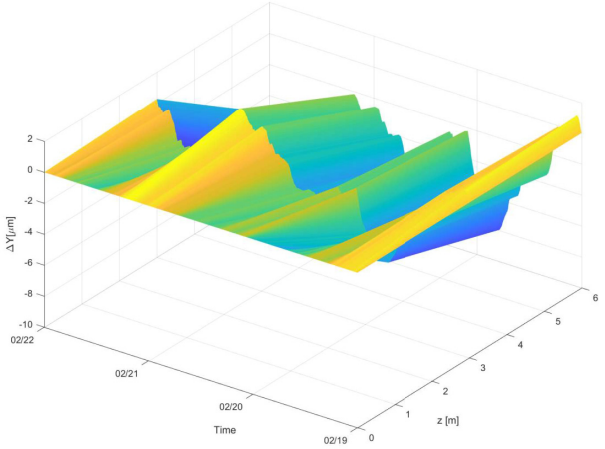


Figure 4 Hydrostatic Level Measurements of Hutch2.2.

A global solution to insulate the building was proposed. Initial analysis has shown that the variation can be reduced by a factor of 30 through insulation of the North and West faces as well as improved performance through shading of the exposed roof. Furthermore, where forced air ventilation was traditionally used, the new hutches will employ radiant panels to remove short term thermal oscillations and pressure fluctuations.

The FEE is a separate structure and measurements of this area show a diurnal change of approximately 10 μm (see Table 2). Comparing the building motion measurements with the outside temperature a clear correlation can be derived.

Table 2: Floor Deformation

Condition	West-East	North-South
Current	1.8 μm	12.63 μm
Roof Shading	1.2 μm	8.16 μm
Foam 20cm	0.07 μm	0.65 μm
Foam + Shading	0.06 μm	0.29 μm

Vibration

A series of measurements were taken in the location of the future NEH2.2 hutch to measure the vibration on the basement level. As shown in Figure 5 many external sources can induce vibration on the floor of the hutch.

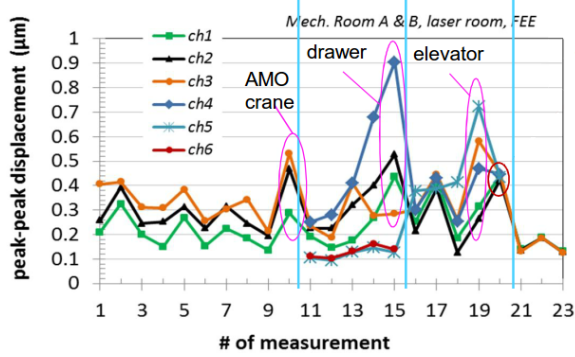


Figure 5 Vibration Measurements in NEH.

While it will be possible to restrict much of this noise, it is proposed to include an accelerometer in the hutch to identify and veto data above a given threshold level.

Cooling

The monochromator consists of a pre-focusing mirror, flat mirror and grating, providing a fixed exit angle. Up to 200W beam power will irradiate the monochromator. To preserve the beam quality, all the optics shall be water-cooled. Particularly challenging is the case of the flat mirror. During the scan, the beam position on the flat mirror will change with energy, inducing a significant temperature variation along its length. This temperature variation results in a aspherical thermal ‘bump’ around the beam footprint, impossible to correct entirely with a bender.

A scheme will be implemented with variable length cooling that will allow optimization of the mirror cooling to change with the changing footprint and location of the beam.

CONCLUSION

The NEH2.2 beamline is progressing through its preliminary design stage, with the LJE expected to be operational in June 2020 and RIXS June 2021.

ACKNOWLEDGMENTS

The authors would like to acknowledge the L2S-I Team, specifically Lance Lee, Ernesto Paisier & Xianchao Cheng.

MAGSTAT V3: AN IN-VACUUM VARIABLE-GAP QUADRUPOLE WITH ROTARY PERMANENT MAGNETS

V. Pinty, H. Popescu, N. Jaouen, F. Marteau, P. Prout

Synchrotron SOLEIL, L'Orme des Merisiers, Saint-Aubin, 91190 Gif-sur-Yvette, France

Abstract

MAGSTAT is a quadrupole designed to magnetize samples with a variable magnetic field in flow density and in directions. Four rotary permanent magnets allow the user to specify a direction for the field and changing in situ the gap between the poles drives the field intensity. The first prototype was realized in 2016 on the SEXTANTS beamline in the framework of SOLEIL-MAXIV collaboration; a second version has been manufactured for MAXIV Softlmax beamline. This third version shows a significant evolution of the mechanical design, guaranteeing a much better stiffness in high field configurations. Samples up to Ø74mm can be placed in this quadrupole, and the tiny ones which may fit in a Ø10mm circle or smaller, can be magnetized with a 1T local field. The angle of each magnet is driven by a dedicated stepper motors with a big reduction ratio. The total gap is ensured by a single motor, and its motion is symmetrically transferred to the magnets through an Archimedean spiral. The first prototype is installed permanently at COMET endstation dedicated to the coherent scattering of soft X-ray in transmission for imaging magnetic materials via the Fourier Transform Holography or ptychography techniques.

SPECIFICATIONS

The initial specifications were:

- The quadrupole should fit in CF100 DN flange so it can be transferred to or removed from the sample through the CF100 vacuum chamber fittings.
- The horizontal magnetic field should be driven by four motorized rotating magnets, with a variable motorized gap.
- The magnetic field should reach ~1T, at minimum gap on the center of the quadrupole.
- All motorized movements should be encoded.

FIRST AND SEDOND MAGSTAT PROTOTYPES

Mechanical Description

In order to drive magnets rotations, each magnet has a dedicated UHV stepper motor and is coaxially mounted on it. The maximum field of 1T is reached only when gap of the magnets is about 12mm, with Ø26mm permanent magnets made of NdFeB. The closest motor size is Ø22mm, with the highest reduction ratio, the output torque is 1.5N.m.

Each motorized magnet block is mounted on a linear translation oriented towards the centre of the poles. To drive the four linear translations, the motorized magnets

mounts are locked in a double Archimedean spiral (green part in Fig. 1) path which crosses the translation path [1].

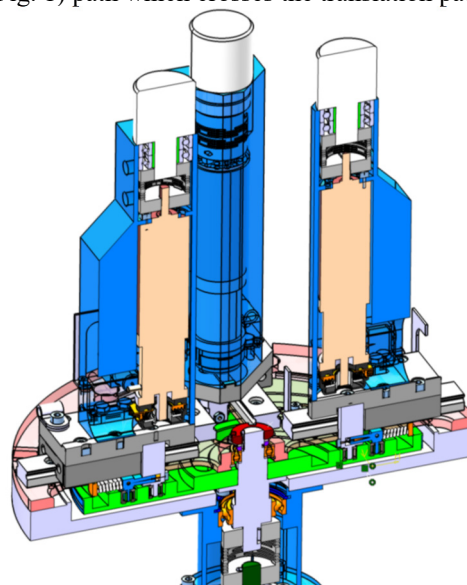


Figure 1: Section view of CAD V1 MAGSTAT prototype.

This solution ensures a great radial compactness since there is only one motor for the four symmetric linear displacements, and it is coaxially mounted with respect to the poles.

Performance

The first prototype (Fig. 2), realized in 2016 was able to achieve good performance in most field configurations and is being use on the SEXTANTS beamline.

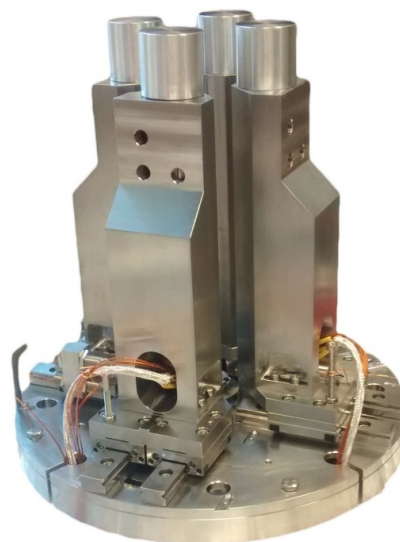


Figure 2: MAGSTAT V1 prototype main parts overview. Bottom disk diameter is less than Ø100mm.

However, the lack of vertical stiffness for very low gap configurations tended to lock the whole system at the closest gap and disorient magnets angle. Each magnet block is mounted on a double miniature guideways which relatively low stiffness comes to be critical. Although the distance between the magnet and the guideways is reduced to the minimum, it is still significant for the lever arm. The major problem is the length of the magnets motors, with their three stages planetary gearboxes, that lead to such a lever arm.

THIRD MAGSTAT PROTOTYPE

Mechanical Description

The apparent lack of stiffness compared to the force coming from the magnets leads to a complete redesign of the four magnet blocks (magnets, motor and mounting parts), while using most of the parts of the first prototype, especially the same motors. The general gap setting system is reused as it was found efficient.

To get a better stiffness, the magnets motors are mounted horizontally, so the distance between the poles and the guideways is shorter. The mechanical driving to connect the motor output to the magnet rotation is ensured by multiple gear wheels and a worm gear. The small size requirement was a condition hard to meet with this new layout but was achievable by allowing the magnets block to be nested one within the other in close gap (Fig. 3).

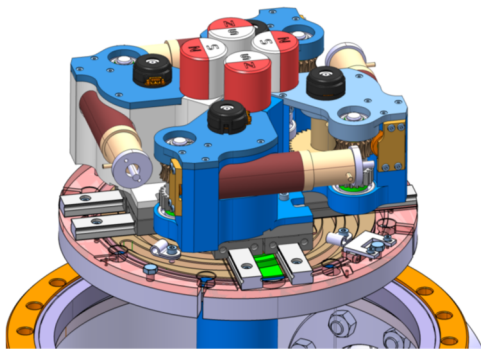


Figure 3: 3D overview of CAD V3 MAGSTAT prototype.

Expected Performance

This new design decreased the height of the motor blocks by near a third, hence guaranteeing a much better vertical stiffness.

The other improvement is about the output torque for the magnet rotations which is tenfold by the worm gear and set irreversible, preventing the motors to heat too much under vacuum with a high stop current.

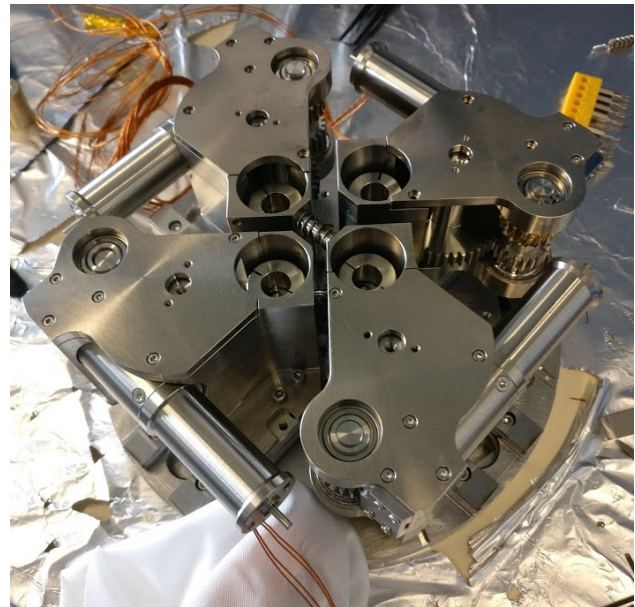


Figure 4: MAGSTAT V3 prototype main parts overview. Magnets are not mounted on the picture.

Small improvements had also been made to ensure that the magnets could not lock in a close gap position by helping the central motor with return springs mounted on several pistons (Fig. 4).

Manufacturing

All these mechanical improvements made the mounting block of each magnet much more complicated to manufacture. Due to the force magnitude and non-magnetic requirements, the motor mount is mainly machined out of a Ø100mm single titanium (TA6V) rod (Fig. 5).



Figure 5: Main magnet mounting part.

MECHANICAL PROPERTIES

Table 1: Torque and Momentums

	V1 [N.m]	V3 [N.m]
Magnet shaft theoretical maximum torque output	1.5	11
Central shaft theoretical Maximum torque output	18.4	18.4*
Lever arm maximum parasitic momentum	36.5	24

* Central torque requirement is less in V3 since there are return springs.

PERSPECTIVES

The third MAGSTAT prototype will be mounted on COMET endstation by the end of 2018, and will allow to operate with higher magnetic field, up to 1T along with safer drive of the gap.

ACKNOWLEDGMENTS

The authors are grateful for financial support through the Swedish Research Council funded Cooperation in the field of synchrotron light research between SOLEIL and MAX IV.

REFERENCES

- [1] V. Pinty, "MAGSTAT a high vacuum gap-variable permanent rotary magnets quadrupole", in *Synchrotron SOLEIL Highlights 2016*, Gif-sur-Yvette, France, May 2016, p. 86.

DESIGN & DEVELOPMENT OF AN INNOVATIVE 6 AXIS SAMPLE MANIPULATOR

M Purling [†], Diamond Light Source Ltd., Oxfordshire, UK

Abstract

The accurate positioning & alignment of sample specimens within the experimental test chamber on a beam line is always a challenge. The ability to move in any direction and angle to very precise increments with repeatable positioning is crucial for being able to focus on the exact part of the sample required in the correct orientation. This is more complex when the sample is required to work within the Ultra High Vacuum environment and cooled to cryogenic temperatures of below 20k. Initially in conjunction with St Andrews University, Diamond Light Source Ltd. have developed their own manipulator for this purpose, it has six degrees of freedom for alignment of the sample and easy remote sample plate loading via a transfer arm system. (Fig.1 & Table 1)

This paper describes the developments made from initial design to working manipulators with increased functionality for bespoke requirements on four different beam lines within Diamond.

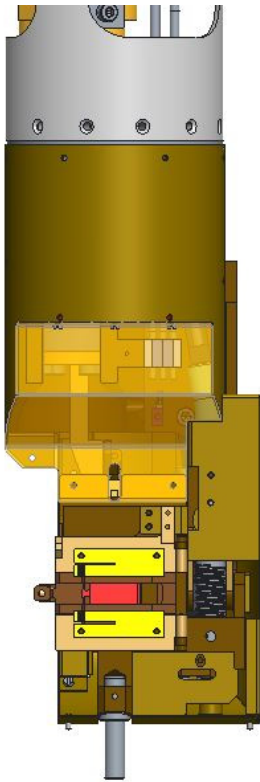


Figure 1: Manipulator Lower Half.

Table 1: Manipulator Motion Specification

Axis	Range	Resolution	Repeatability
x	+/-12mm	0.5 micron [1]	1 micron [1]
y	+/- 12mm	0.5 micron [1]	1 micron [1]
z	100mm	1 micron [1]	1 micron [1]
Polar	360°	100 nrad [2]	10 µrad [2]
Azimuth	+/- 90°	0.01°	+/- 0.05°
Tilt	-10/+45°	0.1°	+/- 0.05°

DRAIN CURRENT MEASUREMENT

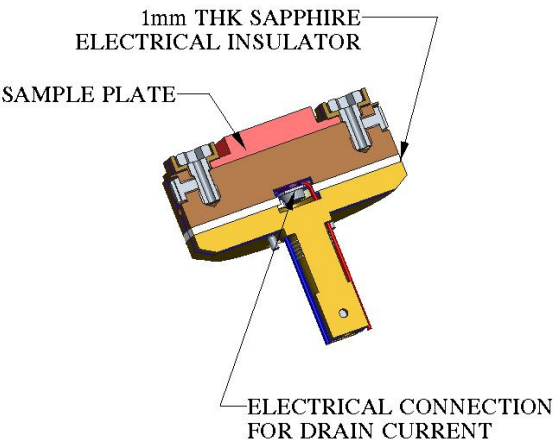


Figure 2: Section Showing Drain Current Connection.

Certain types of experiments, Photo Emission Spectroscopy and Absorption Spectroscopy use & measure the drain current flowing to the sample. It is important that the sample remains at a neutral potential but electrons are allowed to flow to the sample replacing ones emitted during the experiment. A new azimuth drive (Fig. 2) was designed to enable this to be done. A top and bottom made from copper, for good thermal conduction that are separated with a 1mm thick piece of sapphire which kept the top & the sample electrically isolated from earth. A wire is connected to the underside of the top and this is used for the drain current is measurement.

Sapphire was used as it has the properties of an excellent electrical insulator, $1 \times 10^{14} \Omega\text{cm}$ [3], with good thermal conductivity.

[†] martin.purling@diamond.ac.uk

FULL 180° GRAZING ANGLE

The original manipulator had restricted angle access to the sample surface, this would inhibit using the manipulator for some experiments where the photons at the sample surface edges are of interest. For this type of experiment the full 180° grazing angle is required. The angle limitation was caused by the tilt bearing position physically blocking the x-ray beam. To improve this the sample was raised by 6 mm so that it was above the tilt axis (Fig. 3), this allowed the beam to have unimpeded access to the sample surface with a full 180° grazing angle. There was a compromise where the sample surface no longer rotated centrally around the polar axis.

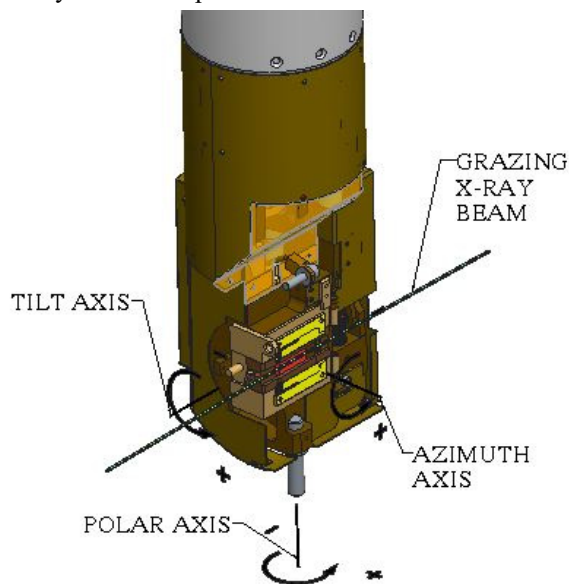


Figure 3: Diagram Showing Manipulator Axis and Grazing X-ray beam.

THERMAL SHIELD IMPROVEMENTS

To achieve lower sample temperatures the cold end of the manipulator is enclosed within an assembly of thin copper sheets to make a thermal shield. Access for insertion and removal of the sample plate is done via a door; it can be opened and closed with a modified wobble stick within the vacuum chamber. Incorporated in the door there is provision to insert plates with different size slots to accommodate different sample sizes (Fig. 4). These plates are to ensure that the minimum amount of the sample surface/plate is exposed the internal temperature of the experimental vessel. The slots are required to allow for grazing angle experiments.

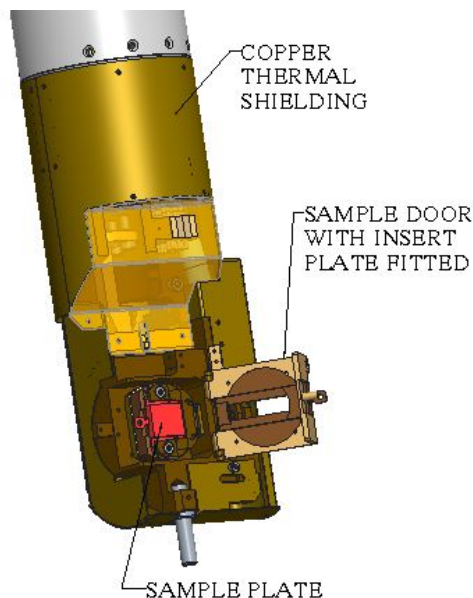


Figure 4: Thermal Shielding with Sample Door Open.

HEATING AND COOLING

To be able to heat and cool the sample plate would make the manipulator much more versatile. The target max higher temperature is 600k while the target min lower temperature is between 20k and 10k. A more complex Azimuth drive assembly is in development consisting of a tungsten filament inside a faraday cup for heating. This is thermally isolated from the copper using a ceramic outer cover (Fig. 5). The cooling is still done using a helium cryostat and the copper braid from the original design.

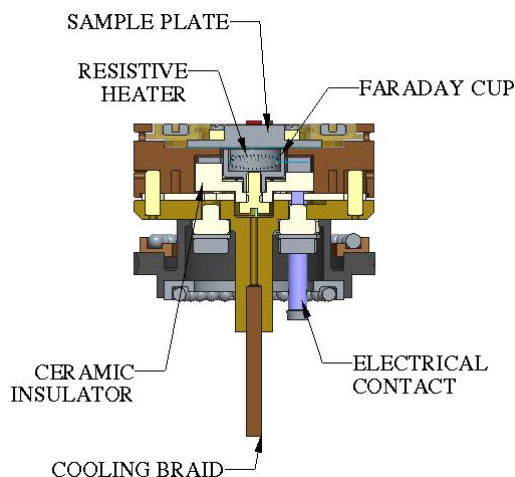


Figure 5: Thermocouple Position on Sample Plate.

ACCURATE SAMPLE TEMPERATURE MEASUREMENT

The original manipulator had the thermocouple for measuring sample temperature mounted on the stem of the azimuth drive; directly connected to the cold thermal braid. This could give an unrealistic sample temperature. The first change was to move the thermocouple to the top plate. Ideally attaching the thermocouple directly on the sample plate (Fig. 6) would give the most accurate reading. A new design is being developed to incorporate this with two contacts making the electrical connection to the azimuth drive assembly.

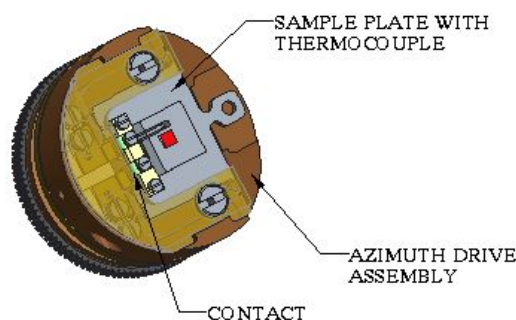


Figure 6: Thermocouple Position on Sample Plate.

FUTURE DEVELOPMENTS

As more experience is gained using the manipulator, it can be seen that there are ways that it could be developed further. Among these are:

- Increased Azimuth rotational range, full 360° (+/- 180°) without effecting the cooling time.
- Tilt bearing redesign so that the sample azimuth axis and tilt axis are aligned without restricting the grazing angle.
- Reduction in component parts to reduce complexity and make easier to assemble.
- Wider sample temperature range (lower & higher limits)
- Easier sample plate clamping.
- Gold plating of the thermal shielding to help reduce the sample temperature and improve emissivity.

REFERENCES

- [1] Vacgen, <http://www.vacgen.com>
 [2] Huber, <http://www.xhuber.com>
 [3] Goodfellow, <http://www.goodfellow.com>

NOVEL COMPREHENSIVE UHV LENS CHANGER AT THE PETRA III BEAMLINES P22, P23 AND P24

J. Raabe[†], K. Ederer[†], C. Schlueter, R. Grifone, D. Novikov
 Deutsches Elektronen-Synchrotron DESY, Notkestraße 85, 22607 Hamburg, Germany

Abstract

We present the design of a compact UHV-compatible X-ray transfocator for beryllium compound refractive lenses (CRL).

CRLs are nowadays commonly applied for beam focusing, collimation and aperture matching in a lot of experimental techniques based on synchrotron radiation. Aim of the current project was the development of a low-maintenance lens for the reliable use under ultrahigh vacuum conditions. We discuss two variants of the device, one designed for 2D lenses and the other one operating with 1D lenses. Precise and reproducible alignment is achieved by pneumatic actuators that press the lens stacks against a high precision prism. All actuators and position sensors are placed outside the UHV vessel. Alignment is facilitated by integrated beam monitors and alignment apertures. The transfocator construction allows an easy adaptation for any desired number of lens stacks. In the current version, the 2D lens changer adapts 12 stacks of up to 8 single lenses each, and the 1D variant – 8 single lenses or apertures.

INTRODUCTION

Refractive optics is of key importance for synchrotron beamlines aiming for micrometer and sub-micrometer beam sizes. Small dimensions of the lenses allow for very compact and cost effective solutions for beam focusing applications [1, 2]. Consequently, CRLs became widespread in the synchrotron community, particularly for hard X-ray beamlines.

Three new beamlines went into operation in the Ada Yonath hall at the high brilliance PETRA III storage ring at DESY (Hamburg, Germany) in 2017. At all beamlines compound refractive lenses are employed for in-vacuum X-ray beam focusing, collimation and conditioning [3].

In this project, great importance was attached to a robust and low maintenance design of the lens changing mechanics which was implemented with some minor variation at all three beamlines. Here we present a lens changer design, with particular emphasis on 2D focusing requirements at the In-situ and Nano Diffraction beamline P23 and at the Chemical Crystallography beamline P24.

LENS CHANGER DESIGN

The beamline optical configurations require the positioning of lenses in the optic hutches in an UHV environment, making a compact and scalable design, high reliability and low-maintenance operation as well as com-

pliance with the stringent DESY vacuum guidelines key objectives of the design task.

Requirements

Basic specifications for the lens changer include :

- Main functionality: high precision for positioning of the lenses
 - with exact coaxial orientation of the lenses to the synchrotron radiation beam and to each other
 - high positional reproducibility
- UHV environment with extremely low residual hydrocarbon content
- Simplified adjustment mechanics with four motorized degrees of freedom for alignment with respect to the X-ray beam – y (horizontal, perpendicular to the beam), z (vertical), pitch and yaw
- all alignment mechanical parts should stay outside of vacuum for easy service and troubleshooting
- Integrated alignment screens
- CF-flange viewport(s) for inspection and alignment
- flexible remote control via a TCP/IP interface

Design of P23 Transfocator

The general design of the transfocator is comprised of a vacuum vessel with lens stacks, alignment prism, out of the vacuum support and positioning mechanics. Single lenses are stacked in groups depending on experimental requirements (i.e. energy, focusing conditions, photon flux optimization). To achieve optimal focussing at discrete energies one can select suitable combinations of lens stacks carrying different numbers of lenses [4].

The lens stacks are pressed with a spring sheet into a high precision prism. The prism is the core element of the design. It has very tight shape and position tolerances and serves as a reference plane for reproducible alignment and ensures exact positioning. The manufacturer we have chosen provides a permitted variance of the guide plane parallelism to the reference planes of 2µm over the whole length of a range [300...1000] mm.

The stacks are inserted into the beam path by a rotational lever mechanics pushed by pneumatic drives. The simple and robust layout inside the vessel allows for fast and reliable switching between different configurations.

For alignment and beam monitoring, pinholes and X-ray fluorescence screen are incorporated into the system.

The assembly is shown in Figure 1.

[†] jana.raabe@desy.de
[†] katrin.ederer@desy.de

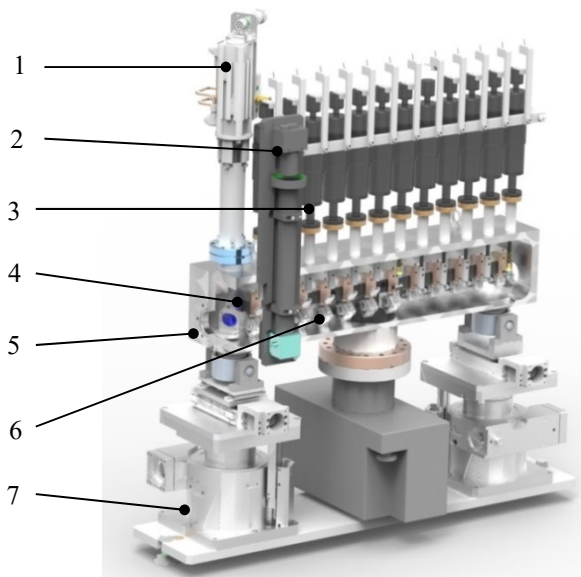


Figure 1: Rendered image of the 2D lens changer with fluorescence screen (1), camera and optics (2), pneumatically driven translation actuators (3), prism (4), UHV vessel (5), lens stack (6) and support construction (7).

Support Construction

The lens changer can be easily aligned in the beam by precise parallel kinematics, offering two translational and two rotational degrees of freedom.

The alignment of vessel and prism is done via a combination of two vertical and two horizontal individually driven translation stages placed under the UHV vessel (Figure 2). Two Huber Z-stages (5103.A20-90) are used to adjust height and pitch.

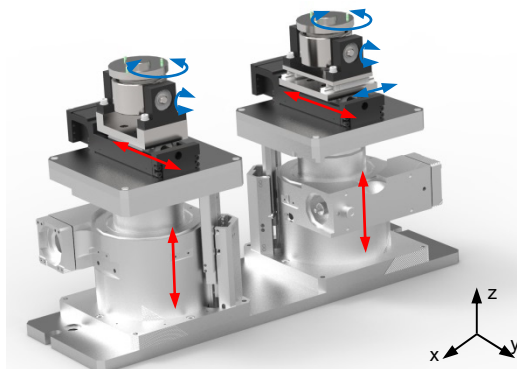


Figure 2: Rendered image of the support stage.

Two Misumi linear travels (LX3005-B1-A3038-125) adjust translation in y across the beam and the yaw rotation around the vertical z axis. Further rotational and translational rails and deep groove ball bearing compensate the angular and geometrical displacements (marked in blue) between vessel and ground plate that occur due to the movements.

Vacuum Chamber

The vacuum vessel consists of a base chamber and a sideward cover as shown in Figure 3. It has a length of

662mm, a width of 153mm and a height of 153mm. All inner components are arranged on the milled out rear panel and therefore positioned in a well controllable relation to each other.

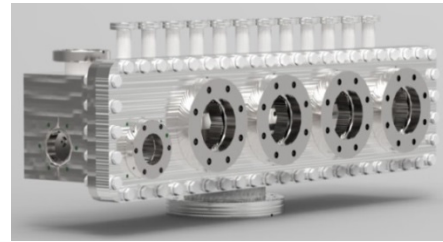


Figure 3: Rendered image of the vessel.

The cover has integrated viewports for easy inspection of the lenses. The main vessel components are sealed with a FKM O-ring seal (Viton®). The calculated groove filling was chosen to be as high as possible and lies between 84 and 98% which is in the specified tolerances to ensure optimal sealing. For high vacuum quality all parts went under a thorough cleaning process and assembly under ISO class 5 clean room conditions. Baking of the chamber is not necessary under these premises. Residual gas analysis shows that the system fulfills the DESY vacuum guidelines [5] and the emitted gas is free of hydrocarbons. A base pressure of 1.8×10^{-8} mbar was reached.

Furthermore DN40 CF Flanges are chosen to connect the chamber to other beamline components and a DN100 connects the Ion pump on the bottom. An additional DN40 viewport gives direct visibility onto the DESY standard diamond fluorescence screen incorporated into the system [6]. The CVD diamond screen with an integrated graphitized cross can be put into the center of lens axis immediately after the upstream port. The 12 DN16 flanges for the translational feedthroughs sit on the top of the vessel.

Positioning Mechanics

Details of the 2D mechanics are shown Figure 4. 2D lenses are delivered in circular metal frames. These frames are combined to firm stacks that exhibit cylindrical reference plane for alignment. The stacks are held loosely by a lever which can rotate in a lug. During the assembly the height of the lug is adjusted to ensure an optimal pivot point.

The stacks are pressed against the reference prism by pneumatic drives and the lever mechanism. For precision alignment a spring sheet pushes the reference planes of the lens stack into the prism planes. When removed from the beam, or in case of air pressure loss, the frames slide out of the X-ray path and a spring plate at the end of the travel ensures a gentle hold.

The insertion of a lens stack into the beam is implemented in two stages. In the beginning, there is no direct mechanical contact between the levers and pneumatic actuators: in a first step the force transmission is implemented in a contactless manner over repulsing permanent magnets built into the lever and the pneumatic drive tip. Under the magnet, adapted to the pneumatic drive rod,

sits a small ball, so that in a second step the end of the rod has contact just in one point to the lever. This construction ensures both a damping of the mechanical impact by the drives and a self-aligning low contact motion transmission and allows avoiding complex adjustments in the force transmission mechanism.

The MDC linear feedthroughs with a travel length of 1 inch are mounted to the 12 DN16 flanges of the vacuum vessel (Model K075-ABLM-1).

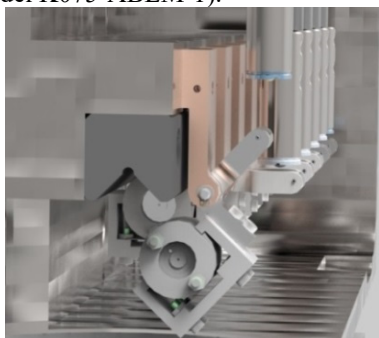


Figure 4: Detailed view on the 2D mechanics.

The 1D lenses differ from the 2D ones by a square holder form. The focusing direction of a 1D lens is parallel to one of the frame edges. Therefore, the lens changer prism is mounted under a 45° angle to align the rectangular lens frames in the vertical or horizontal planer (Figure 5). Extensions of the pneumatic drives press the lens stacks against the prism. Lateral stability of the stack holder is ensured by guide rails placed inside the vacuum vessel. [7]

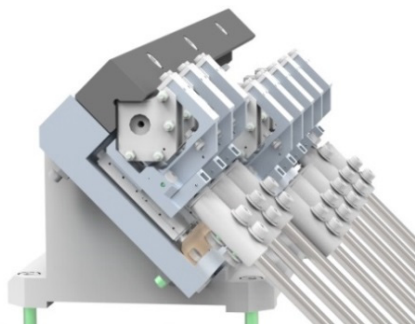


Figure 5: Detailed view on the 1D mechanics.

Alignment and Control

For easy alignment two built in apertures allow fast beam positioning parallel to the main axis.

According to the experimental requirements, different lens combinations can be set remotely from the beam line control cabin. A control box with an Acromag XT1112 16 channel I/O modules was designed to switch the FESTO valve terminal used for driving the pneumatic feedthroughs. Communication is facilitated via the ModBus protocol in the Tango middleware. The interface is fully integrated in the user software and allows for automated lens changes during experimental runs.

Example of Performance

First test for focusing showed good reproducibility and repeatability results for intermediate focus sizes, lens

positioning in the prism and alignment by the parallel kinematic.

Figure 6 demonstrates the results of the first test of the 2D translocator at beamline P23. Total beam intensity loss of about -40% was observed after focusing with a stack of 4 beryllium lenses with 500μm radius. After focusing, the flux density in the focal spot was increased by several orders of magnitude.

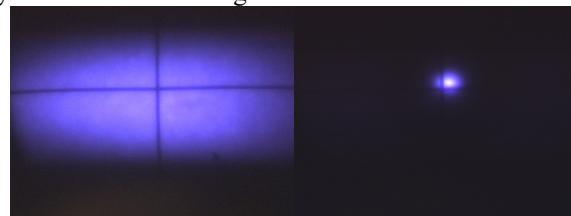


Figure 6: Focused beam at 10.367keV.

CONCLUSION

We have presented two UHV compatible lens changer designs for 1D and 2D lenses for the use at synchrotron radiation beamlines. All active elements are placed outside the vacuum vessel, which allowed a compact vacuum chamber design and facilitates easy access for repair and maintenance work. Alignment aperture and fluorescent screens are integrated into the vacuum vessel. The design can be easily adapted for any number of lens stacks.

ACKNOWLEDGEMENTS

We would like to thank the DESY workshop for excellent quality and manufacturing on short notice, the beamline technology group for the advice and manpower support, Ilja Schostak for the help and development of the electronics. Our thanks also go to Martin Tolkien for fruitful discussion and advice. We want to thank Wolfgang Drube for support and guidance.

REFERENCES

- [1] B. Lengeler *et al.*, “Imaging by parabolic refractive lenses in the hard X-ray range”, in *Journal of Synchrotron Radiation*, pp. 1153–1167, 1999.
- [2] B. Lengeler *et al.*, “Refractive x-ray lenses”, in *J. Phys. D Appl. Phys.* 38, A218–A222, 2005.
- [3] W. Drube *et al.*, “The PETRA III extension”, in *Proc. AIP*, vol. 1741, 020035, 2016.
- [4] K. Klementiev *et al.*, “Powerful scriptable ray tracing package xrt”, in *SPIE*, vol. 92090A, Sept. 2014.
- [5] U. Hahn, K. Zapfe, “Guidelines for UHV-Components at DESY”, Technical Specification, No: Vacuum 005/2008, Version 1.6/22.09.2010.
- [6] M. Degenhardt *et al.*, “CVD diamond screens for photon beam imaging at PETRA III”, in *Journal of Physics: Conference Series*, vol. 425, 192022, 2013.
- [7] C. Schlueter *et al.*, “New HAXPES application at PETRA III” in *Synchrotron Radiation News*, unpublished. doi:10.1080/08940886.2018.1483656

TRAINING THE NEXT GENERATION OF ENGINEERS FOR PHOTON BASED LIGHT SOURCES

S.M.Scott, Diamond Light Source, OX11 0DE Didcot, UK

Abstract

The continued increase in the number of Light Sources, their beamlines and the need for upgrades of both machine and beamlines requires an increasing supply of suitably qualified and experienced engineers. If there is a world wide shortage of Engineers where will facilities find these engineers and how can they be trained to the required level?

This paper discusses these issues by looking at the growth of demand for engineers within light sources, the evidence of shortages of engineers, the changes in attitudes to work by younger people, the skills necessary, training opportunities and the issues in attracting people into the light sources industry.

GROWTH OF LIGHT SOURCES

The first observation of radiation from accelerating electrons was in 1947. At first, synchrotron radiation was obtained from electron synchrotrons built for other purposes such as for high-energy physics. Dedicated machines started to appear in the 1970's and since then there has been a constant increase in the number of synchrotrons operating throughout the world. As well as an increasing number of facilities, the size and complexity of each synchrotron is increasing. The larger number of beamlines per facility, the demands for higher levels of stability, smaller beam sizes, higher power and faster throughput all require Engineers with a high level of expertise and experience.

IS THERE A WORLD SHORTAGE OF ENGINEERS ?

Some of the recent headlines would indicate a shortage of engineers in many parts of the world.

"By 2025, we might need 500,000 engineers, said Olof Persson, chief executive, of Volvo Group, the world's second-biggest truckmaker" [1].

"Peter Löscher, chief executive of Siemens, Europe's largest engineering group, said "the skills shortage, particularly in Germany, is a big issue" [1].

"Washington Post editorial published on August 4th 2011 warns of an approaching disaster in the shortage of professional engineers in the US."

As well as the media sound bites there are well researched reports.

"According to a recent Engineering labour market study by Engineers Canada, the country's rapid growth in the mining, energy, and transportation sectors, coupled by the anticipated retirement of approximately 95,000 Canadian engineers in the next 7 years, has resulted in a worrisome shortage of experienced engineering talent" [2].

The "skills panorama" are part of the European commission and monitor skills shortages. They report that across the EU, the top five skill shortage occupations include engineering professionals [3].

Within the UK, the Royal Academy of Engineering's report highlighted a shortage of Engineers within the UK across all sectors of the economy [4], the Institution of Engineering and Technology (IET) 2017 skills survey [5] concluded that engineering skills shortages and gaps continued to be a huge problem for employers.

In India, about 1.5 million engineers graduated from more than 3,500 engineering colleges across India in 2014. But at a recent meeting to discuss the Indian aerospace industry the conclusion was that only 4 to 7 per cent of engineers are actually fit for jobs in the core engineering sectors [6].

However one of the problems in developing a global view is the lack of reliable data. In a recent report by Emma Smith [7], she concludes that while the shortage debate has a long history, it is one that is characterized by poor quality data as well as methodological and conceptual challenges.

IS THERE A SHORTAGE OF ENGI- NEERS FOR LIGHT SOURCES?

If accessing a shortage of Engineers worldwide is difficult, can we say anything about the shortage within the light source community?

One way of examining the need would be to review the number of vacancies that exist. The vacancy pages of the web sites of each facility may give information as well as generic web sites such as www.lightsources.org. The problem with this approach is that the recruitment and supply of staff varies between facility and country. For example SOLEIL Light source have a limit in staff numbers as part of the legal structure and any shortfalls have to be met with contractors. In the USA, some beamlines are operated by university departments that are separate from

the overall facility organization, this makes it difficult to determine if there is a shortage within the light source community.

THE POSITION IN THE UK

In the UK, it is easy to state the position. The UK has one synchrotron and all its permanent staff are employed directly by the facility and this makes the vacancy position easy to measure. The position is that there is a very definite shortage of mechanical, electrical and controls engineers. The reasons may be very much due to local conditions including high demand from other local high technology companies, expensive housing costs as well as a national shortage especially for electrical engineers. The decision to leave the European Union has also not helped.

IMPROVING THE DATA

It would be an advantage to have more data from other countries. This could help in developing a strategy that could be adopted that could help all facilities tackle such a shortage if it really exists.

A STRATEGY TO ADDRESS SHORTAGE

Making the Light Source Community a Desirable Destination.

For anyone searching for a new job, a career at a Synchrotron is not likely to be high on the agenda. Within each country the number of people employed within light sources is dwarfed by that in other industries such as Automotive, Aerospace or Energy. To address this we need more people to be aware that such industries as ours exist and that we have a number of unique selling points over other industries. These could include the following;

- Much of the work done at light sources is aimed at helping mankind including the research into environmental issues and understanding disease.
- An industry where collaboration is of prime importance.
- Much of the engineering is state of the art at the forefront of technology.
- Usually function far outweighs issues of cost.
- The work is varied and interesting

One of the areas where light sources can be improved is their own web sites which can be dominated by the scientific output and not highlight the engineering which enables such ground breaking science to be performed. Social media is now the prime method of engagement and such avenues such as facebook, twitter, linkedin, Insta-gram, youtube, google+ and snapchat need to be used more effectively to tell some of the stories about developments at light sources and increase awareness.

Increase Recruitment of Graduates

Many industries have substantial graduate recruitment programmes and spend appropriate resources on recruitment and training. They therefore tend to attract the best graduates often well before their final year by offering sponsorship.

For light sources to become attractive to good graduates then the opportunities need to be highlighted or improved. One area that could be developed would be to provide opportunities for graduates to visit facilities in other countries. This could be short-term visits, training courses, or secondments. Highlighting the international nature of the community and location of facilities in some very attractive parts of the world could help with recruitment.

At Diamond there are close ties in the science community to universities but this has not been so for the engineering community. Recently Diamond Engineers have been developing closer ties to universities with strong Electrical Engineering departments. This has produced a number of advantages including the following:

- Highlighting career opportunities at Diamond
- Identifying potential projects for final year students
- Creating opportunities for Diamond staff to give guest lectures to demonstrate how skills and knowledge gained at university is applied in real life.
- Identifying where specialist facilities and equipment at universities could be used for solving problems at Diamond.

Improve Training Opportunities for Existing Staff

Training of existing staff is critical, not only to improve skills and knowledge but also to help with staff retention. For some facilities training can be an issue, with insufficient staff to provide the training or not having the required skills to deliver such training. Sharing of training resources would of potential benefit. Such resources could be online videos, webinars and manuals. Diamond are organising a training course for engineers who are early in their career at light sources. As well as providing some training in some of the basic issues regarding light sources it also provides a face to face opportunity to meet engineers from other light sources and help develop social networks.

Staff Sharing

With a number of facilities, undergoing upgrades then there are certain skills that are in high demand during these long shutdowns. This for example includes survey and alignment specialists. The additional staff required are only needed during the shutdown so could there be a

system established where suitable staff are available for loan from other facilities

Changing Attitudes to Work

There are changing attitudes to work. Previous generations may have expected to stay with one company for a good part of their working lives. Now there seems to be an assumption that younger people will have a much more fluid career with frequent changes of employment. This change means that there will be a much higher turnover of staff and so recruitment and training systems will have to be modified to reflect these changes.

A recent report on attitudes [8] reported that "Our respondents are imploring business leaders to take the lead in solving the world's problems, to shift organizations' motives from inordinately focusing on making profit to balancing social concerns, and to be more diverse, flexible, nurturing of and generous with its employees." This focus on solving the world's problems very much fits into the light source community and so if this could be highlighted than it would make a career in light sources attractive,

Increasing Diversity

In some areas, such as nationality Diamond are very diverse, but the percentage of female engineers in the UK is very low and although many countries the percentage is higher there is still more that can be done to attract girls into engineering. It is well known that female role models are very important so any efforts to increase visibility of women in engineering should be encouraged. In some fields efforts are made to ensure that there is a balanced representation in organising committees and speakers at conferences. This is a sensitive subject and there is no suggestion that women should be selected irrespective of their ability but given equivalent abilities a gender balance should be the long term aim.

TRAINING

Training has a key role to play not only in increasing skills level but also to help with staff retention. Training can comprise of not only technical skills but also the soft skills in communication and team work. With a potential higher level of turnover the demands of training increase and a cyclic training scheme needs to be established. At Diamond we are starting to establish in house training in such areas as motion control, EMC, vacuum technology. We have also identified a need to provide a basic grounding in the wider aspects of synchrotron Engineering so we are organising a week's course which is aimed at engineers early in their career at light sources. This is open to engineers from other light sources.

As well as recruiting experienced staff, fresh graduates and apprentices, Diamond are encouraging existing staff to upskill with day release to college.

Beamlines

End Stations

FUTURE ACTION

There are a number of actions that could be taken to address the possible skills gap within the light source community.

These could include the following:

- Sharing of information about skills shortages
- Greater visibility of Engineering on facility websites
- Development and sharing of training resources
- Sharing of staff by secondment between facilities
- Highlighting female engineers as role models
- Closer liaison with Universities

CONCLUSION

As the technology behind third generation synchrotron light sources and free electron lasers becomes evermore challenging the importance of having a good supply of skilled and experienced engineers has never become more critical.

Although there is some data indicating a world wide shortage of engineering skills there is no data to indicate a shortage within the light source community except in the UK.

If there is a shortage, there are a number of actions that could be taken. This includes opportunities for coordinated and shared training, increased publicity on the role of engineering and staff sharing. The author would like to further develop these ideas and welcome collaborations and discussions with staff in other organisations and facilities.

REFERENCES

- [1] Financial Times, May 26 2013.
- [2] Engineers Canada: "Engineering Labour Market in Canada: Projections to 2025", June 2015, Ottawa, Canada.
- [3] Skills Panorama: www.skillspanorama.cedefop.europa.eu
- [4] Royal Academy of Engineering: "Jobs and Growth - The importance of Engineering skills to the UK economy", Sept. 2012, London, UK.
- [5] The Institution of Engineering and Technology: "Skills and Demand in Industry - 2017 Survey", Herts, UK, 2017.
- [6] OneIndia News, 28 May 2015.
- [7] E. Smith, "Shortage or surplus? A long-term perspective on the supply of scientists and engineers in the USA and the UK", Leicester, UK. Review of Education, vol. 5, no. 2, Jan. 2017, pp. 171-199.
- [8] "2018 Deloitte Millennial Survey": <https://www2.deloitte.com/content/dam/Deloitte/global/Documents/About-Deloitte/gx-2018-millennial-survey-report.pdf>.

THPH40

423

FRONTEND SLITS FOR CLOSELY-SPACED WIGGLER BEAMS

S. Sharma[†], C. Amundsen, F. DePaola, J. Tuozzolo, NSLS-II, BNL, 11973 Upton, NY, USA

Abstract

A high energy x-ray (HEX) beamline facility will be constructed at NSLS-II for R&D in energy storage technologies using different x-ray imaging techniques. A 4.3 Tesla superconducting wiggler will be used to produced x-rays of total power of approximately 56 kW in 8 keV – 200 keV range. The nominal horizontal fan of ~ 10 mrad will be split into three closely spaced beams of 0.2 mrad, 1.0 mrad and 0.2 mrad fans. Each beam is required to have a frontend slit with four distinct apertures. The conventional L-shape design of the slit is not feasible for these closely spaced beams because of constraints on side cooling and horizontal travel of the slits. In this paper we propose two solutions for these slits using a beam pass-through design, vertical-only travel and optimized cooling configurations.

INTRODUCTION

NSLS-II is presently designing a state-of-the-art HEX beamline facility for fundamental research in energy storage technology and associated materials [1]. The facility will support three beamlines integrating multiple high energy x-ray imaging techniques. The beamlines will enable in-situ experiments on real materials and systems under real operating conditions.

The x-ray source will be a 4.3 Tesla superconducting (SC) wiggler that will produce highly intense x-rays of total power of 56 kW in 8 keV – 200 keV range. As shown in Fig. 1(a) this source has a large horizontal fan of 9.87 mrad as compared to the narrow vertical fan of 0.88 mrad. The peak power density is 28.4 kW/mrad².

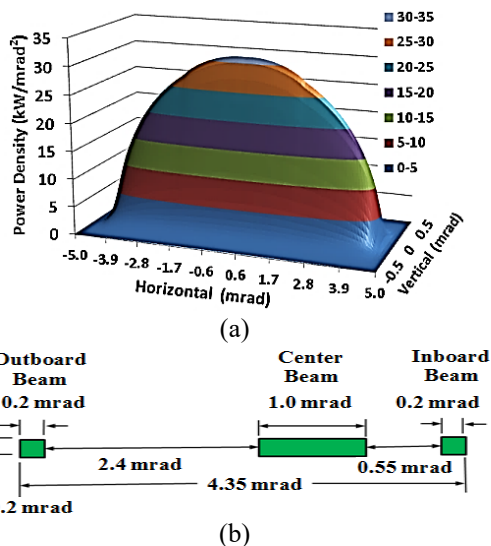


Figure 1: HEX wiggler x-ray source and beams, (a) power distribution of 4.3 Tesla SC wiggler, (b) 3 beams, fan sizes and spacings.

[†] sharma@bnl.gov

A fixed mask in the frontend, placed at 18 m from the source, divides the horizontal fan into three beams of 0.2 mrad (outboard), 1.0 mrad (center) and 0.2 mrad (inboard) as shown in Fig. 1(b). The separation between the outboard and center beams is 2.4 mrad, whereas it is only 0.55 mrad between the center and inboard beams.

Three slits are provided downstream of the fixed mask to reduce the beam size for each beamline independently (Fig. 2(a)). The conventional design of a pair of L-shaped slits is not possible for these closely spaced beams because there is no room for any significant horizontal travel. The HEX slits will, therefore, have four discreet apertures [2] ranging from a full beam size exiting the mask to a smallest size of (0.05 mrad H x 0.05 mrad V). The apertures for the center-beam slit, separated vertically by ~ 10 mm, are shown in Fig. 2(b). Each slit will also act as a beam stop. Single axis high-precision linear stages will be used to provide vertical motion to the slits for remotely selecting one of the apertures.

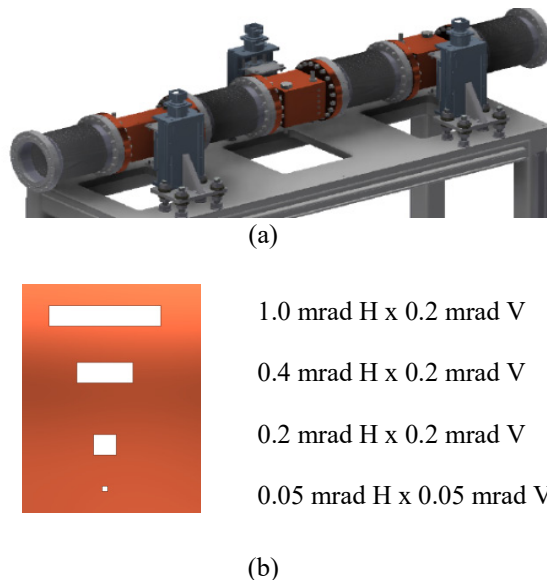


Figure 2: Slits in the HEX frontend, (a) 3-slits assembly on a table, (b) 4 apertures of the center-beam slit with vertical separation of ~ 10 mm.

Two slit designs are described in this paper, one for the case when the narrow spacing between the beams is not sufficient to include cooling channels of reasonable size ($> \phi$ 6 mm). This design will be applicable to the center and inboard beams. The second design, applicable to outboard beam, is for the case where it is possible to include cooling channels between the beams, even if slightly smaller than ϕ 6 mm. For comparison both designs are discussed with respect to the center-beam slit.

SLIT DESIGNS

Slit Design 1

The first slit design for the center beam is illustrated in the CAD model shown in Fig. 3. The model is oriented looking into the beam direction. For clarity the upstream flange (ϕ 200 mm) is removed. Overall length of the slit in the beam direction is 280 mm. Beam apertures are created on a surface (A) inclined at 10.8° from the vertical plane. Each aperture also has top and bottom tapered surfaces in order to further reduce the incident beam power density.

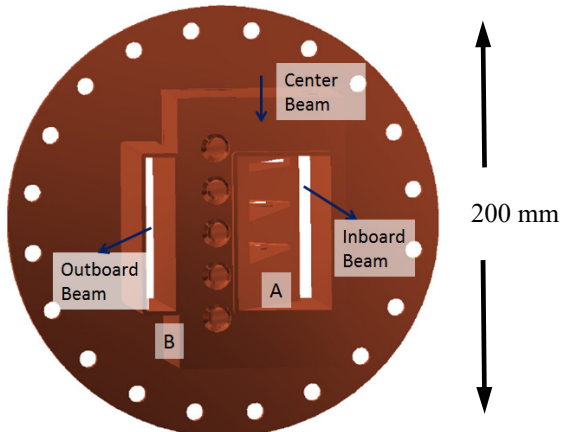


Figure 3: Slit design 1 for the center-beam slit. Apertures are created on the inclined surface (A).

Apertures for the inboard and outboard beams are made to be pass-through apertures taking into account the vertical travel of the slit. The center and inboard beams share the same vacuum space machined in a single part from CuCrZr. A separate rectangular chamber is machined for the outboard beam mainly to avoid water-to-vacuum joints on surface (B). This part is also made from Cu-CrZr. The two parts are then edge welded to the upstream and downstream CuCrZr flanges.

Because of high power density of the wiggler beam the cooling channels must be within a 3 – 8 mm range from the beam footprint. This is achieved by a cooling channels configuration shown in Fig. 4. Cooling channels C (see sectional view, Fig. 4(a)) of ϕ 9.5 mm are blind-drilled parallel to the inclined surface A (Fig. 3). Another set of channels D of the same diameter are blind-drilled perpendicular to surface B to connect with channels C. Both sets of channels are plugged at the entrances. Channels E and F are then drilled parallel to surface B to interconnect channels C and D, respectively. These channels are of ϕ 16 mm except at the entrances where the standard geometry for a 16 mm tapered plug is used. Custom tapered plugs are used for these channels as shown in (Fig. 4(b)). The stems of these plugs have two diameters, 6 mm in the middle to connect 2 water channels of ϕ 9.5 mm in series, and 16 mm at the end to plug the channels of ϕ 16 mm.

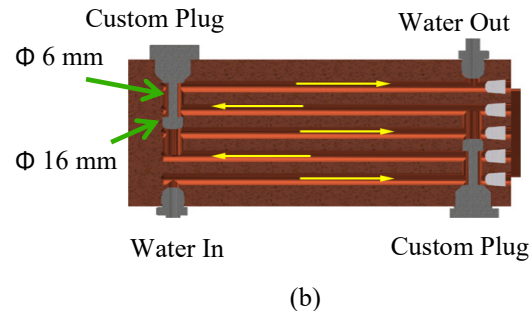
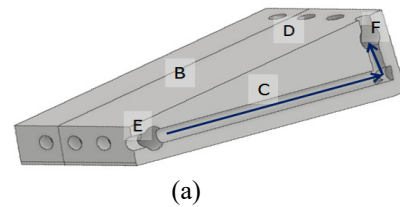


Figure 4: Cooling channels configuration, (a) C and D channels of ϕ 9.5 mm interconnected by channels E and F of ϕ 16 mm, (b) custom plugs for connecting the channels in series.

Slit Design 2

In slit design 2, water channels of smaller diameter (ϕ 5.5 mm) are provided in the narrow spacings between the beams. This slit design, shown in Fig. 5 without the flanges, is simpler due to symmetric cooling on the two sides of the apertures. Beam-intercepting surfaces A and B are inclined at 8.8° from the vertical plane. Overall length of this design is 150 mm including the 2 flanges (ϕ 200 mm). Inboard and outboard beams have pass-through apertures. These beams share the vacuum space with the center beam. The four apertures are EDM wire cut into the inclined surfaces with wire parallel to beam direction. No additional beam intercepting surfaces are created with these wire cuts as they were in the first design.

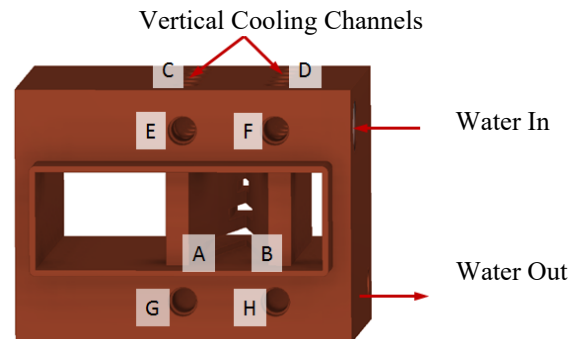


Figure 5: Slit design 2 with beam-intercepting inclined surfaces A and B. Vertical cooling channels C and D are interconnected by horizontal channel E, F, G and H.

Six vertical cooling channels of ϕ 5.5 mm (C and D) are blind-drilled on each side of the apertures. These are connected by 4 horizontal channels, E, F, G and H, of ϕ 9.5 mm. Series connections between the vertical channels are made by 4 custom plug-stems similar in design as in

Fig. 4. All channel entrances are plugged by Lee© plugs. Water inlet and outlet are provided on the side surface as shown in the figure.

FINITE ELEMENT ANALYSIS

ANSYS finite element (FE) analyses were performed for both the designs. The wiggler beam was positioned at different parts of the slits to ensure that the worst condition was not missed. Heat transfer film coefficient for the cooling channels was assumed to be $0.01 \text{ W/mm}^2\text{K}$. A conservative maximum temperature-rise criterion of 300°C under normal operation was used for CuCrZr. A higher limit, 400°C , was used for rare upset conditions.

Temperature contours for slit design 1 are shown in Fig. 6 for three different cases. Case 1 is for normal operation when the central part of the wiggler beam passes through one of the apertures, $0.2 \text{ mrad H} \times 0.2 \text{ mrad V}$ aperture for instance. In this case a maximum temperature rise, ΔT_{max} , of 99.5°C is obtained (see Fig. 6(a)).

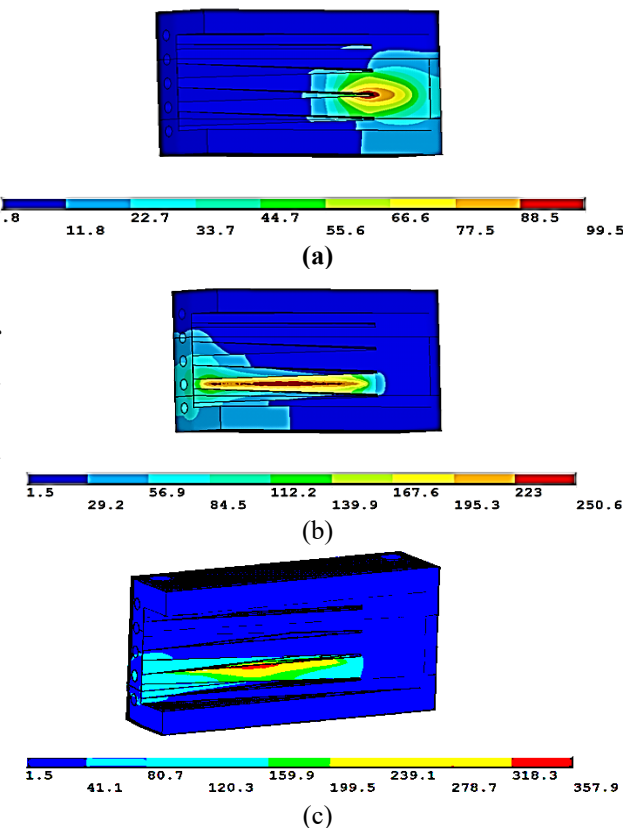


Figure 6: Temperature contours for slit design 1, (a) beam at the center of an aperture, (b) beam on a beam-stop position, (c) beam on an inclined edge (upset condition).

In case 2 the slit is used as a beam stop. The wiggler beam is parked on the inclined surface between any two apertures. For this case a ΔT_{max} of 250.6°C is calculated (Fig. 6(b)) which is sufficiently lower than the acceptable value of 300°C . The third case is for upset conditions such as a failure of the vertical motion stage or controller. In this case the beam can be incident on an inclined edge

resulting in a ΔT_{max} of 357.9°C . This is also lower than the acceptable value of 400°C .

Figure 7 shows temperature contours for slit design 2. When the beam is centered on one of the apertures a ΔT_{max} of 194.5°C is obtained (Fig. 7(a)). When this slit is used as a beam stop, ΔT_{max} is 269.1°C . Because of cooling channels of smaller diameter, there is a significant bulk water temperature rise of 21.6°C and 57.3°C , respectively. This design has no inclined edge which means that upset conditions do not result in a higher temperature.

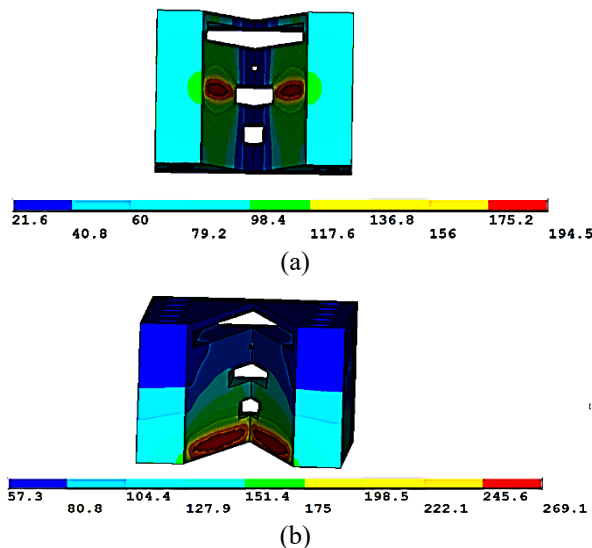


Figure 7: Temperature contours for slit design 2, (a) beam at the center of an aperture, (b) beam on a beam-stop position.

CONCLUSION

Conventional L-shape slit design is not feasible for the closely-spaced HEX wiggler beams. For such beams we have described two slit designs based on discreet vertical apertures and optimized cooling channel configurations. In the first design the cooling channels run parallel to the main inclined surface. Vertical cooling channels between the beams are used in the second design. Custom plugs are used in both designs to connect the cooling channels in series. FE analyses show acceptable temperatures for both slit designs under all beam-intercept cases.

ACKNOWLEDGMENTS

The authors thank our colleagues A. Broadbent, O. Chubar, G. Fries, M. Lucas and Z. Zhong for their contributions and support.

REFERENCES

- [1] *High Energy Engineering X-ray Scattering (HEX) Facility*, Preliminary Design Report for the NSLS-II Project, April 13, 2018.
- [2] Z. Zhong, A. Broadbent, *RSI for the Superconducting Wiggler Source and Front End for the HEX Beamline*, NSLS-II-27ID-RSI-001, Version 2, March 2018.

NEW HOLDER FOR DUAL-AXIS CRYO SOFT X-RAY TOMOGRAPHY OF CELLS AT THE MISTRAL BEAMLINE

R. Valcárcel*, N. González, C. Colldelram, A. J. Pérez-Berná, A. Sorrentino, E. Pereiro,
 ALBA Synchrotron Light Source, Cerdanyola del Valles, Spain

Abstract

A new dual-axis sample holder has been designed and built for the Transmission soft X-ray Microscope (TXM) at the MISTRAL beamline (ALBA Synchrotron) [1, 2] to perform cryo-soft X-ray tomography of cells with dual tilt configuration to reduce the missing wedge.

The design, with restricted dimensions $\varnothing 7 \times 30$ mm, enables using commercial Auto-Grid support rings that give rigidity to the sample grid handling. It consists of a guided miniature handle with a spring system that allows sample rotation by 90° around the beam axis inside vacuum and in cryogenic conditions by using the TXM sample loading robot keeping a rotation of $\pm 65^\circ$ at the sample stage. Two magnets fix the positions at 0° and 90° . The two tilt series can be collected consecutively and the use of Au fiducials permits combining both improving the final quality of the 3D reconstructions. In particular, cellular features hidden due to their orientation with respect to the axis of rotation become visible. The main frame is made in aluminium bronze to enhance the thermal conductivity and in addition, all the pieces have undergone an ion implantation treatment in order to reduce friction and improve the anti-seizure property of the parts.

INTRODUCTION

Structural Cell Biology demands detailed structural and functional descriptions of the different cellular components which must be correlated with a topological 3D map of these components at the whole cellular level. In this frame, an emerging technique such as cryo-SXT can provide structural information at the level of a whole cell without further sample preparation except for the cryo-fixation required to prevent radiation damage while collecting the data. The penetration power of soft X-rays in the so-called water window spectral range, between the inner-shell absorption edges of carbon and oxygen (from 284 eV to 543 eV), allows penetrating water layers of up to 10 μm thickness while carbon-rich structures are visualized with good absorption contrast. Thus, frozen-hydrated specimens can be imaged close to their native state providing significant complementary information to existing biological imaging techniques at a spatial resolution of 30 nm. Cryo-SXT generates, as in electron tomography, 3D absorption maps of the specimen from a series of 2D soft X-ray microscopy projections recorded with a CCD [3]. In the current TXM design at Mistral we use TEM grids as sample support on which the cells are grown. Due to the choice of the flat sample support and the reduced distance from the sample to the objective

lens, the available tilt range is $\pm 70^\circ$. This angular restriction results in a region empty of information in the Fourier space, the so-called “missing wedge” (see Fig. 1), which in real space produces an elongation of every point of the reconstructed volume along the beam direction. In addition to this well-known effect, in the reconstructions some cellular features will not be visible due to their orientation with respect to the axis of rotation. A way to reduce the missing-wedge effect in the reconstructed volumes is therefore by doing dual-tilt tomography (see Fig. 1)

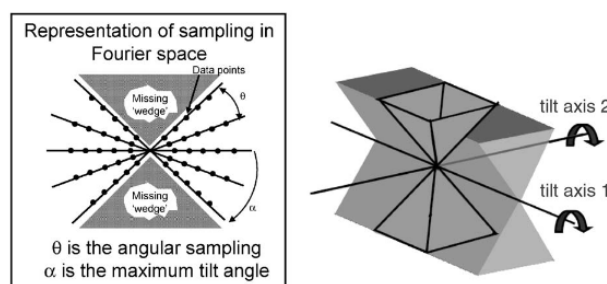


Figure 1: Representation of the sampling in Fourier space showing the limited tilt range (left) leading to a missing wedge 3D reconstruction in a single tilt tomography (right) and the sampling achieved by dual axis tomography which is reduced to a missing pyramid (right). [4]

TECHNICAL SPECIFICATIONS

The dual-axis holder must comply with the following specifications:

- Two orthogonal tilt axis.
- High vacuum compatible (10^{-7} mbar).
- Good thermal conductivity to get 100K at the sample.
- Motions inside TXM.
- Compatibility with AutoGrid sample support.
- Sample visibility in the range $\pm 65^\circ$ degrees for the existing tilt.
- Second tilt with two fixed positions (0° - 90°).

DESIGN

The design consists of tiny mechanism of metal parts that have been treated with an ion implantation process to improve the anti-seizure property and reduce the friction in cryogenic temperatures. The holder body is produced in aluminium bronze to achieve a good thermal conductivity and it is manufactured with precision to fit perfectly in the motorized sample stage of the TXM. The

* rvalcarcel@cells.es

system facilitates the usage of the AutoGrid which securely holds the specimen into the Dual-axis holder. At the same time it provides precise, in-plane specimen rotation perpendicular to the beam. The design has been optimized to maximise sample visibility, even at high-tilt angles. The main advantage is that the rotation can be done inside the TXM (maintaining the cryogenic temperature and the HV). Initially, the specimen can be rotated around a range $\pm 65^\circ$ to acquire the first tilt series. Additionally thanks to the movement of the TXM robot gripper which operates a spring system the holder can be rotated by a fixed 90° angle by means of a simple lever fitted to the top of the holder, which rotates the mobile part while two magnets fix the two-positions at 0° and 90° . These features greatly facilitate the acquisition of a dual-axis tilt series. The whole assembly can be shown as Fig. 2.

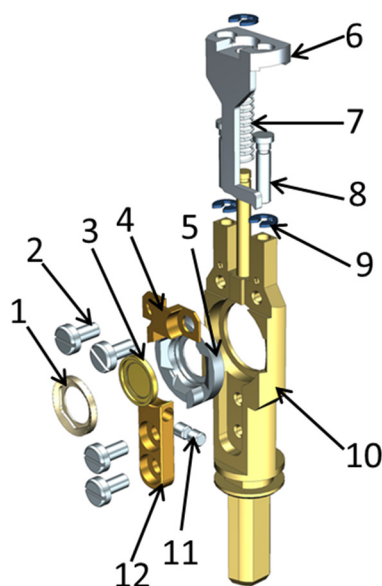


Figure 2: (1) AutoGrid holder, (2) Screw M1x2, (3) AutoGrid, (4) Bushing retainer, (5) Rotating bushing, (6) Holder handle, (7) Spring, (8) Rod, (9) C-clip, (10) Holder base, (11) Magnet, (12) Bushing holder.

MOVEMENTS DESCRIPTION

The dual-axis holder is rotated with the motorized sample stage of the TXM. The first tilt is orthogonal to the beam direction with a maximum tilt angle of $\pm 65^\circ$ without any visual or mechanical interference. This is the main and accurate motorized movement to obtain the tomography images (see Fig. 3).



Figure 3: First tilt with motorized movement.

Then, for the second tilt series, the specimen needs to be rotated inside the dual-axis holder using the gripper robot which will activate the mechanism that achieves the rotation in the axis parallel to the beam. With this sample rotation the second sample position is obtained to perform the second series (see Fig. 4).

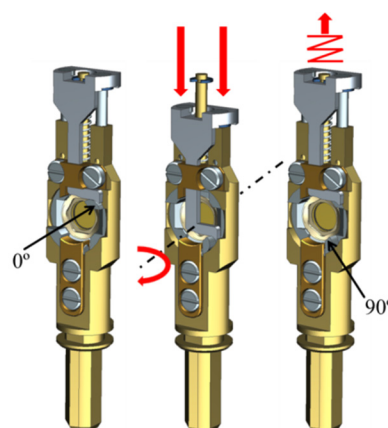


Figure 4: Second tilt with robot help.

At the same time, due to the new dimensions of the dual-axis holders a new sample shuttle that accommodates up to 4 dual-tilt holders has been designed and built. New covers have also been built to protect the sample from contamination during all sample transfers from atmospheric pressure to HV (see Fig. 5).

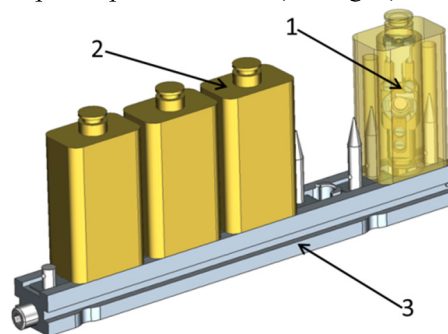


Figure 5: New cartridge. Sample load system. (1) dual-axis holder, (2) hood, (3) shuttle.

ASSEMBLY & TESTS

The sample environment shows the dimensional constraints that exist with the optical components and the shielding system to maintain the cryogenics conditions (see Fig. 6).

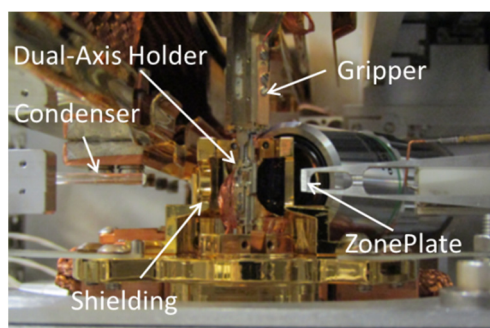


Figure 6: Inside TXM the sample environment.

In order to test the dual-axis holder different types of tests were performed:

Test of the dimensions, using a dummy to check the possible interferences with the rest of the components in the TXM.

Test of all rotation movements, using the TXM itself, first in air conditions and after in HV and cryogenic conditions.

Finally the dual-axis holder was tested with a real sample and the specific conditions of the Mistral TXM.

RESULTS

Figure 7 shows an example of two biological samples with the single tomographies in the two fixed positions (0° - 90°) reconstructed independently and the improved reconstruction obtained by combining both (DT, dual tilt tomography). The 3D DT reconstruction clearly shows an improvement in the visibility of the features marked with arrows such as for instance the mitochondria cristae (bottom row) [5].

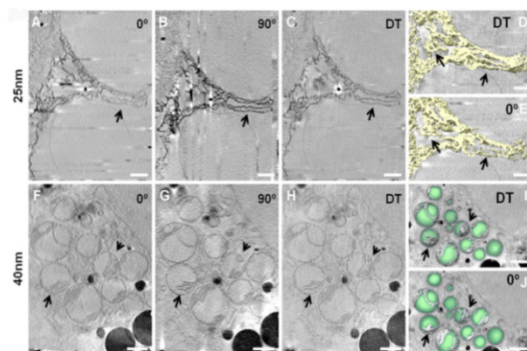


Figure 7: Two 3D DT reconstructions. For the ZP25 is a polyribosome consist of large numbers of ribosomes. For the ZP40 regions with large mitochondria were selected.

CONCLUSION

In summary, the objective of this DT new capability is to improve the final quality of the 3D reconstructions of all cells imaged at the Mistral beamline by reducing the missing-wedge artefacts occurring in single tomography.

ACKNOWLEDGEMENT

The authors wish to acknowledge all the ALBA staff involved in the design and testing of the dual axis holder, in particular: Salvador Ferrer and Javier Conesa. Also they wish to thank all the Blumeprot Group staff, the external workshop involved in the construction and assembly.

REFERENCES

- [1] E. Pereiro *et al.*, "Soft X-ray beamline at ALBA", *J. Synchrotron Rad.*, Vol 16, pp. 505–512, 2009.
- [2] Andrea Sorrentino *et al.*, "MISTRAL: a transmission soft X-ray microscopy beamline for cryo nano-tomography of biological samples and magnetic domains imaging", *J. Synchrotron Rad.*, Vol. 22, pp 1112–1117, 2005
- [3] E. Pereiro and F.J. Chichón, "Cryo-Soft X-ray tomography of the cell", In *eLS*, John Wiley & Sons, Ltd., Hoboken, New Jersey, USA, 2014.
- [4] I. Arslan, J.R. Tong, and P.A. Midgley, "Reducing the missing wedge: High-resolution dual axis tomography of inorganic materials", *Ultramicroscopy*, Vol. 106, pp. 994–1000, 2006.
- [5] Perez-Berna *et al.*, "The dual-axes for soft X-ray cryo-tomography reveals ultrastructural alterations of the host cell during Hepatitis C infection by increasing the isotropic axial resolution", *Microsc. Microanal.*, Vol. 23, Suppl 1, pp. 976-977, 2017.

A HIGH HEAT LOAD DOUBLE CRYSTAL MONOCHROMATOR AND ITS CRYO COOLING SYSTEM FOR HEPS

Hao Liang[†], Gang Cao¹, Lidan Gao, Yongcheng Jiang, Weifan Sheng^{†, 1}, Shanzhi Tang¹, Aiyu Zhou,
 Institute of High Energy Physics, 100049 Beijing, P. R. China,

¹also at University of Chinese Academy of Sciences, School of Physics, 100049 Beijing, China

Abstract

A high heat load double crystal monochromator and its cryo cooling system were designed and their prototypes were fabricated for the future HEPS. The mechanical and cooling structure of the DCM are introduced. The FEA results show the DCM is capable of cooling 870 watts of heat load. The cryo cooling system is also introduced. Test results show the pressure stability of the cryo cooling system is less than 2 mbar RMS. Offline heat load test of the DCM were carried out by a ceramic heater attached to the center of the incident surface of the first crystal, and 834 watts heat load were applied by the heater without boiling the liquid nitrogen. Offline absolute vibration measurement of the second crystal assembly was carried out by a laser interferometer under different cryo pump speed, pressure and heat load conditions, to find out the stability performance accordingly. An absolute vibration of 41 nrad RMS was measured, with the pump running at 45 Hz, which has a cooling capability of 400 watts.

INTRODUCTION

HEPS is a new generation light source which employs multi-bend achromat lattices and aims to reach emittance as low as 60 pm•rad with a circumference of about 1296 m. [1] It will start construction at the end of this year in Beijing. With the new light source there will be very small beam size and high-power density for the monochromator, and cryo cooling of crystals is favourable under those conditions. In the first phase of HEPS there will be 14 beamlines, a batch of cryo cooled monochromators and cryo cooling systems will be needed. Monochromator relates directly with beam intensity and stability issues and affects the overall beamline performance. Beijing Synchrotron Radiation Facility of IHEP is a first-generation light source which contains no cryo cooled optics. It is necessary to develop prototypes of a DCM and a cryo cooling system in order to get a better understanding of the technical challenges during the process and meet the requirements of HEPS beamlines in the future.

The following sections will introduce the design of the DCM and the cryo cooling system, offline heat load test and vibration test, and online test results of the prototypes.

DESIGN OF THE DCM

During the designing phase only, the techniques that had past the proven of principle stage were adopted. By applying those techniques which has never been used in BSRF

before, successful running of both the prototypes was the major target.

Table 1 shows the general specifications of the DCM during design phase.

To have a good stability performance wasn't among the original design objectives of the DCM. Later on, after the prototype was built, with the growing concern on the stability performance, the target was set to 100 nrad.

Table 1: DCM Specifications

Parameter	Description
Energy range:	5-20 keV
Crystal type:	Si<111>
Bragg angle range:	-4°-40°
Angular resolution:	0.5 μrad
Fixed offset:	25 mm (upwards)
Absolute stability of exit beam:	100 nrad
Heat load to be handled:	800 Watts
Rocking-curve broadening:	<10%
1 st crystal size:	30(W)×60(L)×40(T) mm ³
2 nd crystal size:	30(W)×200(L)×30(T) mm ³
1 st crystal adjustment:	fixed
2 nd crystal adjustment:	Pitch, roll, gap
1 st crystal cooling:	Indirect LN ₂
2 nd crystal cooling:	Indirect by copper foils
Vacuum:	10 ⁻⁵ Pa

Cooling of Crystals

To design a high heat load monochromator, a heat load of 870 watts with 2D Gaussian distributions were assumed to irradiate onto the first crystal. Assumed distribution of heat load absorbed on the surface of the first crystal is shown in Fig. 1 and Fig. 2.

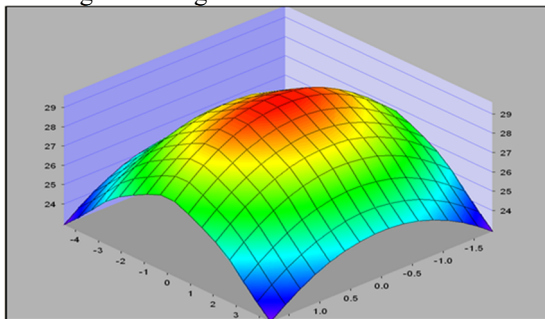


Figure 1: Heat load distribution, total power: 870 watts, power density: 29.6 W/mm², divergencies (RMS): 25(H)×10(V) mrad².

[†] Email addresses: lianghao@ihep.ac.cn and shengwgf@ihep.ac.cn.

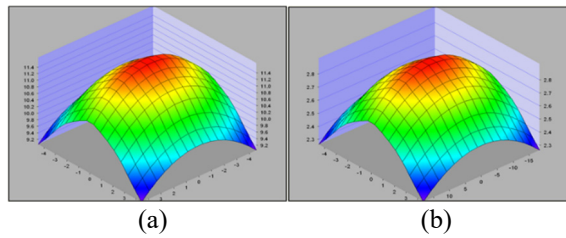


Figure 2: Power distribution: (a) At 5keV, max power density: 11.7W/mm². (b) At 20keV, max power density: 2.9W/mm².

Indirect cooling of the first crystal has been proven effective for high heat load monochromators around the world. [2] [3] Designed cooling structure also adopt side indirect cooling by OFHC blocks as shown in Fig. 3. Liquid nitrogen passes through 16 rectangular channels in both cooling blocks. In addition, in order to release the high heat load on the crystal diffraction surface, the height of the cooling copper block was designed to be slightly higher than the upper surface of the first crystal.

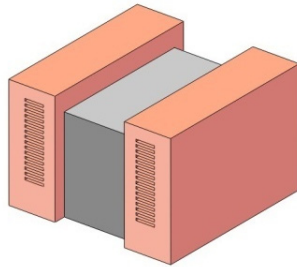


Figure 3: The cooling structure of the first crystal. The first crystal is clamped by 2 OFHC blocks with cooling channels.

The thermal deformation of the first crystal of double crystal monochromator at photon energies of 5keV and 20keV are simulated by FEA. Assuming the thermal contact resistance between the copper blocks and the silicon crystal was $5 \times 10^{-6} \text{ m}^2 \cdot \text{K/W}$, then the corresponding temperature field can be obtained, as shown in Fig.4. The maximum temperature on the crystal is 177K and 111K, respectively. From the temperature field of the first crystal, the stress field can be further obtained, and then the slope error curve was calculated according to the corresponding strain displacement curve, as shown in Fig. 5. The slope error RMS values of 5.82 μrad and 2.65 μrad for 5 keV and 20 keV can be obtained from the figure, respectively. The deformation results meet the requirement. The maximum temperature of wet walls is 86K.

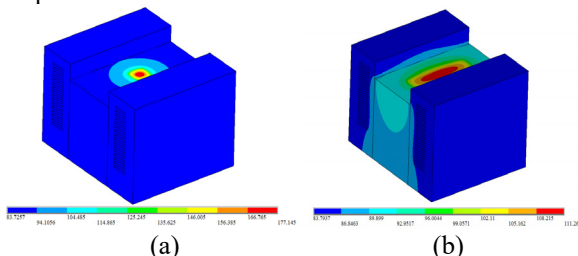


Figure 4: The temperature distribution of first crystal at 5 keV (a) and at 20 keV (b).

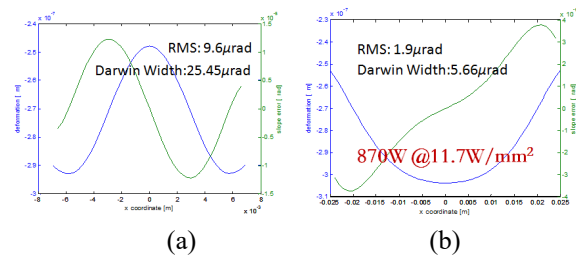


Figure 5: Displacement (blue curves) and slope error (green curves) distribution of first crystal at 5 keV (a) and at 20 keV (b).

Mechanical Design of the DCM

The designed DCM is shown in Fig. 6 (a). It has a granite table supported by an iron frame, with the frame manual adjustment of pitch, roll, yaw, and height of the main axis is possible. Also 2 slide ways to detach the main axis from the chamber or move the whole Bragg axis assembly transverse to the beam. A worm-wheel Bragg axis from Kohzu was used for good mechanical performance. An ion pump was put on top of the chamber, which now seems hard to maintain and decreases eigenfrequency. The liquid nitrogen in and out flanges are hard fixed to the back plate of the chamber, the vibration of the big hard liquid nitrogen pipe will transfer to the Bragg axis by these connections.

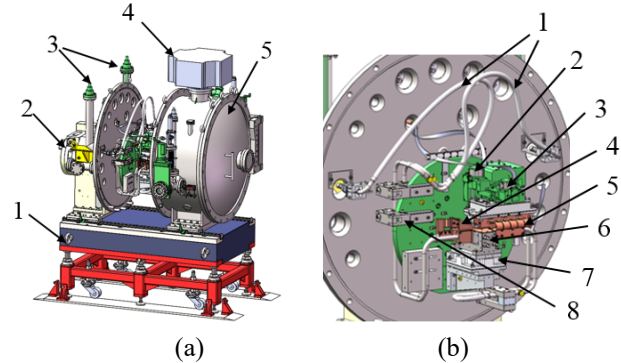


Figure 6: (a) DCM total assembly, (1) Support chassis, (2) The main axis from Kohzu, (3) Liquid nitrogen in and out flange, (4) Ion pump, (5) Vacuum chamber. (b) The internal view of crystal assemblies, (1) Liquid nitrogen pipes, (2) Pitch adjustment stage, (3) Roll adjustment stage, (4) Compton scattering shield, (5) Copper foils, (6) First crystal manifold, (7) Ceramic heat isolator, (8) Pipe clamp.

The interior of the DCM is illustrated in Fig. 6 (b). Note that the pipes were clamped 3 times to suppress resonance. And the temperature difference during low temperature operation was reduced by a ceramic heat isolator. The temperature of isolated part stayed above 270K for a long operation period. A Compton scattering shield was used to protect the second crystal assembly and improve temperature stability of it. The Compton shield worked well after online running. Also heat foils were applied if positive temperature control is required. The first crystal and its manifolds were clamped by bolts with leaf springs to prevent poor thermal contact under low temperature due to shrinkage of the crystal and mechanism.

THE CRYO COOLING SYSTEM

Table 2 shows the specifications of the designed cryo cooling system. It has more capacity than necessary for future needs, such as the maximum cooling power and the operation pressure.

Table 2: Cryo Cooling System Specifications

Parameter	Specification
Maximum cooling power	2500 watts
Pressure of closed loop	0.2–1 MPa
Pressure of open loop	1 Bar
Pressure stability	$\leq \pm 1.5$ kPa
Pump speed	0–100Hz
Maximum flow rate	10 L/min

The system has a closed loop to cool the crystals and a big Dewar in which the heat is taken away by boiling liquid nitrogen via a heat exchanger. The temperature, pressure, are controlled by a heater in a buffer tank. The flow rate is controlled by a variable frequency pump and bypass routes. It can be operated remotely and has full automated process control, which is compatible with EPICs.

The system will operate at high pressure, to prevent the boiling of liquid nitrogen due to high heat load.

OFFLINE TEST

After the prototype had been fabricated and assembled, the basic functions of them were tested first. After that phase the 2 prototypes were connected together to see how well they perform together. With the tuning and testing we gradually increase the complexity of the tests. First, offline heat load test were carried out, then absolute vibrations of the second crystal assembly were measured by laser interferometers with heat load and other variable conditions.

Offline Heat Load Test

Due to the lack of high heat load beamlines in China, the heat load test was carried out by applying a ceramic heater from Watlow. [4] It has a power capability of 967 watts, dimension of 25 mm × 25 mm. Figure 7 shows how it was applied to the surface of the crystal, the measurement of applied power by a Fluke amperemeter, and temperature readings change of PT100 sensors.

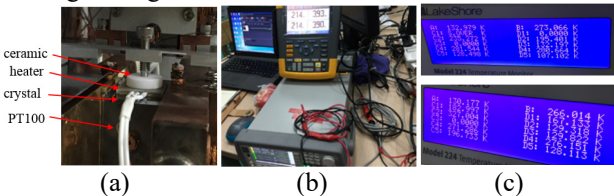


Figure 7: (a) Ceramic heater applied to the first crystal, (b) Applied voltage and current, 214 V×3.9 A=834 W. (c) Temperature rise of the button PT100 sensor (D5, 107 K–128 K, $\Delta T=21$ K), photo above is before heat load was applied, lower photo is after heat load was applied.

To make sure the heat load was properly absorbed by the crystal, Apiezon N grease was applied between the heater and crystal. [5] Also a ceramic heat isolator was used to keep them tight and isolate heat from going upwards to the support structure.

The measured voltage and current was roughly the given power, how much was absorbed can be calculated by the flow rate and temperature rise of liquid nitrogen flow. By calculation the result was 811 watts. The missing power could have been radiated or passed through the ceramic isolator.

The PT100 sensor was glued to the button surface of the first crystal, the glue is thin, but its thermal conductivity is not very high (about 0.22 W/(m·K) at 77 K). [6] The temperature of the crystal is not measured accurately due to temperature gradient and thermal resistance of the glue.

Offline Vibration Measurement

After the heat load success fully applied and no damage seems to be done, vibration measurements with heat load were also carried out.

The offline vibration test was carried out by a laser interferometer 5519 system from Agilent as shown in Fig. 8. This method was used to test the Petra III monochromators. [7]

Both the absolute and relative vibration affect the beam quality. Unfortunately there is just one port can be used to measure the absolute vibration of the second crystal. Since it requires adjustments of mirror when changing the Bragg angle under test, only when the Bragg axis is at 0 degree was tested.

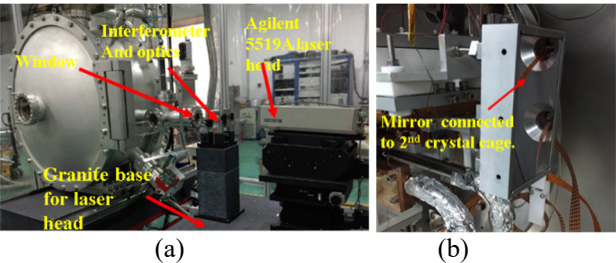


Figure 8: (a) Layout of absolute vibration measurement of the second crystal assembly. (b) Mirror mounted onto the second crystal assembly in the vacuum chamber.

The sampling rate of the interferometer was set to 10000 Hz, and the total points could be collected by the software was 1 million, that gave us 100 seconds of collection time.

The vibration tests were carried out under various conditions with different pump speed: (a) Pressure set to 3.5 bar. (b) Pressure set to 4 bar. (c) No heat load, with motor powered on, pressure at 4 bar. (d) 800 watts of heat load, with a 1-minute period triangular wave. (e) 800 watts of heat load applied in a 1-minute period triangular wave fashion. Also, the pure environment back ground was measured without liquid nitrogen flowing or air conditioner running. The air conditioner of the experiment hall increases the vibration level by about 6 nrad, that's why it was shut down to provide a quieter environment.

Figure 9 shows different results under different conditions. The background level is about 29 nrad, given by the

poor environment of the experiment hall ground with no isolations. However, Sorbothane pads were used under the whole DCM assembly aiming to bring down the vibration [8]. From the figure we can see that the 800 heat load didn't bring up vibration, so the liquid nitrogen was not boiling, the cooling of the crystal was sufficient enough. The best value is 41 nrad and under that pump speed of 45 Hz, which is still very high frequency. By calculation of the liquid nitrogen flow rate and boiling temperature, 400 watts could be taken away before liquid nitrogen boils in the pipe.

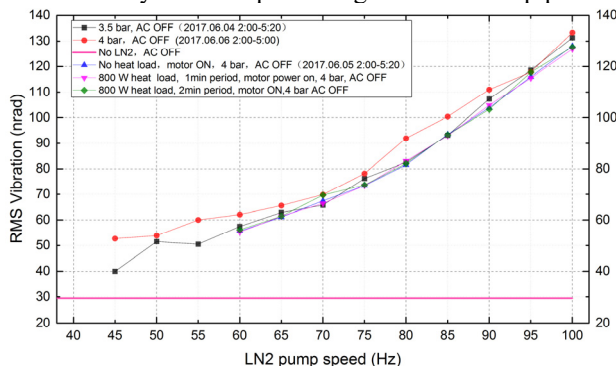


Figure 9: Absolute pitch vibrations under different test conditions. The frequency range is 2 Hz-5000Hz.

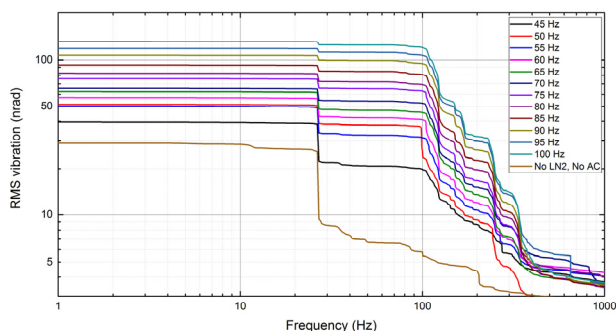


Figure 10: RMS vibrations under different pump speed. The frequency range is 1 Hz to 5000 Hz, but for a clear display the frequency above 1000 Hz is hidden because the values are too small, nearly negligible.

Figure 10 shows the RMS vibrations under different pump speed.

As illustrated in Fig. 10, we can see that the liquid nitrogen mainly contributes mainly to the frequency above 100 Hz. Vibration increases with the increasing pump speed above 100 Hz.

Another thing from the figure it is easy to see that the 25 Hz contributes almost the same at every pump speed, even when there is no liquid nitrogen. It has a contribution of roughly 20 nrad to the total RMS value.

The interferometer optics were mounted by screw rods on magnet base, not hard connected. The magnet base sticks on an iron plate supported by a granite table which stands on 4 levellers. The optics itself has some level of vibrations. As described above, the 25 Hz vibration doesn't increase with the pump speed, so it may be not coming from the DCM itself. It is reasonable to consider 25 Hz as the eigenfrequency of interferometer optics, or just a strong

ground motion, and consider the 100 Hz as the first eigenfrequency of DCM.

Pressure Stability of the Cryo Cooling System

The cooling system has been running for more than 100 days and seems to be working rather well. During the running period the pressure stability was recorded under various parameters, such as different pressure, speed. Figure 11 shows the pressure stability at 4 bar, in a long term and in a short term. The pressure stability is in the range of ± 6 mbar in PV value, and 2 mbar in RMS.

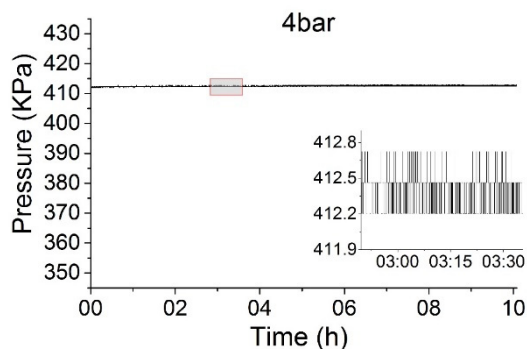


Figure 11: Pressure stability at 4 bar, in a long term (bigger figure) and in a short term (small figure).

ONLINE TEST

Online tests were carried out at beamline 3W1 of BSRF. With a total power of 150W by calculation, only the rocking curve and fixed exit position accuracy can be measured. Test beamline set up is shown in Fig. 12.

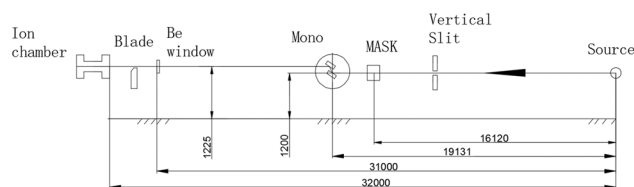


Figure 12: Layout of the online test. The vertical slits defined the acceptance angle by approximately $62 \mu\text{rad}$. No horizontal slits but only a mask.

Rocking Curve Measurement

After finding the Cu K edge, the Bragg axis angle could be roughly related to photon energy. Then rocking curve of 5–20 keV were tested by scanning the pitch angle of the second crystal. Table 3 shows the test results. The calculated values were done by XOP. The reason why the measured value are smaller than calculated ones may be caused by the third harmonics from Si<333> diffraction, as shown in Fig. 13. Or it might be caused by miscut, or misalignment of the crystals.

Table 3: Rocking Curve Test Results

Energy	Calculation	Measured
5 keV	17.78"	15.89"
8.979 keV	8.98"	8.79"
10 keV	7.98"	7.38"
15 keV	5.19"	4.73"
20 keV	3.85"	3.35"

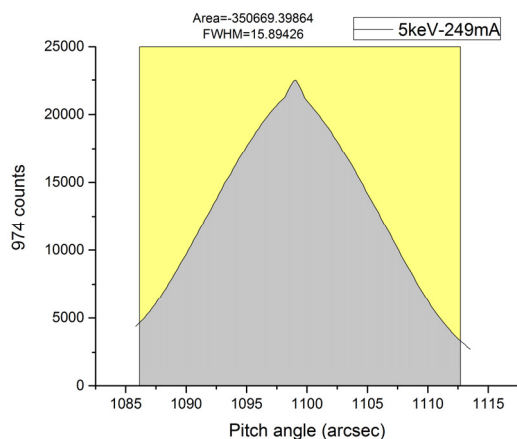


Figure 13: Rocking curve at 5 keV. The small peak on top is signal from 15 keV by Si<333>.

Fixed Exit Position During the Whole Range Scan

The fixed exit position stability during the whole scan was measured by the blade driven by a Kohzu linear stage. The Bragg axis stopped by every 0.5° increment, then the blade scanned the exit beam. During the scan the ion chamber recorded the signal, then derivate the signal, the intensity distribution could be obtained. The beam centre was defined by the FWHM centre of the intensity curve. The result was $\pm 89 \mu\text{m}$ for a Bragg angle range of 5°–24°.

CONCLUSION

The prototype of designed DCM and cooling system had shown the expected performance and meet our very basic requirements.

As for the stability performance, further stability tests should be carried out to see how it performs under lower pump speed, or on different times. For future HEPS, this will not be the final version of DCM, there are still plenty of room for improvements. The absolute stability is still not good enough for some demanding beamlines which require below 20 nrad stability. And for long term stability of the beam position or intensity, a feedback system and piezo driven flexures should be added.

ACKNOWLEDGEMENTS

We thank Lin Zhang for many advices. Great help from colleagues in BSRF are also appreciated. And special thanks to Dr. Ming Li for his vibration analysis software.

REFERENCES

- [1] Yi Jiao *et al.*, “Progress in the Design and Related Studies on the High Energy Photon Source”, *Physics Procedia*, Volume 84, 2016, ISSN 1875-3892, pp. 40 - 46, doi.org/10.1016/j.phpro.2016.11.008
- [2] A. Chumakov *et al.*, “Performance of a silicon monochromator under high heat load”, *J. Synchrotron Rad.* 21, 2014, pp. 315 - 324, doi:10.1107/S1600577513033158
- [3] A. Chumakov *et al.*, “Performance of a cryogenic silicon monochromator under extreme heat load”, *J. Synchrotron Rad.* 11, 2014, pp. 132 - 141, doi: 10.1107/S0909049503026785
- [4] WATLOW company website: <http://www.watlow.com/en/products/heaters/specialty-heaters/ultramic-ceramic-heaters>
- [5] APIEZON company website: <https://www.apiezon.com/products/vacuum-greases/n-grease>
- [6] Lake Shore Cryotronics, Inc., <https://www.lakeshore.com/products/cryogenic-accessories/varnish/pages/overview.aspx>
- [7] P. Kristiansen, J. Horbach, R. Doehrmann, J. Heuer *et al.*, “Vibration Measurements of high-heat-load monochromators for DESY PETRA III extension”, *J. Synchrotron Rad.*, vol. 22, Jul. 2015, pp. 879 - 885, doi.org/10.1107/S1600577515005664
- [8] SORBOTHANE company website: <https://www.sorbothane.com>

ENGINEERING DESIGN AND COMMISSIONING PERFORMANCE OF THE ESM AND SIX SOFT X-RAY BEAMLINES AT NSLS-II*

Y. Zhu, S. O'Hara, M. Idir, E. Vescovo, I. Jarrige, S. Hulbert[†], National Synchrotron Light Source II (NSLS-II), Brookhaven National Laboratory, Upton, New York 11973, USA

Abstract

Two of the five NSLS-II Experimental Tools (NEXT) project insertion-device beamlines developed for the NSLS-II facility at Brookhaven National Laboratory are state-of-the-art soft X-ray beamlines covering the 15 eV-2300 eV photon energy range. The engineering challenges of these two beamlines included: accurate and realistic optical simulations, nearly perfect optical figure and metrology, and advanced diagnostics systems developed in-house. The measured preliminary performance (flux, spot size, resolution) of these two beamlines closely matches the calculated values. Here, the engineering design and performance measurements of these two beamlines are presented.

INTRODUCTION

The Electron Spectro-Microscopy beamline (ESM) and Soft Inelastic X-ray Scattering beamline (SIX), as part of the NEXT project funded by the Department of Energy, have recently been commissioned at NSLS-II and are now in operation.

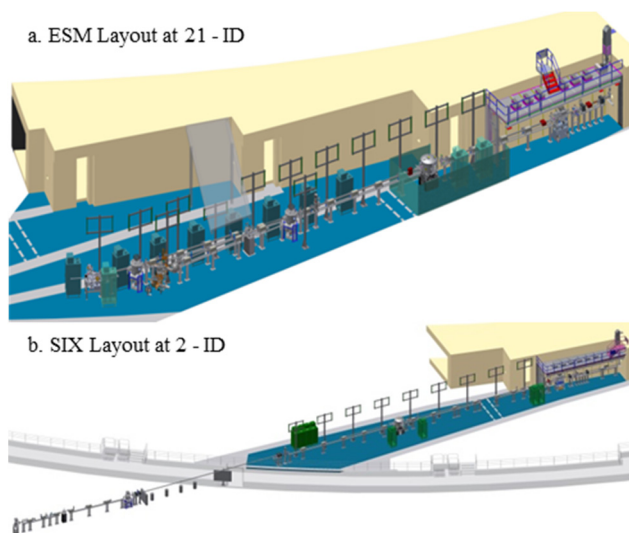


Figure 1: ESM and SIX on the NSLS-II Floor.

ESM is an insertion device beamline installed in sector 21-ID shown in Figure 1(a), a low-beta, non-extended floor space sector of the NSLS-II experimental floor. Two in-line, elliptically polarized undulators (EPU), a 2.8 m long

EPU105 and a 1.4 m long EPU57, serve as the beamline sources to cover a large photon energy range: 15 to 1500 eV. Downstream of a shared plane grating monochromator, the beam is deflected horizontally into one of two branches, the A-branch or P-branch (A for a high-resolution Angle-Resolved PhotoEmission Spectroscopy (μ -ARPES) and P for a full-field photoelectron microscopy (XPEEM)) by vertical selection of one of two identical elliptical cylinder mirrors (M3-A and M3-P).

The 105 m long SIX beamline is installed in sector 2-ID shown in Figure 1(b), a high-beta insertion device straight section feeding beam through an extended floor space sector to a satellite building. The SIX beamline covers the 180-2300 eV photon energy range by using a 3.5 m long EPU57 (upgradable to 7.0m) and is optimized to achieve a resolving power of 100,000 at 1,000 eV.

BEAMLINES OVERVIEW

ESM and SIX adopt the same type of optical scheme [1] (Figure 2; Table 1 lists beamline parameters). A horizontal internally water-cooled plane mirror (M1) serves to remove unwanted power and to separate the rest of the beamline from the Bremsstrahlung cone. The next component, a Variable Line Spacing (VLS) Plane Grating Monochromator (PGM), contains an internally water-cooled plane pre-mirror (M2) which illuminates one of four VLS gratings (300 l/mm, 600 l/mm, 800 l/mm and 1200 l/mm) for ESM and one of three VLS gratings (500 l/mm, 1200 l/mm, and 1800 l/mm) for SIX. The diffracted beam from the gratings is focused, vertically by the VLS grating and horizontally by an elliptical cylinder mirror (M3), at a plane occupied by high precision horizontal and vertical slits which define the energy resolution (vertical) and serve as a secondary source. A refocused image of the secondary source is produced at the sample position by either an ellipsoidal mirror (M4, at SIX and ESM B-branch) or by a KB mirror pair (ESM A).

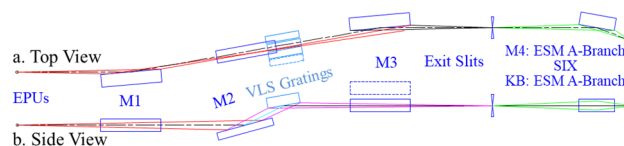


Figure 2: ESM and SIX optical schemes. The dashed rectangles represent the 4th ESM grating and the 2nd ESM M3 mirror.

* Work supported by the U. S. Department of Energy under Contract No. DE-SC0012704.

[†] Hulbert@bnl.gov

Table 1: ESM and SIX Parameters

	ESM	SIX
Source	EPU105, EPU57	EPU57
Energy Range	15 - 200 eV, 200 - 1500 eV	180 - 2300 eV
Resolution (ΔE)	~ 1 meV up to 100 eV ~ 100 meV up to 1000 eV	~ 10 meV at 1,000 eV
Flux	μ -ARPES: 10^{10} - 10^{11} photons/second XPEEM: 10^{11} - 10^{12} photons/second	10^{11} - 10^{12} photons/second
Beam Size at sample (FWHM)	μ -ARPES: ≤ 1 μ m, XPEEM: ≤ 40 μ m	6 μ m (horizontal) \times 0.6 μ m (vertical)

ENGINEERING DESIGN AND IMPLEMENTATION

The engineering challenges presented by the ESM and SIX beamlines included: optics optimization and metrology, high heat load optics cooling solutions, and advanced diagnostics system design for beamline commissioning and operation. Engineering standardization and modularization activities were implemented for the engineering design and implementation of both beamlines. All corresponding components of ESM and SIX share one engineering solution, with detailed parameter values that are dedicatedly optimized for each beamline.

Here, the ESM engineering design and implementation is presented as an example to elaborate the engineering design process for both ESM and SIX.

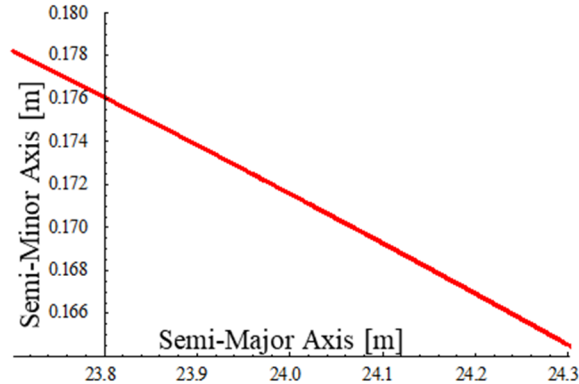
Optics Engineering Design and Metrology

Conventional ray trace software XOP SHADOWVUI [2] was used to perform extensive ray trace simulations to optimize the ESM and SIX optical configurations and parameters. In total, the ESM and SIX beamline optics consist of 11 Au-coated (50 nm thickness) mirrors and 7 VLS gratings. The surface figure of these optics is state-of-the-art in order to maintain the brightness of source photon beams and to achieve the target energy resolution and spot size values at the sample positions. Table 2 shows the optimized optical parameters for the ESM mirrors.

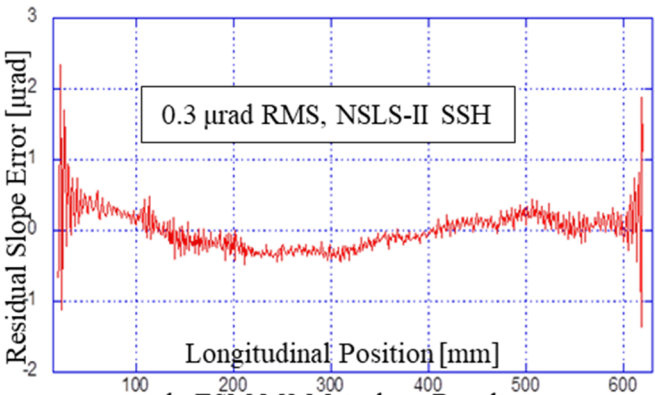
All optical elements were measured in the NSLS-II optical metrology lab using state-of-the-art surface figure measurement tools such as Stitching Shack-Hartman (SSH) [3] and Nano Surface Profiler (NSP) [4]. Figure 3 shows SSH metrology results for a typical focusing mirror (M3) for the ESM beamline.

Table 2: ESM Mirrors Optimized Parameters

Optics	M1	M2	μ -ARPES-Branch			XPEEM-Branch	
			M3-A	KB-H	KB-V	M3-A	M4-P
Object distance (m)	-	-	51.5	6.6	6.925	51.5	9
Image distance (m)	-	-	3.5	0.7	0.375	3.5	3
Grazing angle ($^{\circ}$)	1.25	2.2-15.5	1.5	2.5	2.5	1.5	2.5
Deflection Direction	Inboard	Upward	Outboard		Upward	Inboard	
Mirror shape	Plane	Plane	Elliptical Cylinder				Ellipsoid
Optical active area (L(mm) \times W(mm))	535 \times 16	515 \times 22	600 \times 15	335 \times 15	300 \times 10	600 \times 15	600 \times 15
Longitudinal RMS slope error (μ rad)		< 0.2		< 0.1		< 0.5	



a. ESM M3 Optimized Profile



b. ESM M3 Metrology Result

Figure 3: ESM M3-A mirror: optimized surface figure and metrology results. The residual slope error of this horizontally-focusing mirror is 0.3 μ rad RMS, less than the specified value of 0.5 μ rad.

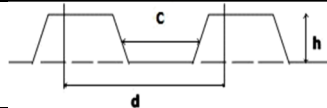
Four laminar VLS gratings are employed at ESM to cover the full 15 – 1500 eV energy range and for different applications. They are: one low energy grating (LEG, 800 l/mm), one medium energy grating (MEG, 600 l/mm), one high intensity grating (HIG, 300 l/mm), and one high energy grating (HEG, 1200 l/mm), covering the 15-100 eV, 50-200 eV, 50-300 eV, and 200-1500eV energy ranges, respectively. To optimize its diffraction efficiency over a wide energy range, the HEG grating was ruled with a sagittally-varying groove depth, ranging from 6 nm to 12 nm across the grating width. GSolver [5] software was used to optimize the grating groove parameters. After ruling, the four ESM gratings were sent to the SOLEIL optical metrology lab and metrology beamline to measure their VLS parameters, groove profiles, and diffraction efficiency. The

metrology results showed that the four gratings’ optical performance meets design requirements. Table 3 lists the optimized grating parameters and the Figure 4 shows a comparison of calculated and measured efficiency for the three fixed-groove-depth gratings.

To eliminate the distortion induced by mechanical mounting, all optics were mounted in their holders and tested as assembled units in the NSLS-II optical metrology lab. Adjustments to the clamping mechanisms were made to optimize surface figure before the optics were installed at the beamlines. Table 4 lists the surface slope errors of the four ESM gratings before and after adjustment. The results show that the grating assemblies were adjusted into the acceptable range.

Table 3: Optimized ESM Grating Parameters

	LEG	MEG	HIG	HEG	
Energy Range (eV)	15 - 100	50 - 200	50 - 350	200 - 1500	
Constant C _{eff}	3 @ 50eV	3 @ 100eV	2 @ 200 eV	2 @ 900 eV	
Line Density	$a_0 + a_1 \times w + a_2 \times w^2 + a_3 \times w^3 + \dots$ <i>where; w: longitudinal distance, and w = 0 defines the grating center.</i>				
VLS Parameters	a ₀ (l/mm)	800	600 l/mm	300 l/mm	1200 l/mm
	a ₁ (l/mm ²)	0.123453	0.0933142	0.0582427	0.231924
	a ₂ (l/mm ³)	1.14027×10^{-5}	8.74344×10^{-6}	5.1248×10^{-6}	2.05878×10^{-5}
	a ₃ (l/mm ⁴)	1.00155×10^{-9}	7.84354×10^{-10}	4.7664×10^{-10}	1.90434×10^{-9}
Meridional RMS slope error (μrad)	< 0.1				
Groove Depth (nm)	48.5	36	30	6 - 12	
Duty Cycle		0.7		0.65	



Duty Cycle = $\frac{c}{d}$; (h: groove depth; c: width of groove; d: period length)

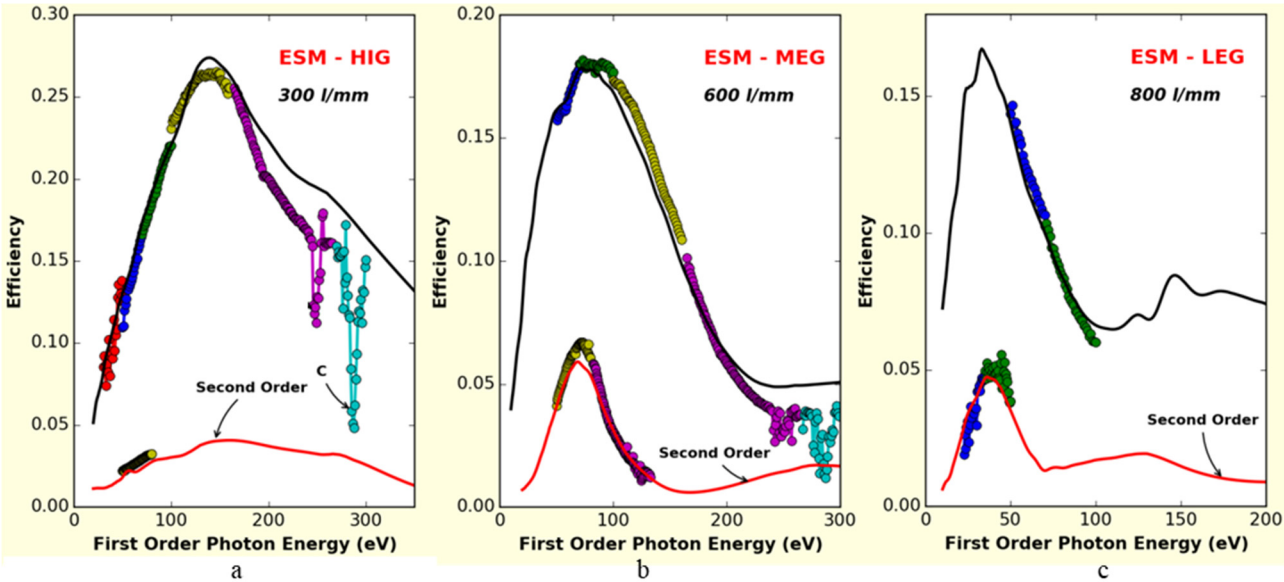


Figure 4: Calculated vs. measured efficiencies for the ESM HIG, MEG, and LEG gratings. Solid and dotted lines represent the calculated and measured efficiency, respectively.

Table 4: ESM Gratings Slope Errors (Unit: nrad)

		MED	HIG	LEG	HEG
SOLEIL (LTP)	Clamped	259	195	180	150
NLSL-II (SSH)	Clamped	182.3	144	-	-
	Adjusted	106.2	85.4	106.4	101

Thermal Cooling Scheme

With the EPU's in the ESM and SIX beamlines operating at their highest output power setting and the NLSL-II ring current set to its maximum value (500 mA), the maximum power incident on the first optical element (M1) is more than 1.2 kW. An integral water-cooling scheme was utilized for the M1 and M2 mirrors at both ESM and SIX, while an indirect water-cooling solution was employed for all gratings. Finite element analysis (FEA) simulations were performed using ANSYS [6] to optimize the structural parameters for the M1 and M2 mirror assemblies and the grating assemblies. Figure 5 shows the power absorbed by the first three ESM optics in its low energy range.

The FEA simulations reveal that the longitudinal slope errors of the M1 and M2 mirrors and the gratings are closely linear over their useful optical areas. That is, the thermal bump shape is almost circular in all three cases. Beam performance degradation in the diffraction plane (vertical) induced by the deformation of M1 (sagittal direction) and M2 (longitudinal direction) can be corrected by tuning the VLS PGM adjustable parameter (C_{eff} [7]). The ESM M1 and M2 thermal deformation and beam vertical profile correction results at 15 eV photon energy are shown in Figures 6 and 7, respectively.

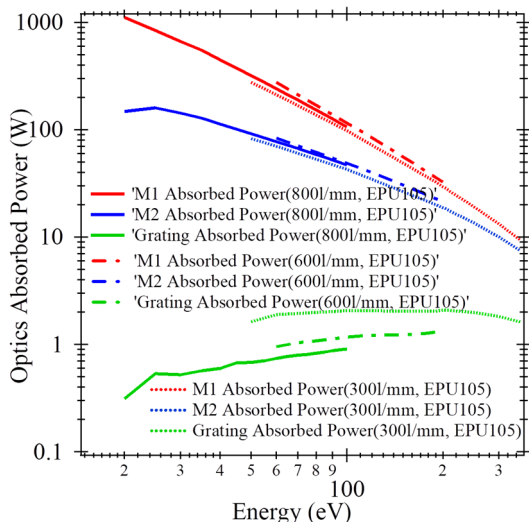


Figure 5: Power absorbed by the ESM M1 and M2 mirrors and gratings in the low energy range (15 - 300 eV). The first two mirrors (M1 and M2) and the gratings absorb 1.1 kW, 159 W, and 1.1 W of worst-case power, respectively.

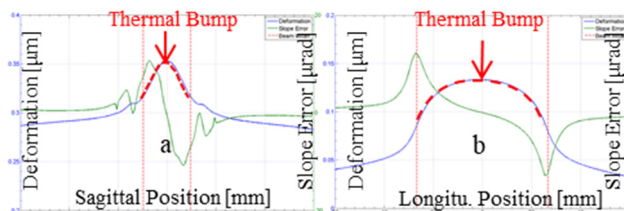


Figure 6: ESM M1 and M2 optical surface deformation: (a) The sagittal radius of curvature of ESM M1 is 461 m and slope error is $< 1 \mu\text{rad}$; (b) The tangential radius of curvature of ESM M2 is 7.4 km and slope error is $< 1 \mu\text{rad}$.

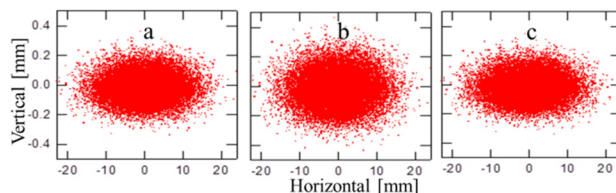


Figure 7: ESM beam spot at the exit slit plane, at 15 eV photon energy: (a) without heat load, $C_{\text{eff}} = 2.8503$, $\sigma_{\text{vert.}} = 83.48 \mu\text{m}$, $\sigma_{\text{horiz.}} = 6.0206 \text{ mm}$; (b) with heat load, $C_{\text{eff}} = 2.8503$, $\sigma_{\text{vert.}} = 107.02 \mu\text{m}$, $\sigma_{\text{horiz.}} = 6.0252 \text{ mm}$; (c) after correction, $C_{\text{eff}} = 2.8661$, $\sigma_{\text{vert.}} = 82.89 \mu\text{m}$, $\sigma_{\text{horiz.}} = 6.0252 \text{ mm}$.

Diagnostics Components Design

A set of beamline diagnostics instrument, developed in-house, was used to align, characterize, and monitor the beam during commissioning of the ESM and SIX beamlines. Figure 8 shows some of the types of diagnostic components installed at these beamlines.

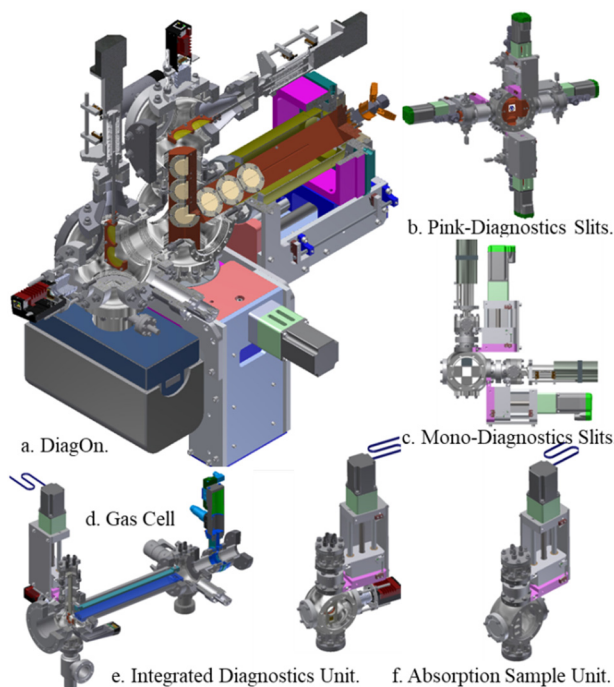


Figure 8: ESM and SIX diagnostics components: (a) DiagOn [8], first developed at SOLEIL, is used to characterize insertion device emission. NLSL-II DiagOn has ex-

tended its function to provide source and beamline alignment adjustments during operation; (b), (c) Diagnostic slits, used in pink or monochromatic beam locations to trim scattered light and monitor beam position through measurement of the current drawn from the blades; (d) Gas cell, used to measure energy resolution and calibrate the beam energy; (e) Integrated diagnostics unit: one YAG crystal, one Au mesh, and one photodiode to measure the beam intensity and observe the beam profile. This unit can be also combined with the gas cell to perform energy calibration; (f) Absorption sample unit, used to calibrate beam energy, scan beam position, and measure beam intensity by measuring photo-emitted current from standard sample wires mounted in the unit.

COMMISSIONING AND PERFORMANCE

The ESM and SIX beamlines have been commissioned and operations have commenced. Preliminary test results are reported here.

The ESM and SIX EPU emission has been characterized using the NSLS-II DiagOn and the intensity diagnostic components described above. Figure 9 (a) shows the evolution of angular distribution of emission, at 2 mA ring current, from ESM EPU105 as the gap is opened from 64.2 mm to 66.8 mm, around 236 eV photon energy. The angular distributions match simulations. Figures 9(b) and 9(c) show the beam positon at different times. These images were used to align the electron beam in the storage ring. Figure 9(d) demonstrates that the DiagOn can be used at standard operating current values (320 mA shown) by scanning the upstream white beam slits when set to a small angular opening.

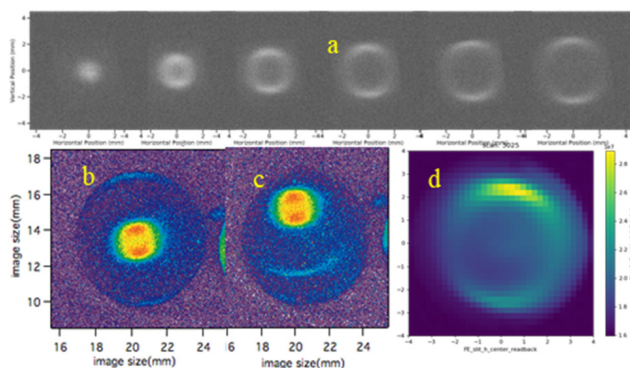


Figure 9: ESM EPU105 emission characterized using the NSLS-II DiagOn.

Figure 10 shows the ESM flux output in the low energy range (30 - 200 eV). In this figure, the black and red curves show measured flux values taken at 10 mA ring current, scaled to 500mA current, with 1 mm \times 1mm and 10 mm \times 10mm front end slit openings, respectively.

CONCLUSION

In conclusion, ESM and SIX have successfully accomplished commissioning, and the preliminary test results have closely achieved the calculated values.

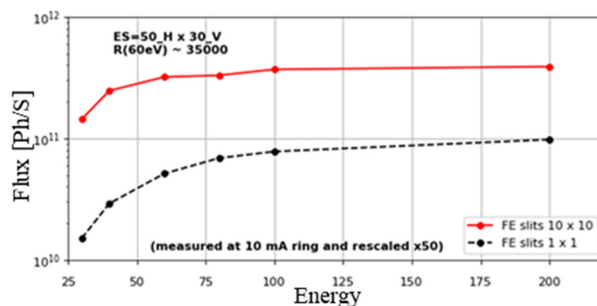


Figure 10: Measured ESM flux between 25 eV and 200 eV. The measured energy resolution at the ESM and SIX beamlines is shown in Figure 11. Figure 11(a) shows a measured energy resolution at SIX of 9 meV at 244.2 eV photon energy. Figure 10(b) shows measured energy resolution of 1.6 meV at 64.83 eV photon energy.

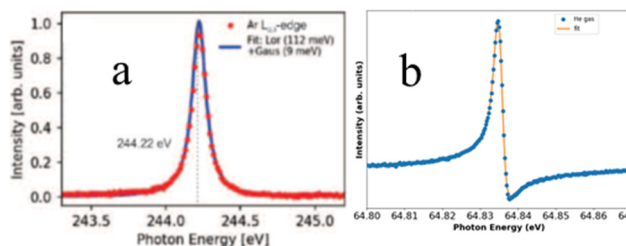


Figure 11: ESM and SIX measured energy resolution.

ACKNOWLEDEMENTS

The authors acknowledge Oleg Tchoubar and Nathalie Bouet for their support for NSLS-II DiagOn development, and the SOLEIL optical metrology group for ESM grating metrology and efficiency evaluation.

REFERENCES

- [1] R. Reininger *et al.*, "The electron spectro-microscopy beamline at National Synchrotron Light Source II: A wide photon energy range, micro-focusing beamline for photoelectron spectromicroscopies", *Rev. Sci. Instrum.*, vol. 83(2), Feb. 2012, DOI: 10.1063/1.3681440.
- [2] Xop Shadowvui, <http://www.esrf.eu>.
- [3] M. Idir *et al.*, "A 2 D high accuracy slope measuring system based on a Stitching Shack Hartmann Optical Head", *Optics Express*, Vol. 22, no. 3, Feb. 2014, pp. 2770-2781, DOI: 10.1364/OE.22.002770.
- [4] Qian *et al.*, "Nano-accuracy measurements and the surface profiler by use of Monolithic Hollow Penta-Prism for precision mirror testing", *Nuclear Instruments and Methods in Physics Research Section A*, vol. 759, Sept. 2014, pp. 36-43, DOI: 10.1016/j.nima.2014.03.043.
- [5] Gsolver, <http://www.gsolver.com>.
- [6] ANSYS, <http://www.ansys.com>.
- [7] R. Reininger *et al.*, "A soft x-ray beamline capable of canceling the performance impairment due to power absorbed on its optical elements", *Rev. Sci. Instrum.*, vol. 79-3, Mar. 2008, DOI: 10.1063/1.2897587.
- [8] K. Desjardins *et al.*, "The DiagOn: an undulator diagnostic for SOLEIL low energy beamlines", in *Proc. IEEE Nuclear Science Symposium Conference Record*, Dresden, Germany, Oct. 2008, pp. 2571-2574, DOI: 10.1109/NSSMIC.2008.4774883.

overall architecture and crystal geometry had to be considered within certain boundary conditions imposed by existing installations.

To optimize stability there is considerable incentive to reduce the number and stroke of crystal translations required to maintain fixed exit and therefore to reduce the beam offset between the incoming and outgoing X-rays. The ESRF DCM adopts a maximum of 2 crystal pairs, fixed 1st crystals, 200mm long 2nd crystals requiring only 1 linear translation to ensure fixed exit and a 10mm downwards deflection of the exit beam.

CONCEPTUAL DESIGN

The project has been divided into 2 main sub projects: “Bragg axis” and “Crystal cage” as shown in figure 2. Sub-division at this level does not compromise the integrated design approach of the overall device and provides straightforward pathways for re-use or modification of the two sub-assemblies for future requirements.

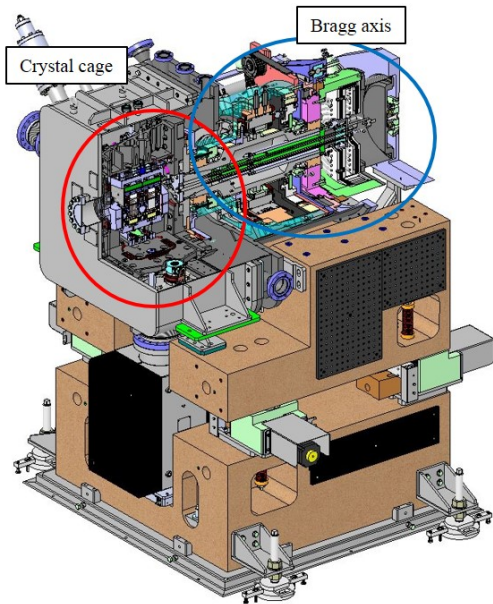


Figure 2: ESRF DCM prototype project structure.

BRAGG AXIS

The “Bragg axis” defines all components behind the crystal cage. This includes the Bragg shaft and bearings, the Bragg motor and ex – vacuum encoder, the cryogenic feeder line management system, all ex – vacuum displacements and the main support structure.

Bragg drive motor

Most current ESRF monochromators use an external, rear mounted stepper motor and reduction gears (worm wheel, gearbox...) for the Bragg drive. More recently, we have seen DCMs exploiting “direct drive torque motors”:- a type of brushless permanent-magnet synchronous motor, with the payload directly connected to the rotor, thus using no additional transmission elements. The frameless, hollow shaft architecture allows

the motor to be ideally positioned between the Bragg bearings and close to the crystals. The large number of poles ensures the angular resolution required. Table 2 compares the 2 drive techniques.

Table 2: Direct Drive Torque Motor vs. Stepper Motor & Gears

Parameter	Torque Motor	Stepper & Gears
Max speed	High	Medium (ratio dependent)
Wear & maintenance	Non (non-contact)	High
Radial parasitic forces	Low	Preload dependent
Aptitude to multiple scans	Good	Limited by backlash & wear
Theoretical resolution	Limited by encoder	Smallest step size
Frictional torque sensitivity	High	Lower
Friction losses	None	Preload dependent
Backlash	N/A	Wear dependent
Heat generation	High (requires cooling)	Lower
Integration	Simple (frameless, hollow shaft)	Complex (gearing or end drive)

Given the numerous advantages of the direct drive motor, the ESRF DCM prototype has been manufactured with this drive option. The ESRF has previous experience of controlling similar motors for applications other than monochromators.

The only identified drawbacks are higher thermal load, minimized by ESRF designed cooling and thermal insulation, and higher sensitivity to torque variation, managed by careful balancing of rotating parts and counterweights.

Bragg bearings

The two (contradictory) principal concerns in guiding the Bragg angle axis are radial stiffness and low frictional torque. Minor guiding errors can be corrected by fine tuning of the second crystal position whereas poor radial stiffness will degrade stability and is far more complex (or impossible) to correct.

The consequence of frictional torque is the limitation of the theoretical minimum angular step size, due to the “stick – slip” effect.

Low frictional torque is generally the main motivation for specifying air bearings. However, the radial stiffness of air bearings is significantly lower than that of angular contact bearings. Table 3 compares the two bearing types.

Table 3: Comparison Between Air and Angular Contact Bearings

Parameter	Air	Angular contact
<i>Typical values, geometry dependent</i>		
Frictional torque	None	2Nm (depends on axial preload)
Runout	25nm	2µm
Wobble	0.1µrad	5 - 10µrad
Radial stiffness	350N/µm	2000N/µm

Radial stiffness being the primary concern in the choice of Bragg shaft bearings, the ESRF DCM prototype was manufactured using two pairs of angular contact bearings in “X” configuration. The bearing arrangement is inspired from established precision spindle geometry and axial preload is optimised for the highest possible radial stiffness whilst maintaining acceptable frictional torque.

Bragg Encoder

Specified absolute angular precision on the Bragg angle is 2 – 5µrad, and angular stability required is 15nrad, even when scanning, which defines an upper limit for encoder resolution.

To guarantee this level of performance, the encoder must be placed as close as possible to the crystals. This argues for the integration of an absolute encoder to the crystal plate, inside the vacuum vessel. The most suitable commercially available option is the Renishaw absolute encoder, providing 1.45nrad resolution with 32 bits encoding.

There is concern over the lifetime of the encoder read heads positioned where they are likely to be exposed to scatted radiation. Two solutions have been deployed:

Position the read heads behind the main crystal plate, where the sensitive electronics will be out of direct line of site of primary scattering and will benefit from radiation attenuation afforded by the main crystal plate. Local shielding is also implemented close to the read heads.

Integrate a second, identical encoder on the air side of the Bragg axis, as close as possible to the crystals. This encoder will be more efficiently protected from radiation and when implemented in parallel with the in-vacuum encoder, permits evaluation of the angular error induced by possible Bragg shaft twist and provides backup in the event of in-vacuum encoder failure.

Cryogenic Feeder Line Management

Most DCMs at the ESRF are subject to absorbed power densities which can attain hundreds of W/mm², requiring cryogenic crystal cooling. LN₂ feeder lines must enter the vacuum environment at a fixed point and follow the move-ment of the Bragg axis during scans (see Fig. 3).

It has been demonstrated that up to 85% of the total inertia seen by the Bragg drive motor is due to the displacement of these feeder lines. This is a severe performance

limitation, especially when using direct drive motors, for which torque should be kept as constant as possible.

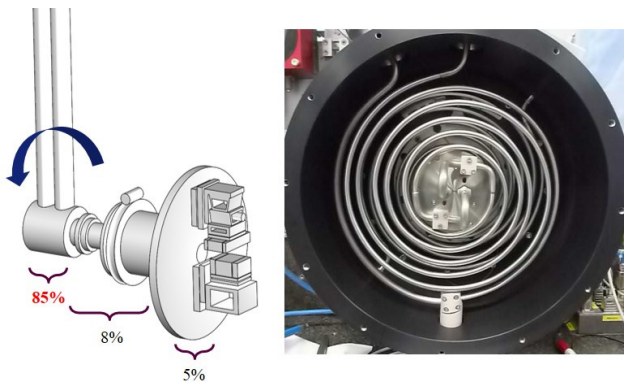


Figure 3: Feeder line management.

Hence there is a strong case for a well-balanced rotating mass and fixed feeder lines which do not perturb Bragg displacement during scanning. A novel deformable spiral tube system has been designed, supplying LN₂ to the crystals for cooling and thermally stabilized water to critical elements to ensure dimensional stability. The coils deform during scanning, allowing +/- 10 degrees angular displacement of the Bragg axis while the feeder lines remain fixed. For larger displacements (between scans), a stepping motor drive synchronised to the Bragg torque motor guides the external LN₂ feeder lines over the required angle.

CRYSTAL CAGE

The “crystal cage” defines all components beyond the end of the Bragg axis. This includes the crystals themselves, their cooling system, alignment and displacement mechanics, the online metrology system, the support structure (plateau) and a conical interface to the Bragg shaft.

Plateau and Cone

To guarantee minimum deformation over the full scan range, a high stiffness plateau is mandatory. Crystal parallelism per degree of Bragg scan in the non-mechanics-assisted mode (A) is defined as $\Delta\Theta/\Theta = 0.3 \mu\text{rad/deg}$. This is then the target for stiffness optimization processes for all static components.

In addition, the plateau structure needs to be thermally stable despite heat loads caused by photon scattering. From the first design calculations, temperature differences of 2.7K provoke parallelism errors of up to $\Delta\Theta = -4.81\mu\text{rad}$ and $\Delta\phi = 36.81\mu\text{rad}$. These calculations reveal the necessity to thermally control the structure.

The plateau structure was optimized in a design-calculation loop to identify lower stiffness zones and to determine deformation of the cage under gravity when loaded with the various component masses (see figure 4).

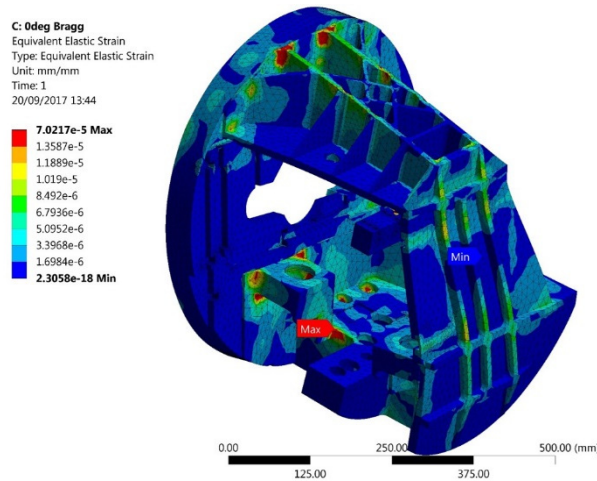


Figure 4: Plateau FEA - strain under gravity load

The structure is composed of four parts using 7075 aluminium alloy for high conductivity and good machinability. It integrates a water circuit to thermalize the structure, reducing temperature gradients.

Crystal Clamping and Cooling

The ESRF DCM comprises two pairs of crystals in an innovative assembly (see figure 5).

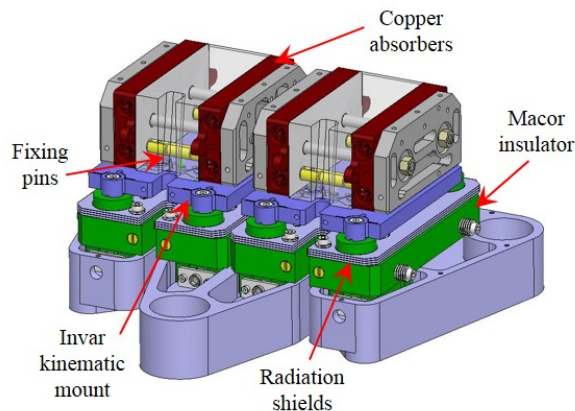


Figure 5: 1st crystal clamping setup.

Silicon crystals are fixed to an Invar plate in order to minimize differential expansion. Further, these plates integrate flexural kinematic mounts to reduce resulting forces on the crystals due to differential thermal expansion. Fixation pins traversing the crystals and screws from the bottom fix the crystals to the Invar plates. Copper absorbers are clamped to the crystal sides to extract the absorbed power.

Dynamic measurements of the assembly confirm high stiffness: a first Eigen mode of over 390Hz. Optical measurements were performed to assess relative deformation of the crystal due to clamping of the cooling blocks. Data was taken at 2 and 4 bars clamping pressure: a maximum relative P-V deformation along the meridional axis of 12.55nm was observed for 4 bars, with a resulting radius of curvature of $\approx 50\text{km}$.

Both crystal pairs are directly cooled. Finned channels through the 1st crystal cooling blocks optimise heat exchange. The second crystal set is cooled in series with the 1st and future developments should allow improved thermal matching between the 2 crystals.

Fastjack

The Fastjack is a high precision linear actuator integrated to the plateau in tripod configuration to position the 2nd crystal. Three Fastjacks will operate from the horizontal plane ($\Theta_{\text{Bragg}} = 80\text{deg}$) to the vertical plane ($\Theta_{\text{Bragg}} = 2\text{deg}$).

The 2 stage actuator comprises a long stroke driven by a stepper motor, and a 2nd stage for fast position errors correction using a piezo actuator. The stepper actuator is specified for a minimum incremental motion (MIM) of 100nm; the piezo actuator and its regulation loop should achieve a MIM of a few nanometres with an actuation bandwidth of 100Hz. Careful design optimisation has been performed for both maximum stiffness and nano-positioning capabilities. Long travel displacement is ensured by a precision screw / nut and guiding by a ball bush guide.

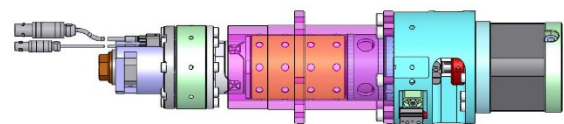


Figure 6: ESRF Fastjack.

Together with the DCM embedded metrology system, the 3 actuators will optimise position repeatability the stability of the 2nd crystals. During a scan or at fixed energy, repeatability and stability of around 15nrad implies about 5nm displacement at the actuator level.

The Fastjack is capable of a stroke of 30mm, a speed of up to 8mm/s, acceleration rate of 100mm/s^2 , and an actuation force above 100N. Specified lifetime is $\sim 10^7$ cycles under UHV conditions. Water-cooling is also integrated.

Online Metrology

To maintain crystal parallelism to within defined specifications over the entire scan range is perhaps the most challenging aspect of the entire DCM design: intrinsic dynamic behaviour and thermal gradients make it impossible to envisage such stability uniquely through passive mechanical design. Based upon the severity of the specifications for parallelism stability, an online metrology system, using multiple radiation resistant Fabry - Perot interferometer heads, has been integrated to monitor the angular drifts of the 2nd crystal and allow correction of its position in real time.

Overlap of the crystals at higher Bragg angles severely restricts accessibility to the diffracting surface for positional metrology and direct exposure to high levels of scattered radiation for prolonged periods may limit component lifetime. Consequently, the interferometer beams will target the rear face of the crystals. This is already a significant challenge and a major improvement over existing systems.

Parallelism between the crystalline planes and the rear of the crystal is supposed fixed.

A dedicated metrology frame carries 3 interferometers to monitor pitch, roll and fixed exit translation of each of the two 2nd crystals. The position of the 1st crystals - directly attached to the Bragg axis - is considered fixed. However, on the prototype, this will be monitored, as will any possible differential displacement of the metrology frame itself. Thus, a total of 15 interferometers are deployed (3 for each crystal and 3 for the metrology frame). Figure 7 shows the schematic layout.

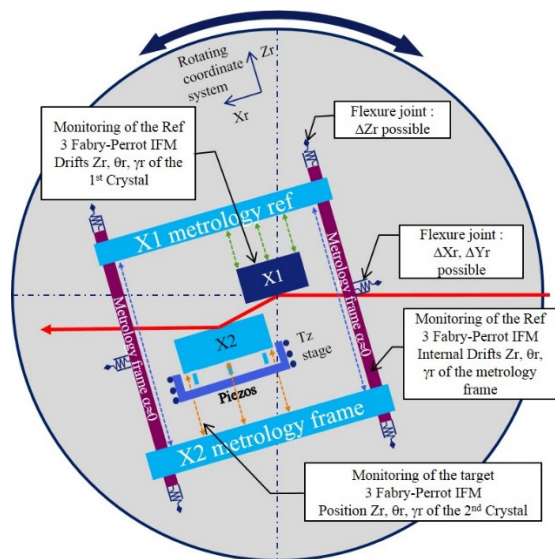


Figure 7: Online crystal metrology schematic layout.

As requested, the DCM can continue to operate in a degraded performance mode in the event of failure of the online metrology system.

FIRST RESULTS

Bragg Axis

By using the torque motor with a linear controller and the in-air position encoder, first tests give a minimal incremental motion and a repeatability of $0.25 \mu\text{rad}$. This is still above final specifications, but performance is expected to improve following further tests using an optimized control algorithm (see Figure 8).

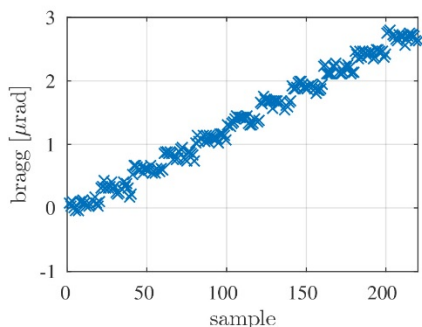


Figure 8: Bragg axis resolution in air.

Fastjack

The first tests of the Fastjack show promising results. In-air tests with a load of 5kg show a minimal incremental motion of about 15nm over a stroke of 30mm. Further, the dynamic performance of the actuator was pushed to a bandwidth of over 100Hz by using advanced control algorithms. This was achieved using a feedback loop consisting of the online metrology system and a real-time controller (see Figure 9).

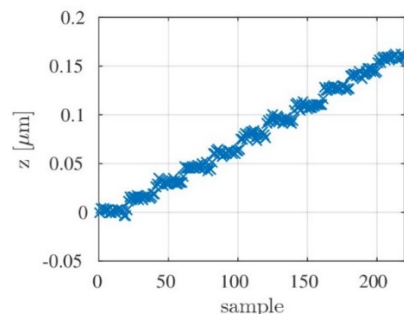


Figure 9: Fastjack resolution in air.

At the time of writing, the measurements are limited by the in-air performance of our reference Interferometer, which shows a noise level of about 10nm. By moving the setup from the in-air test bench to the vacuum chamber of the DCM, a further performance improvement is expected.

CONCLUSION

Derived from the expected performance of the ESRF EBS, specifications for a new generation DCM are extremely challenging and impose exhaustive reconsideration and optimisation of every identified weakness in current designs.

This has been the driving philosophy behind the ESRF DCM prototype project and following a comprehensive design phase, manufacture is now complete and assembly, alignment and initial metrology are being performed in house. First results from off-line lab metrology are encouraging and installation and commissioning on ESRF's X-ray microscopy beamline ID21 are foreseen before the 18 month EBS shutdown (December 2018 – mid 2020).

ACKNOWLEDGEMENTS

The authors would like to thank all ESRF staff involved in the DCM prototype project, including:

H.P. van der Kleij, M. Lesourd, L. Rousset, R. Grivelet, P. Voisin, A. Vivo, M. Cotte, M. Salomé, K. Martel, D. Bugnazet, R. Hino, K. Amraoui

List of Authors

Bold papercodes indicate primary authors; ~~crossed-out~~ papercodes indicate 'no submission'

— A —

Aballe, L. **THPH15**
Abeykoon, M. **THPH19**
Abliz, M. **THPH24**
Abu-Hanieh, T.H. **TUPH01**
Adachi, J. **THPH23**
Adam, M.J.P. **WEPH01, WEPH04**
Adamson, L.W.S. **THPH01**
Adler, S. **THPH31**
Akiyama, K. **THPH33**
Al Shehab, M.M. **TUPH32, TUPH33**
Al-Najdawi, M.A. **WEPH02**
Alexandre, P. **TUPH12**
Allézy, A.P. **TUPH14**
Amores, L. **THPH06, THPH21**
Amundsen, C. **THPH41**
Anders, A. **TUPH14**
Andreazza, W. **TUPH36, WEPH03**
Andresen, S. **THOAMA01**
Anklamm, L.C.A. **WEOAMA06**
Anton, J.W.J. **WEOPMA04**
Appathurai, N. **WEPH01**
Araujo, W.R. **WEPH12**
Armenta, R. **THPH02**
Arrachart, C.A. **TUPH03**
Arruda, L.C. **WEPH39**
Assoufid, L. **WEOPMA04, THPH27**
Attenkofer, K. **THPH33**

— B —

Baboulin, D. **FROAMA07**
Baker, N. **THOPMA04**
Baker, R. **FROAMA07**
Bandke, D.B. **TUPH37**
Baptiste, K.M. **TUPH14**
Barada, A.H. **WEPH35**
Barkway, G.R. **WEPH04**
Baron, N.B. **TUPH03**
Barrett, R. **THOAMA06, FROAMA07**
Bartalesi, A. **THPH03**
Barthe-Dejean, C. **THOAMA03**
Béchu, N. **TUPH03, TUPH11**
Bühner, A. **THPH31**
Becheri, F. **WEPH06**
Beckhoff, B. **WEOPMA06**
Ben El Fekih, R. **TUPH12**
Benda, E. **THOPMA02**
Bernard, P. **FROAMA07**
Berruyer, G. **WEPH40, FROAMA07**
Berteaud, P. **TUPH03**
Beye, M. **THPH31**
Biacsi, J.C. **TUOPMA06, TUPH35**

Billett, B. **TUPH04**
Birri, M. **THPH04**
Bizen, T. **TUOPMA05**
Blache, F. **TUPH03**
Blanchet, Blanchet, C. **WEPH20**
Boiesan, T. **WEPH05**
Bonney, J. **FROAMA07**
Borrel, J. **TUPH02**
Botta, S. **THOPMA03**
Bourenkov, G. **WEPH20**
Bourgoin, C.B. **TUPH03**
Brajuskovic, B. **TUPH04**
Brendike, M. **FROAMA07**
Briquez, F. **TUPH03**
Brochard, T. **TUOPMA06, TUOPMA07**
Brumund, P.M. **TUOPMA07, TUPH08, FROAMA07**
Buda, S. **THPH19**
Bueno, C.S.N.C. **TUPH43, WEPH39, THPH12**
Buice, E.S. **TUPH14**
Burt, M.H. **THPH05**
Butler, D.J. **TUPH34**

— C —

Caliari, R.M. **WEOAMA01**
Calvi, M. **TUOPMA03**
Campmany, J. **WEPH06, WEPH24**
Canova, H.F. **WEPH39**
Cao, G. **FROAMA02**
Capatina, D. **WEPH07, THOPMA02**
Cappadoro, P.L. **TUPH26**
Carballedo, A. **THPH15**
Carcy, A.C. **THPH09**
Carlson, M. **WEPH05**
Carter, J.A. **TUPH04, THOAMA05**
Casas, J.J. **TUPH30**
Castagna, J.C. **THOAMA02, THPH06, THPH21**
Cedillos, A.G. **TUPH05**
Celestre, R.S. **THPH07**
Chan, W.S. **WEPH30**
Chang, C.-H. **THPH06**
Chang, C.F. **THPH08**
Chang, C.H. **TUPH06, TUPH19**
Chang, C.H. **WEPH38, THPH08, THPH29**
Chang, C.Y. **WEPH38, THPH08, THPH29**
Chang, S.H. **WEPH38, THPH08, THPH29**
Chen, B.Y. **WEPH41**
Chen, C.S. **WEPH30**
Chen, C.Y. **WEPH38**
Chen, H.W. **THPH08**
Chen, J.-R. **THPH07**
Chen, J.X. **TUPH27, WEPH08, WEPH32, WEPH34**

Chen, M.L.	TUPH07
Cheng, Y.Y.	WEPH30
Cherukuvada, H.	THPH35
Chiu, C.C.	WEPH38, THPH08, THPH29
Choi, H. J.	WEPH18
Chow, K.	TUPH14
Chubar, O.V.	TUPH26
Chung, T.Y.	TUPH06
Chung, Y.-C.	WEPH30
Cianciosi, F.	TUPH08
Ciccone, L.	WEPH36
Claudioano, G.V.	TUPH09, WEOAMA04, WEPH31, THPH12
Clavel, C.	WEPH40
Clute, T.K.	THOPMA02
Cocco, D.	THOPMA05, THPH34, THPH36
Colldelram, C.	TUPH30, THPH14, THPH15, THPH16, THPH17, THPH43
Collette, C.G.R.L.	WEOAMA02
Collins, J.T.	THOPMA02
Collins, S.P.	THPH05
Connatser, R.W.	TUPH10
Connolley, T.	THOAMA04
Corwin, T.M.	TUPH26
Couprie, M.-E.	TUPH03
Cutler, G.D.	TUPH14

— D —

Da Silva Castro, J.	TUPH03, TUPH11, TUPH12
da Silva, M.B.	TUPH43
Dabin, Y.	TUPH02, THOAMA06, FROAMA07
Dakovski, G.L.	THPH36
Davies, S.	THOAMA04, THOPMA04
de Oliveira, C.	TUPH03
de Oliveira, H.G.P.	TUPH43, WEPH39
De Santis, S.	TUPH14
DeBeer, S.D.	WEOAMA06
Defever, J.	THPH36
Dehaeze, T.	WEOAMA02
Dejus, R.J.	TUPH23
Deng, R.B.	TUOPMA02, TUPH16
DePaola, F.A.	TUOPMA08, TUPH13, THPH41
Desjardins, D.K.	WEPH36, THPH09, THPH32
Di Giacomo, M.	THOAMA03
Diete, W.	WEPH42
Dill, F.U.	THPH10, FROAMA06
Doehrmann, R.	THOPMA03
Dommach, M.	TUOPMA01
Donahue, R.J.	TUPH14
Donnelly, A.T.	TUPH23
Dooryhee, E.D.	THPH19
Doose, C.L.	TUPH23
Downey, J.S.	TUPH29, THPH24
Drakopoulos, M.	THOAMA04
Du, H.W.	TUOPMA02
Duarte, R.M.	TUPH14

Dubuisson, J.M.	TUPH03
Ducotté, L.	FROAMA07
Ducourtieux, S.	THKA01
Dufresne, E.M.	THPH26
Duller, G.M.A.	TUPH34
Duraffourg, M.	WEPH03
Duval, J.P.	TUPH03

— E —

Ebbeni, M.	TUOPMA04
Ederer, K.	THPH39
Einfeld, D.	TUPH35
Endo, K.	THPH33
Engblom, C.	WEPH42
Eom, I.	THPH28
Erdmann, M.	THOPMA02
Ermakov, A.	TUPH15
Ewald, F.	TUPH02
Eybert, L.	TUOPMA06

— F —

Falkenberg, G.	THOPMA03
Fan, Y.	WEPH09
Farré París, F.	THPH18
Faussete, R.	TUPH13
Fauth, F.	THPH18
Feng, Y.	TUPH39, THPH11
Ferreira Sanchez, D.	THPH04
Ferreira, V.Z.	WEOAMA04, THPH12
Ferrer, S.	THPH14, THPH17
Fiedler, S.	WEPH20
Field, R.C.	TUPH05
Filippetto, D.	TUPH14
Fisher, M.V.	WEPH16
Fliegauf, R.	WEOPMA06, THPH30
Focker, G.J.	WEPH03
Foerster, M.	THPH15
Fonda, E.	WEPH14
Fonseca, E.B.	TUPH09
Fonseca, P.T.	TUPH09, WEPH39
Fontserè Recuenco, A.	THPH14, THPH17
Forcat Oller, S.	TUPH39, THPH11
Freitas, P.P.S.	WEPH26
Fuchs, F.	WEPH11

— G —

Gangnant, P.	THOAMA03
Gao, F.	TUPH16
Gao, L.	WEPH10, THPH42, FROAMA02, FROAMA03
Garcia-Fernandez, M.	THOPMA04
Garrevoet, J.	THOPMA03
Gehrmann, T.	WEPH20
Geraldes, R.R.	WEOAMA01, WEOAMA04, WEPH31, THPH12

Gevorgyan, A.A.	WEPH23, WEPH24, THPH17	Hsu, M. Y.	WEPH41
Ghose, S.	THPH19	Hu, X.	TUOPMA02
Gießel, T.	WEPH11	Huang, D.-G.	TUPH21
Gilmour, A.	WEPH12	Huang, H.C.	THOPMA04
Giorgetta, J.L.	THPH09	Huang, J.C.	TUPH19
Gnewkow, R.G.	WE0AMA06	Huang, L.	WEPH38, THPH08, THPH29
Goerlitz, M.	THPH13	Huang, Y.-S.	WEPH38
Goirand, L.	TUOPMA06, TUOPMA07, TUPH08, TUPH35	Huber, L.	TUOPMA03
González Fernández, J.B.	THPH14, THPH16, THPH17, THPH18	Huber, N.	WEPH21
Gonzalez, H.	FROAMA07	Hubert, N.	TUPH11
Gonzalez, N.	THPH14, THPH15, THPH16, THPH17, THPH43	Hulbert, S.	FROAMA05
Gottwald, A.	THPH25	Hwang, C.-S.	TUPH06, TUPH19
Graber, T.	THOPMA02	Hwang, S-M.	THPH28
Grant, R.K.	TUPH24	Hyun, H.J.	THPH28
Grötzsch, D.	WE0AMA06		
Green, S.	THPH05	Idir, M.	FROAMA05
Grifone, R.	THPH39	Igarashi, N.	TUPH20
Grizolli, W.C.	WEOPMA04, THPH27	Ikeya, Y.	FROAMA08
Grolimund, D.	THPH04	Ishii, H.	TUPH20, THPH23
Gudkov, D.	TUPH36	Islam, Z.	WEOPMA04
Guillet, S.	THPH36	Izzo, S.J.	WEPH22
Guo, D.Z.	TUPH18		
— H —		— J —	
Haas, E.	THPH19	Jahn, D.	WEPH20
Haeffner, D.	THOPMA02	Jain, A.K.	TUPH13, TUPH23
Hammond, N.P.	TUPH17, TUPH24	James, J.H.	THPH06, THPH21
Han, H.	FROAMA03	Janis, A.J.	WEPH04
Han, J.H.	WEPH17, WEPH18	Jaouen, N.	THPH37
Han, Q.	FROAMA03	Jarjays, S.J.	THOAMA06
Haouz, A.	WEPH36	Jarrige, I.	FROAMA05
Hara, H.	THPH33	Jaski, M.S.	TUPH13, TUPH23
Harder, D.A.	TUPH26	Jaski, Y.	TUPH29, THOPMA02, THPH24
Hardin, C.L.	THOPMA05, THPH34, THPH36	Jasso, T.	WEPH26
Harkins, J.P.	TUPH14	Jeangerard, D.	WEPH36
Hasanaj, S.	WEOPMA07	Jeong, S.-H.	WEPH17
Hashimoto, A.H.	TUPH25	Ji, D.	TUPH41
He, H.Y.	WEPH08, WEPH34, TUPH27	Jiang, Y.C.	FROAMA02
He, P.	TUPH18	Jiang, Z.	TUOPMA02, TUPH16, TUPH41
Hellert, T.	TUPH14	Jiao, Y.	TUPH41
Herbeaux, C.	TUPH03, TUPH11	Jobert, N.	TUPH11, WEPH14
Hidaka, Y.	TUPH26	Jöhri, H.	TUOPMA03, WEOPMA03
Hindermann, M.	TUOPMA03	Johnson, M.J.	TUPH14
Hirschi, P.	WEOPMA03	Jover-Mañas, G.	THPH14, THPH17
Ho, H.C.	TUPH21	Juanhuix, J.	THPH16
Hoehl, A.	THPH20	Jung, J.-Y.	TUPH14
Holfelder, I.	WEOPMA06	Jung, Y.G.	WEPH17
Holmes, M. R.	THOAMA02, THPH06, THPH21	Junqueira Leão, R.	WEPH26
Holz, M.	TUPH37		
Hora, J.	WEOPMA03	— K —	
Horswell, I.	THPH05	Kaestner, B.	THPH20
Howell, G.E.	THOAMA04, THOPMA04	Kahnt, M.	THOPMA03
Hsu, K.H.	TUPH21, WEPH13	Kamma-Lorger, C.	THPH14, THPH17
		Kang, H.-S.	WEPH17, WEPH18
		Kang, L.	TUPH27, WEPH08, WEPH32,

Kanngießer, B.	WEPH34	Leitner, M.	TUPH14
Kaser, H.K.	WE0AMA06	Léonardon, J.	TUPH35
Kayser, Y.	THPH25	Lepage, F.	TUPH03, TUPH11
Kearney, S.P.	WEOPMA06	Lestrade, A.	TUPH03
	WE0AMA05, WEOPMA04, THPH26, THPH27	Leyge, J.F.	TH0AMA03
Keller, A.	TUOPMA03	Li, C. H.	TUPH41
Kelly, J.H.	WEPH15	Li, J.	THPH05
Kenesei, P.	WEOPMA04	Li, M.	WE0AMA03, THPH42, FROAMA03
Kikuchi, T.	TUPH25	Li, Q.	TUPH18
Kim, D.E.	WEPH17	Li, X. Y.	WEPH41
Kim, K.S.	THPH28	Li, Z. L.	WEPH09
Kim, M-J.	THPH28	Liang, H.	WE0AMA03, FROAMA02
Kim, S.	THPH28	Lin, C.J.	TUPH21
Kim, S.	THPH28	Lin, J.M.	WEPH38
Kim, S.H.	WEPH18	Lincoln, F.C.	TUOPMA08, WEPH29
Kim, S.H.	THPH28	Liu, B.Q.	TUPH18
Kim, S.N.	WEPH18, THPH28	Liu, C.Y.	WEPH30
Kishimoto, H.	FROAMA08	Liu, C.Y.L.	THPH08
Kitamura, H.	TUPH19	Liu, D.G.	WEPH38, THPH29
Kitegi, C.A.	TUPH26	Liu, F.	WEPH20
Klein, R.	THPH30	Liu, J.	TUPH23
Knopp, J.J.	WEPH16, THOPMA02	Liu, L.	WEPH34, TUPH27, WEPH08
Kolbe, M.	THPH25	Liu, X.	TUPH24
Kolodziej, T.	THPH27	Liu, X.	FROAMA03
Kosuge, T.	TUPH20, THPH23	Liu, Y.	TUOPMA02, TUPH22
Kraus, H.	WEOPMA02	Liu, Z.	TUPH28, WEPH16, WEPH22
Kroth, S.	THPH30	Llonch, M.L.	THPH14, THPH17
Krüger, H.	THPH31	Locher, M.	TUOPMA03
Krzywiński, J.	TUPH39, THPH11	Lubeck, J.	THPH30
Kuan, C.K.	TUPH21, WEPH13	Luiz, S.A.L.	WEPH31
Kuo, C.Y.	TUPH06	Luo, T.H.	TUPH14
		Lutton, F.	TH0AMA03
		Lyubomirskiy, M.	THOPMA03

— L —

La Civita, D.	FROAMA04
Labat, M.	TUPH11
Ladrera Fernández, J.	THPH14
Lai, L.	WEPH41, THPH29
Lai, L.W.	TUPH41
Lai, W.Y.	TUPH07, TUPH21, WEPH13
Lale, M.A.	TUPH04
Laluc, B.	THOPMA01
Lang, K.	THPH27
Langer, B.	WEPH11
Le Jollec, A.	WEPH36
Lecomte, P.	TH0AMA03
Lee, C.	THPH28
Lee, H.-G.	WEPH17, WEPH18
Lee, H.-S.	WEPH17
Lee, L.	WEPH38, THPH08, THPH29
Lee, L.	WEPH19, THOPMA05
Lee, M.H.	THPH08, THPH29
Lee, S.B.	WEPH17, WEPH18
Lee, S.H.	TUPH29, THPH24
Leemann, S.C.	TUPH14
Leitner, D.	TUPH14

— M —

Ma, Y.	TUPH18
Maag, St.	WEOPMA07
Maccallini, E.	TUPH18
Macdonell, S. A.	WEOPMA05
Macrander, A.	THPH27
Magnin-Mattenet, M.	WE0AMA02
Maillard, T.	THOPMA01
Malandrino, G.	FROAMA07
Malfois, M.	THPH14, THPH17
Malzer, W.	WE0AMA06
Manini, P.	TUPH18
Marcos, J.	WEPH06, WEPH24
Marion, P.	TUOPMA06, FROAMA07
Marques, H.P.	TUPH35
Marshall, G.	WEPH20
Marteau, F.	TUPH03, THPH37
Martens, C.	TUPH15
Martin, I.P.S.	TUPH17
Martínez Guil, J.C.	THPH14, THPH17
Mary, A.	TUPH03, TUPH11
Mase, K.	TUPH25

Maser, J. **WEPH16**
Massana, V. **WEPH06**
Mathon, O. **WEPH40, FROAMA07**
Matsuzaki, Y. **FROAMA08**
McElderry, A. **TUPH04**
Meissner, D. **THPH31**
Meneglier, C. **THPH09, THPH32**
Mesa, A.L. **WEPH26**
Meyer, B. **THPH04**
Meyer, Meyer, J. **WEPH20**
Miarnau Marin, A. **WEPH03**
Miarnau Marin, A. **TUPH36**
Michel, C. **THOAMA03**
Michel, F.M. **TUPH03**
Michel, M. **THOAMA03**
Miura, T. **FROAMA08**
Miyazawa, T. **TUPH25**
Mizumoto, S. M. **TUPH19**
Mochizuki, T. **THPH33**
Morand, S.M. **TUPH03**
Moreno, G.B.Z.L. **WE0AMA01**
Moreno, T. **WEPH14**
Mori, T. **TUPH20**
Morton, D.S. **WEPH19, THOPMA05, THPH34, THPH36**
Mountford, B. **THPH35**
Müller, M. **WEOPMA06**
Mulvey, J. **TUPH29, THPH24**
Musardo, M. **TUPH26**
Mykhaylyk, V.B. **WEOPMA02**

— N —

Narayanan, S. **THPH26**
Nasiatka, J.R. **THOPMA06**
Naujoks, U. **TUPH15**
Navrotsky, G. **THOPMA02**
Neuenschwander, R.T. **WEPH26**
Ng, M.L. **WEPH19, THOPMA05**
Nguyen, M.-H. **TUPH03**
Nicolás, J. **THPH16**
Nie, X.J. **WEPH34, TUPH27, WEPH08**
Nikitin, Y. **TUPH30, THPH17**
Ning, C.J. **TUPH27, WEPH08, WEPH34**
Nisbet, G. **THPH05**
Nishimura, H. **TUPH14**
Nitani, H. **TUPH20**
Noonan, J. R. **TUPH04**
Novikov, D. **THPH39**
Nowrouzi, K. **THPH07**
Nudell, J. **TUPH28, WEPH22**
Nue, L. **WEOPMA07**

— O —

O'Dowd, F.P. **THPH36**
O'Hara, S. **FROAMA05**
O'Neill, M.M. **TUPH04**

Oh, B.G. **WEPH17**
Ohashi, H. **FROAMA08**
Ohsawa, T. **THPH33**
Oishi, M. **TUOPMA05**
Olea, G. **WEPH21**
Oliver, T. **TUPH14**
Omelayo, O. **TUPH14, THOPMA06**
Oprondek, S.M. **TUPH29, THPH24**
Ortiz, E. **TUPH39, THPH11**
Osborn, J.R. **TUPH14**
Osier, T.O. **THPH36**
Osipov, T. **THPH21**
Osipov, T.O. **THPH06**
Owens, M.A. **THPH36**

— P —

Padmore, H.A. **THOPMA06, THPH07**
Paiser, E.A. **THPH02**
Pappas, G.C. **TUPH14**
Park, G.S. **THPH28**
Park, J. **THPH28**
Park, J.K. **THPH28**
Park, K.-H. **WEPH17**
Pascarelli, S. **WEPH40**
Pasquaud, J. **TUOPMA07**
Pasquaud, J. **TUPH35**
Pasternak, S. **WEPH40**
Paustian, P. **THPH30**
Peña, G. **THPH17**
Pedreira, P. **THPH18**
Pedrini, B. **WEOPMA03**
Peredkov, S.P. **WE0AMA06**
Pereiro, E. **THPH43**
Pérez-Berná, A.J. **THPH43**
Perng, S.Y. **TUPH21**
Perrin, F. **WEPH40**
Persichelli, S. **TUPH14**
Petit, E. **THOAMA03**
Petrocelli, R. **WEPH06**
Pfister, A. **WEOPMA07**
Pinto, A.C. **WEPH31**
Pinty, V. **THPH32, THPH37**
Placidi, M. **TUPH14**
Platzer, R. **THPH31**
Plumb, P.N. **WEOPMA07**
Pocock, R. **THPH05**
Polli, J.M. **WEPH12**
Pompidor, G. **WEPH20**
Ponthenier, P. **WEPH40**
Popescu, H. **THPH37**
Portmann, G.J. **TUPH14**
Pradervand, C. **WEOPMA03**
Preissner, C.A. **TUPH28, WEPH22**
Prieto, M. **TUPH30**
Prout, P. **THPH37**
Purling, M.F. **THPH38**

— Q —

Qi, T.Z.	TUPH18
Qin, H.L.	WEPH09
Quispe, M.	TUPH32, WEPH23, WEPH24

— R —

Raabe, J.	THPH39
Rah, S.Y.	THPH28
Ramanathan, M.	TUPH29, THPH24
Ramm, T.	TUPH31
Rank, J.	TUPH26
Ravy, S.	TUKA01
Rawcliffe, R.K.	TUPH24
Rühl, E.	WEPH11
Reininger, R.	WEPH16
Ren, Z.L.	TUPH38
Reuss, T.	THPH31
Revenko, R.V.	THOAMA03
Reyes, S.	TUPH14
Ribbens, M.	WEPH14
Ribó, L.	WEPH06, THPH17
Rich, D.W.	THPH36
Richter, M.	THPH30
Riquer, A.	THOPMA01
Ristau, U.	WEPH20
Robin, D.	TUPH14
Rocha, M.C.	WEPH26
Rodrigues, A.R.D.	WEPH26
Rodrigues, F.	WEPH26
Rodrigues, G.L.M.P.	WEPH39
Röhling, M.	THPH31
Roldán, D.	THPH18
Roth, T.	FROAMA07
Rouquié, A.R.	TUPH03
Rowen, M.	TUPH39, THPH11
Roy, D.	THPH32
Ruget, C.	THPH16
Ruijl, T.A.M.	WEOAMA01

— S —

Saemann, E.	THPH31
Saithong, E.	THPH31
Sajaev, V.	TUPH28
Samson, V.A.	THPH04
Samuelsson, S.	TUPH36
Sanchez del Rio, M.	THOAMA06
Sandy, A.	THPH26
Sanfelici, L.	TUPH43, WEOAMA01, WEOAMA04, WEPH39
Sannibale, F.	TUPH14
Saveri Silva, M.	WEOAMA01, THPH12
Savko, M.	WEPH36
Sévelin-Radiguet, N.	WEPH40
Schacht, A.	WEPH42
Schäfers, F.	WEPH11

Scheel, M.	WEPH42, THPH09
Scheidt, K.B.	TUPH35
Schlüter, C.	THPH39
Schlesiger, C.S.	WEOAMA06
Schmidt, O.A.	THOPMA02
Schmidt, T.	TUOPMA03
Schneider, R.M.	WEOAMA01
Scholz, M.	THOPMA03
Schroer, C.G.	THOPMA03
Schropp, A.	THOPMA03
Schwarb, A.	WEOAMA07
Scott, S.M.	THOPMA04, THPH40
Sebdaoui, M.	TUPH03
Seltmann, J.	WEPH27
Senba, Y.	FROAMA08
Senée, F.	TUPH44
Serra Gallifa, X.	THPH18
Seyrich, M.	THOPMA03
Sgobba, S.	WEKA01
Shapiro, D.A.	THPH07
Sharma, G.	TUPH03
Sharma, S.K.	TUOPMA08, TUPH13, TUPH16, WEPH29, THPH41
Shastri, S.D.	WEOAMA04
Sheng, I.C.	WEPH28
Sheng, W.F.	WEOAMA03, FROAMA02
Shepard, W. E.	WEPH36
Shi, H.	WEPH35
Shi, H.	THPH42
Shi, S.	WEOAMA07
Shi, X.	WEOAMA04, WEPH16, THPH27
Shimizu, Y.	FROAMA08
Shoji, M.	TUOPMA05
Shu, D.	WEOAMA05, WEOAMA04, THPH26, THPH27
Shvyd'ko, Yu.	THPH27
Sics, I.	THPH14, THPH17
Sikorski, A.	WEOAMA04, THPH12
Silva, M. H. S.	TUPH09
Simon, C.	TUPH44
Sinn, H.	FROAMA04
Smakulska, D.	WEPH03
Smith, D.M.	WEPH04
Soezeri, S.S.	THOPMA06
Solano, E.	THPH17
Sonoyama, J.	THPH33
Sorrentino, A.	THPH43
Souza, M.S.	WEOAMA04, THPH12
Spataro, C.J.	TUPH13, WEPH29
Spiers, J.	THPH05
Stallwood, A.	TUPH34
Stavitski, E.	THPH33
Steier, C.	TUPH14
Stelmach, C.	THPH19
Su, Y.	THPH29
Suh, H.S.	WEPH17

Sun, C. TUPH14
Sun, J.L. TUPH27
Sun, Q.L. TUPH41
Sun, S. TUOPMA02, TUPH22
Sun, Y. WEPH35
Swenson, C.A. TUPH14
Swetin, E. TUPH40

— T —

Tachibana, T. THPH33
Takahashi, S. TUOPMA05
Takeichi, Y. TUPH20
Takenaga, H. THPH33
Takeuchi, T. FROAMA08
Tamura, K. TUOPMA05
Tanabe, T. TUPH26
Tanaka, H. TUPH20, THPH23
Tanaka, M. FROAMA08
Tang, S. WEOAMA03, FROAMA02, FROAMA03
Taniuchi, Y. TUOPMA05
Tao, F. WEPH09
Tarawneh, H. TUOPMA04
Tassan-Viol, J. WEPH03
Tavakoli, K.T. TUPH03, TUPH11
Thiel, A. TUOPMA04
Thoraud, T. S. TUPH12
Thornagel, R. THPH30
Tilmont, M. TUPH03
Tischer, M. TUPH31
Tizzano, W. THOAMA04
Tolentino, H.C.N. WEOAMA01, WEOAMA04
Torchio, R. WEPH40
Trunk, J.T. THPH19
Trutmann, D. WEOPM07
Tsai, Z.-D. TUPH07, WEPH30
Tseng, T.C. TUPH21
Tsuboki, I. FROAMA08
Tsubota, K. THPH33
Tucoulou, R. FROAMA07
Tuozzolo, J.L. TUOPMA08, THPH41

— V —

Valcárcel, R. THPH43
Valléau, M. TUPH03
Van Vaerenbergh, P. TUPH02, TUPH35
Vandenbergh, M.V. TUPH03
Vantelon, D. THPH32
Vétéran, J. TUPH03
Veness, R. TUPH36, WEPH03
Venturini, M. TUPH14
Vescovo, E. FROAMA05
Vignet, J.L. THOAMA03
Vilcins, S. TUPH37
Villanueva, J. THPH17
Villar, F. WEPH40
Virotek, S.P. TUPH14

Volpe, L.M. TUPH09, WEOAMA04, WEPH31, WEPH39

— W —

Wagner, A. WEOPM02
Wakefield, K. TUPH04
Waldron, W.L. TUPH14
Wallén, E.J. TUPH14
Walsh, A. THPH35
Walter, P. THPH06, THPH21
Walters, A. THOPMA04
Walters, D.R. TUPH04
Wang, A.X. TUPH27, WEPH08, WEPH34
Wang, D.-J. WEPH41
Wang, G.Y. TUPH27, WEPH08, WEPH32
Wang, G.Y. WEPH34
Wang, H. TUPH39, THPH11
Wang, H.S. TUPH21, WEPH13
Wang, J. TUPH22
Wang, L. TUPH22
Wang, S.H. TUPH22
Wang, X. TUOPMA03, WEOPM03
Wang, X.J. TUPH18
Wang, X.Q. TUPH38
Wang, Y. TUPH38
Wang, Z.Z. TUPH41
Wansleben, M. WEOPM06
Waterstradt, T. WEPH42
Weitkamp, T. WEPH42, THPH09
Weser, J. WEOPM06
Westfahl Jr., H. WEOAMA01, WEOAMA04
Westferro, F. TUPH29, THPH24
White, S.M. TUOPMA07
Wiemerslage, G.E. TUPH04
Wiljes, P. WEPH33, THOPMA03
Wilkinson, K.G. THPH05
Winarski, R. THOPMA02
Wojcik, W. THPH27
Wright, R.D. TUPH40

— X —

Xiang, S. TUPH16
Xu, G. TUPH41
Xu, H. TUPH38
Xu, T.G. TUPH27

— Y —

Yamada, Y. TUPH20
Yamanaka, M. TUPH25
Yamazaki, H. FROAMA08
Yan, F. TUPH41
Yan, H.Y. WEPH38, THPH08, THPH29
Yang, B.X. TUPH29, THPH24
Yang, C.K. TUPH19
Yang, C.S. TUPH19

Yang, J.	WE0AMA03	Zhang, L.	WEPH19, TH0AMA02 , TH0PMA05,
Yang, Y.C.	TUPH07		THPH34 , THPH36 , FR0AMA01
Yang, F.G.	WEPH37	Zhang, W.	TUPH42
Yin, G.C.	WEPH41	Zhang, W.	TU0PMA02
Yin, L.	TU0PMA02 , TUPH16	Zhao, L.	TUPH44
Yu, J.B.	TUPH27, WEPH08, WEPH32,	Zhou, A.Y.	FR0AMA02
	WEPH34	Zhou, K.	TH0PMA04
Yu, Y.J.	TUPH27, WEPH08, WEPH34	Zhu, D.	WEPH35
		Zhu, D.H.	WEPH08, WEPH34, TUPH27
		Zhu, W.	WEPH09
		Zhu, Y.	FR0AMA05
		Zhu, Y.	TUPH42
		Zientek, J.	TUPH04
— Z —			
Zehnder, K.M.	WE0PMA07		
Zhang, B.	TUPH38		
Zhang, J.S.	TUPH27, WEPH08, WEPH34,		
	WEPH32		

Institutes List

ALBA-CELLS Synchrotron

Cerdanyola del Vallès, Spain

- Aballe, L.
- Becheri, F.
- Campmany, J.
- Carballedo, A.
- Casas, J.J.
- Colldelram, C.
- Farré París, F.
- Fauth, F.
- Ferrer, S.
- Foerster, M.
- Fontserè Recuenco, A.
- Gevorgyan, A.A.
- González Fernández, J.B.
- Gonzalez, N.
- Jover-Mañas, G.
- Juanhuix, J.
- Kamma-Lorger, C.
- Ladrera Fernández, J.
- Llonch, M.L.
- Malfois, M.
- Marcos, J.
- Martínez Guil, J.C.
- Massana, V.
- Nicolás, J.
- Nikitin, Y.
- Pedreira, P.
- Pereiro, E.
- Pérez-Berná, A.J.
- Petrocelli, R.
- Peña, G.
- Prieto, M.
- Quispe, M.
- Ribó, L.
- Roldán, D.
- Ruget, C.
- Serra Gallifa, X.
- Sics, I.
- Solano, E.
- Sorrentino, A.
- Valcárcel, R.
- Villanueva, J.

Alfred-Wegener-Institut

Bremerhaven, Germany

- Andresen, S.

ANL

Argonne, Illinois, USA

- Abliz, M.
- Anton, J.W.J.
- Assoufid, L.
- Benda, E.
- Billett, B.
- Brajuskovic, B.
- Capatina, D.

- Carter, J.A.
- Clute, T.K.
- Collins, J.T.
- Connatser, R.W.
- Dejus, R.J.
- Donnelly, A.T.
- Doose, C.L.
- Downey, J.S.
- Dufresne, E.M.
- Erdmann, M.
- Fisher, M.V.
- Graber, T.
- Grizolli, W.C.
- Haeffner, D.
- Islam, Z.
- Izzo, S.J.
- Jain, A.K.
- Jaski, M.S.
- Jaski, Y.
- Kearney, S.P.
- Kenesei, P.
- Knopp, J.J.
- Kolodziej, T.
- Lale, M.A.
- Lang, K.
- Lee, S.H.
- Liu, J.
- Liu, Z.
- Macrander, A.
- Maser, J.
- McElderry, A.
- Mulvey, J.
- Narayanan, S.
- Navrotski, G.
- Noonan, J. R.
- Nudell, J.
- O'Neill, M.M.
- Oprondek, S.M.
- Preissner, C.A.
- Ramanathan, M.
- Reininger, R.
- Sajaev, V.
- Sandy, A.
- Schmidt, O.A.
- Shastri, S.D.
- Shi, X.
- Shu, D.
- Shvyd'ko, Yu.
- Swetin, E.
- Wakefield, K.
- Walters, D.R.
- Westferro, F.
- Wiemerslage, G.E.
- Winarski, R.
- Wojcik, W.
- Wright, R.D.
- Yang, B.X.
- Zientek, J.

AS - ANSTO

Clayton, Australia

- Cherukuvada, H.

ASCo

Clayton, Victoria, Australia

- Adamson, L.W.S.
- Mountford, B.
- Walsh, A.

AXILON AG

Koeln, Germany

- Diete, W.
- Schacht, A.
- Waterstradt, T.

BCSI

Vancouver, Canada

- Boiesan, T.
- Carlson, M.

Bestec GmbH

Berlin, Germany

- Fuchs, F.
- Gießel, T.

BNL

Upton, Long Island, New York, USA

- Abeykoon, M.
- Amundsen, C.
- Attenkofer, K.
- Buda, S.
- Cappadoro, P.L.
- Chubar, O.V.
- Corwin, T.M.
- DePaola, F.A.
- Dooryhee, E.D.
- Faussete, R.
- Ghose, S.
- Haas, E.
- Harder, D.A.
- Hidaka, Y.
- Hulbert, S.
- Idir, M.
- Jarrige, I.
- Lincoln, F.C.
- Musardo, M.
- O'Hara, S.
- Rank, J.
- Sharma, S.K.
- Spataro, C.J.
- Stavitski, E.
- Stelmach, C.
- Tanabe, T.
- Trunk, J.T.
- Tuozzolo, J.L.
- Vescovo, E.
- Zhu, Y.

CEA/DRF/IRFU

Gif-sur-Yvette, France

- Zhao, L.

CEA/DSM/IRFU

France

- Senée, F.
- Simon, C.

CERN

Geneva, Switzerland

- Andreazza, W.
- Duraffourg, M.
- Focker, G.J.
- Gudkov, D.
- Miarnau Marin, A.
- Samuelsson, S.
- Sgobba, S.
- Smakulska, D.
- Tassan-Viol, J.
- Veness, R.

CLS

Saskatoon, Saskatchewan, Canada

- Adam, M.J.P.
- Appathurai, N.
- Barkway, G.R.
- Janis, A.J.
- Smith, D.M.

CSNS

Guangdong Province, People's Republic of China

- Chen, J.X.
- He, H.Y.
- Liu, L.
- Nie, X.J.
- Ning, C.J.
- Sun, J.L.
- Wang, A.X.
- Wang, G.Y.
- Yu, J.B.
- Yu, Y.J.
- Zhang, J.S.
- Zhu, D.H.

CTEC

MEYLAN, France

- Laluc, B.
- Maillard, T.
- Riquer, A.

DESY Zeuthen

Zeuthen, Germany

- Bandke, D.B.

DESY

Hamburg, Germany

- Adler, S.
- Beye, M.
- Botta, S.
- Bühner, A.
- Dill, F.U.
- Doebrmann, R.
- Ederer, K.
- Ermakov, A.
- Falkenberg, G.
- Garrevoet, J.
- Goerlitz, M.
- Grifone, R.
- Holz, M.
- Kahnt, M.
- Krüger, H.
- Lyubomirskiy, M.
- Martens, C.
- Meissner, D.
- Naujoks, U.
- Novikov, D.
- Platzer, R.
- Raabe, J.
- Ramm, T.
- Reuss, T.
- Röhling, M.
- Saemann, E.
- Saithong, E.
- Schlüter, C.
- Scholz, M.
- Schroer, C.G.
- Schropp, A.
- Seltmann, J.
- Seyrich, M.
- Tischler, M.
- Vilcins, S.
- Wiljes, P.

DLS

Oxfordshire, United Kingdom

- Baker, N.
- Burt, M.H.
- Butler, D.J.
- Collins, S.P.
- Connolly, T.
- Davies, S.
- Drakopoulos, M.
- Duller, G.M.A.
- Garcia-Fernandez, M.
- Grant, R.K.
- Green, S.
- Hammond, N.P.
- Horswell, I.
- Howell, G.E.
- Huang, H.C.
- Kelly, J.H.
- Li, J.
- Liu, X.
- Macdonell, S. A.
- Martin, I.P.S.

- Mykhaylyk, V.B.
- Nisbet, G.
- Pocock, R.
- Purling, M.F.
- Rawcliffe, R.K.
- Scott, S.M.
- Spiers, J.
- Stallwood, A.
- Tizzano, W.
- Wagner, A.
- Walters, A.
- Wilkinson, K.G.
- Zhou, K.

EMBL

Hamburg, Germany

- Blanchet, Blanchet, C.
- Bourenkov, G.
- Fiedler, S.
- Gehrman, T.
- Jahn, D.
- Marshall, G.
- Meyer, Meyer, J.
- Pompidor, G.
- Ristau, U.

ESRF

Grenoble, France

- Baboulin, D.
- Baker, R.
- Barrett, R.
- Bernard, P.
- Berruyer, G.
- Biasci, J.C.
- Bonnefoy, J.
- Borrel, J.
- Brendike, M.
- Brochard, T.
- Brumund, P.M.
- Ciansiosi, F.
- Clavel, C.
- Dabin, Y.
- Dehaeze, T.
- Ducotté, L.
- Einfeld, D.
- Ewald, F.
- Eybert, L.
- Goirand, L.
- Gonzalez, H.
- Jarjays, S.J.
- Léonardon, J.
- Magnin-Mattenet, M.
- Malandrino, G.
- Marion, P.
- Marques, H.P.
- Mathon, O.
- Pascarelli, S.
- Pasquaud, J.
- Pasternak, S.
- Perrin, F.

- Ponthenier, P.
- Roth, T.
- Sanchez del Rio, M.
- Scheidt, K.B.
- Sévelin-Radiguet, N.
- Torchio, R.
- Tucoulou, R.
- Van Vaerenbergh, P.
- Villar, F.
- White, S.M.

FUB

Berlin, Germany

- Langer, B.
- Rühl, E.

GANIL

Caen, France

- Barthe-Dejean, C.
- Di Giacomo, M.
- Gangnant, P.
- Lecomte, P.
- Leyge, J.F.
- Lutton, F.
- Michel, C.
- Michel, M.
- Petit, E.
- Revenko, R.V.
- Vignet, J.L.

Helmut Fischer GmbH

Sindelfingen, Germany

- Anklamm, LC.A.

HUBER Diffraktionstechnik GmbH&Co.KG

Rimsting, Germany

- Huber, N.
- Olea, G.

HZB

Berlin, Germany

- Schäfers, F.

IHEP

Beijing, People's Republic of China

- Gao, L.
- Guo, D.Z.
- Han, H.
- Han, Q.
- He, H.Y.
- He, P.
- Ji, D.
- Jiang, Y.C.
- Jiao, Y.
- Kang, L.
- Li, C. H.
- Li, M.

- Li, Q.
- Liang, H.
- Liu, B.Q.
- Liu, L.
- Liu, X.
- Ma, Y.
- Nie, X.J.
- Qi, T.Z.
- Sheng, W.F.
- Shi, H.
- Tang, S.
- Wang, G.Y.
- Wang, X.J.
- Wang, Z.Z.
- Xu, G.
- Xu, T.G.
- Yan, F.
- Yang, J.
- Yang, F.G.
- Yu, J.B.
- Zhang, J.S.
- Zhou, A.Y.
- Zhu, D.H.

JASRI/SPRING-8

Hyogo, Japan

- Bizen, T.
- Ikeya, Y.
- Kishimoto, H.
- Matsuzaki, Y.
- Miura, T.
- Ohashi, H.
- Oishi, M.
- Senba, Y.
- Shimizu, Y.
- Takahashi, S.
- Takeuchi, T.
- Tamura, K.
- Tanaka, M.
- Taniuchi, Y.
- Tsuboki, I.
- Yamazaki, H.

JASRI

Hyogo, Japan

- Shoji, M.

KEK

Ibaraki, Japan

- Adachi, J.
- Igarashi, N.
- Ishii, H.
- Kikuchi, T.
- Kosuge, T.
- Mase, K.
- Mori, T.
- Nitani, H.
- Takeichi, Y.
- Tanaka, H.

- Yamada, Y.

LBNL

Berkeley, California, USA

- Allézy, A.P.
- Anders, A.
- Baptiste, K.M.
- Buice, E.S.
- Celestre, R.S.
- Chow, K.
- Cutler, G.D.
- De Santis, S.
- Donahue, R.J.
- Duarte, R.M.
- Filippetto, D.
- Harkins, J.P.
- Hellert, T.
- Johnson, M.J.
- Jung, J.-Y.
- Leemann, S.C.
- Leitner, D.
- Leitner, M.
- Luo, T.H.
- Nasiatka, J.R.
- Nishimura, H.
- Nowrouzi, K.
- Oliver, T.
- Omolayo, O.
- Osborn, J.R.
- Padmore, H.A.
- Pappas, G.C.
- Persichelli, S.
- Placidi, M.
- Portmann, G.J.
- Reyes, S.
- Robin, D.
- Sannibale, F.
- Shapiro, D.A.
- Soezeri, S.S.
- Steier, C.
- Sun, C.
- Swenson, C.A.
- Venturini, M.
- Virostek, S.P.
- Waldron, W.L.
- Wallén, E.J.

LNE

Trappes Cedex, France

- Ducourtieux, S.

LNLS

Campinas, Brazil

- Araujo, W.R.
- Arruda, L.C.
- Bueno, C.S.N.C.
- Caliri, R.M.
- Canova, H.F.
- Claudiano, G.V.

- da Silva, M.B.
- de Oliveira, H.G.P.
- Ferreira, V.Z.
- Fonseca, P.T.
- Freitas, P.P.S.
- Gerales, R.R.
- Gilmour, A.
- Jasso, T.
- Junqueira Leão, R.
- Luiz, S.A.L.
- Mesa, A.L.
- Moreno, G.B.Z.L.
- Neuenschwander, R.T.
- Pinto, A.C.
- Polli, J.M.
- Rocha, M.C.
- Rodrigues, A.R.D.
- Rodrigues, F.
- Rodrigues, G.L.M.P.
- Sanfelici, L.
- Saveri Silva, M.
- Sikorski, A.
- Souza, M.S.
- Tolentino, H.C.N.
- Volpe, L.M.
- Westfahl Jr., H.

LNNano

Campinas, Brazil

- Fonseca, E.B.
- Silva, M. H. S.

MAX IV Laboratory, Lund University

Lund, Sweden

- Bartalesi, A.
- Ebbeni, M.
- Tarawneh, H.
- Thiel, A.

MI-Partners

Eindhoven, The Netherlands

- Ruijl, T.A.M.
- Schneider, R.M.

MPI CEC

Mülheim an der Ruhr, Germany

- DeBeer, S.D.
- Peredkov, S.P.

NCTU

Hsinchu, Taiwan

- Hwang, C.-S.

NEOMAX Co., Ltd.

Mishima-gun, Osaka, Japan

- Mizumoto, S. M.

NIMS

Tsukuba, Ibaraki, Japan

- Hashimoto, A.H.
- Yamanaka, M.

NSRRC

Hsinchu, Taiwan

- Chan, W.S.
- Chang, C.-H.
- Chang, C.F.
- Chang, C.H.
- Chang, C.Y.
- Chang, S.H.
- Chen, B.Y.
- Chen, C.S.
- Chen, C.Y.
- Chen, H.W.
- Chen, J.-R.
- Chen, M.L.
- Cheng, Y.Y.
- Chiu, C.C.
- Chung, T.Y.
- Chung, Y.-C.
- Ho, H.C.
- Hsu, K.H.
- Hsu, M. Y.
- Huang, D.-G.
- Huang, J.C.
- Huang, L.
- Huang, Y.-S.
- Hwang, C.-S.
- Kuan, C.K.
- Kuo, C.Y.
- Lai, L.
- Lai, W.Y.
- Lee, L.
- Lee, M.H.
- Li, X. Y.
- Lin, C.J.
- Lin, J.M.
- Liu, C.Y.L.
- Liu, C.Y.
- Liu, D.G.
- Perng, S.Y.
- Sheng, I.C.
- Su, Y.
- Tsai, Z.-D.
- Tseng, T.C.
- Wang, D.-J.
- Wang, H.S.
- Yan, H.Y.
- Yang, C.K.
- Yang, C.S.
- Yang, Y.C.
- Yin, G.C.

Oxford University, Physics Department

Oxford, Oxon, United Kingdom

- Kraus, H.

PAL

Pohang, Kyungbuk, Republic of Korea

- Choi, H. J.
- Eom, I.
- Han, J.H.
- Hwang, S-M.
- Hyun, H.J.
- Jeong, S.-H.
- Jung, Y.G.
- Kang, H.-S.
- Kim, D.E.
- Kim, K.S.
- Kim, M-J.
- Kim, S.H.
- Kim, S.N.
- Kim, S.
- Lee, C.
- Lee, H.-G.
- Lee, H.-S.
- Lee, S.B.
- Oh, B.G.
- Park, G.S.
- Park, J.K.
- Park, J.
- Park, K.-H.
- Rah, S.Y.
- Suh, H.S.

Pasteur Institute, Crystallisation and X-ray Diffraction (PF6)

Paris, France

- Haouz, A.

PML

Liège, Belgium

- Collette, C.G.R.L.
- Dehaeze, T.

PSI

Villigen PSI, Switzerland

- Birri, M.
- Calvi, M.
- Ferreira Sanchez, D.
- Grolimund, D.
- Hasanaj, S.
- Hindermann, M.
- Hirschi, P.
- Hora, J.
- Huber, L.
- Jöhri, H.
- Keller, A.
- Locher, M.
- Maag, St.
- Meyer, B.
- Nue, L.
- Pedrini, B.
- Pfister, A.
- Plumb, P.N.
- Pradervand, C.
- Samson, V.A.
- Schmidt, T.

- Schwarb, A.
- Shi, S.
- Trutmann, D.
- Wang, X.
- Zehnder, K.M.

PTB

Berlin, Germany

- Beckhoff, B.
- Fliegauf, R.
- Gottwald, A.
- Hoehl, A.
- Holfelder, I.
- Kaestner, B.
- Kaser, H.K.
- Kayser, Y.
- Klein, R.
- Kolbe, M.
- Kroth, S.
- Lubeck, J.
- Müller, M.
- Paustian, P.
- Richter, M.
- Thornagel, R.
- Wansleben, M.
- Weser, J.

RIKEN SPring-8 Center

Sayō-cho, Sayō-gun, Hyogo, Japan

- Kitamura, H.

SAES Getters S.p.A.

Lainate, Italy

- Maccallini, E.
- Manini, P.

SESAME

Allan, Jordan

- Abu-Hanieh, T.H.
- Al Shehab, M.M.
- Al-Najdawi, M.A.

ShanghaiTech University

Shanghai, People's Republic of China

- Liu, F.

SINAP

Shanghai, People's Republic of China

- Deng, R.B.
- Du, H.W.
- Gao, F.
- Hu, X.
- Jiang, Z.
- Lai, L.W.
- Li, Z. L.
- Liu, Y.
- Sun, Q.L.

- Sun, S.
- Tao, F.
- Wang, J.
- Wang, L.
- Wang, S.H.
- Xiang, S.
- Yin, L.
- Zhang, W.
- Zhu, W.
- Zhu, Y.

SLAC

Menlo Park, California, USA

- Amores, L.
- Armenta, R.
- Barada, A.H.
- Castagna, J.C.
- Cedillos, A.G.
- Cocco, D.
- Dakovski, G.L.
- Defever, J.
- Feng, Y.
- Field, R.C.
- Forcat Oller, S.
- Guillet, S.
- Hardin, C.L.
- Holmes, M. R.
- James, J.H.
- Krzywiński, J.
- Lee, L.
- Morton, D.S.
- Ng, M.L.
- O'Dowd, F.P.
- Ortiz, E.
- Osier, T.O.
- Osipov, T.O.
- Osipov, T.
- Owens, M.A.
- Paisier, E.A.
- Rich, D.W.
- Rowen, M.
- Shi, H.
- Sun, Y.
- Walter, P.
- Wang, H.
- Zhang, L.
- Zhu, D.

Sokendai, The Graduate University for Advanced Studies

Tsukuba, Japan

- Miyazawa, T.

SOLEIL

Gif-sur-Yvette, France

- Alexandre, P.
- Arrachart, C.A.
- Baron, N.B.
- Ben El Fekih, R.
- Berteaud, P.

- Blache, F.
- Bourgoïn, C.B.
- Briquez, F.
- Béchu, N.
- Carcy, A.C.
- Ciccone, L.
- Couprie, M.-E.
- Da Silva Castro, J.
- de Oliveira, C.
- Desjardins, D.K.
- Dubuisson, J.M.
- Duval, J.P.
- Engblom, C.
- Fonda, E.
- Giorgetta, J.L.
- Herbeaux, C.
- Hubert, N.
- Jaouen, N.
- Jeangerard, D.
- Jobert, N.
- Kitegi, C.A.
- Labat, M.
- Le Jollec, A.
- Lepage, F.
- Lestrade, A.
- Marteau, F.
- Mary, A.
- Menneglier, C.
- Michel, F.M.
- Morand, S.M.
- Moreno, T.
- Nguyen, M.-H.
- Pinty, V.
- Popescu, H.
- Prout, P.
- Ravy, S.
- Ribbens, M.
- Rouquié, A.R.
- Roy, D.
- Savko, M.
- Scheel, M.
- Sebdaoui, M.
- Sharma, G.
- Shepard, W. E.
- Tavakoli, K.T.
- Thoraud, T. S.
- Tilmont, M.
- Valléau, M.
- Vandenberghe, M.V.
- Vantelon, D.
- Vétéran, J.
- Weitkamp, T.

- Gnewkow, R.G.
- Grötzsch, D.
- Kanngießer, B.
- Malzer, W.
- Schlesiger, C.S.

TOYAMA Co., Ltd.

Kanazawa, Japan

- Akiyama, K.
- Endo, K.
- Hara, H.
- Mochizuki, T.
- Ohsawa, T.
- Sonoyama, J.
- Tachibana, T.
- Takenaga, H.
- Tsubota, K.

UCB

Berkeley, California, USA

- Nowrouzi, K.

ULB - FSA - SMN

Bruxelles, Belgium

- Collette, C.G.R.L.

University of Chinese Academy of Sciences

Beijing, People's Republic of China

- Cao, G.

University of Illinois at Chicago

Chicago, USA

- Anton, J.W.J.

USTC/NSRL

Hefei, Anhui, People's Republic of China

- Ren, Z.L.
- Wang, X.Q.
- Wang, Y.
- Xu, H.
- Zhang, B.

XFEL. EU

Schenefeld, Germany

- Dommach, M.
- La Civita, D.
- Sinn, H.

SSRF

Shanghai, People's Republic of China

- Fan, Y.
- Qin, H.L.

Technische Universität Berlin

Berlin, Germany